PROCEEDINGS OF THE
POWER CONVERSION
CONFERENCE — NAGAOKA
1997

PCC-Nagaoka

Volume II

August 3-6, 1997

Nagaoka Grand Hotel,
Hive-Nagaoka

Nagaoka, Japan

Sponsored by
The Industry Applications Society of the IEE Japan
The IEEE Industry Applications Society

IEEE 97TH8266

Proceedings of the Power Conversion Conference-Nagaoka 1997

Volume II



sponsored by

the Industry Applications Society of the IEE Japan

and

the IEEE Industry Applications Society

in cooperation with

the IEEE Industrial Electronics Society,
the IEEE Power Electronics Society,
IEEE Tokyo Section,
Japan Society for Power Electronics,
the Illuminating Engineering Institute of Japan,
the Society of Instrument and Control Engineers,
the Institute of Electrical Installation Engineers of Japan,
the Institute of System, Control and Information Engineers,
the Institute of Electronics, Information and Communication Engineers

IEEE Catalog Number 97TH8266

Note: IEEE holds copyright to the PCC-Nagaoka papers and the conference records on behalf of both IEEE and IEE of Japan. By agreement, IEE of Japan also has certain translation/republication right to these materials.

IEEE Catalog Number:	97TH8266
ISBN SoftboundEdition:	0-7803-3823-5
MicroficheEdition:	0-7803-3824-3
Library of Congress Number:	97-70237

ORGANIZING COMMITTEE

Chairperson: **Akira Nabae** *Tokyo Institute of Polytechnics*
Investigator: **Masao Yano** *Toyo University*
Secretary: **Isao Takahashi** *Nagaoka University of Technology*

Eisuke Masada
University of Tokyo

Tadashi Fukao
Tokyo Institute of Technology

Akeshi Maeda
Tokyo Denki University

Takayoshi Nakano
Shibaura Institute of Technology

Rokuya Ishii
Yokohama National University

Koji Iwata
Chube University

Takamasa Hori
Mie University

Toru Maruhashi
Kobe University

Sakutaro Nonaka
Kinki University

Takeichi Sakurai
Tokyo Electric Power Co.

Taizo Hasegawa
Kansai Electric Power Co.

Isamu Kobayashi
Chubu Electric Power Co.

Minoru Morikuni
Tohoku Electric Power Co.

Hiromasa Higasa
Shikoku Research Institute Inc.

Hisashi Ooi
Electric Power Development Co., Ltd.

Naoe Kawakami
Hitachi Ltd.

Sumio Kobayashi
Toshiba Corp.

Kazuya Furukawa
Mitsubishi Electric Co.

Akira Takai
Fuji Electric Co., Ltd.

Masaaki Obana
Meidensya Co.

Takashi Koga
Toyo Electric Mfg.

Koichi Hirano
Yaskawa Electric Corp.

Jun Nishidai
Nissin Electric Co.

Keisuke Fujisaki
Nippon Steel Corp.

Hironori Shimizu
Shinko Electric Co.

Kozo Hiyoshi
Sharp Corp.

Sinya Tanaka
Sanken Electric Co.

Yoshihiro Sekino
Sanyo Denki Co., Ltd.

Hisatoshi Goshima
Origin Electric Co.

Atsuo Nagai
Nippon Seiki Corp., Ltd.

Masaru Wasaki
TDK Corp.

Tatsuo Naito
JAPAN STORAGE BATTERY Co., Ltd.

Kiyotaka Ikawa
Yuasa Corp.

Toshiaki Sasaki
Railway Tech. Research Institute

Akihiro Tabata
SHINDENGEN Electric Mfg. Co., Ltd.

Kikuji Tsuneyoshi
Mitsubishi Heavy Industries Ltd.

Naotake Kumagai
Mitsubishi Motors Corp.

Tsuneo Kume
Yaskawa Electric Corp.

Masashi Mizoguchi
NETUREN Co., Ltd.

Toru Hirano
Daikin Industries, Ltd.

ADVISORS

Seizaburo Hiura
Mayor of Nagaoka

T. A. Lipo
University of Wisconsin -Madison

B. K. Bose
University of Tennessee

P. C. Sen
Queen's University

K. R. Heumann
Technische Universitat Berlin

F. Profumo
Politecnico di Torino

Jijum Wu
Xian Power Electronic Research Institute

Young-Moon Hwang
Pusan National University

Junichi Nishizawa
Tohoku University

Koosuke Harada
Kumamoto Institute of Technology

Fumio Harashima
University of Tokyo

Yasuzo Uchida
Nagaoka University of Technology

Ichiro Nagata
Hitachi Ltd.

Keiji Nishijima
Toshiba Corp.

Toshio Suzuki
Mitsubishi Electric Co.

Kunihiko Sawa
Fuji Electric Co., Ltd.

Takashi Hirayama
Meidensya Co.

Sumio Nagabuchi
Toyo Electric Mfg.

Rikihiro Madarame
NEMIC-LAMDA K.K.

STEERING COMMITTEE

Chairperson:	**Isao Takahashi**	*Nagaoka University of Technology*
Co-Chairperson:	**Ryuichi Shimada**	*Tokyo Institute of Technology*
Secretary:	**Kiyoshi Ohishi**	*Nagaoka University of Technology*

Tung-Hai Chin
Sophia University

Kouki Matsuse
Meiji University

Gunji Kimura
Tokyo Metropolitan University

Toshimasa Haneyoshi
Tokyo Denki University

Yoichi Hori
University of Tokyo

Kenzo Kamiyama
Utsunomiya University

Shigeru Okuma
Nagoya University

Nobuyuki Matsui
Nagoya Institute of Technology

Katsunori Taniguchi
Osaka Institute of Technology

Yoji Takeda
University of Osaka Prefecture

Atsuo Kawamura
Yokohama National University

Yasuo Haga
Nagaoka National College of Technology

Keiichi Tsuchida
Nagaoka National College of Technology

Seiji Kondo
Nagaoka University of Technology

Toshihiko Noguchi
Nagaoka University of Technology

Itatu Ando
Nagaoka University of Technology

Kazuo Saito
Nagaoka University of Technology

Susumu Horiuchi
Tokyo Electric Power Co.

Seiichi Muroyama
NTT Interdisciplinary Research Lab.

Mitsuyuki Hombu
Hitachi Ltd.

Suzuo Saito
Toshiba Corp.

Ryohei Uchida
Mitsubishi Electric Co.

Kouetsu Fujita
Fuji Electric Co., Ltd.

Yasuo Kataoka
Meidensya Co.

Ichiro Miyashita
Toyo Electric Mfg.

Junji Hirai
Yaskawa Electric Corp.

Yuichi Sakuragawa
NEMIC-LAMDA K.K.

Takayuki Uchida
Society of Electric Vehicle

Kunio Ishibashi
IEE of Japan

TECHNICAL PROGRAM COMMITTEE

Chairperson:	**Ryuichi Shimada**	*Tokyo Institute of Technology*
Co-Chairperson:	**Deepakraj M Divan**	*University of Wisconsin*
Secretary:	**Seiji Kondo**	*Nagaoka University of Technology*
Secretary:	**Yukihiko Sato**	*Tokyo Institute of Technology*

Akagi, Hirofumi
Okayama University

Ando, Itaru
Nagaoka University of Technology

Buja, Giuseppe
University of Padova

Chiba, Akira
Science University of Tokyo

Choi, Jae-Ho
Chungbuk National University

Dawson, Francis P.
University of Toronto

Ehsani, Mehrdad
Texas A&M University

Fujita, Hideki
Chubu Electric Power Co.

Fujita, Kouetsu
Fuji Electric Corporate Research and Development Ltd.

Fukuda, Shoji
Hokkaido University

Hayashi, Yoichi
Aoyama Gakuin University

Heumann, Klemens
Technische Universitat Berlin

Holtz, Joachim
Wuppertal University

Hombu, Mitsuyuki
Hitachi Ltd.

Hwang, Young Moon
Busan National University

Ikeda, Haruo
Railway Technical Research Institute

Irie, Hisaichi
Osaka Electro-Communication University

Ise, Toshifumi
Osaka University

Ishida, Muneaki
Mie University

Ishikawa, Tadao
Central Research Institute of Electric Power Industry

Ito, Youichi
Sanken Electric Co., Ltd.

Itoh, Yuzo
Hokkaido University

Iwakane, Takanobu
Yaskawa Electric Corp.

Iwata, Makoto
Sanken Electric Co., Ltd.

Jahns, Thomas M.
Massachusetts Institute of Technology

Jinzenji, Toshimasa
Sanyo Denki Co.

Kanmachi, Toshiyuki
Sendai National College of Technology

Kataoka, Yasuo
Meidensha Co.

Kaushik, Rajashekara
Delphi Energy & Engneering

Kawamura, Atsuo
Yokohama National University

Kaynak, Okyay
Bogazici University

Kim, Moon Hwan
Korea Electrotechnology Research Institute

Kitano, Jun-ichi
Central Japan Railway Co.

Koyama, Masato
Mitsubishi Electric Corp.

Kubota, Hisao
Meiji University

Kuroki, Kazuo
Fuji Electric Corporate Research and Development Ltd.

Lorenz, Robert D.
University of Wisconsin - Madison

Matsuda, Yasuo
Hitachi Ltd.

Matsui, Keiju
Chubu University

Matsui, Mikihiko
Tokyo Institute of Polytechnics

Matsui, Nobuyuki
Nagoya Institute of Technology

Matsuo, Hirofumi
Nagasaki University

Matsuse, Kouki
Meiji University

Miki, Ichiro
Meiji University

Miyashita, Kunio
Hitachi Ltd.

Morimoto, Masayuki
Mitsubishi Heavy Industries Ltd.

Morimoto, Sigeo
Osaka Prefecture University

Murai, Yoshihiro
Gifu University

Naitoh, Haruo
Toshiba Corp.

Nakagawa, Toshiko
Tokyo Denki University

Nakajima, Tatsuhito
Tokyo Electric Power Co.

Nakaoka, Mutsuo
Yamaguchi University

Nishikata, Shoji
Tokyo Denki University

Ogasawara, Satoshi
Okayama University

Ogata, Tsutomu
NTT Integrated Information & Energy Systems Laboratories

Ogihara, Yoshiya
Nisshin Electronic Co., Ltd.

Oguchi, Kuniomi
Ibaraki University

Ohishi, Kiyoshi
Nagaoka University of Technology

Ohmae, Tsutomu
Hitachi Ltd.

Ohnishi, Kohei
Keio University

Ohshima, Masaaki
Tokyo Electric Power Co.

Ohyama, Kazunobu
Daikin Industries Ltd.

Okuma, Shigeru
Nagoya University

Panda, Sanjib Kumar
National University of Singapore

Peng, Fang-Zheng
Oak Ridge National Lab.

Rahman, M.A.
Memorial University of Newfoundland

Rajagopalan, Venkatachari
Universite du Quebec

Rashid, Muhammad H.
Indiana-Purdue University

Sakui, Masaaki
Toyama University

Schroeder, Dierk
Technishe Universitat Munchen

Sen, Paresh C.
Queen's University

Senjyu, Tomonobu,
University of the Ryukyus

Shimizu, Toshihisa
Tokyo Metropolitan University

Su, Guijia
Sanken Electric Co., Ltd.

Sugimoto, Hidehiko
Fukui University

Sul, Seung-Ki
Seoul National University

Tadakuma, Susumu
Chiba Institute of Technology

Takahara, Eimei
Toshiba Corp.

Takahashi, Isao
Nagaoka University of Technology

Takeda, Yoji
Osaka Prefecture University

Tamura, Yoshiaki
Toshiba Corp.

Tanaka, Shigeru
Toshiba Corp.

Tanaka, Toshihiko
The Polytechnic University, Japan

Taniguchi, Katsunori
Osaka Institute of Technology

Terashima, Masayuki
Meidensha Co.

Uceda, Javier
Universidad Politecnica de Madrid

Uchida, Ryohei
Mitsubishi Electric Corp.

Umita, Hidetoshi
Fuji Electric Corporate Research and Development Ltd.

Van Wyk, J.D.
Rand Afrikaans University

Vas, Peter
University of Aberdeen

Watanabe, Hiroshi
Tokyo Metropolitan Institute of Technology

Yanase, Takao
Fuji Electric Corporate Reserach and Development Ltd.

TABLE OF CONTENTS

Volume I :

O1 Electric Vehicle

O1 - 1 Traction Control of Electric Vehicle Based on the Estimation of Road Surface Condition --- Basic Experimental Results Using the Test EV "UOT Electric March"---
Yoichi Hori, Yasushi Toyoda, Yoshimasa Tsuruoka : (University of Tokyo) 1

O1 - 2 A High Performance Drive System for Electric Vehicle
Yoshinobu Sato, Kouetsu Fujita, Takao Yanase, Shigenori Kinoshita, Kenji Endo : (Fuji Electric Corporate R&D, Ltd.) 9

O1 - 3 Energy Saving Vector Control Strategies for Electric Vehicle Motor Drives
Sadegh Vaez, V. I. John*, M. A. Rahman**: (*Queen's University, **Memorial University of Newfoundland)* 13

O1 - 4 Driving Characteristics of Anti-Directional-Twin-Rotary Motor on Electric Vehicle Simulator
Nobukazu Hoshi, Kantaro Yoshimoto**, Atsuo Kawamura** : (*Ibaraki University, **Yokohama National University)* 19

O1 - 5 A Control Method of an Inverter-Fed Six-Phase Pole Change Induction Motor for Electric Vehicles
Masato Mori, Takayuki Mizuno, Tadashi Ashikaga, Isao Matsuda :(Meidensha Corporation) 25

O1 - 6 High Performance Design of an Interior Permanent Magnet Synchronous Reluctance Motor for Electric Vehicles
Shinichiro Kawano, Hiroshi Murakami, Noriyoshi Nishiyama, Yasufumi Ikkai, Yukio Honda, Toshiro Higaki : (Matsushita Electric Industrial Co., Ltd.) 33

O2 Traction Systems

O2 - 1 Development of Power Supply System for Yamanashi Maglev Test Line
*H. Ikeda*1, S. Kaga*1, Y. Osada*2, J. Kitano*2, K. Ito*3, Y. Mugiya*3, H. Ito*3, K. Tutumi*4 : (*1 Railway Technical Research Institute, *2 Central Japan Railway Company, *3 Toshiba Corporation, *4 Hitachi, Ltd.)* 37

O2 - 2 Harmonics Control of the 20MVA PWM Inverter Fed LSM Drive System for the Yamanashi Maglev Test Line
*Yusuke Yamauchi*1, Hiroaki Tanitsu*1, Jun-ichi Kitano*1, Shigeo Kaga*2, Yoshihiro Tagami*3, Yoshinori Otsuka*3, Naoki Morishima*3 : (*1 Central Japan Railway Company, *2 Railway Technical Research Institute, *3 Mitsubishi Electric Corp.)* 43

O2 - 3 Optimization of Readhesion Control of Shinkansen Trains with Wheel-Rail Adhesion Prediction
Tomoki Watanabe, Akihiro Yamanaka*, Toshio Hirose*, Katsuyoshi Hoshi*, Shigeru Nakamura* : (*Railway Technical Research Institute, **East Japan Railway Co.)* 47

O2 - 4 Improvement of Re-Adhesion for Commuter Trains with Vector Control Traction Inverter
Ikuo Yasuoka, Takuma Henmi, Yooske Nakazawa, Ikuya Aoyama : (Toshiba Corporation) 51

O2 - 5 Harmonic Compensator for 50Hz Fed AC Railway Vehicles
Masamichi Ogasa, Jens Onno Krah**, Joachim Holtz** : (*Railway Technical Research Institute, ** University of Wuppertal)* 57

O2 - 6 Permanent Magnet Synchronous Motor Control System for Railway Vehicle Traction and Its Advantages
Keiichirou Kondou, Kouichi Matsuoka :(Railway Technical Research Institute) 63

O3 Induction Motor Control (1)

O3 - 1 Position Estimation in Induction Machines Utilizing Rotor Bar Slot Harmonics and Carrier Frequency Signal Injection
M. W. Degner, R. D. Lorenz : (University of Wisconsin-Madison) 69

O3 - 2 Sensorless Speed Estimation Based on Primary and Secondary Resistance Estimation and Output Voltage Compensation of Induction Motor
Kan Akatsu, Atsuo Kawamura : (Yokohama National University) 73

O3 - 3 Sensorless Vector-Controlled Induction Motor Drive System with Rotor Resistance Estimation Using Parallel Processing with Floating Point DSP
Teodor Pana : (Technical University of Cluj-Napoca) 79

O3 - 4 A Speed-Sensorless IM Drive with Modified Decoupling Control
Somboon Sangwongwanich, Surapong Suwankawin : (Chulalongkorn University) 85

O3 - 5 **Sensorless Speed Control of an Induction Motor with No Influence of Resistance Variation**
Toshiyuki Kanmachi, Isao Takahashi** : (*Sendai National College of Technology, ** Nagaoka University of Technology)* 91

O4 Induction Motor Control (2)

O4 - 1 **An Auto-Tuning Method for Vector Controlled Induction Motor Drives Considering Stator Core Loss**
Hiroaki Yamamoto, Kohji Tanaka, Ichiro Miki : (Meiji University) 97

O4 - 2 **High-Torque and High-Efficiency Control in Induction Motor Drives**
Lishi Wang, Hirohito Funato, Kenzo Kamiyama : (Utsunomiya University) 103

O4 - 3 **Vector Control of an Induction Motor for the Field Weakening Region with Tuning of the Magnetizing Inductance**
*D. H. Choi*1, M. H. Shin*1, T. K. Lee*2, S. B. Cho*3, D. S. Hyun*1 : (*1 Hanyang University, *2 Ansung National University, *3 Doowon Technical College)* 107

O4 - 4 **Precise Torque Control of Induction Motor with On-Line Parameter Identification in Consideration of Core Loss**
Toshihiko Noguchi, Paiboon Nakmahachalasint**, Narin Watanakul** : (*Nagaoka University of Technology, **Thammasat University)* 113

O4 - 5 **Multi-Star Induction Motors Fed by Voltage Source Inverters**
H. Stemmler, R. Deplazes : (The Swiss Federal Institute of Technology) 119

O5 Permanent Magnet Motor Control

O5 - 1 **For Practical Use Position and Speed Sensorless Salient-Pole Brushless DC Motor Drives**
Nobuyuki Kasa, Hiroshi Watanabe : (Tokyo Metropolitan Institute of Technology) 127

O5 - 2 **Fully Digital Implementation of PMSM Servo Based on a Novel Current Control Strategy**
Jia Wu, Dongsheng Zhang, Yongdong Li : (Tsinghua University) 133

O5 - 3 **Sensorless Starting and Low Speed Drive of Cylindrical Brushless DC Motor Using Eddy Current at Un-Known Load**
Mutuwo Tomita, Hideyuki Yamaguchi**, Shinji Doki*, Shigeru Okuma* : (*Nagoya University, ** Aichi Electric Co., Ltd.)* 139

O5 - 4 **Initial Rotor Position Estimation of Salient-Pole Brushless DC Motors by Artificial Neural Network**
Tomonobu Senjyu, Naomitsu Urasaki, Katsumi Uezato : (University of the Ryukyus) 145

O5 - 5 **Dynamic Matrix Control (DMC) for the Step Motion of Synchronous Motor**
Sun Hexu, Ge Baoming, Chi Yan, Zang Xiaojie, Li Wenjiang : (Liaoning Technology University) 151

O5 - 6 **Advantageous Use of a Dual Operation, Linear and Switching Power Module in Drive Control with no Deadtime**
Kenji Yanagawa, Takeshi Tohya, Kouki Matsuse : (Meiji University) 157

O6 Active Power Filter

O6 - 1 **A Control Method of Active Power Filter in Unsymmetrical and Distorted Voltage System**
Yasuhiro Komatsu, Takao Kawabata : (Ritsumeikan University) 161

O6 - 2 **A New Control Method for Active Power Filters with Voltage Detection**
Yukihiko Sato, Hidenori Chigira*, Teruo Kataoka** : (*Tokyo Institute of Technology, **Tokyo Denki University)* 169

O6 - 3 **Novel Active Filter System Composed of Inverter Bypass Circuit for Suppression of Harmonic Resonance at the Yamanashi Maglev Test Line**
*Ikuo Kawaguchi*1, Haruo Ikeda*1, Jun-ichi Kitano*2, Yoshiya Ogihara*3, Miyokazu Syogaki*3, Hiroshi Morita*3 : (*1 Railway Technical Research Institute, *2 Central Japan Railway Company, *3 Nissin Electric Co., Ltd.)* 175

O6 - 4 **Design of Harmonic Current Detector and Stability Analysis of a Hybrid Parallel Active Filter**
Santhiphong Khositkasame, Somboon Sangwongwanich : (Chulalongkorn University) 181

O6 - 5 **Development of Dispersion Type Active Filter**
Katsuhiro Shinzen, Masakatsu Nomura*, Masayuki Terashima*, Fumimasa Anan**, Kiyomi Yamasaki : (*Meidensha Corporation, **Kyushyu Electric Power Co.)* 187

O6 - 6 **An Adaptive Noise Canceling Theory Based Single-Phase Shunt Active Power Filter**
Chen Weiji, Chen Wenhong*, Ma Xiaojun**, Chen Jianye**, Wang Zhonghong**, Han Yingduo** : (*University of Macau, **Tsinghua University)* 191

O7 Utility Network Applications (1)

O7 - 1 Transformerless Reactive Series Compensators with Voltage Source Inverters
H. Stemmler, A. Beer : (The Swiss Federal Institute of Technology) 197

O7 - 2 Series Power Line Compensator Using Self-Commutated Inverter
Hirokazu Tokuda, Naoya Eguchi*, Satoshi Uemura**, Ryuichi Shimada** : (*Fuji Electric Corporate R&D, Ltd., ** Tokyo Institute of Technology)* 203

O7 - 3 Continuous Operation Control during Electric Power Network Faults in an Adjustable Speed Generation System with a Flywheel Excited by a DC Link Converter
Tohru Nishio, Kiyoshi Minoguti*, Seinosuke Uno*, Motoo Futami**, Mitsuyuki Hombu**, Masaya Ichinose**, Akihiro Maoka** : (*The Kansai Electric Power Co., Inc., **Hitachi, Ltd.)* 209

O7 - 4 Stabilization of Electric Power System Using the Variable Speed Flywheel Generator
Satoshi Uemura, Shinichi Nomura, Ryuichi Shimada : (Tokyo Institute of Technology) 215

O7 - 5 Design Procedure and Performance Evaluations of Utility-Interactive Bidirectional Resonant DC Link Three Phase ZVS-PWM Power Conditioner
T. Shimizu, M. Kurokawa, Y. Matsumoto, A. Chibani, M. Nakaoka : (Yamaguchi University) 219

O8 PWM (1)

O8 - 1 A State-Space Modeling and a Neutral Point Voltage Control for an NPC Power Converter
Chiharu Osawa, Yasushi Matsumoto, Tetsuya Mizukami, Satoru Ozaki :(Fuji Electric Corporate R&D, Ltd.) 225

O8 - 2 Neutral Point Potential and Unity Power Factor Control of NPC Boost Converters
Shoji Fukuda, Yasumasa Matsumoto : (Hokkaido University) 231

O8 - 3 DC Ripple Current Reduction Method on a Single Phase PWM Voltage Source Converter
Toshihisa Shimizu, Yasuhiro Fujioka, Gunji Kimura : (Tokyo Metropolitan University) 237

O8 - 4 A Simple Sensorless Method for Sinusoidal PWM Converters
Itaru Ando, Isao Takahashi*, Kouji Utsunomiya** : (* Nagaoka University of Technology, **Takaoka Electric Mfg. Co., Ltd.)* 241

O8 - 5 Line Voltage Sensorless Three Phase PWM Converter by Tracking Control of Operating Frequency
Tokuo Ohnishi, Kentarou Fujii : (The University of Tokushima) 247

O8 - 6 Transient Oscillation Suppression of Input Filter Voltage and Current for Current-Source Three-Phase PWM AC/DC Converter
Koji Toyama, Takaharu Takeshita, Nobuyuki Matsui : (Nagoya Institute of Technology) 253

O9 PWM (2)

O9 - 1 Harmonic Evaluation of Carrier-Based PWM Methods Using Harmonic Distortion Determining Factor
Shoji Fukuda, Kunio Suzuki : (Hokkaido University) 259

O9 - 2 Unified PWM Technique for Real Time Power Conversion
Dae-Woong Chung, Seung-Ki Sul*, Joohn-Sheok Kim** : (*Seoul National University, **Inchon City University)* 265

O9 - 3 Walsh Function Based Synthesis Method of PWM Pattern for Full-Bridge Inverter
Seiji Kondo , Krit Choeisai : (Nagaoka University of Technology) 271

O9 - 4 Indirect Current Control Scheme in PWM Voltage-Sourced Converter
Jae-Ho Choi, Hyong-Cheol Kim, Joo-Sik Kwak : (Chungbuk National University) 277

O9 - 5 Development of Multiple Space Vector Control for Direct Connected Parallel Current Source Power Converters
Ryuichi Abe, Yoshiaki Nagai*, Kazuhiko Tsuyuki*, Hiroyuki Nishikawa**, Takeo Shimamura**, Akira Kawaguchi**, Kazuhiko Shimada** : (*Electric Power Development Co., Ltd., **Toshiba Corporation)* 283

O9 - 6 A Novel Control Strategy on Single-Phase PWM Current Source Inverter Incorporating Pulse Area Modulation
Katsuya Hirachi, Yasuharu Tomokuni : (Yuasa Corporation) 289

O10 Soft Switching (1)

O10 - 1 Design and Analysis of a Novel Soft-Switched Push-Pull Boost Converter
Yu-Ming Chang, Jia-You Lee*, Kuan-Hui Fang** : (*National Cheng Kung University, **Delta Electronics Incorporation)* 295

O10 - 2 Performance of Series-Resonant AC Link Inverter
Masahito Hayashi, Kouki Matsuse : (Meiji University) 301

O10 - 3 A Basic Study on a Parallel Resonant Link Converter for a High Frequency Link System
Mikihiko Matsui, Toshio Akiyama : (Tokyo Institute of Polytechnics) 305

O10 - 4 New Developments in Resonant DC Link Inverters
Deepak Divan, Ian Wallace : (Soft Switching Technologies Corporation) 311

O10 - 5 Improvement of Performance of a Series Resonant DC Link PWM Inverter
Hiroki Ishikawa, Yoshihiro Murai : (Gifu University) 319

O10 - 6 A Novel Resonant DC Link Circuit with Two Level PWM Control Scheme and Its Application to Three-Phase Voltage-Fed Converter Operating at New Pulse Vector Modulation
Arihi Kambe, Manabu Kurokawa, Ali Chibani , Mutsuo Nakaoka : (Yamaguchi University) 325

O11 Power Supply Systems

O11 - 1 Active EMI Filter for Switching Noise of High Frequency Inverters
Isao Takahashi, Akihiro Ogata*, Hidetoshi Kanazawa**, Atsuyuki Hiruma** : (*Nagaoka University of Technology, **Toshiba Corporation)* 331

O11 - 2 Low Cost Power Factor Correction (PFC) Converter Using Delay Control
K. C. Lee, B. H. Cho : (Seoul National University) 335

O11 - 3 High-Efficiency Power Supply for Resistive Loads with Sinusoidal Input Current
*L. Rossetto*1, L. Malesani*1, G. Spiazzi*1, J. A. Pomilio*2, M. Monacchi*3 : (*1 University of Padova, *2 UNICAMP, *3 Whirlpool Europe)* 341

O11 - 4 Distortion-Free Regulated AC Power Supply Using Variable Capacitance Device
Akihiko Katsuki, Hidetatsu Iwata, Takeshi Matsui : (Kyushu Institute of Technology) 347

O11 - 5 Improvement of Reactance Compensator Using Variable Active-Passive Reactance with Output Filter
Hirohito Funato, Atsuo Kawamura**, Takao Watanabe*, Kenzo Kamiyama* : (*Utsunomiya University, **Yokohama National University)* 355

O12 Simulation of Power Converter Systems (1)

O12 - 1 The Instantaneous Power Theory Based on Mapping Matrices in Three-Phase Four-Wire Systems
Hyosung Kim, Hirofumi Akagi** : (*Cheonan Technical College, **Okayama University)* 361

O12 - 2 Periodic Steady-State Analysis by a Modified Shooting Method for a Power Electronic Circuit
Toshiji Kato, Wataru Tachibana : (Doshisha University) 367

O12 - 3 Simulation Method for Phase-Shift Controlled AC-AC Converters Based on Switching Vector
Jorma Kyyra, Sami Valiviita : (Helsinki University of Technology) 373

O12 - 4 A Novel Simulation Scheme of Power Electronics System with the Parallel Inference Machine (PIM)
E. Masada, J. Baba, H. Wakamiya, M. Tamura : (The University of Tokyo) 379

O12 - 5 State Vector Equation Based Computer Simulation Approach of Digitally Controlled Power Conversion Circuits and Systems
Syed Mobin Ulhaq, Mutsuo Nakaoka*, Hiroshi Takano** : (*Yamaguchi University, **Hitachi Medical Co., Ltd.,)* 385

O13 Simulation of Power Converter Systems (2)

O13 - 1 A Study on Power Factor and Efficiency Correction of AC-DC Boost Converter by Partial Resonant Type Using a L^2SC
Hyun-Woo Lee, Ki-Young Suh*, Young-Chul Kim*, Jung-Ham Chun*, Katsunori Taniguchi** : (*Kyung-Nam University, ** Osaka Institute of Technology)* 391

O13 - 2 Analysis and Improvement of Input Current Waveforms for Discontinuous-Mode Boost Converter with Unity Power Factor
Katsunori Taniguchi, Yukio Nakaya : (Osaka Institute of Technology) 399

O13 - 3 Interleaved Boost Power Factor Corrector Operating in Discontinuous-Inductor-Current Mode
C. H. Chan, M. H. Pong : (Hong Kong University) 405

O13 - 4 Computer-Aided Simulation Technique of Digitally Controlled Switched-Mode Power Conversion Circuits and Systems Using State Variable Matrices
H. Takano, S. Mobin Ulhaq**, M. Nakaoka** : (*Hitachi Medical Corporation, **Yamaguchi University)* 411

O13 - 5 General Approach to a Novel Average-Current-Mode Control of the Constant Frequency Power Converters
Marko Jankovic, Predrag Ninkovic : (EE Institute

Nikola Tesla) 419

O13 - 6 The Characteristics Analysis of PWM Inverter-Fed 3-Phase Induction Motor from View Point of Saturation
Katsumi Kamimoto, Naoyuki Andoh**, Yoshihiro Murai** : (*Daido Institute of Technology, **Gifu University)* 425

O14 Modeling and Analysis of PE System (1)

O14 - 1 The IGBT - An Optimized Device for System Integration
L. Lorenz : (Siemens AG) 431

O14 - 2 Modified Charge-Control Equation for More Realistic Simulation of Power Diode Characteristics
K. J. Tseng, S. Pan : (Nanyang Technological University) 439

O14 - 3 Combined Optimality and Robustness Assessments for Interconnected Power Converters - Theoretical and Experimental Results
Catalin Burlacu, Hiroyuki Ohsaki, Eisuke Masada : (The University of Tokyo) 445

O14 - 4 Dual Slope Integrator Type Delta Modulator for High Performance Voltage Source Inverters
K. M. Rahman, M. A. Choudhury*, M. Rezwan Khan*, M. A. Rahman**: (*Bangladesh University of Engg. & Tech., **Memorial University of Newfoundland)* 451

O14 - 5 Development of a General Tokamak Circuit Simulation Program and Some Application Results to the JT - 60 Power Supply System
Makoto Matsukawa, Tetsuo Aoyagi, Yushi Miura : (Japan Atomic Energy Research Institute) 457

O14 - 6 Genetic Algorithm Based Control for Power Converters
J. Baba, E. Masada : (The University of Tokyo) 463

O15 Control and Applications (1)

O15 - 1 Adaptive Signal Processing System for Accurate Zero-Crossing Detection of Cycloconverter Phase Currents
Sami Valiviita, Seppo J. Ovaska, Jorma Kyyra : (Helsinki University of Technology) 467

O15 - 2 Switching-Ripple-Based Current Sharing for Paralleled Power Converters
David J. Perreault, Kenji Sato, John G. Kassakian : (Massachusetts Institute of Technology) 473

O15 - 3 Isolated Three-Phase AC-to-DC Bidirectional Converter with a Small Number of Switches
Akira Takeuchi, Hisahito Endo, Seiichi Muroyama, Satoshi Ohtsu : (NTT Integrated Information & Energy Systems Lab.) 479

O15 - 4 Immunity Test Results of a Quick Power Failure Detector of Uninterruptible Secondary Battery System
Satoshi Miyazaki, Masaaki Ohshima*, Fuminori Nakamura**, Yuushin Yamamoto**, Shinzo Tamai**, Haruyoshi Mori** : (*Tokyo Electric Power Co., Inc., **Mitsubishi Electric Corp.)* 483

O15 - 5 Parallel Redundant Operation of UPS with Robust Current Minor Loop
Youichi Ito, Osamu Iyama : (Sanken Electric Co., Ltd.) 489

O15 - 6 Compensation Method of AC-to-DC Converter Characteristics under Unbalanced Three-Phase AC Side Voltage
Yoshiaki Okui, Masayuki Mouri**, Tsutomu Mizuno**, Hajime Yamada** : (*Sanyo Denki Co., Ltd., ** Shinshu University)* 495

O16 Motion Control and Soft Computing

O16 - 1 Digital Robust Speed Servo System with Complete Avoidance of Output Saturation Effect
Kiyoshi Ohishi , Tomonori Mashimo : (Nagaoka University of Technology) 501

O16 - 2 A DSP-Based Servo System Using Generalized Predictive Control
K. S. Low, K. Y. Chiun, K. V. Ling : (Nanyang Technological University) 507

O16 - 3 Analysis and Control of Grasping Motion by Two Cooperative Robots
Kyunghwan Kim, Yoichi Hori : (The University of Tokyo) 513

O16 - 4 Control and Diagnosis for AC Drives and UPS Systems Using Soft Computing
Yasuhiko Dote, Richard G. Hoft** : (* Muroran Institute of Technology, ** University of Missouri-Columbia)* 519

O16 - 5 New Digital Redesign Method by N-Delay Control and Its Application
Hiroshi Fujimoto, Atsuo Kawamura : (Yokohama National University) 525

Volume II :

P1 Induction Motor Control (3)

P1 - 1 **Improvement of Lower Side Speed Control Characteristics of an Induction Motor without a Speed Sensor**
Yoichi Ohmori, Masashi Takagi, Tomoaki Kiriya : (Toyo Electric Mfg. Co., Ltd.) 531

P1 - 2 **High Performance Sensorless Control of Induction Motor Drives for Industry Applications**
*G. Griva*1, C. Ilas*2, J. F. Eastham*3, F. Profumo*1, P. Vranka*4 : (*1 Politecnico di Torino, *2 Polytechnic of Bucharest, *3 Bath University, *4 University of Miskolc)* 535

P1 - 3 **A New Hybrid Vector Control for Induction Motor without Speed and Position Sensors ---Frequency Hybrid Approach Using New Indirect Scheme---**
Shinji Shinnaka : (Kanagawa University) 541

P1 - 4 **Behavior of Sensorless Induction Motor Drives in Regenerating Mode**
Hisao Kubota, Kouki Matsuse*, Yoichi Hori** : (*Meiji University, **The University of Tokyo)* 549

P1 - 5 **Sensorless Control for Induction Motor Drives Based on New Speed Identification Scheme**
Shyh-Shing Perng, Yen-Shin Lai**, Chang-Huan Liu* : (*National Taiwan Inst. of Tech., **National Taipei Inst. of Tech.)* 553

P1 - 6 **Transient Response of Speed Sensorless Control Method Based on Phase Difference**
Junichi Tsuchiya, Kazuhiro Watanabe*, Toshihisa Simizu*, Gunji Kimura*, Ikuo Watanabe**, Koji Naniwa** : (*Tokyo Metropolitan University, **Oriental Motor Co.)* 559

P2 Induction Motor Control (4)

P2 - 1 **Improvement of Thrust of Linear Induction Motor Using Modified Ladder Slits**
Tadashi Yamaguchi, Masaki Ito, Keiju Matsui : (Chubu University) 563

P2 - 2 **Novel Prediction Method of Acoustic Magnetic Noise Emitted by Inverter-Fed Induction Motor System**
Bin Kaku, Ichiro Miyashita*, Satoru Sone** : (*Toyo Electric Mfg. Co., Ltd., **The University of Tokyo)* 567

P2 - 3 **A Speed Calculation Method for Induction Motor Based on Voltage Decoupling Control Principle**
Zeng Yuenan, Feng Duoshen**, Chen Boshi* : (*Shanghai University, **Guangdong University of Technology)* 573

P2 - 4 **High-Power Drive Using Wound Rotor Induction Motor and Two Current Controlled Inverters**
Yoshitaka Kawabata, Emenike C. Ejiogu, Kazuhide Nishiyama, Takao Kawabata : (Ritsumeikan University) 579

P2 - 5 **Stability Analysis and Design Guidelines for a Speed-Sensorless Induction Motor Drive**
Surapong Suwankawin, Somboon Sangwongwanich : (Chulalongkorn University) 583

P3 Motor Control Technology

P3 - 1 **Improving the Start and Restart Behavior through State Recognition of AC Drives**
Hangwen Pan, Lothar Springob**, Joachim Holtz* : (*University of Wuppertal, ** VECTRON Electronik)* 589

P3 - 2 **Speed Control of Ultrasonic Motors by Discrete Time Variable Structure Control**
Tomonobu Senjyu, Satoru Yokoda, Katsumi Uezato : (University of the Ryukyus) 595

P3 - 3 **A New Sensorless Control Method for a General Class of Linear Pulse Motors**
Dong-Eui Chang, Yang-O Kim*, In-Joong Ha*, Moonhwan Kim**, Kook Hun Kim* (*Seoul National University, **Korea Electrotechnology Research Institute)* 601

P3 - 4 **Robust Vibration Suppression Control Using System Identification of Minor Control-Loop System**
Seiji Hashimoto, Kenji Hara, Hirohito Funato, Kenzo Kamiyama : (Utsunomiya University) 607

P3 - 5 **P-I and I-P Controllers in a Closed Loop for DC Motor Drives**
F. I. Ahmed, A. M. El-Tobshy, A. A. Mahfouz, M. M. S. Ibrahim : (Cairo University) 613

P3 - 6 **A Proposition of Design Method for Modified Repetitive Control System with Corrected Dead Time Using Sensitivity Function Shaping and Its Application to Motor Control System**
Hidehiko Sugimoto, Kazuo Washida : (Fukui University) 619

P3 - 7 **A Two-Dimensional Homopolar Linear DC Motor with New Position Detectors**
Yijia Wang, Masaki Yamaguchi, Yoshio Kano : (Tokyo University of Agriculture & Technology) 625

P3 - 8 **Propulsion Control Experiments in Mass-Control Mode of an Underwater Travelling Marine-Express Model Vehicle ME02**
K. Yoshida, L. Shi, H. Takami : (Kyushu University) 631

P3 - 9 **Design Tradeoffs and Technology Outlook of Highly Compact Integrated AC Motors**
Jie (Jay) Chang : (Rockwell International Corporation) 637

P4 New Synchronous Motors and Their Control

P4 - 1 **Axial Type Flat PM Motor with Large Air Gap**
Masayuki Sanada, Shigeo Morimoto, Yoji Takeda : (Osaka Prefecture University) 643

P4 - 2 **Performance of PM/Reluctance Hybrid Motor with Multiple Flux-Barrier**
Shigeo Morimoto, Masayuki Sanada, Yoji Takeda : (Osaka Prefecture University) 649

P4 - 3 **A Rotor Design of a Permanent Magnet-Type Bearingless Motor Considering Demagnetization**
Masahide Ooshima, Satoru Miyazawa*, Akira Chiba*, Fukuzo Nakamura*, Tadashi Fukao** : (*Science University of Tokyo, **Tokyo Institute of Technology)* 655

P4 - 4 **Torque/Current Ratio Improvement of Reluctance Motor under Consideration of Teeth Design and Current Waveform**
Takashi Kosaka, Nobuyuki Matsui : (Nagoya Institute of Technology) 661

P4 - 5 **Automatic Learning Control-Based Auto Gain Parameter Tuning DC Brushless Servo Motor Drive Systems**
Kenji Inoue, Junji Yoshitsugu**, Shin Shirogane**, Prasanna Boyagoda**, Mutsuo Nakaoka** : (*Shinko Electric Co., Ltd., **Yamaguchi University)* 667

P4 - 6 **A Real-Time Estimation Method of Brushless DC Servomotor Parameters**
Hisashi Takahashi, Takashi Kenjo*, Hirokazu Takeuchi** : (*Polytechnic University of Japan, **Sagamihara Vocational Training School)* 673

P4 - 7 **Driving Method for Delta-Connected Brushless-Sensorless Motor**
*Tadashi (Ted) Sakurai*1, Motoki Sakurai*2, Masao Arimoto*3, Sumio Kaneko*4 : (*1 Sakura Lab., *2 Sophia University, *3 Nagaoka College, *4 maxon Japan)* 679

P5 Utility Network Applications (2)

P5 - 1 **A Practical Approach to Minimize the Zero-Sequence Current Harmonics in Power Distribution Systems**
Pekik A. Dahono, Radpandji E. Widjaya, Syafrudin, Qamaruzzaman : (Bandung Institute of Technology) 683

P5 - 2 **New Current Feedback Control Method for Solar Energy Inverter Using Digital Signal Processor**
Tsukasa Takebayashi, Hirofumi Nakata, Masaki Eguchi, Hirokazu Kodama : (SHARP Corporation) 687

P5 - 3 **A New Scheme for Maximum Photovoltaic Power Tracking Control**
Hidehiko Sugimoto, Huian Dong : (Fukui University) 691

P5 - 4 **A New Microcontroller Based Solar Energy Conversion Modular Unit**
F. Huang, Gao Zhimin**, T. Forughian*, D. Tien* : (*Ngee Ann Polytechnic, **Sennheiser Electronic Asia Pte Ltd.)* 697

P5 - 5 **Ring-Shaped Flywheel Energy Storage Systems with Superconducting Levitation**
Hidekazu Teshima, Taichi Tawara**, Jun Kobuchi**, Tatsuo Suzuki**, Ryuichi Shimada** : (*Nippon Steel Corporation, **Tokyo Institute of Technology)* 701

P5 - 6 **Development of Uninterruptible Secondary Battery System**
Masaaki Ohshima, Satoshi Miyazaki*, Katsuhisa Inagaki**, Hitoshi Kikuchi**, Hitoshi Nirasawa** : (*Tokyo Electric Power Co., Inc., **Toshiba Corporation)* 707

P5 - 7 **A Hybrid Single-Phase Power Active Filter for High Order Harmonics Compensation in Converter-Fed High Speed Trains**
Takashi Maeda, Tomoki Watanabe*, Abdallah Mechi**, Takashi Shiota**, Katsuji Iida** : (*Railway Technical Research Institute, ** Toyo Electric Mfg. Co. Ltd.)* 711

P5 - 8 **A New Method for Separating AC Component of Instantaneous Real Power and Imaginary Power Suitable for Active Filters**
Atsushi Nakata, Akiteru Ueda, Akihiro Torii : (Aichi Institute of Technology) 719

P5 - 9 **Development of 60MVA SVC (Static Var Compensator) Using Large Capacity 8kV and 3.5kA Thyristors**
Taizo Hasegawa, Yoshiharu Aoshima*, Tadashi Sato*, Osamu Kondo**, Tatsuya Matsukawa** : (*The Kansai Electric Power Co., Inc., **Nissin Electric Co., Ltd.)* 725

P5 - 10 **SVC Control Considering the Impedance on the Higher Side of the Power System**
Takao Akiyama, Kimiyoshi Tamura, Junichi Shimomura, Masafumi Ichihara, Masayuki Terashima : (Meidensha Corporation) 731

P5 - 11 **Power System Stabilizing Control Using High Speed Phase Shifter (HSPS)**
Toshifumi Ise, Takanori Hayashi, Junichi Ishii, Sadatoshi Kumagai : (Osaka University) 735

P5 - 12 Robust Power System Stabilizer Design with H_∞ Optimization Method and Its Experiment on a Hardware Simulator
Yeonghan Chun, Takuhiko Ohashi*, Yoichi Hori*, Kook Hun Kim**, Jong Bo Ahn**, Seok Joo Kim** : (*The University of Tokyo, **Korea Electrotechnology Research Institute)* 741

P5 - 13 D. C. Power System for Superconducting Fusion Test Facility LHD
*H. Chikaraishi*1, S. Tanahashi*1, S. Yamada*1, O. Motojima*1, T. Satoh*2, H. Niwa*2, T. Uede*3, Hiue*3 : (*1 National Institute for Fusion Science, *2 Aichi Electic Co., Ltd., *3 Fuji Electic Co., Ltd.)* 747

P5 - 14 The Design of Control Configuration of Variable Speed Generator System
Yuzo Itoh, Nobuhito Nozawa : (Hokkaido University) 751

P6 PWM (3)

P6 - 1 A Novel Three-Phase Sinusoidal PWM Voltage Source Inverter and Its Application for Photovoltaic Power Generation System
Sakutaro Nonaka : (Kinki University) 755

P6 - 2 Characteristics of a Novel PWM Inverter Circuit with a L-C Filter Connected with DC Link
Kenji Amei, Masaaki Sakui, Hiroshi Fujita : (Toyama University) 759

P6 - 3 A Voltage Source Three Phase PWM Converter with Chopper Circuit
Keiju Matsui, Tomohiro Katayama*, Shinichi Takase**, Yue Yang** : (* Chubu University, **Neturen Co., Ltd.)* 765

P6 - 4 Analysis and Design of Three-Phase Boost PWM Converter against Power Disturbances
Ki-Tae Park, Jun-Koo Kang, Seung-Ki Sul : (Seoul National University) 773

P6 - 5 Effect of Parasitic Capacitance of Power Device on Output Voltage Deviation during Switching Dead-Time in Voltage-Fed PWM Inverter
Kichiro Yamamoto, Katsuji Shinohara, Hiroyuki Ohga : (Kagoshima University) 777

P6 - 6 New Current-Controlled PWM Rectifier-Voltage Source Inverter without DC Link Components
Kenichi Iimori, Katsuji Shinohara*, Osamu Tarumi*, Zixum Fu*, Mitsuhiro Muroya** : (*Kagoshima University, **Kagoshima National College of Technology)* 783

P6 - 7 Generalized Harmonic Loss-Factor As a Novel Important Quality Index of PWM Techniques
S. Halasz, B.T. Huu : (Technical University of Budapest) 787

P7 Soft Switching (2)

P7 - 1 A Loss-Less Passive Snubber for Soft Switching Boost-Type Converters
Hiroshi Nomura, Kenichiro Fujiwara : (Kochi National College of Technology) 793

P7 - 2 New Switching Sequence for Three Phase Converter with ZVS Using a Transformer
Shinya Ofuji, Tetsuya Oshikata, Yoshiaki Matsuda : (Shindengen Electric Mfg. Co., Ltd.) 797

P7 - 3 Analysis of Self-Excited Resonant DC-DC Converter to Determine Oscillation Condition
Yasuyuki Kanai, Nobuhiko Yamashita, Naoki Murakami, Toshiaki Yachi : (NTT Integrated Information & Energy System Laboratories) 801

P7 - 4 New DC-DC Resonant Converter As Active Filter
*I. Nagy*1, P. Korondi*1, E. Masada*2, Z. Puklus*3 : (*1 Technical University of Budapest, *2 The University of Tokyo, *3 Szechenyi College)* 805

P7 - 5 Single-Switch Auxiliary Resonant Converters
Masa-aki Shimada, Mantaro Nakamura : (Sanken Electric Co., Ltd.) 811

P7 - 6 Analysis and Simulation of Series-Resonant High-Frequency AC-Linked DC-AC Converter Realizable by Inverter Modules
Jinsheng Wei, Muneaki Ishida, Takamasa Hori : (Mie University) 815

P7 - 7 Comparative Transient and Steady-State Performances of Three Resonant PWM Inverter-Controlled DC-DC Converters Using High-Voltage Transformer and Cable Parasitic Circuit Components
J. M. Sun, L. Gamage*, M. Nakaoka*, H. Takano**, T. Hatakeyama** : (*Yamaguchi University, **Hitachi Medical Corporation)* 821

P7 - 8 Performance Characteristics of the Combined Zero-Voltage Switching Inverter with the Auxiliary Input-Current Controller
Lishan Tu, Fujio Kurokawa*, Hirofumi Matsuo*, Nanjo Aoike** : (*Nagasaki University, **Toshiba Lighting & Technology Corporation)* 827

P8 Modeling and Analysis of PE System (2)

P8 - 1 Simulation and Analysis of Hybrid Systems Using Probabilistic Techniques
Fadia M. A. Ghali, M. M. Abd El Aziz**, F. A.*

Syam : (*Electronics Research Institute, **Cairo University)* **831**

P8 - 2 Modeling Analysis and Simulation of Motor Parameter Variation in Vector Controlled Electrical Drives
Goran Rafajlovski, Emil Ratz**, D. Manov* : (*University "St. Kiril and Metodij", **Technical University of Sofia)* **837**

P8 - 3 Effect of Slot-Combination on Electromagnetic Vibration of Squirrel-Cage Induction Motor under Loaded Condition
Isao Hirotsuka, Kazuo Tsuboi*, Fuminori Ishibashi** : (*Chubu University, **Toshiba Corporation)* **843**

P8 - 4 Analysis and Computer Simulation of Cycloconverter Operation Based on the Energy Equation
I. Katz, M. A. Slonim : (Ben-Gurion University of the Negev) **849**

P8 - 5 Steady-State Performance Analysis of Shaft Generator Systems
Shoji Nishikata, Akihiro Odaka, Yohei Koishikawa : (Tokyo Denki University) **853**

P8 - 6 Dynamic Model of Fluorescent Lamp Implemented in PSpice
K. J. Tseng : (Nanyang Technological University) **859**

P8 - 7 Stability Analysis and Performance Evaluation of AC Side Current Control System of Voltage Type Converters
A. Draou : (University of Sciences and Technology of Oran) **865**

P9 Measurement and Control

P9 - 1 The Use of a Single Microprocessor Board to Control Two Independent Inverters
I. A. El-Kassas, L. N. Hulley**, W. Shepherd** : (*College of Technology Al-Ahsa, **University of Bradford)* **871**

P9 - 2 Rapid Prototyping Tool for a Fuzzy Logic Based Soft-Starter
M. Rajendra Prasad, V. V. Sastry : (Indian Institute of Technology) **877**

P9 - 3 Accurate Measurement of Instantaneous Voltage for Power Electronics Circuits
Tung-Hai Chin, Motomu Nakano, Takashi Hirayama : (Sophia University) **881**

P9 - 4 Analysis of the Tuned-Average Current-Mode Control of the Constant Frequency DC/DC Converters
Predrag Ninkovic, Marko Jankovic : (EE Institute Nikola Tesla) **885**

P10 Control and Applications (2)

P10 - 1 Analysis of Single Phase Diode Rectifiers with Power Factor Correction Circuits
Akiteru Ueda, Toshiko Shinohara, Masaru Matsubara, Akihiro Torii : (Aichi Institute of Technology) **891**

P10 - 2 Improvement of Current Waveform for 200V Input Single-Phase Rectifiers Using Modified Voltage-Doubler Circuit
Kenichiro Fujiwara, Hiroshi Nomura : (Kochi National College of Technology) **897**

P10 - 3 Power Factor and PWM Controller TDA 16888
M. Herfurth, L. Lorenz : (Siemens AG) **901**

P10 - 4 Improved Circuit of AC Choppers for Single-Phase Systems
Nabil Abd El-Latif Ahmed, Kenji Amei, Masaaki Sakui : (Toyama University) **907**

P10 - 5 A New Topology for Single Phase UPS Systems
Gui-Jia Su, Tetuhiko Ohno : (Sanken Electric Co., Ltd.) **913**

P10 - 6 A Design Concept of DC Filters for Magnet Power Supplies
Hyosung Kim, Jaeho Choi** : (*Cheonan National Technical College, **Chungbuk National University)* **919**

P10 - 7 Electric Load Controlled by Computer Simulator Having Power Regeneration Ability
Itaru Ando, Isao Takahashi*, Yuichi Tanaka**, Mitsuo Ikehara** : (* Nagaoka University of Technology, **Tsuken Electric Co., Ltd.)* **925**

P10 - 8 New NPC Multi-Level Four-Quadrant DC-DC Converter Controlled by the Integrated-Voltage-Control Method
Hideyuki Okui, Hisaichi Irie** : (*Osaka Polytechnic College, **Osaka Electro-Communication University)* **931**

P11 Industrial Applications

P11 - 1 Induction Motor Control for Electric Vehicle Application Using Low Resolution Position Sensor and Sensorless Vector Control Technique
*Giuseppe Guidi*1, Hisao Kubota*2, Yoichi Hori*3 : (*1 Universita Degli Studi Dell Aquila, *2 Meiji University, *3 The University of Tokyo)* **937**

P11 - 2 Residual Capacity Estimation of Sealed Lead-Acid Batteries for Electric Vehicles
Takahiro Yanagihara, Atsuo Kawamura : (Yokohama National University) **943**

P11 - 3 Total Efficiency of a Hybrid Electric Vehicle
Sadao Imai, Nobuaki Takeda, Yusuke Horii : (Mitsubishi Motors Corporation) **947**

P11 - 4 Maximum Adhesive Force Control in Super High Speed Train
Yoshiki Ishikawa, Atsuo Kawamura : (Yokohama National University) **951**

P11 - 5 Compensation of Voltage Drop Using Static Var Compensator at Sectioning Post in AC Electric Railway System
Keiji Kawahara, Shin-ichi Hase*, Yoshifumi Mochinaga*, Yasuji Hisamizu*, Takashi Inoue** : (*Railway Technical Research Institute, ** West Japan Railway Company)* **955**

P11 - 6 Optimal Formation of Trainsets
Satoru Ito, Klemens Heumann** : (*Hitachi, Ltd., **Technische Universitat Berlin)* **961**

P11 - 7 3300V 400A, 600A and 1200A High Power IGBT Modules with High Reliability for Traction Applications
Akira Tanaka, Mutsuhiro Mori, Hirokazu Inoue, Yoshihiko Koike, Tadao Kushima, Hideo Shimizu, Kiyoshi Nakamura, Ryuichi Saito : (Hitachi, Ltd.) **967**

P11 - 8 Efficient Ozonizer Using PDM and PWM Controlled Resonant Inverter and Its Performance Evaluations
Y. Konishi, S. P. Wang**, M. Ishibashi**, Y. L. Feng**, M. Nakaoka** : (*Fuji Electric Co., Ltd., **Yamaguchi University)* **971**

P11 - 9 Innovative Development of Electromagnetic Induction-Based Fluid-Heating System Using Resonant PWM Inverter
A. Kajiyama, B. Guo*, M. Nakaoka*, Y.Uchihori** : (*Yamaguchi University, **Seta Kosan Chemical Industry Co., Ltd.)* **977**

P11- 10 Switching Modes and Short-Circuit Considerations in Very High Frequency, Very High Power Resonant Inverters for Induction Heating Applications
E. J. Dede, J. Jordan*, V. Esteve*, J.M. Espi**, A. Ferreres** : (*G. H. Elin International, **University of Valencia)* **983**

P11- 11 New Type of Ballast for HID Lamps Using Distributed Constant Line
Masato H. Ohsato, Hideki Ohguchi*, Toshihisa Shimizu*, Gunji Kimura*, Hiroyuki Takagi** : (*Tokyo Metropolitan University, **Kandenko Corporation)* **987**

P11- 12 All Digital Controlled Three-Phase UPS without Inverter-Transformer
Akihiko Kanouda, Yoshimi Sakurai, Kenji Kubo, Keizou Shimada, Hideaki Kunisada, Hideyasu Umetsu : (Hitachi, Ltd.) **991**

P11- 13 Steady-State Characteristics of an Overload-Protected Frequency-Compensated Current-Feedback Magnetic Multivibrator
Akihiko Katsuki, Masaki Ouchiyama, Tomoko Takeshita : (Kyushu Institute of Technology) **997**

P11- 14 Rare-Metal Free Thin Film Solar Cell
Hironori Katagiri, Masato Nishimura, Takeshi Onozawa, Shinichi Maruyama, Masato Fujita, Toshiyuki Sega, Taku Watanabe : (Nagaoka National College of Technology) **1003**

P11- 15 A Method to Measure EMI Due to Electric Field Coupling on PCB
Bryan M. H. Pong, Angus C. M. Lee : (Hong Kong University) **1007**

P11- 16 Novel Digital Control Topology of a High Power Resonant DC-DC Converter for X-Ray High-Voltage Applications
H. Takano, T. Hatakeyama*, L. Gamage**, J. M. Sun**, M. Nakaoka** : (*Hitachi Medical Corporation, **Yamaguchi University)* **1013**

AUTHORS INDEX

A

Abe, R. 283
Ahmed, F. I. 613
Ahmed, N. A. E. L. 907
Ahn, J. B. 741
Akagi, H. 361
Akatsu, K. 73
Akiyama, Takao 731
Akiyama, Toshio 305
Amei, K. 759, 907
Anan, F. 187
Ando, I. 241, 925
Andoh, N. 425
Aoike, N. 827
Aoshima, 725
Aoyagi, T. 457
Aoyama, I. 51
Arimoto, M. 679
Ashikaga, T. 25
Aziz, M. M. A. E. 831

B

Baba, J. 379, 463
Beer, A. 197
Boyagoda, P. 667
Burlacu, C. H. 445

C

Chan, C. H. 405
Chang, D. E. 601
Chang, J. 637
Chang, Y. M. 295
Chen, B. 573
Chen, J. 191
Chen, W. 191
Chi, Y. 151
Chiba, A. 655
Chibani, A. 219, 325
Chibani, S. 325
Chigira, H. 169
Chikaraishi, H. 747
Chin, T. H. 881
Chiun, K. Y. 507
Cho, B. H. 335
Cho, S. B. 107
Choeisai, K. 271
Choi, D. H. 107
Choi, J. 919
Choi, J. H. 277
Choudhury, M. A. 451
Chun, J. H. 391
Chun, Y. 741
Chung, D. W. 265

D

Dahono, P. A. 683
Dede, E. J. 983
Degner, M.W. 69
Deplazes, R. 119
Divan, D. 311
Doki, S. 139
Dong, H. 691
Dote, Y. 519
Draou, A. 865

E

Eastham, J. F. 535
Eguchi, M. 687
Eguchi, N. 203
El-Tobshy, A. M. 613
Ejiogu, E. C. 579
El-Kassas, I. A. 871
Endo, H. 479
Endo, K. 9
Espi, J.M. 983
Esteve, V. 983

F

Fang, K. H. 295
Feng, D. 573
Feng, Y. L. 971
Ferreres, A. 983
Forughian, T. 697
Fu, Z. 783
Fujii, K. 247
Fujimoto, H. 525
Fujioka, Y. 237
Fujita, H. 759
Fujita, K. 9
Fujita, M. 1003
Fujiwara, K. 793, 897
Fukao, T. 655
Fukuda, S. 231, 259
Funato, H. 103, 355, 607
Futami, M. 209

G

Gamage, L. 821, 1013
Ge, B. 151
Ghali, Fadia M. A. 831
Griva, G. 535
Guidi, G. 937
Guo, B. 977

H

Ha, I. J. 601
Halasz, S. 787
Han, Y. 191
Hara, K. 607
Hase, S. 955
Hasegawa, T. 725
Hashimoto, S. 607
Hatakeyama, T. 821, 1013
Hayashi, M. 301
Hayashi, T. 735
Henmi, T. 51
Herfurth, M. 901
Heumann, K. 961
HigakI, T. 33
Hirachi, K. 289
Hirayama, T. 881
Hirose, T. 47
Hirotsuka, I. 843
Hiruma, A. 331
Hisamizu, Y. 955
Hiue, 747
Hoft, R. G. 519
Holtz, J. 57, 589
Hombu, M. 209
Honda, Y. 33
Hori, T. 815
Hori, Y. 1, 513, 549, 741, 937
Horii, Y. 947
Hoshi, K. 47
Hoshi, N. 19
Huang, F. 697
Hulley, L. N. 871
Huu, B. T. 787
Hyun, D. S. 107

I

Ibrahim, M. M. S. 613
Ichihara, M. 731
Ichinose, M. 209
Iida, K. 711
Iimori, K. 783
Ikeda, H. 37, 175
Ikehara, M. 925
Ikkai, Y. 33
Ilas, C. 535
Imai, S. 947
Inagaki, K 707
Inoue, H. 967
Inoue, K. 667
Inoue, T. 955
Irie, H. 931
Ise, T. 735
Ishibashi, F. 843
Ishibashi, M. 971
Ishida, M. 815
Ishii, J. 735
Ishikawa, H. 319
Ishikawa, Y. 951
Ito, H. 37
Ito, K. 37
Ito, M. 563
Ito, S. 961
Ito, Y. 489
Itoh, Y. 751
Iwata, H. 347
Iyama, O. 489

J

Jankovic, M. 419, 885
John, V. I. 13
Jordan, J. 983

K

Kaga, S. 37, 43
Kajiyama, A. 977
Kaku, B. 567
Kambe, A. 325
Kamimoto, K. 425
Kamiyama, K. 103, 355, 607
Kanai, Y. 801
Kanazawa, H. 331
Kaneko, S. 679
Kang, J. K. 773
Kanmachi, T. 91
Kano, Y. 625
Kanouda, A. 991
Kasa, N. 127
Kassakian, J. G. 473
Katagiri, H. 1003
Kataoka, T. 169
Katayama, T. 765
Kato, T. 367
Katsuki, A. 347, 997
Katz, I. , 849
Kawabata, T. 161, 579
Kawabata, Y. 579
Kawaguchi, A. 283
Kawaguchi, I. 175
Kawahara, K. 955
Kawamura, A. 19, 73, 355, 943, 951
Kawano, S. 33
Kenjo, T. 673
Khan, M. R. 451
Khositkasame, S. 181
Kikuchi, H. 707
Kim, H. 361, 919
Kim, H. C. 277
Kim, J. S. 265
Kim, K. 513
Kim, K. H. 601, 741
Kim, M. 601
Kim, S. J. 741
Kim, Y. C. 391
Kim, Y. O. 601
Kimura, G. 237, 559, 987
Kinoshita, S. 9
Kiriya, T. 531
Kitano, J. 37, 43, 175
Kobuchi, J. 701
Kodama, H. 687
Koike, Y. 967
Koishikawa, Y. 853
Komatsu, Y. 161
Kondo, O. 725
Kondo, S. 271
Kondou, K. 63
Konishi, Y. 971
Korondi, P. 805
Kosaka, T. 661
Krah, J. O. 57
Kubo, K. 991
Kubota, H. 549, 937
Kumagai, S. 735
Kunisada, H. 991
Kurokawa, F. 827
Kurokawa, M. 219, 325
Kushima, T. 967
Kwak, J. S. 277
Kyyra, J. 373, 467

L

Lai, Y. S. 553
Lee, A. C. M. 1007
Lee, J. Y. 295
Lee, K. C. 335
Lee, T. K. 107
Li, W. 151
Li, Y. 133
Ling, K. V. 507
Liu, C. H. 553
Lorenz, L. 431, 901
Lorenz, R. D. 69
Low, K. S. 507

M

Ma, Z. 191
Maeda, T. 711
Mahfouz, A. A. 613
Malesani, L. 341
Manov, D. 837
Maoka, A. 209
Maruyama, S. 1003
Masada, E. 379, 445, 463, 805
Mashimo, T. 501
Matsubara, M. 891
Matsuda, I. 25
Matsuda, Y. 797
Matsui, K. 563, 765
Matsui, M. 305
Matsui, N. 253, 661
Matsui, T. 347
Matsukawa, M. 457
Matsukawa, T. 725
Matsumoto, Y. 219
Matsumoto, Yasumasa 231
Matsumoto, Yasushi 225
Matsuo, H. 827
Matsuoka, K. 63
Matsuse, K. 157, 301, 549
Mechi, A. 711

Miki, I. 97
Minoguti, K. 209
Miura, Y. 457
Miyashita, I. 567
Miyazaki, S. 483, 707
Miyazawa, S. 655
Mizukami, T. 225
Mizuno, Takayuki 25
Mizuno, Tsutomu 495
Mochinaga, Y. 955
Monacchi, M. 341
Mori, H. 483
Mori, Masato 25
Mori, Mutsuhiro 967
Morimoto, S. 643, 649
Morishima, N. 43
Morita, H. 175
Motojima, O. 747
Mouri, M. 495
Mugiya, H. 37
Mugiya, Y. 37
Murai, Y. 319, 425
Murakami, H. 33
Murakami, N. 801
Muroya, M. 783
Muroyama, S. 479

N

Nagai, Y. 283
Nagy, I. 805
Nakamura, Fukuzuo 655
Nakamura, Fuminori 483
Nakamura, K. 967
Nakamura, M. 811
Nakamura, S. 47
Nakano, M. 881
Nakaoka, M. 219, 325, 385, 411, 667, 821, 971, 977, 1013
Nakata, A. 719
Nakata, H. 687
Nakaya, Y. 399
Nakazawa, Y. 51
Nakmahachalasint, P. 113
Naniwa, K. 559
Ninkovic, P. 419, 885
Nirasawa, H. 707
Nishikata, S. 853
Nishikawa, H. 283
Nishimura, M. 1003
Nishio, T. 209
Nishiyama, K. 579
Nishiyama, N. 33
Niwa, H. 747
Noguchi, T. 113
Nomura, H. 793, 897
Nomura, M. 187
Nomura, S. 215
Nonaka, S. 755
Nozawa, N. 751

O

Odaka, A. 853
Ofuji, S. 797
Ogasa, M. 57
Ogata, A. 331
Ogihara, Y. 175
Ohashi, T. 741
Ohga, H. 777
Ohguchi, H. 987
Ohishi, K. 501
Ohmori, Y. 531
Ohnishi, T. 247
Ohno, T. 913
Ohsaki, H. 445
Ohsato, M. 987
Ohshima, M. 483, 707
Ohtsu, S. 479
Ohtsuka, Y. 43
Okui, H. 931
Okui, Y. 495
Okuma, S. 139
Onozawa, T. 1003
Ooshima, M. 655
Osada, Y. 37
Osawa, C. 225
Oshikata, T. 797
Ouchiyama, M. 997
Ovaska, S. J. 467
Ozaki, S. 225

P

Pan, H. 589
Pan, S. 439
Pana, T. 79
Park, K. T. 773
Perng, S. S. 553
Perreault, D. J. 473
Pomilio, J. A. 341
Pong, M. H. 405, 1007
Prasad, M. R. 877
Profumo, F. 535
Puklus, Z. 805

Q

Qamaruzzaman, S. 683

R

Rafajlovski, G. 837
Rahman, K. M. 451
Rahman, M. A. 13, 451
Ratz, E. 837
Rossett, L. 341

S

Saito, R. 967
Sakui, M. 759, 907
Sakurai, M. 679
Sakurai, T. 679
Sakurai, Y. 991
Sanada, M. 643, 649
Sangwongwanich, S. 85, 181, 583
Sastry, V. V. 877
Sato, K. 473
Sato, T. 725
Sato, Y. 9
Sato, Y. 169
Satoh, T. 747
Sega, T. 1003
Senjyu, T. 145, 595
Shepherd, W. 871
Shi, L. 631
Shimada, Kazuhiko 283
Shimada, Keizou 991
Shimada, M. 811
Shimada, R. 203, 215, 701
Shimamura, T. 283
Shimizu, H. 967
Shimizu, T. 219
Shimizu, Toshihisa 237, 559, 987
Shimomura, J. 731
Shin, M. H. 107
Shinnaka, S. 541
Shinohara, K. 777, 783
Shinohara, T. 891
Shinzen, K. 187

Shiota, T. 711
Shirogane, S. 667
Slonim, M. A. 849
Sone, S. 567
Spiazzi, G. 341
Springob, L. 589
Stemmler, H. 119, 197
Su, G. J. 913
Sugimoto, H. 619, 691
Suh, K. Y. 391
Sul, S. K. 265, 773
Sun, H. 151
Sun, J. M. 821, 1013
Suwankawin, S. 85, 583
Suzuki, K. 259
Suzuki, T. 701
Syam, F. A. 831
Syogaki, M. 175

T

Tachibana, W. 367
Tagami, Y. 43
Takagi, H. 987
Takagi, M. 531
Takahashi, H. 673
Takahashi, I. 91, 241, 331, 925
Takami, H. 631
Takano, H. 385, 411, 821, 1013
Takase, S. 765
Takebayashi, T. 687
Takeda, N. 947
Takeda, Y. 643, 649
Takeshita, Takaharu 253
Takeshita, Tomoko 997
Takeuchi, A. 479
Takeuchi, H. 673
Tamai, S. 483
Tamura, K. 731
Tamura, M. 379
Tanahashi, S. 747
Tanaka, A. 967
Tanaka, K. 97
Tanaka, Y. 925
Taniguchi, K. 391, 399
Tanitsu, H. 43
Tarumi, O. 783
Tawara, T. 701
Terashima, M. 187, 731
Teshima, H. 701
Tien, D. E. 697
Tohya, T. 157
Tokuda, H. 203
Tomita, M. 139
Tomokuni, Y. 289
Torii, A. 719, 891
Toyama, K. 253
Toyoda, Y. 1
Tseng, K. J. 439, 859
Tsuboi, K. 843
Tsuchiya, J. 559
Tsuruoka, Y. 1
Tsuyuki, K. 283
Tu, L. 827
Tutumi, K. 37

U

Uchihori, Y. 977
Ueda, A. 719, 891
Uede, T. 747
Uemura, S. 203, 215
Uezato, K. 145, 595
Ulhaq, S. M. 385, 411
Umetsu, H. 991
Uno, S. 209
Urasaki, N. 145
Utsunomiya, K. 241

V

Vaez, S. 13
Valiviita, S. 373, 467
Vranka, P. 535

W

Wakamiya, H. 379
Wallance, I. 311
Wang, L. 103
Wang, S. P. 971
Wang, Y. 625
Wang, Z. 191
Washida, K. 619
Watanabe, H. 127
Watanabe, I. 559
Watanabe, K. 559
Watanabe, Takao 355
Watanabe, Taku 1003
Watanabe, Tomoki 47, 711
Watanakul, N. 113
Wei, J. 815
Widjaya, R. E. 683
Wu, J. 133

Y

Yachi, T. 801
Yamada, H. 495
Yamada, S. 747
Yamaguchi, H. 139
Yamaguchi, M. 625
Yamaguchi, T. 563
Yamamoto, H. 97
Yamamoto, K. 777
Yamamoto, Y. 483
Yamanaka, A. 47
Yamasaki, K. 187
Yamashita, N. 801
Yamauchi, Y. 43
Yanagawa, K. 157
Yanagihara, T. 943
Yanase, T. 9
Yang, Y. 765
Yasuoka, I. 51
Yokoda, S. 595
Yoshida, K. 631
Yoshimoto, K. 19
Yoshitsugu, J. 667

Z

Zang, X. 151
Zeng, Y. 573
Zhang, D. E. 133
Zhimin, G. 697

Improvement of Lower Side Speed Control Characteristics of an Induction Motor without a Speed Sensor

Yoichi Ohmori, Masashi Takagi and Tomoaki Kiriya
Toyo Electric Mfg. Co., Ltd.
338-1 Kamisoyagi Yamato-shi Kanagawa Pref. 242 Japan
Fax: +81-462-63-2947, Phone:+81-462-64-5781
E-mail:kiri@lab.toyodenki.co.jp

Abstract - **Various methods for improvement of speed control performance in the low speed region of an induction motor without a speed sensor are proposed. However, most of those methods seem to have various problems for practical use. In this paper, a speed estimation method with new primary resistance identification is proposed. The better performance of speed control in very low frequency range under the full load condition is possible without deterioration of speed and torque control response by the proposed method. And speed reversal operations at acceleration over 30r/min/sec through zero frequency have been achieved under full load condition.**

I.INTRODUCTION

Recently, a speed sensor-less vector controlled inverter is merchandised in many, and it becomes the main stream of inverters which drive an induction motor. But, it is difficult to operate in the low speed as several r/min without large ripples of the speed and the torque. The reasons are that relative accuracy of primary voltage detects or voltage control of an induction motor becomes worse following the decrease of primary voltage, and that values of motor parameters such as primary resistance used in a controller have errors. Moreover, operation with zero frequency and slow speed reversal operation through zero frequency can't be realized easily. It causes that speed estimation becomes impossible by stator and rotor being separated completely electrically under the zero frequency condition.

To solve the above problems, the method [1] which estimates the rotor position by injecting harmonic currents into the motor which the structure of the rotor is devised, and the method [2][3] which estimates the flux position by utilizing saliencies induced by magnetic saturation in the motor and by injecting harmonic currents into the motor are proposed. Very low speed operations under the zero or nearly zero frequency have been realized with above methods.

But the former method can't be applied to a general purpose motor being produced at present. And when for example the latter method is applicable to the motor which has a closed slot rotor, it is likely to require difficult adjustment which depends on the motor. It is because of the spatial distribution of inductance in the motor warps with the influence of saturation of secondary leakage flux which depends on secondary current. Moreover new torque ripple and acoustic noise are likely to come out by injecting the harmonic currents.

In this paper, a new primary resistance identification method is proposed. Slow speed reversal operation of a general purpose motor through zero frequency has been achieved by using the proposed method. It doesn't almost need to adjust much the proposed method by using auto-measuring function [4] of the motor parameters together.

II.SPEED SENSORLESS VECTOR CONTROL

A block diagram of the speed sensorless vector control is shown in Fig. 1. The secondary and primary linkage flux vectors ψ_{2i}, ψ_1, torque T, speed ω_m of the motor are calculated from detected primary current vector i_1 and voltage vector v_1. A speed regulator outputs a torque command T* so that the calculated speed follows its command. A torque and flux controller supply directly the PWM inverter with a switching signal so that the calculated torque and flux will follow their commands.

The secondary linkage flux vector ψ_{2i} is given by (1). The vectors are represented in a stationary d-q coordinate system. Where speed ω_m is calculated by (6). Another secondary linkage flux vector ψ_{2v} which is used for slip angular velocity calculation is given by (2). The second term in the integral in the (2) is added to suppress the

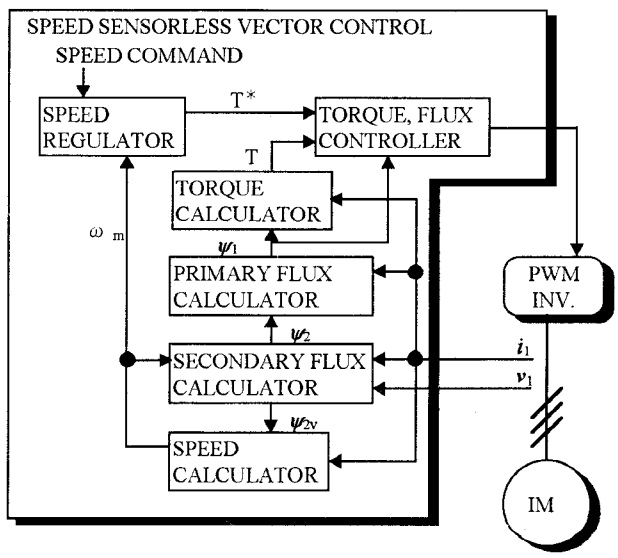


Fig. 1 Control block diagram

integration drift caused by error signal involved in vector i_1 and v_1. K is varied with the speed ω_m as (3) to stabilize this system, especially at high speed region. The primary linkage flux vector ψ_1 and torque T are calculated from (4) and (5), respectively. Where i_{1d}, i_{1q} and ψ_{1d}, ψ_{1q} are the components of i_1 and ψ_1, respectively. The speed is obtained by subtracting the slip angular velocity ω_S from the angular velocity of rotation of the ψ_{2v} as indicated in (6). The slip angular velocity is obtained by (7). Where ψ_{2vd}, ψ_{2vq} are the components of ψ_{2v}.

Where,

R_1: Primary resistance R_2: Secondary resistance
L_1: Primary inductance L_2: Secondary inductance
M: Mutual inductance ω_m: Rotor speed.

$$\psi_{2i} = \int \left(\frac{M}{L_2} R_2 i_1 - \frac{R_2}{L_2} \psi_{2i} + j\omega_m \psi_{2i} \right) dt \tag{1}$$

$$\psi_{2v} = \int \left[\frac{L_2}{M} \left(\mathbf{v}_1 - R_1 \mathbf{i}_1 \right) - K \left(\psi_{2v} - \psi_{2i} \right) \right] dt - \left(\frac{L_1 L_2}{M} - M \right) \mathbf{i}_1 \tag{2}$$

$$K = K_A \omega_m \tag{3}$$

$$\psi_1 = \frac{M}{L_2} \psi_{2i} + \left(L_1 - \frac{M^2}{L_2} \right) i_1 \tag{4}$$

$$T = \psi_{1d} i_{1q} - \psi_{1q} i_{1d} \tag{5}$$

$$\omega_m = \omega - \omega_S \tag{6}$$

$$\omega_S = R_2 \frac{M \left(\psi_{2vd} i_{1q} - \psi_{2vq} i_{1d} \right)}{L_2 \left(\psi_{2vd}^2 + \psi_{2vq}^2 \right)} \tag{7}$$

By employing the direct torque controller based on spatial vector theory as mentioned above, torque frequency-response with corner frequencies above 1krad/sec has been experimentally measured [5]. And 90rad/sec of speed frequency-response has been experimentally obtained [5] because the rotation speed can be calculated quickly from calculated flux and detected currents by the speed calculator.

III.INFLUENCES OF PRIMARY RESISTANCE VARIATION

If the primary resistance R_1 varies with the temperature, the error involved in calculating ψ_{2v} using (2) increases particularly in the low speed region. This increases the error in the slip angular velocity calculated from ψ_{2v}. This also leads to an increase in the error in the calculated speed value ω_m as Fig.2, when the R_1 setting is varied between +20% ~ -20% of the actual value. In this figure, a 100% load is applied during measurement. Similar characteristics hold also for errors in torque calculation.

As mentioned above, the R_1 error influences a characteristic specially in the low speed. Therefore, the R_1 error decides whether the speed reversal operation done more slowly can be made or not. So, the primary resistance identification method without speed sensor is proposed in the next chapter.

IV.PRIMARY RESISTANCE IDENTIFICATION

A primary resistance identification is realized by (8)-(10). Error value ε is obtained by vector product with the primary current vector i_1 and a flux error vector which is obtained by subtracting the voltage model flux ψ_{2v} obtained by (2) from the current model flux ψ_{2i} obtained by (1) as indicated in (8). Where ψ_{2id}, ψ_{2iq} are the components of ψ_{2i}. The error value ε is amplified by PI controller as (9). And the primary resistance can be modified by (10). Where K_{rp} is proportional gain, K_{ri} is integral gain, R_{1n} is initial value of R_1.

$$\varepsilon = i_{1d} \left(\psi_{2iq} - \psi_{2vq} \right) - i_{1q} \left(\psi_{2id} - \psi_{2vd} \right) \tag{8}$$

$$G_r = \left(K_{rp} + \frac{K_{ri}}{S} \right) \varepsilon \tag{9}$$

$$R_1 = R_{1n} \left(1 + G_r \right) \tag{10}$$

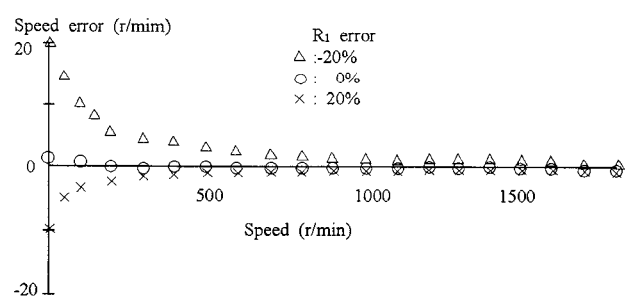


Fig. 2 Speed errors without R_1 identification

The reason why the primary resistance identification by the method as the mentioned above is possible is given in the following.

Fig.3 shows vectors diagram at powering. A chain line in the figure is parallel in the direction of the vector i_1 and the line passes the tip of the current model flux ψ_{2i}. A broken line is at right angle to the direction of the vector i_1 and the line passes the tip of the voltage model flux ψ_{2v}. The voltage model flux is obtained by integrating a voltage vector E which is obtained by subtracting the primary voltage vector v_1 from a voltage drop vector depended on R_1 as indicated by (2). Therefore when R_1 is reduced, the vector E approaches the vector v_1 along a dotted line in the Fig. 3 and the voltage model flux ψ_{2v} approaches the chain line along the broken line. When there is the voltage model flux ψ_{2v} of the bottom side of the chain line, the error value ε obtained by (8) is negative value. The other way when there is the voltage model flux ψ_{2v} of the upside of the chain line, the error value ε is positive value. Hence R_1 has only to be made small in the case of $\varepsilon<0$ to draw the ψ_{2v} to the chain line near. In the case of $\varepsilon>0$, R_1 must be increased. In other words, R_1 is adjusted by (9),(10) so that the voltage model flux ψ_{2v} may become on the chain line. It is the same in the case of regenerating shown in Fig.4 as well. If a difference between the voltage model flux ψ_{2v} and the current model flux ψ_{2i} is caused by R_1 error, R_1 is supposed to be identified properly and the voltage model flux ψ_{2v} is supposed to correspond to the current model flux ψ_{2i} when the voltage model flux ψ_{2v} exists on the chain line.

The proposed R_1 identification method can compensate for not only R_1 error but also detected voltage error. Because of the voltage detection error in the direction which is the same as current vector i_1 is compensated for completely, compensations of forward voltage drop of switching elements in the inverter don't need to be made accurate any more.

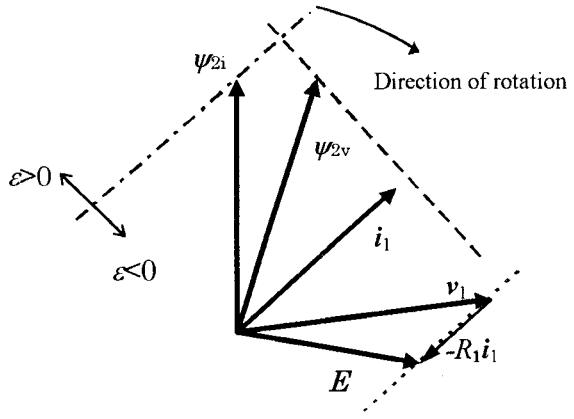


Fig. 3 Vectors diagram at powering

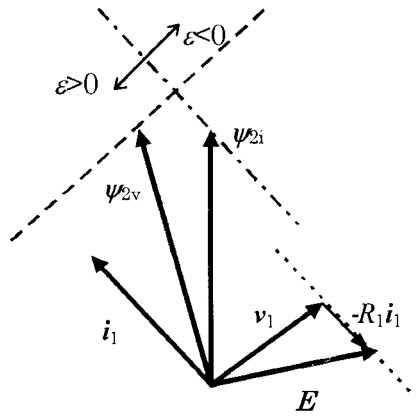


Fig. 4 Vectors diagram at regenerating

V.EXPERIMENTAL RESULTS

Fig. 5 shows the flux calculator with the primary resistance identification method indicated in the blocks made over.

Experiments went by the control composition of substituting the block of the Fig. 5 for the block of SECONDARY FLUX CALCULATOR in the Fig. 1. The rating of the induction motor used for the experiment is 200V, 7.5kW, 1800r/min. The electrical parameters of the motor were set into the inverter by the auto-measuring function [4]. A torque sensor for torque measurement and a DC motor driven by a thyristor Leonard system for generating load torque are directly coupled to the induction motor.

Fig. 6 shows an actual speed waveform, an output waveform of the torque sensor and a phase current waveform when the speed command was changed -300r/min to 300r/min in the acceleration of 30r/min/sec from. The DC motor gave about load torque of 100% to the induction motor. It also shows that the operation state of the induction motor moved to positive speed operation with powering from negative speed operation with regenerating. The speed reversal operation done very slowly through zero frequency was attained with just a few speed ripple. Because temperature rise in the induction motor was about

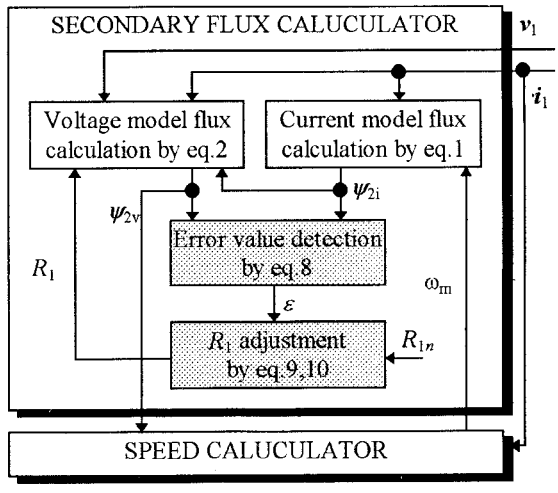


Fig. 5 Flux calculator with R_1 identification

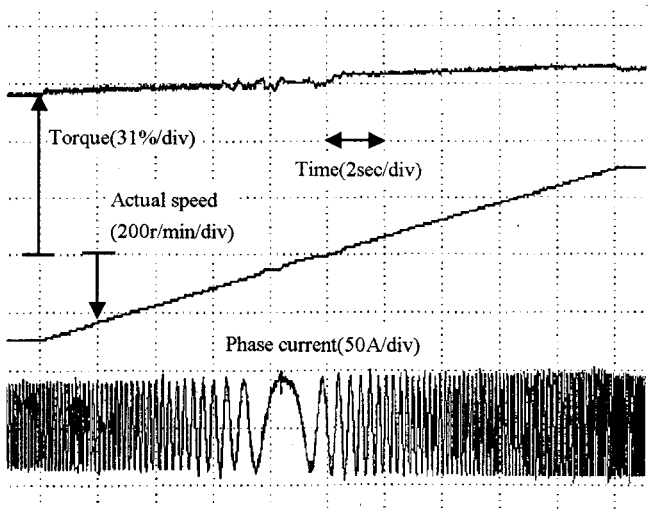


Fig. 6 Speed reversal operation with R_1 identification method under the full load condition (-300r/min → 300r/min)

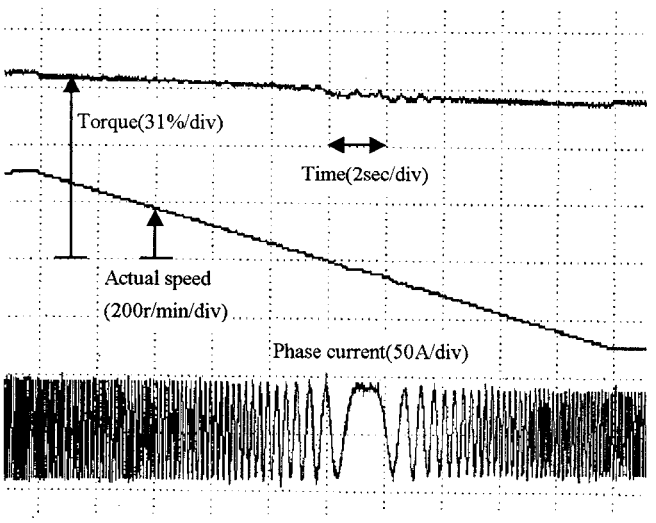


Fig. 7 Speed reversal operation with R_1 identification method under the full load condition (300r/min → -300r/min)

25°C, about actual 10% of R_1 was supposed to be big in this experiment.

Fig. 7 shows the waveform which is the same as the Fig. 6 when the speed command was changed from 300r/min to -300r/min in the acceleration of -30r/min/sec. In the same way as this figure, the speed reversal operation done very slowly has been achieved.

On the other hand, in the case of a conventional controller without R_1 identification, the induction motor was accelerated suddenly in the negative speed direction by the load torque because it stopped providing a torque suddenly before the frequency became zero.

VI.CONCLUSION

The method of a primary resistance identification for a vector control without a speed sensor was proposed. It was confirmed by experiment that the method was effective in the improvement of the operation characteristic around zero frequency. Then, the speed reversal operation done very slowly which was difficult at before, became possible. This method can be applied to the various induction motors without any adjustments.

REFERENCES

[1] R.D.Lorenz and M.J.Corley, "Rotor Position and Velocity Estimation for a Permanent Magnet Synchronous Machine at Standstill and High Speeds," Proc.of IEEE/IAS pp.36-41, 1996.

[2] M.Schroedl, "Sensorless Control of AC Machines at Low Speed and Standstill Based on the "INFORM" method," Proc.of IEEE/IAS pp.270-277, 1996.

[3] F.Blaschke, "Sensorless Direct Field Orientation at Zero Flux Frequency," Proc.of IEEE/IAS pp.189-196, 1996.

[4] Y.Ohmori, T.Nakanishi and H.Kobayashi, "A SPEED SENSORLESS SPATIAL VECTOR CONTROLLED INVERTER ADDED AN AUTO-MEASURING FUNCTION," EPE-SEVILLA pp.3-452-3-457 1995.

[5] I.Miyashita and Y.Ohmori, "IMPROVEMENT OF ROBUSTNESS ON SPEED SENSORLESS VECTOR CONTROL OF INDUCTION MOTOR," EPE-FIRENZE 4-660-4-665, 1991.

High Performance Sensorless Control of Induction Motor Drives for Industry Applications

G.Griva*, C.Ilas**, J.F.Eastham***, F.Profumo*, P.Vranka****

* Dipartimento di Ingegneria Elettrica, Politecnico di Torino, C.so Duca degli Abruzzi 24, 10129, Torino, Italy, Fax: +39-11-564.7199, Tel.: +39-11-564.7159, e-mail: grivag@athena.polito.it

** Dept. of Electrical Engineering, Polytechnic of Bucharest, Spl. Independentei 313, 77206 Bucharest, Romania, Fax: +40-1-3120412, Tel.: +40-1-4.100.400, e-mail: costel@alpha.amotion.pub.ro

*** School of Electrical and Electronic Engineering, Bath University, Claverton Down, Bath BA2 7AY, U.K., Fax: +44-1225-826.305, Tel.: +44-1225-826.056, e-mail: J.F.Eastham@bath.ac.uk

**** Dept. of Electrical Engineering, University of Miskolc, Egyetemavaros, 3515 Miskolc, Hungary, Fax: +36-46-361.740, Tel.: +36-46-365.111, e-mail: elkvp@gold.uni-miskolc.hu

Abstract - This paper deals with some aspects concerning the implementation of a sensorless induction motor control for industry applications. The proposed control method uses an adaptive rotor flux observer and a suitable adaptation law for the speed estimation. The theoretical analysis of this method has been presented in [1-5]. It has been found that this method is superior to many other methods when the performance versus complexity criterion is considered [1], [4]. The adaptation law is obtained by a general one, valid for any induction motor parameter estimation [5].
A comparison between the floating and the fixed point DSP implementation of the proposed method is presented. In fact, the appearance of new and powerful fixed point DSP microcontrollers makes the fixed point solution very attractive for many industrial applications, such as the retrofit ones, the conveyors control, and a lot of manufacturing process control. Different algorithm implementation issues, such as the on-line computation of the observer gain matrix and of the discrete motor model are discussed in this paper. Simulation and experimental results for the two cases (fixed and floating point DSP implementation) are shown.

Introduction

Sensorless drive systems have a structure similar to that of the classical field oriented drives, but instead of measuring the rotor speed, the shaft speed is only estimated. The absence of the shaft sensor leads to several benefits, but reduces the speed range operation and makes the control algorithm more complex [1-5]. To have a simultaneous estimation of the rotor flux and the speed, several solutions have been proposed in the last ten years. In [4], it was shown that the solution using an adaptive linear state observer (Luenberger Observer) and an adaptation mechanism can be a very attractive solution, in respect to the performance versus complexity criterion. This method has a thorough theoretical basis [3], that also explains its superiority to other methods [2].
For industrial applications, some improvements have to be done in the algorithm implementation in such a way that a cheaper controller system can be designed and used. It is expected that the new fixed-point DSP microcontroller TMS320C240 would become a very popular solution for industry applications during the next years, since it reduces all the control hardware to one chip [6]. Although this processor has a reasonable computation power, the simplicity of the control algorithm is a benefit for at least two reasons: it allows more other functions (such as communication, automatic generation of reference) to be performed by the system and it normally leads to smaller computation errors due to truncation. For a lot of control algorithms, including most of the speed estimation ones, the accuracy also depends drastically on the sampling time, so that the algorithm simplicity has a double effect on precision.

In this paper a very simple speed and flux estimation algorithm is presented. The algorithm is implemented in both fixed and floating point representation, and the two solutions are compared in simulations and experimentally.

The Simplified Speed and Flux Estimation Algorithm

As the four electrical equations of an induction motor form a linear system with a variable parameter (the rotor speed), the Extended Luenberger Observer (ELO) [1,4], that is an adaptive linear observer, can be used to estimate the state vector. The motor and the observer are described by the following equations:

$$\text{(Motor):}\ \begin{cases}\dot{x} = Ax + Bu \\ y = Cx\end{cases} \qquad \text{(Obs.):}\ \begin{cases}\dot{\hat{x}} = \tilde{A}\hat{x} + Bu + L(\hat{y} - y) \\ \hat{y} = C\hat{x}\end{cases} \tag{1}$$

The matrices A, B, and C describe the induction motor electrical equations, where the model output y is the stator current, while L is the observer gain matrix. The state vector x has as elements the orthogonal components, in the fixed reference frame, of the stator current and rotor flux: (i_{ds}, i_{qs}, λ_{dr} and λ_{qr}). The A matrix depends on the rotor speed. If the rotor speed is estimated and used by the observer, its matrix will be denoted $\tilde{A}$ instead of A, as they are distinct due to the difference between the estimated and the real speed. Because of this variation with speed of the matrix A the selection of the observer gain matrix L is not a straightforward problem. A traditional approach [2], [3] uses a gain matrix whose elements depend on the rotor speed so that the eigenvalues of (A - LC) are proportional with those of A, so that the observer is a stable system. The speed is estimated by an adaptation mechanism obtained from the hyperstability theory [5]:

$$\hat{\omega}_r = \tilde{\omega}_r = K\int e_y^T A_{er}\hat{x}dt$$

where $A - \tilde{A} = (\omega_r - \tilde{\omega}_r)A_{er}$ and $e_y = y - \hat{y}$

In Fig.1, the scheme of the speed sensorless FOC induction motor drive, with Extended Luenberger Observer (ELO) speed estimation.

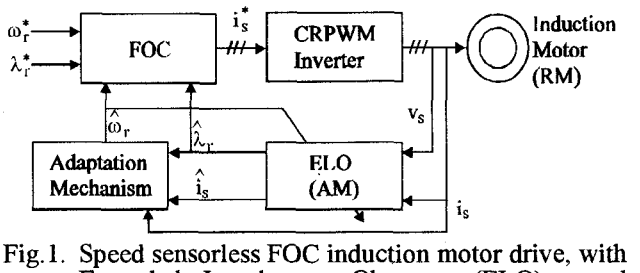


Fig.1. Speed sensorless FOC induction motor drive, with Extended Luenberger Observer (ELO) speed estimation.

For our scheme this means:

$$\hat{\omega}_r = \tilde{\omega}_r = K\int e_y^T A_{er}\hat{x}dt = K\int[-e_{iqs}\hat{\lambda}_{dr} + e_{ids}\hat{\lambda}_{qr}]dt \quad (2)$$

where $K>0$ is an arbitrary constant.
In a digital implementation the discrete equivalent of Eq.1 and Eq.2 has to be used. The state equation in the linear observer will be:

$$\hat{x}(k+1) = A_d\hat{x}(k) + B_d u + L_d(y(k) - \hat{y}(k)) \quad (3)$$

with the matrices given by:

$$A_d = e^{Ah},\quad B_d = \int_0^h e^{At}Bdt$$

$$e^{Ah} \cong I + Ah + \frac{A^2h^2}{2!} + \ldots \quad (4)$$

If the gain matrix L for the continuos time observer is computed according to the traditional approach, then the discrete gain matrix L_d is obtained from L by a similar relation. Due to the complex structure of A_d it is not possible to find simple formulae to compute the L_d elements so that the eigenvalues proportionality is kept.
The algorithm simplification starts with the implementation of Eq.4. If only the first three terms in the series are retained, an analytical expression of A_d can be obtained. It has the following form:

$$A_d = \begin{bmatrix} c_{11} & c_{12}\hat{\omega}_r & c_{13}^1 + c_{13}^2\hat{\omega}_r^2 & c_{14}\hat{\omega}_r \\ -c_{12}\hat{\omega}_r & c_{11} & -c_{14}\hat{\omega}_r & c_{13}^1 + c_{13}^2\hat{\omega}_r^2 \\ c_{31} & c_{32}\hat{\omega}_r & c_{33}^1 + c_{33}^2\hat{\omega}_r^2 & c_{34}\hat{\omega}_r \\ -c_{32}\hat{\omega}_r & c_{31} & -c_{34}\hat{\omega}_r & c_{33}^1 + c_{33}^2\hat{\omega}_r^2 \end{bmatrix} \quad (5)$$

where c_{ij} are constants depending on the A coefficients and on the sampling time h, while $\hat{\omega}_r$ is the estimated rotor speed. Using this relation the discrete equivalent of A can be easily obtained by only eight multiplications. In a similar way it can be found that B_d is practically independent on the speed, so it is no need to compute it on-line. Using these results (A_d - L_dC) is obtained to be:

$$A_d - L_dC = \left[\begin{array}{cc|cc} c_{11}-l_{11} & c_{12}\hat{\omega}_r - l_{12} & c_{13}^1 + c_{13}^2\hat{\omega}_r^2 & c_{14}\hat{\omega}_r \\ -c_{12}\hat{\omega}_r - l_{21} & c_{11}-l_{22} & -c_{14}\hat{\omega}_r & c_{13}^1 + c_{13}^2\hat{\omega}_r^2 \\ \hline c_{31}-l_{31} & c_{32}\hat{\omega}_r - l_{32} & c_{33}^1 + c_{33}^2\hat{\omega}_r^2 & c_{34}\hat{\omega}_r \\ -c_{32}\hat{\omega}_r - l_{41} & c_{31}-l_{42} & -c_{34}\hat{\omega}_r & c_{33}^1 + c_{33}^2\hat{\omega}_r^2 \end{array}\right]$$

This form suggest that L_d may be chosen as:

$$L_d = \begin{bmatrix} c_{11}-\lambda_1 & c_{12}\hat{\omega}_r \\ -c_{12}\hat{\omega}_r & c_{11}-\lambda_1 \\ c_{31} & c_{32}\hat{\omega}_r \\ -c_{32}\hat{\omega}_r & c_{31} \end{bmatrix} \quad (6)$$

with λ_1 a desired eigenvalue. In this way (A_d - L_dC) will have as eigenvalues λ_1 (two times) and the two eigenvalues given by the block in the lower right corner. It can be proved that for small sampling times the eigenvalues of this block are always stable, so that the observer is stable if λ_1 is correctly chosen.
In this way the algorithm for speed and fluxes estimation is reduced to the following operations:

- compute the A_d matrix according to the last value of the estimated speed $\hat{\omega}_r$, by eight multiplications, according to Eq.5;
- compute the new coefficients of the L_d matrix, by two multiplications, according to Eq.6;
- compute the new estimate of the state vector (stator currents and rotor fluxes) according to Eq.3;
- compute the new estimate of the rotor speed according to Eq.2.

The evaluation of the integral in Eq.2 can be done by a simple rectangular approximation without affecting the precision.

Simulation Results

The algorithm implementations in floating point and fixed point have been tested by simulation on the same speed sensorless scheme of the field oriented induction motor drive on which the experimental results have been obtained. The induction motor rated quantities and parameters are shown in the Appendix, while the structure of the sensorless drive is presented in Fig.1. To simplify the analysis, the following assumptions have been made:

- ideal inverter (the voltage references are applied directly to the motor terminals);
- parameters tuning;
- absence of noise on the measured stator currents and voltages.

Fig.2 shows the results obtained for no-load starting conditions (0 to 1000 rpm speed reference step), followed by a torque step (at the rated value) after 0.56 seconds.
As it can be seen, the estimation errors are larger in the case of the fixed point algorithm, which makes all the calculations for the flux and speed estimation and for the control tasks using 16 bit integers. There is quite a relevant error for the shown estimated quantities, i.e. speed and stator currents. As a consequence, the estimated speed tends to have oscillations that could lead to an undulate motor speed. To avoid this situation the proportional term in the PI regulator on the speed loop has to be kept not too high, with a negative impact on the dynamic performance of the system. To allow the comparison of the results, the PI regulator parameters for the floating point implementation have been set at the same value of those used for the fixed point one.
To increase the global precision of the estimation we need to represent some of the variables in the algorithm on 32 bits. The equations that are susceptible of greater errors due to the finite length representations are the flux and the speed equation. If either of these are estimated with the variables expressed on 32 bits, the global precision increases very much. For example, in Fig.3 are presented the results obtained for the same test conditions, when the speed estimation is done on 32 bits. The estimated quantities are now very close to the real ones and the system behavior is quite similar to that using the floating point algorithm. As a direct consequence the coefficients of the speed regulator can be increased, so that the dynamic performance is improved. Again, for comparison purposes, the PI regulator parameters for the floating point scheme have been set at the same value of those used for the fixed point one (the value of the proportional gain is higher than the one used to obtain the results shown in Fig.2).

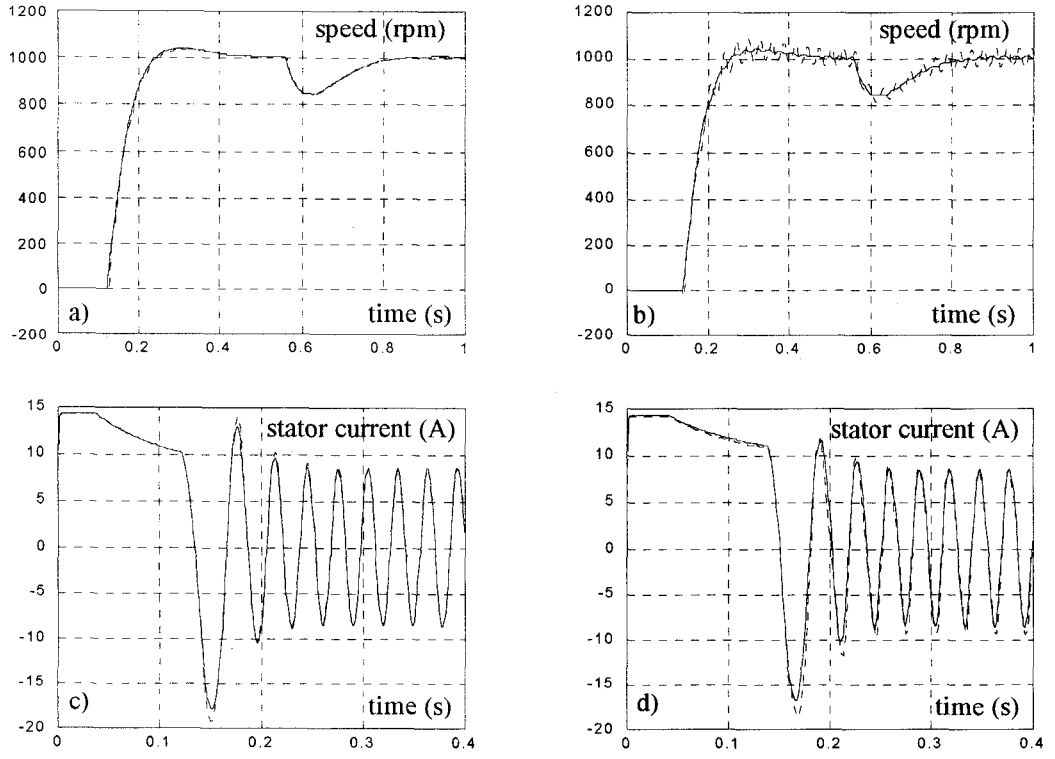


Fig.2: Simulation results for the sensorless induction motor drive using the floating point (a, c) and respectively the fixed point (b, d) algorithm implementation. In the fixed point implementation all variables are represented on 16 bits:
a, b: real (solid line) and estimated (dashed line) speed;
c, d: real (solid line) and estimated (dashed line) stator current on the stationary 'd' axis.

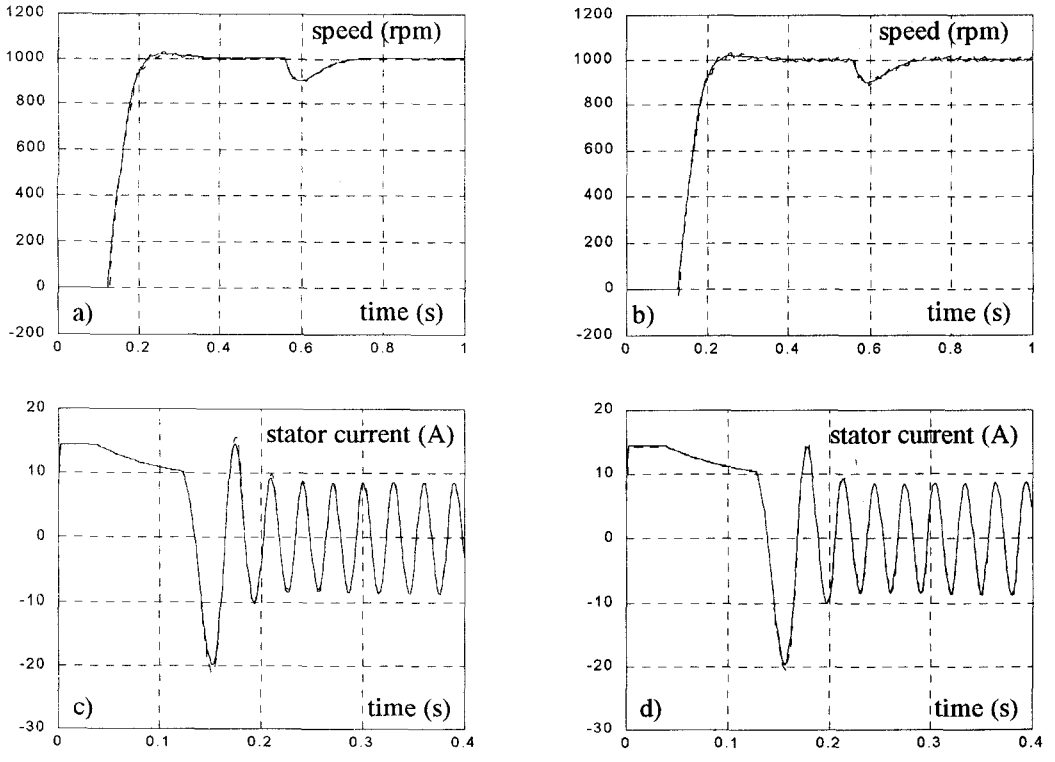


Fig.3: Simulation results for the sensorless induction motor drive using the floating point (a, c) and respectively the fixed point (b, d) algorithm implementation. In the fixed point implementation the variables in the speed estimation equation are represented on 32 bits:
a, b: real (solid line) and estimated (dashed line) speed;
c, d: real (solid line) and estimated (dashed line) stator current on the stationary 'd' axis.

Experimental Results

The floating point and fixed point algorithms have also been tested experimentally on the field oriented induction motor drive that has been previously simulated (induction motor rated quantities and parameters shown in the Appendix). The structure of the sensorless drive is again the one of Fig.1. All the control and estimation tasks for either the floating point and the fixed point implementations of the described sensorless scheme have been performed using a floating point DSP, the TMS320C30 by Texas Instruments. This DSP allows to perform operations either in floating point or in fixed point (and the data length can be chosen by the user). The sampling time for the acquisitions, for the outputs and for the calculations has been set at 200μs. The time needed to perform all the input/output and calculation tasks is 180μs.

A BJT inverter has been used, with the main switches rated 1200 V, 50 A. The switching frequency is 2.5 kHz.

Fig.4 shows the experimental results obtained for the same conditions that have been tested in simulation, i.e. no-load starting conditions (0 to 1000 rpm speed reference step), followed by a torque step (at the rated value). The stationary d axis current (Fig.4c,d) is shown in stationary conditions with no load. Again, the fixed point implementation has been made using 16 bit data for the flux and speed estimation and for the control tasks. These results are quite similar to those shown in Fig.2, with larger estimation errors in the case of the fixed point algorithm. It can be seen that even in the floating point implementation there are estimation errors which are larger than those in Fig.2a,c (where ideal conditions have been supposed). This is due to the presence of noise on the measured quantities and probably to detuning on the motor parameters, as it was shown in the analysis on the noise and parameters detuning effects, made in [1]. The proportional gain in the PI regulator on the speed loop has been kept not too high to avoid too large speed ripple in the fixed point algorithm (for comparison, the PI gains used in the floating point implementation are set at the same values used for the fixed point implementation).

In Fig.5 are presented the experimental results obtained for the same test and operating conditions, when the speed estimation is performed on 32 bits. Again, the experimental results are very similar to those shown in Fig.3, except for the presence of non-idealities, as already mentioned in the comment to Fig.4. The estimated quantities are very close to the real ones. The proportional gain in the PI regulator on the speed loop is higher than that used in the fixed point 16 bit implementation, leading to a better dynamic behavior.

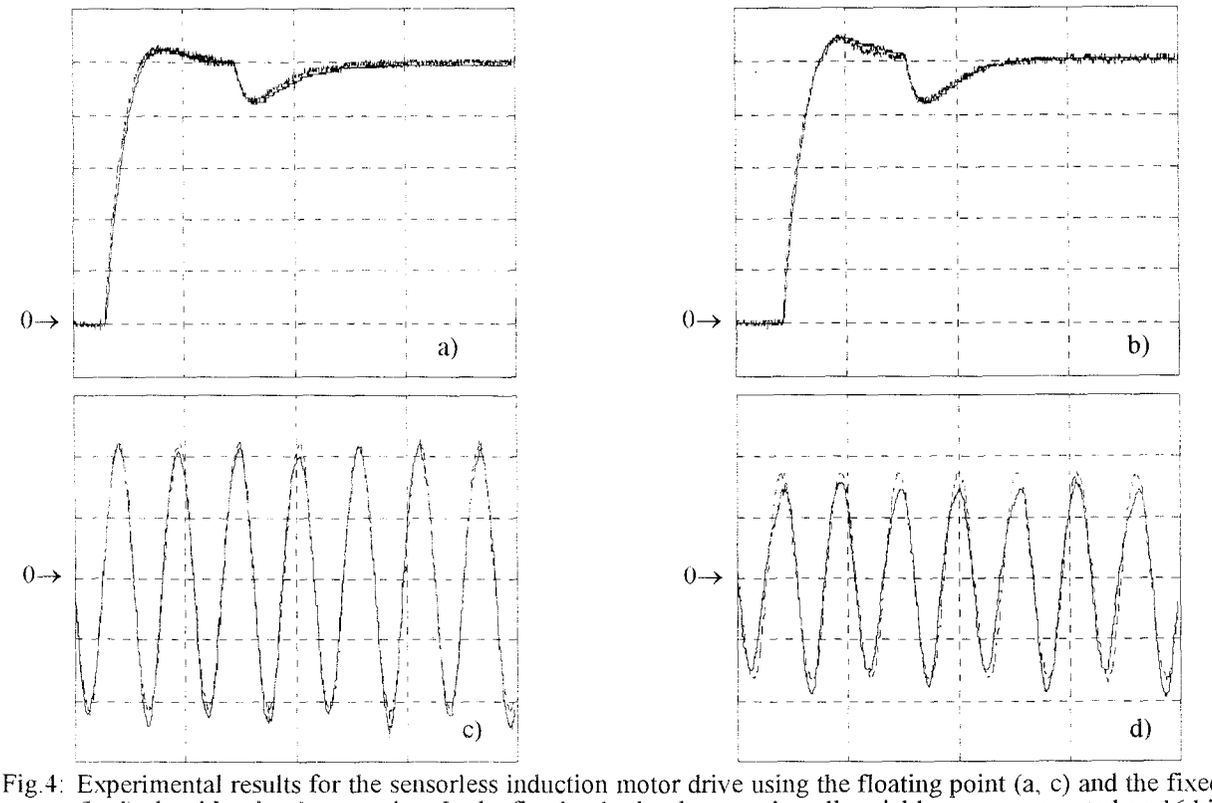


Fig.4: Experimental results for the sensorless induction motor drive using the floating point (a, c) and the fixed point (b, d) algorithm implementation. In the fixed point implementation all variables are represented on 16 bits: a, b: real (solid line) and estimated (dashed line) speed: time scale: 250 ms/div; vertical scale: 200 rpm/div; c, d: real (solid line) and estimated (dashed line) stator current on the stationary 'd' axis: time scale: 50 ms/div; vertical scale: 5 A/div.

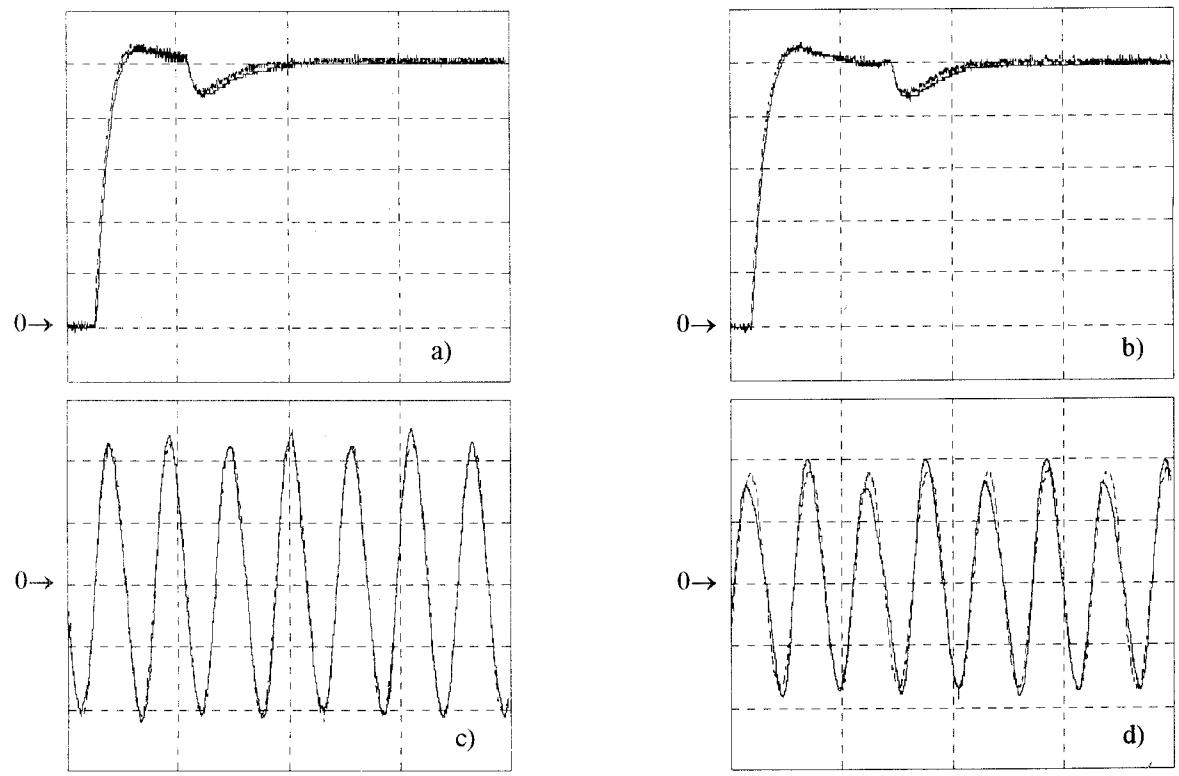


Fig.5: Experimental results for the sensorless induction motor drive using the floating point (a, c) and the fixed point (b, d) algorithm implementation. In the fixed point implementation the variables in the speed estimation equation are represented on 32 bits:
a, b: real (solid line) and estimated (dashed line) speed: time scale: 250 ms/div; vertical scale: 200 rpm/div;
c, d: real (solid line) and estimated (dashed line) stator current on the stationary 'd' axis: time scale: 50 ms/div; vertical scale: 5 A/div.

Conclusions

In this paper the possibility of using the fixed point processors in high performance sensorless induction motor drives has been discussed. The subject has become of greater relevance due to the appearance of new fixed point DSP microcontrollers expected to become a standard for the industry applications during the next years. The speed estimation method chosen for the fixed point implementation is the one that has been previously found optimal in respect with the performance versus complexity criterion. Further simplifications in the algorithm have been proposed to decrease the computation time and to minimize the errors due to the finite length representation. The simulation tests have shown that it is no important difference between the performance of the sensorless system using the fixed point and respective the floating point implementation.

Appendix

The induction motor parameters are:

Rated Output Power:	4	kW
Rated Torque	20	Nm
Rated Voltage:	250	V
Rated Frequency:	50	Hz
Rated Flux:	0.611	Vs
Poles:	4	
Rated Speed:	1430	rpm
Max Speed:	3000	rpm
Rated Power Factor:	0.87	
Rated efficiency:	0.85	
Inertia:	0.006	kg m^2
Stator Resistance:	0.6592	Ω
Rotor Resistance:	0.472	Ω
Stator Leakage Inductance:	4.29	mH
Rotor Leakage Inductance:	4.29	mH
Main Inductance	58.2	mH

References

[1] C.Ilas, A.Bettini, L.Ferraris, G.Griva, F.Profumo: "Comparison of Different Schemes without Shaft Sensors for Field Oriented Control Drives", Conf.Rec.IEEE-IECON'94, Bologna, Italy, September 1994, pp. 1579-1589, published on "Sensorless Control of AC Motor Drives" edited by K.Rajashekara, A.Kawamura, K.Matsuse, IEEE Press, pp.30-39.

[2] H.Kubota, K.Matsuse: "Speed Sensorless Field-Oriented Control of Induction Motor with Rotor Resistance Adaption", *IEEE Transactions on Industry Applications*, Vol. IA-30, No.5, 1994.

[3] H.Kubota, K.Matsuse, T.Nakano: "New Adaptive Flux Observer of Induction Motor for Wide Speed Range Motor Drives", Conf.Rec.IEEE-IECON'90, pp. 921-926.

[4] G.Griva, F.Profumo, C.Ilas, R.Magureanu, P.Vranka: "A Unitary Approach to Speed Sensorless Induction Motor Field Oriented Drives Based on Various Model Reference Schemes", Conf.Rec.IEEE-IAS'96, San Diego, USA, October 1996, pp. 1594-1599.

[5] C.Ilas, R.Magureanu: "A General Adaptation Mechanism and its Applications to Induction Motor Direct Field Oriented Drives", Conf.Rec.IEEE-ISIE'96, Warsaw, Poland, June 1996, pp. 923-928.

[6] "TMS320C240, TMS320F240 DSP Controllers" - Data Book, Texas Instruments, 1997.

A New Hybrid Vector Control for Induction Motor without Speed and Position Sensors

----- Frequency Hybrid Approach Using New Indirect Scheme -----

Shinji Shinnaka, Members, IEEE, IEE Japan
Kanagawa University
3-27-1 Rokkakubashi, Kanagawa-ku, Yokohama 221 JAPAN
Fax: +81-45-491-7915 Phone: +81-45-481-5661
E-mail: shinnaka@cc.kanagawa-u.ac.jp

Abstract – This paper proposes a new hybrid vector control scheme for induction motors without speed and position sensors. It has the following interesting and distinguished features. Employed field orientation is pure rotor flux orientation. Field orientation scheme requires neither velocity nor position estimation at all. It is a completely seamless hybrid of indirect and direct orientation schemes and indirect one is quite new and simple. Estimates of both rotor and stator fluxes can be obtained. It is completely free from variation of rotor electrical parameters in most of operation cases. Instant estimate of rotor velocity for speed control is available. Rigorous numerical experiments are carried out in order to examine torque response with constant velocity in both of motoring and regenerating operations, torque response in four-quadrant operation with variable velocity, and speed response to variable command in which maximum and minimum values are 500 and 1(rad/sec) respectively, acceleration and deceleration are ± 400(rad/sec^2). Result shows high potential usefulness of proposed hybrid scheme.

I . INTRODUCTION

A number of sensorless vector control schemes have been proposed for seeking practically usable performance so far[1].[4]. In addition to difference on oriented flux and orientation methodology, taking account of estimation methods for such velocity, slip-frequency, flux, variation of reported schemes might diverge. However it still remains as a question what kind of scheme will be able to meet best rigid servo control specification requiring instant and accurate torque response, dynamic variable speed response and load accommodation over wide range etc.

One of potential candidates for such will be hybrid scheme that can exploit preferable characteristics of several schemes. De Doncker et al.[5] proposed a vector control scheme where orientation could be changed between rotor flux, stator flux and air-gap flux, and making transition of indirect vector control in the low velocity range to direct vector control in high velocity range. Bose et al.[6] proposed a vector control scheme which is basically direct vector control with stator flux orientation in whole velocity range, but use indirect one only for start-up at zero-velocity and shut down, where indirect and indirect modes are changed discontinuously. Tajima et al.[7] proposed another switching type vector control scheme where two methods of generating synchronous angular frequency in indirect form are used and they are discontinuously switched to each other before and after zero-crossing of synchronous angular frequency. One of them is based upon mechanical velocity model of motor with load and requires its mechanical dynamics.

This paper proposes a new hybrid vector control scheme for induction motors without speed and position sensors. It is newly developed and has the following interesting features distinguished from previous ones.

1) Employed field orientation is pure rotor flux orientation for all operation condition, which is the most preferable for vector control to yield linear torque response[2],[3].
2) Our field orientation scheme requires neither velocity nor position information of rotor at all. Consequently no sensors and no algorithmic estimators for such information are necessary for field orientation. It is free from estimation problems such as limitation of dynamic operation range ensuring validity of estimate, accuracy of estimate, speed of estimation etc[6].
3) It is a hybrid of indirect and direct orientation schemes where hybridization is made linearly in frequency domain. It is completely seamless and requires no switching of indirect and direct orientation schemes at all.
4) As byproduct of field orientation process, estimates of both rotor and stator fluxes are obtained. Therefore flux controller can be easily realized if necessary to control transient response as well as level of rotor flux.
5) Our field orientation scheme needs rotor parameters such as time constant only for transient control of flux. But it does not at all for operation keeping rotor flux level constant, which is the case encountered in servo control. In other words, in most of operation cases it is

0-7803-3823-5/97/$10.00© 1997 IEEE

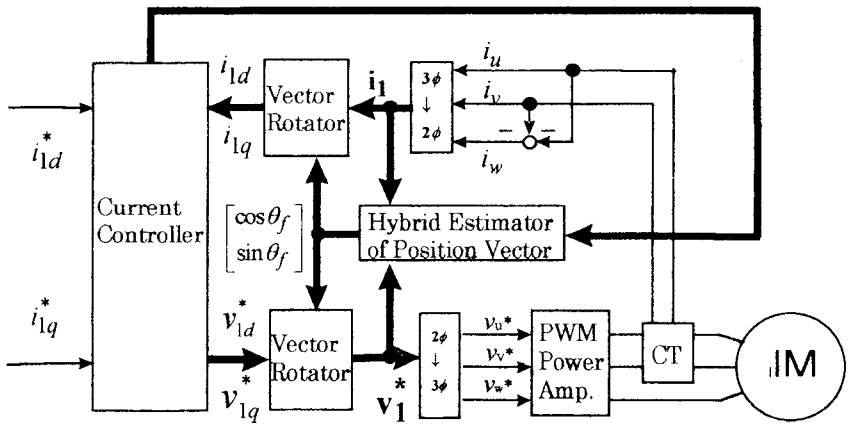


Fig. 1 Configuration of an example of proposed hybrid vector control system for induction motors

completely free from variation of rotor parameters caused by change of temperature and/or flux level of the motor.

6) If necessary such as for speed control, estimate of rotor velocity can be obtained via a simple calculation with synchronous frequency generated in the hybrid orientation process. Since our velocity estimation requires no dynamics and is instant, it is possible to attain relatively wide speed control band for instance 100(rad/sec) for a class of one(kW) induction motors.

II. FREQUENCY WEIGHTED HYBRID ESTIMATION OF FLUX POSITION

In order to establish vector control oriented to rotor flux, position information on rotor flux is essentially necessary. In the case that position or velocity information of the rotor cannot be obtained directly by sensor it must be estimated or generated appropriately. However it would be difficult for single scheme to attain better estimation or generation of the flux position both in every aspect of performance and over wide dynamic operation range. From this standpoint, we estimate or generate the flux position using complex schemes simultaneously, especially one good in low velocity range and the other good in high velocity range.

Let θ denote the flux position of the rotor. What we need to realize vector control is its sinusoidal values such as $cos\theta$ and $sin\theta$, which we refer to as 2x1 position vector $[cos\theta \quad sin\theta]^T$ in the following. According to the above manner, let $[cos\theta_1 \quad sin\theta_1]^T$ be position vector estimate by scheme 1 and $[cos\theta_2 \quad sin\theta_2]^T$ by scheme 2.

We produce single final estimate $[cos\theta_f \quad sin\theta_f]^T$ by combining two estimates as follows:

$$\begin{bmatrix} cos\theta_f \\ sin\theta_f \end{bmatrix} = F(s)\begin{bmatrix} cos\theta_1 \\ sin\theta_1 \end{bmatrix} + (1-F(s))\begin{bmatrix} cos\theta_2 \\ sin\theta_2 \end{bmatrix} \quad (1)$$

where F(s) is a weighting factor with low-pass characteristics of F(0)=1 and appropriate frequency band width.

Our hybrid estimation has the following features

1) Two estimates by different schemes are hybridized in sense of linear weighting in frequency domain.
2) Hybridization is seamless in frequency domain.
3) Weighting factor characterizing final estimate can be easily obtained and changed by designing a low-pass filter.

Figure 1 shows block diagram of an example of proposed vector control system with current controller, where thick line indicates line of vector signal consisting of several scalar signals, hybrid position estimator gets signals both in synchronous and stationary frames, and output of the position estimator is fed to a couple of vector rotators as final estimate of position vector of normalized rotor flux. In this example, voltage command is used as stator voltage information for simplicity. Of course, actual value of voltage can be used if additional cost of measurement is allowed.

III. NEW INDIRECT VECTOR CONTROL SCHEME

We here show a new rotor flux oriented indirect vector control scheme , which requires no velocity information of rotor at all, consequently is inherently free from velocity sensor of rotor.

We can derive the following relationship between velocity ω of d-q coordinates and interior states of induction motor.

$$\omega L_{1t} i_{1q} = -\left(v_{1d} - R_1 i_{1d} - s\phi_{1d} + \omega\phi_{2nq}\right) \quad (2)$$

$$\omega\phi_{1d} = v_{1q} - \left(sL_{1t} + R_1\right) i_{1q} - s\phi_{2nq} \quad (3)$$

$$(s+W_2)\phi_{2nd} = R_{2n}i_{1d} + (\omega - \omega_{2n})\phi_{2nq} \quad (4)$$

$$(s+W_2)\phi_{2nq} = R_{2n}i_{1q} - (\omega - \omega_{2n})\phi_{2nd} \quad (5)$$

with newly defined normalized parameters and normalized state as

$$L_{1t} = L_1 - \left(\frac{M}{L_2}\right)M \quad (6)$$

$$W_2 = \frac{R_2}{L_2} \quad (7)$$

$$R_{2n} = \left(\frac{M}{L_2}\right)^2 R_2 \quad (8)$$

$$\phi_{2n} = \left(\frac{M}{L_2}\right)\phi_2 \quad (9)$$

where non-mentioned symbols of variables and parameters follows conventional meaning, and suffix d, q attached to variables indicates d, q element of signals in d-q coordinates respectively.

It should be noted that coordinates velocity ω in equations (2)-(5) is arbitrary. Allowable selections of the velocity ω for deriving rotor flux oriented indirect vector control schemes are such that d-axis can synchronize with normalized rotor flux. We can easily derive such three selections as follows:

1) Selection based on equation (2)

$$\omega L_{1t}i_{1q} = -(v_{1d} - R_1 i_{1d} - s\phi_{1d}) \quad (10)$$

sustaining

$$\omega\phi_{2nq} = 0 \quad (11)$$

2) Selection based on equation (3)

$$\omega\phi_{1d} = v_{1q} - (sL_{1t} + R_1)i_{1q} \quad (12)$$

sustaining

$$s\phi_{2nq} = 0 \quad (13)$$

3) Selection based on equation (5)

$$\omega = \omega_{2n} + \frac{R_{2n}i_{1q}}{\phi_{2nd}} \quad (14)$$

sustaining

$$(s+W_2)\phi_{2nq} = 0 \quad (15)$$

Every selection in equations (10), (12), (14) requires stator or rotor flux in rotor flux orientation. These can be observed by means of observer. We can easily derive basic equation for the observer, which yields estimates of stator and/or rotor flux in rotor flux orientation in equations (10), (12), (14), from equation (5) as follows:

$$(s+W_2)\phi_{2nd} = R_{2n}i_{1d} \quad (16)$$

$$\phi_{1d} = L_{1t}i_{1d} + \phi_{2nd} \quad (17)$$

which also sustains such convergence of q-element of rotor flux as

$$(\omega - \omega_{2n})\phi_{2nq} = 0 \quad (18)$$

Conventional rotor flux oriented indirect vector control scheme, so called slip frequency type vector control scheme exploits selection 3) with equation (16). In stead of conventional sensorless schemes based on equation (14) in selection 3), selection 1) or 2) can be utilized. We here newly propose an indirect vector control with rotor flux orientation based on selection 2) along with equations (16), (17).

Basic but key points of our proposed scheme for generating synchronous angular velocity are arranged in the following compact form.

$$\hat{\phi}_{2nd} = \frac{R_{2n}}{s+W_2}i_{1d} \quad (19)$$

$$\hat{\phi}_{1d} = L_{1t}i_{1d} + \hat{\phi}_{2nd} \quad (20)$$

$$\omega = \frac{v_{1q} - (sL_{1t} + R_1)i_{1q}}{\hat{\phi}_{1d}} \quad (21)$$

It can be clearly understood that our indirect scheme has the following features.

1) It inherently requires no velocity or position information of the rotor at all. Subsequently it is free from velocity estimation and its associated problems[6].
2) Since equation (13) does not necessarily mean $\phi_{2nq} = 0$ in every case. There is possibility that usable operation range would be limited.
3) Both rotor and stator fluxes are observed via single observer. Flux observer is basically the same as that of conventional indirect vector control.
4) In most of the case that stator d-current (magnetizing current) i_{1d} is set to be constant, generating synchronous frequency can be completely free from rotor parameter, and consequently from influence of its variation. We point out that in this case the following relationship is sustained,

$$\phi_{1d} = L_1 i_{1d} \quad (22)$$

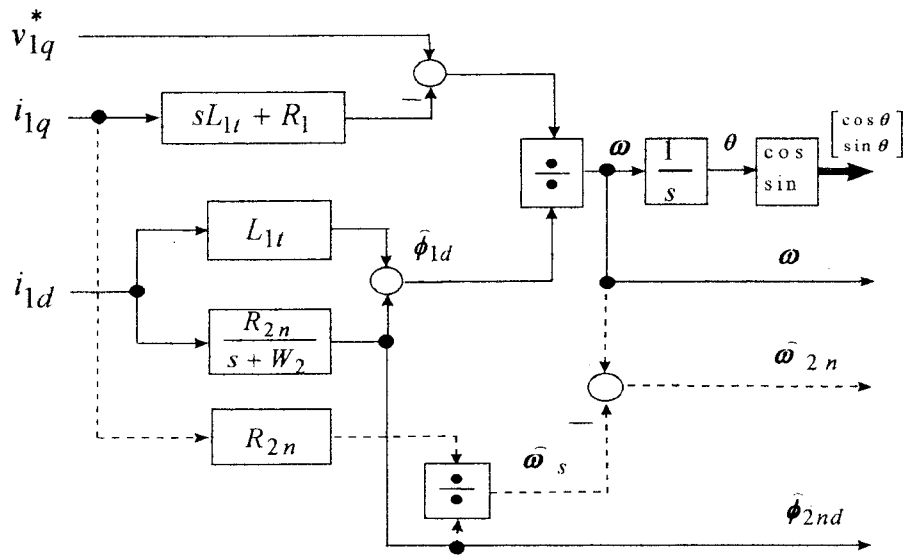


Fig. 2 Main part of proposed indirect scheme where position vector, synchronous angular frequency, estimate of rotor flux and estimate of electrical angular velocity of rotor are produced

and the observer can be also simplified.

5) Division by signal is necessary in performing the process in equation (21) just like in equation (14) of convention. In the case that stator d-current is set to be constant, this can be avoided.

Since torque is generated linearly to stator q-current(producing torque current) command once field orientation with current control is attained and stator d-current is held constant, torque command is given in conventional manner.

In situation that velocity of rotor has to be controlled rather than torque, speed controller must be implemented, which requires rotor velocity. In our vector control, electrical angular velocity of rotor can be easily and instantaneously estimated in the following manner

$$\hat{\omega}_s = \frac{R_{2n}}{\hat{\phi}_{2nd}} i_{1q} \tag{23}$$

$$\hat{\omega}_{2n} = \omega - \hat{\omega}_s \tag{24}$$

where $\omega, \hat{\omega}_s, \hat{\omega}_{2n}$ are synchronous angular frequency generated in accordance with equations (19)-(21), estimate of slip angular frequency and estimate of angular velocity of rotor, respectively. Note that estimate of normalized rotor flux $\hat{\phi}_{2nd}$ has been already available in process of generation of synchronous angular frequency.

As clearly seen from equations (23), (24), estimation of angular velocity requires no dynamics and is instant. This means that time delay of estimation to actual varying velocity is almost minimized, and that relatively wide speed control band can be attained.

Figure 2 shows as an example a block diagram of main part in proposed indirect vector control scheme, where voltage command is used for cost decreasing stead of measured voltage, generated synchronous frequency ω is integrated to yield possible position θ of normalized rotor flux, and this position is converted into its associated position vector. As depicted by dashed line, estimate of electrical velocity of rotor can be easily obtained if necessary for speed control as well as estimate of normalized rotor flux.

IV. DIRECT SCHEME WITH HIGH-PASS FILTER

Now let us establish the high-frequency part $\begin{bmatrix}\cos\theta_2 & \sin\theta_2\end{bmatrix}^T$ of position vector in equation (1). We access to this objective via approach of direct vector control.

Stator equation in stationary frame can be expressed in such induced voltage form as

$$s\boldsymbol{\phi}_{2n} = \boldsymbol{v}_1 - \left[sL_{1t} + R_1\right]\boldsymbol{i}_1 . \tag{25}$$

Multiplying both sides of the above equation by (1-F(s))/s , where F(s) is a low-pass filter, yields

$$\left(1 - F(s)\right)\phi_{2nd}\begin{bmatrix}\cos\theta \\ \sin\theta\end{bmatrix} = \frac{\left(1 - F(s)\right)}{s}\left(\boldsymbol{v}_1 - \left[sL_{1t} + R_1\right]\boldsymbol{i}_1\right) \tag{26}$$

where ϕ_{2nd} denotes normalized rotor flux in synchronous frame exactly oriented to rotor flux, In most operation cases that magnitude of the rotor flux vector is controlled to be constant, equation (26) is reduced to

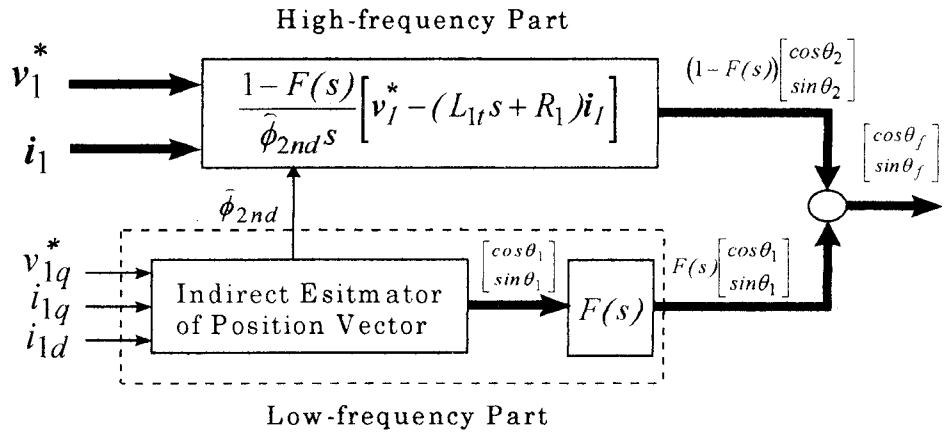


Fig. 3 Configuration of hybrid estimator of position vector

$$\left(1-F(s)\right)\begin{bmatrix}\cos\theta\\ \sin\theta\end{bmatrix}=\frac{\left(1-F(s)\right)}{\phi_{2nd}\,s}\left(v_1-\left[sL_{1t}+R_1\right]i_1\right). \quad (27)$$

Equation (27) describes the relationship between high-passed position vector of rotor flux and stator vector signals.

Basically according to equation (27), we estimate high-frequency part of the position vector in equation (1). In practice, some of measured variables in equation (27) can be replaced by their estimates such as command signals.

It might be pointed out that our basic estimating equation requires pure integration, which is unstable, and is unusable in practice. However this first glance is not necessarily true. Select weighting factor F(s) of low-pass characteristics with F(0)=1 as in form of

$$F(s)=\frac{f_0}{s^n+f_{n-1}s^{n-1}+\cdots+f_1s+f_0} \quad (28)$$

which can be easily designed so as to have both desired stability and specified low-pass characteristics. Then the filter directly applied to stator variables of voltage and current results in

$$\frac{1-F(s)}{s}=\frac{s^{n-1}+f_{n-1}s^{n-2}+\cdots+f_1}{s^n+f_{n-1}s^{n-1}+\cdots+f_1s+f_0}. \quad (29)$$

It should be noted that the filter (1-F(s))/s no longer have high-pass characteristics, it generally have band-pass or low-pass characteristics, and that it is as stable as desired, and does require neither pure nor approximated integration at all. This features make our direct scheme with filter distinguished from conventional direct ones that take pure or approximated integration and is almost under unstable condition.

It should be also noted that high-passed position vector is not generally a unit vector, and that its reasonable estimation needs information of normalized rotor flux magnitude as clearly shown in equation (27). This requirement makes no problem so long as it is utilized as a part of our hybrid position estimator where estimate of normalized rotor flux is available.

Figure 3 shows an example of our hybrid position estimator where our new indirect scheme in equations (19)-(21) is employed to realize basic estimator in low frequency part of the estimator, and above explained direct scheme with filter as high-frequency part. It is seen that estimate of normalized rotor flux obtained from the flux observer in indirect part is fed to direct part (high-frequency part). We note as results of rigorous numerical experiments that once indirect part is realized in hybrid position estimator as in the structure it can functions in all dynamic range, subsequently such estimates yielded from indirect part as rotor flux, stator flux, slip angular frequency, electrical velocity of rotor can be available in all dynamic range.

VI. NUMERICAL EXPERIMENTS

In order to examine basic performance of the proposed hybrid scheme, extensive numerical experiments have been taken. We show some of them as examples.

Parameters of the motor used in the numerical experiment is shown in TABLE I. Low-pass filter F(s) in hybrid vector control for the above motors is selected as follows:

$$F(s)=\frac{50}{s+50}$$

Both d and q current controllers are designed so as to attain band width of 2000(rad/sec), and d-current(magnetizing current) command is set to rated value 10(A). In addition to current loop, decoupling loop is made for overcome of nonlinearity depending on rotor velocity.

TABLE. I
Motor Parameters for Numerical Experiment

rated power	760(W)	R_1	0.407(Ω)
maximum load	500(%)	L_{1t}	3.46(mH)
rated d-current	10(A)	R_{2n}	0.385(Ω)
rated q-current	10(A)	W_2	15.3(Ω/H)
rated velocity	100(rad/sec)	pole pair	3
rated torque	7.57(Nm)	moment of inertia J_m	0.0179(kg m^2)
torque coefficient K_t	0.757(Nm/A)	friction coefficient D	0.001(Nm/(rad/sec))

Results of three classes of experiments such as torque control for constant velocity, torque control for variable velocity and variable speed control are shown as examples.

A. Torque control for constant velocity

The purpose of this experiment is to examine characteristics of torque response of the induction motor driven by proposed scheme where velocity of the motor is regulated constant by load machine.

1) Experiment A-1(100% motoring operation)

Q-current(torque producing current) command is set to positive rated value i.e. +10(A) and rotor velocity regulated by load machine is changed from positive 100(rad/sec) to 80,60,40,20,0 (rad/sec) sequentially in stepwise manner. Figure 4 shows the results where part (a) depicts d-current, its command and estimates of d-component of normalized rotor flux and stator flux, part (b) q-current, its command and produced torque, part (c) synchronous angular frequency and electrical angular velocity of rotor, part (d) mechanical angular velocity of rotor and its estimate. It is observed that in spite of change of rotor velocity from rated velocity to standstill torque is produced appropriately at constant value 7.57(Nm). Estimate of rotor velocity is also fine, which is not used in this torque control.

2) Experiment A-2

(100% regenerating operation)

After q-current command is changed to negative rated value i.e. −10(A) and rotor velocity regulated by load machine is changed from positive 100(rad/sec) to 80,60,40,20,0 (rad/sec) sequentially in stepwise manner. Figure 5 shows the results similar to that of Experiment A-1 of 100% motoring operation. i.e. in spite of change of rotor velocity from rated velocity to standstill torque is produced appropriately at constant value −7.57(Nm) and rotor velocity is properly estimated.

From extensive experiments including above two, it is concluded that our hybrid vector control scheme can produce stable torque independent on constant velocity of rotor in both motoring and regenerating operations including standstill.

B. Torque control for variable velocity

The purpose of this experiment is to examine characteristics of torque response of induction motor under four-quadrant operation with variable velocity where load machine is free. We have special interest on hybridization phenomenon around 50(rad/sec) of synchronous angular frequency.

As a q-current command rectangular signal of amplitude 10(A) and period 5(secs) is applied to the hybrid vector control system. Figure 6 shows the results.

It is observed from part (b) that except for around zero-crossing of synchronous angular frequency torque is produced very properly, and that torque response is seamless around hybridizing frequency 50(rad/sec). Torque vibration, which is relatively small compared with average torque, starts just before zero-crossing of synchronous frequency and decreases quickly after zero-crossing. The influence of small torque vibration to both synchronous frequency and rotor velocity can not be seen in parts (c), (d). And estimation of rotor velocity is also carried out properly as seen in part (d).

It should be noted that small torque vibration is related to zero-crossing of not rotor velocity but synchronous frequency, and that generations of both torque and synchronous angular frequency are proper around hybridizing angular frequency. In this example, maximum rotor velocity exceeds five times of rated value.

C. Variable speed control

The purpose of this experiment is to examine characteristics of speed control of the induction motor driven by proposed scheme. Our interests on speed control are focused on the following.

1) Is it possible to attain speed band width of more than 50(rad/sec) in class of one(kW) motors? Moment of inertia of this class is small enough to attain speed band width of 100(rad/sec) if actual and instant velocity of rotor is available, Success depends highly on performance of velocity estimation. As long as we know no conventional sensorless vector control schemes have attained stable band width of more than 50(rad/sec)
2) Is it possible to track velocity command with angular acceleration of 400(rad/sec^2)? Is it possible to track velocity command which decreases from rated to slow velocity with deceleration of -400(rad/sec^2) and keeps the slow velocity including standstill?

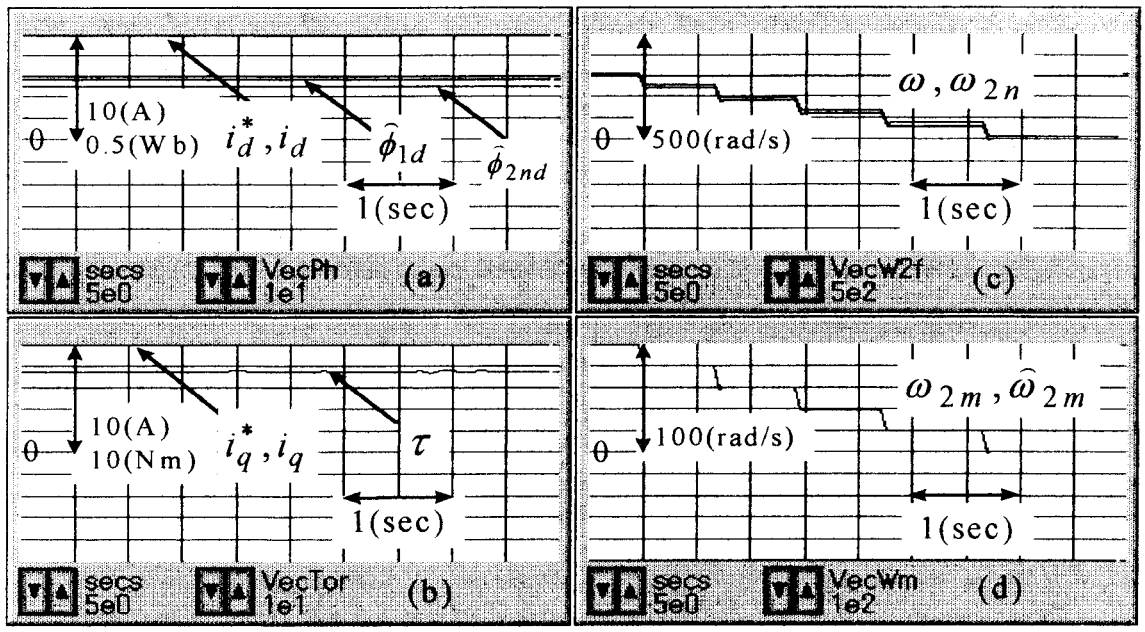


Figure 4 Result of experiment A-1 of100% motoring operation with constant speed

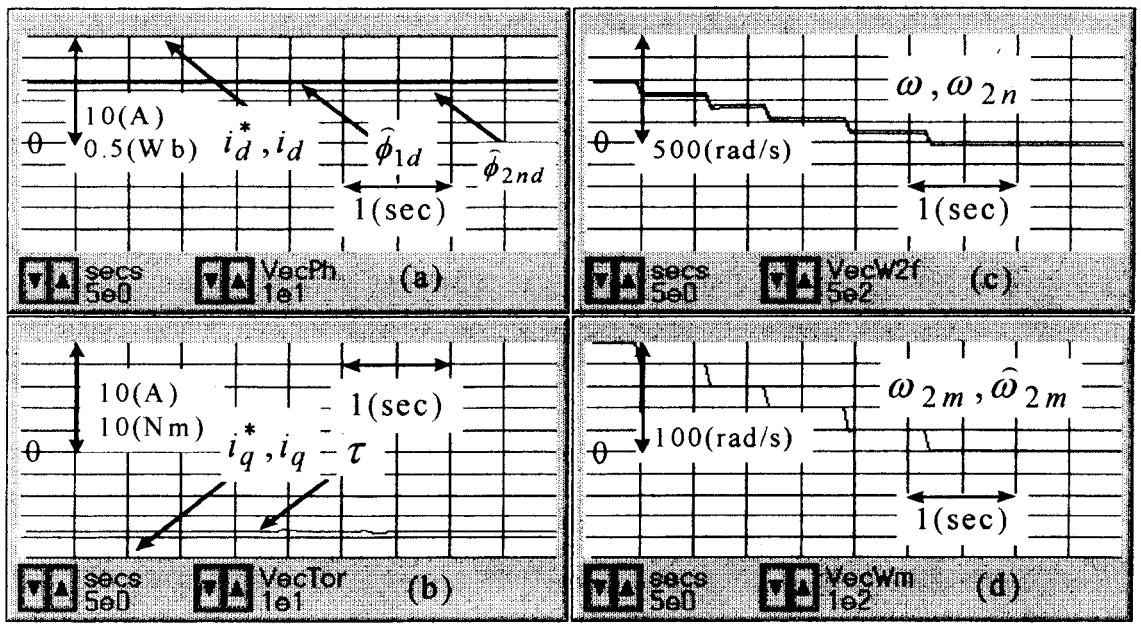


Figure 5 Result of experiment A-2 of 100% regenerating operation with constant speed

1) Experiment C-1(Step response)

We utilize step response of speed control for examining speed band width. Figure 7 shows an example of results of experiments where PI controller is employed as speed controller and is designed to attain band width of 100(rad/sec). As observed from time constant 0.01(sec) of step response, band width of 100(rad/sec) is successfully attained as designed.

2) Experiment C-2(Tracking response)

In order to examine tracking capability, we prepare velocity command in which maximum and minimum values are 500 and 1(rad/sec) respectively, acceleration and deceleration are positive and negative 400(rad/sec^2) in mechanical angular frequency respectively. Figure 8 shows tracking response to this velocity command.

In the figure both velocity command and actual controlled velocity are depicted. Velocity estimation is successful and the difference between actual and estimated values of velocity is non-visibly small. It can be seen that our expected tracking performance is well attained.

VI. CONCLUDING REMARKS

This paper have proposed a new hybrid vector control scheme for induction motors without

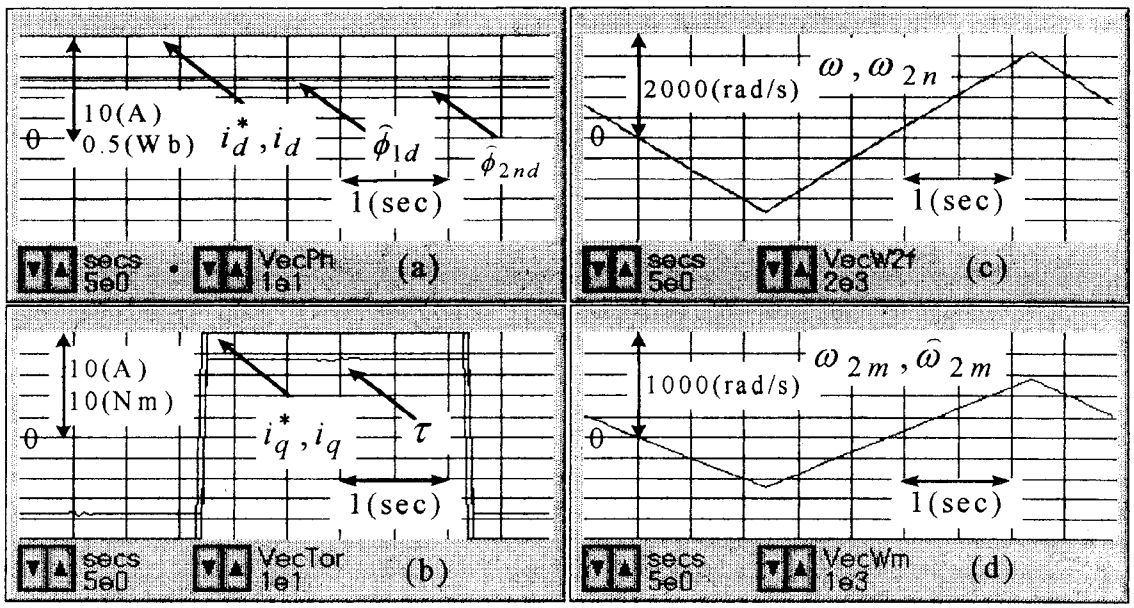


Figure 6 Result of experiment of four-quadrant operation with 100% torque

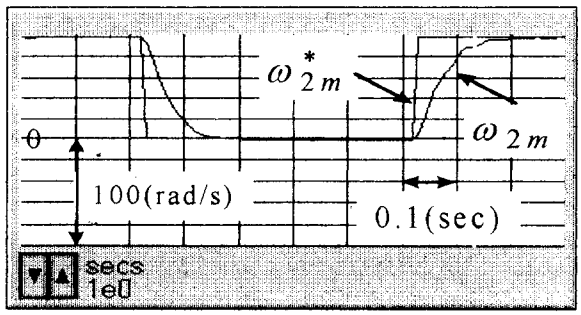


Figure 7 Result of experiment C-1
(step response of speed control)

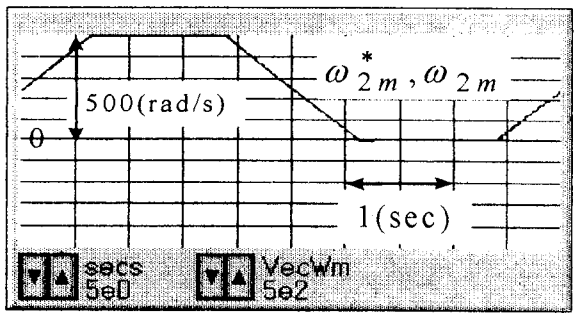


Figure 8 Result of experiment C-2
(tracking response of speed control)

velocity and position sensors. Although presented examination of performance of our scheme is limited to numerical experiments, a number of results show us high potential usefulness. One will be able to understand easily its potentiality by comparison with both algorithmic simplicity and performance in numerical experiments of conventional schemes. Experiment with hardware is now in preparation.

REFERENCES

[1] B. K. Bose(editor), "Power electronics and variables frequency drives", IEEE press, 1997

[2] H. Ohnishi and K. Miyachi, "Principle of constant magnitude regulation of secondary flux based on slip frequency in induction motor drive", Proc. Int. Conf. on Electrical Machines, Part 1, pp. 203-206, 1982

[3] S. Shinnaka, N. Sakakibara and H. Fukazawa, "A unified vector analysis for vector control of induction motors". Trans. of Society of Instrumentation and Control Engineers(Japan), Vol. 30, No. 7, pp. 760-766, July, 1994

[4] K. Rajashekara, A. Kawamura and K, Matuse, "Sensorless control of AC motor drives, Speed and position sensorless operation", IEEE press, 1996

[5] R. W. De Doncker and D. W. Novotony, "The universal field oriented controller", IEEE trans. Ind. Appl. Vol. 30, pp. 92-100, Jan./Feb., 1994

[6] B. K. Bose, M. G. Simoes, D. R. Crecelius, K. Rajashekara and R. Martin, "Speed sencorless hybrid vector controlled induction motor drive", IEEE IAS Ann. Mtg. pp. 137-143, 1995

[7] T. Tajima, H. Umida and H. Tetsutani, "Zero-cossing speed control by sensorless vector control with instantaneous speed estimation", IEE Japan industrial applications society, national convention recordⅢ, pp.219-220, 1996

Behavior of Sensorless Induction Motor Drives in Regenerating Mode

Hisao Kubota Kouki Matsuse
Dept. of Electrical Engineering
Meiji University
1-1-1, Higashi-mita, Tama-ku
Kawasaki 214
JAPAN
Phone: +81-44-934-7296
Fax: +81-44-934-7909
E-mail: kubota@isc.meiji.ac.jp
matsuse@isc.meiji.ac.jp

Yoichi Hori
Dept. of Electrical Engineering
The University of Tokyo
2-11-16, Yayoi, Bunkyo-ku
Tokyo 113
JAPAN
+81-3-3812-2111 Ext. 7680
+81-3-5800-3865
hori@kaya.t.u-tokyo.ac.jp

Abstract–**This paper presents two kinds of sensorless vector control methods of induction machines which work stably even in regenerating mode. These methods take the stator resistance variation into account.**

I. INTRODUCTION

A lot of sensorless induction motor drive methods have been proposed[1]-[11]. For most methods, the mismatch of the stator resistance affects the speed estimation in low speed range. The method proposed in [11] utilizes the instantaneous reactive power and does not need the stator resistance value. Therefore this method is robust against the stator resistance variation. However, this method is unstable in the regenerating mode.

This paper proposes two kinds of sensorless induction motor drive methods which are robust against the stator resistance variation and are stable in powering and regenerating modes. One is based on the instantaneous reactive power measurement. The other is based on the on-line stator resistance identification. Advantages and disadvantages for both methods are discussed.

II. SPEED ESTIMATION USING INSTANTANEOUS REACTIVE POWER

An induction motor can be described by following equations in the stationary reference frame.

Stator:

$$\boldsymbol{v}_s = (R_s + \sigma L_s \mathrm{P})\boldsymbol{i}_s + (M/L_r)\mathrm{P}\boldsymbol{\psi}_r \tag{1}$$

Rotor:

$$\mathbf{0} = M\boldsymbol{i}_s/\tau_r + (1/\tau_r + \mathrm{P})\boldsymbol{\psi}_r - \omega_r \mathbf{J}\boldsymbol{\psi}_r \tag{2}$$

where

$\boldsymbol{i}_s = \begin{bmatrix} i_{ds} & i_{qs} \end{bmatrix}^{\mathrm{T}}$: Stator Current

$\boldsymbol{\psi}_r = \begin{bmatrix} \psi_{dr} & \psi_{qr} \end{bmatrix}^{\mathrm{T}}$: Rotor Flux

$\boldsymbol{v}_s = \begin{bmatrix} v_{ds} & v_{qs} \end{bmatrix}^{\mathrm{T}}$: Stator Voltage

$\mathbf{J} = \begin{bmatrix} 0 & -1 \\ 1 & 0 \end{bmatrix}$

R_s, R_r : Stator and Rotor Resistance
L_s, L_r : Stator and Rotor Self Inductance
M : Mutual Inductance
σ : Leakage Coefficient, $\sigma = 1 - M^2/(L_s L_r)$
τ_r : Rotor Time Constant, $\tau_r = L_r/R_r$
ω_r: Motor Angular Velocity (Electric Angle)
P : d/dt

Instantaneous reactive power into the rotor is described by the stator variables or rotor variables as follows:

$$q = (\boldsymbol{v}_s - \sigma L_s \mathrm{P}\boldsymbol{i}_s) \times \boldsymbol{i}_s \tag{3}$$

or

$$q = \frac{M}{L_r}\left\{-\omega_r \boldsymbol{\psi}_r{}^{\mathrm{T}}\boldsymbol{i}_s - \frac{1}{\tau_r}(\boldsymbol{\psi}_r \times \boldsymbol{i}_s)\right\} \tag{4}$$

where $\times$: vector product.

For the sensorless drives, the motor speed or the rotor flux cannot be measured, so these variables are replaced by the estimated ones.

$$\hat{q} = \frac{M}{L_r}\left\{-\hat{\omega}_r \hat{\boldsymbol{\psi}}_r{}^{\mathrm{T}}\boldsymbol{i}_s - \frac{1}{\tau_r}(\hat{\boldsymbol{\psi}}_r \times \boldsymbol{i}_s)\right\} \tag{5}$$

In [11], the motor speed is estimated by the following equation.

$$\hat{\omega}_r = \mathrm{K_P}(q - \hat{q}) + \mathrm{K_I}\int (q - \hat{q})\mathrm{d}t \tag{6}$$

The rotor flux is estimated by Eq.(2) with the estimated speed. Although this algorithm does not need the stator resistance value, it becomes unstable in the regenerating mode.

In this paper, we propose the estimation of the motor speed and the rotor flux by the Extended Kalman Filter algorithm and the superimposition of the M-sequence signal on the magnetizing current command in order to stabilize the estimation and satisfy the Persistent Excitation condition (PE condition).

An induction machine can be described by following nonlinear state equation with the rotor flux and the motor speed as state variables.

$$\frac{\mathrm{d}}{\mathrm{d}t}\boldsymbol{x} = \boldsymbol{f}(\boldsymbol{x}) + \mathbf{G}\boldsymbol{w} \tag{7}$$

where $\boldsymbol{x} = \begin{bmatrix} \psi_{dr} & \psi_{qr} & \omega_r \end{bmatrix}^{\mathrm{T}}$

$$f(x)=\begin{bmatrix} -\psi_{dr}/\tau_r - \omega_r\psi_{qr} + Mi_{ds}/\tau_r \\ \omega_r\psi_{dr} - \psi_{qr}/\tau_r + Mi_{ds}/\tau_r \\ 0 \end{bmatrix}$$

w is the system noise, $\mathbf{G}$ is the weighting matrix of w.
Output equation is

$$y = h(x) + z \tag{8}$$

where $h(x) = q$ and z is the measurement noise.
The state equation is discretized and the rotor flux and the motor speed are estimated by using following Extended Kalman Filter algorithm.

$$\hat{\boldsymbol{x}}_{k|k} = \hat{\boldsymbol{x}}_{k|k-1} + \mathbf{K}_k\left[\boldsymbol{y}_k - \boldsymbol{h}_k\left(\hat{\boldsymbol{x}}_{k|k-1}\right)\right] \tag{9}$$

$$\hat{\boldsymbol{x}}_{k+1|k} = \boldsymbol{f}_k\left(\hat{\boldsymbol{x}}_{k|k}\right) \tag{10}$$

$$\mathbf{K}_k = \hat{\mathbf{P}}_{k|k-1}\mathbf{H}_k{}^{\mathrm{T}}\left[\mathbf{H}_k\hat{\mathbf{P}}_{k|k-1}\mathbf{H}_k{}^{\mathrm{T}} + \mathbf{P}_{vk}\right]^{-1} \tag{11}$$

$$\hat{\mathbf{P}}_{k|k} = \hat{\mathbf{P}}_{k|k-1} - \mathbf{K}_k\mathbf{H}_k\hat{\mathbf{P}}_{k|k-1} \tag{12}$$

$$\hat{\mathbf{P}}_{k+1|k} = \mathbf{F}_k\hat{\mathbf{P}}_{k|k}\mathbf{F}_k{}^{\mathrm{T}} + \mathbf{G}_k\mathbf{P}_{wk}\mathbf{G}_k{}^{\mathrm{T}} \tag{13}$$

where

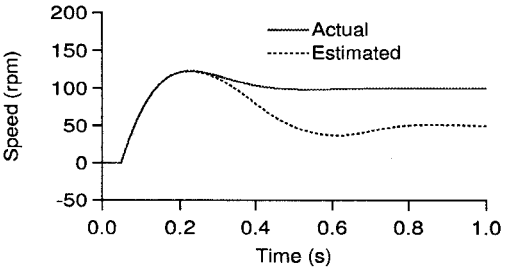
$$\mathbf{F}_k = \left.\frac{\partial \boldsymbol{f}_k(\xi_k)}{\partial \xi_k}\right|_{\xi_k=\hat{\boldsymbol{x}}_{k|k}} \qquad \mathbf{H}_k = \left.\frac{\partial \boldsymbol{h}_k(\xi_k)}{\partial \xi_k}\right|_{\xi_k=\hat{\boldsymbol{x}}_{k|k-1}}$$

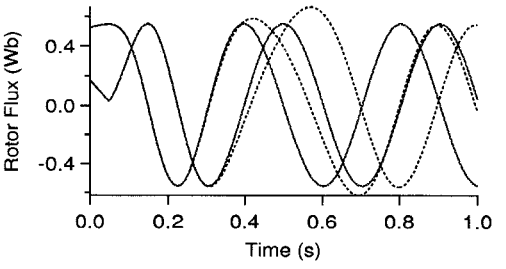
$\mathbf{P}_{wk}$, $\mathbf{P}_{vk}$: Covariance of the system noise and the measurement noise.
Fig. 1 shows the simulation results of the speed estimation in regenerating mode. The induction motor is controlled with a speed sensor and the estimated speed is not used for the control. The load torque is constant at -10Nm and the speed command changes from 0 to 100rpm at t=0.05s. Fig.(a) is the results for the algorithm proposed in [11]. The estimated speed is much less than the actual one. Fig.(b) shows the results for the proposed method. The amplitude of the M-sequence signal superimposed on the magnetizing current command is 1 [A], about 10% of the ratings. Although a little estimation error arises during transient condition, the estimated speed converges to the actual value.

Disadvantages of this method is that the differentiation of the stator current and the superimposition of the high frequency component on the magnetizing current are necessary. It makes the system sensitive to leakage inductance mismatch. When the leakage coefficient in the Extended Kalman Filter is 0.98 times as much as the actual one, the speed estimation become unstable as shows in Fig.1(c).

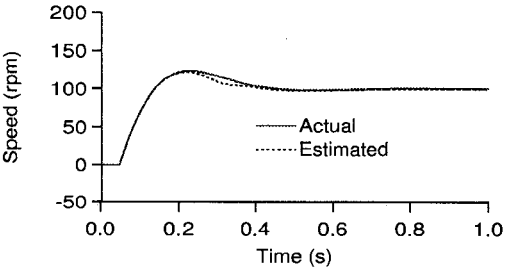
Table1 Ratings of Tested Induction Machine

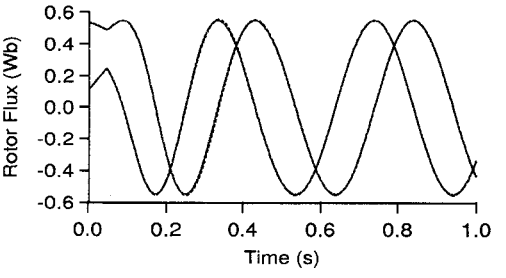
3.7kW 200V 15A
4poles 1420rpm at 50Hz



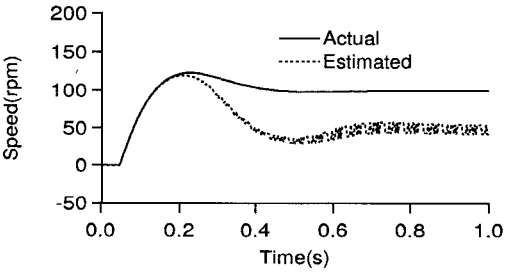


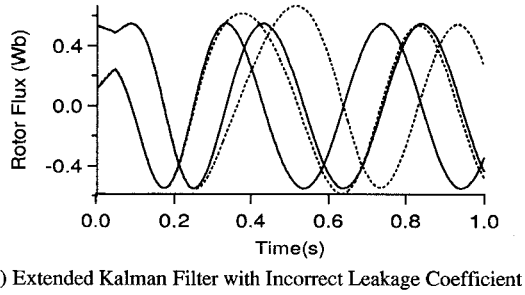
(a) Method in [11]





(b) Extended Kalman Filter with Correct Leakage Coefficient





(b) Extended Kalman Filter with Incorrect Leakage Coefficient

Fig.1 Simulation Results of Speed Estimation using Instantaneous Reactive Power

III. SPEED ESTIMATION WITH ON-LINE STATOR RESISTANCE ADAPTATION

From Eqs.(1) and (2) the induction motor is described following nonlinear state equation with the stator current, the rotor flux, the motor speed, and the stator resistance as state variables.

$$\frac{\mathrm{d}}{\mathrm{d}t}\boldsymbol{x} = \boldsymbol{f}(\boldsymbol{x}) + \mathbf{G}\boldsymbol{w} \tag{14}$$

where $\boldsymbol{x} = \begin{bmatrix} i_{ds} & i_{qs} & \psi_{dr} & \psi_{qr} & \omega_r & R_s \end{bmatrix}^{\mathrm{T}}$

$$\boldsymbol{f}(\boldsymbol{x}) = \begin{bmatrix} a_{11}R_s i_{ds} + a_{12} i_{ds} + a_{13}\psi_{dr} + a_{14}\omega_r \psi_{qr} - a_{11} v_{ds} \\ a_{11}R_s i_{qs} + a_{12} i_{qs} + a_{13}\psi_{qr} - a_{14}\omega_r \psi_{dr} - a_{11} v_{qs} \\ a_{31} i_{ds} + a_{32}\psi_{dr} - \omega_r \psi_{qr} \\ a_{31} i_{qs} + a_{32}\psi_{qr} + \omega_r \psi_{dr} \\ 0 \\ 0 \end{bmatrix}$$

$\boldsymbol{w}$ is the system noise, $\mathbf{G}$ is the weighting matrix of $\boldsymbol{w}$.

$$a_{11} = -1/(\sigma L_s)$$
$$a_{12} = -(1-\sigma)/(\sigma \tau_r)$$
$$a_{13} = M/(\sigma \tau_r L_s L_r)$$
$$a_{14} = M/(\sigma L_s L_r)$$
$$a_{31} = M/\tau_r$$
$$a_{32} = -1/\tau_r$$

Output equation is

$$\boldsymbol{y} = \boldsymbol{h}(\boldsymbol{x}) + \boldsymbol{z} \tag{15}$$

where $\boldsymbol{h}(\boldsymbol{x}) = \begin{bmatrix} i_{ds} & i_{qs} \end{bmatrix}^{\mathrm{T}}$

Applying the Extended Kalman Filter algorithm, the state variables are estimated.

Fig. 2 shows the simulation results of the speed and stator resistance estimation in regenerating mode. The actual stator resistance gradually increases after t=0.5s. The load torque changes from -10Nm to -15Nm at t=0.7s. The leakage coefficient in the Extended Kalman Filter is 0.90 times as much as the actual one. The estimated speed and stator resistance agree with those actual value even in the transient condition.

Fig.3 shows the simulation results when the stator resistance is not identified. In this case, the state variables are the stator currents, rotor fluxes, and the motor speed. This type of the speed estimation method has been reported in [7] and [8]. From this figure, we can see that the speed estimation by the 5th order Extended Kalman Filter without stator resistance identification does not work well in the regenerating mode.

IV. CONCLUSION

Two kinds of speed estimation methods for sensorless induction motor drives are proposed. One is based on the instantaneous reactive power measurement. This method can be used if the correct leakage coefficient is available. The other is based on the stator resistance identification using the Extended Kalman Filter algorithm. This method is robust against the stator resistance variation and is stable in powering and regenerating modes.

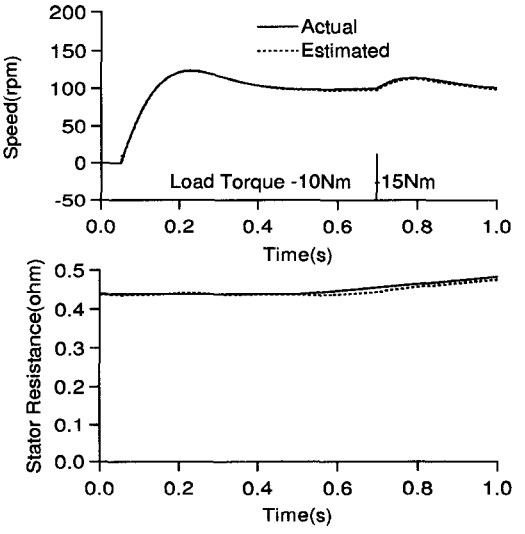


Fig.2 Simulation Results of Speed and Stator Resistance Estimation using 6th order Entended Kalman Filter (Incorrect leakage Coefficient)

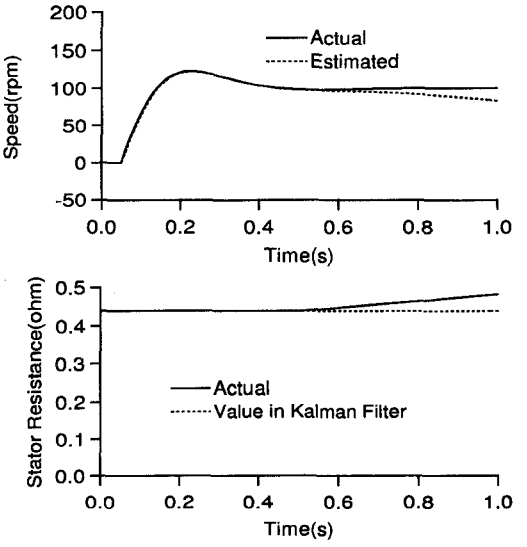


Fig.3 Simulation Results of Speed Estimation using 5th order Entended Kalman Filter (without Stator Resistance Estimation)

REFERENCES

[1]H.Kubota, K.Matsuse, T.Nakano, "DSP-Based Speed Adaptive Flux Observer of Induction Motor" IEEE Trans. on Ind. Appl., Vol.29, No.2, 1993

[2]T.Ohtani, N.Takada, and K.Tanaka, "Vector control of induction motor without shaft encoder," in Conf. Rec. of 1989 IEEE IAS Annual Meeting, pp.500-507

[3]C.Schauder, "Adaptive speed identification for vector control of induction motor without rotational transducers," in Conf. Rec. of 1989 IEEE IAS Annual Meeting, pp.493-499

[4] H.Tajima, Y.Hori, "Speed sensorless field orientation control of induction machine," in Conf. Rec. of 1991 IEEE IAS Annual Meeting, pp.385-391

[5] S.Tamai, H.Sugimoto, M.Yano, "Speed sensor-less vector control of induction motor with model reference adaptive system," in Conf. Rec. of 1987 IEEE IAS Annual Meeting, pp.189-195

[6] S.Doki, S.Sangwongwanich, and S.Okuma, "Implementation of Speed-Sensor-Less Field-Oriented Vector Control using Adaptive Sliding Observer," in Conf. Rec. of IECON '92, pp.453-458

[7] Henneberger, B.J.Brunsbach, and Th.Klepsch, "Field-Oriented Control of Synchronous and Asynchronous Drives without Mechanical Sensors using Kalman Filter," in Conf. Rec. of EPE, 1991, pp.664-671

[8] Y.R.Kim, S.K.Sul, and M.H.Park, "Speed Sensorless Vector Control of an Induction Motor Using an Extended Kalman Filter," in Conf. Rec. of 1992 IEEE IAS Annual Meeting, pp.594-599

[9] J.Holtz, "Speed Estimation and Sensorless Control of AC Drives," in Conf. Rec. of IECON '93, pp.649-654

[10] H.Kubota, and K.Matsuse, "Speed Sensorless Field Oriented Control of Induction Machines using Flux Observer," in Conf. Rec. of IECON '94, pp.1611-1615

[11]F.Z. Peng, T.Fukao, "Robust Speed Identification for Speed-Sensorless Vector Control of Induction Motors", IEEE Trans. on Industry Applications Vol.30, No.5, pp.1234-1240, 1994

SENSORLESS CONTROL FOR INDUCTION MOTOR DRIVES BASED ON NEW SPEED IDENTIFICATION SCHEME

Shyh-Shing Perng*, Yen-Shin Lai**, *Member, IEEE,* and Chang-Huan Liu*, *Member, IEEE*

* Dept. of Elect. Eng., National Taiwan Inst. of Tech., Taipei, Taiwan, R. O. C.

** Dept. of Elect. Eng., National Taipei Inst. of Tech., Taipei, Taiwan, R. O. C.

Abstract **- A sensorless controller, which is based upon the proposed synchronous speed identification scheme [1], for induction motor drives is presented in the paper. In comparison with previous results [2-3] which involve temperature-sensitive parameters, including rotor and/or stator resistors, the proposed MRAS synchronous speed identification scheme requires *neither* rotor time constant *nor* stator resistance in both reference and adjustable models.**

It is shown in this paper that the new sensorless controller for induction motor drives consists of feedforward control of stator voltage[4] and the new MRAS synchronous speed identification scheme, and does *not* invoke rotor resistance and voltage sensors. Simulation and experimental results will be presented to confirm the theoretical analysis.

Nomenclature

X_D^U

U:

r referring to the rotor flux frame

D:

d d-axis component

q q-axis component

s stator component

r rotor component

x^* reference or command value of x

$\hat{x}$ estimated (calculated) or feedback value of x

Symbols

ω_e	synchronous speed
ω_r	rotor speed
ω_s	slip frequency
p	differential operator
R_r	rotor resistance
R_s	stator resistance
L_r	rotor self-inductance
L_s	stator self-inductance
L_m	mutual inductance
σ	total leakage factor; $\sigma = 1-(L_m^2/L_s L_r)$
τ_r	rotor time constant; $\tau_r = L_r/R_r$
Ts	sampling period of digital implementation
s	slip
$v_s^r = v_{ds}^r + jv_{qs}^r$	stator voltage
$i_r^r = i_{dr}^r + ji_{qr}^r$	rotor current
$i_s^r = i_{ds}^r + ji_{qs}^r$	stator current
$i_m^r = \frac{L_r}{L_m} i_r^r + i_s^r$	magnetizing current
$\lambda_r^r = L_m i_s^r + L_r i_r^r$	rotor flux
$\lambda_s^r = L_s i_s^r + L_m i_r^r$	stator flux

I. INTRODUCTION

To improve the performance of dynamic response of induction motor drives, the conventional V/F control scheme has been replaced by vector control [5], which requires accurate information about the mechanical speed or position for field orientation. The field oriented control can be achieved at the cost of using additional shaft sensors, thereby increasing the size and reducing the robustness of the whole drive system.

To overcome these issues, "sensorless control", without using any shaft sensor, becomes a trend for the design of induction motor drives. A variety of methods have been proposed which heavily rely upon plant parameters. A comprehensive review of sensorless control of induction motor drives can be found in reference [6].

Sensorless induction motor drives based upon the theory of Model Reference Adaptive System (MRAS) [7] provide an alternative way for the development. However, the method shown in [2] requires both rotor *and* stator resistors, and integral operation which involves initial value problem. Although, integration operation is not required in [8], rotor time constant which is sensitive to temperature variation, is still necessary for the adjustable model.

To deal with this problem, a novel sensorless controller [1] based on model reference adaptive system has been proposed and demonstrated by experimental and simulation results. The proposed MRAS scheme requires *neither* rotor time constant *nor* stator resistance in both adjustable and reference models. Furthermore, since *no* integral operation is required, the proposed scheme provides wider bandwidth for speed control.

Although rotor resistance is not required in the new

0-7803-3823-5/97/$10.00© 1997 IEEE

MRAS scheme [1], the vector controller still requires the rotor resistance for the calculation of slip frequency. A new sensorless controller, which does not require rotor resistance and voltage sensors, for induction motor drive control will be presented. Simulation and experimental results will be presented to confirm the theoretical analysis.

II. THEORY

A. A New MRAS Scheme

Although the new MRAS scheme [1] for synchronous speed identification has been presented, a brief review relevant to the development of the new sensorless controller for induction motor drives is given as follows.

The motor voltage referring to rotor flux frame, can be derived as follows.

$$v_s^r = R_s i_s^r + p\lambda_s^r + j\omega_e \lambda_s^r \tag{1}$$

$$v_{ds}^r = R_s i_{ds}^r + p\lambda_{ds}^r - \omega_e \lambda_{qs}^r \tag{2}$$

$$v_{qs}^r = R_s i_{qs}^r + p\lambda_{qs}^r + \omega_e \lambda_{ds}^r \tag{3}$$

Equations (2) and (3) are substituted into (4), which is the reactive power of machine, thereby resulting in (5).

$$Q = v_{qs}^r i_{ds}^r - v_{ds}^r i_{qs}^r \tag{4}$$

$$Q = \omega_e \left(\lambda_{qs}^r i_{qs}^r + \lambda_{ds}^r i_{ds}^r\right) + i_{ds}^r p\lambda_{qs}^r - i_{qs}^r p\lambda_{ds}^r \tag{5}$$

Substituting the stator flux equation shown in (6) into (5), the reactive power equation can be rewritten as shown in (7).

$$\lambda_s^r = \lambda_{ds}^r + j\lambda_{qs}^r = L_s i_{ds}^r + j\sigma L_s i_{qs}^r \tag{6}$$

$$Q = \omega_e \left[\sigma L_s \left(i_{qs}^r\right)^2 + L_s \left(i_{ds}^r\right)^2\right] + i_{ds}^r \sigma L_s p i_{qs}^r - i_{qs}^r L_s p i_{ds}^r \tag{7}$$

According to the theory of MRAS , (4) and (7) can be used as the reference and adjustable models, respectively, to identify the synchronous speed. The block diagram for the new MRAS synchronous speed identification scheme is shown in Fig. 3. Notice that the reactive power shown in (4) and (7) does *not* contain *either* rotor resistance *nor* stator resistance. Moreover, the calculations of reactive power for both reference and adjust models as shown in (4) and (7), respectively do *not* require any integration operation.

The proposed MRAS has been proved [1] to be hyperstable using the theory of Hyperstability [9]. Therefore, the synchronous speed is identified and converges to the real value; more details about the development and proof can be found in [1].

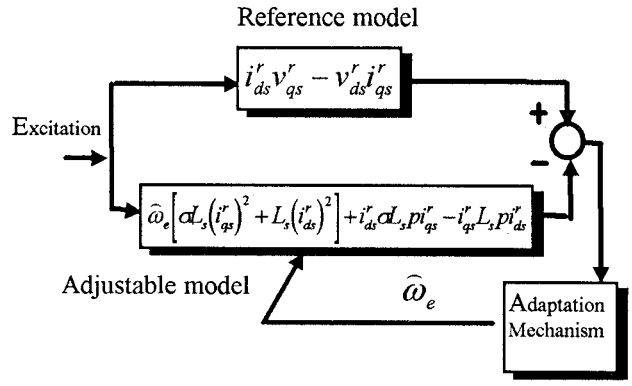


Fig. 1. The proposed synchronous speed identification scheme based upon MRAS

B. Feedforward Control of Stator Voltage

The stator voltage equation of induction motor drives is

$$v_{ds}^r = \left(R_s + \sigma L_s p\right) i_{ds}^r - \left(\omega_e \sigma L_s\right) i_{qs}^r + \frac{L_m}{L_r}\left(p\lambda_{dr}^r - \omega_e \lambda_{qr}^r\right)$$

$$v_{qs}^r = \left(R_s + \sigma L_s p\right) i_{qs}^r + \left(\omega_e \sigma L_s\right) i_{ds}^r + \frac{L_m}{L_r}\left(p\lambda_{qr}^r + \omega_e \lambda_{dr}^r\right) \tag{8}$$

Assume that the torque producing current, i_{ds}^r, is constant and equals to its command value, $i_{ds}^{r\,*}$, then in the steady state the stator voltage command can be shown as follows.

$$v_{ds}^{r\,*} = R_s i_{ds}^{r\,*} - \left(\omega_e^{\,*} \sigma L_s\right) \hat{i}_{qs}^r + \Delta v$$

$$v_{qs}^{r\,*} = R_s \hat{i}_{qs}^r + \left(\omega_e^{\,*} L_s\right) i_{ds}^{r\,*} \tag{9}$$

where

$$\Delta v \equiv \frac{L_m}{L_r}\left(-\omega_e^{\,*} \hat{\lambda}_{qr}^r\right) \tag{10}$$

C. Flux Control

The well-known current model of rotor flux is

$$p\lambda_r^r = \frac{L_m}{\tau_r} i_s^r - \frac{1}{\tau_r}\lambda_r^r - j\left(\omega_e - \omega_r\right)\lambda_r^r \tag{11}$$

and the corresponding q-axis component is

$$p\lambda_{qr}^r = \frac{L_m}{\tau_r} i_{qs}^r - \frac{1}{\tau_r}\lambda_{qr}^r - \left(\omega_e - \omega_r\right)\lambda_{dr}^r \tag{12}$$

Therefore, λ_{qr}^r is affected by the torque producing current, i_{qs}^r, and the following relationships result

provided that the derivative of λ_{qr}^r equals to zero.

① if $\lambda_{qr}^r = 0$, then $i_{qs}^r = \frac{\tau_r}{L_m}(\omega_e - \omega_r)\lambda_{dr}^r$

② if $\lambda_{qr}^r < 0$, then $i_{qs}^r < \frac{\tau_r}{L_m}(\omega_e - \omega_r)\lambda_{dr}^r$

③ if $\lambda_{qr}^r > 0$, then $i_{qs}^r > \frac{\tau_r}{L_m}(\omega_e - \omega_r)\lambda_{dr}^r$

Recalling that $\lambda_{qr}^r \propto -\Delta v$ as shown in (10), λ_{qr}^r is controlled by adding an additional voltage component, $k_v \Delta v$, to v_{qs}^{r*}, thereby changing i_{qs}^r and λ_{qr}^r, where k_v is a constant.

Furthermore, the voltage equation for the q-axis component can be derived from (8) and (12), and is rewritten as follows.

$$v_{qs}^r = (R_s + \frac{L_m^2}{L_r\tau_r} + \sigma L_s p) i_{qs}^r + \sigma L_s \omega_e i_{ds}^r + \frac{L_m}{L_r}(\frac{-1}{\tau_r}\lambda_{qr}^r + \omega_r \lambda_{dr}^r) \quad (13)$$

If the voltage shown in (9) is fed to the motor, and assume that $\omega_e = \omega_e^*$, $i_{ds}^r = i_{ds}^{r*}$, and $\lambda_{dr}^r = L_m i_{ds}^{r*}$, the above equation becomes

$$\sigma L_s p i_{qs}^r = -\frac{L_m^2}{L_r\tau_r} i_{qs}^r + \frac{L_m}{L_r}\frac{1}{\tau_r}\lambda_{qr}^r + \frac{L_m}{L_r}(\omega_e - \omega_r)\lambda_{dr}^r \quad (14)$$

The torque producing current derived from (14) is

$$i_{qs}^r = \frac{\frac{L_m}{L_r}\frac{1}{\tau_r}\lambda_{qr}^r + \frac{L_m}{L_r}(\omega_e - \omega_r)\lambda_{dr}^r}{\sigma L_s p + \frac{L_m^2}{L_r\tau_r}} \quad (15)$$

Substituting (15) into (12), the relationship between the torque producing current and the derivative of q-axis flux component can be derived and is shown as follows.

$$p\lambda_{qr}^r = \frac{-\sigma L_s p[\frac{1}{\tau_r}\lambda_{qr}^r + (\omega_e - \omega_r)\lambda_{dr}^r]}{\sigma L_s p + \frac{L_m^2}{L_r\tau_r}} \quad (16)$$

$$= -\sigma L_s (\frac{L_r}{L_m} p i_{qs}^r)$$

Equation (16) shows that load variation causes fluctuation of q-axis flux component. To overcome this deterioration, the fluctuation is compensated by adding $k_d p i_{qs}^r$ term to the flux model shown in (12). Fig. 2 shows the block diagram, derived from (12), of λ_{qr}^r. and the compensation for the flux fluctuation caused by the variation of torque producing current. Therefore, the rotor flux is still under orientation even in transient state.

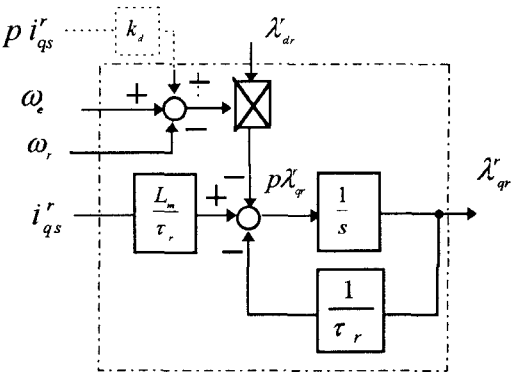


Fig. 2. Block diagram of flux compensation, where $k_d = \sigma L_s L_r / \lambda_{dr}^r$

D. *Sensorless Controller of Induction Motor Drives*

Fig. 3 shows the system configuration of the sensorless controller based upon the proposed MRAS scheme. As shown in Fig. 3, the synchronous speed is identified and provided by the proposed MRAS. Moreover, the voltage command is calculated using feedforward voltage control method shown in (9).

Moreover, due to the zero initial value of synchronous speed the stator voltage, shown in (9), is zero at the instance of start up. To deal with this issue, the error of torque producing currents is fed to generate the required stator voltage command as shown in Fig. 3.

It is important that shaft speed and rotor resistor cannot be identified simultaneously for an induction motor drive without using additional excitation signal [10]. In the proposed sensorless controller shown in Fig. 3, rotor resistor is not required. Although stator resistor is used for feedforward voltage control, it has been demonstrated [10] that both stator resistance and shaft speed can be identified at the same time. Therefore, the proposed sensorless controller for induction motor drives provides robustness to parameter variations.

III. SIMULATION AND EXPERIMENTAL RESULTS

A. *Hardware Configuration*

The MRAS-based sensorless induction motor drive shown in Fig. 3 has been realized using a single-chip-based control board which consists of an INTEL 80196 MC® single-chip microprocessor, protection circuits, current detection circuits, and decoding circuit. Fig. 4 shows the block diagram of hardware configuration. As shown in Fig. 4, the object code generated by the cross-assembler using personal computer is downloaded into the in-circuit emulator (ICE) which emulates the target system in real time for on-line debug.

One of the features of the 80196 MC single-chip microprocessor is its embedded PWM generator which generates the three-phase PWM gating signals according to the command voltage using traditional natural-sampled sinusoidal pulse-width modulation (SPWM) technique.

Several protection circuits are included in the single-chip microprocessor board and will cause trip whenever one of the events, including over voltage, under voltage, regeneration voltage, over current, and over load, occurs. The current detection circuits transform the load current signals into the acceptable voltage level, –0.5 ~ +5.5V, of the embedded A/D converter of 80196 MC single-chip microprocessor. It is worthy of note that the sampling time of A/D is around 15 μ sec/channel.

Although the output pulses of incremental encoder of induction motor is not fed into the controller, a decoding circuit is built in the single-chip microprocessor board for measurement purpose and further applications.

B. Software Design

For the implementation of the sensorless controller shown in Fig. 3 using software, it is necessary to derive the discrete-time representations of the equations. To simplify the calculations of transforming the continuous-time equations to the related discrete-time forms, the so called "backward rule" of Euler's formula is considered and is shown as follows [11].

$$p = \frac{z-1}{T_s z} \tag{17}$$

Equation (19), derived by substituting (17) into (18), illustrates the associated discrete-time representation for proportional-integer (PI) control, using speed control as an example.

$$i_{qs}^{s*} = \left(k_p + \frac{k_i}{p}\right)\left(\omega_r^* - \hat{\omega}_r\right) \tag{18}$$

$$i_{qs}^{s*}(k+1) = i_{qs}^{s*}(k) + \left(k_p + k_i T_s\right)\Delta\omega_r(k+1) - k_p\Delta\omega_r(k) \tag{19}$$

where

$$\Delta\omega_r \equiv \left(\omega_r^* - \hat{\omega}_r\right)$$

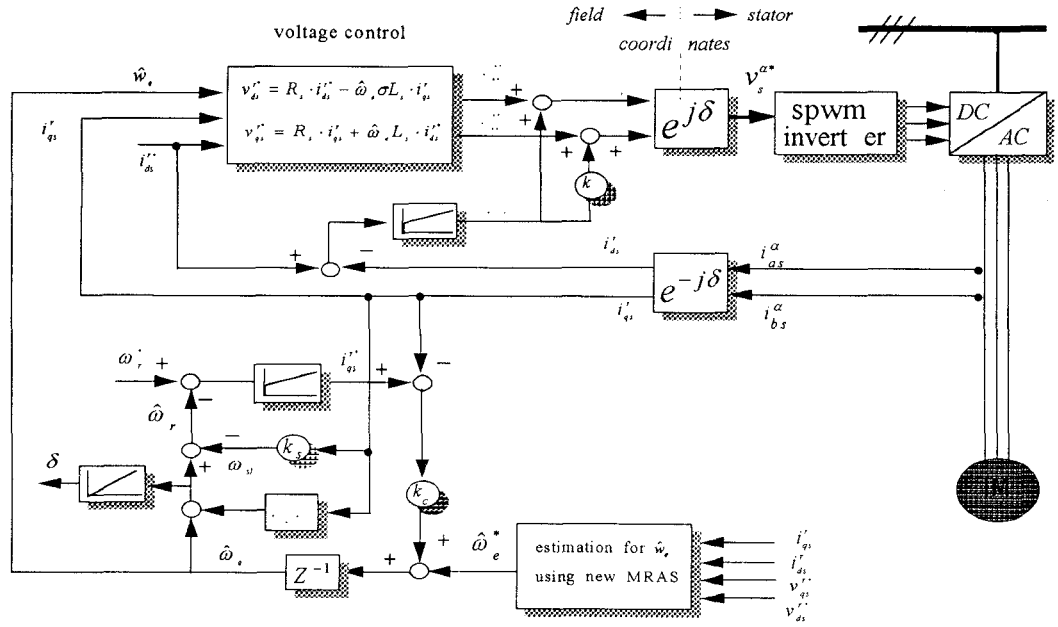


Fig. 3. System configuration of the sensorless controller

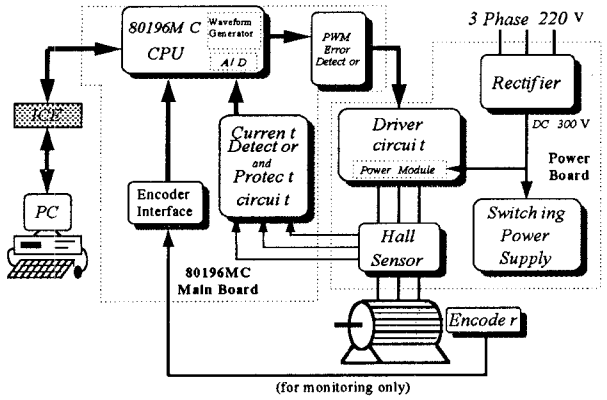


Fig. 4. Hardware configuration of the implementation of the sensorless controller

C. *Results*

The simulation work has been carried out using Simulink™ and the controller has been realized using software based on a single chip microprocessor, MC 80196, board.

Figs. 5 and 6 illustrate the simulation and experimental results using speed command equal to ±1000 rpm and ±200 rpm as examples, respectively. As shown in Figs. 5 and 6, the simulation results agree with experimental results very well confirming the theoretical analysis.

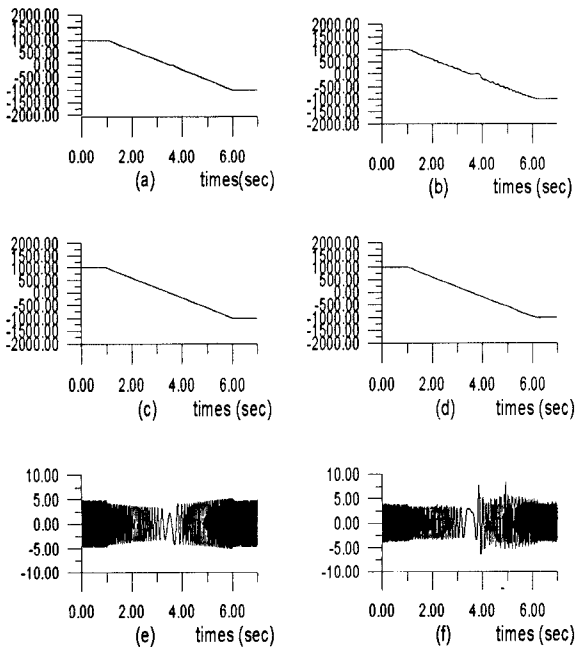


Fig. 5. Illustration of experimental and simulation results, ±1000 rpm , 2 Nt.-m;(a) speed response, simulation; (b). speed response, experiment ;(c) estimated speed, simulation; (d) estimated speed, experiment; (e) current for phase A, simulation; (f)current for phase A, experiment .

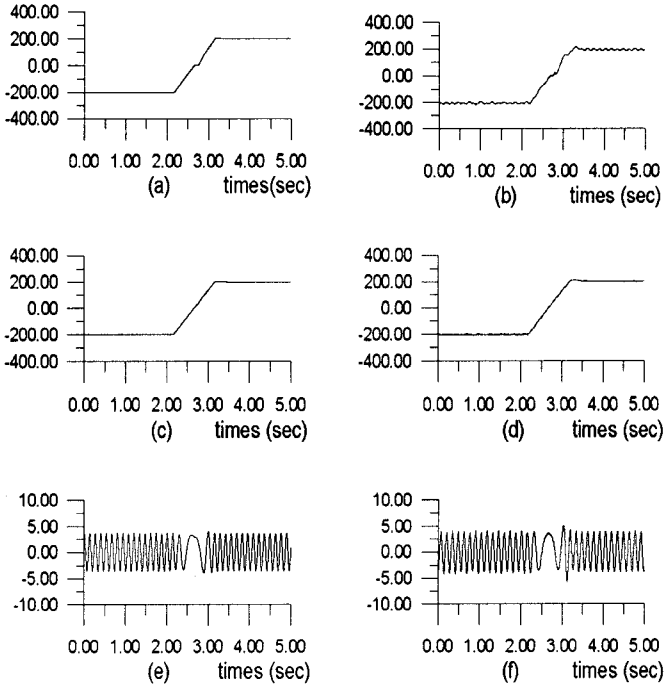


Fig. 6. Illustration of experimental and simulation results, ±200 rpm , 2 Nt.-m;(a) speed response, simulation; (b). speed response, experiment ;(c) estimated speed, simulation; (d) estimated speed, experiment; (e) current for phase A, simulation; (f)current for phase A, experiment .

IV. CONCLUSION

A novel sensorless controller based on MRAS scheme, requiring *neither* rotor time constant *nor* stator resistance in both adjustable and reference models, for induction motor drives has been presented in this paper. The proposed sensorless controller does not require rotor resistance, and thereby increasing the robustness to parameter variations.

The proposed sensorless controller is demonstrated using simulation and experimental results confirming the theoretical analysis.

V. ACKNOWLEDGMENTS

The authors gratefully acknowledge the financial support given by the National Science Council under the grants NSC86-2213-E-010-075 and NSC86-2622-E-011-005R .

VI. REFERENCES

1. S. S. Perng, Y. S. Lai ,and C. H. Liu, "A novel sensorless controller for induction motor drives," to appear in *EPE'97*.
2. C. Schauder, Adaptive speed identification for vector control of induction motors without rotational

transducers, *IEEE IAS Conf. Rec.*, pp. 493-499, 1989. (also see *IEEE Trans. Ind. Appl.*, Vol. 28, No. 5, pp. 1054-1061, 1992.)
3. F. Z. Peng and T. Fukao, Robust speed identification for speed-sensorless Vector control of induction motors, *IEEE IAS Conf. Rec.*, pp. 419-426, 1993. (also see *IEEE Trans. Ind. Appl.* ,Vol. 30, No. 5, pp. 1234-1240, 1994.)
4. T. Okuyama, N. Fujimoto, T. Matsui and Y. Kubota, "A high performance seed control scheme for induction moor without seed and voltage sensors," *Con. Rec. of IEEE IAS Ann. Meet.*, pp. 106~111, 1986.
5. F., Blaschke, "The principle of field orientation as applied to the new TRANSVECTOR closed loop control system for rotating field machines," Siemens Review, Vol. 34, pp. 217-220, 1972.
6. J. Holtz, Speed estimation and sensorless control of AC drives, Proceedings of *IEEE IECON*, Vol. 2, pp. 649-654, 1993.
7. Y. D. Landau, Adaptive control: the model reference approach, Marcel Dekker, Inc, New York, 1979.
8. H. Tajima and Y. Hori, Speed sensorless field orientation control of the induction machine, *IEEE IAS Conf. Rec.*, pp. 385-391, 1991.
9. V. M. Popov, Hyperstability of automatic control systems, Springer-Verlag, New York, 1973.
10. S. Shinnaka, "A unified analysis on simultaneous identification of velocity and rotor resistance of induction motors," *Trans. IEE Japan*, Vol. 113-D, No. 12, pp. 1483-1484, 1993.
11. G. F. Franklin, J. D. Powell, and M. L. Workman, Digital control of dynamic systems, Addison-Wesley, Reading, Massachusetts, 1990.

Transient Response of Speed Sensorless Control Method Based on Phase Difference

Junichi Tsuchiya, Kazuhiro Watanabe,
Toshihisa Simizu, Gunji Kimura
Dept. of Electrical Eng., Tokyo Metropolitan University
1-1, MinamiOhsawa, Hachioji-shi, Tokyo 192-03, JAPAN
Phone: +81-426-77-2747 Fax: +81-426-77-2737
e-mail tsuchiya@eei.metro-u.ac.jp

Ikuo Watanabe, Koji Naniwa
ORIENTAL MOTOR CO.
1400 Shikoda, Kashiwa-shi, Chiba, 277, JAPAN
Phone: +81-471-45-6500 Fax: +81-471-46-3276

Abstract **- A simple speed control is needed for small induction motors. Previously, authors have proposed a simple speed sensorless control method for small induction motors. In this method, the load torque is estimated from the phase difference between the stator current and the stator voltage, and the drive frequency is calculated from the estimated torque. As a result, the average speed of the induction motor is kept constant. This paper presents the principle of this method and the transient responses of torque fluctuations and speed commands with 90W induction motor.**

I . INTRODUCTION

In recent years, many kinds of adjustable speed drive techniques for induction motors have been developed, and the induction motor drives have been used in many applications. In many cases, the speed sensor is often used for the constant speed control of the induction motors[1]. However, a speed sensor cannot be mounted in some cases, such as motor drives in a hostile environment, high-speed motor drives, etc. Several field-oriented induction motor drive methods without speed-sensors have been proposed[2]-[4]. These methods have the disadvantage that the control is complex and a high performance CPU is necessary. Therefore, the cost of these methods is high. On the other hand, the simple and lower-cost control method is requested in small induction motors, etc. Moreover, the stator current of a small induction motor is small and the fluctuation of the amplitude of current by the load fluctuation is small. Therefore, it is difficult to estimate the speed from the fluctuation of the amplitude of current.

Previously authors proposed a simple sensorless speed control method for small induction motors by using a simple control method[5]. We paid attention to the phase difference between the stator current and the voltage, because the fluctuation of the phase difference by the load fluctuation is detected easily. In this method, the speed fluctuations are estimated by the phase difference between the stator current and the voltage. The inverter frequency command is calculated by using data tables that have been measured beforehand, and is adjusted to compensate for the fluctuation of rotational speed. The calculation of this control method is very simple. However, The controller cannot respond instantaneously because the detection of the phase is two times a cycle.

This paper presents the principle of this method and the transient responses of torque fluctuations and speed commands with 90W induction motor.

II . PRINCIPLES

In controlling the speed of induction motors without a speed sensor, it is important to estimate the fluctuation of the load torque. Generally, a load torque can be presumed from the information of the stator current waveform as a general method. However, for reason of the problems stated above, it is hard to detect the accurate stator current of small induction motors. On the other hand, the phase difference time between the zero-crossing of the stator current and that of the stator voltage can be detected easily. Fig.1 shows the measurement scheme of the phase difference time. The two sinusoidal waves of

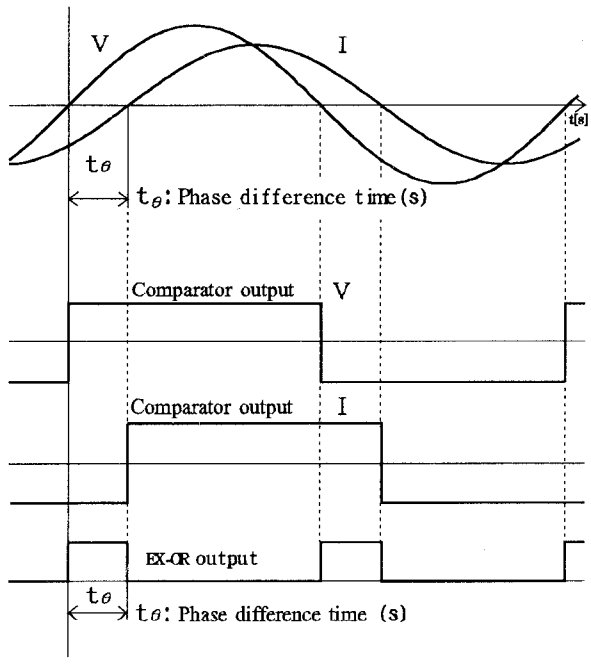


Fig.1 Measurement of the phase difference time

voltage and current represent the filtered stator voltage and filtered stator current. Since the EXCLUSIVE-OR (EX-OR) output is the time difference between comparator outputs of voltage and current, the phase difference time is detected by measuring the EX-OR output.

Fig.2 shows the relationship between load torque and phase difference time on condition that the 90W motor rotates at specific speed. As the load torque increases, the phase difference time decreases. Thus the load torque at a certain rotor speed can be obtained from the phase difference time, and the motor slip that arises the phase difference is the slip for the constant speed. The operating frequency of inverter is adjusted to compensate for the slip, and the motor can maintain the constant speed.

Fig.3 shows the relationship between the operation frequency and the phase difference time when the rotational speed of the 90W induction motor is kept to 300rpm,600rpm,900rpm,1200rpm, respectively. This relationship has been measured beforehand, and is stored in a memory as a data table. In order to regulate the rotor speed to the target speed, the operation frequency of inverter is selected by referring the table. Although the table contains only four kinds rotational speed, the operation frequency at another speed command is calculated by using a linear interpolation.

III . Configuration of Control System

Fig.4 shows the configuration of the control system. The filters reduce the noise from the detected stator current and stator voltage of the induction motor. The detection circuit of phase difference is composed of

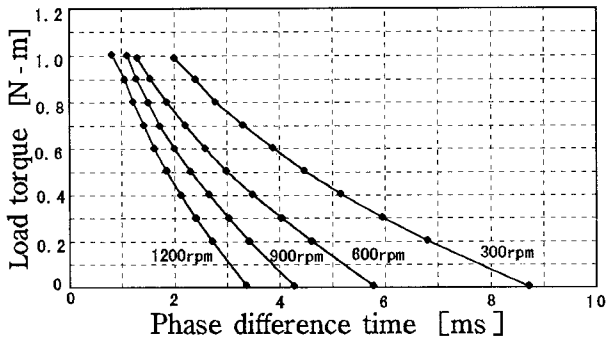


Fig.2 Characteristics of the torque versus the phase difference time

comparators and an EX-OR circuit, and generates a pulse of which the width is equivalent to the phase difference time. The digital counter converts this pulse width into a digital value. The microprocessor stores the data table shown in Fig.3 to adjust the rotational speed, and calculates a command frequency, which corresponds to the preset rotational speed. The PWM inverter receives this signal and drives the induction motor at the corrected frequency. The microprocessor is a single-board 8-bit computer.

IV . Experimental Results of Steady-State Torque Characteristics

Fig.5 shows the characteristics of steady state-torque versus rotational speed of the 90W motor. As shown in Fig.5, the rotational speed slows down as load torque increases at no control condition. When the proposed control system is applied, the rotational speed is kept

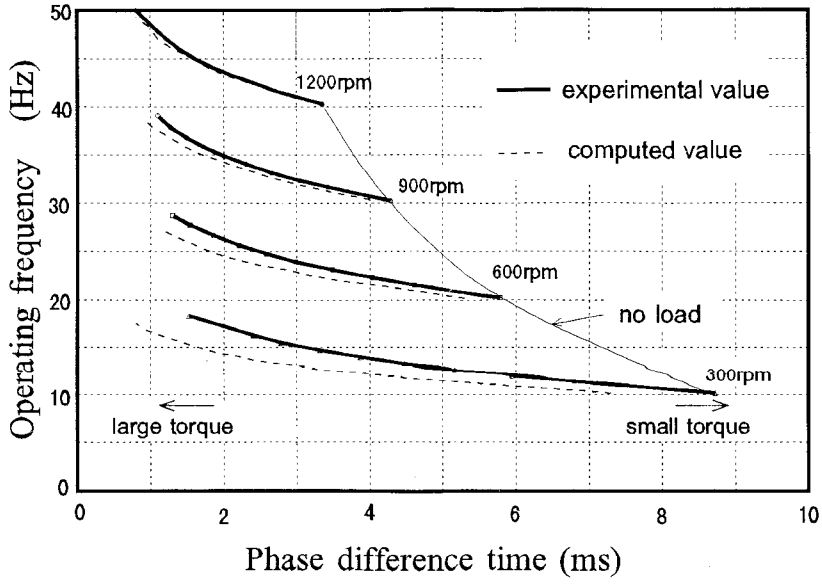


Fig.3 Relation between operating frequency and phase difference time

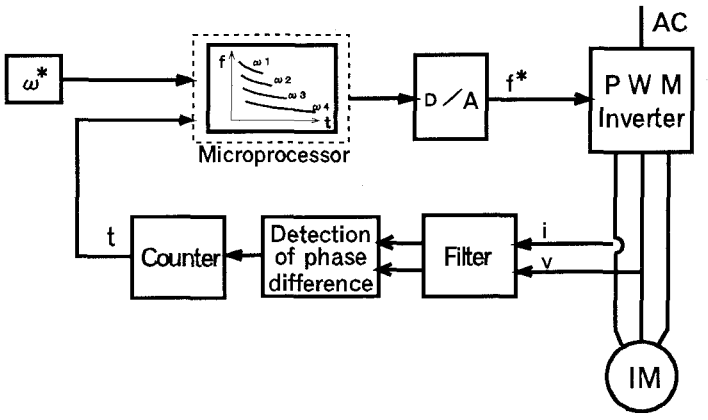


Fig.4 Block diagram of the control system

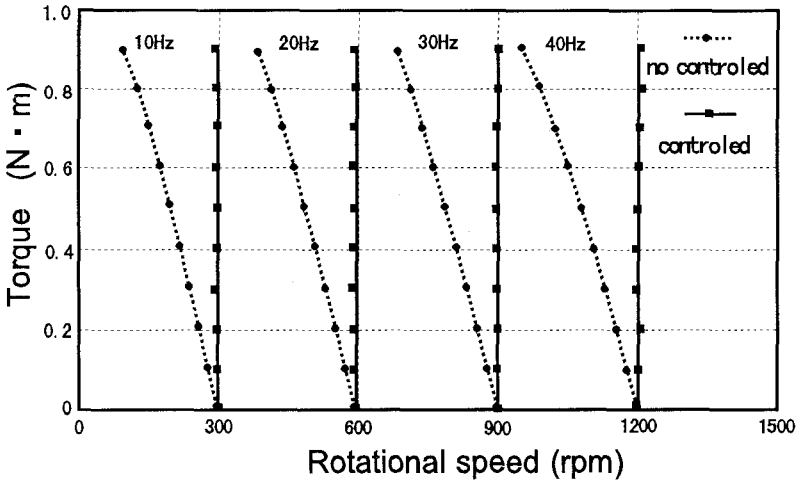


Fig.5 Torque– speed characteristics

almost constant. In the experiment, the precision of the speed error is about ±3%. It is suspected that the factors of the speed error are the following: the temperature characteristic of the motor is not considered, noise caused by the PWM inverter are large, etc.

V . Transient Response Characteristics

Steady state torque characteristics were obtained. However, the motor was to suffer a sudden change in load torque, and the rotational speed would vary for a moment. The transient response when the speed instruction is made from 600rpm to 1200rpm is shown in Fig.6. The frequency of the inverter changes when the speed instruction is changed and the phase difference time changes at once. The rise time and the fall time in the rotational speed are fast within 50ms.However, because the phase difference vibrates transitionally, the convergence time in the rotational speed is about 200ms.

Fig.7 shows the experimental results of rotational speed variation when load torque is varied in a step change. The load torque is varied from zero to the rated torque and is varied from the rated torque to zero, and the response time is about 300 millisecond.

VI . Examination of Delay of Responses.

1) Interval of sampling phase difference time : The interval of sampling the phase difference time is two times an inverter frequency cycle as shown in Fig. 1. Therefore, the maximum delay time of sampling is about 25ms when the rotation speed is 600rpm(the frequency of the inverter is about 20Hz).

2) The delay time of the low-pass filter : The voltage and current pass through the low-pass filter to remove the noise. the delay time of the filter is 22ms.

3) Time constant of primary winding of the induction

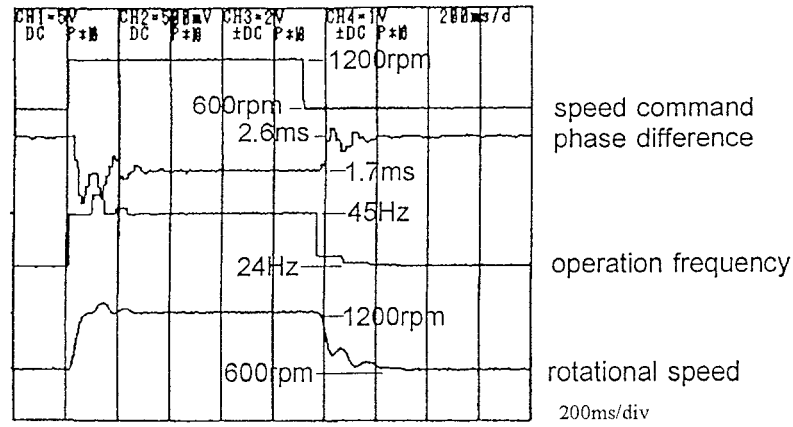


Fig.6 The transient response of the speed instruction.

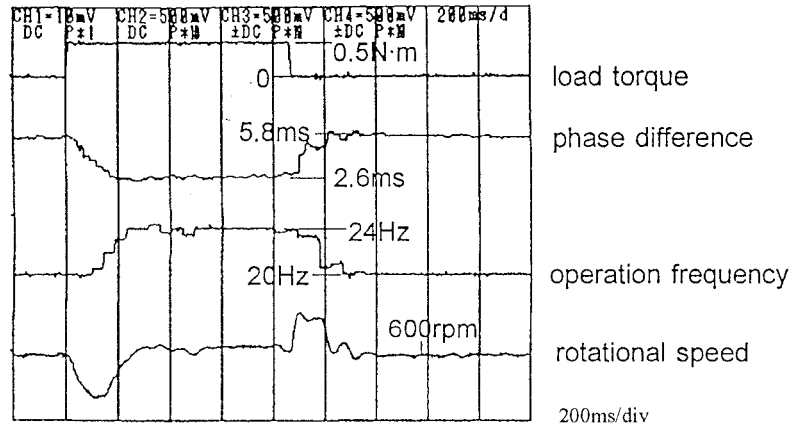


Fig.7 The transient response of torque change.

motor : The transition response time of the step change of torque is simulated. That time constant is 10 milliseconds or less.

4)Mechanical time constant of the moment of rotor inertia: The moment of rotor inertia according to the measurement is 2.52×10^{-4}kg·m^2. Time that the rotor speed accelerates from 600rpm to 1200rpm is approximately calculated. That time is about 32ms.

The transient response time is a total of the above-mentioned factor. Because the error detection is delayed, the transient response of the torque change is slow. The transient response of the speed instruction is faster than the transient response of the torque change.

VII . CONCLUSIONS

In this paper, a new simple control method for small induction motors is proposed. The features of the method are that a speed-sensor is not used, and only the phase difference time between the voltage and current is used. Moreover, the inverter frequency is determined by a simple calculation. Using this method, the torque-speed characteristics are improved greatly, and the effectiveness of this control method is confirmed by experiments.

The transient response times of torque fluctuations and speed commands are measured by the experiment. That time is from 100ms to 300ms. This response time is slower than the one of the vector control. However, this control system is useful for sufficient use of controlling an average speed. Therefore, this method is simple and can be easily applied to a lot of applications of the induction motor.

REFERENCES

[1] B.K.Bose,"Adjustable Speed AC Drive System,"IEEE Press,1980

[2] H.Kubota, K.Matsuse, "Speed Sensorless Field-Oriented Control of Induction Motor With Rotor Resistance Adaptation," IEEE Trans. Industry Applicat., vol.30, no.5, pp.1219-1224, 1994

[3] H.Kubota, K.Matsuse, "DSP-Based Speed Adaptive Observer of Induction Motor," IEEE Trans. Industry Applicat., vol.29, no.2, pp.344-348, 1993

[4] T.Ohtani, N.Takada, K.Tanaka, "Vector control of induction motor without shaft encoder," in Conf. Rec. 1989 IEEE IAS Ann. Mtg., pp.500-507.

[5] Y. Yuan, J. Tsuchiya, etc. "A Simple Speed Control Method for Small Induction Motor Based on Phase Difference," IEEE International Conference on Industrial Electronics, Control, and Instruction, vol.1, 1995, pp.306-310.

Improvement of Thrust of Linear Induction Motor Using Modified Ladder Slits

Tadashi Yamaguchi, Masaki Ito and Keiju Matsui
Department of Electrical Engineering, Chubu University
1200, Matsumoto-cho, Kasugai 487, JAPAN
Fax: +81-568-51-1141, Phone: +81-568-51-1111
E-mail: yamachu@solan.chubu.ac.jp

Abstract — This paper presents a method to improve the thrust of a linear induction motor (LIM). LIMs are used in many industrial applications such as high speed material transport systems and the like, because they can obtain the thrust directly without auxiliary mechanisms like gears and links in addition to the simple structure. In this paper, we propose a secondary conducting plate with novel shape ladder slits in order to improve the thrust. The usefulness of the proposed novel ladder slits is discussed by experiments and analytical computation results.

I. INTRODUCTION

Linear induction motors (LIMs) are used in many industrial applications such as high speed material transport systems and the like. It is one of features to be able to obtain the thrust directly without auxiliary mechanisms like gears and links in addition to the simple structure. LIM has many advantages, such as (i) simple structure, (ii) easy maintenance, (iii) less environmental pollution, etc. Consequently, LIMs are put into practical use as transport systems in the clean rooms of factories and hospitals.

A flat conducting plate made of aluminum or copper is adopted as a secondary conducting plate, or a reaction plate, because the structure becomes very simple. Therefore, it is very difficult to analyze the state of eddy current flows in the flat reaction plate. The flow of eddy currents, or eddy current path, however, has a significant effect on the thrust. Only transverse component of the eddy current makes the thrust. In other words, binding effectively the eddy current path to the transverse one is one of thrust improvements. Studies for a reaction plate with ladder slits have already been reported [1]. The ideas for such reaction plate come from the rotor of the squirrel cage induction motor. The shape of the reaction plate becomes complicated, so that the simple structure, which is one of advantages of LIM, is deteriorated. It is very important for the optimum design of the reaction plate under consideration of proper current path in order to obtain the improved thrust. Otherwise, it will make the thrust worse to reshape the reaction.

In this paper, we propose a novel ladder shape of the reaction plate for the purpose of improving the thrust of LIM. Only the shape of the reaction plate is changed and the secondary core is not, so that an advantage of LIM as a simple structure is not deteriorated. Onuki, et al. have been presented the same shape of the reaction plate from the different point of view [2].

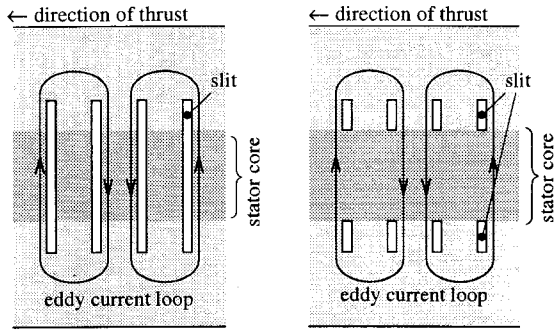
The usefulness of the proposed reaction plate is confirmed by experimental and analytical computation results.

II. MODIFIED LADDER SLITS

In recent years, various researches have been studied for the improvement of thrust of LIM. In such studies, the improvement of the thrust have been performed by the reaction plate with ladder slits, especially for LIMs with primary side on ground [1],[2]. In general, the conventional reaction plate with slits has many long slits at the center as shown in Fig.1 (a) and the reaction plate is sticked in the slits by the stator core in order to improve the permeance. However, this method makes sure to deteriorate an advantage of LIM of simple structure. In a case that only the reaction plate is processed with respect to the slits and the secondary core remains intact, the conductivity of the reaction plate may be reduced and the thrust may become worse if we make too many slits in no consideration of the eddy current path. From such point of view, we propose a new reaction plate with slits shown in Fig.1 (b). It has many slits on only both sides of the edge of region over the stator core in parallel to the effective primary eddy current flow, which is modified from the conventional reaction plate with long slits shown in Fig.1 (a).

Fig.2 shows a slit effect for the eddy current. The definition of eddy current paths and regions is shown in Fig.2. Symbols α and β are the eddy current path without silts and that with slits, respectively, and symbols A and B are the region over the stator core and its both side, respectively. Eddy current in region A flows naturally in vertical to the direction of the thrust such as the path α shown in Fig.2, because the flux density in A is assumed to be almost constant throughout the reaction plate. Therefore, there is no need to make slits in A. Otherwise, its conductivity is reduced less than that of the conventional reaction plate. In region B, a magnitude of normal component of flux density is not zero. However the eddy current makes a turn in region B where the generated trust is very small. Therefore, the trust can be made larger, since the eddy current path α is changed into β by making slits in B.

0-7803-3823-5/97/$10.00© 1997 IEEE



(a) conventional (b) proposed

Fig.1. Reaction Plates with Ladder Slits.

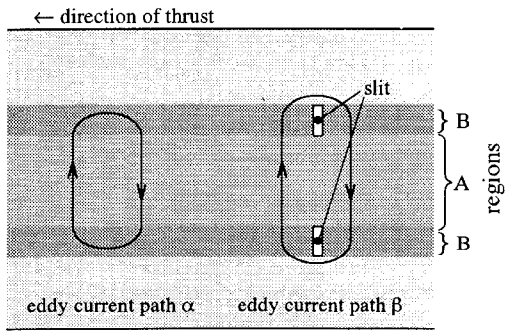


Fig.2. Slit Effect for Eddy Current.

III . Numerical Analysis

For obtaining the eddy current path in the reaction plate, the finite element method using electric vector potential $\boldsymbol{T}$ is applied. In a case that the reaction plate is sufficiently thin and eddy currents and magnetic scalar potential do not vary in the normal direction to the reaction plate, the fundamental equation of electric field in a reaction plate is described using T as normal component of electric vector potential $\boldsymbol{T}$ as follows [3],[4] :

$$\mathrm{rot}\left(\frac{1}{\rho}\mathrm{rot}T\right) = \mu_0 \frac{\partial T}{\partial t} + \frac{\partial B}{\partial t}, \quad \rho = \sigma h \qquad (1)$$

where ρ is the siemens, μ_0 is the magnetic permeability in the air, B is the normal component of the applied magnetic flux density to the reaction plate, σ is the electric conductivity, and h is the thickness of the reaction plate.

The applied magnetic flux density B is varying sinusoidally, so the electric vector potential T is also varying sinusoidally. Therefore, $\partial B/\partial t$ and $\partial T/\partial t$ in (1) can be regarded as $j\omega B$ and $j\omega T$ of the complex function, respectively. The electromotive force in each region on the reaction plate can be expressed by means of shifting of the applied magnetic flux density as shown in Fig.6 (a). To evaluate slits, electric conductivity σ of the elements of the slit is assumed to be very small [5]. Equation (1) is solved by using a standard finite element method with first-order triangular elements.

IV . Experimental Equipments and Conditions

Fig.3 shows the experimental equipment of LIM and a force gauge. It is designed to measure the thrust of locked LIM. The stator core is installed on the ground and the secondary core is set up on the carrier which can move smoothly in the direction of the thrust. A force gauge locks the secondary core and measures the thrust of locked LIM. The secondary core is a lump of iron and the stator core is made of laminated iron. The reaction plate, or a secondary conducting plate is made of copper. Thickness of the reaction plate is 5 mm. The air gap between the reaction plate and the stator core is 1 mm. Table I shows the dimensions and rating values of LIM.

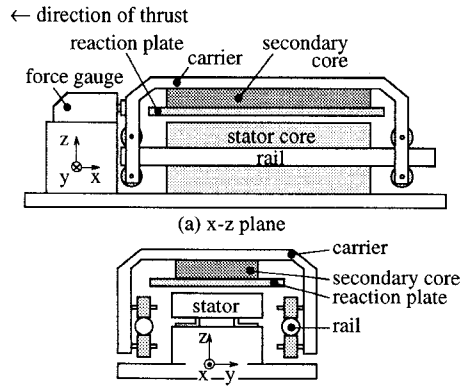


Fig.3. Linear Induction Motor.

TABLE I
DIMENSIONS AND RATING VALUES OF LIM

Dimensions			Rating Values	
parts	length (mm)	width (mm)	number of phase	3
			rated voltage (V)	220
stator core	225	30	rated current (A)	4.9
secondary core	380	85	frequency (Hz)	60
reaction plate	380	130		

Fig.4 shows an electric circuit configuration for the experiments. The source current is controlled by a programmable controller shown in Fig.4 intermittently, which is turned on for 3 sec. and turned off for 117 sec., in order to reduce heat effects on the characteristics of the thrust which is generated by iron and copper losses in experiments. A wattmeter and a force gauge has peak-hold function, so that experimental results in this paper are maximum values obtained by them.

Fig.5 shows a reaction plate with the proposed novel slits. It has many slits which are cut from the point over the edge of stator core to the outside in parallel as described above. The distance of slits between both sides in vertical direction to the thrust is 30 mm, since the width of the stator core is 30 mm. The slit length is 10 mm because there is leakage flux in this region, which are described the later experimental results.

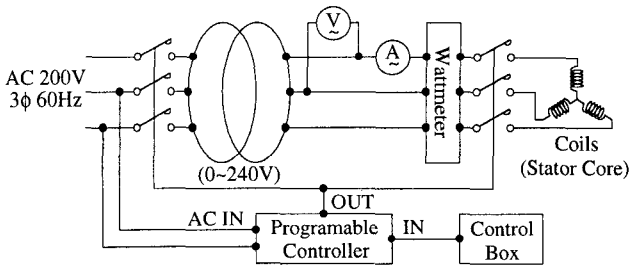


Fig.4. Electric Circuit of LIM.

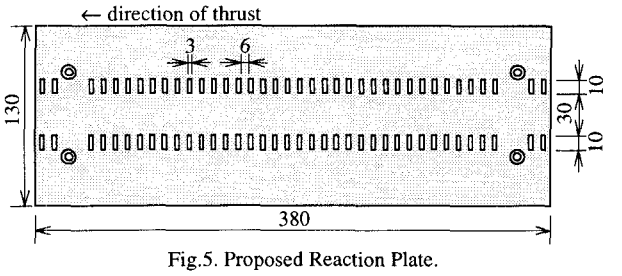
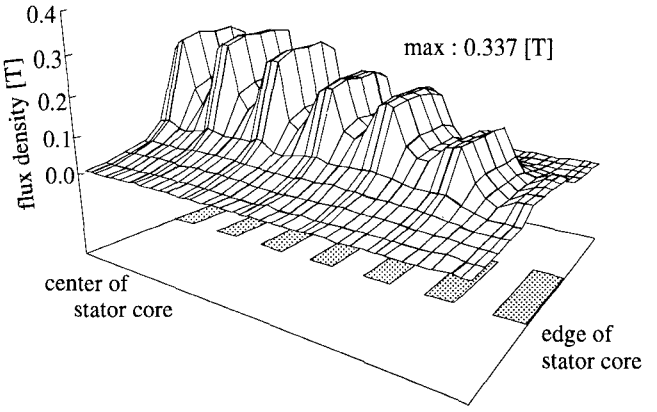


Fig.5. Proposed Reaction Plate.

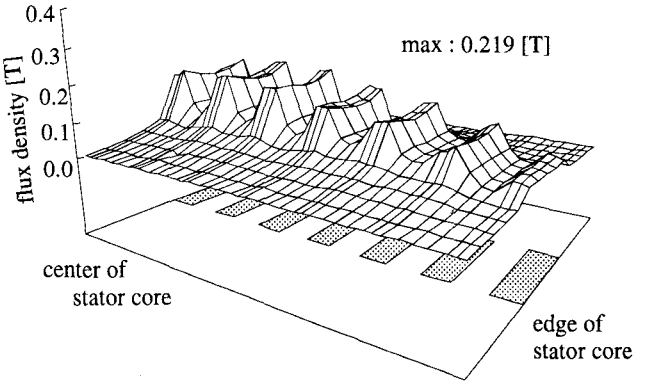
V . Experimental Results

Fig.6 shows the waveforms of z-axis component of flux density with the secondary core or without. They are measured by a gauss meter at the point 1 mm away from the stator core. With the secondary core, the gap length between the stator core and the secondary core is 5 mm. The input voltage is 220 V. The stator core takes a form such as a comb in order to set up the three phase windings. Tooth regions of the stator core are also shown in the figure as shaded rectangles. From this figure, it is found that the amplitude of flux density is neither flat and nor sinusoidal. It is considered that the shape of the stator core like a comb makes effects on the actual flux. Existence of the secondary core makes effects on the magnitude of flux density. The magnitude is about one and a half times as much as that without the secondary core. Without the secondary core, it is considered that the leakage flux seems to be concerned the edge of the tooth as shown in Fig.6 (b). On the other hand, with the secondary core, the flux density over each tooth is almost flat. The magnitude of the flux density becomes gradually smaller as parts from the center of stator core according to the state of the three phase winding as shown in Fig.7. It can be seen that there is leakage flux throughout the reaction plate. The magnitude of leakage flux is about a quarter times as mush as that on the tooth.

Fig.8 shows characteristics of the thrust using the proposed reaction plate. Results without slits are also shown in the same figure. Measurements are done during the input phase voltage is varied every 20 V from 100 to 220 V. The most left points show measured values when the input phase voltage is 100 V and the most right points show ones at 220 V. From this figure, it is found that (i) thrusts using proposed reaction plate is always larger than that without slits and (ii) its difference becomes larger as the input phase voltage becomes larger. The increased rate of the thrust between the novel reaction plate and the reaction plate without slits is about 3.2 %.



(a) with secondary core



(b) without secondary core

Fig.6. Flux Density Distributions.

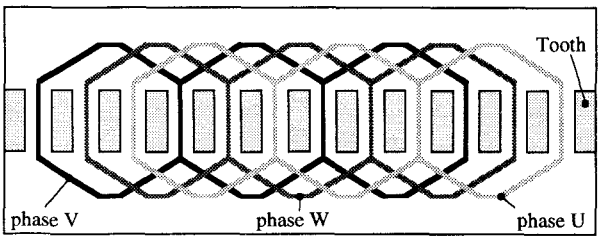


Fig.7 Winding Coils in Stator Core.

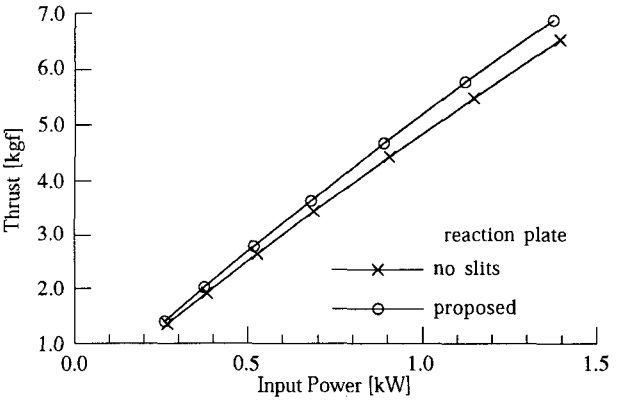


Fig.8. Characteristics of Thrust.

VI . Analyzed Model

Fig.9 shows an analyzed model of the proposed reaction plate in the numerical analysis, which is one half of the whole region due to the symmetry of the model. The effect of rivet hole is assumed to be neglected because the hole is distant from the center of the reaction plate. Table II shows the analyzed data. The flux density shown in Fig.6 (a) is applied as the applied flux density in the finite element analysis.

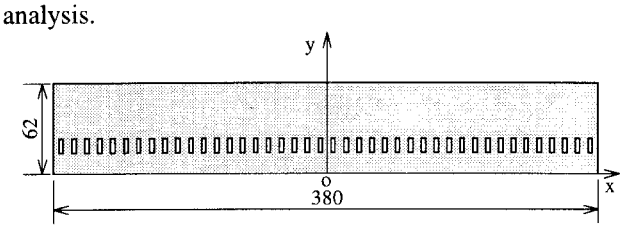


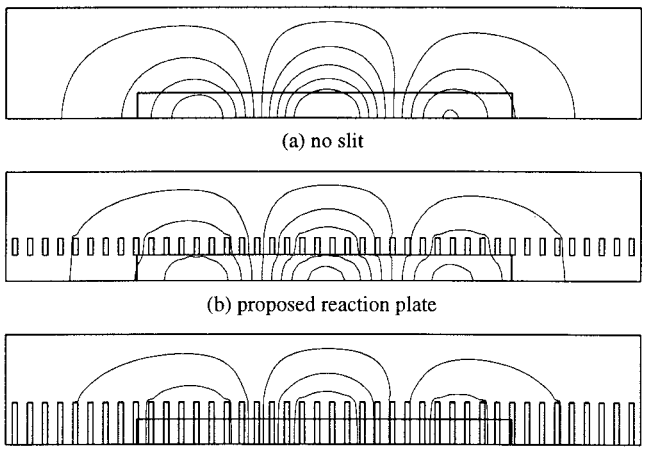
Fig.9. Analyzed Model.

TABLE II
ANALYZED DATA [4]

number of elements	9,880
number of nodes	5,334
number of unknowns	4,927
number of non-zero entries in matrix	18,925

V . Calculated Results

Fig.10 shows eddy current paths in a reaction plate with (a) no slit, (b) proposed slits and (c) conventional slits, which are calculated by using the 2-Dimensional finite element method. It is found that eddy current path is bound by the slits. Using a proposed reaction plate, the component of eddy current path in vertical to the direction of the thrust is increased in the region B shown in Fig.2. Using a conventional reaction plate, the component of eddy current path in vertical to the direction of the thrust is also increase, however, the eddy current is decreased because the resistance of the reaction plate is increased by means of making slits.



(a) no slit

(b) proposed reaction plate

(c) conventional reaction plate

Fig.10. Eddy Current Paths in Reaction Plate.

VIII . Conclusions

We propose a novel reaction plate with modified ladder slits to improve the thrust of LIM. It has many slits in parallel to the effective primary current flow. The flow of eddy currents in the reaction plate is made effectively change by the slits and the thrust improvement can be implemented by this method. Using the finite element method, the effect of slits for the flow of eddy currents can be obtained. These results are verified by experiments.

Acknowledgement

The authors wish to acknowledge the offer to the linear induction motor and an adequate discussion by Dr. M. Karita of Shinko Electric Co., Ltd.

References

[1] T. Koseki, S. Sone and D. Ebihara : "Analysis of secondary eddy current path of a linear induction motor," *in Proceedings of Linear Drive symposium, IEE Japan*, LD-92-100, pp.21-29, 1992.

[2] T. Onuki, Y. Kamiya and W. Jeon : "Three-Dimensional Finite Element Analysis of Slitted Plate in Linear Induction Motor," *Transactions of IEE Japan*, vol. 144-D, No.11, pp.1122-1129, 1994.

[3] S. J. Salon, B. Mathewson and S. Uda : "An Integro-Differential Approach to Eddy Currents in Thin Plates," *IEEE Trans. on Magnetics*, vol. MAG-19, No.6, pp.2405-2408, 1983.

[4] D. Rodger and N. Atkinson : "Finite Element Method for 3D Current Flow in Thin Conducting Sheets," *IEE-Proceeding*, vol. 135, Pt. A, No.6, pp.369-374, 1988.

[5] M. Tsuchimoto, A. Fukaya and T. Honma : "An Analysis of Eddy Current Testing with Sheet Current," *IEEE Trans on Magnetics*, vol. 29, No. 6, pp.2455-2457, 1993.

Novel Prediction Method of Acoustic Magnetic Noise Emitted by Inverter-fed Induction Motor System

Bin Kaku Ichiro Miyashita
Technical Research Laboratory
Toyo Electric Mfg. Co., Ltd.
338-1 Kami-soyagi, Yamato-shi
Kanagawa Pref. 242, Japan
Tel: +81-462-64-5781
Fax: +81-462-63-2947
E-mail: kaku@lab.toyodenki.co.jp

Satoru Sone
Electrical Engineering Dept.
the University of Tokyo
Hongo 7-3-1, Bunkyo-ku
Tokyo 113, Japan
Tel: +81-3-3812-2111(Ext. 6678)
Fax: +81-3-5802-3380
E-mail: sone@sone.t.u-tokyo.ac.jp

Abstract - **When an induction motor is driven by an inverter, the acoustic magnetic noise caused by the time harmonics of motor input is becoming a serious environmental problem. A novel prediction method of acoustic magnetic noise emitted by the inverter-fed motor system is presented in this paper. By this novel method, the acoustic magnetic noise vs. harmonic current characteristic function (NHCC function) is defined first, and then based on it, the acoustic magnetic noise can be predicted by the calculation of harmonic currents of motor. The principle of this method and the determination of NHCC function are introduced. At last, some experimental results are shown to verify the effectiveness of this novel method.**

I. INTRODUCTION

It is well-known that the acoustic magnetic noise is a problem inherited with the invention of induction motor, basically, it is caused by space harmonics of motor[1]. Due to several decades' efforts of many researchers, the noise has been reduced to a tolerant low level through the optimum design of motor. However, nowadays almost all the induction motors are driven by inverters. Inverter produces a supply voltage or current that is rich in time harmonics. These time harmonics considerably enhance the acoustic magnetic noise and cause a serious environmental problem. There are two reasons that make the prediction of acoustic magnetic noise very important.

(1) Environmental noise management.

When a motor is installed and driven by an inverter, how much noise can be generated from the motor is the matter that users care about. When the same motor is driven by different inverters, the noise characteristics are different, and when using the same inverter to drive different motors, the noise characteristics are also different one by one. For the purpose of managing the environmental noise, a simple method of predicting the acoustic magnetic noise emitted by inverter-fed motor system is eagerly required.

(2) Evaluation of low acoustic magnetic noise PWM methods.

Because the adoption of inverter causes a new motor noise problem, the low acoustic magnetic noise PWM techniques are demanded. For the purpose of developing low acoustic magnetic noise PWM methods, predicting the acoustic magnetic noise emitted by inverter-fed motor system is a very useful tool to evaluate the low acoustic magnetic noise characteristics of the PWM methods.

Some typical prediction methods of acoustic magnetic noise are introduced in references, generally, it contains following steps [1][2]:

(1) Analyzing the motor internal magnetic force.
(2) Calculating the mechanical resonant frequencies of motor.
(3) Calculating the sound radiation efficiency of motor.
(4) Synthesizing the acoustic magnetic noise of motor from the data obtained above.

Unfortunately, because the mechanical properties of motor are not so easy to be grasped, the methodology is still not sufficiently advanced to give the accurate results. Especially considering the influence of saturation, eccentricity, and slotting, the calculation can only be performed approximately.

In this paper, a novel prediction method of acoustic magnetic noise caused by time harmonics is introduced. This method is based on the authors defined **NHCC** function, the acoustic magnetic noise vs. harmonic current characteristic function which reflects the response of acoustic magnetic noise to a single harmonic current. This function represents the inherent properties of motor, like the resistance or inductance of motor. The **NHCC** function can be determined by experiment. By this method, the acoustic magnetic noise can be predicted by following steps:

(1) Measuring **NHCC** function of motor.
(2) Analyzing the frequency spectrum of motor current.
(3) Predicting the acoustic magnetic noise from the analyzed harmonic currents and measured **NHCC** function.

0-7803-3823-5/97/$10.00© 1997 IEEE

II. ACOUSTIC MAGNETIC NOISE CAUSED BY A SINGLE HARMONIC CURRENT

A. Basic Idea of Novel Method

For easy comprehension of this novel method, the basic idea of this novel method is better to be related first. It is well-known that in the control theory, the impulse response function $g(t)$ of system is a very important concept. It is defined as the output response of the system when the input is an unit impulse function $\delta(t)$. If the impulse response $g(t)$ of system is obtained, the system output $y(t)$ for any input $x(t)$ can be evaluated. This is shown in Fig.1. The noise prediction problem can be described as that the input of system (motor) are the harmonic currents, the output is acoustic magnetic noise. For the purpose of calculating the system output, the acoustic magnetic noise, similar to the concept of the impulse response function $g(t)$, a **NHCC** function is defined as the response of acoustic magnetic noise to a single harmonic current. Based on the **NHCC** function, the acoustic magnetic noise can be evaluated as the response to all the harmonic currents and it is also shown in Fig.1.

Calculation of system output:

Input System (motor) Output (response)

$x(t)$ $y(t)=\int_0^t g(\tau)\,x(t-\tau)\,d\tau$

Impulse response function $g(t)$

Prediction of acoustic magnetic noise:

Input System (motor) Output (response)

Harmonic currents i_j Acoustic noise L=equation (9)

NHCC function

Fig.1 Basic idea of novel method

B. Sound Pressure Level Caused by A Single Harmonic Current

Supposing that the fundamental current of motor is I_1 and there is only a single harmonic current denoted as I_h. The flux densities corresponding to these currents are B_1 and B_h. According to the theory about the mechanism of acoustic magnetic noise of motor[1], the radial magnetic forcewave caused by B_1 and B_h can be considered as the main reason causing the acoustic magnetic noise. In this case, the sound power W radiated from the motor can be expressed below [3]:

$$W=\left(\frac{\sqrt{2}\pi f H_m}{4\mu_0}\right)^2\times\frac{B^2_1 B^2_h \rho c \sigma S}{\left[\left(1-\frac{f}{f_{mec}}\right)^2+\left(\frac{2Df}{f_{mec}}\right)^2\right]^2}$$
$$=C\times B^2_1 B^2_h \qquad (1)$$

where H_m is a constant relating to the geometric dimension and the material properties of motor, f is the frequency of the radial magnetic forcewave, f_{mec} is the mechanical resonance frequency, D is the damping coefficient, μ_0 is the permeability constant, ρ is the density of medium, c is the speed of sound in the medium (the value of ρc for air at the room temperature is 415 N • s / m^3), σ is the radiation efficiency (also called the sound radiation factor). S is the area of the motor surface.

From the equation (1), it can be found that if frequency f of the radial magnetic forcewave is not changed, the sound power W emitted by motor is only determined by B_1 and B_h. Generally, the flux density B is proportional to the current, so the flux density B_1 and B_h can be expressed as:

$$\left.\begin{aligned} B_1 &= K_1 I_1 \\ B_h &= K_h I_h \end{aligned}\right\} \qquad (2)$$

where the K_1 and K_h are the constants related to the number of windings and the permeance.

The sound power level L_w can be given by:

$$L_w = 10\log\frac{W}{W_0}$$
$$= 10\log\frac{D\times I^2_1\times I^2_h}{W_0} \qquad (3)$$

where D is a constant.

The sound pressure level L at the area A can be expressed as:

$$L = L_w - 10\log A$$
$$= 10\log\frac{D\times I^2_1\times I^2_h}{W_0} - 10\log A \qquad (4)$$

C. Sound Pressure Level Variance Caused by Amplitude Variance of A Single Harmonic Current

Now it is assumed that the frequency and amplitude of fundamental current I_1 are not changed, the frequency of the single harmonic current is also not changed, but the amplitude of the single harmonic current I_h is changed from

I_{h1} to I_{h2} . From equation (4), the corresponding sound pressure level are:

$$\left.\begin{aligned} L_1 &= 10\log\frac{D\times I^2_1\times I^2_{h1}}{W_0} - 10\log A \\ L_2 &= 10\log\frac{D\times I^2_1\times I^2_{h2}}{W_0} - 10\log A \end{aligned}\right\} \quad (5)$$

The variance of the amplitude of the single harmonic current results in the variance of the sound pressure level ($\Delta L = L_2 - L_1$) and it can be expressed as follows:

$$\Delta L = L_2 - L_1 = 20\log\frac{I_{h2}}{I_{h1}} \quad (6)$$

Equation (6) shows how sound pressure level varies with the variation in amplitude of the single harmonic current.

III. DEFINITION OF NHCC FUNCTION

Like the impulse response function $g(t)$ is very important for analyzing the system response to any input, the **NHCC** function is also very important for predicting the acoustic magnetic noise. **NHCC** function is the response of acoustic magnetic noise to a single harmonic current. It is defined below:

The ideal sinusoidal voltage source V_1 is added with a pure single harmonic voltage component V_0, then supply them to motor. This causes a single harmonic current I_0 flowing in the motor and generate the acoustic magnetic noise L_0. The relationship between the generated acoustic magnetic noise L_0 and the rms value of the pure single harmonic current I_0 , is called acoustic magnetic Noise vs. Harmonic Current Characteristic function, i.e, $L_0=f(I_0)$, abbreviated as **NHCC** function. The description of the definition of **NHCC** function is also shown in Fig.2.

Obviously, **NHCC** function reflects the inherent characteristic of motor, like the resistance R_1, R_2 or the inductance L_1, L_2 of motor and it can also be determined by the experiment like the determination of R_1, R_2 or L_1, L_2 . The **NHCC** function reflects, or includes all the information about the mechanical properties such as material property, the dimension, the mechanical resonant frequency, and so on. By making use of **NHCC** function, the acoustic magnetic noise can be calculated very easily and accurately even though the mechanical properties are not considered so that by this novel method, the difficulties like the calculation of mechanical resonant frequency can be escaped.

IV. DETERMINATION OF NHCC FUNCTION

The **NHCC** function can be obtained by the experiment,

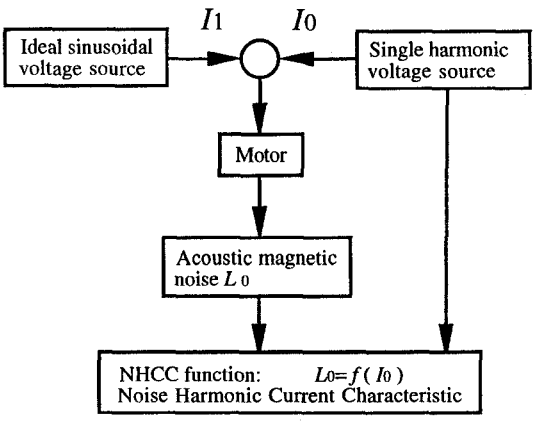


Fig.2 Definition of **NHCC** function

the details about it are introduced in section 7. During the experiment, the motor is running in rated status, and the fundamental current I_1 is kept I_1=30 A, its frequency f_1 is kept f_1=50 Hz. The pure single harmonic current I_0 can not be kept a constant because it is decreased as its frequency is increased. So the whole frequency range is divided into several small ranges and only in these small ranges, the amplitude of the single harmonic current I_0 is kept a certain value respectively. In section 6, it can be proved that the selection of the amplitude of the single harmonic current I_0 has no influence on the noise prediction. The acoustic magnetic noise L_0 is measured while the frequency of the single harmonic current I_0 is changed. Fig.3 is the measured **NHCC** function of a 7.5 kw induction motor.

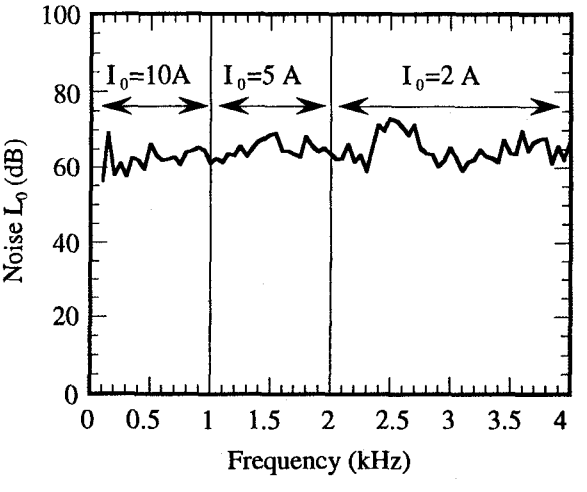


Fig.3 Measured **NHCC** function

V. PREDICTION OF ACOUSTIC MAGNETIC NOISE

Now the actual case is considered. As a matter of fact, there are many harmonic components in motor current. Supposing the harmonic currents are i_1, i_2, i_3, ... i_j , where j is the frequency of harmonics. The corresponding acoustic magnetic noise is L_1, L_2, L_3, ...L_j, which are

generated by the single harmonic component respectively. So the total acoustic magnetic noise (L) is given by:

$$L = 10\log\left(\sum_{j=1}^{\infty} 10^{\frac{L_j}{10}}\right) \tag{7}$$

From Fig.3, the harmonic currents that have the same harmonic frequencies with $i_1, i_2, i_3, \ldots\ldots i_j$ are denoted as $I_{0_1}, I_{0_2}, I_{0_3}, \ldots\ldots I_{0_j}$. The corresponding acoustic magnetic noise is $L_{0_1}, L_{0_2}, L_{0_3}, \ldots\ldots L_{0_j}$, which are generated by the single harmonic component $I_{0_1}, I_{0_2}, I_{0_3}, \ldots\ldots I_{0_j}$ respectively. The I_{0_j} and L_{0_j} are used as the reference values, and from equation (6),

$$L_j - L_{0j} = 20\log\frac{i_j}{I_{0j}} \tag{8}$$

From equation (8), L_j can be derived and substitute it into equation (7) , the following equation can be obtained, which is used to predict the acoustic magnetic noise caused by the time harmonics.

$$L = 10\log\left(\sum_{j}^{\infty} 10^{\frac{L_{0j}}{10}} \times \left(\frac{i_j}{I_{0j}}\right)^2\right) \tag{9}$$

Here is an example to show how to use equation (9) and **NHCC** function to predict the acoustic magnetic noise.

Supposing that motor is running in rated state, and by the simulation, the motor harmonic currents are calculated and listed as,

$$i_{500\,\mathrm{Hz}} = 0.5\,(\mathrm{A}),$$
$$i_{1250\,\mathrm{Hz}} = 0.8\,(\mathrm{A}),$$
$$i_{2500\,\mathrm{Hz}} = 0.3\,(\mathrm{A}),$$

From Fig.3, the reference values corresponding to these three frequencies are,

$$I_{0_500\,\mathrm{Hz}} = 10\,(\mathrm{A}), \quad L_{0_500\,\mathrm{Hz}} = 62.5\,(\mathrm{dB}),$$
$$I_{0_1250\,\mathrm{Hz}} = 5\,(\mathrm{A}), \quad L_{0_1250\,\mathrm{Hz}} = 65.0\,(\mathrm{dB}),$$
$$I_{0_2500\,\mathrm{Hz}} = 2\,(\mathrm{A}), \quad L_{0_2500\,\mathrm{Hz}} = 72.5\,(\mathrm{dB}).$$

Substituting these values into equation (9), the acoustic magnetic noise can be predicted, and the result is L=54.2 (dB).

VI. DISCUSSIONS

A. Selection of Reference Value I_0 in NHCC function

As shown in Fig.3, for measuring the **NHCC** function, the amplitude of the single harmonic current is selected as follows, $I_{0(j=0\sim1\mathrm{kHz})}$=10 A from the frequency 0 to 1 kHz,

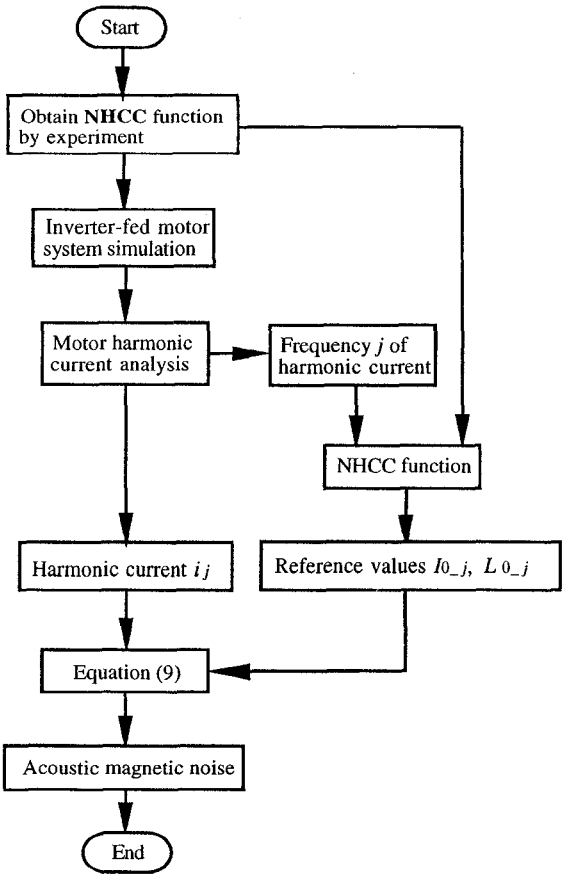


Fig.4 Flow of predicting acoustic magnetic noise

$I_{0(j=1\sim2\mathrm{kHz})}$=5 A from frequency 1 kHz to 2 kHz, and $I_{0(j=2\sim4\mathrm{kHz})}$=2 A from frequency 2 kHz to 4 kHz. These reference values can be selected arbitrarily if the acoustic magnetic noise generated by these single harmonic current is laud enough to be measured easily. In our experimental equipment, because there is a limitation to supply the single harmonic voltage, the amplitude of the single harmonic current becomes lower and lower as its frequency is increased. Here, it can be proved mathematically that the arbitrary selection of the reference value has no influence on the calculation of the acoustic magnetic noise by using equation (9).

Assuming that the reference value I_{0_j} is changed into I'_{0_j} , and the corresponding acoustic magnetic noise is changed from L_{0_j} into L'_{0_j}. From equation (8),

$$L'_{0j} - L_{0j} = 20\log\frac{I'_{0j}}{I_{0j}} \tag{10}$$

And the I_{0j}' can be expressed as,

$$I'_{0j} = I_{0j} \times 10^{\frac{L'_{0j} - L_{0j}}{20}} \tag{11}$$

In this case, the acoustic magnetic noise L' can be predicted by substituting the above relations into equation (9), and this results in the following equation:

$$L' = 10\log\left\{\sum_j^n 10^{\frac{L'_{0j}}{10}} \times \left(\frac{i_j}{I'_{0j}}\right)^2\right\}$$

$$= 10\log\left\{\sum_j^n 10^{\frac{L'_{0j}}{10}} \times (i_j)^2 \times \left(I_{0j} \times 10^{\frac{L'_{0j}-L_{0j}}{20}}\right)^{-2}\right\}$$

$$= 10\log\left\{\sum_j^n 10^{\frac{L_{0j}}{10}} \times \left(\frac{i_j}{I_{0j}}\right)^2\right\} = L \qquad (12)$$

From equation (12), it can be understand that if the reference value I_{0_j} is changed, the corresponding reference value L_{0_j} is also changed, so the selection of the reference value I_{0_j} has no influence on the calculation of the acoustic magnetic noise by using equation (9)

B. Prediction of Acoustic Magnetic Noise for Any Motor's Running States

The **NHCC** function shown in Fig.3 is measured under the condition that the motor is running in rated state, so the fundamental frequency is f_1=50 Hz and the fundamental current is I_1=30 A. In some kinds of application, such as the VVVF (Variable Voltage Variable Frequency), the motor current and frequency are changed depending on the different running state. In this case, equation (9) and the **NHCC** function shown in Fig.3 can not be used directly. To solve this problem,

(1) If there is an ideal sinusoidal voltage source that its output frequency can be changed free, according to the same procedures mentioned above, a group of **NHCC** functions with different fundamental frequencies and currents can be obtained. Based on this group of **NHCC** functions, the prediction of the acoustic magnetic noise for any motor's running states can be performed easily.

(2) If there is only an ideal sinusoidal voltage supply with a constant frequency f_1=50 Hz, the **NHCC** function shown in Fig.3 and the equation (9) should be modified somewhat.

For example, considering a certain running state of motor that the fundamental frequency is $f'_1 < 50$ Hz and the current is $I'_1 < 30$ A. In this case, the acoustic magnetic noise can be predicted approximately by the following equation.

$$L = 10\log\left(\sum_j^{\infty} 10^{\frac{L_{0j+50-f'_1}}{10}} \times \left(\frac{I'_1}{I_1}\right)^2 \times \left(\frac{i_j}{I_{0j+50-f'_1}}\right)^2\right) \qquad (13)$$

where the added item of $(I'_1 / I_1)^2$ is because that the **NHCC** function shown in Fig.3 is measured under the condition that I_1=30 A, if the fundamental frequency is not changed but only the amplitude of the fundamental component is changed from I_1 to I'_1, this causes the change in acoustic magnetic noise. Doing the same derivation mentioned above in section 2 and 5 cause the added item of $(I'_1 / I_1)^2$ in equation (13). The added subscript of $0j + 50 - f'_1$ means that the acoustic magnetic noise caused by fundamental component with frequency of 50 Hz and the harmonic component with the frequency of $0j$ Hz, is considered approximately the same to the acoustic magnetic noise caused by fundamental component with frequency of f'_1 Hz and the harmonic component with the frequency of $0j + 50 - f'_1$ Hz.

VII. EXPERIMENTAL RESULTS.

To verify the effectiveness of this novel method, some experiments are performed. Fig.5 shows the experimental system. The motor is 7.5 kW induction motor, the rated values are V_1=200 V , I_1=30 A, f_1=50 Hz. First, for the purpose of examining the equation (6), the experimental system is configured as: switch K1, K2 are on, switch K3 is off. The ideal voltage source supplies the fundamental component of voltage V_1. The inverter is used as the single pure harmonic voltage source V_0. These two voltages are

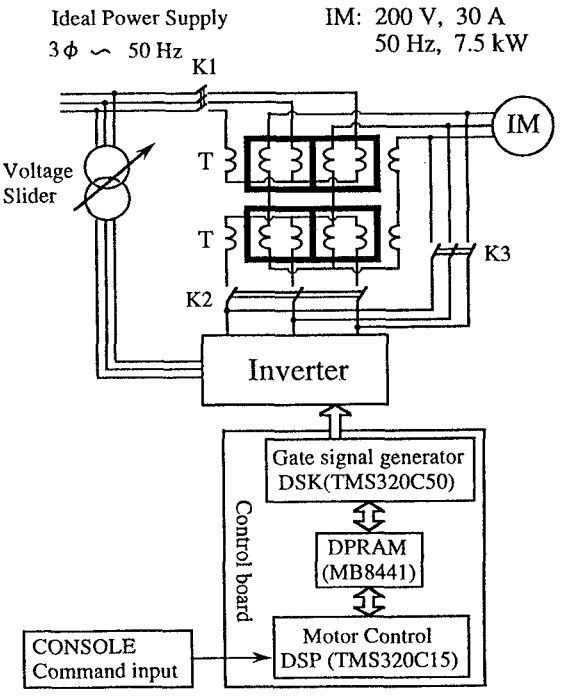


Fig.5 Experimental system

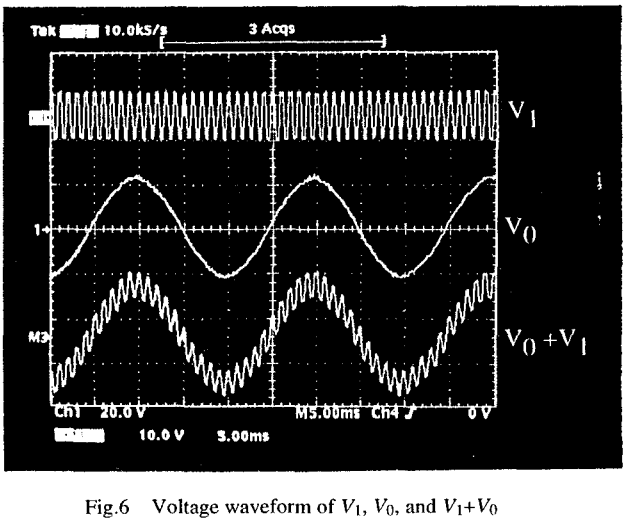


Fig.6 Voltage waveform of V_1, V_0, and V_1+V_0

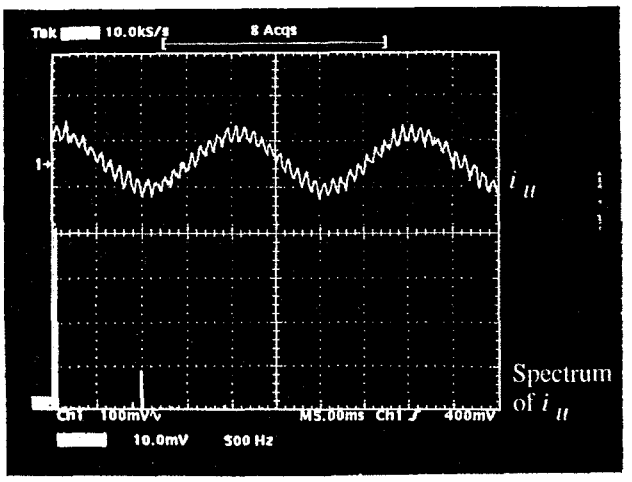


Fig.7 Current waveform and its spectrum

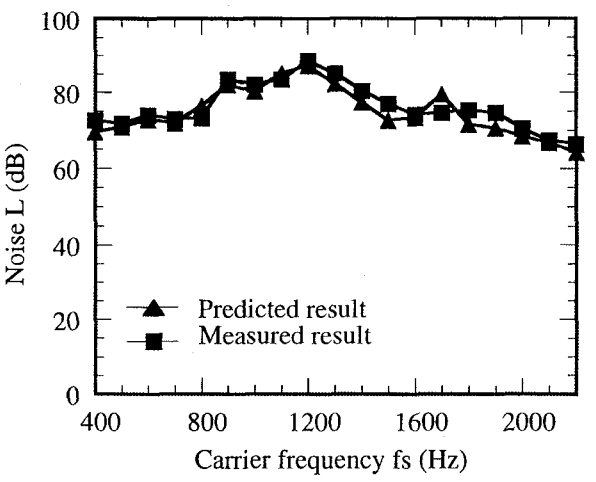


Fig.9 Predicted result and experimental result.

supplied to motor through the transformer T. The inverter is running in one-pulse mode. The frequency of the single harmonic current is determined by the frequency of inverter output. The amplitude of the single harmonic current is controlled by adjusting the input DC link voltage of inverter through the voltage slider. Fig.6 shows their waveforms and Fig.7 shows the motor current waveform and its spectrum, where the frequency of the fundamental component is f_1=50 Hz, the frequency of the inverter output is f_s=1000 Hz.

From Fig.7, it can be seen that the inverter output can be considered as a single harmonic source approximately. Now the frequency and amplitude of fundamental current I_1 are not changed, the frequency of the single harmonic current is also not changed, but the amplitude of the single harmonic current I_h is changed from I_{h1} to I_{h2} and then the noise corresponding to I_{h1} and I_{h2} is measured. So the variance of acoustic magnetic noise ΔL can be calculated. The result is shown in Fig.8. By this result, equation (6) is proved.

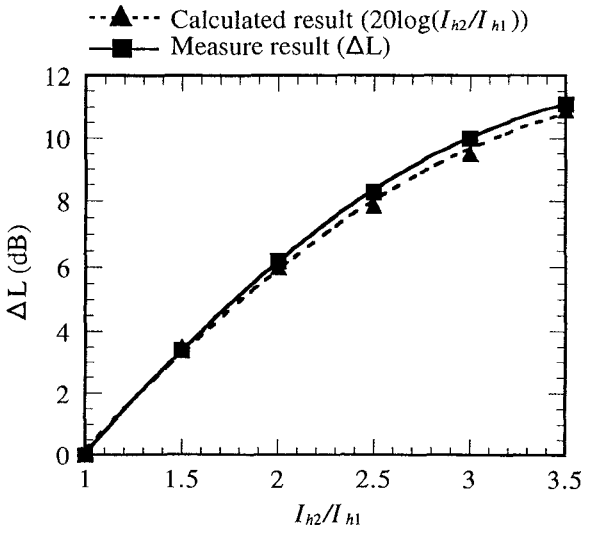


Fig.8 Relation between noise change (ΔL) and single harmonic current change rate (I1/I2)

Next, the experimental system is configured as K1, K2 are off, K3 is on so that the motor is driven by an inverter directly. Fig.9 shows the experimental results and the predicted results of the acoustic magnetic noise. It can be seen that they have good accordance with each other and the effectiveness of this novel method is proved.

VIII. CONCLUSIONS

In this paper, a **NHCC** function, the acoustic magnetic noise vs. harmonic current characteristic function is defined, and based on this function, a novel prediction method of acoustic magnetic noise caused by the time harmonics and emitted from inverter-fed motor system is introduced. By this method, the acoustic magnetic noise can be predicted very easily and accurately even though the mechanical properties of motor are not calculated so that the difficulties like calculation of mechanical resonant frequency and noise radiation efficiency can be escaped. The experimental results have proved the effectiveness of this method.

References:

[1] Ronnie J. M. Belmans, Dirk Verdyck, Willy Geysen, Raymond D. Findlay:" Electro-Mechanical Analysis of the Audible Noise of an Inverter-Fed Squirrel-Cage Induction Motor ", *IEEE Trans on Industry Applications* , Vol.27, No.3, pp 539-544, May/June, 1991

[2] Z.Q.Zhu, D.Howe, Ceng FIEE :" Improved method for pridition of electromagnetic noise radiated by electrical machines ", *IEE Proc.-Electr, Power Appl.*, Vol. 141, No.2, March 1994

[3] P.L.Timar, J.C.S.Lai; " Acoustic noise of electromagnetic origin in an ideal frequency-converter-driven induction motor", *IEE Proc.-Electr, Power Appl.*, Vol. 141, No.6, pp341-346, November 1994

A Speed Calculation Method for Induction Motor Based on Voltage Decoupling Control Principle

Zeng Yuenan*, Feng Duoshen** and Chen Boshi*
*Research Institute of Electrical Machinery and Control Engineering, Shanghai University
149 Yanchang Road, Shanghai, China, 200072
Fax: +86-56635364, Phone: +86-56653211,
**Research Institute of Automation, Guangdong University of Technology
729 Dongfengdong Road, Guangzhou, China, 510090
Fax: +86-87766069, Phone: +86-87613450,

Abstract — **A new simplified equivalent model of induction motor is proposed firstly in this paper, which is derived based on the voltage decoupling control principle of induction motor. The model consists of two subsystems, one is rotor flux subsystem and another is torque current subsystem, that is identical with that of DC-motor. According to this model, a speed calculation method is presented for a speed sensorless vector-controlled induction motor drive system, which is using integration of the difference between the command of torque current and the torque component of stator current. The validity of the proposed method is verified by computer simulation results.**

I . INTRODUCTION

The method of vector-controlled induction motor has been employed generally as a high performance control method. In order to apply the vector-controlled induction motor drive system to various of industry applications, speed sensorless vector-controlled induction motor drive system is required. From the regard, the method of vector-controlled induction motor without speed sensor is presented. The emerging of this method has attracted the research workers attention in the field of electrical drives. The method has become one of the investigating problems that the research workers most attach importance to and represents an important developing direction of the induction motor drive control technology.

In the speed sensorless vector-controlled induction motor drive systems, the important mater is that how can obtain the message of motor rotary speed accurately. A great deal of methods about obtaining the speed have been proposed so far [1] [2] [3] [4] [5]. In this paper, a speed calculation method is presented that using integration of the difference between the command of torque current and the torque component of stator current, which is obtained based on a new simplified equivalent model of induction motor that is proposed firstly in this paper.

The paper is outlined as follows: in the second section, a new simplified equivalent model of induction motor is derived based on the voltage decoupling control principle, it consists of two subsystems, one is rotor flux subsystem and another is torque current subsystem. The model is a self-balance system and is identical with that of DC-motor. The third section, according to the proposed induction model, a speed calculation method is presented, which using integration of the difference between the command of torque current and the torque component of stator current. The computer simulation results are given in the fourth section, the results are accordant with that of the theory analysis completely and show that the speed calculation method is validity. Finally, the fifth section concludes this paper.

II . THE EQUIVALENT MODEL OF INDUCTION MOTOR

The objective of the voltage decoupling control for induction motor is that decomposes the model of induction motor into two independent subsystems, one is d-axis rotor flux subsystem and another is q-axis torque current subsystem [6] [7]. Therefor the rotor flux and the torque component of the stator current are controlled separately in their respective subsystem. However, the equivalent model of induction motor shown in [6] [7] can not be directly used to analysis and design speed sensorless vector-controlled induction motor drive system. This is because that when the coupling voltage terms between d-axis and q-axis are canceled, the term of backward electromotive force in q-axis subsystem is canceled at the same time. In the case of speed sensorless, the model becomes a self-unbalance system.

In order to solve the problem, a new simplified equivalent model of induction motor is proposed in this paper based on the voltage decoupling control principle.

The dynamic equations of squirrel-cage induction motor in the synchronous rotary d-q coordinate that is oriented with rotor flux-axis are expressed as follows.

$$V_{ds} = (R_s + L_{ls}P)i_{ds} - \omega_s L_{ls} i_{qs} + \frac{L_m}{L_r} P\Psi_r \,, \qquad (1)$$

$$V_{qs} = \omega_s L_{ls} i_{ds} + (R_s + L_{ls}P)i_{qs} + \frac{L_m}{L_r}\omega_s \Psi_r \,, \qquad (2)$$

$$0 = -\frac{R_r}{L_r} L_m i_{ds} + \left(\frac{R_r}{L_r} + P\right)\Psi_r \,, \qquad (3)$$

$$0 = -\frac{R_r}{L_r} L_m i_{qs} + \omega_{sl}\Psi_r \,, \qquad (4)$$

$$T_e = n_p \frac{L_m}{L_r}(i_{qs}\Psi_r) \ , \tag{5}$$

$$T_e - T_L = \frac{J}{n_p} \times \frac{d\omega_r}{dt} \ , \tag{6}$$

where $L_{ls} = L_s\left[1-\left(L_m^2/L_sL_r\right)\right]$, $\omega_{sl} = \omega_s - \omega_r$, $\Psi_r = \Psi_{dr}$. The meanings of the parameters are as follows.

V_{ds}, V_{qs}: d-axis and q-axis component of stator voltage.

i_{ds}, i_{qs}: d-axis and q-axis component of stator current.

R_s, R_r: stator and rotor resistance.

L_s, L_r: stator and rotor autoinductance.

L_m: stator/rotor mutual inductance.

L_{ls}: stator leakage inductance.

ω_s: primary synchronous angular frequency.

ω_r: rotor rotary angular frequency.

ω_{sl}: slip angular frequency.

Ψ_r: rotor flux linkage

Ψ_{dr}: d-axis component of rotor flux linkage.

T_e, T_L: electromagnetic and load torque.

J : moment of inertia.

n_p: pairs of magnetic pole.

P: differential operator.

Substituting $\omega_{sl} = \omega_s - \omega_r$ and equation (4) into the fourth term of the right side in equation (2), therefor the equation (2) can be rewritten as follows

$$V_{qs} = \omega_s L_{ls} i_{ds} + (R + L_{ls}P) i_{qs} + \frac{L_m}{L_r}\omega_r \Psi_r \ , \tag{7}$$

where $R = \left[R_s + (L_m \backslash L_r)^2 R_r\right]$. According to equations (1) (3) (5) (6) (7), the equivalent model of induction motor in d-q coordinate as shown in Fig.1 can be obtained. In the figure, $T_r (= L_r \backslash R_r)$ is named as rotor loop time constant. It can be seen from Fig.1 that there is coupling electrical potential terms between V_{ds} and V_{qs}, namely

$$V_{q \to d} = \omega_s L_{ls} i_{qs} \ , \tag{8}$$

$$V_{d \to q} = -\omega_s L_{ls} i_{ds} \ . \tag{9}$$

Let the given stator voltage V input to induction motor includes two components. One is $V_{q \to d}$ or $V_{d \to q}$ that used to compensate the coupling electrical potential terms between V_{ds} and V_{qs}, which acts as decoupling, and another is V_{ds}' or V_{qs}' that used to control rotor flux or control the torque component of stator current, namely:

$$V_{ds} = V_{ds}' - V_{q \to d} \ , \tag{10}$$

$$V_{qs} = V_{qs}' - V_{d \to q} \ . \tag{11}$$

Under the given voltage V affecting, the coupling electrical potential terms are compensated. Then an equivalent model of induction motor can be obtained, shown as Fig.2.

It can be seen form Fig.2 that the equivalent model of induction motor is decoupled in d-q coordinate and decomposed into two subsystems, one is d-axis rotor flux subsystem and another is q-axis torque current subsystem. Its structure is similar to that of the independent exciting DC-motor.

Assuming that the rotor flux Ψ_r is constant $(\Psi_r = \Psi_r')$ below the base-frequency, therefor the d-axis subsystem can be omitted. Under the condition of rated exciting, a new simplified equivalent model of induction motor as shown in Fig.3 is obtained. In the figure, n is referred to as revolution, GD^2 is referred to as flywheel inertia, and

$$C_e = \frac{L_m}{L_r} \times \frac{2\pi \cdot n_p}{60} \times \Psi_r' \ ,$$

$$C_m = n_p \times \frac{L_m}{L_r} \times \Psi_r' \left(= \frac{30}{\pi} \times Ce \right) .$$

The simplified equivalent model of induction motor described in Fig.3 is a self-balance system and is identical with that of DC-motor under rated exciting.

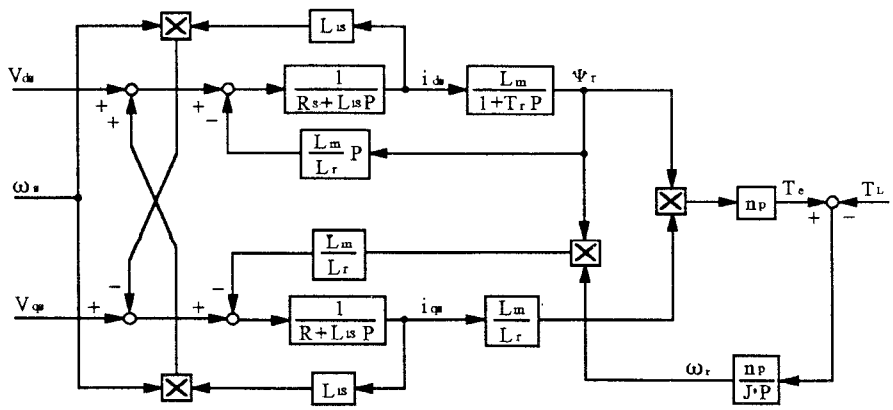


Fig. 1. The equivalent model of induction motor in d-q coordinate

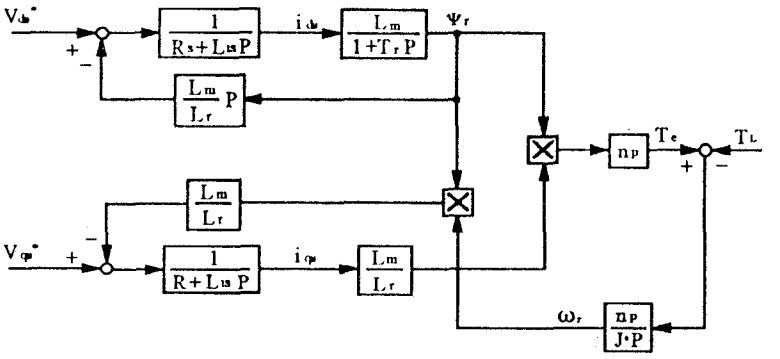


Fig.2 Decoupled equivalent model of induction motor

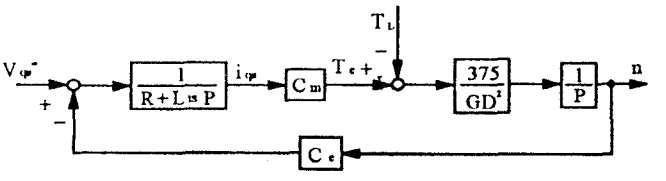


Fig. 3. Simplified equivalent model of induction motor

Ⅲ. SPEED CALCULATION METHOD

Assuming that the synchronous rotary coordinate is oriented with the direction of the rotor flux (Ψ_r) and Ψ_r is kept constant ($\Psi_r = \Psi_r^*$). Then the simplified equivalent model of induction motor shown in Fig.3 can be formulated as follows.

$$V_{qs}^* = (R + L_{ls}P)i_{qs} + C_e \times n \ , \tag{12}$$

$$n = C_m \times \frac{375}{GD^2}\int (i_{qs} - i_{dL})dt \ , \tag{13}$$

where $i_{dL} = T_L / C_m$. It can be seen from the equation (13) that the integration of the difference between the i_{qs} and the i_{dL} is the rotary speed of induction motor.

Because, in the equation (13), the i_{qs} is an only current component that can be detected, so a speed calculation mechanism is constructed as follows.

$$\hat{n} = C_m \times \frac{375}{GD^2}\int (i_{qs}^* - i_{qs})dt \ , \tag{14}$$

namely, using the integration of the difference between the command i_{qs}^* of torque current, which is the output of the speed adjuster, and the torque component of stator current to calculate the speed.

According to equation (12), let V_{qs}^* is

$$V_{qs}^* = (R + L_{ls}P)i_{qs}^* + C_e \times \hat{n} \ , \tag{15}$$

that is used to produce the component of torque current. Hence, according to equations (12) (14) (15), a simplified system configuration of speed sensorless induction motor drive system as shown in Fig.4 is obtained...

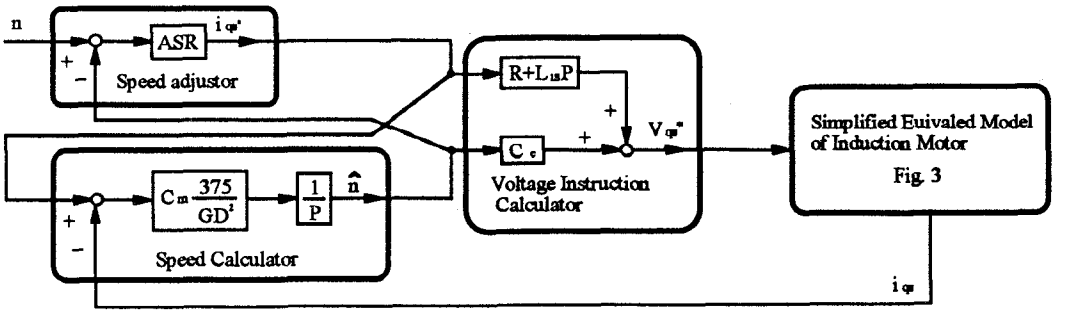


Fig.4 Simplified system configuration of speed sensorless induction drive system

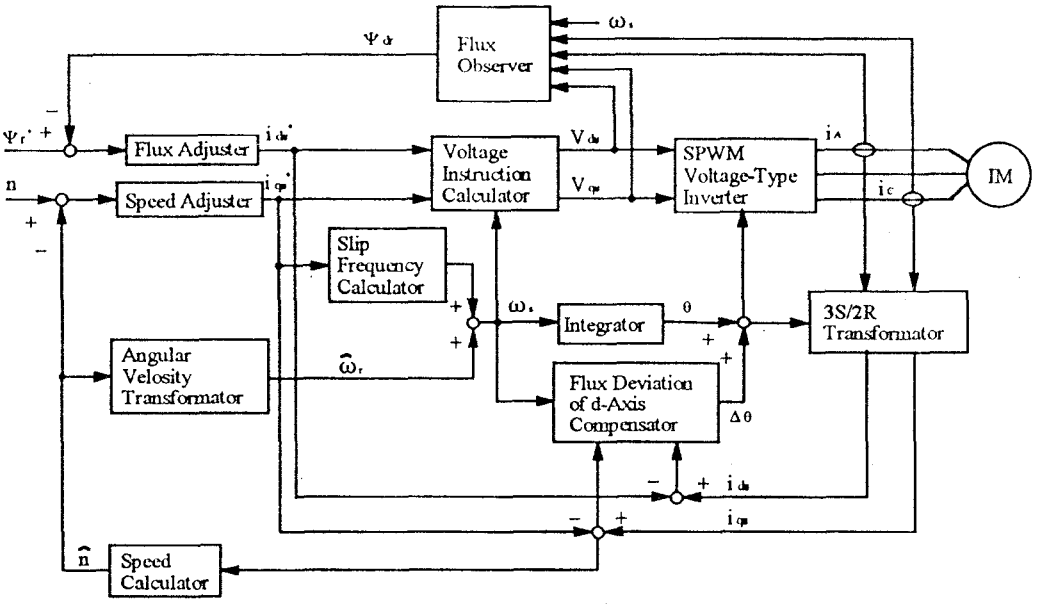


Fig.5 Block diagram of speed sensorless vector-controlled induction motor drive system

Let V_{ds}^* is as follows

$$V_{ds}^* = (R_s + L_{ls}P)i_{ds}^* , \tag{16}$$

that is used to produce exciting current of rotor flux. According to equation (16) and the conditions of slip frequency vector control

$$i_{ds}^* = \frac{\Psi_r^*}{L_m} , \tag{17}$$

$$\omega_{sl} = \frac{L_m}{T_r \Psi_r^*} i_{qs}^* , \tag{18}$$

as well as equations (12) (14) (15), a block diagram of speed sensorless vector-controlled induction motor drive system fed by voltage source as shown in Fig.5 is obtained

In the dynamic state and when the rotor resistance variation, a compensatory link of d-axis flux linkage deviation [1] is introduced into the Fig.5, so as assuring the control reference d-axis is oriented with the direction of rotor flux quickly and accurately. In thr figure, the model of flux observer is refered to [7].

It can be proved that:

(1) The calculated speed is identical with the actual speed in the steady state, but there is an error between them in the dynamic state.

(2) The steady precision of the calculated speed is independent of the inertia.

(3) When the parameter of rotor resistance variates, there is an error between the calculated speed and the actual speed in the steady state. The error is $\Delta n = \Delta R \times i_{qs}^*$.

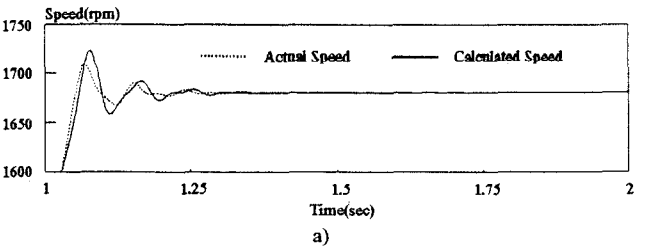
Ⅳ. SYSTEM SIMULATION EXPERIMENTS

The parameters of induction motor used in the simulation experiments are listed in the appendix A.

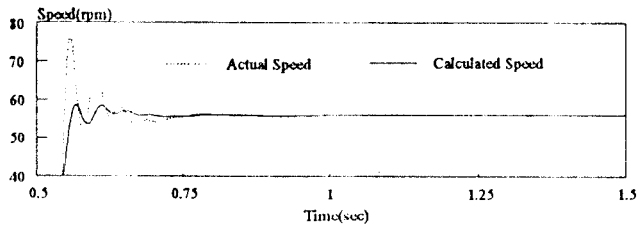
For simplified and easily distinguished, in the figures shown as bellows, the induction motor speed response of computer simulation and the calculated speed by equation (14) are refereed to as actual speed and calculated speed respectively. The d-axis component of rotor flux linkage is refered to as d-axis flux linkage and q-axis component of rotor flux linkage is refereed to as q-axis flux linkage, in the computer simulation experiments. The electrical torque response of computer simulation is refereed to as torque.

1) Computer simulation experiment one

The induction motor starting experiments results of computer simulation are shown in Fig.6 under rated load. Fig.6 a) and b) are motor speed response and calculated speed of computer simulation respectively under rated given 1680 rpm and lower given 56 rpm.



a)

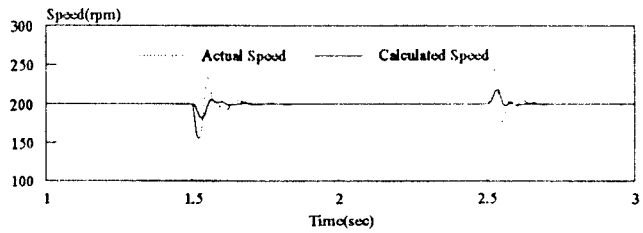


b)

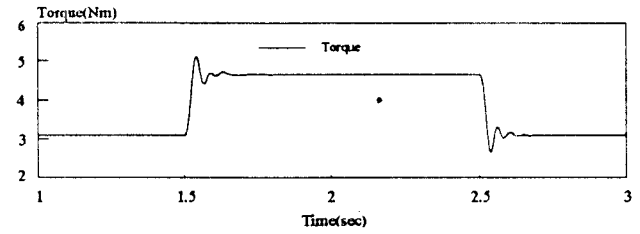
Fig.6 The Speed curves of computer simulation

2) Computer simulation experiment two

Under given speed 200 rpm and rated load, the motor operates stably. At 2s the load is decreased to 50% of rating and at 3s the load is added to 50% of rating, the speed response and calculated speed of computer simulation is shown in Fig.7 a) and the torque response is shown in Fig.7 b).



a)

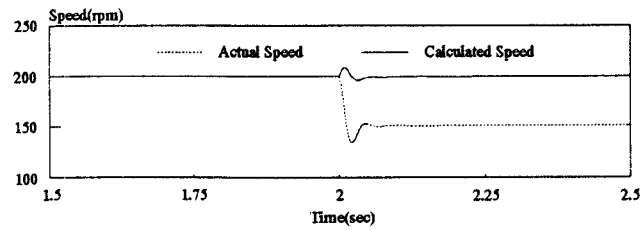


b)

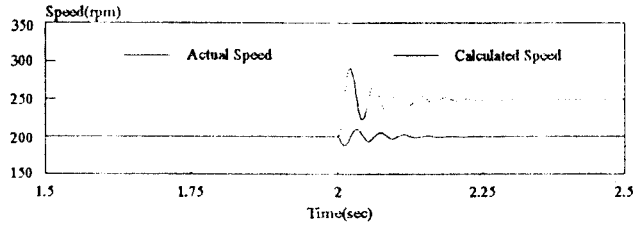
Fig.7 The experiment curves of computer simulation

3) Computer simulation experiment three

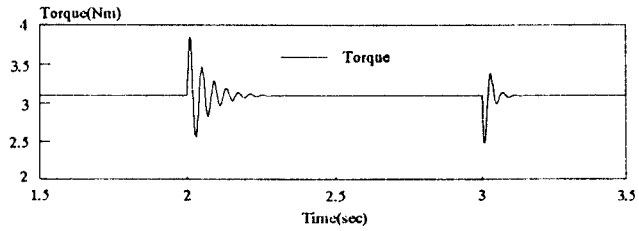
The experiment results of computer simulation are shown in theFig.8 when rotor resistance is changed abruptly, under given speed 200 rpm and rated load. Fig.8 a) is the speed curves when rotor resistance is added to 50% of rating and Fig.8 b)is the speed curves when rotor resistance is decreased to 50% of rating. Fig8. c)and d) show the torque response and rotor flux linkage rsponse respectively when rotor resistance is decreased to 50% of rating at 2s and added to 50% of rating at 3s.



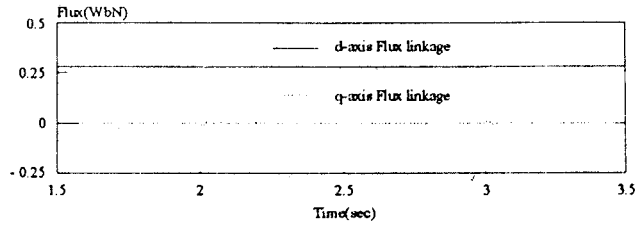
a)



b)



c)

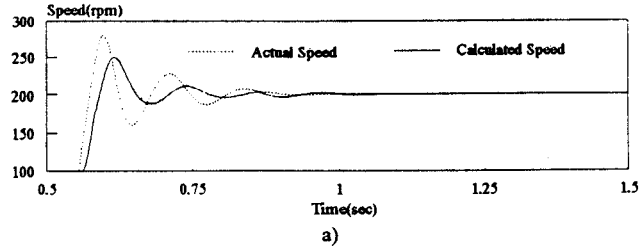


d)

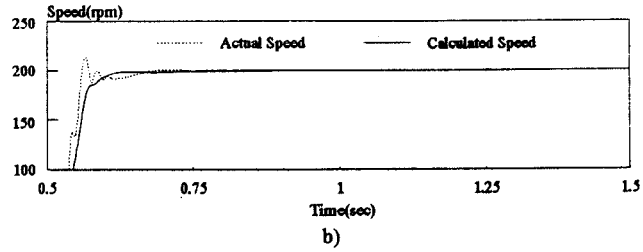
Fig.8 The experiment curves of computer simulation

4) Computer simulation experiment four

Under given speed 200 rpm and rated load, the simulation experiment results are given in the Fig.9 when inertia is changed. Fig.9 a) is the speed curves of computer simulation when the inertia is 4 times larger than the rating. Fig.9 b) shows the speed curves of computer simulation when the inertia is 4 times less than the rating.



a)



b)

Fig.9 The speed curves of computer simulation

It can be seen from Fig.6 and Fig.7 that the performance of proposed control method is satisfactory.

The Fig.8 shows that When rotor resistance is changed, there is an error between the calculated speed and the actual speed of computer simulation, the error is about 50 rpm. Fig.9 shows that the steady-state accuracy of calculated speed have no relation to the inertia when the system is steady.

V. CONCLUSIONS

In this paper, a new simplified equivalent model of induction motor is proposed firstly, based on the voltage decoupling control principle. According to the model, a speed calculation method is presented. The method's validity is verified by computer simulation experiments. According to the simulation results, the conclusions are made as follows.

1) The speed adjustment range from rated value 1680 rpm to lower speed 56 rpm is achieved in the paper. The Adjustable-speed ratio is 1:30.
2) The value of the calculated speed is identical with that of the actual speed in the steady state but there is an error in the dynamic state, when rotor resistance is equal to the rating. However, when the rotor resistance is changed, there is a static error between them, the error is $\Delta n = \Delta R \times i_{qs}^{*}$
3) The steady value of calculated speed doesn't be affected by the changed load inertia, and is identical with that of the actual speed.

Appendix A

The parameters of induction motor used in the computer simulation are as follows:

Table 1: Induction Motor Parameters

Voltage	90 V
Current	4.2 A
Frequency	60 Hz
Torque	3.1 Nm
Revolution	1680 rpm
Phase	3
np	2
J	0.001 Kgm^2
Rs	1.2 Ω
Rr	1.03 Ω
Ls	0.0805H
Lr	0.08377H
Lm	0.0777H

REFERENCES

[1] YAMAMOTO, etal., The method of speed sensorless control, The national conference of electrical association, Japan,1989.

[2] Colin Schauder, Adaptive Speed Identification for Vector Control of Induction motor without Rotational Transducers, IEEE Trans. on Ind. Appl., Vol.28, No.5, 1992.

[3] Lazhard Ben-Brahim and Atsuo Kawamura, A fully Digitized Field-Oriented Controlled Induction Motor Drive Using only Current Sensors, IEEE Trans. on Ind. Electron., Vol.39, No.3, 1992.

[4] Lazhard Ben-Brahim, etal., Implementation of an Induction Motor Speed Estimation Using Neural Networks, IPEC-Yokohama'95.

[5] Zeng Yuenan, Feng Duosheng, etal., Digitized Vector Controlled Induction Motor Drive Systems Using Only Current Sensors, Proceedings of CAVD'93, China.

[6] Kouhei Ohnishi, etal., Decoupling Control of Secondary Flux and Secondary Current in Induction Motor Drive with Controlled Voltage Source and Its Comparison with Voltage/Hertz Control, IEEE Trans. on Ind., Appl., Vol.21, 1985.

[7] Xu Dazhong, The principle on AC-Motor Drives, Proceedings of Zhejiang University, China, 1991.

[8] Chen Boshi, Automatic Control System on Electric Drives, Proceedings of Shanghai University, China, 1991.

High-Power Drive Using A Wound Rotor Induction Motor and Two Current Controlled Inverters

Yoshitaka Kawabata, Emenike C. Ejiogu,
Kazuhide Nishiyama, Takao Kawabata,
Dept. of Electrical & Electronic Engineering
Ritsumeikan University
1-1-1, Nojihigashi, Kusatsu-shi, Shiga, 525, Japan
Fax: +81-775-61-2663, Phone: +81-775-66-1111
E-mail: mpe40024@bkc.ritsumei.ac.jp

Abstract — **New configurations for high-power and high performance drives suitable for steel rolling mill drives will be presented. Three-level inverters using 6 inch GTOs, can deliver 10,000kVA output. But in case of drives rated more than several thousands kW, this capacity is still insufficient. Usually, for such drives, two three-level inverters have been combined using bulky, expensive inter-phase reactors.**

To solve these problems, a new configuration using a wound rotor induction motor and two inverters, is proposed.

In this configuration, outputs of two inverters are combined directly within the machine, the novel features that can be obtained with be explained.

I. INTRODUCTION

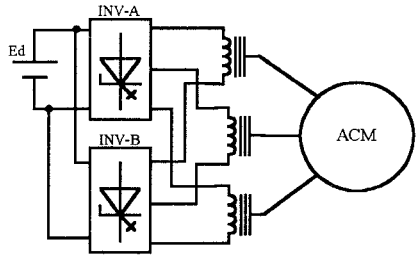
For high power and high performance drives such as steel rolling mill drives, synchronous machines or induction machines, cyclo-converters have been usually adopted until three or four years ago.

In the last four years, the three-level inverter using 4inch GTOs or 6inch GTOs drives have been adopted in place of cyclo-converters, where the drive ratings are less than several thousands kW. However, in the case of drives rated more than several thousands kW, these inverter capacity are still insufficient. Therefore, more than two inverters have been combined using inter-phase reactors as shown in Fig.1(a). But inter-phase reactors have problems of acoustic noise, losses and magnetic saturation.

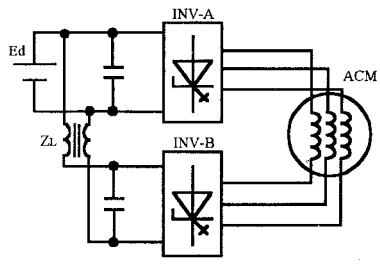
Almost three years ago, to solve these problems, Dr. H. Stemmler and the last author independently proposed new drive configurations using the open winding AC motor, such as shown in Fig.1(b) [1][2].

These configurations can combine the output of two inverters without inter-phase reactors. However, in these configurations, if the DC circuit of one inverter is earthed, then the potential of the other inverter becomes high, and therefore high insulation specification is needed.

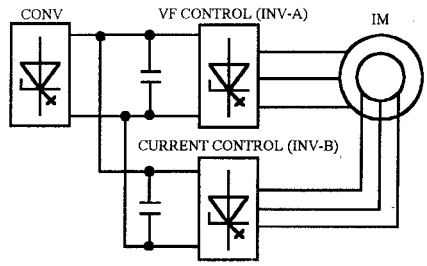
The authors proposed new high-power drive configurations using V/F controlled inverter in the stator of the wound induction motor and a current controlled voltage source inverter in the rotor side (TYPE VC), as shown in Fig.1(c)[3]. In these configurations, the stator and the rotor are electrically isolated, therefore high insulation specification is not needed as in Fig.1(b).



(a) Usual Inter-Phase Reactor Circuit



(b) Open-Winding AC Motor Using Common DC Power Source



(c) Wound Rotor Induction Motor Using V/F Controlled Inverter and Current Controlled Inverter

Fig.1. Previously Proposed Configurations of High-Power Motor Drives

However, the stator magnetizing current is not completely decoupled from the rotor torque current.

II. NEW CONFIGURATION

To solve this problem, in this paper, the adoption of current controlled inverter in both the stator and the rotor (TYPE CC), as shown in Fig.2 will be proposed.

In this configuration, the currents, $i_{\gamma 1}$, $i_{\gamma 2}$, $i_{\delta 1}$ and $i_{\delta 2}$ are completely decoupled, therefore excellent control performance can be obtained.

In case of the TYPE VC, the total magnetizing current, i_{γ}, is determined by the stator side INV-A through its voltage, and the torque current, i_{δ}, is controlled mainly by the rotor side INV-B. On the other hand, in case of the TYPE CC, the magnetizing current, i_{γ}, can be supplied from both inverters by arbitrary sharing as shown in Fig.3(a).

The sharing of voltage for torque current under synchronous speed and above synchronous speed is explained in Fig.3(b) and (c). By doing so, the torque current, i_{δ}, is controlled by both inverters.

III. CONTROL SYSTEM

3-1 Frequency Control

The motor speed is determined by the sum or the difference of the frequency of two inverters. The most simple frequency control strategies are lines A1 shown in Fig.4. In case of these lines, using two inverters of 20Hz rated frequency, the speed corresponding to 40Hz can be obtained. But when the effective frequency is under 20 Hz, undesirable power circulation occurs, and this may cause some deterioration of the efficiency. To minimize this power circulation, frequency control strategies is improved as line A2 of Fig.4. In case of these lines, the region where the two inverters operate in f1+f2 fashion increases, and hence the power circulation is decreased.

3-2 Decoupled Current Control

The magnetizing current, i_{γ}, and the torque current, i_{δ}, of both the stator and the rotor are controlled by a decoupled current controller using matrix theory as shown in Fig.5. Thus, all rotor variables are converted to the stator windings by turn ratios. In this controller, the coupling elements in the matrix A concerning the stator and the rotor currents are decoupled by the matrix B.

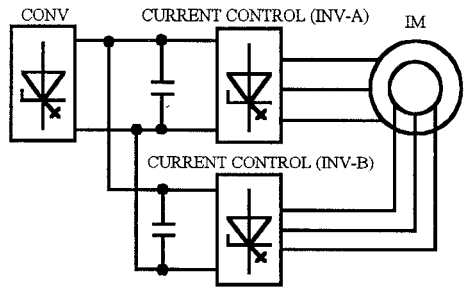
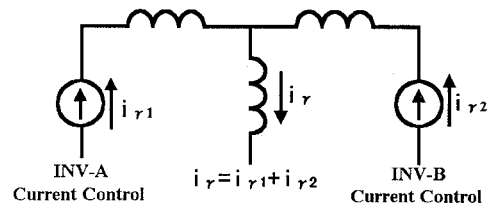
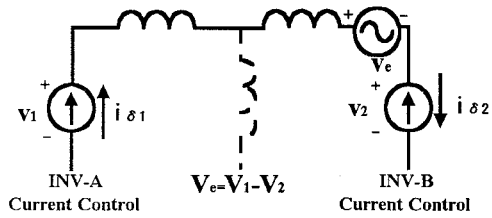


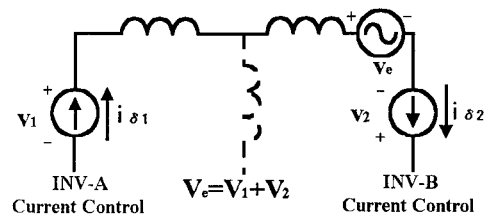
Fig.2 Proposed New Configuration



(a) Sharing of Magnetizing Current



(b) Sharing of Voltage for Torque Current Under Synchronous Speed



(c) Sharing of Voltage for Torque Current Above Synchronous Speed

Fig.3 Sharing of Magnetizing Current and Voltage for Torque Current

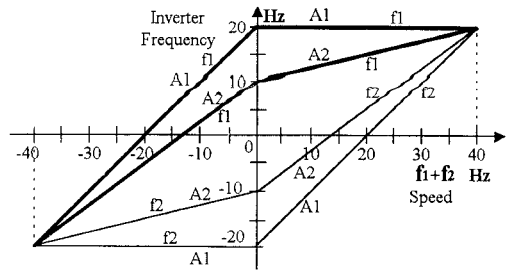


Fig.4 Frequency Control Strategies

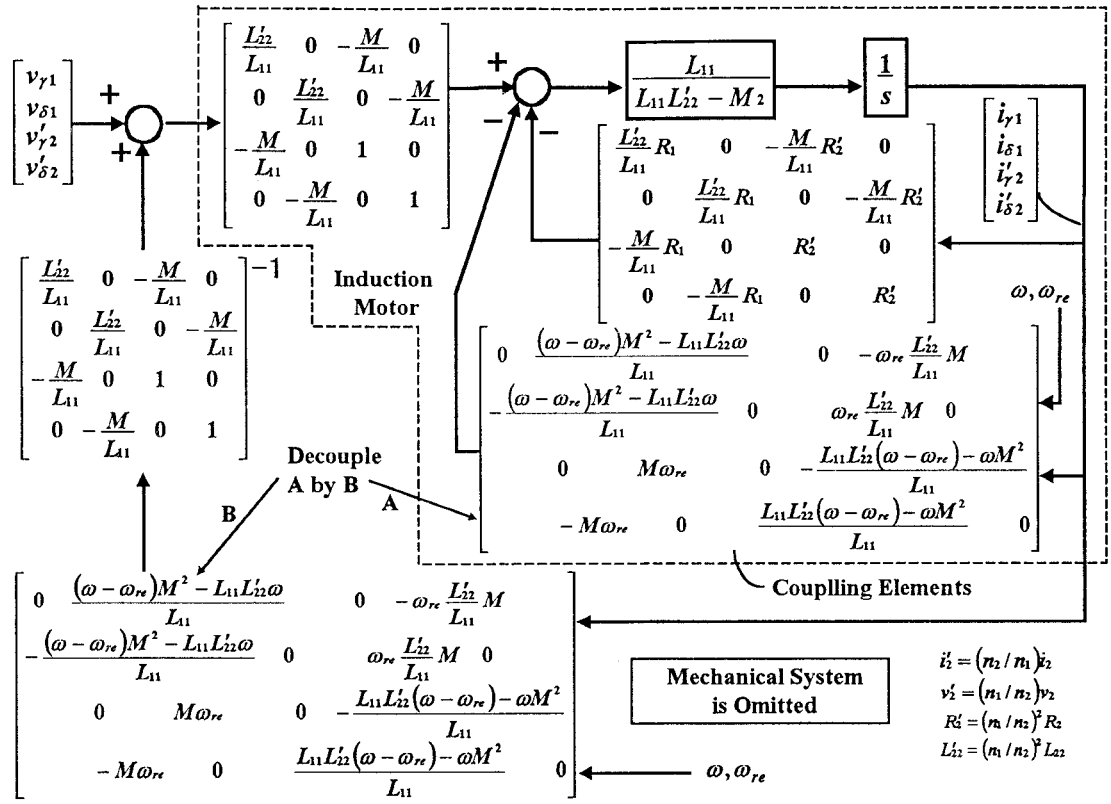


Fig.5 Decoupled Current Controller Using Matrix Theory

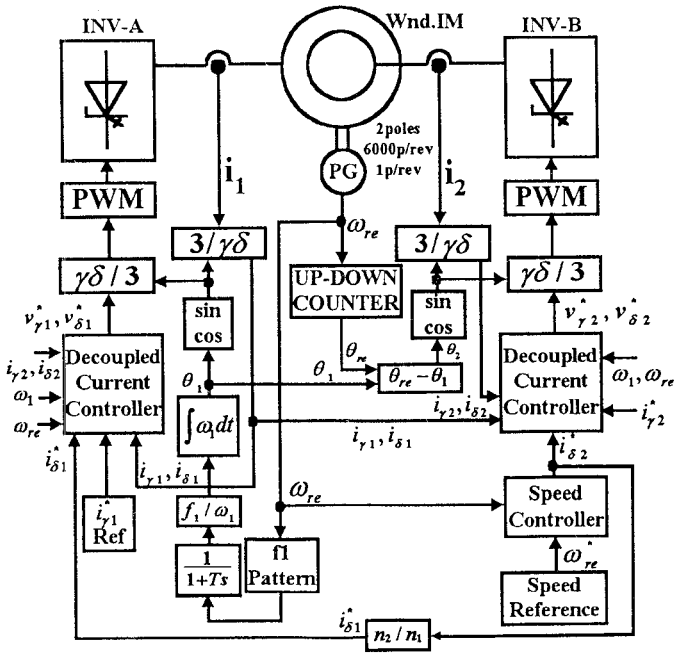


Fig.6 Control System

As explained in Fig.3, the stator and the rotor magnetizing or torque currents are linked by the winding ratio (n_1 / n_2), so the ratio of command value of the stator and the rotor currents is determined to be

$$i_{\gamma 2} / i_{\gamma 1} = n_1 / n_2,\ i_{\delta 2} / i_{\delta 1} = n_1 / n_2 .$$

Using this current controller, the complete decoupling control of magnetizing current, i_γ, and the torque current, i_δ, can be achieved in both the stator and the rotor sides.

3-3 *Total Control System*

The total control system using DSP (TMS320C40) is as shown in Fig.6.

The frequency, f1, of INV-A is controlled according to the motor speed which correspond to the effective frequency, by the pattern A1 of Fig.4. The primary flux position, θ_1, of INV-A is obtained by software counting of f_1 and is reset once every cycle. The rotor position, θ_{re}, is counted 6000 pulse / revolution of the encorder and is reset 1 pulse / revolution. The secondary flux position, θ_2, of INV-B is determined by the calculation of $\theta_{re} - \theta_1$. As a result, the frequency, f2, of INV-B is determined automatically as line A1 of f2 shown in the Fig.4.

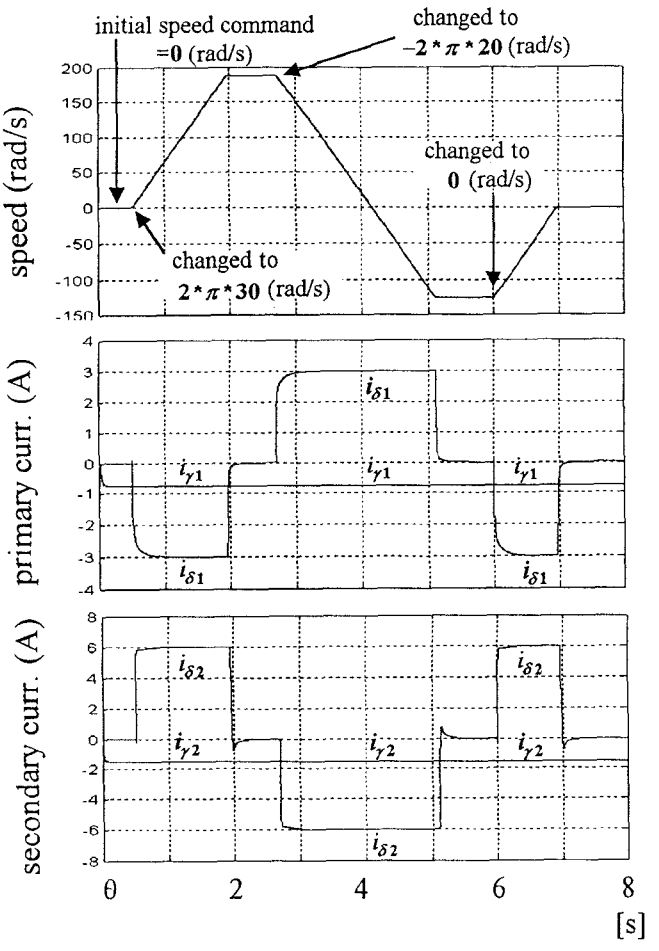


Fig.7 Simulation Result of Decoupling Controller of Fig.5

A simulation result of this controller is as shown in Fig.7. In this simulation, MatLab is used and the inverters are simulated as ideal amplifiers. The magnetizing ampere-turn is equally shared by INV-A and INV-B, that is $i_{\gamma 1}{}^{*}$=-0.75A, $i_{\gamma 2}{}^{*} = (n_1 / n_2) i_{\gamma 1}^{*}$=-1.5A. The motor constants for this study are as shown in the appendix. In the result of simulation, the torque current is changed, the magnetizing current is not effected. It can be seen that the couplings between the magnetizing current and the torque current are completely decoupled in both the rotor and the stator sides. The TYPE CC configuration can realize superior performance owing to this complete decoupling.

IV. FEATURES

In this configuration, the couplings between the magnetizing current and the torque current are completely decoupled in both the rotor and the stator sides.

In the result of simulation, it can be seen that four currents, $i_{\gamma 1}$, $i_{\gamma 2}$, $i_{\delta 1}$ and $i_{\delta 2}$ are completely decoupled, therefore this proposed configuration can realize superior control performance.

V. CONCLUSION

We are now studying the cases of the TYPE VC and the TYPE CC of the proposed configurations by a experimental set using a small motor and DSP. We would like to present experimental results at the next opportunity.

APPENDIX

Constants of the Motor for Experimental Study
Rated Capacity: 0.75kw, Winding ratio: 2 : 1,
Primary:200V, 3A, R1=3.19ohm, L11=0.295H, R2=1.00ohm, L22=0.0715H, L12=0.140H, J=0.192kgm, 4poles

REFERENCE

[1] H.Stemmler: " Configurations of High-Power Voltage Source Inverter Drives ", EPE'93, p7-14

[2] T.Kawabata: "Consideration Concerning Circuit Configurations of High-power Inverters", Conference of IEEJ Society for Semiconductor Power Converter, SPC-94-8, Jan.29, 1994

[3] T.Kawabata, et al.: "New Configuration of High-Power Inverter Drives", ISIE'96, Warsaw, June 17-20, 1996

Stability Analysis and Design Guidelines for A Speed-Sensorless Induction Motor Drive

Surapong Suwankawin, Somboon Sangwongwanich
Dept. of Electrical Eng. Faculty of Engineering Chulalongkorn University
Payatai Bangkok 10330 Thailand
Tel +662-2186533 Fax. +662-2518991

Abstract-- **In this paper, we propose a novel stability analysis for speed sensorless vector control systems based on the parametric approach which results in the analytical necessary conditions for stability. It is pointed out that the system can be unstable in the low-speed region with regenerative load. Assigning an appropriate feedback gain of the flux observer, however, can render the stability and reduce the unstable region. As a guideline for designing the adaptive PI gain, it is shown that the integral gain determines the tracking speed of the estimator during acceleration/deceleration while the sensitivity to current measurement noises depends on the proportional gain. In addition, to avoid an oscillation in the speed estimator, a suitable corner frequency of the adaptive PI gain is required as a design trade-off.**

I. Introduction

In the recent years, a large number of speed-sensorless drive systems have been developed and applied to several industries. Among them, the popular approach to estimate the rotor speed is based on model adjustment methods, and the stability limitation of which was pointed out in [1,4]. However there are two important problems which remain to be solved. Firstly, the results in stability analysis were constrained by the linearization or averaging process. Therefore, in this paper we will introduce a new approach for stability analysis based on the Routh-Hurwitz criterion which gives exact stability conditions covering also those mentioned in [1,4].

Secondly, the adaptive gain of the speed estimator is often found out by trial and error due to lack of design criterions [2]. Therefore, a design guideline for the adaptive gain taking into account also measurement noises will in addition be given. We can, as a result, design a suitable speed estimator to achieve the performance goal which will be confirmed by experiment.

II. Adaptive Observer

Following the induction motor model for the voltage source type inverter, we can express a full-order adaptive observer on the stator reference frame ($\alpha - \beta$ axis) [3,4] which estimates the rotor flux and speed simultaneously as

$$\frac{d\hat{\vec{i}}_s}{dt} = A_{11}\hat{\vec{i}}_s + \hat{A}_{12}\hat{\vec{\lambda}}_r + B_1\vec{v}_s - H_1'(\hat{\vec{i}}_s - \vec{i}_s) \quad (1)$$

$$\frac{d\hat{\vec{\lambda}}_r}{dt} = A_{21}\hat{\vec{i}}_s + \hat{A}_{22}\hat{\vec{\lambda}}_r - H_2'(\hat{\vec{i}}_s - \vec{i}_s) \quad (2)$$

$$\hat{\omega}_m = (k_p + k_I\int dt)(\hat{\vec{i}}_s - \vec{i}_s)^T pJ\hat{\lambda}_r \;;\; (k_p, k_I > 0) \quad (3)$$

wherein

$$A_{11} = -\left(R_S + R_r M^2 / L_r^2\right)/\sigma L_S \bullet I$$

$$\hat{A}_{12} = \left(R_r / L_r\varepsilon\right)\bullet I - p\hat{\omega}_m/\varepsilon \bullet J$$

$$A_{21} = \left(M R_r / L_r\right)\bullet I, \quad \hat{A}_{22} = -\varepsilon\hat{A}_{12}$$

$$B_1 = 1/\sigma L_S,\ \sigma = 1 - M^2/L_S L_r,\ \varepsilon = \sigma L_S L_r / M$$

H_1', H_2' are the observer's gains, and " $\wedge$" denotes the estimated value.

The overall speed sensorless vector control system is depicted in Fig. 1

III. Stability Analysis

From the equations of motor model and observer, it can be derived that the stator current error will satisfy the following equations (see [4,6] for further details) :

$$e_1 = G(s)\, pJ\hat{\lambda}_r\,(\hat{\omega}_m - \omega_m) \quad (4)$$

$$G(s) = -\frac{s}{\varepsilon}\left[s^2 I + s(xI + yJ) + mI + nJ\right]^{-1} = \begin{bmatrix} G_{11}(s) & G_{12}(s) \\ G_{21}(s) & G_{22}(s) \end{bmatrix} \quad (5)$$

where

$$e_1 = \hat{\vec{i}}_s - \vec{i}_s$$

$$m = [\frac{R_r}{L_r}(h'_1 + \frac{R_s}{\sigma L_s} + \frac{h'_3}{\varepsilon}) + p\omega_m(h'_2 + \frac{h'_4}{\varepsilon})]$$

$$n = [\frac{R_r}{L_r}(h'_2 + \frac{h'_4}{\varepsilon}) - p\omega_m(h'_1 + \frac{R_s}{\sigma L_s} + \frac{h'_3}{\varepsilon})]$$

$$x = [h'_1 + \frac{R_s}{\sigma L_s} + \frac{R_r}{\sigma L_r}], \quad y = [h'_2 - p\omega_m]$$

$$H'_1 = \begin{bmatrix} h'_1 & -h'_2 \\ h'_2 & h'_1 \end{bmatrix}, H'_2 = \begin{bmatrix} h'_3 & -h'_4 \\ h'_4 & h'_3 \end{bmatrix} \quad (6)$$

It should be noted that equations (4) and (5) are the general form of error equations for most model-adjustment based speed estimators. As a consequence, we can apply the analysis given in the following to those speed estimators as well. We can see that equations (3) and (4) form the familiar closed-loop system composed of the output error transfer function $G(s)$ together with the PI speed estimator of the adaptive observer as shown in Fig.2. To carry out the stability analysis easily, we will transfer the estimation error system from the stator frame ($\alpha - \beta$) to rotor flux frame $(d-q)$, and then simplify the error system to be a single-input-single-output (SISO) system considering also measurement noises as shown in Fig. 3 (See [5,6] for more details). $G'_{22}(s)$ is calculated to be

$$G'_{22}(s) = \frac{s^3 + x s^2 + (\omega_o^2 + m)s + \omega_o^2 x + \omega_o n}{-\varepsilon[(s^2 + xs - \omega_o^2 - \omega_o y + m)^2 + ((2\omega_o + y)s + \omega_o x + n)^2]} \quad (7)$$

where ω_o is the angular frequency of the estimated rotor flux.

Since we usually have to select a high PI gain to obtain a fast tracking of the real rotor speed, the location of the zeros of $G'_{22}(s)$ must be restricted to the left-half plane only. To determine the condition for all roots of the numerator of $G'_{22}(s)$ (zeros) to lie strictly in the left-half plane (stable zeros), we apply the Routh-Hurwitz criterion and obtain the following necessary and sufficient conditions:

$$\omega_o > \omega_c = -\frac{n}{x}(critical\ frequency) \quad (8.A)$$

$$x > 0 \quad (8.B)$$

$$\omega_o n < mx \quad (8.C)$$

where m, n and x depend on motor parameters, and feedback gains H'_1, H'_2 as given in (6).

If the operating frequency ω_o goes lower than this critical frequency ω_c, an unstable zero will appear on real axis. The pole at the origin of the adaptive PI gain will move toward this unstable zero as shown in Fig. 4, and the speed estimation system will be unstable regardless of the adaptive gain used. This unstable phenomena corresponds to the operation in generator mode with large enough regenerative load which usually occurs in the elevator application. Experimental results in Fig. 5 demonstrates this phenomena. The motor speed command is 120 rpm (12.6 rad/s) together with regenerative load $T_L \cong$ -9.7 Nm and slip ω_{sl} = -11.7 rad/s, and the operating frequency ω_o must be 13.5 rad/s. In this case, we set the feedback gains H'_1, H'_2 to zeros and it can be calculated from equation (6), and (8.A) that

$$\omega_c = \frac{p\omega_m}{1 + \frac{R_r L_s}{L_r R_s}} \quad (9)$$

According to the motor parameters in the appendix, the operating point ω_o = 13.5 rad/s is lower than the critical frequency (ω_c = 0.66 $p\omega_m$ = 16.6 rad/s), and the instability of speed identification results in speed error and the exceed torque and slip command (T_m^* = -11.5 Nm, ω_{sl}^* = -14 rad/s). Fortunately, the speed error does not diverge, but approaches a steady-state non-zero value ($\cong$ 35 rpm), instead. This is because both the operating frequency and the critical frequency depend on the rotor speed are changed continuously during the transient response, and finally become equal at new values ω'_o, ω'_c. The new operating frequency ω'_o can be calculated from the experimental result as $\omega'_o = p\hat{\omega}'_m + \omega_{sl}^*$ = 2*12.6-14 = 11.2 rad/s, while the new critical frequency ω'_c is given by equation (9) as : ω'_c = 11.2 rad/s. The unstable zero on the real axis of $G'_{22}(s)$ then becomes a zero at the origin which cancels out the effect of PI gain and causes a steady-state error. Normally when the instability occurs, the operating point of the system will move onto the boundary between the stability and instability.

This analytical condition does agree with the result derived by the averaging analysis [4], and an appropriate output error feedback gain of the adaptive observer (H'_1, H'_2) can be used to enlarge the stable region to render the stability as shown in Fig 6, and 7 (ω_c = 0.5 $p\omega_m$. = 12.6 rad/s). There is, now no unstable zero, and the motor speed can be regulated with the torque command corresponding to load.

Since the boundary for stability is the point when $\omega_o = \omega_c$,considering that $\omega_o = p\omega_m + \omega_{sl}$ and $\omega_c = \frac{p\omega_m}{1+\eta}$ when η can be changed by feedback gain h_3', we can find that the stability boundary is given by

$$\omega_m = -\frac{(1+\eta)}{\eta}\frac{R_r}{p|\lambda_r|^2}T_m \quad (10)$$

From the condition (8.A) and equations (6), (10) we can compare conceptually the unstable region on the torque-speed plane for the systems with and without error feedback as shown in Fig. 8 .

Fortunately, for normal rated slip frequency and motor parameters, the remaining conditions (8.B, 8.C) always hold. The condition 8.C is similar to the one derived by linearlization method [1] which can cause instability for some system as well. (See [5,6] for further details)

IV. A Design Guideline for Adaptive PI Gain

Following the block diagram in Fig. 3, we can give a design guideline for the adaptive PI gain of the speed estimation based on three criterias.

[1] Tracking Performance

Normally due to the mechanical inertia, the waveform of motor speed during the acceleration and deceleration can be considered as a ramp function. So it is reasonable to focus only on the tracking performance against the ramp response. The speed estimation error e_{ss} corresponding to the ramp response of motor speed can be calculated from Fig. 3 as:

$$\frac{\omega_m - \hat{\omega}_m}{\omega_m} = \frac{1}{1 + (-C^2)G'_{22}(s)(K_P + K_I/s)}$$

$$e_{ss} = \lim_{s\to 0} s \times \frac{R}{s^2} \times \frac{1}{1 + (-C^2)G'_{22}(s)(K_P + K_I/s)} = \frac{R}{(-C^2)G'_{22}(s)\big|_{s=0} K_I} \quad (11)$$

where $R = T_m/J$, $C = p|\hat{\lambda}_r|(t)$, $G'_{22}(s)\big|_{s=0}$ is nearly constant

over the entire range of speed (see Fig. 9)

The result in (11) implies that a good tracking performance can be achieved with a high K_I gain or, speaking in another way, we can design K_I according to the specification of the tracking error for ramp response as shown by the experimental results in Fig. 11 which compares the low and high integral gain used in the speed identification. In the case of low integral gain, the steady-state speed error e_{ss} is about 45 rpm and the motor speed acceleration R is about 272 rad/s^2, while the one calculated from equation (11) is 274 rad/s^2 and the overall system response time is about 450 ms. On the other hand, the system with high integral gain gives us a good tracking performance which steady-state error e_{ss} is about 10 rpm, while the speed acceleration R is about 2 times of the system with low integral gain (573 rad/s^2) and the overall system response time is just 150 ms. From the above result, we can conclude that the slow tracking performance will cause the motor torque T_m to be less than the commanded torque T_m^* , and it also distorts the stator current i_s , especially its amplitude during the acceleration which results in the slow response.

[2] Robustness to Measurement Noises

As the current error is used in speed estimation (equation (3)), the effect of current measurement noises on the estimated speed is given by the following transfer function.

$$\frac{\hat{\omega}_m}{\eta_I} = \frac{C(Kp + K_I/s)}{1 + (-C^2)\, G'_{22}(s)\,(Kp + K_I/s)} \qquad (12)$$

Current measurement noises can be either 1) an DC offset or 2) a high-frequency noise or 3) a low frequency noise around ω_o. It should be reminded that the noise in equation (12) is viewed from the rotating frame, and as such its frequency must be shifted from the frequency on stator frame by ω_o. For the low frequency noise, its frequency on the rotating frame will be around zero, and from equation (12) and Fig. 10, it is seen that the effects of this noise is governed by $G'_{22}(s)$ only. However, for the remaining noises whose frequency is shifted to a high frequency above ω_o, their effect is roughly given by $C K_P$ because $G'_{22}(s)$ is small in high frequency range (Fig. 9). As a result, we can reduce the effects of measurement noises by choosing a low K_P gain. This conclusion is confirmed by the experimental results shown in Fig. 12-a and 12-b.

[3] Stability Margin

It seems as if both results in (11) and (12) are independent and enough to fulfill our performance goal, but if we select a high K_I gain for fast tracking of speed, and a low K_P gain to attenuate noises, oscillation may occur as shown in Fig. 12-c. The reason for this phenomena can be explained from the Bode plot in Fig. 9 where we can see that the phase shift of $G'_{22}(s)$ is about -90° at the frequency nearly equal to the operating frequency ω_o. Therefore, the phase lag of the adaptive PI gain with a high corner frequency (high K_I and low K_P) will reduce the phase margin of the system, and may consequently cause the oscillation. The design trade-off for K_P and K_I gain is that the corner frequency should be less than the operating frequency (Fig. 12-d).

V. Conclusion

In this paper, we analyzed the stability of the speed sensorless vector control system using the Routh-Hurwitz criterion, and derived the conditions for the existence of the unstable zeros which, in turn, causes the instability of the speed estimation system. Our approach conforms well with the linearization method and the averaging analysis previously reported. We also gave a design guideline for the adaptive PI gain to fulfill the tracking performance and robustness against measurement noises of the sensorless system. All theoretical results were confirmed by experiments.

Appendix

Motor's parameters:

Rs = 1.84 [Ohm], Rr = 0.885 [Ohm]

Ls = 131 [mH], Lr = M = 120 [mH], p=2

Acknowledgment

This research was financially supported by the National Electronics and Computer Technology Center (NECTEC) of Thailand.

References

[1] C. Schauder, Adaptive Speed Identification For Vector Control of Induction Motors Without Rotational Transducers, Conf. Record of IEEE/IAS Annual Meeting 1989, pp. 493-499.

[2] H. Kubota, K. Matsuse, Speed Sensorless Field-Oriented Control of Induction Motor with Rotor Resistance Adaptation, IEEE Trans. on Ind. Appl., Vol. IA-30, No. 5, 1994, pp. 1219-1224.

[3] S. Sangwongwanich, Generalized Controllers for Induction Motor Drive Systems, Proc. of PCC- Yokohama 1993, pp 450-455.

[4] S. Sangwongwanich, Speed Sensorless Vector Control of Induction Motors-Stability Analysis and Realization-, Conf. Record of IPEC-Yokohama, 1995, Vol.1, pp. 310-315.

[5] S. Sangwongwanich, Speed Sensorless Induction Motor Drive Systems -Structure and Stability-, Conf. record PEMC-Budapest, 1996, Vol.2, pp. 78-85.

[6] S. Suwankawin, S. Sangwongwanich, Stability Analysis of Speed Sensorless Vector Control System, Proc. of ICPE, 1995, pp 403-408.

[7] S. Tamai, H. Sugimoto, M.Yano, Speed Sensorless Vector Control of Induction Motor Applied Model Reference Adaptive System, Conf. Record of IEEE/IAS Annual Meeting 1985, pp. 613-620.

[8] T. Okuyama et al., Simplified Vector Control System Without Speed Sensor and Voltage Sensors-Effects of Setting Errors in Control Parameters and Their Compensation, Trans. of IEE Japan, Vol 110-D, No. 5, 1990, pp. 477-480.

[9] S. Sangwongwanich, S. Suwankawin, A Speed-Sensorless IM Drive with Modified Decoupling Control, PCC-Nagaoka, 1997, (to be appeared).

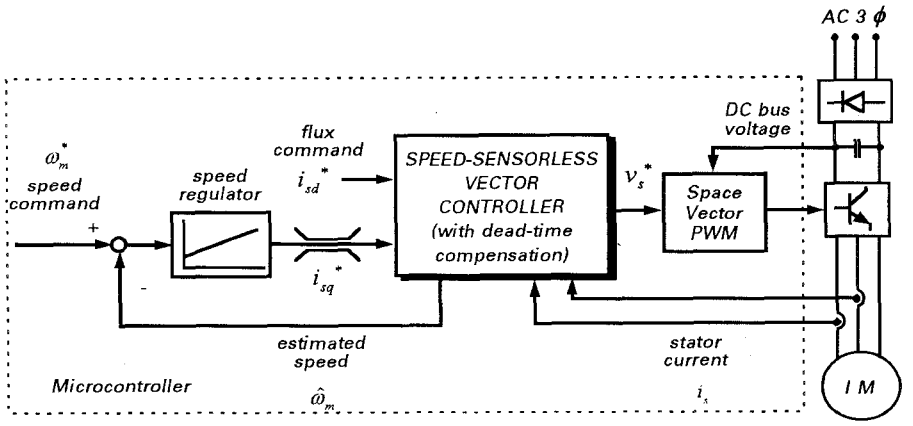


Fig. 1 Experimental Setup of Speed Sensorless Vector Control System

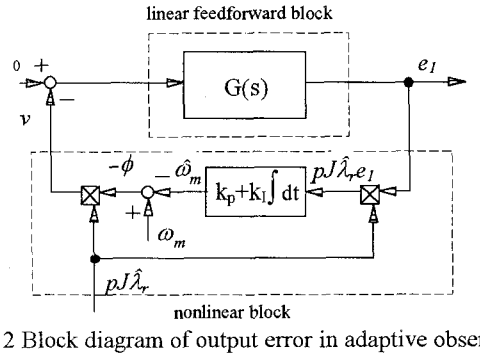


Fig. 2 Block diagram of output error in adaptive observer

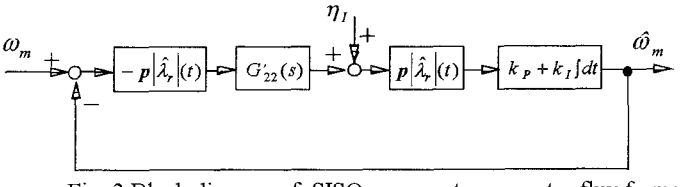


Fig. 3 Block diagram of SISO error system on rotor flux frame

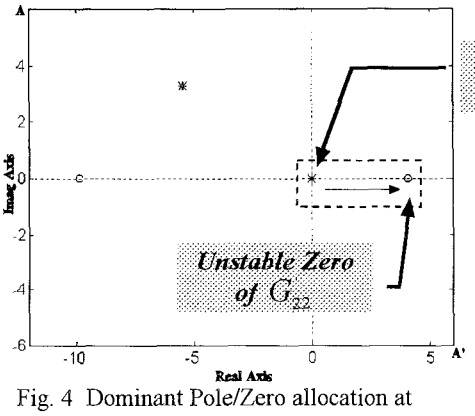


Fig. 4 Dominant Pole/Zero allocation at regenerating operation

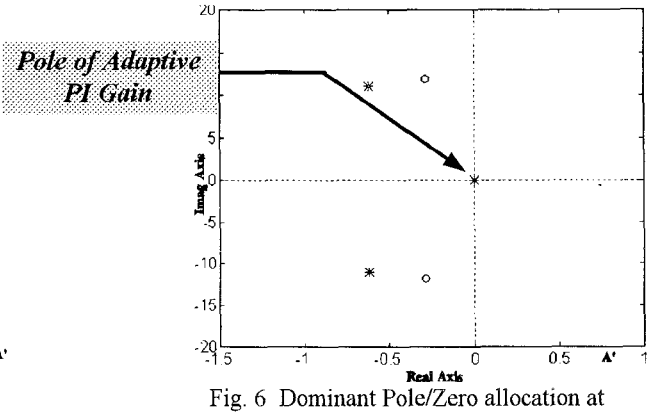


Fig. 6 Dominant Pole/Zero allocation at regenerating operation with error feedback

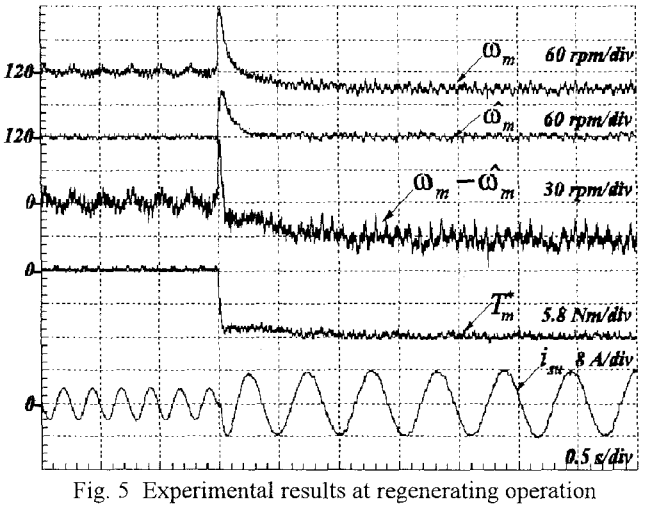


Fig. 5 Experimental results at regenerating operation without eror feedback

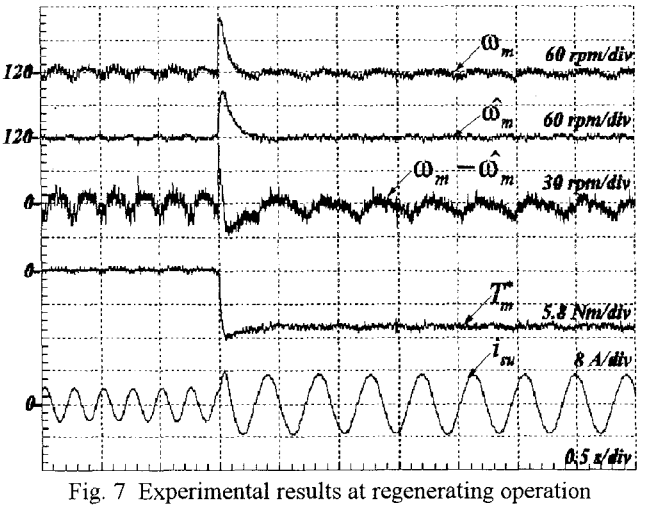


Fig. 7 Experimental results at regenerating operation with error feedback ($H_2' = -0.25R_s I$)

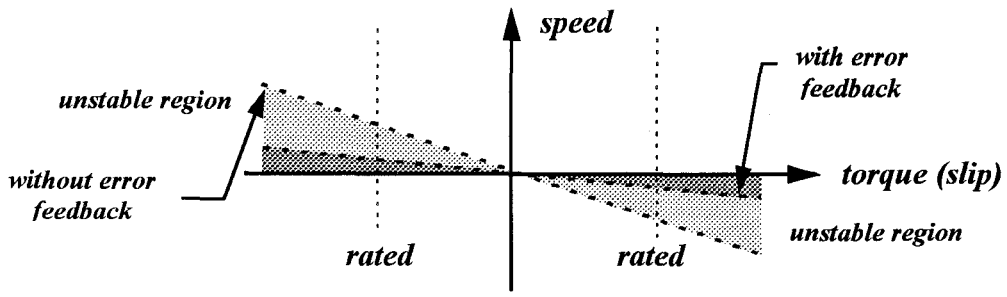


Fig. 8 Area of unstable region in the sensorless system

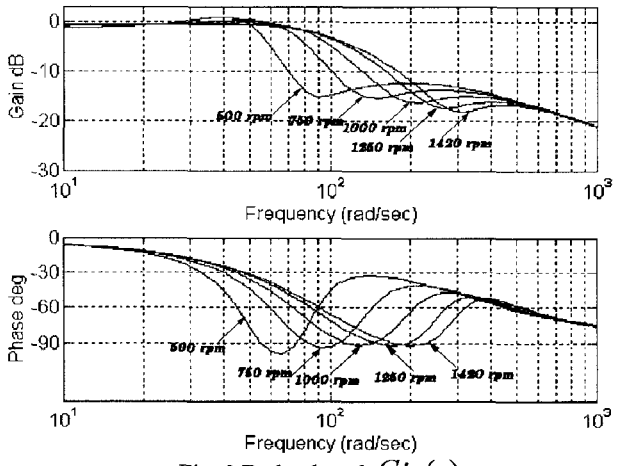


Fig. 9 Bode plot of $G'_{22}(s)$

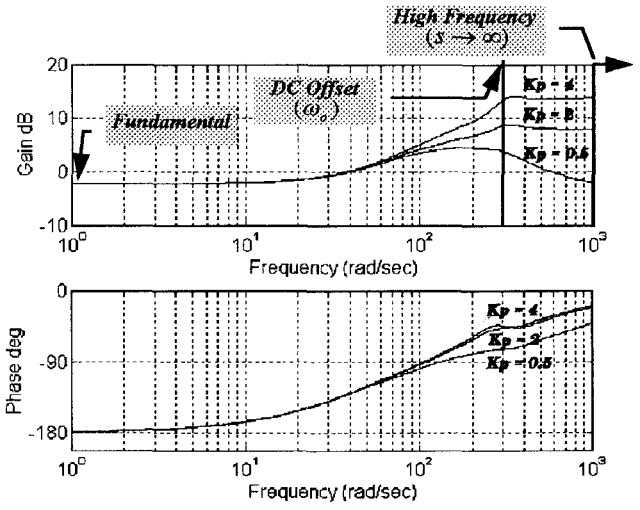


Fig. 10 Bode plot of transfer function corresponding to measurement noises

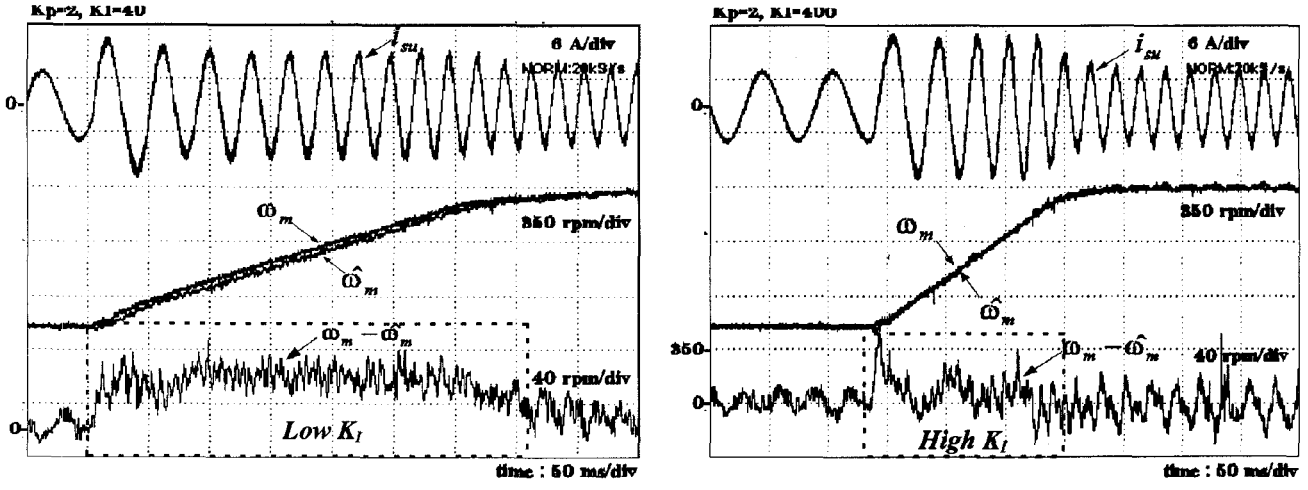


Fig. 11 Experimental results of acceleration ramp response (500 -> 1420 rpm)

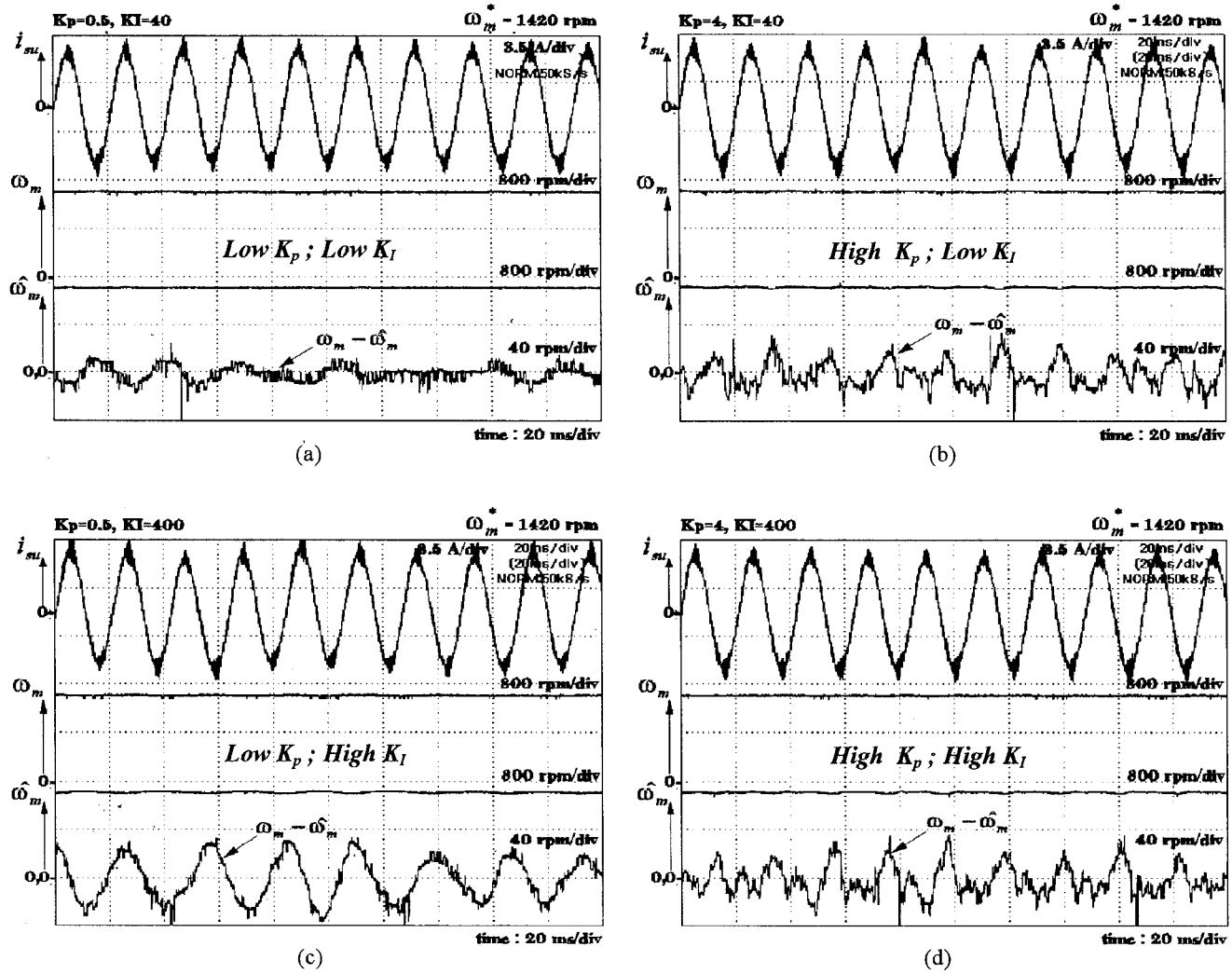


Fig. 12 Experimental results at steady state for different PI gains (motor speed : 1420 rpm)

Improving the Start and Restart Behavior through State Recognition of AC Drives

Hangwen Pan, Lothar Springob*, Joachim Holtz, *Fellow,IEEE*

University of Wuppertal, 42097 Wuppertal, Germany
Fax: +49-202-4392924 Phone: +49-202-4392967
* VECTRON Electronik , Krefeld , Germany

Abstract — **The paper presents control strategies for abnormal operating conditions of ac drive systems. These improve the total performance as well as the ruggedness of the system. Two methods to start a rotating motor through state recognition are described. Two cases are distinguished according to whether the back emf exists or not. In either case the normal operation can be reestablished as fast as possible on return of the power supply following a power interruption. Discussions and experimental results are presented for both failure conditions, based on V/f control and on sensorless field oriented control.**

1. Introduction

For a general purpose PWM inverter induction motor system V/f control scheme is widely used. The conventional V/f control keeps the ratio of stator voltage to frequency constant. The distinctive feature is that speed sensor is not needed. Recently the field-oriented control (FOC) of induction motor becomes gradually mature for more industrial applications [1]-[4]. The sensorless, self-commissioning and parameter-insensitive version of FOC provides an attractive choose to control a general purpose ac drive.

Besides the normal performance requirements adequate solution to abnormal operating conditions should also be implemented in such drive systems. The operation strategies following a power interruption are important in many production processes. After a power interruption, the motor will possibly go on rotating for a considerable time, especially motors with large inertia loads. Reestablishing the normal operation as fast as possible on return of the power supply is a desirable feature, which enhances the performance and ruggedness of the drive system.

In the last several years some operation strategies to counteract a power interrupt have been proposed. In [5] a dc braking mode is proposed to reduce the wait time for restart. Restart is only enabled after complete standstill is detected. According to this method the drive system is subjected to large speed variations. Recovery of normal operation needs much time. Therefore, the approach may not be adequate for many production processes. In fact it is not necessary to restart a motor from zero speed.

Different options for reconnecting a rotating motor are discussed In [6]. The authors propose a frequency control method to provide tripless operation after power interruption. Forced standstill is avoided. The drive system works in current-limit mode until the frequency controller reduces the operating frequency near at the rotor velocity. However, the existing air-gap flux is not considered. A fast recovery of normal operation is then difficult to obtain. Furthermore, to avoid the overcurrent trip, a period of wait time must be elapsed in order that the air-gap flux has nearly vanished before the restarting.

In [7] the problem of short power interruptions was solved by temporarily recovering energy from the rotating masses to maintain the dc link voltage at an appropriate level. The drive system operates then in the generating mode. The electrical power for the control circuits is drawn from the dc link circuit. This proposal suggests thus a design concept for a tripless operation by keeping the motor always under control.

Besides power interruption, there are also other causes that make motor rotate at arbitary speed on start. Depending on the motor states prior to restarting, two cases of starting conditions must be considered:

1. The motor rotates at arbitary speed while being electromagnetically deenergized. Such situation may occur with a fan drive located in an air duct, in which an air draft already exists from sources other than the fan drive. The air flow will act upon the fan blades and make them rotate. The drive motor may assume any speed and direction of rotation, depending on the existing air flow. The same situation exists also when a power interrupts.
2. The motor rotates while being electromagnetically energized. Such case is encountered after a short power interruption. An air-gap flux induced voltage will be present in such case.

In both cases, a large transient current will be produced if the motor is started from zero frequency. The drive system will then change over to the current-limit mode, as the starting frequency is generally different from the corresponding angular velocity of the rotor. Even an overcurrent trip could occur.

In this paper two methods are described, which facilitate starting a rotating motor through state recognition. The

0-7803-3823-5/97/$10.00© 1997 IEEE

first method applies if a residnal air-gap flux exists. The states to be recognized include the rotor speed, the angular position and the amplitude of the back emf. The state recognition is executed within a few milliseconds.

The second method is a frequency search run. It applies when no residnal air-gap flux exists. The frequency searching process can be completed within two or three seconds.

Experiments on drive systems with V/f control, and with sensorless field oriented control, respectively, show that the combination of these two methods can be generally used to facilitate start or restart of a general purpose ac drive under any initial operating conditions.

2. RESTART OF AN ENERGIZED ROTATING MACHINE

This chapter describes the first method, in which the back emf of the rotating machine is estimated.

If the power supply returns again in short time (within several hundred miliseconds) after the inverter had to be shut down due to a undervoltage protection, a fast restart was considered as impossible. Starting the motor with arbitrary field angle δ and zero initial stator voltage, e.i. treating

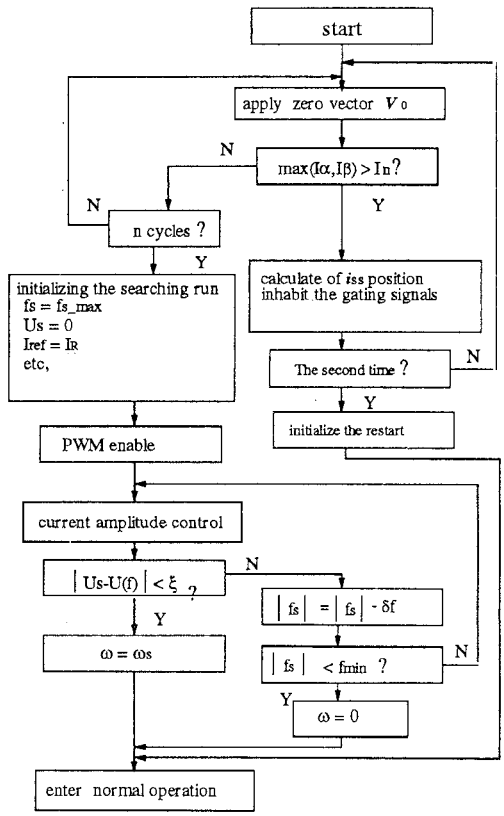


Fig.1 Program flow chart

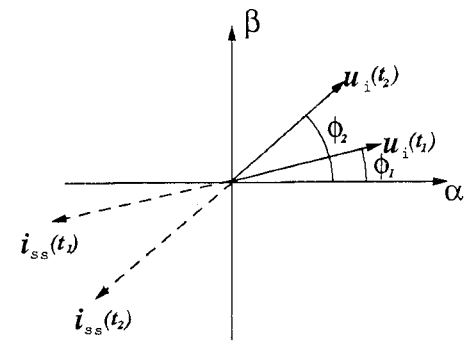


Fig.2 Recognition of the back emf u_i

the motor as in standstill, would create great current transients (Fig.4a). Even if the field oriented control is equipped with the speed sensor, the same problem will also appear, if the states of the motor by restarting is not known.

However, after the states of the motor, e.i. the position, amplitude and the rotating speed of the back emf u_i, has been detected, the motor can be taken under normal control at once. As shown in the program flow chart in Fig.1, the controller decides firstly whether or not u_i exists on restarting. To determine that the motor will be short-circuited by applying stator voltage zero vector v_0. On the existence of u_i a quite big stator current will be detected. The stator current of the short-circuited motor, i_{ss}, is determined by stator resistance r_s, stator leakage inductance $l_{s\sigma}$ and u_i. When u_i is still large, i_{ss} will rise very rapidly. The amplitude of i_{ss} can be easily limited, as clarified in Fig.1. As soon as i_{ss} reaches the rated current, the inverter will be turned-off by inhabiting all of the gating signals. The motor is then open-circuited. Through the measurement of i_{ss} at two different times the rotating speed as well as the position and amplitude of u_i are quickly obtained. The parameter r_s and $l_{s\sigma}$ are assumed to be known through the self-commissioning. Fig. 2 illustrates the recognization process. The stator current of the short-circuited motor, i_{ss}, is mearsured at t_1, t_2, respectively. The corresponding position of the back emf is ϕ_1, ϕ_2, which is determined by Equ. 11. After the mearsurements the stator current returns to zero by inhabiting the inverter. Then the motor is ready for the restart, basing on the recognized motor states.

Next the sensorless field oriented control and V/f control will be discussed separately.

a. Operation with sensorless field oriented control

The following equations describe the dynamic behavior of an induction machine in the synchronous reference frame:

$$\boldsymbol{u}_S = r_S \boldsymbol{i}_S + \frac{d}{d\tau}\boldsymbol{\Psi}_S + j\omega_S \boldsymbol{\Psi}_S \qquad (1)$$

$$0 = r_r \boldsymbol{i}_r + \frac{d}{d\tau}\boldsymbol{\psi}_r + j(\omega_s - \omega)\boldsymbol{\psi}_r \quad (2)$$

$$\boldsymbol{\psi}_s = l_s \boldsymbol{i}_s + l_h \boldsymbol{i}_r \quad (3)$$

$$\boldsymbol{\psi}_r = l_h \boldsymbol{i}_s + l_r \boldsymbol{i}_r \quad (4)$$

where

ω_s	stator frequency,
ω	angular velocity of the rotor,
l_s	stator inductance,
l_r	rotor inductance,
l_h	mutual inductance.

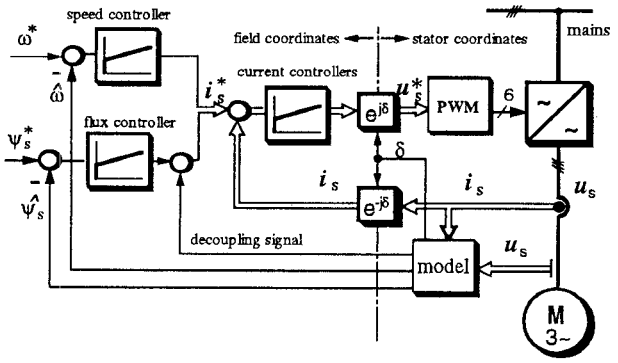


Fig.3. Sensorless ac drive system with stator field oriented control

The block diagram of a sensorless ac drive system with stator field orientation is shown in Fig.3. The phase relationship between $\boldsymbol{u}_s$ and $\boldsymbol{i}_s$ of an induction motor in the reference frames (the stator stationary reference frame α - β and the field oriented synchronous reference frame d - q) is shown in Fig.4.

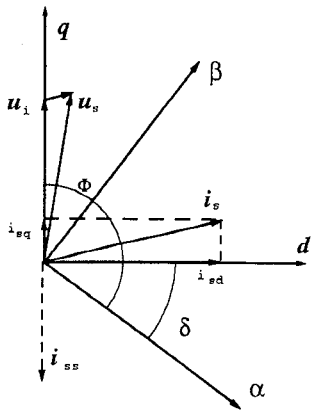


Fig.4. Vector diagram of an induction motor

With stator field orientation, equation (1) can be written as:

$$u_{sd} = r_s\, i_{sd} + \frac{d}{d\tau}\psi_{sd} \quad (5)$$

$$u_{sq} = r_s\, i_{sq} + \omega_s \psi_{sd} \quad (6)$$

The field angle δ as well as the initial stator voltage components, according to equations (5) and (6), at the moment that the controller enters the field oriented control again, can be consequently decided as follows:

$$u_{sd}(0) \approx 0 \quad (7)$$

$$u_{sq}(0) \approx \omega_s \psi_{sd} \approx l_{s\sigma} \frac{\Delta i_{ss}}{\Delta t} \quad (8)$$

$$\delta = arctan\left(\frac{I_{ss\beta}}{I_{ss\alpha}}\right) + 90^0 \quad (9)$$

where

Δt the interval, in which the voltage zero vector is applied,

Δi_{ss} the stator current amplitude at the end of interval Δt,

$I_{ss\alpha}$, $I_{ss\beta}$ the components of i_{ss}

Fig.5 gives out the restarting processes of a sensorless field oriented controlled drive system, with and without the recognition of the motor states.

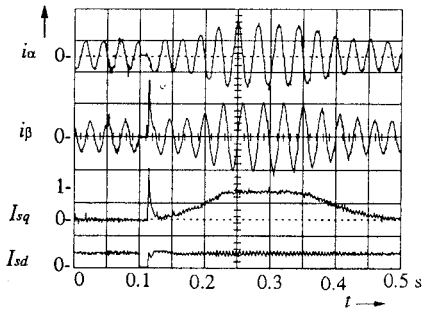


Fig.5a. Without state recognition
Interrupt time = 20ms

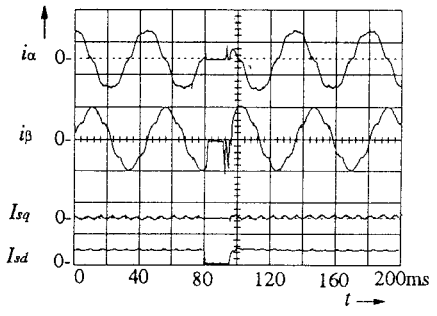
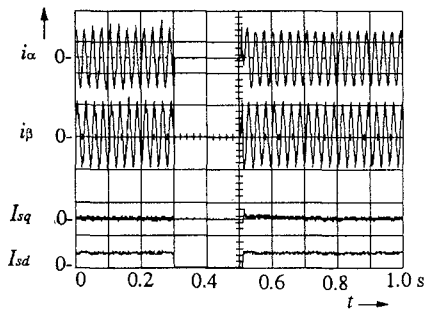


Fig.5b. With state recognition
Interrupt time = 16ms



5c: with state recognition
interrupt time = 200ms

Fig.5. Restarting the drive system with field oriented control

b. with V/f control

Fig. 6 shows the block diagram of a V/f control.

For V/f control the method to recognize the states of the motor is the same as described above. The determination of f means that the initial phase of u_s is found. The stator frequency and the stator voltage amplitude are also decided through the measurement of i_{ss}. The initial values for

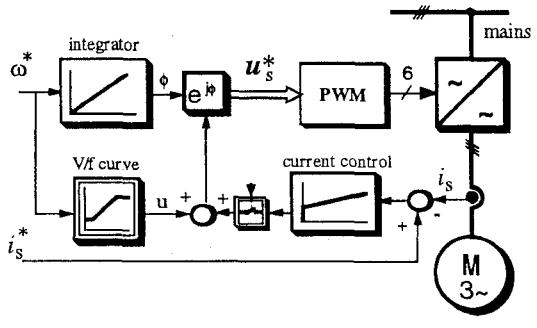


Fig.6. V/f controlled drive system

restart are expressed as:

$$u_s \approx l_{s\sigma} \frac{\Delta i_{ss}}{\Delta t} \tag{10}$$

$$\varphi = arctan\left(\frac{I_{ss\beta}}{I_{ss\alpha}}\right) + 180^0 \tag{11}$$

$$\omega_s = \frac{\varphi_2 - \varphi_1}{t_2 - t_1} \tag{12}$$

where

ϕ_1, ϕ_2 the detected angles of the bach emf at the two times respectively

t1, t2 the corresponding moment, whan the angles are detected

Fig.7 shows a V/f controlled restarting process.

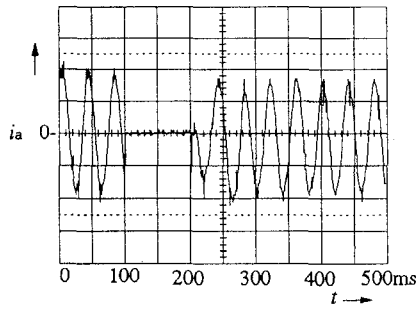


Fig.7. V/f controlled restarting with state recognition, power interruption time=100ms

After the state recognition the drive system enters the normal operation in two steps. At first a current controller is set to be active until the relationship between the stator frequency and the stator voltage amplitude arrives at a constant value. It means that a constant flux level is firstly recovered. More generally to say, the V/f curve is firstly reached. Then the motor can be accelerated to the required speed with a frequency ramp function. In the most cases, the reached flux level in the first step is not just the rated value. It depends on the relationship between the reference value of the current controller and the load. The rated magnetizing level will be gradually reached under the V/f control in the second step.

c. comparision of the two controls

According to the above description, both of the restarting processes, with sensorless field oriented control and with V/f control, show that the normal operation can be quite quickly recovered, after u_i is recognized. It is worthwhile to note that the parameter r_s or $l_{s\sigma}$ has no influence on the determination of the position of u_i.

Thus the existence of u_i is advantegous to recognize the states of the motor. In fact, if u_i has not disappeared after the shutdown of the inverter, the reduction of the rotational speed is negligible, because the air-gap flux stays only so long as several times of the rotor time-constant. The influence of such power interrupt within several hundred miliseconds on these loads, which has large inertias, will thus be almost totally eliminated through the fast restarting with the state recognition of the motor.

It is interesting to observe that.in the sensorless FOC the normal control is already recovered as soon as the flux angle d and the rotating speed of the rotor are recognized. The motor can be accelerated meanwhile the rated flux

level is recovered. In V/f control a longer transient process will be experienced, since the acceleration of the motor is only possible in the second step.

3. RESTART OF A DEENERGIZED ROTATING MACHINE

In this chapter the second method is introduced for cases in which the back emf is absent.

The back emf will be judged as negligible, if the stator current does not reach a predetermined minimum value when the zero-vector v_0 is applied continuely for several milliseconds, a period of time in the scale of the stator transient time-constant. Then the rotor speed is determined by a frequency search run.

The search run begins at maximum stator frequency and zero stator voltage. A constant current is injected into the motor using a current controller. The reference value of the current controller is chosen as I_R, *where* I_R is the rated stator current.

The output of the current controller is the stator voltage amplitude u_s. If u_s reaches the voltage value, which corresponds to the stator frequency on the V/f curve, the rotor speed is found and the search run terminates. Fig.8 illustrates the searching process.

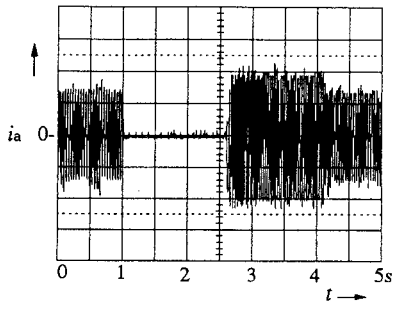


Fig.8. Restart by frequency search

The principle of this searching process can be explained with Fig.9, in which the voltage-frequency characteristics of an induction motor in steady-state are depicted. Curves 1-5 are corresponding the rotating speed of 150-750/min. The searching starts from point A along the constant-current V-f curve. At the cross-point between the constant-current V-f curve and the constant flux V/f curve is approximately the rotor rotating frequency.

When the stator frequency f_s is much larger than the rotor rotating frequency f_m, e.i. the slip is quite large. The injected current flows almost only through the rotor loop. Little air-gap flux can be built up. As f_s approaches f_m, the

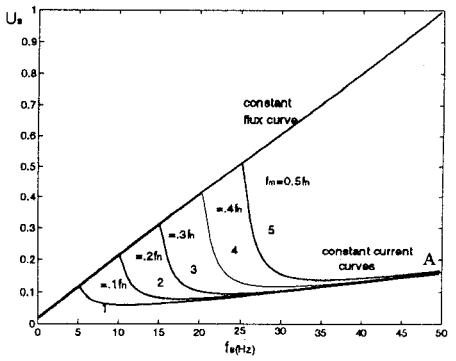


Fig.9 Steady-state voltage-frequency characteristics
I_{sref} = constant = 0.7

stator voltage, e.i. the voltage on the constant-current V-f curve, rises rapidly. As soon as this voltage reaches the value on the constant flux V/f curve corresponding to the stator frequency, the drive system can enter normal operation. During this progress the air-gap flux has be gradually built up. The electrical torque begins to be produced before the arrival of the factual rotor frequency. A little of acceleration can be observed at motor with light loads. However as long as the searching run is completed with reasonable rapidness, this acceleration effect on the factual speed is negligible.

4. DESIGN OF THE CURRENT CONTROLLER

In this chapter the design of the current controller concerning about the frequency searching run are discussed.

Since the principle of the searching run bases on the steady-state characteristics of the motor, the searching of the frequency proceeds on only when the current reaches the reference value, lest the rotor frequency be missed. As a consequence the character of the current controller decides directly the rapidness of the searching.

In the process of frequency searching, the air-gap flux is gradually built up. A steep voltage peak on the constant-current V-f curve at frequencies near rotor frequency can be observed. Therefore the output of the current controller should rise very rapidly in this range, otherwise the current cannot be maintained at constant level.

In our control algorithmus the parameter are so set that the frequency searching goes on relative quickly when the stator frequency f_s is wide distanted from f_m. But the searching process will be slowed down at frequencies near f_m. At the

same time the stator voltage will be raised more rapidly to counteract the gradually increased counter emf. Thus the rotor speed can be reliably and quickly found. The stator current is maintained nearly at a constant level

Fig.11 indicates the experiment results on a V/f controlled drive system. The drop in the envelop of the current is apparent with constant parameter current controller. With adaptive parameter the stator current is nearly kept at constant level. Almost one second less is needed for the searching run.

In order to recognize the rotor velocity exactly, the

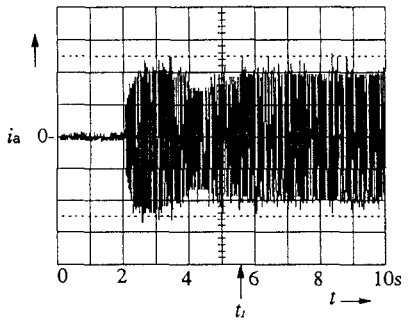


Fig.11a. with constant parameter, t_s=3.55s

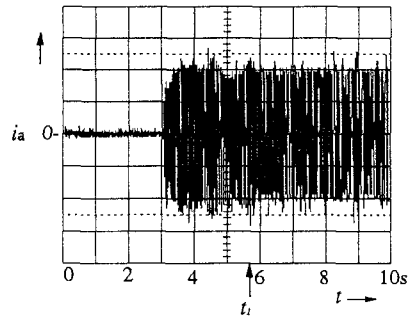


Fig11b. with adaptive parameter, t_s = 2,6s

Fig 11. The searching processes with different parameter. The rotor frequency f_m = 33Hz, f_m is found at time t_1

current reference I_{ref} should in principle be chosen according to the load, since the V/f curve relates itself only to one stator current for one load. However the load is often difficult to predicate. The current reference can be chosen in the range of (0.7-1.0)I_R or simply equal to I_R. The reason is as follows: If I_{ref} is too small, the rotor frequency to be searched can be possiblly lost, e.i. there will be no cross-point between the constant-current V-f curve and the constant-flux V/f curve (Fig.12).

While I_{ref} is equal to I_R and the motor is not loaded, the found frequency is only of an error of the rated slip-frequency. Nevertheless too large reference current is also not preferable, because the motor would be much over-magnetized. In addition to extra energy losses and extra frequency error, a long period of transient process might be necessary to get the current down to the rated magnetizing level after the searching run is finished.

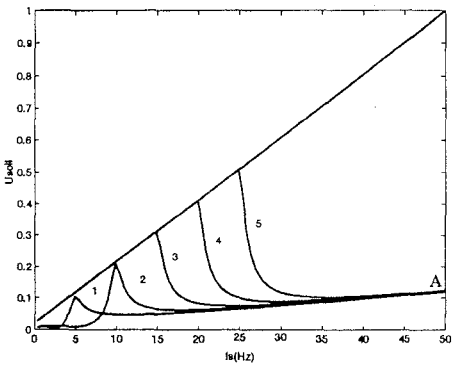


Fig.12. Steady-state frequency-voltage characteristics. I_{sref} = constant = 0.5

5.REFERENCE

[1] J.Holtz," State of the Art of Controlled AC Drives without Speed Sensor", IEEE Intern. Conf. on Power Electronics and Drive Systems PEDS'95, Singapore,pp.1-6

[2] J.Jiang, J.Holtz," Speed Sensorless AC Drive for High Dynamic Performance and Steady State Accuracy", Conf.Rec.IEEE-IECON'95

[3] I.Miyashita, A.Imayanagida, T.Koga," Recent Industrial Application of Speed Sensoeless Vector Control in Japan", Conf.Rec.IEEE-IECON'94, pp.1573-1578

[4]. C.Schauder,"Adaptive Speed Identification for Vector-Control of Induction Motors without Rational Transducers", IEEE-IAS Ann.Meet., 1989,pp. 493-499

[5] U.Baader, M. Depenbrock and G. Gierse," Direct Self Control of Inverter-fed Induction Machine, a Basis for Spped Control without Speed-Measurement", in Conf. Record IEEE Ind. Appl. Sociaty Annual Meeting (1989) pp.486-492

[6] B.J. Seibel, R.J. Kerkman and D. Leggate,"Inverter Control During Overload and Following Power Interruption", IEEE Trans. on Ind.Appl. (1992), pp. 567-573

[7] J. Holtz and W. Lotzkat," Controlled AC Drives with Ride-Through Capability at Power Interruption", in Conf. Record IEEE Ind. Appl. Sociaty Annual Meeting (1993)

[8] K. Koga, R. Ueda and T. Sonoda," Evaluation on Operating Performances of Three Typical V/f Control Schemes in PWM Induction Motor System", in Record of IEEE Conf. on IECON (1991), pp.701-706

Speed Control of Ultrasonic Motors by Discrete Time Variable Structure Control

Tomonobu Senjyu , Satoru Yokoda, and Katsumi Uezato

Faculty of Engineering, University of the Ryukyus
1 Senbaru Nishihara-cho Nakagami Okinawa 903-01 Japan

Abstract **– Ultrasonic motor(USM) has many useful features as a servomotor. In this paper, we propose a speed control system for travelling wave type USM using variable structure control based on adaptive control theory. We construct the control system which includes variable structure self tuning regulator connecting an integrator. Then, steady-state speed error has been reduced when heavy load torque is applied to the motor. In the proposed speed control system, high performance adjustable speed performance is maintained even if parameter values have not been identified sufficiently. The effectiveness and validity of proposed controller is demonstrated by experiments.**

I. Introduction

Ultrasonic motor(USM) has many useful features, including low speed, high torque, silent drive, and no magnetic field generation. This motor has especially large holding torque and quick response characteristics, making it ideal for use as a servomotor[1].

The drive principle of USM has complex mechanism such that the rotor is moved by ultrasonic vibration force of piezoelectric elements inside the stator. Therefore, it is difficult to control the motor's speed and/or position based on minute mathematical models[2]. Accordingly, the controllers for USM have been mostly designed using PI controller. However PI controller cannot maintain the control performance in the case that operating point or load torque variation occur frequently.

Authors have been proposed speed/position controllers for USM using adaptive control[3][4]. These controllers are effective for characteristic variations caused by drive conditions change because it identifies the plant parameters online. But, in these works, the control performances were undesirable when parameter identification was not implemented sufficiently such that starting the motor and large variation of the reference speed. It is important problem for servo system where the reference speed is arbitrary given and the motor starts and stops frequently.

Another approaches to deal with the uncertainty, variable structure control using sliding mode has received much attention for application of electric drives[5]. In such application, there is a problem that sliding mode control speed drive systems needs acceleration signals which is difficult to acquire in actual systems. In recent years, there have been reported a design method of discrete time variable structure control for plant with unknown parameters[6]. This control algorithm does not use state variables but uses present and past input-output signals.

In order to control the speed of USM, it is necessary to control the resonant frequency of the motor almost continuously, even when a large step reference speed is given. Further, in the servo system, it is necessary to reduce quickly the steady-state speed error between the reference speed and the actual speed.

For the purpose of solving these problems, in this paper, we propose a speed servo control system for USM by variable structure control based on adaptive control theory. we construct the control system which include variable structure self tuning regulator(VS-STR) connecting an integrator. The integrator prevents large variation of the control input. Then, the drive frequency is provided almost continuously for a large step reference signal, and steady-state speed error has been reduced when heavy load torque is applied to the motor.

Firstly, the drive system used in this paper and speed characteristics of USM are shown in Section II. Speed control system by conventional self tuning controller is shown in Section III. Section IV presents speed control system by VS-STR with integrator. The effectiveness and validity of proposed controller is demonstrated by experiments in Section V. Finally, conclusions of this paper are summarized in Section VI.

II. Drive System of USM

In this paper, drive frequency is used as a control input of USM. The drive system for speed control of USM is shown in Fig. 1. The load and rotary encoder are connected with the motor via coupling, and the motor speed is measured by the rotary encoder. The microcomputer calculates the control input, and the drive frequency data is transmitted to a programmable frequency oscillator which generates the switching signals to the MOS-FET driver. Then the inverter generates the two-phase alternating voltages V_A and V_B as shown in Fig. 2, for application to the USM. The design specification of the tested USM is shown in Table 1.

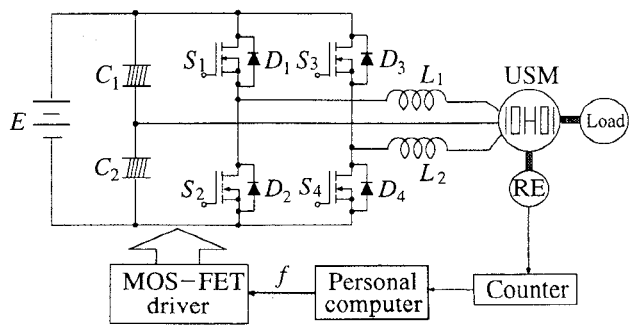


Fig. 1. Drive system for USM

0-7803-3823-5/97/$10.00© 1997 IEEE

Table 1. Design specification of tested USM.

Drive frequency	40 kHz
Drive voltage	100 Vrms
Rated torque	0.314 Nm
Rated output power	3 W
Rated speed	9.0 rad/s
Temperature	$-10 \sim +50$ ℃
Weight	0.240 kg

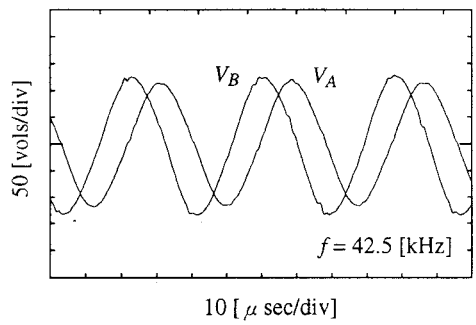
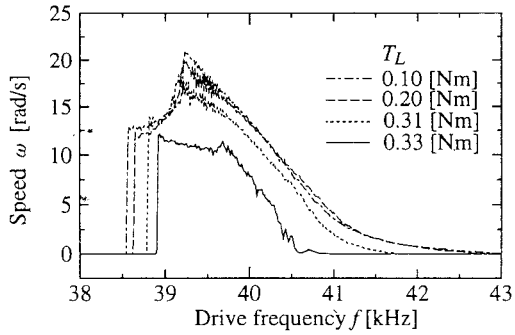
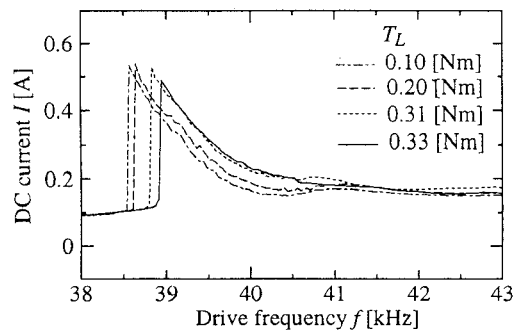


Fig. 2. Output voltages of two-phase inverter.



(a) Revolving speed.



(b) DC current.

Fig. 3. Characteristics for drive frequency against load torque.

Figure 3 shows the drive frequency versus motor speed, dc current supplied to the two-phase inverter against load torque. In Fig. 3(a), since the revolving speed of the USM is proportional to the vibration force of piezoelectric transducer, the revolving speed has a maximum at the mechanical resonant frequency f_r of the motor.

This frequency, however, varies with applied load torque and then the variation of the motor speed is large as load

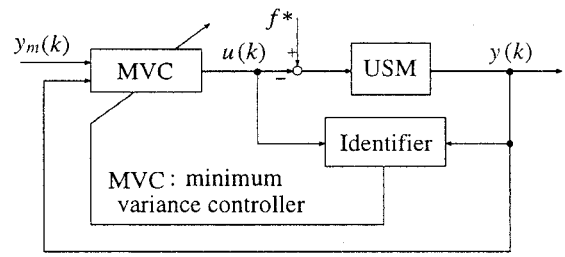


Fig. 4. Block diagram of speed control system by self tuning controller.

torque is applied. Because electromechanical conversion is not performed effectively around the frequency f_r. Then, the dc current which is supplied to the inverter increases around the mechanical resonant frequencies as shown in Fig. 3(b), i.e., the input power increases and we cannot drive stably in the extent of the frequency.

From Fig. 3, the motor is highly nonlinear particularly in the drive frequency below the resonant frequency, therefore we restrict the variation of the drive frequency from 40.0 to 44.0[kHz].

III. Control System by Conventional Self Tuning Controller

USM possesses non-linear speed characteristics, deriving the mathematical model of the motor directly is rather involved. We introduce a simplified mathematical model for USM which is expressed by difference equation. Then design a speed controller using self tuning controller (STC) which is suitable for controlling the time varying and unknown plant.

The block diagram of speed control system using STC is shown in Fig. 4, where $y_m(k)$ is the commanded speed, $y(k)$ is the actual rotor speed, $u(k)$ is the control input (drive frequency), and f^*(=42.0[kHz]) denotes the biased drive frequency, respectively.

We propose a simplified mathematical model for USM in the form of Eq. (1) and thenconstruct the speed controller assuming that the plant parameters are known

$$A\,y(k) = q^{-d}B\,u(k) + w(k) \tag{1}$$

$$\left.\begin{aligned} A &= 1 + a_1 q^{-1} + \cdots + a_n q^{-n} \\ B &= b_0 + b_1 q^{-1} + \cdots + b_m q^{-m} \end{aligned}\right\}$$

where, d is the control delay, q^{-1} is the backward shift operator, $w(k)$ denotes the white noise, n and m are the model orders, respectively.

The adaptive speed controller based on STC is designed with the generalized minimum variance control low, which is designed to minimize the following cost function J_1 [7][8]

$$J_1 = E\left[\{y(k+d) - y_m(k+d)\}^2 + \lambda\{u(k) - u(k-1)\}^2\right] \tag{2}$$

where, $E[\cdot]$ is the expectation operator, and λ denotes the control weight which restricts the variation of control input.

The control input $u(k)$ which minimizes the cost function J_1 is obtained by $\partial J_1/\partial u(k)=0$ taking into account $\partial y(k+d)/\partial u(k) = b_0$ as follows

$$\left\{ B\,R + \frac{\lambda}{b_0} \right\} u(k) = y_m(k+d) - H\,y(k) + \frac{\lambda}{b_0} u(k-1). \quad (3)$$

In Eq. (3), polynomials R and H are determined by following Diophantine equation

$$1 = A\,R + q^{-d} H \quad (4)$$

$$\left.\begin{aligned} R &= 1 + r_1 q^{-1} + \cdots + r_{d-1} q^{-(d-1)} \\ H &= h_0 + h_1 q^{-1} + \cdots + h_{n-1} q^{-(n-1)}. \end{aligned}\right\}$$

The plant parameters are identified by conventional recursively least square method.

IV. Control System by VS-STR with Integrator

A. Speed controller design

Self tuning control shown in section II is effective to control the speed of USM, but when the plant identification is not completed, the self tuning control gives undesirable response.

In order to overcome this problem, we define this motor with error equation using the identified parameters based on input-output relation of the motor and construct the controller by VS-STR connecting an integrator. Then, the original problem of tracking a reference speed has been replaced with the problem of regulating speed error $e(k)$ to zero. Figure 5 shows the block diagram of speed control system using VS-STR with integrator, where, $y_m(k)$ denotes the reference speed, $y(k)$ denotes the actual revolving speed, $u'(k)$ denotes the control input, $f(k)$ denotes the system input(drive frequency of two phase voltages applied to the USM). We give an error model expressed by a differential equation in order to construct the STR using u' and y :

$$Ae(k) = q^{-d} B u'(k) + w(k) \quad (5)$$

$$\left.\begin{aligned} A &= 1 + a_1 q^{-1} + \cdots + a_n q^{-n} \\ B &= b_0 + b_1 q^{-1} + \cdots + b_m q^{-m} \end{aligned}\right\}$$

where, d is the time delay, q^{-1} is the backward shift operator, $w(k)$ denotes white noise.

The STR is designed so as to minimize the following variable $s(k+d)$[6]

$$s(k+d) = C\,e(k+d) \quad (6)$$

where, C is the polynomial defined by

$$C = 1 + c_1 q^{-1} + \cdots + c_n q^{-n}.$$

The control input is decomposed of equivalent control part and non-linear control part as

$$u'(k) = u_{eq}(k) + v(k). \quad (7)$$

The equivalent control input u_{eq} is determined to achieve $s(k+d) = s(k)$

$$\{B\,R + \lambda\}\, u_{eq}(k) = -H\,e(k) + s(k) \quad (8)$$

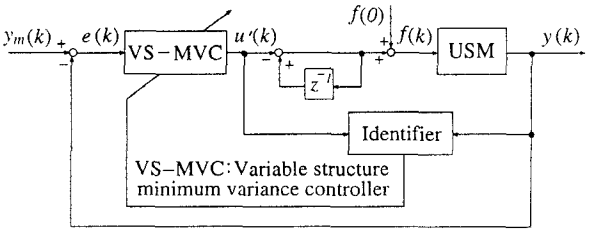


Fig. 5. Block diagram of speed control system by VS-STR with integrator.

where, λ denotes the control weight, R and H are determined by the Diophantine equation (Eq. (4)).

The non-linear control input v is chosen as

$$v(k) = -\eta\,|e(k)|\,\frac{s(k)}{|s(k)| + \delta} \quad (9)$$

where, η and δ are positive constants.

The drive frequency is determined by Eq. (10)

$$f(k) = f(k-1) + u'(k). \quad (10)$$

Equation (10) prevents large variation of the control input.

B. Parameter identification

The controller must know the motor parameters in order to calculate the control input $u'(k)$. There are many parameter identification algorithms and for simplicity this paper adopts the conventional recursive least squares method.

The objective of parameter identification based on the recursive least squares method is to find the parameter vector θ which minimizes the following cost function J_2 [9]

$$J_2 = \sum_{k=0}^{N} \beta^{N-k} w^2(k)$$

$$= \sum_{k=0}^{N} \beta^{N-k} \left\{ e(k) - z^T(k)\theta \right\}^2 \quad (11)$$

where

$$\left.\begin{aligned} \theta^T &= [-a_1\ -a_2\ \cdots\ -a_n\ b_0\ b_1\ \cdots\ b_m], \\ z^T(k) &= [e(k-1)\ e(k-2)\ \cdots\ e(k-n) \\ &\qquad u'(k-d)\ u'(k-d-1)\ \cdots\ u'(k-d-m)] \end{aligned}\right\}$$

and β $(0<\beta\leq 1)$ denotes the forgetting factor. The convergence of the parameter identification becomes fast with small β and the parameter identification algorithm is effective for time varying system. However, when the forgetting factor β is too small, the identification becomes sensitive to system noise[10].

The identification algorithm is finally obtained as follows by solving $\partial J_2/\partial\theta = 0$

$$P(N) = \frac{1}{\beta}\left\{ P(N-1) - \frac{P(N-1)z(N)z^T(N)P(N-1)}{\beta + z^T(N)P(N-1)z(N)} \right\} \quad (12)$$

$$\widehat{\theta}(N) = \widehat{\theta}(N-1) - \frac{P(N-1)z(N)}{\beta + z^T(N)P(N-1)z(N)}\ *$$

Table 2. Control parameters in the experiment

Sampling period	T_s=5.0[ms]
Model orders	n=m=2
Delay time	d=2
Control weight	λ=10
Forgetting factor	β=0.99

$$* \left[z^T(N)\widehat{\theta}(N-1) - e(N)\right]. \qquad (13)$$

Equations (12) and (13) are the identification algorithm based on the recursively least square method.

V. Experimental Results

In order to evaluate the control performance of the proposed controller, the experimental results of the proposed control scheme are compared with that of the conventional self tuning controller[3].

A. Speed control by conventional STC

The experimental parameters used in the experiments are shown in Table 2.

Figure 6 shows the experimental results of speed control by conventional STC, where Fig. 6(a) shows the speed, Fig. 6(b) depicts the drive frequency, Figs. 6(c) and 6(d) show the estimated parameters a_i and b_j. In Fig. 6(a), the tracking performance to the reference speed is poor to the parameter identification has been completed as shown in Figs. 6(c) and 6(d). After an adaptation transient, the actual speed tracks the reference, but steady-state error remain in low speed range.

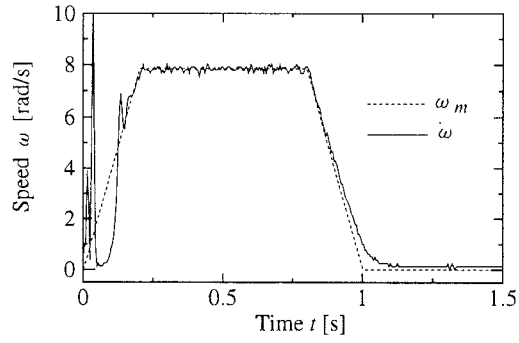
Figure 7 shows the experimental results of speed control with load torque (0.31Nm:rated torque) when the reference speed has been changed at t=1 and 2 second. The response of the actual speed is worse when the reference speed is changed because the variation of plant parameters become large as shown in Figs. 7(c) and 7(d).

As pointed out above, the conventional STC would occur undesirable responses when plant identification is not completed, such as starting the motor and large variation of the reference speed.

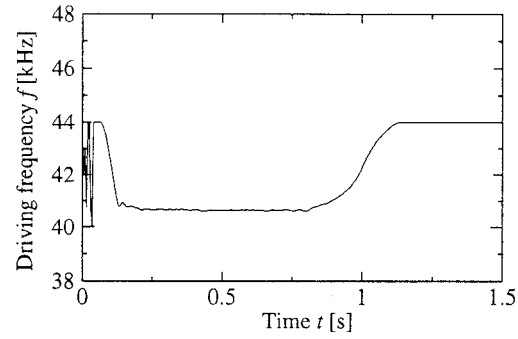
B. Speed control by VS-STR with integrator

The experimental results of speed control by proposed control scheme are shown here. Control parameters in the experiments are identical to the speed control by conventional STC, except for control weight λ=30, feedback control gain η=0.3 and δ=0.1 which is added to the denominator of Eq. (9) in order to eliminate chattering. Polynomial C in Eq. (6) is chosen as C=$1 - q^{-1} + 0.25q^{-2}$ whose zeros are inside the unit disk.

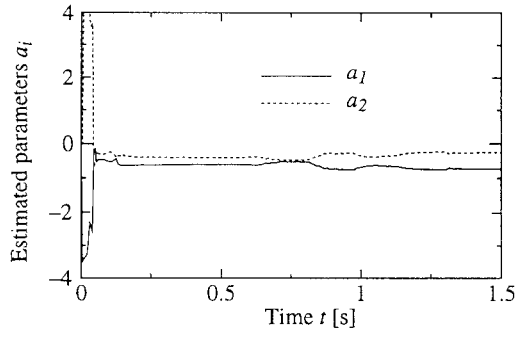
Figure 8 shows the experimental results of speed control with load torque by proposed control scheme. In Fig. 8(a), the actual speed tracks the reference speed from starting the motor compared with Fig 6(a). Fig. 8(b) shows the control input u' which is given by VS-STR. Then, the integrator prevents large variation of the drive frequency f.



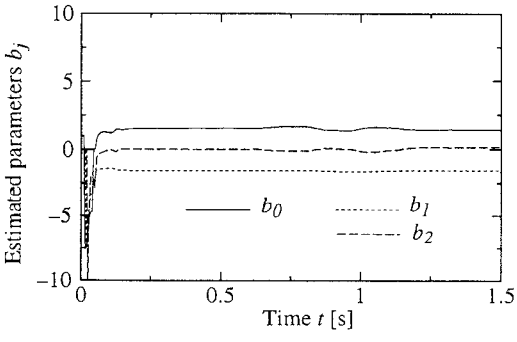
(a) Speed



(b) Control input

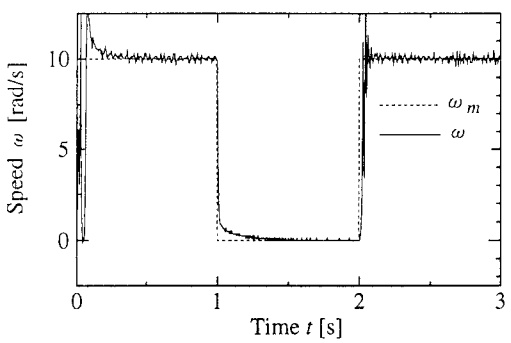


(c) Estimated parameters a_i

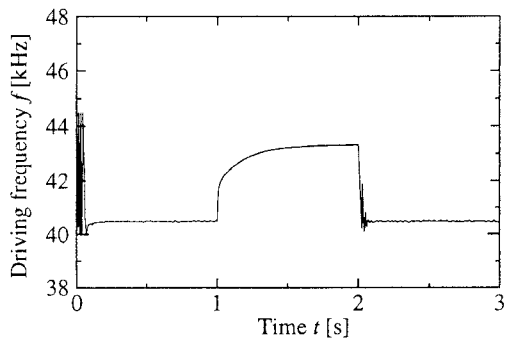


(d) Estimated parameters b_j

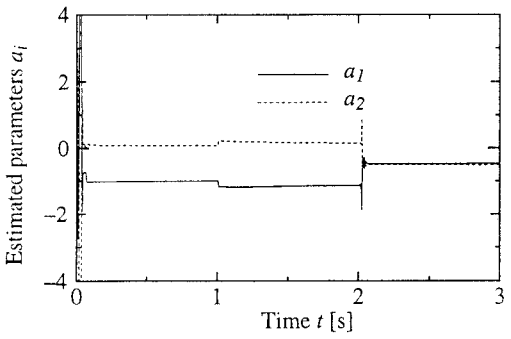
Fig. 6. Speed control by conventional STC (T_L=0.0[Nm]).



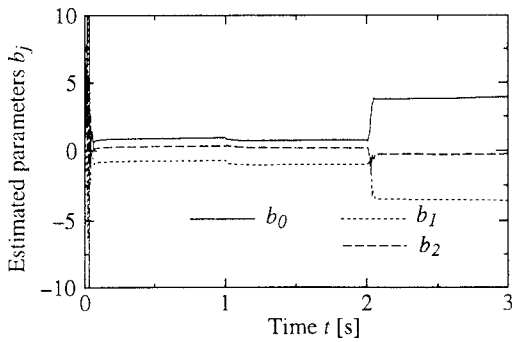
(a) Speed



(b) Control input

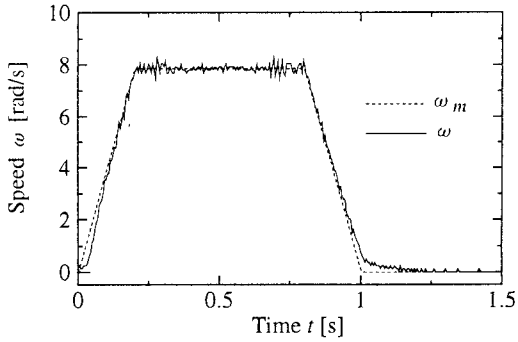


(c) Estimated parameters a_i

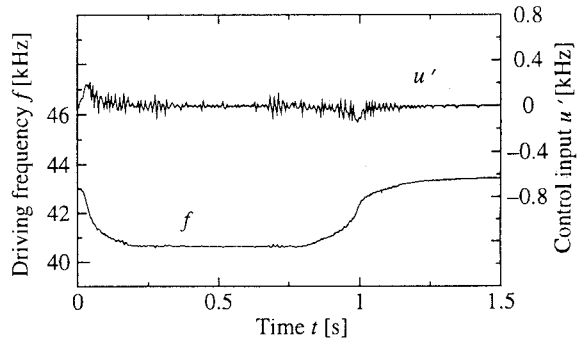


(d) Estimated parameters b_j

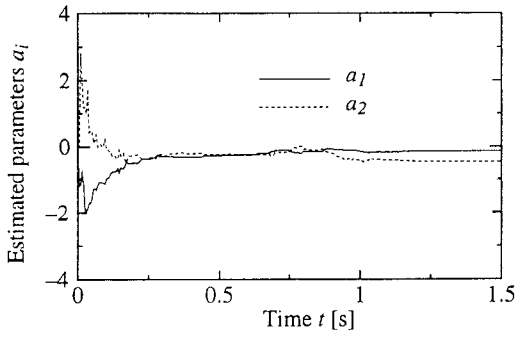
Fig. 7. Speed control by conventional STC (T_L=0.31[Nm]).



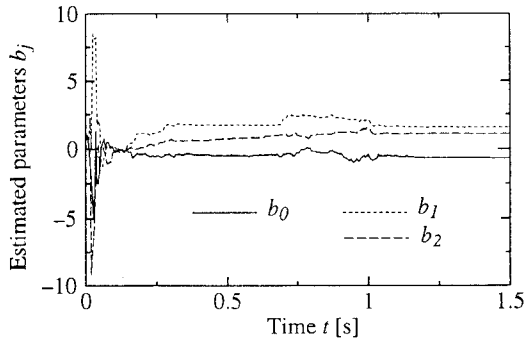
(a) Speed



(b) Control input

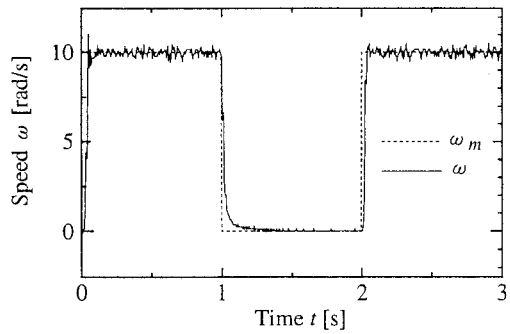


(c) Estimated parameters a_i

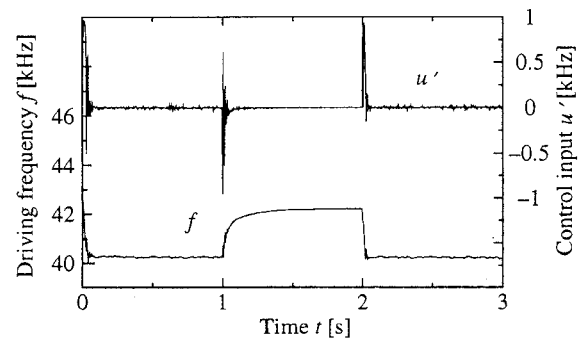


(d) Estimated parameters b_j

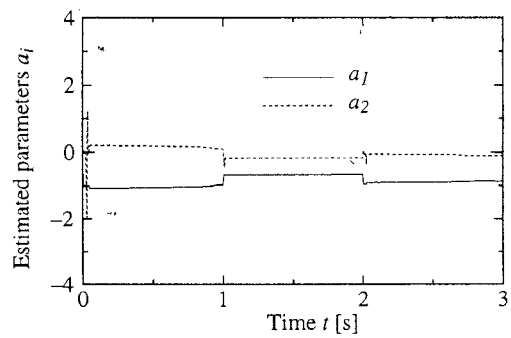
Fig. 8. Speed control by proposed controller (T_L=0.20[Nm]).



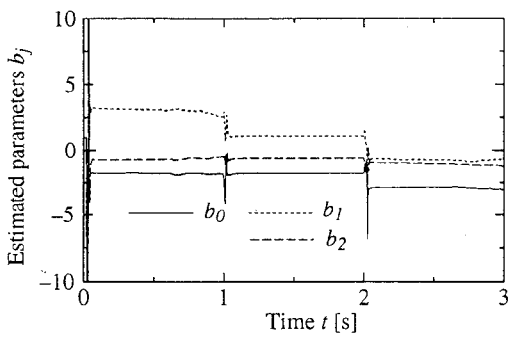
(a) Speed



(b) Control input



(c) Estimated parameters a_i



(d) Estimated parameters b_j

Fig. 9. Speed control by proposed controller (T_L=0.31[Nm]).

Figure 9 shows the experimental results by the proposed control scheme when the reference speed has been changed at t=1 and 2 second. In Fig. 9(a), the actual speed tracks quickly to the reference speed without large overshoot or undershoot, regardless of load torque is applied(0.31[Nm] : rated torque). In the proposed control scheme, since the variable structure term has no system parameters and the control input u' is independent on a system input f, good tracking performance is maintained at any cases. Figs. 9(c) and 9(d) show the identified parameters. Although the parameter variation is large when the reference speed has been changed, after that, the plant parameters are identified stably.

VI. Conclusions

In this paper, we proposed a speed control system for travelling wave type USM using variable structure control based on adaptive control theory. We constructed the control system which includes variable structure self tuning regulator connecting an integrator. Then, steady-state speed error has been reduced when heavy load torque is applied to the motor. In the proposed speed control system, high performance adjustable speed performance is maintained even if parameter values have not been identified sufficiently.

References

[1] T. Kenjyo and T. Sashida, An Introduction of Ultrasonic Motor, Oxford Science Publications, 1993.

[2] P. Hagedorn and J. Wallaschek, "Travelling Wave Ultrasonic Motors, Part I: Working Principle and Mathematical Modelling of the Stator", *Journal of Sound and Vibration*, Vol. 155, No. 1, pp. 31-46, 1992.

[3] T. Senjyu, H. Miyazato, and K. Uezato, "Adjustable Speed Control of Ultrasonic Motors by Adaptive Control", *IEEE Trans. PE.*, Vol. 10, No. 5, pp. 191-200, February 1996.

[4] T. Senjyu, H. Miyazato, and K. Uezato "Quick and Precise Position Control of Ultrasonic Motors Using Hybrid Control", *Electrical Engineering in Japan*, Vol. 116, No. 3, March, 1996.

[5] V. I. Utkin, "Sliding Mode Control Design Principles and Applications to Electric Drives", *IEEE Trans. IE.*, Vol. 40, No. 1, pp. 23-36, 1993.

[6] K. Furuta, "VSS-Type Self Tuning Control", *IEEE Trans. IE.*, Vol. 40, no. 1, pp. 37–44, 1993.

[7] D. W. Clarke, "Self-Tuning Control of Nonminimum-phase Systems", *Automatica*, Vol. 20, No. 5, pp.501-517, 1984.

[8] M. J. Grimble, "A control weighted minimum-variance controller for non-minimum phase systems," *Int. J. Control*, Vol. 33, No.4, pp.751-762, 1981.

[9] M. Terao, K. Kanai, *Introduction to Robust Adaptive Control*, Ohmsha, 1989 (in Japanese).

[10] P. Anderson, "Adaptive Forgetting in Recursive Identification Through Multiple Models", *Int. J. Control*, Vol. 42, No. 5, pp. 1175-1193, 1985.

A New Sensorless Control Method for a General Class of Linear Pulse Motors

Dong-Eui Chang† Yang-O Kim† In-Joong Ha†
Moonhwan Kim‡ Kook Hun Kim‡

† School of Electrical Engineering Seoul National University, Seoul, Korea 151-742
Fax:+82-2-878-8198, Phone:+82-2-880-7312, E-mail:ijha@asrisdt200.snu.ac.kr

‡ Power Plant Control Team, Korea Electrotechnology Research Institute, P.O.Box 20,Changwon, Korea 641-120
Fax:+82-551-80-1476, Phone:+82-551-80-1441, E-mail:mhkim@keri.re.kr

Abstract - This paper describes a sliding-mode type observer to identify the rotor position and velocity of a hybrid-type linear pulse motor(LPM). Since the observer's error dynamics of a hybrid-type LPM is highly nonlinear, the performance of the proposed observer is analyzed using an approximated error model. The optimal choices of the proposed observer gains are also discussed. Our extensive simulation study shows that the proposed observer can identify rotor position and velocity within 3% and is quite robust with respect to uncertainties in system model including mechanical parameters and load force.

I. Introduction

The position information is essential for high performance control of linear pulse motors(LPM). Actually, encoders have been widely used for sensing accurately rotor position. These position sensors, however, make the motor system expensive and mechanically unreliable. For this reason, various methods for identifying rotor position and velocity have been proposed recently. Most of the prior works consider sensorless control of permanent magnet synchronous motors(PMSM) whose dynamics are the same as those of permanent magnet LPM.

In [4], the dq model of the PMSM was used to develop an observer for estimating the electrical and mechanical states of the motor from current and voltage measurements. The dq transformation is useful to transform the highly nonlinear motor dynamics into a simple nonlinear system which is relatively easy to manipulate. In [5], this transformation was incorporated into a gain-scheduling technique to achieve good observation performance. More recently, a nonlinear reduced observer for sensorless control of PMSM was proposed in [7], which is based on a reduced motor model obtained through a novel state transformation. Though these methods seem well suited for sensorless control of the PMSM, they are not likely to be applied directly to hybrid-type LPM. This is because the dq transformation technique no longer simplifies the highly nonlinear dynamics of the hybrid-type LPM, which involve variable reluctance(VR) components. On the other hand, the method of identifying rotor position proposed in [6] is based on the information of winding flux linkages obtained from the measurement of stator voltages and currents. This method is, in priciple, based on pure integration of some measured and/or computed quantities and, with some modification, seems to be applicable to hybrid-type LPM.

It is known that the sliding-mode type observer, which was first proposed in [2], converges faster than the conventional linear observers due to the so-called "shearing effect" and provides some robustness with respect to model uncertainties. The chattering effect, which is known to be a drawback of the sliding-mode controller [3], is not any more a serious problem in the sliding-mode type observer since it happens only in the computation at CPU, and hence, cannot excite any hidden fast dynamics.

In this context, this paper presents a sliding-mode type observer for sensorlss control of hybrid-type LPM. Sufficient conditions for convergence of the proposed observer are given. The error dynamics can be made locally linear and stable. Furthermore, the effect of external load force can be minimized by considering it as an exogenous disturbance and applying well-known disturbance rejection methods. Simulations were carried out to justify further the practical use of the proposed observer for sensorless control of a general class of LPM.

II. Main Result

When no magnetic saturation occurs, the dynamic equations of an LPM can be described in state space as follows.

$$\frac{d\mathbf{x}}{dt} = A(\mathbf{x})\mathbf{x} + h(\mathbf{x}, \mathbf{u}, F_L), \ \mathbf{y} \ = \ C\mathbf{x}, \qquad (1)$$

where

$$\mathbf{x} \triangleq [i_1, i_2, v, x]^T \ , \ \mathbf{u} \triangleq [V_1, V_2]^T \qquad (2)$$

$$A \triangleq \begin{bmatrix} -\frac{R_s}{L(i_1,x)} & 0 & 0 & 0 \\ 0 & -\frac{R_s}{L(i_2,x-\frac{P}{4})} & 0 & 0 \\ 0 & 0 & -\frac{B}{M} & 0 \\ 0 & 0 & 1 & 0 \end{bmatrix} \qquad (3)$$

$$h(\mathbf{x},\mathbf{u},F_L) \triangleq \begin{bmatrix} -\frac{1}{L(i_1,x)}(E(i_1,v,x)-V_1) \\ -\frac{1}{L(i_2,x-\frac{p}{4})}(E(i_2,v,x-\frac{p}{4})-V_2) \\ \frac{1}{M}(F_e(i_1,i_2,x)-F_L) \\ 0 \end{bmatrix} \quad (4)$$

$$C \triangleq \begin{bmatrix} 1 & 0 & 0 & 0 \\ 0 & 1 & 0 & 0 \end{bmatrix} \quad (5)$$

In (1), V_k is the stator voltage of phase $k = 1, 2$, i_k is the stator current of phase $k = 1, 2$, x is the rotor position, v is the rotor velocity, and p is the length of each pitch. Here, M, B, and F_L denote rotor mass, viscous friction coefficient, and external load force, respectively.

On the other hand, the function $L : \mathbf{R}^2 \to \mathbf{R}$ represents stator inductance and can be described as follows.

$$L(i,x) \triangleq L_0 + \tilde{L}_e(x) + \tilde{L}_o(x)\mathrm{sgn}(i), \quad (6)$$

where L_0 is a constant and the functions $\tilde{L}_e$, $\tilde{L}_o$ of x are p-periodic. And, the function $E : \mathbf{R}^3 \to \mathbf{R}$ represents the back emf and is defined by

$$E(i,v,x) \triangleq v\left\{g(x) + \tilde{L}_e'(x)i + \tilde{L}_o'(x)|i|\right\}, \quad (7)$$

where $'$ denotes the derivative with respect to x. And g is also a function of x.

Finally, the function $F_e : \mathbf{R}^3 \to \mathbf{R}$ represents the generated force and has the following form.

$$F_e(i_1,i_2,x) \triangleq F(i_1,x) + F(i_2,x-\frac{p}{4}), \quad (8)$$

where

$$F(i,x) \triangleq g(x)i + \frac{1}{2}\tilde{L}_e'(x)i^2 + \frac{1}{2}\tilde{L}_o'(x)|i|i. \quad (9)$$

Notice that in the RHS of (9), the first term represents the force component due to permanent magnet(PM), while the other two terms represent the force component due to VR.

Here, the functions $\tilde{L}_e$, $\tilde{L}_o$, and g as well as the constant L_0 are determined by the flux distribution due to PM and the geometric structure of stator and rotor. In particular, they are periodic due to the uniformity of pitches. Specifically speaking,

$$\begin{aligned} g(x+p) &= g(x), \\ \tilde{L}_e(x+p) &= \tilde{L}_e(x), \\ \tilde{L}_o(x+p) &= \tilde{L}_o(x), \\ L(i,x) &> 0, \qquad \forall x \in \mathbf{R} \end{aligned} \quad (10)$$

In practice, the stator currents i_1, i_2 and the stator voltages V_1, V_2 can be measured easily with inexpensive electrical sensors. So, we regard i_1 and i_2 as the system output and V_1 and V_2 as the system input. On the other hand, the load force F_L is regarded as a disturbance for which no exact information is available. Based on this observation, we propose a sliding-mode type observer for the state observation of the above system, (1).

$$\frac{d\hat{\mathbf{x}}}{dt} = A(\hat{\mathbf{x}})\hat{\mathbf{x}} - H\mathbf{z} - K(\hat{\mathbf{x}})\mathrm{sgn}(\mathbf{z}) + \hat{h}(\hat{\mathbf{x}},\mathbf{u}), \quad (11)$$

where

$$\hat{\mathbf{x}} \triangleq [\hat{i}_1, \hat{i}_2, \hat{v}, \hat{x}]^T, \quad (12)$$

$$\mathbf{z} \triangleq [z_1,\ z_2\ ]^T \triangleq C(\hat{\mathbf{x}} - \mathbf{x}) \quad (13)$$

$$\mathrm{sgn}(\mathbf{z}) \triangleq [\mathrm{sgn}(z_1),\ \mathrm{sgn}(z_2)\ ]^T \quad (14)$$

$$\hat{h}(\hat{\mathbf{x}},\mathbf{u}) \triangleq h(\hat{\mathbf{x}},\mathbf{u},0) \quad (15)$$

$$H \triangleq \begin{bmatrix} H_1 \\ O_{2\mathrm{x}2} \end{bmatrix}, \quad K(\hat{\mathbf{x}}) \triangleq \begin{bmatrix} K_1 \\ K_2(\hat{\mathbf{x}}) \end{bmatrix} \quad (16)$$

Here, $\hat{\mathbf{x}}$ is the estimate of $\mathbf{x}$; and H_1 and K_1 are 2 x 2 constant matrices, while K_2 is a 2 x 2 matrix function depending on $\hat{\mathbf{x}}$. On the other hand, $O_{2\mathrm{x}2}$ denotes the 2 x 2 zero matrix.

Now, we describe how to determine $K(\hat{\mathbf{x}})$ for the convergence of state observation error. For notational convenience, we will sometimes be sloppy in indicating the dependence of K and K_2 on $\hat{\mathbf{x}}$ by just writing K and K_2 instead of $K(\hat{\mathbf{x}})$ and $K_2(\hat{\mathbf{x}})$.

The sliding gain K is constant in [2], where a sliding-mode type observer was first considered for nonlinear systems. With K constant, however, it is hard to stabilize the dynamics of the observation error as is desired. Here, the choice of K is quite free. In fact, K can be a function of the state estimation $\hat{\mathbf{x}}$. As the result, the stabilization of observation error dynamics can be accomplished relatively easily.

Let

$$\mathbf{e} \triangleq [e_1, e_2, e_3, e_4]^T \triangleq \hat{\mathbf{x}} - \mathbf{x} \quad (17)$$

From (1) and (11), we then can derive the dynamics of observation error as follows.

$$\frac{d\mathbf{e}}{dt} = A(\hat{\mathbf{x}})\mathbf{e} - H\mathbf{z} - K\mathrm{sgn}(\mathbf{z}) + \Delta h, \quad (18)$$

where

$$\begin{aligned} \Delta h &\triangleq [\Delta h_1, \Delta h_2, \Delta h_3, \Delta h_4]^T \\ &\triangleq \hat{h}(\hat{\mathbf{x}},\mathbf{u}) - h(\mathbf{x},\mathbf{u},F_L) + \{A(\hat{\mathbf{x}}) - A(\mathbf{x})\}\mathbf{x} \end{aligned} \quad (19)$$

Note that the detailed expression of Δh is as follows.

$$\begin{aligned} \Delta h_1 \triangleq\ & -\frac{1}{L(\hat{i}_1,\hat{x})}(E(\hat{i}_1,\hat{v},\hat{x}) - V_1 + R_s i_1) \\ & + \frac{1}{L(i_1,x)}(E(i_1,v,x) - V_1 + R_s i_1) \end{aligned} \quad (20)$$

$$\begin{aligned} \Delta h_2 \triangleq\ & -\frac{1}{L(\hat{i}_2,\hat{x}-\frac{p}{4})}(E(\hat{i}_2,\hat{v},\hat{x}-\frac{p}{4}) - V_2 + R_s i_2) \\ & + \frac{1}{L(i_2,x-\frac{p}{4})}(E(i_2,v,x-\frac{p}{4}) - V_2 + R_s i_2) \end{aligned} \quad (21)$$

$$\Delta h_3 \triangleq \frac{1}{M}(F_e(\hat{i}_1,\hat{i}_2,\hat{x}) - F_e(i_1.i_2,x)) + \frac{1}{M}F_L \quad (22)$$

$$\Delta h_4 \triangleq 0 \quad (23)$$

Now, we present the method of choosing H and K for the stabilization of the above observation error dynamics. For this aim, we define a sliding manifold χ

by

$$\chi \triangleq \{\mathbf{e} \in \mathbf{R}^4 \mid e_1 = e_2 = 0\} \tag{24}$$

First, we analyze the observation error dynamics in the reaching mode, i.e., the mode in which the trajectory of observation error reaches the sliding manifold χ. We assume that $|\Delta h_1|$ in (20) and $|\Delta h_2|$ in (21) are bounded, that is, there exists a constant $b > 0$ satisfying

$$|\Delta h_k(t)| \leq b, \quad \forall t \geq 0\ , \quad k = 1, 2 \tag{25}$$

This assumption will be justified later. For computational convenience, we choose the 2 x 2 matrices H_1 and K_1 in (16) by diagonal matrices as follows.

$$H_1 \triangleq \begin{bmatrix} H_{11} & 0 \\ 0 & H_{22} \end{bmatrix},\ K_1 \triangleq \begin{bmatrix} K_{11} & 0 \\ 0 & K_{22} \end{bmatrix} \tag{26}$$

Here, the constants H_{11}, H_{22}, K_{11}, and K_{22} are chosen to satisfy the following conditions.

$$H_{11} > 0,\ H_{22} > 0,\ K_{11} > b,\ K_{22} > b \tag{27}$$

Then, the trajectory of observation error always reaches the sliding manifold χ within a finite time, as shown below.

Simple operation gives the following inequality:

$$\begin{aligned} \tfrac{d}{dt}(\tfrac{1}{2}\|\mathbf{z}\|^2) &= \mathbf{z}^T\dot{\mathbf{z}} \\ &= -(\tfrac{R_s}{L(\hat{i}_1,\hat{x})} + H_{11})|e_1|^2 - (\tfrac{R_s}{L(\hat{i}_2,\hat{x}-\frac{p}{4})} + H_{22})|e_2|^2 \\ &\quad -K_{11}|e_1| - K_{22}|e_2| + e_1\Delta h_1 + e_2\Delta h_2 \\ &\leq -(\tfrac{R_s}{L(\hat{i}_1,\hat{x})} + H_{11})|e_1|^2 - (\tfrac{R_s}{L(\hat{i}_2,\hat{x}-\frac{p}{4})} + H_{22})|e_2|^2 \\ &\quad -(K_{11}-b)|e_1| - (K_{22}-b)|e_2| \\ &\leq -(K_{11}-b)|e_1| - (K_{22}-b)|e_2| \end{aligned} \tag{28}$$

By (10) and (27), this implies that there exists a constant $\eta > 0$ such that

$$\frac{d}{dt}(\frac{1}{2}\|\mathbf{z}\|^2) \leq -\eta\|\mathbf{z}\| \tag{29}$$

This shows that the trajectory of observation error reaches χ within a finite time less than $\frac{\|\mathbf{z}(0)\|}{\eta}$, and thereafter, never leaves χ. In other words, the observation error for stator currents reduces to zero within a finite time. From (20), (21), (27), and (28), we can see that the role of H_1 is to accelerate the reaching speed. On the other hand, the role of K_1 is to assure that reaching the sliding manifold χ occurs within a finite time, and hence its choice depends on the magnitudes of the observation errors for v and x during the reaching mode. Hence, as long as K is chosen large enough to satisfy (27), the assumption in (25) is well justified during the reaching mode.

Next, we analyze the observation error dynamics in the sliding mode and propose a method of determining K_2 such that the observation errors for v and x approach zero. Since in the sliding mode the trajectory of observation error remains in χ, the fourth-order differential equation for observation error dynamics in (18) may be approximated with a second-order differential equation by assuming $\mathbf{z} \equiv \mathbf{0}$. In fact, the observation error dynamics on the sliding manifold χ can be formally derived using the so-called "equivalent control" method [1].

During the sliding mode, the switching term in (18) is active to keep

$$\mathbf{z} \equiv \mathbf{0} \tag{30}$$

Hence it formally holds that

$$\dot{\mathbf{z}} \equiv \mathbf{0} \tag{31}$$

So, the substitution of (30) and (31) into (18) yields

$$\mathrm{sgn}(\mathbf{z}) = K_1^{-1}\begin{bmatrix} \Delta h_1 \\ \Delta h_2 \end{bmatrix} \tag{32}$$

By (18) and (30) - (32), the observation error dynamics on the sliding manifold χ are given by

$$\begin{aligned} \frac{d}{dt}\begin{bmatrix} e_3 \\ e_4 \end{bmatrix} &= \begin{bmatrix} -\frac{B}{M} & 0 \\ 1 & 0 \end{bmatrix}\begin{bmatrix} e_3 \\ e_4 \end{bmatrix} \\ &\quad -K_2(\hat{\mathbf{x}})K_1^{-1}\begin{bmatrix} \Delta h_1|_{\mathbf{z}\equiv\mathbf{0}} \\ \Delta h_2|_{\mathbf{z}\equiv\mathbf{0}} \end{bmatrix} + \begin{bmatrix} \Delta h_3|_{\mathbf{z}\equiv\mathbf{0}} \\ 0 \end{bmatrix} \end{aligned} \tag{33}$$

Assuming that the observation errors are small, we approximate (33) linearly by neglecting higher order terms. Then, it can be shown through some calculation that the observation error dynamics on χ are given by

$$\frac{d}{dt}\begin{bmatrix} e_3 \\ e_4 \end{bmatrix} = \tilde{A}(\hat{\mathbf{x}})\begin{bmatrix} e_3 \\ e_4 \end{bmatrix} + \begin{bmatrix} \frac{1}{M}F_L \\ 0 \end{bmatrix} \tag{34}$$

where

$$\tilde{A}(\hat{\mathbf{x}}) \triangleq \check{A}(\hat{\mathbf{x}}) - K_2(\hat{\mathbf{x}})K_1^{-1}B(\hat{\mathbf{x}}) \tag{35}$$

$$\check{A}(\hat{\mathbf{x}}) \triangleq \begin{bmatrix} -\frac{B}{M} & \frac{1}{M}D_3F_e(\hat{i}_1,\hat{i}_2,\hat{x}) \\ 1 & 0 \end{bmatrix} \tag{36}$$

$$B(\hat{\mathbf{x}}) \triangleq \begin{bmatrix} D_2f_1(\hat{i}_1,\hat{v},\hat{x}) & D_3f_1(\hat{i}_1,\hat{v},\hat{x}) \\ D_2f_2(\hat{i}_2,\hat{v},\hat{x}) & D_3f_2(\hat{i}_2,\hat{v},\hat{x}) \end{bmatrix} \tag{37}$$

$$f_1(\hat{i}_1,\hat{v},\hat{x}) \triangleq -\frac{1}{L(\hat{i}_1,\hat{x})}(E(\hat{i}_1,\hat{v},\hat{x}) - V_1 + R_s\hat{i}_1) \tag{38}$$

$$f_2(\hat{i}_2,\hat{v},\hat{x}) \triangleq f_1(\hat{i}_2,\hat{v},\hat{x}-\frac{p}{4}) \tag{39}$$

We first propose the method for determining $K_2(\hat{\mathbf{x}})$ for the case of

$$\det B(\hat{\mathbf{x}}) \neq 0 \tag{40}$$

(i) Choose a constant Hurwitz matrix A^* such that when $\tilde{A}(\hat{\mathbf{x}}) = A^*$ for all $\hat{\mathbf{x}} \in R^4$, the observation error dynamics in (34) has the desirable dynamic characteristics of a linear time-invariant system with F_L as an exogenous disturbance.

(ii) Solve (35) for $K_2(\hat{\mathbf{x}})$ with $\tilde{A}(\hat{\mathbf{x}}) = A^*$. In other words, take $K_2(\hat{\mathbf{x}})$ by

$$K_2(\hat{\mathbf{x}}) \triangleq (\check{A}(\hat{\mathbf{x}}) - A^*)B(\hat{\mathbf{x}})^{-1}K_1 \tag{41}$$

When (40) does not hold, the gain in (41) will become infinitely large. As a matter of fact, when

$$\det B(\hat{\mathbf{x}}) = 0\ , \tag{42}$$

there exists no K_2 satisfying (35) with $\tilde{A}(\hat{\mathbf{x}}) = A^*$. Fortunately this special case seldom happens. Moreover, even in this case, it is still possible to choose K_2 such that $\tilde{A}(\hat{\mathbf{x}})$ is critically stable at each $\hat{\mathbf{x}}$. This is because the rank of $B(\hat{\mathbf{x}})$ is 1 even when (42) holds.

Then, our task reduces finally to finding the Hurwitz matrix A^* that minimizes the effect of the load force F_L in (34). Recall that this is a well-known linear system problem [9]. It also may be another good method to augment the proposed state observer with a load force observer [8].

III. Simulation Results

To demonstrate the practicality of the observer in Section II proposed for sensorless control of a hybrid-type LPM, we present some simulation results. The model parameters of the hybrid-type LPM used in our simulation are given in Table.1 and Fig.1. Note that in this sample motor, $\tilde{L}_e = 0$.

The overall sensorless velocity controller consists of current controller, velocity controller, and force controller, where the information of rotor position is provided by the sliding-mode type observer in (11). The usual PI controller is used as the current controller for direct control of stator currents. On the other hand, the following feedback-linearizing controller is used as the force controller, which is a simple direct extension of the one in [10] to a more general dynamic model in (1).

$$i_k^* \triangleq f(u, \hat{x} - \frac{(k-1)}{4}p),\ k = 1, 2 \tag{43}$$

where

$$f(u,\hat{x}) \triangleq \begin{cases} 0 & \text{if } g(\hat{x}) = 0 \text{ or } u = 0 \\ u/g(\hat{x}) & \text{if } g(\hat{x}) \neq 0, D(u,\hat{x}) = 0, u \neq 0 \\ \frac{-|g(\hat{x})| + \sqrt{|g(\hat{x})|^2 + 2\mathrm{sgn}(g(\hat{x}))D(u,\hat{x})u}}{D(u,\hat{x})}, & \text{otherwise,} \end{cases} \tag{44}$$

$$D(u,\hat{x}) \triangleq \mathrm{sgn}(g(\hat{x}))\tilde{L}_e'(\hat{x}) + \mathrm{sgn}(u)\tilde{L}_o'(\hat{x}) \tag{45}$$

where i_k^* is the current command for i_k to track, $k = 1, 2$ and $\hat{x}$ is the estimate of x provided by the observer in (11). Here, the force command u is chosen as the well-known IP controller for successful set point tracking.

$$u \triangleq -K_P\hat{v} + K_I \int (v^* - \hat{v})\, dt, \tag{46}$$

where v^* is the velocity command. The block diagram of the overall closed-loop system constructed for simulation study is given in Fig.2.

In the first simulation, a step velocity command of 0.5m/s was applied to the motor at rest initially under no external load force. And the initial vlaues of rotor position and velocity estimates were chosen to be $0.1p$ and 0.1m/s, respectively. Recall that $0.5p$ in a linear motor corresponds to π electrical radian in a rotational motor. From the simulation result depicted in Fig.3, we can see that the observation error is reduced rapidly within 30ms. To confirm that this is generally true, we have repeated the simulation as above for different initial values of rotor position estimate. Fig.4 shows the time histories of the observation errors of rotor position and velocity for each of the four cases: $\hat{x}(0) = 0.1p,\ -0.1p,\ 0.4p,\ -0.4p$.

The second simulation was performed to test the robustness of the observer with respect to uncertainties in the mechanical parameters, mass M and viscous friction coefficient B. Also in the simulation, a step velocity command of 0.5m/s was applied to the motor and the robust performance of the proposed observer was evaluated individually for each mechanical parameter. From now on, we will denote, respectively, by M_o and B_o the values of M and B used in the observer. Fig.5 shows the simulation results for the cases of $M_o = 0.5M$ and $M_o = 2M$. From Fig.5 we can see that the uncertainty in mass only affects the transient responses of the observer but not its steady-state responses. On the other hand, Fig.6 shows the simulation results for the cases of $B_o = 0.5B$ and $B_o = 2B$. It can be seen from Fig.6 that the position observation is robust with respect to the uncertainty in the viscous friction coefficient. Nonetheless, the velocity estimate contains about 2% error at steady-state.

In the last simulation, a step external load force of 3N was applied to the motor which was running at a constant velocity of 0.5m/s. The simulation result is shown in Fig.7. As expected, the load force gives rise to some velocity observation error, but it is only about 3% of the running velocity. The result in Fig.7 also suggests that the effect of the load force on position observation should be negligible.

IV. Conclusion

We have presented a sliding-mode type observer for sensorless control of the hybrid-type LPM. Through extensive simulation study, we have shown that the proposed observer can provide the information of rotor position and velocity with quite good accuracy and, furthermore, is robust with respect to uncertainties in system model including mechanical parameters and external load force. Some sufficient conditions for convergence of the proposed observer were described but need to be further refined.

REFERENCES

[1] V. Utkin, "Variable Structure Systems with Sliding Mode," *IEEE Trans. Automat. Contr.*, vol.AC-22, no. 2, pp. 212-222, 1977.

[2] J. Slotine, J. Hedrick and E. Misawa, "On Sliding Observers for Nonlinear Systems," *Trans. ASME -J. of Dynamic Systems, Measurements and Control*, vol.109, pp. 245-252, 1987.

[3] J. Slotine and W. Li , *Applied Nonlinear Control,* Prentice-Hall, Inc., Englewood Cliffs, NJ, 1991.

[4] L. Jones and J. Lang, "A State Observer for the Permanent-Magnet Synchronous Motor," *IEEE Trans. I.E.*, vol. 36, no. 3, pp. 374-382, August 1989.

[5] T. Low, T. Lee and K. Chang, "A Nonlinear Speed Observer for Permanent-Magnet Synchronous Motors," *IEEE Trans. I.E.*, vol. 40, no. 3, June 1993.

[6] N. Ertugrul and P. Acarnley, "A New Algorithm for Sensorless Operation of Permanent Magnet Motors," *IEEE Trans. I.E.*, vol. 30, no. 1, January/February 1994.

[7] J. Solsona, M. Valla and C. Muravchik, "A Nonlinear Reduced Order Observers for Permanent Magnet Synchronous Motors," *IEEE Trans. I.E.*, vol. 43, no. 4, August 1996.

[8] N. Matsui, T. Makino and H. Satoh, "Autocompensation of Torque Ripple of Direct Drive Motor by Torque Observer," *IEEE Trans. I.A.*, vol. 29, no. 1, January/February 1993.

[9] C. Chen , *Linear System Theory and Design,* Holt, Rinehart and Winston, 1984.

[10] S.H.Chu and I.J.Ha, "Control of Hybrid Step Motors via a Simplified Linearization Technique," *International Journal of Control*, vol.61, no.5, pp. 1143-1167, 1995.

Table 1: Model parameters of the sample motor.

Parameter	Value
R_s	7 Ω
L_0	30 mH
M	0.63 kg
B	20 Ns/m
p	1.6 mm

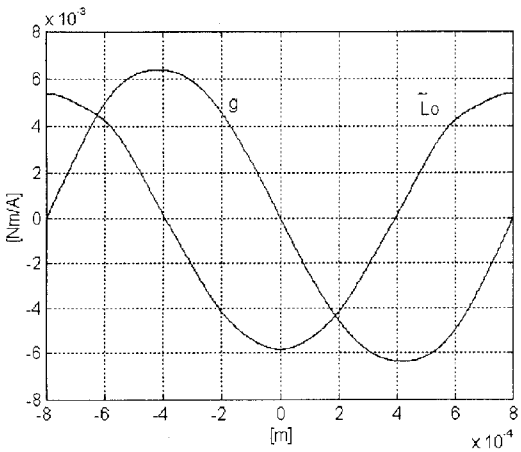


Fig.1 Wave forms of g and $\tilde{L}_o$.

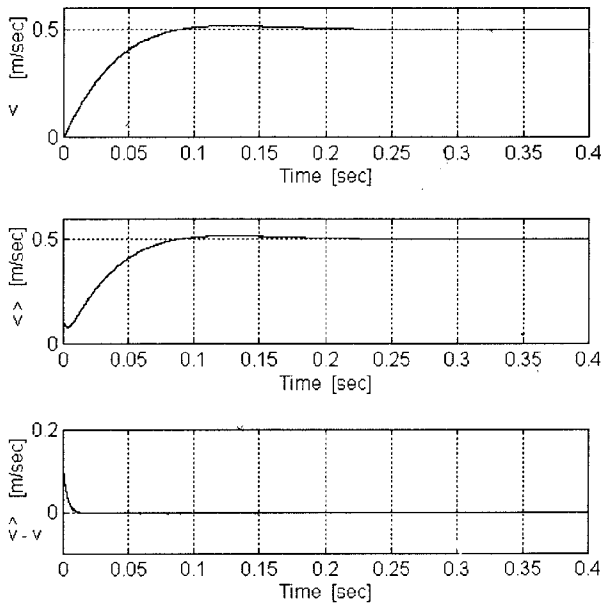


Fig.3 Time responses of the closed-loop system to a step velocity command of 0.5m/sec.

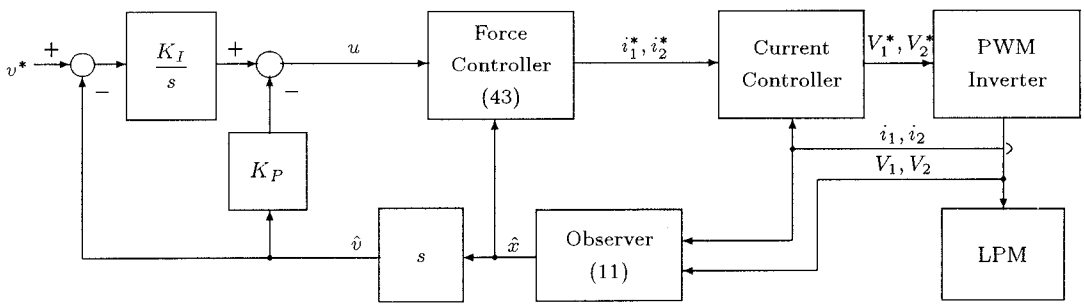
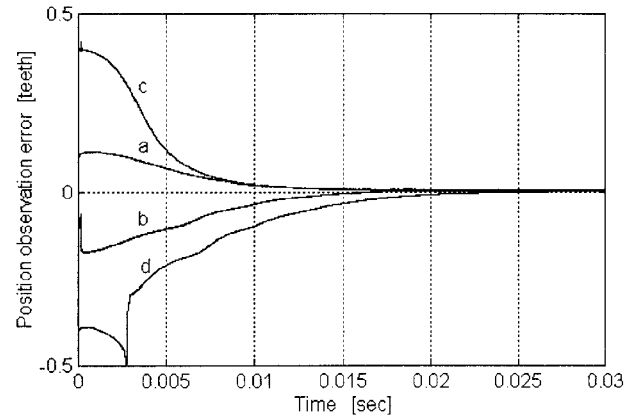


Fig.2 Configuration of the closed-loop system



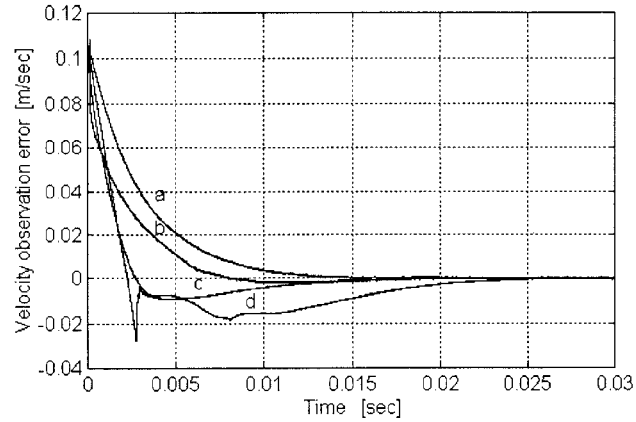
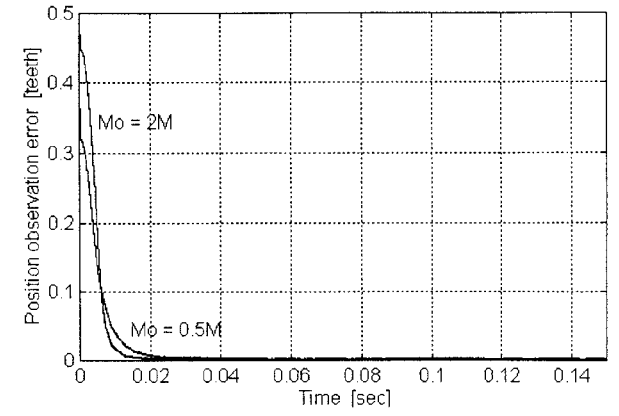


Fig.4 Time-histories of observation errors.
(a) $\hat{x}(0) = 0.1p$, (b) $\hat{x}(0) = -0.1p$
(c) $\hat{x}(0) = 0.4p$, (d) $\hat{x}(0) = -0.4p$



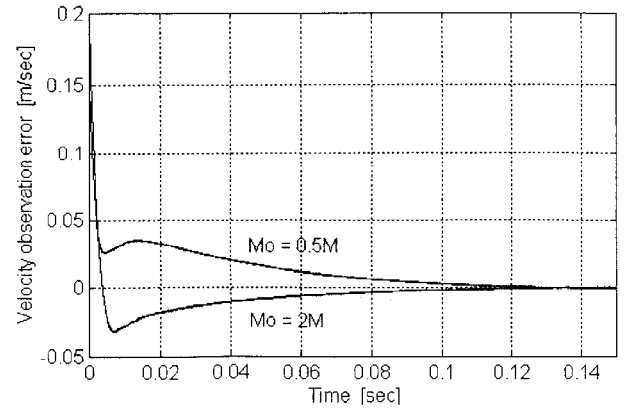
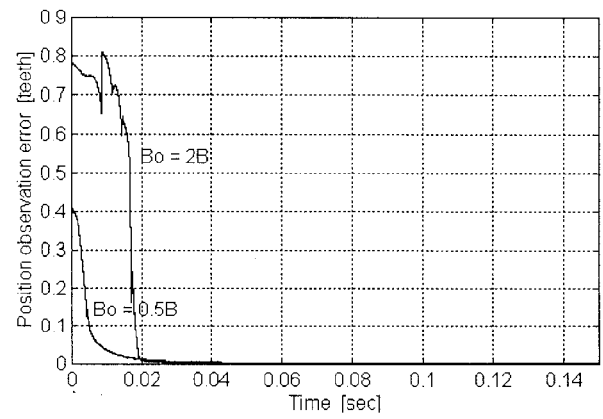


Fig.5 Effect of the uncertainty in M.



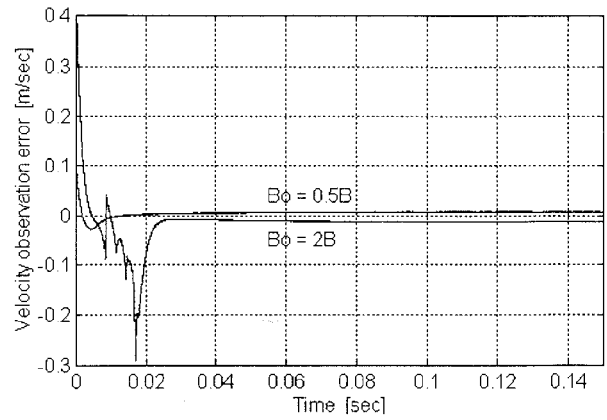
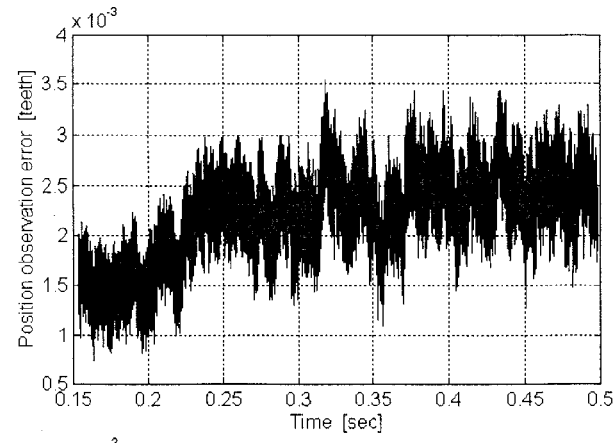


Fig.6 Effect of the uncertainty in B.



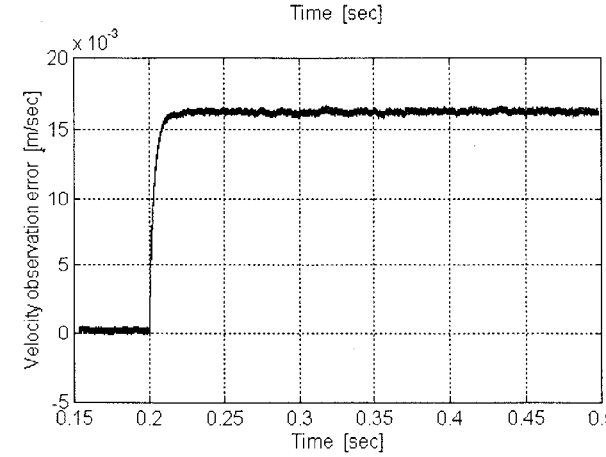


Fig.7 Effect of a load force F_L.

Robust Vibration Suppression Control using System Identification of Minor Control-Loop System

Seiji Hashimoto, Kenji Hara, Hirohito Funato and Kenzo Kamiyama

Department of Electrical and Electronic Engineering
Utsunomiya University
2753 Ishii-cho, Utsunomiya-shi
Tochigi-ken 321 JAPAN
Phone: +81-28-689-6089 Fax: +81-28-689-6009
E-mail: t3962054@cc.utsunomiya-u.ac.jp

Abstract— **In the vibration suppression control with a wide band width for resonant plants, it is a requisite to identify a plant with high accuracy. However, the more complicated the plant is, the more difficult its system identification becomes.**

In this paper, the authors propose to identify a modified plant with a minor control loop (MCL), feedbacked just with an output, instead of identifying an original plant itself. Regarding to the design of the MCL, the original plant is modified to have an optimal damping factor. To identify the modified plant, the Auto-Regressive eXogenous(ARX) model and least squares method are applied. Through this system identification, the authors can derive an exact uncertainty between the nominal and identified parameters. Therefore, a robust vibration suppression control system, which has a wide band width, can be systematically designed.

The effectiveness of the proposed design method for a 2-mass resonant system is demonstrated through simulations and experiments.

I. Introduction

In many industrial fields, a servo has been widely applied to drive a complicated load like a rolling mill, a large scale space structure and a high-rise building. Recently, the cut-off frequency of drive systems is getting higher and higher. On the other hand, the natural frequency of load systems is getting lower and lower because of their low stiff structures. Since the frequencies of these systems are getting closer, they form resonant systems. Therefore, the servo system generates a vibration between the electrical motor drive and the mechanical load. To overcome this problem, various control strategies have been proposed[1]-[5].

In the vibration suppression control for such a system, whose typical model is a 2-mass resonant plant as shown in Fig.1, it is a requisite to identify the plant model with high accuracy[6]. However, identifying the plant with high accuracy is difficult particularly when the plant is very complicated.

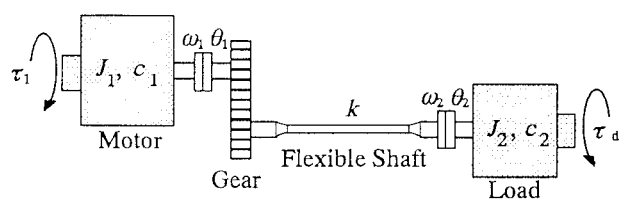


Fig. 1. A two-mass resonant plant.

In this paper, the authors propose a novel design method to identify the plant with high accuracy using system identification of a modified plant with a minor control loop (MCL), feedbacked just with an output, instead of identifying an original plant itself. In this design of the MCL system, first, the original plat is modified to have an optimal damping factor which can make the system identification easy to result in suppressing the vibration. Second, the well-known Auto-Regressive eXogenous(ARX) model is utilized in the system identification, and the parameters of the ARX model are obtained by the least square method. Then, the authors can derive an accurately identified plant which results in an exact uncertainty calculated by the nominal and identified parameters. Finally, a robust vibration suppression control system, which has a wide band width, can be systematically designed by the design method. In this paper, the authors apply the proposed design method to two different types of control system, a position control system and a speed control system, in order to evaluate its applicability for servo systems.

Through simulations and experiments, the proposed method exhibits excellent performance for vibration suppression control of a 2-mass resonant plant which leads to a vibration suppression technology applicable to a more complicated flexible structure[7].

II. Design of position control system using system identification of minor control loop

A. Design of Minor Control-Loop System

An original 2-mass resonant plant with a minor control loop (MCL) is shown in Fig.2. The resonance characteristic of the original plant is modified by the MCL. In its design, the plant is feedbacked just with an output θ_1, i.e., the MCL system, because of its simplicity of structure as well as stabilization. According to the design of the minor feedback gain f_y of the MCL,

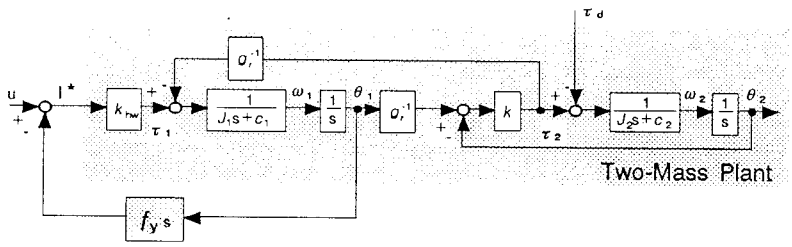


Fig. 2. The two-mass plant modified by the minor control loop.

TABLE I
NOMINAL PARAMETERS OF THE TWO-MASS PLANT.

g_r	gear ratio	4	
k_{hw}	hardware gain	5.244	[Nm/rad]
k	shaft stiffness	13.78	[Nm/rad]
J_1	motor inertia	4.764×10^{-4}	[kg-m^2]
J_2	load inertia	8.60×10^{-3}	[kg-m^2]
c_1	coefficient of motor viscosity	1.3×10^{-3}	[Nm/rad/s]
c_2	coefficient of load viscosity	6.89×10^{-2}	[Nm/rad/s]

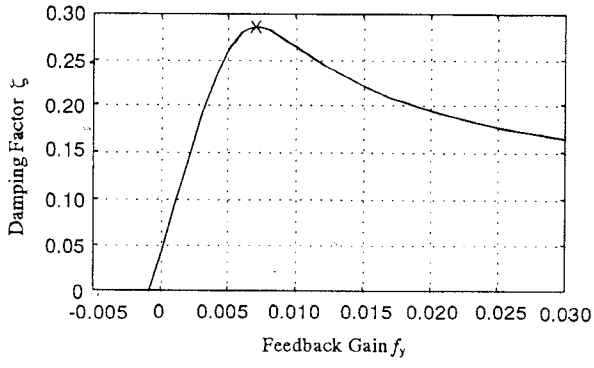


Fig. 3. $f_y - \zeta$ plane.

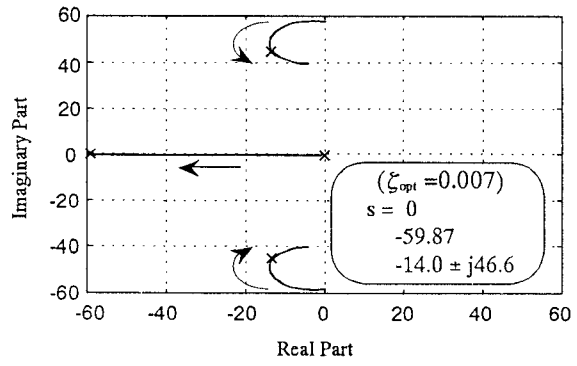


Fig. 4. Root locus of the minor control-loop system (θ_2/u).

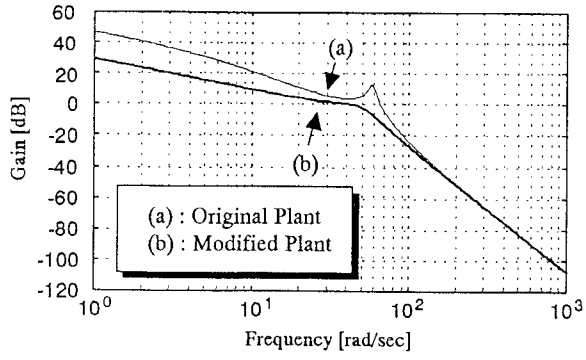


Fig. 5. Gain plots of the original and the modified plants(θ_2/u).

a damping factor ζ of the characteristic equation of the modified plant is maximized under the condition of stability. The characteristic equation G_{ce} of the MCL system is given by:

$$G_{ce} = s^4 + (\frac{f_y k_{hw}}{J_1} + \frac{c_2}{J_2} + \frac{c_1}{J_1})s^3 + (\frac{c_1 c_2}{J_1 J_2} + \frac{k}{g_r^2 J_1} + \frac{k}{J_2} + \frac{c_2 f_y k_g}{J_1 J_2})s^2 + (\frac{c_1 k}{J_1 J_2} + \frac{c_2 k}{g_r^2 J_1 J_2} + \frac{f_y k k_g}{J_1 J_2})s \quad (1)$$

The condition of stability is derived by the Hurwitz stability criterion. In this case, the feedback gain $f_y > -0.000888$ can stabilize the MCL system consisting of nominal parameters as shown in Table I.

Fig.3 and Fig.4 show $f_y - \zeta$ plane and the root locus of the modified plant in the variation of the feedback gain f_y, respectively. It is noticed that the minor feedback gain f_y has an optimal value which can maximize the damping factor ζ of the MCL. From Fig.3, the optimal value of the feedback gain f_{yopt} is 0.007 and the optimal damping factor ζ_{opt} is 0.287. For reference, the damping factor of the original plant without the MCL is 0.0446.

Fig.5 shows the gain plots of the modified plant at the time of ζ_{opt} and that of the original plant without the MCL. Both of them are calculated using the nominal parameters. From the Fig.5, it is verified that the resonance characteristic can be modified by the MCL. Therefore, it can be more easy and accurate to identify the modified plant rather than to identify the original plant itself.

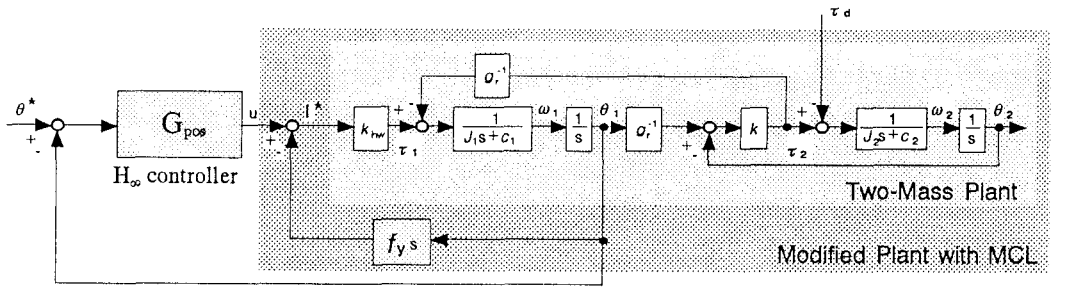


Fig. 8. The $\mathcal{H}_\infty$ control system with the MCL.

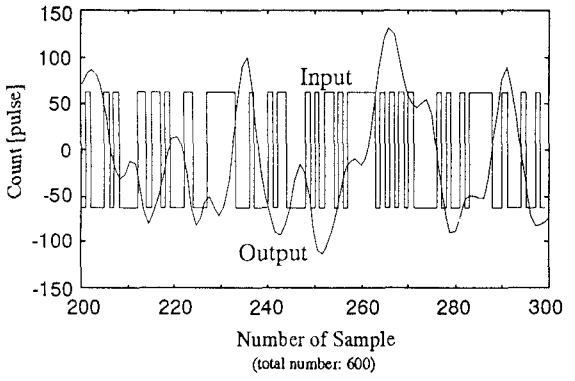


Fig. 6. Time response of input u and output θ_2.

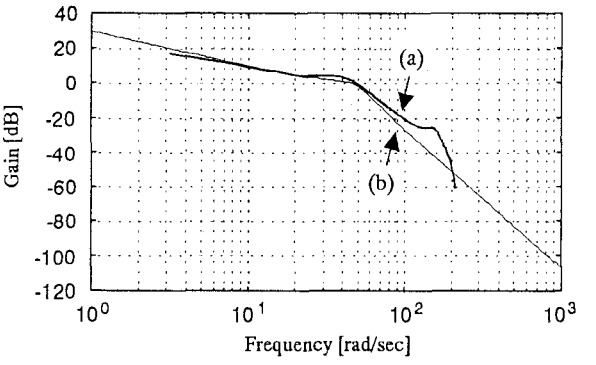


Fig. 7. Gain plots of the modified plant.

B. System Identification

The authors apply the system identification to the modified plant with the minor control loop (MCL) which has the optimal damping factor ζ_{opt}. A portion of input and output data, i.e., u and $y = \theta_2$, is shown in Fig.6. The authors consider the identification model of the modified plant as the Auto-Regressive eXogenous(ARX) model defined as the following:

$$A(q)y(k) = B(q)u(k) + w(k) \tag{2}$$

where q^{-1} is a shift operator and w is a white noise, and derive the polynomials $A(q)$ and $B(q)$ using the batch least squares method. As a result, the polynomials whose order is the sixth are given as:

$$\begin{aligned} A(q) &= 1 - 1.980q^{-1} + 1.2175q^{-2} - 0.2774q^{-3} \\ &\quad +0.4478q^{-4} - 0.6064q^{-5} + 0.2155q^{-6} \quad (3) \\ B(q) &= 0.0209q^{-2} + 0.1357q^{-3} + 0.08828q^{-4} \\ &\quad -0.0531q^{-5} + 0.0236q^{-6} - 0.0147q^{-7} \quad (4) \end{aligned}$$

The gain plot of the identified model is shown with the mark (a) in Fig.7. This model is also compared with the modified plant which is composed of the nominal parameters with the mark (b). The identified model can be considered as the real plant because of its high accuracy by this approach. Therefore, the error between (a) and (b) is considered as an uncertainty of nominal parameters and unmodeled dynamics of the real 2-mass plant.

C. Design of Major Control-Loop System

C.1 Design of the $\mathcal{H}_\infty$ Controller

In case of applying the robust control to a model with an uncertainty which has high accuracy, the conservativeness for the band width of the control system can be improved[8],[9]. Therefore, the authors utilize the $\mathcal{H}_\infty$ control to design a major control loop under an accurately modified plant. The $\mathcal{H}_\infty$ control system including the minor control loop (MCL) is shown in Fig.8.

The authors define the identified ARX model as the real plant P and the modified plant with MCL composed by the nominal parameters as nominal plantP_n. Then, the multiplicative uncertainty Δ_m is derived from the following:

$$\Delta_m(s) = \frac{P(s) - P_n(s)}{P_n(s)} \tag{5}$$

Fig.9 shows the gain plot of this multiplicative uncertainty Δ_m. If there is no restriction of hardware, the band width can be widen up to 50[rad/sec] because of its zero-cross frequency.

The $\mathcal{H}_\infty$ controller is systematically designed for the nominal plant model P_n under the condition of the following.

(1) The control system should be stable even though unmodeled dynamics, i.e., Δ_m, exist in the MCL.
(2) The cut-off frequency of the position control system should be 20 [rad/sec] at least.
(3) The order of the $\mathcal{H}_\infty$ controller is to be as low as possible.

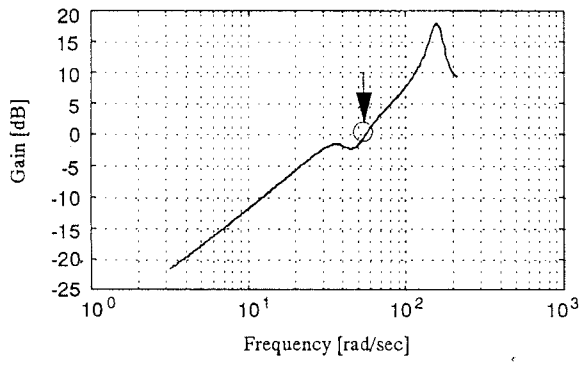


Fig. 9. Gain plot of the multiplicative uncertainty Δ_m.

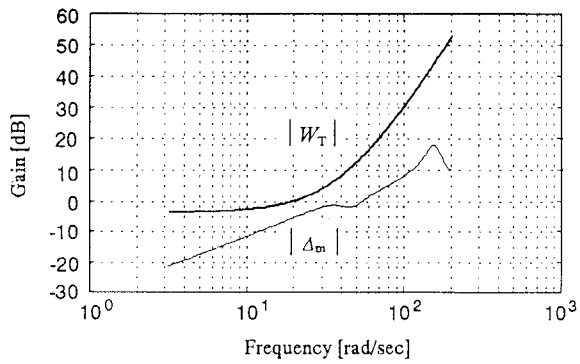


Fig. 10. Gain plots of W_T and Δ_m.

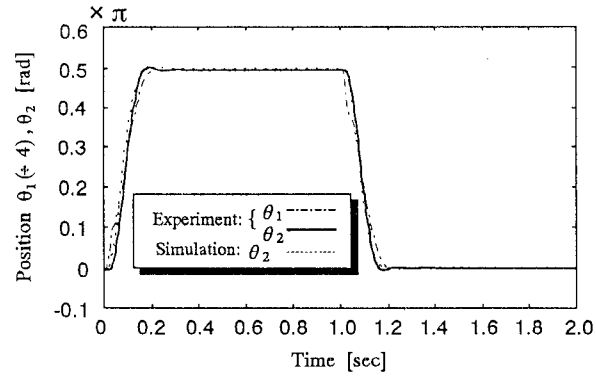


Fig. 11. Simulation and experimental results of the proposed control system.

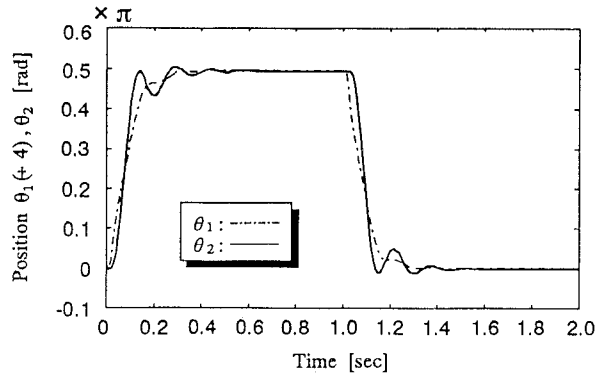


Fig. 12. Experimental result of the *PI* control system.

From the second condition, the zero-cross frequency of a weighting function W_T, which is for the complementary sensitivity function T, is made larger than 20 [rad/sec] from the following equation:

$$|T(j\omega)| < |W_T(j\omega)|^{-1} \quad , \qquad \forall\omega \tag{6}$$

From the first condition, however, the weighting function W_T should satisfy the following:

$$|\Delta_m| < |W_T(j\omega)| \quad , \qquad \forall\omega \tag{7}$$

Therefore, the weighting function W_T is selected as the following equation:

$$W_T = \frac{(1/40s+1)^4}{1.5} \tag{8}$$

Fig.10 shows the gain plots of the weighting function W_T and the multiplicative uncertainty Δ_m. It is verified that the zero-cross frequency of the weighting function W_T is larger than 20 [rad/sec] and the gain of the weighting function W_T is larger than that of Δ_m at any frequency range.

According to a weighting function W_S, which is for the sensitivity function S, it is recommended to be the first order like an integrator as the following, since its dynamics is directly reflected in the $\mathcal{H}_\infty$ controller.

$$W_S = \frac{9.06}{s} \tag{9}$$

As a result of these weighting functions, the $\mathcal{H}_\infty$ controller G_{pos} is designed as the following:

$$G_{pos} = \frac{1771s(s+13.96\pm j46.58)(s+59.87)}{s(s+40\pm j45.32)(s+85.53)(s+2023)} \tag{10}$$

C.2 Simulation and Experimental Results

Fig.11 shows simulation and experimental results of proposed control system to a step position reference. In this figure, the dashed line shows simulation result of load position θ_2. The dash-dot line and the thick solid line show experimental results of motor position θ_1 and load position θ_2, respectively. Since the experimental result agrees with the simulation, it is verified that the identified model P and the multiplicative uncertainty Δ_m has been identified with high accuracy. Fig.12 also shows experimental result at the time when a conventional *PI* controller plus velocity feedback are used for the comparison. The $\mathcal{H}_\infty$ controller derived by using the proposed design method can also suppress the load position vibration as shown in Fig.11.

III. Design of Speed Control System Using System Identification of Minor Control Loop

A. Design of Minor Control-Loop System

In this chapter, the proposed design method is applied in designing of a speed control system as well as designing of the previously mentioned position control

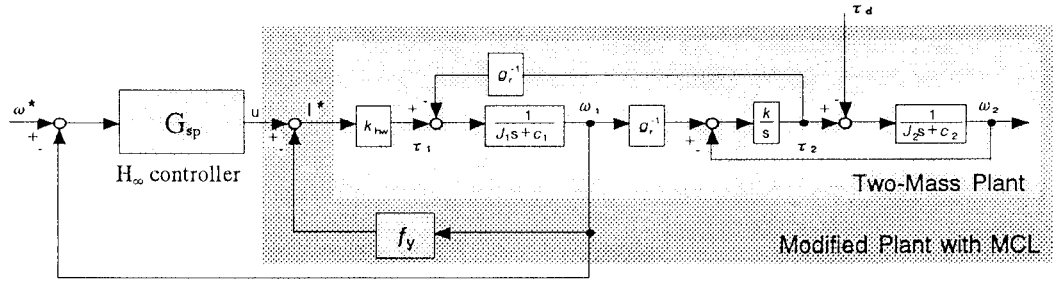


Fig. 13. The speed control system with the MCL.

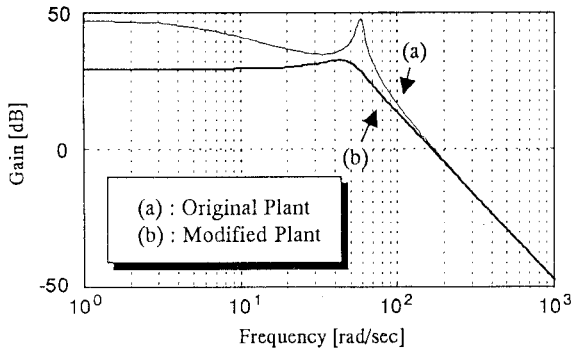


Fig. 14. Gain plots of the original and the modified plants(ω_2/u).

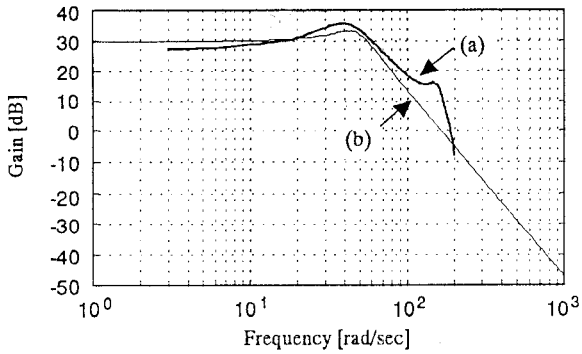


Fig. 15. Gain plots of the modified plant.

system. Its design strategy is quite the same to that of the position control system. Fig.13 shows a speed control system which includes the $\mathcal{H}_\infty$ controller and the minor control loop (MCL). The parameters of 2-mass resonant plant is also shown in Table I. The MCL system is constructed with a motor speed(ω_1) feedback as shown in Fig.13. The characteristic equation, $f_y - \zeta$ plane and root-locus of the MCL system are the same except that one zero pole in the s-plane is disappeared. Therefore, the optimal minor feedback gain and the optimal damping factor are $f_{yopt} = 0.007$ and $\zeta_{opt} = 0.287$, respectively. Fig.14 shows the gain plots of the original and the modified plants with the nominal parameters for speed control system.

B. System Identification

The modified plant with the minor control loop (MCL) for speed control system (ω_2/u) is also identified by the batch least squares method using the *ARX* model whose order is the sixth. The mark (a) in Fig.15 shows gain plot of identified model. The mark (b) shows that of the modified plant, which is composed of the nominal parameters. From Figs.7 and 15, it is noticed that the real 2-mass plant has the second vibration mode at high frequency range.

C. Design of Minor Control-Loop System

C.1 Design of the $\mathcal{H}_\infty$ Controller

Using the proposed approach, however, the system can be stabilized by the $\mathcal{H}_\infty$ controller even though unmodeled dynamics shown in Figs.7 and 15 exist in the original plant.

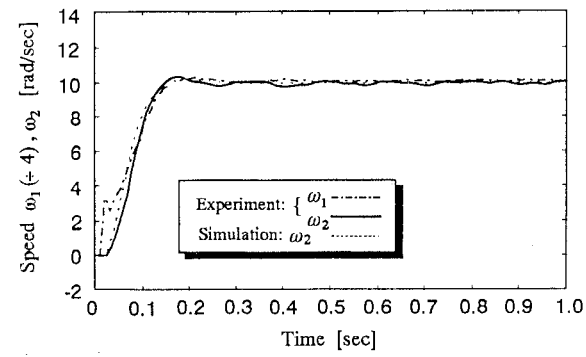


Fig. 16. Simulation and experimental results of the proposed control system.

The $\mathcal{H}_\infty$ controller G_{sp} can be designed by the similar way mentioned in section C.1. In this case, the weighting functions are selected as the following:

$$W_T = \frac{(1/40s+1)^3}{1.5} \tag{11}$$

$$W_S = \frac{12.44}{s} \tag{12}$$

Then, the $\mathcal{H}_\infty$ controller is designed by

$$G_{sp} = \frac{1090(s+13.96 \pm j46.58)(s+59.87)}{s(s+64.14 \pm j40.48)(s+49770)} \tag{13}$$

C.2 Simulation and Experimental Results

Fig.16 shows simulation and experimental results of proposed control system to a step speed reference. In

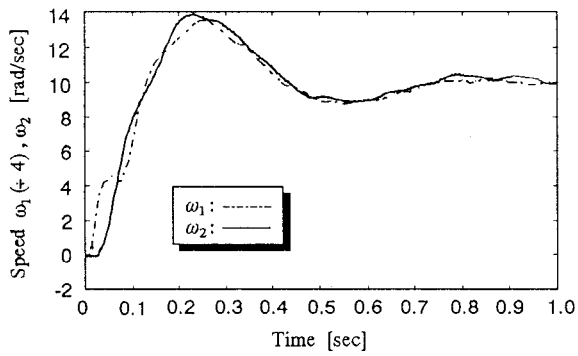


Fig. 17. Experimental result of the *PI* control system.

this figure, the dashed line shows a simulation result of load speed ω_2. The thick solid line and the dash-dot line show experimental results of load speed ω_2 and motor speed ω_1, respectively. Fig.17 also shows experimental result at the time when a conventional *PI* controller plus velocity feedback is used for the comparison.

IV. Conclusion

The authors demonstrated the robust vibration suppression control using the system identification for the modified plant by introducing a minor control loop. Both the position control and the speed control systems exhibit excellent performance. The advantages of the proposed design method are as the following:

- The original plant can be easily modified and stabilized by introducing the output-based minor control loop.
- The minor control-loop system can be identified with high accuracy.
- The conservativeness of the design specifications for the band width of the major control system can be improved.
- Ideal vibration suppression can be performed by the $\mathcal{H}_\infty$ control design and the system identification methods.

This project is supported by the Grant-in-Aid for Japan Society for the Promotion of Science Fellows.

References

[1] Y. Hori, " Comparison of Torsional Vibration Controls based on the Fast and Slow Disturbance Observers ", Proceedings of 1995 International Power Electronics Conference(*IPEC*), pp. 440-446, 1995.

[2] S. Ouchi, T. Mita and K. Yano, " Active Vibration Control of a Motor System by Using $\mathcal{H}_\infty$ control Theory ", *Trans. on Industry Applications of IEE Japan*, Vol. 113-D, No. 3, pp. 325-332, 1993.

[3] J. K. Ji, S. K. Sui and M. H. Park, " LQG Based Speed Controller for Torsional Vibration Suppression in 2-Mass System ", *IECON'93*, pp. 1157-1162, 1993.

[4] Y. Hori, H. Sawada and Y. Chun, " On Optimal Estimation Speed of Disturbance Observer used in the Slow Resonance Ratio Control ", *Trans. on Industry Application of IEE Japan*, Vol. 117-D, No. 1, pp. 50-56. 1997.

[5] S. Hashimoto, H. Funato, K. Kamiyama, " Torsional Vibration Suppression Control in a Three-Mass Motor Drive by First-Order $\mathcal{H}_\infty$ Speed Controllers ", Proceedings of the 7th International Power Electronics & Motion Control Conference(*PEMC*), Vol. 1, pp. 115-119, 1996.

[6] T. Kimura, S. Hara and T. Tomisaka, " $\mathcal{H}_\infty$ Control with Minor Feedback for a Pneumatic Actuator System ", 35th IEEE Conference on Decision and Control(*CDC*), TM11-4, 1996.

[7] W. Gawronski, " Balanced Control of Flexible Structures ", Springer, 1996.

[8] J. C. Doyle, B. A. Francis and A. R. Tannenbaum, " Feedback Control Theory ", Macmillan Publishing Company, 1992.

[9] L. Ljung and T. Glab, " Modeling of Dynamic Systems ", PTR Prentice Hall, Englewood Cliffs, NJ, 1994.

[10] M. Iwasaki and N. Matsui, " Mechanical Parameter Measurement of 2-Mass Resonant System ", Proceedings of 1995 International Power Electronics Conference(*IPEC*), pp. 453-457, 1995.

[11] K. Ohnishi, N. Matsui, and Y. Hori, " Estimation, Identification, and Sensorless Control in Motion Control System ", Proceedings of the IEEE, VOL. 82, No. 8, pp. 1253-1265, 1994.

P - I and I - P Controllers In A Closed Loop For DC Motor Drives

F. I. Ahmed
Professor of Power Electronics
Faculty of Engineering, and Vice-President of
Cairo University, Cairo, EGYPT

A. M. El-Tobshy
Professor of Power Electronics, Faculty of
Engineering, Cairo University
Cairo, EGYPT

A. A. Mahfouz
Assistant Professor of Power Electronics
Faculty of Engineering
Cairo University
Cairo, EGYPT
Fax: +202-5723486, Phone: +202-5613156
E-mail: elkousy @ cairo. eun.eg

M. M. S. Ibrahim
Ph.D. Candidate of Power Electronics
Faculty of Engineering
Cairo University
Cairo, EGYPT
Fax: +202-3608453, Phone: +202-3483986

Abstract—**The traditional Proportional-Integral (P - I) controller, which has been widely used for the speed control of dc motor drives, has been compared with the relatively new Integral-Proportional (I - P) controller which first discussed in the year of 1978. This paper presents some improvements in this important field of industries. Theoretical studies for (P - I) and (I - P) controllers in the S-domain are presented, and the transfer functions for both are derived. Simulation results due to step response in S-domain and Z-domain are presented for both controllers. Experimental studies are discussed in detail. The performance of the two controllers due to step input reference and their behavior to sudden change in reference speed and sudden change in load are discussed. The simulation and the experimental results indicate the superiority of (I - P) controller over (P - I) controller.**

I. Introduction

A variety of engineering applications, such as: material conveyors, paper mills, transportation systems etc., require very accurate speed tracking, fast response and high precision. For many years, dc motor drives have been widely used in such applications, and in spite of the fact that ac motors are rugged, cheaper and lighter, dc motor controlled by a thyristor converter is still a very popular choice in particular applications. In spite of the fuzzy logic is getting emphasis in process control applications [1], [2], the conventional controllers [3] - [5] are an option in applications where low cost is the primary concern. The proportional-integral (P - I) is one of the conventional controllers and it has been widely used for the speed control of dc motor drives. The major features of the (P - I) controller are its ability to maintain a zero steady-state error to a step change in reference and its simple and straight-forward microprocessor implementation. On the other hand (P - I) controller has some disadvantages: the undesirable speed overshoot, the sluggish response due to sudden change in load torque and the sensitivity to controller gains K_i and K_p.

Takahashi, Harashima and Kondo [6] suggested a new method of control called integral-proportional (I - P) as a trial to solve the main problems of (P - I) controllers. This paper discusses the two controllers theoretically and experimentally as applied in speed control of dc motor of 0.5 kW, and it finds some improvements in this field. Experimental work has been carried out to verify the theoretical results.

II. Mathematical Models

The (P - I) controller has a proportional as well as an integral term in the forward path, the block diagram with a (P - I) controller for a dc motor drive is shown in Fig. 1. The integral controller has the property of making the steady-state error zero for a step change, although a (P - I) controller makes the steady-state error zero, it may take a considerable amount of time to accomplish this. Fig. 2 shows (I - P) controller along with a dc motor drive, where the proportional term is moved to the feedback path and it acts like a feedback compensation. The analysis in S-domain is discussed in this section to study the transient and the steady-state behavior for both controllers.

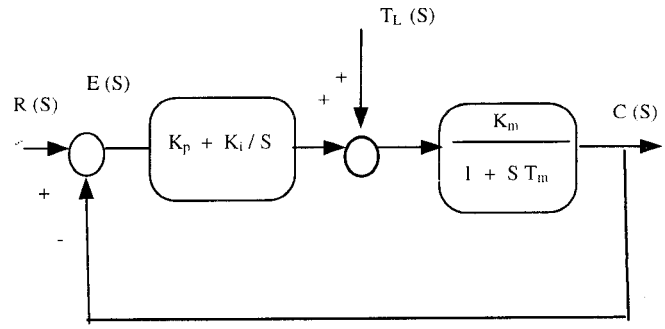


Fig. 1. Block diagram with P - I controller.

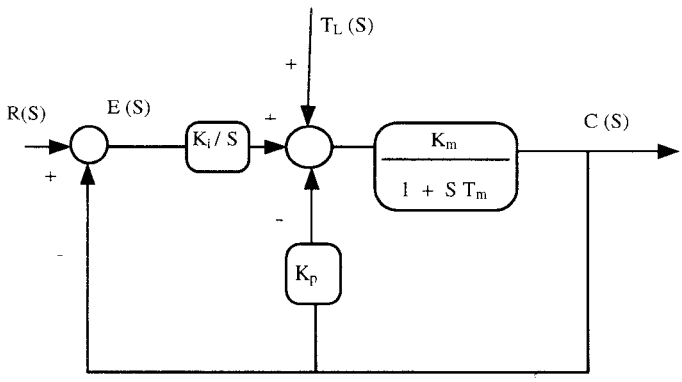


Fig. 2. Block diagram with I - P controller.

A. P - I Controller

The closed loop transfer function between the output C(S) and the input R(S) is given in (1).

$$\frac{C(S)}{R(S)} = \frac{K_m(S K_p + K_i)}{T_m S^2 + (1 + K_m K_p) S + K_m K_i} \quad (1)$$

Where K_i and K_p are the integral and the proportional gains of (P - I) or (I - P) controller, T_m is the mechanical time constant of motor, and K_m is the motor gain constant.

The transfer function between the output C(S) and the load torque disturbance $T_L(S)$ is given in (2).

$$\frac{C(S)}{T_L(S)} = \frac{S(1 + S T_m)}{T_m K_p S^2 + (K_m + T_m K_i + K_p) S + K_i} \quad (2)$$

B. I - P Controller

The closed loop transfer function between the output C (S) and the input R (S) is given in (3).

$$\frac{C(S)}{R(S)} = \frac{K_i K_m}{T_m S^2 + (1 + K_m K_p) S + K_m K_i} \quad (3)$$

The transfer function between the output C(S) and the torque disturbance T_L (S) is given in (4).

$$\frac{C(S)}{T_L(S)} = \frac{S(1 + S T_m)}{T_m K_p S^2 + (K_m + T_m K_i + K_p) S + K_i} \quad (4)$$

From (1) and (3), (P - I) and (I - P) controllers have the same characteristic equations, and it can be seen that the zero introduced by the (P - I) controller is absent in the case of the (I - P) controller. Therefore the overshoot in the speed, for a step change in the input reference R (S), is expected to be smaller for the (I - P) control. Equations (2) and (4) are exactly the same, therefore, the response to a load disturbance is expected to be very similar for both (P - I) and (I - P) controllers.

III. Simulation Results

Simulation studies are made due to step input reference in the S-domain and Z-domain. Appendix I shows the parameters of the motor used for the simulation studies. Fig. 3 shows (P - I) and (I - P) controllers due to step input reference at $\zeta < 1$: the overshoot for (P - I) controller is equal to 34.8%, while for (I - P) controller is 27.2%. The settling time for (P - I) is 0.375 s, while for (I - P) is 0.455 s. It is clear that (I - P) has longer delay time. Table I summerizes the results for the two controllers in digital form.

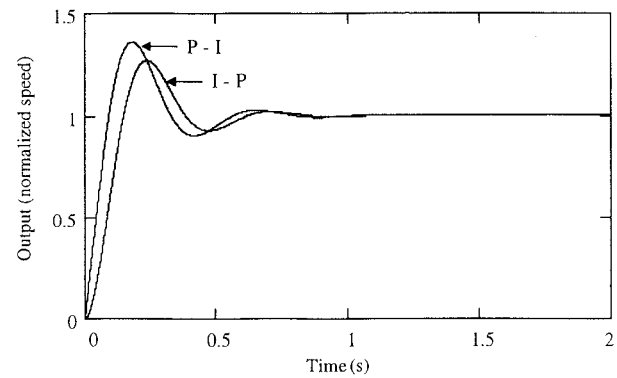


Fig. 3. P - I and I - P controllers step response.
$\zeta < 1$, $K_P = 1.5$, $K_I = 30$.

TABLE I
PERCENTAGE OVERSHOOT AND SETTLING TIME USING DIFFERENT GAIN FACTORS

Gain		% Overshoot		Settling time (s)	
K_i	K_p	P - I	I - P	P - I	I - P
1	2.36	20.45	4.55	0.36	0.5
0.5	3	3.4	0	0.36	0.61
0.3	3.5	0	0	0.18	1.07
5	3	40.3	26.3	0.13	0.13
1.5	3	48	5.77	0.25	0.25
K_i[a]	2.04	0	0	0.035	0.03

[a] K_i = 0.714 for (P - I) and 2.5 for (I - P), these are optimal values, which depend on the closed loop transfer functions [8].

IV. Experimental Work

A. System Description

For the experimental work a closed-loop system is built which consists of : 0.5 kW dc motor-generator separately excited, the parameters of the motor are in Appendix I, tacho-generator 0.06 V/r/min as a feedback voltage, a powerful data acquisition instrument 12 bit resolution, and a personal computer AT 80286. A fully-controlled thyristors bridge is also built where the firing angle is controlled using Relative Firing Angle Method, with this method the firing angle is controlled by lenghtening or shortening the interval between two successive thyristors triggerings [7]. Fig. 4 shows the schematic diagram of experimental set up.

B. Program and Flowchart

The main program is written in C language and is linked with the assembly program which controls the firing angle α. The program can be described using the following steps:

1. P - I or I - P controller is selected using a menu, then the coefficients K_p and K_i are entered via the keyboard.
2. The program starts to read using the analog to digital card, the reference and the error values.
3. Depending on the controller type, the output voltage from controller is calculated.
4. Cos α is calculated using an interpolating, polynomial, and from the look-up table the angle α is known and using a programmable peripheral interface, the assembly program reads the value.

Fig. 5 shows the main flowchart of the program.

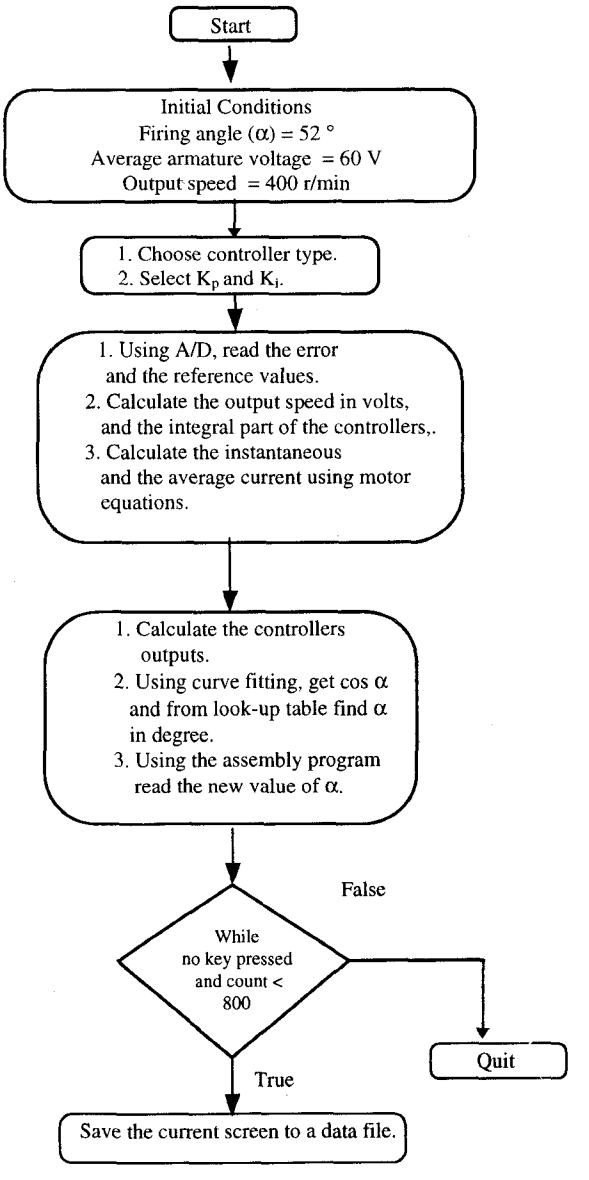


Fig. 5. Main flowchart.

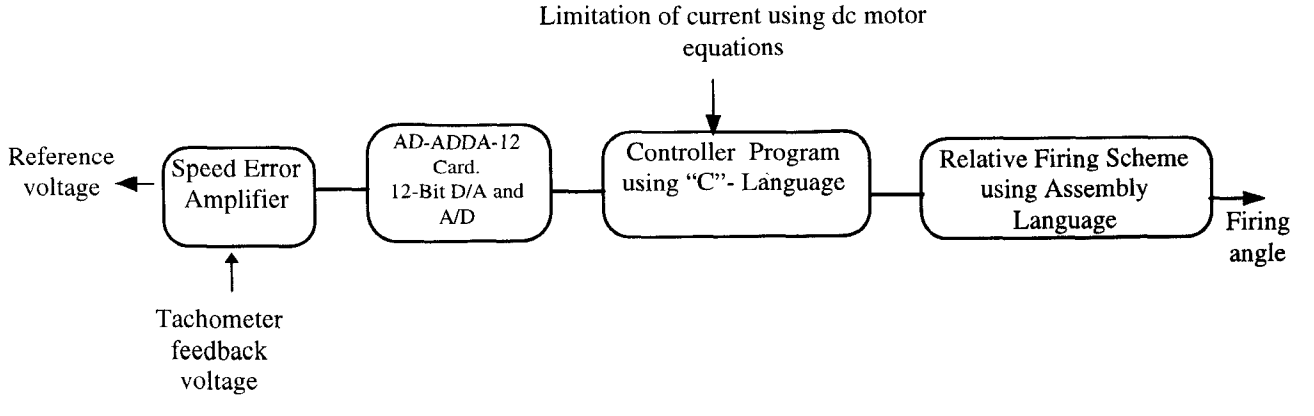


Fig. 4. Schematic diagram of experimental set up.

C. Experimental Results

Theoretical studies as a primarily step are made to choose the suitable coefficients K_p and K_i [8]. The sampling rate T affects the time response because it depends upon the execution time of program and the speed of computer used. Using the same conditions for both controllers: e.g., gain coefficients, reference voltage and required output speed, the performance of both controllers are studied. Fig. 6 and Fig. 7 show the speed time response for (P - I) and (I - P) controllers due to step response, Fig. 8 and Fig. 9 show the instantaneous current time response of both controllers (P - I) and (I - P). Table II summerizes the differences between the two controllers at required speed equal 600.79 r/min, where (I - P) controller has smaller overshoot and a very fast response and thus the starting current is limited. The performance of sudden change in reference speed and sudden change in load are tested experimentally for both controllers. Fig. 10 and Fig. 11 show the instantaneous current time response due to sudden change in reference speed, (P - I) controller has a fast response and a large overshoot in current occurs. Fig. 12 and Fig. 13 show the speed response due to sudden change in load, for (P - I) controller, the time to reach the steady state condition is 8.9 s and the settling time T_s is 7.4 s [9], while for (I - P) controller the time to reach the steady-state condition is 5.36 s and the settling time T_s is 4.63 s.

TABLE II
COMPARISON BETWEEN P - I AND I - P CONTROLLERS DUE TO STEP RESPONSE

Performance characteristics	P - I	I - P
Starting current at rated voltage 130V	1.2 A	0.8 A
Steady-state speed	488.33 r/min	558.33 r/min
Percent maximum overshoot	34.13	21.79
Settling time	11.23 s	0.729 s
Time to reach the steady-state value	12.89 s	5.135 s

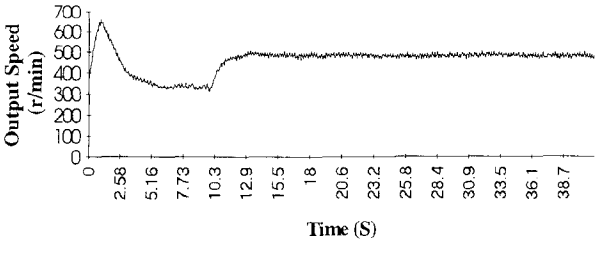


Fig. 6. P - I Speed response.
$K_p = 3$, $K_i = 5$

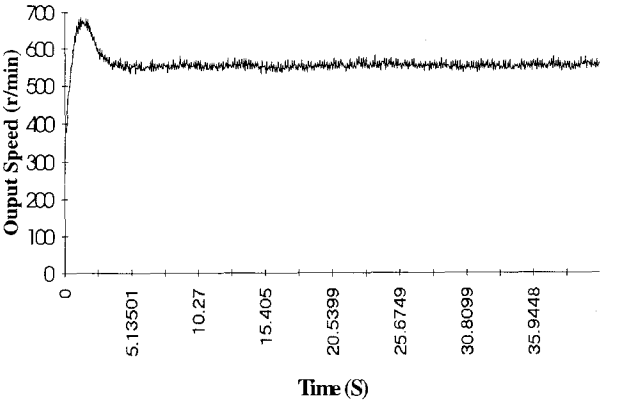


Fig. 7. I - P Speed response.
$K_p = 3$, $K_i = 5$

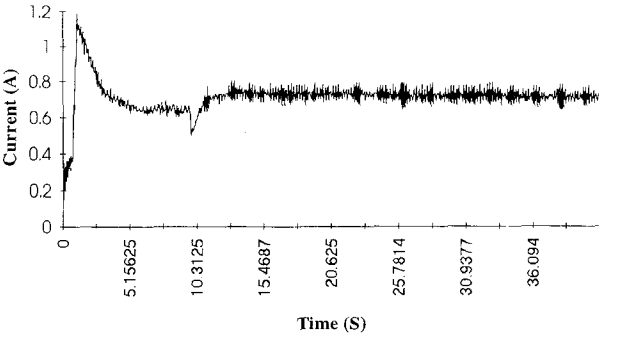


Fig. 8. P - I Instanteneous current response.
$K_p = 3$, $K_i = 5$

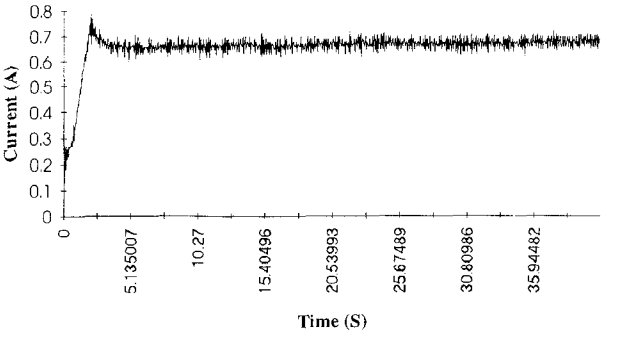


Fig. 9. I - P Instanteneous current response.
$K_p = 3$, $K_i = 5$

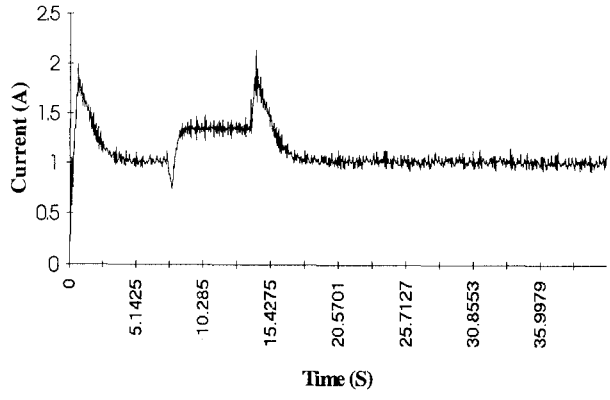


Fig. 10. P - I Instanteneous current response due to sudden change in reference speed.
$K_p = 3$, $K_i = 1.5$

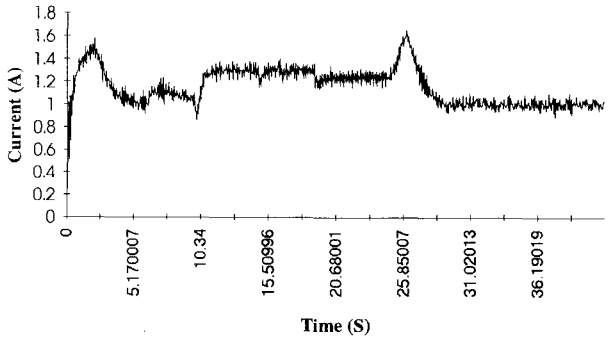


Fig. 11. I - P Instanteneous current response due to sudden change in reference speed.
$K_p = 3$, $K_i = 1.5$

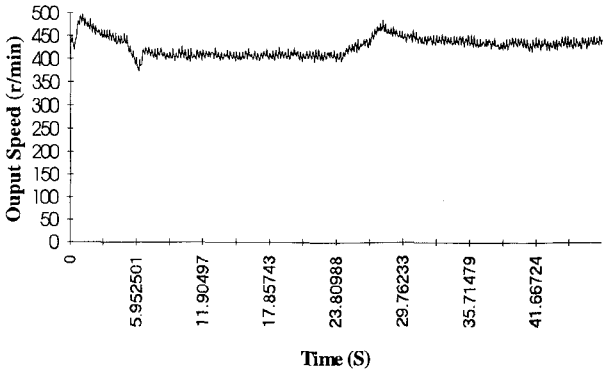


Fig. 12. P - I Speed response due to sudden change in load.
$K_p = 3.5$, $K_i = 0.3$

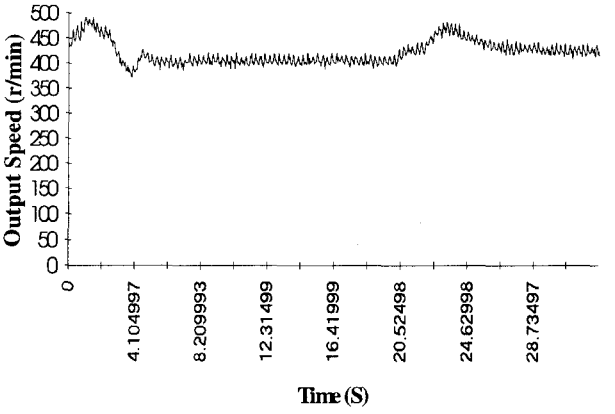


Fig. 13. I - P Speed response due to sudden change in load.
$K_p = 3.5$, $K_i = 0.3$

V. Conclusions

The project is intended to demonstrate the successful application of (I - P) controller to a phase-controlled converter dc separately excited motor-generator system. (I - P) controller's performance was compared with that of conventional (P - I) system. (I - P) controllers show some important advantages: the overshoot in speed is limited, thus the starting current overshoot is reduced. Also, using the suitable coefficient gains, (I - P) controllers offer a good load recovery characteristics. Analysis in S-domain and Z-domain shows the advantages of (I - P) controller. Thus (I - P) can be implemented using analog components. Analog ciruits are still required where: the low cost is required, the experience for high technology is not necessary, or where the replacement for modern control is difficult. Moreover, the simulation and experimental studies clearly indicate the superior performance of (I - P) controller, because it is inherently adaptive in nature. From the above derivation (I - P) controllers can replace (P - I) for the speed control of dc motor drives.

VI. Future Recommendations

The wide advances of computers and software languages will make the controllers' algorithm much easier to implement, the sampling time and the execution time can be reduced. Using (I - P) controller as a current feedback loop may give good controlling results. The experimental set up can be used to test the (I - P) self-tuning adaptive controller and the (I - P) adaptive variable gain controller. Also (I - P) impulse response can be tested experimentally. To prove the simplicity of (I - P) controller, a comparatively study is already started between (I - P) and fuzzy controller.

VII. Acknowledgment

The authors wish to express their gratitude to the staff of Power Electronics Laboratory, Faculty of Engineering, Cairo University, Egypt, for their encouragement and assistance in the laboratory work.

VIII. Appendix I

Motor's Parameters

The motor used in this experiment is dc separately excited, rating 0.5 kW at rated voltage 220 V, and the motor's parameters are as follows:

Armature resistance	=	7.72 Ω
Armature inductance	=	0.16273 H
Back e.m.f constant	=	1.25 V/rad/s
Mechanical inertia	=	0.0236 Kg · m^2
Friction coefficient	=	0.003 N · m/rad/s
Rated armature current	=	2.7 A
Speed	=	1500 r/min

IX. References

[1] Gilberto C. D. Sousa, and Bimal K. Bose, "A fuzzy set theory based control of a phase-controlled converter dc machine drive," *IEEE Trans. Industry Applications*, vol. IA-30, no. 1, January/February 1994, pp. 34-43.

[2] N. Manaresi, R. Rovatti, E. Franchi, R. Guerrieri, and G. Baccarani, "Automatic synthesis of analog fuzzy controllers: a hardware and software approach," *IEEE Trans. Industrial Electronics*, vol. IE-43, no. 1, February 1996, pp. 217-225.

[3] R. Moffat, Paresh C. Sen, R. Younker, and Mohamed M. Bayoumi, "Digital phase-locked loop for induction motor speed control," *IEEE Trans. Industry Applications*, vol. IA-15, no. 2, March/April 1979, pp. 176-182.

[4] KiyosHi OHishi, Masato Nakao, Kouhei Ohnishi, and Kunio Miyachi, "Microprocessor-controlled dc motor for load-insensitive position servo system," *IEEE Trans. Industrial Electronics*, vol. IE-34, no. 1, February 1987, pp. 44-49.

[5] M. OKyay Kaynak, Fumio Harashima and Seiji Kondo, "Microprocessor controlled position servo system with a sliding mode," in *Proceedings of the 1982 Microelectronics in Power Electronics and Electric Drives Conference*, ETZ, Darmstadt, West Germany, pp. 273-279.

[6] O. Kaynak, A. D. Abbaszadeh and S. Nazlibilek,"Digital speed control system with integral-proportional control," *IFAC Control in Power Electronics and Electrical Drives*, Lausanne, Switzerland, 1983, pp. 501-506.

[7] Guy Olivier, Victor R. Stefanovic, and Georges-Emile April, "Microprocessor controller for thyristor converter with an improved power factor, " *IEEE Trans. Industrial Electronics and Control Instrumentation*, vol IECI-28, no. 3, August 1981, pp. 188-194.

[8] Fang L. Luo and Roland J. Hill, "Fast response and optimum regulation in digitally controlled thyristor converters," *IEEE Trans. Industry Applications*, vol. IA-22, no. 1, January/ February 1986, pp. 10-17.

[9] Benjamin C. Kuo, *Automatic Control Systems*, New Delhi: Prentice- Hall, 1983, p. 327.

A Proposition of Design Method for Modified Repetitive Control System with Corrected Dead Time Using Sensitivity Function Shaping and its Application to Motor Control System

Hidehiko SUGIMOTO Kazuo WASHIDA
Department of Electrical and Electronics Engineering,Fukui University
9-1,Bunkyou,3-choume,Fukui 910,JAPAN
Fax:+81-776-27-8749, Phone:+81-776-27-8563
E-mail: sugimoto @ powerel.fuee.fukui-u.ac.jp

Abstract- For a conventional modified repetitive control system, designing of its pre-compensator so as to maximize the lowpass filter band width has been considered to contribute to the improvement of its control performance such as its tracking performance for reference input and its insensitivity to disturbance. The control performance of the control system, however, basically depends on its sensitivity function in the main frequency bands possessed by the reference input and disturbance. This fact suggests that the control performance of the control system should be evaluated using its sensitivity function. Therefore, the sensitivity functions of the conventional modified repetitive control system and the modified repetitive control system with corrected dead time already proposed by the authors were first calculated. The results of the calculation showed that the expansion of the lowpass filter band width did not necessarily result in improved sensitivity function of the control system in the intended frequency band.

Therefore, a new design method applicable both for the conventional modified repetitive control system and our proposed modified repetitive control system with corrected dead time was proposed. This newly proposed design method is based on calculation of its sensitivity function and design the system so as to minimize its sensitivity function . In addition, investigation was finally carried out to prove that designing a modified repetitive control system with corrected dead time according to this newly proposed method provides for great improvement in its control performance.

The overall results of the investigations thus conducted by the authors revealed that a modified repetitive control system with corrected dead time, if so designed using the newly proposed method as to minimize its sensitivity function , can achieve further improvement in its control performance.

I. Introduction

In a control system where reference input or disturbance is periodic, its control performance such as its tracking performance for the reference input or its insensitivity to the disturbance can be improved by the use of a repetitive compensator with a dead time element having the same period as the reference input or disturbance built into it as its internal model. If the object to be controlled by the system is strictly proper, however, the incorporation of such a repetitive compensator alone into it is not sufficient for its stabilization, which can only be attained by its modification with a lowpass filter added to the repetitive compensator [1].

In the conventional modified repetitive control system thus obtained, designing of its pre-compensator so as to maximize the lowpass filter band width, thereby producing the effect of the internal model principle, has been assumed to contribute to the improvement of its control performance [2]. The control perfornance of the system, however, basically depends on its sensitivity function in the main frequency bands possessed by the reference input and disturbance. This fact suggests that the control performance of the system should be evaluated using its sensitivity function.

First of all, therefore, this paper deals with this matter, focusing on the fact that a modified repetitive compensator with a first-order lag element used as its lowpass filter, as generally so done, functions only as a PI compensator in the frequency band given by multiplying 1/(reference input period) by integer, the proportational gain of which is 1 with its integral time equal to the time constant of the lowpasss filter [3] in order to show that the sensitivity function of the modified repetitive control system can be simply expressed as a meromorphic function in the above-mentioned frequency band. In addition, this paper indicates that the sensitity function of a modified repetitive control system with corrected dead time already proposed by the authors [3], although it cannot be expressed as a simple meromorphic function, can be easily determined by numerical calculation. This paper then confirms that in the modified repetitive control system and the modified repetitive control system with corrected dead time, their sensitivity functions cannot be necessarily improved in the intended frequency band only by practicing the conventional concept of designing its pre-compensator so as to maximize the lowpass filter band width through an example of its design.

Therefore, as a new guideline for designing a conventional modified repetitive control system and our proposed modified repetitive control system, this paper proposes a new design method for both systems, which is based on calculation of its sensitivity function and design the systems so as to minimize these sensitivity functions. In addition, this paper describes the results

0-7803-3823-5/97/$10.00© 1997 IEEE

of the investigation conducted to prove that designing a modified repetitive control system with corrected dead time according to this newly proposed method provides for great improvement in its control performance.

The overall results of the investigations described in this paper showed that a modified repetitive control system designed with corrected dead time by the newly proposed method for designing it as to minimize the sensitivity function improves in its control performance.

II. Modified Repetitive Control System and Its Sensitivity Function

A. Modified Repetitive Control System

Fig.1 shows the configuration of a modified repetitive control system.

P(s) represents the object to be controlled by the system, C(s) a pre-compensator and H_F(s) a modified repetitive compensator. In H_F(s), dead time L is equal to the period of reference input and F(s) indicates a lowpass filter.

It should be noted that the control system dealt with in ths paper is based on single-input/single-output.

This system shows exponential asymptotic stability when the following two conditions are met [1].

$$\textcircled{1} \quad \frac{P(s)C(s)}{1+P(s)C(s)} \quad , \tag{1}$$

is a stable meromorphic function with no unstalble pole-zero cancellation between P(s) and C(s).

$$\textcircled{2} \quad \left|\frac{F(s)}{1+P(s)C(s)}\right|_\infty < 1 \quad . \tag{2}$$

F(s) is generally expressed in

$$F(s)=\frac{1}{Ts+1} \quad , \tag{3}$$

as a first-order lag element with gain constant 1 and time constant T.

B. Sensitivity Function of Modified Repetitive Control System

If the first-order lag element represented by (3) is used as F(s), Fig.1 allows modified repetitive compensator H_F(s) to be given by the following expression:

$$H_F(s)=\frac{1}{1-F(s)\,e^{-Ls}}=\frac{1}{1-\frac{1}{Ts+1}e^{-Ls}} \tag{4}$$

However, this modified repetitive compensator functions only as a PI compensator in the frequency band given by multiplying 1/(reference input or disturbance period) by integer, the proportional gain of which is 1 with its integral time equal to time constant T of the lowpasss filter [3]. Therefore, in the frequency band given by multiplying 1/(reference input or disturbance period) by integer, modified repetitive compensator H_F(s) can be expressed as:

$$H_F(s)=1+\frac{1}{Ts} \quad . \tag{5}$$

The above allows sensitivity function S of the modified repetitive control system to be given in the above-mentioned frequency band ($\omega=2\pi n/L$, n=0, 1, 2, ···) by the following expression:

$$S=\frac{1}{1+P(s)C(s)H_F(s)}=\frac{1}{1+P(s)C(s)(1+\frac{1}{Ts})} \quad , \tag{6}$$

as a simple meromorphic function.

III. Modified Repetitive Control System with Corrected Dead Time and Its Sensitivity Function

A. Modified Repetitive Control System with Corrected Dead Time

This control system is designed so that the dead time of the dead time element built into it as its internal model is corrected to make its period L' smaller than period L of the reference input or disturbance, thereby improving the gain of the modified repetitive compensator in the frequency band given by multiplying 1/(reference input or disturbance period) by integer in order to improve the system's tracking performance for the reference input or its insensitivity to the disturbance [3]. Corrected dead time L' is determined by the following equation:

$$L'=L\left\{1-\frac{1}{2\pi k}tan^{-1}\left[\frac{2\pi kT}{L}\right]\right\} \quad (k>0) \quad , \tag{7}$$

where k indicates a variable determined by the frequency band in which to improve th gain of the modified repetitive compensator with corrected dead time [3].

It should be noted that the above-mentioned conditions for stabilization of the modified repetitive control system, ① and ②, which do not contain dead time L, can be applied to the modified repetitive control system

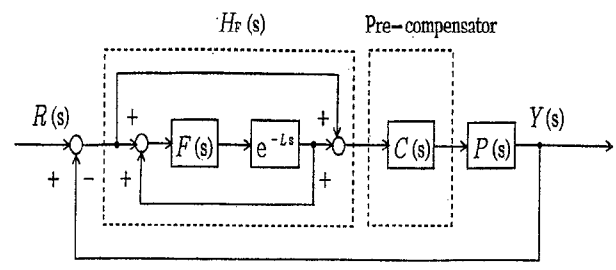


Fig.1 Modified repetitive control system

with corrected dead time, designed only with L changed to L', for its stabilization.

Modified repetitive compensator with corrected dead time $H_F'(s)$ can be given by (4) with L changed to L', which becomes the following expression:

$$H_F'(s)=\frac{1}{1-F(s)\,e^{-Ls}}=\frac{1}{1-\dfrac{1}{Ts+1}e^{-Ls}} \quad . \qquad (8)$$

Fig.2 shows the gain diagrams for two design examples one each of modified repetitive compensators without and with corrected dead time, which will be respectively described later as Case 2 for modified repetitive compensator $H_F(s)$ with reference input period L = 0.062832s (angular frequency ω = 100rad/s) and lowpass filter time constant T = 0.00165s and as Case2' for modified repetitive compensator with corrected dead time $H_F'(s)$ with the same lowpass filter time constant as in Case 2 and the reference input period corrected by (7) with k = 1 to determine L' = 0.0612s. From Fig.2, it can be seen that modified repetitive compensator with corrected dead time $H_F'(s)$ improves greatly in its gain in the frequency band given by multiplying 1/(reference input period) by integer.

B. Sensitivity Function of Modified Repetitive Control System with Corrected Dead Time

Sensitivity function of modified repetitive control system with corrected dead time S' can be given by the following expression:

$$S'=\frac{1}{1+P(s)C(s)H_F'(s)}=\frac{1}{1+P(s)C(s)\dfrac{1}{1-\dfrac{1}{Ts+1}e^{-Ls}}} \quad . \qquad (9)$$

By setting

$$s=j\omega \qquad \omega=\frac{2\pi n}{L} \quad (n=0,1,2,\cdots) \quad , \qquad (10)$$

in (9), this sensitivity function S' can be easily determined by numerical calculation.

IV. Proposition of A new Design Method for Modified Repetitive Control System with Corrected Dead Time

This section takes up a motor including its current control system as the object to be controlled in order to describe design examples of the conventional modified repetitive control system and our proposed modified repetitive control system with corrected dead time to be applied to the speed control system for the motor. Through these design examples, a new design method for a modified repetitive control system is proposed, which is based on the design concept that the system should be designed with corrected dead time in such a way as to minimize its sensitivity function.

A. Object to Be Controlled and Modified Repetitive Control System

A motor including its current control system (with a rated output of 400W and a rated speed of 3000rpm) is taken up as the object to be controlled to configure the speed control sytem of the motor with a modified repetitive control system applied to it as illustrated in Fig.3. In this control system, reference input is a triangular wave with period L of 0.062832s (ω = 100rad/s) and maximum angular speed of $\pm$1rad/s (maximum rotating speed$\fallingdotseq\pm$9.5rpm). The current control system is controlled so that it constitutes a first order lag element with time constant Ti = 1/2000s. Torque constant K_T of the motor is 0.316N·m/A. The moment of combined inertia of the motor and load J is 0.00125kg·m^2.

B. Design Example of Modified Repetitive Control System

1) Pre-compensator and lowpass filter: The object to be controlled is a second order lag element. Therefore, the pre-compensator of a modified repetitve control system is designed as a first order element represented by the following expression:

$$C(s)=\frac{b_1 s+b_0}{s+a_0} \quad , \qquad (11)$$

so that the root of $1+P(s)C(s)=0$ can be freely determined. In addition, the absolute values of λ_1, λ_2 and λ_3 detrmined as roots of $1+P(s)C(s)=0$ are set at 1000 corresponding to 1/2 of the absolute value of the pole of the current control system which is 2000, and roots λ_1, λ_2 and λ_3 are expressed as

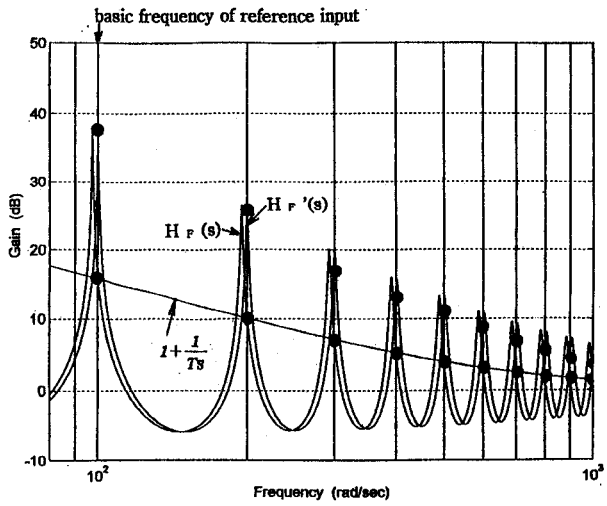


Fig.2 Gain diagrams of $H_F(s)$ and $H_F'(s)$ (L=0.062832s, T=0.00165s, k=1, L'=0.0612s)

$$\left.\begin{aligned}\lambda_{1,2}&=-1000\left(\zeta\pm j\sqrt{1-\zeta^2}\right)\\ \lambda_3&=-1000\end{aligned}\right\},\qquad (12)$$

with ζ as a variable in order to design pre-compensator $C(s)$.

Then, the pre-compensator $C(s)$ thus designed is used to deterine the gain diagram of function $1+P(s)C(s)$, based on which to determine lowpass filter $F(s)$ satisfying the limit of condition ② for stabilization of the system.

Fig.4 shows the diagram obtained by designing $C(s)$ using (12) with ζ set at four different values: $\zeta = 1$ for binomial-coefficient standard type pole placement, $\zeta = 0.5$ for Butterworth standard type pole placement, and $\zeta = 0.71$ and $\zeta = 0.87$ in between the first two values and determining their corresponding $F(s)$ values satisfying the limit of condition ② for stabilization of the system as Case1 to Case4, which are as follows:

$$Case1{:}\zeta=1.00,\ C(s)=\frac{2s+1980}{s+1000},\ T_L=0.0005,\ T=3T_L=0.0015$$

$$Case2{:}\zeta=0.87,\ C(s)=\frac{2.5s+1980}{s+730},\ T_L=0.00055,\ T=3T_L=0.00165$$

$$Case3{:}\zeta=0.71,\ C(s)=\frac{3s+1980}{s+415},\ T_L=0.00071,\ T=3T_L=0.00213$$

$$Case4{:}\zeta=0.50,\ C(s)=\frac{4s+1980}{s},\ T_L=0.00124,\ T=3T_L=0.00372$$

where T_L indicates the time constant of the lowpass filter which satisifies the limit of condition ② for stabilization of the system. The comparison of the four cases shows that Case1 allows the time constant of the lowpass filter to be set at the smallest value, thus enabling its band width to be most expanded.

2) Evaluation of modified repetitive control system using its sensitivity function : With time constant T of lowpass filter $F(s)$ set three times T_L to allow a margin for stabilization of the system, sensitivity function S for each of the four cases was calculated using (6). Fig.5 shows the results of the calculation.

From this figure, it can be seen that designing the four cases with time constant T of lowpass filter $F(s)$ set three times T_L causes the sensitivity function of Case4 where the lowpasss filter band width is the narrowest to become smaller than that of Case1 where the lowpass filter band width is the widest in the frequncy band of approximately 1000rad/s or below where the frequency component possessed by reference input is large.

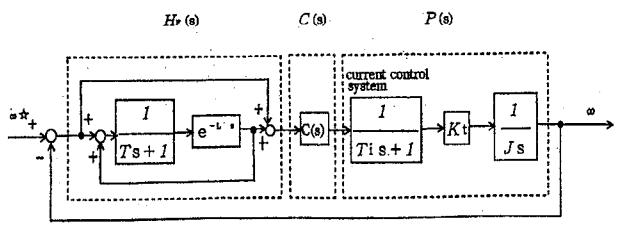


Fig.3 Motor speed control system used modified repetitive control system

C. Design Example of Modified Repetitive Control System with Corrected Dead Time

1) Pre-compensator and lowpass filter : Pre-compensator $C(s)$ of a modified repetitive control system with corrected dead time is designed in the same way as in the case of the above-described design examples of a modified repetitive control system represented as Case1 to Case4. Therefore, time constant T_L of lowpass filter $F(s)$ satisfying the limit of condition ② for stabilization of the system is the same as in Case1 to Case4 described in IV.B above.

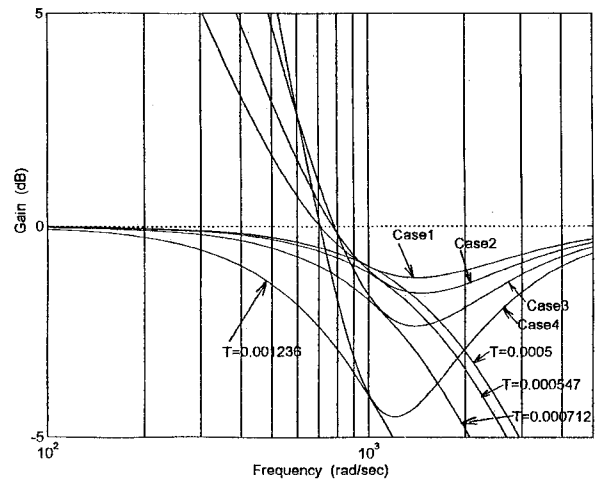


Fig.4 Examination of stability condition ②
(gain diagrams of each $F(s)$ and each function $1+P(s)C(s)$)

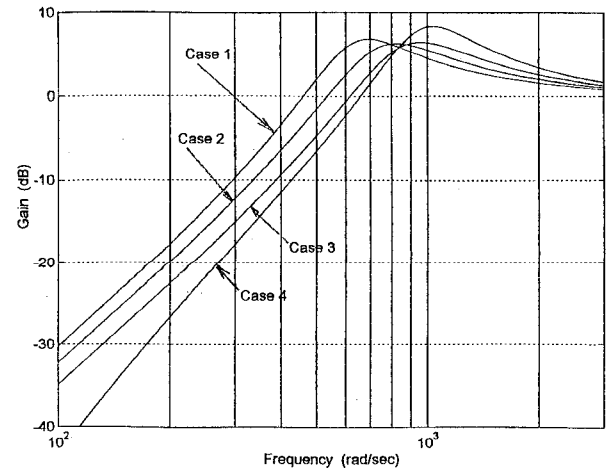


Fig.5 Gain diagrams of sensitivity function S
(Case1,Case2,Case3,Case4 $T=3T_L$)

2) Designing of modified repetitive control system with correction of its dead time: This section deals with the designing of a modified repetitive control system with its dead time corrected to L'. In the control system, reference input is a triangular wave, which is the basic frequency with the largest spectrum. Therefore, (7) with k set to 1 is used to determine L' for each of Case1 to Case4 with time constant T of lowpass filter $F(s)$ set three times T_L to allow a margin for stabilization of the system, designing it as Case1' to Case4', respectively.

The modified repetitive control system with corrected dead time thus designed as Case1' to Case4' (which, respectively, correspond to Case1 to Case4 designed with their respective dead times corrected to L') have pre-compensator $C(s)$, time constant T of lowpass filter $F(s)$ and corrected dead time L' given below for each of the four cases:

$$Case1': \zeta=1.00,\ C(s)=\frac{2s+1980}{s+1000},\ T=0.0015,\ L'=0.0613$$

$$Case2': \zeta=0.87,\ C(s)=\frac{2.5s+1980}{s+730},\ T=0.00165,\ L'=0.0612$$

$$Case3': \zeta=0.71,\ C(s)=\frac{3s+1980}{s+415},\ T=0.00213,\ L'=0.0607$$

$$Case4': \zeta=0.50,\ C(s)=\frac{4s+1980}{s},\ T=0.00372,\ L'=0.0593$$

3) Evaluation of modified repetitive control system with corrected dead time using its sensitivity function : Sensitivity function S' of the modified repetitive control system with corrected dead time for each of the four cases is determined by numerical calculation using (9). Fig.6 shows the results of the calculation. From this figure, it can be seen that the sensitivity function of Case2', where the control system is designed with time constant T of lowpass filter $F(s)$ set three times T_L, is better than other cases.

D. Comparison of Conventional Modified Repetitive Control System and Modified Repetitive Control System with Corrected Dead Time for Their Sensitivity Functions

To compare the conventional modified repetitive control system and our propsed modified repetitive control system with corrected dead time for their control performances, Fig.7 shows the sensitivity functions of modified repetitive control system Case2 (with $T=3T_L$) and modified repetitive control system with corrected dead time Case2' (with $k=1$). This figure clearly reveals that a modified repetitive control system, if designed with with corrected dead time, can improve greatly in its sensitivity function .

E. Proposition of A Design Method for Modified Repetitive Control System with Corrected Dead Time

These overall results allow the authors to propose a design method for a modified repetitive control system, which is based on the concept that it should be designed with corrected dead time in such a way as to minimize its sensitivity function.

V. Simulation of Motor Speed Control Systems based on Conventional Modified Repetitive Control System and Modified Repetitive Control System with Corrected Dead Time

From Fig.5, it is found that a conventional modified repetitive control system can have its sensitivitu function minimized if designed using a pre-compensator represented by Case4 with time constant T of lowpass

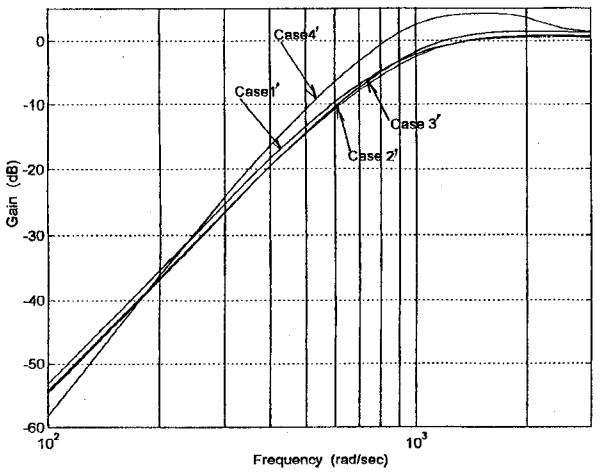


Fig.6 Gain diagrams of sensitivity function S' (Case1',Case2',Case3',Case4' $T=3T_L, k=1$)

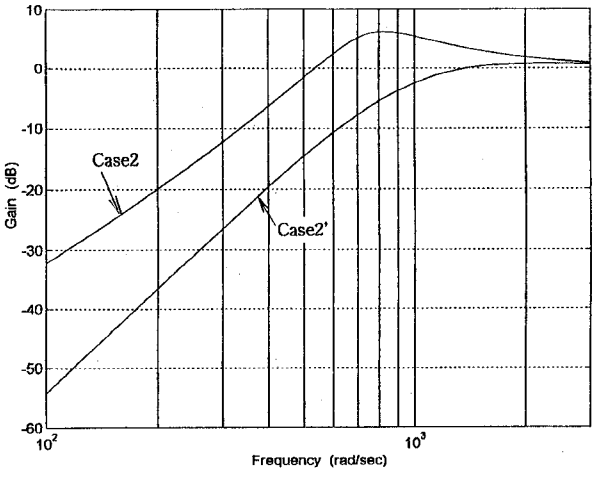


Fig.7 Gain diagrams of sensitivity function S and S' (Case2,Case2' $T=3T_L, k=1$)

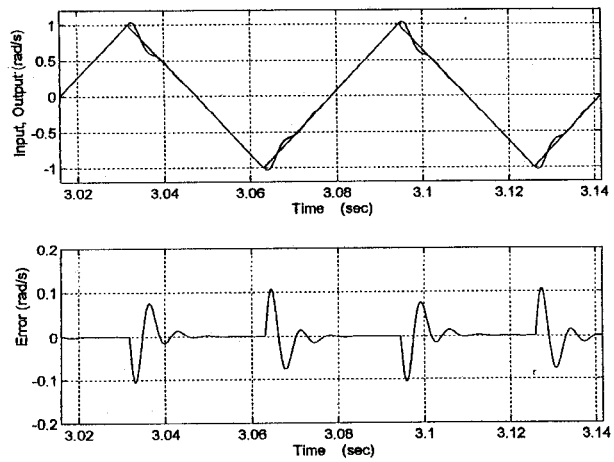


Fig.8 Simulation result of motor speed control system (Case4, L=0.062832s, T=0.00372s, response in the 50th period)

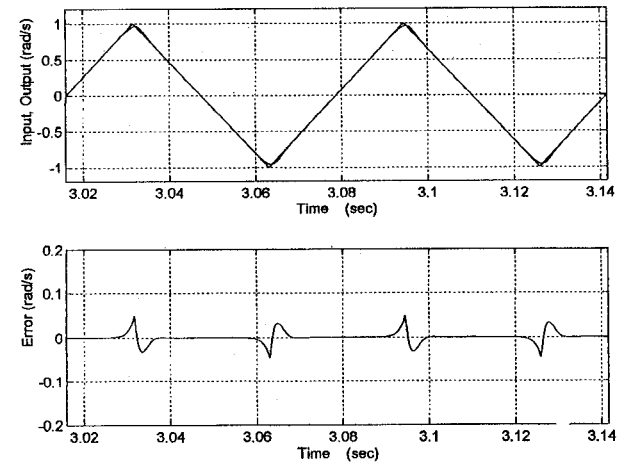


Fig.9 Simulation result of motor speed control system (Case2', k=1, L'=0.0612s, T=0.00165s, response in the 50th period)

filter F (s) set three times T_L. Fig.8 shows the results of the simulation made on this case.

Then, similar simulation was made on our proposed modified repetitive control system with corrected dead time designed using a pre-compensator represented by Case2' with time constant T of lowpass filter F (s) set three times T_L, which gives a smaller sensitivity function value than any other design example of our proposed modified repetitive control system with corrected dead time. Fig.9 shows the results of the simulation. From this figure, it can be clearly seen that a modified repetitive control system, if designed with corrected dead time, shows great improvement in its control performance.

All of these results confirm that a modified repetitive control system should not be designed with the lowpass filter band width expanded, but with corrected dead time in such a way as to minimize its sensitivity function in order to allow the improvement of its control performance to be achieved effectively.

VI. Conclusion

This paper confirms:

(a) Designing of a conventional modified repetitive control system or our proposed modified repetitive control system with corrected dead time with a pre-compensator designed so as to expand the lowpass filter band width does not necessarily result in the improvement of its sensitivity function in the intended frequency band.

(b) Designing of a modified repetitive control system as one with corrected dead time enables its sensitivity function to be improved greatly.

The above led the authors to propose a design method for a modified repetitive control system, which is based on the design concept that it should be designed with corrected dead time in such a way as to minimize its sensitivity function.

References

[1] M.Nakano, T.Inoue, Y.Yamamoto and S. Hara, *Repetitive Control System*: JSICE Press,1986.

[2] O.Kaneko and R. Kawatani, "A Synthesis of Modified Repetitive Control System Using the Loop Shaping Design Procedure", Collection of Papers Presented to JSICE,Vol.31,No. 8, 1144/1151 1995.

[3] H.Sugimoto and K. Washida,"Weft Inserting Motion Control of Rapier Weaving Machine -A Proposition of Modified Repetitive Control System With Corrected Dead Time-" JIEE,SPC-96-100,IEA-96-21,1996.

Introduction of Authors

Hidehiko SUGIMOTO

He entered Mitsubishi Electric Corporation in April,1959 and completed the postgraduate course at Nagoya Institute of Technology in March, 1973 . Thereafter, he transferred to Fukui University, becoming an assistant professor in April, 1990 and a professor in April, 1992, where he has been engaged in the development and research related to power electronics and motor control. He has obtained a doctorate in this field. In 1989, he received a prize from JIEE for his paper presented to the society.

Kazuo WASHIDA

He graduated in mechanical engineering from Fukui University in March, 1974 and entered Industrial Technical Center of Fukui Prefecture as its research staff in April of the same year. As a senior researcher in the Weaving Section of the center, he has been engaged in the development and research of textile machines. In April, 1996, he entered Fukui University to take its doctor's course in system design engineering.

A Two-Dimensional Homopolar Linear DC Motor with New Position Detectors

Yijia Wang, Masaki Yamaguchi, and Yoshio Kano
Tokyo University of Agricalture & Technology
2-24-16, Nakamachi, Koganei-city, Tokyo 184, JAPAN
Fax: +81-423-85-6374, Phone: +81-423-88-7130
E-mail: kano@cc.tuat.ac.jp

Abstract — **This paper presents a novel two-dimensional homopolar linear dc motor (LDM) which can realize the motion two-dimensionally. For precise position control purposes, two kinds of position detecting methods are proposed. The position in one direction is detected by means of a capacitive sensor with feedback loop which makes the output of the sensor largely immune to the variation of gaps between electrodes. The position detection in the other direction is achieved by exploiting the inductance difference between the two driving coils, instead of using an independent sensor. From the experimental results, good thrust distributions and satisfactory linearity of the detecting methods are obtained. The maximum detecting error is 0.9% and 1.7% respectively.**

I. Introduction

Homopolar linear dc motors have been used for linear motion for some times. The main feature of the homopolar LDM is that the magnetic field only experiences one direction, thus there is no need for mechanical or electronic commutation and no force ripple. Because of the good linearity of their force-current relationship as well as their low inertia, these machines have been used in positioning applications, particularly in the OA machine industry. Recently, the research on two-dimensional linear motors has attracted more attention[1][2]. In this work an attempt is made by the authors to add two additional coils to a conventional homopolar LDM to construct a two-dimensional (2-D) homopolar LDM, without paying much penalty on the motor performance and the complexity of mechanical mechanism.

In this paper the prototype of this kind of 2-D homopolar LDM and its thrust characteristics are described. Also, for precise position control purposes, position detecting is indispensable. Since the special structure of the 2-D homopolar LDM, space saving becomes crucial. Moreover, to keep the price low and to improve the robustness of the system it is also necessary to minimize the number of sensors. Therefore the position in the x direction is detected by means of a flat capacitive sensor with feedback loop which is capable of reducing the influence due to the gap variation. Sensorless method is used to realize the position detection in the y direction. Experiments show that the motor has good thrust characteristics and the proposed position detecting methods give satisfactory linearity and accuracy.

II. Motor Topology and Analysis

A. Two-Dimensional Arrangement

The layout of the proposed 2-D homopolar LDM is shown in Fig.1. The basic structure is similar to its 1-D counterpart. Homopolar magnetic flux flows from the permanent magnet to the yoke and returns via two end yokes. The difference between them lies in the movable parts. As seen from Fig.1, two coils contributing to the motion in the x direction (x-coils) are fixed in a plate. X-coils along with the plate constitutes the x-mover and can slide freely with the aid of four x-bearings supported by two V-shaped edges of the yoke. The motion in the y direction can be accomplished by another two rectangular air core coils (y-coils) which are placed side-by-side on a plane inside a carriage framework. The carriage is also supported by means of four y-bearings mounted on the x-mover. The coils are supplied with a dc current from flexible leads. The stroke in the x and y direction is 200mm and 40mm, respectively.

The specifications of the prototype of the 2-D homopolar LDM is indicated in Table I.

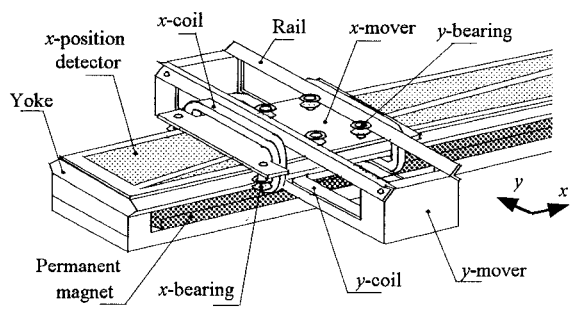


Fig.1 Layout of the 2-D homopolar LDM

TABLE I
Motor Specifications

Item		Value
Mass of the motor		7.2kg
Mass of the mover		0.58kg
PM materials		ferrite (FB4X)
Yoke dimensions		400(l) x 77(w) x 45(h) mm
PM dimensions		300(l) x 60(w) x 5(h) mm
Stroke	x	200mm
	y	40 mm
Thrust constant	x	7.6N/A
	y	6.6N/A
Coil resistance	x	18.4Ω
	y	24.8Ω
Self-inductance of coils	x	65mH
	y	56mH
Mutual inductance		15mH

B. Thrust Characteristics

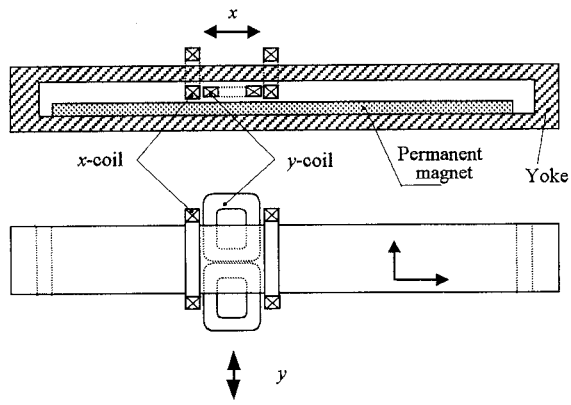


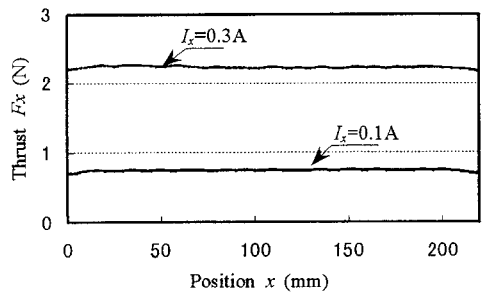
Fig.2 Cross-Sectional View of the 2-D Homopolar LDM

The cross-sectional view is shown in Fig.2. When a dc voltage is switched across the coils, it gives rise to a current i which interacts with the magnetic field B to create a force F.

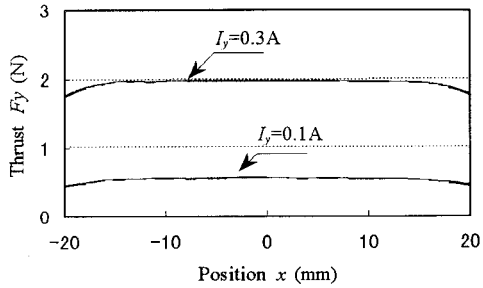
$$\vec{F} = i\vec{X} \times \vec{B} \qquad (1)$$

where $\vec{X}$ is the length of the conductor exposed to the magnetic field. The flux density provided by the magnet is determined primarily by the magnet material and its reluctance path.

Fig.3 (a) and (b) show the thrust distributions with respect to the x and y directions, respectively. The thrusts are nearly equal over the entire range of the stroke in the x direction and the range of -15mm to +15mm in the y direction, whereas F_y dropped substantially near the ends of the stroke because of the uneven distribution of the flux density in the y-direction. The thrust constant in the x and y direction is 7.6N/A and 6.6N/A, respectively.



(a) Thrust distribution versus x position



(b) Thrust distribution versus y position

Fig.3 Thrust Distribution Characteristics

Ⅲ. Position Detection in the x Direction

A. Conventional Structure

The linear capacitive position sensor is realized in simple configurations of high performance where relatively long linear displacement of a order of 200mm are measured. The printed circuit board pattern is readily achievable through a well-established low-cost technology. This device is designed in such a way that there is a moving electrode which has no electrical connection to the static electrodes other than by capacitance as shown in Fig.4. The moving electrode E_0 passes between the fixed electrodes E_1 and E_2. E_0 behaves as a common electrode. In practice, the common electrode is forced to be at virtual ground potential, which confines the electric field to the space between the electrodes without fringing. The influence of the parasitic capacitances of the cable would be eliminated via shield drive technique.

Using the terminology in Fig.4, we get

$$C_1 - C_2 = -\frac{2\varepsilon_0 wl}{g} \cdot \frac{x}{L} \qquad (2)$$

where ε_0 is the dielectric constant of free space, s, w and L are determined by the detector dimension. If the gap length between electrode E_0 and E_1,E_2 is a constant, the difference of C_1 and C_2 is proportional to the displacement of movable electrode E_0. The electronic circuitry has been designed for detecting the capacitance variation[3]. Thus C_1-C_2 can be represented by the amplitude of the output sine voltage V_0

$$V_0 = -\frac{2\varepsilon_0 wlk_0}{g} x \qquad (3)$$

where k_0 is the amplifier gain.

Usually gap length g is very small and from (3) it can be seen that V_0 is so sensitive to the g variation that little change of g would lead to the inaccuracy of the position detecting and hence spoil the linearity. To some extent, it is possible to achieve good performance with careful mechanical design. However, to eliminate the mechanical misalignments totally is difficult, especially for sensors with long stroke. Here improvements are made on the electronic

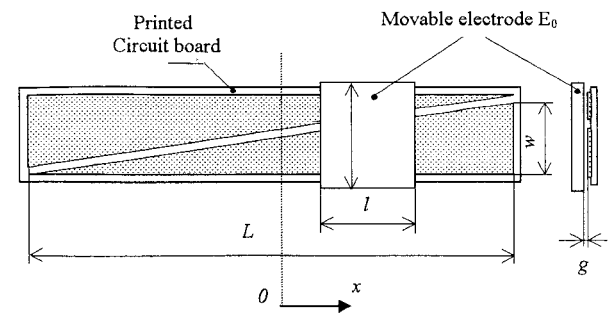


Fig.4 Structure of the Detector

converting circuitry to compensate the mechanical flaw.

B. Improvement of Linearity Using Feedback

We note the fact that

$$C_1+C_2=\frac{\varepsilon_0 wl}{g}. \tag{4}$$

It is clear that the sum of C_1 and C_2 is only the function of g, if the dielectric of air is taken as the same as ε_0 and keeps constant under certain temperature and humidity. This indicates that C_1+C_2 can represent the fluctuation of gap length g.

Based on such a consideration, a feedback loop is added to the conventional open loop configuration of the position detector electronic circuitry as shown in Fig.5. In principle V_1+V_2 would not vary as long as g remains unchanged. We set a reference voltage, V_R, for V_1+V_2, and to employ $V_R-(V_1+V_2)$ to control the magnitude of the sinusoidal oscillator's output voltage, V_S, so as to compensate V_1 and V_2 to make V_1-V_2 be less affected by the variation of the gap length between electrodes.

The detector's output voltage, V_x, is given by

$$V_x=-\frac{2k_3k'K(V_B+ak_2V_R)}{g+2aC'_0k_1k_2K}x, \tag{5}$$

where

- a ratio of output voltage to control voltage of the oscillator.
- $C'_0=\varepsilon_0 wl/2$ (F·m),
- $k'=\varepsilon_0 wl/L$ (F),
- k_1 signal processing circuit gain in feedback channel,
- k_2 feedback amplifier gain,
- k_3 detector amplifier gain,
- x measured position (m),
- K conversion coefficient of capacitance-voltage converter (V/F),
- V_B base value of V_S (V),
- V_E error voltage for controlling the oscillator (V),
- V_R reference voltage for V_1+V_2 (V),
- V_x output voltage of the detector (V).

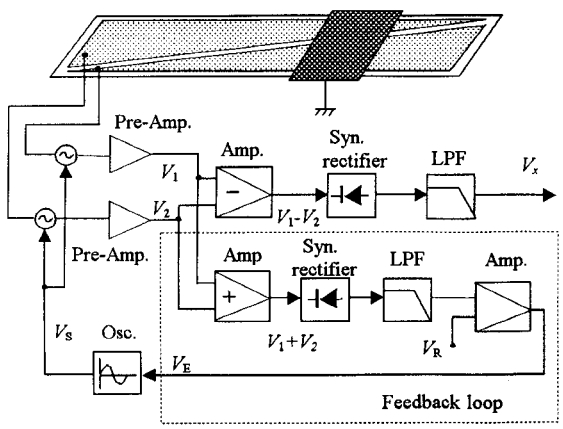


Fig.5 Configuration of the Circuitry

Because a, C'_0, k_1, k_2 and K are all positive, from this expression we find that the detector output voltage V_x is less affected by the fluctuation of gap g than that in (3), if setting appropriate loop gains to guarantee $2aC'_0k_1k_2K > g$. Expression (5) explains the existence of the feedback loop can compensate gap variation due to machining and which results in the detecting error.

C. Experimental Results

The linear capacitive position is tested for the measurement accuracy and linearity. The actual position is measured by a laser displacement meter (Anritsu KL-137).

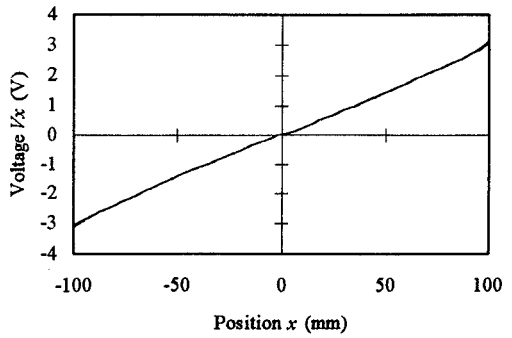
Measurements are performed for different positions of the detector. As shown in (5), the detector is not sensitive to the gap variation because of the existence of the feedback loop, or $2aC'_0k_1k_2K$. In this study, the values of relevant parameters are:

a=15, $C'_0=1.99\times10^{-14}$ (F·m)
$K=1.5\times10^{10}$ (V/F), V_R=1.5(V),
k_1=0.5, k_2=1.5,
V_B=0.66(V).

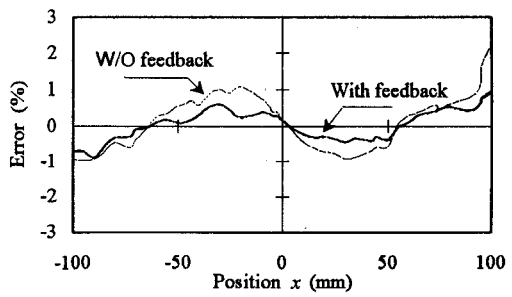
Among them a, C'_0, V_B and K are determined by the detector dimension and design specifications, which will make

$$2aC'_0k_1k_2K=4.5mm \gg g. \tag{6}$$

Then the influence of the gap distance variation can be attenuated. Fig.6 shows the linearity of the position sensor



(a) Relationship between the detector output voltage V_x and position x (with feedback)



(b) Error distribution

Fig.6 Position detecting characteristics

with and without feedback loop. From Fig.6 (b) it is clearly found that the maximum non-linearity error is decreased by 61%, from 2.3% to 0.9% via feedback loop when the feedback gain k_2 is set to 1.5. Despite of the effectiveness of the proposed method, the maximum error is reduced by 61%, not as large as expected from (5). Two reasons may be considered for this. One is the existence of possible skew angle between the movable electrode and fixed electrodes, which results in the uneven gap distance between the movable electrode, E_0, and the fixed electrodes, E_1 and E_2, whereas the proposed method is based on the assumption that E_0 is parallel to E_1 and E_2. The other is that C_1-C_2 versus position x is non-linear near the two ends of the stroke because of the fringing. Although the position detecting method has limitations on eliminating the non-linearity error due to the gap variation, it is already very useful for capacitive position detector with significant errors due to the mechanical misalignment.

IV. Position Detection in the y Direction

A. Principle

As mentioned above, to keep the price low and to improve the robustness of the system it is necessary to minimize the number of sensors. Principles for sensorless operation of electrical machines are generally based on either advanced observers or special characteristics of the motor[4][5]. In our case the position detection in the y direction is realized by exploiting the inductance difference between the two driving coils as y-movers moves. From Fig.2 we know that the two y-coils are inserted in the air-gap between the yoke and the permanent magnet. It can be imagined that the coil self-inductance depends on the y-mover's position. However, the inductance variation is so small (the maximum variation from y=0 to y=±20mm is 7mH) that accurate measurement of coil inductance is difficult. In this research work, signal injection method is employed to detect the unbalance voltage of the electric bridge formed by y-coils and two additional resistors $R1$.

The bridge's equivalent circuit is shown in Fig.7. V_d is the voltage applied to the y-coils to drive the mover. V_S is the injected sinusoidal signal. Voltages e and e_M represent the back electromotive force (EMF) of the y-coils and the induction voltage due to the mutual inductance, respectively. $M(y)$ is the mutual inductance between the x-coils and y-coils. Ideally the two y-coils share the same resistance R and the same inductance L when the mover is situated in the center of the stroke. If the y-mover is off- centered, ΔL occurs, which would lead to the unbalance of the bridge. To develop a sensorless position detection method, the first step is to set up an equation which can describe the position characteristics. The output voltage of the bridge can be expressed by the equation below

$$V_0 = \Delta L \frac{dis}{dt} + \Delta L \frac{di_y}{dt} + 2e + 2M \frac{di_x}{dt} \qquad (7)$$

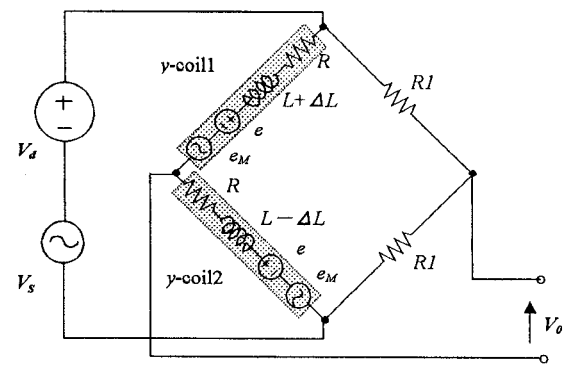


Fig.7 Equivalent circuit of the bridge connection

where i_S is the current due to V_S, i_x and i_y are the driving current flowing in the x-coils and y-coils respectively.

Since V_s is an injected sinusoidal signal which has constant amplitude and constant frequency, i_S is also a sinusoidal signal and has constant amplitude. Note that the first term in (7), being proportional to ΔL, is what we need to estimate the mover position. The second term is due to the variation of the y-coil driving current. The third term usually appears as a dc voltage. The fourth term reflects the influence of current flowing in x-coils through mutual-inductance. If the motor operates at constant speed, di_x/dt and di_y/dt are zero. The back EMF can be eliminated by a dc-isolating circuitry. Then the detected voltage V_0 is amplitude-modulated by ΔL, and has linear relationship with ΔL. If the motor is working in transient state with relative high speed, particularly in the starting or stopping stage, di_x/dt or di_y/dt is not negligible. It is clear that di_x/dt and di_y/dt are objectionable, and their existence would result in error and hence make the position detection method impractical, unless proper technique is employed to get rid of them. But, to precisely predict di_x/dt and di_y/dt is difficult,

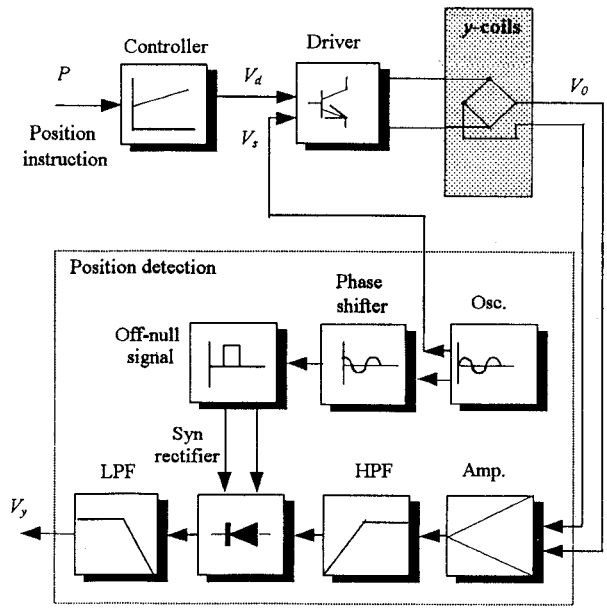


Fig.8 Block diagram of the y position detecting circuitry

because they vary from control objectives. For an ordinary control system, at least several milliseconds are required to adjust the system to a steady state. Based on this consideration, a frequency of 5kHz with a peak to peak magnitude of 0.1V sinusoidal injected signal has been chosen, which makes V_S readily be identified and most of di_x/dt and di_y/dt be eliminated by a high pass filter (HPF) with a cut-off frequency of 3.7kH$_z$. The overall structure of hardware implementation of the position detection is shown in Fig.8.

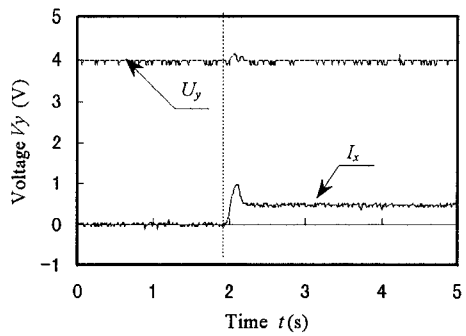
Basically it is an oscillator plus a signal processing circuit converting the ΔL dependent amplitude-modulated voltage to a dc position signal. The sine signal injected to the driver is superimposed on the driving voltage and added to the y-coils.

B. Position Detection Characteristics

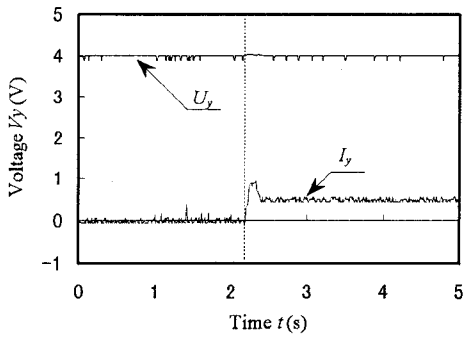
To investigate the position detection characteristics, it is necessary to evaluate the significance of the influence of di_y/dt and di_x/dt. Firstly, the dc component of the bridge's output voltage is set to zero by adjusting the value of $R1$. This step is of vital importance for the position detecting resolution. Then a simulation of transient operation of the detector is performed. In our case, the bridge's output voltage, V_0, is in several mV order which is too weak to be captured. So we choose current variation as a reference to observe its influence on the sensor output voltage. Fig.9 is the results of this simulation. Fig.9 (a) shows the influence on the output voltage of position detection as i_x rise from zero to 1A abruptly and reduces to 0.5A within 200ms while Fig.9 (b) shows the influence as i_y varies in the same pattern, all in the case of y=20mm when ΔL reaches its maximum value. The plots indicates that di_x/dt contributes around 2.0% and di_y/dt contributes less than 0.5% of the instantaneous errors of their full scale value (4V), under the worst situation. This phenomenon can be explained by the fact that $M(y)$ is larger than ΔL. It is believed that in practical application, the dynamic errors would be below these values. The existence of the second and fourth terms in (7) is insignificant after being processed.

Fig.10 shows the results of position estimation reflecting the non-linearity. It demonstrates that the error is within 1.7% over the entire range when x-mover is in a certain position of x=100mm. The error is attributed to the non-linearity of y-coil's self-inductance versus y-position. Another possible reason is the phase shift of the bridge output voltage which eventually affects the output of the signal processing circuit as y-mover travels.

The above results are all obtained when the x-mover locates in the center of x stroke (x=100mm), It is necessary to further observe the relationship between the detector output voltage and the x position. Fig.11 shows the y position detector's output voltage drift error with the x-mover moving whereas the y-mover maintains stationary at y=20mm. The maximum error is 0.6% which is considered coming from the misalignment of the y-coils fabrication other than the end effect of the yoke since the

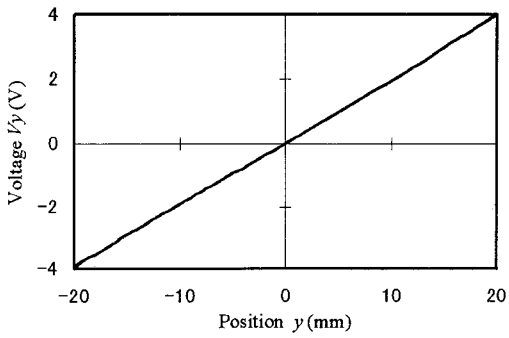


(a) Influence of I_x on the output voltage

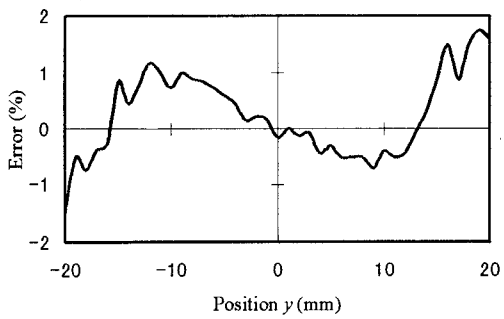


(b) Influence of I_y on the output voltage

Fig.9 Influence coil currents on detector output voltage (y=20mm)



(a) Output voltage with respect to position y



(b) Error distribution

Fig.9 Non-linearity of the proposed detecting method (x=110mm)

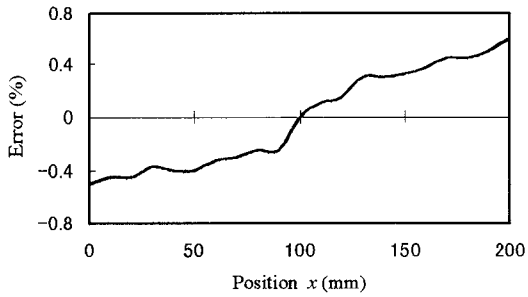


Fig.11 Position detection error in the y direction with respect to position x (y=20mm)

detector's output voltage unilaterally drifts.

Although there is a little dynamic deviation if driving currents varies sharply, it is very useful for the cases when mounting of the position sensor becomes unfeasible. This dynamic error is expected to be further eliminated by advanced signal processing technique.

V. Conclusion

In this paper a novel 2-D homopolar LDM has been presented. By adding two additional coils to a traditional homopolar LDM, two-dimensional motion can be realized over the ranges of ±100mm and ±20mm. The structure of this kind of motor is simple and the motor is easy to be manufactured. Two kinds of position detecting methods are proposed for the motor. From experiments, the following results are obtained:.

1) The thrusts are uniformly distributed over most of the stroke ranges. The thrust constant in the x and y direction is 7.6N/A and 6.6N/A, respectively

2) A flat capacitive position sensor which is capable of reducing the influence of gap variation between electrodes is employed to detect the x position, the maximum discrepancy being 0.9%.

3) The sensorless position detecting method is used to estimate the y position by means of the inductance difference of the two y-coils. The proposed position detecting method provides good linearity and the error is under 1.7%.

Since the motor proposed in this work is only a prototype, the optimal design is necessary which would be the future research topic.

References

[1] D. Ebihara, T. Takahashi, and M. Watada, "Two-Dimensional Servo Control of Surface Motor",*Trans. IEEJ*, vol.115-D, No.9, pp.1186—1191, 1995.

[2] K.Yamazaki and G.Kimura,"Development of a New Type Three-Dimensional Surface Motor", *Trans. IEEJ*, vol.115-D, No.9, pp.1194—1195, 1995.

[3] Y.Kano, J. Shishido, and S. Sato,"Cubic Type Linear DC Motor," *LDIA'95 Nagasaki*, Japan, pp.445—448,1995

[4] T.Matsuo and T.A. Lipo,"Rotor Position Detection Scheme for Synchronous Reluctance Motor Based on Current Measurement", *IEEE Trans. on IAS*, vol.31,No.4, pp.860—868, 1995.

[5] S. Ostlund and M. Brokemper,"Sensorless Position Detection from Zero to Rated Speed for an Integrated PM Synchronous Motor Drive", *IEEE Trans. on IAS*, vol.32, No.5, pp1158—1165, 1996.

Propulsion Control Experiments in Mass-Control Mode of an Underwater Travelling Marine-Express Model Vehicle ME02

K. Yoshida, L. Shi and H. Takami
Department of Electrical and Electronics Engineering, Graduate School of
Information Science and Electrical Engineering, Kyushu University
10-1 6-chome Hakozaki Higashi-ku, Fukuoka 812, JAPAN
Phone: +81-92-642-3905, Fax: +81-92-633-2710

Abstract - **A unique linear synchronous motor (LSM) vehicle ME02 is designed to travel underwater based on the theory of new combined levitation and propulsion for the Marine-Express. This paper presents a stable underwater-propulsion-control experiment in a mass-control mode where the vehicle is sustained by guide-rollers. In this mode, ME02 vehicle can run with guide-rollers contacting with the LSM guideway both in repulsive-mode and in attractive-mode by controlling the lift force to be a required value. The experiment in our Laboratory has shown that ME02 vehicle had been controlled successfully to run underwater in mass-control mode by applying the decoupled-control method of lift and thrust forces.**

I . Introduction

In 1989, the Marine-Express (ME) project, of which the basic concept is an amphibious linear motor (LM) train able to run both on land and under the water, was initiated in our University. A theory of new combined levitation and propulsion for the ME was proposed by Yoshida. In the sea the ME can levitate and travel simultaneously by controlling force vector of LSM in attractive-mode to compensate its buoyancy. On land it does by controlling force vector of LSM in repulsive-mode [1].

The first underwater LM vehicle ME01 which is driven by linear induction motor has successfully travelled underwater in a repulsive-mode levitation [2]. To simulate an actual ME vehicle driven by superconducting LSM, the second underwater LM vehicle ME02 with permanent magnet (PM) on board is designed and manufactured to run in the same water tank [3]. ME02 is controlled by lift and thrust forces of LSM to follow the demand propulsion and levitation patterns according to the decoupled-control method which treats independently the two forces. The attractive- and repulsive-mode levitations during a standstill have been realized successfully in our Laboratory [4][5].

In the ME02 system, it is possible to operate flexibly vehicle in a levitation mode using no guide-rollers and in a mass-control mode sustained by guide-rollers, by controlling armature current and mechanical load-angle. Especially in mass-control mode, an effective or equivalent mass can be loaded arbitrary through guide-rollers on the guideway by regulating the lift force to realize a stable running with the minimum friction loss between rollers and guideway.

This paper presents propulsion-control experiments of ME02 in the mass-control mode, where the equivalent weight is regulated to be 1.274 kg and 0 kg on the guideway by controlling the levitation force independently of the propulsion force. ME02 vehicle is controlled to run in the water tank following the demand propulsion patterns with the lift force kept constant.

II . Model Vehicle ME02 and its Characteristics

Fig. 1 shows ME02 running underwater in the water tank. ME02 is 105 cm long, 12 kg in weight, 17 cm in diameter and streamlined with dorsal and tail fins. Fig. 2 shows the cross-section of a 1/25-th scale model vehicle ME02. It has fifteen-pole PM underneath the body and the LM guideway of iron-cored long stator is enclosed by stainless steel in the water tank. Vehicle is levitated and propelled by only one pair of armature and PM. In Fig.2, when upper guide-rollers contact with the guideway, the airgap-length δ is 9mm. δ is 12mm with lower guide-rollers contacted with the guideway. Airgap sensors are located near the ends of vehicle, apart by 15.4 cm from the lower guide-roller, it is thus possible that one sensor sinks down about



Fig.1. ME02 running underwater in water tank

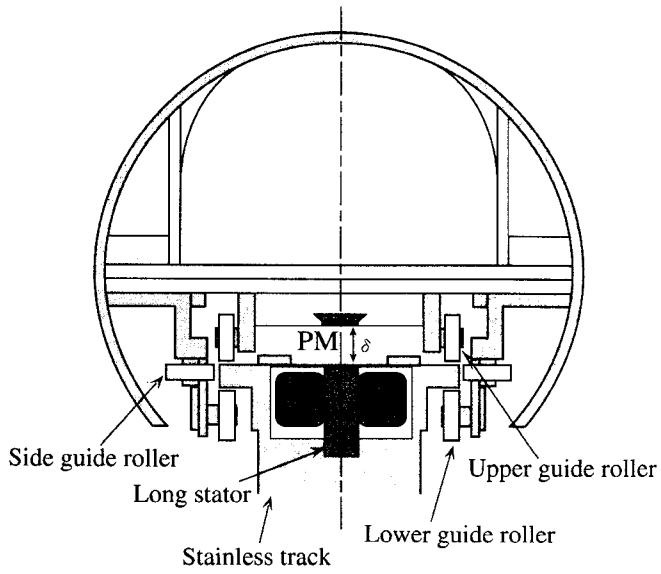


Fig.2. Transverse cross-section of ME02

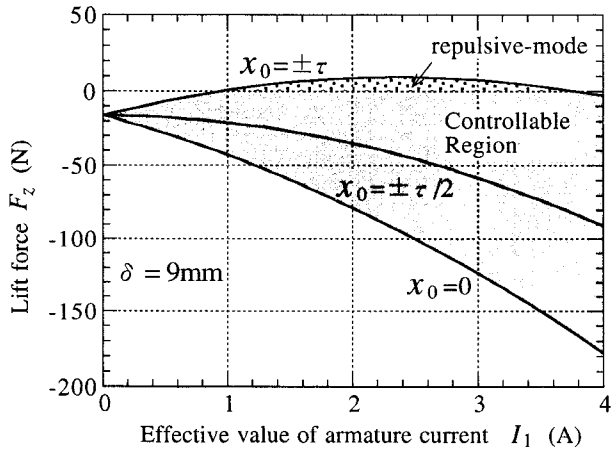


Fig.4. Lift force vs. armature current with a parameter of x_0

0.9mm and another rises up about 3.8mm from the state (δ =9 mm) at which the vehicle is supported by the upper guide-rollers on the guideway. Fig.3 shows that the front-sensor sinks down about 0.9 mm and rear-sensor rises up about 3.8mm. The possible maximum pitching-angle ϕ_m limited by guide-rollers is about 0.29° as shown in Fig.3.

The analytical formulas for PM LSM Maglev system are derived by solving the multi-layer boundary-value field problem using Magnetic Vector Potential (MVP) transfer-matrix method [6][7]. In this LSM system, the thrust force F_x and the lift force F_z can be given in the following analytical form:

$$F_x = K_{F0}(\delta_e) I_1 \sin\frac{\pi}{\tau} x_0 \tag{1}$$

$$F_z = -K_{zs}(\delta_e) I_1{}^2 - K_{zMs}(\delta_e) I_1 \cos\frac{\pi}{\tau} x_0 - K_{zM}(\delta_e) \tag{2}$$

where K_{F0}, K_{ZS}, K_{ZMS}, K_{ZM} are the coefficients of thrust and lift forces, I_1 effective value of armature current, τ the pole pitch, x_0 mechanical load-angle and $\delta_e = kc\delta$ effective airgap-length modified by Carter's coefficient.

At δ = 9mm, the relationship between lift force and armature current with a parameter of mechanical load-angle is shown in Fig. 4. Shade and dotted parts in controllable regions illustrate the attractive- and repulsive-modes, respectively. In these experiments, the buoyancy of water is a little smaller than the weight of the vehicle as mentioned below. Therefore by controlling I_1 and x_0, we can realize mass-control-mode propulsion in both attractive-and repulsive-mode in the controllable region of Fig.4 as mentioned in section Ⅳ .

Ⅲ. Equations of Motion and Control System

The equations of propulsion and levitation motion is simply described as follows:

$$M_x \ddot{x}_2 = F_x - K_{dx} \dot{x}_2{}^2 \tag{3}$$

$$M_z \ddot{z}_2 = F_z + F_L - Mg - K_{dz} \dot{z}_2{}^2 \tag{4}$$

where M is the mass of the vehicle, M_x the equivalent mass in the x direction and M_z the equivalent mass in the z direction, F_x the thrust force, F_z the lift force, F_L the buoyancy of vehicle due to water, g the acceleration of gravity. K_{dx}, K_{dz} are the coefficients of running resistance in the x- and z- directions, $\dot{x}_2$, $\ddot{x}_2$, $\dot{z}_2$, $\ddot{z}_2$ the speeds and accelerations of vehicle in the x- and z- directions, respectively.

In the control strategy as shown in Fig.5, to realize a decoupled-control for levitation and propulsion, first we determine command force F_x^*, F_z^* required for the vehicle to follow the demand position, speed and acceleration patterns according to the control rule based

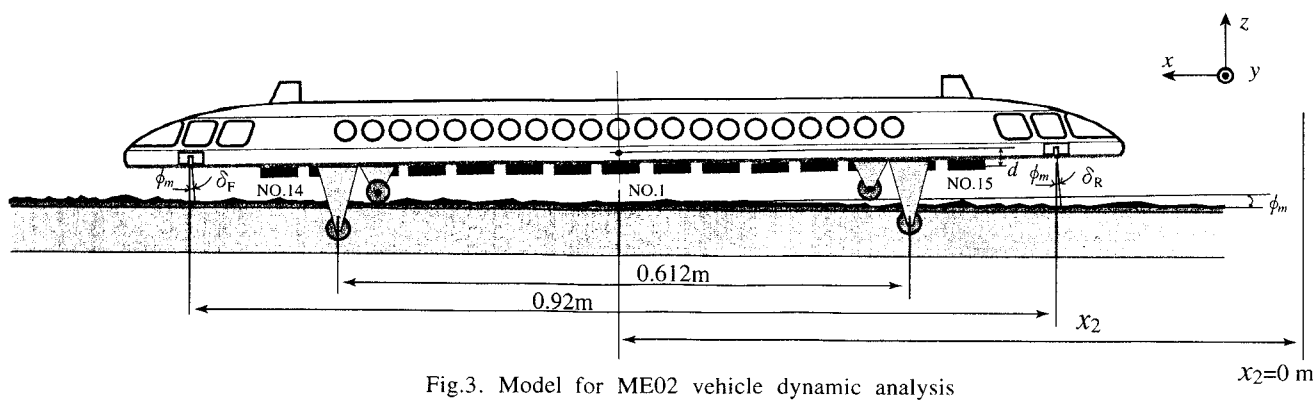


Fig.3. Model for ME02 vehicle dynamic analysis

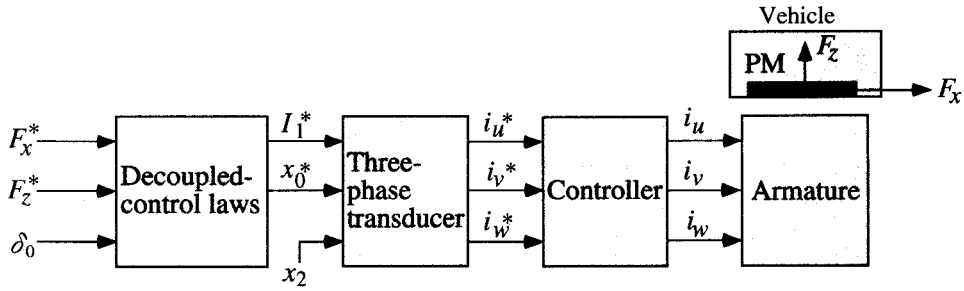


Fig.5. Decoupled control system

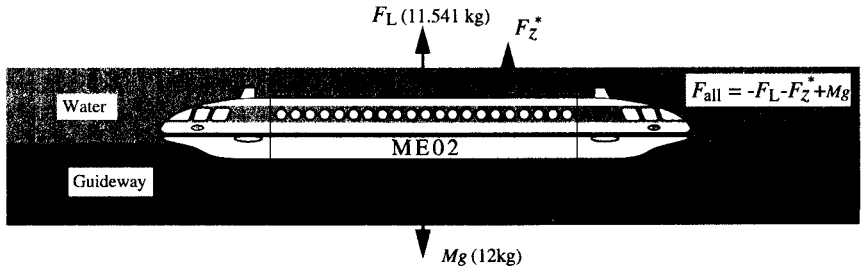


Fig.6. The relationship of forces in the z-direction

on the optimal servo-control theory. Then, we calculate the command armature current I_1^* and mechanical load-angle x_0^* from F_x^*, F_x^* and the demand airgap-length δ_0 by using a 2-dimensional interpolation method for Digital Signal Processor (DSP) [1]. Signals of the command 3-phase instantaneous currents are put into the inverter. When the vehicle is propelled in a mass-control mode, the lift force F_z^* is kept constant during the running period.

In the control system for ME02, the airgap- and position-sensors on board are used to detect the vehicle states, respectively. The detected state-signals of the vehicle are collected by Integrated Vehicle Instrument System (IVIS) and transmitted to on-the-ground control system through water and air by high speed modem and transmitters. Receivers catching the transmitted signals, position-and-speed calculation and control units, A/D and D/A converters, a host computer sending the demand patterns, a current-source inverter supplying the command 3-phase currents to LSM armature winding, and so on, are included in the on-the-ground control system [8]. To carry out the real-time calculation-and-control at high speed, DSP (TMS320C25) is applied in the experimental control system.

Ⅳ. Experimental Results and Discussions

To *simulate* experimentally the ME running on land in a mass-control mode, we control the lift force F_z^* to be 0.459 kg in a repulsive-mode. As a result, the equivalent force F_{all} loaded on the guideway become 'zero' with the buoyancy of water to minimize a friction loss of guide-rollers in Fig.6. Fig.7 shows the results of this experiment.

In Fig.7, shaded regions are the positioning period in which command armature current and mechanical load-angle are determined to bring the vehicle to the starting position. From Figs.7(a) and (b), it is known that the vehicle has been controlled to run following the demand position- and speed-patterns for propulsion. But in this case when the equivalent force F_{all} is 0 kg, a head-up pitching motion happened sharply in the going-motion (period from 5 to 14 sec) as shown in Fig.7(g). It did when the command thrust force changed continuously into the breaking force to follow the constant speed pattern as shown in Fig.7(h). In the return-motion (period from 17 to 26 sec), it happened with delay time of about 2 sec because the water flow produced by the going-motion remained. Figs.7 (c) and (d) show the airgap-length measured by front and rear gap-sensors, respectively. From these data, the pitching-angle was calculated. Figs.7(e) and (f) show the airgap-lengths δ_{Fg}, δ_{Rg} between upper guide-rollers and guideway. Lower guide-rollers limit δ_{Fg} and δ_{Rg} to 3 mm at maximum as shown in Fig.3. It is found from Figs.7(e) and (f) that the vehicle floats with no contact over the guideway during an impact pitching-motion.

Figs.7 (i) and (j) show the command armature-current I_1^*, complemental mechanical-load-angle $x_0'^*$, which is defined by $x_0'^* = \tau - x_0^*$, required for the vehicle to follow the propulsion demand pattern.

For an actual ME running underwater, a buoyancy is generally several times as large as the weight itself. The large buoyancy should be compensated for the ME to travel along the LM guideway. In the following experiment, the vehicle for a repulsive-mode experiment mentioned above is also used and the vehicle weight is a little larger than the buoyancy of water. But the generality of an attractive-mode operation is not lost because an equivalent weight loaded on the guideway is used. Fig.8 shows the experimental results of *simulating* actual ME running underwater in an attractive-mode. The equivalent weight is regulated to be 1.274 kg loaded on the guideway by a lift force F_z^* equal to - 0.815 kg and the buoyancy of water about 11.541 kg as shown in Fig.6.

From Figs.8 (a), (b), it is known that the vehicle has been controlled to run following the demand patterns satisfactorily. Figs.8 (c) and (d) show that airgap-lengths measured by front and rear gap-sensors were almost kept a constant value of 9mm. That is to say, the front- and rear - rollers were always contacted with the guideway during all the periods as shown in Fig.8 (e) and (f). No pitching-motions were produced as shown in Fig.8 (g). Figs.8 (h), (i) and (j) show the command armature-current I_1^*, complemental mechanical-load-

angle $x_0'^*$ and thrust force F_x^* in this mass-control-mode propulsion. It is distinct that the effective-value of armature-current is about 1/3rd that in Fig.7 (i) because there is a large attractive-force between PM on board and iron-core in the LSM armature guideway.

Comparing Fig.7 and Fig.8, we know clearly that although it is hoped to propel the vehicle with minimum friction loss of rollers on the guideway, the propulsion control with the equivalent weight equal to 1.274 kg is more stable in the mass-control propulsion. So, when a pitching-motion happens, the left force F_z^* is regulated to increase suitably the equivalent weight on the guideway and a stable no-pitching propulsion can be realized in the mass-control mode.

V. CONCLUSIONS

Mass-control-mode motions both in repulsive-mode on land and in attractive-mode under the water have been simulated easily by ME02 running under the water. The propulsion experiments in a mass-control mode have been realized successfully by controlling the lift force to be a required constant value, under the conditions that the buoyancy of water is a little smaller than the vehicle weight. The decoupled-control strategy and control system have enabled ME02 to realize a stable propulsion following very well the demand patterns.

To restrain pitching motion and to realize a stable running with a soft contact on the guideway in the mass-control mode, an equivalent weight on the guideway should be regulated to be a suitable positive-value both in repulsive- and attractive-modes. As a experimental simulation of actual ME, it is true for the ME to run on land and/or under the water.

These experiments have also verified the theory of new combined levitation and propulsion for the amphibious LM vehicle ME. Complete levitation and propulsion control test of ME02 is being carried out now.

REFERENCES

[1] K.Yoshida, H. Takami and L. Shi : " Decoupled-Control Method for Levitation and Propulsion in Amphibious Train Marine-Express", *Memoirs of the Faculty of Engineering, Kyushu University*, **Vol. 55, No. 4**, pp.467-489, 1995.

[2] K.Yoshida, H. Muta and N. Teshima : " Underwater Linear Motor Car ", *Journal of Applied Electromagnetics in Materials 2*, pp.275-280, 1991.

[3] K. Yoshida and A. Sakurai ; " A Basic Study on Underwater Linear Synchronous Motor Model Vehicle ME02", *Committee for the study of the Marine Express Concept, ME Report*, **No. 3**, pp.1-10, 1992.

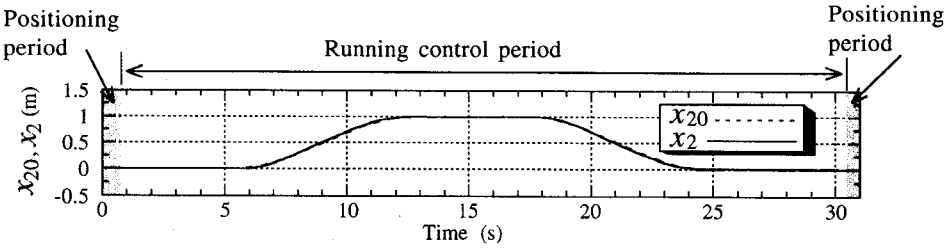
[4] K.Yoshida, H. Takami and L. Shi : " Attractive-Mode Levitation Control During a Standstill of an Underwater Travelling Marine-Express Model Vehicle ME02", *Proc. of ICEMA'96 China*, pp.175-178, 1996.

[5] K. Yoshida, H. Takami, L.Shi and A.Sonoda : " Standstill levitation-control by underwater LM car ME02 as a simulator of land travelling Marine-Express", *Record of 1996 Joint Conference of Electrical and Electronics Engineering in Kyushu*, p.429.

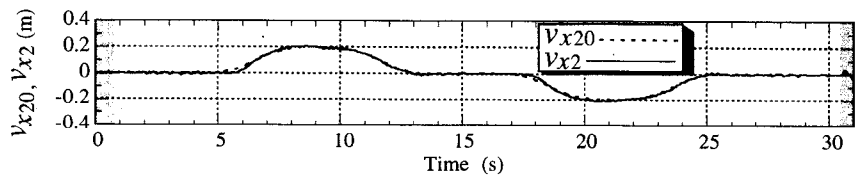
[6] K. Yoshida and H. Weh : " A method of modeling permanent magnet for analytical approach to electrical machinery", *Archiv, für Elektrotechnik*, **Vol. 68, No. 4**, pp.229-239, 1985-5.

[7] K. Yoshida and H. Weh : " Theory of a Controlled-PM Linear Synchronous Motor ", *Proc. of 10th Inter. Conf. on Maglev'88*, pp.259-268, 1988.

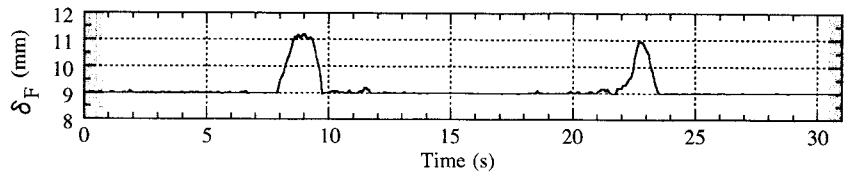
[8] K. Yoshida, H. Takami, N. Shigemi, Y. Nagano and A.Sonoda : " Repulsive-Mode Levitation and Propulsion Control of a Land Travelling Marine-Express Model Train ME03", *Proc. of LDIA'95 Nagasaki*, pp.41-44, 1995.



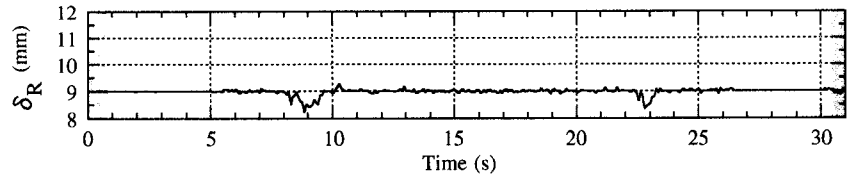
(a) Demand and measured vehicle-positions



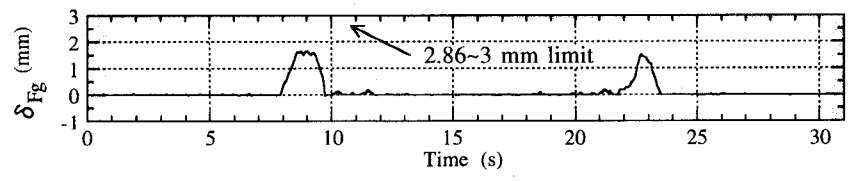
(b) Demand and measured vehicle-speeds



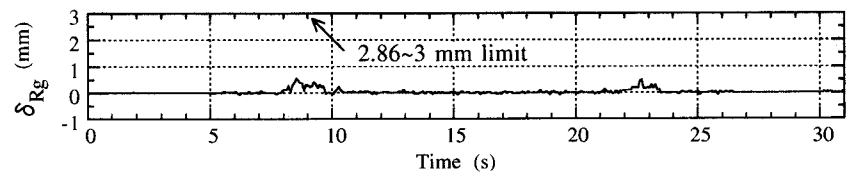
(c) Measured airgap-length by front sensor



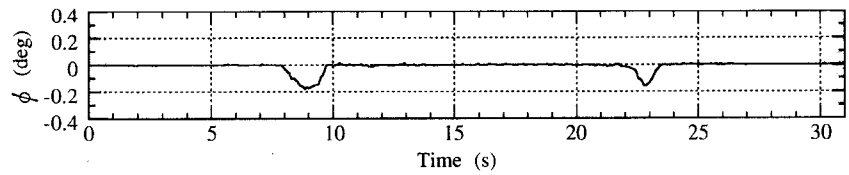
(d) Measured airgap-length by rear sensor



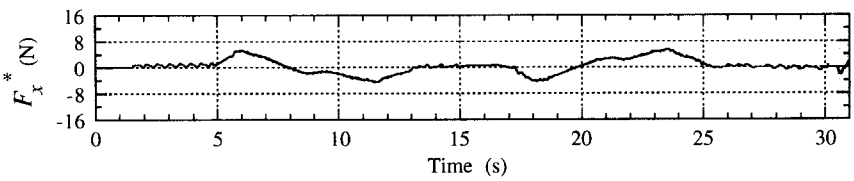
(e) Airgap-length between front upper-guide-roller and guideway



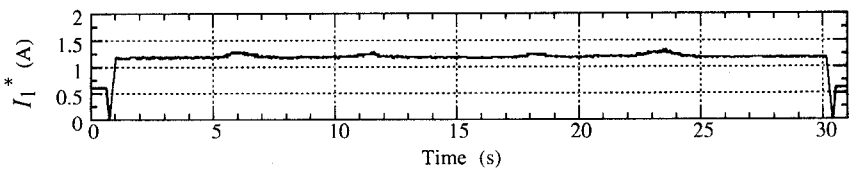
(f) Airgap-length between rear upper-guide-roller and guideway



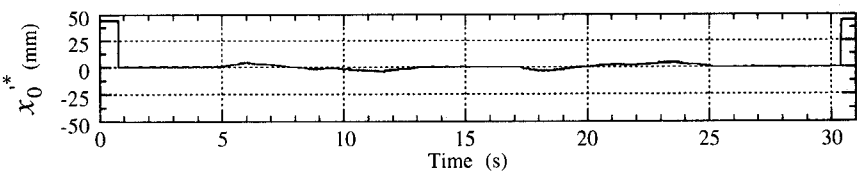
(g) Measured pitching-angle



(h) Command thrust-force

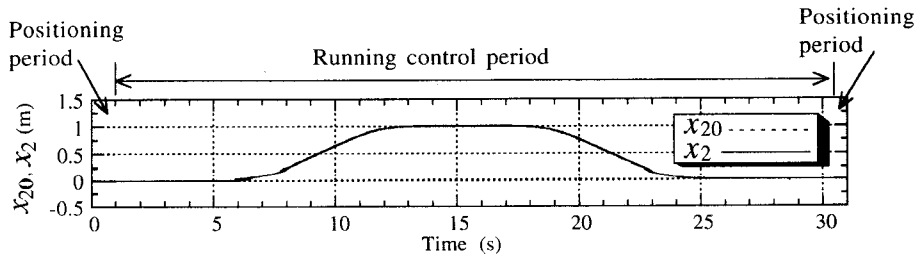


(i) Command effective-value of armature-current

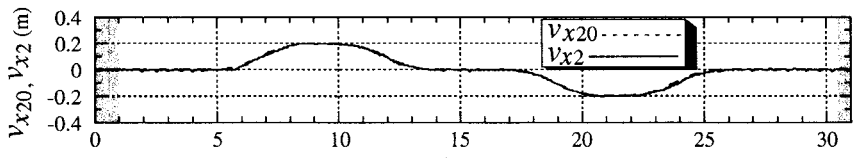


(j) Command mechanical load-angle

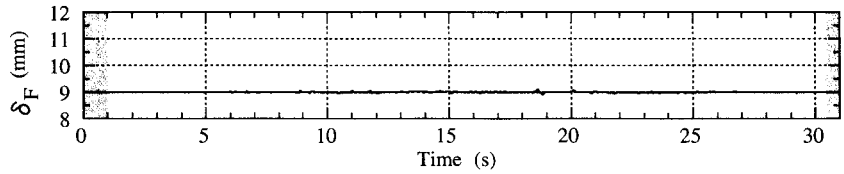
Fig.7. Running experiments in a mass-control mode with the equivalent weight regulated to be 'zero' by the lift force F_z'=0.459kg



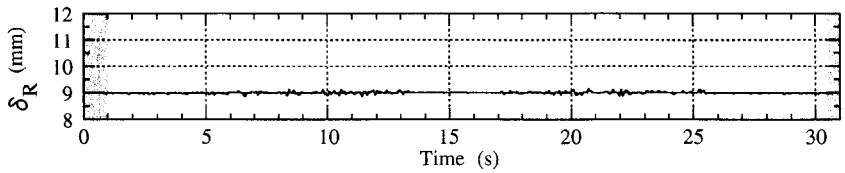
(a) Demand and measured vehicle-positions



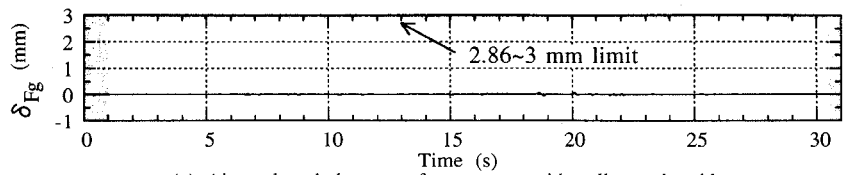
(b) Demand and measured vehicle-speeds



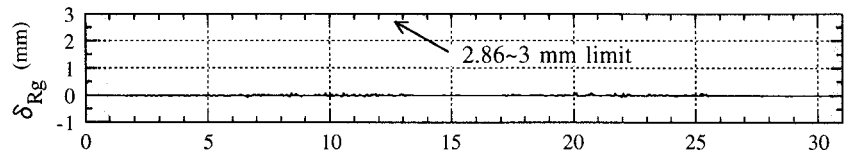
(c) Measured airgap-length by front sensor



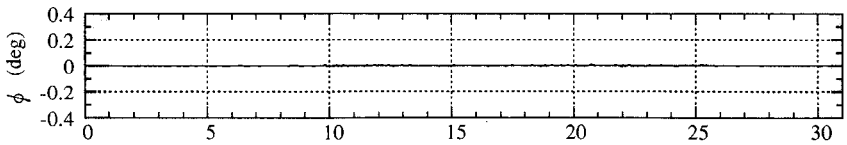
(d) Measured airgap-length by rear sensor



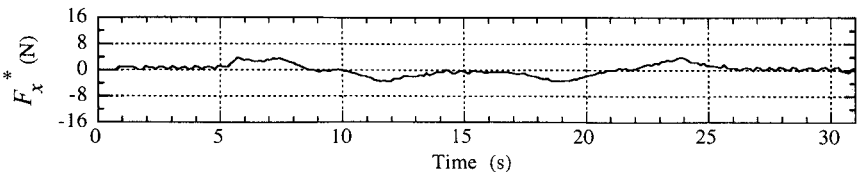
(e) Airgap-length between front upper-guide-roller and guideway



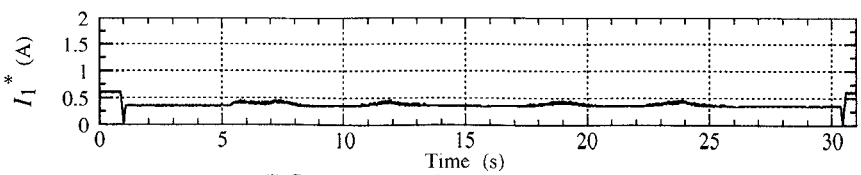
(f) Airgap-length between rear upper-guide-roller and guideway



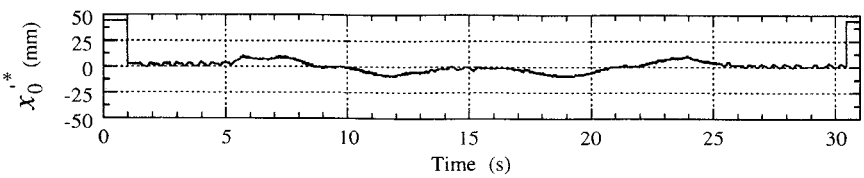
(g) Measured pitching-angle



(h) Command thrust-force



(i) Command effective-value of armature-current



(j) Command mechanical load-angle

Fig.8. Running experiments in a mass-control mode with the equivalent weight regulated to be 1.27kg by the lift force F_z^*=-0.815kg

DESIGN TRADEOFFS AND TECHNOLOGY OUTLOOK OF HIGHLY COMPACT INTEGRATED AC MOTORS

Jie (Jay) Chang, Ph.D., Sr. Member IEEE
Science Center, Rockwell International Corporation.
1049 Camino Dos Rios
Thousand Oaks, CA 91320, U.S.A
Email: jchang@rsc.rockwell.com

Abstract: Integrated AC motors offer many desirable features, such as high compactness, reduced material cost, reduced engineering time for installation or integration, and better protection against short circuiting and over-voltage due to dv/dt induced voltage reflection waves. This paper discusses the basic considerations of temperature sensitive component selection, device availability, design tradeoffs, and reduction of the dc-link capacitor which is the weakest component in the system. Preliminary experimental results are reported to verify the design concept. A brief technology outlook is given to prepare future challenges.

I. Introduction

There are increasing demands for compactness and high power density for integrated AC motor drives. In industry and commercial applications, integrated AC motors are becoming popular in textile fiber drives, motive mining machinery, spindles of machine tools, hermetic pumps, and motion controls in the power range of fractional to 30 Hp. Also, in today's all-electrical vehicle and more-electrical aircraft applications, the integrated AC motor is an interesting technology for achieving compactness and reduced-weight design to meet more stringent requirements of on-board power and actuator control systems.

Many of today's existing integrated motor products are restrained in a mechanical repackaging, where the power inverter is physically mounted onto or inside the motor housing frame. While this arrangement effectively reduces the power cable length, thus reducing the over-voltage spikes caused by high dv/dt and line voltage reflection, several important design issues remain unaddressed. The concerns arise primarily from new power converter design constraints, including elevated ambient temperature inside the motor housing, more confined space volume, and geometric dimensions. This paper discusses the following issues:

1. Availability and selection of temperature sensitive power semiconductor devices and passive energy storage components.
2. Improvement of the control and power converter topology to better fit integrated motors.
3. Further technology outlook and opportunities in overall motor-drive system optimization.

II. Selection of Active and Passive Power Devices for Elevated Ambient Temperatures

The major technological obstacle for the elevated temperature high power density power converter for integrated AC motors is the unavailability of high temperature power components, such as high power semiconductor switching devices, large value of dc-link capacitors, as well as control electronics devices and passive components. Consequently, challenges presented to the designers for the next level of innovations include alternative power devices, total optimization of topology and whole system, thermal management and cost-effective design.

A. Selection of temperature sensitive silicon power devices

An integrated motor/drive is a pair of motor and power converters that are pre-matched in power rating and are tightly packaged as a single unit. The present generation of integrated motor/drives commonly consists of a power converter and a fan-cooled motor which are thermally decoupled from each other by using two independent heat sinks and cooling systems. The intention is to provide a benign local cooling condition for a conventional power converter whose major components are sensitive to elevated temperatures caused by the motor heat flux. Though effective in thermally isolating the power electronics from the motor frame heat sink, this decoupled structure is probably not the optimal design for high compactness, minimum material usage, and reliability. This approach, however, will likely continue until high temperature power electronic devices and better optimal topology become available and cost effective.

Improved compactness can be achieved when power electronics reside inside the motor housing This effectively elevates the ambient temperature of the power converter by 20° to 40°C (depending upon individual cooling and packaging) above the industry standard ambient temperature, 40°C. This easily pushes power electronics devices, such as IGBTs operating at the edge of the maximum allowable junction temperature. In many cases, substantial derating is necessary to achieve acceptable design reliability. System level

optimization and tradeoffs must therefore be given to provide a reliable, compact, yet affordable design.

Although IGBTs are popular power devices for today's variable-frequency power inverters, they are rated for operation below or at 125°C. The devices are typically derated to zero operating power at 150°C, as shown in Fig. 1. The temperature effects on power semiconductor device parameters include on-resistance or on-stage forward voltage drop, break down voltage, leakage current and switching speed [2]. A power electronics engineer must understand the change of the power device's characteristics versus the temperature rise and to further incorporate the characterizations into the circuit design to ensure a proper and reliable operation. For example, the effects of temperature on leakage current, forward on-stage voltage drop, and switching speed are important because they might significantly increase total power losses, thus increasing thermal stress and cooling requirement for integrated motors.

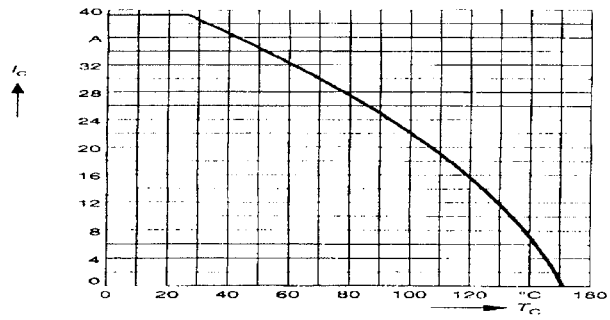


Fig. 1. An IGBT(1200V, 25A) current derating characteristics

As an alternative to high power switching devices, MOS controlled thyristors (MCT) are capable of operation at higher temperatures [4]. In addition, MCTs have been reported to have higher current density and lower conduction loss in comparison with existing IGBT devices [4,5]. A brief comparison of key specifications of IGBT and MCT devices at elevated temperature is shown in Table I below.

A new generation of MCTs is expected to have a higher maximum junction temperature than IGBTs [5]. New MCTs are specified to operate reliably at 150°C without current derating. This would improve the power silicon utilization factor at elevated temperature. A higher maximum junction temperature allows higher base plate or heat sink temperature; thus providing tolerance to higher ambient temperature and reducing the heatsink design requirement. Lower conduction and switching loss induces a smaller temperature difference between the junction and the base plate, which also supports higher base plate temperature. The key specifications given in the second row of Table 1 allow the device base plate temperature in reliable operation to reach the maximum expected motor case temperature for class F insulation. In this case it is even possible to have the power devices directly heat-sinked to the motor frame, eliminating the need for separate heat sinks, thermal isolation and the second cooling system. This is expected to yield a more compact and economical design for integrated motor/drive systems than the conventional approach.

Table I. Comparison of IGBTs and MCTs At Elevated Temperature

Device	Conduction Loss	Current Density	Rated Operating Temperature	Derating needed At 150 C
IGBT	100%	100%	125 C	100%
MCT	70%	200%	>150 C	0%

B. Selection of temperature sensitive dc-link power components

Design of power electronic systems for use at elevated temperatures, such as power converters for integrated motors, requires high voltage and high energy density passive devices that can withstand these temperatures. Of all the passive devices, including resistors, inductors, and magnet components, perhaps none are so problematic as capacitors, especially high voltage and high value capacitors for power switching or conditioning applications. Capacitors made with an insulator with a higher dielectric constant exhibit unstable capacitance and high leakage current at elevated temperatures. In selection of dc-link capacitors, characteristic data for commercially available aluminum electrolytic capacitors is seldom provided above 105°C. The problem of isolated hot spots induced by surge currents in the dc-link is compounded by the dielectric's weakness of being prone to breakdown when exposed to elevated temperatures. This effect can induce catastrophic component failure, with a case rupture or explosion. This unfortunate problem needs to be solved for harsh-environment applications. Since the lack of elevated temperature capacitors is a major constraint in developing high temperature power converters, design tradeoffs and system topology optimization are necessary to reduce the dc-link capacitance to a minimum.

III. Power Converter Topology

A. Adaptive PWM control to reduce DC-link capacitors

Various power converter topologies have been evaluated for integrated motor applications. Considering the cost effectiveness, a rectifier-inverter configuration with adaptive PWM control and optional soft-switching, as shown in Fig. 2, is suitable for low-cost non-regenerative integrated drive. Motor technology selection and tradeoffs will be discussed in section IV.

Traditional PWM control assumes the dc voltage input is constant. It requires large electrolytic capacitors in the dc-link to filter out harmonics at six times line frequency (6 f_1) and reduce the dc voltage peak-peak ripple to 2-3% at loaded

condition. This becomes a very difficult design requirement for

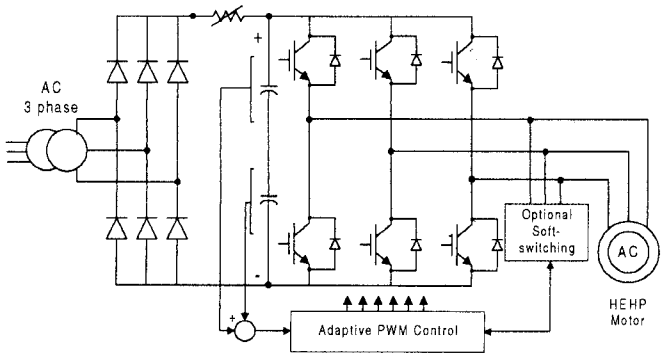


Fig.2. Adaptive PWM control and optional soft-switching

integrated motors because high value and high voltage capacitors are problematic and not available at elevated temperature as aforementioned. An adaptive PWM controlled inverter scheme has been developed. The proposed PWM incorporates the dc-bus voltage variation in each PWM cycle to produce desired output based upon time-averaging principle. This PWM method is therefore less sensitive to dc-bus voltage variation and benefits the deduction of the dc capacitor size. Together with modern AC motor technology with interior permanent rotor, the optimal design proposed in this paper reduces the dc-link capacitor by 60-70% in comparison with the conventional design.

The tail current during a power device turn off has been observed to increase as the device junction temperature increases. Soft switching technique [5-7] could play a more important role in elevated temperature converters than in conventional converters.

B. Coordinated Dual-Bridge PWM control for Regenerative integrated AC motors

The dual-bridge power converter with coordinated PWM control is an interesting configuration for regenerative integrated motors. The merit of this configuration is to control

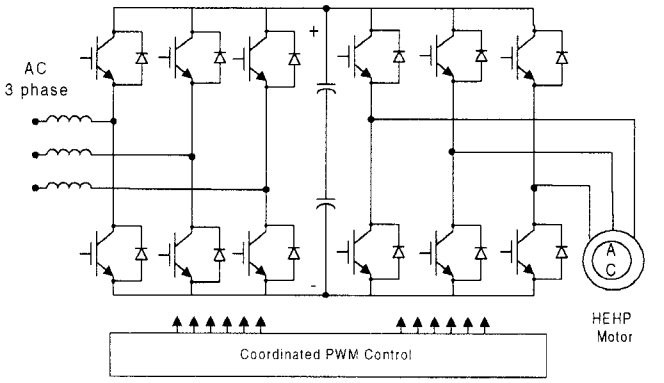


Fig 3. Coordinated PWM control of a dual-bridge converter

the switching instants of two PWM bridges in a coordinated fashion such that the load reactive current can be circulated back to utility lines instead of circulating between the load and the dc-link energy storage component. However, careful design is needed to avoid resonant overvoltage during energizing and line power recovery.

IV. Motor Technology Selection

To minimize the total thermal losses and reduce the requirement for heat dissipation, a high efficient motor is very desirable for the integrated motors. Reducing the dc-link capacitors needs to minimize the reactive load current circulating between the motor magnetizing inductor and the dc-link capacitor. This can be achieved by using an optimally designed high power factor motor. Comparative studies and simulation have been carried out for two groups of motors rated at 3 Hp, 460 V, four pole with a base speed of 3000 and 10000 rpm, respectively. The comparison results from different motor designs [12] are given in Tables 2 and 3, where PM is a synchronous AC motor with an optimized permanent magnet rotor design, and SR and IM are synchronous reluctance, and cage inductance motors, respectively. P_{out} is the motor output power and CPSR represents constant power speed range.

Table 2: Motor Performance Comparison (3,000 Rpm)

Motor type	T_e (p.u.)	P_f (kw)	P_{cu} (kw)	η (%)	Power factor cosϕ	Speed (rpm)	CPSR	PM (Tesla)
PM	1.0	0.004	0.032	91.29	0.93	3,000	>5.0	0.86
SR	1.0	0.006	0.075	82.72	0.55	3,000	2.5	0.0
IM	1.0	0.005	0.080	81.10	0.82	3,000	2.5	0.0

Table 3: Motor Performance Comparison (10,000 rpm)

Motor type	T_e (p.u.)	P_f (kw)	P_{cu} (kw)	η (%)	cosϕ	Speed (rpm)	CPSR	PM (Tesla)
PM	4.5	0.147	0.010	88.94	0.88	10,000	>5:1	0.86
SR	4.5	0.186	0.039	78.71	0.53	10,000	2.5:1	0.0
IM	4.5	0.190	0.040	76.21	0.78	10,000	2.5:1	0.0

Obviously, the optimized PM motor has higher efficiency, improved power factor, and wider speed range in comparison with other motors.

V. A Design Example and Experimental Results

Based on the comparative technology study, AC machines with permanent magnet rotor become a favorable choice for highly compact integrated motors.

The voltage and flux equations in the synchronous reference frame can be expressed by:

$$V_d = r_d i_d - w_r \lambda_d \quad (1)$$

$$V_q = r_s i_q + w_r \lambda d \quad (2)$$

$$\lambda_d = L_d i_d + \lambda_m \quad (3)$$

$$\lambda_q = L_q i_q \quad (4)$$

The motor electromagnetic torque is given by:

$$T_e = \frac{3}{2}\frac{p}{2}\left[\lambda_d i_q - \lambda_q i_d\right] = \frac{3}{2}\frac{p}{2}\left[\lambda_m + \left(L_d - L_q\right) i_d\right] i_q \quad (5)$$

Various system schemes of PM motor drives have been reported [8-10] based on the conventional PWM control. To the author's best knowledge, the overall optimization and tradeoffs of the combination of power converter and motor have not been sufficiently investigated. It is necessary to further evaluate and verify the total optimal design approach and the potential benefits, which is proposed and reported in this paper. Digital simulations are performed and shown in Figure. 4. Figure 4 (b) illustrates that significant unbalances in motor phase currents are produced by the effect of large dc-bus variations if the inverter is controlled by the conventional PWM. In practice, it is not surprising to see such V_{dc} variations at elevated temperature equipment because of the lack of high value and high voltage capacitors, capacitor degradation, or size limits.

The dc bus variation in Figure 4 is simulated under the condition of losing one input phase. However, regardless of whether the variation is caused by reduced dc-link capacitors or loss of one input phase, the effects of the V_{dc} variation on the motor current and speed control remain the same. The unbalanced motor phase currents would often excite an unstable operation of the AC motor. The simulated situation is also very similar to that of single-phase powered AC drives.

In comparison with Figure 4(b), Figure 4(c) shows improved current waveform controlled by the proposed adaptive PWM method. As shown in Fig. 4, the performance under adaptive PWM control is less sensitive to large variation of the inverter dc-bus voltage. It maintains good stability of the motor speed control for a 3Hp 460 V PM motor, even though the dc-link capacitor is reduced to 50 uF. The adaptive PWM control should be beneficial for the dc-link capacitor reduction in both high temperature and conventional temperature operation, and for both three-phase or signal-phase converter configurations.

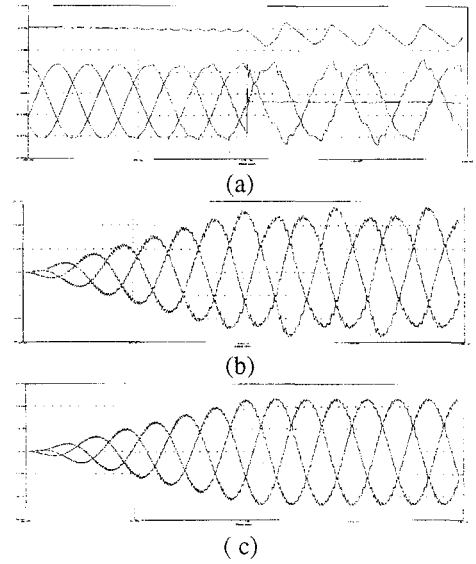
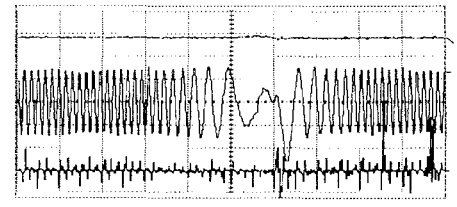


Fig. 4. Control stability comparison between conventional and adaptive PWM.

Experimental Results

A 3 HP Lab prototype of a compact integrated motor is prototyped using an AC motor with an interior permanent rotor. The dc-link capacitor of the prototype is reduced to 50 uF based on the simulation results. The tested motor current waveform and the dc capacitor's voltage and current waveform in a $\pm$ 1800 rpm speed reversal are shown in Figure 5. The motor is under volts/Hz control mode while it can be controlled in high performance modes, such as sensorless field orientation. The motor maintains a good stability and control during the start and speed reversals, as well as during normal operation.



Trace 1: DC capacitor voltage, 100V/div
Trace 2: Motor current, 5A/div
Trace 3: DC capacitor current, 2A/div
Time: 2 sec/div

Fig. 5. Waveform in a speed reversal of $\pm$ 1800 rpm.

VI. Outlook of Future Technology and Opportunities

A. Elevated temperature control devices and components.

In addition to high voltage power electronics devices and components, reliable active and passive microelectronics ICs and components are indispensable for controlling the power converters at elevated temperature. Potential markets, such as automotive and aerospace industries, have led semiconductor manufactures to begin developing electronics devices and components for elevated temperature operations. Table 4 provides an outlook of availability of control electronic devices for elevated ambient temperature operation at 125°C.

The fundamental limitation of the silicon integrated circuit is the excessive generation of carriers by the thermal energy. In the temperature range above 150°C, silicon on insulator (SOI) technology is used for processing new family of integrated circuits. The SOI wafer contains a thin silicon layer over a thick buried oxide layer on a bulk silicon substrate. The leakage current at high temperature can be reduced by a two orders of magnitude by using SOI technology. However, the market may not be fully open for this technology until the cost of SOI chips is close to those of industry or automotive grade chips. This in turn needs a driving force from large volume productions, including, perhaps, future power electronic systems for automotive, aerospace, and industry applications at elevated temperatures.

Table 4 Outlook of elevated temperature control components

Device	Description	Replacement Of Industry Standard Parts	Technology Availability
DSP	32 bit, floating point, 50 Mhz	TMS320C32 or TMS320C31	Yes
PROM (OPTROM)	Size > 1M, . Speed < 120nsec	27Cxxx	Yes
PGA or OTPGA	OTPGA		Yes
PAL	30 ns propagation delay	22V10	Yes
Quad Compactor	Quad voltage compactors	LM139	Yes
Quad or dual Amp	Unity Gain Bandwidth > 1MHZ	TL084 or TL082	Yes
A/D converter	A/D converter & sample/hold, 12 bit, 10 us , +- 10V	AD1674	Yes
D/A	, 12 bit, +- 10 V	ADC312	Yes
Mux and Demux	16-1 or 8-1 +- 10 V	ADG506	Yes
Bipolar transistors / MOSFET	> 30 mA.		Yes
Optical coupler	I_D=16 mA, 2500 V RMS, Faraday shield	TLP559	No

B. Electronics motors with zero DC-link capacitor

AC-AC power conversion [1] is a technology trend in variable speed AC motor drives. A simplified circuit schematic is shown in Fig. 6. AC-AC PWM converter performs a direct power conversion in one stage without using passive energy storage components in a dc-link. The PWM voltage waves of phase-to-neutral and line-to-line output are given in Fig.7.

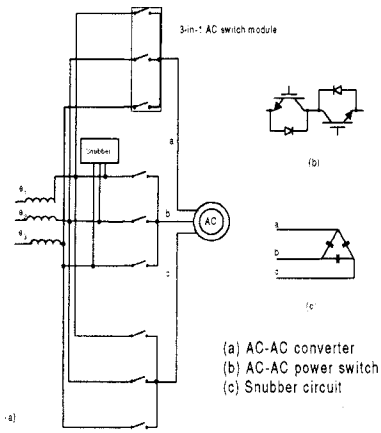
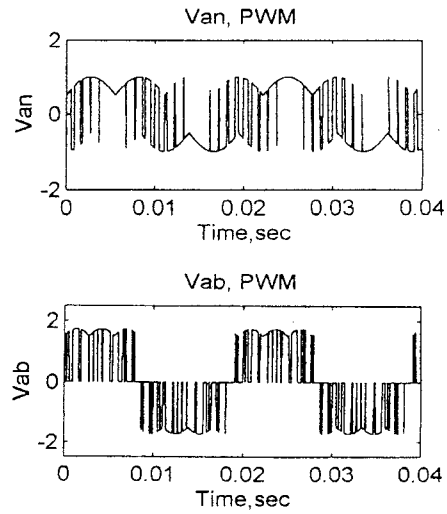


Fig. 6. Basic AC-AC converter fed Smart AC Drive

Main technology payoffs of this topology can be found for future smart electronic motors, including (a) eliminating large dc-link electrolytic capacitors and increases product life expectancy; (b) meeting market expectations on low current harmonic distortion without using costly harmonics filters; (c) providing value-added power products by increasing input wave-form power to near unity; (d) a more compact design with a smaller footprint; (e) inherent power regeneration to provide true four-quadrant operation.



(a) Phase phase-to-neutral voltage
(b) Line-to-line output voltage

Fig. 7. Simulated output voltage waves of AC-AC converter.

The main technical challenges include:

- Bilateral high power switches.
- Low switching-loss and safe commutation.
- New control approach to increase voltage throughput.
- Optimal hardware and software co-design.

VII Conclusions

Basic considerations of temperature sensitive power device selection, component availability, reduction of the dc-link capacitors and design tradeoffs of power converters at elevated temperature for integrated motors have been discussed. Preliminary experimental results are reported to verify the concept. By a totally optimized design, overall integrated motors can be very compact, less weight with low cost while offering improved performance for high power density integrated motors and actuators. A brief technology outlook has been given to prepare future challenges.

Acknowledgments

The author wishes to thank his colleagues at Rockwell Science Center and Rockwell Automation for their valuable inputs, assistance and discussions, especially Dr. Sujeet Chand, Mr. Steve Chiu and Dr. Z.M. Zhao. Special thanks are due to all colleagues at Electronic Circuit Development, Research and Technology Center of Boeing North American, for their invaluable technical supports, especially Dr. Zef Shanfield, Dr. Dave Seib and Dr. Gene Dines. Funding support received from Boeing and HiTeC program is gratefully acknowledged.

References

[1] L. Gjugyi and B. Pelly, "Static Frequency Changes", Wiley, 1996.

[2] J. Bromstead, et al., "Silicon Device Performance Measurements to Support Temperature Range Enhancement", Auburn University, 1994.

[3] H. Kurnia, D. Divan, K. Shenai, "High Temperature Turn Off Performance of IGBTs in Resonant Converters", WEMPEC Report, 1995.

[4] V. Temple, D. Watrous, S. Arthur and P. Kendle, "MOS-Controlled Thyristor Power Switches", PCIM, Nov. 1992.

[5] E. Yang, V. Temple and S. Arthur, "Switching Loss of 600V Gent and Gen-2 P-MCTs in Soft-Switching", APEC, 1995, pp. 746-754.

[6] R.W. De Doncker, D.M. Divan and G. Venkataramanan, "Design Methodologies for Soft-Switched Inverters." IEEE-IAS Conf. 1998, pp. 758-766

[7] H. Li, N. Kurkut, et al., "High Temperature Characteristics of IGBTs in Soft and Hard Switching Converters", APEC, 1995, pp. 733-735.

[8] Z.M. Zhao, L.Y. Xu and A El-Antably, "Strategies and Computer-aided Package for Design and Analysis of Induction Machines for Inverter-Driven Variable Speed Systems", IEEE IAS Annual Meeting, 1995, pp. 523-529.

[9] Jahns T.M., "Flux-Weakening Operation of an Interior Permanent Magnet Synchronous Motor Drive", IEEE Trans Ind. Appl., Vol. IA-23, No.4, Jul/Aug 1986, pp. 681-689.

[10] Sneyers, B., Novotny D.W. and Lipo T.A., "Field Weakening in Buried Permanent Magnet ac Motor Drives", IEEE Trans. Ind. Appl., Vol. IA-21, No. 2, Mar/Apr 1991, pp. 398-407.

[11] Bose, B.K., "A High Performance Inverter-Fed Drive System of an Interior Permanent Magnet Synchronous Machine", IEEE Trans. Ind. Appl., Vol. IA-24, No. 6, Sep/Oct 1988, pp. 987-997.

[12] Zhao Z. M., "Quantitative Optimization for Added Magnet in Synchronous Reluctance Machines", Rockwell work report, 1997.

Axial Type Flat PM Motor with Large Air Gap

Masayuki Sanada, Shigeo Morimoto, Yoji Takeda
Dept. of Electrical and Electronic Systems, College of Engineering
Osaka Prefecture University
1-1 Gakuencho, Sakai, Osaka 593, JAPAN
Fax: +81-722-52-6782, Phone: +81-722-52-1161 Ext. 2265
E-mail : sanada@gto.ees.osakafu-u.ac.jp

Abstract --- **An axial type flat permanent magnet motor (AFPM motor) is used for audio visual equipment and information actuators, and so on. However, it is limited to small capacity with small air gap.**

In this paper, the characteristics of the AFPM motor with large air gap to protect and/or separate between the rotor and the stator for new applications are examined. Tested motor has 8mm air gap length and 170W out put capacity. Maximum efficiency of the tested motor is about 80%, and if the air gap length is spread to 12mm, the tested motor keeps 66% efficiency.

Moreover, it is shown that the steady state characteristics of the AFPM motor driven by the 6-step inverter can be estimated with the *d-q* coordinates modeling.

I. INTRODUCTION

There is an application such as the pump application in the water, which demands the sealing separation between rotating part and the motor. It is generally used that the motor power transmit to the load by magnetic coupling for this purpose. The radial type permanent magnet (PM) motor with large air gap and the partition to reduce the size of the equipment has been examined [1]. However, this radial construction becomes somewhat complex.

The equipment construction can be simplified, if an axial type flat PM motor (AFPM motor) with large air gap and partition has enough performance. The total thickness of the equipment can be decreased. Moreover, reliability of the system is improved by reduction of mud sticking. This AFPM motor has been used for audio visual equipment and information actuators, and so on. However, it is limited to small capacity with small air gap [2].

In this paper, the characteristics of the AFPM motor with large air gap to protect and/or separate between the rotor and the stator for new applications are examined.

Moreover, it is shown that the steady state characteristics of the AFPM motor driven by the 6-step inverter can be estimated with the *d-q* coordinates modeling.

II. STRATEGY OF CHARACTERISTICS ANALYSIS

A. Basic Equation of PM Motor

Generally, the steady state characteristics of a PM motor driven by the sinusoidal PWM inverter can be calculated with the *d-q* coordinates model. The voltage equation of a PM motor in the *d-q* coordinates are expressed as follows [3],[4].

$$\begin{bmatrix} v_d \\ v_q \end{bmatrix} = \begin{bmatrix} R & -\omega L_q \\ \omega L_d & R \end{bmatrix} \begin{bmatrix} i_d \\ i_q \end{bmatrix} + \begin{bmatrix} 0 \\ \omega \phi_a \end{bmatrix} \quad (1)$$

$$V_a = \sqrt{{v_d}^2 + {v_q}^2} \quad (2)$$

where,

i_d, i_q : *d*- and *q*-axis components of armature current,
v_d, v_q : *d*- and *q*-axis components of terminal voltage,
ϕ_a : $= \sqrt{3/2}\,\phi_f$
ϕ_f : maximum flux linkage due to permanent magnet per phase,
R : armature resistance,
L_d, L_q : *d*- and *q*-axis components of armature self-inductance,
V_a : terminal voltage on a steady state,
ω : electrical angular velocity.

Fig. 1 shows the basic vector diagram of the PM motor in the *d-q* coordinates. The phase angle β between the phase of an induced voltage by the permanent magnet and phase of an armature current is controlled more than 0° in the flux-weakening control. As shown in Fig. 1, the permanent magnet flux ϕ_a is demagnetized by the *d*-axis

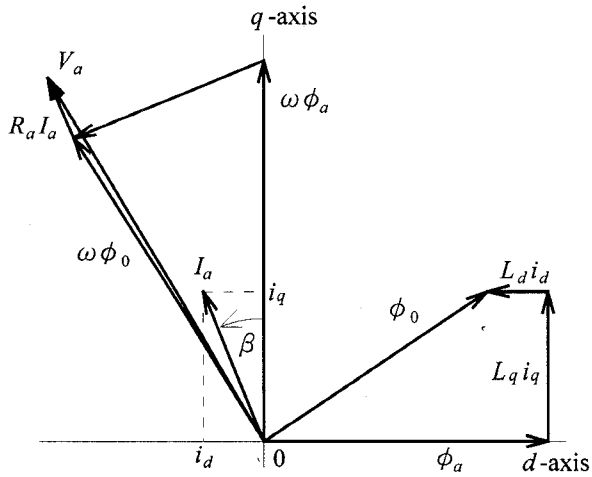


Fig. 1. Vector diagram of the PM motor.

armature reaction $L_d i_d$. This operation is similar to the field-weakening control in the dc machines. As the result, the terminal voltage V_a becomes small.

As the armature linkage flux and the armature winding inductance becomes small in the large air gap PM motor, terminal voltage can be kept low level in the high speed condition. This advantage is preferable for high speed pump application and so on.

Generally, the PM motor is driven by the i_d=0 control, because the torque is in proportion to the current and free from the demagnetization of permanent magnet. In the i_d=0 control, the phase angle β always keeps 0°.

The torque of PM motor is given by the following equation.

$$T = \mathrm{P_n}\{\phi_a + (L_d - L_q)\, i_d\} i_q. \qquad (3)$$

where,

T : torque,

$\mathrm{P_n}$: number of pole pair.

The magnet torque is expressed by the term of $\mathrm{P_n}\,\phi_a i_q$, and the reluctance torque is expressed by the term of $\mathrm{P_n}\,(L_d - L_q)\, i_d\, i_q$ in the equation (3). As the tested AFPM motor does not have the saliency, only the magnet torque can be obtained. If the motor has the inverse saliency such as a interior PM motor, the positive reluctance torque can be also obtained by the negative *d*-axis current.

B. Voltage and Current Equation of 6-Step Inverter Driven AFPM Motor

The basic equation is guaranteed strictly under the condition of the sinusoidal flux distribution and current.

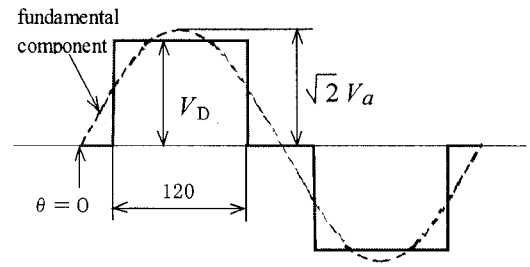


Fig. 2. Trapezoidal voltage and its fundamental component.

And it is able to calculated the characteristics of a PM motor driven with the PWM inverter which has distributed armature winding. However, voltage and current wave form of PM motor driven with 6-step inverter becomes trapezoidal, and includes many harmonic component. Figure 2 shows trapezoidal voltage wave form and its fundamental component.

The characteristics of the AFPM motor driven by the 6-step inverter can be calculated with the *d-q* coordinates model considering the following fundamental component.

$$V_a' = \frac{\sqrt{6}}{\pi} V_D \qquad (4)$$

$$I_a' = \frac{3}{\pi} i_D \qquad (5)$$

where,

V_a', I_a' : fundamental component of the armature voltage and current,

V_D : amplitude of the trapezoidal voltage wave form,

i_D : rms value of the trapezoidal current.

In this paper, characteristics calculation of the AFPM motor is used the revised voltage and current equation shown in Eq.(4) and Eq.(5).

III. TESTED MOTOR CONSTRUCTION

Figure 3 shows the scheme of the tested motor. The specifications of the tested motor are shown in Table 1. It has 3-phases 6-coils concentrated winding stator, 8-poles Nd-Fe-B permanent magnet rotor.

As the aluminum ring can be used to prevent scattering of permanent magnet in the axial construction, it is able to sustain the magnet without damage to the motor characteristics. The stator is constructed with the ferrite core which has a good high-frequency characteristics,

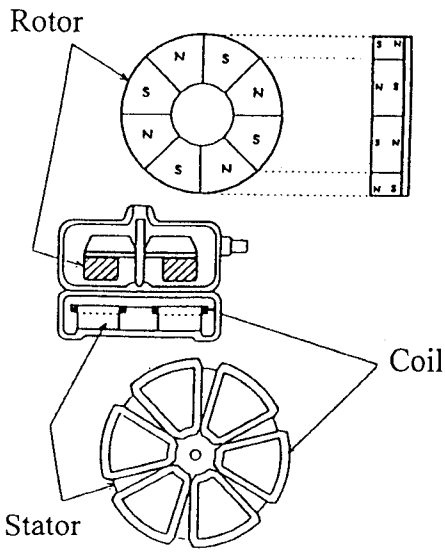


Fig. 3. Scheme of the tested motor.

TABLE I Specification of the tested motor.

Item	Value [Unit]
Stator winding	3-phase 6coils
Stator diameter	96 [mm]
Turns of coil	50 [turns]
Number of rotor poles	8 [poles]
Rotor diameter	80 [mm]
Permanent magnet	Nd-Fe-B
Air gap length	8 [mm]
Rated voltage	110 [V]
Rated speed	9000 [rpm]
Rated torque	2 [kg-cm]

because the number of pole pair of the tested motor is 4 and fundamental frequency becomes twice as high as the normally designed motor [5]. The tested motor has 8mm air gap length and 4mm rotor yoke thickness. As a permanent magnet is magnetically equal to the air, the length of d-axis flux path and the q-axis path becomes almost equal. As the tested motor is non-salient machine d- and q-axis inductance becomes the same value. This tested motor is driven with the $i_d = 0$ control.

Figure 4 shows the scheme of the experimental system. The motor is driven with the 6-step inverter. The rotor position is detected by the hole sensor [6].

Figure 5 shows experimental results of the phase voltage and phase current wave form. As the phase difference between voltage and current is almost zero, it can be seen that the tested motor is driven with the $i_d = 0$ control mode. As the current wave form is nearly the trapezoidal, the revised equation can be used to estimate the steady state characteristics.

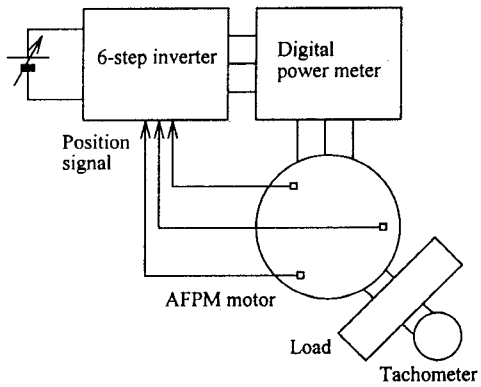
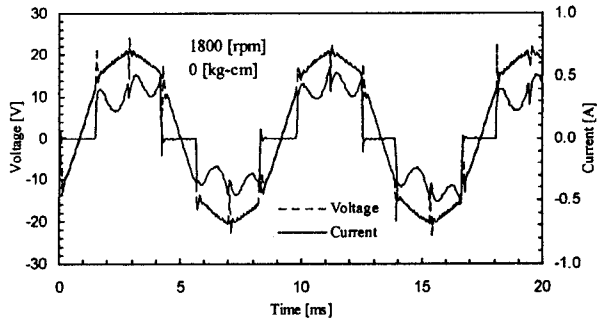
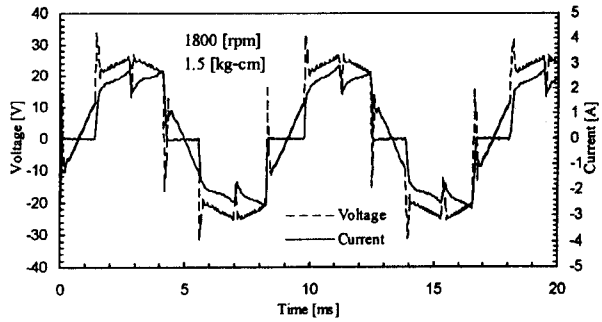


Fig. 4. Characteristics measurement system.



(a) No-load condition.

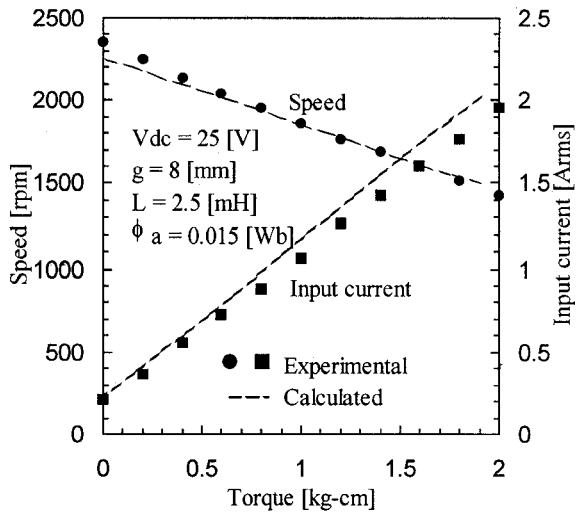


(b) 1.5kg-cm load condition.

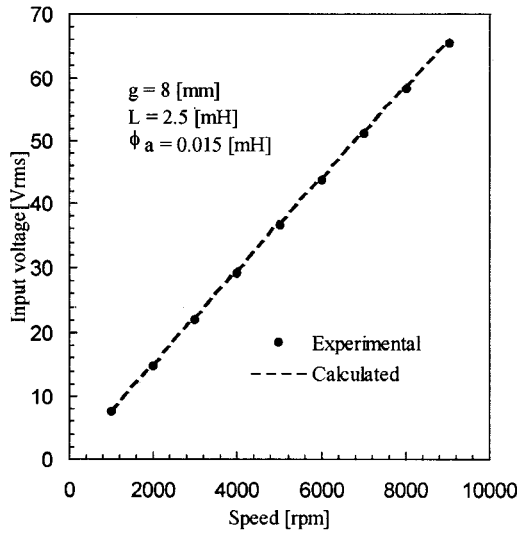
Fig. 5. Wave form of voltage and current.

IV. ANALYSIS AND EXPERIMENT OF CHARACTERISTICS

Figures 6 and 7 show the calculated steady state characteristics of the tested motor, compared with the experimental characteristics. Table 2 shows the analytical parameter. In Figs. 6 and 7, the plotted points express the experimental results and broken line shows calculated results. The calculated results agree well with the experimental results. The steady state characteristics of the AFPM motor driven by the 6-step inverter can be calculated with the d-q coordinates model considering the fundamental component. Figure 6(a) shows torque versus speed and current characteristics under the condition of 25V dc-link voltage.



(a) Torque versus speed, current characteristics.



(b) No load characteristics.

Fig. 6. Steady state characteristics of the AFPM motor.

TABLE II Analytical parameter.

Item	Value [Unit]
Armature linkage flux	0.015 [Wb]
Winding inductance	2.5 [mH]
Winding resistance	1.2 [Ω]

1500rpm speed is obtained in the 2kg-cm load condition, and input current is about $2A_{rms}$/phase. Figure 6(b) shows characteristics in the no load condition. Nevertheless this tested motor has many rotor pole, terminal voltage is only 65V at 9000rpm speed. Figure 7 shows the induced voltage characteristics. The induced voltage is about 10V at 1500rpm.

As the linkage flux is small due to the large air gap, induced voltage becomes very small in comparison with

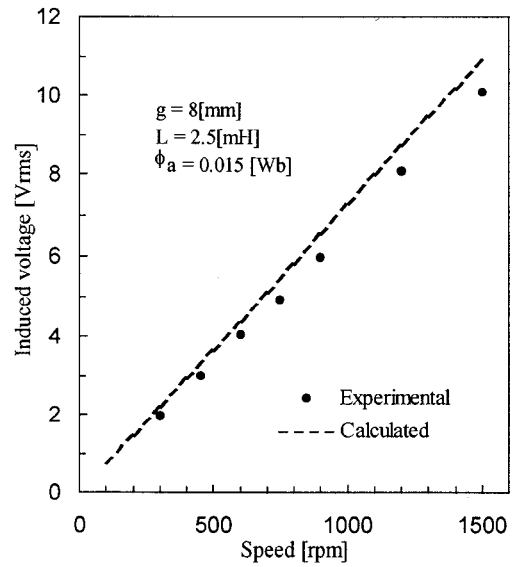


Fig. 7. Induced voltage characteristics.

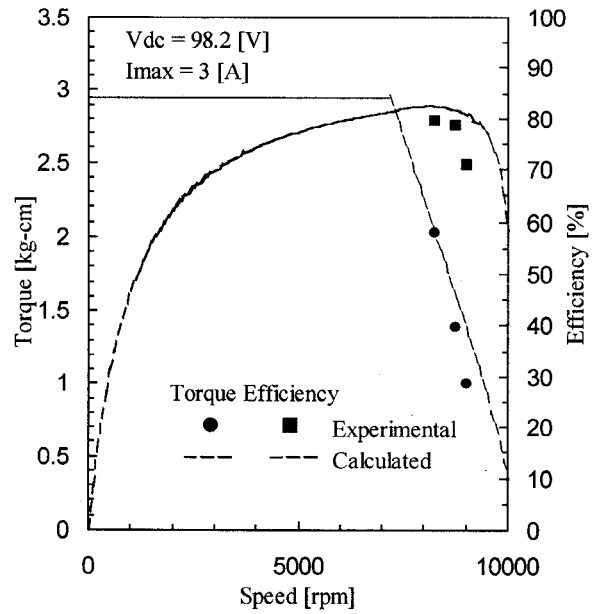


Fig. 8. Speed versus torque, efficiency characteristics.

the normally designed PM motor as shown in Fig. 7. Therefore, the voltage has the room at very high speed region. The cost of inverter and controller can be decreased for the application which using utility source as the flux-weakening control is not need.

Figure 8 shows the steady state characteristics under the 98.2V dc-link voltage and 3A current limit condition. Maximum torque is about 3kg-cm and terminal voltage is saturated at 7000rpm speed. And the load torque is decreased in the region higher than 7000rpm. As a result, 8260rpm speed is obtained at 2kg-cm load and 9000rpm at

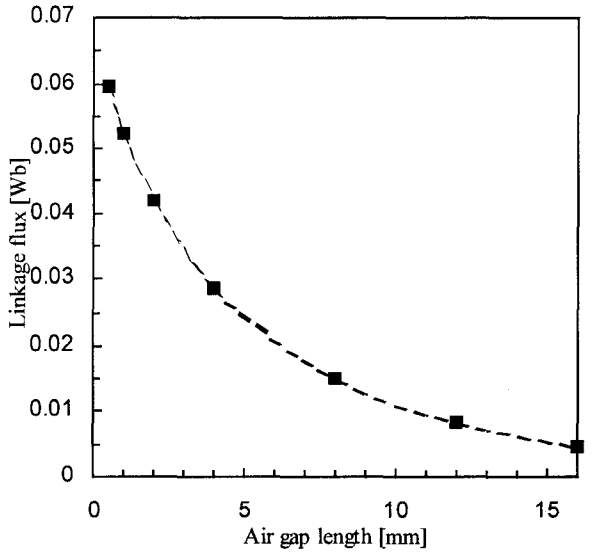


Fig. 9. Relation between gap length and linkage flux.

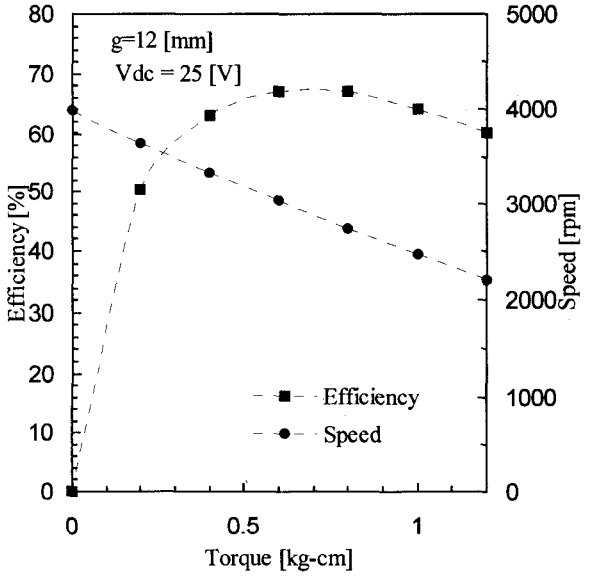


Fig. 10. Steady state characteristics with 12mm air gap length.

1kg-cm load condition. Maximum efficiency of the tested motor with 8mm air gap is about 80% in spite of large air gap and small armature linkage flux.

It is important that the relation of motor characteristics between air gap is clarified for the application demands partition between the rotor and stator. Figure 9 shows air gap versus armature linkage flux characteristics calculated by FEM. As shown in Fig. 9, the linkage flux at 12mm air gap is about half at 8mm air gap, for example.

Figure 10 shows the steady state characteristics with 12mm air gap length. At 2200rpm and 1.2kg-cm load condition, the tested motor still keeps 66% efficiency instead of the large air gap.

V. CONCLUSIONS

In this paper, the AFPM motor with large air gap was reported. This AFPM motor driven with the 6-step inverter under utility source shows good performance. And it was shown that the steady state characteristics of the PM motor driven by the 6-step inverter can be calculated with the *d-q* coordinates model with the fundamental component of voltage and current.

This AFPM motor is expected to new applications such as the maintenance-free pump.

REFERENCES

[1] Y. Nakamura, *et, al.* : "Brushless DC Motor with Large Airgap", T. IEE Japan, Vol. 117-D, No. 4, pp. 519-525 (1997).

[2] H. Takano, *et, al.* : "Optimum Values for Magnet and Armature Winding Thickness for Axial-field Permanent Magnet Brushless DC Motor", Record of 1990 IEEE-IAS Ann. Meeting, pp. 157-162.

[3] S. Morimoto, et, al. : "Motor Parameters and Operating Limits of PM Motor", T. IEE Japan, Vol. 110-D, No. 11, pp. 1171-1176 (1990).

[4] S. Morimoto, et, al. : "Variable Speed Drive System of Permanent Magnet Synchronous Motors with Flux-weakening Control", T. IEE Japan, Vol. 112-D, No. 3, pp. 292-298 (1992).

[5] K. Zaizen, et, al. : "A Novel type of Axial PM Motor with Large Airgap", Record of JIASC '95, No. 116.

[6] M. Sanada, et, al. : "An Axial Type PM Motor with Large Air Gap", Proc. of IEEJ Tech. Meeting on RM, RM-95-146, pp.59-64 (1995).

Performance of PM/Reluctance Hybrid Motor with Multiple Flux-Barrier

Shigeo Morimoto, Masayuki Sanada, Yoji Takeda
Dept. of Electrical and Electronic Systems
Osaka Prefecture University
1-1 Gakuen-cho, Sakai, Osaka 593 JAPAN
Fax : +81-722-52-6782, Phone : +81-722-52-1161 Ext. 2265
E-mail : morimoto@gto.ees.osakafu-u.ac.jp

Abstract —— **This paper examines several performances of synchronous motors, where the rotor has three slits per pole and thus a saliency exists. One synchronous reluctance motor and four PM/Reluctance Hybrid motors are produced and tested. Both of stator and rotor of all prototype motors are the same, but the volume of permanent magnet inserted into the slits is adjusted and as a result the magnet flux is different. The effects of adding magnet into the rotor on the machine parameters and the operating performance are examined by the various experimental results and the theoretical studies. It is shown that the prototype motor can offer a great choice of design varieties of speed versus power characteristics by adjusting the volume of permanent magnet and it can be applied to many applications.**

I. INTRODUCTION

Inverter-driven synchronous motors are widely used in high-performance variable-speed drives. Recently, the synchronous motors producing a reluctance torque such as an interior permanent magnet synchronous motor (IPM motor) and a synchronous reluctance motor are attracting attention to many applications for example an electric vehicle, a compressor drive. A typical schematic diagram of SM drive system is shown in Fig. 1. The armature current vector (namely *d*- and *q*-axis current components) is decided based on the control strategy from the command (torque or speed), and the current-regulated voltage-source PWM inverter drives motor so that the instantaneous armature currents follow their commanded values. In such drive system, many kind of current vector control strategies are proposed. The maximum torque per ampere control [1] is useful for producing the maximum torque considering the current constraint. In consideration of a ceiling voltage, the flux-weakening control [2, 3, 4] is very useful for a high-speed constant power operation, which is desired in traction and spindle drive applications. The optimal control strategy to expand the output capability considering both voltage and current constrains has been proposed [5]. The performances of optimally controlled synchronous motors are greatly influenced by the motor parameters, and the relationships between the motor parameters and the operating performance have been examined in detail [4, 5, 6, 7, 8].

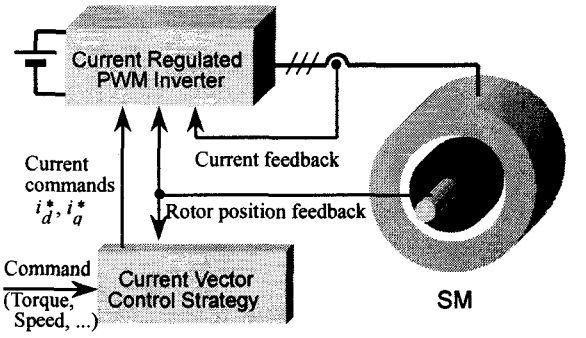


Fig. 1. Typical schematic diagram of SM drive system.

This paper examines various characteristics of the prototype synchronous motors, where a stator structure and a rotor structure of all motors is the same. The rotor of prototype motor has three slits per pole that work as a flux-barrier. The permanent magnets are inserted into the slits and the volume of permanent magnet is adjusted to control the magnet-flux linkage. The effects of adding magnet into the rotor on the machine parameters and the operating performance are discussed based on the various experimental results and the theoretical studies.

II. MOTOR MODEL AND BASIC SPEED VS. POWER PERFORMANCE

In this paper, the synchronous motors are modeled by a *d-q* reference frame circuit. The voltage equation and the torque are expressed by

$$\begin{bmatrix} v_d \\ v_q \end{bmatrix} = \begin{bmatrix} R_a+pL_d & -\omega L_q \\ \omega L_d & R_a+pL_q \end{bmatrix} \begin{bmatrix} i_d \\ i_q \end{bmatrix} + \begin{bmatrix} 0 \\ \omega \phi_a \end{bmatrix}, \qquad (1)$$

$$T = P_n \phi_a i_q + P_n (L_d - L_q) i_d i_q \ , \qquad (2)$$

where

i_d, i_q	d- and q-axis components of armature current,
v_d, v_q	d- and q-axis components of terminal voltage,
ϕ_a	$=\sqrt{3}\,\phi_e$,
ϕ_e	rms value of flux-linkage due to permanent magnet per phase,
R_a	armature resistance,
L_d, L_q	d- and q-axis components of armature self-inductance,
p	$=d/dt$,
P_n	number of pole pairs,
I_a	$=\sqrt{i_d^2 + i_q^2} = \sqrt{3} I_e$,
I_e	rms value of phase current,
V_a	$=\sqrt{v_d^2 + v_q^2}$.

As shown in (1) and (2), the performances of synchronous motors depend on the motor parameters such as the magnet-flux linkage and the inductance. From the past works [5, 6], it is clarified that an outline of speed versus power characteristics, where the ceiling voltage V_{am} and the ceiling current I_{am} are considered, deeply depends on the factor of $\phi_{d\text{-}min} = \phi_a - L_d I_{am}$. In the case of $\phi_{d\text{-}min} > 0$, there is a theoretical finite maximum speed limit owing a ceiling voltage V_{am}. On the other hand, the maximum speed limit becomes infinite when $\phi_{d\text{-}min} \leqq 0$, especially the condition of $\phi_{d\text{-}min} = 0$ gives an ideal wide constant power operating performance. Furthermore, the relationships between the motor parameters and the operating performance has been examined in detail based on the normalized motor model [7, 8].

Fig. 1 shows the simulated speed versus power characteristics, where the inductance L_d and L_q are kept constant values and the magnet-flux linkage ϕ_a is changed.

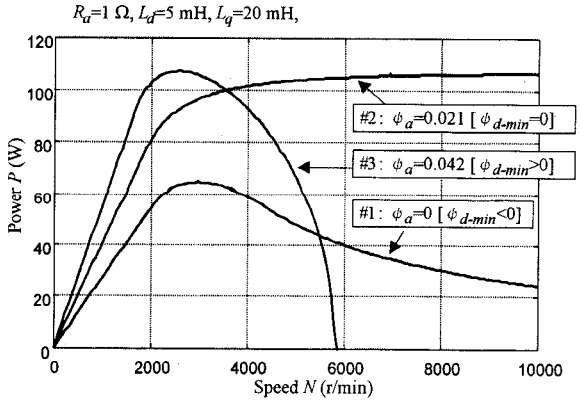


Fig. 1. Typical speed versus power characteristics under voltage and current constraints (V_{am}=30 V, I_{am}=4.16 A).

It shows that adjusting a magnet-flux linkage can control the pattern of speed vs. power performance. The power capability of a synchronous reluctance motor, which corresponds to the case of $\phi_{d\text{-}min} < 0$, can not exceed the capability of a hybrid motor satisfying the condition of $\phi_{d\text{-}min} = 0$.

III. Prototype PM/Reluctance Hybrid Motors

A. Motor Structure

We designed and produced five prototype motors. They have the same structure of stator and rotor. The dimensions of prototype motors are listed in Table 1. The rotor cross-section and the photograph of the prototype motor are shown in Fig. 2 and Fig. 3, respectively. There are three slits per pole, which work as a flux-barrier in the d-axis flux path. Therefore the motor has a saliency where the d-axis

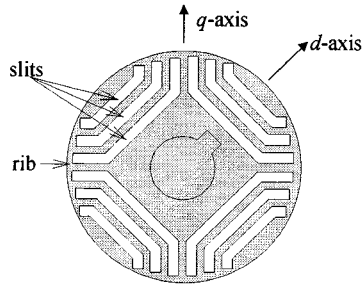


Fig. 2. Cross-section of rotor.

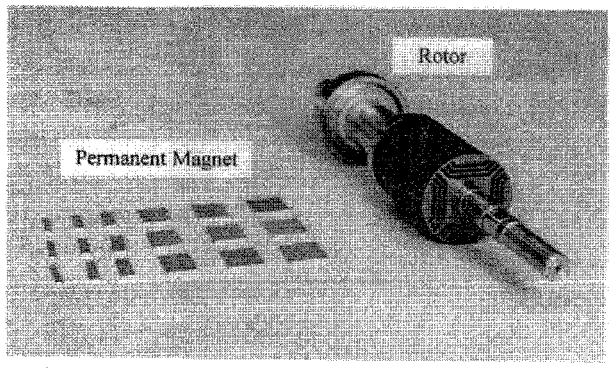


Fig. 3. Photograph of rotor and permanent magnet for prototype motor.

Table 1. Dimensions of prototype motors.

Number of pole pairs	2
Stator outer diameter	73 mm
Stator inner diameter	30.5 mm
Rotor outer diameter	29.9 mm
Air gap length	0.3 mm
Axial length	45.3 mm

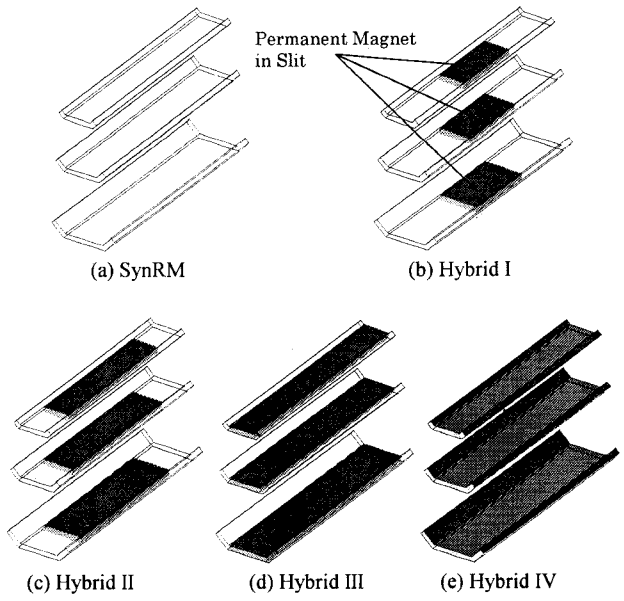


Fig. 4. Arrangement of permanent magnets in slits per pole.

Table 2. Volume of permanent magnet and flux-linkage.

	Volume of PM*1 (mm^3)	Normalized PM Volume*2	ϕ_a (Wb)
SynRM	0	0	0
Hybrid I	2350	1.0	0.0152
Hybrid II	4700	2.0	0.0355
Hybrid III	7050	3.0	0.0580
Hybrid IV	10960	4.7	0.0907

*1 : Neodymium-Iron-Boron

*2 : PM volume of Hybrid I is standard.

inductance L_d is less than the q-axis inductance L_q. This motor is a synchronous reluctance motor called SynRM in this paper. Inserting the segmental permanent magnets shown in Fig. 3 into the slits as shown in Fig. 4, four types of PM/reluctance hybrid motors (Hybrid I, II, III and IV) are obtained. The volume of permanent magnet and its normalized value based on the PM volume of Hybrid I are listed in Table 2.

SynRM without permanent magnet is a complete synchronous reluctance motor. Hybrid I and II have a two-part hybrid rotor comprising axially separated permanent magnet part and reluctance part [9]. The permanent magnet part where the permanent magnets are inserted into the slits corresponds to an IPM motor and the reluctance part without permanent magnet corresponds to a synchronous reluctance motor. Both Hybrid III and IV are complete interior permanent magnet motors.

If the magnetic saturation is ignored, adding permanent magnet to the rotor slits does not influence the inductance

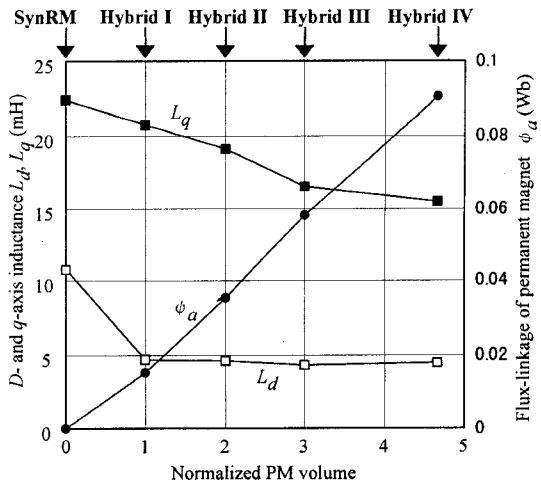


Fig. 5. Measured motor parameters of prototype motors.

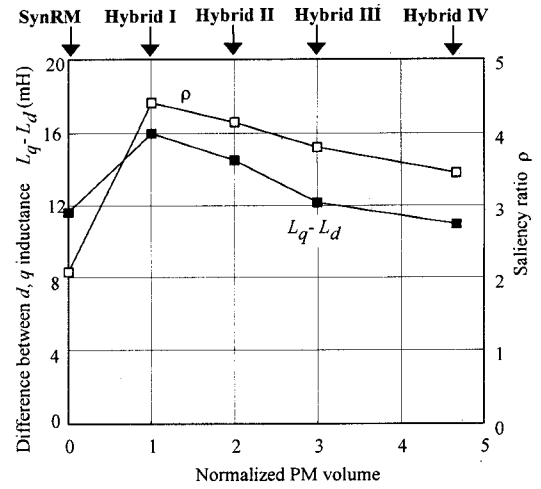


Fig. 6. Difference between q- and d-axis inductance and saliency ratio of prototype motors.

value of both L_d and L_q but increases the magnet-flux linkage ϕ_a because a permeability of permanent magnet closes with that of air. Therefore the reluctance torque is kept constant for any motors and the magnet torque increases as magnet volume increases.

B. Motor Parameters

Fig. 5 shows the measured motor parameters as a function of a normalized permanent magnet volume. The d- and q-axis inductance are measured at the operating condition that N=1000 r/min, I_e=2.4 A (rating) and β=45 degrees, where the current phase angle β is a reading angle of an armature current vector from the q-axis [$\beta=\tan^{-1}(-i_d/i_q)$]. Fig. 6 shows the difference between the q-axis inductance and the d-axis inductance and a saliency ratio ρ ($=L_q/L_d$) obtained from Fig. 5.

SynRM has a relatively large d-axis inductance compared

with other motors. This is reason why the flux in d-axis direction passes through the rib area in rotor. As the saliency of the prototype synchronous reluctance motor (SynRM) is small, the high performance drive can not be expected. In order to improve the performance of a synchronous reluctance motor, a large saliency ratio over 6 is desired and it will be realized by the axially laminated rotor structure [10, 11]. The flux density of the rib area increases by adding permanent magnet into the slits and as a result L_d decreases due to magnetic saturation. The d-axis inductance of Hybrid I becomes half of that of SynRM. Thus adding magnets to SynRM is effective for increasing both of saliency ratio and reluctance torque as shown in Fig. 6. The effect due to a saliency is most effective in Hybrid I because its saliency ratio and L_q- L_d are maximum of all prototype motors.

IV. Performance of Prototype Motors

In order to examine and compare the performance of five prototype motors, various experimentation have been carried out, where all motors are driven by the same PWM inverter and the same controller.

Fig. 7 shows the current phase angle versus torque characteristics at the rated current (I_e=2.4 A). The torque increases and the optimum phase angle producing maximum torque decreases as the volume of magnet increases.

Fig. 8 shows various characteristics of five motors at 3000 r/min. Each motor is controlled by the maximum torque per ampere control method, where the current phase angle β is optimally controlled according to the operating

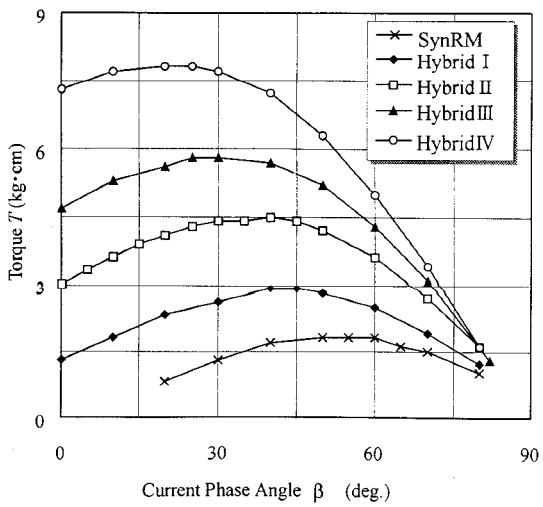
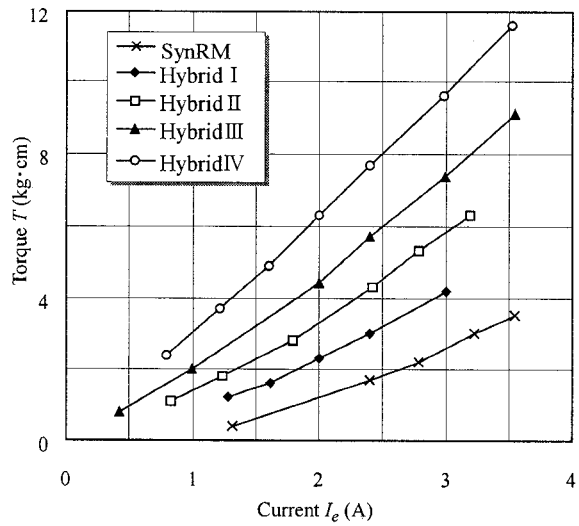
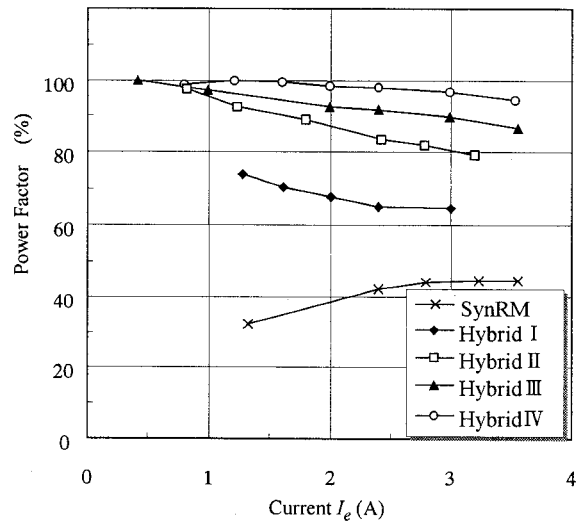


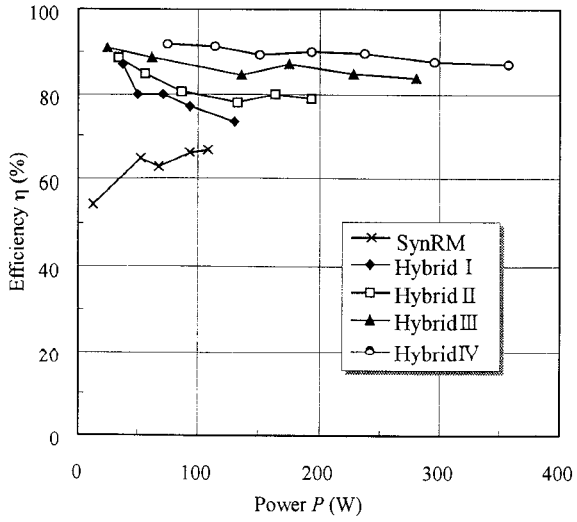
Fig. 7. Current phase angle versus torque characteristics. (I_e=2.4 A)



(a) Current versus torque characteristics.



(b) Current versus power factor characteristics.

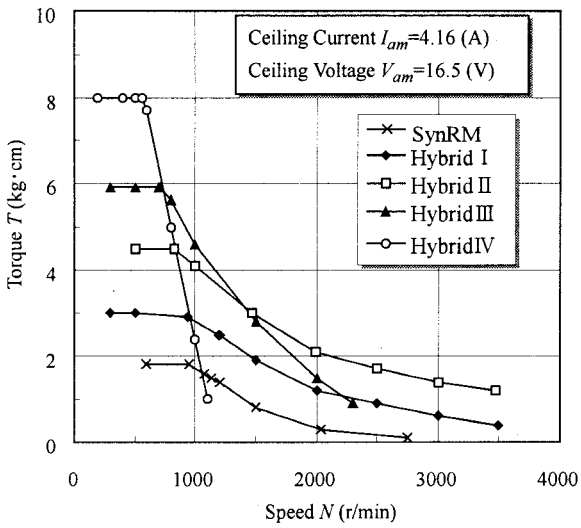


(c) Power versus efficiency characteristics.

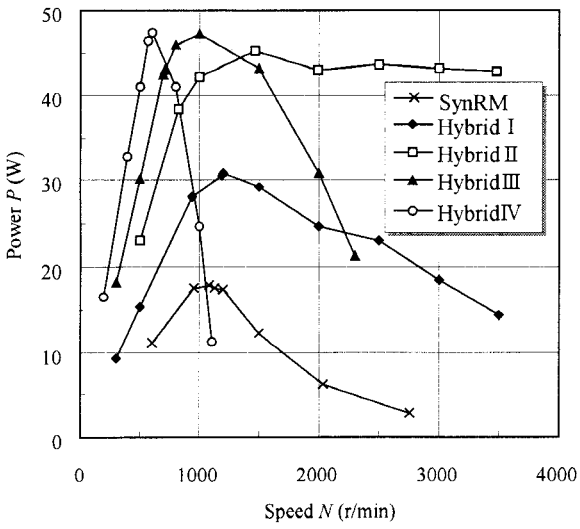
Fig. 8. Various characteristics of prototype motors at 3000 r/min.

condition. Both power factor and efficiency are greatly improved as the magnet flux increases; especially Hybrid IV is operated with a high power factor over 95 % and a high efficiency over 90 %. In this constant torque-operating region, it seems that the performance such as a maximum torque, power factor and efficiency can be improved by increasing magnet-flux linkage. In such case, however, the terminal voltage becomes large and the base speed decreases taking a ceiling voltage into account.

The speed versus torque and power characteristics are shown in Fig. 9, where both constraints of voltage and current are considered (a ceiling voltage V_{am}=16.5 V, a ceiling current $I_{am}=\sqrt{3}\,I_{em}$ =4.26 A; rating). All motors are controlled by a maximum torque per ampere control in the low speed region and by a flux-weakening control in the high-speed region over the base speed. The outline of speed versus torque and power characteristics changes depending on the magnet-flux linkage. It is shown that there is a trade-off between the maximum torque in the constant torque region and the constant power speed range. Hybrid IV can produce the largest torque, but the constant power speed range is limited. Such motor is suitable for the servo drive applications such as an industrial robot. On the other hand, Hybrid II has a largest constant power speed range over 4. Moreover a high power factor and a high efficiency operation is maintained in the flux-weakening

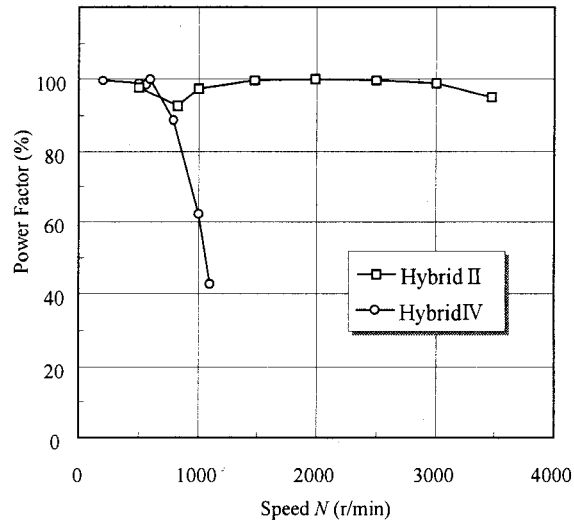


(a) Speed versus torque characteristics.

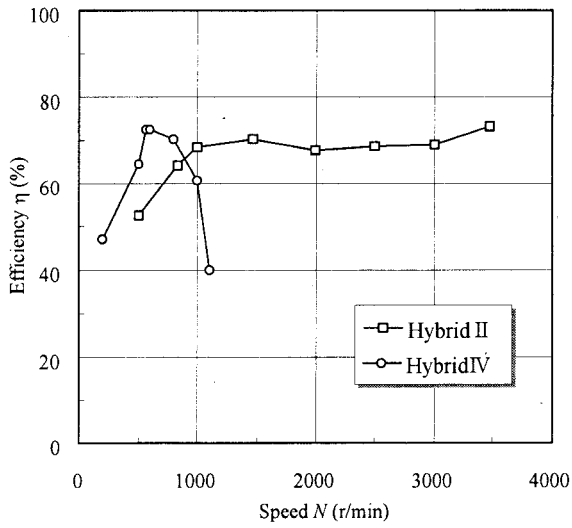


(b) Power versus torque characteristics.

Fig. 9. Current phase angle versus torque characteristics.



(a) Speed versus power factor characteristics.



(b) Speed versus efficiency characteristics.

Fig. 10 Power factor and efficiency of Hybrid II and IV at same operating condition in Fig. 9.

controlled constant power-operating region as shown in Fig. 10. The efficiency in Fig. 10 (b) is relatively low because the low ceiling voltage is selected in the experiment and thus the base speed is comparatively low. If the base speed becomes higher, the efficiency will be improved, which is supposed from the efficiency in Fig. 8 (c). The performance of Hybrid II is suitable for the traction drive applications such as an electric vehicle.

From various experimental results, it seems that the prototype motors can offer a great choice of design varieties of speed versus torque characteristics by adjusting the volume of permanent magnet in the slits. Thus such motors can be adapted to many applications even if they consist of the same stator and the same rotor.

V. CONCLUSIONS

This paper has examined the performance of various synchronous motors such as a synchronous reluctance motor, an interior permanent magnet synchronous motor and a hybrid motor with two-part rotor. These motors consist of the same rotor and the same stator, and are driven by the same inverter. The effects of adding magnets into the rotor on the machine parameters and the operating performance are examined. It has been confirmed that the volume of the permanent magnet inserted into the slits can control a speed versus power performance. Thus the proposed motor can offer a great choice of design varieties of the speed versus power characteristics.

REFERENCES

[1] T. M. Jahns, G. B. Kliman and T. W. Neumann, "Interior permanent-magnet synchronous motors for adjustable-speed drives," *IEEE Trans. Ind. Appl.*, vol. 22, pp. 738-747, July/Aug. 1986.

[2] T. M. Jahns, "Flux-weakening regime operation of an interior permanent-magnet synchronous motor drive," *IEEE Trans. Ind. Appl.*, vol. 23, pp. 681-689, July/Aug. 1987.

[3] B. K. Bose, "A high-performance inverter-fed drive system of an interior permanent magnet synchronous machine," *IEEE Trans. Ind. Appl.*, vol. 24, pp. 987-997, Nov./Dec. 1988.

[4] S. Morimoto, T. Ueno, M. Sanada, Y. Takeda, T. Hirasa and A. Yamagiwa, "Effects and Compensation of Magnetic Saturation in Flux-Weakening Controlled Permanent Magnet Synchronous Motor Drives," *IEEE Trans. Ind. Appl.*, vol. 30, pp. 1632-1637, Nov./Dec. 1994.

[5] S. Morimoto, Y. Takeda, T. Hirasa and K. Taniguchi, "Expansion of operating limits for permanent magnet motor by current vector control considering inverter capacity," *IEEE Trans. Ind. Appl.*, vol. 26, pp. 866-871, Sep./Oct. 1990.

[6] R. F. Schiferl and T. A. Lipo, "Power capability of salient pole permanent magnet synchronous motors in variable speed drive applications," *IEEE Trans. Ind. Appl.*, vol. 26, pp. 115-123, Jan./Feb. 1990.

[7] W. L. Soon, T. J. E. Miller, "Field-weakening Performance of Brushless Synchronous AC Motor Drives," *IEE-Proc.-Electr.Power Appl.*, vol.141, No. 6, pp. 331-340, Nov. 1994.

[8] S. Morimoto , M. Sanada , Y. Takeda, K. Taniguchi, "Optimum Machine Parameters and Design of Inverter Driven Synchronous Motors for Wide Constant Power Operation," *Proc. IEEE IAS Ann. Meet.*, pp. 177-182, 1994.

[9] B. J. Chalmers, L. Musaba, D. F. Gosden, "Variable-frequency Synchronous Motor Drives for Electric Vehicles," *Proc. IEEE IAS Ann. Meet.*, pp. 717-724, 1995.

[10] W. L. Soong, D. A. Staton and T. J. E. Miller, "Design of a new axially-laminated interior permanent magnet motor," *Proc. IEEE IAS Ann. Meet.*, pp. 27-36, 1993.

[11] T. Matsuo and T. A. Lipo, "Current Sensorless Field Oriented Control of synchronous reluctance motor," *Proc. IEEE IAS Ann. Meet.*, pp. 672-678, 1993.

A Rotor Design of a Permanent Magnet-Type Bearingless Motor Considering Demagnetization

Masahide Ooshima Satoru Miyazawa
Science University of Tokyo Suwa College, 5000-1, Toyohira, Chino, Nagano, 391-02 ,JAPAN
Fax:+81(266)1231, Phone:+81(266)73-1201, E-mail:moshima@sd.suwa.sut.ac.jp

Akira Chiba Fukuzo Nakamura
Science University of Tokyo, 2641, Yamazaki, Noda, Chiba, 278, JAPAN
Fax:+81(471)24-3104, Phone:+81(471)24-1501 Ext.3700, E-mail:CXJ10200@niftyserve.or.jp

Tadashi Fukao
Tokyo Institute of Technology, 2-12-1 Ookayama, Meguro Tokyo, 152, JAPAN
Fax:+81(3)5734-2903, Phone:+81(3)5734-2188, E-mail:tfukao@ee.titech.ac.jp

Abstract – Characteristics of a surface-mounted permanent magnet-type bearingless motor have reported by the authors. Thin permanent magnets are employed to generate radial forces efficiently. However, thin permanent magnets have a crisis of demagnetization because not only q-axis fluxes but also additional radial force ones exist in the motor magnetic field. The maximum q-axis and radial force currents limited by the demagnetization have been already made clear for a particular machine configuration using Finite Element Method. However, these results are not theoretically verified. In this paper, a limitation of demagnetization is analytically derived. The maximum current is found as a parameter of a permanent magnet thickness.

I. INTRODUCTION

Bearingless motors have attracted attentions in high speed motors, for machine tools, turbomolecular pumps, blood pumps and so on[1]-[4]. The bearingless motors have functions of magnetic bearings as well as motors. Thus, these have some advantages as follows; a) no contact b) no lubrication c) easy maintenance, etc. High speed and high power can be achieved, because the shaft can be shorter than that of the conventional motors with the magnetic bearings. In addition, the numbers of inverters, electric wires and control circuits can be decreased. As a result, cost can be also decreased.

In the bearingless motors proposed by the authors, additional 2-pole radial force windings as well as conventional 4-pole motor windings are wound in a stator iron core. The air-gap flux densities are unbalanced by the radial force fluxes in the 4-pole revolving magnetic field. As a result, the electromagnetic forces are generated in radial directions and the motor shaft can be successfully levitated and rotated. The bearingless motors with this principle can be applied to various conventional motors[2]-[10].

The surface-mounted permanent magnet-type bearingless motors have been researched[4],[7]-[9]. The characteristics at no load were previously found by the authors and confirmed by a constructed prototype machine. In the surface-mounted permanent magnet-type machines, thin permanent magnets and small air-gap lengths are preferred to generate the radial forces effectively. However, thin permanent magnets are easy to be demagnetized. Thus, it is very important to consider demagnetization of permanent magnets.

Both additional radial force fluxes and conventional q-axis torque fluxes exist in the motor magnetic field. It is undesirably possible that both the radial force fluxes and q-axis ones pass through a permanent magnet against the pre-magnetization direction. This condition is the most critical for demagnetization. Therefore, the permanent magnet thickness, the numbers of turns of both motor and radial force windings and the current ratings are necessary to be designed so that the permanent magnets are not demagnetized.

The most critical area in the permanent magnets with q-axis and radial force currents has been made clear. Under a limitation of demagnetization, the maximum current has been previously reported by the authors employing Finite Element Method [11].

In this paper, the flux densities on the surfaces of permanent magnets are numerically derived as a function of the motor and radial force winding currents. The flux densities in the critical area for demagnetization are decreased as the current is increased. When the flux densities are the minimum values, where the permanent magnets

0-7803-3823-5/97/$10.00© 1997 IEEE

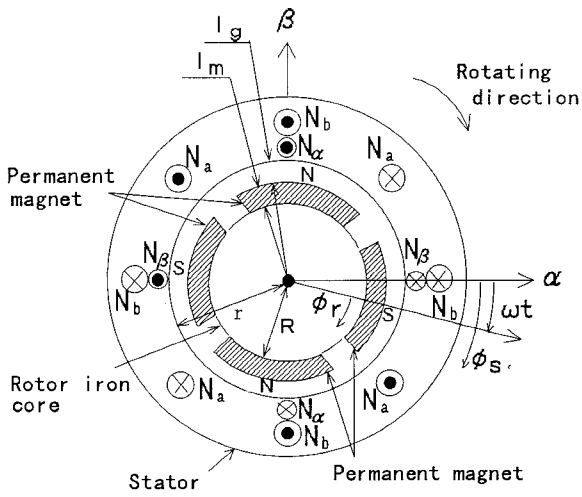
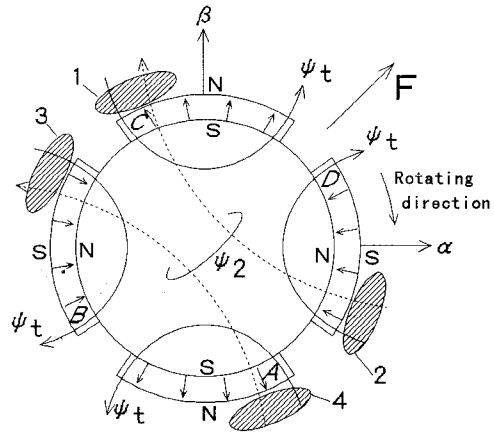
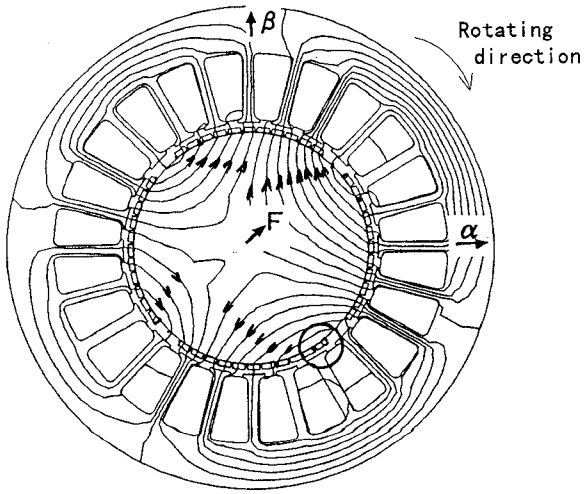


Fig. 1. Cross section of permanent magnet-type bearingless motor.



(a) q-axis and radial force fluxes.



(b) The most critical flux distribution.

Fig.2 Flux orientation and most critical flux distribution.

are slightly demagnetized, the motor and radial force winding currents are the maximum. Thus, the maximum q-axis and radial force currents can be analytically obtained from the flux densities. It is confirmed that the calculated maximum currents are corresponding to those obtained by Finite Element Method. Moreover, the relationship between the permanent magnet thickness and the maximum currents is found. It is effective for the design of permanent magnet thickness and current ratings in bearingless motors.

Ⅱ. Critical Area for Demagnetization

Fig.1 shows the cross section of the surface-mounted permanent magnet type-bearingless motor. In the stator, 2-phase windings are drawn for simplicity although 3-phase windings are wound. Both 4-pole motor windings N_a, N_b and 2-pole radial force windings N_α, N_β are wound in the same stator iron core. The permanent magnets are mounted on the rotor iron core constructing 4-poles.

Fig.2(a) shows q-axis and radial force fluxes. In this case, the q-axis current flows in the positive direction in the motor winding N_b, then the q-axis fluxes Ψ_t are generated. The rotor is rotated in clockwise direction. In the areas *A, B, C* and *D*, the q-axis fluxes pass through the permanent magnets opposite to the pre-magnetization direction. Thus, these four areas are critical for demagnetization.

Suppose that the radial force winding current is negative in the radial force winding N_α and it is positive in the winding N_β, respectively. Then, the resultant radial force fluxes Ψ_2 are generated as shown in Fig.2(a). The flux densities in the air-gaps 1 and 2 are increased, and those in the air-gaps 3 and 4 are decreased. As a result, the radial force F is generated as shown in Fig.2(a) due to the unbalance of the air-gap flux densities.

In Fig.2(a), both the q-axis fluxes Ψ_t and radial force fluxes Ψ_2 pass through the area *A* opposite to pre-magnetization direction of the permanent magnet. Thus, the area *A* is the most critical area for demagnetization in this case. Fig.2(b) shows the most critical flux distribution obtained by Finite Element Method. The part denoted by a circle in Fig.2(b) shows the most critical area corresponding to area *A* in Fig.2(a). It can be seen that there exists few fluxes within the circle.

The thickness of permanent magnets on the rotor iron core should be designed so that permanent magnets are not demagnetized, even if both the q-axis and radial fluxes pass through in permanent magnets. The maximum currents are determined by the permanent magnet thickness, the number of turns of windings and so on. In the later chapters, the flux densities on the surfaces of permanent magnets and the currents are theoretically derived.

Ⅲ. Air-Gap Flux Density

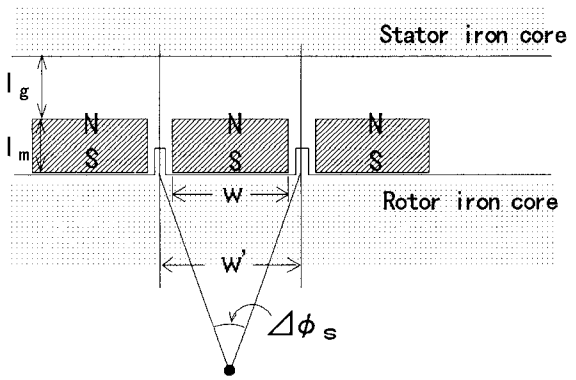


Fig. 3. Enlarged cross section.

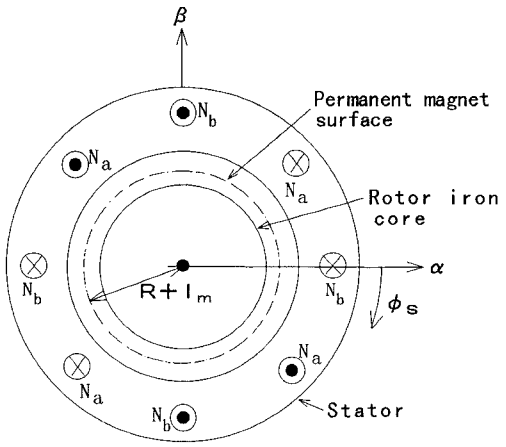


Fig. 4. MMF of motor winding

A. Field excitation of permanent magnets

Fig.3 shows an enlarged cross section around rotor surface of the permanent magnet-type machine. Some small projections are fabricated on the rotor iron. Permanent magnets are mounted between small projections. Let us define the width of a permanent magnet and the width between the small projections as w and w', respectively, as shown in Fig.3. Let us also define the stack length of the rotor as l. The area S of a permanent magnet and the area S' between small projections can be represented as wl and wl', respectively. Thus, S/S' is area density of permanent magnets on rotor surface. The thickness of permanent magnet and the air-gap length are defined as l_m and l_g, respectively. In the following analyses, the permeance in the small projections, magnetic saturation and slot ripples are neglected for simplicity. The peak value of the air-gap flux density B_{gp} can be represented as [9]

$$B_{gp} = \frac{l_m}{l_m + l_g}\frac{S}{S'}B_r \qquad (1)$$

where B_r is the residual flux density of the permanent magnets.

B. MMF of motor winding

Suppose that the permanent magnets are removed on the rotor iron surface as shown in Fig.4. In this condition, let us derive the air-gap flux density when only the motor windings are excited. Only q-axis fluxes Ψ_t by the q-axis currents exist in the motor magnetic field. Let us define the effective number of turns of motor windings N_a and N_b as n_4. Let us also define the angular positions in the stator and rotor coordinates as ϕ_s and ϕ_r, respectively, as shown in Fig.1. Assuming the MMF distribution is sinusoidal, the MMFs A_a and A_b of the motor windings N_a and N_b, respectively, for unit current can be defined as

$$A_a = -n_4 \cos 2\phi_s \qquad (2)$$

$$A_b = -n_4 \sin 2\phi_s \qquad (3)$$

The motor winding currents i_a and i_b are controlled to be perpendicular to each other. The amplitude of motor winding currents and the rotational angular speed are defined as I_q and ω, respectively. The motor winding currents i_a and i_b can be represented

$$i_a = -I_q \sin 2\omega t \qquad (4)$$

$$i_b = I_q \cos 2\omega t \qquad (5)$$

From (2),(3),(4) and (5), the resultant MMF of the motor windings can be written as

$$A_4 = A_a i_a + A_b i_b = -n_4 I_q \sin 2(\phi_s - \omega t) \qquad (6)$$

Permeance P between the rotor and the stator iron cores for a small angle $\Delta\phi_s$ can be written as

$$P = \frac{\mu_0 l \Delta\phi_s}{\ln\left(1+\frac{l_m + l_g}{R}\right)} \qquad (7)$$

where μ_0 is a permeability of the air. R is the radius of the rotor iron core. Then, the air-gap flux Ψ_g for the angle $\Delta\phi_s$ can be written as

$$\Psi_g = \frac{A_4}{2}\cdot P = -\frac{\mu_0 l \Delta\phi_s n_4 I_q}{2\ln\left(1+\frac{l_m + l_g}{R}\right)} \sin 2(\phi_s - \omega t) \qquad (8)$$

The flux densities along with the surface of permanent magnets can be derived. The radius is (R+l_m) from the center in the stator coordinate, as shown in Fig.4. The air-gap flux density $B_{gM4}(\phi_s)$ can be written as

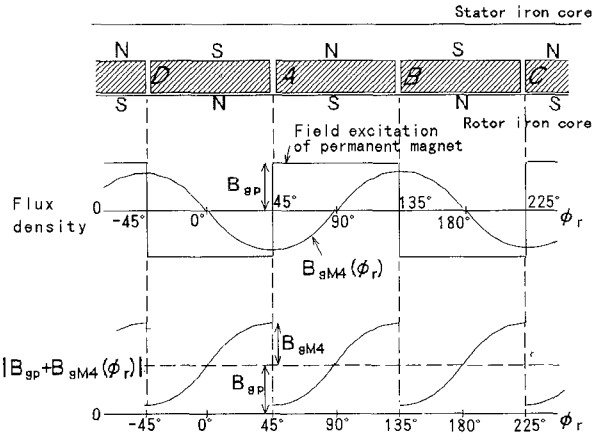


Fig. 5. Flux density in air-gap.

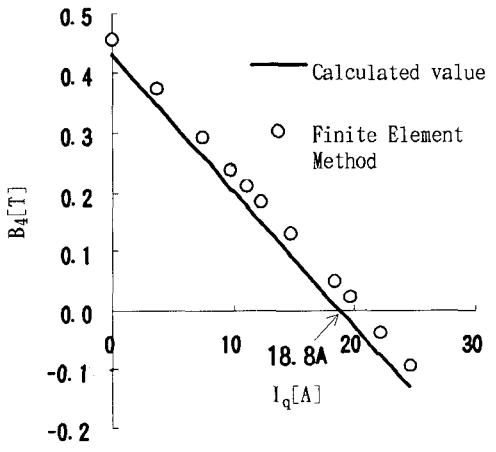


Fig. 6. Flux density on surface of permanent magnet vs. q-axis current.

$$B_{gM4}(\phi_s)=\frac{\Psi_g}{(R+l_m)\cdot\Delta\phi_s l}=-\frac{\mu_0 n_4 I_q}{2(R+l_m)\ln\left(1+\frac{l_m+l_g}{R}\right)}\sin 2(\phi_s-\omega t) \quad (9)$$

C. Air-gap flux density

Fig.5 shows the flux distribution of the field excitation of permanent magnets in the air-gap along the rotor surface. Namely, the horizontal axis is the angular position ϕ_r in the rotor coordinate. Four permanent magnets are symmetrically mounted on the rotor iron core surface. The flux distribution of permanent magnets results in the square wave. The peak value is B_{gp} as derived in (1). Fig.5 also shows the distribution of the air-gap flux density by MMF of the motor winding currents obtained from (9) substituting $\phi_r = \phi_s - \omega t$. The amplitude B_{gM4} of the flux density $B_{gM4}(\phi_s)$ can be written from (9) as

$$B_{gM4}=\frac{\mu_0 n_4 I_q}{2(R+l_m)\ln\left(1+\frac{l_m+l_g}{R}\right)} \quad (10)$$

In Fig.5, areas *A, B, C* and *D* in the permanent magnets show the most critical areas for a demagnetization corresponding to Fig.2(a). The q-axis fluxes pass through the areas *A, B, C* and *D* opposite to a per-magnetization direction of the permanent magnets. Understandably from Fig.5, in the areas *A, B, C* and *D*, the sign of $B_{gM4}(\phi_r)$ is opposite to that of the field excitation of permanent magnets. The air-gap flux density can be represented as $|B_{gp}+B_{gM4}(\phi_r)|$. It can be seen that the flux densities in the area *A, B, C* and *D* are the smallest in any angular position. Thus, the areas *A, B, C* and *D* are the most critical for a demagnetization. The flux density B_4 on the surface of permanent magnet in the most critical areas can be written from Fig.5, (1) and (10) as

$$B_4 = B_{gp} - B_{gM4} = \frac{l_m}{l_m+l_g}\frac{S}{S'}B_r - \frac{\mu_0 n_4 I_q}{2(R+l_m)\ln\left(1+\frac{l_m+l_g}{R}\right)} \quad (11)$$

Fig.6 shows the relationship between the amplitude I_q of the q-axis current and flux density B_4. The solid line in Fig.6 shows the calculated value from (11). The plotted points show the values previously obtained by the Finite Element Method. It can be seen that the calculated values are almost corresponding to the ones obtained by Finite Element Method. However, the calculated results are slightly smaller. The difference of 0.03T can be explained as follows; Some small projections are fabricated on the rotor iron core as shown in Fig.3. Thus, some fluxes go around a loop of "permanent magnet→air→small projection→rotor iron core→permanent magnet". Thanks to the small projections, the flux density on the permanent magnet surface is high if compared with the case without the small projections. In deriving (11), the existence of small projections was neglected for simplicity. Thus, the calculated values are slightly smaller than those by Finite Element Method.

IV. Current Value under Limitation of Demagnetization

A. Maximum value of q-axis current

In general, critical flux densities of permanent magnets in demagnetization are determined depending on a kind of permanent magnet and a temperature, etc. In this research, as referred in

TABLE I
SPECIFICATIONS OF A PROTOTYPE MACHINE

Radius of rotor iron core R		23mm
Air-gap length l_g		1mm
Permanent magnet		Sm-Co
Residual flux density Br		1T
Thickness l_m		1mm
Area density of mounted permanent magnet	S/S'	0.86
Effective number of turns of motor winding	n_4	72.7turns
Effective number of turns of radial force winding	n_2	30.6turns

[11], Sm-Co permanent magnets are employed. A limitation of demagnetization is defined as 5% decrease in a residual flux density at a temperature of 100℃. From the Finite Element Method using a prototype machine, the critical flux densities at the center and on the surface of permanent magnets were 0T and 0.14T, respectively. The B_4 in (11) shows the flux density on the surface of permanent magnet. It is equal to 0 under a limitation of demagnetization. One can obtain the maximum q-axis current $I_{q(max)}$ by equating B_4=0 in (11) and solving I_q as follows;

$$I_{q(max)} = \frac{l_m}{l_m + l_g}\frac{S}{S'}B_r \frac{2(R+l_m)\ln\left(1+\frac{l_m+l_g}{R}\right)}{\mu_0 n_4} \qquad (12)$$

Table I shows specifications of a prototype machine. Substituting these values into (12), one can obtain $I_{q(max)}$=18.8A. On the other hand, the maximum q-axis current is about 20A by Finite Element Method from Fig.6. It is found that the analytical result by Finite Element Method is almost corresponding to the theoretical ones obtained from (12).

B. Maximum value of radial force winding current

In Section *A*, the flux density was derived in the case when only the q-axis current exists. In this section, let us consider both the q-axis and radial force winding currents are flowing. The additional radial force fluxes as well as the q-axis ones are generated. The peak value B_{gM2} of the air-gap flux density caused by only the radial force fluxes can be derived by referring (10) as

$$B_{gM2} = \frac{\mu_0 n_2 I_2}{2(R+l_m)\ln\left(1+\frac{l_m+l_g}{R}\right)} \qquad (13)$$

where n_2 is the effective number of turns of the radial force windings. I_2 is the amplitude of the radial force winding current. Thus, the flux density B on the surface of the most critical area with both the q-axis and the radial force winding currents can

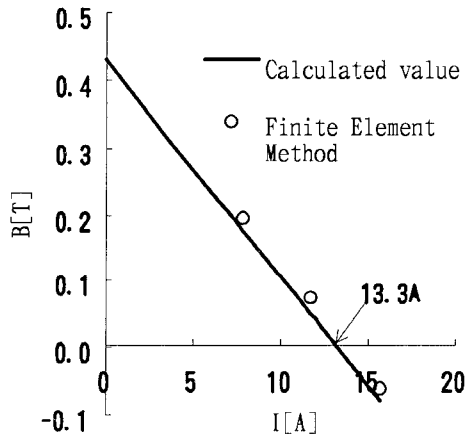


Fig. 7. Flux density at permanent magnet surface vs. q-axis and radial force winding currents.

be written from (1), (10) and (13) as

$$B = B_{gp} - B_{gM4} - B_{gM2} = \frac{l_m}{l_m+l_g}\frac{S}{S'}B_r - \frac{\mu_0 n_4 I_q}{2(R+l_m)\ln\left(1+\frac{l_m+l_g}{R}\right)} - \frac{\mu_0 n_2 I_2}{2(R+l_m)\ln\left(1+\frac{l_m+l_g}{R}\right)} \qquad (14)$$

It can be understood in (14) that the flux density B is a function of both the q-axis and the radial force winding currents. As mentioned in Chapter IV, Section *A*, the flux density B is equal to 0 under a limitation of demagnetization. Thus, if either I_q or I_2 is decided, the maximum value of another current can be obtained by (14).

Let us consider the situation that I_q=I_2=I to confirm that (14) is valid. Substitution of I into I_q and I_2 in (14) yields,

$$B = \frac{l_m}{l_m+l_g}\frac{S}{S'}B_r - \frac{\mu_0(n_4+n_2)I}{2(R+l_m)\ln\left(1+\frac{l_m+l_g}{R}\right)} \qquad (15)$$

Fig.7 shows the relationship between the flux density B on the surface of the most critical area and the current I in the motor and radial force windings. The calculated values by (15) are almost corresponding to the analyzed values by Finite Element Method. The plotted values by the Finite Element Method are slightly higher than the calculated ones due to the existence of small projections. As mentioned in chapter IV, Section *A*, the critical flux density on the surface of permanent magnet is set to 0T. Thus, the maximum current $I_{(max)}$ can be written substituting B=0 into (15) and solving I, as

$$I_{(max)} = \frac{l_m}{l_m + l_g} \frac{S}{S'} B_r \frac{2(R + l_m) \ln\left(1 + \frac{l_m + l_g}{R}\right)}{\mu_0 (n_4 + n_2)} \quad (16)$$

In a prototype machine, substituting the values in Table I into (16), the calculated $I_{(max)}$ is 13.3A. On the other hand, $I_{(max)}$ is about 13A from analyzed result by Finite Element Method, and close to the calculated value by (16).

Summarizing above, the maximum values of q-axis and radial force winding currents by analysis are theoretically verified with FEM results.

In designing permanent magnet-type bearingless motors, the current ratings are properly decided considering the capability of motor load, the weight of shaft, the radial force and so on. A q-axis current is proportional to output torque in general, and a radial force winding current is also proportional to an applied radial force to the shaft. The permitted range of the currents, which the permanent magnets are not demagnetized, can be numerically decided by $B \geqq 0$ in (14) using the thickness of permanent magnets, the radius of rotor iron core and so on. The equations derived analytically in this paper are effective in deciding the current ratings.

V. Conclusion

In the permanent magnet-type bearingless motors, the additional radial force fluxes as well as the q-axis ones exist in the motor magnetic field. Thus, the problem with respect to the demagnetization of permanent magnets mounted on the rotor iron core is very important. The currents under a limitation of demagnetization must be found in the motor design.

In this paper, the relationships between the flux densities and the currents under a limitation of demagnetization are analytically derived. It is confirmed that the maximum currents by the derived equations are almost corresponding to ones by Finite Element Method. The derived equations are effective in design of the permanent magnet thickness, the current ratings and so on.

References

[1] R. Bosch, "Development of a bearingless electric motor," in *Proc. ICEM'88*, vol.3, pp.373-375.

[2] R. Schob, "Applications of the Lateral-Force-Motor(LFM)," in *Proc. IPEC-Yokohama*, 1995, pp.358-363.

[3] M. A. Rahman, T. Fukao, and A. Chiba, "Principles and developments of bearingless AC motors," in *Proc. IPEC-Yokohama*, 1995, pp.1334-1339.

[4] Y. Okada, S. Shimura and T. Ohishi, "Horizontal Experiments on a PM Synchronous Type and Induction Type Levitated Rotating Motor," in *Proc. IPEC-Yokohama*, 1995, pp.340-345.

[5] C. Michioka, T. Sakamoto, O. Ichikawa, A. Chiba and T. Fukao, "A Decoupling Control Method of Reluctance-Type Bearingless Motors Considering Magnetic Saturation," in *IEEE Trans. IAS*, vol.32, No.5, 1996, pp.1204-1210.

[6] S. Nomura, A. Chiba, F. Nakamura, K. Ikeda, T. Fukao and M. A. Rahman, "A radial position control of induction type bearingless motor considering phase delay by the rotor squirrel cage," in *IEEE, Power Conversion Conf. (PCC-Yokohama)*, 1993, pp.438-443.

[7] J. Bichsel, "The bearingless electrical machine," in *NASA-CP-3152-PT-2*, 1992, pp.561-573.

[8] M. Oshima, S. Miyazawa, T. Deido, A. Chiba, F. Nakamura and T. Fukao, "Characteristics of a Permanent Magnet Type Bearingless Motor," in *Proc. IEEE Trans. IAS*, vol.32, No.2, 1996, pp.363-370.

[9] M. Oshima, S. Miyazawa, T. Deido, A. Chiba, F. Nakamura and T. Fukao, "An Analysis and Characteristics of a Permanent Magnet Type Bearingless Motor," in *IEEJ, Trans.*, vol.115, No.9, 1995, pp.1131-1139 (written in Japanese).

[10] T. Ohishi, Y. Okada and S. Miyamoto, "Levitation Control of IPM Type Rotating Motor," in *Proc. 5th Int. Symp. Magnetic Bearing*, Kanazawa, 1996, pp.327-332.

[11] A. Chiba, S. Onoya, T. Kikuchi, M. Ooshima, S. Miyazawa, F. Nakamura and T. Fukao, "An analysis of a Prototype Permanent Magnet-Type Bearingless Motor using Finite Element Method," in *Proc. 5th Int. Symp. Magnetic Bearing*, Kanazawa, 1996, pp.351-356.

Torque/Current Ratio Improvement of Reluctance Motor under Consideration of Teeth Design and Current Waveform

Takashi Kosaka, Nobuyuki Matsui
Nagoya Institute of Technology
Gokiso, Showa, Nagoya 466, JAPAN
Fax: +81-052-735-5442, Phone: +81-052-735-5420
E-mail: kosaka@elcom.nitech.ac.jp

Abstract— The developed torque of reluctance motors depends on the inductance space distribution and the current waveforms. Generally, the inductance distribution includes the space harmonics, which have the major effects on the torque ripple under the sinusoidal current drive. The torque ripple can be compensated for by modifying the instantaneous current waveforms.

A combination of space harmonics of inductance and time harmonics of current is studied in the paper from the standpoint of instantaneous torque. The analysis shows the combination of space and time harmonics can improve the torque/current^2 ratio, while the torque ripple can be suppressed within a reasonable range. From this result, the design of stator and rotor teeth is examined under considerations of applied current waveforms.

I. Introduction

The major advantages of Reluctance Motors(RM) are the simple and rugged motor construction, higher efficiency and low cost power electronics controller [1]-[3]. Unlike the conventional ac motors, the generated torque of RM is determined by a product of the square of winding current amplitude and the rate of change of inductance with respect to a rotor position. Since the torque is proportional to the square of winding current, the unipolar current drive by a simple power converter is possible. However, RM has essentially the torque ripple and the magnetic noise depend on its saliency, so that the applications might be limited.

Authors have proposed the torque ripple suppression by modifying current waveforms [4]. In this scheme, the linear relation between torque and current can be obtained under the assumption of sinusoisal inductance space distribution characteristic [4]. The inverter-fed bipolar sinusoidal current drive or C-dump Circuit-fed unipolar sinusoidal current drive can be used [5].

This paper presents the examination of a special combination of space harmonics of inductance and time harmonics of current from the standpoint of instantaneous torque. A certain combination of space harmonic of inductance with a certain time harmonic of current produces a non-oscillatory torque, while the torque ripple can be suppressed in a reasonable range. Since the space harmonics distribution of inductance are closely related to the design of teeth configuration, this study shows that the combination of motor teeth design with current control strategy can improve the torque/current^2 ratio without increasing the torque ripple.

II. Test Motor and Inductance Characteristics

Figs.1 and 2 show the construction of the test motor and inductance characteristics. In Fig.2(a), inductance distribution with respect to the rotor position is measured by impedance method and θ is electrical angle. The origin of θ is defined to the rotor position where U-phase stator tooth and corresponding rotor tooth are in the aligned position. Since the stator has a concentric winding, the mutual inductance between phases can be neglected and the self-inductance of each winding should be considered. Fig.2(b) shows the spectrum of self-inductance which is obtained by DFT.

III. Unipolar Sinusoidal Current Drive of RM

The torque produced by the three phase RM can be expressed in (1) by neglecting the magnetic saturation.

$$\tau = \frac{m}{2}\left[{i_u}^2\frac{\partial L_u}{\partial\theta} + {i_v}^2\frac{\partial L_v}{\partial\theta} + {i_w}^2\frac{\partial L_w}{\partial\theta}\right] \qquad (1)$$

where, m is the number of pole pairs.

Considering the space harmonics, the inductances of each phase are given in (2),

$$\left.\begin{aligned} L_u(\theta) &= L_{g0} + L_{g2}\sum_{n=1}^{\infty}\{l_{2n}\cos 2n\theta\} \\ L_v(\theta) &= L_{g0} + L_{g2}\sum_{n=1}^{\infty}\{l_{2n}\cos n(2\theta+\frac{2}{3}\pi)\} \\ L_w(\theta) &= L_{g0} + L_{g2}\sum_{n=1}^{\infty}\{l_{2n}\cos n(2\theta-\frac{2}{3}\pi)\} \end{aligned}\right\} \qquad (2)$$

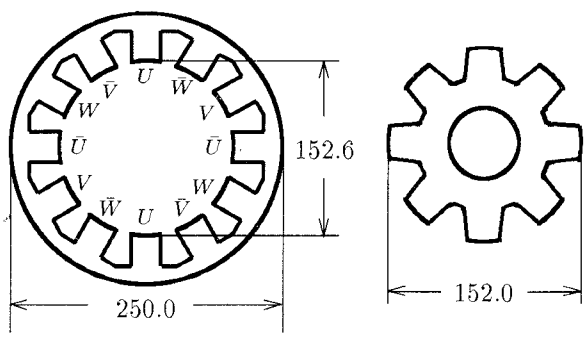
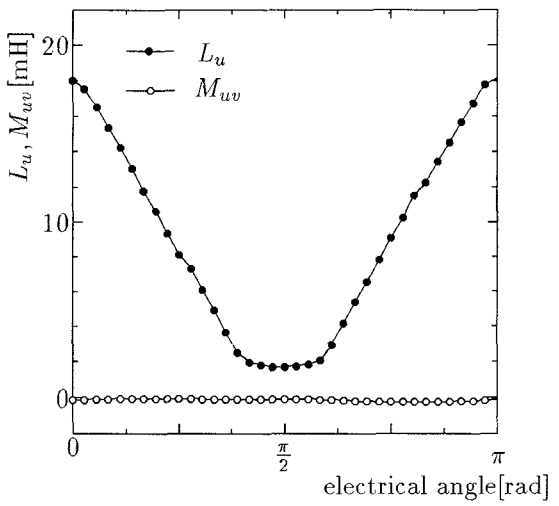
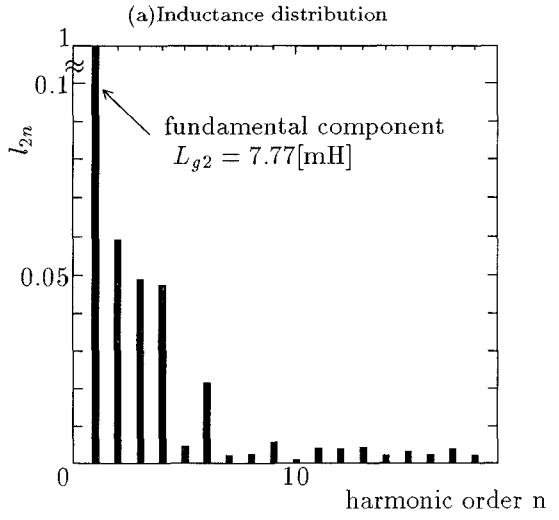


Fig. 1. Construction of test motor.



(a)Inductance distribution



(b)Inductance spectrum

Fig. 2. Inductance characteristics of the test motor.

where L_{go} and L_{g2} are the dc component and the fundamental amplitude of inductance and l_{2n} and n are the relative amplitude of harmonics and harmonic order.

On the assumption that the winding current can be controlled by using the conventional current minor loop, the sinusoidal full-wave rectified current, named unipolar sinusoidal current given by equation (3), can be applied to the motor through unipolar drive circuit such as C-dump Circuit and 'H'-bridge inverter.

$$\begin{bmatrix} i_u \\ i_v \\ i_w \end{bmatrix} = \sqrt{2} I_1 \left| \begin{bmatrix} \cos(\theta + \varphi_1) \\ \cos(\theta + \varphi_1 - \frac{2}{3}\pi) \\ \cos(\theta + \varphi_1 + \frac{2}{3}\pi) \end{bmatrix} \right| \tag{3}$$

where φ_1 is a leading phase angle of current. From (1),(2) and (3), the generated torque of RM under this current drive is given in (4).

$$\tau = \frac{3}{2} m {I_1}^2 L_{g2} (\sin 2\varphi_1 + \sum_{n=2}^{\infty} \tau_{rip}) \tag{4}$$

where, the first term is the non-oscillatory torque which can be obtained from the fundamental component of inductance and takes the maximum torque/current^2 ratio at $\varphi_1 = \pi/4$ rad. The second term is the torque ripple generated by the space harmonics of inductance, where τ_{rip} is given by;

$$\left.\begin{array}{rcl} n & = & 3k-1 \\ \tau_{rip} & = & -l_{2n} n \sin(2(n+1)\theta + 2\varphi_1) \\ n & = & 3k \\ \tau_{rip} & = & -2 l_{2n} n \sin(2n\theta) \\ n & = & 3k+1 \\ \tau_{rip} & = & -l_{2n} n \sin(2(n-1)\theta - 2\varphi_1) \\ & & (k = 1,\ 2,\ \cdots) \end{array}\right\} \tag{5}$$

From (5), it is clear that frequencies of torque ripples under the unipolar sinusoidal current drive are $6n$ times the source frequency.

IV. Torque Improvement of RM by Using the 3rd Current Harmonic

A. Generation Mechanism of Non-Oscillatory Torque

The non-oscillatory torque generated by the fundamental component of inductance under the unipolar sinusoidal drive is considered on the basis of U-phase torque equation. Substituting the fundamental component of inductance in (2) into the first term in (1), the generated torque in U-phase is obtained in (6).

$$\begin{aligned} \tau_u &= \frac{m}{2} {i_u}^2 \frac{\partial L_u}{\partial \theta} \\ &= \frac{m}{2} {I_1}^2 \{1 + \underbrace{\cos 2(\theta + \varphi_1)}_{A}\} \cdot (-2 L_{g2} \sin 2\theta) \\ &= \frac{m}{2} {I_1}^2 L_{g2} \{-2\sin 2\theta - \sin(4\theta + 2\varphi_1) \\ &\qquad + \underline{\sin 2\varphi_1}\} \end{aligned} \tag{6}$$

Following the same procedure, generated torque in V- and W-phases can be obtained. Due to the symmetry, the first and second terms in (6) are cancelled by the corresponding terms of V- and W-phases and the resulting torque is determined by the third term in (6). It is noted here, the third term is introduced by the 2θ-component of part A in (6) which is obtained by the square of current. Since that, superimposing the 3rd harmonic of current to the original fundamental current, the resulting non-oscillatory torque can be increased because of the additional 2θ-component.

B. Increasing of Non-Oscillatory Torque by Using the 3rd Harmonic of Current

From the discussion above, generated torque is examined here under the current drive given in (7).

$$\begin{aligned} \begin{bmatrix} i_u \\ i_v \\ i_w \end{bmatrix} = \sqrt{2} I_1 & \left| \begin{bmatrix} \cos(\theta + \varphi_1) \\ \cos(\theta + \varphi_1 - \frac{2}{3}\pi) \\ \cos(\theta + \varphi_1 + \frac{2}{3}\pi) \end{bmatrix} \right. \\ & \left. + i_3 \begin{bmatrix} \cos 3(\theta + \varphi_3) \\ \cos 3(\theta + \varphi_3 - \frac{2}{3}\pi) \\ \cos 3(\theta + \varphi_3 + \frac{2}{3}\pi) \end{bmatrix} \right| \end{aligned} \tag{7}$$

where, i_3 is the proportion of the amplitude of 3rd harmonic with respect to the amplitude of fundamental of

current and φ_3 is the leading phase angle of the 3rd harmonic. The corresponding torque is given in (8).

$$\tau = \frac{3}{2} m {I_1}^2 L_{g2} \quad \{ \quad \sin 2\varphi_1 + 2i_3 \sin(3\varphi_3 - \varphi_1) - 2i_3 \sin(6\theta + 3\varphi_3 + \varphi_1) \} \quad (8)$$

In (8), the first term is the non-oscillatory torque generated by a combination of the fundamental component of inductance and the fundamental component of current. The second term is also the non-oscillatory torque generated by a combination of the fundamental component of inductance and the fundamental and the 3rd harmonic of current and takes the maximum torque/current^2 ratio at $\varphi_1 = \varphi_3 = \pi/4$ rad. It is noted here that the non-oscillatory torque is increased by the amount of $2i_3$ by superimposing the 3rd harmonic of current.

C. *Torque Compensation by the 3rd Space Harmonic of Inductance*

Here, the torque ripple compensation by using the space harmonic of inductance is examined under the unipolar current drive in (7). It is also assumed that $\varphi_1 = \varphi_3 = \pi/4$ rad is held to obtain the maximum torque/current^2 ratio. The torque equation is given in (9).

$$\tau = \frac{3}{2} m {I_1}^2 L_{g2} \quad [\quad (1 + 2i_3 - 3l_6 {i_3}^2) - \{6l_6(1 + {i_3}^2) - 2i_3\} \sin 6\theta + (3l_6 {i_3}^2 \cos 12\theta)] \quad (9)$$

where, l_6 is the proportion of the amplitude of 3rd space harmonic with respect to the amplitude of fundamental of inductance. From the second term in (9), the torque ripple whose frequency is 6θ can be eliminated by the condition below.

$$6l_6(1 + {i_3}^2) - 2i_3 = 0 \quad (10)$$

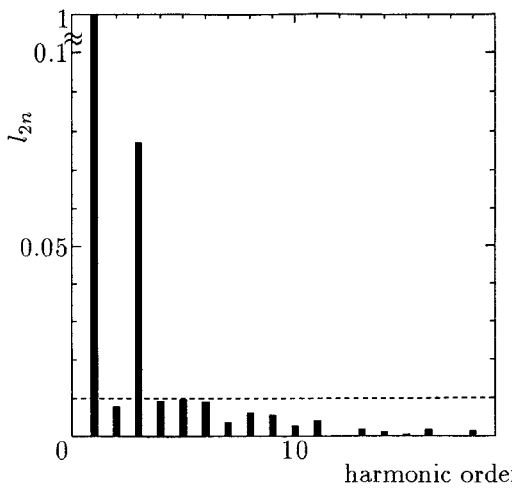


Fig. 3. Inductance spectrum under optimum motor design.

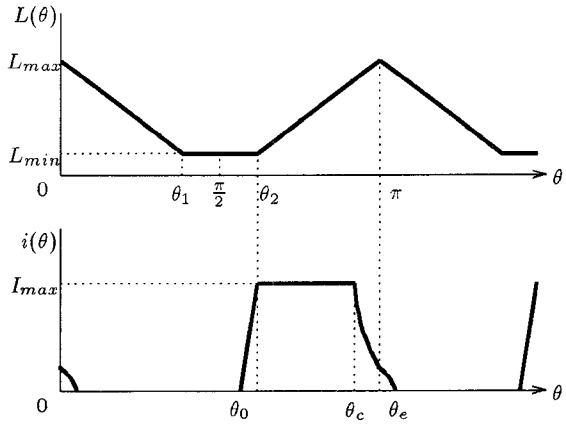


Fig. 4. Concept of pulse current drive.

Using $l_6 = 0.049$ in test motor, (10) is solved for i_3 and $i_3 = 0.15$ is obtained. Under this condition, torque/current^2 ratio can be improved by 27%, while the second term in (9) can be eliminated and the third term is only 0.3% compared to the non-oscillatory torque.

The discussion above leads to the following design strategy. The motor should be designed so that the 3rd space harmonic of inductance might be included but higher harmonics of inductance should not be included. Fig.3 is one of examples obtained by computer simulations, where higher space harmonics of inductance are effectively eliminated.

V. Instantaneous Torque Simulation

A. *Comparisons of Torque/Current^2 Ratio*

Here, comparisons of the generated torque under the pulsewise current drive and the proposed current drive are given. For the pulsewise current drive shown in Fig.4, the optimum pulse profile should be determined to obtain the maximum torque/ current^2 ratio. Supposing that the maximum current is limited by the current

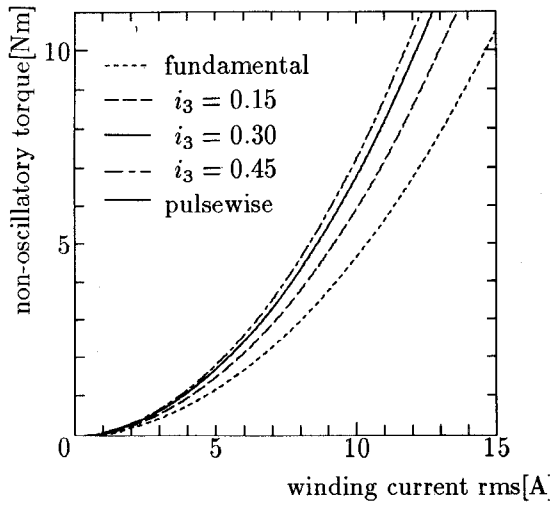
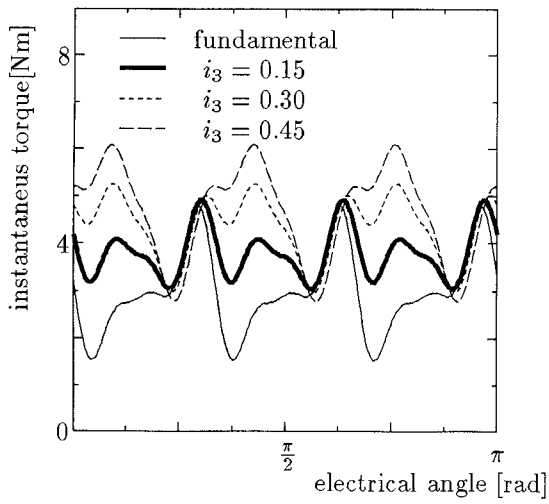
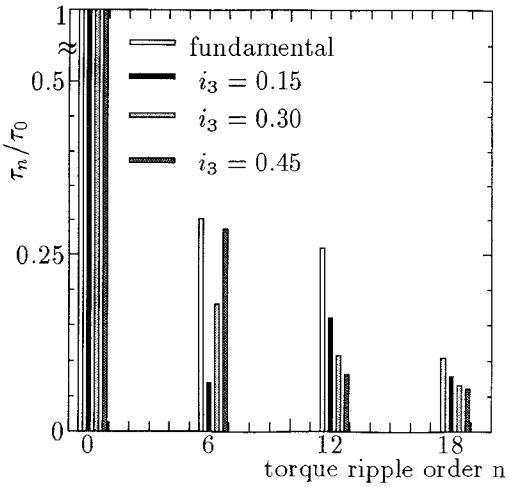


Fig. 5. Torque-Current Characteristics(calculated at 1000rpm).



(a)Instantaneous torque waveforms



(b)Instantaneous torque spectra

Fig. 6. Instantaneous torque characteristics (calculated at 1000rpm, I_{rms}=8A).

minor loop, the transient current is obtained in (11) by neglecting the winding resistance.

$$V = \frac{d(Li)}{dt} = \dot{\theta}\{L(\theta)\frac{di(\theta)}{d\theta} + i(\theta)\frac{dL(\theta)}{d\theta}\} \quad (11)$$
$$\begin{cases} V = V_{dc} & (\theta_0 \le \theta < \theta_1) \\ V = -V_{dc} & (\theta_c \le \theta < \theta_e) \end{cases}$$

Inductance is linearized as in (12).

$$\begin{cases} L(\theta) = L_{max} - k(\theta - \frac{\pi}{2}) & (0 \le \theta < \theta_1) \\ L(\theta) = L_{min} & (\theta_1 \le \theta < \theta_2) \\ L(\theta) = L_{min} + k(\theta - \theta_2) & (\theta_2 \le \theta < \pi) \\ & (k = const.) \end{cases} \quad (12)$$

By using (11) and (12), optimum $I_{max}, \theta_0, \theta_c$ can be obtained to make the torque/current^2 ratio maximum. The result is given in Fig.5. For the proposed current drive, as previously stated, the maximum torque/current^2 ratio is realized by $\varphi_1 = \varphi_3 = \pi/4$ rad. The torque-current characteristics are simulated for the fundamental current and $i_3 = 0.15, 0.30, 0.45$. As stated, torque ripple can be fully eliminated for $i_3 = 0.15$. Allowing the torque ripple to some extent, the torque/current^2 ratio can be more improved. To examine this, torque-current characteristics in Fig.5 show that the torque-current characteristics for $i_3 = 0.30, 0.45$ are coincident with that for pulsewise current drive and higher torque is generated for the same winding current in case of $i_3 = 0.45$, compared to the pulsewise current drive.

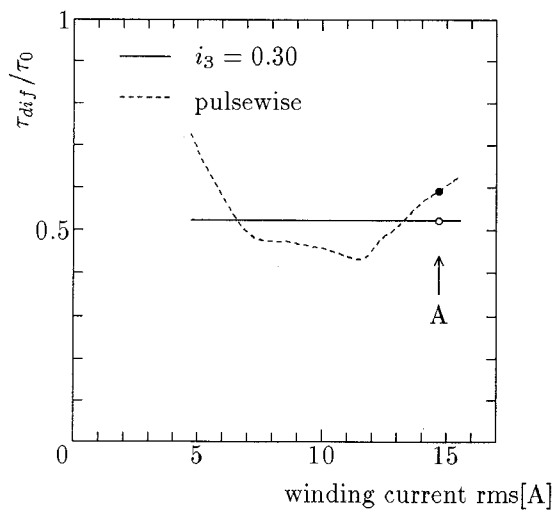


Fig. 7. Relative Torque ripple-current characteristics (calculated at 1000rpm).

B. Comparisons of Torque Ripple

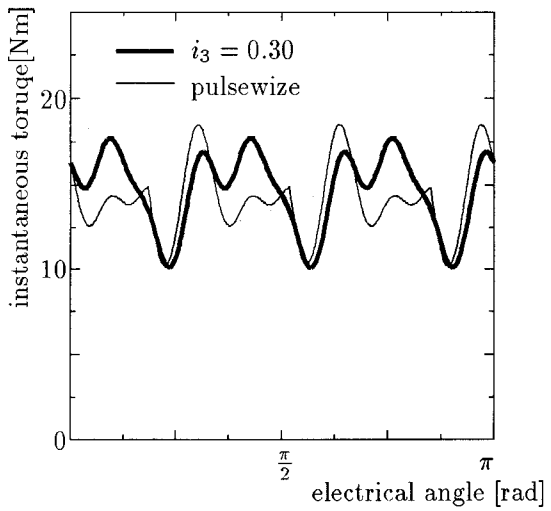
Fig.6 shows the comparisons of torque ripple for the fundametal and the proposed current drives. From Fig.6(a), the current drive for $i_3 = 0.15$ shows better instantaneous torque characteristic than the fundamental current drive. Fig.6(b) shows the torque ripple with 6θ-component is greatly reduced in the proposed scheme.

Fig.7 shows the comparisons of torque ripple for pulsewise and the proposed current drives. In the figure, τ_0 is the non-oscillatory torque and τ_{dif} is the peak-to-peak value of the instantaneous torque. From the figure, the current drive for $i_3 = 0.30$ shows better torque ripple characteristics in lower and higher current level and nearly the same torque ripple characteristics in the medium current region. The rated current of the test motor is 15A, and Fig.8 shows the instantaneous torque profile and spectra in the rated condition.

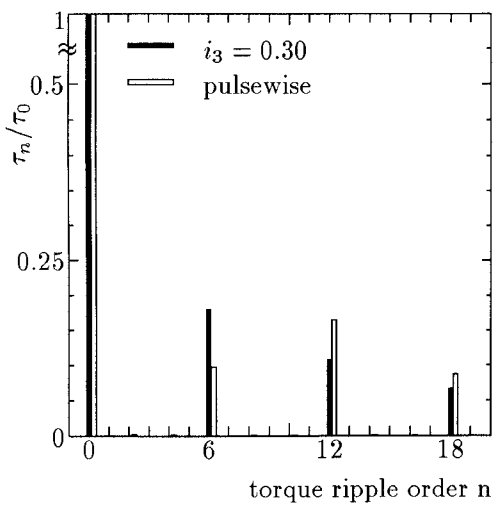
VI. Experimental Verification of Improvement of Torque/Current^2 Ratio

A. System Configuration

Fig.9 is the experimental system configuration. DSP(TI, TMS320C50) is used as a controller. The position sensor is a resolver(Tamagawa Seiki, Smartsyn, sampling rate 250μs) and output is converted to 12-bit digital signal through a R/D Transducer(Tamagawa



(a)Instantaneous torque waveforms



(b)Instantaneous torque spectra

Fig. 8. Instantaneous torque characteristic (calculated at 1000rpm ,I_{rms}=15A).

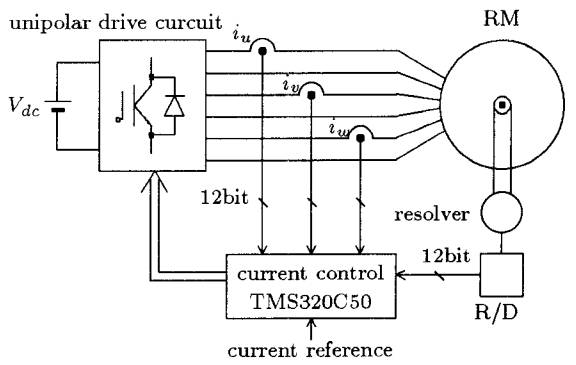


Fig. 9. System configuration.

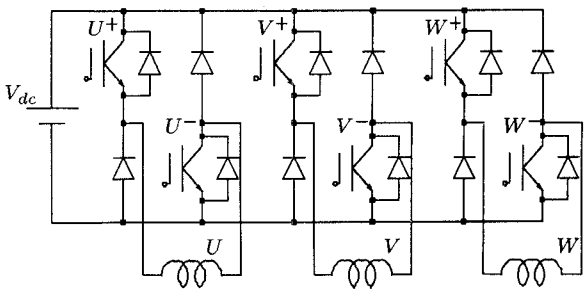


Fig. 10. Unipolar drive circuit.

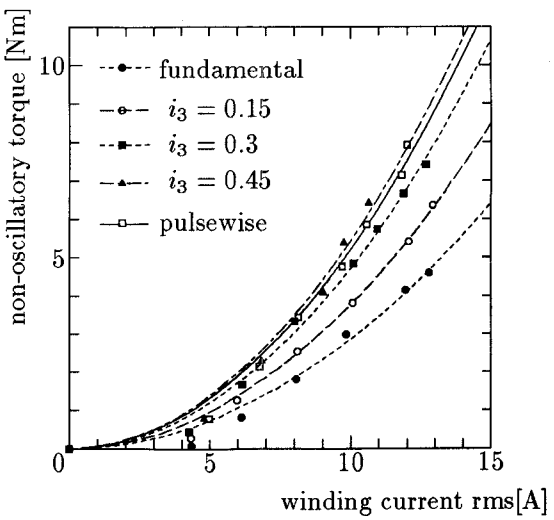


Fig. 11. Torque-current characteristic (measured value at 1000rpm).

Seiki, Smartcoder AU6800). Winding current are detected by Hall-CT(LEM, LA-55-P) and output is converted to 12-bit digital signal through A/D converter(B.B, AD674A).

The converter is shown in Fig.10. The load is an eddy current brake.

B. Experimental Result

Fig.11 shows the torque-current characteristics for various current drive schemes. The rotational speed is 1000rpm. As predicted from the analyzes, the proposed current drive schemes present the improved torque/current^2 ratio as shown TABLE I.

VII. Conclusions

In this paper, the instantaneous torque of the reluctance motors is analyzed under consideration of current harmonics and space harmonics of inductance. As a result, for the given motor, the optimum current waveforms can be determined to achieve the maximum torque/current^2 ratio and minimum torque ripple. The experimental study verify the effectiveness of proposed current drive. To improve the maximum torque/current^2 ratio while maintaining the minimum torque ripple, the 3rd space harmonic of inductance plays an important role. The simulation studies have proved that, by a proper design of the stator and rotor teeth dimensions, the motor can present higher torque/current^2 ratio and torque ripple free characteristic.

TABLE I

TORQUE/CURRENT^2 RATIO IN EACH CURRENT DRIVE

type of drive current	torque/current^2 ratio
only fundamental	1.00 ($0.0285Nm/A^2$)
fundamental+$i_3 = 0.15$	1.32
fundamental+$i_3 = 0.30$	1.65
fundamental+$i_3 = 0.45$	1.91
pulsewise current	1.83

REFERENCES

[1] T.J.E.Miller, "Switched Reluctance Drives", IEEE/IAS Ann. Meeting, Tutorial Course Text.(1990)

[2] A.V.Radun, "Design Considerations for the Switched Reluctance Motor", Proc. of IEEE/IAS Ann.Meeting, pp.290-297, 1994.

[3] B.C.Mecrow, "Fully pitched-winding switched-reluctance and stepping-motor arrangements", IEE Proceedings-B, vol.140, No.1, pp.61-70, Jan., 1993.

[4] N.Matsui, N.Akao, T.Wakino, "High-Precision Torque Control of Reluctance Motors", IEEE Trans. on Industry Applications, vol.27, No.5, pp.902-907, 1991.

[5] Wakino, Matsui, "Some Considerations on Torque Control of SRM", Proc. of IEEJ, SPC-90-20, pp.77-86, 1990.

Automatic Learning Control-Based Auto Gain Parameter Tuning DC Brushless Servo Motor Drive Systems

Kenji Inoue* Junji Yoshitsugu** Shin Shirogane** Prasanna Boyagoda**

and Mutsuo Nakaoka**

*Development Laboratory of New Products
Shinko Electric Co., Ltd.
100,Takegahana,Ise City,Mie Prefecture,516 Japan
Fax: +81-596-36-3974, Phone: +81-596-36-3180
E-mai: inoue@servo.shinko-elec.co.jp

**Department of Electrical and Electronics Engineering,
The Graduate School of Engineering and Sience
Yamaguchi University
2557,Tokiwa-dai,Ube City,Yamaguchi Prefecture,
775 Japan
Fax: +81-836-35-9449, Phone: +81-836-35-9946
E-mail: nakaoka@pe-news1.eee.yamaguchi-u.ac.jp

Abstract **In this paper, described is an advanced control method of system parameter auto-tuning implementation for AC servo system using fuzzy reasoning logic with automatically learning control function.**
This method includes three features;
(i) It is not necessary to input some kinds of fuzzy rules to the servo system before starting auto-tuning operation. Thus, fuzzy rules can be automatically produced in learning logical process.
(ii) Any knowledge and information about system parameter tuning technique are not required.
(iii) Both high speed response and robustness can be obtained.
The feasible effectiveness of this auto-tuning processing approach for AC servo system are practically confirmed through experimental results.

I. Introduction

In general, an AC servo has been widely used in numerical control machines and robotics, in which high level of motion control technology has been required. In case of these applications, the parameter gains in AC servo system have been adjusted by skilled workers in order to get the optimum performance.

In recent years, AC servo has been incorporated to many kinds of factory automated machine. It has attracted special interest as a motion carrier system between processes used in semiconductor manufacturing factory.

Significant demand of "easy to use" increases for these expanding applications. To satisfy this demand, auto-tuning technology have been applied to servo systems from a practical point of view. Many kinds of auto-tuning technology have been proposed so far. In many cases, a step signal is inputted into AC servo and the characteristics of its response are measured and servo gains are adjusted according to fuzzy rules stored in a control system in advance[1],[2].

In case of fuzzy reasoning type of auto-tuning method, designer should define the type and specification of load prepared by user and set fuzzy rules so as to be suitable for the load as much as possible. In General, it takes a lot of time to make the rules however a designer has enough knowledge about tuning technique. On the other hand, fuzzy adaptive control method or fuzzy learning control method are applied to AC servo to reduce the adjusting time[3],[4]. But, it still remains a serious problem that fuzzy rules should be set by designer. For this reason, it is necessary for a designer who well knows about adjusting technique to decide what kind of rule should be set.

An advanced auto-tuning method proposed here is the way that the whole processes of auto-tuning can be executed automatically only by inputting the start command. In this paper, an advanced auto-tuning method with learning control function is introduced and the effectiveness of this conceptual procedure are confirmed by some experimental results.

II. Auto-Tuning Method

Fig.1 shows the schematic flow chart of this auto-tuning method. When starting the auto-tuning operation, the parameters of load linked to AC servo motor are estimated. Initial values of control gains and fuzzy rule sets used in the following auto-tuning process are produced by the estimated

0-7803-3823-5/97/$10.00© 1997 IEEE

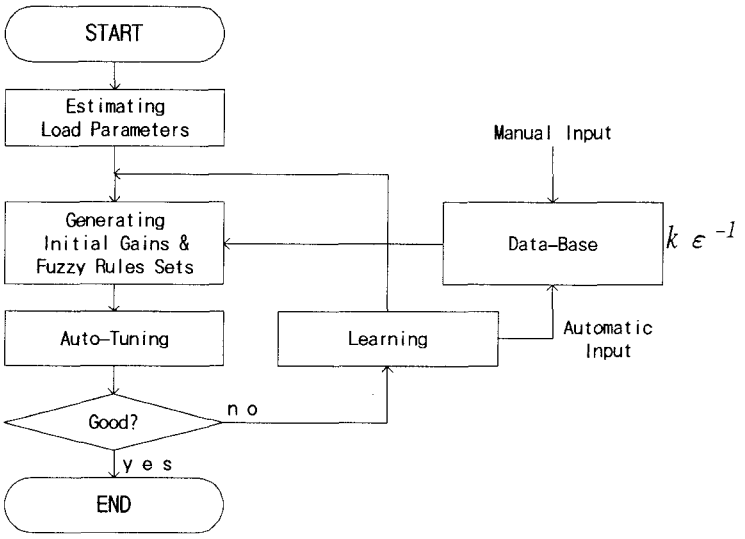


Fig.1 Schematic Flow Chart

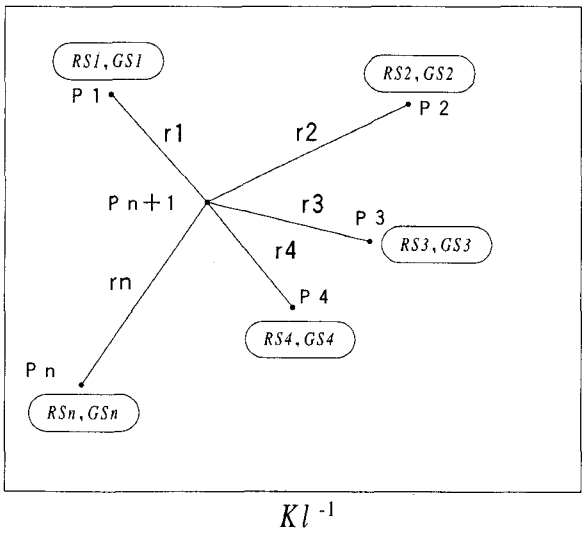


Fig.3 Plane of $K\ \varepsilon^{-1}$-Kl^{-1}

load parameters and data stored in data-base.

In auto-tuning process, step disturbance signal is inputted into a speed control loop and characteristics of the loop are calculated from the step response and the servo gains are adjusted to derive the optimum characteristics according to the characteristics and the fuzzy rule sets.

In learning process, fuzzy rule set is made according to trends of control characteristics derived by changing servo gains and measuring step responses and is stored in the data-base. After completing learning process, The auto-tuning process will be started again.

In following discussions, each step of auto-tuning are described in detail.

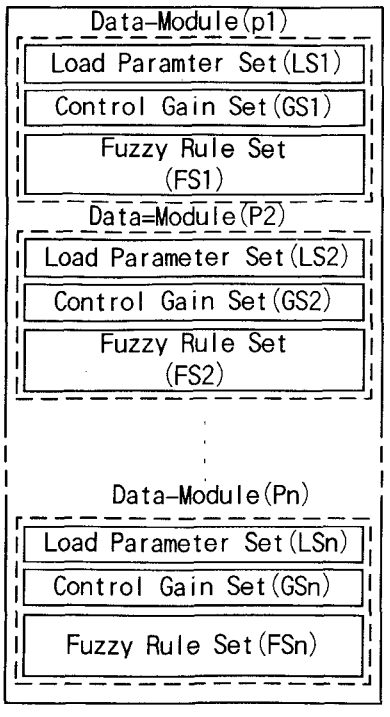


Fig.2 Structure of Data-Base

A. Estimating load parameters

Load parameters are estimated by measuring step response derived by inputting the disturbance signal. Load can be considered to be two-mass system consisted of a spring constant and a load inertia. Friction and backlash are supposed to be negligible. In this case, it is not necessary to estimate the load parameters accurately. For this reason, simple trapezoidal integration method is used.

B. Generating fuzzy rule sets

PI gains and the fuzzy rule sets used in following auto-tuning process are produced by the estimated load parameters and the data modules stored in the data-base. As illustrated Fig.2, the data-base consists of some data modules which were produced in learning process. The data module consists of load a parameter set, a control gain set and a fuzzy rule set.

Fig.3 shows how to produce fuzzy rule sets and initial PI gains used in the following process. *RS i* and *GS i* are a fuzzy rule set and a control gain set respectively which are derived by *i* number of learning execution. Distance *r i* between Pn+1 and Pi is calculated as following equation;

$$r_i = \sqrt{\log^2(\frac{KE_i}{KE_{n+1}}) + \log^2(\frac{Kl_i}{Kl_{n+1}})} \qquad (1)$$

Fuzzy rule sets of Pn+1 used in the following auto-tuning

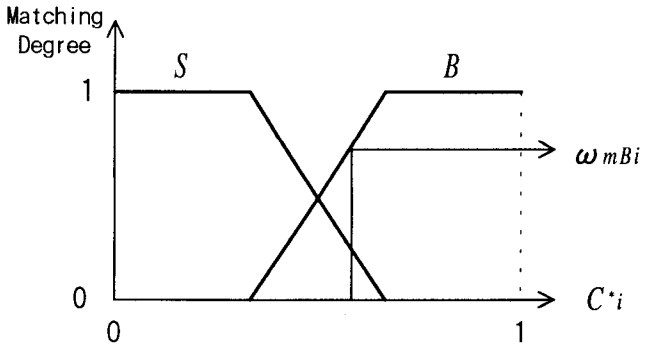


Fig.4 Member-Ship Function of ri

process can be expressed as following conditional equations;

$$if\ ri = B\ then\ RSi \tag{2}$$

where, i=1~n

RSi; fuzzy rule set of Pi.

$$\omega Si = \mu Ri(ri) \tag{3}$$

It means that the smaller ri is the more effective RSi is.

Fig.4 shows the member-ship functions of antecedent of the equation(2).

Following conditional equations are a sample of RSi;

$$if\ D = B\ then\ \Delta Kp = P \tag{4-1}$$

$$if\ D = S\ then\ \Delta Kp = N \tag{4-2}$$

$$if\ I = H\ then\ \Delta Kp = P \tag{4-3}$$

$$if\ I = L\ then\ \Delta Kp = N \tag{4-4}$$

$$if\ D = B\ then\ \Delta Tp = P \tag{4-5}$$

$$if\ D = S\ then\ \Delta Tp = N \tag{4-6}$$

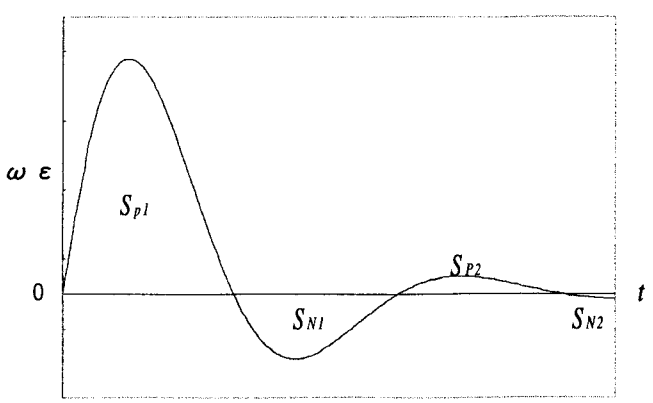


Fig.5 Extraction of D

$$if\ I = H\ then\ \Delta Tp = P \tag{4-7}$$

$$if\ I = L\ then\ \Delta Tp = N \tag{4-8}$$

Equation(2) can be considered to be a kind of hierarchical fuzzy-rule.

Kp and Tp can be derived from the following equations;

$$Kp = Kp + \Delta Kp \tag{5}$$

$$Tp = Tp + \Delta Tp \tag{6}$$

Initial PI gains can be calculated by following conditional equations;

$$K_{p0} = \frac{\sum_{i=1}^{n} \omega si \cdot K_{p0i}}{\sum_{i=1}^{n} \omega si} \tag{7}$$

$$Tp_0 = \frac{\sum_{i=1}^{n} \omega si \cdot Tp_{0i}}{\sum_{i=1}^{n} \omega si} \tag{8}$$

GSi consists of a proportional gain Kp and an integral time constant Tp. The auto-tuning process is started to execute with $Kp0$ and $Tp0$.

C. Auto-tuning

Dynamic characteristics of AC servo are calculated by measuring step response caused by inputting step disturbance reference. D and I are treated as extracted values.

D is corresponded to damping factor of control loop and is derived by separating $\omega\ \varepsilon$ into positive part and negative one and calculating the summation of each part as shown in Fig.5.

$$D = \left| \frac{\sum_{i=1} S_{Ni}}{\sum_{j=1} S_{Pj}} \right| \tag{9}$$

I is corresponded to response speed of control loop. As shown in Fig.6, I consists of three member-ship functions. I is introduced by integrating the absolute value of the filter output of which input is derived by differentiating $\omega\ \varepsilon$. For example, in case where I is H, the matching degree is corresponded to the value of I_H which is derived from the high pass filter.

$\triangle Kp$ and $\triangle Tp$ are calculated from $\triangle Kp$ and $\triangle Tp$ as

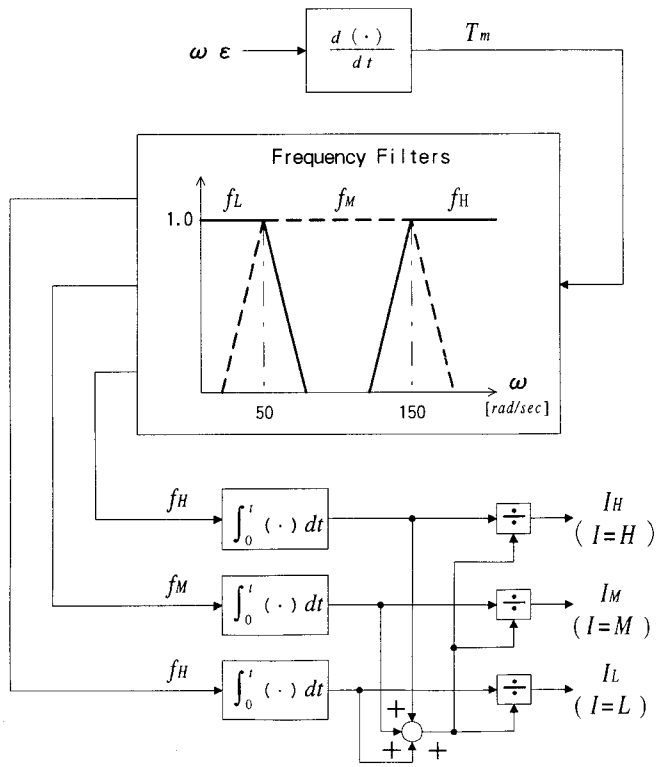


Fig.6 Extraction of I

following equations;

$$\Delta Kp = \frac{\sum_{i=1}^{n} \omega si \cdot \Delta Kpi}{\sum_{i=1}^{n} \omega si} \qquad (10)$$

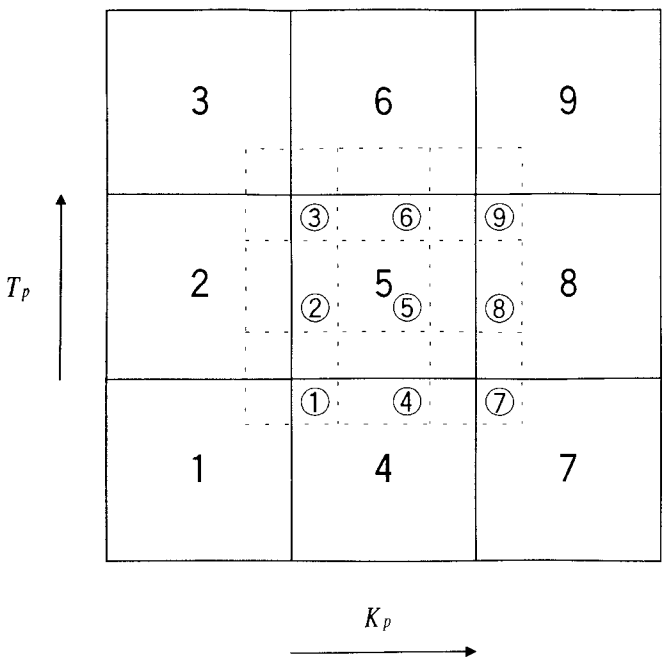


Fig.7 Plane of PI Gains

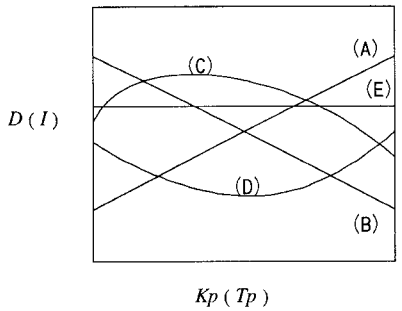


Fig.8 Characteristics of D-K

$$\Delta Tp = \frac{\sum_{i=1}^{n} \omega si \cdot \Delta Tpi}{\sum_{i=1}^{n} \omega_i} \qquad (11)$$

D. Learning control

If desirable characteristics can not be derived in setting numbers of auto-tuning execution, the learning control will be started.

First, D and I are extracted by measuring the characteristics of a servo system at every 9 points selected in whole range of PI gain plane as shown in Fig.7. A point which has the minimum value of D is selected as the first optimum point. In this case, point 5 is assumed to be the first optimum point.

Second, D and I are extracted again at every 9 points in local area of PI gain plane around the first optimum point. The local area is surrounded by dotted lines as shown in Fig.7. A point has minimum value of J in the nine points is selected as the second optimum point.

J which is a kind of performance index is expressed by following equation;

$$J = \sqrt{\log^2\left(\frac{D}{D_{opt}}\right) + \log^2\left(\frac{I}{I_{opt}}\right)} \qquad (12)$$

In this case, ⑤ is assumed to be the second optimum point. PI gains of this point are saved into the data base as a control gain set. Alteration trends of D and I versus Kp and Tp are investigated by changing Kp and Tp and measuring its step response.

Fig.8 shows 5 curves of alteration trend of D versus Kp. Each curve can be expressed as following conditional equations;

(A) $if\ D = B\ then\ \Delta Kp = P$ (13-1)

if $D = S$ *then* $\Delta Kp = N$ (13-2)

(B)*if* $D = B$ *then* $\Delta Kp = N$ (13-3)

if $D = S$ *then* $\Delta Kp = P$ (13-4)

(C)*no rule* (13-5)

(D)*no rule* (13-6)

(E)*no rule* (13-7)

Alteration trends of *Kp-I*,*Tp-D* and *Tp-I* can be also transformed to conditional equations in the same manner.

Ⅲ. Experimental Results

Fig.9 shows the construction of a prototype made to confirm the effectiveness of the auto-tuning method.

Whole auto-tuning processes are executed by software in the personal computer. PI gains and disturbance signal are sent to the servo driver via RS422 type of network. The motor speed is detected as a analog signal by a F/V converter of which input is the output pulse of the encoder connected to the servo motor. The torque reference calculated by the control software of the AC servo driver is transformed to an analog signal with 16-bit D/A converter. These analog signals are inputted into the board with a 12-bit A/D converter every 1.0 msec and 500 points of converted data are saved into the memory area in the personal computer.

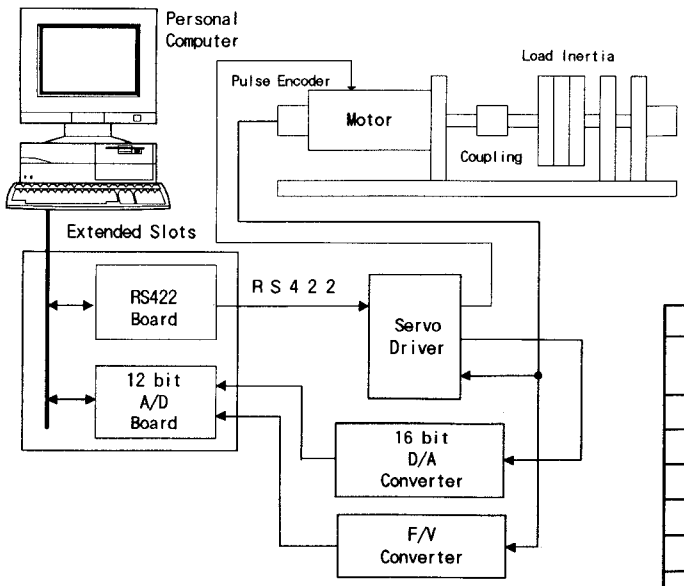


Fig.9 Feasible AC Servo System Structure Control by Computer Software

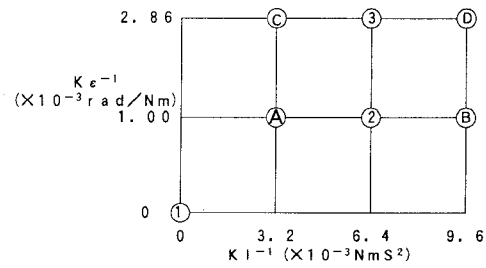


Fig.10 Plean of $K\ \varepsilon^{-1}$—KI^{-1}

In estimation process, the saved data are used to estimate a spring constant and a load inertia by the trapezoidal integration method. In auto-tuning process and learning process, the data are used to calculate *D* and *I*. Spring constant can be changed by replacing the coupling linked the motor and the load. The load inertia can be increased up to 9.6 [NmS²] by connected the load rings to the shaft.

Fig.10 shows the auto-tuning points on $K\ \varepsilon^{-1}$-KI^{-1}plane. Point 0,1 and 2 are the point in which learning control process is already performed and the control gains sets and fuzzy rules are saved into the data-base.

The experimental results are derived in case where the number of fuzzy rules set N is 1,2 and 3. N=1 is the case

Table 1 Experimental Results of $K\ \varepsilon$ and KI

Measuring Points	Design Values		Experimental Results	
	$K\ \varepsilon$ [Nm/rad]	$K\ I$[Nmsec²]	$K\ \varepsilon$ [Nm/rad]	$K\ I$[Nmsec²]
2	1000	156	1854.3	163.0
3	350	156	347.2	124.3
A	1000	312	1538.8	319.7
B	1000	104	1720.4	114.5
C	350	312	412.1	342.7
D	350	104	347.2	124.3

Table 2 Experimental results of *D*, *I* and *J*

N	1			2			3		
Measuring Points	*D*	*I*	*J*	*D*	*I*	*J*	*D*	*I*	*J*
1	0.189	0.594	0.328	0.189	0.594	0.328	0.189	0.594	0.328
2	1.46	0.839	1.84	0.270	0.537	0.104	0.255	0.558	0.111
3	0.403	0.624	0.526	0.255	0.480	0.045	0.338	0.617	0.367
A	1.32	0.839	1.74	0.166	0.497	0.410	0.160	0.522	0.448
B	1.13	0.847	1.60	0.272	0.561	0.142	0.328	0.541	0.283
C	0.396	0.609	0.500	0.170	0.450	0.400	0.204	0.587	0.258
D	0.387	0.606	0.477	0.323	0.520	0.259	0.271	0.590	0.183

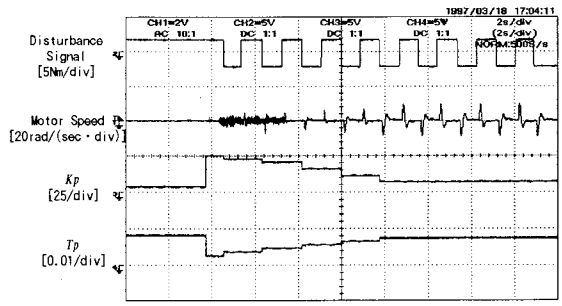


Fig.11 Wave-form of Auto-Tuning Operation

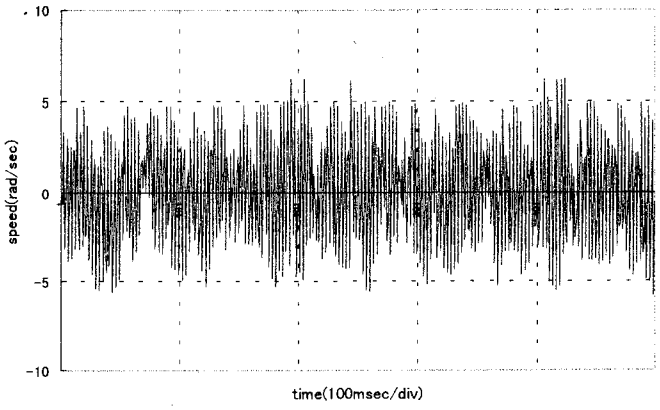


Fig.12 Wave-form of Motor Speed(N=1)

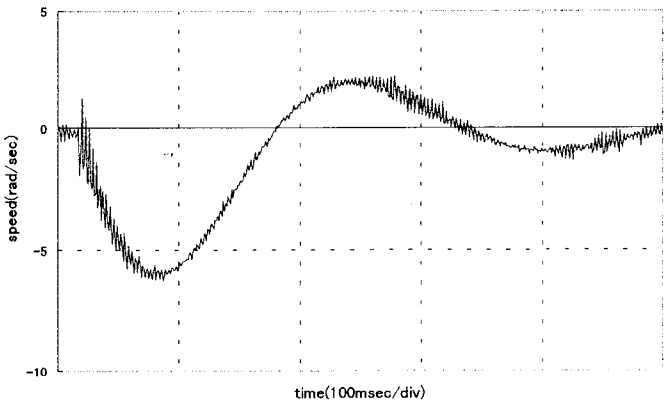


Fig.13 Wave-form of Motor Speed(N=2)

where the data module of point 0 is used. In case of N=2, the data modules of point 0 and 1 are used. As for N=3, the data modules of point 0,1 and 2 are used.

Table 1 shows the results of estimating the load parameters. The load inertia values are considered be comparatively accurate. But, the estimating error of the spring constant is seem to be large in all cases. The estimating values are also different from the design value of the coupling as indicated in Table 1. To derive more accurate estimating values, data sampling period should be set smaller and the calculating method should be changed to high level one. But, in this case these error level can be acceptable and does not have any influences on the auto-tuning performance.

Table 2 shows the results of auto-tuning operation.

In case of N=1, *D* values are large in all conditions. In some cases, mechanically vibration is occurred. On the other hand, in case where N is 2 or 3, *D* exists between 0.1 and 0.4. For this reason, the responses are considered to be desirable.

Fig.11 shows the wave-forms of auto-tuning operation at point 2 in N=3. When starting auto-tuning mechanical vibration occurs, but after a few steps of auto-tuning operation the response becomes stable and desirable. Fig.12 and Fig.13 show the step responses at point B in case where N is 1 and 2 respectively. In Fig.12 mechanical vibration occurs. But, in Fig.13, the responses are desirable and do not contain a large level of vibration.

Ⅳ.Conclusion

An advanced Fuzzy auto-tuning method with learning control is introduced. Without any kinds of strategy on tuning servo gains, the optimum fuzzy rules can be generated automatically in learning process. Furthermore, the auto-tuning performance increases with increasing learning times. From the experimental results, the effectivenesses of this auto-tuning method are proved.

References

[1] Inoue K and Nakaoka M, "An Advanced DC Brush-less Servo Drive System and Its Practical Evaluations", International Journal of Electronics-Special Issue on Power Electronics, Vol.80, No.2, pp.223-233, 1996.

[2] Ahmed R S and Rattan K S, "Real-time Tracking Control of A DC Motor using A Neural Network", Proceeding of the IEEE National Aerospace Electronics Conference, No.2, pp.593-600, 1995.

[3] Karr C.L., "Design of an Adaptive Fuzzy Logic Controller Using Genetic Algorithm", Proceeding of 4th International Conference on Genetic Algorithm,pp.450-457, 1991.

[4] Chiricozzi E,Parasiliti F,Tursini M and Zhang D Q, "Fuzzy Self-Tuning PI Control of PM Synchronous Motor Drivers", International Journal of Electronics,Vol.80, No.2,pp.211-221,1996.

A Real-time Estimation Method of Brushless DC Servomotor Parameters

Hisashi Takahashi, Takashi Kenjo, and Hirokazu Takeuchi
(Polytechnic University of Japan) (Sagamihara Vocational Training School, Kanagawa, Japan)
4-1-1 Hashimotodai, Sagamihara, Kanagawa 229-11, JAPAN
Fax : +81-427-63-9150 phone : +81-427-63-9138
E-mail : hisasan@uitec.ac.jp

Abstract **- This paper deals with an estimation method of the load inertia/torque, motor's cogging torque, winding resistance and back-emf constant of a brushless DC servomotor operating in a system. The method requires no modification of the system hardware, as the quantities needed for estimation are the winding current, applied voltage, motor speed and rotor position, which can all be taken from the connectors of a normal driver or controller. Time required for data acquisition and computation is discussed for applying this technique to construct a controller capable of coping with varying inertia and load torque.**

I. INTRODUCTION

Motor control devices used in robots and automatic control must be highly functional as well as robust against varying load and motor characteristics. Motor drive devices are generally designed to be stable for a certain load torque range. However, for achieving a stable and high-response control for a wide range of electrical and mechanical parameters, it is necessary to estimate these values while the motor is running and to adjust the servo gain and other system constants using the estimated quantities.

We propose a simple method for estimating the inertia and load torque as well as winding resistance and back-emf constant of a three-phase brushless DC motor. We will discuss the possibility of applying this technique for real-time estimation of the necessary quantities while operating at an accuracy level needed for stable control. The effect of cogging torque is also discussed, together with the estimation accuracy of the fluctuating torque during operation.

II. DEFINITION OF BACK-EMF AND TORQUE CONSTANTS

Of the various parameters of a brushless DC motor as well as a conventional brush DC motor, the back-emf constant K_E and torque constant K_T are the two most important ones: they are usually the same thing in the physical sense and have a large influence on other parameters.

While Hendershot and Miller [1] discuss the definitions for the back-emf and torque constant for several cases, we shall first present our definition of these parameters within the context of the present theory. The back-emf appearing across each phase winding is assumed to be given by:

$$\begin{aligned} e_U &= K_E\omega\{\cos(\theta)+h_5\cos(5\theta)\},\\ e_V &= K_E\omega\{\cos(\theta-\gamma)+h_5\cos(5\theta+\gamma)\},\\ e_W &= K_E\omega\{\cos(\theta+\gamma)+h_5\cos(5\theta-\gamma)\}. \end{aligned} \quad (1)$$

Here γ is $(2/3)\pi$, and K_E the back-emf constant. As indicated by these equations, the back-emf is proportional to the angular speed ω. θ is the rotating angle, which can be obtained by integrating ω with respect to time t. We assume that the back-emf is basically sinusoidal but may involve some harmonic components. As shown typically in Figure 1, the major component is the fifth, which is expressed in the above equations, and its magnitude h_5 is around 0.05 or less. The seventh harmonic component is considered to be negligible compared to the fifth component. With these back-emfs, torque T is assumed to be given by

$$\begin{aligned} T = K_T\big[&i_U\{\cos(\theta)+h_5\cos(5\theta)\}\\ &+i_V\{\cos(\theta-\gamma)+h_5\cos(5\theta+\gamma)\}\\ &+i_W\{\cos(\theta+\gamma)+h_5\cos(5\theta-\gamma)\}\big]. \end{aligned} \quad (2)$$

Here the proportionality factor K_T is the torque constant and i_U, i_V and i_W are the instantaneous currents for each phase.

Now, the electric power supplied to the back-emf source of the three phases is

$$P_E = e_U i_U + e_V i_V + e_W i_W. \quad (3)$$

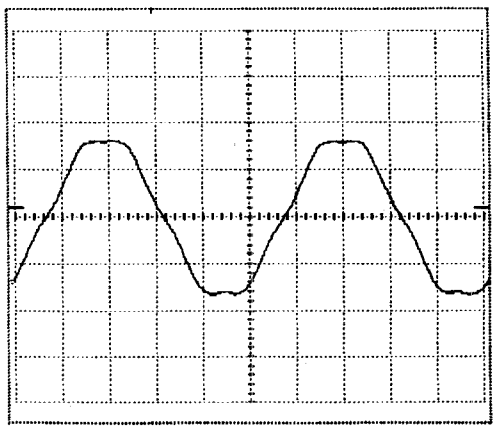


Fig.1. Back-emf waveform.

This is considered to be consumed as mechanical power P_M, which is the torque (T) multiplied by angular speed ω, so $P_E=P_M$. From this, we have the basic relationship:

$$K_E = K_T . \tag{4}$$

Thus K_E and K_T are the same thing, so hereafter we use K_E. It is well known that T and h_5 can be obtained from the emf waveform observed when the motor is made to run as generator at constant speed by another motor, so we can calculate torque from (2). However, here we need to estimate K_E and other parameters while the motor is running. We thus propose a simplified expression to calculate T derived from (2) as shown in Appendix:

$$T \cong \sqrt{\frac{3}{2}} K_E I_{ef} \tag{5}$$

where

$$I_{ef} = \sqrt{{i_U}^2 + {i_V}^2 + {i_W}^2} . \tag{6}$$

This is satisfactory for a harmonic component of less than 3% (h_5=0.03), even when the winding current is modulated by the motion ripple due to large cogging torque. When the fifth harmonic component is around 5%, (5) is a fairly good approximation when the motor is running at a constant speed with a moderate load.

Note that when the motor is driven in the 120-degree conduction mode from a DC supply, instead of sinusoidal voltage operation, a satisfactory approximation is given by

$$T = 1.16 K_E I_{ef} . \tag{7}$$

The average current I_{av} supplied by the DC source when operated on the sinusoidal base, is related to the effective current as follows:

$$I_{ef} = \frac{\pi}{2} I_{av} . \tag{8}$$

Hence we have

$$T = \sqrt{\frac{3}{2}}\left(\frac{\pi}{2}\right) K_E I_{av} \cong 1.92 K_E I_{av} . \tag{9}$$

Recall that for a brush DC motor, the torque constant K_{DC} is defined as:

$$T = K_{DC} I_{DC} \tag{10}$$

where I_{DC} is the armature current. A comparison of these two equations shows the analogy between our definition of the torque constant for a brushless DC servomotor and that of a brush DC motor.

III. Estimation Principles

A. Estimation of winding resistance and back-emf constant

When running at a fairly constant speed, the back-emf constant K_E and winding resistance R can be computed from

$$K_E = \frac{V_P}{\omega} - \frac{pLI_F}{\sin\phi} \tag{11}$$

$$R = \frac{p\omega L}{\tan\phi} \tag{12}$$

where V_P is the voltage amplitude, L the sum of self and mutual inductances of each phase, ω the rotational angular speed, I_F the magnitude of the fundamental component of the winding current, ϕ the phase angle between the voltage and current, and p the number of pole pairs.

Thus I_F and the phase angle ϕ are needed. Even when the motor is driven by sinusoidal voltages, the current waveforms contain harmonic components caused by, for example, the rotor's magnetization pattern and the stator's slot/teeth shapes. To remove the harmonic components in the computation of I_F and ϕ, we use integration over one cycle as follows:

$$I_F = \sqrt{\left(\frac{1}{\tau}\int_{t_1}^{t_1+\tau} v_S i_U dt\right)^2 + \left(\frac{1}{\tau}\int_{t_1}^{t_1+\tau} v_C i_U dt\right)^2} \tag{13}$$

$$\phi = \tan^{-1}\left(\frac{\int_{t_1}^{t_1+\tau} v_C i_U dt}{\int_{t_1}^{t_1+\tau} v_S i_U dt}\right) \tag{14}$$

where τ is the cycle period, t_1 an arbitrary point in time, i_U the instantaneous U-phase current, v_S=sin($p\theta$) and v_C=cos($p\theta$).

Though these equations involve integration which require some computational time, this poses no problem since the variations of R or K_E due to temperature rise occur over longer time spans.

B. Estimation of moment of inertia and load torque

If we assume that motor torque, which is balanced with the inertial load and other components of load torque, changes very little during a sampling cycle of Δt, the total moment of inertia J and load torque T_L can be computed from the following equations.

$$J = \frac{I_{ef}(t_1) - I_{ef}(t_2)}{\left(\frac{d\omega}{dt}\right)_{t_1} - \left(\frac{d\omega}{dt}\right)_{t_2}} \sqrt{\frac{3}{2}} K_E \tag{15}$$

$$T_L = \frac{I_{ef}(t_2)\left(\frac{d\omega}{dt}\right)_{t_1} - I_{ef}(t_1)\left(\frac{d\omega}{dt}\right)_{t_2}}{\left(\frac{d\omega}{dt}\right)_{t_1} - \left(\frac{d\omega}{dt}\right)_{t_2}} \sqrt{\frac{3}{2}} K_E . \tag{16}$$

where t_1 and t_2 are the points of time when samplings are taken (rotor position must be the same for t_1 and t_2). The load torque T_L involves not only the load torque coupled to the test motor but also the fluctuation or loss torque within

the test motor, including the cogging torque. These equations involve speed differentiations, so that J and T_L must be estimated when the motor's speed is changing in magnitude. In practice, the speed variation from t_1 to t_2 must be at least 10% for estimation.

C. Measuring torque ripples when running

Once J is determined using (15), however, we can determine T_L from sampling data taken from a constant-voltage operation using

$$T = \sqrt{\frac{3}{2}} K_E I_{ef} = J\frac{d\omega}{dt} + T_L \tag{17a}$$

or

$$T_L = \sqrt{\frac{3}{2}} K_E I_{ef} - J\frac{d\omega}{dt}. \tag{17b}$$

Here the time differentiation of speed must be computed from data sampled at very proximate rotor angles. As will be shown later, not only the average load torque but even cogging torque and other fluctuating torque can be detected sufficiently by this method (whereas the torque values estimated from (16), shown in Fig. 7, show a irregular fluctuations when the voltage is changing.)

D. Correction of sampling data and statistical treatment

The quantities for estimation computations contain various sorts of noise and quantization errors due to analog-to-digital conversion. To reduce the effect of quantization and noise, we apply corrections by the method of least squares. There is still, however, the possibility that the computed values will have a statistical distribution. As it was confirmed that the estimated resistance and back-emf constant concentrate in the vicinity of the true value, we use a simple average for these. As for the inertia and the torque, the computed values show a scattered distribution, so we take the mode.

IV. Estimation System and Experimental Results

A. Estimation system

Figure 2 shows a block diagram for our system. The section within the dotted line is the portion added to the normal drive/control system of a brushless DC servomotor. Thus the estimation section does not require any modification of the existing drive/control system; in other words, the quantities needed for estimation computation are taken from the connectors of conventional hardware. The relevant data for the test machine are shown in Table 1 and Figure 3.

B. Resistance and back-emf constant estimation

In the experiment, several sample resistors of known resistance were connected in series between the motor and drive circuit to compare the estimated values and real resistance within a wide range.

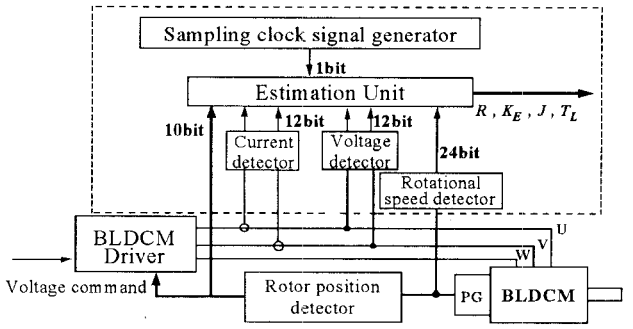


Fig.2. Block diagram for the estimation system.

Table 1 Specifications and ratings of test motor.

Rated output	100 W	Winding resistance	2.6 Ω/phase
Rated speed	3000 rpm	Inductance	8.59 mH/phase
Torque constant	0.154 NmA^{-1}	Mutual inductance	2.67 mH/phase
Back-emf constant	0.154 $Vsrad^{-1}$	Moment of inertia	3.137×10^{-5} kgm^2
Number of poles	4	Stator diameter	75 mm
Number of slots	6	Rotor diameter	35.6 mm
Stator's internal diameter	36 mm	Windings	3-phase concentrated
		Rotor magnet	samarium-cobalt

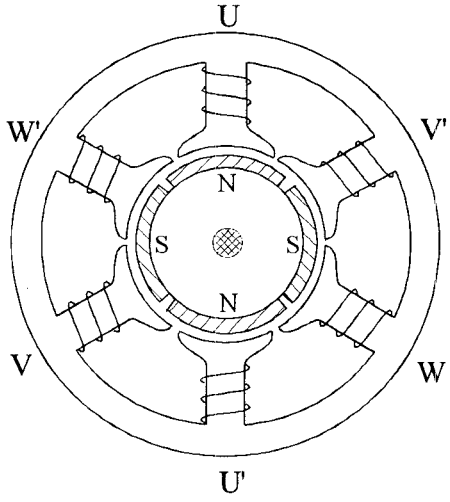


Fig.3. Cross-sectional diagram of test motor.

As the load for the test motor we mounted a brush DC motor whose torque can be adjusted by the armature current. (The DC motor is used in brake mode.)

Figure 4 shows the relation between the computed resistance and the added resistance values. Since the winding resistance at room temperature is 2.6Ω, the estimation accuracy is excellent.

Figure 5 shows the computed back-emf constant as a function of the added resistance. Though in theory the back-emf constant is independent of the winding resistance plus the added resistance, a 10% reduction is seen in the estimated value when a resistor of 3.5Ω is added to the winding of 2.6Ω. The error is considered to occur due to the change of time constant when a resistor is added.

However, the resistance variation of an actual motor due to temperature rise will be at most 50%, so the estimation error for K_E would be less than 5%.

C. Inertia

For estimation of inertia using (15), five discs of different moment of inertia (up to 150 times the motor moment of inertia) were attached to the motor. Figure 6 shows the plotted relation between the actual moment of inertia and estimated mode values; the straight line represents the ideal relation. Clearly the result is very satisfactory.

D. Torque and torque ripples

In Figure 7 the curves represent the estimated torque for two types of brake, for which (16) was used. The above curve is the result when a brush DC motor is coupled to the test motor as the brake, so the system is subjected to the brake machine's slot cogging. (The brake motor's armature has 13 slots.) The below curve is obtained when a rippleless hysteresis brake was used as the load. Here we observe that:

1) irregular fluctuations are seen, even though statistical treatment was carried out,
2) but the average value for both cases, shown by the dotted straight line, matches the actual load torque.

Thus, the estimation method is satisfactory for determining the average torque, which is the estimated frictional/viscous load torque or the brake torque. Figure 8 shows the relation between the estimated torque and the applied brake torque. Thus the estimation results are in good agreement over a certain range.

Now, we need to examine the torque ripples. The large fluctuations in these samples are thought to have several causes:

1) Cogging torque: the torque ripples generated by the interaction between the stator teeth and rotor's permanent magnets.
2) Additional cogging torque due to stator's winding currents.
3) Torque ripple due to fifth harmonics.
4) Brake machine's torque ripples.

In order to detect torque ripples during a constant-voltage drive using (17b), we conducted another experiment, which results are shown in Figure 9. The motor is driven at a constant voltage with an inertial disc of 0.0001kgm^2 and hysteresis brake, and 40 samplings were taken at each position as before. The effective current defined by (6) was nearly the same for each rotating angle. The curve is very smooth with 12 peaks, caused by the superposition of three different waves, i.e., 12, 4, and 2 cycles per rotation.

The four peaks are likely to be the effects of eddy-current that depend on the stator position. For some reason, e.g. due to the bolts or calking rivets, the eddy current that flows when a magnetic pole passes this position may be higher than that for other positions. Four poles pass per rotation. These peaks are not found in the static measurement of cogging torque shown in Figure 10, though the gentle two-cycle wave can be noticed. Curve (a) is the measured no-current cogging, while curves (b) and

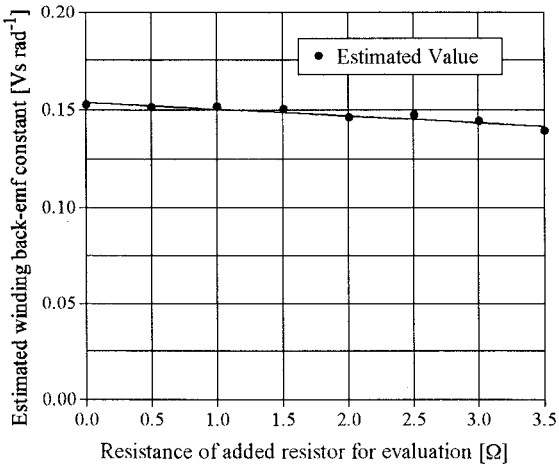


Fig.5. Estimated back-emf constant.

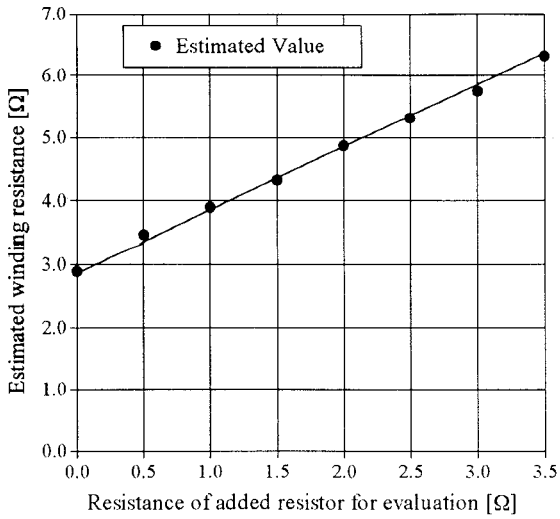


Fig.4. Estimated winding resistance.

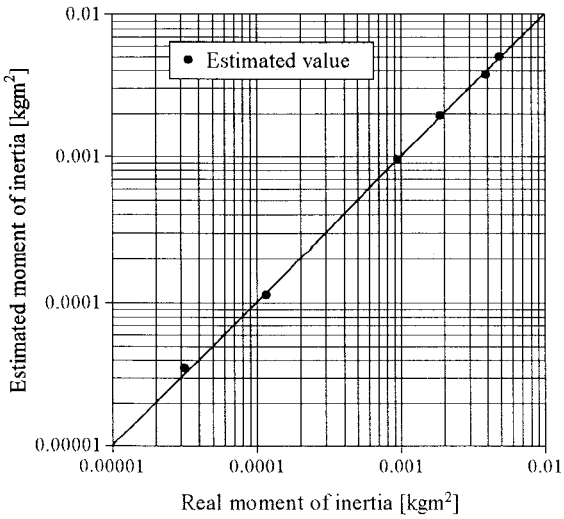
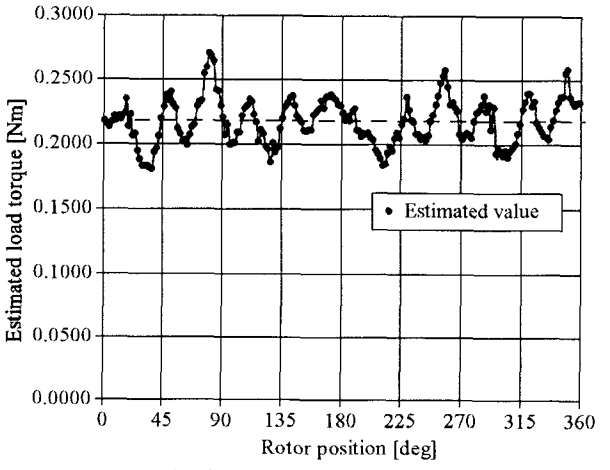


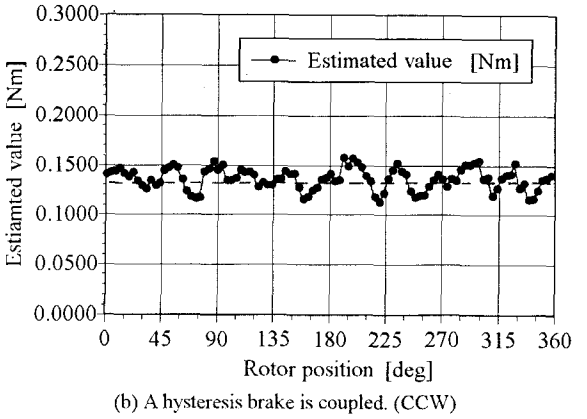
Fig.6. Estimated moment of inertia.

(c) show the cogging torque when a sinusoidal current is supplied to each winding with 120-degree differences.

Chigiri et.al[2], in their linear theory, claim that cogging torque is independent of winding current. However, as shown in Figure 10 the cogging torque increases and the phase shifts with current for our test motor, and this was confirmed by computation that took into account non-linear characteristics of the permanent magnet[3]. Moreover the fifth harmonic current produces torque ripples which have the same frequency as cogging. As seen in Figure 8, other types of torque ripple are also created inside the motor. Theoretically the curve in this figure, which is based on (17b), represents the load torque, the cogging torque and these low frequency ripples, but not the torque ripple due to the fifth harmonics, and this is confirmed by a simulation calculation.



(a) A brush DC motor is coupled. (CW)



(b) A hysteresis brake is coupled. (CCW)

Fig.7. Relationship between rotary angle and estimated load torque.

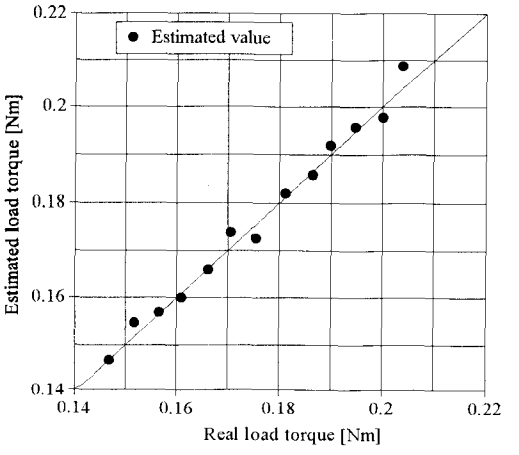


Fig.8. Estimated load torque.

V. Discussion and Conclusion

Our parameter estimation method is not very sophisticated and only requires simple hardware. A major advantage when applied to motion control is that it is possible to compute, from accurate information on winding resistance R, back-emf constant K_E, angular speed ω and winding inductance L, the optimum pulse-width modulation command to set the winding current at a desirable value, without using a current sensor. Here L can be treated as a fixed value, while ω is directly measured, so the important parameters are K_E and R. For estimation of these parameters, data for one cycle are sufficient for integration based on (13) and (14) corresponding to the statistical effect, that is, half rotation for a four-pole motor. Thus, if the motor speed is 600rpm, the time needed for data collection is as short as 50ms. The computation time using the sampled data depends on the CPU's execution rate, requiring only a second or so. Although R and K_E vary with temperature, sampling and computation time is much shorter than the thermal time constant of these parameters.

Because cogging and other factors cause the total torque

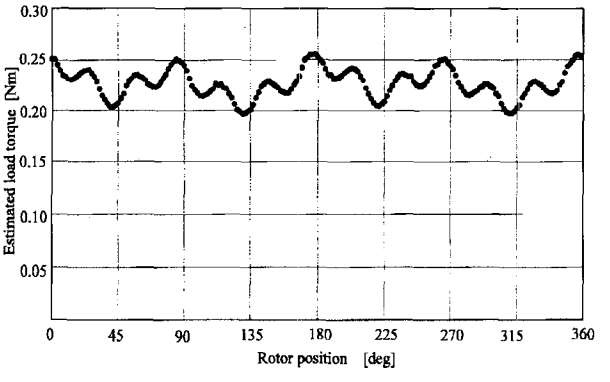


Fig. 9 Estimated load torque containing cogging and other ripples.

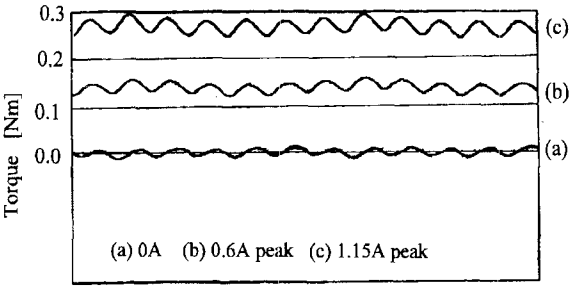


Fig.10. Cogging torque measured at low speed, with sinusoidal current supplied. As the current increases amplitude increases and the phase shifts.

to vary with rotor angle, sampling must be done at various rotor angles when estimating moment of inertia and load(frictional/viscous) torque. To carry out statistical treatment, at least 20 data are needed for each position. Thus, two seconds are required to obtain 20 data for a motor running at 600rpm. For a four-pole motor, however, two samplings can be taken per rotation, so data collection would require one second (at 600rpm). Meanwhile, the time needed to compute J and T_L from the sampled data should take no longer than a second.

In situations where the moment of inertia stays relatively constant, the estimated moment of inertia can be used to compute the load torque much faster by using the approximation of (17b).

However, in applications where the moment of inertia changes, data acquisition time can be a major obstacle in the real-time estimation of torque based on (16). If the variation of inertia during the sampling time in this method is less than 5% or so, one solution is to take advantage of several rotor positions where the cogging torque is nearly identical. Thus, in a four-pole motor with an ideal construction, there are 24 such positions, and in the absence of other unpredictable periodical effects, a single rotor revolution should suffice for sampling.

Unfortunately, real motors often have unpredictable rippling effects as seen in our experiment, and this can only be avoided by using a carefully constructed motor with predictable cogging characteristics.

Another possible technique to reduce sampling time is to continually update part of the data set, in which case data collection time will consist only of that time necessary to obtain the newly added data (say, two or three) instead of the entire set of 20.

In conclusion, the most important parameter is the back-emf constant, and we presented a method for estimating it on a real-time basis while the motor is running. Winding resistance can be estimated at the same time. Our technique of identifying the moment of inertia is very satisfactory in terms of accuracy. However, to achieve real-time estimation, the time spent on data collection and computation must be cut down considerably. We have discussed some strategies, and concluded that the most effective approach is to increase the number of sampling points. For this careful design of the motor itself is critical.

APPENDIX
DERIVATION OF EQUATION (5)

We assume that the sine-wave voltage applied to U is in phase with e_U and inductance L is negligible. Current i_U in this case is given by

$$i_U = I_0\{\cos(\theta) + H_5(5\theta)\}. \quad \text{(A1)}$$

Similar forms are assumed for i_V and i_W.

Equation (5) then becomes

$$T = \left(\frac{3}{2}\right)K_E I_0\{(1+h_5H_5)+(h_5+H_5)\cos(6\theta)\}. \quad \text{(A2)}$$

Since h_5H_5 is much smaller than 1, we obtain

$$T \cong \left(\frac{3}{2}\right)K_E I_0\{1+(h_5+H_5)\cos(6\theta)\}. \quad \text{(A3)}$$

Since H_5 is much larger than h_5 we further simplify as follows:

$$T \cong \left(\frac{3}{2}\right)K_E I_0\{1+H_5\cos(6\theta)\}. \quad \text{(A4)}$$

Meanwhile

$$i_U{}^2 + i_V{}^2 + i_W{}^2 = \left(\frac{3}{2}\right)\{(1+H_5{}^2)+2H_5\cos(6\theta)\}. \quad \text{(A5)}$$

If $H_5 < 0.3$, from this we can obtain the following approximation

$$\sqrt{i_U{}^2 + i_V{}^2 + i_W{}^2} \cong \sqrt{\frac{3}{2}}\{1+H_5\cos(6\theta)\}. \quad \text{(A6)}$$

(Even when $H_5 \cong 0.5$ this approximation is satisfactory for our purpose.)

We obtain (5) from (A4) and (A6).

When the motor is running at an almost constant electrical angular speed ω, we can put $\theta = \omega t$. From (A3) we see that the torque contains a ripple component with an angular frequency of 6ω, or 12 cycles in a four-pole motor. The cogging also has 12 cycles because of six teeth and four magnetic poles. (12 is the least common multiple of 4 and 6.)

REFERENCES

[1] J.R.Hendershot Jr. and TJE Miller, *Design of Brushless Permanent-magnet Motors*. UK: Oxford University Press,1994, Chapter 7.

[2] T.Chigiri, T.Shimada, T.Watanabe, O.Ichinokura and T.Jinzenji, "Current Control Method for Zero Torque Ripple and Maximum Efficiency of Brushless DC Motor," *J. IEEJ*, vol.116-D, No.12, pp.1276-1282, 1996.

[3] T.Kenjo, H.Takahashi, H.Takeuchi and K.Marushima, "*Effect of Winding Current on CoggingTorque in a Brushless Motor*," *IEEJ*, RM-97-19, 1997.

Driving Method for Delta-Connected Brushless-Sensorless Motor

Tadashi (Ted) SAKURAI(*1), Motoki SAKURAI(*2), Masao ARIMOTO(*3), Sumio KANEKO(*4)
(*1):SAKURA lab, (*2):SOPHIA Univ., (*3):NAGAOKA College, (*4):maxon Japan
(*1):3-7-3-301 Hazawa, Nerima-ku, Tokyo, JAPAN 176
Tel.& Fax.:+81-3-3991-6234 or (office)Tel.&Fax.:+81-3-3261-3606
E-mail: sakulab@twics.com or CXX00137@niftyserve.or.jp

Abstract - **Developing our new driving method for a brushless DC motor, we report a manner of the motor operation by using "vector chart" in this time, and make the feedback operation clear in the method.**

As the results, we drive the motor at more than 16,000 rpm of the rotation and start quickly the rotation without any sensing elements in the motor, i.e. sensorlss driving motor.

I. Introduction

To get more power converting efficiency and to reduce noises or mechanical vibrations at driving brushless DC motor, we have reported a new driving method used a delta connected three phase motor and a 12 phase/steps combination of the driving voltages (a half current flows when the driving voltage opens at one terminal of the delta connected motor), so that we have realized better sine shape current on the phase of the delta connected brushless motor.[1]

Increasing number of the phase/steps from 12 to 48, it is better for the sine shape current to flow in the motor phase. The percentages of the power sine shape current to the total power current is 92.9% by the 12 phase/steps and 95.8% by the 48 phase/steps.[2]

Also, it is important to start rotation of a brushless motor, so that we have adopted a feedback circuits in Fig.1 using a back-E.M.F.as well as known. The back-E.M.F signal is picked up when the driving terminal is opened referring to the phase 1, 5 and 9 - "OPN" in Table 1. And by using this way, we drive the motor synchronously at a setting number of the rotation.[3] An actual feedback circuit is that a differential voltage between the back-E.M.F. and the reference voltage regarding to the power supply voltage controls the number of the rotation by changing frequency of the O.S.C. Please refer to the circuits in Fig.5.

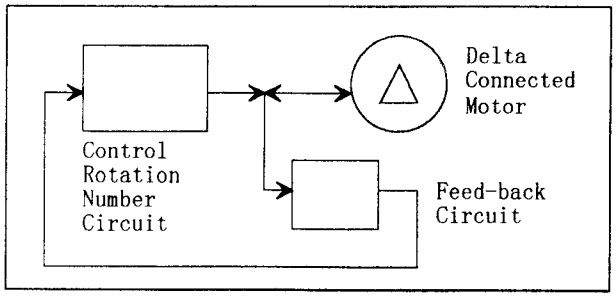


Fig.1 Block Diagram for Control System

II. Vector

A. Definition and Function

Based on the past experiment to driving the delta connected motor, we understand the manner of the motor operated as sine shape current function closely, even the power supply is a DC voltage. Then, we try to put " Vector chart" on our new driving system.

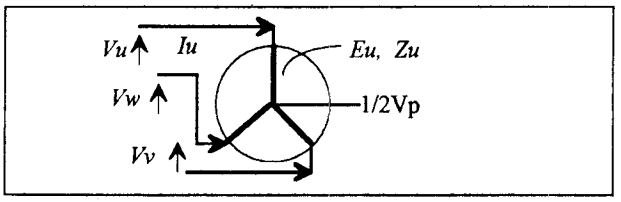


Fig.2 Equivalent Star Connected Motor

Phase	1	2	3	4	5	6	7	8	9	10	11	12	13/ 1
Vu	OPN	Vp	Vp	Vp	Vp	Vp	OPN	GND	GND	GND	GND	GND	OPN
Iuv	N/2	N	N	N	N/2	0	S/2	S	S	S	S/2	0	N/2
Vv	GND	GND	GND	GND	OPN	Vp	Vp	Vp	Vp	Vp	OPN	GND	GND
Ivw	S	S	S/2	0	N/2	N	N	N	N/2	0	S/2	S	S
Vw	Vp	Vp	OPN	GND	GND	GND	GND	GND	OPN	Vp	Vp	Vp	Vp
Iwu	N/2	0	S/2	S	S	S	S/2	0	N/2	N	N	N	N/2
Vu	OPN	Vp	Vp	Vp	Vp	Vp	OPN	GND	GND	GND	GND	GND	OPN

NOTE : OPN = opened terminal voltage Vp = supplied Power voltage
N, S = N, S electromagnetic pole by the full current.
N/2, S/2 = electromagnetic pole by the half current.
0 = non electromagnetic pole by no current (the shorted terminals).

Table 1. 12 Phase Driving Voltage and Electromagnetic Poles

We drive and control the delta connected motor by a DC voltage, so that we consider that the motor is a star connected motor with the neutral point of a half power supply voltage. Names of each voltages and currents are in Fig. 2.

The vector equation and conditions are followings. Please refer to them in Fig.3.

$$\boldsymbol{Vu} = \boldsymbol{Eu} + \boldsymbol{Iu} \cdot \boldsymbol{Zu} \text{ (vector)} \quad (1)$$

$$\textbf{Power out (Po)} \leq \textbf{Eu}\cdot\textbf{Iu}\cdot\cos\alpha \quad (2)$$

$$\Delta V = \textbf{Eu}\cdot\sin\beta \quad (3)$$

We explain the vector equation and conditions.

A motor rotes following the vector equation (1) generating a back E.M.F.,Eu against a supply voltage Vu.

When a motor starts the rotation, and when a motor rotates as stable, the power output of the motor should keep the condition (2). Here, if a number of rotation is constant, the motor changes the factor of cos α for the load of the motor. If the load of the motor needs less power output, the α increases and the current Iu increases ! However, if the load increases over, the motor stops immediately due to less power of the Eu·Iu.

To control the motor as a DC brush motor, we put (3) to feedback the back E.M.F. to controlling the number of the rotation.

B. Vector chart

Fig 3. shows the vector chart at the phase 1 of Table 1. In this case, the Vu is opened, OPN, then the value is 1/2 Vp due to balanced voltage between the power supply(Vw) and Ground(Vv). And the back E.M.F., Eu advances an angle β to the line voltage Vu. So that the real voltage of the Eu is ΔV.

C. Line voltage

Also you can see the Δ V (BEMF) in Fig.4. The measuring data of the line voltage Vu changes the value due to the phase steps. The phase 1 is as same vector phase as in Fig.3, and the opened terminal shows the back E.M.F., Eu with a voltage of 1/2 Vp. The second Eu in the phase 7 is the just other side of a sine shape of the Eu.

D. Control ΔV

For the controlling Δ V, we adopt feed back circuits in Fig.5. There are two points to manage the Δ V. The first point is that the Δ V is on a half of the power supply voltage (1/2 Vp). The second one is that the value is related to the starting rotation of the motor.

For the first point above it is not so difficult to cut the DC voltage by using a differential amplifier and to transfer the signal to a OSC circuit by a current mirror circuit. In this case, Δ V is set as a Vf, about 0.7 volts. Of course, we should consider the range of operation voltage Vp, if it is more than 5 volts, and we use voltage dividers for both of inputs, the 1/2 Vp and the back E.M.F.

For the 2nd point, we should accelerate the rotation of the motor from 0 r.p.m to a setting number, i.e. 16,000 rpm. So, even the back E.M.F. in the starting point is a

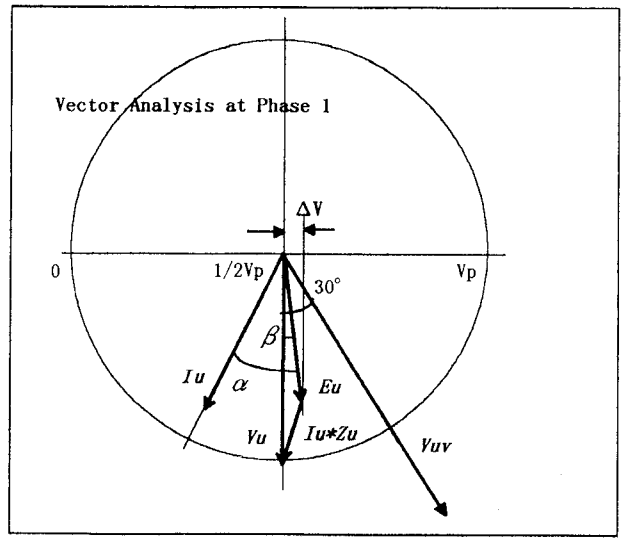


Fig.3 Vector chart at Phase 1

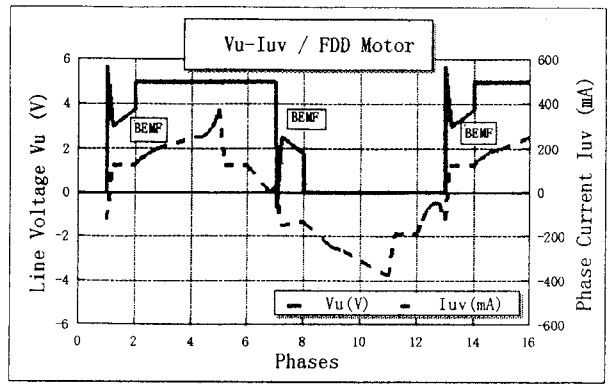


Fig. 4 Wave-form for Line Voltage and Phase Current

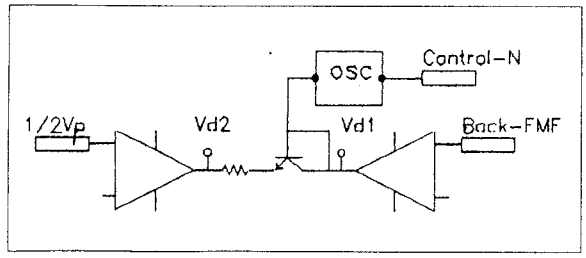


Fig.5 Feed Back Circuits

small, it is need to keep the starting rotation number less than 1/10 for setting rotation. In opposition, it is needed quick response at the normal rotation to change the Δ V for the rotation following the motor load. Then, we put a nonlinear element(transistor/ diode) and a tuning resistance in series to manage the Δ V.

When the motor stops, the value of the back E.M.F.is the same as other input voltage, 1/2 Vp in Fig. 5. Then, the OSC circuit oscillates at lower frequency, and the bigger driving current flows in the motor coil to generate bigger torque in the rotating field. Also, in this system, the field is

closely sine shape due to driving 12 combined voltages in an electrical period.

III. Results

A. Feed Back Voltage, ΔV vs. Rotation, N

Fig.6 shows a curve of Δ V and N for much conditions of power supply voltages and loads. There are two areas; Δ V ≒0.6 V and less than 0.6 V. The first area is to control the number of the rotation. So, the slope means a response of the changing the power supply and the load on the motor. And we can set the slope by changing serial resistance in Fig.5

It is not clear the curve at lower voltages of Δ V, but there is the starting feed back characteristics. As referring to Fig.5, when the motor stops, the Δ V is zero and the number of the rotating field is 789 rpm by the OSC circuit.

After lower rotating motor, the Δ V increases quickly the value and goes into the first area at the Δ V≒0.6 V. The starting rotation is shown in Fig.9 and explained it in section D.

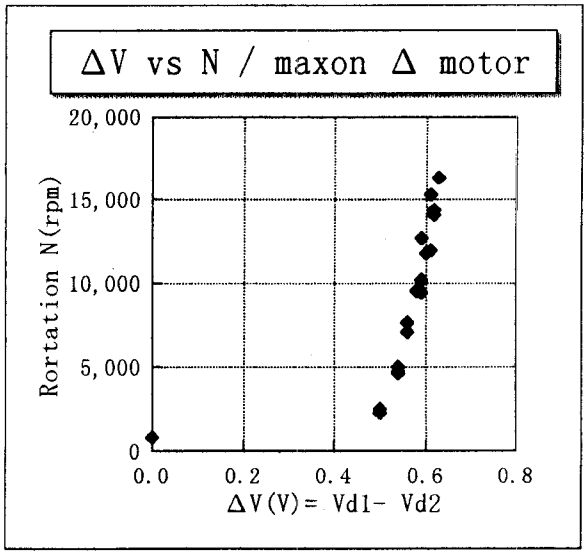


Fig. 6 Feed Back Δ V and the Rotation, N

B. Power Supply Voltage, Vp vs. Rotation, N

Fig.7 shows the rotation N vs. the power supply voltage Vp for a standard "maxon EC motor" which operates over the rotation of 16,000 rpm with sensors (hall elements). We can do it by our sensorless system, and get the same as the ratio of N/Vp as 1,281 rpm/V in the data sheet of the motor (EC032-060-31EBB200B).

For the wide range of the power supply voltage in Fig.7, from 1.5 V to 13.0 V, we should consider the voltage operation range of the feed back circuit. Especially, if the this system is made in an IC, we should use a 5 V power supply voltage separately for the control. There are many kinds of motors and applications, so that the feed back circuits should be modified in case by case.

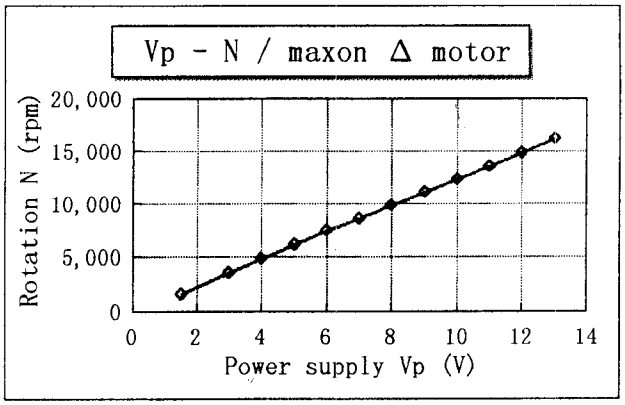


Fig. 7 Power Supply Voltage and the Rotation, N

C. Motor Driving Power, Pp vs. N and Line Current, Ip

It is necessary to check load capability because this motor operates as a synchronous motor and stops quickly when over load. To test a torque of the motor, we connect a generator (DC motor) with its resistance load to the motor and change the loads. Then, the X-axis shows the output power level of the generator's power including R-loads. This motor has a capacity of power consumption of 40 watts and needs max. current of 15 Ampere, but due to our power supply limitation, those data do not fill in the chart.

At each power supply voltage, the rotation N is decreasing by increasing loads, and the line current is increasing. Those functions are clear by referring the vector chart of Fig.3 and also by controlling voltage Δ V. Increasing the loads makes the back E.M.F. delayed and smaller by the feed back circuit, then the current Iu increases to keep the vector chart.

For this feedback function, one of condition to have a wide operation voltage range of the motor is to use a lower inductance in the rotating field coils. The testing motor, maxon Δ motor uses a coreless winding and the inductance

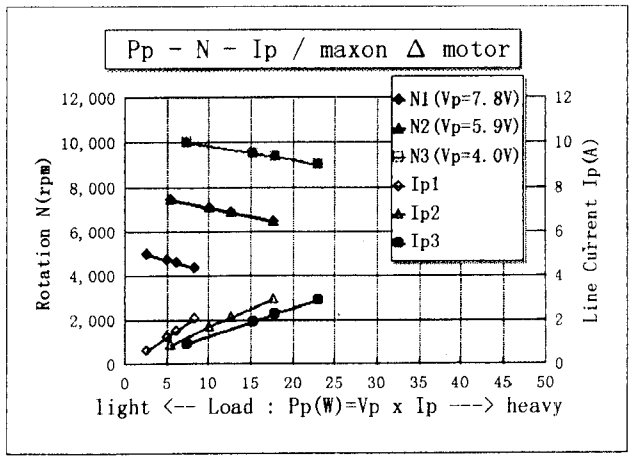


Fig. 8. Rotation, N and Line Current v.s. Motor Driving Power

of 0.015 mH (Lu), then, the operation is keeping the angle α low and driving the motor wide. This point is also to make the motor higher rotation over 16,000 rpm.

D. Starting Rotation

Fig. 9 shows the starting rotation at 12 V of the power supply voltage and reaches the rotation of 12,600 rpm within 1 second. The figure shows a current saturation of 3A due to our power supply limitation. Normally the motor needs a maximum current of 15A in the specification. Then, the starting time takes less time at the normal operation. Anyway, we can start the motor for much conditions of Fig.8 without any problems, even under the limitation of 3A..

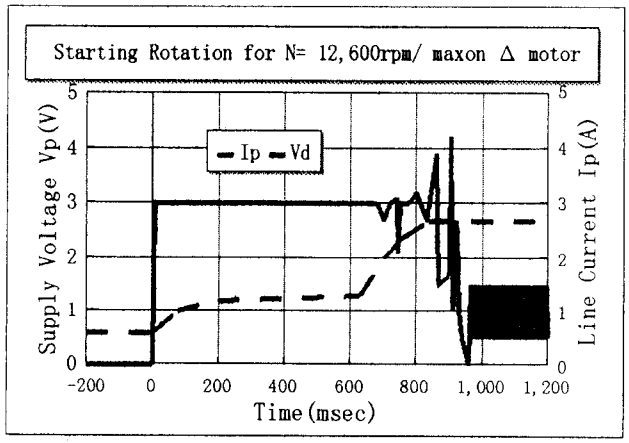


Fig. 9. Starting Rotation Time

IV. Next steps

A. Best of the Δ V

We mentioned a little about the Δ V before, but the best value of the Δ V is zero after starting rotation. Because the current Iu sites closely on the line voltage Vu, so that all of the flowing currents order to functions of the switching voltage Vu. If the current Iu delays from the line voltage Vu, there are much strong pulse current and voltage on the lines.

On the other hand, the Δ V is needed for the starting rotation and for a margin to driving motor. We should decide the balance of the Δ V on motors and those applications.

Then, we try to develop a hard wear for them as next step.

B. Digital Signal Processor

Recently a digital signal processing device becomes popular for ãny kind of control systems. It is a solution by a soft ware for the Δ V. We can use the device not only for above controlling Δ V, but also for a fail safe of this driving system. Also, we will try to do them.

Reference

[1] T.Sakurai: "Driving Method for a Delta-Connection Brushless Motor (1st report)" 1993 National convention record I.E.E. Japan -Industry Application Society - pp257-260

[2] T.Sakurai,M.Arimoto,M.Sakurai:"Driving Method for a Delta-Connec -tion Brushless Motor "1996 National convention record I.E.E. Japan" pp4-272--4-473

[3] T.Sakurai,M.Arimoto, M.Sakurai,K.Takizawa: "Driving Method for a Delta-Connection Brushless Motor (2nd report)"1996 National conven -tion record I.E.E. Japan -Industry Application Society - pp201-204

A Practical Approach to Minimize the Zero-Sequence Current Harmonics in Power Distribution Systems

Pekik A. Dahono, Radpandji E. Widjaya, Syafrudin, and **Qamaruzzaman**

Electrical Energy Conversion Research Laboratory,
Department of Electrical Engineering, Bandung Institute of Technology,
Jl. Ganesa No. 10, Bandung 40132, Indonesia
Tel : 62-22-2503316 Fax : 62-22-2508132

Abstract

In this paper, a simple and practical approach to minimize the zero-sequence current harmonics in 3-phase 4-wire power distribution system is proposed. The zero-sequence current harmonics are minimized by using a combination of a very low zero-sequence impedance transformer and a very high zero-sequence impedance transformer. The very low zero-sequence-impedance transformer is shunt connected to the load and the very high zero-sequence impedance transformer is series connected to the source. The series connected transformer will act as a zero-sequence current isolator between the source and load and, therefore, almost all of zero-sequence currents which are generated by the load will flow through the shunt connected transformer. Experimental results are included to verify the proposed approach.

Introduction

Recent surveys on three-phase four-wire electric power distribution systems with computer and nonlinear loads show excessive currents in the neutral conductor[1-2]. The neutral currents are fundamentally zero-sequence current harmonics which are mostly consists of triplen current harmonics. The excessive zero-sequence current harmonics in the neutral conductor increases the risk of wiring failure, transformer overheating, elevated of neutral potentials, and elevated EMF levels [3].

An active power filter to cancel the zero-sequence current harmonics in the neutral conductor was proposed in [4]. This approach, however, is complicated and expensive. An another approach to minimize the zero-sequence current harmonics is by using a zigzag transformer which is shunt connected to the load[5]. Because the zigzag transformer has a very low zero-sequence impedance, most of the zero-sequence current harmonics which are generated by the loads will circulate through the zigzag transformer. The effectiveness of this approach, however, is strongly determined by the ratio of the zero-sequence impedance of the zigzag transformer to the zero-sequence impedance of the source. Unfortunately, the zero-sequence impedance of the source is sometimes unknown and difficult to determine.

In this paper, a combination of a zero blocking transformer and a zero passing transformer is proposed to minimize the zero-sequence current harmonics in three-phase four-wire electric power distribution systems. Experimental results are presented to verify the proposed approach.

Zero-Passing Transformer

The zero-passing transformer is a transformer that having a very low zero-sequence impedance. This transformer is shunt connected with the load as shown in Fig. 1. Besides having a very low zero-sequence impedance the transformer has very high both positive- and negative-sequence impedances. Thus, the zero-passing transformer has no effect on the positive and negative sequence harmonics.. The single-phase equivalent circuit of a system having a shunt connected zero-passing transformer is shown in Fig. 2. The neutral current flowing through the source after the connection of zero-passing transformer can be calculated as follow :

$$I_{NS} = \frac{Z_{op}}{Z_{op}+Z_{os}} I_N \qquad (1)$$

where

I_{NS} = the source neutral current after compensation
I_N = the source neutral current before compensation
Z_{os} = the zero-sequence impedance of the source
Z_{op} = the zero-sequence impedance of zero-passing transformer.

Eqn. (1) shows that the effectiveness of zero-passing transformer in reducing the zero-sequence current harmonics is strongly dependent on the ratio of zero-sequence impedance of the source to zero-sequence impedance of the zero-passing transformer. Unfortunately, the zero-sequence impedance of the source is difficult to determine. Moreover, the zero-sequence impedance of the source is changing with the power system operating conditions. In [5], insertion of an inductance between the source and zero-passing transformer neutrals was proposed to solve this dependency problem. By using this method, however, the neutral voltage of the load

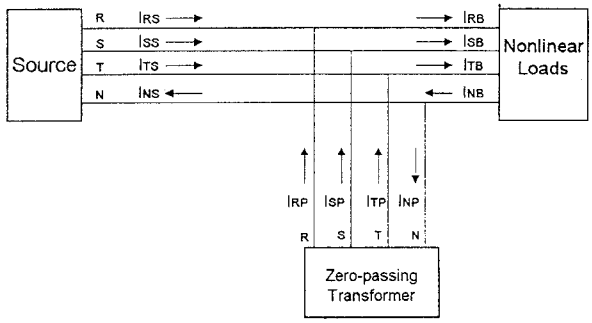
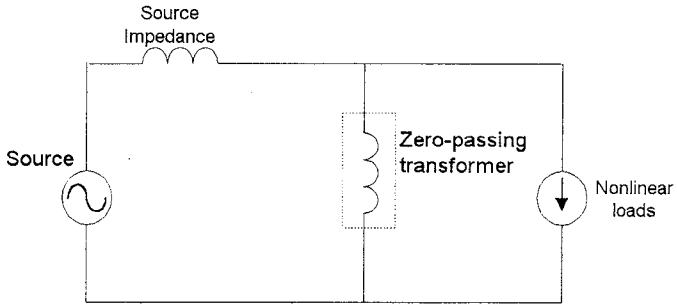


Fig. 1. Three-phase four-wire distribution system with a shunt connected zero-passing transformer.



. Fig. 2. Single-phase equivalent circuit of Fig. 1.

Table 1. Rating of zero-passing transformers.

Connection	Zigzag	Y-Δ	T
kVA	0.666 $V_{ll}I_N$	1.155 $V_{ll}I_N$	0.718 $V_{ll}I_N$

will be different to the neutral of the source. Moreover, a stray ground current problems can happen if the neutral of the power system is grounded at several points.

The zero passing transformer can be implemented by using a zigzag, Y-Δ, or T connected transformer. KVA rating comparison among these three types of transformer is shown in Table 1. This Table shows that the zigzag connected transformer has the smallest kVA requirement. In this Table, V_{ll} and I_N are the line-to-line voltage and compensated neutral current, respectively.

Besides of the dependency on the ratio of zero-sequence impedances of the source to the zero-passing transformer, a shunt connected zero-passing transformer can be a problem if the source generates a zero-sequence voltage harmonics. Under this condition, the neutral current can be even higher than before the shunt transformer is connected.

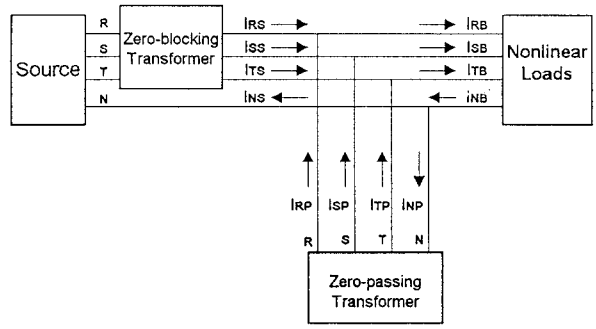


Fig. 3. Combination of zero-blocking and zero-passing transformers.

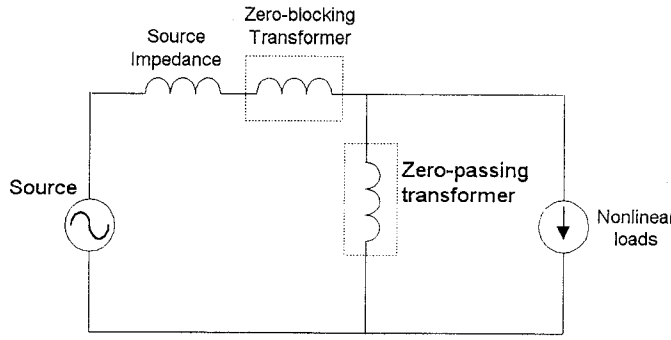


Fig. 4. Single-phase equivalent circuit of Fig. 3.

Combination of Zero-Passing and Zero-Blocking Transformers

To solve the previous mentioned problems, a combination of zero-passing and zero-blocking transformer is proposed. The zero-blocking transformer is a series connected transformer as shown in Fig. 3. The single-phase equivalent circuit of a system having a combination of zero-passing and zero-blocking transformer is shown in Fig. 4. The zero-blocking transformer is a transformer that having a very high zero-sequence impedance and having very-low both positive- and negative-sequence impedances. Thus, the series connected zero-blocking transformer has no effect on the positive and negative sequence harmonics. The schematic diagram of a zero-blocking transformer is shown in Fig. 5. The zero-blocking transformer windings are just several turns but the winding should be able to conduct the full load currents. To prevent the core saturation due to the zero-sequence currents, the core should have a small air gap.

The zero-blocking transformer has two functions. The first is preventing the load zero-sequence current harmonics

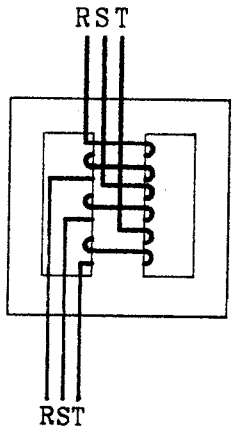


Fig. 5. Zero-blocking transformer.

from flowing into the source. The second is preventing the flow of zero-sequence current harmonics when the source generates the zero-sequence voltages. The second function is important when the power is generated by an inverter. To be effective, the zero-sequence impedance of the zero-blocking transformer should be much higher than the source zero-sequence impedance.

Experimental Results

In order to verify the proposed approach, an experiment in a television broadcasting station has been done. In this station, most of the loads are electronic equipment with simple rectifier diodes as the power supplies. In order to improve the reliability of the power system, all of the loads are supplied through an uninterruptible power supply system. Fig. 6 shows the measured phase current waveform. The rms value of this current is 35.5 A. Because the loads are balanced the other phase currents are almost the same. The neutral current waveform is shown in Fig. 7. The rms value of this current is 56.8 A. Though the loads are almost balanced, it can be seen that the rms value of the neutral current is much higher than the phase current. The neutral current is mostly consist of the third current harmonic.

To reduce the neutral current, a combination of zigzag transformer and zero-blocking transformer was designed. With only zigzag transformer is connected, the neutral current is increased to 70 A. The waveform is shown in Fig. 8. This is occurred because the UPS inverter generates also the zero-sequence voltage harmonics.

Fig. 9 shows the phase current waveform after the combination of zero-passing and zero-blocking transformers are connected. The rms value of phase current is reduced to 29.9 A. Fig. 10 .shows the neutral current waveform and spectrum after compensated. The rms value of the neutral current is reduced significantly to 3.16 A. Tables 2 and 3 show the analysis results before and after compensation. The total power factor measured at the source is increased from 0.75 to 0.9. Thus the proposed approach is also useful to solve low power factor problem due to harmonics.

In this experiment, the zero blocking transformer is implemented as shown in Fig. 5 with six turns cable for each phase. The size of the zero blocking transformer is much smaller compared to the zigzag ones.

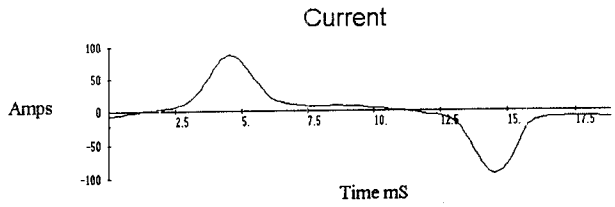


Fig. 6. Phase current waveform before compensation.

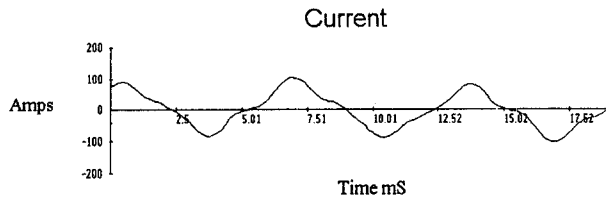


Fig. 7.Neutral current waveform before compensation.

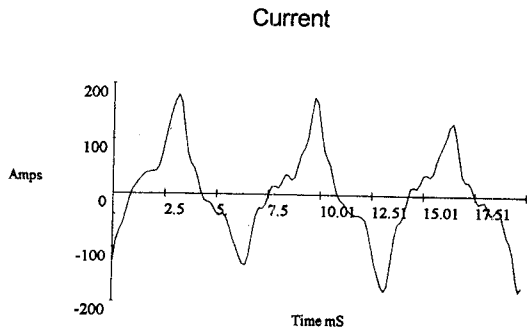


Fig. 8. Neutral current waveform when zero-passing transformer only is connected.

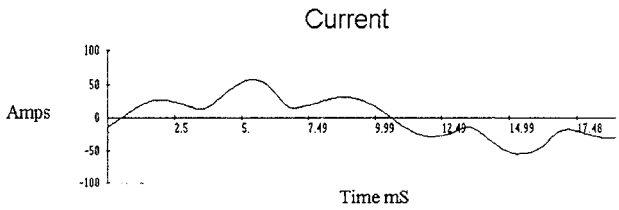


Fig.7. Phase current waveform after compensation.

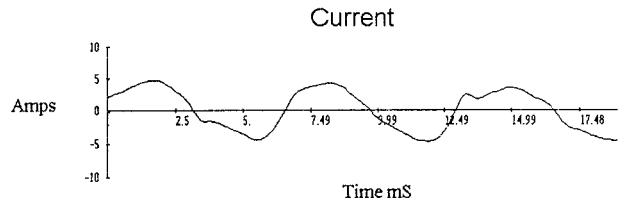


Fig. 8. Neutral current waveform after compensation.

Table 2. Result analysis of the measured phase current waveforms.

Description	Before compensation	After compensation
RMS current	35.5 A	29.9 A
Peak current	92.7 A	55.6 A
THD rms	61.5 %	36.8 %
THD Fund	78 %	39.6 %
kW	5.9	5.9
kVA	7.8	6.6
kVAR	1	1.3
Total PF	0.75	0.9
DPF	0.99	0.98

Experimental results in the laboratory shown that the proposed approach has also the following merits :

- Balancing the load, and
- Protecting the load from the danger of broken neutral conductor.

These two features are very important for utility in reducing the power distribution losses and increasing the power quality. At present, the proposed compensation approach is under field test at several places in Indonesia. The results will be published in the next occassion.

Table 3. Result analysis of the measured neutral current waveforms.

Description	Before compensation	After compensation
RMS current	56.8 A	3.16 A
Peak current	106.2 A	4.79 A
THD rms	98.8 %	99.8 %

Conclusion

In this paper, a combination of zero-passing and zero-blocking transformer is proposed to minimize the zero-sequence harmonics in three-phase four-wire power distribution system. Experimental results show that the proposed approach can reduce significantly the neutral current and improve the power factor. Because no power electronic control nor tuning is required, the proposed approach is much simpler, cheaper, and reliable compared to the approaches using active filters or passive LC filters.

References

[1] A. Liew, Excessive neutral currents in three-phase fluorescent lighting circuits, IEEE Trans. Ind. Appl., July/August 1989.

[2] T. M. Gruzs, A Survey of neutral currents in three-phase computer power systems, idem, July/August 1990.

[3] T. Q. Tran, et. al., Electric shock and elevated EMF levels due to triplen harmonics, IEEE Trans. Power Delivery, April 1996.

[4] P. N. Enjeti, et. al., Analysis and design of a new active power filter to cancel neutral current harmonics in three-phase four-wire electric distribution systems, idem, Nov./Dec. 1994.

[5] P. P. Chorea, Application of zigzag transformers for reducing harmonics in the neutral conductor of low voltage distribution system, Conf. Rec. IEEE Ind. Appl. Soc. Ann. Meet., 1990.

New Current Feed back Control Method for Solar Energy Inverter using Digital Signal Processor

Tsukasa TAKEBAYASHI, Hirofumi NAKATA,
Masaki EGUCHI, Hirokazu KODAMA
Solar Energy System Group SHARP Corporation
282-1 Hajikami, Shinjo-cho, Kitakatsuragi-gun, Nara 639-21 JAPAN
Fax: +81-7456-2-8254 , Phone: +81-7456-8-1161
E-mail: taket@shinjo.sharp.co.jp nakata@shinjo.sharp.co.jp

Abstract — **A solar energy inverter for photovoltaic systems connected with electric utility lines has been developed. It is a power conditioner with a high-frequency transformer link for residential use at level of power 3 kW. This paper describes a new synchronous current feed back control method using a digital signal processor (DSP). An adaptive finite impulse response filter is introduced into control.**

This paper also suggested a new method for detecting a power outage. It gives frequent changes to frequency of inverter output voltage using a distortion on inverter output current.

I. Introduction

Recently, with increasing concern about global environmental protection, the need to produce pollution-free natural energy has pointed us towards alternative sources of energy. Solar energy, especially, is a positive choice. The spread of residential photovoltaic (PV) systems connected with electric utility lines are being promoted in Japan.

Size reduction, simplification and performance improvement of inverters, a peripheral device used in PV systems, are preferable for wider use of them. We have developed a solar energy inverter with a high-frequency transformer-link which is based on a DSP.

This paper presents a new synchronous current feedback control method using the DSP. The use of it realizes the significant size reduction and simplification of the control circuit. This approach also appears to have the greatest potential for the reduction of the output current distortion. The suggestion for a new method for detecting a power outage of electric utility lines is discussed for inverter performance improvement.

II. Power Circuit

A simplified schematic of power circuit for the inverter with a high-frequency transformer link [1] is shown in Fig.1. The inverter converts dc power to ac power (50/60Hz) and feeds to electric utility lines. The power circuit of inverter consists of a high-frequency inverter bridge, a high-frequency transformer, diode-bridge rectifiers, a DC filter, a low-frequency inverter bridge and an AC filter.

The following procedure explains how ac power is generated from dc power of solar batteries. The inverter has three conversion stages. First the high-frequency inverter bridge inverts dc voltage to high-frequency ac (38kHz). AC voltage is sinusoidal pulse wave modulated (A) at the side of primary of the transformer. Next it is rectified by diode-bridge rectifiers at the side of secondary of the transformer (B). Then it changes into a full wave form (C) filtered by the DC filter. Finally, the low-frequency inverter bridge reverses it at zero crossing points. Therefore, a full sine wave (D) outputs to electric utility lines from the inverter.

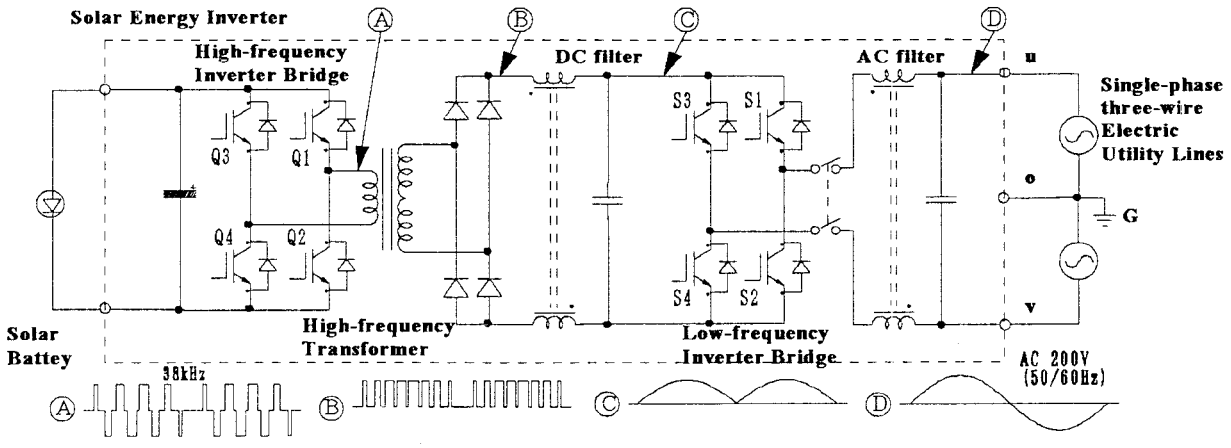


Fig.1. Simplified Schematic of Inverter Power Circuit

Ⅲ. New Current Feed back Control Method

This section explains new current feedback control method using the DSP. The purpose of this control is to output sine waves (as shown in Fig.1 C) for a half-period of a commercial sine wave repeatedly. The current waves are in phase with voltage of electric utility lines V_{UL}. Sine waves are obtained by an integration of a current error wave form in order which is the difference between an output current wave form and a desired current wave form.

An adaptive finite impulse response (FIR) filter was introduced into current feedback control. It's a filter in which the filter coefficients are updated in real time in order for the output of the filter and desired output to agree. The adaptive algorithm of filter coefficients is based on the synchronized filtered-X LMS[2], which has been widely used for the periodic sound and vibration control. It has been improved for inverter control. A structure of current feedback control shown in Fig.2. Equation (1) shows an input signal $x(n)$ of the adaptive FIR filter W ($x(n)$ is an zero crossing pulse train of voltage V_{UL}).

$$x(n) = \sum_{m=0}^{\infty} \delta(n - mN) \tag{1}$$

$N = T/2\Delta t$: the number of sampling data between zero crossing points
T : period of voltage V_{UL}
Δt : sampling period
n : sampling time

Also, (2) shows an output signal $y(n)$ of the filter W.

$$y(n) = \sum_{i=0}^{I-1} w_i(n) \sum_{m=0}^{\infty} \delta(n - mN - i) \tag{2}$$

$I = N$: tap number of the filter W

If the element $\delta(n-mN-i) = 1$ in the case of $i=n-mN$, (2) is rewritten as (3).

$$y(n) = w_{n \bmod N}(n) \tag{3}$$

Equation(3) means the filter coefficient w_i is outputted in order.

Based on the output signal $y(n)$, the DSP executes the PWM operations so that the high- frequency inverter bridge is driven. Then, output current is detected and inputted in the DSP via an a/d converter. The DSP compares a desired current signal $Ic(n)$ and an absolute value of output current $Io(n)$. Therefore, the DSP obtains an inverter error signal $e(n) = Ic(n) - Io(n)$. In addition, $e(n)$ is filtered by the FIR filter A in order to remove high frequency noises included in output current I_{INV}. The filtered error current signal $e^*(n)$ is obtained. If we assume that the transfer function $C(z)$ (which is expressed as a path from the output side of the filter W to the output side of the filter A) is a delay of time d, (4) for the update of the filter coefficient $w_i(n)$ is found by minimizing the equation $E(n) = \{ e^*(n) \}^2$ using the method of the steepest descent.

$$\begin{aligned} w_i(n+1) &= w_i(n) + \mu e^*(n) \sum_{m=0}^{\infty} \delta(n - mN - i - d) \\ &= w_i(n) + \mu e^*(n) x(n - i - d) \end{aligned} \tag{4}$$

μ : step-size parameter which has a small positive value

In the actual operations, we utilize (5) in order to reduce the amount of calculation at the DSP.

$$\begin{aligned} w_i(n+1) &= w_i(n) + \mu e^*(n) \sum_{m=0}^{\infty} \delta(n - 2mN - i - d) \\ &= w_i(n) + \mu e^*(n) r(n - i - d) \end{aligned} \tag{5}$$

It means that the DSP executes adaptive operations of the filter coefficient w_i during a half-period of voltage V_{UL}. In addition, the DSP carries out operations of the filter B to remove a high-frequency component of the filter coefficient train during the remain of the half period.

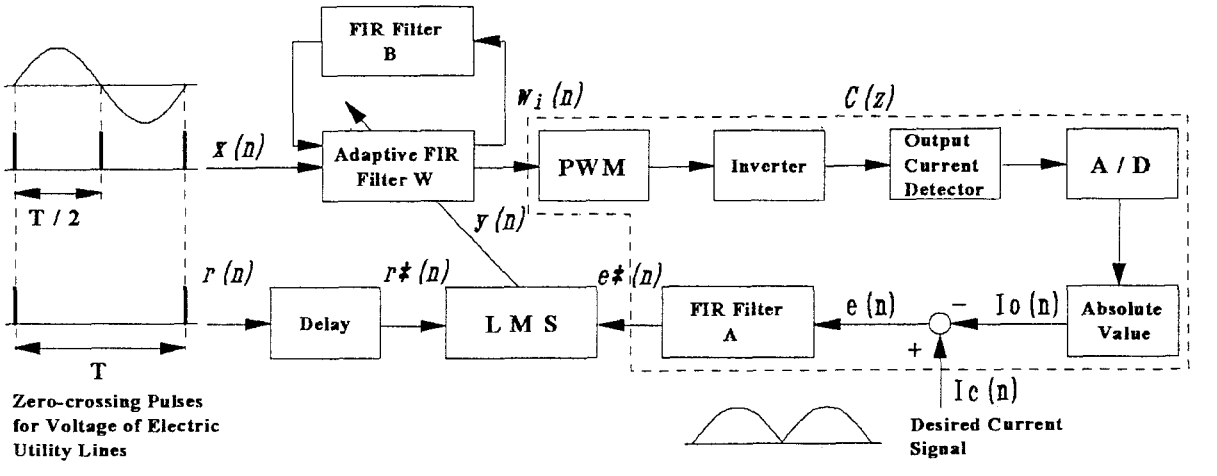


Fig.2. Block Diagram of Current Feed back Control

Ⅳ. New method for detecting a power outage

In the event of a power outage, a solar energy inverter for PV systems connected with electric utility lines must automatically detect a power outage and stop operations of the system. Because maintenance personnel that check electric utility lines is danger of receiving an electric shock if PV systems charge electric utility lines in the event of a power outage.

In general inverter voltage or frequency deviate from a standard range in the event of a power outage. The inverter monitors them and detects a power outage. This method is called a passive prevention technique. However, the method can not perfectly detect a power outage in the case that inverter output power and electric load power connected to systems balance by chance. There is another method in order to detect a power outage in the case described above. It is a method that the inverter gives frequent changes to inverter output power or frequency, and the inverter detects voltage, current or frequency changes of electricity utility lines appearing in the event of a power outage. The method is called an active prevention technique.

This section explains a new method that gives frequent changes to inverter output frequency using a distortion on inverter output current in the active prevention technique. The accuracy of a power outage detection can be significantly increased by the method. It will be discussed in detail as follows.

To give a change to frequency of inverter output voltage V_{INV}, it is necessary to change frequency of pulses that are generated by zero-crossing points in voltage V_{UL} of electric utility lines. New method makes a part of zero-crossing points for inverter output current I_{INV} distort slightly. Voltage V_{INV} is the same frequency as voltage V_{UL} in normal conditions of electric utility lines, but is the same frequency as current I_{INV} in the event of a power outage. Distorted output current is shown in Fig.3. There are two kinds of distortions:

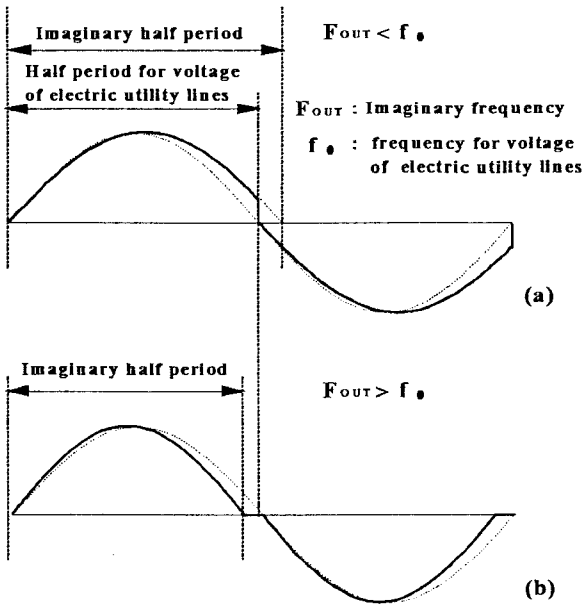


Fig.3. Inverter Output Current in Normal Conditions

a. The value of current I_{INV} is not zero but left at zero-crossing points (Fig.3-a).

b. The value of current I_{INV} is zero at zero-crossing points and there is a term that zero value continues (Fig.3-b).

Here I would like to define the term, "imaginary half period F_{OUT}" in Fig.3. In the event of a power outage, it means half period of voltage V_{INV} that is changed by a distortion of current I_{INV}. In the case of "a.", frequency F_{OUT} of voltage V_{INV} is less than frequency f_0 of voltage V_{UL} and in the case of "b.", it is more than frequency f_0 in the event of a power outage.

The inverter output current wave (Fig.3.) is obtained from (6) that is another form (3).

$$y(n) = w_{\mathrm{int}\{\alpha(n \bmod N)\}}(n) \qquad (6)$$

α : time scale factor

If $\alpha < 1$, imaginary frequency is less than frequency F_{UL} as in Fig.3-a. If $\alpha > 1$, imaginary frequency is more than frequency F_{UL} as in Fig.3-b.

Fig.4 shows relationship between imaginary frequency F_{OUT} of current I_{INV} and frequency F_{IN} of voltage at the point of connected to electric utility lines. In normal conditions of electric utility lines, frequency F_{IN} is equal to frequency f_0 of voltage V_{UL}, but is equal to frequency of current I_{INV} in the event of a power outage.

In unbalanced conditions of reactive power and electric loads, frequency of voltage V_{INV} goes up or down according to an advance or a delay of a current phase in electric loads in the event of a power outage. Frequency F_{IN} changes and goes into an frequency abnormal area (ex. 50Hz: $F_{IN} < 49.8$Hz or $F_{IN} > 50.2$Hz), then the distortion of current I_{INV} is increased and imaginary frequency F_{OUT} is changed as frequency F_{IN} is changed furthermore.

On the other hand, in balanced conditions of reactive power and electric loads it is difficult to occur a change of frequency F_{IN} as described above.

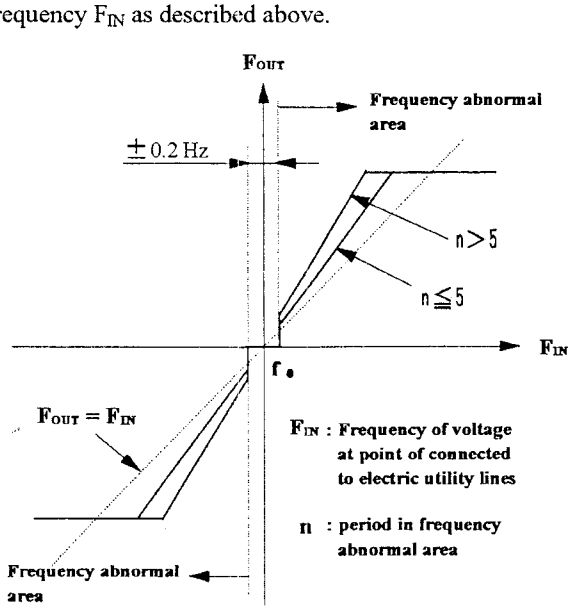


Fig.4. Relationship between frequency F_{IN} and F_{OUT}

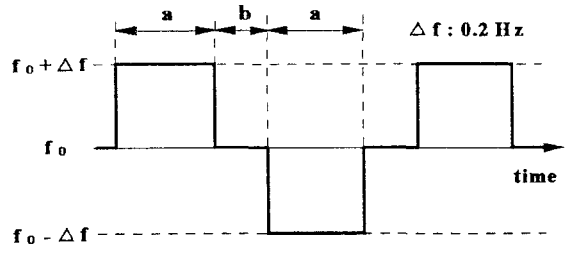


Fig.5. Changes in imaginary frequency F_{OUT}

In order to solve the problem, new method makes the distortion of current I_{INV} change frequently in normal conditions of electric utility lines. As the result, imaginary frequency F_{OUT} is changed more than f_0 or less than f_0. The change is shown in Fig.5. Frequency F_{OUT} is changed into $f_0+\Delta f$ during the period *a*, f_0 during the period *b* and $f_0 -\Delta f$ during the period *a*. The method in normal conditions makes frequency of voltage V_{INV} change furthermore in the event of a power outage.

In regard to a change direction of frequency F_{IN}, the method allows for changing into the opposite direction against a natural direction depending on a phase of electric loads. If frequency F_{IN} is not more than a threshold value for detecting a power outage within five periods after frequency F_{IN} goes into a frequency abnormal area in the event of a power outage, the method makes the distortion of current I_{INV} increase and makes inclination of characteristics for input-output frequency come to increase (Fig.4.).

V. Experimental Results

An experiment using power supply controller (400V, 30A) and RLC loads was run to confirm new method for inverter current feedback control and detecting a power outage availability. To perform them, a DSP [TI TMS320C209] was used. The ratio of frequency F_{OUT} in normal conditions of electric utility lines as in Fig.5, a:b was 7:3 and the change of frequency F_{OUT} was approximately $\pm$0.2 Hz of frequency 50/60 Hz. The inverter was performed in 3 kW, 200 V.

The experimental results that are total harmonic distortion for inverter output current are shown in Fig.6. They are included total degree from first to forty-ninth. For characteristics of new method with frequent changes to frequency, measurements were made, and the results were compared with characteristics of old one without frequent changes to frequency. The experimental results agree approximately with those in range of high power. The total harmonic current distortion is less than 1% at level of power 3 kW.

In addition, the experimental results that are detecting a power outage are shown in Fig.7. Active power ΔP and reactive power ΔQ were changed in range of $\pm$300W, $\pm$ 300Var. In guidelines for PV systems connected to electric utility lines, inverters must stop systems between 0.5 sec and 1.0 sec after detecting a power outage. Stopping time of all experiments (Fig.7.) satisfied above conditions and sufficient results were obtained. Experimental results prove the availability of new method for detecting a power outage.

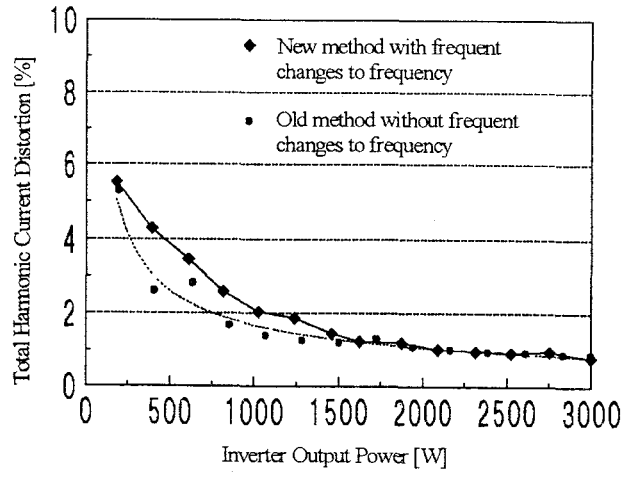


Fig.6. Total Harmonic Current distortion

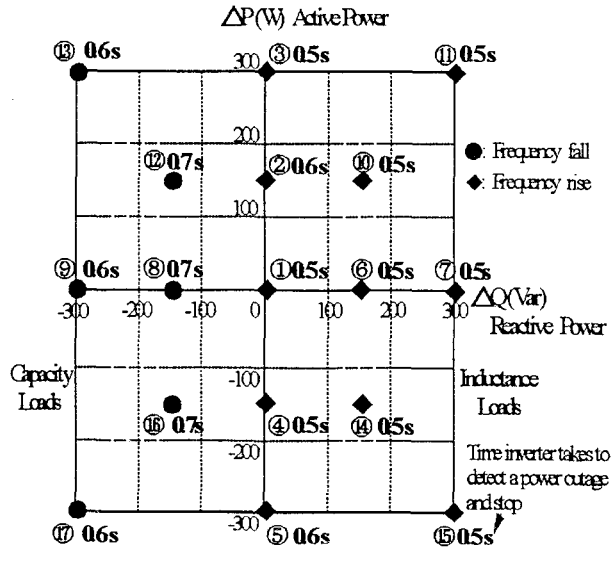


Fig.7. Experimental Results for detecting a power outage

VI. Conclusion

The objective of this paper was to suggest the new current feed back control method that an adaptive FIR filter is introduced. Inverter performance for switching technology was significant improved and the total harmonic current distortion is less than 1% at level of power 3 kW.

This paper also suggested new method for detecting a power outage by current distortion. It has allowed us to detect a power outage perfectly in balanced conditions of reactive power and electric loads.

Further developments will be made in the future.

References

[1] M.Eguchi, H.Kodama, T.Takebayashi, H.Nakata, "Digital Control Method for Utility Interactive Inverter using DSP ", SPC-96-7, pp. 61-68, January 1996.

[2] H.Hamada, K.Ito, I.Miyasaka, S.Uto, "Synchronized Filtered-X Algorithm and Its Application to Active Noise Control", JSME, No.920-78, 1992, pp. 116-118,

A New Scheme For Maximum Photovoltaic Power Tracking Control

Hidehiko Sugimoto, *Member, JIEE* , Huian Dong, *Member, JIEE*
Department of Electrical and Electronics Engineering, Fukui University
9-1, Bunkyo , 3-chome, Fukui-shi 910, JAPAN
Fax:+81-776-27-8749, Phone:+81-776-27-8563
E-mail:sugimoto@powerel.fuee.fukui-u.ac.jp

***Abstract*—It is shown that the derivative (dp_s/de_s) of output power(p_s) with respect to output voltage(e_s) of photovoltaic array is equal to zero at maximum power point. This kind of relationship is independent on the insolation and temperature. This property may be utilized to perform maximum power tracking control, that is, in all insolation and temperature levels, the maximum power point can be obtained by regulating dp_s/de_s toward zero. Based on this concept, a new scheme of maximum power tracking control is proposed, and applied to an utility interactive photovoltaic power conditioning system. Where the boost chopper is arranged responsible for maximum power tracking control, the inverter responsible for unity power factor control and constant dc input voltage control. The relating design method is described. The usefulness and validity of proposed method are verified by simulating analysis. Compared to conventional methods, it behaves considerable high tracking performance.**

***Index Terms*—photovoltaic array, maximum power tracking control, unity power factor control, constant dc voltage control, utility interactive photovoltaic power conditioning system, chopper, inverter.**

I . INTRODUCTION

As the conventional energy sources are dwindling fast, solar photovoltaic(PV) energy offers a very promising alternative, because it is free, abundant, pollution-free, and distributed throughout the earth. The researches on the photovoltaic(PV) power source have received much attention to not only space applications but also terrestrial applications. However, the present energy conversion efficiency of PV arrays are still quite low. Therefore, in order to achieve maximum utilization efficiency, the technique, called maximum power point(MPP) tracking control to extract the maximum possible power from the PV array, is essential one in the systems powered by PV array. The PV arrays exhibit an extremely non-linear voltage-ampere characteristic, which varies with array temperature and solar insolation(or illumination) at all times. It makes the locating of maximum power point complex. The conventional locating method of the MPP [1][2], generally say, is based on the comparison of the output powers of two different operating point. This kind of method makes the PV powered systems operate mostly around the MPP with a fluctuation but not at the MPP. Particularly, at the case of frequently changing insolation and temperature, its tracking speed appears not fast enough. Therefor, there still remains a problem at quickly and accurately determining the location of the MPP on the operating curves.

At this paper, the attention is paid to the e_s-dp_s/de_s characteristic of PV array, where the quantity dp_s/de_s is the derivative of output power(p_s) with respect to output voltage(e_s) of PV array. It is shown that derivative dp_s/de_s is equal to zero at MPP under various insolations and temperatures. Based on such a property a new scheme for the maximum power point tracking is proposed. This is, the MPP is located by controlling dp_s/de_s into zero. Theoretically it can drive the PV powered system accurately and quickly operate at any MPP due to the change of insolation or/and temperature. To verify this concept, an typical utility interactive PV power conditioning system is taken as its an application example. This system consists of PV array, boost chopper, single-phase inverter and utility line. In this system, the boost chopper is arranged responsible for maximum power tracking control, the inverter responsible for unity power factor output current control and constant dc voltage control of the dc side of the inverter to prevent the dc side over-voltage. In addition, since the output of the PV array must contain inherent ripples due to the single-phase inverter, the dp_s/de_s can still be directly detected out without the other additional means even if the system is operating at the MPP. The results simulated by the proposed method show it has considerable high tracking performance.

II . CHARACTERISTICS OF PV ARRAY

First of all, let us briefly review PV array. The PV arrays exhibit a non-linear voltage-ampere characteristic. It is expressed by:

$$i_s = I_{PH} - I_0 \exp(\frac{q}{KT} e_s - I_0). \qquad (1)$$

Where i_s: array output current ,
e_s: array output voltage,
I_0: array saturation current,
T: array temperature in K,
I_{PH}: light-generated current,
K/q: Boltzman's constant.

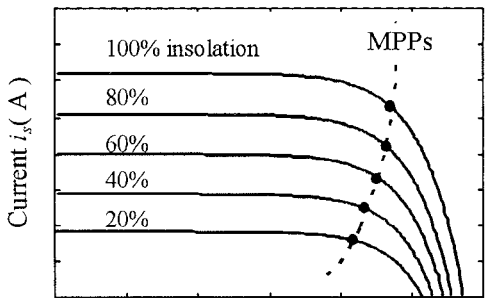


Fig.1 Voltage-ampere characteristic curves of PV array

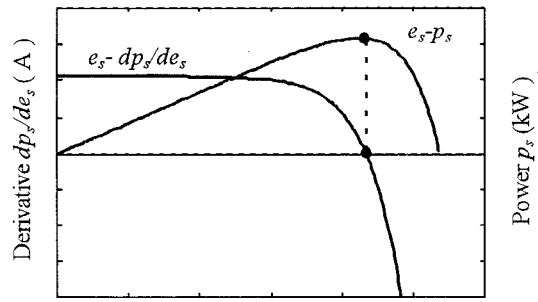


Fig.2 e_s-p_s and e_s-dp_s/de_s characteristic curves of PV array

Fig.1 shows their characteristic curves corresponding on different insolation (at a constant temperature). It can be seen that the MPPs vary with the change of insolation (of course, also with the change of temperature). Therefor, in order to obtain the maximum output power from the PV array at various array insolation and temperature levels. it is necessary to use some suitable means so as to determine the location of the MPP on the operating curves. One possible method is that, decrement the output voltage e_s of PV array and then compare the new power with the old power. If Δp_s is positive, the decrementing is continued in the same direction, if Δp_s is negative, the output voltage e_s will be incremented, and so forth until the MPP is reached. However this method would make the PV operate mostly around the MPP but not at the MPP, and its tracking speed appears not fast enough, particularly to frequently changing insolation and temperature.

Now, let's look at the other characteristics of PV array. The voltage-power characteristic can simply be written by

$$p_s = I_{PH} e_s - I_0 e_s \exp(\frac{q}{KT} e_s - I_0) \cdot \qquad (2)$$

and the relationship between output voltage e_s and derivative (dp_s/de_s) of output power with respect to output voltage is deduced as follows:

$$\frac{dp_s}{de_s} = I_{PH} - I_0 \exp(\frac{q}{KT} e_s)\left(\exp(-I_0) + \frac{q}{KT} e_s\right) \cdot \qquad (3)$$

The derivative quantity dp_s/de_s is a monotonous and continuous function of output voltage e_s. Its unit is ampere and its value will be equal to the short-circuit current of PV array when the output voltage e_s approaches to zero. Fig.2 shows the characteristic curves of (2) and (3), and their relationship. It is shown that the MPP must correspond to such a point where the dp_s/de_s is equal to zero. This kind of relationship keeps true at various insolation and temperature. In other words, it is independent of insolation and temperature. Thus, whether the system operate at MPP may be identified through checking if the dp_s/de_s is equal to zero. As such, the dp_s/de_s=0 might be selected as the maximum power command of a maximum power tracking system with the dp_s/de_s feedback loop. The controlling the dp_s/de_s toward zero means controlling operating point into MPP. According to this concept, a new control scheme for maximum power tracking is presented and applied to the following system.

III. Design of Control System

Fig.3 shows a typical utility interactive PV power conditioning system, It consists of PV array, boost chopper, single-phase inverter, utility line, and the corresponding controllers. With the power conditioner within the dotted line, the dc power from PV array is converted to single-phase 60Hz ac and fed to the utility line. The basic requirements from this system are:

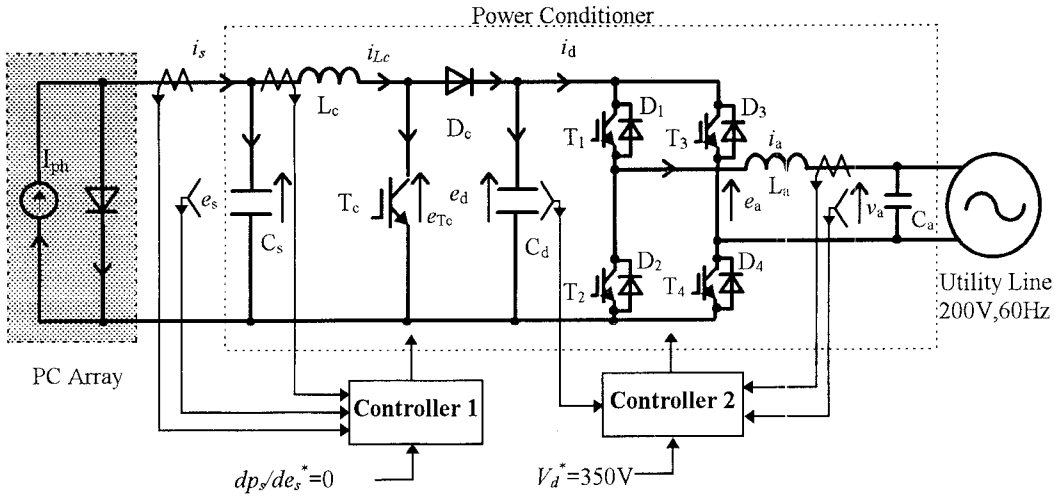
1. operate at MPP under various insolation and temperature levels in all times.
2. maintain sinusoidal output current in phase with the utility voltage (i.e. unity power factor).

Here, we arrange the boost chopper responsible for maximum power tracking control, the inverter responsible for unity power factor output current control, and also responsible for constant dc voltage control in order to prevent the charged voltage of link capacitor C_d in the inverter dc side from exceeding the voltage rating of capacitor C_d or switch devices.

A. Maximum Power Tracking Control

1)Modeling of the booster chopper: The booster is of two operating state, on or off. When switch Tc is turned on, the energy from the PV array is stored in the inductor L_c, and when T_c is turned off, the energy is delivered to the dc link capacitor C_d and the inverter. Assuming T_c is an ideal switch, the on state of the booster chopper can be expressed by the state space equation:

$$\begin{cases} C_s \dfrac{d}{dt} e_s = i_s - i_{Lc} \\ L_c \dfrac{d}{dt} i_{Lc} = e_s \end{cases}, \qquad (4)$$



Controller 1:maximum power tracking control
Controller 2:unity power factor output current control and constant dc voltage control

Fig.3 Schematic configuration of an utility interactive PV power conditioning system

the off state can be given by :

$$\begin{cases} C_s \dfrac{d}{dt} e_s = i_s - i_{Lc} \\ L_c \dfrac{d}{dt} i_{Lc} = e_s - e_d \end{cases} \quad (5)$$

By the state space averaging method, the resulting state space averaging equation can be represented as follows:

$$\frac{d}{dt}\begin{bmatrix} e_s \\ i_{Lc} \end{bmatrix} = \begin{bmatrix} 0 & \frac{1}{C_s} \\ \frac{1}{L_c} & 0 \end{bmatrix}\begin{bmatrix} e_s \\ i_{Lc} \end{bmatrix} + \begin{bmatrix} 0 \\ \frac{1}{L_c} \end{bmatrix} e_{Tc} + \begin{bmatrix} \frac{1}{C_s} \\ 0 \end{bmatrix} i_s \quad (6)$$

Where $e_{Tc}=(1-D)e_d$, D is duty ratio ($0 \leqq D \leqq 1$). (6) is a set of non-linear equations. Set MPP as equilibrium point, then the linearized state-space averaging equations are found as:

$$\frac{d}{dt}\begin{bmatrix} \Delta e_s \\ \Delta i_{Lc} \end{bmatrix} = \begin{bmatrix} -\frac{A}{C_s} & -\frac{1}{C_s} \\ \frac{1}{L_c} & 0 \end{bmatrix}\begin{bmatrix} \Delta e_s \\ \Delta i_{Lc} \end{bmatrix} + \begin{bmatrix} 0 \\ -\frac{1}{L_c} \end{bmatrix} \Delta e_{Tc} \quad (7)$$

Where $A=(I_0 q/KT)\exp(e_{s0}q/KT)$, subscript 0 denote equilibrium point. From (7), it is seen that the PV array voltage e_s can be controlled by adjusting the duty ratio of the booster chopper. Further, the dp_s/de_s can be controlled by controlling e_s. So we may consider such a MPP tracking controlling system that consists of a e_s voltage feedback control loop and a dp_s/de_s feedback control loop, and the e_s control loop, as a minor one, is inserted within the dp_s/de_s feedback control loop. Of course, the input command $(dp_s/de_s)^*$ of the overall control system should be set zero, i.e., MPP is desired value. Where the feedback PV array derivative dp_s/de_s is compared with the command $(dp_s/de_s)^*$, and the resulting error generates the array voltage command e_s^* through the dp_s/de_s compensator, then through the e_s control loop, the duty ratio is adjusted, and so forth until the dp_s/de_s shift to zero. When the insolation or/and temperature changes, the corresponding MPP can be fast achieved by the feedback control system. Note that whether this method is practicable depends on the possibility of detecting out dp_s/de_s from PV array at MPP. In this system, the inhere property of single-phase inverter results in ripples in the output of the PV array. So the dp_s/de_s still may be directly detected out without the other additional means even though the system already is operating at MPP.

2)Design of e_s voltage feedback control loop: Based on the above considerations and through the following control means:

- decoupling control to weaken the coupling intensity between e_s and i_{Lc}
- over-current protecting control to prevent the switch T_c from damaging.
- current feed-back control of capacitor C_s to improve the response of voltage e_s

a complete control algorithm may be given

$$e_{Tc} = K_{ci}\left[K_{ce}(e_s^* - e_s) - (i_s - i_c)\right] + e_s, \quad (8)$$

Where K_{ci}, K_{ce} denote proportional gain. Substituting (8) into (7), at the equilibrium point, the transfer function relating Δe_s^* to Δe_s is deduced as:

$$\frac{\Delta e_s(s)}{\Delta e_s^*(s)} = \frac{\frac{K_{ci}K_{ce}}{L_c C_s}}{S^2 + (\frac{K_{ci}}{L_c} + \frac{A}{C_s})S + \frac{K_{ci}K_{ce}}{L_c C_s}} \quad (9)$$

3)Design of *dps/des* feedback control loop: putting the e_s control loop into the dp_s/de_s control loop, the reference voltage e_s^* comes from the dp_s/de_s compensator. At the equilibrium point, the $\Delta(dp_s/de_s)$ and Δe_s has the following relationship:

$$\frac{\Delta(\frac{dp_s}{de_s})}{\Delta e_s} = -\frac{I_0 q}{KT}(2+\frac{qe_{s0}}{KT})\exp(\frac{qe_{s0}}{KT}) = -B. \tag{10}$$

So, the block diagram of the maximum power tracking control system may be constructed as Fig.4. For eliminating steady-state error, the dp_s/de_s compensator is selected as K_P/S. Then the closed loop transfer function of dp_s/de_s is obtained as follows:

$$\frac{\Delta\frac{dp_s}{de_s}(s)}{\Delta\left(\frac{dp_s}{de_s}\right)^*(s)} = \frac{BK_P}{S^3+(\frac{K_{ci}}{L_c}+\frac{A}{C_s})S^2+\frac{K_{ci}K_{ce}}{L_cC_s}S+BK_P} \tag{11}$$

Although the poles of this system are affected by the variation of insolation and temperature, since these poles can be located freely, the influences can be greatly reduced by selecting appropriate value of the coefficient K_{ci}, K_{ce}, K_P.

B. Design of Unity Power Factor Output Current Control And Constant dc Voltage Control System

With the inverter, through pulse width modulation (PWM), the maximum dc power obtained by the boost chopper is transformed to ac power , and meanwhile the output current is kept in phase with ac utility voltage. In addition, at the dc side the over high charged voltage of capacitor C_d might cause demanding of some relating devices. In order to ensure the system operate normally, it is also necessary to limit the dc side voltage within a certain range. Hence, according to these considerations, similarly we could take a dual loop control construction, where the unity power factor current control loop is set within the constant dc voltage control loop.

1)Design of unity power factor output current control loop: Set the reference current i_a^* as follows:

$$i_a^* = I_a^* \sin\omega_a t \tag{12}$$

where ω_a is the angular frequency of the utility voltage. The phase angle $\theta_a = \omega_a t$ can be obtained by PLL(phase-locked loop) principle to synthesize the utility voltage. Notice that I_a^* is a time function and come from the compensator of dc voltage control loop which will be designed bellow. The output voltage (or control voltage)

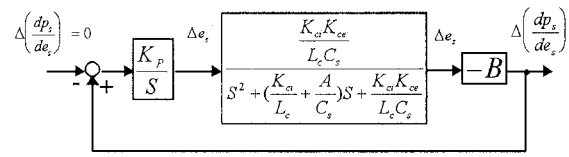


Fig.4 Block diagram of maximum power tracking control system

command e_a^* of the inverter may be given by

$$e_a^* = L_a\frac{di_a^*}{dt} + v_a \,. \tag{13}$$

As e_a^* in this formula easily is affected by the change of parameter La and the solution error of di_a^*/dt, we improve it by a feedback control of current i_a:

$$e_a^* = e_a' + \omega_a L_a I_a^* \cos\theta_a + v_a, \tag{14}$$

where $e_a' = K_{ai}(I_a^*\sin\theta_a - i_a)$, K_{ai} is a proportional gain. If the frequency of carry wave is much large than the one of inverter control voltage and the high frequency components of the output current mostly are filtered with a suitable ac filter, the fundamental component of the invert output voltage would be proximately equal to the control voltage. Hence, in design processing it is reasonable to assume that the control voltage e_a^* of the inverter is equal to its practical output voltage e_a. From (13) and (14), the following equation

$$(K_{ai}+L_a\frac{d}{dt})i_a = I_a^*(K_{ai}\sin\theta_a + \omega_a I_a\cos\theta_a) \tag{15}$$

is obtained. Since the equation is of non-linearity due to the time function I_a^*, solving i_a is difficulty. For the reason, we limit the change of I_a^* at the moment 0, $2\pi/\omega_a$,...$2k\pi/\omega_a$(k=0, 1,....)(this kind of dealing method also is essential in dc voltage control loop). So, at a period of $2\pi/\omega_a$, the frequency domain solution of current i_a is found as:

$$i_a(s) = \frac{I_a^*\omega_a}{K_{ai}+L_aS}\cdot\frac{K_{ai}+L_aS}{S^2+\omega_a^2} = I_a^*\frac{\omega_a}{S_2+\omega_a^2}\cdot \tag{16}$$

Therefor, (14) may well be used as the control voltage of the inverter for the unity power factor current control.

2)Design of constant dc voltage control loop: In the dc side of the inverter, if the current i_{Dc} flowing through diode Dc is considered as a disturbance, the dc side voltage e_d can be controlled through controlling the input current i_d. On the other hand, the e_d also depends on the following relationsiop:

$$e_d = \frac{e_a i_a}{i_d}. \tag{17}$$

Where the all quantities are transient value. Notably, the waveshape of $e_a i_a$ is similar to a single-phase diode-bride rectified one, there must be a certain ripple in the output of the PV array even if at MPP. (17) can be divided into two parts:

$$e_a i_a = \frac{V_a I_a}{2} + \frac{\omega_a L_a I_a^2 \sin 2\theta_a - V_a I_a \cos 2\theta_a}{2}. \quad (18)$$

Where V_a, I_a are root-mean square values. The first term of (18) represents the dc component, second term is the ac component with a frequency $2f_a$. Because what we want to do is over-voltage protection, it is sufficient enough for this requirement to only control the dc component (V_d) of e_d to a certain value. The dc component of e_d is related to $V_a I_a/2$, and V_a belongs to utility voltage, an uncontrolled quantity. As a result, I_a may is selected as a controlled quantity. By controlling the amplitude of I_a, then controlling the amplitude of i_d, the dc component V_d is controlled to an constant value(here 350V). In addition, for preventing that the time function I_a^* cause dc component in the ac current i_a, One possible method is to limit the change of I_a^* at the moment 0, π/ω_a,...$k\pi/\omega_a$(k=0, 1,....). For marching the dealing method mentioned previously, here, the change of I_a^* is limited at t=0, $2\pi/\omega_a$,...$2k\pi/\omega_a$(k=0; 1,....). As such, the block diagram of the dc voltage control system may be constructed as Fig.5. Where the sample cycle is $2\pi/\omega_a$. The integral element is for eliminating steady-state error of dc component V_d. Fig.5 is a non-linear block diagram. At the equilibrium point, its linearized transfer function is:

$$\frac{\Delta V_d}{\Delta V_d^*} = \frac{\frac{V_a K_{PV}}{2e_d^* C_d T_V} S + \frac{V_a K_{IV}}{2e_d^* C_d T_V}}{S^3 + (\frac{1}{T_V} - \frac{I_{do}}{C_d V_d^*}) S^2 + (\frac{V_a}{2C_d T_V V_d^*} K_{PV} - \frac{I_{d0}}{C_d T_V V_d^*}) S + \frac{V_a K_{IV}}{2C_d T_V V_d^*}}$$

Similarly, the poles of this system can be located freely.

IV. Simulation Results

For verifying the proposed method, the main circuit parameters of Fig.3, as given in Table I, is used for simulation. As the poles of the designed control systems can be freely located by adjusting the compensator parameters, through trial and error method, the suitable parameter values of comensators, which ensure the system steadily operate to the insolation variation from 100W/m^2 to 1kW/m^2 and temperature variation from-50°C to 100°C, were found as Table II. The simulated results under insolation 1kW/m^2 and temperature 25°C are plotted in Fig.6, Fig.7 and Fig.8. Fig.6 shows the maximum power tracking performance using the proposed method. The relationship is clearly seen that the PV array output its maximum power as long as the derivative dp_s/de_s is equal to zero. In addition, as stated above, in such a system the output power of PV array contains a few ripples as shown

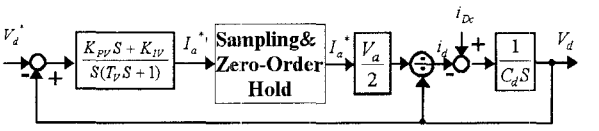


Fig.5 Block diagram of constant dc voltage control system

TABLE I Circuit Paremeters

utility line	200V, 60Hz
array short-circuit current	16.5A
array open-circuit voltage	268V
capacitor Cs	470μF
capacitor Cd	2820μF
capacitor Ca	8μF
inductor Lc	1mH
inductor La	13.6mH

TABLE II Compensators Paremeters

K_P	642.5
K_{ce}	0.5774
K_{ci}	1.750
K_{PV}	0.4530
K_{IV}	9.109
T_V	0.0104
K_{ai}	1.360

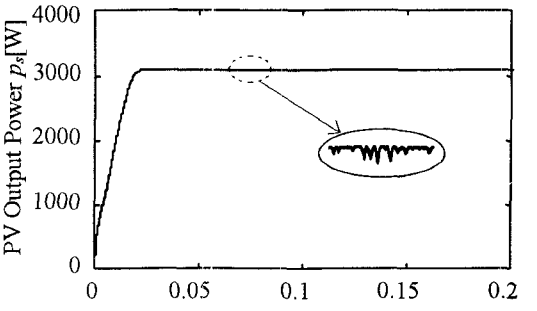


Fig.6(a) Transient response of output power

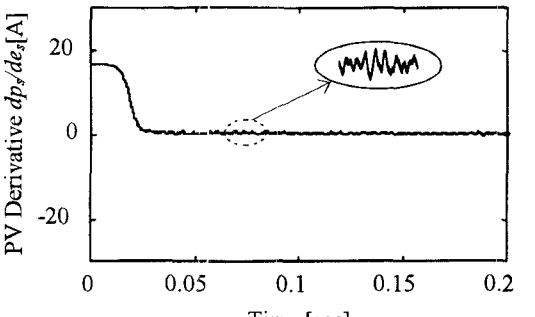


Fig.6(b) Transient response of dp_s/de_s

in the detail part of Fig.6. And just with the aid of them, the dp_s/de_s can be directly detected out even if during the operating at the MPP, without another addition means. Fig.7 shows the unity power factor output current control performance. Fig.8 shows the constant dc voltage control

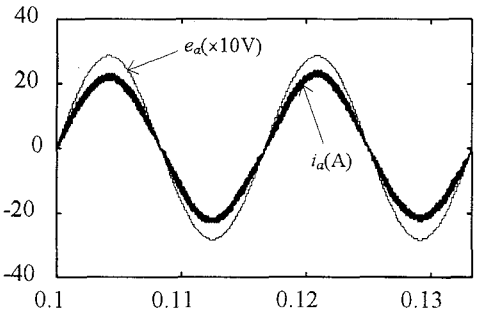


Fig.7 Unity power factor control performance

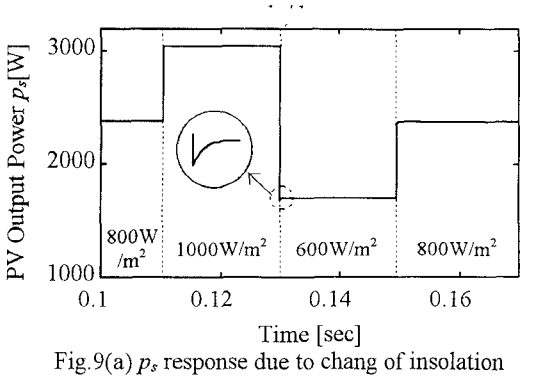


Fig.9(a) p_s response due to chang of insolation

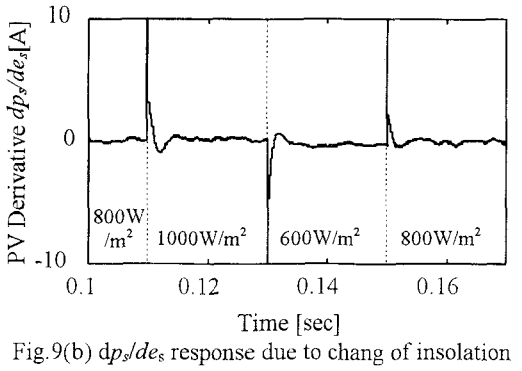


Fig.9(b) dp_s/de_s response due to chang of insolation

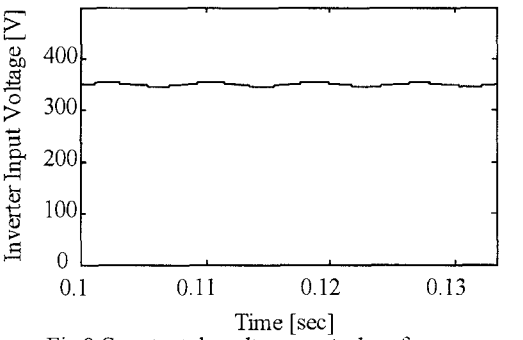


Fig.8 Constant dc voltage control performance

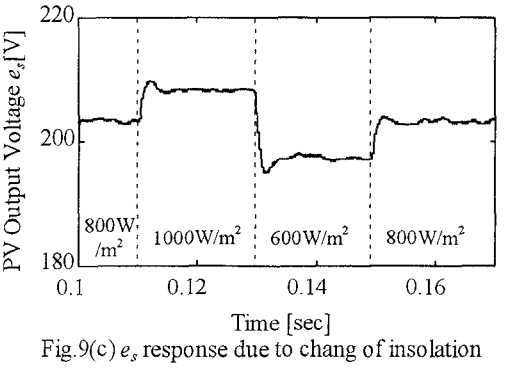


Fig.9(c) e_s response due to chang of insolation

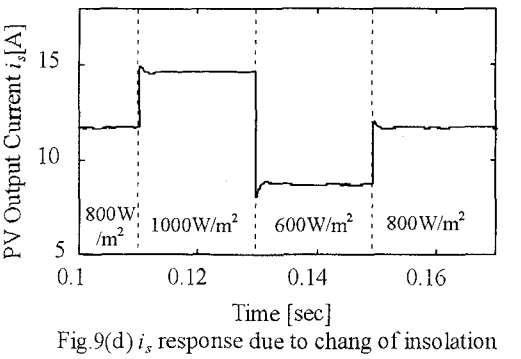


Fig.9(d) i_s response due to chang of insolation

performance. As desired, the dc component of the inverter input voltage is controlled to 350V. Fig.9(a)(b)(c)(d) show the transient response of PV array output quantities, voltage e_s, current i_s, power p_s and derivative dp_s/de_s, to a insolation change of 800W/m^2→1kW/m^2→600W/m^2 at 25°C, respectively. As can be seen, it can track new MPPs in very short time. So the tracking performances was improved by the proposed method.

V. Conclusions

The property, the PV array must output maximum power when its dp_s/de_s is equal to zero, is paid attention, and based on it a new method for maximum power tracking was proposed. The maximum power tracking was implemented through controlling the derivative dp_s/de_s toward zero with the feedback loop of dp_s/de_s. A 3kW utility interactive PV power conditioning system was used as an application example and the relating design method was described. The simulated results shown that the accuracy and rapidity of the maximum power tracking were significantly improved by the proposed method.

Reffrences

[1] B.K.Bose, et al: "Microcomputer Control of a Residential Photovoltaic Power Conditioning System," *IEEE Trans. Ind. Applicat.*, vol.IA-21, No.5, pp.1184-1191, 1985.

[2] M.Makino, et al: "Digital Control Method for a Photovoltaic Power System", in *Proceedings of IPEC-Yokohame'95*, Yokohama, Japan, April 3-7, 1995, pp.197-202.

A New Microcontroller based Solar Energy Conversion Modular Unit

F. Huang* Gao Zhimin** T. Forughian* D. Tien*
*Ngee Ann Polytechnic **Sennheiser Electronic Asia Pte Ltd
Singapore 599489 Singapore 120709
Fax: +65 –4676504 E-mail: huf@np.ac.sg

Abstract: This paper presents the design and the implementation of a new microcontroller based solar energy conversion modular unit. The unit consists of an array of solar panels, a step-up chopper, a single-phase inverter, an ac mains power source, and a microcontroller based control unit. The novelty of this unit is that the switching device of the chopper is not only used for power conversion but also for Maximum Power Point (MPP) detection.

In the existing MPP trackers, the MPP is detected by hardware. The parameters of the hardware subject to the changes of the environmental conditions. In the new unit the MPP is determined by a simple embedded software. With this new approach, the modularization of the conversion from solar power to electric power at its maximum power point can be made more compact and more reliable.

I. INTRODUCTION

With the cost of solar cells decreasing, the conversion of solar energy to electric energy is increasingly becoming economically viable. This is particular true in a tropical country like Singapore where there is abundant solar energy available through out the year.

To harvest the vast solar energy, it would be desirable if the energy conversion modular units are simple, reliable, and of low cost and high efficiency. High efficiency can be achieved by controlling the modular unit operating at its maximum power extraction. There are two basic approaches in maximizing the power extraction:

(a) using automatic sun tracker;
(b) searching for the MPP conditions.

In automatic sun tracker systems, the solar panels are controlled to follow the movement of the sun[1]. Due to the high cost and the energy consumption of the sun tracker, this approach may not be suitable for energy conversions at a small to medium power range.

In searching for the MPP condition, many methods have been tried. The "look-up-table", the "perturb and observe", and the "current sweep" are some of the fundamental approaches. Neural Network approach[2] and Fuzzy Logic approach[3] are also reported.

This paper presents the design and the implementation of a solar energy conversion modular unit with a "current sweep" approach[4]. In this unit, the MPP detection and the energy conversion are implemented by using a single power switching device and its driving circuit. In addition, the MPP is detected through a simple software embedded in a microcontroller. The unit controlled by the microcontroller operates in two different modes: the tracking mode and the conversion mode.

In the tracking mode, the switching device of the chopper is controlled in such a way that its current increases exponentially. In the conversion mode, the chopper converts the low voltage energy to high voltage energy. During the tracking mode, the panel voltage is sampled and the MPP is detected. During the conversion mode, the desired panel voltage corresponding to the MPP is maintained by controlling the on-off time of the power switching device in the step-up chopper.

II. MODULAR UNIT DESCRIPTION

A. General

The circuit diagram of the solar energy conversion modular unit is shown in Figure 1. The unit is designed at 500 W using 10 solar panels connected in series and in parallel. The specifications of the solar panel are given in Table 1.

The output voltage across the 10 solar panels is between 40 - 100 V. The unit will be disabled if the voltage drops below 40 V. The panel voltage is converted to a higher voltage through a step-up chopper. An inverter consisting of Insulated Gate Bipolar Transistors (IGBT) is then used to convert the dc voltage at the output of the chopper to mains supply.

The unit starts with testing the panel voltage, if it is higher than 40 V, the MPP detection procedures are

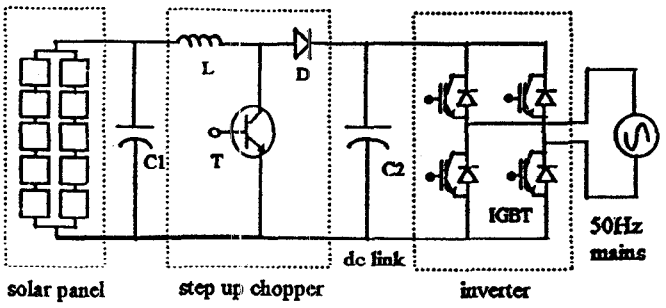


Figure 1 Circuit diagram of the modular unit

Table 1: Power specifications.

Model	M55
Rated power	53 W
Current:	3.05 Amps
Voltage:	17.4 Volts
Short circuit current:	3.35 Amps
Open circuit voltage:	21.7 Volts

initiated. Within 10 milliseconds, the MPP will be detected and the voltage corresponding to the MPP will be memorized. In the next 1 minute, the step-up chopper is controlled to maintain the panel voltage at a level around its MPP.

B. MPP Detector

The maximum power point corresponds to the peak of the power

$$p(t) = v(t)i(t) \tag{1}$$

where v(t) and i(t) are solar panel terminal voltage and output current. Under the MPP condition, the derivative of p(t) with respect to v(t) and i(t) is zero

$$\frac{dp(t)}{dv} = 0; \text{ and} \tag{2}$$

$$\frac{dp(t)}{di} = 0; \tag{3}$$

To detect the MPP, the panel current can be swept through from zero to its maximum value in a certain period of time. Assuming the sweeping current is

$$i(t) = f(t) \tag{4}$$

the power of the panel along this sweep current is

$$p(t) = v(t)f(t) \tag{5}$$

The panels deliver maximum power when the derivative of p(t) is zero

$$\frac{dp(t)}{dt} = 0; \text{ or} \tag{6}$$

$$v(t)\frac{df(t)}{dt} + f(t)\frac{dv(t)}{dt} = 0 \tag{7}$$

The sweeping current can be further assumed that

$$f(t) = k\frac{df(t)}{dt} \tag{8}$$

where k is a constant.

Equation (7) can be simplified to

$$\left(k\frac{dv(t)}{dt} + v(t)\right)\frac{df(t)}{dt} = 0 \tag{9}$$

Assuming the derivative of f(t) is not zero in the sweeping period, then the condition

$$k\frac{dv(t)}{dt} + v(t) = 0 \tag{10}$$

can be used to detect the MPP.

To define the function of the sweeping current, (8) is solved

$$f(t) = Ae^{\frac{t}{\tau}} \tag{11}$$

where A is an arbitrary constant of the general solution. If k in (8) is selected as a negative real number and A is selected as the maximum sweeping current, I_{max}, the sweeping current becomes an exponential function decreasing, with a time constant $\tau = k$, from I_{max} to zero.

C. Control Implementation

The modular unit is designed in such a way that the control information based on the detected MPP is up-dated every one minute. The first ten milliseconds in every one minute is used to find the MPP information. After this 10 ms, the unit is controlled to convert the solar energy under the MPP condition for the rest of the time before the next cycle comes.

A single control circuit is designed for both the MPP detection and the control of power conversion. Figure 2 shows the diagram of the control circuit. The input of the control circuit is the feedback signal from the panel voltage. The output is a current source to drive the power transistor in the chopper circuit.

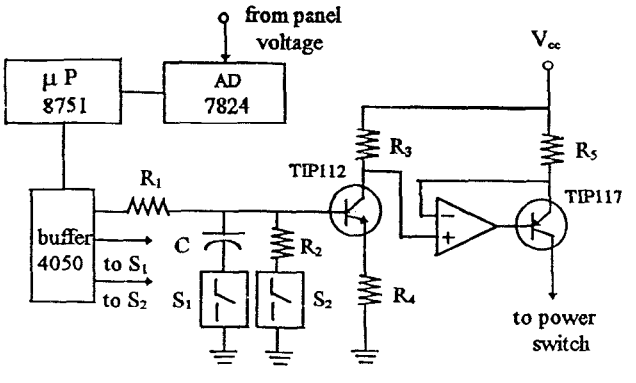


Figure 2 Control circuit of the modular unit

In the MPP detection mode, an exponential sweeping current is generated. Referring to Figure 2, at the beginning, S_1 is kept close and S_2 is kept open. A voltage step increase at the output of the buffer will result in an exponential increase of the voltage across the capacitor. The time constant, $\tau = RC$ is designed to be 10 ms. The two Darlington transistors TIP112 and TIP 117 function as voltage to current source converter. The exponential increase of the voltage at the base of the TIP112 results in an exponential increase of the current at the collector of the TIP117.

Once the microcontroller initiated the sweeping current, it starts to obtain the information of the panel voltage. The panel voltage is sampled every 100 μs. The conversion of the voltage from analog to digital values is done by AD 7824 which is a 8 bits, 4 channels IC with a conversion time of 2.5μs. Starting from the second point of the converted voltage, the condition, shown in (10) is tested.

The MPP condition (10) can be described in a digital form

$$(k'+1)\times v(i+1) - v(i) = 0 \qquad (12)$$

where $k' = \tau \cdot \Delta t$, $\Delta t = 100$ μs, and $i = 1, 2, 3 \cdots\cdots$.

Testing of the MPP condition is programmed in software. The program simply tests whether the following condition is held

$$| (k'+1)\times v(i+1) - v(i) | \leq \varepsilon \qquad (13)$$

where ε is a very small value. If the condition is satisfied, the detection mode will be terminated and the conversion mode will be initiated. The last value of the panel voltage is memorized. This voltage is used as the reference in the conversion mode.

In the conversion mode, both S_1 and S_2 are kept open. The voltage to current converter (TIP112 and TIP117) is now working in switching mode, not in amplifying mode.

The panel voltage is sampled every 5 μs. The sampled voltage, which is the actual panel voltage, is compared with the reference voltage in the microcontroller.

When the actual voltage is higher than the reference one, a logic high is produced at the output of the microcontroller. This pulse, through the voltage to current converter, turns on the power transistor in the chopper circuit. When the actual voltage falls below the reference voltage, the microcontroller produces a logic low. This logic low then switches off the power transistor. The control of the panel voltage under its MPP condition, is achieved by controlling the on-off duration of the power transistor.

The control of the inverter which converts DC to single phase or three phase AC power for solar energy conversion has been well described [5,6].

III. TEST RESULTS

The modular unit is tested with two solar panels connected in series. Figure 3 and 4 show the waveforms of the panel voltage, current and power at two different illumination levels. An exponential current is repeatedly generated in every 40 ms. The sweeping current takes about 10 ms. Setting the interval between two sweeping currents at 20 ms is only for testing of the MPP detection. Under normal operation of the modular unit, the interval between two sweeping currents should be 1 minute.

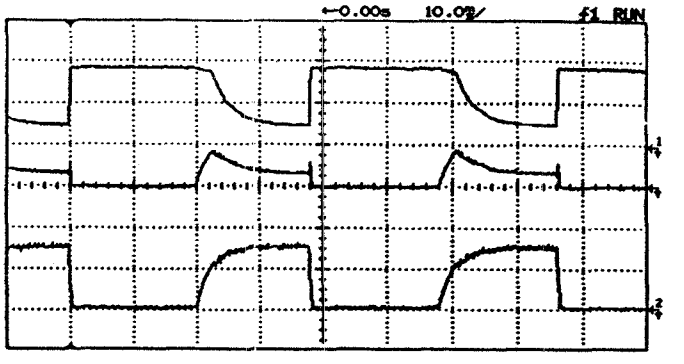


Figure 3 MPP detection at illumination level A
a) panel voltage, 20v/div (top)
b) panel output power, 50W/div (middle)
c) panel output current, 1A/div (bottom)

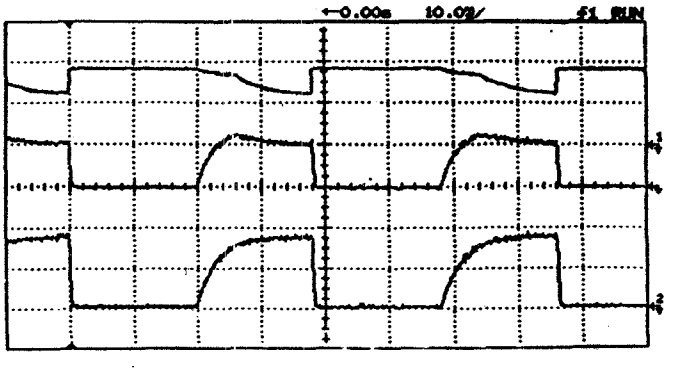


Figure 4 MPP detection at illumination level B
a) panel voltage, 20v/div (top)
b) panel output power, 50W/div (middle)
c) panel output current, 1A/div (bottom)

Once the MPP is detected, the voltage or current at this sampling point are memorized and used as the reference information. To control the actual panel voltage or current in a band of the reference, hysteresis control is used. Figure 5 shows the voltage across the solar panel when the panel voltage is controlled. As shown in the Figure, when the power switch is in the off-state (high

voltage), the panel voltage is built up. After it reaches the top limit, the switch is switched on, the charging current through the inductance increases. This, in turn, results in the panel voltage drops. When the voltage drops below the low limit, the switch is cut off again. The current built up in the inductance discharges through the dc link. Meantime, the panel voltage is building up again. This is repeated in every 80μs. Figure 6 shows the panel output current when the current is controlled.

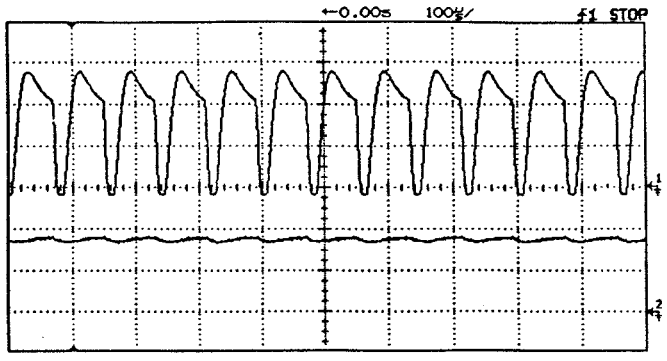


Figure 5 Voltage controlled power conversion (20V/div, 100μs/div)
a) voltage across the power switch (top)
b) voltage across the solar panel (bottom)

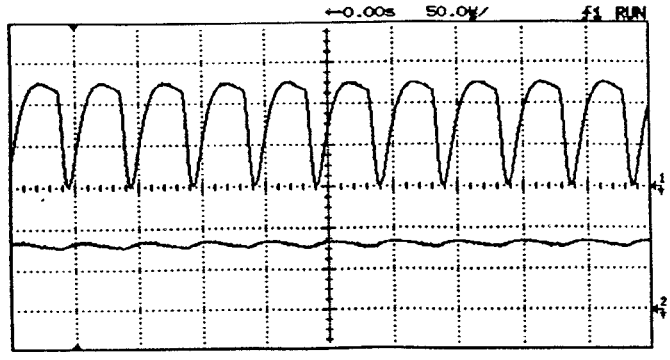


Figure 6 Current controlled power conversion (20v/div, 1A/div, 50μs/div)
a) voltage across the power switch (top)
b) panel output current (bottom)

IV. CONCLUSIONS

A new microcontroller based solar energy conversion modular unit has been designed and implemented. In the new modular unit, the MPP detection and the power conversion are realized by using the same hardware circuit. In the existing MPP detectors, the detection of the MPP is achieved by analog computing, analog comparison, and analog hold. In contrast to the existing ones, in the new unit, the MPP is detected by software which is embedded in a microcontroller. It can be concluded that with the new design the solar energy converter can be made more compact, reliable, and cost effective.

References

[1] A. Konar and A.K. Mandal, "Microprocessor based automatic Sun tracker," IEE Proceedings A, Vol:138, Iss:4, p237-41, July 1991

[2] T. Hayama, S. Kouzuma, and T. Imakubo, "Identification of optimal operating point of PV modules using neural network for real time maximum power tracking control," IEEE Transactions on Energy Conversion, Vol:10, Iss:2, p360-7, June 1995

[3] H.M. Mashaly, and A.M. Sharaf, "Fuzzy logic controller for photovoltaic-unility interfacing scheme," in Proceedings of the 7th Mediterranean Electrotechnical Conference, 1994, vol. 2, p.715-18

[4] M. Bodur and M. Ermis, "Maximum power point tracking for low power photovoltaic solar panels," in Proceedings of the 7th Mediterranean Electro-technical Conference, 1994, vol. 2, p.758-61

[5] K. Harada and Gen Zhao, "Controlled power interface between solar cells and AC source," IEEE Trans. on Power Electronics, Vol.8, No.4, Oct. 1993, p.654-62

[6] R.M. Hilloowala and A.M. Sharaf, "A rule-based fuzzy logic controller for a PWM inverter in photo-voltaic energy convsion scheme," in Conf. Rec. of the IEEE Industry Applications Society Annual Meeting, New York, 1992, Vol.1, p.762-9

Ring-shaped Flywheel Energy Storage Systems with Superconducting Levitation

Hidekazu Teshima
Advanced Technology Research Laboratories, Nippon Steel Corporation
3-35-1 Ida, Nakahara-ku, Kawasaki 211, JAPAN
Fax : +81-44-752-5759, Phone : +81-44-777-4111, E-mail : hteshima@lab1.nsc.co.jp

Taichi Tawara, Jun Kobuchi, Tatsuo Suzuki, and Ryuichi Shimada
Research Laboratory for Nuclear Reactors, Tokyo Institute of Technology
2-12-1 O-okayama, Meguro-ku, Tokyo 152, JAPAN
Fax : +81-3-5499-7217, Phone : +81-3-5734-3328

Abstract **- This paper proposes an energy storage system that combine two new concepts: a ring-shaped flywheel and superconducting levitation. The ring-shaped flywheel differs from conventional disk-shaped flywheels in that it can be applied to large-scale electric power storage systems like pumped storage power generation systems. Superconducting levitation is automatically-stable noncontacting levitation without control and is suitable as support mechanism for the ring-shaped flywheel that has no shaft and hub. To evaluate the feasibility of this new combination, a small-scale prototype was built and tested to investigate the stiffness of superconducting levitation and the properties of the ring, such as horizontal vibration and rotational loss.**

I. Introduction

The need for energy storage technology has been ever increasing with increase in electric power demand, expansion of electric power demand gap between the daytime and nighttime, and utilization of natural energy sources, among other factors. Of the energy storage technologies under development, that of utilizing the rotational kinetic energy of a flywheel is already commercialized to compensate for load variations in such short time as seconds or minutes and assures high reliability [1]. For daily load leveling, however, the conventional flywheel energy storage system with a disk-shaped flywheel supported with mechanical bearings had two main problems. First, it was difficult to make a flywheel large enough for a practical energy scale. Second, the bearing loss was large enough to reduce the overall efficiency of the system over a long period of continuous operation.

This paper proposes a superconductively-levitated ring-shaped flywheel as one solution to these problems. The results of evaluation with a small-scale prototype are also presented.

II. Concept and Structure of Experimental Apparatus

A. Ring-shaped flywheel

The energy E stored in the flywheel is given by

$$E = (1/2)\, I\, \omega^2 \propto M\, R^2\, \omega^2. \quad (1)$$

where I, ω, M, and R are the moment of inertia, angular velocity, mass, and outermost diameter of the flywheel, respectively. When the flywheel rotates, the resultant centrifugal force produces stresses in the flywheel. There is the following relationship between the allowable stress σ_a of the material of the flywheel and the maximum speed wmax at which the flywheel can rotate:

$$\sigma_a \propto \rho\, R^2\, \omega_{\max}{}^2. \quad (2)$$

where ρ is the density of the material of the flywheel. From (1) and (2), the following equation is derived:

$$E = K_s\, M\, (\sigma_a / \rho). \quad (3)$$

where Ks is a shape factor. The first prerequisite to increase the amount of stored energy is to select a material with high specific strength (σ_a/ρ) for the flywheel. The further increase in the amount of stored energy, however, requires the size and mass M of the flywheel to be increased.

Fig.1 conceptually illustrates the conventional disk-shaped flywheel and the new ring-shaped flywheel. The increase in the size of the conventional disk-shaped flywheel involves the following problems : (1) When the flywheel rotates, the

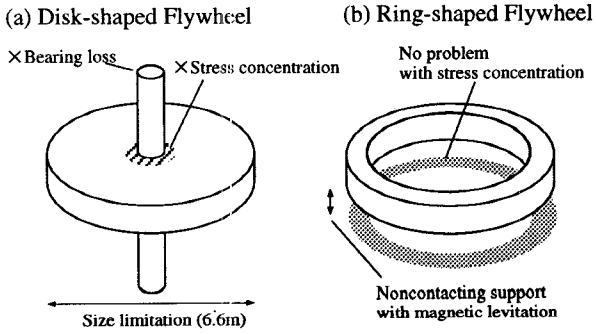


Fig.1. Problems of conventional disk-shaped flywheel and features of new ring-shaped flywheel.

resultant centrifugal force makes the internal stress to peak at the center of the flywheel and sometimes causes stress concentration there. The maximum amount of energy that can be stored is limited by the material strength of not the periphery of the flywheel where a large part of the energy is stored, but the center part of the flywheel where only a small part of the energy is stored. (2) When the flywheel is increased in size, the merit of increased energy storage is more than offset by the demerit of increased bearing load. (3) Available equipment makes it difficult to fabricate and transport a disk-shaped flywheel with a diameter greater than the present maximum of 6.6 m.

The above problems can be solved when increasing the size of a ring-shaped flywheel without rotating shafts [2]. The ring-shaped flywheel carries the centrifugal force with the tension of the ring, so that stress concentration at the center does not occur. Since the flywheel rotates only where a large amount of energy is stored, the stored energy density or the stored energy relative to the flywheel weight increases. The ring shape without shafts, however, created the new problem of the inability to support the flywheel with conventional bearings.

B. Superconducting Levitation

One possible support mechanism for the ring-shaped flywheel is the magnetic levitation of the entire ring. Since the flywheel becomes mechanically noncontacting as a result, the bearing loss due to friction, for instance, can be sharply reduced. The absence of rotating shafts, however, makes it difficult to achieve the stable levitation and rotation of the ring-shaped flywheel as compared with the disk-shaped flywheel. Conventional magnetic levitation with magnets is essentially unstable [3] and is stabilized by a complicated control system. The ring-shaped flywheel calls for a magnetic levitation mechanism of still higher stability.

Superconducting levitation using the pinning effect is intrinsically stable levitation and is suitable as support mechanism of the ring-shaped flywheel. Fig.2 shows the concept of superconducting levitation. The magnetic flux lines from the magnet are pinned by the bulk superconductor. This pinning effect is responsible for restoring force to the levitation position of the magnet in both horizontal and vertical directions and ensures the stable levitation of the magnet. The restoring force acts only in the direction where the magnetic field is nonuniform. When superconducting levitation is applied to a flywheel, the resistance to the rotation of the flywheel can be made small enough to be ignored by making the magnetic field uniform in the rotational direction. It is pointed out that superconducting levitation using the Meissner effect is small in levitation force. With superconducting levitation using the pinning effect, a high enough levitation force to carry a practical weight is accomplished by the development of high-performance and large-size bulk superconductors [4,5]. Fig.3 shows an example of bulk superconductors commercially available.

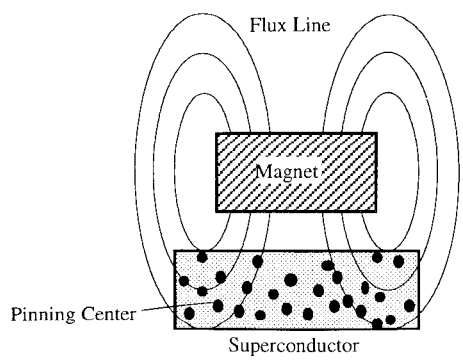


Fig.2. Schematic diagram of superconducting levitation due to pinning effect.

C. Structure of Prototype

Figs.4 and 5 show the appearance and structure, respectively, of an experimental superconductively-levitated ring-shaped flywheel used in the present study. The ring was made of iron and measured about 280 mm in diameter. It was fitted with levitation and drive Nd-Fe-B permanent magnets as shown in Fig.5. Its total weight and inertial moment were 7.63 kg and 0.107 kg·m^2, respectively. The ring was driven by a permanent-magnet synchronous motor method. Permanent magnets were installed vertically opposed to each other as synchronous motor poles in the outside surface of the ring. Drive coils were installed in three phases between the top and bottom magnets. A pattern indicating rotational angle information was printed on the top surface of the ring. The pattern was read with a reflection-type optical sensor to detect the rotational angle of the ring and to ensure the synchronism of the ring with the synchronous motor.

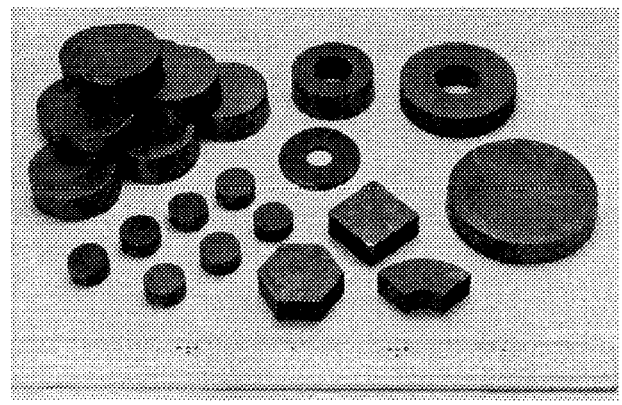


Fig.3. Appearence of bulk superconductors commercially available.

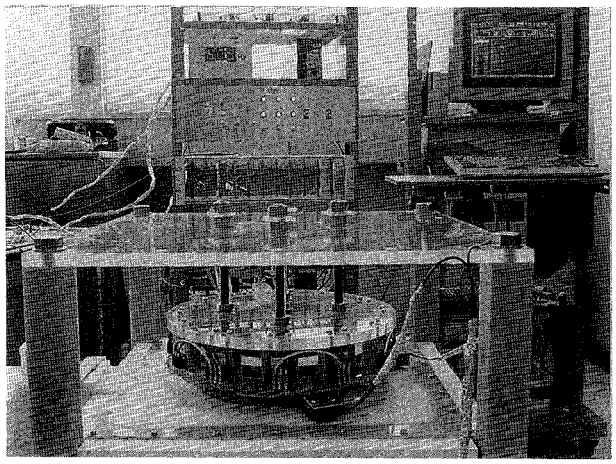


Fig.4. Appearence of prototype ring-shaped flywheel with superconducting levitation.

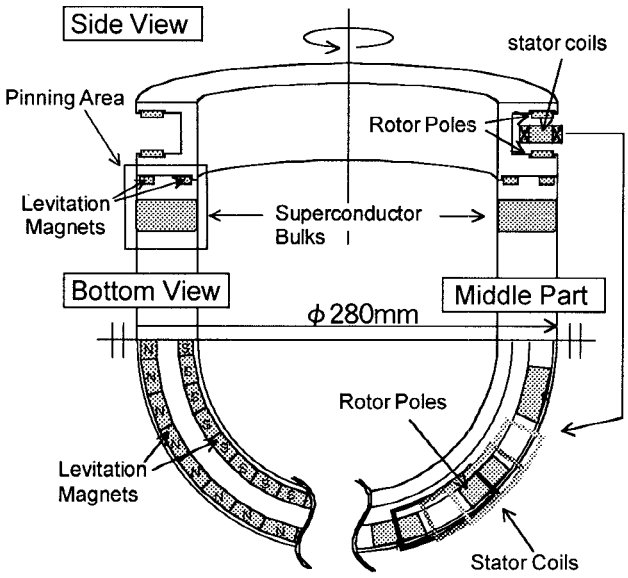


Fig.5. Structure of prototype ring-shaped flywheel with superconducting levitation.

As levitation magnets, 36 trapezoidal magnets were closely installed in the circumferential direction in the bottom surface of the ring. The circumferential magnetic field distribution at a position of 7 mm simulating the actual levitation gap exhibited pulsations of about 50 Gauss at 10-deg intervals by reflecting the trapezoidal shape of the magnets. Sixteen bulk Y-Ba-Cu-O superconductors, made by the modified quench and melt growth process and measuring 46 mm in diameter, were arranged in a ring pattern as opposed to the levitation magnets. To magnetically support the ring-shaped flywheel using superconducting levitation, the flux of the levitation magnets must be pinned by the bulk superconductors. With the ring suspended from above, the bulk superconductors were refrigerated by liquid nitrogen with an appropriate gap (called the initial gap) to pin the flux of the levitation magnets.

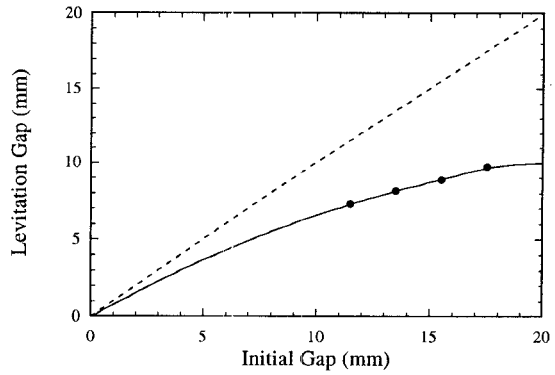


Fig.6. Relationship bewteen initial gap and levitationgap.

III. Results and Discussion

A. Levitation Gap and Spring Constant

Fig.6 shows the relationship between the initial gap and the actual levitation gap. Relative to each initial gap, impact force is horizontally applied to the ring that is levitated and still. The change with time in the resultant vibration of the ring was measured with a laser displacement meter. Fig.7 shows the vibration wave form of the ring when the levitation gap was 8.9 mm. Superconducting levitation is found to attenuate the horizontal vibration of the ring. It is assumed that superconducting levitation can be approximately by the one-degree-of-freedom model shown in Fig.8 or an object of the mass m is connected with the spring constant k and the damping coefficient c [6]. The spring constant k of the one-degree-of-freedom model is given by

$$k = m\,(2\pi / T\ )^2 . \qquad (4)$$

where T is the period of vibration. Fig.9 shows the

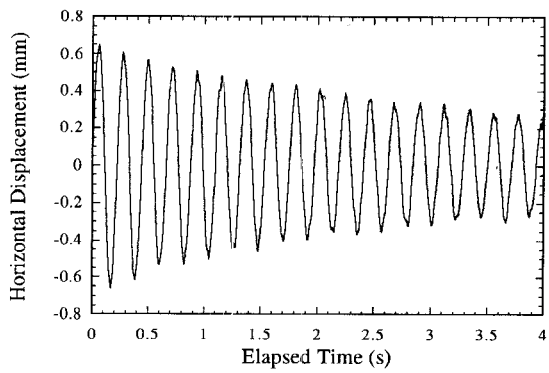


Fig.7. Wave form of horizontal vibration of ring at a levitation gap og 8.9mm.

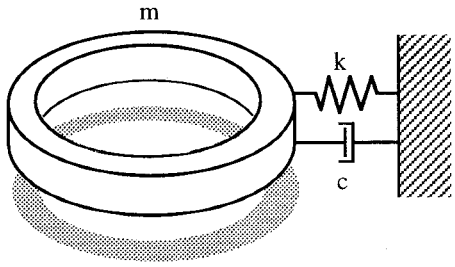


Fig.8. One-degree-of-freedom model, where m is mass, k is spring constant, and c is damping coefficient.

relationship between the initial gap and the spring constant as obtained from the period of the vibration wave form and (4). Decreasing the initial gap increases the number of the flux lines pinned by the bulk superconductors, the spring constant, and the stiffness of magnetic bearings.

B. Magnitude of Horizontal Vibration and Eccentricity Adjustment (Balancing) during Acceleration

Fig.10 shows the change with time in the magnitude of horizontal vibration of the ring when rotated at a speed of 0.36 rps. The minute vibrations observed in the wave form are regarded as the vibrations of the ring that did not fully stop after the application of the rotational torque and are ignored here. From Fig.10, the deviation (eccentricity) between the center of gravity and the center of rotation of the ring-shaped flywheel is about 0.1 mm. The magnitude of horizontal vibration of the ring during rotational acceleration with a levitation gap of 8.9 mm is shown in relation to the speed in Fig.11. The eccentricity of the ring was adjusted by attaching balancing weights in suitable positions. Before the ring was balanced, its vibration became excessive near 4.2 rps so that it could not be accelerated any more. After the ring was balanced, the amplitude of vibration in the vicinity of 4.6 rps or the resonance point could be made fully small by the damping mechanism of superconducting levitation. In

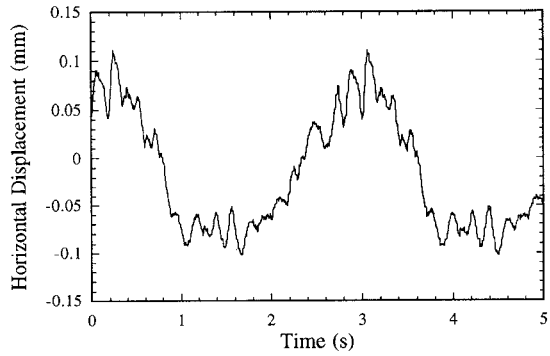


Fig.10. Change with time in horizontal vibration of ring rotating at 0.36 rps.

the region where the resonant frequency was exceeded, the ring-shaped flywheel could be operated. The resonant frequency of 4.6 rps agrees well with that predicted from the spring constant obtained for the ring that is levitated and still.

C. Rotational Loss

Fig.12 shows the change with time in the speed of the ring-shaped flywheel when freely rotated in air and helium gas. Figs.13 (a) and (b) are linear and logarithmic plots, respectively, of the speed-rotational loss relationship of the ring-shaped flywheel in air and helium gas as obtained from Fig.12. In Fig.13 (b), straight lines indicating the loss components proportional to the square and cube of the rotational speed (square and cubic losses) are also shown as auxiliary lines. In helium, the square loss is predominant over almost the entire speed range. In air, the line indicating line as the speed increases. The difference between the rotational loss in air and the rotational loss in helium is also shown in Fig.13 (b). This difference corresponds to the decrease in windage loss due to the difference in density between air and helium. Since the difference is proportional

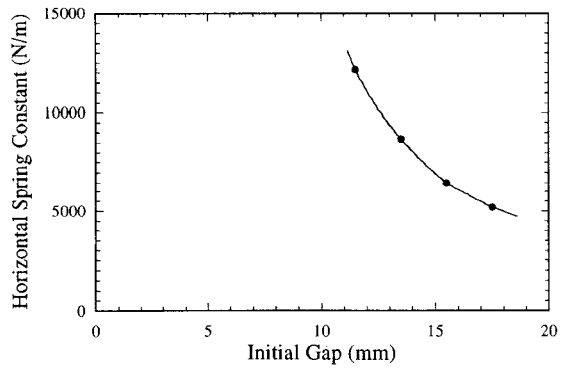


Fig.9. Relationship between initial gap and spring constant of ring.

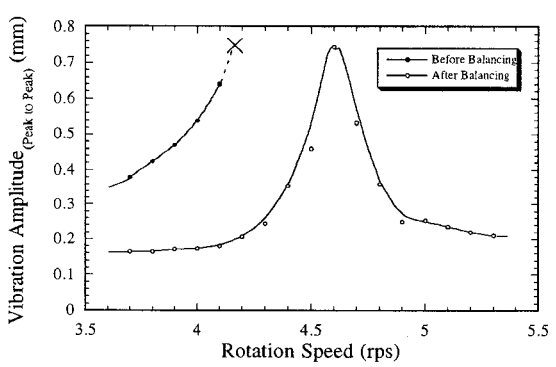


Fig. 11. Relationship between horizontal vibration amplitude and rotational speed of ring before and after balancing.

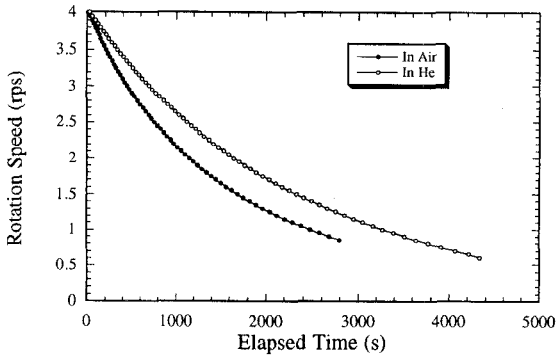


Fig.12. Change with time in rotational speed of ring rotating freely in air and helium.

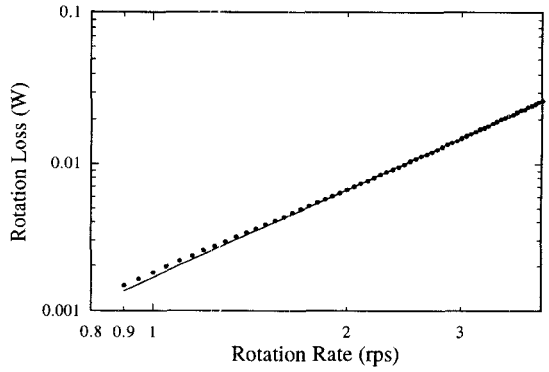


Fig.14. Relationship between rotational loss and rotational speed of ring when loss component proportinal to cube of rotational speed is deduced from measured total energy loss.

to the cube of the rotational speed in the entire speed region, it can be conducted that the windage loss is proportional to the cube of the rotational speed.

Since the windage loss can be eliminated by rotating the flywheel in a vacuum in a commercial system, the cubic loss was separated from the measured total energy loss. The results are given in Fig.14. The rotational loss proportional to the square of the rotational speed over almost the entire speed range. Near 1 rps, however, the rotational loss slightly deviated from the square loss. This points to the presence of linear loss. The linear loss and the square loss are thought to reflect the hysteresis loss and the eddy current loss, respectively.

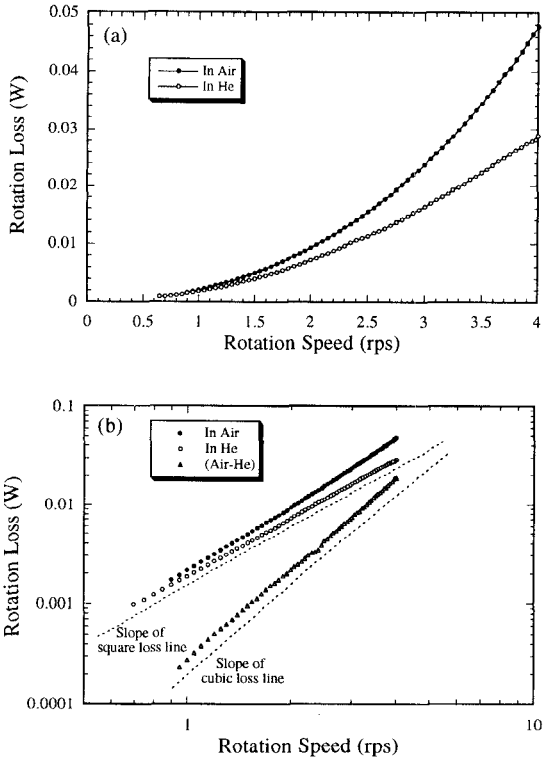


Fig.13. Relationship between rotational loss and rotational speed of ring in air and helium. (a) Linear plot and (b) logarithmic plot.

In this experimental work, the proportion of the square loss is large, probably for the following causes:

(1) Loss due to the eddy current that flows through the winding conductors of the drive coils

(2) Loss due to the eddy current that flows through the materials of construction of the ring

When the rotational loss was measured by pulling the drive coils away from the ring to estimate the loss due to cause (1), the loss component proportional to the square of rotational speed was reduced to 54%. This means that the contribution of cause (1) to the square loss is 46%. To reduce this loss, such a mechanism is required that pulls the drive coils off the ring when the ring is idle without energy input or output.

The magnetic field pinned by the bulk superconductors is suspected as the fluctuating magnetic field that causes the eddy current to flow through the material of construction of the ring. Fig.15 shows the magnetic field measured at certain points at the bottom surface of the ring while the ring was levitated and rotated. The presence of a fluctuating magnetic field of about 100 Gauss and with a period of 22.5 degree was found. The period of 22.5 degree reflects the arrangement of the 16 bulk superconductors in the ring pattern. To reduce the loss due to cause (2), it is necessary to improve the uniformity of the magnetic field to be pinned by tightly arranging the bulk superconductors and by increasing the size of the bulk superconductors and decreasing their number.

IV. SUMMARY

This paper has proposed a new energy storage system or a ring-shaped flywheel with superconducting levitation. A small-scale prototype was built and evaluated. The following findings were obtained:

(1) The spring constant or stiffness of the levitated ring can be adjusted by changing the initial gap.

(2) Eccentricity adjustment is also effective in supporting the ring-shaped flywheel with superconducting levitation. A

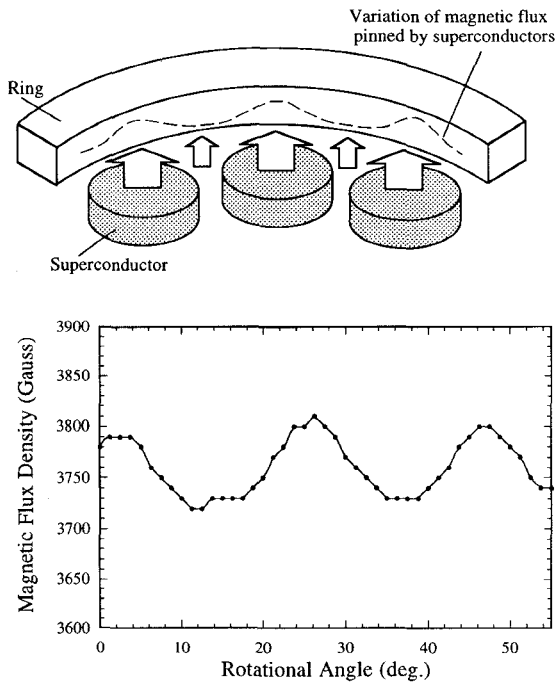


Fig.15. Circumferential magnetic field measured at bottom surface of levitated ring.

damping mechanism with superconducting levitation alone allows the rotational speed of the ring to exceed the resonant frequency.

(3) The resonant frequency of the ring during its rotational acceleration can be predicted from the spring constant measured when the ring is levitated and still.

(4) The windage loss of the ring-shaped flywheel is proportional to the cube of its rotational speed.

(5) About a half of the loss component proportional to the square of the rotational speed is due to the eddy current that flows through the winding conductors of the drive coils.

(6) The remaining half of the loss component proportional to the square of the rotational speed is due to the eddy current that is caused to flow through the material of construction of the flywheel by the magnetic field pinned by the bulk superconductors.

REFERENCES

[1] H. Chikaraishi et al., "Applications of large flywheel motor generator as power source for short-period load leveling device and uitility line power stabilization device", in Proceedings of IPEC-Tokyo, 1990, pp.585-592

[2] T. Ogata et al., "New concept flywheel - ring flywheel generator -",in Proceedings of PCC-Yokohama, 1993, pp.587-591

[3] S. Earnshaw, "On the nature of the molecular forces which regulate the constitution of the luminiferous ether", Trans. Camb. Phil. Soc., vol.7, Part I, pp.97-112, 1842

[4] M. Morita et al., "Processing and properties of QMG materials", Physica C 235-240, pp.209-212, 1994

[5] H. Teshima et al., "Compariosn of the levitation forces of melt-processed YBaCuO superconductors for different magnets", Physica C 269, pp.15-21, 1996

[6] H.Teshima, "Combination of additional noncontact dampers and superconducting levitation using melt-processed YBaCuO bulk superconductors", Jpn. J. Appl. Phys., vol.36, pp.68-75, 1997

Development of Uninterruptible Secondary Battery System

Masaaki Ohshima, Satoshi Miyazaki, Katsuhisa Inagaki, Hitoshi Kikuchi, Hitoshi Nirasawa
Tokyo Electric Power Co. Inc.
4-1 Egasaki-cho Tsurumi-ku
Yokohama-shi, 230, JAPAN
Fax: +81-45-585-8520, Phone: +81-45-585-8505
Toshiba Corporation
1 Toshiba-cho Fuchu-shi
Tokyo-to, 183, JAPAN
Fax: +81-423-40-8078, Phone: +81-423-33-2566
E-mail (corresponding author only) : inagaki@peken.fuchu.toshiba.co.jp

Abstract — **This paper presents the system configuration and control schemes of USBS(Uninterruptible Secondary Battery System), which acts as BESS when no fault occurs in commercial power network and functions as UPS in case of fault of the network. If some fault such as a voltage interruption occurs on the network, USBS disconnects critical loads from it at instant, and supply power to them as a UPS. It takes less than 2ms to restart supplying power to the loads in case of emergency, so there happens no damage on them. Simulations and experimental tests are carried out to confirm feasibility of the proposed system.**

I. Introduction

Batteries, which can store electric energy, are under development for realizing BESS (Battery Energy Storage System). On the other hand, UPS (Uninterruptible Power-supply System) is widely penetrated to protect critical loads from power interruption.

In this paper, we propose and develop the control schemes of USBS (Uninterruptible Secondary Battery System), BESS with function of UPS. USBS operates as a BESS to level load curve in case of no failure in the commercial power network. If some fault in the power network such as a voltage interruption occurs on power source, USBS disconnects critical loads from the network at instant, and continues to supply power to them as a UPS (UPS-mode). As it takes less than 2ms to restart supplying power to the critical loads when power source fault occurs, there happens no damage on the loads.

At first we will propose the configuration of USBS and its control schemes. Next we will discuss about the control algolism of PCS (Power Conversion System) and a.c. switch. Self-turn-off semiconductor switch such as IGBTs are supposed to use in the a.c. switch connecting loads to a power network, but we will show non-self-turn-off semiconductor switch such as thyristors can be also used in this a.c. switch. Finally we report on the simulated and experimental results considering various faults of power networks and have confirmed feasibility of the proposed system.

II. Mains circuit

Fig.1 shows the configuration of the proposed USBS. In consideration there is one USBS in one building, a USBS supplies emergency power to a whole building. There are two buses in the building, one is a bus for normal loads, the other one is a bus for critical loads such as computers. These two buses are connected through an a.c. switch made by semiconductor power devices. We suppose to use self-turn-off semiconductor devices such as IGBTs in this a.c. switch, but we can also use non-self-turn-off semi-conductor devices, as shown later. Battery is also connected to the bus for critical loads through a power converter, and the bus for normal loads is connected to commercial power network directly.

III. Control schemes

In daytime, when whole loads in the building need much power, USBS discharges the battery to assist power networks. At night, when the loads need small power, USBS charges batteries. We call these operational modes LL(Load Leveling)-mode. Once a fault is detected in the network, USBS disconnects the emergency bus from the network, and provide power to critical loads from the battery. We call this operational mode UPS-mode.

The transition from LL-mode to UPS-mode should have been finished as fast as possible, but some voltage interruption is inevitable during the mode transition. So we should survey the acceptable voltage fluctuation which assures no damage to the loads. Fig.2 shows the acceptable voltage fluctuate range we can assume to continue to supply power. This graph means that there happens no damage in the loads even if 100% voltage drop within 2ms or 25% voltage drop within 10ms occurs.

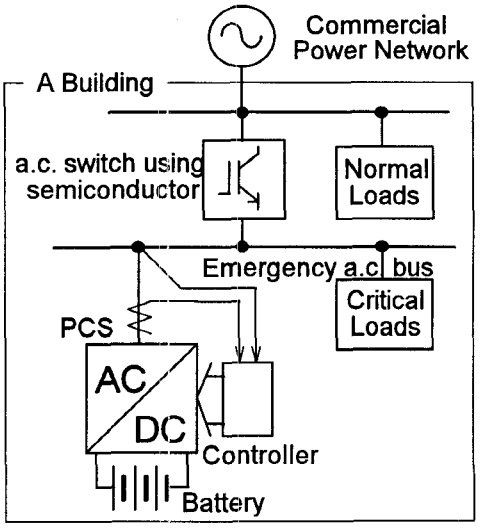


Fig.1 Configuration of USBS

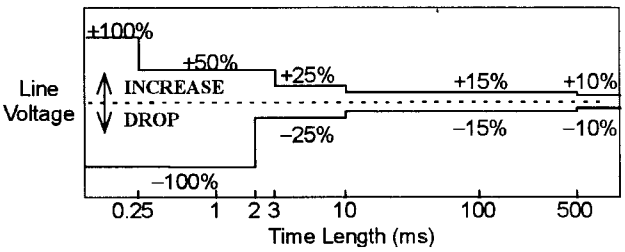


Fig.2 Defined acceptable voltage change domain

This voltage criterion is defined in consideration of ANSI(American National Standards Institute), CBEMA(Computer and Business Equipment manufactures Association), US Navy, and IEC standard.

Fig.3 shows the control block. In LL-mode the ACR is in use. It controls AC currents and DC charging or generating currents change with AC currents. It also keep input power factor unity. In UPS-mode the AVR is in use to keep load voltage assured to be almost uninterruptible, as defined in Fig.2. These ACR and AVR are constructed by PI controller with feed-forward path of output voltage reference. This feed-forward path cancels the influence of network voltage in LL-mode, and assist output voltage start up quickly in transition from LL-mode to UPS-mode.

The proposed USBS is requested high efficiency in LL-mode, and high speed response in UPS-mode. To realize these conflicting demands, USBS has adopted different carrier frequency between the two modes. USBS runs in low switching frequency in LL-mode to achieve high efficiency. In UPS-mode, higher carrier frequency is adopted to achieve high speed response.

IV Opration of the A.C. Switch

A. How to Detect Network Voltage Faults

When a fault such as voltage interruption, low or high frequency, phase jump, is detected in the commercial power network, USBS disconnects the network. We have to detect these faults as quickly as possible.

In proposed USBS, voltage amplitude failure is detected on q-axes voltage. 3-phase network voltages are detected and transformed into dq-axes components. The equation of this transformation is shown as follows.

$$\begin{pmatrix} v_d \\ v_q \end{pmatrix} = \begin{pmatrix} \cos(\omega t) & \cos\left(\omega t - \frac{2}{3}\pi\right) & \cos\left(\omega t + \frac{2}{3}\pi\right) \\ \sin(\omega t) & \sin\left(\omega t - \frac{2}{3}\pi\right) & \sin\left(\omega t + \frac{2}{3}\pi\right) \end{pmatrix} \begin{pmatrix} v_u \\ v_v \\ v_w \end{pmatrix} \quad (1)$$

where ω is the power network frequency. In steady state, d-axes component of network voltage becomes zero, so q-axes voltage indicates the amplitude of network voltage. Checking whether this q-axes component fills the acceptable voltage change domain defined in Fig.2 or not, the USBS detects if some fault occurs in the power network or not.

In an actual plant, when q-axes component has dropped more than 25% during 1msec, the controller judges a power source fault occurs and turns to UPS-mode (start up output voltage) within next 1msec. The required sampling rate of the controller (including dq-axes conversion, voltage fault detection) is more than 10kHz.

B. How to Use Non-Self-Turn-Off Devices

Self-turn-off semiconductor devices such as IGBTs are supposed to use for the a.c. switch connecting a bus for normal loads with a bus for critical loads in order to disconnect it as quick as possible when some fault occurs on the network. But non-self-turn-off semi-conductor devices such as thyristors can be also used in this a.c. switch if PCS output currents may assist turn off action. We will discuss the method to adopt non-self-turn-off devices to the a.c. switch

To achieve the required performance as shown in Fig.2, the PCS should assist the turn-off action of them. As a PCS can output fixed voltage that decrease the switch currents to zero, for example, when the direction of switch current is shown in Fig.4, PCS must output immediately voltage as shown in the figure to decrease switch current. The switching pattern of PCS is decided by the direction of each switch current.

Let me consider how long does it take to decrease switch currents to zero at the worst case. Fig.5 shows more simple equivalent circuit for Fig.4. In this circuit, we consider the current waveform when voltage V_{DC} is added to this circuit. At the time t=0, we suppose the switch current is i_s, DC voltage is V_{DC}.

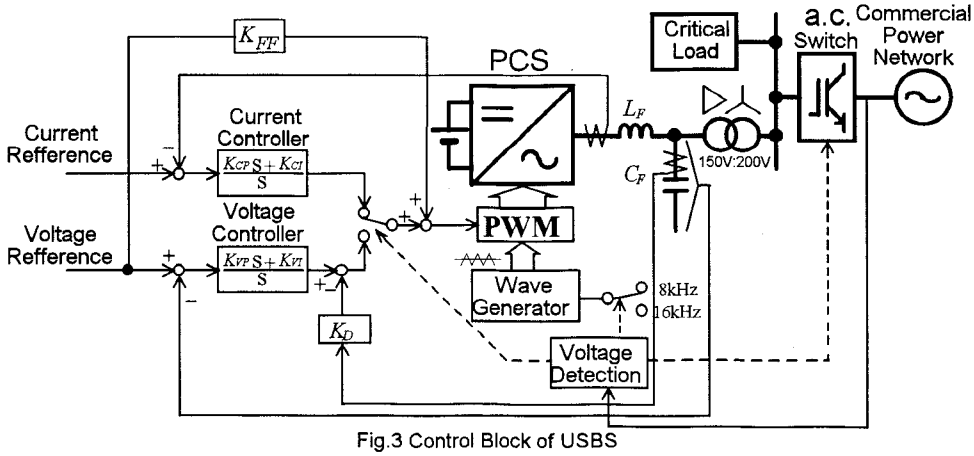


Fig.3 Control Block of USBS

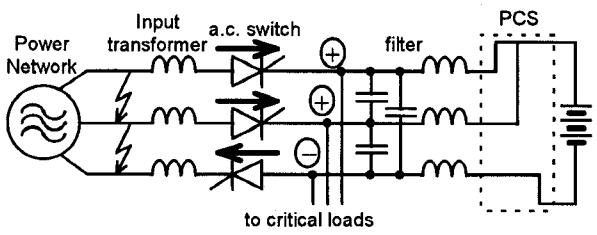


Fig.4 Equivalent circuit using thyristors

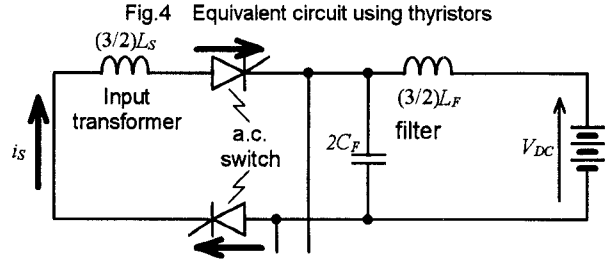


Fig.5 Simple equivalent circuit of Fig.5

Seeing from the side of DC power supply, the input transformer and the filter capacitor are connected in parallel. The impedance of the filter capacitor is much higher than the impedance of the input transformer, so we can ignore the current flowing into the capacitor, and circuit equation becomes as follows.

$$V_{DC} = -\frac{3}{2}(L_S + L_F)\frac{\Delta i_S}{\Delta t} \qquad (2)$$

where L_S is the impedance of the input transformer, L_F is the impedance of the filter reactance.

Suppose that L_F is 5%IX and L_S is 5%IX, so

$$L_S = L_F = \frac{0.05}{2\pi f} \quad (\text{where } f = 50\text{Hz}) \qquad (3)$$

and the maximum value of Δi_s is 141% (peak value at rated load), the minimum battery voltage is 135% (average value of rectifying voltage). Considering these value, it takes about 0.5msec to decrease the switch current to zero. If L_F and L_S are larger, it takes longer to decrease the currents to zero.

This consideration is under no load condition, but the impedance of loads are much higher than that of input transformer, so we can ignore the current flowing to the loads. Fig.6 shows the current waveform considering the filter capacitor and the rated R-L loads. It takes about 0.7ms to decrease the switch currents to zero.

V. Simulations and Experiments

Fig.7, 8, 9shows test results using a 3kW experimental system to confirm the basic ability of the proposed system. Fig.7 shows the waveforms at transferring from LL(generating)-mode to UPS-mode, Fig.8 shows those from LL(charging)-mode to UPS-mode, Fig.9 shows those UPS-mode to LL-mode. In all cases the critical loads voltage waveforms satisfy the uninterruptible criterion. Experimental conditions are listed in Table 1.

Fig.10, 11 show the simulation results with a 50kW plant with thyristor a.c. switches. Simulation conditions are listed on Table.2. The uninterruptible criterion defined in Fig.2 is also shown in the load voltage waveforms. In all cases, the transition from LL-mode to UPS-mode meets the defined condition. In.Fig.10, a short pulse appears on load voltage wave forms. This pulse voltage decrease the a.c. switch currents to zero.

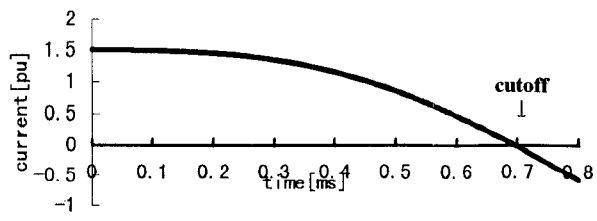
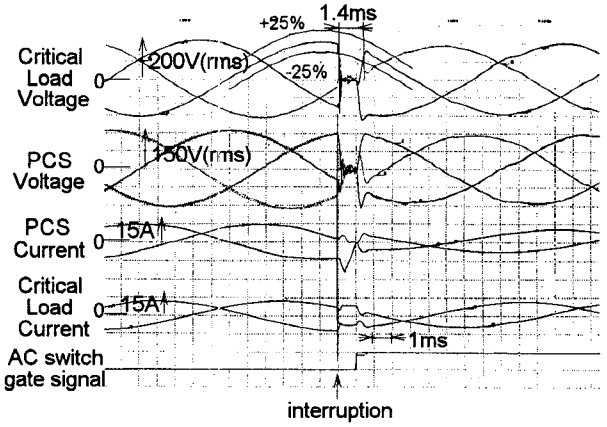
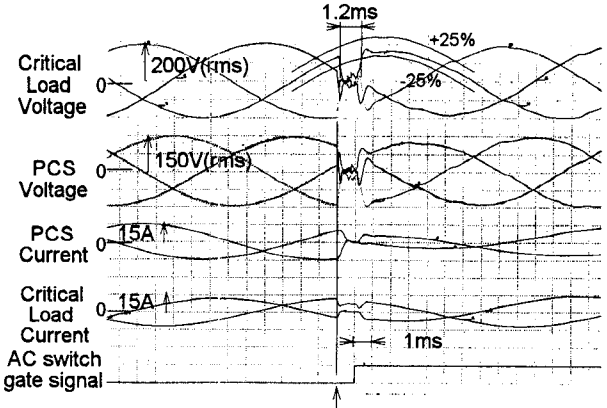


Fig.6 Switch current waveform at cutoff action. (considering filter capacitor and loads)



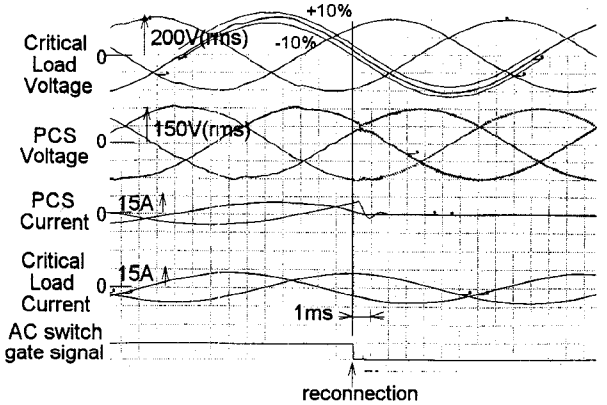
LL-mode(generating 3kw)→UPS-mode(RLload 1.7kVA P.F.=0.6)

Fig.7 Experimental results



LL-mode(charging 3kw)→UPS-mode (RL load 1.7kVA P.F.=0.6)

Fig.8 Experimental results



UPS-mode (RL load 1.7kVA P.F.=0.6) → LL-mode (0kW)

Fig.9 Experimental results

VI. Conclusion

This paper presented a new power system termed USBS, which operates as BESS in case of no fault in commercial power networks and operates as UPS when some fault occurs in them. Even if commercial power supply has stopped, it has taken less than 2ms to restart supplying power, so it has given no damage to critical loads such as computer systems

References

[1] K. Inagaki et. al, "A New Control Method for Uninterruptible Secondary Battery System", in Record of National convention of IEE-J, 1996

[2] Japanese Electrical-Machinery Association, "The Users Guideline of Semiconductors in General UPS with AC Outputs", JEM-TR 185/186, 1993

[3] CBEMA(American computer manufacture organization), "Computer Power-Supply Design Standard", 1987

[4] ANSI standard, C-84-1, 1993

[5] IEC standard (proposal), 1993

[6] US Navy standard 20

TABLE I PARAMETERS IN EXPERIMENT

Line Voltage	200V–50Hz
DC Voltage	320V
Output Capacity	3.0kVA
Load condition	RL load 1.7kVA(P.F. = 0.6)
Switching Frequency	8kHz(LL-mode), 16kHz(UPS-mode)
Output filter	L_F = 5%P.U. C_F = 2.5%P.U.

TABLE II PARAMETERS IN SIMULATIONS

Line Voltage	200V–50Hz
DC Voltage	320V
Output Capacity	50kVA
Load condition	50kVA RL load, P.F. = 0.7 (Fig.11) 50kVA Rectifier load ,C.F. = 2.5 (Fig.12)
Switching Frequency	8kHz(LL-mode), 16kHz(UPS-mode)
Output filter	L_F = 5%P.U. C_F = 2.5%P.U.

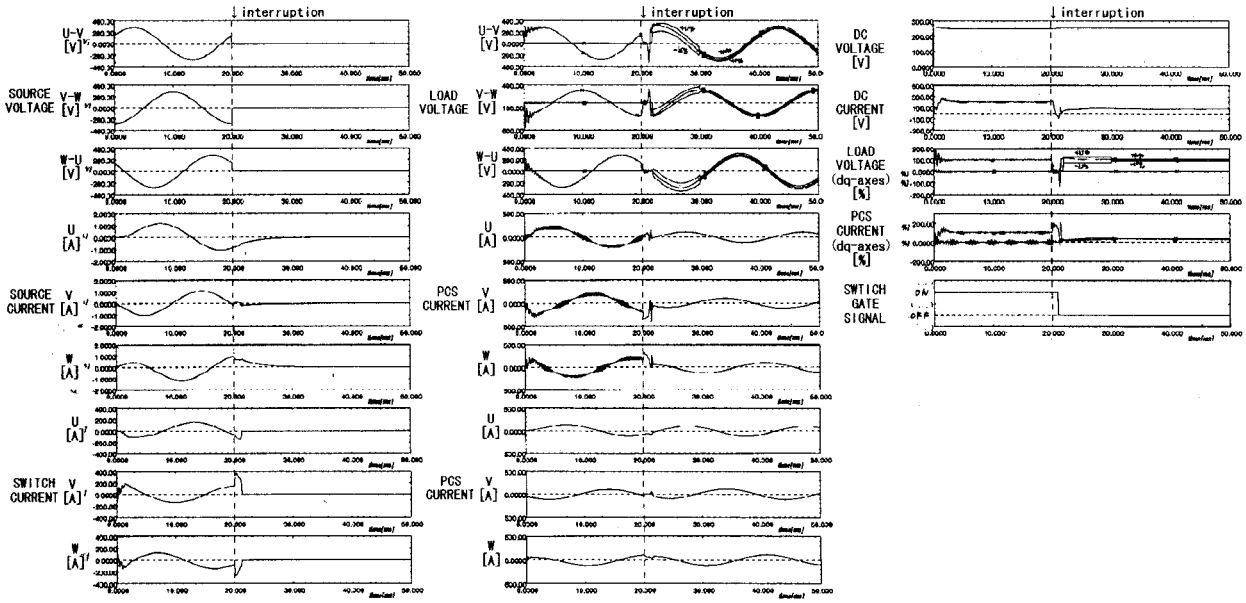


Fig.10 Simulation Results LL-mode(generating 50kw)→UPS-mode(RL load 50kVA P.F.=0.7)

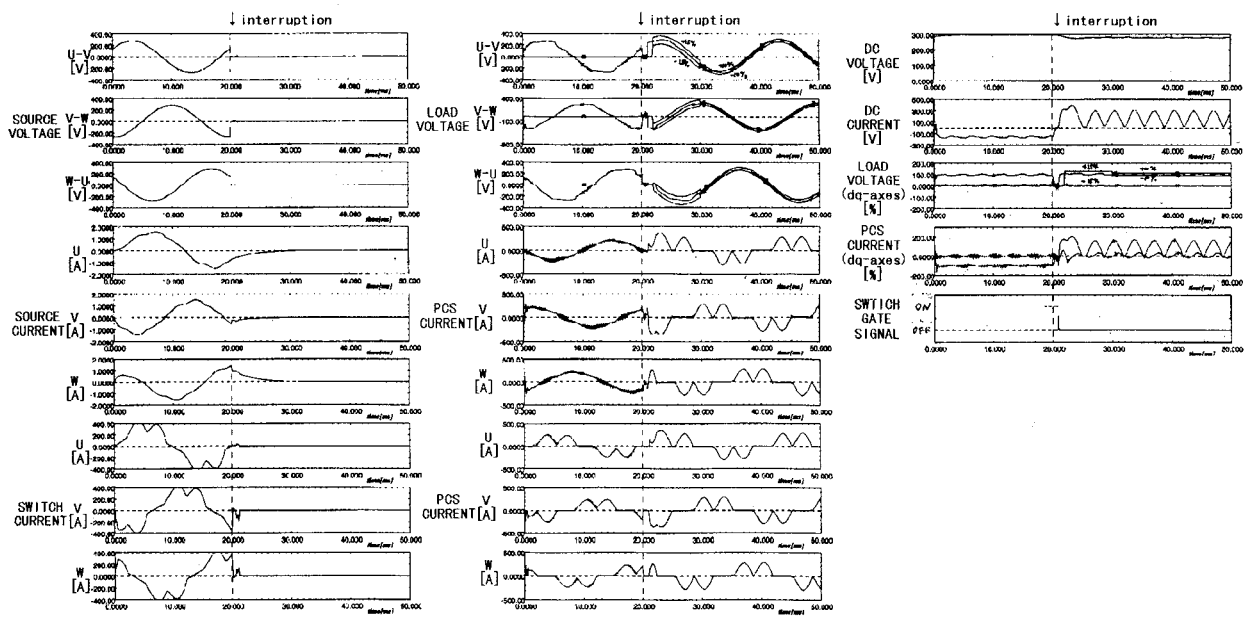


Fig.11 Simulation Results LL-mode(charging 50kw)→UPS-mode(Rectifier load 50kVA C.F.=2.5)

A Hybrid Single-Phase Power Active Filter For High Order Harmonics Compensation in Converter-fed High Speed Trains

Takashi Maeda &Tomoki Watanabe
Railway Technical Research Institute
2-8-38, Hikari, Kokubunji Tokyo 185 JAPAN
Tel. (81) 425-73-7284 Fax. (81) 425-73-7259

Abdallah Mechi, Takashi Shiota & Katsuji Iida
Technical Laboratory Toyo Electric Mfg. Co.Ltd.
338-1 Kami-Sohyagi, Yamato- shi Kanagawa Pref., 242
JAPAN Tel. (81)462-64-5781 Fax. (81) 462-63-2947

Abstract—To study the problem of the injected harmonic currents into the overhead line by the modern AC rolling stock, a mini model is presented. A Hybrid Active Power Filter composed of a controlled PWM converter in series with a passive filter is proposed for the compensation of the injected harmonic current. Finally, the results of a two control strategies for the generation of the compensating reference are presented.

I. INTRODUCTION

The PWM controlled line-side converters of the modern AC rolling stock inject the harmonic currents into the overhead line. When they coincide with the variable resonance frequency of the line distributed constants, theirs resonating currents can be considerably higher in amplitude. As a results, the efficiency of the substations protection systems is decreased .

To solve this problem many techniques have been studied. The adaptive optimal Pulsewidth modulation [1, 2, 3] was considered. This technique consists of the identification of the resonances and theirs respective harmonic energy is estimated on board the vehicle. The results are used to adapt the pulse width control of the line-side converter such that the harmonic excitation and resulting oscillation of the supply system are avoided. By this approach, the Complexity increases, and the high order harmonics still persist.

The three-level converters approach [4] on the line-side was also considered for the same purpose. As a result, the effective switching frequency is doubled and the individual voltage steps at switching are reduced to one half. However, the number of power switches doubles. Complexity and cost increase, and high order harmonics still persist.

The idea of active filters, which has been discussed and tested in stationary power systems [5, 6, 7], is another alternative to the problem. The closed-loop three-phase power active filter is considered as a successful tools for the total compensation of both harmonics and reactive power. However, when it comes to the practical-application, it is always suggested to combine the static filter and the active filter in order to minimize the size and the cost. More than that, their control algorithm is intended for three-phase, and they deal with the total harmonic compensation which is too costly in our case.

The single-phase power active filter for compensation of the PWM controlled line-side converters harmonics was proposed [8, 9]. the first was based only on the analytical analysis but the second was based on the control strategy of a single-phase power active filter. Good result was obtained in the mini-model experimental test . However, it was insufficient for the field test because the leakage inductance of the power transformer was not considered. In addition, an intermediate heavy auto-transformer was needed for the connection of the power active filter to the main transformer. Then, a 200 (kVA) single-phase power active filter (APF) was presented [10], and the results were partially satisfied because of the unbalance in the leakage inductances of the power transformer.

In this paper, a mini model is presented and it is composed of a new designed power transformer with four secondary windings provided for the four single phase PWM AC/DC converters unit which perform the PWM rectification and inject the harmonic currents into the source and a hybrid single-phase power active filter (HAPF) connected to the fifth secondary winding of the transformer. The HAPF is composed of a controlled PWM converter in series with a passive filter resonating at the same frequency as the injected harmonic one. Finally, the results of a two control strategies for the generation of the compensating reference are presented.

II. SYSTEM CONFIGURATION

Fig.1 shows an outline of the mini model. It is composed of a power transformer with four secondary windings provided for the four single phase PWM AC/DC converters unit which perform the PWM rectification and inject the harmonic currents into the source, and the HAPF is

0-7803-3823-5/97/$10.00© 1997 IEEE

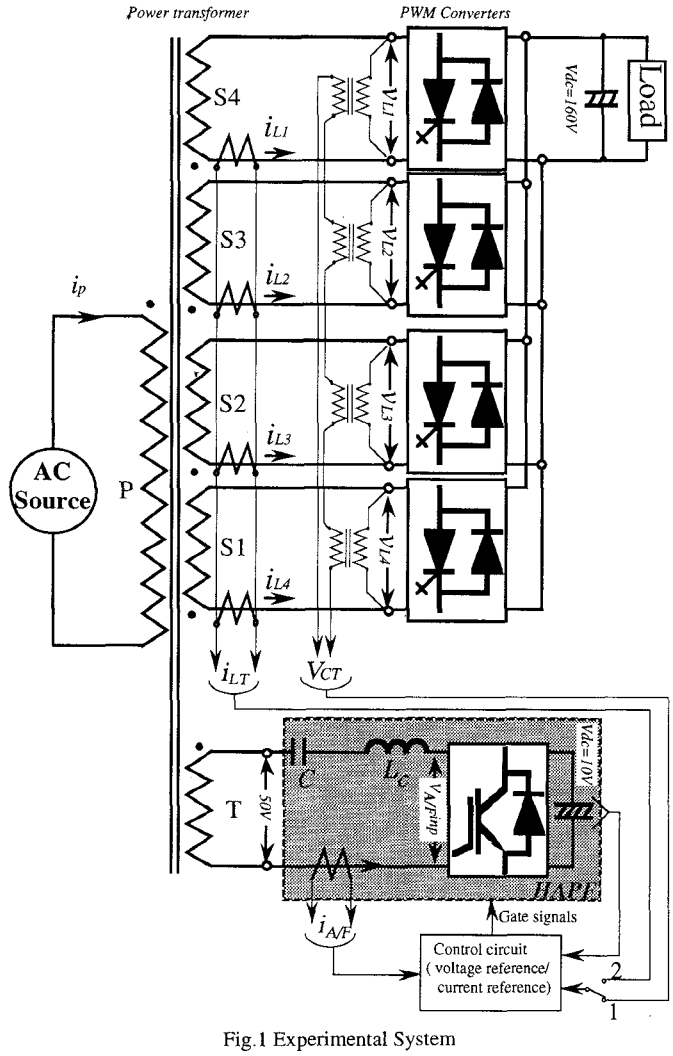


Fig.1 Experimental System

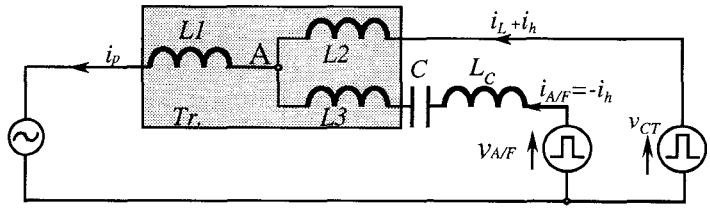


Fig.2 System Equivalent Circuit

connected to the fifth secondary winding of the power transformer. The AC capacitor of the HAPF has two principal goals: To minimize the weight of the APF by the elimination of the auto-transformer used for the connection of the power switching devices to the fifth secondary winding of the transformer. Further, when it is connected in series with the leakage inductance and the AC reactor, they give the effect of a passive filter.

3. System Equivalent Circuit

Fig.2 shows an equivalent circuit to the total system. Where, the power transformer and the line are modelled by three leakage inductances (L1, L2, L3), the equivalent reaction of the four line-side converters is represented by the voltage v_{CT} and the HAPF is represented by the series connection of the capacitor C, the inductor L_C and the voltage v_{AF}.

4. Power Transformer

The power transformer is designed with the following considerations;

1) the winding impedance to which the A/F should be connected (T1//T2) is lower than the primary winding impedance.

2) The smoothing AC reactors of The four AC/DC converters are eliminated and their values are considered in the design of the leakage inductances of the secondary windings.

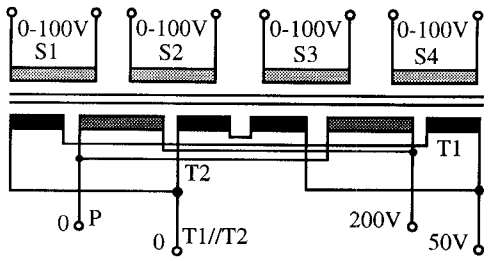


Fig.3. Windings configuration

Table I
Reactance matrix[mH]

	S1	S2	S3	S4	T1//T2
S1	*4.496*	*-0.137*	*0.034*	*0.118*	*0.115*
S2	—	*6.503*	*3.288*	*0.093*	*0.002*
S3	—	—	*6.734*	*-0.031*	*0.009*
S4	—	—	—	*4.496*	*0.153*
T1//T2	—	—	—	—	*0.086*

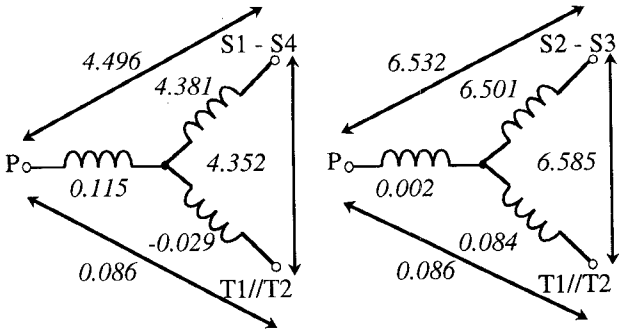


Fig.4. Distribution of the Leakage inductance of the Tansformer

5. Resonance Circuit

The resonance circuit consists of a band pass series resonance LC filter with te same frequency as the effective switching one of the converters ω_s. The harmonic contents of the input current is determined by bandwidth of the filter, ω_s/Q. The Q of the filter, $Q = Z_r/R_L$ is function of the load and the characteristic impedance of the LC circuit including the the leakage between the primary and (T1//T2) windings, $Z_r = \sqrt{L/C}$. As it is complicated to design the appropriate values of C and the L_C necessarily for the resonance between the primary and (T1//T2) windings, a simple and efficient method is used. As shown in Fig. 5, it consists of short circuiting the primary winding in one side and the four secondary windings in parallel in the other side, then a variable-voltage/variable-frequency generator in series with a capacitor C is connected to the fifth winding. First, the voltage is increased. Then, the resonance frequency is determined by changing the switching frequency until the current flowing between the primary and (T1//T2) windings became a sine waveform. Once the resonance frequency is known, the L_C and C are designed as follows:

The series capacitor C value is selected in the way that, it's fundamental flowing current can be sufficient for the control of the DC voltage. The L_C value is selected in the way that, the quality factor Q is minimum. Connected in series with the L_C and the leakage inductance between the primary and (T1//T2) windings of the power transformer, they should resonate at the compensating frequency. Fig. 6 shows the results of the resonance experiment with C = 100 μF and L_C = 35μH.

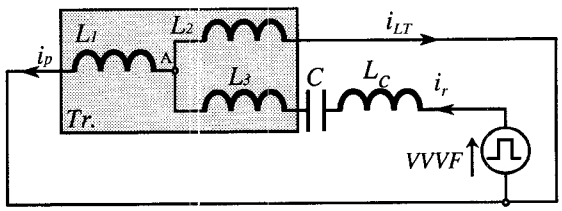


Fig.5. Resonance test equivalent circuit

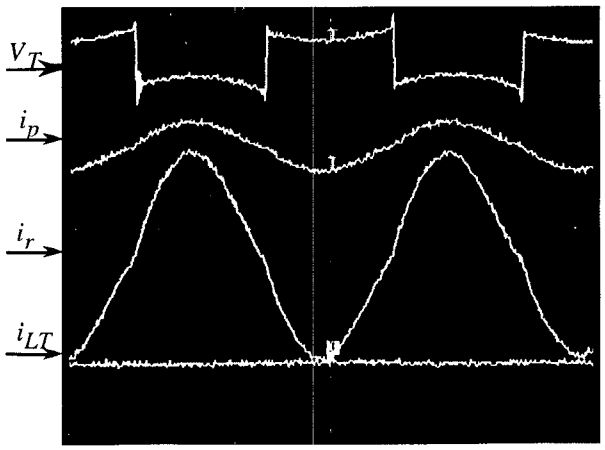


Fig.6. Waveforms of the Resonance Experiment

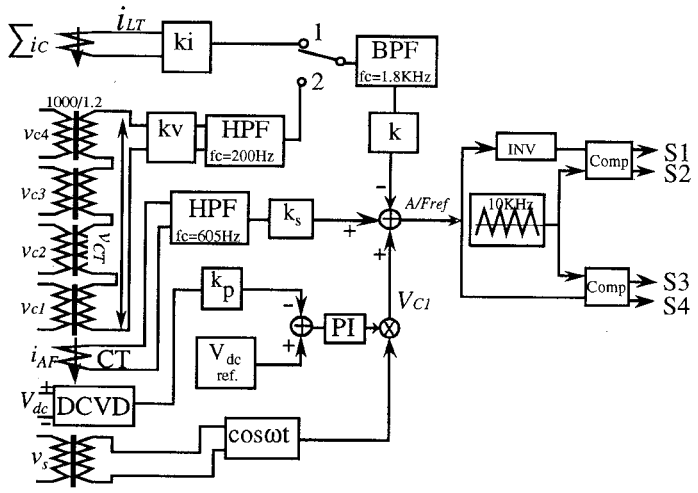


Fig.7. Control System

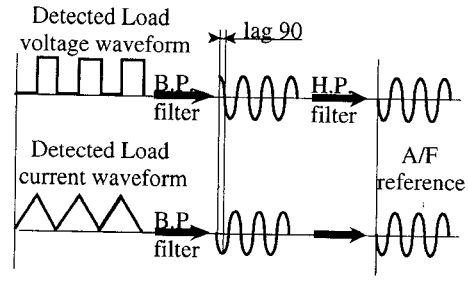


Fig.8. Detection Methods

5. Control Method

In general, to compensate for the harmonic current produced any source, the compensator should be a suppressor or a source of the same harmonic currents. That means; it should have the capability to inject the inverse of the same harmonic currents to the source for canceling or have the capability to accept the same harmonic current by creating a much flowing path easier than that of the source. As shown in Fig. 7, the physical meaning of the voltage and current detection methods is the determination of the A/F reference which should be in phase (or inverse) to the harmonic currents to be compensated. Hence, theoretically, they are the same. But as a methods, they are different.

2) Voltage detection method: the detected voltage waveform is a rectangular one with 90 in lag to the real harmonic current flowing into the source. First, it is made in phase with the injected harmonic currents flowing into the source by the use of high-pass filter. Then, the unwanted low (including the fundamental) and high order harmonics are eliminated by band-pass filter with a cut-off frequency equal to that of the injected one.

1) Current detection method : In Fig. 8, the detected current waveform is almostly the same as the real harmonic currents flowing into the source. Therefore, only a band-pass filter with a cut-off frequency equal to that of the injected one, is use to eliminated the unwanted low (including the fundamental) and high order harmonics from the A/F reference.

The A/F reference is selected by one of the two methods (1-2). The input current $i_{A/F}$ is detected through a current transformer (CT) and a high pass filter then multiplied by a constant k_S to form the damping voltage. The detected DC voltage V_{dc}, AC voltage v_s are used for the loss compensation (DC voltage control).

Once the reference voltage is determined , the on-off times of the inverter switches (IGBTs) is decided by comparing the reference and its inverse to a 10kHz triangular waveform. Then, the PWM patterns are transmitted by an optical system (transmitter-receiver) to the driving circuit.

V. EXPERIMENTAL RESULTS

Fig. 9 shows the HAPF and the primary current waveforms of the system and spectrum of the primary current of the power transformer when the HAPF is out of service. The experimental constants and conditions are presented in table II.

Fig. 10 shows the experimental result using the voltage detection method and Fig. 11 shows the experimental result using the current detection method.

Using both methods, the harmonic currents injected into the source are reduced to a minimum level (-20dB). In the region around the cut-off frequency, the voltage detection method gives better results than the current detection one. However, in the region around the double cut-off frequency (3.6kHz), the harmonic components increases only in the case of the voltage detection method. That is because, the double cut-off frequency harmonics components exist in the

detected voltage waveform itself and it is difficult to eliminate it by first order band-pass filter.

To be more realistic, the line distributed constants were simulated by the insertion of two parallel L-types LC filters with a constant resonance frequency of 1.8kHz between the source and the primary winding of the power transformer. In Fig.12(a), the injected harmonic currents become considerably higher in amplitude and in Fig.12(b) they are almostly eliminated when the HAPF is in service.

From Table IV showing the data of the filed test and the laboratory test conducted on the Star21 super express train of the japanese east railway and on the mini-model respectively, it can be concluded that; in the field test, the needed compensating power is 1.3 times the injected one. However, in the mini-model test using the resonance method, they are almost the same. More than that, the compensator DC voltage is reduce to 1/5.

Table II
experimental constants and conditions

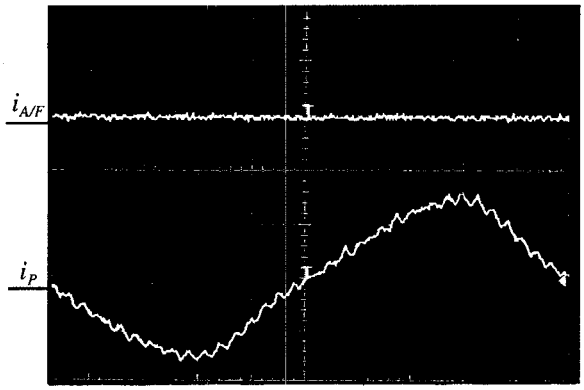
Source voltage [V]	200
Converters input voltage[V]	100
Convertyers DC voltage [V]	160
HAPF input voltage [V]	50
HAPF DC voltage [V]	10
Lc [μH]	35
C [μF]	100
Switching Frequency [kHz]	10

Table III
Compensation Efficiency

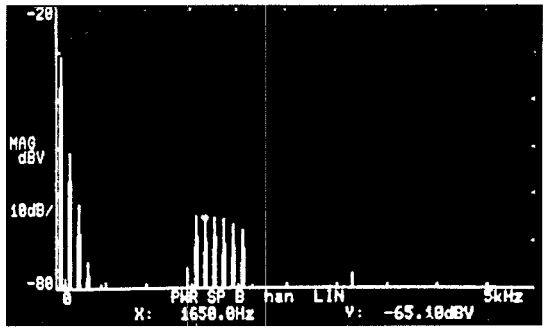
Frequency[Hz]	I_p Harmonic Components [dB]		
	A/F-off	A/F - on	
		Voltage Detection	Current Detection
1450	-74	-83	-80
1550	-65	-75	-77
1650	-64	-83	-97
1750	-64	-90	-75
1850	-66	-80	-74
1950	-65	-76	-95
2050	-68	-75	-75

Table IV
Comparative data

	Field test	Mini-Model
Source voltage [V]	25000	200
Total power [kVA]	3000	1
Injected harmonic power[kVA]	120	0.22
Compensator power[kVA]	160	0.23
Compensator input voltage[V]	405	50
Compensator output voltage[V]	400	10



a) Waveforms



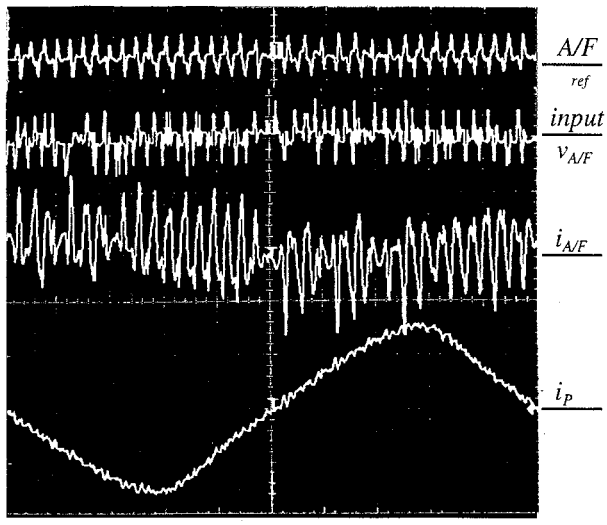
b) i_P Spectrum (19A=-35dB)

Fig. 9 waveforms before Compensation

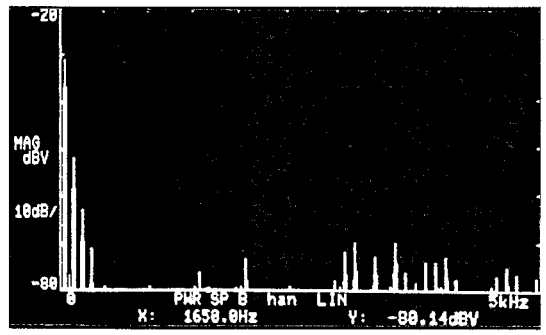
VI. CONCLUSIONS

A hybrid single-phase power active filter for high order harmonics compensation is presented.

A new leakage power transformer design is proposed as a new model for the AC rolling stock.

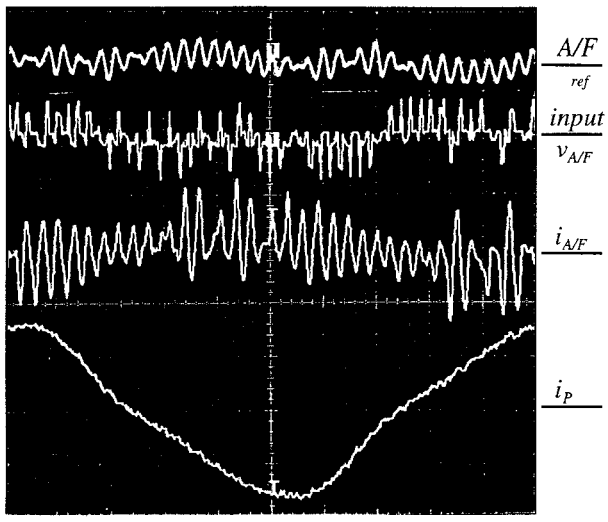


a) Waveforms

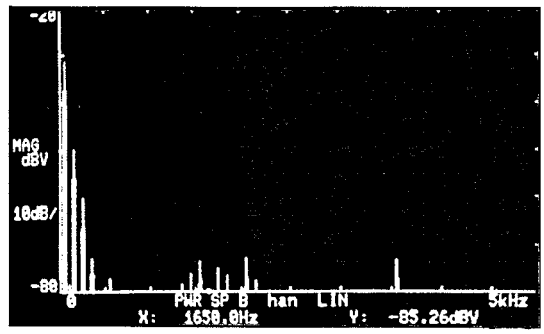


b) i_P Spectrum (19A=-35dB)

Fig.10 Voltage Detection Method

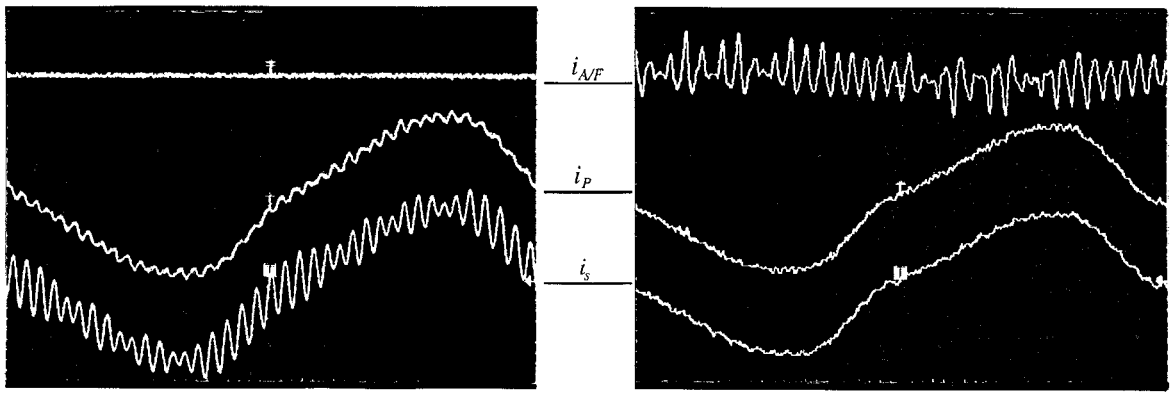


a) Waveforms



b) i_P Spectrum (19A=-35dB)

Fig. 11 Current Detection Method



a) Before compensation

a) After compensation

Fig.12 Current Waveforms with consideration of the Line Distributed Constants

The voltage control and current detection methods for the determination of the compensating reference are carried out and it is shown that the good results are given by the current detection method.

Using the proposed compensator design based on the resonance method, the active compensator size can be extremely reduce by the reduction of the needed compensating power and the DC voltage of the inverter.

Finally. For the power conditioning in the AC rolling stock the active filtering is the best and the cheapest method if it is well used

VII. REFERENCES

[1] J. Holts and J. O. Krah, "Adaptive Optimal Pulsewidth Modulation for the Line-Side Converter of Electric Locomotives", European Conference on Power Electronics and Applications EPE, Aachen, pp. 567-572, 1989.

[2] J. Holts and J. O. Krah, "Suppression of Time-Varying Resonances in the Power Supply Line of AC Locomotives by Inverter Control", IEEE Trans. Ind. Electron., vol. 39, NO. 3, pp. 223-229, 1992.

[3] M. Meyer and A. Sonnenmoser, "A hysteresis Current Control for Parallel Connected Line-Side Converters of an Inverter Locomotive", European Conference on Power Electronics and Applications EPE, Brighton, pp. 102- 108, 1993.

[4] L. Hennrich, "460 Series Locomotives for the Swiss Federal Railways (SBB)", Eisenbahntechnische Rundschau., vol. 81, NO. 7, pp.216-226, 1992.

[5] H. Akagi, Y. Kanazawa, and A. Nabae, "Instantaneous reactive power compensators comprising switching devices without energy storage components", IEEE Trans. Ind. Appl., vol. IA-20, pp. 625-631, 1984.

[6] F. Z. Peng, H. Akagi, and A. Nabae, "Compensation Characteristics of the Combined System of Shunt Passive and Series Active Filters", IEEE Trans. Ind. Appl., vol. IA-29, No. 1 pp. 144-152, 1993.

[7] H. Akagi, "Trends in Active Power Line conditioners", IEEE Trans. Power Electro., May 1994.

[8] M. Meyer, "Active Power Filters for Locomotives-A Concept for Improved Efficiency and Low Distortion Currents", 23rd Annual Power Electronics Specialists Conference, Toledo (Spain), pp. 389-396, 1992.

[9] T. Watanabe, T. Maeda & H. Ueno - A. Mechi & K. Iida, "Single-Phase Power Active Filter for High Order Harmonics Compensation "IEE-JAPAN-IAS'95, International Session, vol. 2 pp. 35-40.

[10] T. Watanabe, T. Maeda & H. Ueno - M. Sekimoto & K. Hoshi - A. Mechi, T. Shiota & K. Iida, "A Single-Phase Power Active Filter Restraining High Harmonics in AC Electric Motor Vehicle", IEE-JAPAN-IAS'96, vol. 3 pp. 423-427.

A New Method for Separating AC Component of Instantaneous Real Power and Imaginary Power Suitable for Active Filters

Atsushi Nakata, Akiteru Ueda, Akihiro Torii
Aichi Institute of Technology
1247, Yachigusa, Yakusa-cho, Toyota, 470-03, JAPAN
Fax: +81-565-48-0010, Phone: +81-565-48-8121, Ext.2016
E-mail:aueda@ee.aitech.ac.jp

Abstract — In a control system of active filters, the p-q theory can be used for the calculation of higher harmonic currents. A high pass filter of the first order is usually used for separating ac components of instantaneous real power (p) and instantaneous imaginary power (q). But, in that system transient response for a load change is not high enough. We propose a new control system in which ac components are derived from p and q using a moving average value calculation method. By the proposed system, control response and accuracy are very good even in the case of an abrupt load change.

I . INTRODUCTION

Recently, harmonic interference in power systems is a problem that is caused by the spread of power electronics equipment, and an active power filter is expected as its countermeasure. The p-q theory for calculating an instantaneous power has often been used for the calculation of compensation current references of a three-phase active power filter[1]. In the p-q theory, a dc component of the instantaneous real power p corresponds to the fundamental wave effective power, and an ac component of the instantaneous imaginary power q corresponds to the fundamental wave reactive power. The compensation current references can be calculated by removal of the dc component of p and q, and by inverse transformation of the ac component of p and q.

The first-order high pass filter (HPF) with a cut-off frequency of 5-35 Hz is usually used for the detection of the ac component of both p and q[2][3][4]. The problems of the system are as follows:

1) The active power filter becomes unstable because of a insufficient response of the HPF in the case of a load change, although the HPF with low cut-off frequency can detect an ac component with high accuracy.
2) The accuracy of the detected ac component is insufficient, although the response of the HPF with high cut-off frequency is good.

In this paper, we propose a new control system in which ac components are derived from the instantaneous real power and the instantaneous imaginary power using a moving average value calculation method. In the proposed system, a HPF using the moving average value calculation method is utilized for detecting the ac component of both p and q. The proposed system can acquire an ac component with high accuracy, and the response of the HPF used in the proposed system has a desirable characteristic. The feasibility of the proposed system by simulation and some experimental results are shown.

II . HARMONIC DETECTION SYSTEM

Fig.1 shows a conventional harmonic detection system and Fig.2 shows a proposed harmonic detection system using moving average value calculation. The HPF is used in the conventional system as shown in Fig.1, and a moving average calculation circuit is used in place of HPF as shown in Fig.2.

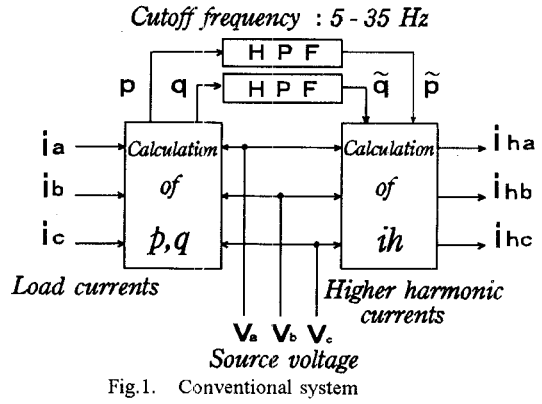


Fig.1. Conventional system

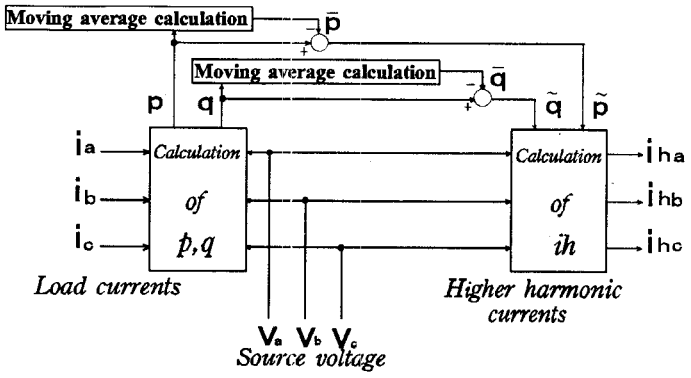


Fig.2. Proposed system

A. Calculation of p and q

Transformation of the three-phase source voltages v_a, v_b and v_c and the three-phase load currents i_a, i_b and i_c into the α - β orthogonal coordinates gives the following expressions:

$$\begin{bmatrix} v_\alpha \\ v_\beta \end{bmatrix} = \sqrt{\frac{2}{3}} \begin{bmatrix} 1 & -1/2 & -1/2 \\ 0 & \sqrt{3}/2 & -\sqrt{3}/2 \end{bmatrix} \begin{bmatrix} v_a \\ v_b \\ v_c \end{bmatrix} \quad (1)$$

$$\begin{bmatrix} i_\alpha \\ i_\beta \end{bmatrix} = \sqrt{\frac{2}{3}} \begin{bmatrix} 1 & -1/2 & -1/2 \\ 0 & \sqrt{3}/2 & -\sqrt{3}/2 \end{bmatrix} \begin{bmatrix} i_a \\ i_b \\ i_c \end{bmatrix}. \quad (2)$$

The instantaneous real power p and the instantaneous imaginary power q are calculated as follows:

$$\begin{bmatrix} p \\ q \end{bmatrix} = \begin{bmatrix} v_\alpha & v_\beta \\ -v_\beta & v_\alpha \end{bmatrix} \begin{bmatrix} i_\alpha \\ i_\beta \end{bmatrix} \quad (3)$$

$$= \begin{bmatrix} \bar{p} + \tilde{p} \\ \bar{q} + \tilde{q} \end{bmatrix}, \quad (4)$$

where $\bar{p}$ and $\bar{q}$ denote the dc components of p and q and $\tilde{p}$ and $\tilde{q}$ denote the ac components of p and q. The fundamental wave effective component corresponds to $\bar{p}$, and the fundamental wave reactive component corresponds to $\bar{q}$.

B. Calculation of $\tilde{p}$ and $\tilde{q}$

In the conventional system, a HPF is used to obtain $\tilde{p}$ and $\tilde{q}$ from p and q as shown in Fig.1. In the proposed system, $\tilde{p}$ and $\tilde{q}$ are calculated by the moving average value calculation circuit. The characteristics of the circuit are described in the next section.

C. Calculation of ih

The three-phase harmonic currents can be calculated by

$$\begin{bmatrix} i_{ha} \\ i_{hb} \\ i_{hc} \end{bmatrix} = \sqrt{\frac{2}{3}} \begin{bmatrix} 1 & 0 \\ -1/2 & \sqrt{3}/2 \\ -1/2 & -\sqrt{3}/2 \end{bmatrix} \begin{bmatrix} v_\alpha & v_\beta \\ -v_\beta & v_\alpha \end{bmatrix}^{-1} \begin{bmatrix} \tilde{p} \\ \tilde{q} \end{bmatrix}. \quad (5)$$

Eq.(5) is the inverse transformation of Eqs.(1)-(3).

III. CHARACTERISTIC OF FILTER

In the p-q theory, the fundamental components in load currents are converted into dc component of p and q. When the source frequency is 60 Hz, the (6n±1) order harmonics of load currents are converted into 360n Hz, where n is an integer. The desirable characteristics of the filter, which calculate $\tilde{p}$ and $\tilde{q}$ from p and q, are that the gain is equal to 1 and the phase difference is equal to 0.

A. Conventional HPF

The first-order HPF is usually used for the acquisition of p and q. Fig.3 shows the bode diagram and Fig.4 shows the step response, where the cut-off frequency of the first order HPF is assumed to be 10 Hz.

In Fig.3, the characteristics of the first order HPF at 360 Hz are that the gain is 0.99 and that the phase difference is 1.59 degrees. In Fig.4, since the time constant of the HPF is 15.9ms, which corresponds to the cut-off frequency of 10Hz, 47.7ms is needed to decrease the dc component to a magnitude of 5% of the initial value.

The HPF is designed for a specific load. Therefore the HPF can acquire $\tilde{p}$ and $\tilde{q}$ with high accuracy when a load is constant in a specific condition. When the cut-off frequency is higher, the HPF works well in case of the load variation. Using the HPF with high a cut-off frequency, however, the ac component cannot be detected $\tilde{p}$ nor $\tilde{q}$ with high accuracy.

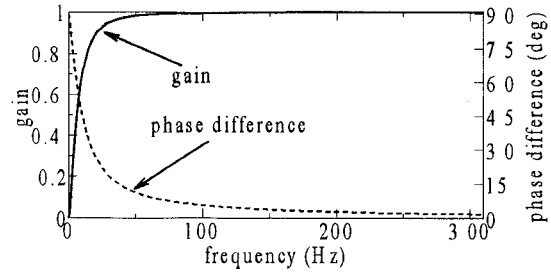


Fig.3. The bode diagram of conventional system

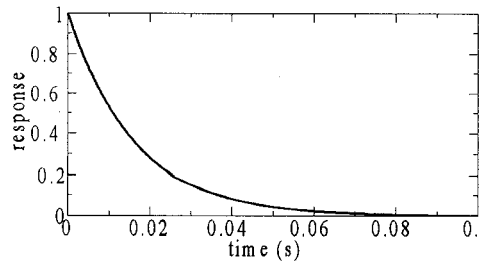


Fig.4. The step response of conventional system

B. HPF using moving average calculation method

The moving average is an operation which calculates the average value within a shifted period. The method is considered to be a kind of a digital filter[5][6].

In general, a discrete-time signal can be presented by a function X(nT), where T is a sampling time and n is an integer. The moving average value X(nT) is given by

$$X(nT)=\frac{1}{N}\sum_{k=n-N}^{n-1}x(kT)\ , \qquad (6)$$

where N denote a data sampling number.

In the proposed system, the moving average calculation method, which is described in Eq.(6), is used to obtain $\bar{p}$ from p. Similarly $\bar{q}$ is obtained from q. Therefore, $\tilde{p}$ and $\tilde{q}$ are given by

$$\tilde{p}=p-\bar{p} \qquad (7)$$

$$\tilde{q}=q-\bar{q}. \qquad (8)$$

Since the moving average value calculation circuit shown in Fig.2 eliminates dc components in p and q, the circuit is a kind of a HPF. We call it a moving average HPF.

In the following consideration, the sampling number of the moving average calculation method is 64 and the sampling time is 43.4 μ s .

In Fig.5, the characteristic of the moving average HPF at 0 Hz is that the gain is 0 and that the phase difference is 90 degrees and the characteristics of the moving average HPF at 360, 720 and 1080 Hz are that the gain is 1.0 and that the phase difference is 0 degrees. In Fig.6, 2.78ms is needed to decrease the dc component to a magnitude of 0% of the initial value. In conclusion, the moving average HPF has excellent gain and phase difference characteristics and has a quick response.

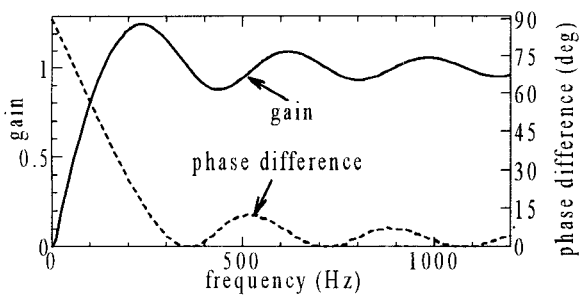


Fig.5. The bode diagram of moving average HPF

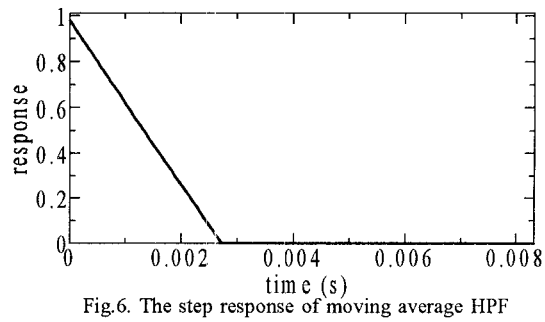


Fig.6. The step response of moving average HPF

IV. SIMULATION

The load is assumed to be a three-phase thyristor bridge rectifier of phase control angle 0, with source voltage of 100V, ac frequency of 60 Hz and dc load current of 10A. The source voltage of phase-a is shown in Eq.(9).

$$v_a=100\sin(\omega t),\ \omega=2\pi\times 60 \qquad (9)$$

A. Simulation in a constant load

The load current of phase-a at a constant load is assumed in Eq.(10):

$$i_a=\frac{20\sqrt{3}}{\pi}(-1)^n\sum_{n=0}^{3}\sin(6n\pm 1)\omega t \qquad (10)$$

The approximation of a function by the first 19th order terms of harmonic components is used.

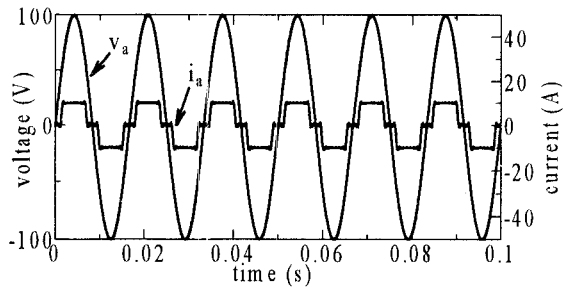


Fig.7. Load current and source voltage waveforms used in simulation

Fig.7 shows the waveforms of the load current i_a and the source voltage v_a given by Eqs. (9) and (10). Fig.8 shows the waveforms of p and q given by Eq. (3). The instantaneous imaginary power q does not contain a dc component since the phase control angle is 0. Therefore we do not discuss q, $\bar{q}$ and $\tilde{q}$, here.

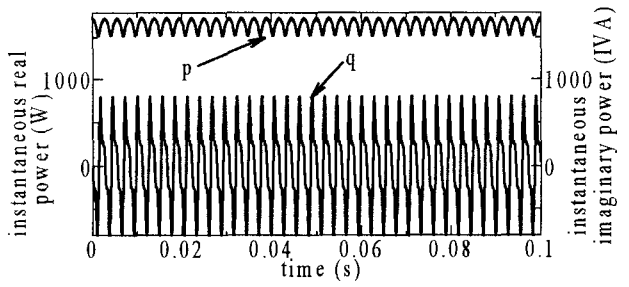


Fig.8. Detection results of instantaneous power

The waveforms of p, $\bar{p}$ and $\tilde{p}$ in a conventional system is simulated as shown in Fig.9. A HPF with 10 Hz cut-off frequency is used in the system. Fig.10 shows the simulated waveforms of p, $\bar{p}$ and $\tilde{p}$ in the proposed system.

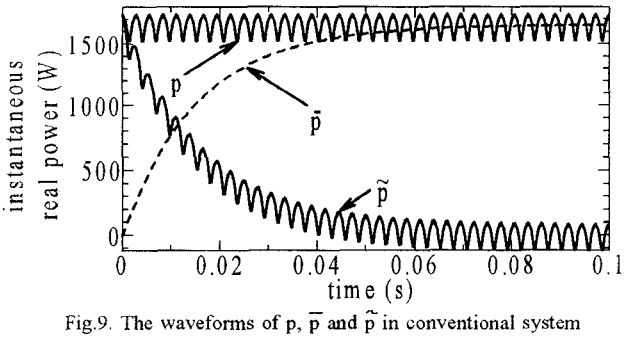


Fig.9. The waveforms of p, $\bar{p}$ and $\tilde{p}$ in conventional system

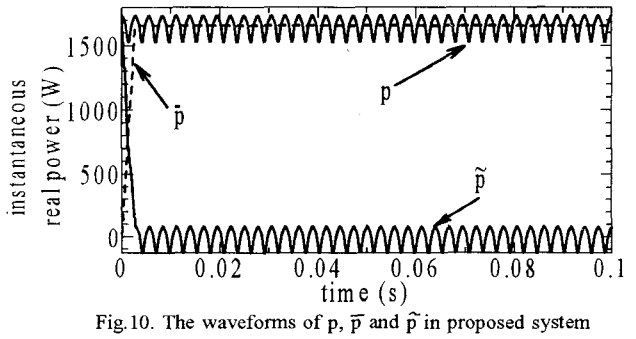


Fig.10. The waveforms of p, $\bar{p}$ and $\tilde{p}$ in proposed system

In Fig.9, the dc component decreases to 1% in 80ms, which is determined by the time constant of the HPF. In Fig.10, the dc component decreases to 0% is (N×T), which is determined by the averaging period. The proposed system using the moving average HPF improve the detection responses of $\tilde{p}$ and $\tilde{q}$.

B. Simulation in case of a load change

The load change is assumed to be the absolute value of a sinusoidal function with frequency of 10 Hz. The load current with dc load change is approximated by the following expression:

$$i_a = |sin(\omega t/6)| \frac{20\sqrt{3}}{\pi} (-1)^n \sum_{n=0}^{3} sin(6n \pm 1)\omega t \ . \quad (11)$$

The waveforms of the source voltage and load current are shown in Fig.11. The simulated waveforms of p and q are shown in Fig.12.

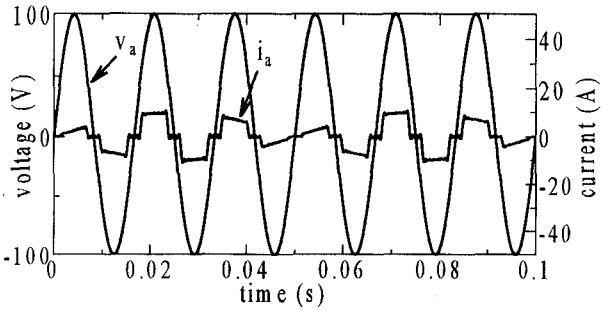


Fig.11. Load current and source voltage waveforms used in simulation

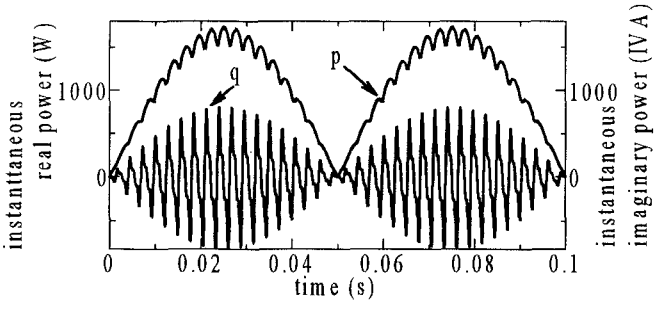


Fig.12. Detection results of instantaneous power

Since the waveform of q shown in Fig.12 does not contain the dc component, we only discuss the waveform of p, here. The simulated waveforms of p, $\bar{p}$ and $\tilde{p}$ in a conventional system using the HPF with 10 Hz cut-off frequency are shown in Fig.13. The HPF cannot remove the dc component, since the time constant of the HPF is in the same order of the fluctuation of the load. Consequently, the active filter becomes unstable since the effective power flows out and flows into the capacitor or the reactor of the active power filter. Fig.14 shows the simulated waveforms of p, $\bar{p}$ and $\tilde{p}$ in the proposed system. The simulated $\tilde{p}$ contains a much smaller dc component than the conventional system, since the time constant of the moving average HPF is much smaller than that of the fundamental frequency of the load current(i_a).

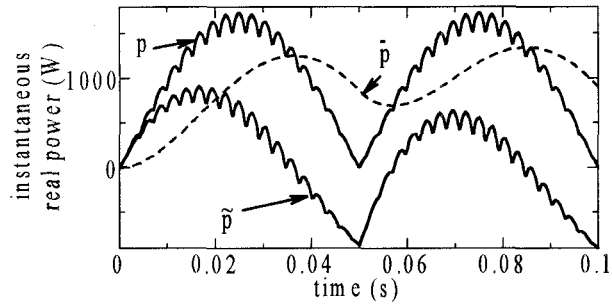


Fig.13. Conventional system with high pass filter

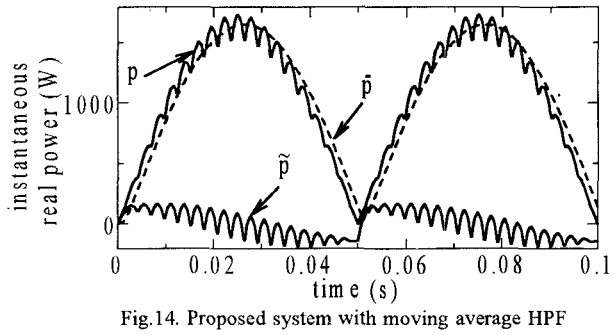


Fig.14. Proposed system with moving average HPF

V . COMPENSATION OF HARMONIC CURRENTS

We simulated compensated harmonic currents which are in a constant load condition and in a fluctuated load condition. Assume that the active power filter is ideal. Fig.15 shows simulated results of compensated harmonic currents in a constant load. The thin curve denotes the theoretical input current, the broken curve denotes the simulated result of a conventional active power filter and the thick curve denotes the simulated result of the proposed active power filter. The theoretical input current is expressed by

$$i_a = \frac{20\sqrt{3}}{\pi} sin(\omega t) \ , \qquad (12)$$

where ω is $2\pi \times 60$. The compensated harmonic currents, which are obtained by the conventional system and by the proposed system, agrees well with the theoretical currents. At the beginning of the compensation, however, the input current obtained by the conventional active power filter does not agree with the theoretical value due to the large time constant of a HPF.

The simulated waveforms of the compensated harmonic currents in a changing load are shown in Fig.16. The simulation results of the conventional system differ from the theoretical waveform due to a large time constant of the HPF. Here, the theoretical input current is expressed by

$$i_a = |sin(\omega t/6)| \frac{20\sqrt{3}}{\pi} sin(\omega t) \ . \qquad (13)$$

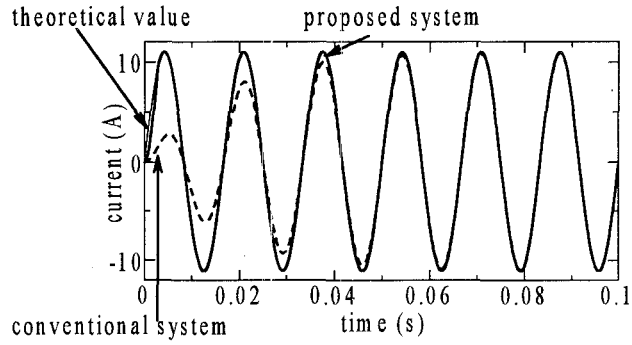


Fig.15. Source currents after compensation by active filter in a constant load

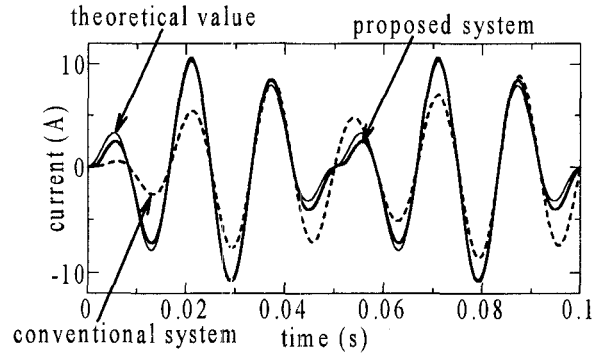


Fig.16. Source currents after compensation by active filter in a changing load

On the contrary, the waveform of the proposed system agrees well with the theoretical waveform. The proposed system shows very good characteristics of the input current in comparison with the conventional system.

VI . EXPERIMENTAL RESULT

An experimental model is set up using a digital signal processor (DSP; TI TMS320C25) . The DSP calculates the p which is used to compensate the input harmonics. The sampling time of the DSP is 43.4 μ s and the number of the data is 64.

The parameters for the experiment are as follows. The source voltage is 150V and the ac frequency is 60 Hz. The harmonics generation load is a three-phase thyristor bridge rectifier with RL circuit in dc side, where the resister(R) equals 190 Ω and the inductance(L) equals 300mH. Transient characteristics are examined when the load is suddenly switched on. Before the experiment, preliminary simulation is done in the same condition as

the experiment to examine transient characteristics.

The simulated transient waveforms are shown in Fig.17. The waveforms show simulated $\tilde{p}$ of the conventional system (broken line) and simulated $\tilde{p}$ of the proposed system (solid line). Fig.18 shows experimental results of the measured p (top) and $\tilde{p}$ (bottom). The experimentally obtained $\tilde{p}$ agree well with the simulated $\tilde{p}$. Therefore excellent characteristics of the proposed system are confirmed by the model tests.

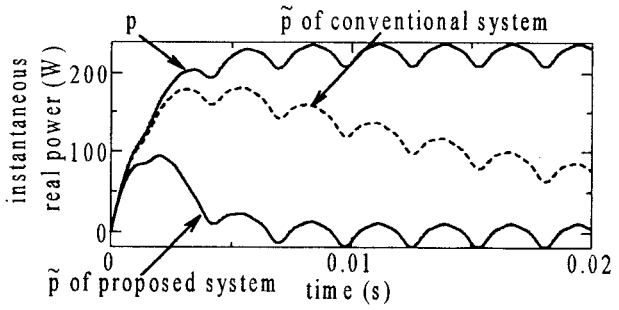
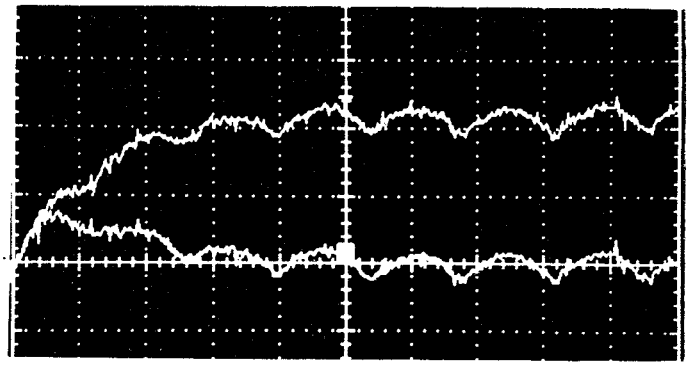


Fig.17. Simulated waveforms of RL transient circuit


Fig.18. Experimental waveforms

Vertical:83.3[W]/div Horizontal:2.0ms/div

Ⅶ. CONCLUSION

A new control system is proposed which is suitable for an active filter characterized in deriving method of the ac component of the instantaneous real power. The proposed system uses the moving average value calculation method for deriving the dc value of p. By subtracting the dc value, ac components of p are obtained accurately and in quick response even in the case of an abrupt load change. The operating performance of the proposed system is confirmed by digital simulation and laboratory model tests.

REFERENCES

[1] H.Akagi, Y.Kanazawa, and A.Nabae,"Instantaneous reactive power compensators comprising switching devices without energy storage components,"IEEE Trans.on Ind.Appl., vol.IA-20,p.625,1984.

[2] J.Haefner, M.Aredes and K.Heumann,"A combined system of a passive filter and a shunt active power filter to reduce line current harmonics,"IPEC-Yokohama'95, pp388-393

[3] H.Fujita, H.Akagi, and A.Nabae,"Control schemes and compensation characteristics of an active filter connected in series with a passive filter,"T,IEE Japan, Vol. 110-D, No.6, '90, 637

[4] F.Z.Peng, H.Akagi, and A.Nabae,"A new approach to harmonic compensation in power systems-A combined system of shunt passive and series active filters,"IEEE Trans.on Ind.Appl.,vol.IA-26,pp.983,1990.

[5] N.Ahmed and, T.Natarajan,"Discrete-Time Signals and Systems," Prentice-Hall, Inc.1983

[6] A.Papoulis,"Signal analysis," McGraw-Hill, Inc.1977

Development of 60MVA SVC(Static Var Compensator) using large capacity 8kV and 3.5kA thyristors

Taizo Hasegawa Yoshiharu Aoshima Tadashi Sato
The Kansai Electric Power Co., INC.
3-3-22, Nakanoshima, Kita-ku, Osaka, JAPAN

Osamu kondo Tatsuya Matsukawa
Nissin Electric Co., Ltd.
47, Umezutakase-cho, Ukyo-ku, Kyoto, JAPAN

Abstract - A static var compensator (SVC) of 154kV and 60MVA ratings was developed with the largest capacity thyristors of 8kV and 3.5kA in the world. The SVC was commissioned in The Kansai Electric Power Company in 1996 and has shown good performance. This paper presents the following items, i.e. system design of the SVC (hardware and software), field test results and effects of SVC application.

I. INTRODUCTION

We have constructed a static var compensator (SVC) of 154kV and 60MVA in Higashi-Osaka substation, The Kansai Electric Power Co., with the aim of replacing a shunt reactor which have been operated in substation for long period. Furthermore the SVC makes it possible to stabilize 154kV bus voltage more steadily. In this paper, the SVC's design and components are described and its effects of stabilizing the voltage, which are measured in the commissioning, are also mentioned. As particular points of the SVC, 8kV-3.5kA-6inch light-triggered thyristors are used, which are newly developed by Japanese three manufacturers, and the SVC has the thyristor-controlled -transformer (TCT) part only, which means the SVC can output lagging reactive power only.

II. PURPOSE OF SVC

Higashi-Osaka substation is main one to feed to the south area of Osaka Pref. To compensate the voltage fluctuation caused by the change of reactive power in network, the substation has several shunt reactors, which operation is controlled by programmable controller. As the results of reactive power control by shunt reactor switching, the voltage is adjusted in stepwise and circuit breakers for shunt reactors are operated frequently. In the occasion of replacing 60 MVA shunt reactor, which have been under operation for long period, the SVC is adopted to keep voltage continuously stable. the SVC can also realize rapid response to reactive power change with switching reactor current by thyristor equipment. To replace shunt reactor, it is also required to output lagging reactive power. So the thyristor-controlled-transformer (TCT) type SVC is selected, which doesn't have any capacitor (or filter) part for leading reactive power. Concerning the harmonic currents from the SVC, the guideline's limits are considered. As thyristor equipment, newly developed 8kV-3.5kA thyristor elements are expected to be used practically for the first time.[1]

III. DESIGN AND COMPONENTS OF SVC

As the SVC has the roles to supply lagging reactive power instead of shunt reactor and to settle steadily 154kV bus voltage in substation, it is decided that the SVC's voltage and capacity ratings are 154kV and 60MVA (lag) respectively. The SVC is connected to the secondary side of each of 275kV/154kV main transformers (No.5 or No.6) with 154kV Gas Insulated Switchgear (GIS). The SVC is thyristor-controlled-transformer type consisting of a high-impedance transformer, thyristor equipment, control panel, so on. The single line diagram and the layout are shown in Figure 1 and Figure 2. The high-impedance transformer is connected directly to GIS in its primary side and to thyristor equipment each phase in its secondary side via busduct.

A. High-impedance transformer (Hi-Z TR)

High-impedance transformer (Hi-Z TR) has the fundamental capacity of 60MVA, equal to the SVC capacity, and the harmonic capacity of 15MVA to withstand harmonic currents from thyristor. The leakage impedance of Hi-Z TR is large percent impedance of 76% to work as the reactance for reactive power output. Hi-Z TR has another function to supply the suitable voltage of 5kV per phase to each thyristor module as the secondary voltage of Hi-Z TR. From the point of constitution, considering the transportation limit of Hi-Z TR, three single phase transformers of 20 MVA per each tank were produced. In construction work, they were connected each

0-7803-3823-5/97/$10.00© 1997 IEEE

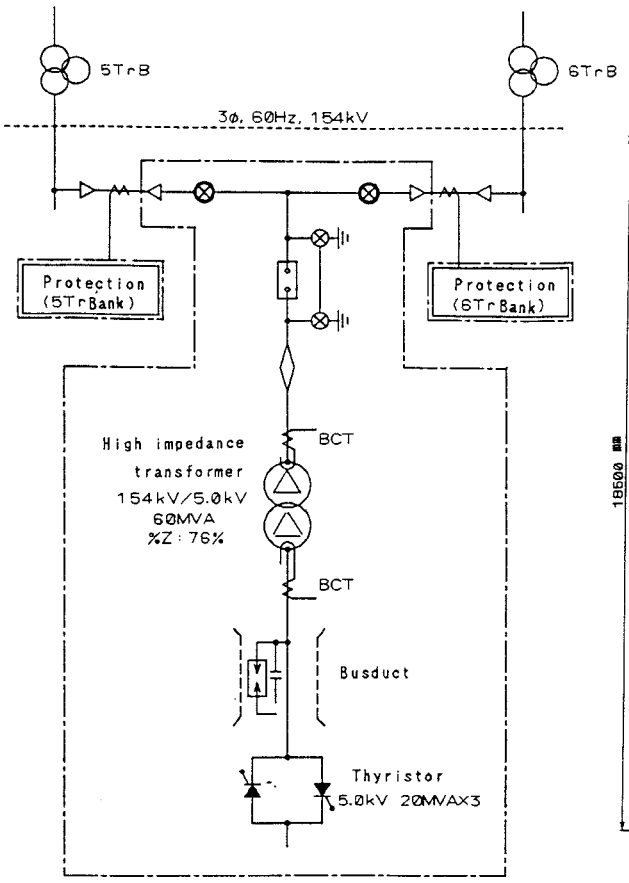


Fig. 1 Single line diagram

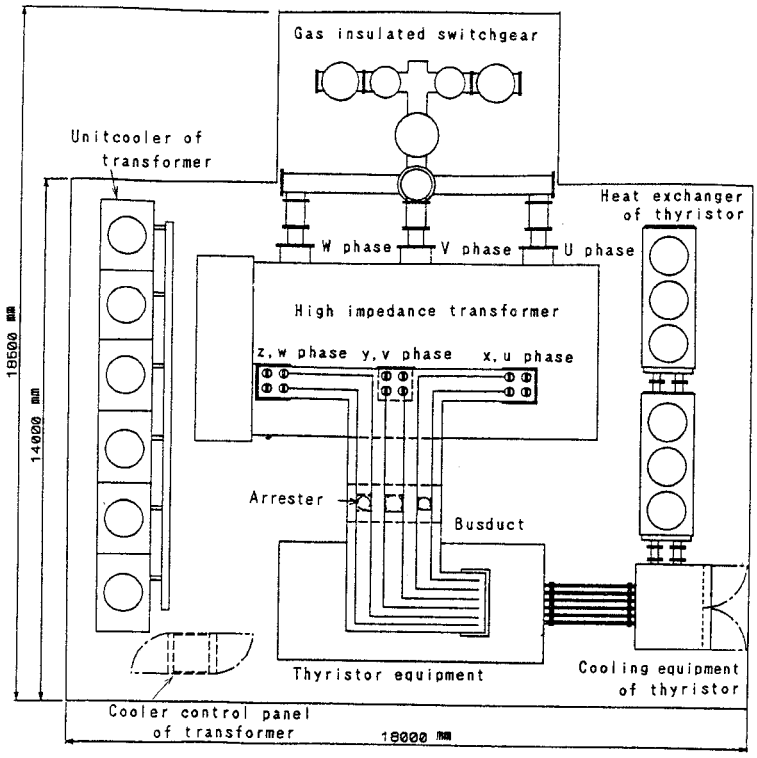


Fig. 2 Layout of the SVC

other into delta winding in the 154kV primary side, whereas the secondary windings remain independent to make it convenient to connect to thyristor equipment. To reduce the sound level, the transformer tank was surrounded with double-layered shield walls. The cooling of Hi-Z TR is by circulating oil and forced air type unit-coolers, one of which is spare.

B. Thyristor equipment

Thyristor element of the SVC is 8kV-3.5kA-6inch light-triggered one developed for HVDC transmission system by Japanese three manufacturers. As the SVC is three phases system, three thyristor modules were made by three thyristor manufacturers. One module per phase by one manufacturer includes stacked four elements, set into two series-one parallel in one arm and anti-parallel of two arms, and also snubber circuit, anode reactor, so on. Three modules were piled up insulated each other shown in Figure 3 and the whole of them was installed in an aluminum cubicle. Thyristor stack is cooled by demineralized water with snubber resistor and anode reactor. One pulse-generator panel is attached to one module, which transmits optically triggering pulse signal to thyristor element gate and monitors thyristor voltage, current, cooling water flow, temperature, so on for protection. The cooling system is circulating demineralized water and forced air type and common for three modules. The cooling water flow for each module is adjusted by valve independently and suitably. One spare of circulating pump and cooling fan is prepared for increasing reliability.

C. Control panel

One control panel is also installed in the aluminum cubicle to send triggering timing pulse signals to three pulse-generator panels electrically. The control panel has direct digital control (DDC) unit which calculates triggering angle of thyristors according to the selected control programme. DDC also monitors 154kV bus voltage, triggering angle, so on. To allow operational flexibility, the following control programmes were

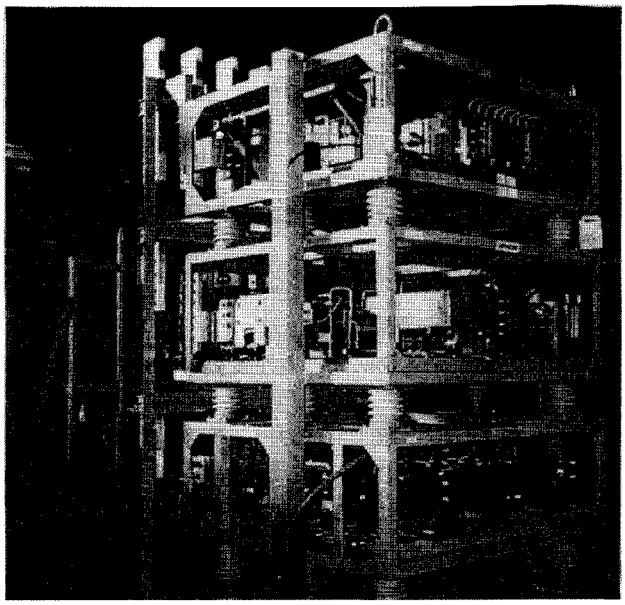


Fig. 3 Thyristor modules

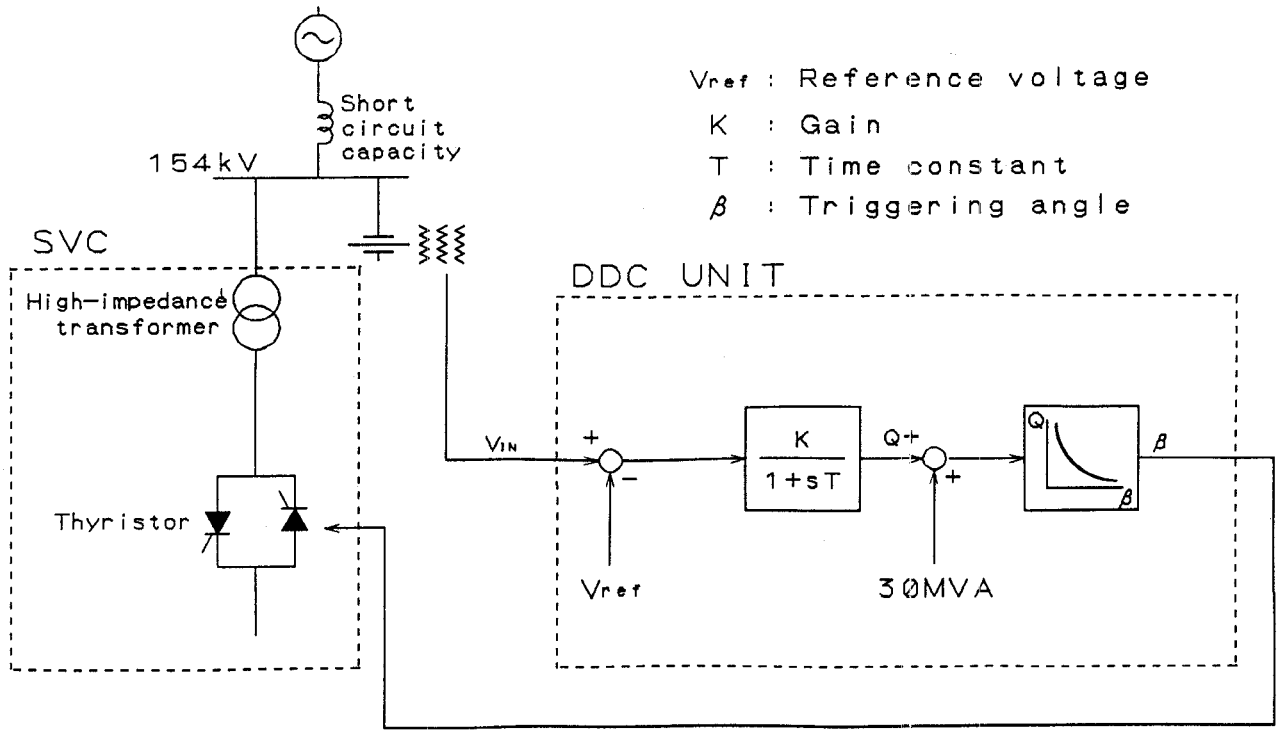


Fig. 4 Block diagram of AVR control

prepared in DDC unit.

1) Automatic Voltage Regulation (AVR) control : The block diagram of AVR control is shown in Figure 4. It is normal feedback control with reference versus actual voltages. Feedback gain and time constant are decided considering the short circuit capacity of network and the response optimization of the SVC. The reference voltage is set automatically as scheduled or manually by operator.

2) Fixed output operation : As same as shunt reactor, SVC can output constant reactive power with fixed triggering angle of thyristor.

IV. FACTORY AND FIELD TESTS

Three thyristor modules by different manufacturers were tested from the point of three phases system. After piling assembly of three thyristor modules in factory, heat-run test with low voltage, one of factory tests, was done. Figure 5 shows the waveforms of thyristor voltage and current in heat-run test. Though thyristor modules and corresponding pulse-generator panels were simultaneously operated with control panel for the first time, they showed good switching characteristics as three phases system. Then, in commissioning period at substation site, heat run test with full voltage was done, the waveforms being shown in Figure 6. In both tests, different manufacturer's thyristor elements of three phases showed no discrepancies in triggering or switching characteristics, so that the SVC was proved to have sufficient performance as three phases system.

V. EFFECTS OF SVC APPLICATION

At the final stage of commissioning, the SVC was examined in its effects. The SVC is operated mainly with AVR control to stabilize 154kV bus voltage according to reference voltage. Figures 7-(1) and 7-(2) show two tipical results on AVR control operation. Case (1) is voltage stabilization in the period when three shunt reactors were switched on. In oscillogram, it is found that voltage fluctuation is better compensated with SVC than without SVC. Case (2) is that bus voltage was settled in two levels of the selected reference voltage of 146kV then 144kV. The SVC controlled its output reactive power stepwise according to the reference voltage, and bus voltage was settled steadily in both levels. As shown in two cases, the better effects of voltage stabilization have been realized than the occasion without the SVC constructed. After completing commissioning, the SVC has been taken into service in substation.

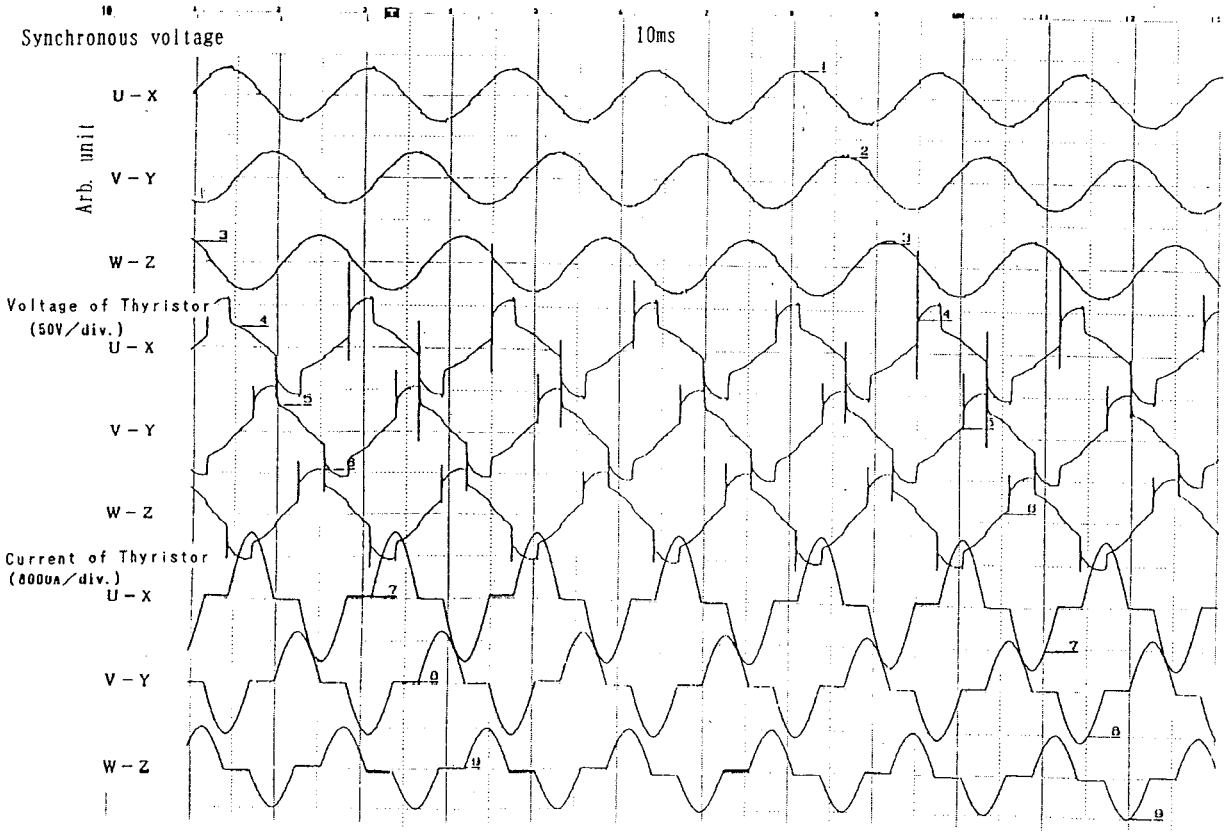


Fig. 5 Oscillogram of thyristor voltage and current in heat run test (in factory)

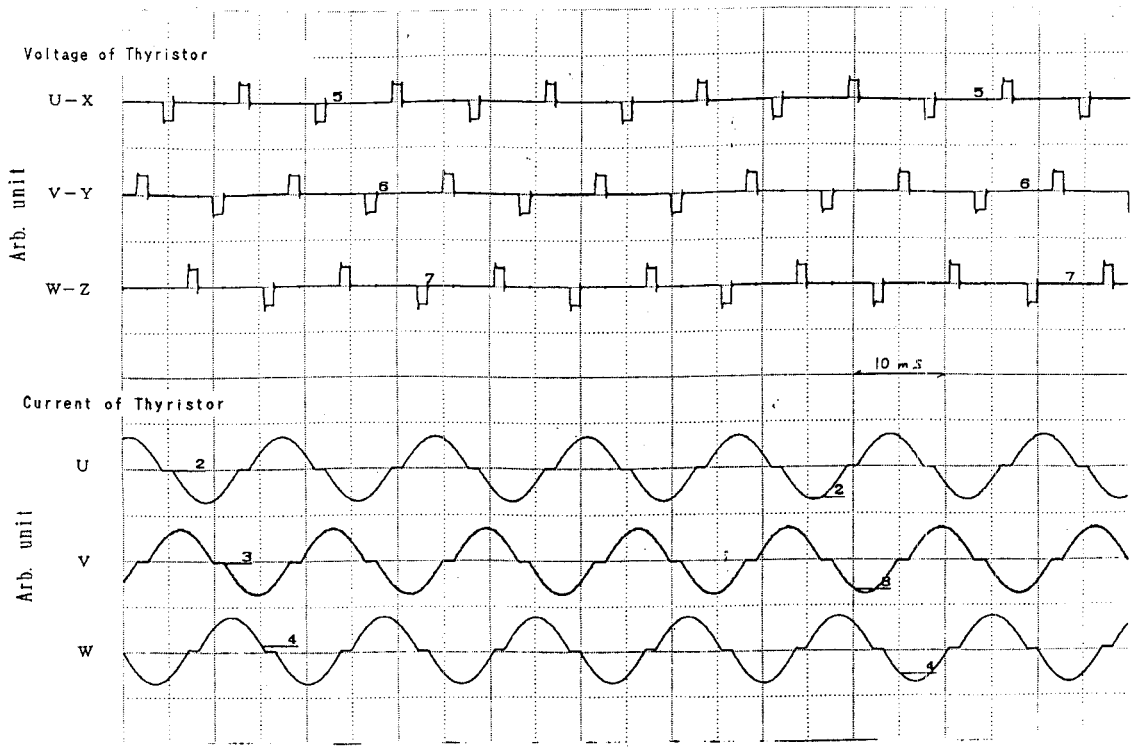


Fig. 6 Oscillogram of thyristor voltage and current in heat run test (in site)

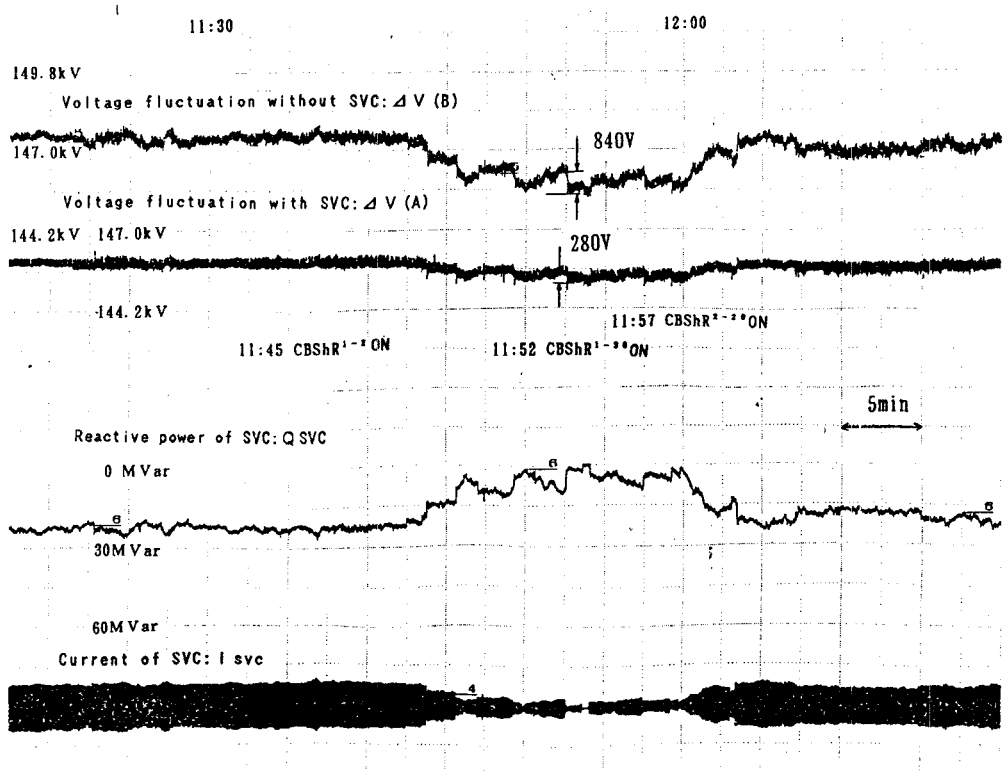


Fig. 7-(1) Oscillogram of voltage fluctuation and SVC output (shunt reactors operated)

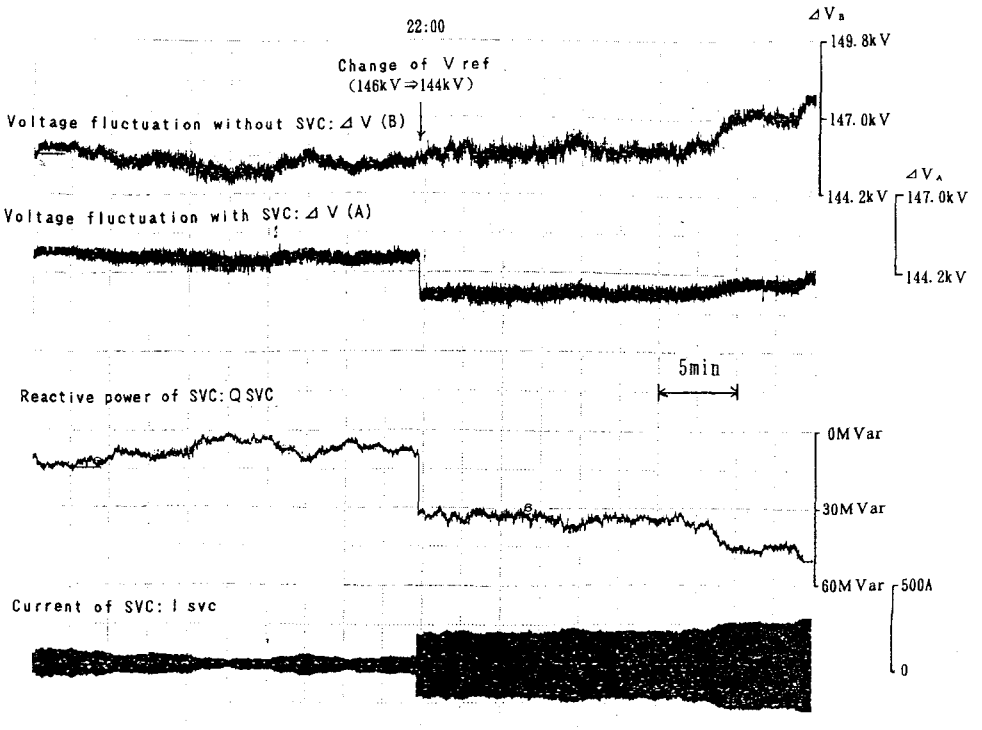


Fig. 7-(2) Oscillogram of voltage fluctuation and SVC output (reference voltage changed)

VI. CONCLUSION

154kV and 60MVA SVC was constructed in Higashi-Osaka substation. For thyristor equipment, three different manufacturers' thyristor elements were used. In tests or commissioning, the SVC showed good results on thyristor switching as three phases system and on bus voltage stabilization. The SVC has been operated successfully more than one year.

REFERENCES

[1] Y. Aoshima, et al, "The 154kV 60MVA SVC (Static Var Compensator) installed in Higashi-Osaka Substation of The Kansai Electric Power Co., Inc." the Nissin Electric Review, vol.41, No.3, pp.23-27, Nov., 1996

SVC Control Considering the Impedance on the Higher Side of the Power System

Takao Akiyama*, Kimiyoshi Tamura, Junichi Shimomura,
Masafumi Ichihara, Masayuki Terashima
Development Department 1, Product Development Laboratory, Meidensha Corporation
1-17 Ohsaki 2-chome, Shinagawa-ku, Tokyo 141, Japan
Fax: +81-3-5487-1598, Phone: +81-3-5487-1582
E-mail: akiyama@ohsaki.meidensha.co.jp

Abstract— **In a previous paper[1], we proposed a new control method for SVC which is utilized to control the voltage of an operating point. The proposed method keeps the control characteristics of SVC constant even if the reactance of the power source side fluctuates, while the control response of the conventional method is easily affected by fluctuations in the power source side reactance. We applied the model reference adaptive control (MRAC) method in the proposed method. However, we did not take load fluctuations into consideration in the previous paper. Load fluctuations during control operation cause an undesirable fluctuation in the adaptive parameter, and may disturb the power system or make SVC control unstable. In this paper, we describe a new control method that we have developed to maintain the stability of SVC, even if load fluctuations occur.**

I. Introduction

The standard SVC system consists of a voltage sensor at an operating point, a controller, an inverter which produces the current calculated by the controller, and a condenser. A PI-controller is usually applied to stabilize the voltage of the operating point (hereinafter referred to as SVC control).

The power source side impedance (hereinafter referred to as *Lpp*) at an operating point fluctuates according to changes in the bank or distribution line in the substation. The conventional SVC control method does not take fluctuations in *Lpp* into consideration. The PI gain in the conventional method is adjusted to a sufficiently small value that fluctuations in *Lpp* do not affect the control response. As a result, the settling time of the control response becomes late.

In order to design a controller that provides a constant response even if *Lpp* fluctuates during control operation, we applied the model reference adaptive control (MRAC) method [1][2].

In our previous paper [1], we did not take load fluctuations into consideration. The reference model consists of the power source side reactance and the time-invariant power source. The proposed method is applicable to a case where the load fluctuates in a narrow range during control operation. Load fluctuations cause fluctuations in the adaptive parameter, whereas it is desirable that the adaptive parameter fluctuate only when *Lpp* fluctuates. If load fluctuations are taken into consideration in the reference model, the controller would become very complex. We propose a simple method to decrease fluctuations in the adaptive parameter in a case where the load fluctuates over a wide range.

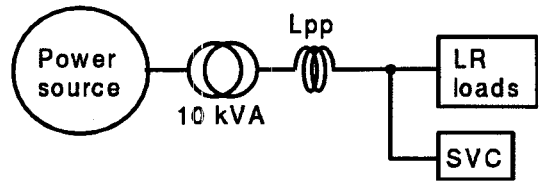


Fig. 1. Configuration of experiments

The configuration of our experiments and the operating point of SVC are shown in Fig.1.

II. An adaptive SVC control system [1]

We derived the transfer function of a conventional SVC control system, while assuming the following: (1) SVC can be considered as an ideal current source, (2) the power source side impedance (*Lpp*) consists only of reactance, (3) the load impedance is so much greater than *Lpp* that most of the SVC's current flows to the power source side, (4) the gain of the controller of a DC voltage is so small that it is able to neglect the active current of SVC, (5) the RMS of the voltage at the operating point is calculated using a 4th ITAE minimized low-pass filter (LPF) having a cut-off frequency of 20 Hz.

The RMS of the voltage is calculated as follows. Detected RS,TS interphase voltages is transformed into RS,ST,TR interphase voltages. The RMS of the voltage is then calculated by low-pass filtering of the output of a three-phase rectifier whose input is the RS,ST,TR interphase voltages. The output of a three-phase rectifier includes a large amount of higher harmonics, the main element of which is the 6th harmonic. The 4th LPF, whose cut-off frequency is 20 Hz, is necessary to attenuate these harmonics sufficiently[3]. These calculations are performed by DSP.

According to these assumptions, the transfer function of a conventional SVC control system is described as (1):

$$e_{qF} = \frac{(c_0\omega L_{pp}K_p s + c_0\omega L_{pp}K_i)\cdot e_{qREF}}{s^5 + c_3 s^4 + c_2 s^3 + c_1 s^2 + c_0(1+\omega L_{pp}K_p)s + c_0\omega L_{pp}K_i} \quad (1)$$

where e_{qF} is the RMS of a voltage at an operating point, e_{qREF} is the reference value of e_{qF}, K_p, K_i are PI gains of the SVC controller, $c_0 \sim c_3$ are the coefficients of the 4th LPF, $\omega = 2\pi \cdot 50$.

A new control parameter K_L is inserted after the output of the PI controller. If K_L is adjusted adequately according to the fluctuations in L_{pp}, variations in the control response are suppressed.

The adaptive law of K_L is designed by the method of Lyapunov [2] and is described as (2):

$$K_L = \alpha \cdot \int e^T P_B y_{pc} dt + \beta \cdot e^T P_B y_{pc} \qquad (2)$$

where e is a vector representing the difference between the states of the model and the plant. The first to fourth elements of e represent the difference between the states of the 4th LPF of the model and the plant, and the fifth element of e represents the difference between the state of the model's PI controller and the plant's PI controller. y_{pc} is the output of the PI controller of the plant and is also a reference value of the reactive current of SVC. P_B is a vector calculated using the solution matrix of the Lyapunov equation and the control vector of the state equation which represents the 4th LPF. α, β are certain positive values.

Under ideal conditions, equation.(2) ensures that the state error (e) tends toward zero and the adaptive parameter (K_L) tends toward an appropriate value after several step responses.

An actual plant has a variety of disturbances and there are errors of modeling. These disturbances cause fluctuations in K_L. The conditions in which SVC control operates are far from ideal. The adaptive law in (2) is not sufficient to stabilize the fluctuations in K_L, and the unstable fluctuations in K_L make SVC control unstable.

We have therefore improved the adaptive law. The improved adaptive SVC control system is shown in Fig.2.

The adaptive law was improved as follows. The 1st LPF (eFIL) and a dead zone (DZ) are positioned after $e^T P_B$. Noise included in the states of the 4th LPF (LPFp) of the plant is attenuated. This noise is from the higher-harmonics distortion of the voltage of the operating point.

Furthermore, a filter (PFIL) is installed. PFIL operates as a dead time element for a large state error ($e^T P_B$) which is caused by fluctuations in L_{pp} or large load fluctuations. PFIL eliminates the pulse-like noise (PLN) which is caused by small load fluctuations. If the load fluctuates in a narrow range, the noise included in the 4th LPF (LPFp) exceeds the dead zone (DZ) and becomes PLN. The sign of PLN is according to the direction of load fluctuation. The sign of PLN is positive when the load fluctuates so that the voltage of the operating point decreases, and it is negative when load fluctuates so that the voltage of the operating point increases. K_L drifts in a certain direction according to the state of loading or unloading. To prevent K_L from drifting, PFIL eliminates PLN having a time range less than the dead time of PFIL.

The 1st LPF (KLFIL) is positioned according to the calculation of (2). When K_L fluctuates beyond a certain range, re-identification starts. A rectangle signal whose amplitude is $\pm$ 1 V is added to the voltage reference of the operating point (e_{qREF}), for the purpose of convergence to an adequate value of K_L.

These improvements stabilize the fluctuations in K_L. K_L fluctuates adequately according to the fluctuations in L_{pp}. We obtained the same experimental results of step response even when L_{pp} fluctuated. Experiments were performed in which L_{pp}=0.31 mH, 0.75 mH, and 1.6 mH. Fig.3 shows the step responses of a conventional SVC control system in which the PI gain is fixed assuming L_{pp}=0.75 mH. Fig.4 shows the step responses of an adaptive SVC control system. K_L was converged to an adequate value according to L_{pp} by several step responses. The reactance of the reference model was 0.75 mH, and the PI gain of the adaptive SVC control system was the same as that of the conventional SVC control system.

III. Consideration of load fluctuations

Load fluctuations cause fluctuations in the voltage of the operating point, leading to fluctuations in the adaptive parameter K_L. If a load fluctuation causes a fluctuation of K_L, re-identification (IDSG in Fig.2) brings K_L to an appropriate value. If K_L fluctuates over a wide range due to load fluctuations, SVC tends to become unstable before K_L reaches an appropriate value. Even if SVC does not become unstable, the power system is disturbed by re-identification. It is therefore desirable that re-identification be completed in a shorter time.

We compensate for the fluctuations in the adaptive parameter caused by load fluctuations as follows. A reactive current identical to the load reactive direct current is added to the reference value of the SVC current. SVC reacts speedily to fluctuations in voltage caused by fluctuations in the load reactive current, and the fluctuations in K_L become smaller.

SVC is not able to produce active power. The method of compensation for fluctuations in the load active current cannot be the same as that of the load reactive current. SVC compensates for a fluctuation in voltage caused by a fluctuation in the load active current with a reactive current. P_B in (2) is the coefficient which weights the state error (e). The fifth element of P_B weights the difference between the output of an integrator of the model and the plant. Not only fluctuations in voltage but also fluctuations in the output of the integrator cause fluctuations in K_L, when the load fluctuates.

The aim of SVC control is the stabilization of a voltage. The output of the integrator of the plant does not necessarily have to be coincident with that of the model. If the fifth element of P_B is set at zero, the difference between the output of the integrator of the model and

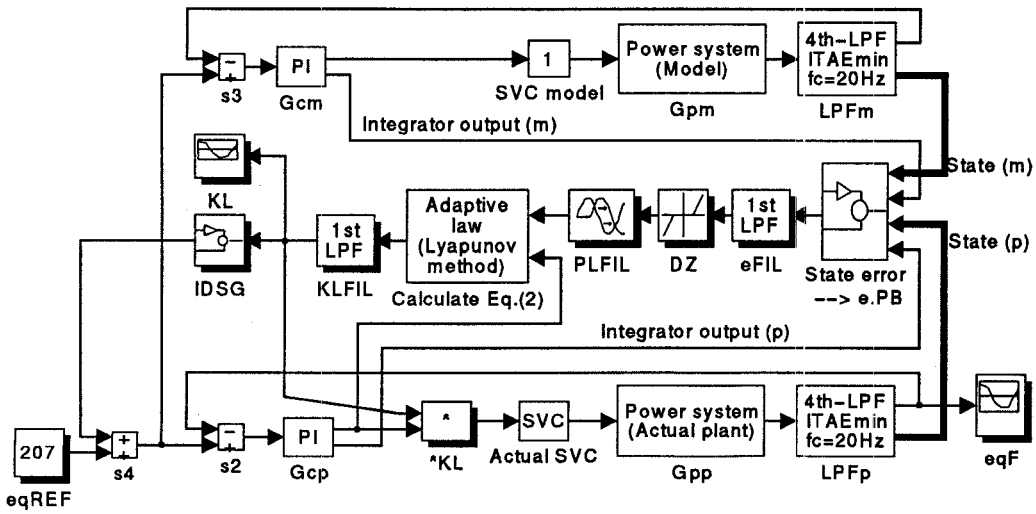


Fig. 2. Adaptive SVC control system

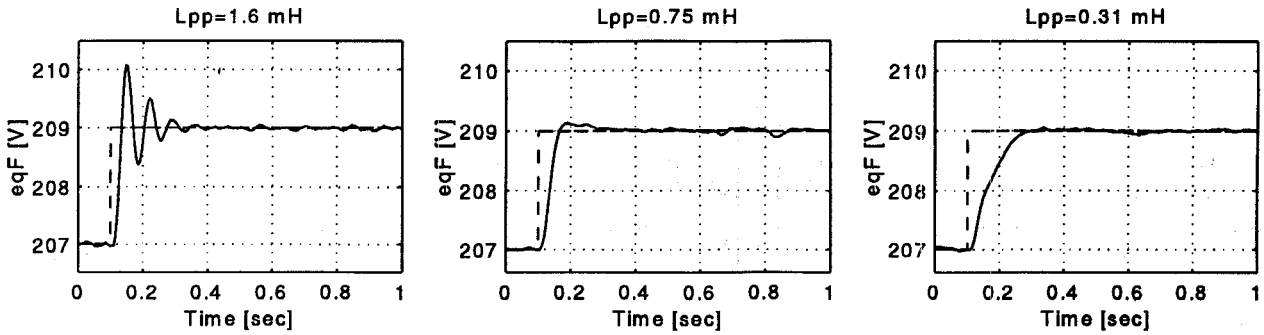


Fig. 3. Step responses by conventional SVC control (fixed PI gain)

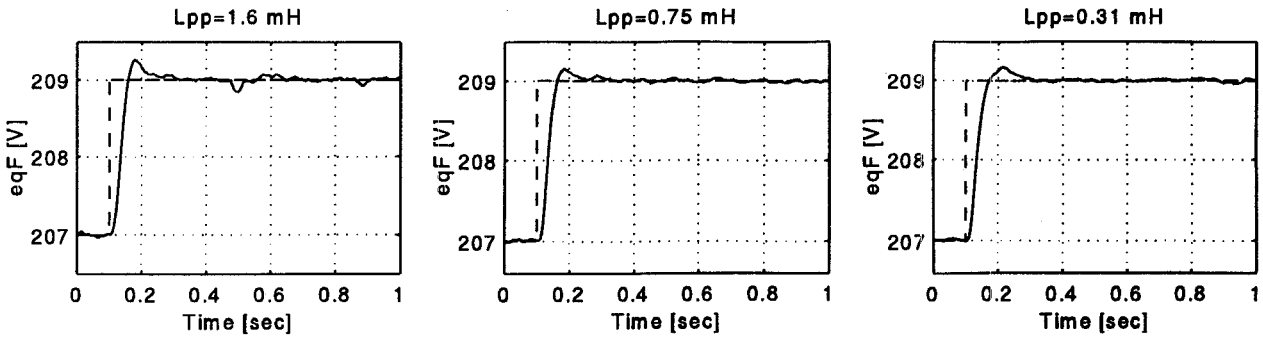


Fig. 4. Step responses by adaptive SVC control

that of the plant does not promote the fluctuations in K_L.

We confirmed the effect of this compensation by conducting experiments. A 60 mH reactance and a 7.7 Ω resistance were loaded and unloaded under conditions where the power source side reactance (L_{pp}) was 0.75 mH and the power source side resistance was 0.13 Ω. The experiment with compensation was compared to the experiment without compensation. Fig.5 and 6 show the experimental results. The thick lines in the figures indicate the period of re-identification. The load was loaded, and then unloaded.

Fig.5 shows the results of loading and unloading of reactance. The compensation for load reactive current suppresses fluctuations in K_L and makes the period of re-identification significantly shorter. Fig.6 shows the results of loading and unloading of resistance. Although the results are not the same as in the Fig.5, the compensation of P_B makes the period of re-identification shorter.

IV. Conclusion

We configured an SVC control system based on the model reference adaptive control method derived from the method of Lyapunov. This method is applicable under ideal conditions. An actual power system has a variety of disturbances, however, and the stability of the adaptive parameter was easily affected by such disturbances. We therefore added new filters to the conventional adaptive law. These filters attenuate the noise included in the state error between the model and the plant, thus stabilizing fluctuations in and suppressing drifting of an adaptive parameter.

For the purpose of suppressing fluctuations in the adaptive parameter caused by large load fluctuations, a reactive current identical to the load reactive direct current was added to the reference value of the SVC current, and the difference between the output of the integrator of the model and that of the plant was ignored in the adaptive law. This compensation made the period of re-identification shorter.

Henceforth, we plan to reduce the disturbances caused by re-identification.

Acknowledgments

The authors would like to acknowledge the suggestions made by many people in connection with this study.

References

[1] T.Akiyama et al: "SVC Control Considering the Impedance on the Higher Side of the Power System" 1997 National Convention Record I.E.E Japan, 935

[2] T.Jinguji et al: "Design of Model Reference Adaptive Control Systems via the Method of Lyapunov" Transactions of the Society of Instrument and Control Engineers, Vol.11, No.6, pp650-655.

[3] T.Chiba et al: "High-Precision Voltage Measuring Method using Fast Sampled Data for Electric Power Systems" The Transactions of The Institute of Electrical Engineers of Japan, Vol.113-B, No.5, 1993, pp553-561.

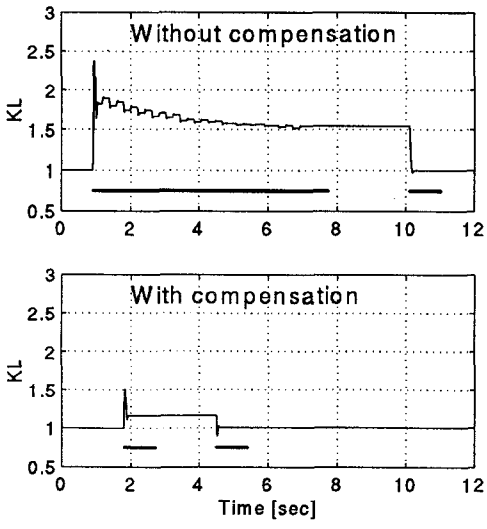


Fig. 5. In the case of load fluctuation (reactance)

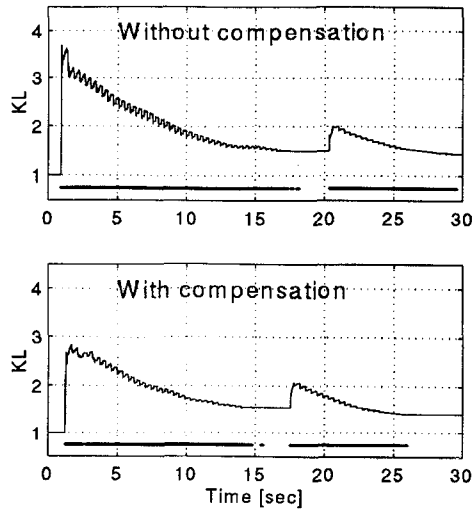


Fig. 6. In the case of load fluctuation (resistance)

Power System Stabilizing Control Using High Speed Phase Shifter (HSPS)

Toshifumi ISE, Takanori HAYASHI, Junichi ISHII and Sadatoshi KUMAGAI
Department of Electrical Engineering, Faculty of Engineering, OSAKA University
2-1, Yamada-oka Suita, Osaka, 565 JAPAN
FAX: +81-6-879-7263, TEL: +81-6-879-7695
E-mail: ise@pwr.eng.osaka-u.ac.jp

Abstract **--- A High Speed Phase Shifter (HSPS) presented here is composed of three sets of a single phase PWM inverter which are connected in series to a power system, and another PWM inverter to control the dc link voltage of inverters at a specified value which is connected in parallel to a power system. The configuration is same as a UPFC (Unified Power Flow Controller). The experimental mini model for 10kVA transmission line was developed and its performance for power system stabilizing control was examined. It was shown that not only transient stability but also dynamic stability can be improved by the HSPS.**

I. INTRODUCTION

Recently, much attentions have been paid on control of power systems by power electronics technology such as SVC using self-commutated inverters, SMES, static phase shifters and so on[1]-[5]. Among them, the High Speed Phase Shifter (HSPS) which is composed of series and parallel inverters connected in series and parallel with power line, respectively, is the most advanced system. Three or four variables can be controlled independently depending upon its configuration. Although several studies have been reported on their control scheme, the control performance has been verified only on computer simulations [6]-[8]. In order to verify their ability on a real power system, a mini model of the HSPS on the 10kVA model transmission line was developed, and the performance on power system stabilizing control was tested. The control algorithm for power system stabilization is based on a very simple idea producing decelerating energy by the HSPS to counterbalance the accelerating energy of the generator. Two configurations of the HSPS which are without and with an energy storage device using a superconducting coil, have been tested and their results have been compared.

II. CONFIGURATION OF THE SYSTEM

The two configurations of the HSPS studied in this paper is shown in Fig.1 and 2. As for the HSPS shown in Fig.1, the active and reactive power from the series inverter, that is P_S and Q_S, can be controlled independently, but the parallel inverter is controlled to maintain the dc voltage of inverters at a specified value. Although the active power P_p from the parallel inverter depends on active power P_S from the series inverter, the reactive power Q_p from the parallel inverter can be controlled independently. Hence, this controller can control three variables, that is P_S, Q_S and Q_p, independently. This configuration is sometimes refereed as UPFC (Unified Power Flow Controller). In this paper, the series inverter is applied to power system stabilizing control and the parallel inverter is used only to maintain the DC link voltage.

On the other hand, the HSPS with energy storage is shown in Fig.2 The active and reactive power from the series inverter, that is P_S and Q_S, can be controlled independently, and the output active and reactive power from the parallel inverter, that is P_p and Q_p, can also be controlled independently. These power can be utilized for many purposes of power quality control, such as power system stabilization, harmonic current and voltage compensation, line voltage compensation for voltage sags, swells and so on, and saving sensitive loads from short duration power outages. The parallel inverter charges the superconducting magnet current from zero to a specified value and maintains the average current at a certain value, while the chopper is controlled to keep the dc side voltage of inverters at a specified value. In this paper, the series inverter is controlled to perform power system stabilizing control and the parallel inverter is controlled to supplying power losses of the HSPS system

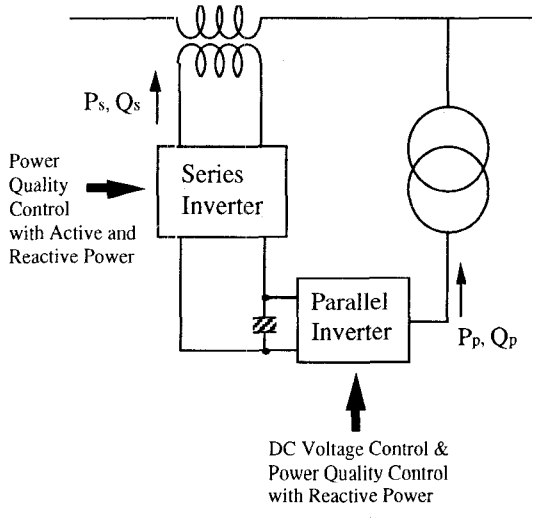


Fig.1. Configuration of the HSPS without Energy Storage.

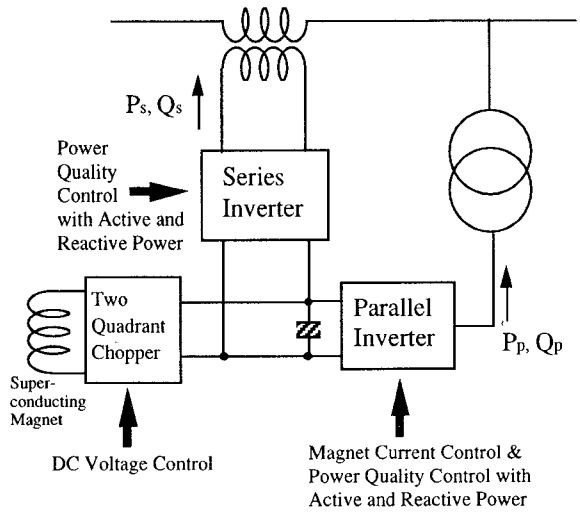


Fig.2. Configuration of the HSPS with Energy Storage.

III. CONTROL SCHEME

The series inverter is controlled so as to perform power system stabilizing control. The active and reactive power of the series inverter, that is P_S and Q_S, are proportional to deviations of angular velocity of generator ($\Delta\omega$) and bus voltage of the generator terminal (ΔV_G), respectively.

$$P_S=-K_D\Delta\omega,\quad Q_S=K_V\Delta V_G$$

The equivalent function of the series inverter can be expressed as shown in Fig.3. It can be seen as an equivalent variable resistor and capacitor or inductor. The control algorithm for power system stabilization is based on the idea producing decelerating energy by the HSPS to counterbalance the accelerating energy gained during faults and the reactive power is controlled so as to compensate the voltage deviations.

The parallel inverter is controlled as shown in Fig.4 depending upon the configuration without and with a superconducting coil for energy storage.

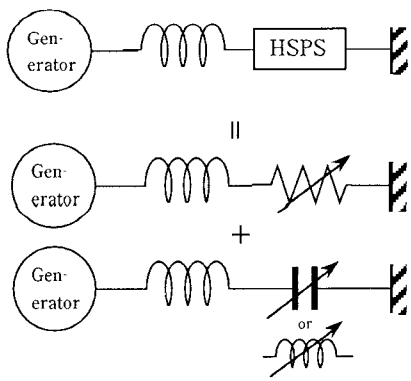


Fig.3. Equivalent Function of the Series Inverter.

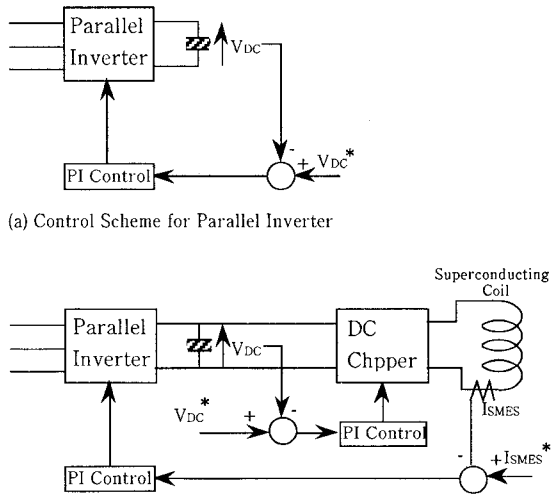


Fig.4. DC Voltage and Current Controller.

IV. EXPERIMENTAL SYSTEM

The configuration of the experimental system is shown in Fig.5 and specifications of the model HSPS are shown in Table 1. In the main circuit, three sets of single phase series inverters and one three phase parallel inverter are connected together to the common dc bus, and the primary side of transformers of single phase inverters are connected in series to the transmission line. The control circuit of the HSPS is composed of a PLL (Phase Locked Loop) circuit which detects the frequency and the phase angle of the line voltage, a DSP (Digital Signal Processor) and some logic circuits for PWM modulation. According to the modulation index (M) and voltage phase (θ) for the series inverters which are given from power system stabilizing controller, the DSP calculates sinusoidal reference voltage, and on-off switching signals are generated in the PWM modulation circuit. For the parallel inverter, instantaneous three phase current reference signals are calculated by DSP from the amplitude of current which is given from dc voltage (V_{DC}) controller or coil current (I_{SMES}) controller depending upon the configuration, and ac current control is carried out in the PWM control circuit.

The ratings of line to line voltage of the model transmission line is 460V and the generator G is 10kVA. This model simulates 2000MVA, 500kV transmission line, and the HSPS was connected to the place which is equivalently 240km far from the generator in order to show the effectiveness of the HSPS for power system stabilizing control. The three phase line short circuit (3LS) for five cycles(=50msec) can be occurred at the generator bus as shown in Fig.5.

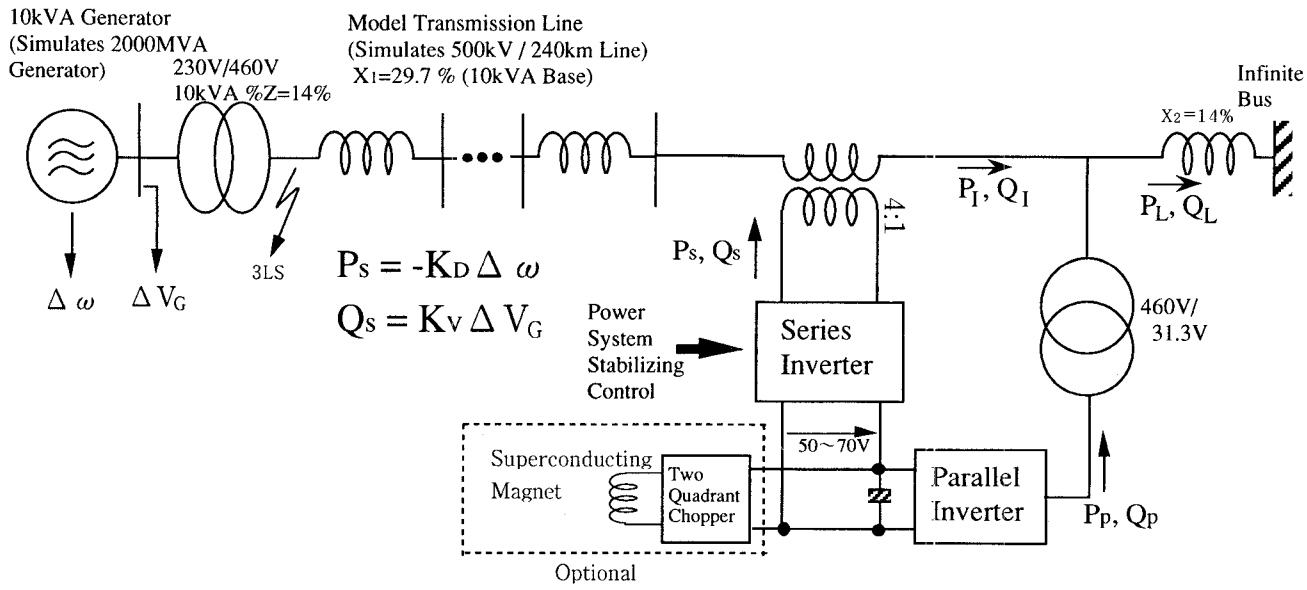


Fig.5. Configuration of the HSPS in the Model Transmission Line.

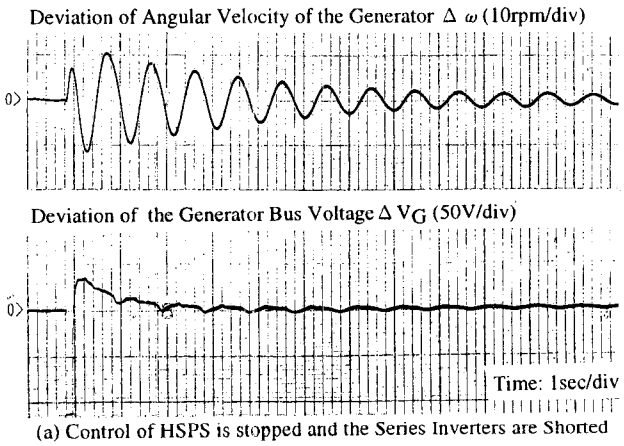
Table 1. Specifications of the Experimental HSPS.

Series Inverters	
Transformers	Primary Voltage : 460V Secondary Voltage : 115V
Inverters	Single phase PWM Inverter Power Rating : 2.6kVA, 3 sets DC Voltage : 50 ~ 70V Power Devices : IGBT PWM Carrier Frequency : 2.2kHz
Parallel Inverter	
Transformer	Primary Voltage : 460V Secondary Voltage : 31.3V
Inverter	Three phase PWM Inverter Power Rating : 4.6kVA DC Voltage : 70V Power Devices : IGBT PWM Carrier Frequency : 3.3kHz
Chopper	Power Rating : 10kW Input DC Voltage : 70V
Supercon-ducting Magnet	Energy : 10kJ Inductance : 1.078H Current : 140 A Conductor : NbTi

V. EXPERIMENTAL RESULTS

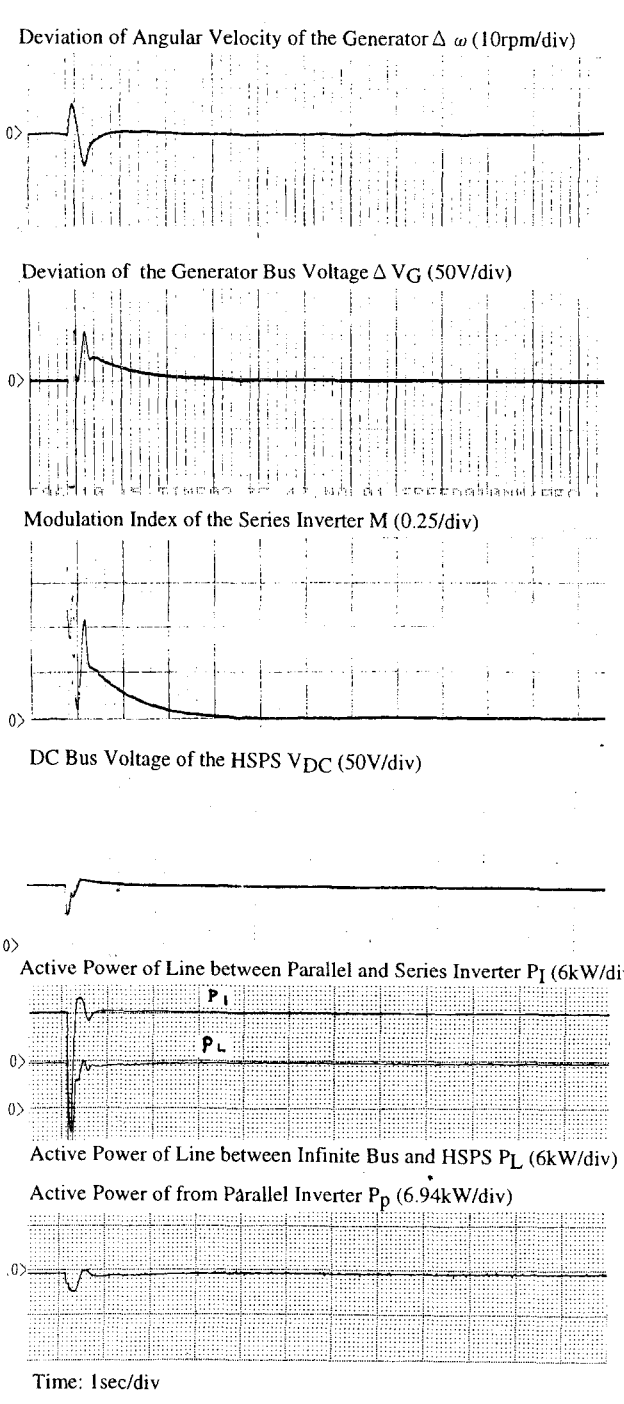
Experiments of power system stabilizing control were carried out. Fig.6 shows experimental waveforms of power system stabilizing control after the five cycle three phase line short circuit (3LS). Fig.6(a) shows the waveforms when the HSPS was stopped and the series inverters were shorted. Fig.6(b) shows waveforms for the case without the superconducting coil for energy storage and (c) for the case with the coil. From comparison of Fig.6(a), (b) and (c), deviation of angular velocity was quickly damped by the HSPS, although the HSPS is connected far from the generator. The deviation of the generator. terminal voltage ΔV_G became a little larger in Fig.6(b) and (c) than (a). This peak voltage was caused by the injected voltage by the series inverters.

Fig.6 also shows the active power Pp from the parallel inverter, when power system stabilizing control shown in was carried out. From these figures, it is shown that the active power Pp during power system stabilizing control is constant with the superconducting coil, while Pp for the case without the superconducting coil was changed in order to maintain the dc voltage. Therefore, disturbances to the power system are lower with the superconducting coil than without the coil.

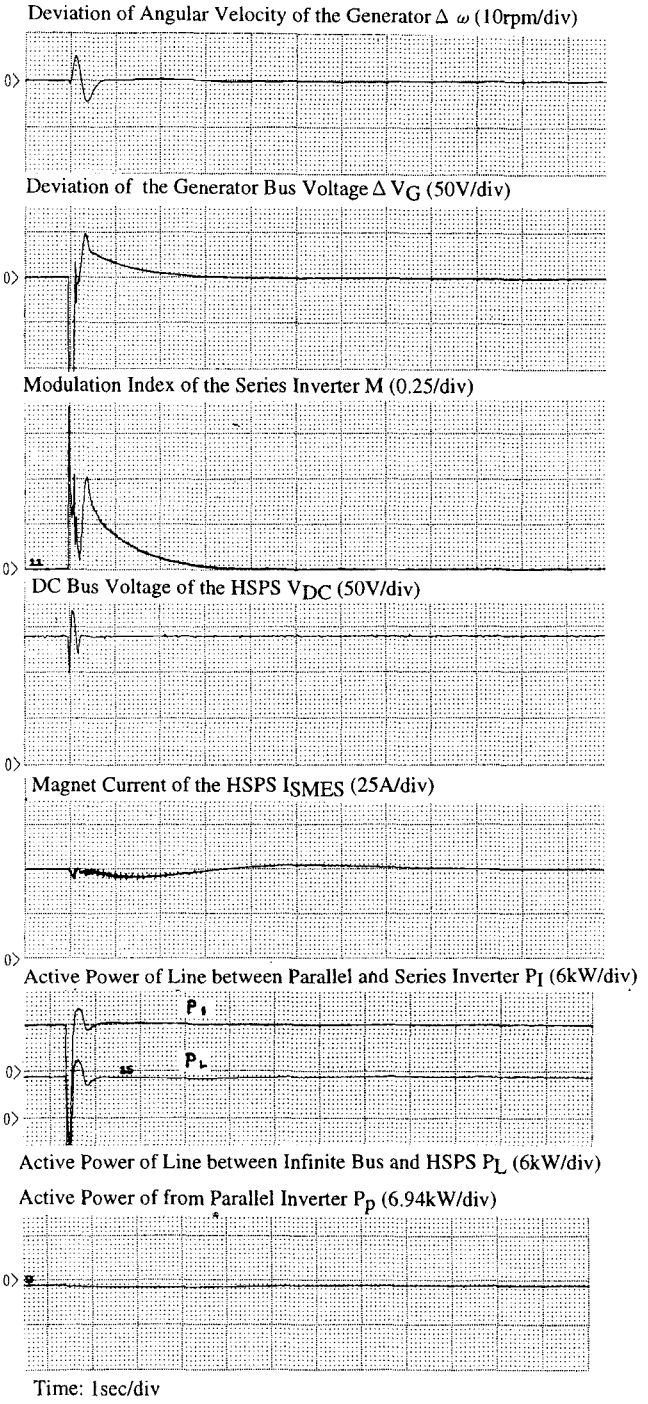


(a) Control of HSPS is stopped and the Series Inverters are Shorted

Fig. 6. Experimental Results of Transient Stability.



(b) With control of the HSPS



(c) With control of the HSPS with Energy Storage

Fig. 6. Experimental Results of Transient Stability.

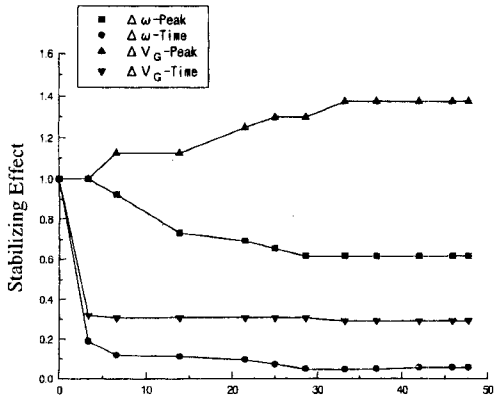


Fig.7. Changing of Power System Stabilizing Effect

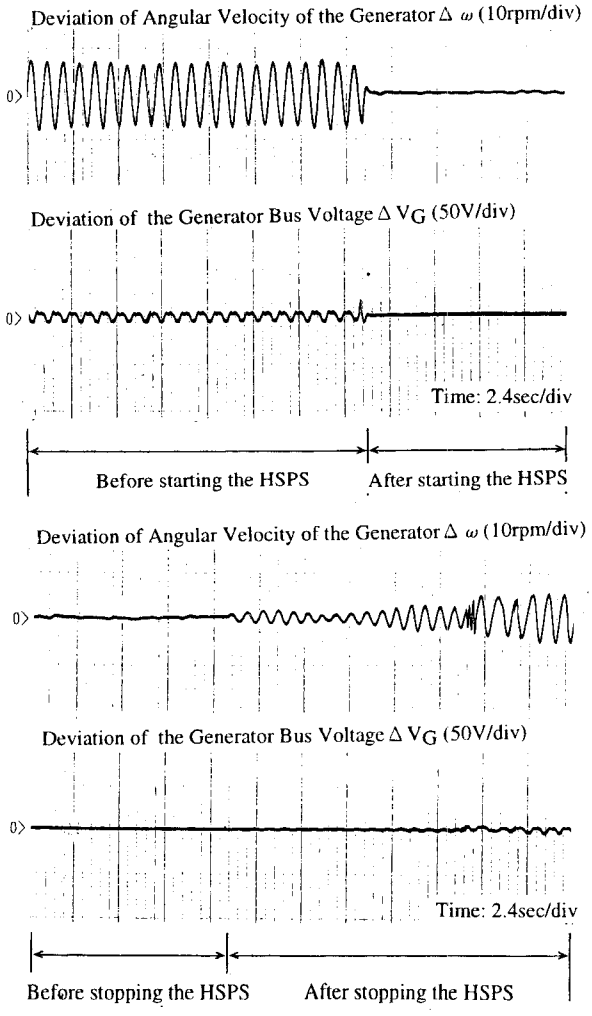


Fig.8. Experimental Results of Dynamic Stability.

The required power rating for the series inverters was studied by limiting the modulation index M for the series inverters Fig.7 shows changing of power system stabilizing effect by limiting the power rating of the series inverter. The limitation was carried out by applying upper limit for modulation index M. From the figure, it was shown that only 15% of the transmitted power (8kW) was required for the series inverters.

Fig. 8 is an experimental results, when transmitted power was increased to 9.5kW and some oscillations were occurred without the control of HSPS at steady state. After starting the HSPS the oscillations were quickly damped by the control of the HSPS, and after stopping the HSPS, oscillations occurred again and synchronism was lost after all. The HSPS can improve not only transient stability but also dynamic stability, and increase the transmitted power as shown above. Remarkable effects on power system stabilizing control by HSPS were verified experimentally as shown above.

Further studies are needed for stabilizing control scheme in a real power systems with multi-generators and effective utilization of power converters of the HSPS, such as compensation of voltage and current harmonics distortions simultaneous with the power system stabilizing control.

VI. Conclusions

As a series type power system controller, High Speed Phase Shifter (HSPS) with an energy storage device and a parallel inverter was designed and experiments of power system stabilizing control in a model transmission line with a 10kVA generator were carried out. Remarkable effects on power system stabilizing control by the HSPS were verified experimentally. Further studies are needed for effective utilization of active and reactive power from the parallel inverter.

Acknowledgments

This work was financially supported in part by the Kansai Electric Power Co. Inc. and the Grant-in-Aid for Scientific Research (B) (Project No.07455120) supported by the Ministry of Education, Science, Sports and Culture. The authors would like to gratefully express our thanks to co-workers in carrying out experiments.

References

[1] S. Mori, K. Matsuno, T. Hasegawa, S. Ohnishi, M. Takeda, M. Seto, S. Murakami and F. Ishiguro, "Development of a Large Static Var Generator Using Self-Commutated Inverters for Improving Power System Stability," IEEE Trans. on Power Systems , Vol.8, No.1, pp.371-377, Feb. 1993.

[2] T.Ise, Y.Murakami and K.Tsuji, "Simultaneous Active and Reactive Power Control of Superconducting Magnet Energy

Storage Using GTO Converter," IEEE Trans. on Power Delivery, Vol.1, No.1, pp.143-150, Jan.1986.

[3] Y.Mitani, K.Tsuji and Y.Murakami, "Application of Superconducting Magnet Energy Storage to Improve Power System Dynamic Performance," IEEE Trans. on Power System, Vol.3, No.4, pp.1418-1425, Nov. 1988.

[4] B.Ooi, S.Dai and X.Wang, "Solid-State Series Capacitive Reactance Compensators," IEEE Trans. on Power Delivery, Vol.7, No.2, pp.914-919, April 1992.

[5] G.Joos and J.Espinoza, "Three Phase Series Var Compensation based on a Voltage Controlled Current Source Inverter with Supplemental Modulation Index Control," 25-th IEEE Power Electronics Specialists Conference PESC'94 Record, pp.1437-1442, June 20-25, 1994 Taipei, Taiwan.

[6] A.A.Edris, "Enhancement of First-Swing Stability Using a High-Speed Phase Shifter," IEEE Trans. on Power Systems , Vol.6, No.3, pp.1113-1118, Aug. 1991.

[7] M.R.Iravani, P.L.Dandeno and D.Maratukulam, "Applications of Static Phase Shifters in Power Systems," IEEE Trans. on Power Delivery, Vol.9, No.3, pp.1600-1608, Jul. 1994.

[8] F.Jiang, S.S.Choi and G.Shrestha, "Power System Stability Enhancement using Static Phase Shifter," IEEE Trans. on Power Systems , Vol.12, No.1, pp.207-214, Feb. 1997.

Robust Power System Stabilizer Design with H_∞ Optimization Method and Its Experiment on a Hardware Simulator

Yeonghan Chun*, Takuhiko Ohashi*, Yoichi Hori*
Kook Hun Kim**, Jong Bo Ahn**, Seok Joo Kim**

* Department of Electrical Engineering
The University of Tokyo
Hongo 7-3-1, Bunkyo-Ku
Tokyo 113, Japan

** Power plant control innovation team
Korea Electrotechnology Research Institute
Sungjoo-Dong Changwon
Kyoungnam 641-120, Korea

Abstract— **This paper presents an application result of H_∞ optimization method to the design of Power System Stabilizer(PSS). The trade off relations between performance and robustness are used for the decision procedure of the weighting functions. As the purpose of the PSS is to increase system damping, weighting functions are determined to put weights on the robustness not only in the high frequency region but also in the low frequency range. The designed PSS is confirmed through experiments on a hardware simulator.**

I. Introduction

The system modes of swings consist of the local mode, interarea mode, and intramachine mode whose frequency ranges are 0.8 to 1.8 Hz, 0.2 to 0.5 Hz, and 1.8 to 2.5 Hz respectively. These power swings should be damped to prevent oscillatory instability, which limit the power transfer ability. Power system stabilizer is applied for this purpose as a supplementary excitation controls. For the linear power system stabilizer(PSS) to be practical, it should provide damping for the swing modes in large power systems over a wide range of operating conditions.

H_∞ optimization method is a frequency domain design tool which can be generally applied to multivariable systems. One of the characteristics of the H_∞ optimization theory is that plant uncertainty can be modeled directly in the stage of design. Chow et. al. applied the H_∞ optimization method to PSS already[7]. In the approach, the specifications were given by only the uncertainty models. As the control problem is to juggle the trade offs between the performance and the robustness, performance weights should be considered together with the uncertainty models. The proposed performance index and weighting functions can add damping over wide range of frequencies for the suppression of the local mode. DGKF algorithm[10] was used to solve the optimization problem.

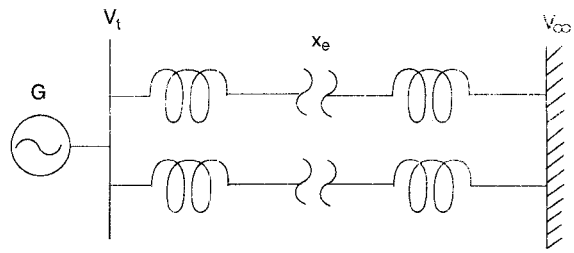


Fig. 1. Single-machine infinite-bus system

II. Single-machine infinite-bus system

The test system of single-machine infinite-bus system is shown in Fig. 1. The system is for the test of local mode of oscillation. Hardware simulator used for the test has the same configuration with Fig. 1. Even though the inter-tie mode or inter-machine modes can not be produced by this configuration, local mode can be produced by disturbances like line-fault or load changes.

III. Problem formulation for H_∞ optimization

The aim of the PSS is to increase system damping at the expected frequency range. This control objective is different from the general regulating problem. For example, the designed compensator should guarantee the steady state error specifications in general regulating problems, which causes high DC gain. In the case of PSS, the control purpose is to add damping especially at the range of local mode of oscillation. This performance specification is weaker than general regulating problem in a sense that steady state error need not to be considered in PSS. This is why governor controls mechanical power and steady state error. Therefor we can put more weights on robustness specifications, which can be understood by the tradeoffs between per-

0-7803-3823-5/97/$10.00© 1997 IEEE

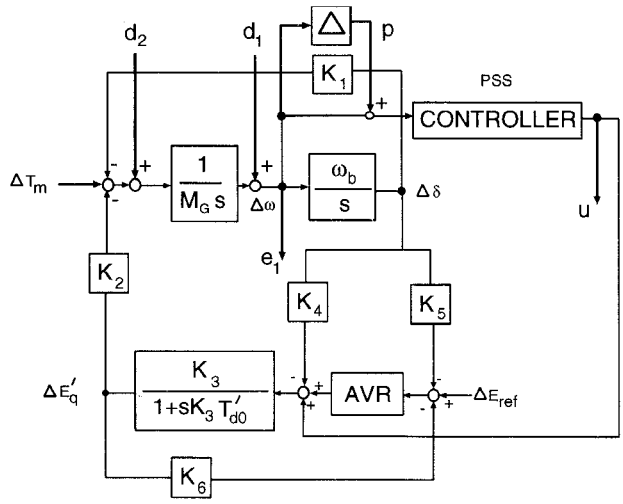


Fig. 2. Performance index without weighting functions

formance and robustness.

IV. Performance index and weighting functions

The design specifications addressed in Section III can be written in the single measure of performance index given by (1) together with corresponding weighting functions.

$$\min_{\text{stabilizing } K} \left\| \begin{array}{ccc} T_{e_1 d_1} W_1 & T_{e_1 d_2} W_2 & T_{e_1 p} W_3 \\ W_u T_{u d_1} W_1 & W_u T_{u d_2} W_2 & W_u T_{up} W_3 \end{array} \right\|_\infty < \gamma \quad (1)$$

Weighting functions together with performance index determines robustness and performance of the closed loop system. Therefore it is very important to decide weighting functions to get desired controller.

In this section, we give a way of deciding weighting functions for the Power System Stabilizer(PSS) comparing that of servo control case. These weighting functions should be applied together with the performance index given in Fig. 2.

The typical weighting functions for servo control were suggested as given by (2) $\sim$ (6)[14].

$$W_1 = \frac{1}{s+\epsilon_1} \quad (2)$$

$$W_2 = \frac{1}{s+\epsilon_2} \quad (3)$$

$$W_3 = \frac{s}{\epsilon_3 s+\alpha} \quad (4)$$

$$W_u = \frac{s}{\epsilon_4 s+\beta} \quad (5)$$

$$W_{e_1} = 1 \quad (6)$$

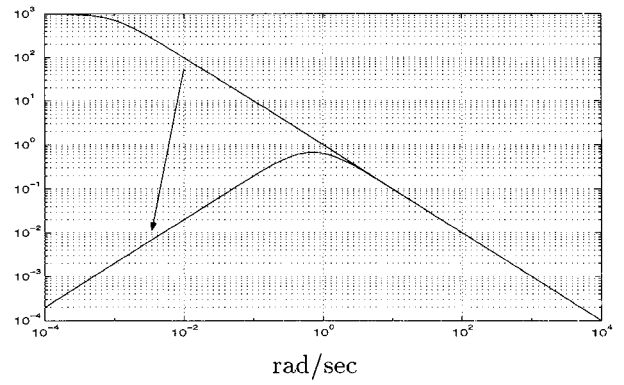


Fig. 3. Tuning of weighting function W_1

A. Weighting Function W_1

In servo control case, the weighting function W_1 is given by (7), where $\epsilon_1 \simeq 0$

$$W_1 = \frac{1}{s+0.001} \quad (7)$$

This is why ϵ_1 should be sufficiently small to guarantee the small steady state error. Fortunately we don't have to consider steady state error in the stage of designing the PSS, because governor is working in the outer loop. The only objective of the PSS is to put damping in the frequency range of 0.2 to 2.5 Hz. Therefore we cut the weighting function W_1 as shown in (8) and Fig. 3. This means that the low frequency performance has been sacrificed. This procedure is very important for the controller to be robust to the uncertainty of the parameters according to different operating points.

$$W_1 = \frac{s}{(s+1)(s+0.5)} \quad (8)$$

B. Weighting Function W_2

The weighting function W_2 given by (3) has its physical meaning that it shapes step torque disturbance. The step disturbance is too strict considering the real disturbances of the power system which PSS should suppress. As our objective of designing PSS is to give damping over the desired frequency ranges, 0.2 Hz $\sim$ 2.5 Hz, we tune the weighting function W_2 like (9).

$$W_2 = \frac{s}{(\frac{1}{0.2*2\pi}s+1)(\frac{1}{2.5*2\pi}s+1)} \quad (9)$$

Fig. 4 shows the bode magnitude plot of tuned weighting function W_2. The torque disturbance modeling can cover speed or position disturbance. This can be explained by that velocity is obtained by integration of torque.

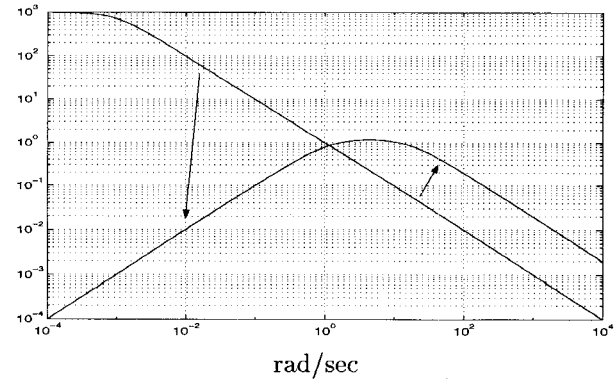


Fig. 4. Tuning of weighting function W_2

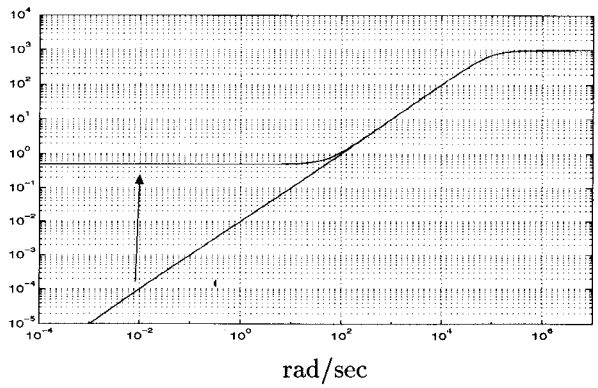


Fig. 5. Tuning of weighting function W_3

C. Weighting Function W_3

The weighting function W_3 given by (4) has its physical meaning that it shapes high frequency sensor noise and high frequency plant uncertainty. More important factor to consider in the weighting function W_3 is plant uncertainty rather than sensor noise in the case of PSS design. The weighting function W_3 that meets the objective is represented by (10) and Fig. 5. The weights at low frequency was increased to consider robustness at low frequency range too, but the weights at low frequency should be less than one.

$$W_3 = \frac{s+50}{10^{-3}s+100} \tag{10}$$

D. Weighting Function W_u

The weighting function W_u has its physical meaning that we would like to suppress frequency weighted control effort. The shape of the weighting function W_u is given in (11) and Fig. 6.

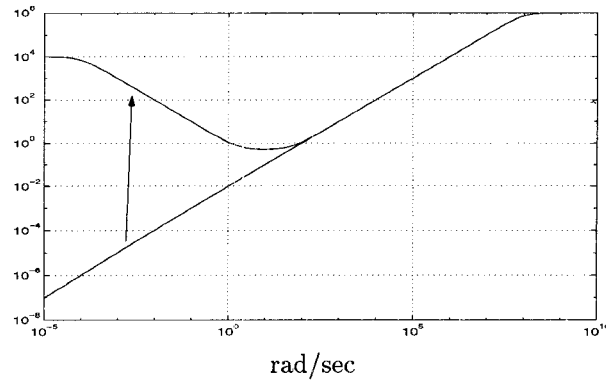


Fig. 6. Tuning of weighting function W_u

$$W_u = \frac{(0.5s+1)(0.02s+1)}{(s+10^{-4})(s+10^{-8})} \tag{11}$$

The reason why the weights at the frequency range below 0.5 rad/sec was increased is that the controller should be insensitive to the signal below 0.5 rad/sec.

V. Description of the Simulator

Fig. 7 shows the structure of the simulator. In the experiment of Case 1, switch S_1 was opened and reclosed to generate disturbances.

Though electric loads can be modeled both at the generator side and at the infinite bus side, only the load in the infinite bus side was connected for the experiment.

The exciter is digital type developed by Korea Electrotechnology Research Institute(KERI) and Korea Heavy Industry. AVR is PI type whose parameters are given by (12).

$$AVR = (K_{PR} + \frac{K_{IR}}{s}), \tag{12}$$

where $K_{PR} = K_{IR} = 6$.

VI. Experimental Results

As the PSS should work in the wide range of operating points, the designed PSS has been tested in three operating conditions. The different operating points were decided by generation level as given by Table 1. The experimental results shows that the PSS does not affect transient stability. In the case of voltage regulating property, the performance has been degraded only in Case 1.

A. Case 1 : when real power is 0.88 pu

The generator is weakly coupled with power systems when generation level is high. the system is transiently

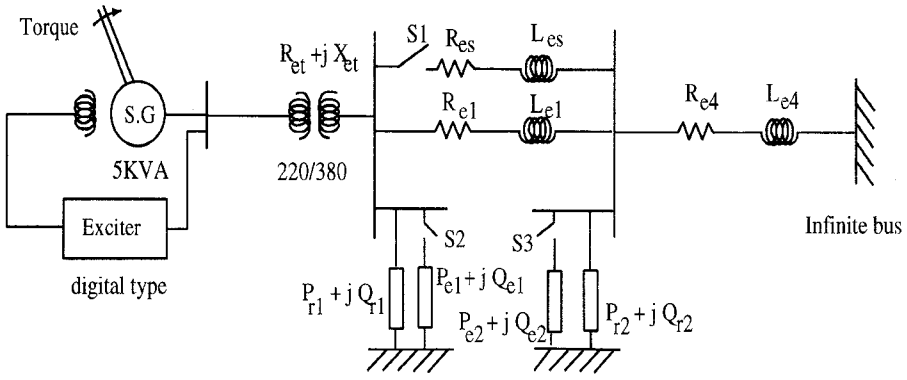


Fig. 7. Structure of the experimental system

TABLE 1

TEST OPERATING POINTS AND DISTURBANCE TYPE

	case 1	case 2	case 3
P(pu)	0.88	0.5	0.2
Q(pu)	0.1	0.08	0.1
disturbance type	one-line open and close	line-to-ground fault(0.1sec)	line-to-ground fault(0.1sec)

unstable due to the one-line-to-ground fault when generation level is 0.88 pu. Therefore disturbance of the system was modeled by one-line open and re-close. Fig. 8 shows the experiment results of real power and terminal voltage. In the experiment, the opened line was re-closed at 4.7 seconds when PSS was not applied, and at 3.95 seconds when PSS was applied. The voltage regulating performance was degraded by the application of PSS in this case, but power oscillation has been improved considerably.

B. Case 2 : when real power is 0.5 pu

The generator is coupled with the power systems stronger than Case 1. The disturbance was modeled by one-line-to-ground fault for 0.1 seconds, because the system is transiently stable against the one-line-to-ground fault for 0.1 seconds. Fig. 9 shows the experimental results of real power and terminal voltage. The voltage regulation property was not degraded in this case.

C. Case 3 : when real power is 0.2 pu

The disturbance was modeled by one-line-to-ground fault for 0.1 seconds as in Case 2. Fig. 10 shows the experimental results of real power and terminal voltage. The voltage regulation property was not degraded, either.

VII. CONCLUSION

H_∞ optimization method has been applied to the PSS design. Performance index, basic weighting functions, and a tuning method was proposed for this purpose. To test the robustness of the designed PSS, experiment was conducted over three operating points with generation levels of 0.88 pu, 0.5 pu, and 0.2 pu, respectively.

ACKNOWLEDGMENT

The authors would like to express our sincere thanks to Korea Heavy Industry & Construction Corporation for technical advice and financial support.

REFERENCES

[1] F.P. Demello and C. Concordia, "Concepts of Synchronous Machine Stability as Affected by Excitation Control", IEEE Transactions on Power Apparatus and Systems, Vol. PAS-88, No. 4, April 1969, pp. 316-329.

[2] E.V. Larsen and D.A. Swann, "Applying Power System Stabilizers: Part *I*: General Concepts", IEEE Transactions on Power Apparatus and Systems, Vol. PAS-100, No. 6 June 1981, pp. 3017-3024.

[3] E.V. Larsen and D.A. Swann, "Applying Power System Stabilizers: Part *II*: Performance Objectives and Tuning Concepts", IEEE Transactions on Power Apparatus and Systems, Vol. PAS-100, No. 6 June 1981, pp. 3025-3033.

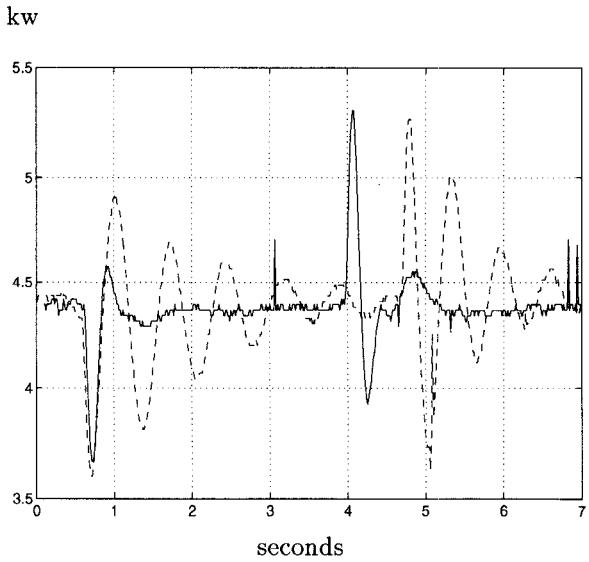
[4] E.V. Larsen and D.A. Swann, "Applying Power System Stabilizers: Part *III*: Practical Considerations", IEEE Transactions on Power Apparatus and Systems, Vol. PAS-100, No. 6 June 1981, pp. 3034-3046.

[5] M.L. Crenshaw, et. al., "Excitation System Models for Power System Stability Studies", IEEE Committee Report, IEEE Transactions on Power Apparatus and Systems, Vol. PAS-100, No. 2, February 1981, pp. 494-501.

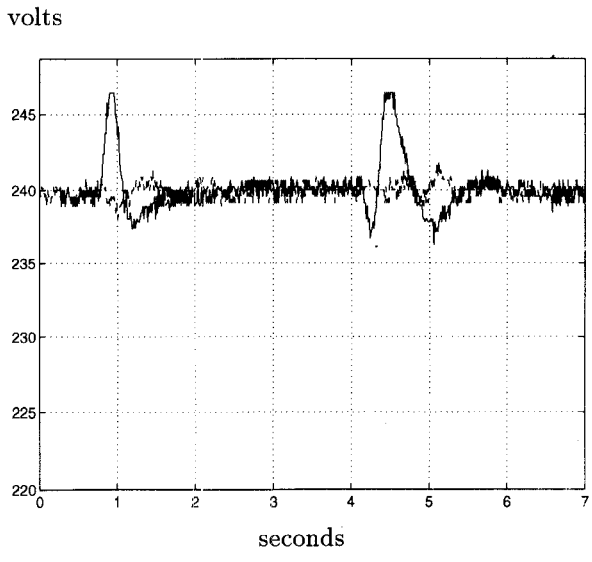
[6] P. Kundur, M. Klein, G.J. Rogers, and M.S. Zywno, "Application of Power System Stabilizers for Enhancement of Overall System Stability", IEEE Transactions on Power Systems, Vol. 4, No. 2, May 1989, pp. 614-626.

[7] J.H. Chow, L.P. Harris, M.A. Kale, and H. Othman, "Robust Control Design of Power System Stabilizers Using Multivariable Frequency Domain Techniques", International Journal of Robust and Nonlinear Control, Vol. 2, 1992, pp. 123-138.

[8] B.A. Francis, *Lecture Notes in Control and Information Sciences : A Course in H_∞ Control Theory*, Springer-Verlag, New York, USA, 1987.

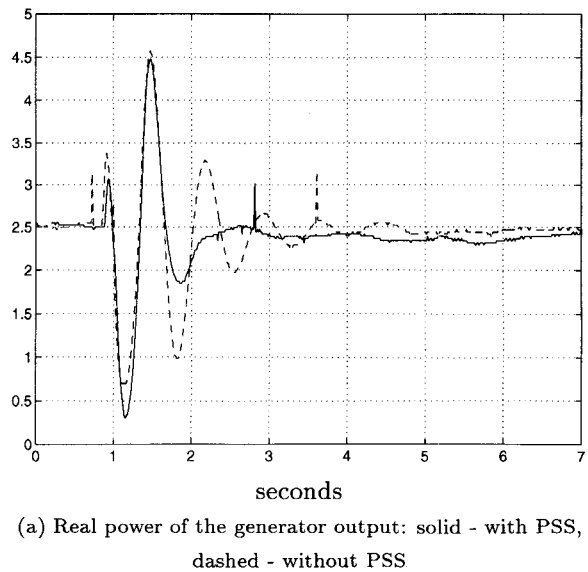


(a) Real power of the generator output: solid - with PSS, dashed - without PSS

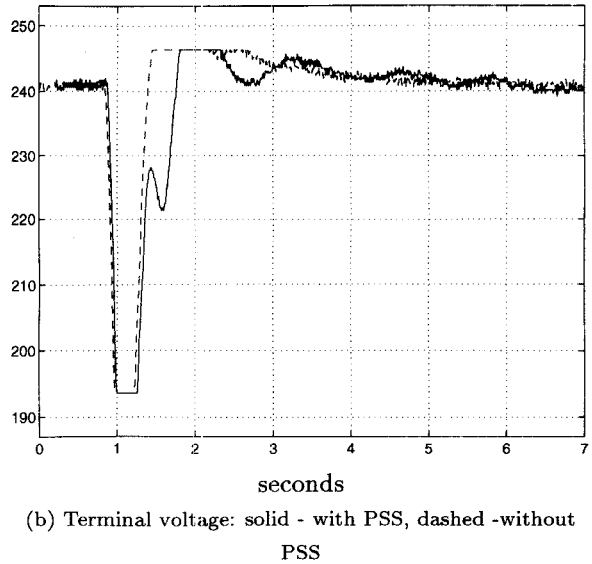


(b) Terminal voltage: solid - with PSS, dashed -without PSS

Fig. 8. Case 1 : Real power and terminal voltage ($P = 0.88, Q = 0.1$)



(a) Real power of the generator output: solid - with PSS, dashed - without PSS



(b) Terminal voltage: solid - with PSS, dashed -without PSS

Fig. 9. Case 2 : Real power and terminal voltage ($P = 0.5, Q = 0.08$)

[9] K. Glover and J. Doyle, "State-space formulae for all stabilizing controllers that satisfy an H_∞ norm bound and relations to risk sensitivity", Systems and Control Letters 11, 1988, pp 167- 172.

[10] J. Doyle, K. Glover, P. Khargonekar, and B. Francis, "State-space solutions to standard H_2 and H_∞ problems", IEEE Transactions on Automatic Control, vol. 34, no. 8, 1989, pp. 831-847.

[11] J. Doyle, B.A. Francis, and A.R. Tannenbaum, *Feedback Control Theory*, Macmillan, 1992.

[12] J.M. Maciejowski, *Multi-variable Feedback Design*, Addison Wesley, 1989.

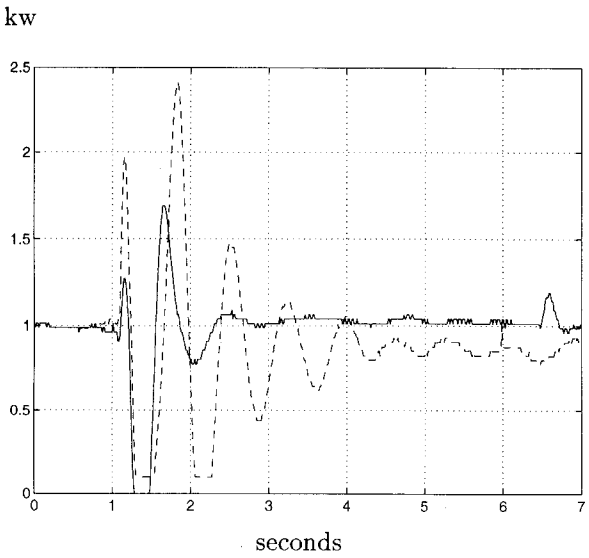
[13] J. Sefton and K. Glover, "Pole/zero Cancelations in the General H_∞ Problem with Reference to a Two Block Design", Systems and Control Letters 14, 1990, pp. 295-306.

[14] Y.H. Chun and Yoichi Hori, "On Decision of the Performance Index and the Weighting Functions for the Application of H_∞ Optimization Method to Servo Systems", Submitted to IEEE/ASME Transactions on Mechatronics, 1996.

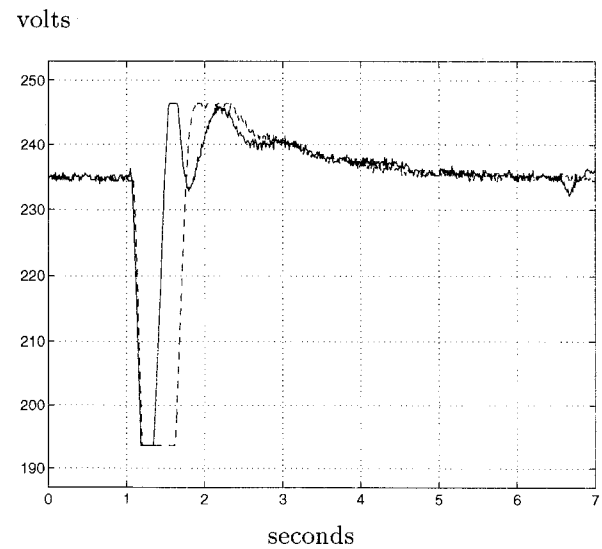
[15] R.Y. Chiang and M.G. Safonov, "Real K_m-synthesis via generalized Popov multipliers", ACC/TP9, 1992, pp. 2417-2418.

[16] H. Kwakernaak , "Robust Control and H_∞ Optimization - Tutorial Paper", Automatica, Vol. 29, No. 2, 1993, pp. 255-273.

[17] H. Kwakernaak, "Progress in the Polynomial Solution of the Standard H_∞ Optimal Control Problem", the 11th IFAC World Congress, Vol. 5, 1990, pp. 122-129.



(a) Real power of the generator output: solid - with PSS, dashed - without PSS



(b) Terminal voltage: solid - with PSS, dashed - without PSS

Fig. 10. Case 3 : Real power and terminal voltage ($P = 0.2, Q = 0.1$)

[18] G.J. Balas and J.C. Doyle, "Robustness and Performance Trade-Offs in Control Design for Flexible Structures", IEEE Transactions on Control Systems Technology, Vol. 2., No. 4, December 1994, pp. 352-361.

[19] G.J. Balas, J.C. Doyle, K. Glover, A. Packard, and R. Smith, *μ-Analysis and Synthesis Toolbox : User's Guide*, MuSyn Inc., Minneapolis MN, USA, 1991.

[20] R.A. Hyde, *The Application of Robust Control to VSTOL Aircraft*, Ph.D. Dissertation, Girton College, Cambridge, 1991.

[21] Y. Hori, "Comparison of Vibration Suppression Control Strategies in 2-mass system Including a Novel Two-Degree-of-Freedom H_∞ Controller", IEEE 2nd AMC Workshop, 1992, pp. 409-416.

[22] H.S. Lee and M. Tomizuka, "Robust High-Speed Servo-Controllers for Micro positioning Systems", IEEE AMC Workshop, 1994, pp. 633-642.

[23] Y.H. Chun and Y. Hori, "Rolling Mill Controller Design with H_∞ Sensitivity Minimization", ASCC, vol. 2, 1994, pp. 629-632.

[24] Y.H. Chun and Y. Hori, "A Unifying Design of H_∞ Controller and PI Speed Feedback for High Precision Position Control of Flexible System", KACC international session, 1994, pp. 553-556.

[25] Y.H. Chun and Y. Hori, "On Weighting Functions for H_∞ Controller and Its Experiment of 2-mass System with Low Frequency Resonance", Proceedings of IFAC Motion Control, Munchen, 1995, pp. 165-172.

D.C. Power System for Superconducting Fusion Test Facility LHD

H. Chikaraishi, S. Tanahashi, S. Yamada, O. Motojima,
T. Satoh* , H. Niwa*, T. Uede** and Hiue**
National Institute for Fusion Science
Oroshi 322-6, Toki-shi, Gifu, 509-52, Japan
Fax: +81-572-58-2616, Phone: +81-572-58-2130, Email: hchikara@nifs.ac.jp
* Aichi Electric Co., Ltd, Kasugai, Aichi, Japan,
** Fuji Electric Co., Ltd, Ichihara, Chiba, Japan

Abstract — **The Large Helical Device (LHD) is a fusion plasma test facility that has three sets of superconducting helical coils and three sets of superconducting poloidal coils. This paper introduces a power system to excite these coil. The system consists of large current thyristor rectifiers, quench protection circuits, control system and superconducting dc power feeders. Several components are developed for this power system. A dc circuit breaker using a small power fuse and a vacuum circuit breaker realize a compact and low cost quench protection circuit. Superconducting dc power feeder, that joins power supply and a coil, moves a large cryogenic joint box to far away from LHD main structure.**

Introduction

In these years, large scale superconducting coils are researched for fusion test facilities such as the Large Helical Device (LHD) that is just constructing in National Institute for Fusion Science (NIFS) in Japan [1]. As the result, 1 GJ class superconducting magnets using 30 kA class cable are developed and constructed.

Regarding to the power supplies to excite these coils, 6 dc power supplies for steady state excitation are constructed and setting in the main experimental building. Superconducting flexible dc feeders, that capacity is 32 kA and 2 kV, are now constructing and setting to join coils and power supplies.

In these power supplies, new type of 30 kA class dc opening switch, that consists of a small vacuum breaker and power fuses, is used for quench protection circuit. The prototype of this switch is tested and confirmed its operation but there may be difference between actual circuit and prototype in such as large current system. Therefore a reliability tests using actual quench protection circuits are executed in 1995 and 1996.

In following sections, first we will introduce the outline of LHD. Next, the power supplies, they consist of thyristor rectifiers, quench protection systems and superconducting power feeders are introduced. Finally, the result of reliability test of protection system is described.

I. Out Line of the LHD

The LHD is a helical type fusion device which is a kind of magnetic confinement type fusion device. In this type, all of magnetic field is generated by coil currents and it doesn't need any plasma current and every magnets generate only static field with dc current Therefore this device can operate in steady state. From view point of magnets, this is very suitable for application of superconducting materials because dc operation leads high current density and small power consumption in conductors. At the same time, the using of superconducting magnets remove ohmic heat generation that limits steady state operation of high field magnets. With these reason, the all of the magnets in LHD are wound with superconducting cable.

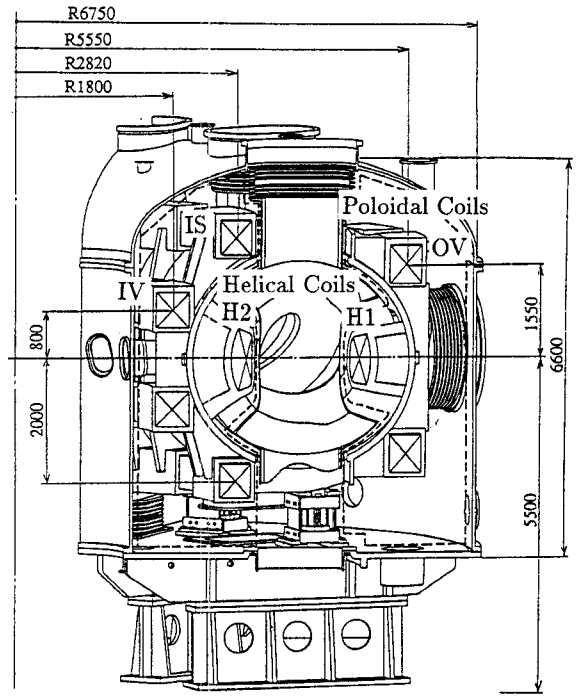


Fig. 1. Cross-section of the Large Helical Device (LHD), Which is a Fusion Plasma Test Facility using Superconducting Coils.

Figure 1 shows a cross section of the LHD. As this figure shows, the LHD has 3 poloidal coil sets , which are designated as OV, IS and IV, and 2 helical coils, which are designated as H1 and H2. These poloidal field coils are wound with NbTi CICC cable and helical coils are wound with pool boiling NbTi cable. Each helical coil is divided in 3 blocks which designated as HI, HM and HO. Usually, corresponding blocks of H1 and H2 coils are connected in series and form 3 helical coils sets. Table I shows a current ratings and self inductance of these coils.

0-7803-3823-5/97/$10.00© 1997 IEEE

TABLE I. Current Ratings and Self Inductance of Superconducting Coils for LHD.

	HO	HM	HI	OV	IS	IV
For first phase of 3 T operation [kA]	13.0	13.0	13.0	23.5	16.3	15.7
For second phase of 4 T operation * [kA]	17.3	17.3	17.3	31.3	21.7	20.9
Self Inductance [H]	1.38	1.31	1.30	1.24	0.95	0.74

* Helical coils will be sub-cooled by 1.8 K helium for this operation.

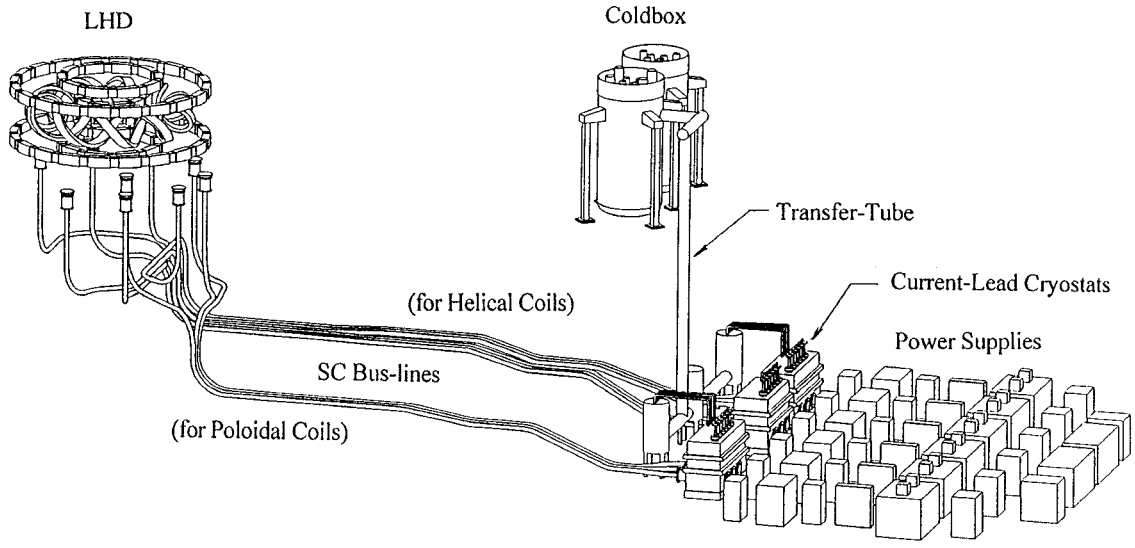


Fig. 2. Bird View of LHD Coil Power System.

TABLE II. Coil Currents for LHD Operation in First Phase. [kA]

	1-o	1-a	1-b	1-c	1-d
HI,HM,HO	13.0				
OV	-20.4	-22.7	-18.2	-19.6	-21.2
IS	-5.2	5.6	-16.0	-6.8	-3.5
IV	10.7	6.2	15.2	8.1	13.4

Figure 2 shows a bird view of LHD coil power systems. The dc power supplies are set about 50 m far from LHD. The superconducting dc feeders connect these power supplies and superconducting coils of LHD.

II. DC POWER SUPPLIES FOR LHD SUPERCONDUCTING COILS

Figure 3 shows a diagram of dc power supplies for steady state excitation of poloidal and helical field coils. This figure contains thyristor rectifiers, dc filters, quick dump circuit, quench protection subsystems and polarity change units.

Table II shows typical coil operation currents of LHD in first experiment phase. It shows that the coil currents flow in uni-direction expect the IS coil, so the power supplies are based on single rectifier. For the IS coil, the current reverses in mode 1-a only and mode change does not so often. Therefore, a mechanical cross switch is used to reverse a current in mode 1-a.

Table III shows specifications of these power supplies for steady state excitation of superconducting coils.

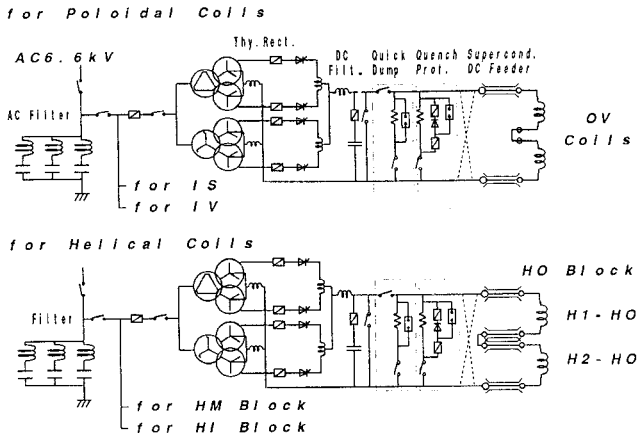


Fig. 3. Circuit Diagram of Power Supplies for LHD.

TABLE III. Specifications of dc power supplies for LHD.

	HO–HI	OV	IS	IV
Voltage [V]	45	33	33	33
Current [kA]	17.3	23.5 (31.3 *)	16.3 (21.7 *)	15.7 (20.9 *)
Voltage ripple	less than 0.5 V			

Current accuracies for all Power supplies	
Measurement error	0.03% of reading value + 4.5A
Control error	0.04% of set value + 6A

(*) indicates the output current for second phase plasma experiments.

TABLE IV. Specification of Superconducting Power Feeder

Item	Specifications
Numbers of power feeders	9
Rated current	32kA
Rated withstanding voltage	5kV at 77K Helium gas
Minimum bending radius	1.5m
Length	45.7-58m
Heat load	0.3 W from 80 K to 4.2K , 3 W from room temp. to 80K

III. Superconducting Power Feeder

In the LHD, cryo junction boxes, that connect superconducting coils and room temperature cables, must be set near the power supplies because of limitation of space and leakage magnetic flux. Therefore, a flexible dc superconducting power feeder is developed [2]. In this section, this feeder is introduced.

Figure 4 shows a configuration of this power feeder. This feeder consist of coaxial five corrugated stainless tubes and a pair of aluminum stabilized NbTi superconducting cable. Because the positive and negative lines are bound tight with small gap and packed in same tube, the leakage magnetic flux, which disturbs plasma confinement, is suppressed to small enough and the electromagnetic force generated by cable is canceled. As shown the figure, liquid helium cools the cables in the center tube and return through a channel configured with inner and next tubes. This return gas make thermal shield between 80K layer and cables, that reduces heat load into the cables. Table IV shows specifications of this cable.

In the LHD operation, it is required that these cables must operate stable while superconducting coils are excited even if helium refrigerator stopped. With this reason, the cables have much aluminum around superconducting wire that can work as a electrical current path and thermal heat sink in a short time. When coil quench protection, which is introduced in next section, works, the coil terminal voltage rises to about 2 kV. If break down is occurs in the cable, the current dump and quench protection becomes impossible. Therefore, higher insulation strength is required in table IV and break down tests with short sample confirm the insulation strength.

As the table shows, this cable can be bent in small radius of 1.5 m when it is carried. With this merit, these cables are built in factory, wound on the drum, carried to facility and set in the building. By using this flexible superconducting feeder, necessary space for setting of feeder is much reduced than copper feeder.

IV. Reliability Test of Quench Protection System

The quench protection circuit is a most important component for a power supply exciting super conducting magnets. Especially, dc circuit breaker is a key device. For this purpose, a novel dc circuit breaker using power

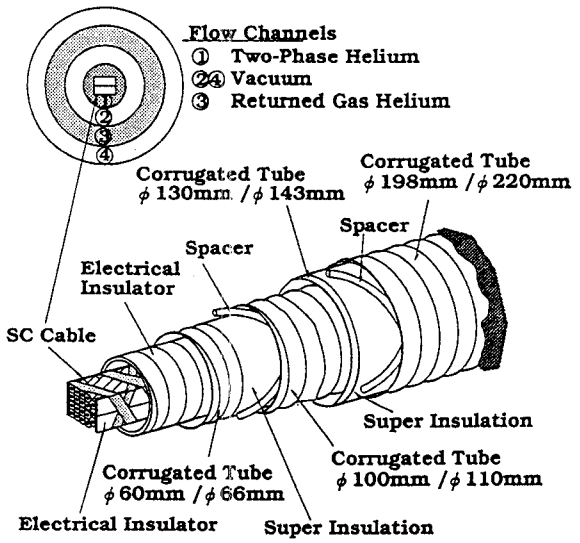


Fig. 4. Configuration of a Flexible Superconducting DC Feeder

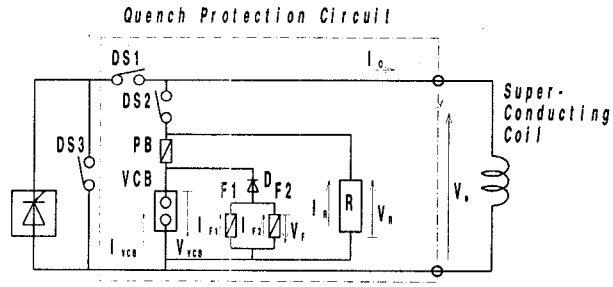


Fig. 5. Diagram of Quench Protection Circuit for OV Power Supply

fuse is developed and tested with model circuit [3]. In the large current circuit, difference of leakage inductance between model and actual circuit may affect operation. With this reason, every quench protection circuit in the actual power supply must be tested. This section describe the quench protection circuit and its reliability tests.

Figure 5 shows the detail of OV quench protection circuit. In this figure, VCB is an ac vacuum circuit breaker and F is a relatively small power fuse with a current rating that is about 3% of the coils. From DS1 to DS3 are disconnectors that have no ability to break the current. R is a dump resistor. The diode serial connected to the fuse blocks the current by dropping forward before VCB opens to avoid preheating of the power fuse. In the figure, PB is a backup pyro-breaker that is triggered and forces commutation to the external resistors if the previous sequence fails.

In this test, a load coil, which has enough inductance and low resistance, is required to keep output current while protection sequence is running. For this purpose, a liquid nitrogen cooled copper coil is built and used as a dummy load coil.

In the beginning of the experiments, a trouble, that a rush current flows through DS2 when it closes, is found out. To suppress this rush current, modification quench

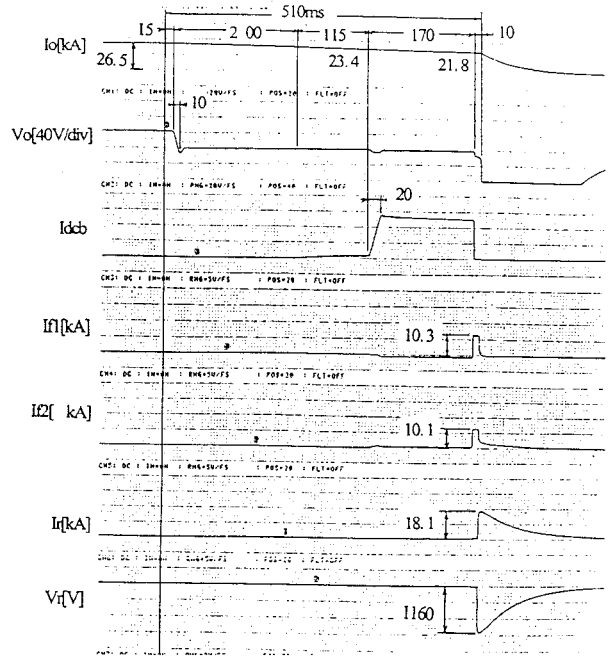


Fig. 6. Experimental Waveforms of Coil Current and Voltage

protection sequence is done. At the same time arcing contacts are installed in DS2. After these correction, no rush current is observed. Finally, the operation sequence is fixed as follows;

1. The dc power supplies turns its output voltage to 0V and DS2 close
2. The dc power supplies generate negative voltage. With this operation, the current flowing in power supplies is transferred to DS2 and VCB.
3. After a short time, the power supply current through DS1 becomes zero; then DS1 opens.
4. VCB opens and the main current is commutated to the power fuse with low voltage.
5. The power fuse melts and opens, then all currents commutate to the dump resistor. At this step, the terminal voltage rises to 2 or 3 kV, but it stays within the rating of the power fuse.

Figure 6 shows one of experimental diagrams of current and voltage waveforms in quench protection. This figure points out that the applied voltage to the VCB is less than 20 V for only 10 ms, the fuse current is zero before the VCB opens, and after the fuse breaks the coil voltage rises to 1.16 kV. By this result, the performance of this dc breaker and reliability are confirmed. This figure shows the above sequence is finished within 510 milliseconds after quench protection signal and it satisfies a request that opening delay must be less than 1 second.

We made 200 shots of operation tests without failure for OV power supplies. Also 100 shots are made for IS and IV power system.

Figure 7 shows melting time of fuses and opening delay of this dc circuit breaker. The opening delay and fuse melt time increase when operating current becomes

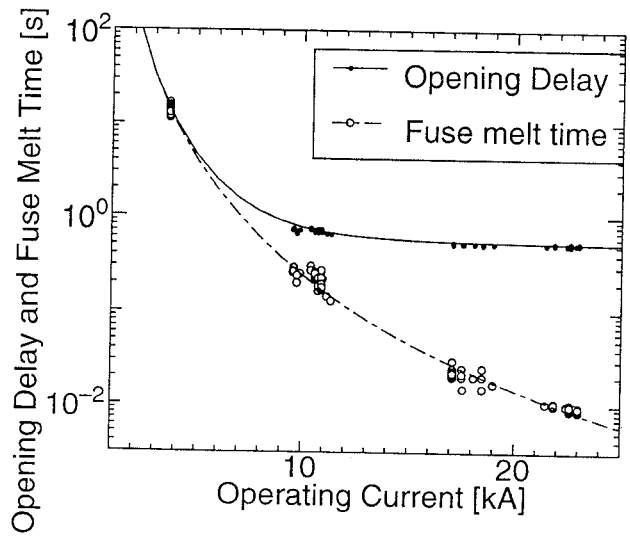


Fig. 7. Melting and Opening delay

small. This points out that this circuit breaker does not suitable for quench protection in small current less than 10% of rating. Therefore other protection method should be considered for the low operating current region. In the LHD, dumping circuit with lower dump resistors and air circuit breaker shown in figure 3 are used in low current region.

At the end of the experiments, a dc current break test with DS1 was performed to confirm the protection in the event that the power supplies or electrical network failed. As a result, we confirmed that DS1 is able to break the dc current of rating, but the arc burns the conductors and they must be replaced after this operation.

V. Conclusions

This paper introduces the outline of power system of the LHD fusion plasma test facility. The flexible dc superconducting power feeder and a dc circuit breaker are successfully developed for this system. In the reliability test for quench protection circuit, total of 400 shots using actual poloidal power supplies are finished in several operation current without any failure.

References

[1] M. MOTOJIMA et al., "Physics and engineering design studies on the LHD", *Fusion Eng. and Design*, vol. 20, pp. 3-14, Jan. 1993

[2] S.YAMADA et al., " Superconducting current feeder system for the Large Helical Device", *IEEE Trans on Mag.*, Vol.32 (Supplement of MT14), 1996

[3] S. TANAHASHI et al., "Design study of power supplies for LHD superconducting magnets", *Fusion Eng. and Design*, vol. 20, pp. 107-111, Jan. 1993

The Design of Control Configuration of Variable Speed Generator System

Yuzo ITOH and Nobuhito NOZAWA

Division of System and Information Engineering,
Faculty of Engineering, Hokkaido University

North 13 West 8, Kita-ku, Sapporo 060 JAPAN

Telephone: +81-11-706-6465 Facsimile: +81-11-706-7890

E-mail address: yuzo@e2.hines.hokudai.ac.jp

Abstract —**In this paper a new designing method for Variable Rotating Speed Generator System (VSGS) is presented. On the other hand the rotor speed of the traditional Synchronous generator system is exactly regulated to the power system frequency by the manner of mechanical governor control, VSGS has no necessity of frequency controlling by a mechanical control system. The machine emplyed in VSGS is a wound type induction machine.**

Nowadays, VSGS is applied for the pumped storage generator system which elevates a running efficiency. And the system with large rotating inertia is used to improve the stability for the step load variation in the power system. As the other utilization, it can be applied for wind turbine system and asynchronous rotary machine which can provide not only electrical reactive power but active power. So, a variable speed generator will be more used as the device of Flexible AC Transmission System (FACTS). For those application of VSGS, the stable and quick response for the system references and step change of power output are required. In order to obtain the steady and transient state behavior of VSGS, the instantaneous vector analysis is employed. To design control system for VSGS, a developed optimal control theory is applied.

The system response of VSGS designed by the proposed method is simulated and is experimented on the case of constant generating mode while the shaft input is increasing. Finally, the effectiveness of the proposed control method for variable speed generator system is confirmed.

I. INTRODUCTION

Variable speed generator system, VSGS, has been gradually applied for a pumped-storage generator system[1] in order to use a surplus electric power efficiently. And it could be utilized for wind turbine generator[2].

The another use of VSGS which is mounted fly-wheel in shaft is proposed. Its system[3] can store and discharge electrical energy as the kinetic energy. Therefore, VSGS is expected to be developed to the important device of FACT.

The VSGS has some merits compared with synchronous generator system and AC generator system. Some of them is listed as follows;

(1) The governor system can be designed loosely against load variation.

(2) The output rating of the power conversion system is less than that of secondary exciting power system.

On the other hand, VSGS has a demerit that the secondary copper loss increases in the out of synchronous speed. The new designing method for VSGS[4] which makes utilization for power generating system possible is proposed.

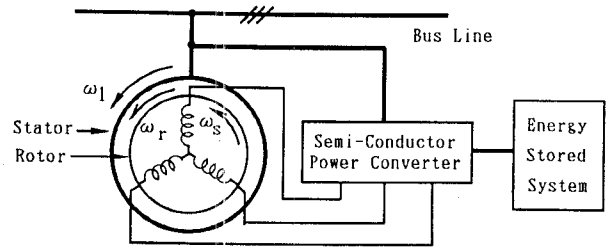


Fig. 1. Variable speed generator system

II. BASIS OF VSGS

The outline of VSGS is shown in Fig. 1. The shaft input torque is supplied and the generated power is sent electrical power system through the stator of induction machine. Secondary excitation is driven by PWM inverter. As the energy storage device, a battery or a fly-wheel system for small power system can be assumed and SMES for huge power system. The maximum of power generating, Pmax, is decided by output rating of stator side of induction machine and the shaft input, Pm, or the rating output power of exciting system, P_2, are smaller than Pmax.

III. MODELING AND DESIGN OF VSGS

In order to solve not a steady state but a transient state, the equation of three phase induction machine is transformed to two phase machine and replaced to that of rotating d-q axis machine.

$$\begin{bmatrix} v_{1d} \\ v_{1q} \\ y_{2d} \\ v_{2q} \end{bmatrix} = \begin{bmatrix} r_1+pL_1 & -\omega_1 L_1 & pM \\ \omega_1 L_1 & r_1+pL_1 & \omega_1 M \\ pM & -\omega_s M & r_2+pL_2 \\ \omega_s M & pM & \omega_s L_2 \end{bmatrix} * \begin{bmatrix} -\omega_1 M \\ pM \\ -\omega_s L_2 \\ r_2+pL_2 \end{bmatrix} * \begin{bmatrix} i_{1d} \\ i_{1q} \\ i_{2d} \\ i_{2q} \end{bmatrix} \quad (1)$$

Where, all machine impedance are converted to d-q component.

In order to use the idea of vector control of induction motor, a primary linkage flux ϕ_1 is introduced and is shown in (2).

$$\phi_1 = L_1 i_1 + M i_2 = \phi_{1d} + j\,\phi_{1q} \tag{2}$$

Substituting (2) to (1), the relation of d-q components flux are obtained as (3).

$$\begin{aligned} \frac{d}{dt}\phi_{1d} &= v_{1d} - r_1 i_{1d} + \omega_1 \phi_{1q} \\ \frac{d}{dt}\phi_{1q} &= v_{1q} - r_1 i_{1q} - \omega_1 \phi_{1d} \end{aligned} \tag{3}$$

In steady state, the term of the left side becomes to be zero. The relation between d-q component current and d-q component primary flux ϕ_1 is decided because the stator side voltage is linked to that of power system. In order to express system variables in electrical variables, the primary flux ϕ_1 is defined by using a flux producing current i_n as (4).

$$\phi_1 = L_1 i_1 + M i_2 = L_1 i_n \tag{4}$$

Finally, the state variable equations on an electrical system are shown in (5).

$$\frac{d}{dt}\begin{bmatrix} i_{nd} \\ i_{nq} \\ i_{2d} \\ i_{2q} \end{bmatrix} = \begin{bmatrix} -\frac{r_1}{L_1} & \omega_1 & \frac{r_1 M}{(L_1)^2} & 0 \\ -\omega_1 & -\frac{r_1}{L_1} & 0 & \frac{r_1 M}{(L_1)^2} \\ \frac{r_1 M}{\delta L_1} & -\frac{\omega r M}{\delta} & -\frac{R}{\delta} & \frac{\omega_1 - \omega r}{\delta} \\ \frac{\omega r M}{\delta} & \frac{r_1 M}{\delta L_1} & -\frac{\omega_1 - \omega r}{\delta} & -\frac{R}{\delta} \end{bmatrix}$$

$$\begin{bmatrix} i_{nd} \\ i_{nq} \\ i_{2d} \\ i_{2q} \end{bmatrix} + \begin{bmatrix} 0 & 0 \\ 0 & 0 \\ \frac{1}{\delta} & 0 \\ 0 & \frac{1}{\delta} \end{bmatrix} \begin{bmatrix} v_{2d} \\ v_{2q} \end{bmatrix} + \begin{bmatrix} \frac{1}{L_1} & 0 \\ 0 & \frac{1}{L_1} \\ \frac{-M}{\delta L_1} & 0 \\ 0 & \frac{-M}{\delta L_1} \end{bmatrix} \begin{bmatrix} v_{1d} \\ v_{1q} \end{bmatrix} \tag{5}$$

Where, $R = r_2 + r_1 (M/L_1)^2$, $\delta = L_2 - M^2/L_1$.

The mechanical equation is presented in (6).

$$\frac{d}{dt}\omega r = \frac{1}{J}\tau - \frac{1}{J} Dr\,\omega r - \frac{1}{J}\tau_{in} \tag{6}$$

Where, ωr is angular velocity of rotor, τ_{in} is shaft input torque, τ shown in (7) is shaft output torque which is equivalent to the power generating, J is moment inertia and Dr is damping coefficient of rotor.

$$\tau = PM\,(i_{nq} i_{2d} - i_{nd} i_{2q}) \tag{7}$$

<Active power and reactive power>

The instantaneous active and reactive power Pe and Pr represented in d-q axis domain are shown in (8) and (9).

$$Pe = v_{1d} i_{1d} + v_{1q} i_{1q} \tag{8}$$

$$Pr = v_{1q} i_{1d} - v_{1d} i_{1q} \tag{9}$$

Provided that the same shall not apply to Pr in transient state.

If the primary voltage v_1 is coincident to d component voltage v_{1d}, q component voltage v_{1q} becomes to be zero. After all, the desired value of active and reactive power, Pe^* and Pr^*, are shown in (10).

$$Pe^* = v_{1d} i_{1d}, \quad Pr^* = -v_{1d} i_{1q} \tag{10}$$

From (1), power factor $\cos\phi$ is given in (11).

$$\cos\phi = Pe^* / \sqrt{(Pe^{*2} + Pr^{*2})} \tag{11}$$

The desired value of d component current i_{1d}^* which produces Pe^* is calculated as (12).

$$i_{1d}^* = Pe^* / v_{1d} \tag{12}$$

The desired value of q component current i_{1q}^* which produces Pr^* is presented in (13).

$$i_{1q}^* = \pm \sqrt{1 - \cos^2\phi^*} \cdot i_{1d}^* / \cos\phi^* \tag{13}$$

(+ : phase lagging, − : phase leading)

On the case of designing the control structure of VSGS by using the primary current references, i_{1d}^* and i_{1q}^*, a quick response of system cannot be obtained for the sake of the long time constant of primary side of VSGS. Therefore, i_{1d}^* and i_{1q}^* had better to be changed to new variables. By using (4), new current references, i_{2d}^* and i_{2q}^*, are chosen.

$$\begin{aligned} i_{2d}^* &= (L_1/M)\quad (i_{nd} - i_{1d}^*) \\ i_{2q}^* &= (L_1/M)\quad (i_{nq} - i_{1q}^*) \end{aligned} \tag{14}$$

The modeling of VSGS (15) is obtained by substituting (6) to (5). From (15), it is found that the order of system is 5 and system input and output are 2, respectively. The explanation of the system coefficient matrix A_c, input coefficient matrix B_c and disturbance matrix E_c are omitted by the space assigned.

$$\begin{aligned} \frac{d}{dt} x(t) &= A_c x(t) + B_c u(t) + E_c d(t) \\ y(t) &= C x(t) \end{aligned} \tag{15}$$

where, $x(t) = [\omega r(t) \quad i_{nd}(t) \quad i_{nq}(t) \quad i_{2d}(t) \quad i_{2q}(t)]^T$

$u(t) = [v_{2d}(t)\, v_{2q}(t)]^T$, $u(t) = [\tau_{in}(t)\, v_{1d}(t)\, v_{1q}(t)]^T$

$y(t) = [i_{2d}(t)\, i_{2q}(t)]^T$

$$C = \begin{bmatrix} 0 & 0 & 0 & 1 & 0 \\ 0 & 0 & 0 & 0 & 1 \end{bmatrix}$$

In the state variable equation (15), the reason why the shaft

input torque $\tau_{in}(t)$ is chosen as a system disturbance is presented as follows;

We can design VSGS which can control the power generating without a precise governor system that regulates the shaft input torque. In addition, such an idea is able to be applied for wind turbine generator system.

After linearizing (15), the discreet system equation (16) is obtained by substituting system parameters and the sampling period Ts.

$$X(k+1)=AX(k)+Bu(k-1)+Ed(k)$$
$$y(k)=CX(k) \tag{16}$$

Where,

$X(k)=[\omega_r(k)\ i_{nd}(k)\ i_{nq}(k)\ i_{2d}(k)\ i_{2q}(k)]^T$

$u(t)=[v_{2d}(k)\ \ v_{2q}(k)]^T$, $d(t)=[\tau_{in}(k)\ \ v_{1d}(k)\ \ v_{1q}(k)]^T$

$y(t)=[i_{2d}(k)\ \ i_{2q}(k)]^T$.

In (16), the delay time caused by control algorithm processing time is considered as one sampling time.

On designing control system, error system technique[5] based on optimal regulator theory which guarantees a stable response and no steady deviation for MI/MO system is used.

The relation between desired signal $R(k)$ and output signal $y(k)$ of the controlled object, $e(k)$ is shown in (17).

$$e(k)=R(k)-y(k) \tag{17}$$

The first difference equation concerning state variables and input variables is presented in (18).

$$\begin{aligned}\Delta X(k+1)&=A\Delta X(k)+B\Delta u(k-1)+E\Delta d(k)\\ \Delta e(k+1)&=\Delta R(k+1)-CA\Delta X(k)\\ &\quad -CB\Delta u(k-1)-CE\Delta d(k)\end{aligned} \tag{18}$$

Where,

$\Delta X(k)=[\omega_r(k)-\omega_r(k-1),\ i_{nd}(k)-i_{nd}(k-1),\ i_{nq}(k)-i_{nq}(k-1),$

$i_{2d}(k)-i_{2d}(k-1),\ i_{2q}(k)-i_{2q}(k-1)]^T$

$\Delta u(k)=u(k)-u(k-1)$, $\Delta y(k)=y(k)-y(k-1)$,

$\Delta d(k)=d(k)-d(k-1)$, $\Delta R(k)=R(k)-R(k-1)$.

From (18), a new equation (19), which is applicable to optimal regulator theory, is obtained.

$$\begin{bmatrix} Xo(k+1)\\ \Delta u(k)\end{bmatrix}=\begin{bmatrix}\Phi & G\\ 0 & 0\end{bmatrix}\begin{bmatrix} Xo(k)\\ \Delta u(k-1)\end{bmatrix}+\begin{bmatrix}0\\ Ir\end{bmatrix}\Delta u(k)$$
$$+\begin{bmatrix}G_R\\ 0\end{bmatrix}\Delta R(k+1)+\begin{bmatrix}G_d\\ 0\end{bmatrix}\Delta d(k) \tag{19}$$

Where,

$$Xo(k)=\begin{bmatrix}e(k)\\ \Delta X(k)\end{bmatrix},\quad \Phi=\begin{bmatrix}Im & -CA\\ 0 & A\end{bmatrix}$$

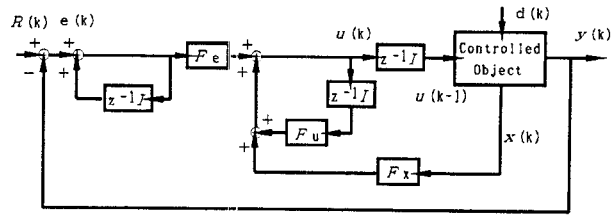


Fig. 2. The control structure

$$G=\begin{bmatrix}-CB\\ B\end{bmatrix},\quad G_R=\begin{bmatrix}Im\\ 0\end{bmatrix},\quad G_d=\begin{bmatrix}-CE\\ E\end{bmatrix}.$$

The optimal control input $\Delta u(k)$ is decided as (20) by solving optimal regulator problem.

$$\Delta u(k)=F_e e(k)+Fx\Delta X(k)+F_u\Delta u(k-1) \tag{20}$$

Where, Feedback gains $[F\ F_u]$ are determined by solving Riccati equation. From (20), control input for the real system is shown in (21). And the control structure is illustrated in Fig. 2.

$$u(k)=F_e\sum_{i=1}^{k}e(i)+FxX(k)+F_u u(k-1) \tag{21}$$

IV. EXPERIMENT AND SIMULATION

<Experimental set-up>

Block diagram of VSGS is shown in Fig. 3. The measured data is stored in the memory of computing system. In case of necessity, the graph of the transient state can be displayed on CRT monitor. To shorten the processing time, DSP (Digital Signal Processor) is used. Time of processing control algorithm is about a third of sampling time Ts (Ts=0.555 msec).

The system constants used on experiment and simulation are listed in Table I.

The optimal feedback gains based on the system constants can be computed by the method mentioned in the previous chapter.

<Experiment>

The system response on the case of shaft input torque of the step-up change is shown in Fig. 4. Pe* and Pr* are 160 W and 0 VAR, respectively. The shaft torque is transformed to the equivalent armature current of DC motor which is mounted to

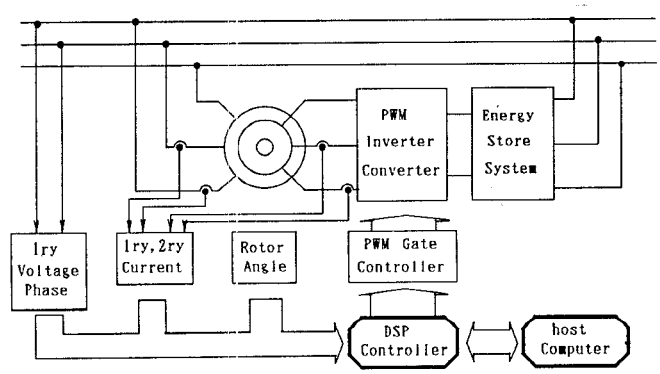


Fig. 3. Experimental set-up of VSGS

Table I Machine constants

Wound type induction motor:			
Output 1kW, 100V, 5.8A,4 poles, 50Hz			
Stator:	resistance	r_1	3.861 Ω
	self inductance	L_1	39.7 mH
	mutual inductance	M	38.7 mH
Rotor:	resistance	r_2	1.77 Ω
	self inductance	L_2	46.0 mH
moment inertia		J	0.077 Kg/m^2
damping factor		Dr	0.001 N·m·s/rad
Inverter input DC voltage		E	50.0V

VSGS shaft is changed in step. $i_{2d}{}^*$ and $i_{2q}{}^*$ are 4.7A and -4.3A. The initial speed of rotor is 1,000 rpm.

Though the speed of VSGS is gradually accelerated because of unbalance between input torque and output torque, the active power, Pe, and reactive power, Pr, are kept in accordance with the desired values. It is assumed that the rough of measured data is caused by PWM inverter driving in the secondary side.

<Simulation>

In Fig. 5, the result of simulation is shown. The condition of simulation are same as that of experiment. The result of system response is almost agree with that of experiment. The torque input is slightly small.

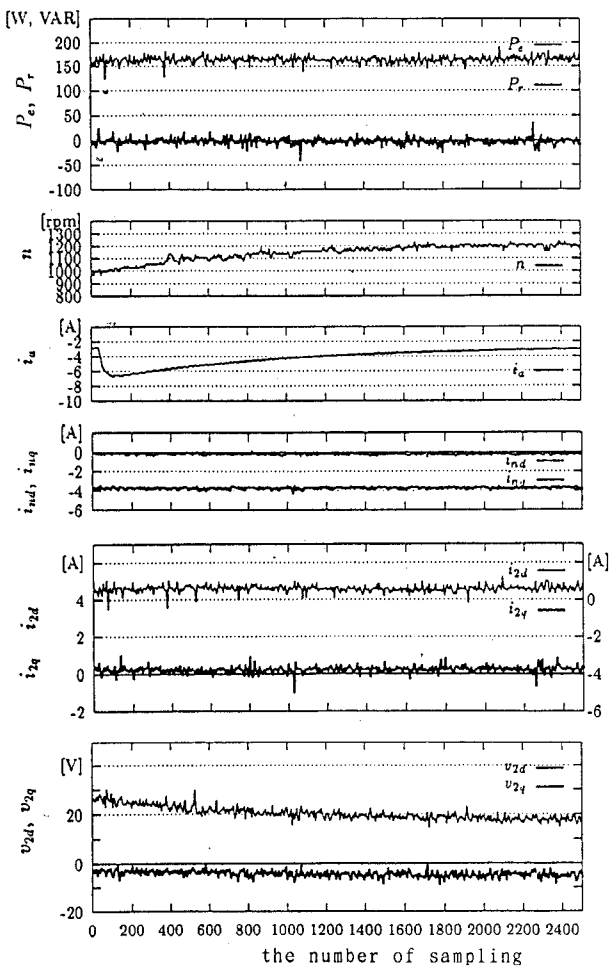


Fig. 4. System response (experiment) of VSGS (step-up of shaft input)

V. CONCLUSION

VSGS which can generate active and reactive power output stably is proposed and the effectiveness and the fine stable response are confirmed in experiment and simulation.

In order to be put VSGS to practical use, some important problems which should be solved are remained. Some of those are as follows.

1) To remove noise of the measured data, a filter may be employed.

2) A two directional power converter system should be used to work at region of the lower and upper side of synchronous speed.

The effectiveness of elevating the stability of electrical power line applied VSGS should be developed in the future.

References

[1]T.Michigami & K.Koyanagi:" The improvement of Power System Stability of an adjustable-speed Pumped-Storage Generator/Motor ",195/204, Vol.114-B, No.2,T.IEE Japan'94.

[2]T.Sato, et al.:" Wind Power System Using a Wound Rotor Induction Machine", 778/783, Vol.114-D, No.7/8, T.IEE Japan '94.

[3]H.Chikaraishi, et al.:" Fast Response Power Stabilizer using the AC-Excited Flywheel Generator", 1254/ 1261, Vol.113-D, No.11, T.IEE Japan '93.

[4]N.Nozawa & Y.Itoh:" Power Control using Variable Speed Generator System", 980/983, National Convention Record IEE Japan '94.

[5]T.TSUCHIYA,et al.:"Modern Control Theory", (in Japanese), Sangyo-tosho.co.,(91)

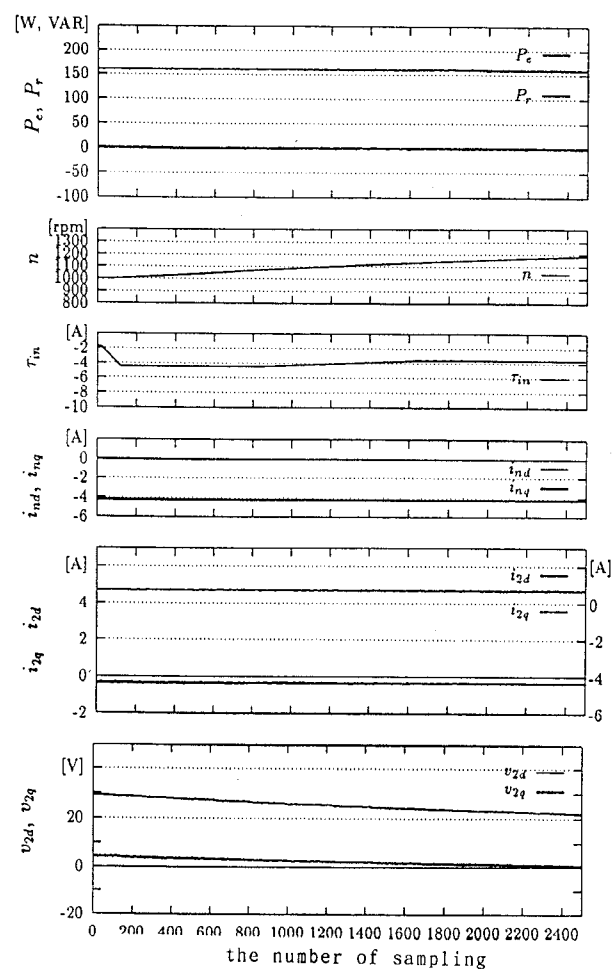


Fig. 5. System response (simulation) of VSGS (step-up of shaft input)

A Novel Three-Phase Sinusoidal PWM Voltage Source Inverter and its Application for Photovoltaic Power Generation System

Sakutaro Nonaka
Dept. of Electrical Engineering, Faculty of Engineering in Kyusyu, Kinki University
11–6, Kayanomori, Iizuka-shi, Fukuoka, 820 Japan.
Fax: +81-948-29-8936, Phone: +81–948–22–5655 ext. 254

Abstract – **In this paper, a novel three-phase sinusoidal PWM voltage source inverter (VSI) is proposed. The inverter has an additional arm to the normal PWM three-phase bridge circuit. The additional arm contributes to reduce the ripple in the ac output current. As an example of the application of this VSI, the utility connected photovoltaic power generation system is shown. In the system, the smooth dc current without pulsation is supplied from PV array, and the VSI provides a sinusoidal ac current for domestic loads and the utility line.**

I. INTRODUCTION

For the voltage source inverter (VSI) and the current source inverter (CSI), the use of the gate turn-off thyristor (GTO) or the IGBT which has self-extinguishing capability, has several merits.

The pulsewidth modulation (PWM) control technique has been applied commonly to the VSI but seldom to the CSI. In the GTO-VSI with PWM control, the waveform of motor phase current is nearly sinusoidal, but the motor terminal voltage has the pulsewidth modulated rectangular wave. The audible noise is a problem one should not ignore. The PWM control technique for the basic circuit of the CSI has been reported by Hitachi Ltd. [1]. As the GTO current of this inverter is basically pulsewidth modulated with trapezoidal modulation of the pulsewidth, the waveform of the motor current shows a tendency to resemble the trapezoidal wave rather than the sinusoidal wave.

The new GTO current source inverter [2][3] with PWM control techniques was proposed by the author in 1985, for the purpose of supplying both the sinusoidal voltage and current to the motor.

Either of two auxiliary GTO's was connected between the neutral of the Y-connected filter capacitors and the positive or negative side of the inverter dc terminal, respectively. The addition of the two auxiliary GTO's has made it possible to produce sinusoidal waveform with ease. The proposed current source inverter has been shown to be able to drive induction motors with little audible noise and reduced torque pulsation [4][5]. A converter with the same circuit arrangement as the inverter was thereafter reported, which can keep input current

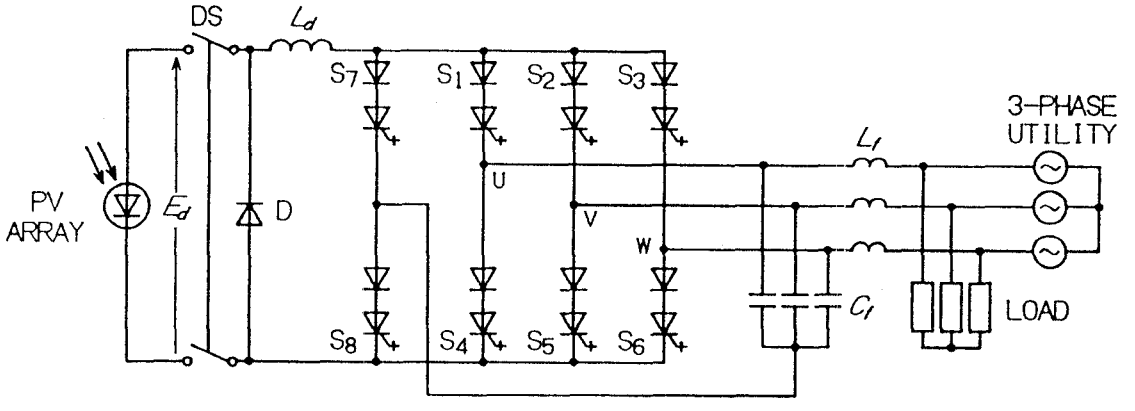


Fig.1. Three-phase sinusoidal PWM current source inverter circuit for PV system.

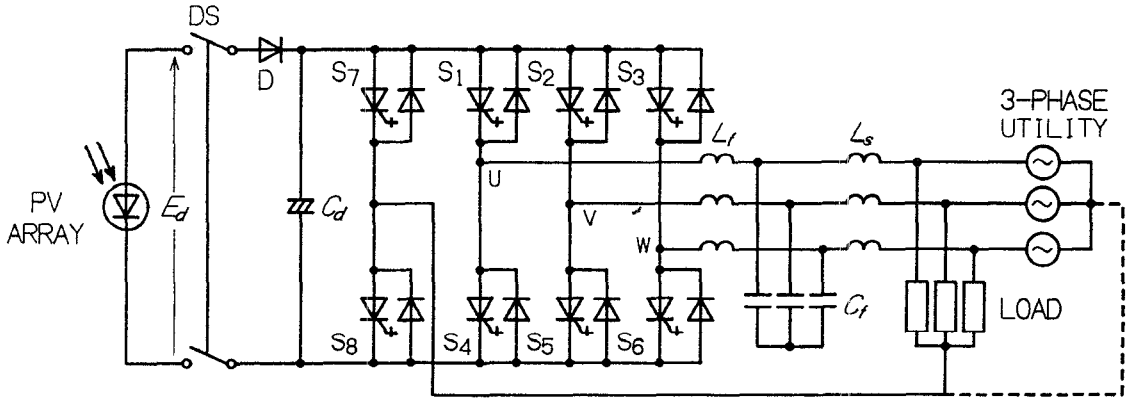


Fig.2. Three-phase sinusoidal PWM voltage source inverter circuit for PV system.

in sinusoidal waveform at unity power factor [6].

As an another application of this three-phase current source PWM inverter, the author reported an utility interactive PV system as shown in Fig.1, [7]. This system can supply the utility with maximum power corresponding to the insolation with sinusoidal current waveform at unity power factor. In this system, the modulation index and firing angle are fixed and there's no need for any feedback control.

In this paper, a novel three-phase sinusoidal PWM voltage source PWM inverter and its application for PV system are described.

Also, in the paper, the circuit configuration, the PWM method and the details of the operation modes are shown.

II. Circuit Configuration

Figure 1 shows a three-phase PWM CSI circuit which composed an important part of the utility-interactive PV system [7].

Figure 2 shows the proposed VSI type circuit configuration in duality of the CSI circuit.

In the VSI circuit, six main GTO's S_1~S_6 with antiparallel diodes, respectively, compose the usual three-phase bridge circuit.

The additional arm consists of GTO's S_7 and S_8 with antiparallel diodes.

L_f indicates the ac filter reactors and C_f is the ac filter capacitors.

L_s indicates the interconnected reactors between the utility and the PV system for controlling the output current. In the dc side, C_d indicates the smoothing capacitor.

The system will be provided the battery instead of the smoothing capacitor C_d.

The neutral point of the auxiliary arm is connected to the neutral of the Y-connected balanced three-phase load or the neutral of the three-phase utility such as the four-wire system if available.

III. PWM Method

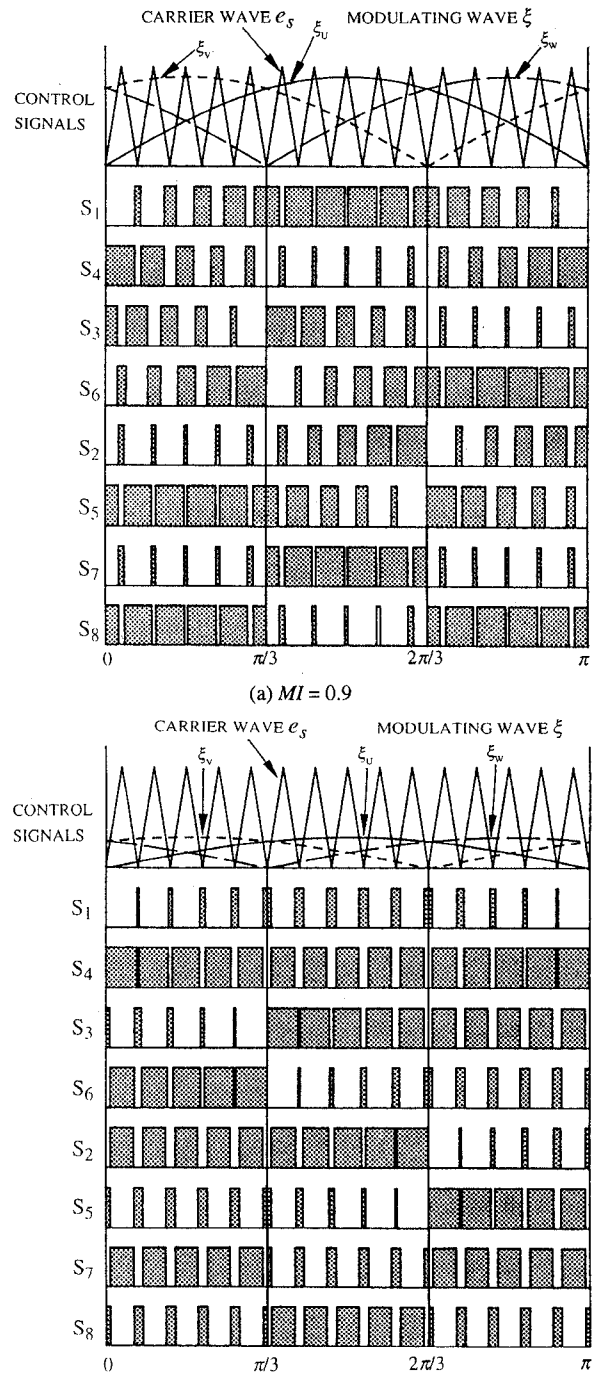
Figure 3 illustrates the generation method of the PWM pattern. The pattern is determined by the points of the intersections of the sinusoidal modulating waves ξ_U, ξ_V and ξ_W for each three-phase voltages and the triangular carrier wave e_s. The modulation index MI is defined as:

$$MI = \frac{\text{amplitude of modulating wave}}{\text{amplitude of carrier wave}}$$

The modulation index MI can be changed by varying the amplitude of the modulating wave while keeping that of the carrier wave.

Figure 3 (a) shows in case of a relatively large MI (=0.9) and Figure 3 (b) in case of a relatively small MI (=0.3).

In this PWM method, a trains of pulses of the PWM pattern are perfectly distributed sinusoidally, regardless of changing the modulation index MI ($0 \le MI \le 1$), and no low-order



(a) $MI = 0.9$

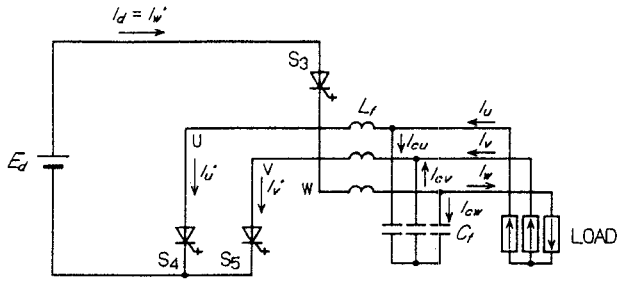
(b) $MI = 0.3$

Fig.3. PWM Method.

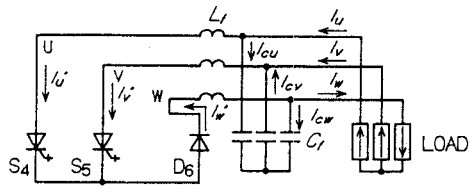
harmonics contain at all in this pattern. The output power factor can be adjusted by shifting the PWM pattern. The firing angle α is defined as a displacement angle between the fundamental of the PWM pattern and the corresponding phase voltage.

IV. Operating Mode

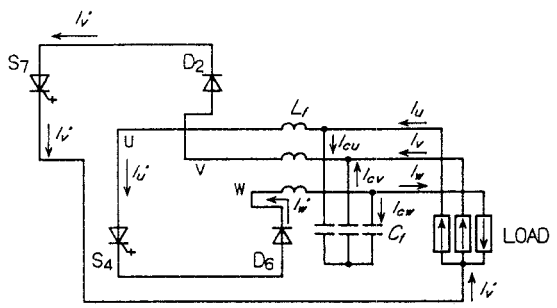
The operation mode is different by the power factor of load. Figure 4 shows the operation modes in $0 \le \omega t < \pi$ at resistance load, that is, the power factor is unity. In this duration, $i_u > 0$, $i_v < 0$, $i_w > 0$.



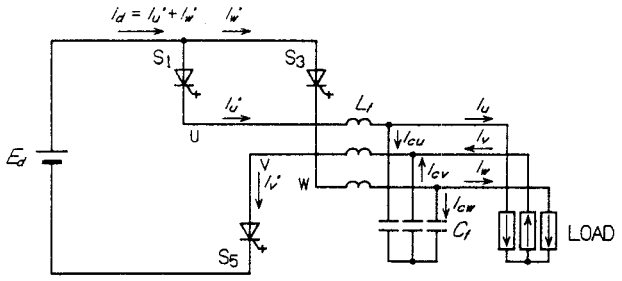
(a) mode 1 (S_3, S_4, S_5, S_8 on)



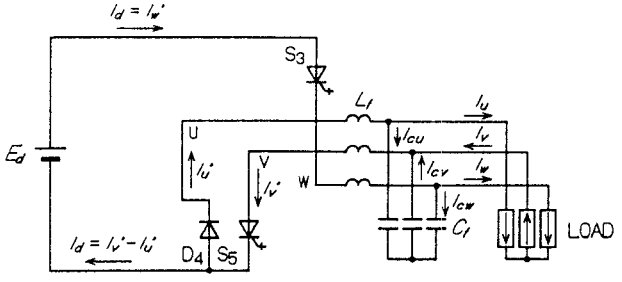
(b) mode 2 (S_4, S_5, S_6, S_8 on)



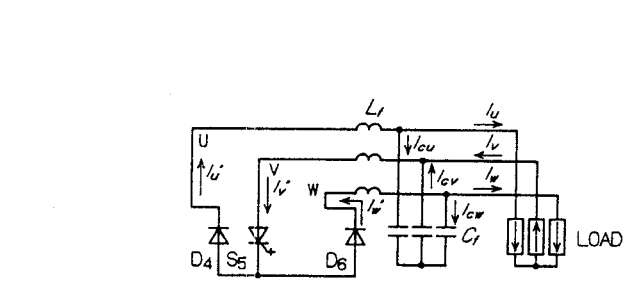
(c) mode 3 (S_2, S_4, S_6, S_7 on)



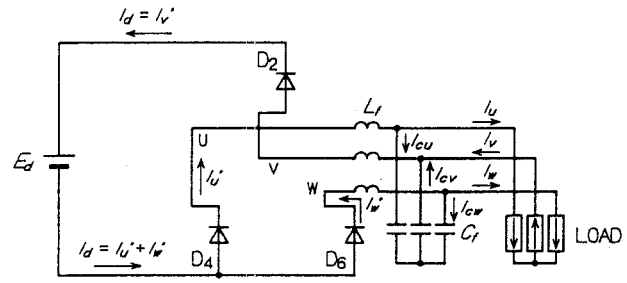
(d) mode 4 (S_1, S_3, S_5, S_8 on)



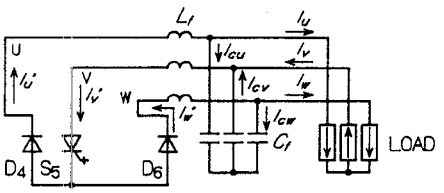
(e) mode 5 (S_3, S_4, S_5, S_8 on)



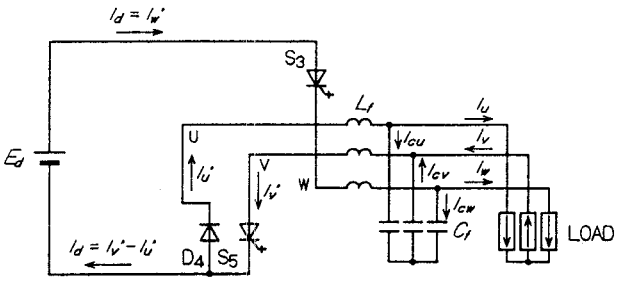
(f) mode 6 (S_4, S_5, S_6, S_8 on)



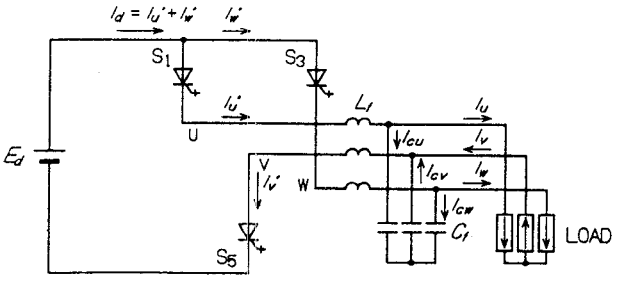
(g) mode 7 (S_2, S_4, S_6, S_7 on)



(h) mode 8 (S_4, S_5, S_6, S_8 on)



(i) mode 9 (S_3, S_4, S_5, S_8 on)



(j) mode 10 (S_1, S_3, S_5, S_8 on)

Fig.4. Example of operating mode.

V. CONCLUSIONS

The proposed three-phase PWM VSI was invented by the author. This VSI circuit configuration is in duality of the three-phase PWM CSI with the auxiliary arm. The VSI provides a very fine sinusoidal three-phase output current.

In an application of PV system, if a storage battery is added in the dc side in order to dc voltage stabilization, the system will be available for uninterruptible power supply (UPS).

The VSI output current is controlled by both of the firing angle α and the modulation index *MI*. The operation mode of VSI is easily changed from inverter action to rectifier action with changing the firing angle α from plus to minus. When α is minus, the VSI acts as a battery charger.

There is no need of a regulator between PV array and battery by proper design of the battery's volt corresponded to the output voltage of PV array. The circuit configuration of the utility-interactive PV system adopted the proposed VSI is very simple.

ACKNOWLEDGMENT

The author wishes to thank Mr. K. Harada for his assistant on the manuscript preparation.

REFERENCES

[1] M. Hombu, S. Ueda, A. Ueda and Y. Matsuda : "A new current source GTO inverter with sinusoidal output voltage and current", in *Proc. IEEE Ind. Appl. Soc. Annu. Meeting*, pp.807–812, Oct. 1984.

[2] S. Nonaka and Y. Neba : "New GTO current source inverter with pulsewidth modulation control techniques", *IEEE Transactions on Industry Applications*, Vol.IA-22, No.4, pp.666–672, 1986.

[3] S. Nonaka and Y. Neba : "Circuit configuration of current source inverter", Japanese patent No.1947733, 1995 (Patent publication No.H6–81546).

[4] S. Nonaka and Y. Neba : "Analysis of PWM GTO current source inverter-fed induction motor drive system", *IEEE Transactions on Industry Applications*, Vol.IA-23, No.2, pp.256–262, 1987.

[5] S. Nonaka and Y. Neba : "PWM GTO current source inverter-fed induction motor drive system", *Trans. Inst. Elec. Eng., Japan*, Vol.107–D, pp.890–897, 1987.

[6] S. Nonaka and Y. Neba : "A PWM GTO current source converter-inverter system with sinusoidal inputs and outputs", *IEEE Transactions on Industry Applications*, Vol.IA-25, No.1, pp.76–85, 1989.

[7] S. Nonaka, K. Kesamaru, T. Murakami, N. Nishi and Y. Neba : "Interconnection system with sinusoidal output PWM current source inverter between photovoltaic arrays and the utility line", *Proc. of 1990 IPEC-Tokyo*, pp.144–151, April 1990.

[8] S. Nonaka : "A novel three-phase sinusoidal PWM voltage source inverter", *Ann. Meeting of IEE of Japan*, No.870, 1997.

Characteristics of a Novel PWM Inverter Circuit with a L-C Filter Connected with DC Link

Kenji Amei Masaaki Sakui Hiroshi Fujita
Toyama University
3190 Gofuku Toyama, JAPAN 930
Fax / Phone:+81-764-45-6712

Abstract-**Characteristics of the inverter circuit which LC filter has connected with each arm of a switching element of DC link is described. Switching component of an output voltage is reduced like the case which a filter has connected on the side of AC. But, LC filter on the side of DC shows effect sufficiently by a small capacity in comparison with the case which is connected on the side of AC of conventional inverter. It is because the voltage which is impressed on a filter is single polarity. As for controlled method, by making potential of control circuit coincide with potential of DC link, it becomes possible not to use expensive isolation amplifier and to detect an output voltage and a DC link voltage. By replacing a filter on the side of AC on the side of DC in this way, efficiency and accuracy of detection were improved.**

I. INTRODUCTION

An output voltage of voltage source type PWM inverter is the square wave which switching component (carrier wave) of a high frequency had synthesis fundamental component (signal wave). When this voltage is impressed on a load such as electric apparatus, an electric current of a high frequency flows and causes increase of iron loss and noise. Moreover, an electromagnetic wave is made to generation and a malfunction is induced on electronic apparatus. For this reason, the low pass filter which is formed of L and C in an output edge of inverter is connected with apparatus as follows.

(1) Like a constant voltage constant frequency power supply, the equipment which output only a voltage of fixed frequency component

(2) The equipment which is directly connected with an electric power system like active power filter

(3) The apparatus which dislikes an occurrence of a noise to the utmost

Therefore, in order to prevent that unnecessary high frequency component flows into a load and an electric power system, it is taken measures.

By using a switching element in a saturation territory, inverter has realized power supply equipment of variable voltage variable frequency efficiently.

But inverter generates unnecessary switching component at the same time, and it has bad effect upon the apparatus which was connected with output of inverter.

As for switching component, since it is the highest frequency component in the voltage which is output from inverter, it is impossible to remove it by control.

In this paper, the low pass filter which was connected with the outside of inverter like a circuit such as a constant voltage constant frequency power supply and an active filter is connected with an inside of DC link and the new inverter circuit which reduces the harmful switching component which is included in an output voltage of inverter is proposed

II. MAIN CIRCUIT CONFIGURATION

The main circuit configuration of PWM inverter which is proposed in this paper is shown in figure 1. On this circuit, the smooth circuit which is formed of L and C is connected with each arm of a usual 3 phase bridge inverter circuit. Inductor is connected over a middle point of two switching elements from neutral point of the capacitor which was connected with DC link in series. Electric power is supplied to a load from neutral point of capacitor. In general, if an AC voltage was impressed on both ends of capacitor, neutral point potential of the capacitor which was connected in series is divided in a ratio of impedance. But, when a DC voltage is impressed, the impedance becomes infinite. For this reason, potential of neutral point of capacitor becomes undefined. By moving neutral point potential of capacitor, a voltage wave of PWM inverter is done smooth and a voltage of a sine wave is output.

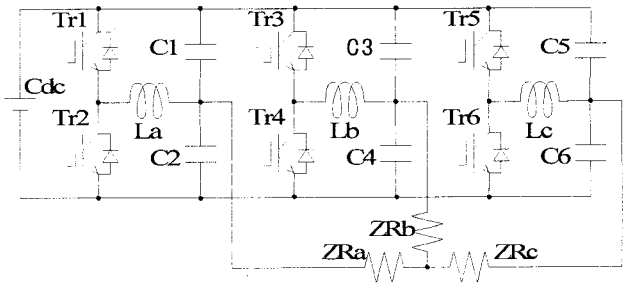


Fig.1. Main Circuit Configuration

Ⅲ. PRINCIPLES OF PROPOSED CIRCUIT

Principles of a proposed circuit is shown below. Though three phase bridge inverter is used in fact, since it can be considered that single phase full bridge inverter is practicing in parallel, in order to simplify an explanation, a case of single phase bridge inverter is explained. A direction of the electric current is described about 4 switching modes and an entire OFF mode of a dead time condition like an analysis of a usual inverter circuit.

1) Mode 1 (T_{r1}, T_{r4} in terms of turn on condition)

When it becomes the condition which T_{r1} and T_{r4} conducted, an electric current flows in the order of T_{r1}, L_a, Z_L, Z_R, L_b, T_{r4}, C_{dc} from DC link capacitor C_{dc}, and a positive voltage is impressed on a load. Electric charge of capacitor C_1, C_4 which was connected with each switching element in parallel has electricity respectively discharged through inductor L_a, L_b.

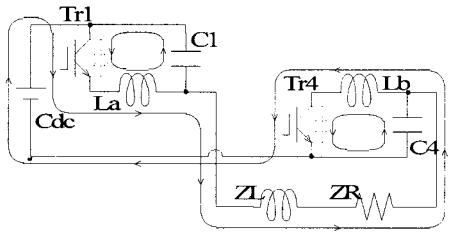


Fig.2.1. Direction of an electric current of mode 1

2) Mode 2 (T_{r1}, T_{r3} in terms of turn on condition)

When it becomes the condition which T_{r1} and T_{r3} conducted, since a load is short-circuited through a switching element and a diode, when it has shifted from mode 1, an electric current flows in the order of Z_R, L_b, D_3, T_{r1}, L_a, Z_L from Z_L. Electric charge of capacitor C_1 has electricity discharged through inductor L_a, and a charging electric current flows to C_3 from L_b.

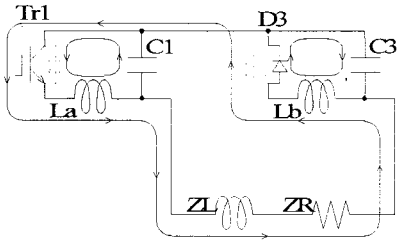


Fig.2.2. Direction of an electric current of mode 2

3) Mode 3 (T_{r2}, T_{r3} in terms of turn on condition)

When it becomes the condition which T_{r2} and T_{r3} conducted, an electric current flows in the order of T_{r3}, L_b, Z_R, Z_L, L_a, T_{r2}, C_{dc} from DC link capacitor C_{dc}, and a negative voltage is impressed on a load. Electric charge of capacitor C_2, C_3 which is connected with each switching element in parallel has electricity respectively discharged through inductor L_a, L_b.

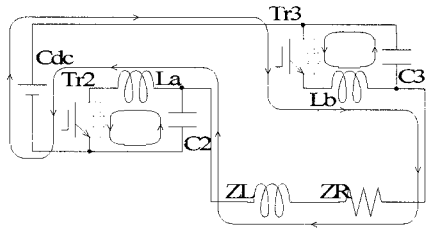


Fig.2.3. Direction of an electric current of mode 3

4) Mode 4 (T_{r2}, T_{r4} in terms of turn on condition)

When it becomes the condition which T_{r2} and T_{r4} conducted, since a load is short-circuited through a switching element and a diode, when it has shifted from mode 3, an electric current flows in the order of L_a, T_{r2}, D_4, L_b, Z_R, Z_L from Z_L. Electric charge of capacitor C_2 has electricity discharged through inductor L_a, and a charging electric current flows to C_4 from L_b.

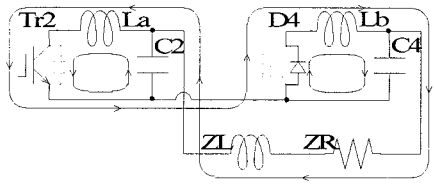


Fig.2.4. Direction of an electric current of mode 4

5) An entire OFF mode (dead time condition)

After above-mentioned mode 1～4, condition (dead time) that all switches certainly become OFF is chosen.

For example, when it has shifted from a condition of mode 1 (T_{r1}, T_{r4} in terms of turn on) in a dead time, an electric current flows in the order of Z_R, L_b, D_3, C_{dc}, D_2, L_a, Z_L from inductor Z_L of a load, and energy of Z_L is regenerated on capacitor C_{dc} of DC link. A charging electric current respectively flows capacitor C_2, C_3 from inductor L_a, L_b through diode D_2, D_3.

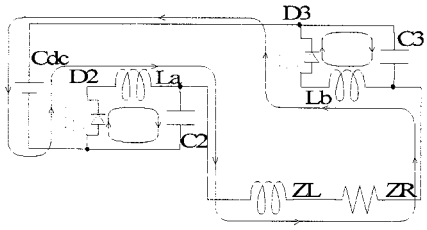


Fig.2.5. Direction of an electric current of OFF mode

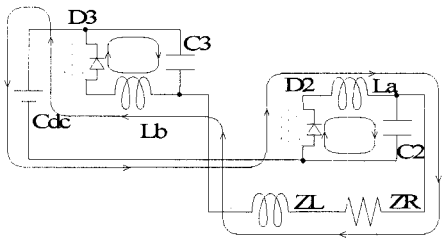


Fig.2.6. Direction of an electric current of OFF mode

In this way, a course of an electric current of this circuit is a total of a course of conventional inverter and a course of a charge, the electric discharge which is caused by L, C which was connected newly. Since switching component has circulated round an inside of DC link, an output voltage of inverter turns into the sine wave which switching component had eliminated.

Ⅳ. Design of L-C Circuit

LC circuit which was connected with each arm repeats a charge, electric discharge by switching. High frequency component of an output voltage is reduced by this. When electric charge of capacitor is short-circuited through inductor, electric current i_{SW} which flows to a switching element is a total of electric current i_f which flows transiently and electric current i_L which is supplied to a load. By considering the maximum electric current which flows to a switching element, method of design of optimum L, C can be derived. When it became the condition which a switching element conducted, equation (1) concerning electric current i_{SW} is obtained from figure 3.

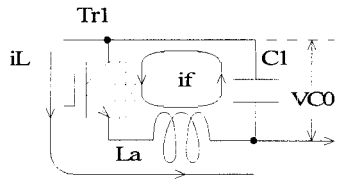


Fig.3. An electric current of a switching element

$$i_{SW} = i_L + i_f \tag{1}$$

Maximum value of i_L depends on a capacity of a load. Moreover, i_f is led by a differential equation of L, C simply. From figure 3, a circuit equation can be shown with (2).

$$L\frac{di_f}{dt} + \frac{1}{C}\int i_f dt = 0 \tag{2}$$

By solving this equation, (3) is obtained.

$$i_f = \frac{V_{C0}}{\sqrt{L/C}} \sin \frac{1}{\sqrt{LC}} t \tag{3}$$

Therefore, an electric current of a charge, electric discharge of LC circuit becomes maximum at time of (4).

$$t_{\max} = \frac{\pi}{2}\sqrt{LC} \tag{4}$$

But, when initial voltage V_{c0} of capacitor is equal to DC voltage V_{dc}, since modulation factor a amounts to about 1, then minimum pulse width $t_{\min}$ is chosen. And, maximum value I_{SW} of an electric current of an element is calculated from (5).

$$I_{SW} = I_L + \frac{V_{C0}}{\sqrt{L/C}} \sin \frac{1}{\sqrt{LC}} t_{\min} \tag{5}$$

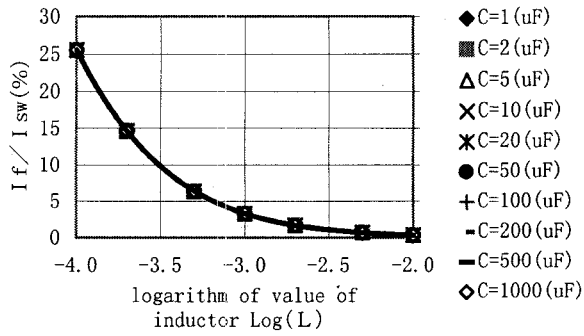


Fig.4. A ratio for an element current of a charging/discharging current of LC circuit

For example a case of DC link voltage Vdc=350V, pulse width tmin=2us at the minimum, a rate of electric current I_f of LC circuit for electric current I_{SW} of a switching element in various L, C is shown in figure 4. It is found that I_{SW} is not influenced by value of C and it is decided by value of L.

Than the above, value of optimum L is obtained by a ratio of I_f and I_{SW}. Moreover, C is obtained by a rate of switching component and fundamental voltage component of an output voltage.

Ⅴ. Control Circuit of Inverter

A block diagram of the feedback control which was used in a suggestion circuit is shown in figure 5. Since the potential which is impressed on a load is equal to neutral point potential of capacitor of LC circuit, by turning DC link potential into standard, an output voltage of inverter can be fed back easily. In addition, by making potential of a ground of control circuit coincide with DC link potential, it becomes possible not to use expensive isolation amplifier and to feed back an output voltage.

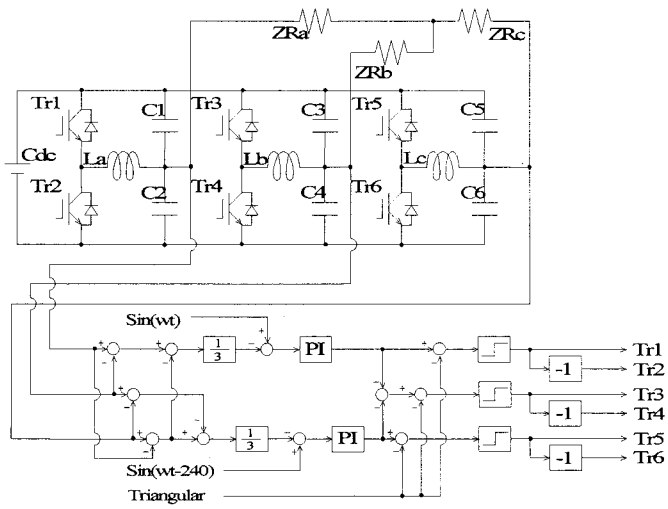


Fig.5. Control circuit of a proposed inverter

The inverter output voltage at the time when DC link potential was turned into standard is respectively shown with V_{aN}, V_{bN}, V_{cN}. Line voltage V_{ab}, V_{bc}, V_{ca} is shown the following (6).

$$\begin{aligned} V_{ab} &= V_{aN} - V_{bN} \\ V_{bc} &= V_{bN} - V_{cN} \\ V_{ca} &= V_{cN} - V_{aN} \end{aligned} \tag{6}$$

Phase voltage V_a, V_b, V_c are shown like (7).

$$\begin{aligned} V_{ab} &= V_a - V_b \\ V_{bc} &= V_b - V_c \\ V_{ca} &= V_c - V_a \end{aligned} \tag{7}$$

Moreover, since connection of this circuit is three phase three lines, (8) is formed.

$$\begin{aligned} V_{ab} + V_{bc} + V_{ca} &= 0 \\ V_a + V_b + V_c &= 0 \end{aligned} \tag{8}$$

Phase voltage can be led to (9) from the above.

$$\begin{aligned} V_a &= \left\{\left(V_{aN} - V_{bN}\right) - \left(V_{cN} - V_{aN}\right)\right\}/3 \\ V_b &= \left\{\left(V_{bN} - V_{cN}\right) - \left(V_{aN} - V_{bN}\right)\right\}/3 \\ V_c &= \left\{\left(V_{cN} - V_{aN}\right) - \left(V_{bN} - V_{cN}\right)\right\}/3 \end{aligned} \tag{9}$$

A deviation of phase voltage and the directive value V_a^*, V_c^* is calculated and an error is amplified using proportional integral controller and is controlled following.

VI. Simulation Results

In order to check characteristic of the proposed main circuit, the voltage which is output from conventional three phase bridge inverter and a proposing circuit was calculated by simulation. And, both calculated results were compared. Then 0.5mH, 10uF were respectively used as for value of inductor and capacitance of LC filter. A resistant load of star connection of 10ohm was used. And, general sine wave-triangular wavy comparative method was used on generation of PWM pulse. Modulation factor is 0.8 and frequency of a signal wave, carrier wave were respectively 60Hz, 10kHz. With both circuits, it was calculated similarly under above-mentioned condition.

A calculated result of an output voltage wave and a frequency analysis of a conventional circuit and a proposed circuit is respectively shown in figure 6.1, figure 6.2. In a conventional circuit, harmonic generation of low order is plentiful, and it is 8.2% at the rate of entire harmonic strain of the 5th degree, the 7th degree, the 11th degree, the 13th degree. But, it is reduced 1.6% in a proposed circuit. With regard to switching component, it is reduced 1.5% from 2.6%. A ratio of fundamental component and the switching component at the time when value of various inductors was connected is shown in figure 7.1. Then, capacitor (fix) of 10uf is connected. Inductor is smaller, and a residual rate of switching component indeed becomes big. In the case of

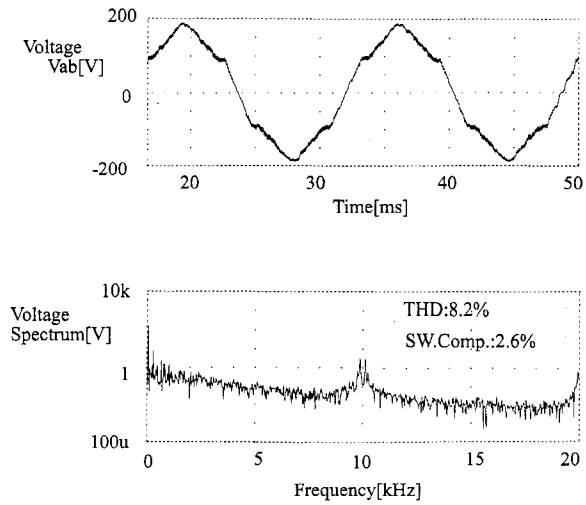


Fig.6.1. Voltage wave of a conventional circuit and the frequency component

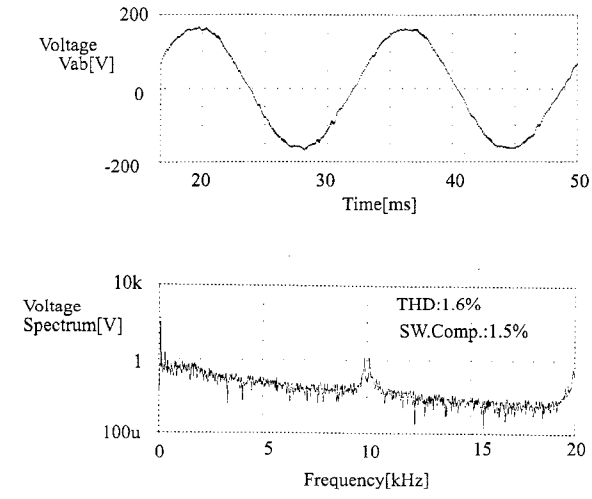


Fig.6.2. Voltage wave of a proposed circuit and the frequency component

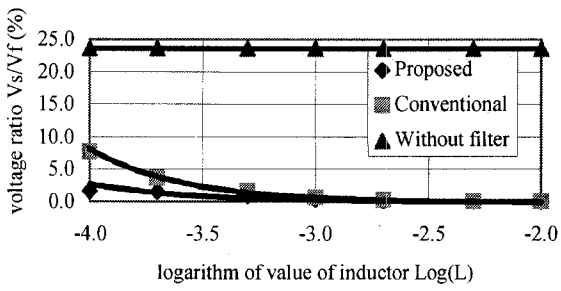


Fig.7.1. A ratio of fundamental component and switching component (C=10uF, fixed)

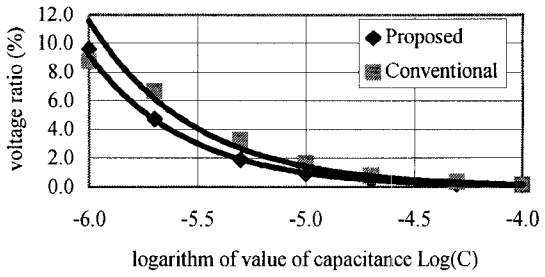


Fig.7.2. A ratio of fundamental component and switching component (L=0.5mH, fixed)

L=0.1mH, a rate of switching component of a proposed circuit is about 1/4 of a conventional circuit, and it is reduced on about 1/2 concerning L=1mH. The relation of value of capacitance and a residual rate of switching component at shown in figure 7.2. In this case, it is found that a proposed circuit controls an outflow of switching component in comparison with a conventional circuit. Than the above, a proposed circuit does not need merely a filter of a smaller capacity than a conventional circuit, and it is found to possess the superior ability which removes a high frequency.

Ⅶ. EXPERIMENTAL RESULTS

In order to verify superiority to introduce feedback control, experiment of two ways of the condition which does not introduce feedback control into a proposed circuit and the condition which introduced feedback control was performed. Then, all conditions such as constant of a circuit element and a generation circuit of PWM pulse made it coincide with a condition of simulation except for a DC link voltage.

1) When feedback control was not introduced

An experimental result of an output voltage wave, an electric current wave and a frequency analysis in the case which does not introduce feedback control is shown in figure 8.1. By simulation, though an amplitude of line voltage of output is 117.8V, it is 136.5V by experiment, and an experimental result is somewhat higher. Total harmonic distortion was 1.9% to the 13th degree from the 5th degree, and a ratio of switching component for fundamental component was 0.65%.

2) When feedback control was introduced

An experimental result of an output voltage wave, an

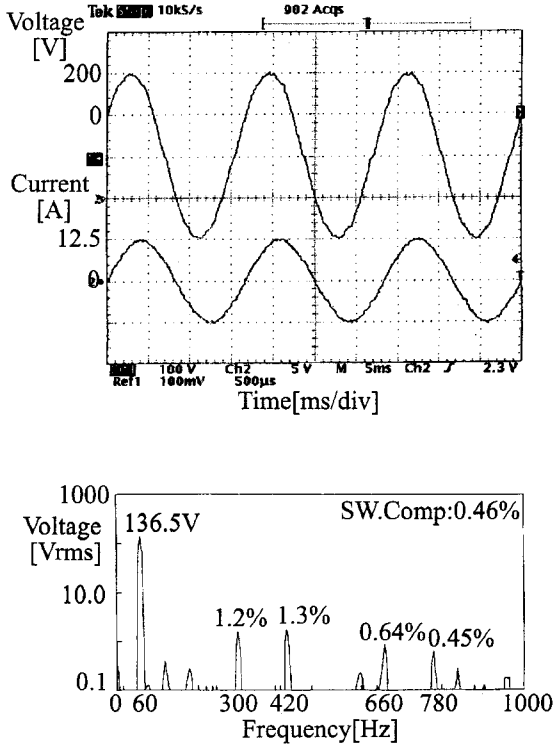


Fig.8.1. Voltage and current wave, frequency analysis of the voltage (Without feed-back control)

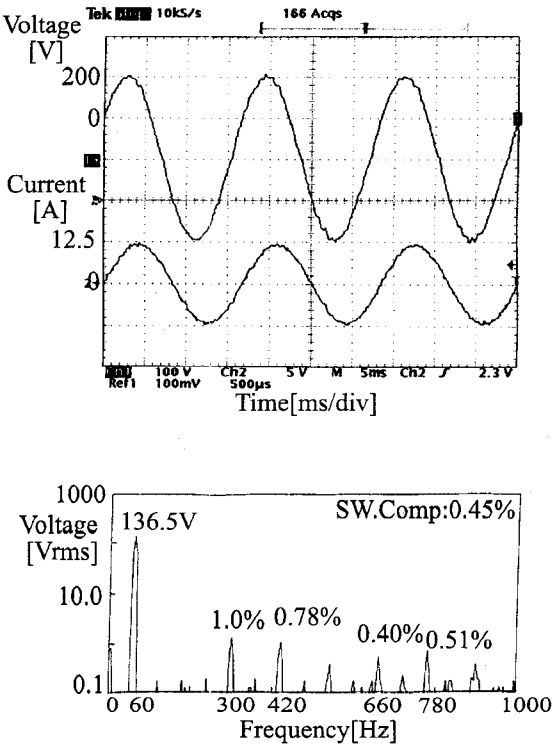


Fig.8.2. Voltage and current wave, frequency analysis of the voltage (with feed-back control)

electric current wave and a frequency analysis in the case which introduced feedback control is shown in figure 8.2. It was adjusted to an output voltage in the case which does not introduce feedback control and directive value of an output voltage was established about 135Vrms. Total harmonic distortion was 1.4% to the 13th degree from the 5th degree, and a ratio of switching component for fundamental component was 0.63%. Than this, it was found that a harmonic distortion of lower order is improved by feedback control.

Ⅷ. CONCLUSION

Formerly, by connecting the low pass filter which was connected with an output edge of inverter with DC link, it became possible to control to outflow unnecessary switching component to the inverter outside. Generation of iron loss of electric apparatus will be reduced by this. And, if the iron core which possesses characteristic of the high frequency which was superior was used on a filter, improvement of efficiency will be expected. Since high frequency component has circulated in only a DC link inside of inverter, generation of a noise is restrained in addition. At the same time, since value of inductor, capacitor of LC filter is reduced in comparison with a conventional circuit, frequency band of the voltage which can be output from inverter is extended. It will be possible to apply a proposed circuit to variable voltage variable frequency (VVVF) power supply.

With regard to controlled method, by making DC link potential coincide with potential of control circuit, an output voltage could be fed back without isolation amplifier. By applying this controlled method, improvement of accuracy of detection of an output voltage and a reduction of a price were realized.

In this way, "the inverter which is gentle to an environment" possesses the superior characteristic which improved efficiency and generation of noise was constructed.

REFERENCES

[1] IEEJ compilation, "A semiconductor electric power convertible circuit", Institute of Electrical Engineers of Japan, 1987

[2] N. Mohan, T. M. Undeland, W. P. Robbins, "Power Electronics: Converters, Applications and Design", New York/USA, J. Wiley & Sons, 1989

[3] IEEJ compilation, "Foundation of Power Electronics", Institute of Electrical Engineers of Japan, 1993

[4] M. Pande, H. Jin, and G.Joos, "Modulated Integral Control Technique for Compensating Switch Delays and Nonideal DC Buses in Voltage-Source Inverters", IEEE Transaction Industrial Electronics, vol. 44, pp. 182-190

[5] K.Yamada et al., "One consideration concerning improvement of a switching wave in PWM inverter", IEEJ, Semiconductor Power Converter society, SPC-95-104

A Votage Source Three Phase PWM Converter with Chopper Circuit

Keiju Matsui, Tomohiro Katayama
Shinichi Takase* and Yue Yang*
Electrical Eng. Dep., Chubu University, Kasugai 487 JAPAN
TEL: 0568-51-1111, FAX: 0568-51-1141
e-mail: keiju@isc.chubu.ac.jp
*Neturen Co.,Ltd. 5893 Tamura, Hiratsuka-city 254 JAPAN

Abstract- This paper presents a novel strategy of PWM converter to control output voltage using the chopper circuit. The voltage source PWM converters are unsuitable to general purpose with wide adjustable voltage range. However, the surge voltage at switching becomes small and the input current waveforms have low harmonics and less resonant oscillations as compared with the current source converters. In this circuit, the input current waveform is controlled by the PWM converter with the fixed optimum voltage modulation factor and the output voltage amplitude is adjusted by chopper circuit with very fast response and precise control. The results are verified by experiments. Finally, a control scheme for an application to ac motor drive is presented and discussed.

I. INTRODUCTION

It is well known that non-linear semiconductor circuits such as rectifiers and the like have been widely applied, so that various harmonics are generated in the power system. From such reasons, the conventional six step thyristor rectifier circuits and the like with large capacities will be restricted to use hereafter. Consequently, the PWM converters using self-turned off switching devices will be put into wide applications, because of generating low harmonics [1]-[4].

There are two types of the PWM converters, that is, voltage source type and current source type. The current source PWM converter has the advantage as compared with the voltage source type because of wide adjustable voltage for various purpose applications. As for the surge voltage generations, however, the current source type has a disadvantage.

In the VS (voltage source) PWM converter, the current path is ensured by the by-pass diode at the turned off instant. Consequently, the turn-off surge voltage does not generate for the voltage source type and snubber circuit is not required except the very large capacity converters. However, the voltage source type is intrinsically a boost converter. Therefore, such converters are unsuitable to the general purpose with very wide adjustable voltage range [5]-[11]. On such backgrounds, the purpose of this paper is to present a novel circuit strategy for the three phase VS-PWM converter. A few characteristics of the VS-PWM converter are to be presented. In this converter, the input current waveform is controlled by the PWM converter with the optimum fixed voltage modulation factor where the input current distortion factor becomes a mimimum value. The output voltage is adjusted by the chopper circuit with very fast response and precise control. In the chopper control circuit, a novel control strategy that directly controls the pulsewidth is presented that differs from the conventional hysteresis comparator method and the like. The results are verified by experiments.

II. CIRCUIT CONFIGURATION AND ITS OPERATION

Fig.1 shows the novel PWM converter circuit configuration that is a voltage source type and constructed in three phases. L is the filter inductor for the input power source. The output of the PWM converter is series-connected with the chopper circuit through the dc link circuit. The chopper circuit is constructed with filter capacitor C, filter inductor L_d, by-pass diode and a switching device.

The control can be separated into the input power control system that controls the input current wave-

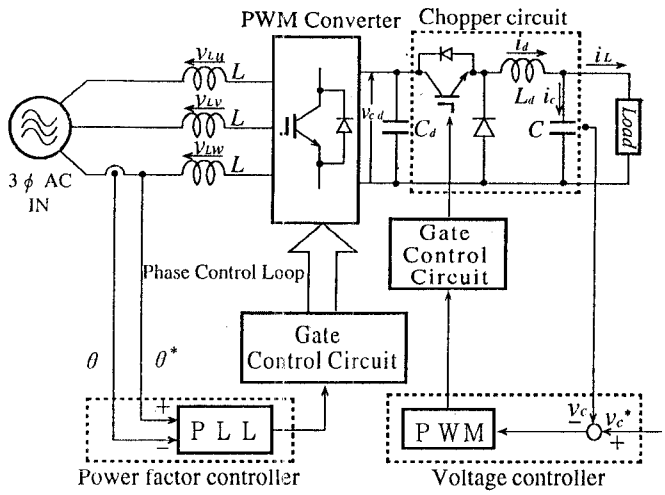


Fig.1 Three phase PWM converter circuit.

form and converts the ac power to the dc link power, and the adjustable output voltage control system with the chopper circuit. In the input power factor control, the voltage modulation factor is previously set to an optimum fixed value. Consequently, the input current waveform becomes an optimum one with a minimum distortion throughout the adjusted whole voltage range. The power factor of the fundamental current becomes cos ϕ= 1 by means of a phase locked loop (PLL) in [12],[13] described later.

In the output voltage control system, the voltage feed back loop with direct pulse control is used so that the controlled output voltage V_c follows the reference voltage V_c^* whose mechanism is described later. In the conventional voltage control system of the chopper circuit, the error signal is compared with the triangular waveform after processing through the PI controller and the like. As compared with the presented direct pulse control system, the output pulse is controlled indirectly, so that transient response deteriorates. On the other hand, the presented direct pulse control can improve significantly the transient characteristics [14].

III. PHASOR DIAGRAM OF PWM CONVERTER

Fig.2 shows the equivalent circuit and the phasor

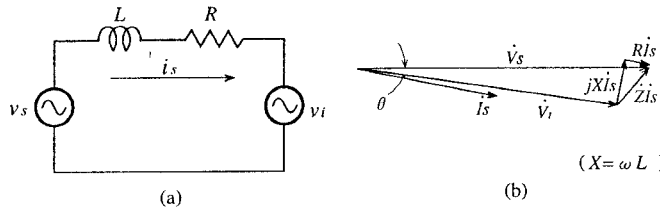


Fig.2 Single phase (a)equivalent circuit,(b)phasor diagram of PWM converter.

diagram of one phase of the three phases PWM converter. The input power $\dot{W}s$ becomes

$$\dot{W}_s = P_s + jQ_s = \dot{I}_s \bar{\dot{V}}_s \quad (1)$$

where Ps: input active power, Qs: input reactive power, $\dot{I}s$: input current, $\bar{\dot{V}}s$: complex conjugate of input suppy voltage $\dot{V}s$, $\dot{V}_I$: fundamental conponent of the converter voltage.

Let the phasor $\dot{V}s$ be a reference phasor as shown and a delay angle of $\dot{V}_I$ be θ, so that the following equation can be obtained. Thus,

$$\dot{I}_s = (\dot{V}s - \dot{V}_I) / \dot{Z} \quad (2)$$

$$\dot{V}_I = V_I (\cos\theta - j \sin\theta) \quad (3)$$

where $\dot{Z}$: line impedance including the filter inductor.

To simplify an analysis, it is assumed that the line resistance R is very small relative to $X = \omega L$, where Z nearly equals jX. Substituting (2) and (3) into (1), we have

$$\dot{W}_s = P_s + jQ_s = \frac{V_s V_I}{X} \sin\theta + j\left(\frac{V_s V_I}{X}\cos\theta - \frac{V_s^2}{X}\right) \quad (4)$$

The voltage drop due to the line impedance becomes very small, so V_I becomes equal to Vs practically for the conventional operation of the PWM converter. From such equations, the active power Ps and the reactive power Qs injected from the power supply to the load can be obtained as shown,

$$P_s = \frac{V_s V_I}{X} \sin\theta \quad (5)$$

$$Q_s = \frac{V_s}{X}(V_I \cos\theta - V_s) \quad (6)$$

On the basis of such discussions, we can make clear a mechanism of the power control by the PWM converter.

The active power can be controlled by the phase angle θ of V_I relative to one of Vs as shown in (5). Actually, in order to make coincide the phasors of Vs and Is, the phase of V_I is adjusted by means of the PLL [15]. For example, in a case of lagging Is as shown, the phase of V_I is made lag in order to make Is lead. The voltage modulation factor is fixed to an optimum value. According to the adjustment of the voltage modulation factor, V_I changes significantly and the term of Qs in (6) changes largely, because θ is small value. For an example, let us consider a case that the output voltage is suddenly lowered. V_I must be decreased in order to increase the output dc link voltage. The term of Qs changes mainly, so that the voltage drop across the circuit becomes also large. At the same time, the voltage drop reduces due to the adjustment of Ps by the PLL. In such manner, the output dc link voltage can be controlled. Because the basic concept of control for the PWM converter is a transfer of power through the inductor that is a storage element of energy, a reactive power control loop is essentially included in the circuit. Thus, we can see that as the control takes just mentioned two step operations, the transient respose of the VS-PWM converter could not become fast.

IV. PHASE LOCKED CONDITIONS

In the proposed control strategy of PWM converter that controls in an optimum fixed voltage modulation factor, the input power factor is controlled by the PLL in which the input current phase is phase-locked to the input supply voltage one. This control loop includes the PWM converter that operates nonlinearly,

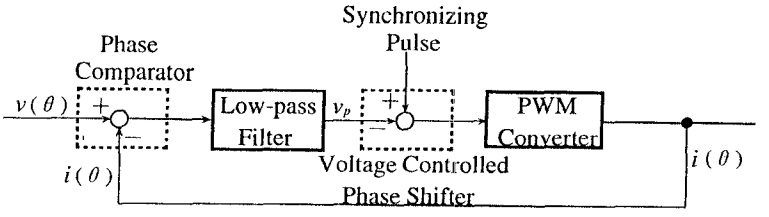


Fig.3 PLL circuit.

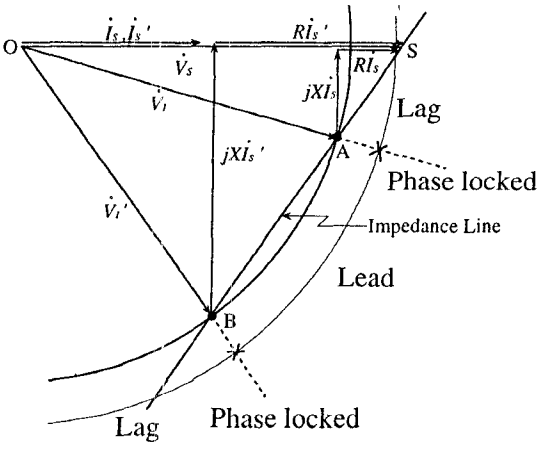


Fig.4 Phasor diagram at phase locked operation.

so the circuit operation also becomes nonlinear. Accordingly, in this chapter, the operating conditions of control scheme not to generate serious problems due to the PLL is to be discussed. The PLL applied to the proposed system is shown in Fig.3. In the figure, the phase comparator compares the phase of input voltage v(θ) and the phase of input current i(θ). After eliminating high frequency harmonic components through the low-pass filter, the output signal controls the phase of synchronizing pulse for the PWM signals from the memories of microcomputer. The controlled pulse by this voltage controlled phase shifter adjusts the input current phase i(θ) by means of the adjustment of the synchronizing pulse phase to the PWM converter. Thus, the phases of the input voltage and the input current coincide with each other by means of the closed loop of the PLL.

Fig.4 shows a phasor diagram at the phase-locked operation between the input current and supply voltage waveforms. A straight line A to B is an impedance line with reference to the supply voltage $\dot{V}s$ and the converter voltage $\dot{V}_l$. For a case of the converter voltage AO as shown, the line voltage drop becomes a segment line, SA. If the head point of the voltage phasor $\dot{V}_l$ is placed from B to A on the circle, the operating point is dislocated from the impedance line, so that the input current phasor $\dot{I}s$ leads $\dot{V}s$. On the other hand, for the region from A to S, $\dot{I}s$ lags $\dot{V}s$. When the converter voltage phasor $\dot{V}_l$ is placed on the point B of the impedance line, the current phasor $\dot{I}s$ becomes phase-locked as shown. Thus, the phase-locked operations are given by two points. At the point B, however, the operating current becomes very large, so that the alternative operating point A is preferred as a phase-locked operating point.

V. OPTIMUM VOLTAGE WAVEFORM OF PWM

Various methods to synthesis the PWM waveforms can be considered. In this paper, by means of the sinusoidal to triangular waves comparison method with constant switching frequency, the PWM converter is controlled. In the proposed control strategy, the voltage modulation factor of the PWM converter is previously determined to an optimum fixed value that can give a minimum distortion factor. The desired

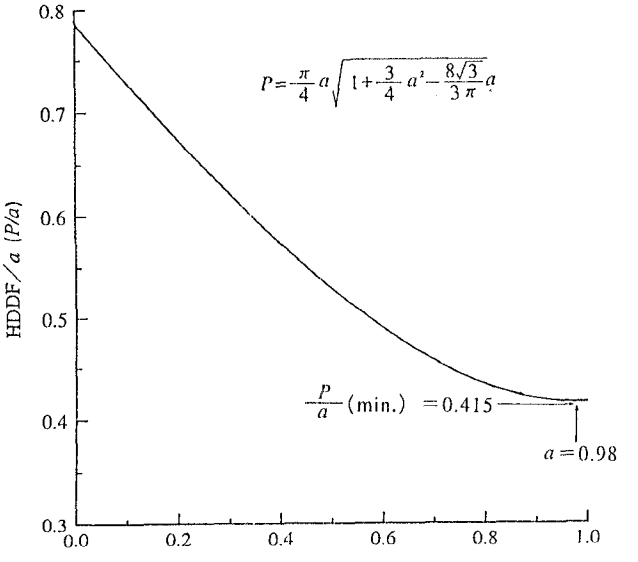


Fig.5 Relation between voltage modulation factor and harmonic distortion determining factor.

output voltage is controlled by the following stage chopper circuit. Various evaluation methods for the PWM waveforms have been presented so far. Recently, an evaluation method by harmonic distortion determining factor (HDDF) has been reported [16]. By this evaluation method, a certain constant voltage modulation factor is determined to obtain the optimum voltage waveform. For an influence to the output, a representation due to the ratio relative to the fundamental component is important. Because the fundamental component of the PWM waveform is proportional to the modulation factor, HDDF in Fig.5 is shown in the ratio relative to the voltage modulation factor. In the region of small a, the distortion ratio to the output becomes larger, but as a approaches to unity, it is reduced and becomes a minimum value, P/a = 0.418 at a = 0.98. According to this reason, the voltage modulation factor of PWM converter is given to the fixed value, a = 0.98.

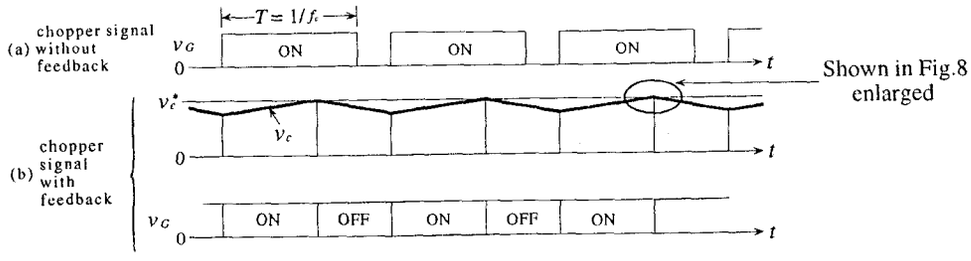


Fig.6 Chopper signal and output waveforms.

VI. CHOPPER CONTROL CIRCUIT

A. Direct Pulse Control Method

In a case of controlling the output pulses, various control methods have been reported. For an example of the conventional one, the error signal that is the difference voltage between the reference and the output is given to the sinusoidal to triangular waves comparator after processing through PI controller. In such a manner, the desired PWM signal can be obtained. This conventional method has been often put into practical use. In this paper, we present an alternative pulse control method, which has very fast transient characteristics. This method has been presented in the area of small capacity switching regulators where the reference and measured value are directly compared every each pulse. In such a relative larger capacity as the proposed converter, the output voltage ripple will increase due to the low switching frequency and the like. Accordingly, it is very important to make clear reasons of the ripple generation. The actual control circuit is to be presented and discussed for the case of this relative high voltage power converters like this system.

Fig.6 shows a relation between the chopper control signal and the output voltage waveform where the controlled value is compared every each pulse. Fig.7 shows the actual control circuit configuration, where the chopper output volatge Vc is detected by the photo coupler through the zenor diode Z. When Vc increases over a precise value of the zenor voltage Vc^*, the photo coupler conducts and the RS switch turns off. Then, the gate signal to the IGBT is prohibited, so the chopper is turned off and Vc is reduced. When the next pulse comes from the pulse generator after one period, the RS switch is turned on again, and the IGBT also turned on. This relationship between the chopper signal V_G, the output voltage V_c and the reference voltage V_c^* is shown in Fig.6(b).

B. Output Current and Voltage Ripples

Above discussion was described conceptually on a basic operating circuit. In the actual control, however, the operation is indirect control through

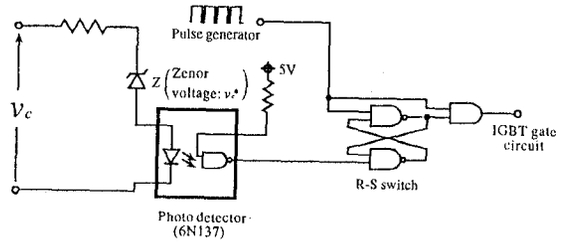


Fig.7 Chopper voltage controlling circuit.

the large capacity filters, so the actual appearance is a little different from such figures. The output voltage V_c is controlled by switching through the LC filter. For such control operation, let us solve an error between the desired value and the controlled variable. For turned on period,

$$v_{cd} - v_c = L_d \frac{di_d}{dt} \tag{7}$$

where an influence to the inductor current due to the capacitor voltage ripple is little for the period of one cycle of the chopper frequency. Consequently, V_{cd} and V_c is constant for this period. Considering $V_c = dV_{cd}$, where d is the duty cycle, we obtain

$$\Delta i_d = \frac{v_{cd}}{f_c L_d} (1-d)\ d \tag{8}$$

where Δi_d is the output current ripple as shown in Fig.8 and f_c is the chopping frequency. As shown, during the turn on period (dT) of the chopper, the current increases linearly to a value represented in (8). During the turned off period ($1\text{-}d)T$, the current is decreased by the same quantities. In the figure, the straight line of the average currents $\bar{i}_d$ that is the load current goes through the midpoints of line segments. When $\bar{i}_d$ is smaller than i_d, the exceeded quantities flows into the smoothing capacitor C. On the other hand, at $\bar{i}_d > i_d$, the current flows out of C. By means of these current flows, the capacitor voltage is increased or decreased, so that the voltage ripple generates. In the figure, such relationship is shown that the actual output capacitor voltage V_c is lower than the reference V_c^* for turn-on, and is higher than V_c^* for turn-off. The capacitor voltage for turn-on can be obtained from (7), where the increasing current equation is integrated. Thus,

$$v_c = \frac{1}{C} \frac{v_{cd}}{L_d} \int (1-d)\ t\ dt \tag{9}$$

For an incremental quantity, this equation is solved. As a result,

$$\Delta v_{c1} = \frac{v_{cd}(1-d)^2 d}{8 L_d C f_c^2} \quad (10)$$

In a similar manner, for decreasing current, the capacitor current can be also given by

$$\Delta v_{c2} = \frac{v_{cd}(1-d) d^2}{8 L_d C f_c^2} \quad (11)$$

The sum of (10) and (11) gives the capacitor voltage ripple. The result becomes

$$\Delta v_c = \Delta v_{c1} + \Delta v_{c2} = \frac{v_{cd}(1-d) d}{8 L_d C f_c^2} \quad (12)$$

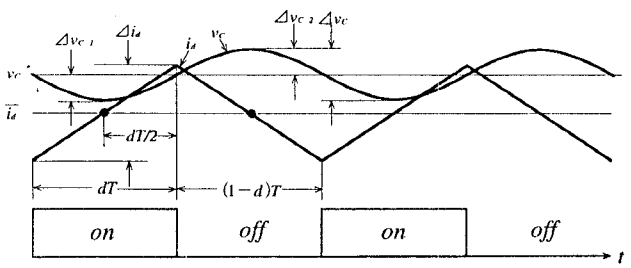


Fig.8 Ripple waveforms of output voltage and current.

VII. EXPERIMENT AND SIMULATION

A. Output Voltage and Current Ripple

Fig.9 shows the output voltage and current ripples, $\triangle v_c$ and $\triangle i_d$, respectively. The inductor current linearly increases for turn-on or decreases for turn-off. The capacitor voltage ripple $\triangle v_c$ follows a parabola that is previously described in Fig.8. The experimantal parameters are V_{cd} = 100V, V_c = 80V, L_d = 3.0 mH, C = 470 μF, f_c = 5.0 kHz and d = 0.8. Calculating the voltage ripple from (12) becomes $\triangle v_c$ = 57 mV which is almost coincident with the experimental results. In spite of the control through large capacity LC filters, pricise voltage control can be obtained by means of the pulse direct control method.

B. Steady State Characteristic of Output Voltage

Fig.10 shows steady state characteristic of output voltage. The voltage modulation factor of input PWM waveform is selected to be a = 0.98 where HDDF/a becomes minimum value, where the voltage reference V_c^* is 100 V. Though the dc link voltage V_{cd} is fairly varied according to the variation of load current, the output volatage V_c is well controlled to a constant value.

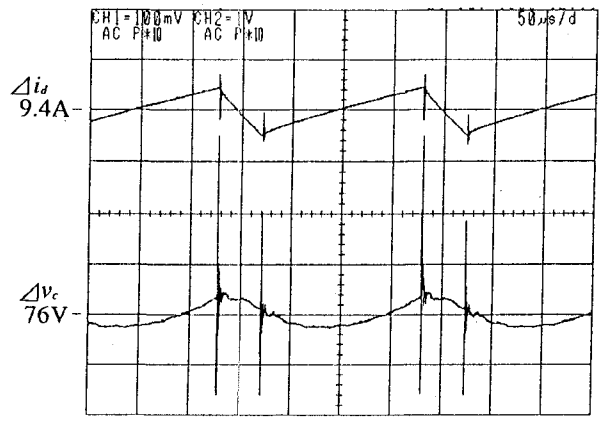


Fig.9 Ripple waveforms of output voltage and current. ($\triangle v_c$: 100 mV/div, $\triangle i_d$: 1.7 A/div, 50 μ sec/div)

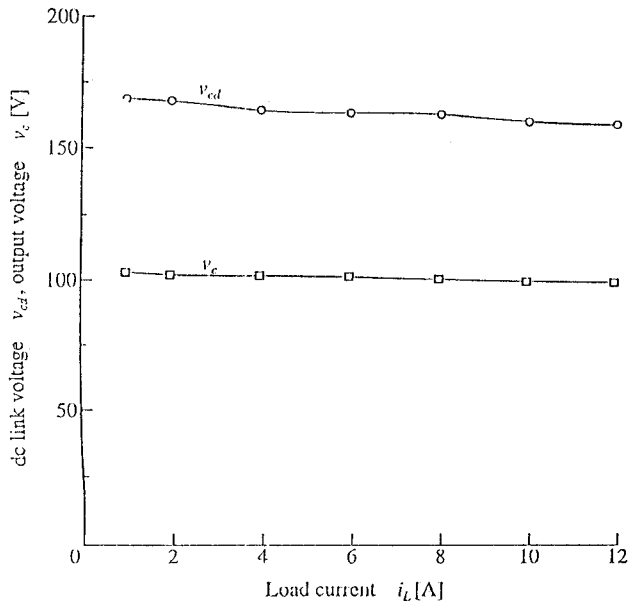


Fig.10 Relation between output voltage and output current.

C. Transient Characteristic Of Output Voltage

Fig.11 shows a transient characteristic at the alteration of the input reference. For the experimental parameters such as the output filters, the same ones previously mentioned are used. For the output voltage control of the conventional VS-PWM converters, various techniques have to be employed to obtain the fast response. On the other hand, the proposed strategy can realize a very fast transient characteristic.

D. Transient Response of Power Factor Control by PLL

Fig.12 shows the input current waveform i at the PLL

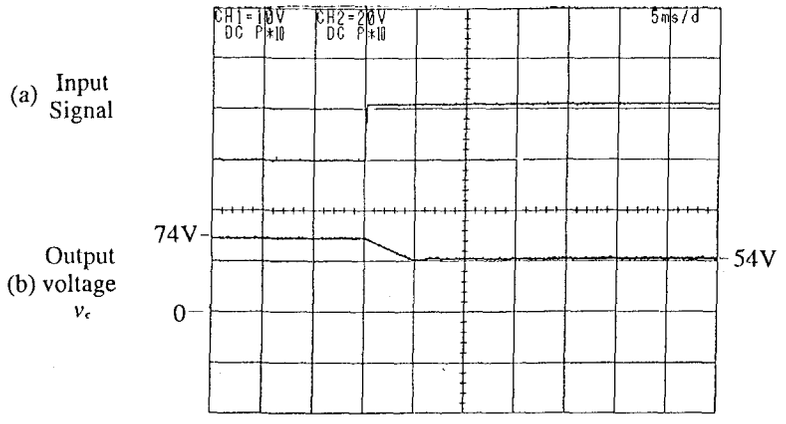


Fig.11 Transient response of output voltage.
(Δv_C : 50 V/div,5 msec/div)

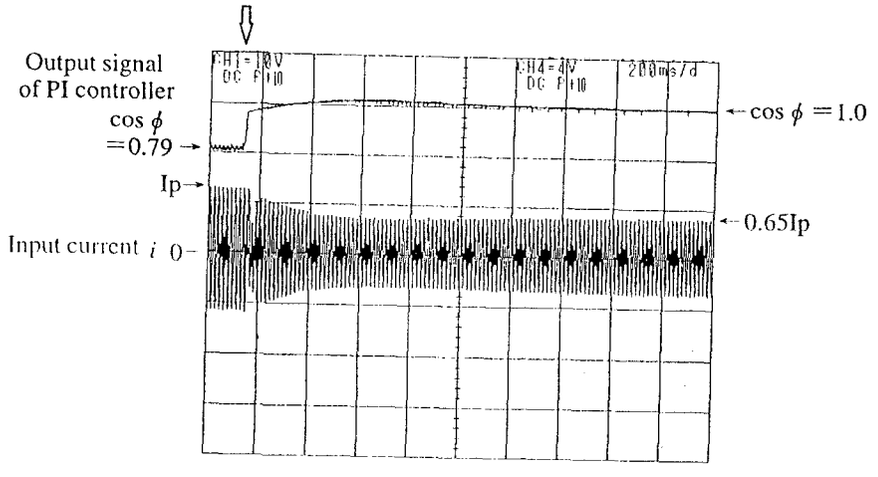


Fig.12 Transient response of power factor control by PLL.
(PI:4V/div, i:16A/div,200msec/div)

control. In the figure, the PLL control turns on at an arrow. The PLL circuit including PI controller is integrated as an IC chip, so it is very easy to employ. For a little disadvantage, the transient response is ralatively slow. Actually, in this experiment, the transient response was slow as shown. For the power factor control, however, it is not necessarily to improve the transient response, considering the purpose of the power factor correction. In the proposed scheme, the actual output voltage is controlled by the chopper circuit with very fast response and precise control.

VIII. APPLICATION TO CONVERTER / INVERTER SYSTEM

Fig.13 shows an application to PWM converter to inverter system for the induction motor drive. The voltage modulation factor for the PWM converter is fixed to obtain the optimum waveform as mentioned above. For the PWM inverter, in the same way, the voltage modulation factor is also fixed to be the optimum value. According to the speed command n^*, the dc output voltage V_c is controlled by the chopper. The obtained voltage V_c proportinal to n^* gives the frequency command ω_1^* to the inverter through VCO (voltage controlled oscillator). For power regeneration, the dc voltage increases and the antiparalleled diode with the IGBT turns on. Consequently, the converter voltage as shown in Fig.4 also increases, so that the current phase leads the input supply voltage one. The leading angle of the input current reaches automatically 180° by means of the PLL function. According to such mechanism, the power regeneration can be successfully performed.

IX. CONCLUSIONS

Novel voltage control strategy for the voltage source PWM converter with the chopper circuit has

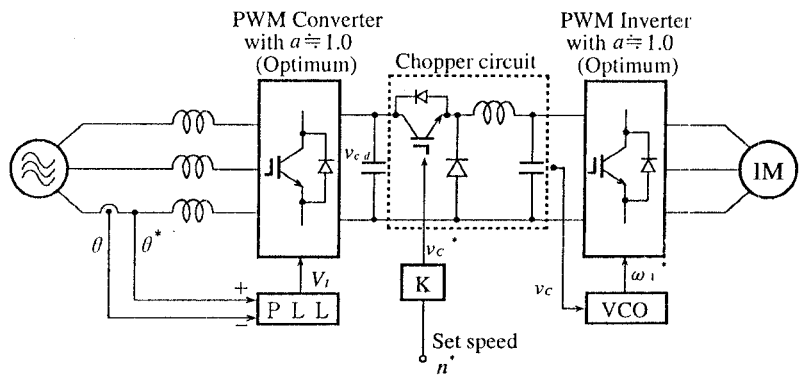


Fig.13 Three phase PWM converter/inverter system.

been proposed and discussed. In this method, the power factor is controlled by the PLL that is very simple control scheme. The response of the input power factor control by PLL becomes slow. However, the delay of the power factor control does not bring a serious problem. The output voltage that is the main controlled variable can be controlled very fast and precise. Voltage source converters are not suited for adjustable wide voltage range. However, by means of connecting the chopper, the problem can be resolved. The proposed PWM converter with an optimum voltage modulation factor produces always optimum current waveforms.

For an example to ac motor drive, a control scheme is proposed where the inverter is also controlled by the optimum modulation factor. We expect this circuit strategy to be applied for alternative general purpose ac motor drives.

REFERENCES

[1] Inoue,"Simple Estimations for Finding the Generating Source of a Harmonic Current and its Equivalent Circuit",Trans.IEE Japan, vol.101-B,pp.451-458, No.8, 1981.

[2] D.G.Kim, T.Nakajima & E.Masada, " Harmonic Analysis of a Capacitor-Filtered Rectifier with Line Impedance", Trans. IEICE Japan,vol.J75-B-I,pp.1316-1322,No.7,1981.

[3] K.Matsui, U.Mizuno & Y.Murai: "Improved Power Regenerative Controls by Using Thyristor Rectifier Bridge of Voltage Source Inverter and a Switching Transistor", IEEE Trans. on Industry Applic. Vol.28, No.5 (1992)

[4] K.Matsui, I.Yamamoto & et al: "A Reduction Method of Harmonic Currents in Power Systems Generated by Switch-ing Regulators", Conference Record of IEEE IAS Annual Meeting, Part II, p.1552 (1993)

[5] K.Matsui & M.Konishi : "A Method of PWM Power Regenerative Control Using DC Reactor for Voltage Source Type Inverter", Trans. IEEJ,vol.110-D,343 (1990)

[6] T.Kataoka, K.Kawakami & J.Kitano : "A Pulsewidth Modulated AC to DC Conveter Using Gate Turn-off Thyristors", Conf. Rec. of IEEE Ind.Appl.Soc.Annu.Meeting,p.966 (1985)

[7] A.Ueda, S.Ueda & M.Honbu: "Control Method and Characteristics of Current Source GTO Converter with Sinusoidal Input Current", Trans.IEEJ,Vol.107-D,1316 (1987)

[8] Y.Sato, H.Miyazawa & T.Kataoka: "A Control Method for Improving AC Input Current Waveform of Current Type PWM Rectifiers", Trans.IEEJ,Vol.112-D,703 (1992)

[9] Y.Sato & T.Kataoka : "State Feedback Control of Current Type PWM AC-to-DC Converters", IEEE Trans.on Ind.Appl.29 p.1090 (1993)

[10] K.Toyama, O.Mizuno, T.Takeshita & N.Matsui " Supression of Transient Oscillation Voltage in Current Source Three Phase PWM AC/DC Converter", Conf.Rec.IEEJ, SPC-96-56 (1996)

[11] T.Yamaguchi,K.Matsui, K.Hayashi, S.Takase & Y.Yang: "A Novel PWM Stategy to Minimize Surge Voltage for Current Sourse Converter", Conf.Rec. IEEE IAS Annnual Meeting, p.1085 (1996)

[12] K.Matsui & N.Sato "A Synchronized Modulation for a Pulse-width Modulated Inverter by using Phase Locked Loops", Trans.IEEJ,Vol.100-B,No.6(1980)

[13] K.Matsui & N.Sato: "A Modulation Technique of PWM Inverter using PLL",Trans,IEEJ, Vol.104,No.4(1984)

[14] Micro Linear Co. : "ML 4812 Power Factor Controller Data Sheet" (1989)

[15] T.Ohnishi: "Three Phase Voltage Fed Type PWM Power Converter by means of Power Factor Control",Trans.IEEJ, Vol.110, No.7(1990)

[16] S.Fukuda, Y.Iwazi and S.Sato : "Introduction of the Harmonic Distortion Determining Factor and its Application to Evaiuating Real Time PWM Inverters" IEEE IAS-93,Part II, p.1127 (1993)

Analysis and Design of Three-Phase Boost PWM Converter against Power Disturbances

Ki-Tae Park, Jun-Koo Kang and Seung-Ki Sul
School of Electrical Engineering
Seoul National University
Shillim-Dong Kwanak-Ku, Seoul, Korea (ZIP 151-742)
e-mail : sulsk@plaza.snu.ac.kr, Fax : +82-2-878-1452, Web: http://eepel.snu.ac.kr

Abstract - **This paper describes the operation of the three phase PWM converter under power disturbances caused by inevitable power faults. The output voltage ripple by input power unbalances - especially caused by a single line-to-ground fault(SLGF) - is analyzed to represent the amplitude of the ripple with some given parameters. This paper also shows that some converters' operation can be unstable when it uses a synchronous frame controller by unbalanced input power resulted from a SLGF. And we discuss a method that makes the converter run within a certain voltage ripple boundary even in the faulted power condition. Finally, the operations of the discussed converter are simulated and experimented to verify the results.**

1. INTRODUCTION

For the reliability of a power electronics system, system designer pays much attention to many kinds of things which may trip the system. One of the causes is the power disturbance by an inevitable fault in a power network system.

Since a converter is directly connected to a power system the first influence by a power disturbance is on the dc link voltage or output voltage of a converter. And by the abnormal dc link voltage, all the other systems would be tripped sequentially. Therefore, it is much important to make the converter system reliable even in the abnormal power conditions[1].

There are many types of power faults and they cause many types of power disturbances in a plant for example undervoltage, overvoltage, voltage sags, and outage. Among them, the power outage is rarely occurred only when the fault is on the same line[2][4]. Therefore, in most power disturbance cases, power is still supplied from a source. Line faults are the most common because lines are exposed to the environment. The most common type of fault are the single line-to-ground faults(SLGF), followed in frequency of occurrence by line-to-line faults(LLF),double line-to-ground faults(DLGF), and balanced three-phase faults[3].

Although a PWM converter has been widely used, few studies have been done about power disturbances caused by power failure. This paper describes and analyzes the operation of a three-phase boost PWM converter, and discuss the converter design providing against the power disturbances caused by single line-to-ground faults(SLGF).

2. MODELING OF THREE PHASE BOOST PWM CONVERTER

A. System Modeling

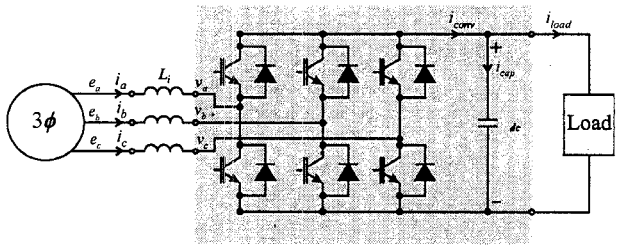


Fig. 1 Three-phase boost PWM converter

A typical three-phase boost PWM converter is shown in Fig. 1. The system equations of the converter where the load spends constant power is followed. If no zero-sequence voltage is assumed, the system voltage equation can be expressed in a synchronous dq frame as followings.

$$e_d^e = L_i \frac{di_d^e}{dt} - \omega L_i i_q^e + v_d^e$$
$$e_q^e = L_i \frac{di_q^e}{dt} + \omega L_i i_d^e + v_q^e \quad (1)$$

Equation(1) is used in the feedforwarded synchronous frame current controller[6].

B. Modeling of Balanced Power

In a normal power condition, three-phase input voltages are balanced. And these balanced voltages are modeled in three-phase form as

$$e_a = E\cos\omega t$$
$$e_b = E\cos(\omega t - (\frac{2\pi}{3} + \alpha)) \quad (2)$$
$$e_c = E\cos(\omega t + (\frac{2\pi}{3} + \alpha))$$

and in synchronous dq frame, as follows.

$$e_d^e = E$$
$$e_q^e = 0 \quad (3)$$

In a balanced system, the input power to the converter is the same with the output power to the load. The power is represented in synchronous dq frame as following.

$$P = \frac{3}{2}(e_d^e i_d^e + e_q^e i_q^e) \quad (4)$$

And for the unity power factor, the q-axis current is controlled to be zero ($i_q^e = 0$). So the power is modeled as (5) and the converter output power can be linearly controlled with the d-axis current in a balanced power condition.

$$P = \frac{3}{2} e_d^e i_d^e \quad (5)$$

C. Control Block Diagram

The control block diagram of the converter is shown in Fig. 2.

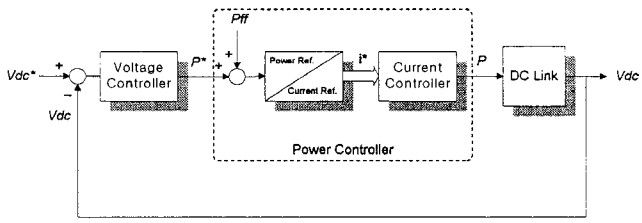


Fig. 2 The control block diagram of the PWM converter

The control block consists of a voltage controller and a power controller, and the power controller can be divided into a part that convert the power reference from the voltage controller to a current reference and a current controller part. A synchronous dq current controller[6] is used as a current controller. In balanced case, input voltage angle $\theta = \cos^{-1}\left(\frac{e_a}{E}\right)$ and $\theta_e = \tan^{-1}\left(\frac{-e_q^s}{e_d^s}\right)$ are equivalent so either angle can be used in a vector rotator. In unbalanced case, only θ_e can keep e_q^e zero and e_d^e becomes dc value with ripple terms.

In power controller, to make a current reference, the following equation is used.

$$i_q^e = 0, \quad P = \frac{3}{2} e_d^e i_d^e$$

Therefore, the current reference can be obtained from one of these following equations.

$$i_d^{e*} = \frac{P^*}{\frac{3}{2} e_d^e} \quad (6)$$

$$i_d^{e*} = \frac{P^*}{\frac{3}{2} E} \quad (7)$$

Equation (6) uses a instantaneous reference voltage and (7) uses a constant reference voltage. In a balanced condition, (6) and (7) operate as the same.

3. Converter Operations by Power Disturbances

A. Modeling of Unbalanced Voltage by Single Line-to-Ground Fault(SLGF)

As shown in the Appendix B, input voltages from the power network where at some place a SLGF occurs can be modeled as follows in worst case.

$$e_d^e = \bar{E} + \tilde{E}\cos 2\omega t$$
$$e_q^e = \tilde{E}\sin 2\omega t \quad (8)$$

where, $\bar{E} = \frac{1+m'}{2}E$, $\tilde{E} = \frac{1-m'}{2}E$,

$$m' = \frac{2}{\sqrt{3}}\sin\left(\frac{2\pi}{3} + \alpha\right)m \quad (9)$$

The sag index m' has the value of $1 \le m' \le 1/3$.

B. Analysis of Output Power under the Unbalanced Voltage

Note that the output power to the load is not always same with the input power from the source in the unbalanced power condition. If the currents of three-phase are unbalanced the instantaneous output and input powers have difference proportional to the inductance. The input power and the output power are represented as follows.

$$p_{in} = \frac{3}{2}(e_d^e i_d^e + e_q^e i_q^e) \quad (10)$$

$$p_{conv} = \frac{3}{2}(e_d^e i_d^e + e_q^e i_q^e) - \frac{3}{2} L_i \left(i_d^e \frac{di_d^e}{dt} + i_q^e \frac{di_q^e}{dt} \right) \quad (11)$$

In the unbalanced condition, the output power of the converter which designed based on a balanced condition has no longer constant value. The aspect of the power is varied according to the power controller scheme.

C. Instantaneous Voltage Reference(IVR) Power Controller

If the power controller is designed with (6) for the faster response to a input voltage variation, the wave forms are given as Fig. 3.

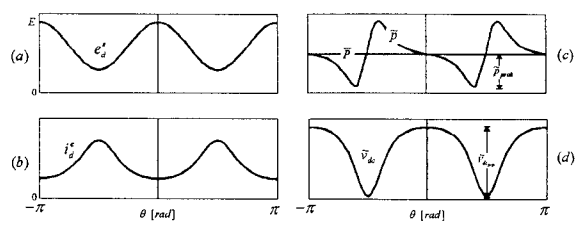
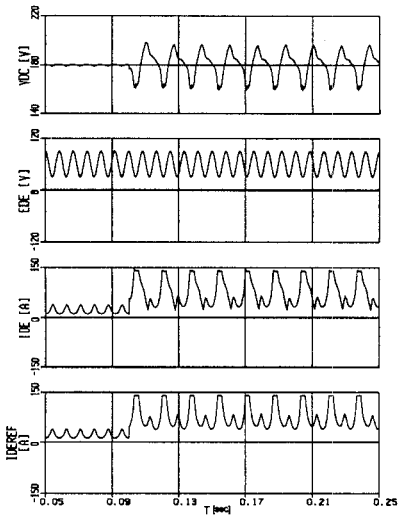
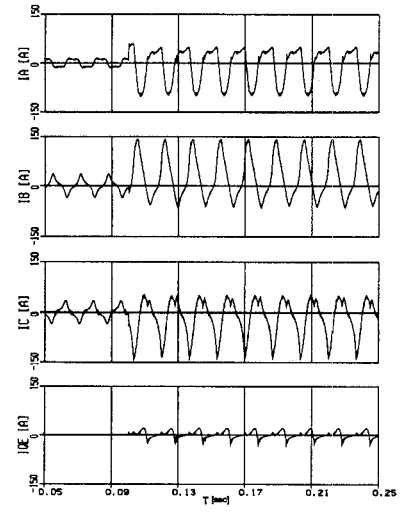


Fig. 3 The wave forms with the instantaneous voltage reference(IVR) power controller
(a) d-axis voltage (b) current reference
(c) output power (d) output voltage

With this power controller, the input power (10) is controlled to be constant. But, because of the second term of (11), the output power has ripple terms. In a SLGF condition, the worst power ripple and the peak of it can be obtained



(a)



(b)

Fig. 4 Simulation wave forms with the IVR power controller
(a) Dc link voltage, d-axis voltage, d-axis current, and d-axis current reference
(b) Phase currents and q-axis current

from following equations.

$$\tilde{p} = -\frac{4\omega L_i P^{*2} \tilde{E} \sin 2\omega t}{3(\bar{E} + \tilde{E}\cos 2\omega t)^3} \tag{12}$$

$$\tilde{P}_{peak} = \frac{4\omega L_i P^{*2} \tilde{E}\sqrt{1-C^2}}{3(\bar{E}+C\tilde{E})^3}, \quad C = \frac{\bar{E}-\sqrt{\bar{E}+24\tilde{E}^2}}{4\tilde{E}} \tag{13}$$

As shown in (13), the ripple peak is proportional to the square of the reference power. So the ripple peak can be larger than the reference power and then it may cause a positive feedback in the outer voltage control loop during some time period.

D. Constant Voltage Reference(CVR) Power Controller

With the constant voltage reference power controller, the output power ripple in a SLGF is given as follows.

$$\tilde{p}_1 = P_{load}\frac{\tilde{E}}{\bar{E}}\cos 2\omega t \tag{14}$$

The output voltage ripple in a SLGF due to the power ripple is given as following if the IVR power controller is used,

$$\tilde{V}_{dc_{pp}} = \frac{L_i P_{load}^{\ 2}}{3C_{dc}V_{dc_0}}\left(\frac{1}{(\bar{E}-\tilde{E})^2}-1\right) \tag{15}$$

and if the CVR power controller is used as follows.

$$\tilde{V}_{dc_{pp}} = \frac{P_{load}\tilde{E}}{\omega C_{dc}V_{dc_0}\bar{E}} \tag{16}$$

4. Design of PWM Converter against Power Disturbances

A. Elimination of the Power Ripple by a Power Controller

Figure 4 shows that a converter using an IVR power controller has following characteristics that 1)it can reduce power ripple when index of voltage sag is not large but 2) it can be unstable to an unbalanced voltage by a SLGF, 3) eliminating the power ripple requires too large device rating as shown in Fig.3 and 4) it generates large harmonic currents. Therefore in practical situation it is a simple but better way to use the CVR power controller, letting the ripple exist and restricting the ripple to a certain range. Of course, there are some complicated compensation schemes for general voltage unbalance cases. From (16), we can obtain the dc link capacitor rating to envelop the output voltage ripple within a certain range $\tilde{V}_{dc_{pp}}$ as follows.

$$C_{dc} = \frac{P_{load}}{2\omega V_{dc_0}\tilde{V}_{dc_{pp}}} \tag{17}$$

5. Experimental Results

Figure 5 shows the response of the converter which uses the CVR power controller. The dc link capacitance is chosen to fit the output voltage within 10[V] in the worse-case SLGF using (19). Table 1 shows parameters of experimental set-up. In Fig.5, the SLGF is occurred at 30[msec], and from that time the ripple of the d-axis voltage appears. This result shows that the converter endures the SLGF without serious voltage ripple and distortion of the current wave forms.

TABLE 1. Experiment parameters

Rating power	6.5[kW]
Interface inductor	1.5[mH]
Input line-to-line voltage	110[V]
DC link voltage	180[V]
DC link capacitor	6800[uF]

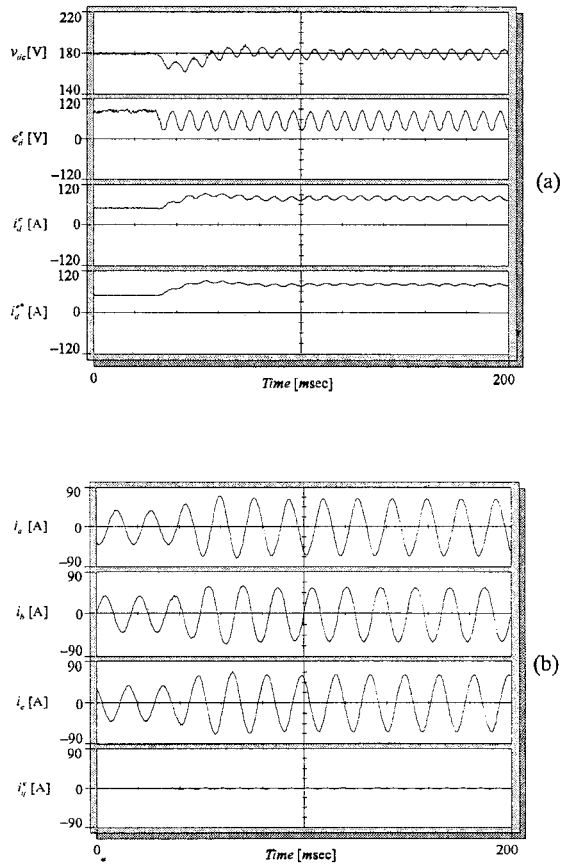


Fig. 5 The response of the converter using the constant voltage reference power controller to a worst-case SLGF.
(a) Dc link voltage, d-axis voltage, d-axis current, and d-axis current reference
(b) Phase currents and q-axis current

6. CONCLUSIONS

In this paper, a three-phase boost PWM converter under power disturbance condition – especially under unbalanced sags by a SLGF -- was analyzed and discussed how the converter can be designed to endure the sags by a SLGF.

It introduced the power controller to analyze and design the converter under unbalanced power and calculated the ripple power and the ripple voltage by a SLGF.

This study showed why, with some control scheme, the converter may be tripped or not properly operated by a SLGF, and proposed how to make the converter endure the SLGF.

REFERENCES

[1] F. L. Hoadley, " AC drive operation during power Failures," in *Power Quality Conference*, pp. 1-13, October 1993.

[2] M.F. McGranaghan, D.R. Mueller, and M.J. Samotyj, "Voltage sags in industrial systems," *IEEE Transactions on Industry Applications*, vol. 29, no. 2, pp. 397-403, March/April 1993.

[3] A.R. Bergen, *Power Systems Analysis*, ch. 13. Prentice-Hall, 1986

[4] D. S. Dorr, "Power quality study - 1990 to 1995 initial results," in IEEE-APEC Conference, pp. 303-308, 1992.

[5] M. Carrescia and G. Griva, "Voltage sags analysis and statistical distribution, as a function of amplitude and duration, for a typical MV distribution system in Italy," in *IEEE-IAS Conference*, vol.2, pp. 192-195, 1996.

[6] T. M. Rowan and R.J. Kerkman, " A new synchronous current regulator and analysis of current-regulated PWM inverters," *IEEE Transactions on Industry Applications*, vol. 22, no. 4, pp. 678-690, July/August 1986.

[7] C. Becker, W.B. Jr., K. Carrick, T. Diliberti, C. Grigg, J. Groesch, B. Hazen, T. Imel, D. Koval, D. Mueller, T. S. John, and L. E. Conrad, "Proposed chapter 9 for predicting voltage sags(dips) in revision to IEEE std 493, the gold book," *IEEE Transactions on Industry Applications*, vol. 30, no. 3, pp. 805-822, May/June 1994.

[8] W.-I. Tsai, Y.-Y. Sun, and M.-T. Tsai, "Effect of voltage unbalance and harmonics on three-phase PWM ac-to-dc converters with instantaneous power feedback," *T. IEE Japan*, vol. 115-D, no. 1, pp. 21-29, 1995.

APPENDIX A

Voltage modelling at SLGF

When single-line-to-ground fault occurs at the primary side of Δ-Y transformer, the voltage phasor diagram of the secondary side can be shown as fig. A and from this figure voltage equations are obtained as follows

$$e_a = E\cos\omega t$$
$$e_b = mE\cos(\omega t - (\frac{2\pi}{3} + \alpha)) \quad \text{(A.1)}$$
$$e_c = mE\cos(\omega t + (\frac{2\pi}{3} + \alpha))$$

where sag index m is $\frac{1}{\sqrt{3}} \le m \le 1$ (A.2)

angle α is $\frac{\pi}{3} - \cos^{-1}(\frac{1}{2m})$ (A.3)

With 3 to 2 phase transformation (A.1) becomes (A.4).

$$E_d^s = E\cos wt$$
$$E_q^s = -\frac{2}{\sqrt{3}}mE\sin(\frac{2\pi}{3} + \alpha)\sin wt = -m'E\sin wt \quad \text{(A.4)}$$

where the sag index m' has the value of $1 \le m' \le 1/3$.

Finally, we can obtain voltage in SLGF with synchronous reference frame as follows.

$$e_d^e = \overline{E} + \widetilde{E}\cos 2wt \qquad e_q^e = \widetilde{E}\sin 2\omega t$$

where, $\overline{E} = \frac{1+m'}{2}E$, $\widetilde{E} = \frac{1-m'}{2}E$

$$m' = \frac{2}{\sqrt{3}}\sin(\frac{2\pi}{3} + \alpha)m$$

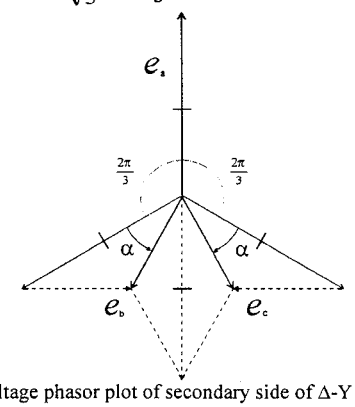


Fig. A Voltage phasor plot of secondary side of Δ-Y transformer at SLGF .

Effect of Parasitic Capacitance of Power Device on Output Voltage Deviation during Switching Dead-Time in Voltage-Fed PWM Inverter

Kichiro Yamamoto Katsuji Shinohara Hiroyuki Ohga
Department of Electrical and Electronics Engineering, Faculty of Engineering, Kagoshima University
Address: 21-40, Korimoto, 1 chome, KAGOSHIMA 890, JAPAN
Fax: +81-99-285-8414, Phone: +81-99-285-8411
E-mail: yamamoto@eee.kagoshima-u.ac.jp

Abstract - The PWM inverter, which is operated by the high carrier frequency, is influenced by the switching dead-time. In this paper, the effect of the parasitic capacitance of the power device on the voltage deviation during switching dead-time is investigated and a numerical method to analyze the output voltage deviation in consideration of the parasitic capacitance of the power device is proposed. Furthermore, this method is applied to a permanent-magnet ac servo motor drive system and the voltage deviation and the phase current waveforms are calculated. Finally, the calculated results are compared with the experimental results in order to confirm the validity of the analysis.

I. INTRODUCTION

With appearance of high-speed switching devices, the switching frequency tends to be raised in voltage-fed PWM inverters, recently. The PWM inverter, which is operated by the high carrier frequency, is influenced by the switching dead-time. The switching dead-time, which is unavoidable to prevent the shoot-through phenomena, causes the voltage deviation between the ideal PWM waveform and the actual output PWM waveform. The average value of the output voltage is distorted by the output voltage deviation. In the case that the load is a motor, it is known that the output voltage deviation causes serious problems such as current waveform distortion and increased torque ripples at low speed and light load operation. Though the mechanism of the output voltage deviation was clarified and several compensation were proposed, deterioration of the current waveform remains around zero[1][2]. The deterioration is conspicuous when both the output frequency and voltage are low. Main causes for this deterioration are a parasitic capacitance parallel to the power device[3][4] and zero-current-clamping phenomenon caused by diode[5][6].

In this paper, the effect of the parasitic capacitance of the power device on the voltage deviation during switching dead-time is investigated and a numerical method to analyze the output voltage deviation in consideration of the parasitic capacitance of the power device is proposed. Furthermore, this method is applied to a permanent-magnet ac servo motor drive system and the voltage deviation and the phase current waveforms are calculated. Finally, the calculated results are compared with the experimental results in order to confirm the validity of the analysis.

II. CIRCUIT SCHEME

The circuit and block diagram of Digital Signal Processor (DSP)-based permanent-magnet ac servo motor drive system is shown in Fig.1. The inverter consists of IGBT module. C_1-C_6 are parasitic capacitances of the IGBTs. The rating of the permanent-magnet ac servo motor is 771W and it has six poles. The control circuit mainly consists of DSP (TMS320C25). The reference value of q-axis stator current i_q^* is obtained by the speed PI regulator whose input is the difference between the rotor speed reference ω_r^* and the actual rotor speed ω_r. And the reference value of d-axis stator current i_d^* is equalized to zero. The dq-axes stator voltage references v_{sd} and v_{sq} are obtained by the current PI regulators whose input is the difference between the stator current references i_d^* and i_q^* and the actual stator currents i_d and i_q, respectively. The dq-axes stator voltage references are transformed into the three-phase stator voltage references v_{su}, v_{sv} and v_{sw}. To modulated these references into the PWM form, we use the space vector modulation method. The modulated signals which have the dead-time 4μs drive the gates of IGBT. The sampling period T_s of the position of the rotor and the values of the three-phase stator currents is 132μs.

III. OUTPUT VOLTAGE DEVIATION

A. Without Parasitic Capacitance

To make effect of parasitic capacitance clear, output voltage deviation is explained without parasitic capacitance.

Fig.2 shows the actual waveform of v_u with the dead-time for the polarity of the current i_u. Effect of parasitic capacitance is not considered in Fig.2. The polarity of the current i_u is positive when the current flows into the motor. The positive edge of the gating signal of IGBT S_1 is delayed with respect to the positive edge of the ideal v_u for a dead-time T_{dead}. The positive edge of the gating signal of IGBT S_2 is delayed with respect to the negative edge of the ideal v_u for a dead-time T_{dead}, too. When IGBT S_1 is on-state, the actual v_u is equal to the dc link voltage. When IGBT S_2

0-7803-3823-5/97/$10.00© 1997 IEEE

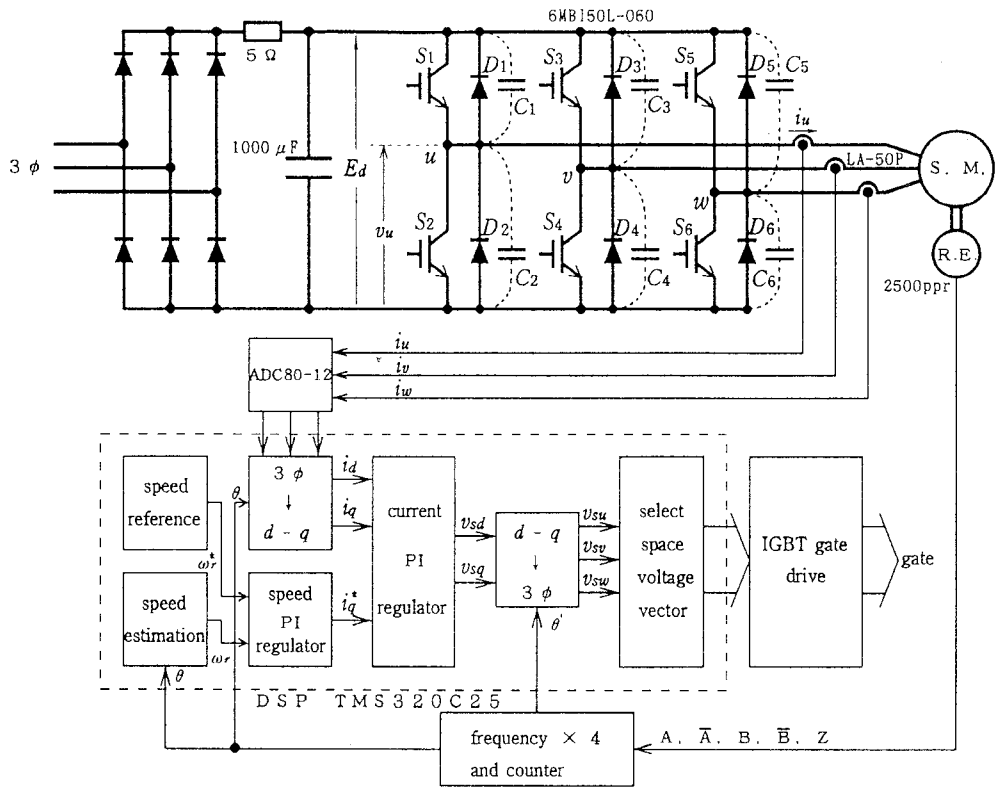


Fig.1. Circuit and block diagram of DSP-based permanent-magnet ac servo motor drive system.

is on-state, the actual v_u is zero. During the period that both S_1 and S_2 are off-state, the actual v_u depends on the polarity of the current i_u. In the case that the current i_u is positive, the current i_u flows through the bottom diode D_2 and the actual v_u is zero. In the case that the current i_u is negative, the current i_u flows the upper diode D_1 and the actual v_u is equal to the dc link voltage.

In comparison the ideal v_u with the actual v_u, it is found that the actual v_u has lag times. There are two kinds of the lag time. One is short and the other is long. The short one is only turn-off time T_{off} of IGBT. On the other hand, the long one is the sum of the dead-time T_{dead} and turn-on time T_{on} of IGBT. These lag time causes output voltage deviation.

B. With Parasitic Capacitance

In this subsection, effect of parasitic capacitance on the output voltage deviation is explained. Fig.3 illustrates the output voltage deviation when the phase current flows through an IGBT. The parts of the output voltage deviation are shaded in Fig.3. The polarity of the current i_u is positive in Fig.3. In the period A, the phase current i_u flows through the upper IGBT S_1. When the upper IGBT is turned off, the period B begins. The upper parasitic capacitance C_1 is charged and the bottom parasitic capacitance C_2 is discharged in the period B. In this time, the output voltage v_u is as the following[4]:

$$v_u = Ed - \frac{1}{C_1+C_2}\int i_u\, dt \qquad (1)$$

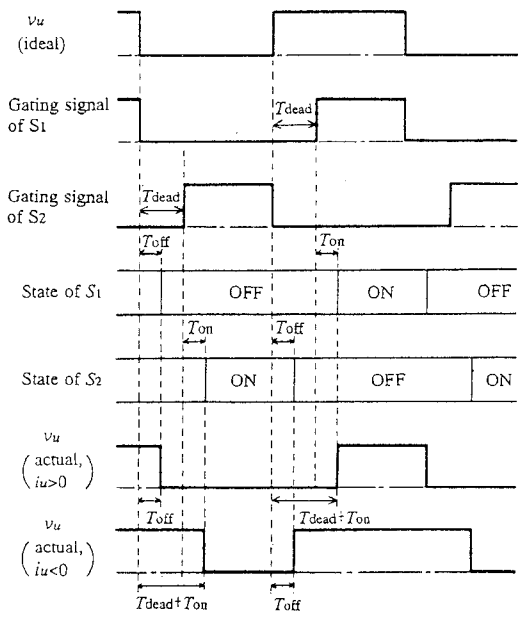
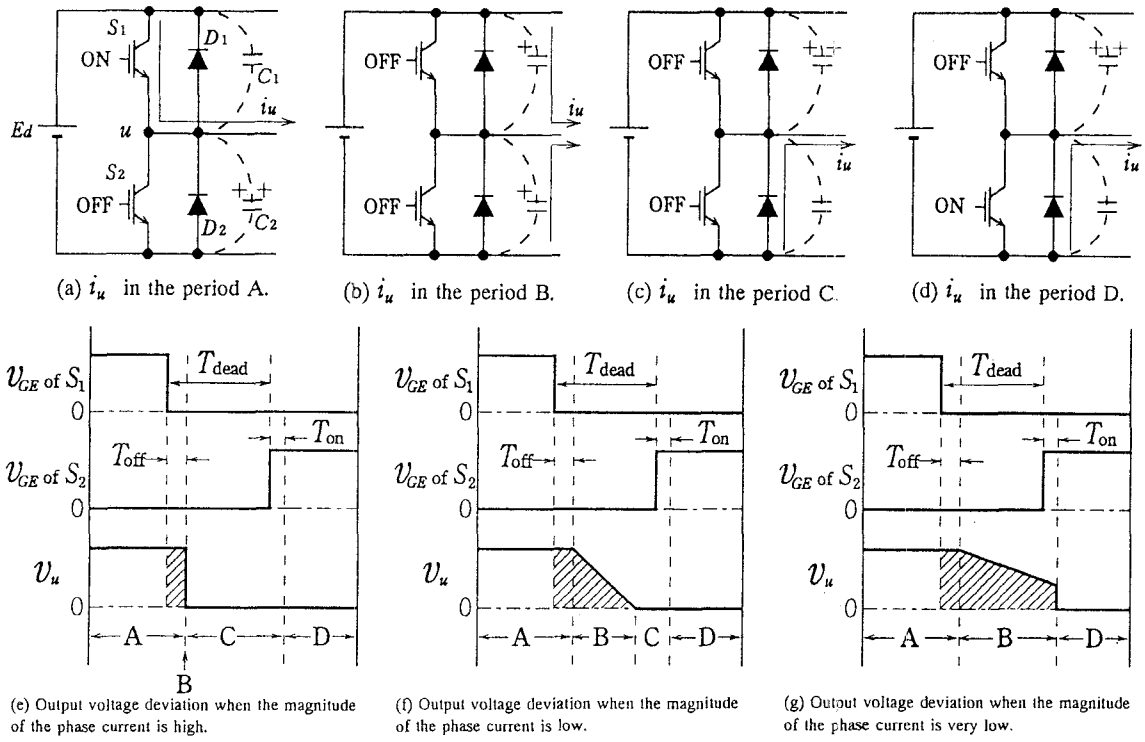


Fig.2. Actual v_u for the polarity of the current i_u (without parasitic capacitance).

When both charge of C_1 and discharge of C_2 are finished, the output voltage v_u becomes zero. In the period C, the current i_u flows through the bottom diode D_2. Though the bottom IGBT S_2 is turned on at the end of the period C, the current i_u remains flowing through the bottom diode D_2 in the period D. In the case that the magnitude of the phase current i_u is high at the moment when the upper IGBT S_1 is turned off, the upper parasitic



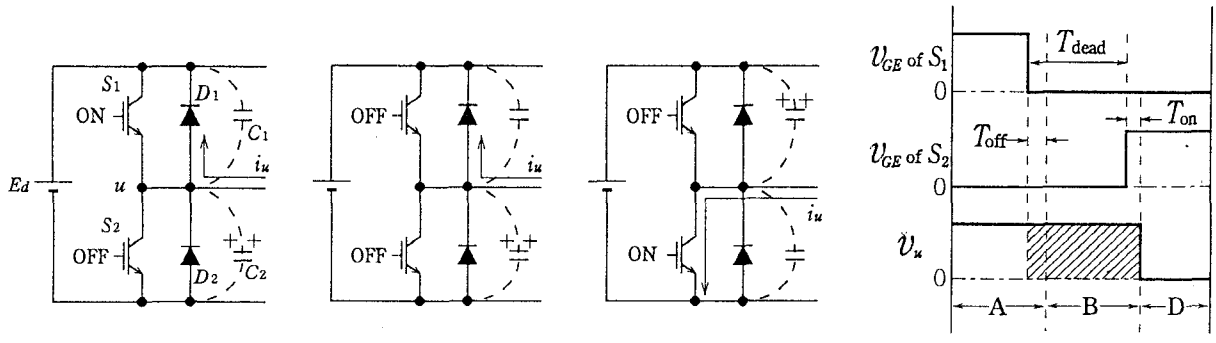
(a) i_u in the period A. (b) i_u in the period B. (c) i_u in the period C. (d) i_u in the period D.

(e) Output voltage deviation when the magnitude of the phase current is high.

(f) Output voltage deviation when the magnitude of the phase current is low.

(g) Output voltage deviation when the magnitude of the phase current is very low.

Fig.3. Illustrating the output voltage deviations when the phase current flows through an IGBT (with parasitic capacitance).



(a) i_u in the period A. (b) i_u in the period B. (c) i_u in the period D. (d) Output voltage deviation.

Fig.4. Illustrating the output voltage deviation when the phase current flows through a diode (with parasitic capacitance).

capacitance C_1 is charged immediately and the bottom parasitic capacitance C_2 is discharged immediately, too. Therefore, the output voltage v_u changes with lag time T_{off} as shown in Fig.3(e). In the case that the magnitude of the phase current i_u is low at the moment when the upper IGBT S_1 is turned off, both charging the upper parasitic capacitance C_1 and discharging the bottom parasitic capacitance C_2 make the output voltage v_u change slowly as shown in Fig.3(f). In this case, the output voltage v_u changes with lag time more than T_{off}. In the case of very low current, the bottom IGBT S_2 is turned on before the finish of charging C_1 and discharging C_2 because the output voltage v_u changes more slowly. This turn-on of the bottom IGBT S_2 charges the upper parasitic capacitance C_1 and discharges the bottom parasitic capacitance C_2 immediately. Therefore, the output voltage v_u changes to zero immediately as shown in Fig.3(g). In this case, the output voltage v_u changes with lag time $T_{dead}+T_{on}$.

Fig.4 illustrates the output voltage deviation when the phase current i_u flows through a diode. The polarity of the current i_u is negative in Fig.4. In the period A, the phase current i_u flows through the upper diode D_1. In the period B, the upper IGBT S_1 is turned off but the phase current i_u flows through the upper diode D_1 nevertheless. At the end of the period B, the turn-on of the bottom IGBT S_2 charges the upper parasitic capacitance C_1 and discharges the bottom parasitic capacitance C_2. As a result, the output voltage v_u changes to zero immediately. In this case, the change of v_u is independent of the parasitic capacitances C_1, C_2 and the output voltage v_u changes with lag time $T_{dead}+T_{on}$.

As described above, when phase current flows through an IGBT and the current is low, output voltage deviation

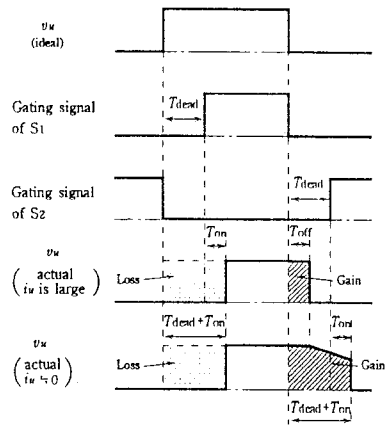


Fig.5. Effect of parasitic capacitance on output voltage deviation (i_u>0).

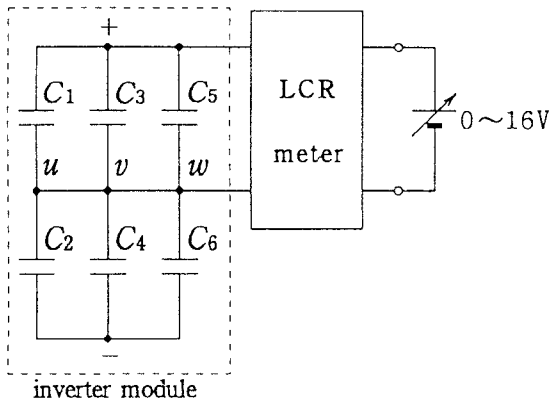


Fig.6. Measurement circuit for parasitic capacitance.

consists of lag time and amplitude deviation. As it is clear from Fig.5, output voltage v_u is reduced by the output voltage deviation when phase current i_u is high but v_u is not reduced when i_u is very low. Therefore, conventional compensation for only the lag time makes current waveform distortion serious around zero.

IV. Measurement of Parasitic Capacitance

The parasitic capacitance of IGBT (6MB50L-060) which was used in our system, was measured. During the measurement, between gate and emitter of all IGBT were connected to privent turn-on of IGBT. And output terminal u, v and w also were connected each other. Upper arms were applied dc voltage and the parasitic capacitance of upper arms were measured by LCR meter (Fig.6). The parasitic capacitance of an arm is one third of that of the upper arms. The average value of parasitic capacitances of upper and lower arm, C_{av}, is shown in Fig.7. It is found that the parasitic capacitance depends on the collector-emitter voltage V_{CE} and its value was several nano farad.

V. Mathematical Method Analysis

Replacing the integral part of second term in (1) to Q_u for phase u and using the dq transformation for three-phase voltage v_u, v_v and v_w give the following:

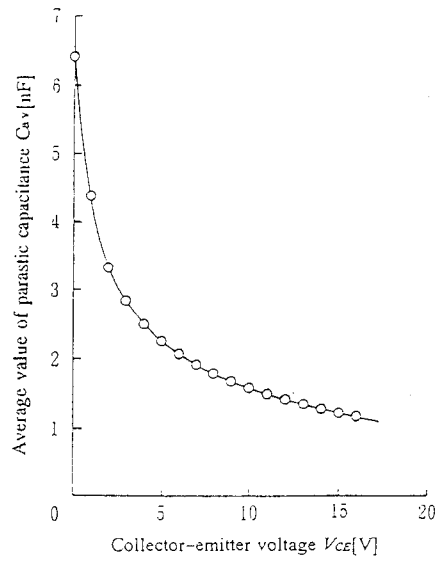


Fig.7. Parasitic capacitance of IGBT (measured).

$$v_d=-\frac{1}{C1+C2}\sqrt{\frac{2}{3}}\{Q_u\cos\omega_e t+Q_v\cos(\omega_e t-\frac{2}{3}\pi)+Q_w\cos(\omega_e t+\frac{2}{3}\pi)\} \quad (2)$$

$$v_q=\frac{1}{C1+C2}\sqrt{\frac{2}{3}}\{Q_u\sin\omega_e t+Q_v\sin(\omega_e t-\frac{2}{3}\pi)+Q_w\sin(\omega_e t+\frac{2}{3}\pi)\} \quad (3)$$

We also obtain the following differential equation for Q_u .

$$pQ_u=i_u=\sqrt{\frac{2}{3}}\,(i_d\cos\omega_e t-i_q\sin\omega_e t) \quad (4)$$

In the same way, we obtain the differential equations for Q_v and Q_w as follows:

$$pQ_v=i_v=\sqrt{\frac{2}{3}}\{i_d\cos(\omega_e t-\frac{2}{3}\pi)-i_q\sin(\omega_e t-\frac{2}{3}\pi)\} \quad (5)$$

$$pQ_w=i_w=\sqrt{\frac{2}{3}}\{i_d\cos(\omega_e t+\frac{2}{3}\pi)-i_q\sin(\omega_e t+\frac{2}{3}\pi)\} \quad (6)$$

The following equations are used for the ac servo motor and controller.

$$pi_d=(v_d-Ri_d+\omega_e L_q i_q)/L_d \quad (7)$$

$$pi_q=(v_q-Ri_q-\omega_e L_d i_d-\omega_e\Phi_f)/L_q \quad (8)$$

$$p\omega_r=\left[-D\omega_r+\frac{P}{2}\{(L_d i_d+\Phi_f)i_q-L_q i_q i_d\}-T_{load}\right]/J \quad (9)$$

$$i_d^*=0 \quad (10)$$

$$i_q^*(n)=K_{p\omega}\{\omega_r^*(n)-\omega_r(n)\}+\frac{K_{p\omega}}{\tau_\omega}\sum_{m=0}^{n}\{\omega_r^*(m)-\omega_r(m)\}T_{samp} \quad (11)$$

$$v_{sd}(n+1)=K_{pi}\{i_d^*-i_d(n)\}+\frac{K_{pi}}{\tau_i}\sum_{m=0}^{n}\{i_d^*-i_d(m)\}T_{samp} \quad (12)$$

$$v_{sq}(n+1)=K_{pi}\{i_q^*(n)-i_q(n)\}+\frac{K_{pi}}{\tau_i}\sum_{m=0}^{n}\{i_q^*(m)-i_q(m)\}T_{samp} \quad (13)$$

where p is the derivative operator d/dt, R is the armature resistance, L_d and L_q are the d-and q-axes inductance,

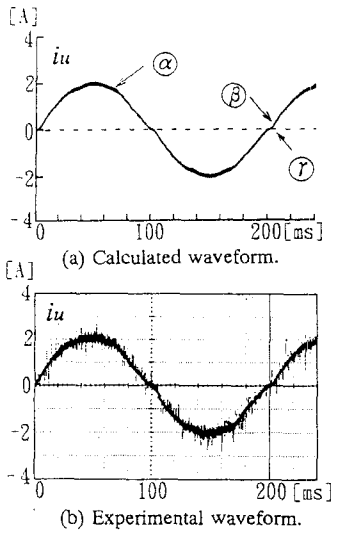
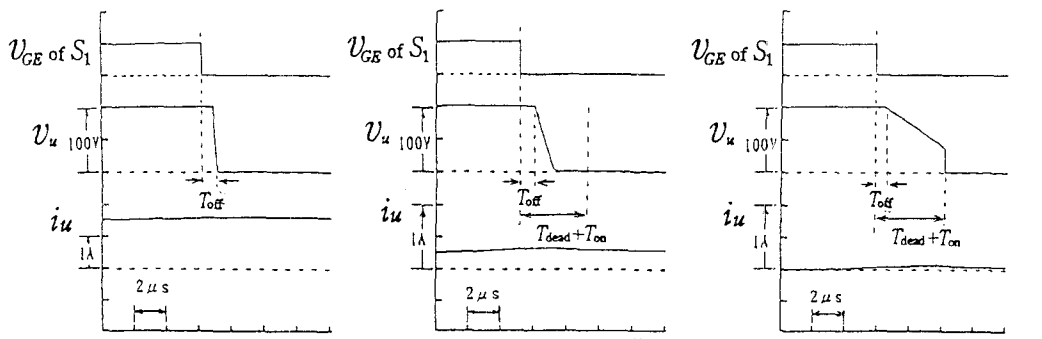


Fig.8. Calculated and experimental waveforms of phase current (iu*peak=2A, 100rpm).

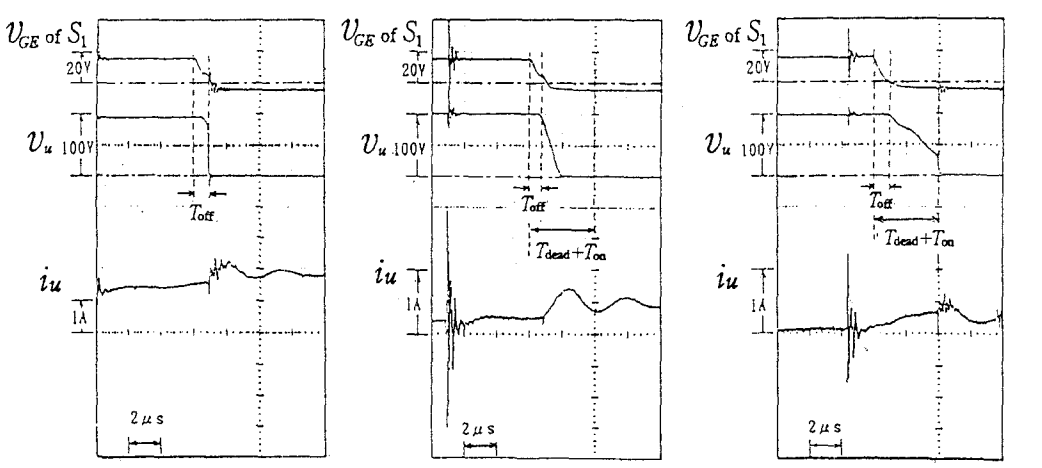
TABLE I
CONSTANTS OF MACHINE AND INVERTER

Parameter	Symbol	Value
Rated output power		771W
Pole number	P	6
Armature resistance	R	0.61 Ω at 20 ℃
d-axis inductance	Ld	2.75mH
q-axis inductance	Lq	3.01mH
Flux of field	ϕ_f	0.101Wb
Turn-on time of IGBT	T_{on}	Typ. 0.6μs (max. 1.0μs)
Turn-off time of IGBT	T_{off}	Typ. 0.9μs (max. 1.5μs)
Dead-time	T_{dead}	4.0μs
Proportional gain of current regulator	K_{pi}	1.0
Integral time constant of current regulator	τ_i	2.0ms
Sampling period	Ts	132μs
Dc link voltage	Ed	100V



(a) The magnitude of the phase current is high (corresponding to Fig.4.ⓐ).
(b) The magnitude of the phase current is low (corresponding to Fig.4.Ⓑ).
(c) The magnitude of the phase current is very low (corresponding to Fig.4.Ⓒ).

Fig.9. Calculated output voltage deviations when the phase current flows through an IGBT.



(a) The magnitude of the phase current is high.
(b) The magnitude of the phase current is low.
(c) The magnitude of the phase current is very low.

Fig.10. Experimental output voltage deviations when the phase current flows through an IGBT.

ϕ_f is the flux of field, ω_e is the electrical angular velocity, D is the dumping coefficient, P is the number of poles, T_{load} is the load torque and J is the moment of inertia, $Kp\omega$ is the proportional gain of speed regulator, τ_ω is the integral time constant of speed regulator, Kpi and τ_i is the proportional gain and the integral time constant of current regulator, respectively.

In our analysis, we use (2)-(13) for B, C periods in Figs.3 and 4. And we also use (7)-(13) for other periods.

VI. Calculated and Experimental Results

The numerical analysis in consideration of the parasitic capacitance of the power device is applied to a permanent-magnet ac servo motor drive system shown in Fig.1. The constants of machine and inverter are listed in Table I. As shown in the section IV, the parasitic capacitance depends on the collector-emitter voltage V_{CE} and it is not constant. But we use a constant value 2nF in order to simplify the analysis (C_1=C_2=2nF). Fig.8 shows the calculated and the experimental waveforms of phase current i_u. According to our experimental condition, the peak of the u phase current reference i_u*peak was 2A. The carrier frequency f_c was 3780Hz and the inverter frequency f was 5Hz (100rpm). The waveform distortion around zero is found from Fig.8.

Figs.9 and 11 show the calculated waveforms of output voltage v_u. Figs.10 and 12 show the experimental waveforms corresponding to those in Figs.9 and 11, respectively. The phase current i_u flows through an IGBT in both Figs.9 and 10. The current i_u flows through a diode in Figs.11 and 12, respectively. Figs.9 and 10 demonstrate that the output voltage v_u changes with lag time corresponding to the current magnitude when the current i_u flows through an IGBT. Furthermore, Figs.11 and 12 demonstrate that the output voltage v_u changes with lag time independent of the current magnitude when i_u flows through a diode. It is clear from Figs.8-12 that there is good agreement between the calculated and experimental results.

VII. Conclusion

In this paper, a numerical method to analyze the output voltage deviation in consideration of the parasitic capacitance of the power device was proposed. This method was applied to the permanent-magnet ac servo motor drive system and both the voltage deviation and the phase current waveforms was calculated.

Main conclusions drawn from this study are as follows:
(1)The validity of the analysis was confirmed by comparing the calculated waveforms with that obtained from the experimental.
(2)When the phase current flows through an IGBT, the parasitic capacitance of power device makes the output voltage deviation change corresponding to the magnitude of the current. This is one of causes of the current waveform deterioration around zero in the case of using compensation for output voltage deviation.
(3)When the phase current flows through a diode, the output voltage changes independent of the magnitude of phase current and the parasitic capacitance.

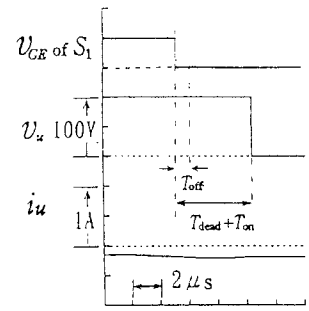


Fig.11. Calculated output voltage deviation when the phase current flows through a diode.

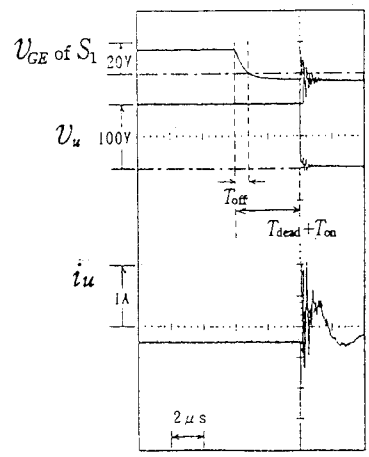


Fig.12. Experimental output voltage deviation when the phase current flows through a diode.

References

[1] R. C. Dodson, P. D. Evans, H. Tabatabaei Yazdi and S. C. Harley, "Compensating for dead time degradation of PWM inveter waveforms, " *IEE PROCEEDINGS*, Vol.137, Pt.B, No.2, pp.73-81, 1990.

[2] K. Yamamoto and K. Shinohara, "Analysis of ac servo motor driven by PWM inverter with switching dead-time and compensation for output voltage deviation," *Trans. Inst. Electr. Engng. Jap.*, 116-D, (9), pp.924-933, 1996.

[3] R. B. Sepe and J. H. Lang, "Inverter nonlinearities and discrete-time vector urrent control," *IEEE Trans. Ind. Applicat.*, vol. IA-30, pp.62-70, Jan./Feb. 1994.

[4] Joohn-Sheok Kim, Jong-Woo Choi and Seung-Ki Sul, "Analysis and Compensation of voltage distortion by zero current clamping in voltage-fed PWM inverter," in *IPEC-Yokohama Conf. Rec.*, pp.265-270, 1995.

[5] Y. Murai, A. Riyanto, H. Nakamura and K. Matsui, "PWM strategy for high frequency carrier inverters eliminating current-clamps during switching dead-time," in *IEEE-IAS Ann. Meet. Conf. Rec.*, pp.317-322, 1992.

[6] K. Yamamoto and K. Shinohara, "Analysis of zero-current-clamping phenomena during switching dead-time in PWM inverter," in *IPEC-Yokohama Conf. Rec.*, pp.1519-1524, 1995.

New Current-Controlled PWM Rectifier-Voltage Source Inverter without DC Link Components

Kenichi Iimori Katsuji Shinohara Osamu Tarumi Zixum Fu Mitsuhiro Muroya*
Department of Electrical and Electoronics Engineering, Faculty of Engineering, Kagoshima University
Address: 21-40, Korimoto, 1 chome, KAGOSHIMA 890, JAPAN
Fax: +81-99-285-8414, Phone: +81-99-285-8411
E-mail: iimori@eee.kagoshima-u.ac.jp

*Kagoshima National College of Technology
Address: 1460-1, Shinko, Hayato-cho, Aira-gun, KAGOSHIMA 899-51, JAPAN

Abstract- **The voltage-source inverters are normally equipped with an electrolytic capacitor in their DC link, the electrolytic capacitor has several disadvantages such as increasing size, limiting converter life and reliability. Therefore several approaches for removing the DC link capacitor have been studied. This paper proposes a new voltage source inverter without DC link components, whose rectifiers is controlled by suitable current feedback to adjust near-sinusoidal AC source current waveforms at unity power factor. The calculated characteristics are described for a 0.75kW induction motor driven by this inverter.**

I. INTRODUCTION

The voltage source inverter without DC link components have already been proposed and verified by the authors, that the inverter made possible the highly reliable four quadrant operation of the induction motor[1]. The rectifier section of this inverter requires the *LC* filter on the AC source side to improve AC source current[2]. However, AC source current may oscillate caused by resonance of this *LC* filter.

In this paper, calculated characteristics are described for a 0.75kW induction motor driven by this inverter, which rectifier is controlled by the current closed loop with *di/dt* feedback. As a result, it can be obtained that the AC source current maintain nearly sinusoidal waveforms with a unity power factor.

II. CIRCUIT CONFIGURATION

The overall system described in this paper is shown in Fig. 1. The main circuit consists of the inverter section, rectifier section and AC filter. There are no smoothing circuit such as electrolytic capacitors and reactors (or resistors) on the DC link.

The inverter section employs the IGBT module as a switching device, and the PWM-controlled signal, which are generated by comparing the sinusoidal modulating waves with the triangular carrier wave, are applied to each inverter gates. The rectifier section also employs twelve IGBT, and the current flow is possible in both direction when a IGBT is in on-state. The control circuit consists of several detectors and logic operations to generate PWM signal for rectifiers.

III. CURRENT CONTROL LOOP FOR RECTIFIER

Figure 2 shows the gate signal of rectifier. There is no erectrolytic capacitor on the DC link in this inverter. Therefore, one of the switches in the upper part of the rectifier and one in the lower part must be on-state, in order to assure continuous current flow of load. The gate signal of the rectifier is so generated during period Ⓐ (in Fig. 2), that the upper part of R-phase switch keeps on-state, and the lower part of S or T phase switch is turn-on each other by the command of PWM pulse generator.

A. *Generation of reference current*

Figure 3 shows generation of the reference current. Based on power balance equation and assuming unity power factor operation, I of the reference current is calculated as follows.

$$I = E_{dc} I_{dc} / \sqrt{3}\, E_{uv} \qquad (1)$$

Where, E_{uv} and I_u are rms values of rectifier input voltage and current, E_{dc} and I_{dc} average values of DC link voltage and current. The averaging interval of E_{dc} and I_{dc} are each 60° of AC source. The three-phase reference current signals i_u^*, i_v^* and i_w^* are obtained by multiplying the AC source phase-voltage waveforms.

$$\begin{aligned} i_u^* &= \sqrt{2}\, I \sin\omega t \\ i_v^* &= \sqrt{2}\, I \sin\left(\omega t - \frac{2}{3}\pi\right) \\ i_w^* &= \sqrt{2}\, I \sin\left(\omega t - \frac{4}{3}\pi\right) \end{aligned} \qquad (2)$$

B. *Generation of PWM signal for rectifier*

From the control circuit of Fig. 1, the

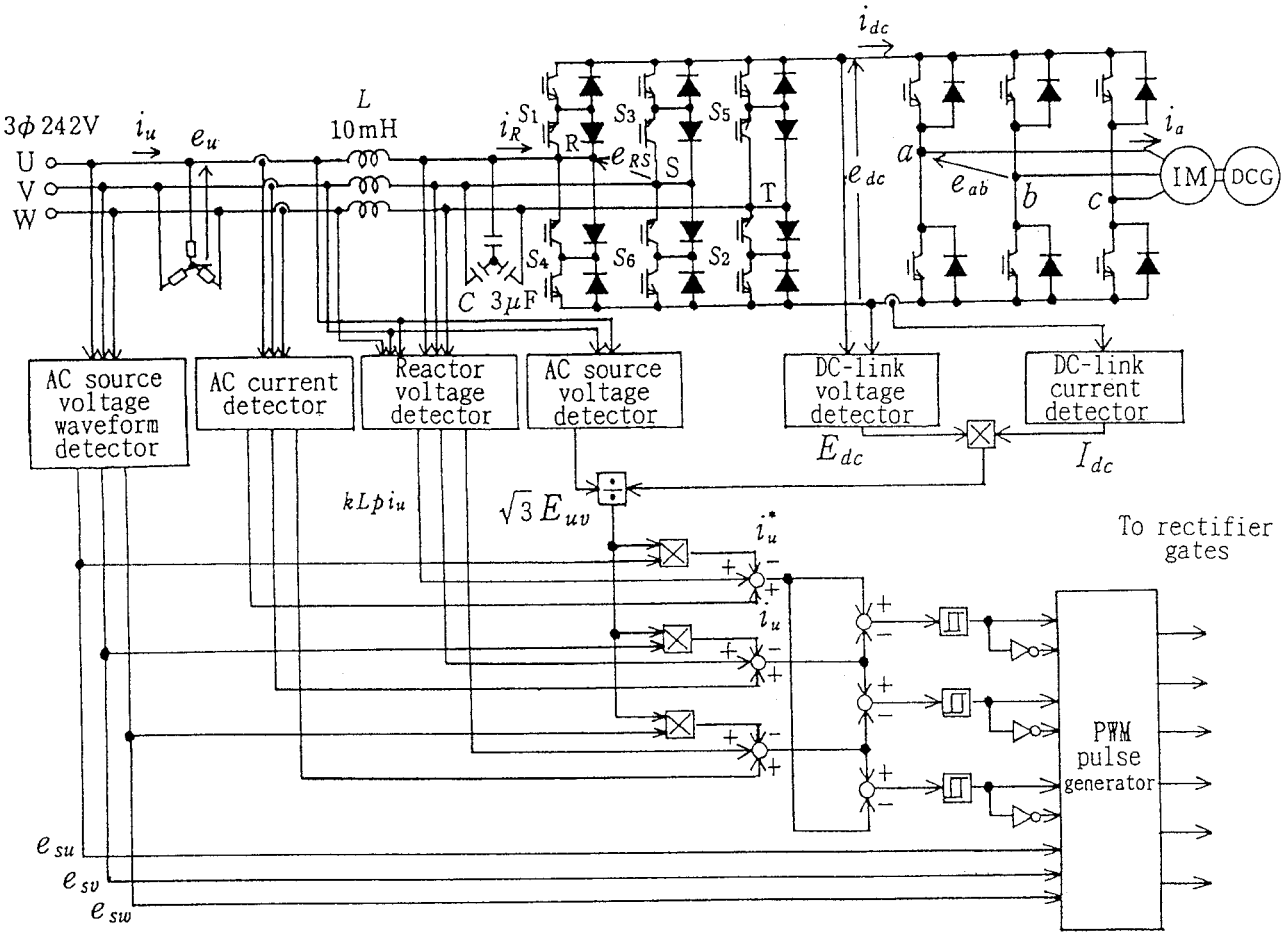


Fig.1. Circuit configulation

three-phase current errors; δi_u^* , δi_v^* and δi_w^* are derived as follows.

$$\delta i_u = i_u - i_u^* + kLpi_u$$

$$\delta i_v = i_v - i_v^* + kLpi_v \quad (3)$$

$$\delta i_w = i_w - i_w^* + kLpi_w$$

where, k is feedback gain, $p=d/dt$.

Figure 4 shows relation between current errors and gate signals. When the S_1 keeps on-state, current error $\delta i_v - \delta i_w$ is compared with hysteresis band width h. In the case of,

$$\delta i_v - \delta i_w > h \quad (4)$$

then S_6 is turned on to reduce S-phase current. Another case of,

$$\delta i_v - \delta i_w < -h \quad (5)$$

then S_2 is turned on to reduce T-phase current. Where, $h=0.015$(A) used in calculation.

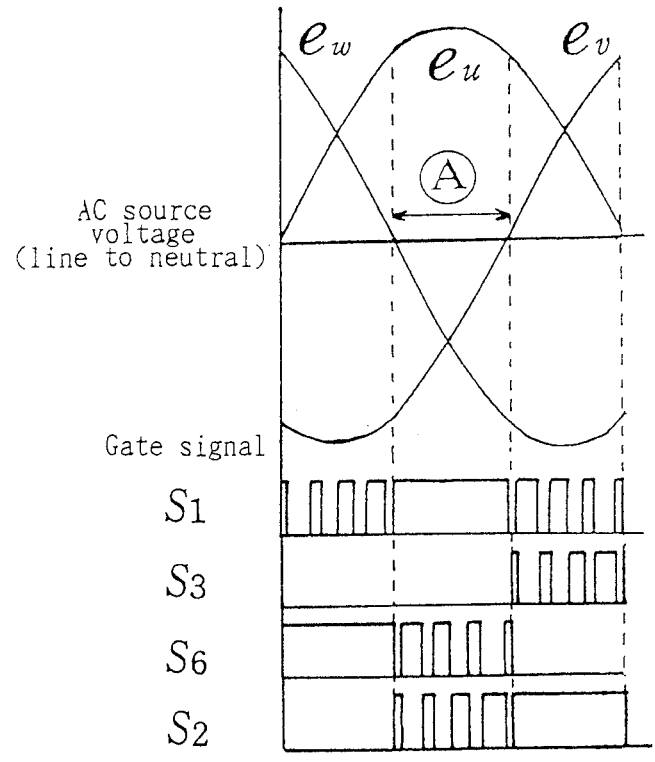


Fig.2. Gate signals of rectifier

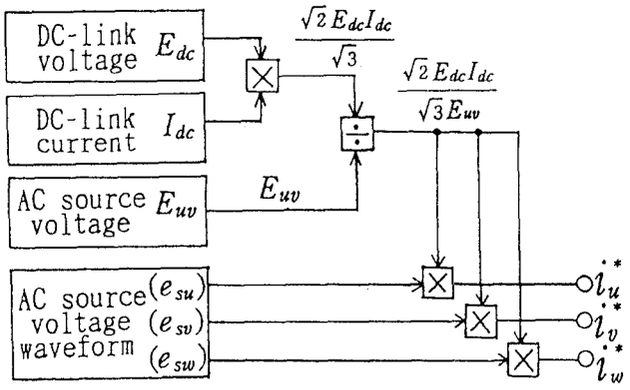


Fig.3. Generation of reference current

TABLE 1.
SPECIFICATION OF THE SYSTEM

Induction motor

P_0 =0.75kW , V=200V, f=60Hz, P=4 pole

r_s =3.45 Ω , r_r =2.09 Ω

L_s =L_r =0.192H, M=0.184H

Converter

L=10mH, C=3 μF

Inverter

Carrier frequency=8820Hz

Modulation index=0.95

Sine−Triangle PWM

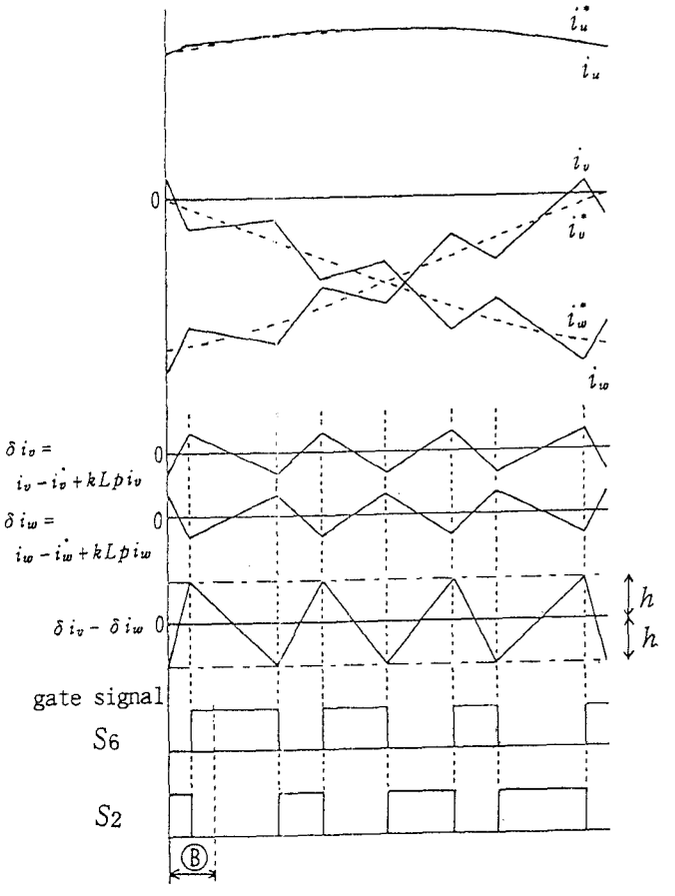


Fig.4. Relation between current errors and gate signals

IV. STEADY STATE ANALYSIS

Figure 5 shows part Ⓑ (in Fig. 4) of the switching waveform formed by combining the inverter with rectifier. For the interval t-t' in Fig. 5, S_1 and S_6 of rectifier are on−state, and the voltage vector of inverter is V_6. Then the equivalent circuit from AC source to induction motor is shown in Fig. 6.

From the equivalent circuit in Fig. 6, the voltage and current equation for variable x are shown as follows,

$$px = A_6 x \qquad (6)$$

where, $x = \left[e_1, e_2, i_u, i_v, e_{CR}, e_{CS}, i_{s\alpha}, i_{s\beta}, \Psi_{r\alpha}, \Psi_{r\beta}\right]^T$

e_1 and e_2 are assumed AC source voltage; $i_{s\alpha}$ and $i_{s\beta}$ the primary currents; and $\Psi_{r\alpha}$ and $\Psi_{r\beta}$ the secondary flux linkages of an induction motor in the α-β stationary co−ordinate. A_6 is 10×10 matrix which is determined by the equivalent circuit in Fig. 6. The turn−on switches are determined by solutions of (6) and current error conditions of expression (4) and (5). Equation (7) is computed by mean of Runge−Kutta method with the time

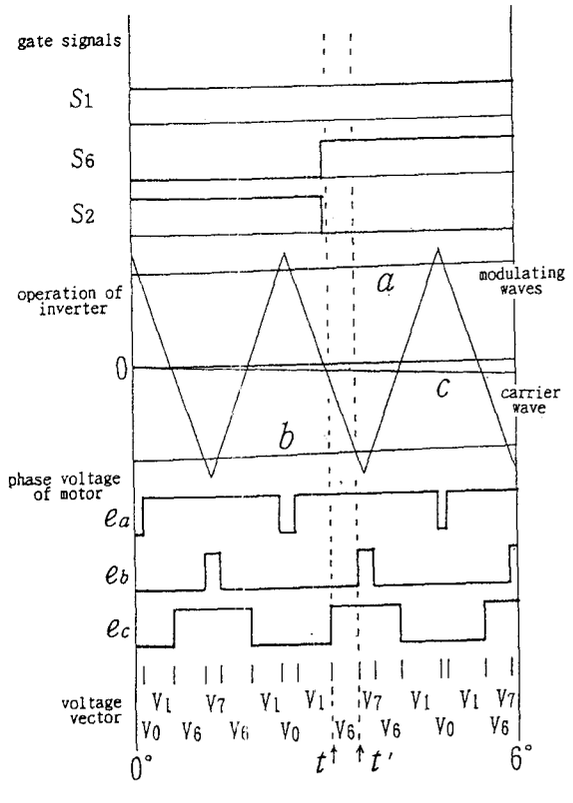


Fig.5. Detailed waveforms of part Ⓑ (in Fig.4)

step Δt . These calculation are continued for the analysis period 360° using matrices A_m ; and A_m is determined by switching waveforms combined with the inverter and rectifier.

V. Voltage and Current Waveforms

Figure 7 shows the calculated waveforms of AC source current i_u , phase voltage e_u , rectifier input current i_R , input voltage e_{RS} , DC−link current i_{dc} , DC−link voltage e_{dc} , motor current i_a , motor voltage e_{ab} . The waveforms are calculated using the constants shown in Table 1, AC 242V rms of source voltage and 60Hz of motor frequency.

Figure 7(a) shows the waveforms with feedback (k=0.000375), in this case, the resonance owing to LC filter is effectively restrained, AC source current i_u maintain near sinusoidal waveforms with a unity power factor.

Figure 7(b) shows the waveforms without feedback (k=0). The resonance owing to LC filter (around 1kHz) can be seen in waveform of i_u , and it is considered that distortion of other waveforms caused by oscillation of i_u .

VI. Conclusion

In this paper, the calculated characteristics are described for a 0.75kW induction motor driven by this new inverter, which rectifier is controlled by the current closed loop with *di/dt* feedback. The results obtained in this paper are summarized as follows.

(1) This inverter makes possible to improve the AC source current waveform, as well as unity power factor operation when induction motor is driven by this inverter.

(2) By adapting of *di/dt* feedback, AC source can be restrained the resonance of LC filter .

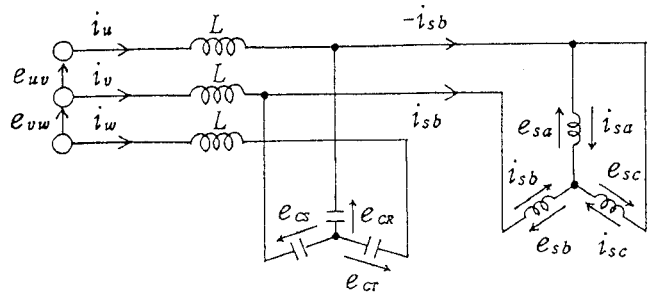
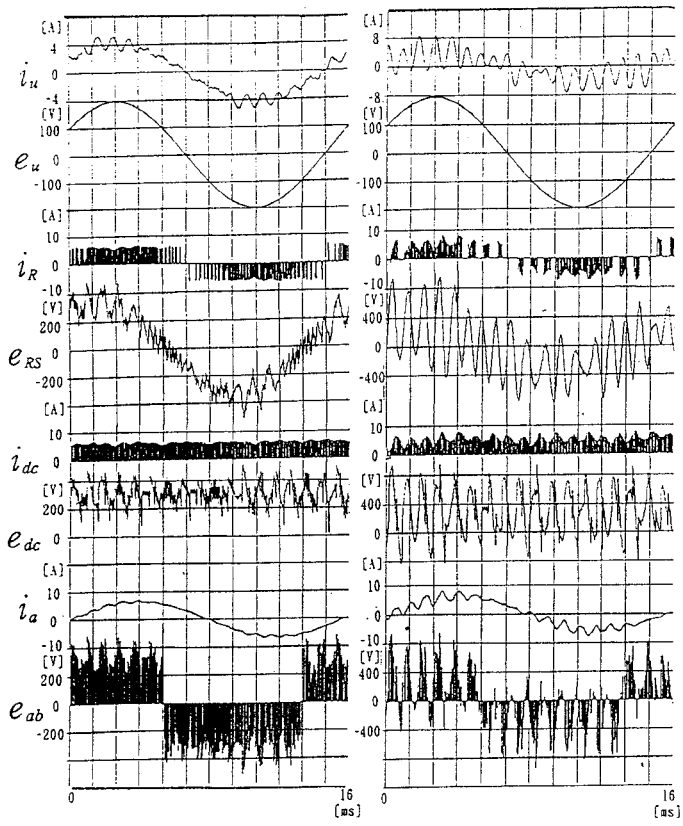


Fig.6. Equivalent circuit in V6 mode (interval t-t' in Fig.5)



(a) with feedback (k=0.000375) (b) without feedback (k=0)

Fig.7. Calculated waveforms with 80% rated load (s=0.139)

References

[1] K. Shinohara, Y. Minari, T. Irisa and Y. Imamura, "Analysis and fundamental characteristics of induction motor driven by voltage source inverter without DC link components", Trans. Inst. Electr. Eng. Jpn, (1989). vol. 109−D No. 9, pp. 637−644, (1989)

[2] Y. Minari, K. Shinohara and T. Irisa, "PWM Rectifier/voltage source inverter without DC link components", IEE Proceeding−B. vol. 140. No. 6. pp. 363−368. (1993)

Generalized Harmonic Loss-Factor As a Novel Important Quality Index of PWM Techniques

S. Halász, B.T. Huu
Technical University of Budapest, Department of Electrical Machines and Drives
1111, Egry József u. 18., Budapest, HUNGARY
Fax: (36-1)-463-3600, Phone: (36-1)-463-3605
e-mail: vgadm@tubelf.vsz.bme.hu

Abstract - Different carrier-based and loss-optimized PWM methods of two- and three-level inverters are examined and compared from the viewpoint of the motor harmonic losses. For the presently used commutation frequencies these losses with a good accuracy are determined from the generalized loss-factors, which are expressed by analytical equations and usually independent of the commutation frequency of the inverter. The generalized loss-factors of bipolar, dipolar and unipolar PWM techniques with three and two phase commutations are compared in details.

I. Introduction

The paper deals with the simple and quick method for the determination of the harmonic losses of the ac motors fed from two- or three-level inverters. This method is based on the analytical equations which are valid for the infinitive value of the commutation frequency [1-4], but in the case of the presently used commutation frequencies these equations obtain the motor harmonic losses with a good accuracy. The other mean merit of this method is that each PWM technique can be described by a single generalized loss-factor curve in the function of the motor fundamental voltage and therefore the method provides a good opportunity for the correct comparison of the different PWM techniques from the viewpoint of the motor harmonic losses.

The carrier-based bipolar, dipolar and unipolar PWM techniques [5-6] are investigated with different shapes of the reference waves. These PWM techniques are presented in Figs. 1-2, where u_{ar} is the *a* phase reference wave and the triangular carrier wave is used.

Besides the usually used three-phase commutation the generalized loss-factor of the rarely used so called two-phase commutation technique will be given too. In this case during 1/6 (or 1/3) of the fundamental period commutations occur only in two phases, while the third one is connected to the positive or negative dc bus-bar.

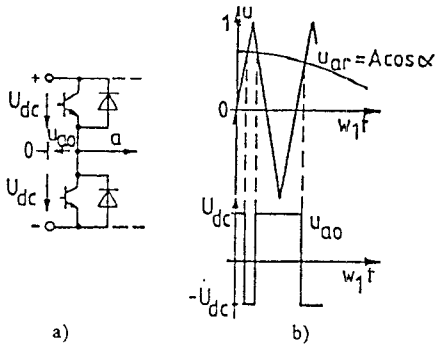


Fig.1. Two-level inverter (a), bipolar PWM technique(b)

II. State of the art

One of the most important quality indexes of the PWM technique in inverter fed ac drives is the motor harmonic losses according to the given inverter commutation frequency. These losses are generally characterized by the loss-factor which for the pure inductive load is given as follows:

$$K_\psi = (L')^2 \sum_{\nu>1}^{\infty} I_\nu^2 = \sum_{\nu>1}^{\infty} \Psi_\nu^2 \ , \qquad (1)$$

where I_ν, Ψ_ν are the harmonic current and the harmonic flux of the order ν, L' is the stator transient inductance and all the values are in p.u. system. The loss-factor can also be computed by analytical equation [1], but the sampling times and the according voltage vectors must be known. The loss-factor curves are usually presented as a function of the fundamental voltage and each curve is valid for a constant number of commutations on the period or for a constant value of commutation frequency.

A more simple and effective calculation of the harmonic losses is based on the use of the generalized loss-factor curves [2-4] which are usually independent of the commutation frequency of the inverter. The generalized loss-factor can be determined as follows:

$$G_{lf} = f_c^2 K_\psi \ , \qquad (2a)$$

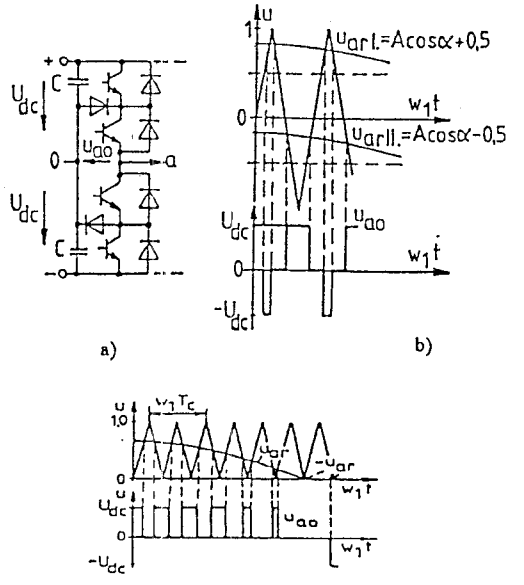


Fig 2. Three-level inverter (a), dipolar (b), unipolar (c) PWM techniques

where f_c is the carrier frequency, or as:

$$G_{\ell m} = m^2 K_\psi , \qquad (2b)$$

where $m = f_c / f_1$ and f_1 is the fundamental frequency (both frequencies are in p.u. system). The first case is more suitable for carrier-based PWM techniques, the second one is more practical for PWM with look-up table (i.e. loss-optimized precalculated PWM). In the latter case the number of the commutations on the fundamental period γ is equal to m. In equations (2a) and (2b) it is assumed that $f_c \to \infty$, so the T_c carrier (or sampling) period must be infinitely small. This assumption permits the analytical determination of the generalized loss-factor as the values of reference waves on each carrier period are taken constant ones. E.g. for bipolar PWM of the two-level inverters with saw-tooth carrier wave the modulation process is presented in Fig. 3. The *bc* line voltages and fluxes are calculated. The line harmonic flux is determined by equation:

$$\Delta\psi_{bc} = \int_o^t (u_{bc} - u_{bc1})dt, \qquad (3)$$

where $u_{bc1} = AU_{dc}\sin(\alpha)$ is the fundamental component of u_{bc}, A is the relative fundamental amplitude of the reference waves and $2U_{dc}$ is the input inverter dc voltage. The square of the rms. value of this flux for a carrier period and after that on fundamental period can be calculated:

$$\Delta\overline{\psi}^2_{bc} = \frac{A^2 U^2_{dc}}{8}\left(1 - \frac{8\sqrt{3}}{3\pi}A + \frac{9}{16}A^2\right). \qquad (4)$$

After division on the square of the rated flux

$$\Psi^2_{bcr} = \frac{6U^2_{dc}}{\pi^4 f_r^2}$$

the generalized loss-factor is obtained:

$$G_{\ell f} = \frac{A^2\pi^4}{48}\left(1 - \frac{8\sqrt{3}}{3\pi}A + \frac{9}{16}A^2\right) \qquad (5)$$

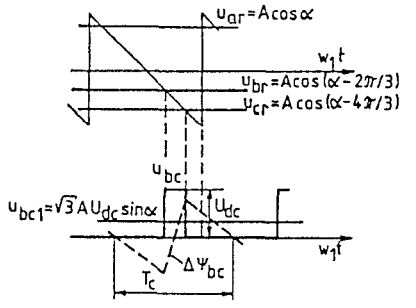


Fig.3. Modulation process for bipolar PWM technique with saw-tooth carrier wave

and after substitution $A = 4f_1/\pi$ the $G_{\ell m}$ is determined too:

$$G_{\ell m} = \frac{\pi^2}{3}\left(1 - \frac{8\sqrt{3}}{3\pi}A + \frac{9}{16}A^2\right) \qquad (6)$$

In the above equations it is assumed that the rated voltage is equal to the maximal inverter voltage $U_{1max}=4U_{dc}/\pi$ and the rated frequency f_r corresponds to this voltage. It is an interesting fact that the zero points of $\Delta\psi_{bc}$ are not in coincidence with the zero points of the carrier waves. Another specialty of saw-tooth carrier waves is that injection of the zero-sequence harmonics in the reference wave does not influence the shape of the line harmonic flux as the u_{br} and u_{cr} reference waves are changed on the same value, therefore the $\Delta\psi_{bc}(t)$ curve in Fig. 3 only is shifted according to the carrier wave. Hence, in case of the saw-tooth carrier wave the generalized loss-factor for $0<A<1$ does not depend on the injection of zero-sequence harmonics in the reference waves.

Sometimes it is better to use the vector interpretation. E.g. in Fig.4 the unipolar modulation process for three-level inverters is presented, where the x and y are the axes of stationary coordinate system. The space vector PWM technique is used. It is well known [5], that in this case the sinusoidal reference waves are modified by adding up u_o zero-sequence component, as follows:

$$u_o = -\frac{1}{2}\left[\max\{u_{ar}, u_{br}, u_{cr}\} + \min\{u_{ar}, u_{br}, u_{cr}\}\right].$$

The simplest calculation is carried out for $\pi/3 < W_1 t < \pi/2$, where $u_{br} = u_{cr}$. The square of the harmonic flux $\Delta\Psi^2 = \Delta\Psi_x^2 + \Delta\Psi_y^2$ is determined and after division by the rated flux $\Psi_r^2 = \frac{4U^2_{dc}}{\pi^4 f_r^2}$ the generalized loss-factors are obtained. Several peculiarities of the generalized loss-factor computation in case of three-level inverters are given in [7].

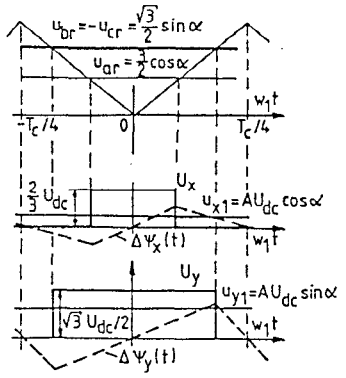


Fig.4. Modulation process for unipolar space vector PWM technique

Table I. Generalized loss-factors of different PWM techniques (three-phase modulation).

PWM technique			Generalized loss-factor G_{lm}	Generalized loss-factor G_{lf}	γ
Two level inverter	Bipolar	$A_3=0$ $0\le A\le 1$	$\frac{\pi^2}{12}\gamma$	$\frac{A^2\pi^4}{192}\gamma$	$1-\frac{8\sqrt{3}}{3\pi}A+\frac{3}{4}A^2$
		$A_3\neq 0$ $0\le A\le A_{max}$			$1-\frac{8\sqrt{3}}{3\pi}A+\left(\frac{3}{4}-\frac{3A_3}{4}+\frac{3A_3^2}{2}\right)A^2$
		Space vector $0\le A\le\frac{2}{\sqrt{3}}$			$1-\frac{8\sqrt{3}}{3\pi}A+\left(\frac{9}{8}-\frac{27\sqrt{3}}{32\pi}\right)A^2$
Three level inverter	Dipolar	$A_3=0$ $0\le A\le 0.3$	$\frac{\pi^2}{48}\gamma$	$\frac{A^2\pi^4}{768}\gamma$	$1-\frac{16}{\pi\sqrt{3}}A+3A^2$
		$A_3\neq 0$ $0\le A\le A_{max}/2$			$1-\frac{16}{\pi\sqrt{3}}A+\left(3-3A_3+6A_3^2\right)A^2$
		Space vector $0\le A\le\frac{1}{\sqrt{3}}$			$1-\frac{16}{\pi\sqrt{3}}A+\left(\frac{9}{2}-\frac{27\sqrt{3}}{8\pi}\right)A^2$
	Unipolar	$A_3=0$ $0\le A\le 1$	$\frac{\pi^2}{12}\gamma$	$\frac{A^2\pi^4}{192}\gamma$	$1-\left(\frac{7}{9}+\frac{\sqrt{3}}{3}\right)\frac{4}{\pi}A+\frac{3}{4}A^2$
		$A_3\neq 0$ $0\le A\le A_{max}$			$1-\left(\frac{7}{9}+\frac{\sqrt{3}}{3}-\frac{2}{3}A_3+\frac{36}{33}A_3^2+\frac{16}{27}A_3^3\right)\frac{4}{\pi}A+\left(\frac{3}{4}-\frac{3}{4}A_3+\frac{3}{2}A_3^2\right)A^2$
		Space vector $0\le A\le\frac{2}{\sqrt{3}}$			$1-(3-\sqrt{3})\frac{4}{\pi}A+\left(\frac{9}{8}-\frac{27}{32}\frac{\sqrt{3}}{\pi}\right)A^2$

If $A_3\ge 1/9$: $A_{max}=3\sqrt{3}A_3/(1+3A_3)^{3/2}$; If $A_3\le 1/9$: $A_{max}=1/(1-A_3)$

The generalized loss-factor can also be computed as the limit of the m^2K_ψ (or $f_c^2K_\psi$) when $m\to\infty$ (or $f_c\to\infty$). With this method the generalized loss-factors of the loss-optimized PWM were obtained. In case of bipolar modulation $\gamma = m = 69$ was the largest number of commutations which could be taken into consideration.

III. Results

The results for both two- and three-level inverters and for triangular carrier waves are presented in Tables I and II. The loss-factor curves as function of the fundamental voltage are presented in Figs.5-7, where:

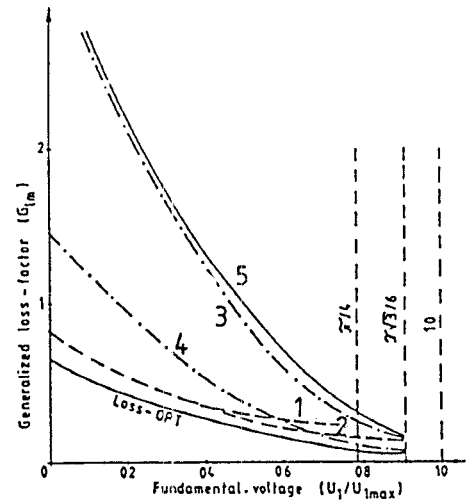
Curves 1 and 2 are the loss-factors of the usually used three-phase modulation technique without and with third harmonic injection of the relative amplitude A_3=0.25 in the reference waves.

Curve 3 is the loss-factor of two-phase modulation [8], where during 1/6 (or 1/3) of the fundamental period commutations occur only in two phases, while the third one is connected to the positive or negative dc bus-bar. In this case for the bipolar modulation the reference waves are presented in Fig.8. It is seen that these waves are obtained by addition of the zero-sequence voltages to the fundamental ones.

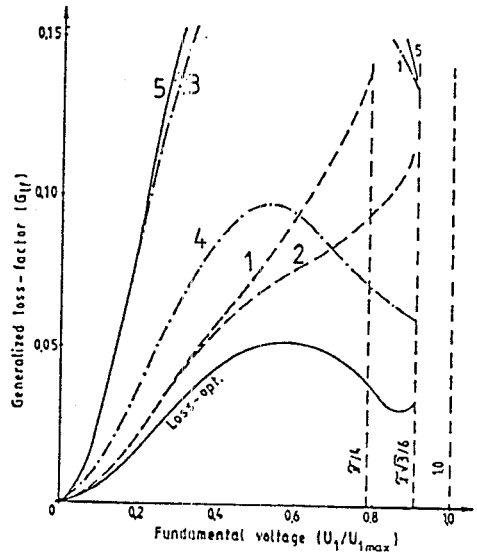
This PWM technique is used by several firms (e.g., by DANFOSS). From Fig.8 one can see that control can beshifted by ±30° or can be modified in such a manner that one phase is connected to the positive (or negative) bar on 120° of the period. Loss-factors for the above modification are presented in Table II too, but all the modifications have about the same value of the loss-factors.

Table II. Generalized loss factors of different PWM techniques (two-phase modulation).

PWM technique			Generalized loss-factor G_{lm}	Generalized loss-factor G_{lf}	γ
Two-level inverter	Bipolar	60° cycle(shift 0°) $0\le A\le\frac{2}{\sqrt{3}}$	$\frac{\pi^2}{6}\gamma$	$\frac{A^2\pi^4}{96}\gamma$	$2-\left(\frac{15}{2\pi}+\frac{4}{\sqrt{3}\pi}\right)A+\left(\frac{9}{8}+\frac{9\sqrt{3}}{32\pi}\right)A^2$
		60° cycle(shift 30°) 120° cycle $0\le A\le\frac{2}{\sqrt{3}}$	$\frac{\pi^2}{6}\gamma$	$\frac{A^2\pi^4}{96}\gamma$	$2-\frac{35\sqrt{3}}{6\pi}A+\left(\frac{9}{8}+\frac{27\sqrt{3}}{64\pi}\right)A^2$
Three-level inverter	Unipolar	60° cycle $0\le A\le\frac{1}{\sqrt{3}}$	$\frac{\pi^2}{12}\gamma$	$\frac{A^2\pi^4}{192}\gamma$	$1-\left(\frac{15}{2\pi}+\frac{4}{\sqrt{3}\pi}\right)A+\left(\frac{9}{4}+\frac{9\sqrt{3}}{16\pi}\right)A^2$
	Dipolar	60° cycle(shift 30°) 120° cycle $0\le A\le\frac{1}{\sqrt{3}}$			$1-\frac{35\sqrt{3}}{6\pi}A+\left(\frac{9}{4}+\frac{27\sqrt{3}}{32\pi}\right)A^2$
	Unipolar	60° cycle $A=0.8$			0.04720
		60° cycle $A=\frac{2}{\sqrt{3}}$			0.01212



a)



b)

Fig.5 . Loss-factors of bipolar PWM techniques, (a) G_{lm}, (b) G_{lf}

Curve 4 is the loss-factor of the two phase modulation too, but for by 3/2 increased commutation frequency. The loss-factor decreases in this case by 4/9 from the original value (curve 3) but the commutation frequency of three- and two-phase modulation becomes the same.

Curve 5 is the loss-factor for the saw-tooth carrier wave. In all the cases the loss-factor for the loss-optimized PWM technique is presented too.

IV. Discussion

The general loss-factor interpretation is valid only as long as the loss-factor $m \to \infty$ (or $f_c \to \infty$) can be done equal to zero. Theoretically this may be true for $0 \le A \le 2/\sqrt{3}$, but in reality the general loss-factor can be used up to A_{max} where over modulation occurs. For the certain PWM technique the loss-factor cannot be zero even with $f_c \to \infty$. E.g for the bipolar modulation when in 1/6th of the period only one phase is commutated the fluxvector path will be hexagonal (Fig.9). In this case with $f_c \to \infty$ and symmetrically distributed pulses the loss-factor will be [9]:

$$k_{\psi 1} = \frac{5\pi^4}{486} - 1 \approx 0.00215.$$

For $f_c \neq \infty$ the loss-factor can be evaluated as the sum of $k_{\psi 1}$ and the depended on f_c^2 (and U_1) loss-factor component. The detailed investigation leads to the next approximate result:

$$k_\psi = k_{\psi 1} + \frac{\pi^4}{486N^2}\left(1 - \frac{U_1}{U_{1\max}}\right),$$

where N is the number of pulses on 1/6th of the period. On the basis of the generalized loss-factor results (Figs.5-7) several important conclusions can be drawn.

A. Two- Level Inverters

For two-level three-phase inverters the bipolar modulation gives acceptable results, but the generalized loss-factors (hence the motor harmonic losses) are by 20-30%higher than for the loss-optimized PWM in the low voltage region and about 30%-150% in the high one.

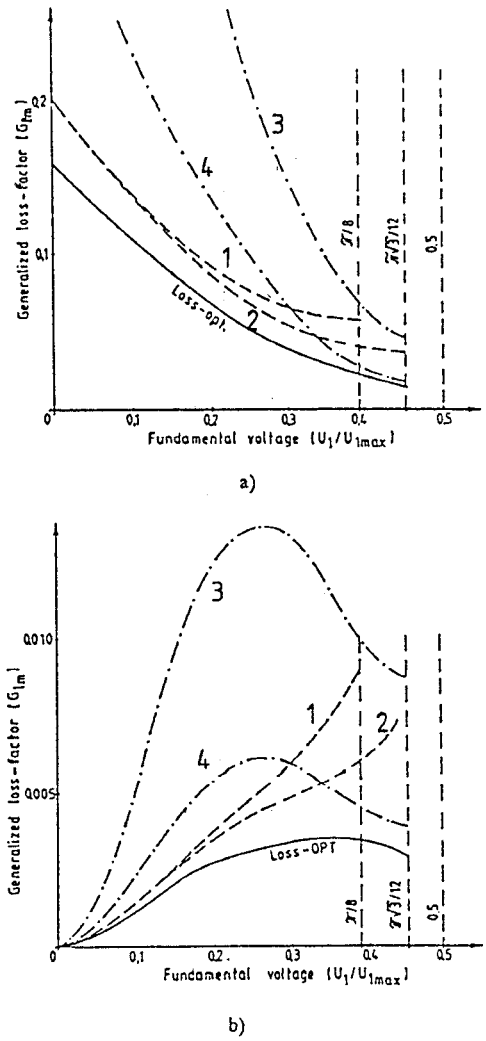


Fig.6. Loss-factors of dipolar PWM technique, (a) G_{lm}, (b) G_{lf}

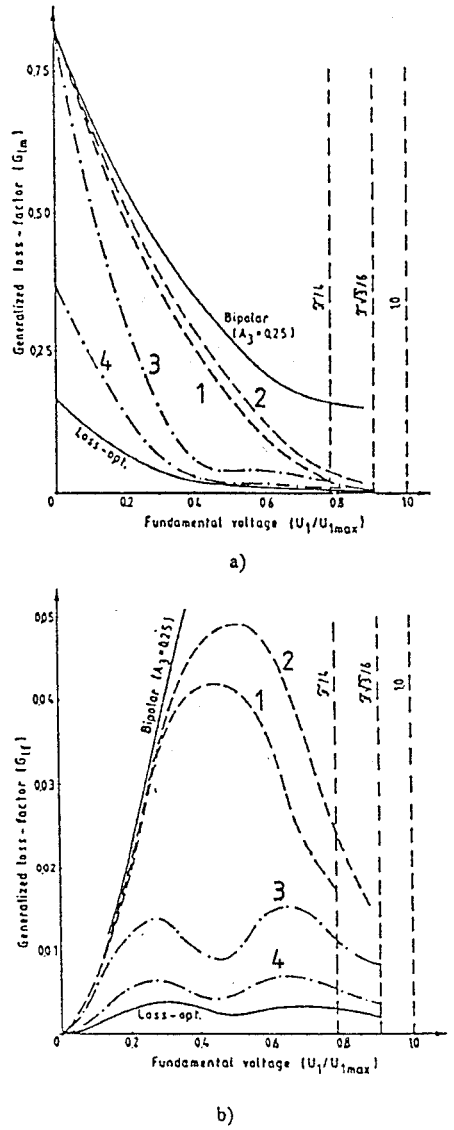


Fig.7. Loss-factors of unipolar PWM technique, (a) G_{lm}, (b) G_{lf}

For the carrier-based PWM technique it is seen that the usually used three-phase modulation with a triangular carrier wave produces the lowest value of the harmonic losses, especially when A_3=0.25. The space vector PWM produces the losses very closed to this case as the space vector PWM virtually has the same quality as the case of A_3=0.2067 [7]. But from Fig.5 it is very clear that for U_1/U_{1max} <0.3 the loss-factor is independent from the third harmonic injection.

The two-phase modulation with the identical commutation frequency (curve 2) produces lower losses in region U_1/U_{1max} > 0.6 even than normal three-phase modulation with A_3=0.25. At the same time this two-phase modulation in the region U_1/U_{1max} <0.4 produces about two times more losses (and torque pulsations) than normal bipolar modulation. The reason for that is the appearance of the high amplitudes voltage harmonics with order $m\pm2$ (or $m\pm1$ in dependence of the control scheme).

The harmonic losses for the saw-tooth carrier wave are very high but the number of commutations on the carrier period - with a better control - can be decreased from 6 to 4. In the latter case the commutation frequency decreases by 2/3 and losses by 4/9. Therefore the loss-factor values will be very close to curve 2. Hence this carrier wave has an advantage in comparison with the triangular one in the voltage region U_1/U_{1max}>0.65.

B. Three-Level Inverters, Dipolar Modulation

The dipolar modulation is used for the low voltage region $U_1/U_{1max}<\pi\sqrt{3}/12$ and all the conclusions which were deduced for the bipolar modulation are valid for the dipolar one too.

C. Three-Level Inverters, Unipolar Modulation.

The unipolar modulation is used for the upper voltage region $U_1/U_{1max}>\pi\sqrt{3}/12$. Unfortunately the loss-factor for the voltage region $U_1/U_{1max}<1/\sqrt{3}$ expressed by very complicated equations , therefore these ones are not presented in Table. II.

From Fig.7 it is seen that the three-phase modulation produces very high loss-factor values in the whole voltage region and the third harmonic injection increases the voltage control region only but does not decrease the loss-factors. In contrast with the bipolar and dipolar modulations the two-phase unipolar modulation considerably decreases the loss-factor even for the same carrier wave (curve 1) and especially for the same commutation frequency (curve 2). In comparison with the loss-optimized PWM the loss-factor of the two-phase modulation becomes acceptable in the voltage region U_1/U_{1max}> 0.4.

The above peculiarity of the unipolar modulation is explained by the absence of the harmonics of order $m\pm2$ $3m\pm2$, $5m\pm2$ etc. in the motor voltage spectra [1].Really, the third harmonic injection increases the amplitudes of the voltage harmonics with order $2m\pm1$, $4m\pm1$, $6m\pm1$ etc.

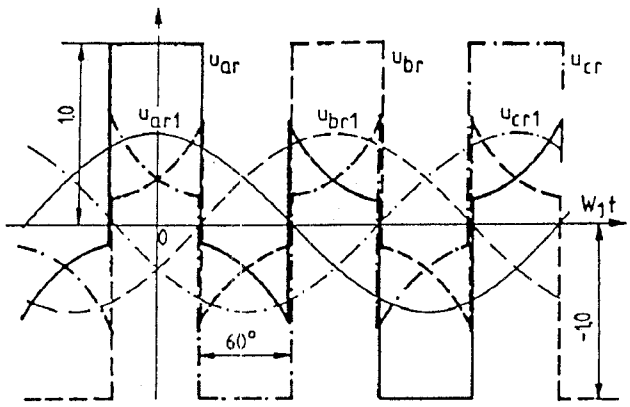


Fig. 8. Reference waves for two-phase modulation

and therefore the motor harmonic losses also increase. In case of the two-phase modulation there cannot be harmonics of order $m\pm2$, 3 $m\pm2$ etc. and therefore the loss-factor does not increase. In the other side the two phase modulation is used the zero value voltage vectors very often and that leads to considerable decreases of the motor harmonic losses [6].

For the three-level inverters the bipolar modulation can be also used, but the loss-factor will be very high (Fig.7).

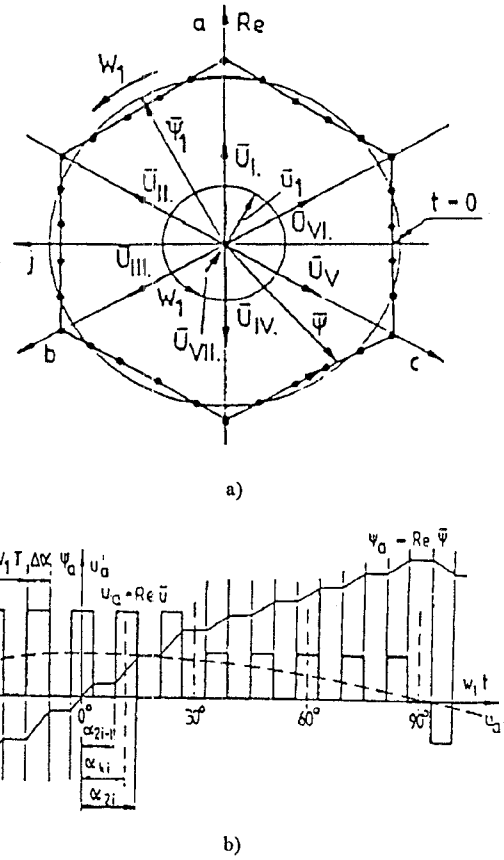


Fig.9 One-phase modulation,symmetrical pulse distribution, a) voltage- and fluxvectors, b) phase voltage and flux vs time.

V. Computation Examples

1. Let us compute the loss-factor for the space vector bipolar PWM and A= 0.5, m = 15 and m = 27.
From Table I. the approximate loss-factors are:

$$m = 15: \; k_\psi = \frac{G_{\ell m}}{m^2} = \frac{0.3535}{225} = 0.001513,$$

$$m = 27: \qquad k_\psi = \frac{0.3535}{729} = 0.0004850.$$

The straight calculation gives the accurate values:

m = 15: $k_\psi = 0.001610$ (deviation: 6.4%),

m = 27: $k_\psi = 0.0004885$ (deviation: 0.7%).

For the dipolar modulation the deviation will be 8..5% and 0.8%, for the unipolar one: 0.4% and 0.13% for the same values m.

In a common case the accuracy of these computation is 1% without third harmonic injection and 2% with it, if $m \geq 39$ for the bipolar, $m \geq 27$ for the dipolar and $m \geq 15$ for the unipolar modulation.

2. The square of the harmonic current rms value is determined as follows:

$$\Delta I^2 = \frac{K_\psi}{(L')^2}.$$

For the bipolar modulation in the low and middle ac motor power range a carrier frequency of always 4 kHz is used. With that and f_r=50Hz, f_c=4000/50=80. The maximal value of generalized loss-factor for the space vector modulation will be G_{lfmax}=0.1232 at $A = \frac{2}{\sqrt{3}}$ (Fig.5b.). Assume L'=0.10 the stator harmonic losses will be:

$$\Delta I^2 = \frac{G_{\ell f\,\max}}{f_c^2 (L')^2} = \frac{0.1232}{80^2 0.1^2} = 0.0019,$$

thus 0.19% from the rated losses of the stator coil, if the stator coil skin effect can be neglected. For the rotor coil the skin effect can increase the harmonics losses by 10-20 times.

For the three-level high power inverters a carrier frequency of about 500Hz is used (f_c=10). According to Fig.6b. the maximal generalized loss-factor of the space vector dipolar modulation is $G_{\ell f\,\max} = 0.0077$ (at $A = 1/\sqrt{3}$) and the stator harmonics losses are:

$$\Delta I^2 = \frac{0.0077}{10^2 0.01^2} = 0.0077 \;\; (0.77\%).$$

For the unipolar modulation with A_3=0 (Fig.7b) G_{lfmax}=0.0429 (at A=0.584) and the stator harmonics losses are:

$$\Delta I^2 = \frac{0.0429}{10^2 0.01^2} = 0.0429 \;\; (4.3\%).$$

For two-phase modulation the maximal value of the loss-factor are (curve 2, Figs. 5b-7b):

$G_{\ell f\,max} = 0.0977$ *at* $A = 0.68$ (bipolar PWM),

$G_{\ell f\,max} = 0.0061$ *at* $A = 0.40$ (dipolar PWM),

$G_{\ell f\,max} = 0.0069$ *at* $A = 0.83$ (unipolar PWM).

Thus the maximal value of harmonics losses for the two-phase modulation lower but - except the unipolar modulation - only if the sampling time by 3/2 times lower than for the three phase modulation.

VI. Conclusions

The generalized loss-factor interpretations provide a good opportunity for the accurate and quick determination of the motor harmonic losses and for the correct comparison of the different PWM techniques. Both two- and three-level inverters are investigated and the generalized loss-factor equations of the different PWM techniques are given.

Acknowledgment

This paper was supported by the Hungarian N.Sc. Fund (OTKA No.T 016021) for which authors express their sincere gratitude.

References

[1] S. Halász, G. Csonka, A.A.M. Hassan, *"Sinusoidal PWM techniques with additional zero-sequence harmonics"*, in Proceedings of the Int..Conf. on Ind. Electronics Control and Instrumentation, Sept. 5-9. 1994., Bologna, Italy, pp.273-289.

[2] S. Fukuda, Y.Iwaji, *"Introduction of the harmonic distortion determining factor and its application to evaluating real time PWM methods"*, in Proc. of the IPEC-Yokohama'95, Yokohama, Japan, 1995. pp.730-735.

[3] F.Jenni, D.Wueest, *"Steuerverfahren für selbstgeführte Stromrichetr"*, Hochschuleverlag, AG an der ETH, Zürich, 1995.

[4] S. Halász, G. Csonka, A.A.M. Hassan, *"Generalized harmonic loss curves of ac motors fed from two and three level inverters"*, In Proc. of the Int. Conf. on Ind. Electronics Control and Instrumentation, August 5-9., 1996. Taipei, Taiwan. \ pp. 957-963

[5] F.Jenni, D. Wueest, *"The optimization parameters of space vector modulation"*, In Proc.of 5th European Conf. on Power Electronics and Applications, Brighton, 1993., pp.376-381.

[6] S.Halász, A.A.M.Hassan, B.T.Huu, *"Optimal control of three level PWM inverters"*, IEEE Trans. on .Ind. Electronics . Vol.44. pp. 96-107, Febr. 1997.

[7] BT.Huu, S. Halász, G. Csonka, *"Generalized harmonic losses of inverter fed ac motors"*, in Proceedings of the 7th Int. Power Electronics and Motion Control Conference, 2-4 Sept., 1996. Budapest, Hungary, pp. 121-125.

[8] P.E. Nielsen, E.Ch.Thomson, M.T. Nielsen, *"Digital voltage vector control with adaptive parameter tunning"*, In Proc. of 3rd European Conf. on Power Electronics and Applications, Aachen, 1989. pp. 313-318.

[9] I.Rácz, *"Betractungen zu Oberwellenproblemen an Asychromotoren bei Stromrichterspeisung"*, Periodica Polytechnica Series EI. Vol. 11. pp.29-57, Nov., 1967.

A Loss-less Passive Snubber for Soft-Switching Boost-type Converters

Hiroshi Nomura and Kenichiro Fujiwara
Kochi National College of Technology
200-1 Monobe, Nangoku, Kochi 783 JAPAN
Phone:+81-888-64-5545, Fax:+81-888-64-5541
E-mail: nomura@ee.kochi-ct.ac.jp

Abstract—**A novel loss-less passive snubber is proposed for the soft-switching boost-type converters. The proposed snubber does not use any auxiliary switches, but uses two snubber capacitors which are charged in parallel and discharged in series automatically. And the discharged energy is recovered effectively (more than 95% recovery) into the output capacitor. Thus the snubber provides zero-voltage switching for the converter main switch reducing the turn-off losses and improves the converter efficiency. The experimental results of a 20kHz DC-DC boost converter and a single-phase AC-DC boost rectifier with the new snubber are presented.**

I. INTRODUCTION

Switch mode power supplies often employ the boost-type converter topologies for DC-DC and AC-DC power conversions. With increased switching frequencies and high-power ratings, verious studies as to reducing switching losses and EMI noise have been made. Soft switching using resonant technique is an attractive approach. While soft switching using loss-less snubbers also gives an effective solution from the viewpoint of converter efficiency and extended utilization of power switching devices [1]-[3].

Most of the loss-less snubbers proposed so far use an auxiliary switch (active snubbers), which tend to increase complexity of both power and control circuits. Therefore, energy-recovery schemes without an auxiliary switch (passive snubbers) are preferable [4]-[7].

The proposed snubber in this paper is a passive one. This unique snubber comprises two identical capacitors which are charged in parallel and discharged in series automatically, recovering all the snubber energy into the output. Although its application is limited to the boost-type converters, the experimental results of a boost DC-DC converter and a boost AC-DC converter confirm the effectiveness of the proposed snubber circuit.

II. PRINCIPLES OF NEW SNUBBER CIRCUIT

A. Basics of capasitor energy recovery

Fig.1 shows a capacitor discharging its initial voltage

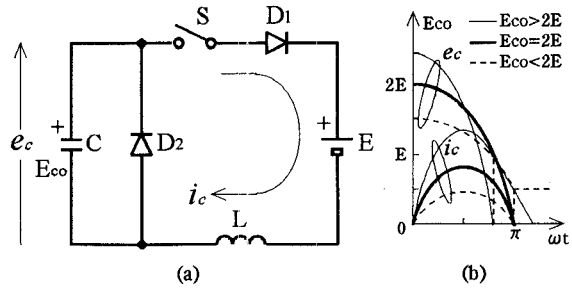


Fig.1 Discharge of capacitor voltage into DC source.
(a)Equivalent circuit. (b)*ec* and *ic* after closing the switch S.

Eco into a DC source resonantly. The diodes D_1 and D_2 represent the uni-directional qualities of both current and voltage as is the case with the actual snubber circuit.

Neglecting the losses in Fig.1, the following equations for *ic* and *ec* after closing the switch S is obtained.

$$ic(t)=\sqrt{C/L}(E_{co}-E)\sin\omega t \qquad (1)$$

$$ec(t)=E(1-\cos\omega t)+E_{co}\cos\omega t \qquad (2)$$

$$where\ \ \omega=1/\sqrt{LC}$$

Fig.1(b) illustrates these equations from which the following rules for capacitor energy recovery are found.

(1) In case E<Eco<2E, a part of the capacitor voltage (2E-Eco) remains un-recovered at $\omega t=\pi$.

(2) In case Eco=2E, *ec* reaches zero at the end of oscillation, then all the capacitive energy is recovered into E.

(3) In case Eco>2E, *ec* reaches zero before $\omega t=\pi$ and *ic* continues to flow through D_2, recovering all the capasitive energy into E when *ic* reduces to zero.

These considerations make it clear that the initial voltage on capacitor Eco should be equal to or higher than twice the source voltage (2E) to achieve a complete energy transfer.

B. Principles of new snubber circuit

The SW in Fig.2 represents any semiconductor switching device, both ends of which have two polarized capasitors connected in parallel. When SW turns off, two capasitors are charged equally by the energy stored in the circuit. The final voltage of each capacitor Ec is usually a

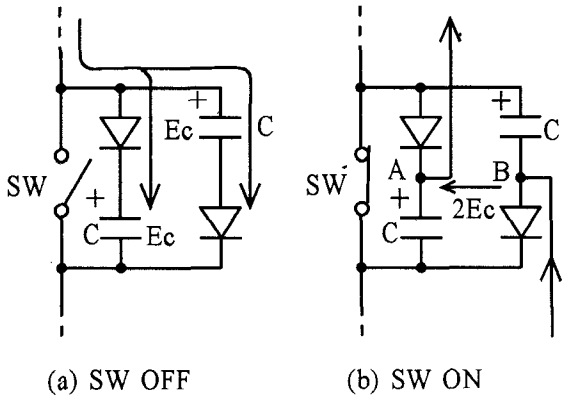


Fig.2 Structure of the new snubber.
(a)Two snubber capasitors are charged in parallel when SW turns off, and (b)discharged in series when SW turns on.

little higher than the source voltage or the load voltage. When SW turns on, these two voltages are superimposed and 2Ec appears across the terminals A and B.

If these terminals are connected with the source or the load in the circuit through an inductor, the capacitor voltages will discharge resonantly to zero, thus recovering the snubber energy from the above discussion. The SW turns off softly at zero voltage by virtue of being in parallel with the capasitors.

III. BOOST DC-DC CONVERTER WITH THE NEW SNUBBER

A. Circuit configulation and operation

The proposed snubber circuit applied to the boost DC-DC converter is shown in Fig.3. To avoid short-circuiting the snubber capacitor at turn-on of the main switch (IGBT), the diode D_2 must be added. This increases the conduction loss of the converter, but it is expected that the soft switching achieved by the loss-less snubber well compensates this defect.

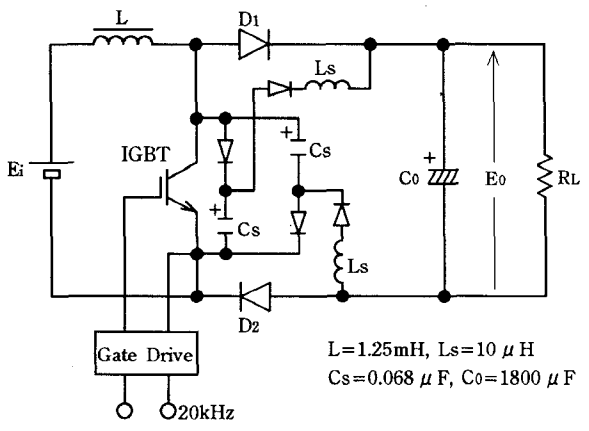


Fig.3 Boost DC-DC converter with the new snubber.

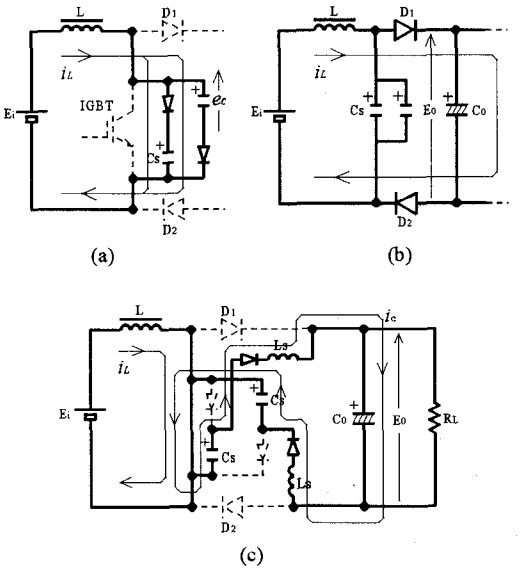


Fig.4 Equivalent circuits during commutation.
(a)charging snubber capacitors immediately after IGBT turns off, (b)snubber voltage clamped at Eo, (c)discharging snubber voltages into Eo immediately after IGBT turns on.

Also two pairs of a resonant inductor in series with a diode are nessesary to assure symmetrical operation and to avoid oscillation of the capacitor voltage.

In Fig.4(a), the main switch turns off at zero voltage and the inductor current i_L is transferred to the snubber capasitors Cs charging them equally up to the output voltage Eo. Assuming that the initial voltage on Cs is zero and the inductor current I_{Lo} at turn-off is kept constant during this mode, each capasitor voltage ec is given as follows.

$$ec(t) = \frac{I_{Lo}}{2C}\, t \qquad (3)$$

When the capacitor voltage reaches Eo, diodes D_1 and D_2 turn on in Fig.4(b). In continuous current mode, the snubber capasitor voltages are clamped at Eo during the off-interval of IGBT. Note that each snubber capacitor in Fig.3 can discharge if its voltage is higher than Eo, while it can be re-charged as long as D_1 and D_2 maintain conduction. In the actual circuit, the stray inductances once push the capasitor voltage higher than Eo, then the excess voltage leaks toward Eo.

In discontinuous current mode, however, the capasitors start to discharge through Co toward the DC source E when the inductor current ceases to flow. This lowers the capasitor voltages resulting in an incomplete energy recovery at turn-on. Hence the new snubber is not effective if the source of a converter operating in discontinuous mode accepts reverse current flow. The circuit configulations like boost AC-DC converters do not have this defect as shown later.

Fig.4(c) shows the current paths at turn-on of the main switch. The superimposed capacitor voltage (initially 2Eo) discharges resonantly into the output voltage Eo. Due to the losses in the actual current path, the capacitor voltage does not completely come down to zero, leaving a small portion of the initial voltage. This residual voltage on capasitor can be minimized by using low-loss components.

B. Experimental Results

In order to verify the basic operations of the circuit, a 20kHz, 600W prototype has been built using the components listed in Fig.3. The source voltage Ei is 100 V and the duty ratio is about 0.5 for a 200V output. The snubber capacitor Cs can be one half of the necessary capacitance to limit the dv/dt on IGBT to a proper value. From equation (3), a maximum inductor current of 20A charging Cs to 200V in 1 μ S gives Cs=0.05 μ F.

Fig.5 shows the voltage and current waveforms of the snubber capacitor which clearly indicate the basic operation of the new snubber circuit. At the turn-off of IGBT, each capacitor voltage rises slowly up to a little higher than the output voltage, then discharges through Ls and Co down to the output voltage Eo as illustrated in Fig.4(a) and (b).

At the turn-on of IGBT, the superimposed capacitor voltage (initially 2Eo) is discharged resonantly into the output voltage Eo. Due to the losses in the current path, the capacitor voltage does not come down to zero leaving a small portion (less than 5V) of the initial voltage. This residual voltage can be minimized by using low-loss components (especially snubber inductor Ls).

Fig.6 shows the converter efficiency with the new snubber and that with the conventional RCD snubber. A high converter efficiency of 95% with a high recovery percentage of about 97% was obtained for the new circuit. The recovery efficiency was calculated by measuring the maximum snubber voltage, assuming losses other than snubber loss of both circuits are the same at the same output power.

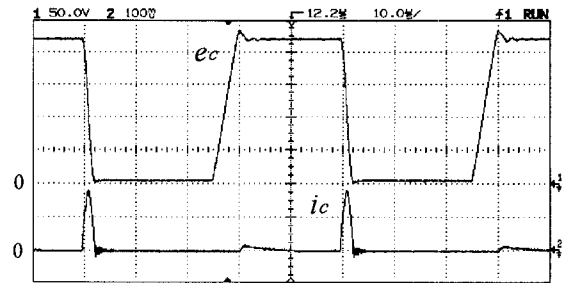


Fig.5 Experimental waveforms of the boost DC-DC converter in Fig.3 at 500W output. Snubber capacitor voltage *ec*:50V/div and snubber capacitor current *ic*:5A/div. time:10us/div

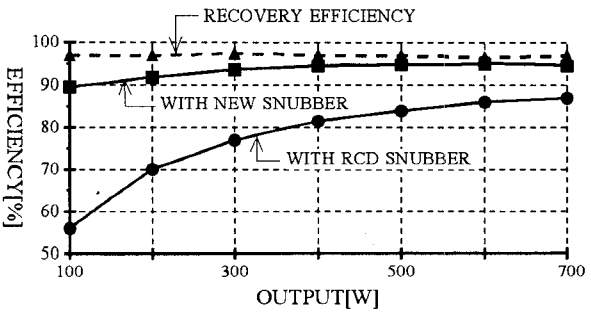


Fig.6 Converter efficiencies with and without snubber energy recovery, and recovery efficiency for the circuit in Fig.3.

IV. BOOST AC-DC CONVERTER WITH THE NEW SNUBBER

High-power-factor boost rectifiers have been developed recently for improving the input current qualities as well as controlling the output power. For these applications, the soft-switching techniques with loss-less means are also important from converter efficiency and EMI stand point of view.

Fig.7 shows a boost AC-DC converter with the new snubber. One of the defects of the basic circuit of Fig.3 that an extra diode (D_2) increases the conduction loss is improved by using two diode bridges DB_1 and DB_2 as shown in Fig.7. The conduction loss durig the off-period can be halved as compared with the basic circuit having a single diode bridge.

During the on-interval of IGBT, the inductor current increases through DB_2, while the output capacitor voltage is blocked by DB_1. During the off-interval, the inductor releases its energy to the output through DB_1, while the snubber voltage is blocked by DB_2 from discharging through the ac source. Therefore, the snubber circuit in this application can work well even in discontinuous current mode, as the snubber voltages are kept high enough for the energy recovery operation.

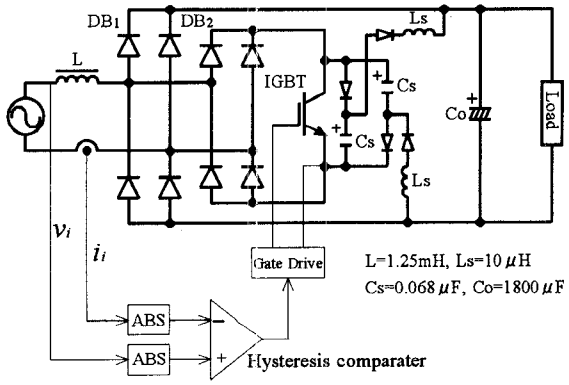


Fig.7 Single-phase boost AC-DC converter with the new snubber and hysteresis control.

A prototype of Fig.7 was built, with the circuit parameters listed in the same figure, to verify the circuit operations. For simplicity, the hysteresis-comparater control was employed. The source voltage is 100V(rms) and the output voltage is controlled manually at 200V by adjusting the reference voltage.

Fig.8 shows the un-filtered input current waveform of the converter together with the source voltage. The switching frequency ranges from about 16kHz to 20kHz.

Fig.9 shows the waveforms of snubber capacitor voltage and current near the zero crossing of the source voltage. It is seen that the capasitor voltage does not come down to zero for few switching cycles. This occurs because near the zero crossing, the main current is not large enough to charge the snubber capacitor up to the output voltage.

A high converter efficiency of 94.3% at 500W output was obtained by virtue of the loss-less soft switching and the reduced conduction loss of Fig.7.

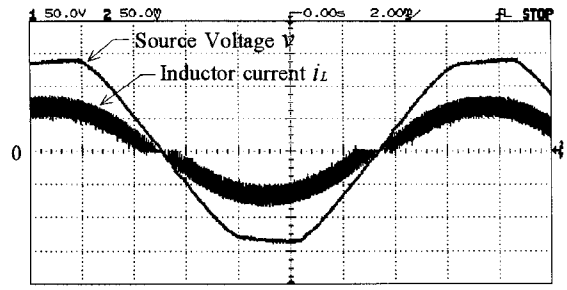


Fig.8 Source voltage and inductor current waveforms for the high-power-factor converter in Fig.7. 50V/div, 5A/div, 2ms/div

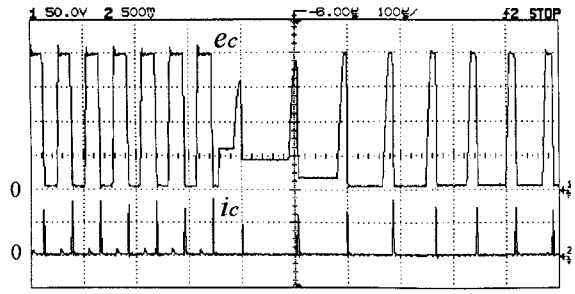


Fig.9 Snubber capacitor voltage *ec* and current *ic* near the zero-crossing of ac source for the high-power-factor converter in Fig.7. 50V/div, 5A/div, 100us/div

V. CONCLUSION

A novel loss-less passive snubber circuit suitable for the boost-type converters is proposed in this paper. The circuit configulation and its operation are simple using only passive components. Experimental results show that the snubber effectively improves the converter efficiency with high recovery efficiency of the snubber energy and reduced turn-off loss of the main switch. Using low-loss components for the snubber circuit, a very high recovery efficiency of about 97% is obtained because of the direct energy conversion.

It is expected that the new snubber is also effective for reducing the EMI noise at turn-off of the convereter. The EMI evaluation and development of other applications of the new snubber are left for the future studies.

REFERENCES

[1] A. Petterteig, J. Lode and T.M. Undeland,"IGBT Turn-Off Losses for Hard Switching and with Capacitive Snubbers", IEEE-IAS 1991 conf. Rec., Vol.2, pp.1501-1507

[2] A. Elasser and D.A.Torrey,"Soft Switching Active Snubbers for DC/DC Converters", IEEE Trans. on Power Electronics, Vol.11,No.5, September 1996

[3] K. Taniguchi, K. Hirachi and H. Irie,"Soft-Switching Circuit for Three-Phase Converter with Unity Power Factor, Trans. IEE Japan, Vol.117-D, No.2, 1997, pp.142-149

[4] S.J. Finney, B.W. Williams and T.C. Green,"RCD Snubber Revisited", IEEE Trans. on Industry Applications, Vol.32, No.1, Jan./Feb. 1996, pp.155-160

[5] X. He, S.J. Finney, B.W. Williams and Z.M. Qian,"Novel Passive Lossless Turn-on Snubber for Voltage Source Inverters", IEEE Trans. on Power Electronics, Vol.12, No.1, January 1997, pp.173-179

[6] M. Nakamura and M. Shimada,"A Single Switch Auxiliary Resonant Converter", 1997 National Convention Record of IEE Japan, Vol.4, No.919, pp.219-220

[7] H. Nomura, K. Fujiwara and K. Ozaki,"A Loss-less Passive Snubber for Soft-Switching Boost Converters", 1997 National Convention Record of IEE Japan, Vol.4, No.921, p.222

New Switching Sequence for Three Phase Converter with ZVS Using a Transformer

Shinya Ofuji , Tetsuya Oshikata , and Yoshiaki Matsuda
Development division Shindengen Electric Mfg.Co.,Ltd.
10-13, Minami-cho,Hanno city, Saitama, 357, Japan

Abstract **— New switching sequence for high power factor three phase converter is presented. By using the switching sequence, we can get a lower cost converter by letting the currents of upper-side-switches and lower-side-switches be unbalanced intentionally.**

Additionally, the three phase converter employs new ZVS topology with a transformer. The transformer makes the circuit design easier and the auxiliary switch for ZVS can switch under ZCS condition.

With these technology, we developed a high power factor, high efficiency, low noise, low cost three phase converter .

I . Introduction

A six-switch-boost-type converter is often used for three phase power factor correction(PFC). By using this topology, unity power factor can be achieved easily with high efficiency, but it is not so easy to make low cost converters. In this paper, new switching sequence is proposed to achieve a lower-cost six-switch-boost-type converter with maintaining unity power factor and high efficiency.

Three phase PFCs often employ soft-switching to make the PFCs be low noise and high efficiency ones.

In this paper, new ZVS topology is presented. It has a transformer which can be considered as a voltage source to achieve ZCS condition on the auxiliary switch.

II . Circuit Configuration

Fig.1 shows the basic circuit of the converter.

Body-diodes of Q1～Q6 are not written, but they are used as components. The dotted line and C1～C6 form the resonant circuit. Without the resonant circuit, the basic circuit configuration is the same as usual PFCs, since the new switching sequence proposed here is an idea of control method.

A. New Switching Sequence

Fig.2 shows input phase voltages. Around 45° , the conventional switching sequence is considered to be Fig.3. In Fig.3, Ec is the sawtooth carrier, Eu～Ew are the reference waves, and GQ1～GQ6 are the gate drive signals of Q1～Q6, respectively. No dead-time is shown for clarity. Judging from the ON/OFF conditions of Q1～Q6, the sequence can be divided into 4 stages (①～④).

The equivalent circuit for Stage ① and ④ is the same. It can be written as Fig.5.

Therefore even if these two stages are changed into one stage, the operation is apparently the same.

For example, if Stage ① is changed into Stage ④, the sequence is ④→②→③→④ (see Fig.6.). In Fig.6, GQ1"～GQ6" are the gate drive signals of Q1～Q6,respectively, when the new switching sequence is employed. GQ4'～GQ6' are shown as references and they are the same as GQ4～GQ6 in Fig.3. And it can be derived from checking Fig.4 that the currents in the upper side switches (Q1～Q3) are reduced comparing to those of the conventional sequence.

Although the currents in the lower side switches (Q4～Q6) increase, the peak values of currents and voltages on them are the same as those of the conventional switching sequence. Therefore lower rate devices can be used for the upper side switches. The new switching sequence may not be used in the case that the switches are selected severely in terms of their losses, because the losses of lower side switches increase by using this new sequence.

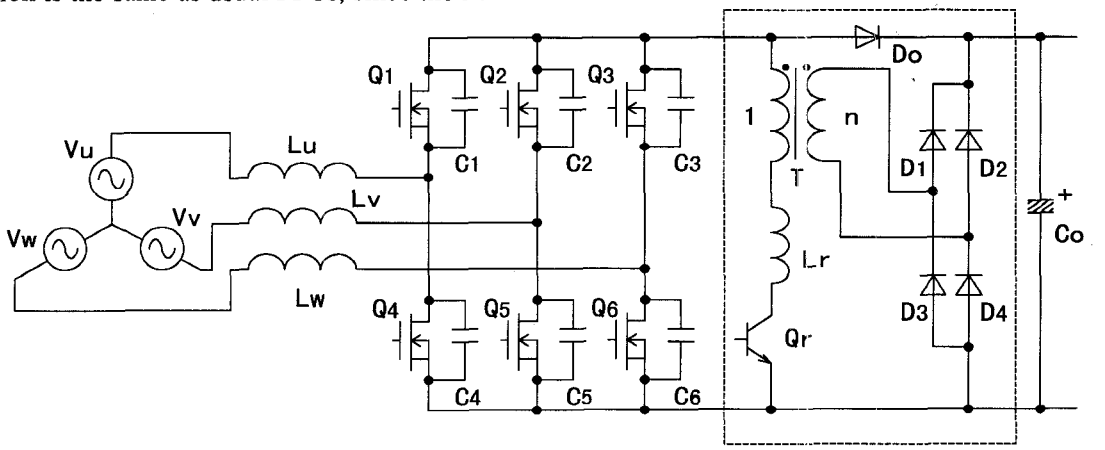


Fig.1 Basic circuit

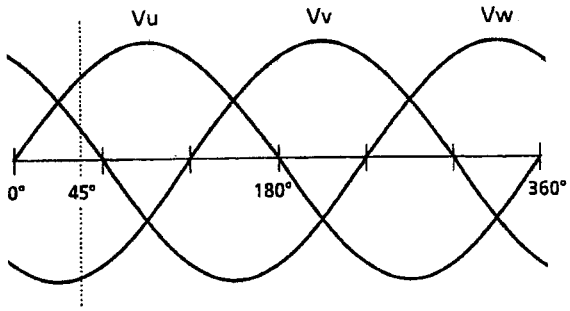


Fig.2 Phase voltages

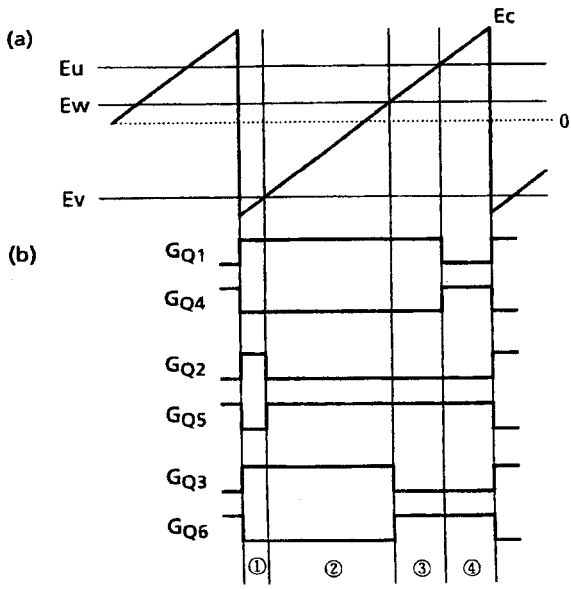


Fig.3 Conventional switching sequence

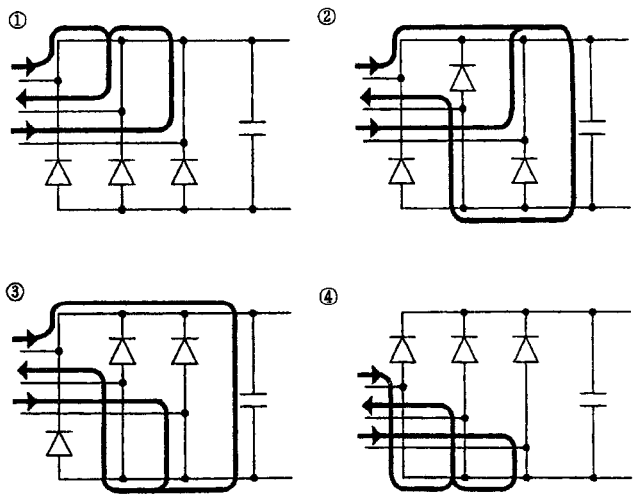


Fig.4 Current-flow

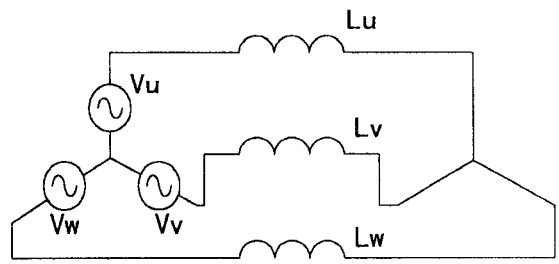


Fig.5 Equivalent circuit for Stage ① and ④

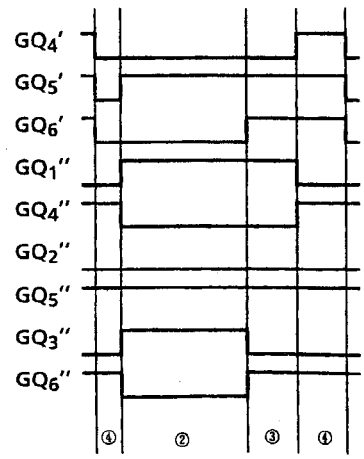


Fig.6 New switching sequence

The new switching sequence can be realized easily by adding an additional circuit on the conventional control circuits. Fig.7 shows an example of additional circuit. Dead time control should be added.

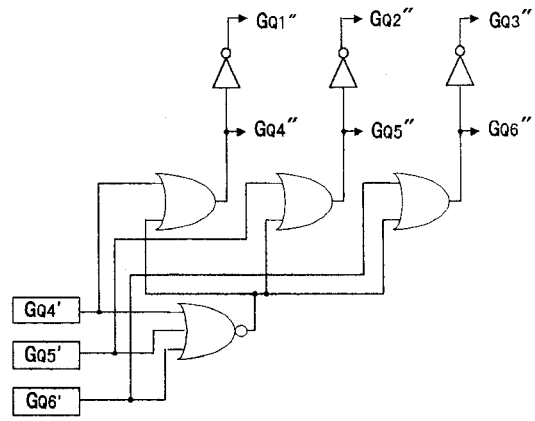


Fig.7 Example circuit

B. Resonant Circuit

Fig.8 shows the resonant equivalent circuit. In Fig.8, Cr=3·C1 (C1=C2···=C6) and IL is the amount of currents in Lu, Lv, Lw, which is considered as a constant current source.

Fig.9 shows typical wave forms of the circuit.

The resonant operation itself can be devided into three stages. Fig.10 shows the equivalent circuits of these stages.

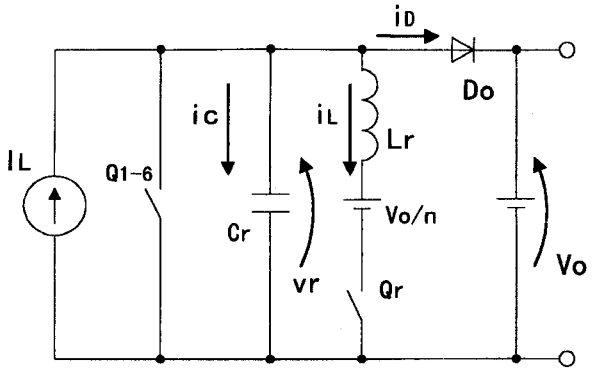


Fig.8 Resonant equivalent circuit

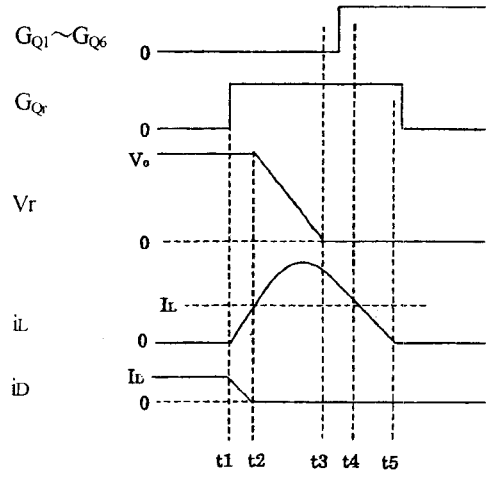


Fig.9 Waveforms

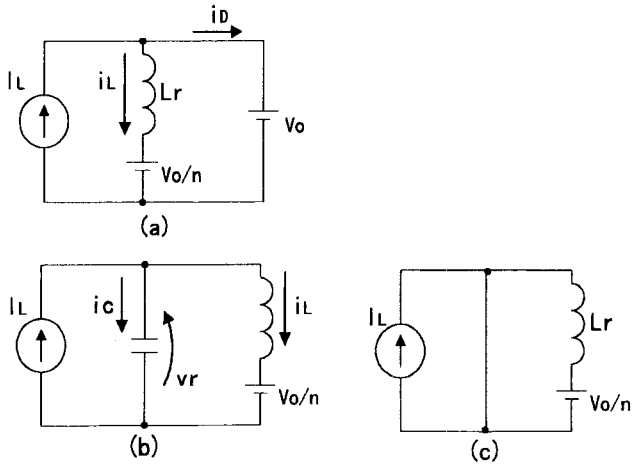


Fig.10 Equivalent circuit of stages

(a) Stage1 (t1~t2)

Before t1, Q1~Q6 are practically off, so iD equals to IL.

At t1, Qr turns on and iL rises linearly. At t2, iL reaches IL and iD drops to zero.

$$i_L = \frac{Vo - Vo/n}{Lr} t \tag{1}$$

The duration of this stage, T12 can be determined:

$$T_{12} = \frac{I_L \cdot Lr}{Vo - Vo/n} \tag{2}$$

(b) Stage2 (t2~t3)

This is the resonant stage.

State equations:

$$Lr \frac{di_L}{dt} = vr - \frac{Vo}{n} \tag{3}$$

$$vr = \frac{1}{c_r} \int (I_L - i_L) dt \tag{4}$$

The stage equations and the duration, T23 can be solved:

$$i_L(t) = I_L + \frac{Vo - Vo/n}{Zo} \sin \omega o t \tag{5}$$

where $Zo = \sqrt{\frac{Lr}{Cr}}$, $\omega o = \frac{1}{\sqrt{Lr \cdot Cr}}$

$$vr(t) = (Vo - Vo/n) \cos \omega o t + \frac{Vo}{n} \tag{6}$$

$$T_{23} = \frac{1}{\omega o} \cos^{-1}\left(\frac{1}{1-n}\right) \tag{7}$$

(c) Stage3 (t3~t5)

After vr drops to zero at t3, iL starts to drop linearly.

State Equation:

$$Lr \frac{di_{Lr}}{dt} = -\frac{Vo}{n} \tag{8}$$

The state equation and the duration, T35 can be solved:

$$i_L(t) = -\frac{Vo}{n \cdot Lr} t + i_L(t3) \tag{9}$$

$$T_{35} = \frac{n \cdot Lr \cdot i_{Lr}}{Vo} \tag{10}$$

In this duration, before iL reaches IL (i.e. t3~t5), the relevant switches of Q1~Q6 should turn on to achieve ZVS on Q1~Q6. And after iL drops to zero at t5,Qr should turn off to achieve ZCS on Qr.

The t4~t5 duration, T34 can be determined:

$$T_{34} = \frac{n-1}{\omega o} \sin(\omega o \cdot T_{23}) \tag{11}$$

The t4~t5 duration, T45 can also be determined:

$$T_{45} = \frac{n \cdot Lr \cdot I_L}{Vo} \tag{12}$$

III. Experimental Results

The advantages were verified on 5kW converters.

To compare the new switching sequence and the conventional one, two converters were made.

- converter A

  The conventional switching sequence is used. Each switch of Q1~Q6 consists of two 500V-50A FETs (80m Ω typ.).

- converter B

  The new switching sequence is used. Each switch of Q1~Q3 consists of one 500V-30A FET(160m Ω typ.) and each switch of Q4~Q6 consists of two 500V-50A FETs (80m Ω typ.).

The difference between converter A and B on power factor and efficiency could not be detected.

Efficiency of 97.8% and power factor of 0.99 at 5kW and 200Vinput.

Fig.11 shows the typical waveforms of converter B. The larger wave is the line voltage and the smaller one is the input current.

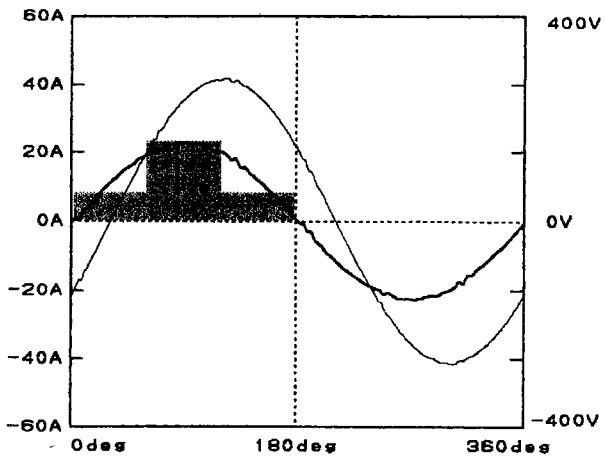


Fig.11 Wavefoms

Fig.12 shows harmonic currents of converter B with IEC standards limit.

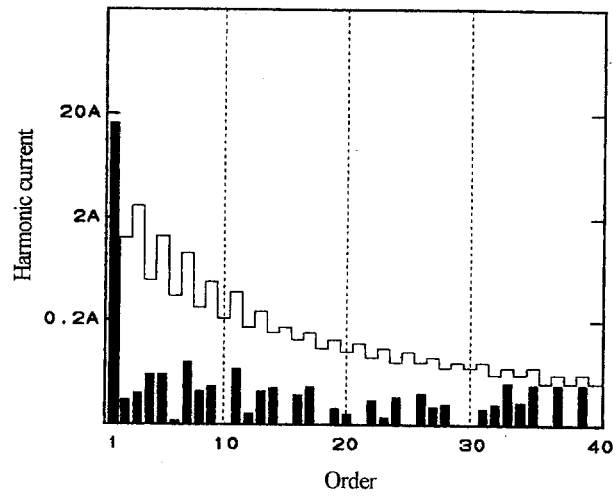


Fig.12 Harmonic currents

IV. Conclusions

A new switching sequence and ZVS topology for high power factor three phase converter is proposed. With these methods, a high efficiency, high power factor, low noise and low cost three phase converter can be made. The Advantages has been verified on 5kW converters.

References

[1] Fred C.Lee et al.: "SOFT-TRANSITION THREE-PHASE PMW CONVERSION TECHNOLOGY", Proc. Of PESC'94

[2] D.Boroyevich and Silva Hiti : "Three-Phase PMW Converter Modeling and Control Design", APEC96 SEMINAR9

ANALYSIS OF SELF-EXCITED RESONANT DC-DC CONVERTER TO DETERMINE OSCILLATION CONDITION

Yasuyuki Kanai*, Nobuhiko Yamashita, Naoki Murakami, Toshiaki Yachi
NTT Integrated Information & Energy System Laboratories
3-9-11 Midori-cho, Musashino-shi, Tokyo 180, Japan
Fax: (*) +81-422-59-2172,Phone:(*) +81-422-59-2029
E-mail Address: ykanai@ilab.ntt.co.jp

ABSTRACT

A method is proposed for analyzing a self-exciting resonant DC-DC converter that gives the theoretical oscillation condition under which the converter can work. This condition was determined by theoretically analyzing the energy transmission between the main-resonant circuit and the resonant gate-driving circuit. Maintaining oscillation requires that the energy supplied by the main-resonant circuit is larger than the conduction power loss caused by the parasitic gate resistance. The analysis also showed that the oscillation area depends on the feedback and gate capacitances. The analytical results agreed with the experimental ones.

1. Introduction

Communication systems require compact highly efficient power-supply modules to save space and energy. Power modules that operate at high frequencies and have fewer components save space. The self-exciting resonant DC-DC converter[1][2] is one such module. It has a self-exciting, zero-voltage-switching (ZVS) inverter that fully utilizes the internal capacitances of the MOSFET circuit elements. The self-excitation is achieved with a minimum number of components, resulting in a highly efficient gate drive. However, determining the oscillation condition by experimentally or with simulation takes a long time. A theoretical approach is thus needed.

We propose a new approach to analyzing a self-exciting resonant DC-DC converter that gives the theoretical oscillation condition under which the converter can work. This condition is identified by theoretically analyzing the energy transmission between the ZVS resonant circuit and the resonant gate-driving circuit. We determined that the energy supplied by the ZVS circuit must be larger than the conduction power loss caused by the parasitic gate resistance to maintain oscillation. We also found that the oscillation area depends on the feedback and gate capacitances. These analytical results agreed with our experimental results.

2. Self-exciting operation

A diagram of the circuit we used is shown in Fig. 1. It was designed to modulate the frequency so that the output voltage is kept a constant. This frequency control is implemented by resonating the gate of the power MOSFET by using a variable reactive network.

To determine the oscillation condition, we translated the circuit to an equivalent one (Fig. 2). The circuitry enclosed by the dotted line is the MOSFET-equivalent circuit; it consists of a gate resistor, three internal capacitors, an ideal switch, and a body-diode. Resonance in the power MOSFET gate is obtained through inductance L_G, capacitance C_{GEX}, and internal MOSFET capacitance C_{GS}. Resonance in the ZVS inverter is obtained through both inductance L_O, capacitance C_{OEX}, and internal MOSFET capacitance C_{DS}. Feedback from the drain to the gate is obtained through both external feedback C_{FBEX} and internal MOSFET capacitance C_{DG}. Capacitor C_P and the secondary circuit (Fig. 1) are assumed to be the resistor[3].

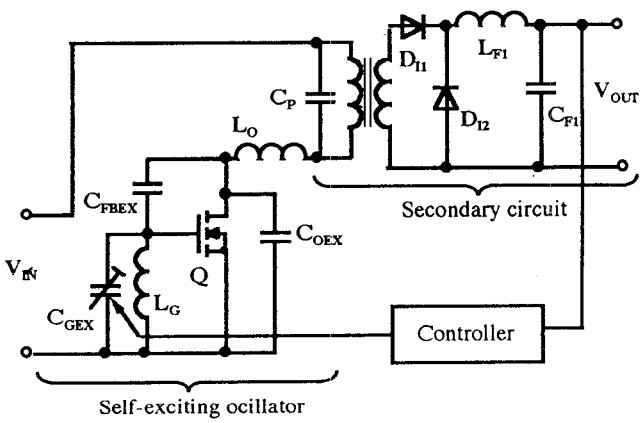


Fig. 1 Circuit diagram of self-exciting resonant DC-DC converter.

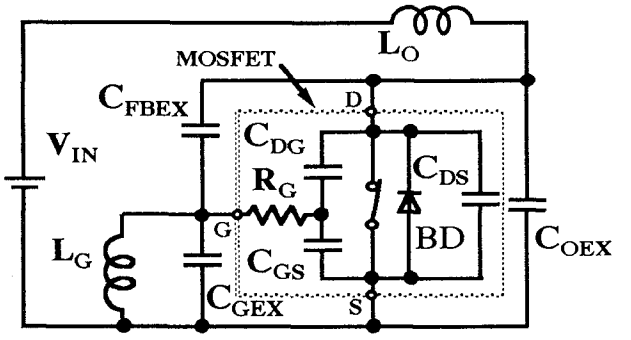


Fig. 2 Equivalent circuit for self-exciting oscillator.

The waveforms for the equivalent circuit are shown in Fig. 3, in which each switching cycle is divided into three topological stages. The equivalent circuit model for each stage is shown in Fig. 4. The operations during the three topological stages are as follows.

Stage Ⅰ (t_2 - t_1): this stage is the resonant stage. MOSFET Q is turned off at t_1, and the body-diode is in the off-state. Inductor L_O and capacitors C_{OEX} and C_{DS} (C_O = C_{OEX} + C_{DS}) generate the resonance for the ZVS inverter. Inductor L_G and capacitors C_{GEX} and C_{GS} ($C_G = C_{GEX} + C_{GS}$) constitute the gate resonant circuit. In this stage, the energy of L_O is distributed to both the gate resonance circuit and capacitor C_O.

Stage Ⅱ (t_3 - t_2): this stage is the voltage clamping interval for MOSFET Q, Which is in the off-state. The body-diode is turned on at t_2, causing inductor current I_{LO} to increase gradually.

Stage Ⅲ(t_1' - t_3): this stage is the energy storage stage.

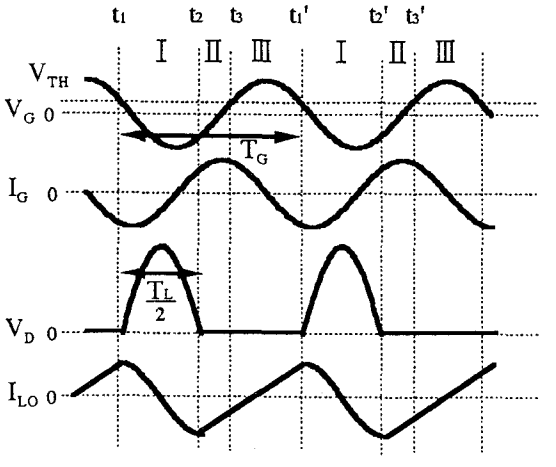


Fig. 3 Waveforms for equivalent circuit.

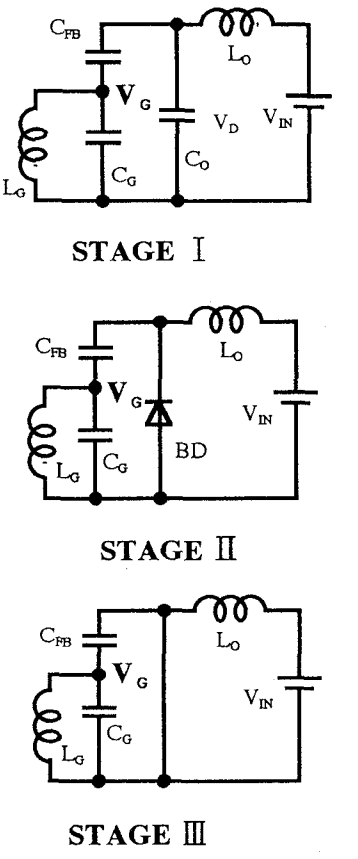


Fig. 4 Equivalent circuits of oscillator.

MOSFET Q is turned on at t_3 and the body-diode is turned off, causing I_{LO} to increase linearally. In this stage, L_O stores energy. To achieve ZVS operation, MOSFET Q is turned on while the body-diode is conducting. When MOSFET Q is turned off, the next cycle begins. The output voltage is controlled by changing the duration of this stage.

3. Analysis

To determine the condition for self-exciting oscillation, the state-equations must be solved. It is impossible, however, to solve higher than 5th-order nonlinear equations. We thus propose that the oscillation condition be identified by theoretically analyzing the energy transmission between the ZVS resonant circuit and the resonant gate-driving circuit. The energy streams are shown in Figs. 5(a) and (b). The ZVS-resonant inductance L_O supplies energy E_{CG} through the gate-resonant circuit in stage Ⅰ (Fig. 5(a)). Energy E_{CG} makes up for the conduction power loss E_{LOSS} caused by the gate-resonance current and internal MOSFET gate-resistance R_G (Fig. 5(b)). To maintain oscillation, energy E_{CG} must be larger than conduction power loss E_{LOSS}. The E_{CG} and E_{LOSS} are described as follows:

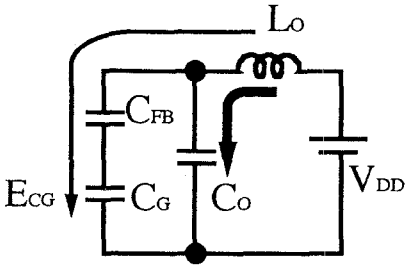


Fig. 5(a) Energy distribution from Lo to the capacitance.

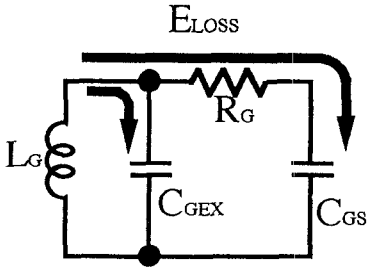


Fig. 5(b) Conduction power loss caused by gate-resonant current and internal MOSFET gate-resistance.

$$E_{CG} = \frac{C_G C_{FB}^2}{(C_{FB}+C_G)\left\{C_O(C_{FB}+C_G)+C_{FB}\cdot C_G\right\}} E_{LO} \quad (1)$$

$$E_{LO} = \frac{1}{2}L_O I_{LO}^2 = \frac{V_{IN}^2}{8L_O}\left(T_G - \frac{T_L}{2}\right)^2 \quad (2)$$

$$E_{LOSS} = \frac{\pi R_G C_{GS}^2 V_{GP}^2}{2\sqrt{L_G C_G}} \quad (3)$$

Here V_{GP} is the amplitude of the gate voltage. T_L is ZVS resonant cycle. T_G is gate resonant cycle. The condition for keeping V_{GP} constant so as to maintain the oscillation can be expressed as follows:

$$E_{CG} = E_{LOSS} \quad (4)$$

$$V_{GP} \geq V_{TH} \quad (5)$$

Here V_{TH} is the MOSFET threshold voltage. The V_{GP} and the oscillation condition are obtained from these equations as follows:

$$V_{GP} = \frac{C_{FB}}{C_{GS}}\sqrt{\frac{2E_{LO}C_G\sqrt{L_G C_G}}{\pi R_G(C_{FB}+C_G)\left\{C_O(C_{FB}+C_G)+C_{FB}C_G\right\}}} \geq V_{TH} \quad (6)$$

The design of this circuit make it easier to vary capacitances C_{FB} and C_G than to vary the inductance. therefore, these capacitances are better parameters for maintaining the oscillation.

4. Experiment

To verify our analytical results, we implemented the self-exciting oscillator shown in Fig. 2 with the following specifications:

V_{IN}=12 V, C_{GEX}=1 - 1000 pF, C_{FBEX} =1 - 1000 pF, C_{OEX}=1000 pF, L_O =3.3 μH, and LG =3.3 μH. The MOSFET Q was a Siliconix Si9950DY.

The oscillations are not self starting, but are initiated by injecting energy into the circuit, which is done by applying a short voltage pulse to the MOSFET gate. When this gate-voltage reaches a sufficiently high level, ringing is initiated in the gate network, causing the circuit to oscillate. Feedback from the drain to the gate is obtained through both C_{FBEX} and the internal MOSFET capacitance.

5. Results and Discussion

The graphical expressions of the amplitude of the gate voltage depended on external gate capacitance C_{GEX} and external feedback capacitance C_{FBEX}, as shown in Fig. 6. The threshold voltage of the MOSFET V_{TH} was 5 V, and the breakdown voltage VB_{GS} was 20 V. Oscillation occurred between V_{TH} and VB_{GS}.

The graphical expression of the oscillation border lines depended on the feedback and gate capacitances, as shown in Fig. 7. The areas under the left side of each border line

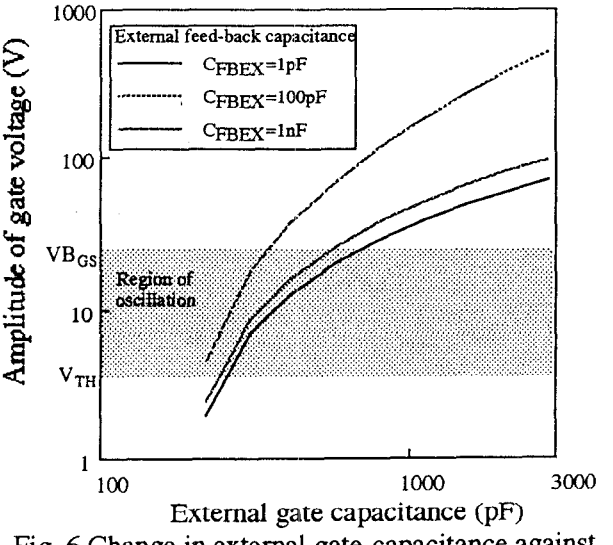


Fig. 6 Change in external gate-capacitance against change in external feed-back capacitance.

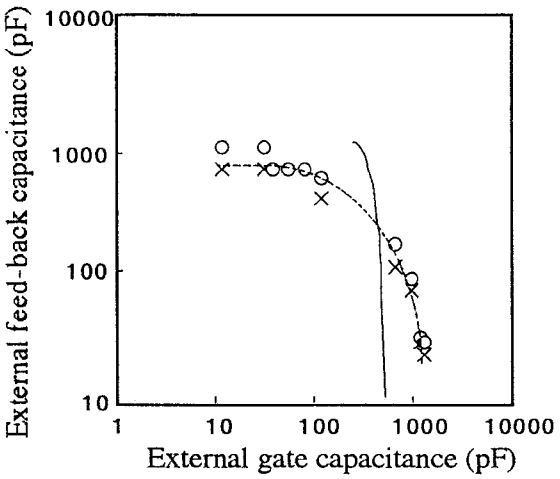


Fig. 7 Oscillation boundaries.

Calculated ——— Measured ---------

○ Oscillation × Non-Oscillation

indicate non-oscillation areas caused by a lack of gate-driving energy. These experimental results also agree with our analysis. The slight difference between analysis and experiment was probably caused by heat-drift of external capacitances.

6. Conclusion

We have proposed an effective method for analyzing a self-exciting resonant DC-DC converter to determine the theoretical oscillation condition under which the converter can operate.

We found that the energy supplied by the ZVS inverter must be larger than the conduction power loss caused by the parasitic gate resistance. Our analytical results agreed with our experimental results.

REFERENCES

[1] W. C. Bowman, J. F. Balicki, F. T. Dickens, R. M. Honeycutt, W. A. Nitz, W. Strauss, W. B. Suiter, and N. G. Ziesse, "A resonant DC-to-DC converter operating at 22 Megahertz," IEEE Applied power electronics conference proceedings, pp. 3-10, 1988.

[2] W. C. Bowman, J. R. Bailey, C. W. Boettcher, M. G. Johnson, F. M. Magalhaes, W. A. Nitz, F. Sarasola, G. R. Westerman, and N. G. Ziesse, "A high density board mounted power module for distributed powering architectures, " IEEE Applied power electronics conference proceedings, pp. 43-54, 1990.

[3] W.A.Nitz, W. C. Bowman, F. T. Dickens, F. M. Magalhaes, W. Strauss, W. B. Suiter, and N. G. Ziesse, "A new family of resonant rectifier circuits for high frequency DC-DC converter applications, " IEEE Applied power electronics conference proceedings, pp. 12-22, 1988.

NEW DC-DC RESONANT CONVERTER AS ACTIVE FILTER

I. Nagy*/**, P. Korondi**, E. Masada***, Z. Puklus****

* Computer and Automation Institute, Hungarian Academy of Sciences, HUNGARY
** Technical University of Budapest, Dept. of Automation, H-1111 Budapest, Budafoki ut 8. F. II. HUNGARY
Fax.:+36-1-463 3163, Phone:+36-1-463 E-mail: nagy@elektro.get.bme.hu
*** The University of Tokyo , Dept. of Electrical Engineering, JAPAN
**** Széchényi College, HUNGARY

Abstract **-- The paper is concerned with the application of a resonant DC-DC converter as a low pass active filter. The converter is a member of a rather new converter family. A short summary of the operation and that of the quantitative relations of the new converter family are presented. To prepare the discussion of the resonant buck converter as active filter its asymmetrical state is studied by two phase symmetrical components. The operation of the buck converter as a low pass active filter applying both commutation angle and switching frequency modulation control are discussed somewhat in detail. Laboratory test results are included.**

I. INTRODUCTION

The paper describes the application of a resonant DC-DC converter as a low pass active filter. The converter is a member of a rather new converter family published earlier [1,2]. This family cannot be found in the wide literature of DC-DC converters [4 ... 27]. The resonant family includes buck, boost and buck & boost (B&B) converters like the conventional DC-DC converters. Each of them has slightly different configurations from the conventional converters leading to significant deviations in operation. Their configurations are based on the conventional buck, boost as well as buck and boost converters but they have a switched capacitance C and a positive and a negative side suffixed by p and n (Fig. 1).

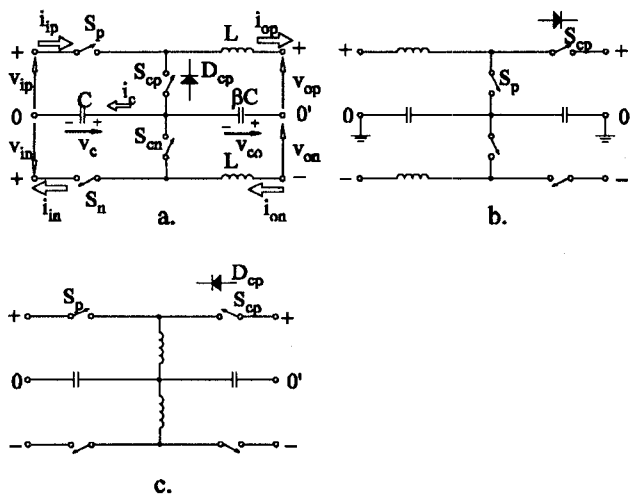


Fig. 1. Buck (Fig.a), Boost (Fig.b), B&B (Fig. c) resonant converters

First a short summary of the operation and that of the qualitative relations of the new converter family are presented. To prepare the discussion of the resonant buck converter as active filter its asymmetrical state is studied by two phase symmetrical components. Three of its control modes are described: Symmetrical, Asymmetrical and General Energy Supply.

The converter as a low pass active filter applying both commutation angle and switching frequency modulation control is discussed somewhat in detail before presenting laboratory test results.

II. OPERATION

The steady-state operation is briefly presented in the simple case when capacitance βC is replaced by short circuit in Fig. 1a and c and by an interrupt in Fig. 1b. Clamping diodes are connected in place of switches S_{cp} and S_{cn} in all three circuits. Discontinuous current conduction in inductance L, and lossless operation, furthermore $v_{ip} = -v_{in} = V_i = const.$ and $v_{op} = v_{on} = V_o = const$ are the other assumptions $(v_{in} < 0)$. The capacitance across the input and output terminals are not shown in Fig.1.

By turning on switch S_p , a sinusoidal current pulse i_i is developed from $\omega t = 0$ to α (Fig.2a, b, c, $\omega = 1/\sqrt{LC}$). It makes the voltage v_c swing from V_{cn} to V_{cp} $(V_{cn} < 0)$. The voltage V_{cp} is V_i in Fig 1a, V_o in Fig 1b and $V_i + V_o$ in Fig 1c. Note that the polarity of the output voltage is reversed in the B&B converter. Reaching $v_c = V_{cp}$ value, the clamping

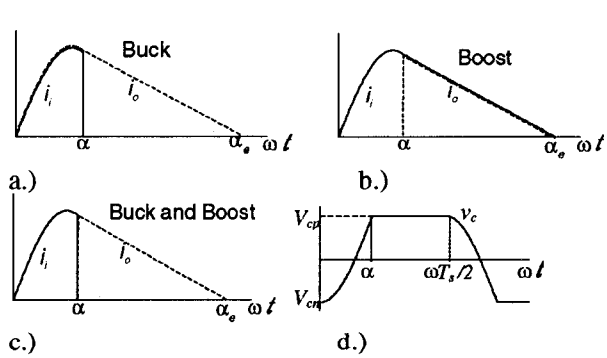


Fig.2 Time functions of input and output currents and voltage v_c

diode D_{cp} turns on and it clamps v_c on the value V_{cp}. The choke current commutates from S_p to D_{cp}. The commutation time is neglected in Fig. 2. The choke (output) current i_o is reduced like a ramp to zero. The output energy delivered by the output current pulse

$$W_{op} = \int_0^{Ts/2} V_o i_o dt = \int_0^{Ts/2} V_i i_i dt + \frac{C}{2}(V_{cn}^2 - V_{cp}^2) = W_{ip} + \Delta W_{cp} \quad (1)$$

W_{ip} is the input energy, ΔW_{cp} is the change in the stored energy of capacitance C in half period $T_s/2$ (Fig.2d). $f_s = 1/T_s$ is the switching frequency. In symmetrical case, $-V_{cn} = V_{cp} = V_i$ and $\Delta W_{cp} = 0$. Similar process takes place in the next half period from $T_s/2$ in the negative side of the converter.

Neglecting the losses, the power balance $V_i I_i = V_o I_o$ where I_i and I_o are average values. i_i and i_o overlap each other in the buck ($I_o \geq I_i$) and in the boost ($I_o \leq I_i$) converter while there is no overlapping in the B&B converter ($I_o \lessgtr I_i$) (Fig.2). Taking into account $V_o/V_i = I_i/I_o$, the voltage ratio is $V_o/V_i \leq 1$ for the buck converter, $V_o/V_i \geq 1$ for the boost converter and $V_o/V_i \lessgtr 1$ for the B&B converter.

Important advantage is the soft switching of S and D. The sinusoidal current in S starts from zero at turning on and the current commutates from S to D practically under zero voltage across S and D.

III. RELATIONS

Applying clamping diodes D_{cp}, D_{cn}, the steady-state behavior can be described by unified way. The input current pulse for all converters in the interval $0 \leq \omega t \leq \alpha$ is

$$i_i = \frac{V_i + V_x}{\sqrt{L/C}} \sin \omega t \quad (2)$$

and the diode current pulse from $\omega t = \alpha$

$$i_D = i_i(\alpha) - \frac{V_o - V_y}{L}\tau \quad (3)$$

where $\tau = 0$ at $\omega t = \alpha$. The voltages V_x and V_y are in Table 1. On the basis of eq. (2) and (3) the relations V_o / V_i can be derived and are included in Table 1 [1].

TABLE 1

	Buck	Boost	B&B	
V_o / V_i	$1-A$	$1/A$	$(1-A)/A$	(4)
V_x	$V_i - V_o$	V_o	V_i+V_o	
V_y	0	V_i	0	
$2I_i V_i$	$2W_o f_s$	$2W_o f_s/(1-A)A$	$2W_o f_s / A$	(5)

$$2W_o = 4\frac{CV_i^2}{2}$$

The quantity A is

$$A = \frac{1+\cos\alpha}{1-\cos\alpha} \quad (6)$$

A has somewhat similar function here as the duty ratio D in the conventional buck, boost and B&B converters in mathematical sense [5]. There is a fundamental difference between A and D in the case of clamping diode. D can directly be changed by the turn on time (T_{on}), by the turn-off time (T_{off}) and by the switching period ($T_s = T_{on} + T_{off} = 1/f_s$) by keeping one of them constant and changing the other two. On the other hand, A can only indirectly be set by f_s in the following way. Provided that V_i and the equivalent load resistance is kept constant, by increasing the switching frequency f_s, that is, the frequency of the output energy pulses delivered by i_o, the output power $P_o = 2V_o I_o$ are increased together with I_o and V_o and $P_i = 2V_i I_i$ [eq. (5) in Table 1]. A is indirectly reduced [eq. (4) in Table 1] and α increases in the direction to $\alpha_{max} = \pi$. As A changes from 1 to 0 the angle α moves from $\alpha_{min} = \pi/2$ to $\alpha_{max} = \pi$. A can also indirectly be changed by varying V_i and/or the load resistance and keeping f_s constant.

IV. EXPERIMENTAL RESULTS
Symmetrical Operation

Laboratory measurements of the buck converter applying MOSFET switches and clamping diodes were carried out. The resonant frequency $f = (1/2\pi)\, 1/\sqrt{LC} = 62$ kHz and the characteristic impedance $Z_c = \sqrt{L/C} = 54.6\Omega$ were in all tests presented here. Two of the results are included now.

The static characteristic for discontinuous (DCM) and for continuous (CCM) choke current conduction mode is shown in Fig. 3. for the buck converter applying clamping diodes. The switching frequency f_s changed from 33 kHz to 105 kHz was the parameter. The value of k in eq. (5) is $2W_o = 1.69*10^{-4}$ Ws (C = 47 nF, V_i = 30 V). Table 2 includes the input power $P_i = 2I_i V_i$ obtained from eq. (5) and the input and output power from measurement and the efficiency at three switching frequencies. The hyperbolic relation between V_o and I_o given by eq (5) is well met.

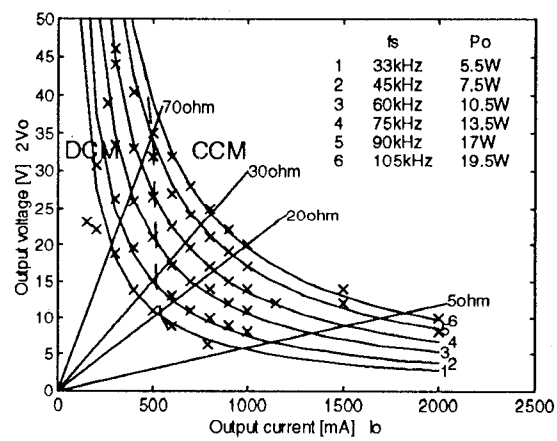


Fig.3. Output Characteristic

The oscilloscope traces of some variables are shown in Fig. 4. The scales are: 20 V/div; 4μs/div. The switching frequency was f_s = 50 kHz. Further tests for active filtering will be presented in the paper.

The tests results support the theoretical considerations.

TABLE 2

f_s[kHz]	33	60	105
P_i from eq. (5) [W]	5.57	10.1	17.8
P_{im} measured [W]	7.6	13	23.5
P_o measured [W]	5.5	10.5	19.5
efficiency $\eta=P_o/P_{im}$	72	81	83

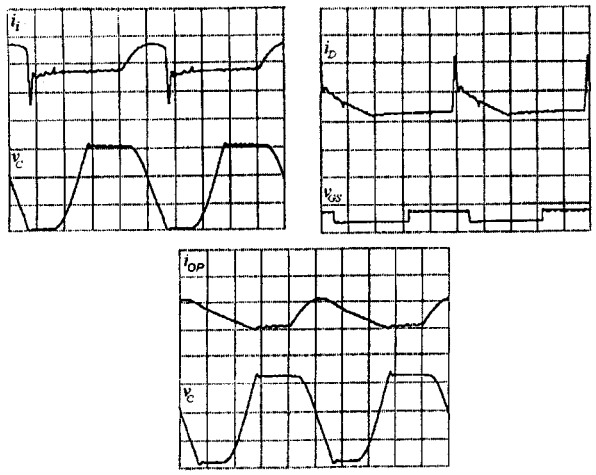


Fig. 4 Oscilloscope traces

V. ASYMMETRICAL OPERATION

To prepare the explanation of the buck converter as active filter its operation is studied in asymmetrical state. The clamping diodes are replaced by switches and in general $v_{ip} \neq - v_{in}$; $v_{op} \neq v_{on}$; $v_{cp} \neq - v_{cn}$. Assuming $\alpha_p = \alpha_n = \alpha$, now there are two control parameters; f_s and A or α. They can be directly set and they can control both the output power and the output voltages v_{op} and v_{on}.

The study of the behavior of the converter is greatly supported by the application of the two phase symmetrical components [3]. The x_p positive and the x_n negative sequence component is defined

$$x_1 = (x_p + x_n)/2 \quad (7)$$

and

$$x_2 = (x_p - x_n)/2 \quad (8)$$

respectively. [Note that $v_{in} < 0$ and $v_{cn} < 0$ and in these cases e.g. $v_{i1} = (v_{ip} - v_{in})/2$ and $v_{i2} = (v_{ip} + v_{in})/2$].

The configuration can be redrawn as shown in Fig. 5.

Here $v_{c2} = (v_{cp} + v_{cn})/2$ where v_{cp} and v_{cn} are peak values and Δv_c is the instantaneous value measured from v_{c2} (Fig.6).

The energy delivered by one positive and one negative current pulse from the input source, respectively

$$w_{ip} = v_{ip} \int i_c dt = v_{ip} C(v_{cp} - v_{cn}) \quad (9)$$

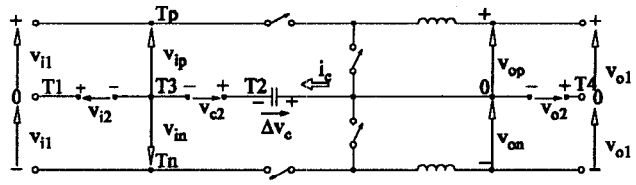


Fig. 5 Buck Converter with symmetrical components

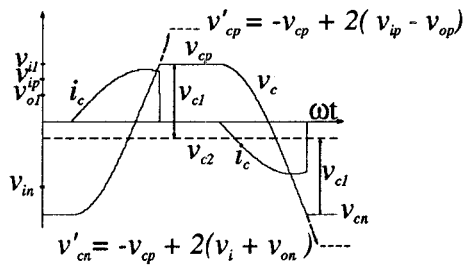


Fig.6 Time functions in asymmetrical case

$$w_{in} = v_{in} \int i_c dt = - v_{in} C(v_{cp} - v_{cn}) \quad (10)$$

The corresponding energy changes in the switched condenser C are

$$\Delta w_{cp} = C(v_{cp}^2 - v_{cn}^2)/2 \quad (11)$$

$$\Delta w_{cn} = C(v_{cn}^2 - v_{cp}^2)/2 \quad (12)$$

the output energy pulses are

$$w_{op} = C(v_{cp} - v_{cn})[v_{ip} - (v_{cp} + v_{cn})/2] \quad (13)$$

$$w_{on} = C(v_{cp} - v_{cn})[-v_{in} + (v_{cp} + v_{cn})/2] \quad (14)$$

The positive and negative sequences component of the output energy pulses are

$$w_{o1} = 2Cv_{c1}v_{i1} \quad (15)$$

$$w_{o2} = 2Cv_{c1}(v_{i2} - v_{c2}) \quad (16)$$

The avarage output energy $w_{o1} = (w_{op} + w_{on})/2$ is determined by v_{c1} and v_{i1}. The difference between the two input energy pulses $w_{o2} = (w_{op} - w_{on})/2$ is determined by v_{i2} and v_{c2} besides v_{c1} in steady-state.

There are three possible control modes by using f_s and angle α as control parameters [eq.(1)] :

- Symmetrical Energy Supply, SES ($w_{op} = w_{on}$)
- Asymmetrical Energy Supply, AES $[w_{op}/w_{on} = v_{ip}/(-v_{in})]$.
- General Energy Supply, GES ($w_{op}/w_{on} = g$).

The results of their study will be summarized.

Symmetrical Energy Supply (SES). The output current pulses deliver the same energy, that is, $w_{op} = w_{on}$ and $v_{op} = v_{on}$ though the input voltages are different. The Δw_{cp} part of the energy stored in C is added to the input energy w_{ip}

and their sum $w_{c1} = w_{ip} + \Delta w_{cp}$ is delivered to the load by the current pulse i_{op} (Fig.7). The same energy $\Delta w_{cn} = \Delta w_{cp}$ is supplied back to C at the end of the negative input current pulse from the input energy w_{in}. The output current pulse i_{on} delivers $w_{on} = w_{in} - \Delta w_{cn}$ energy to the load. The capacitance C plays an energy balancing role. The negative sequence components v_{i2} and v_{c2} are equal, $v_{i2} = v_{c2}$. Terminals $T1$ and $T2$ are short-circuited and the positive sequence component v_{i1} develops across

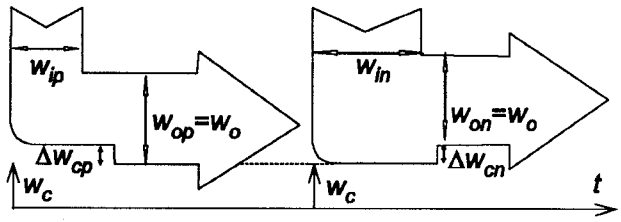


Fig. 7 Energy balance in SES

terminals T_p and $T2$ as well as across $T2$ and T_n. Considering v_{i1} as input voltages we have arrived back to the symmetrical case.

Asymmetrical Energy Supply (AES). The ratio of the two output energy pulses is the same as that of the input voltages $w_{op}/w_{on} = v_{ip}/(-v_{in})$. The total input energy is transferred to the output on the same side: $w_{op} = w_{ip}$ and $w_{on} = -w_{in}$. The capacitance C exchanges no energy between the positive and the negative side. The negative sequence component $v_{c2} = 0$ and $v_{o2} = v_{i2}$.

General Energy Supply (GES). The ratio of the two output energy pulses is arbitrary $w_{op}/w_{on} = g$. Introducing

$$w_{o1} = (g+1)w_{on}/2 \quad (17)$$
$$w_{o2} = (g-1)w_{on}/2 \quad (18)$$

their ratio

$$\frac{w_{o2}}{w_{o1}} = \frac{g-1}{g+1} = \delta = \frac{v_{i2} - v_{c2}}{v_{i1}} \quad (19)$$

that is

$$v_{c2} = v_{i2} - \delta v_{i1} \quad (20)$$

The condenser current pulses are

$$i_{cp} = \sqrt{C/L}(v_{ip} - v_{cn} - v_{op})\sin\omega t \quad (21)$$
$$i_{cn} = -\sqrt{C/L}(-v_{in} + v_{cp} - v_{op})\sin[\omega(t - T/2)] \quad (22)$$

The current pulse i_{cp} alters the C conderser voltage by $2v_{c1}$

$$2v_{c1} = \frac{1}{\omega C}\int_0^{\alpha_p} i_{cp} d\omega t \quad (23)$$

From (17) and (19)

$$\cos\alpha_p = \frac{v_{ip} - v_{op} - v_{cn} - 2v_{c1}}{v_{ip} - v_{op} - v_{cn}} \quad (24)$$

Similarly

$$\cos\alpha_n = \frac{-v_{in} - v_{on} + v_{cp} - 2v_{c1}}{-v_{in} - v_{on} + v_{cp}} \quad (25)$$

Introducing the symmetrical components

$$\cos\alpha_p = \frac{v_- + \Delta v}{v_+ + \Delta v} \quad (26)$$

$$\cos\alpha_n = \frac{v_- - \Delta v}{v_+ - \Delta v} \quad (27)$$

where

$$v_- = v_{i1} - v_{o1} - v_{c1} \quad (28)$$
$$v_+ = v_{i1} - v_{o1} + v_{c1} \quad (29)$$
$$\Delta v = v_{i2} - v_{o2} - v_{c2} \quad (30)$$

In SES $v_{o2} = 0$. and $v_{c2} = v_{i2}$, therefore $\alpha_p = \alpha_n = \alpha$.

In AES $v_{o1} = v_{i1}$ and $v_{o2} = v_{i2}$ futheremore $v_{c2} = 0$. Again $\alpha_p = \alpha_n = \alpha$.

In GES $\alpha_p = \alpha_n = \alpha$ can be met only if $v_{o2} = \delta v_{i1}$ since now from eq. (20).

$$\Delta v = v_{i2} - v_{o2} - v_{c2} = -v_{o2} + \delta v_{i1} = 0 \quad (31)$$

VI. ACTIVE FILTER

The buck converter can be operated as a low pass active filter. The input voltages can have low frequency components superposed on their dc value.

The low frequency components can be filtered out in the output voltages v_{op} and v_{on} by three controllers. The requirements is that $v_{op} = v_{on} = V_o$. Indetical load currents are assumed in the positive and in the negative side of the converter. The converter is supposed to be operated SES mode. The three controllers (Fig. 8):

- Controller 1 controls the positive sequence component of the output voltage v_{o1}.
- Controller 2 controls the positive sequence component of the condenser voltage v_{c1}.
- Controller 3 controls the negative sequence component of the condenser voltage v_{c2}. Controller 1 sets the switching frequency f_s. Reduction in v_{o1} has to be componsated by output energy pulses delivered more frequently. Controller 2 sets the positive sequency component of the commutation angles α_p and α_n, that is, $\alpha_1 = (\alpha_p + \alpha_n)/2$. Reduction in v_{c1} increases α_1. Controller 3 sets the negative sequency component of the commutation angles α_p and α_n, that is, $\alpha_1 = (\alpha_p - \alpha_n)/2$. Its refrence signal is $v_{c2ref} = v_{i2}$ [eq. (20), $\delta = 0$]. Realizing the SES mode perfectly, $\alpha_2 = 0$.

Assuming sinusoidal variation in the input voltage as an example,

$$v_{ip} = V_i - 2V_{im}\cos\Omega t = V_i + 2v_{i2} \quad (32)$$
$$v_{in} = -V_i \quad (33)$$

where $\Omega << \omega$ and V_i= const. v_{ip} can be approximated by a constant value in one or several high frequency period of the converter.

To maintain $v_{op}= v_{on} =V_o = const$, that is, to filter out v_{i2} the condenser voltages v_{c1} and v_{c2} have to be changed slowly with v_{i2} as follows [eq. (15), (16)]

$$\frac{v_{c1}}{V_i} = \frac{1}{2RCf_s}\left(\frac{V_o}{V_i}\right)^2 \frac{1}{1-\Delta} \tag{34}$$

$$\frac{v_{c2}}{V_i} = \frac{v_{i2}}{V_i} = -\Delta \tag{35}$$

where

$$\Delta = \frac{V_{im}}{V_i}\cos\Omega t, \tag{36}$$

$$w_{o1} = w_o = \frac{V_o^2}{Rf_s}, \tag{37}$$

$f_s = \frac{1}{T}$ = switching frequency,

R = load resistance.

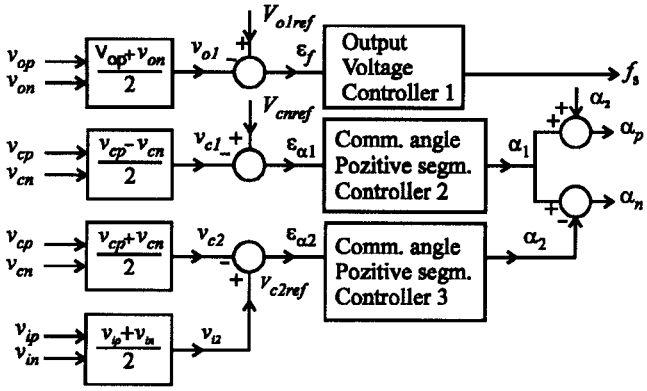


Fig. 8 Controllers operating the buck converter as active filter

On the basis of eq. (34) and (35)

$$v_{cp} = v_{c1} + v_{c2} \tag{38}$$

$$v_{cn} = -v_{c1} + v_{c2} \tag{39}$$

In perfect SES mode $\alpha_p = \alpha_n = \alpha$ and $\alpha_2 = 0$. From eq. (26) ... (30)

$$\cos\alpha = \frac{v_{i1} - V_o - v_{c1}}{v_{i1} - V_o + v_{c1}} \tag{40}$$

where

$$v_{i1} = V_i(1-\Delta) \tag{41}$$

The three controllers can set three variables independetly (Fig. 1 and Fig. 8):

- the switching frequency f_s. by turning on switch S_p and S_n,
- the commutation angle α_p. of clamping switch S_{cp},
- the commutation angle α_n of clamping switch S_{cn}.

The block diagram of one possible way for control in SES is shown in Fig. 8.

The simplest way to accomplish SES is to use clamping diodes and output voltage controller 1. Now in each switching cycle $v_{cp}= v_{ip}$ and $v_{cn}= v_{in}$, that is, $v_{c1}= v_{i1}$ and $v_{c2}= v_{i2}$. As both the voltage between terminal T_p and T_2 and the voltage between terminal T_2 and T_n are v_{i1} (Fig. 5), the converter operates in SES mode, $w_{o1}= w_{o2} =w_o$ and $v_{op} = v_{on}=V_o$, $v_{o2}=0$. Voltage $\Delta v=0$ [eq. (30)]. The commutation angle $\alpha_p= \alpha_n =\alpha$ [eq. (26), (27)] and:

$$\cos\alpha = \frac{V_o}{V_o - 2v_{i1}} \tag{42}$$

When v_{ip} has a sinusoidal component [eq. (32), (33)]

$$v_{i1} = V_i - V_{im}\cos\Omega t \tag{43}$$

To keep the output voltages and powers constant the switching frequency must be changed [eq. (15)]

$$f_s = V_o^2 / 2RCv_{i1}^2 \tag{44}$$

The output power $P_o = 2V_oI_o = 2V_o^2 / R$.

VII. Experimental Results Asymmetrical Operation

One test result is included for asymmetrical operation. The converter was the same as in section IV. In the test $v_{ip}= V_i= 30V$ was constant and $-v_{in}$ was changed from $20V$ up to $40V$ in steps. By setting the switching frequency, the output voltages was kept at $v_{op}= v_{on}= V_o= 15V$ and the output current $I_o= 0.325A$ was kept constant as well. Clamping diodes were used in place of switch S_{cp} and S_{cn}. SES was realized, that is, $w_{o1}= w_{o2} = w_o$. The switching frequency ensuring SES mode and $v_{op}= v_{on}= V_o$ can be calculated from eq. (44).

Fig. 9 and Table 3 shows both the measured and the calculated values of f_s. The measured values are always higher than the calculated ones because the converter losses were neglected in the calculation.

VIII. Conclusions

The new resonant converter family include buck, boost and B&B converters like the conventional DC-DC converters. Sinusoidal rather than square wave currents starts flowing in the controlled switches S_p and S_n in discontinuous current conduction. Switches S_p, S_n and clamping diodes D_{cp}, D_{cn} operate with soft switching. The sinusoidal current starts from zero value in S at turning on and the current commutates from S to D practically under zero voltage across S and D.

The low frequency a.c. voltages in v_{ip} and in v_{in} can be filtered out from v_{op} and v_{on} by changing the switching frequency f_s and the commutation angle α. In the simplest

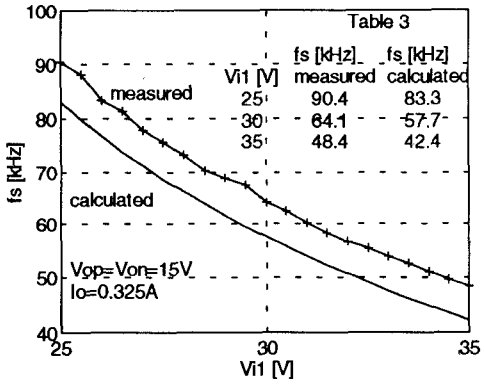


Fig. 9 Switching frequency f_s versus positive sequence component of input voltage

case clamping diodes are applied and only output voltage controller setting f_s is used. Symmetrical Energy Supply (SES) in automatically accomplished, that is, $v_{op} = v_{on} = V_o$, although the two input voltages are different and they can have low frequency components which are filtered out from the output voltages.

ACKNOWLEDGMENTS

The authors wish to thank the Hungarian Research Found (OTKA T-016382) and the Hungarian Academy of Sciences for their financial suport.

REFERENCES

[1] I. Nagy, „Resonant DC-DC Configuration", 3rd European Conference on Power Electronics and Applications, EPE'89, Aachen, Germany, 1989, pp. 1495-1500.

[2] I. Nagy, „DC-DC Converters with Series Commutation", 15th Int. PCI'88, Munich, West Germany, 1988, pp. 360-378.

[3] I. Nagy, „Study of a Quasi-Resonant Converter with Symmetrical Components", Periodica Polytechnica, Mechanical Engineering, Vol. 34, No.1-2, Budapest, Hungary, 1990, pp. 1-32.

[4] K. Harada, „Switching Converter and Magnetics", Vol. 1, 2, 3, Ohmsha, Japan, 1993.

[5] N. Mohan, T. M. Undeland, W. P. Robbins, „Power Electronics" John Wiley & Sons, New-York, 1995.

[6] P. Korondi,. S. H. Yang, H. Hashimoto, F. Harashima, „Sliding mode controller for parallel resonant dual converters", Journal on Circuits, System and Computers, 1995, Vol. 5. no.4.

[7] T. Ninomiya, A. Takeuchi, and T. Kohama, „Beat Phenomenon, Phase-Lock, and Chaotic Oscillation in Resonant Converters", Proceedings of Chinese/Japanese Power Electronics Conference, 1992, pp. 1-8.

[8] J. W. Kollar, H. Sree, U. Drofenik, N. Mohan, F. C. Zach, „A Novel Three-Phase Three-Switch Three-Level High Power Factor SEPIC-Type AC-to-DC Converter", 12th IEEE Applied Power Electronics Conference, Atlanta, USA, 1996.

[9] K. Murata, K. Harada, F. Anan, K. Yamasaki, H. Sakamoto, M. Jinno, Y. Kawata and T. Nakashima, „Intelligent Line-operated Transformer", Proceedings of the 7th Int. Power Electronics&Motion Control Conference , Budapest, Hungary, 1996, Vol.1, pp. 88-91.

[10] K. Hirachi, Y. Nishida, K. G. D. Laknath and M. Nakaoka, „A New Buck-Type Controlled AC-DC Converter with Input Current Harmonics Compensated Output Voltage Ripple Active Filtering Scheme", Proceedings of the 7th Int. Power Electronics&Motion Control Conference , Budapest, Hungary, 1996, Vol.1, pp. 232-238.

[11] N. P. Polyzos, E. C. Tatakis, A. N. Safacas, „Predicting Real Characteristics of Buck Zero-Voltage Switching Quasi-Resonant Converters", Proceedings of the 7th Int. Power Electronics&Motion Control Conference , Budapest, Hungary, 1996, Vol.1, pp. 282-286.

[12] I. Hermann, I. Ipsits, „The Effects of Commutation Process on the Operation of the Flyback Type Power Supplies", Proceedings of the 7th Int. Power Electronics&Motion Control Conference , Budapest, Hungary, 1996, Vol.1, pp. 396-399

[13] M.Ishida, T. Goto, and T. Hori, „Active Filter Using Quasi-Zero-Current-Switching Series- Resonant High-Frequency AC-Linked DC-AC Converter", Proceedings of the 7th Int. Power Electronics&Motion Control Conference , Budapest, Hungary, 1996, Vol.2, pp. 144-148

[14] S. Hamada, A. Kambe, T.Mii, E. Hiraki and M. Nakaoka, „Zero-Voltage Soft-Switching-Based Asymmetrical PWM DC-DC Power Converter with High-Frequency Forward-Flyback Transformer Link", Proceedings of the 7th Int. Power Electronics&Motion Control Conference , Budapest, Hungary, 1996, Vol.2, pp. 220-225.

[15] K. Jezernik, B. Mohorko, „Variable Structure System Control of Unity Power Factor Boost Converter", Proceedings of the 7th Int. Power Electronics&Motion Control Conference , Budapest, Hungary, 1996, Vol.3, pp. 213-217

[16] M. M. Bech, J. K. Pedersen and F. Blaabjerg, „Random Modulation Techniques in Power Conversion – an Update", Proceedings of the 7th Int. Power Electronics&Motion Control Conference , Budapest, Hungary, 1996, Vol.3, pp. 357-365.

[17] Lin Chen, F. P. Dawson, „An adaptive Bandpass Control Filter for Power Engineering Applications", Proceedings of 1995 Int. Power Electronics Conference, IPEC-Yokohama'95, Yokohama, Japan, Vol. 2, pp. 951-955.

[18] K. Wang, G. Hua and F. C. Lee, „Analysis, Design and Experimental Results of ZCS-PWM Boost Converters", Proceedings of 1995 Int. Power Electronics Conference, IPEC-Yokohama'95, Yokohama, Japan, Vol. 2, pp. 1197-1202.

[19] H. Okui, T. Nakagawa and H. Irie, „Circuits for Zero-Voltage Switching Multi-Resonant DC-DC Converter with a Complementary Construction", Proceedings of 1995 Int. Power Electronics Conference, IPEC-Yokohama'95, Yokohama, Japan, Vol. 3, pp. 1362-1367.

[20] F. A. Himmelstoss, L. L. Erhartt, „Simulation Problems for a Low-Loss ZCS Quasi-Resonant PWM-Converter", Proceedings of 1995 Int. Power Electronics Conference, IPEC-Yokohama'95, Yokohama, Japan, Vol.3, pp. 1368-1372

[21] C. A. Canesin, C. M. C. Duarte and Ivo Barbi, „A New Family of Pulse-Width-Modulated Zero-Current Switching DC/DC Converters", Proceedings of 1995 Int. Power Electronics Conference, IPEC-Yokohama'95, Yokohama, Japan, Vol. 3, pp. 1379-1384.

[22] H. Nakano, A. Nabae, Y. Satou, „Comparison of Boost Type Sinusoidal Rectifiers", Proceedings of 1995 Int. Power Electronics Conference, IPEC-Yokohama'95, Yokohama, Japan, Vol. 1, pp. 281-286.

[23] M. P. Kazmierkowski, M. A. Dzieniakowski, „Review of Current Regulation Techniques For Three-Phase PWM Inverters", Proceedings of the IECON'94, Bologna, Italy, 1994, pp. 567-575.

[24] L. Matakas Jr., C. Burlacu, E. Masada, „High Power, High Performance Parallel Connected Multiconverters: Analysis and Control", Proceedings of the IEEE Int. Symposium on Industrial Electronics, ISIE'95, Athens, Greece, 1995, pp.121-126.

[25] Y. Dote, D. F. Akhmetov, „Soft Computing in Power Electronics and Motion Control", Proceedings of the 7th Int. Power Electronics&Motion Control Conference , Budapest, Hungary, 1996, Vol. 2, pp. 56-61.

[26] Yan-Fei Liu, P. C. Sen, Shi-Peng Huang, „Function Control –A Novel Strategy to Achieve Improved Performance of the DC-to-DC Switching Regulators", IEEE Transaction on Ind. Electronics, Vol. 42, Number 2, 1995, pp.186-191.

[27] M. K. Kazimierczuk, A. Abdulkarim, „Current-Source Parallel-Resonant DC/DC Converter", IEEE Transaction on Ind. Electronics, Vol. 42, Number 2, 1995, pp.199-208.

Single-Switch Auxiliary Resonant Converters

Masa-aki Shimada and Mantaro Nakamura
Sanken Electric Co., Ltd.
677, Ohnohara Shimoakasaka, Kawagoe-shi,
Saitama 350-11, JAPAN
Fax: +81-492-66-8084, Phone: +81-492-66-8031

Abstract-**This paper presents new single-switch auxiliary resonant converters which can operate in a soft-switching way without auxiliary switches. In the proposed converter circuits, the capacitors of the resonant circuit act as lossless snubbers which can be expected to reduce the switching losses, the switching stresses and EMI noise on the power semiconductor device. Moreover they are also capable of conventional PWM control. The principle of operation, simulated results, experimental results and other applications are presented to verify the analysis.**

I. INTRODUCTION

Recently, power conversion circuits have been in high power and frequency circuit applications with the advances in power semiconductor device technology. Though the switching devices, such as MOSFETs and IGBTs etc. are generally utilized in the power conversion circuits with PWM control, their performances are not completely suitable for power application under hard-switching. Because their switching behaviors are abrupt during turn-on and turn-off, the switching device has serious high voltage or current stress problems. In addition, the hard-switching circuit operation results in switching losses and switching noise [1].

Soft-switching techniques can solve these problems, because the switching schemes are to turn on and off devices under zero current or voltage conditions. To improve these power devices behavior problems, a number of soft-switching performance PWM converters have been proposed [2].

In this paper, a new single-switch auxiliary resonant boost DC-DC converter, which can operate in a soft-switching way without auxiliary switches, is first proposed, and the operation principles, computer simulation and other application are presented. A 4.8kW experimental circuit using the single-switch auxiliary resonant boost DC-DC converter topology is also carried out.

II. THE PROPOSED SINGLE-SWITCH AUXILIARY RESONANT CONVERTERS

A new single-switch auxiliary resonant boost DC-DC converter is shown in Fig.1. This proposed converter circuit is composed of resonant components, which is consisted of an inductor, L1, in series with switch, S, capacitors, C1 and C2. And what is better, it does not use any auxiliary switches. So the switch, S, can constantly achieve soft-switching, that is, zero-current turn-on due to L1 and zero-voltage turn-off due to C1. In addition these circuit operations can be controlled by a single switch, and it is possible to use conventional PWM control. Since the capacitors of the resonant circuit act as lossless snubbers, losses in the resonant circuit can be reduced.

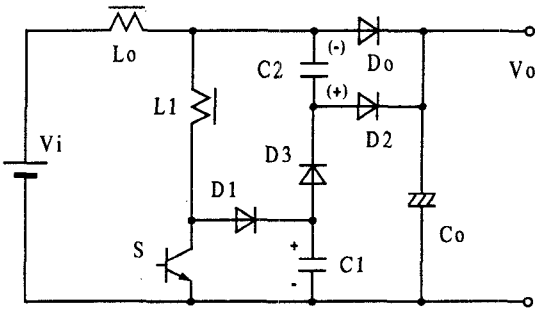


Fig.1. The proposed single-switch PWM boost DC-DC converter.

The proposed soft-switching method by a single switch can be applied to other converters. Figure 2 shows a single-switch auxiliary resonant buck converter. Again, it is ensured that the switching operations are always in soft-switching way.

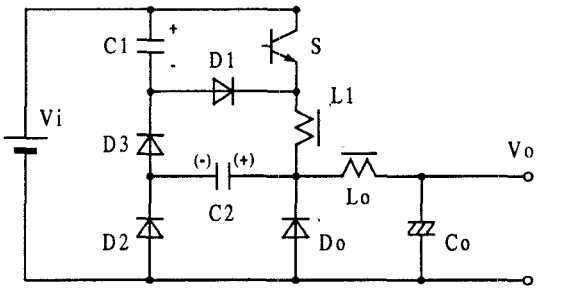


Fig.2. The proposed single-switch PWM buck DC-DC converter.

III. PRINCIPLES OF OPERATION

2.1 Boost Converter

The operation waveforms of the proposed converters are

shown in Fig.3.

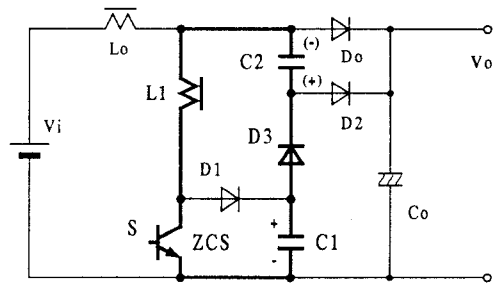
When the switch S is in off-state, energy stored during the previous conduction mode in the boost inductor L0 is transferred to load through the diode, D0. Then the capacitor, C1, is charged with the polarities illustrated in the figure up to the output voltage Vo, but the capacitor, C2, is not. When the switch, S, is turned on and then off under these conditions, the circuit operations can be divided into three different modes as follows (ref. to Fig.4.):

MODE 1 ($t_0 \leqq t \leqq t_1$): When the switch, S, is turned on.

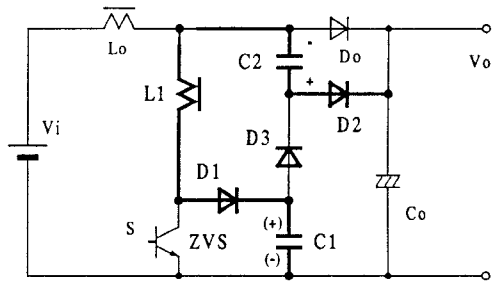
When the switch, S, is turned on at time t_0, current in the diode, D0, is decreased linearly by the inductor, L1. On the other hand, current in the inductor, L1, increases linearly from zero. When the diode current becomes zero, the resonant inductor, L1, and the capacitors, C1, C2, start to resonate, and the energy in C1 is discharged through C1-C2-L1-S loop as shown in Fig.4(a), producing a sinusoidal resonant current. As a result current in the inductor, L1, contains both the L0 current and the resonant current. When the resonant current finished, the energy in C1 is transferred to C2, which is charged up to about the output voltage, Vo. While the switch, S, is in on-state, the energy is stored in L0 for next boost operation.

MODE 2 ($t_2 \leqq t \leqq t_4$): When the switch, S, is turned off.

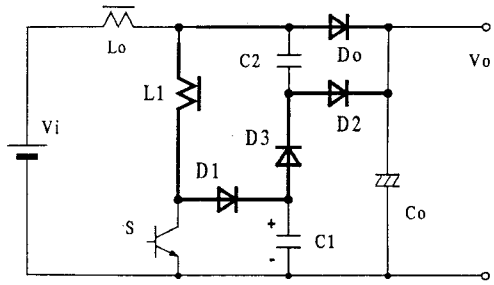
As soon as the switch, S, is turned off at time t_2, the switch current is transferred to C1 through D1. As the voltage of the capacitor, C1, increases due to this charging current, the voltage of the capacitor, C2, is changed, and the energy in C2 is discharged through the diode, D2. When the C1 voltage reaches the output voltage, Vo, at time t_3, the diode, D3, is turned on. In addition, the L1



(a) MODE 1



(b) MODE 2



(c) MODE 3

Fig.4. The operating modes in the single-switch PWM DC-DC converter.

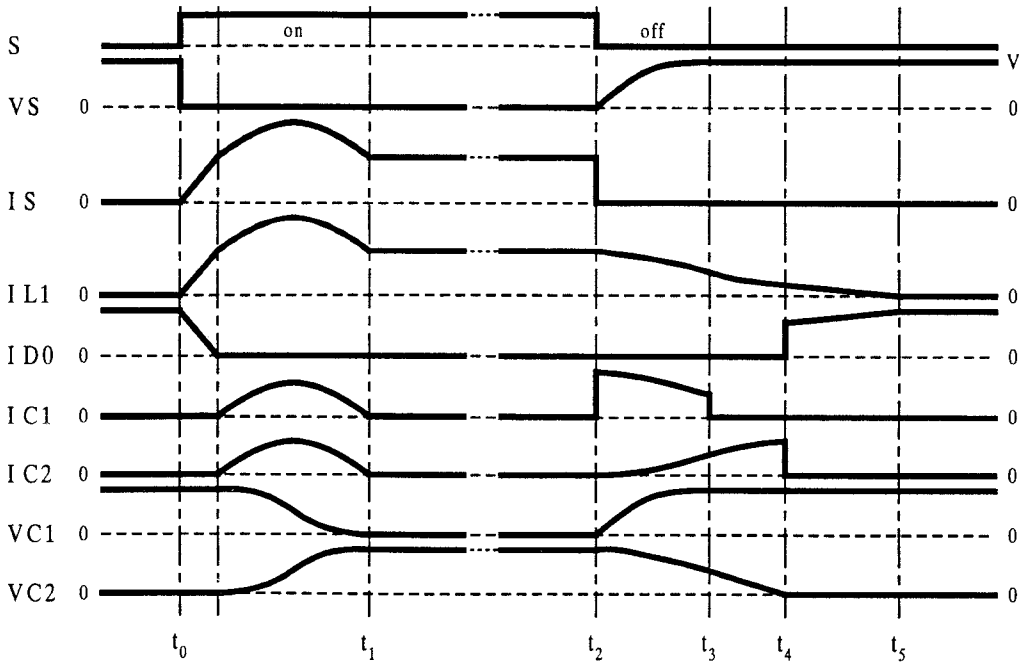


Fig.3. The operation waveforms.

current is transferred to the load through D3-D2, and thus decreases continuously. Then the energy in C2 is also discharged to load through D2.

MODE 3 ($t_4 < t \leqq t_5$)*:* When the power is transferred from the source to the load.

When the C2 voltage goes to zero at time t_4, another operation mode starts, and the current flowed in the capacitor, C2, is transferred to the diode, D0. Afterward, the L1 current decreases linearly by the voltage drop between D1and D2 until time t_5. At the same time, the D0 current increases by the decreased amount of the L1 current.

The above-mentioned operation modes complete one cycle of PWM operation. When S is turned on again, the next cycle starts.

2.2 Buck Converter

When the switch, S, is in off-state, the current in inductor, L0, free-wheels through the diode, D0. During this period, the capacitor, C1, is charged up to the input voltage, Vi. When the S is turned on, the current in the diode, D0, is decreased linearly by the inductor, L1. The energy in C1 is transferred to C2, and produces a resonant current.

When S is turned off at time t_2, the current flowed in the switch, S, is transferred to C1. Then the energy in C2 is discharged.

When the C1 voltage reaches to the input voltage Vi at time t_3, the diode, D3, is turned on, and the L1 current is decreased and transferred to the load. At the same time the energy in C2 is discharged to the load. When the C2 voltage reaches zero, the current is transferred to the diode, D0.

III. Simulation Results

The single-switch auxiliary resonant boost converter as shown in Fig.1. is designed and simulated. Although the diodes are ideal, the switch, S, is composed of on and off variable switch resistances.

The simulation parameters are as follows:

Vi = 200V, Vo = 400V, Po = 10kW, Fs = 20kHz
L1 = 3uH, C1, C2 = 10nF

The simulation results of switching waveforms are shown in Figs.5 and 6. The soft-switching operation is achieved at both turned on and off. Figure 7 shows the simulated voltage and current waveforms of the capacitors C1 and C2 when the switch, S, is turned on. The energy in lossless snubber, C1, is almost transferred to C2 by the resonance. Figure 8 shows the voltage-current locus of the switch, S. The simulation result indicates that the switch, S, achieves lower switching loss performance, because the V-I locus has little area.

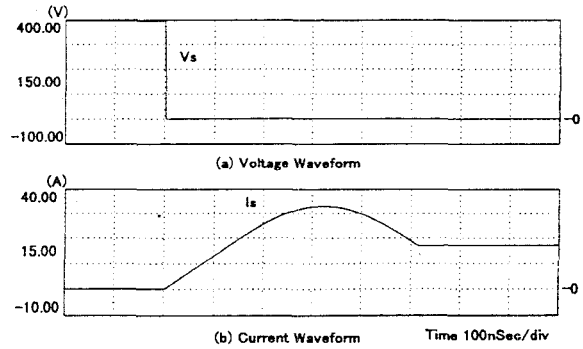


Fig.5. The simulated switching waveforms(Turned on).

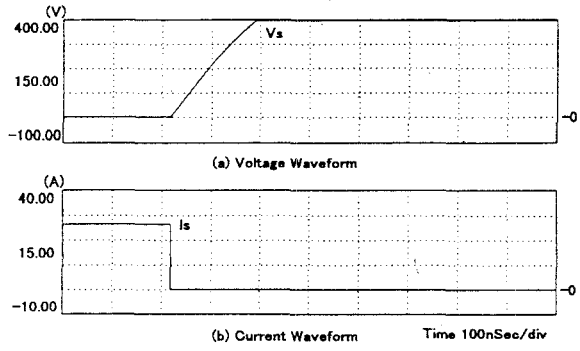


Fig.6. The simulated switching waveforms(Turned off).

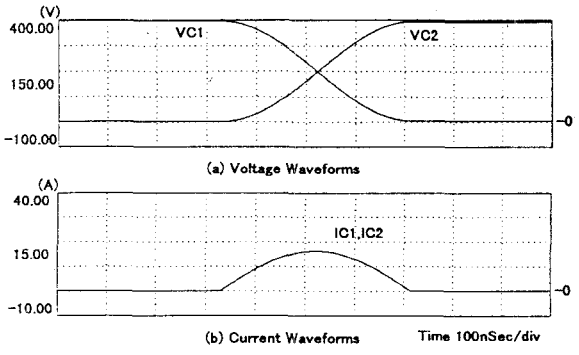


Fig.7. The simulated resonant capacitor waveforms(When S is turned on).

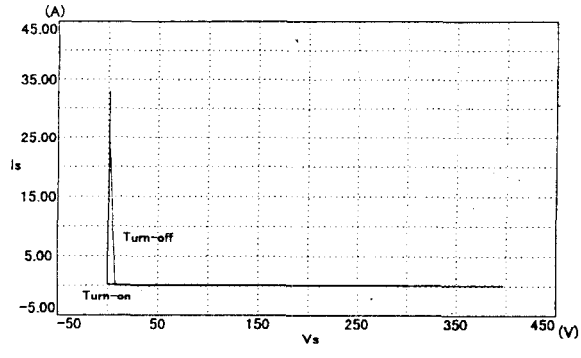
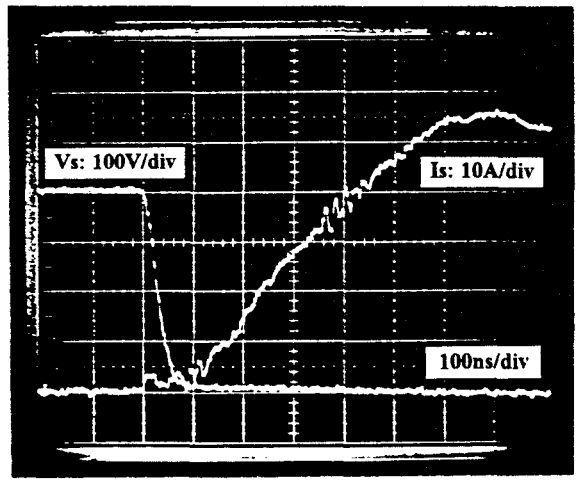


Fig.8. The V-I locus of the switch, S.

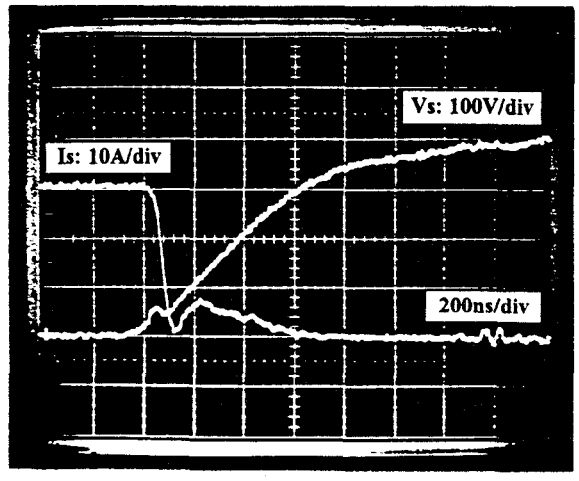
IV. EXPERIMENTAL RESULTS

A 4.8kW prototype DC-DC boost converter using the single-switch auxiliary resonant PWM converter topology as shown in Fig.1 has been built and tested. The converter is switched at a frequency of 16kHz with a duty cycle of 50%. The output voltage is regulated at 400V with 200V input. The resonant circuit component parameters are selected as L1=3uH and C1, C2=47nF. IGBT device is used as the power switch, S.

The experimental switching waveforms are shown in Fig.9 (a) and (b). It can be seen that the switching actions are softer without surge current or voltage than switching waveforms of conventional hard-switching DC-DC boost converter, that is, the *di/dt* at turned on and the *dv/dt* at turned off of the switch, S, waveforms are much lower. And the experimental switching waveforms agree reasonable with the corresponding simulation results in Figs.5 and 6. The switch, S, operates with zero-current-switching during turned on and zero-voltage-switching during turned off respectively. As a result, this single-switch auxiliary resonant DC-DC boost converter significantly can reduce switching losses, switching stresses and EMI noise.



(a) Turn-on



(b) Turn-off

Fig.9. The experimental switching waveforms of the switch, S.

V. CONCLUSIONS

New single-switch auxiliary resonant PWM converters are proposed in this paper. The principles of operation are explained, and the proposed circuit was simulated and experimented. The proposed converters have the following characteristics:

- They can operate in a soft-switching way without auxiliary switches.
- The switch operations can constantly achieve zero-current turn-on and zero-volt turn-off.
- The capacitors of the resonant circuit act as lossless snubbers.
- They can operate with constant switching frequency.

Therefore they can be expected to reduce the switching losses, the switching stresses and EMI noise. The characteristics of the new converters are verified by the obtained results.

REFERENCES

[1] Kunrong Wang, Fred C. Lee, Guichao Hua, and Dusan Borojevic, "A comparative study of switching losses of IGBTs under hard-switching, zero-voltage-switching and zero-current-switching," *IEEE PESC Conf. Rec.*, 1994, pp. 1196-1204.

[2] Guichao Hua and Fred C. Lee, "Soft-switching techniques in PWM converters," *IEEE Trans. on Industrial Electronics*, vol. 42, no. 6, Dec. 1995, pp. 595-603.

Analysis and Simulation of Series-Resonant High-Frequency AC-Linked DC-AC Converter Realizable by Inverter Modules

Jinsheng Wei Muneaki Ishida Takamasa Hori
Mie University
1515, Kamihama, Tsu, Mie, 514, JAPAN
Fax:059-231-9442 Phone:059-231-9674
E-mail:nb40233@cc.mie-u.ac.jp

Abstract— **This paper proposes a new-type series resonant high-frequency AC linked DC-AC converter which simplifies the connection of cycloconverter part using inverter circuit configuration. And different aspects and the same aspects between conventional and proposed converter are compared. A simplified discrete time model is proposed for the simulation and analysis of the transient and steady state performance of proposed converter. Simulation results are validated by experiment results.**

I. INTRODUCTION

In recent years, much efforts have been devoted to developing converters with high frequency link power conversion. And soft switching modes are used to obtain good performances such as low EMI noise, high efficiency and small volume[1] ~ [4],[6],[7]. In [1] ~ [2], real time control methods for ZVS or ZCS HF DC-AC converter were proposed and studied by some researchers. In [3] ~ [4], a kind of Series-Resonant high frequency AC-linked DC-AC converter and its real-time control method was proposed by M.Ishida et.al and developed for use in UPS, or small-size reactive power compensator, but due to its complex cycloconverter configuration it is difficult to be used in practice. In [5], a new cycloconverter configuration was proposed to overcome the above disadvantage, by which the cycloconverter part of converter can be built by two inverter modules. As the same as conventional converter, proposed converter can be operated on the same real time control method and avoid overvoltage caused by imperfect ZCS operation in the series resonant circuit. And the different aspects and the same aspects between conventional converter and proposed converter are compared. And the operation of this converter is verified by experiment. And a time domain model was proposed for the simulation of this converter. However, because of much amount of computation time needed, it has been hard to be used. In this paper, a simplified discrete time domain model is proposed for the faster simulation of this converter. Based on simulation and experimental results, the steady state performances of converter are discussed. The Simulation results are validated by experimental results.

II. SERIES-RESONANT HF AC-LINKED DC-AC CONVERTER

The conventional circuit [4] and proposed circuit of this kind of converter [5] are shown in Fig.1 and Fig.2 respectively. The high frequency(HF) inverter, the resonant circuit and the HF transformer shown in Fig.2 are the same as those shown in Fig.1, but its cycloconverter configuration is different from the cycloconverter of the conventional circuit. This new cycloconverter is composed of two parts: a HF converter with four switches $S_5 \sim S_8$, and a low frequency(LF) inverter with four switches $S_9 \sim S_{10}$. In this circuit, switches (S_1,S_4) or (S_2,S_3) pairs are turned on and off alternatively, by which the high frequency resonant current is produced. And this resonant current is rectified by HF converter into positive or negative flowing energy from secondary side of HF transformer to load side. The proposed converter has the following characteristics which are different from the conventional circuit.

(1) HF inverter, HF converter circuit and low frequency(LF) inverter of cycloconverter can be constructed using three inverter modules, which results in the simplification of the circuit connection.

(2) The switches(S_9^+,S_{10}^+,S_9^-,S_{10}^-) of LF inverter can be low speed switches with low on-state voltage.

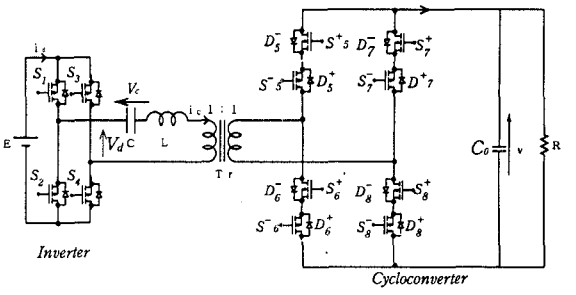


Fig.1. Main circuit of conventional converter

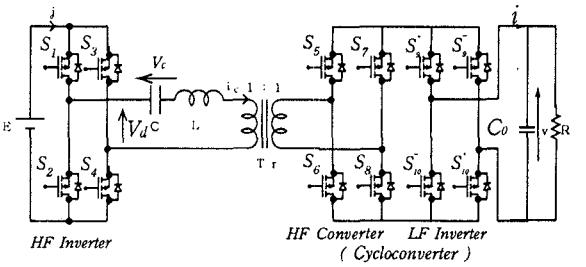


Fig.2. New main circuit of converter

Ⅲ . OPERATION PRINCIPLE

Switches of proposed circuit shown in Fig.1 can be operated in ZCS mode, in which switches of HF inverter and HF converter are turned on and off at the zero-cross timing point of resonant current, which need not to be detected and is fixed to the calculated value of resonant frequency. In this way, switches of proposed circuit are operated at the approximate zero current point. By using the definition method of basic switching sequences in [4], during one half period of resonant current, switching state of all switches is considered as a basic switching sequence. There are four types of basic switching sequences, plus, minus, zero, and off-sequences, as shown in Table 1.

In the HF inverter part, there is the same switching sequences as those proposed in [4]. To compare the switching sequences of the cycloconverter part in the conventional circuit(Fig.1) and the proposed circuit(Fig.2), their equivalent circuits of cycloconverter part are shown in Fig.3 and Fig.4, respectively.

Comparing Fig.3 and Fig.4, it can be found that when output voltage is positive, equivalent circuits of conventional and proposed circuit are the same. But when output voltage is negative, the equivalent connection between HF converter and output capacitor of conventional circuit and proposed circuit are in opposite direction.

Ⅳ . CONTROL METHOD

Here, we also use the control method proposed in [4], which control schematic diagram is shown in Fig.5. Moreover, the predicted output current i* shown in Fig.5 is calculated by the following equation:

$$i^* = i_L + C_0 \frac{dv_{ref}}{dt} + C_0 \frac{v_{ref} - v}{T/2} \quad . \tag{1}$$

The switching sequence is selected by the following rules:

(i) $i^* > \mathrm{Im} \geqq 0 \rightarrow$ Plus sequence is applied in both HF inverter and cycloconverter;

(ii) $-\mathrm{Im} \leqq i^* \leqq \mathrm{Im} \rightarrow$ Off sequence is applied in both HF inverter and cycloconverter;

(iii) $i^* < -\mathrm{Im} \rightarrow$ Minus sequence is applied in HF inverter but plus sequence in cycloconverter,

where Im is the positive threshold value, which determines the rate of off sequences in the switching sequences of the converter. i^* is the predicted output current, by which plus or minus sequence is selected to make the output voltage v coincide with the reference output voltage v_{ref} in one half resonant period T/2.

Ⅴ . ANALYSIS OF PROPOSED CONVERTER

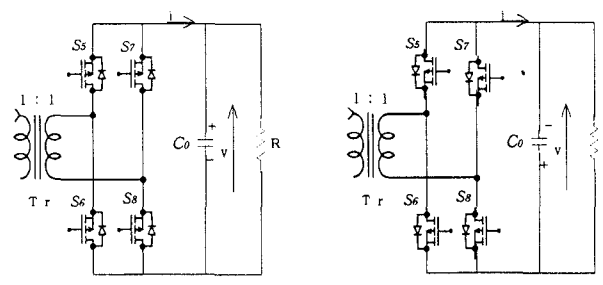
Because the output filter capacitor Co is sufficiently larger than the capacitor C of the resonant circuit, the output voltage v(t) is assumed to be constant during a

Table 1
Basic switching sequences of converter

Inverter Part (Fig.1 or Fig.2)		
Switching Sequence	Former(T/2)	Latter(T/2)
Plus	(S_1,S_4)ON	(S_2,S_3)ON
Minus	(S_2,S_3)ON	(S_1,S_4)ON
Zero	(S_1,S_3)ON or (S_2,S_4)ON	
Off	(S_1,S_2,S_3,S_4)Off	

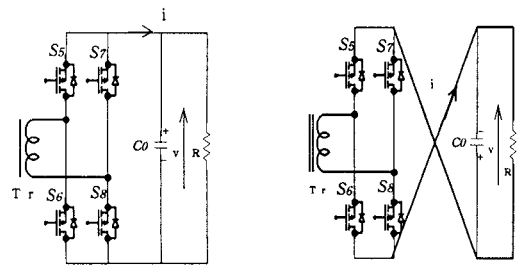
Cycloconverter of Conventional Circuit(Fig.1)		
v>0 ($S_5^+ \sim S_8^+$) ON		
	Former(T/2)	Latter(T/2)
Plus	(S_5^-,S_8^-)ON	(S_6^-,S_7^-)ON
Minus	(S_6^-,S_7^-)ON	(S_5^-,S_8^-)ON
Zero	(S_5^-,S_7^-)ON or (S_6^-,S_8^-)ON	
Off	(S_5^-,S_6^-,S_7^-,S_8^-)Off	
v<0 ($S_5^- \sim S_8^-$) ON		
	Former(T/2)	Latter(T/2)
Plus	(S_5^+,S_8^+)ON	(S_6^+,S_7^+)ON
Minus	(S_6^+,S_7^+)ON	(S_5^+,S_8^+)ON
Zero	(S_5^+,S_7^+)ON or (S_6^+,S_8^+)ON	
Off	(S_5^+,S_6^+,S_7^+,S_8^+)Off	

Cycloconverter of Proposed Circuit(Fig.2)		
v>0 (S_9^+,S_{10}^+) ON		
	Former(T/2)	Latter(T/2)
Plus	(S_5,S_8)ON	(S_6,S_7)ON
Minus	(S_6,S_7)ON	(S_5,S_8)ON
Zero	(S_5,S_7)ON or (S_6,S_8)ON	
Off	(S_5,S_6,S_7,S_8)Off	
v<0 (S_9^-,S_{10}^-) ON		
	Former(T/2)	Latter(T/2)
Plus	(S_6,S_7)ON	(S_5,S_8)ON
Minus	(S_5,S_8)ON	(S_6,S_7)ON
Zero	(S_5,S_7)on or (S_6,S_8)on	
Off	(S_5,S_6,S_7,S_8)Off	



(a) v > 0 (b) v < 0

Fig.3. Equivalent circuit of conventional cycloconverter



(a) v > 0 (b) v < 0

Fig.4. Equivalent circuit of new cycloconverter

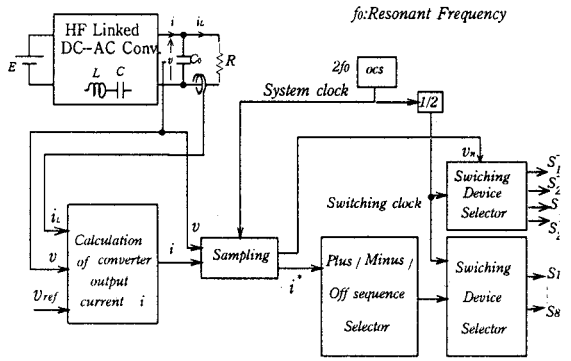


Fig.5. Control schematic diagram

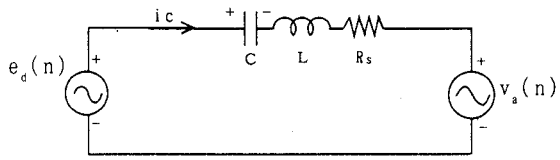


Fig.6 Equivalent circuit of converter

half of the resonant period. During the n th resonant half period $nT/2 \leqq t \leqq (n+1)T/2$, where all variables are denoted by index n, an equivalent circuit can be obtained, which is shown in Fig.6. Here, $e_d(n)$ and $v_a(n)$ are equivalent variables of DC source and output voltage converted into the resonant circuit by the nth switching sequence. And if conversion functions of switching sequence are defined by $D_e(n)$ and $D_v(n)$, $e_d(n)$ and $v_a(n)$ can be expressed as follows:

$$e_d(n)=D_e(n)\cdot e(n);\quad e(n)\equiv E(\frac{nT}{2})$$

$$v_a(n)=D_v(n)\cdot v(n);\quad v(n)\equiv v(\frac{nT}{2}) \qquad (2)$$

Moreover, according to the above proposed switching sequence, $D_e(n)$ and $D_v(n)$ can be adopted by the values shown in Table 2, where the former half resonant period is denoted by Former; and the latter half resonant period is denoted by Latter. And R_s is the equivalent resistance considered as all losses in the converter, which

Table 2

Switching functions

			De(n)	Dv(n)
v >0	Plus	Former	1	1
		Latter	-1	-1
	Minus	Former	-1	1
		Latter	1	-1
	Off	ic >0	-1	1
		<0	1	-1
v <0	Plus	Former	1	-1
		Latter	-1	1
	Minus	Former	-1	-1
		Latter	1	1
	Off	ic >0	-1	-1
		<0	1	1

can be evaluated as follows:

$$R_s=r_T+r_L+4r_{on}+2r_D$$

where r_T is winding resistance of HF transformer, r_L is resistance of resonant inductance, r_{on} is the on state resistance of switch, and r_D is on state resistance of feedback diode.

Since the resonant current of inductor L and resonant voltage of capacitor C change sinusoidally, the n-th resonant current $i_c(n)$ can be evaluated as follows:

$$i_c(t)=\frac{e_d(n)-v_a(n)-v_c(n)}{Z}e^{(-\frac{Rs}{2L})t}\sin\left\{\omega_r(t-\frac{nT}{2})\right\} \qquad (3)$$

During this resonant half period, the peak value resonant current $i_c(n)$ is obtained as follows:

$$i_c(n)=\frac{e_d(n)-v_a(n)-v_c(n)}{Z}e^{(-\frac{(2n+1)T\cdot Rs}{4\cdot 2L})} \qquad (4)$$

where $Z=\sqrt{L/C}$ $T=2\pi\sqrt{LC}$ $\omega_r=1/\sqrt{LC}$. And the peak value of output current of cycloconverter i(n) is found as:

$$i(n)=D_v(n)\cdot i_c(n) \qquad (5)$$

The peak value of resonant capacitor voltage during the (n+1)th resonant half period can be derived and is given by (6):

$$v_c(n+1)=2e_d(n)-2v_a(n)-v_c(n) \qquad (6)$$

And the output voltage can be derived and is given by

$$v(n+1)=v(n)+\int_{nT/2}^{(n+1)T/2}\frac{1}{C_0}D_v(n)\cdot i_c(t)dt$$

$$-\frac{1}{C_0}\int_{nT/2}^{(n+1)T/2}\frac{v(n)}{R}dt$$

$$=D_v(n)\cdot\left\{\alpha e_a(n)-\alpha v_c(n)+v_a(n)(1-\alpha-\beta)\right\} \quad (7)$$

where $\alpha=\frac{2C}{C_0}$, $\beta=\frac{\pi Z\alpha}{2R}$, and R is load resistance.

Based on (1), its discrete time equation can be derived as follows:

$$i^*(n+1)=\frac{v(n)}{R}+C_0\frac{v_{ref}(n+1)-v_{ref}(n)}{T/2}$$

$$+C_0\frac{v_{ref}(n)-v(n)}{T/2} \quad (8)$$

When v_{ref} is sinewave, (8) becomes:

$$(\frac{1}{R}-\frac{C_0}{T/2})v_a(n)D_v(n)+C_0\omega V_{ref}cos(\omega(\frac{(n-1)T}{2}+\frac{T}{4}))$$

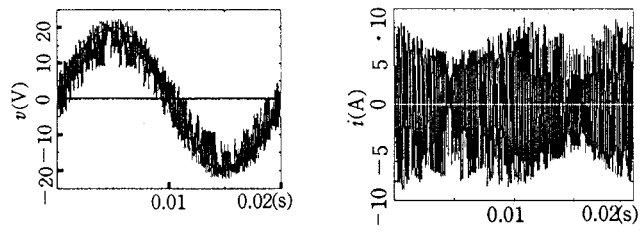
$$+C_0\frac{V_{ref}}{T/2}\sin(\omega(\frac{n-1}{2})T). \quad (9)$$

A. Simulation and Experimental Results

From the above equations, the simulation and analysis of this converter can be performed. The parameters used for the simulation are shown below.

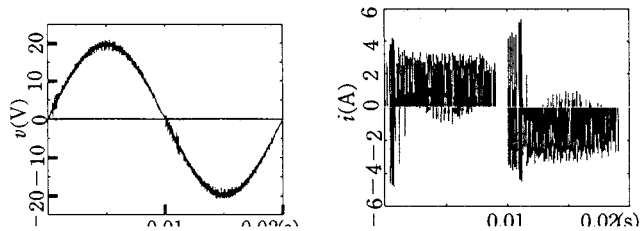
- reference voltage: 20V peak value, 50Hz sinusoidal wave
- DC source voltage: 30V
- load resistance: R=30 Ω
- inductance of resonant inductor: L=77 μ H
- capacitance of resonant capacitor: C=0.1 μ F
- capacitance of AC output filter capacitor: Co=10 μ F
- total resistance in resonant circuit: Rs=3 Ω

When Im=0.4A, 1A and 3.5A, simulation results are obtained as shown in Fig.7, Fig.8, and Fig.9. In this simulation, note that the high frequency oscillations on the output voltage shown in Fig.8(Im=1A) is smaller than that shown in Fig.7 (Im=0.4A). This is good illustration for the role of Im. When Im changes from 0.4A to 1A, the quantity of off sequence in one period of output voltage becomes more, and the oscillations between resonant tank and output capacitor are greatly suppressed because during off sequences the connection between resonant tank and output capacitor is separated. These simulation results agree with the experimental results reported in [3] ~ [4](Similar experimental results are shown in Fig.10). The output voltage and current shown in Fig.9 are simulation results when Im is further increased to 3.5A. In this case, because of more quantity of off sequences applied, output current does not occur to oscillate anymore. But the error between output voltage and reference output voltage becomes larger. Therefore, in practice it is necessary to adopt an adequate Im value so that the output voltage with both less oscillations and smaller steady state error can be obtained.



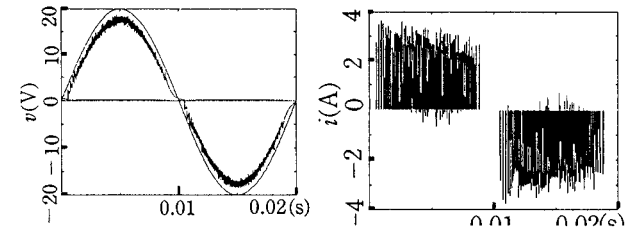
(a) output voltage (b) output current

Fig.7 Output voltage and output current(Im=0.4A)



(a) output voltage (b) output current

Fig.8 Output voltage and output current(Im=1A)



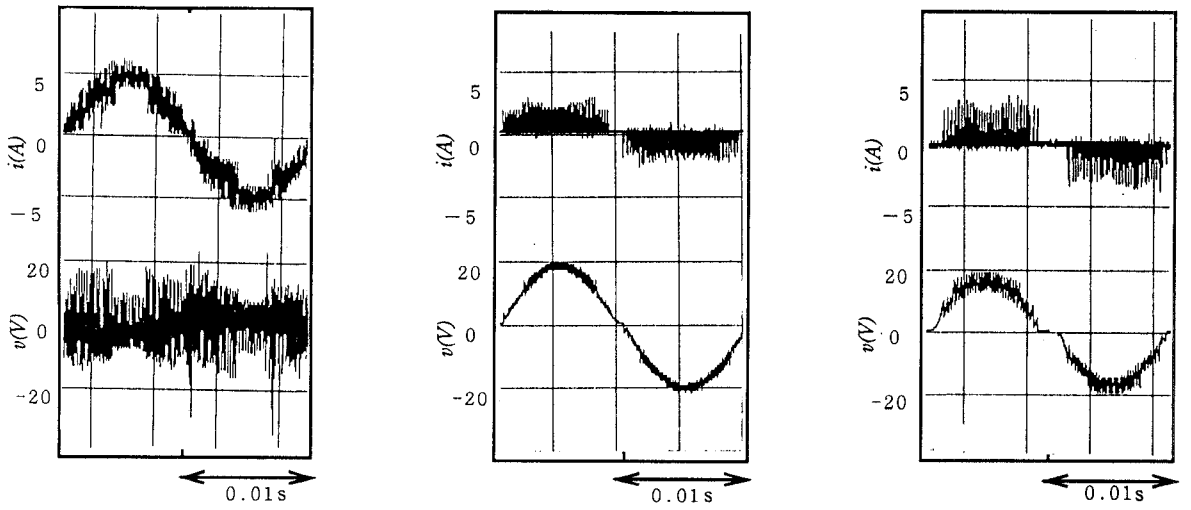
(a) output voltage (b) output voltage

Fig.9 Output voltage and output current(Im=3.5A)

To verify the above simulation results, in Fig.10 and Fig.11 experimental results are shown. When Im changes, the same phenomena as simulation results can be found as shown in Fig.10. When Im is 0.4A, there are much oscillations on output voltage. And when Im is 3.5A, output voltage can not reach to reference voltage, there are larger steady state error between output voltage and reference voltage. Only when Im is 1A, good output voltage waveform can be obtained. Fig.11 shows the case that the output current and output voltage change when Im is kept to 1A but load current is changed. In this case, it can be found that the amplitude of output current increases when load current increases, and larger load current will occur to larger steady error(Fig.11(c)). And to get better output sinewave, it is necessary to change Im according to load current. This indicates it is needed to develop adaptive control method in the further research.

Based on the further observation of experimental results, the following relations can be given:

(1). Smaller Im will results in the unstableness of system and larger resonant current; larger Im will result in the increment of steady error of output voltage and larger resonant current because a lot of off sequences are



(a) Im=0.4A (b) Im=1A (c) Im=3.5A

Fig.10. Experimental results of converter

(L =77[μ H], C =0.1[μ F], C_0 =10[μ F] , E =30[V], V_{ref} =20V, R =30[Ω])

employed.

(2). In the case of the adequate value of Im (Im=1A), the peak value of resonant current will increase when load current increase (Fig.11). The relation between i_{cmax} and i_{Lmax} is shown in Fig.13. It is found that the peak value of resonant current in the maximum value point of i_L is roughly equal to the value of $\pi i_L/2$ +E/Z.

(3). The pulse osillations over output voltage will deduced when the value of output filter capacitor is increased. (Fig.12).

(4). The maximum value of load current is decided by the condition: $E - R_s i_L - 2V_D \geqq v_{ref}$, where $R_e = \pi^2 R_s/8$ where E=30V, R_s =3 Ω , V_D =0.7V, v_{ref} =20V, i_{Lmax} is given by about 2.2A. In the Fig.11(d), this case is shown.

B. Calculation of Converter Efficiency

Based on the above equations and proposed equivalent circuit, we derive the following expressions for the calculation of converter efficiency if ideal zero current switching, which result in no switching losses of all switch devices, are assumed.

$$P_r = \frac{2}{T_o}\sum_{n=1}^{N}\frac{1}{2}i_c(n)\cdot i_c(n)\cdot R_s\cdot\frac{T}{2}+\frac{2}{\pi}i_c(n)\cdot 2V_D \tag{10}$$

$$P_o = \frac{2}{T_o}\sum_{n=1}^{N}\frac{v(n)\cdot v(n)}{R}\cdot\frac{T}{2} \tag{11}$$

$$\eta = \frac{P_r}{P_r+P_o}. \tag{12}$$

where P_r , P_o are the average losses power and average output power of converter during a half period of output AC respectively. And η is the efficiency of converter.

In (9) and (10), N is the number of resonant half period during a half period $T_o/2$ of AC output. i_c (n) and V(n) are, respectively, the peak value of resonant current and the average value of output voltage during the n-th resonant half period. R_s is the total resistance in the equivalent circuit of converter shown in Fig.6, and V_D is on state voltage of feedback diode. The efficiency curves for different values of Im can be calculated as shown in Fig.14.

Note that the efficiency of converter increases with the increment of output power. This is because the oscillations of output current is suppressed by greater load. Moreover, when Im is increased, the efficiency curve shift from lower to upper, i.e., the efficiency of converter increases. However, when Im is increased to a certain value, the increment of efficiency of converter ceases. The reason is that all possible oscillations over output voltage are suppressed when Im is increased. Meanwhile, the further increment of Im will result in the increment of the steady state error of output voltage, which has been illustrated in the simulation results.

VI. CONCLUSION

In this paper, a detailed analysis of a new type of HF DC-AC converter has been presented. This analysis has employed the discrete time model of converter. The model allows a large-signal analysis and simulation of proposed converter. By this analysis, it has shown that adopting an adequate rate of the off-sequence used in the control algorithm proposed in [3] ~ [4] is very important to improvement of the transient and steady state performances of proposed converter. Simulation results are validated by experiment results. The efficiency of converter is related to load power and control parameters.

REFERENCES

[1] Hideki HAYASAKA, Yasushi ABE and etc., " A Method for Improving Output Current Waveform of Series Resonant AC Link Inverter, " PCC − Yokohama' 93, pp.233-237, 1993.

[2] H.Yonemori, and etc., " A New Bidirectional Series-Resonant High-Frequency Linked Power Conversion System Incorporating Instantaneous Sinewave-Modulated Regulation Scheme, " IEEE Trans. on PEL, Vol.6, No.9, pp.1015-1022, 1989

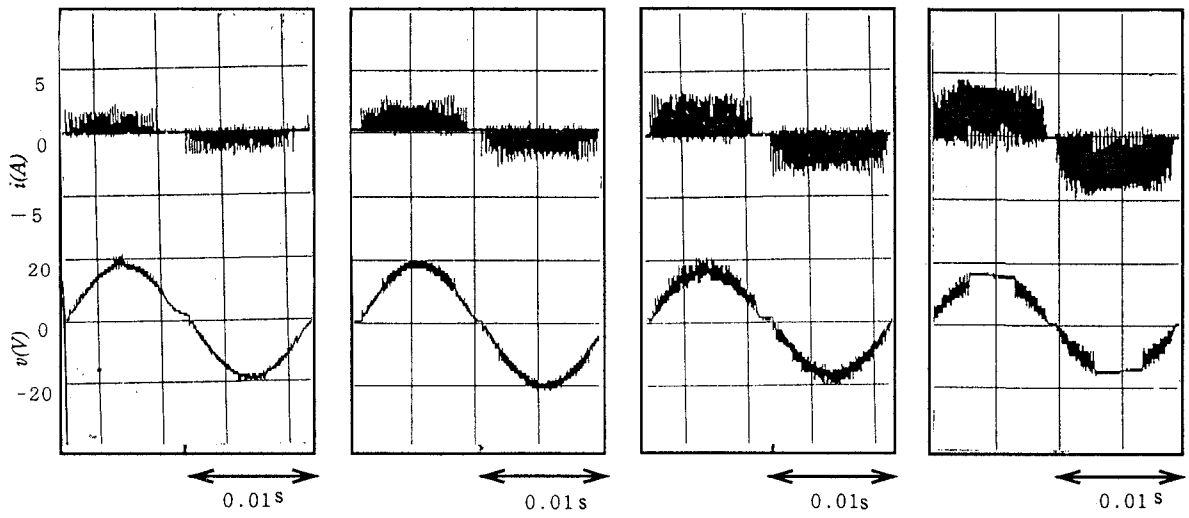
[3] N.Kitano, M.Ishida, and T.Hori,"Open-Loop and Real-Time Control Method of the Series-Resonant HF Linked Converter with DC Input and AC Output," Trans. IEE Japan/IAS, Vol.112-D, No.9, pp.790-798, 1992

[4] M.Ishida, H.Fujino, and T.Hori,"Real-Time Output Voltage Control Method of Quasi-ZCS Series-Resonant HF Linked DC-AC Converter,"IEEE Trans. on PEL, Vol.10, No.6, 1995 pp.776-783, 1995

[5] J.S.Wei, M.Ishida and T.Hori,"Series Resonant High Frequency AC-Linked DC-AC Converter Realizable By Inverter Modules,"1996 Japan/IAS Annual Conf. Record, Vol.3, No.266, pp.259-262, 1996

[6] G.B.Joung, C.T.Rim, and G.H.Cho,"Integral Cycle Model Control of the Series Resonant Converter,"IEEE Trans. on PEL, Vol.4, No.1, pp.83-91, 1989

[7] G.B.Jong, J.G.Cho. and G.H.Cho, " A Generalized Quantum Resonant Converter Using a New Quantum Resonant Module " IEEE Trans. PEL. Vol.7, No.4, pp.76-82,1992



(a) R=100 [Ω] (b) R=30 [Ω] (c) R=15 [Ω] (d) R=8 [Ω]

Fig.11. Experimental results of converter (Im=1[A], C_o =10[μ F])

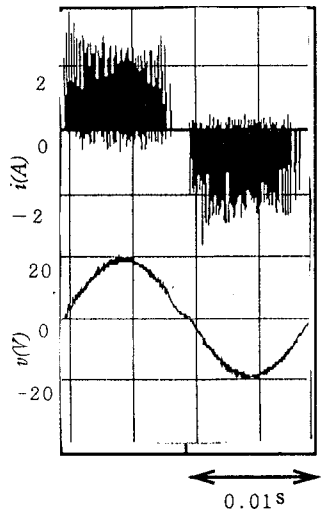


Fig.12 Experimental result of converter (C_o =20[μ F])

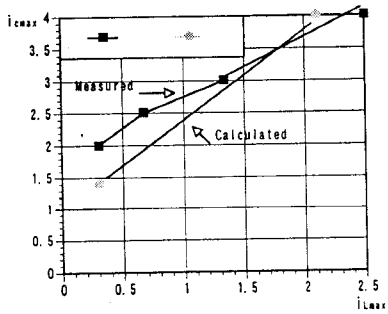


Fig.13 Relation between i_{cmax} and i_{Lmax}

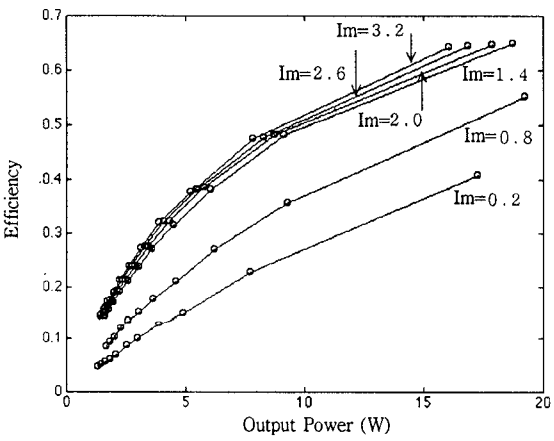


Fig.14 Calculated efficiency curves

Comparative Transient and Steady-State Performances of Three Resonant PWM Inverter-Controlled DC-DC Converters using High-Voltage Transformer and Cable Parasitic Circuit Components

J.M.Sun, L.Gamage and M.Nakaoka
The Graduate School of Engineering and Science,
Yamaguchi University, Yamaguchi, Japan

H.Takano and T.Hatakeyama
R & D Center
Hitachi Medical Corporation, Chiba, Japan

Abstract-The main purpose of this study is to describe some particular characteristic features and inherent benefits of series, parallel and series-parallel resonant tank inverter-fed DC-DC converters for medical-use X-ray high-voltage generator from a practical viewpoint. The method to treat the parasitic resonant circuit parameters of the high-voltage high-frequency transformer used in three typical resonant tank topologies is discussed on the basis of some simulation results, and the simulation results are also verified by experiments.

I .INTRODUCTION

The resonant tank inverter and converter topologies including some energy storage reactive elements has been developed for high-power usages . However, there are not so many descriptions relating to the steady-state characteristics of series resonant converter and parallel resonant converter designed for their practical specifications from application-special aspects.

Thus, this paper describes some particular characteristic features of series, parallel and series-parallel type transformer resonant tank inverter-fed DC-DC converters suitable for medical-use X-ray high-voltage generator, which is produced from a practical viewpoint. The key point of this study is to discuss how to effectively treat the harmful internal parasitic reactive circuit parameters such as the leakage inductance and the secondary-side lumped stray capacitance inside the high-voltage transformer for high-frequency operation.

II RESONANT INVERTER-FED X-RAY GENERATOR

The high-voltage applied to the X-ray tube is called tube voltage and the current flowing through the X-ray tube is called tube current. In practical, relatively lower tube voltage and higher tube current need a shorter exposure time in order to obtain desirable X-ray images for medical diagnosis.

Fig.1 illustrates a schematic power conversion processing system as an inverter-fed type X-ray power generator. The X-ray power generator mentioned above consists of a three-phase phase-controlled thyristor rectifier or a battery, a phase-shifted PWM control-based voltage source high-frequency resonant inverter with a specially-designed high-voltage transformer, a high-voltage diode rectifier connected to the high-voltage cables, and a X-ray tube as a load. The principal features of this X-ray power generator are to make the most use of

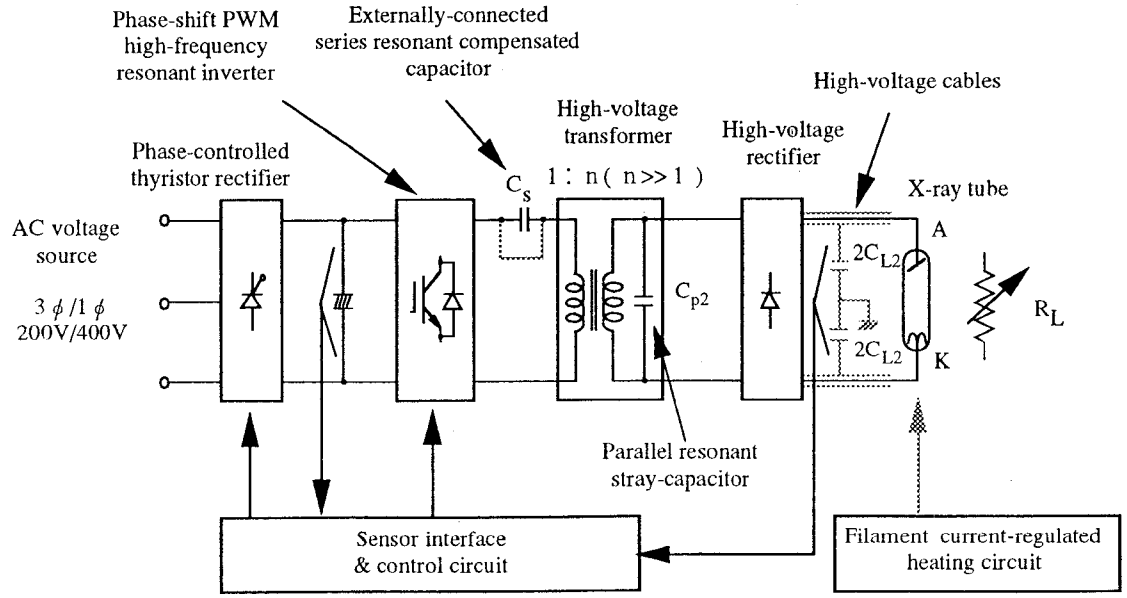


Fig.1 Schematic Main Circuit Configuration of Resonant Inverter-Fed Type X-Ray High-Voltage Generator

the lumped parasitic leakage-inductance and secondary-side lumped capacitance of the high-voltage high-frequency transformer as the LC resonant circuit components in addition to the input-side equivalent capacitance of the high-voltage cables as the DC filter for voltage ripple reduction.

In such a condition, according to the increase of the inverter operating frequency, the leakage inductance of the high-voltage transformer makes enlarge, the impedance in the equivalent load across the output terminal of the inverter including the high-voltage transformer, the high-voltage diode rectifier, the high-voltage cables and the X-ray tube. This enlarged impedance restrains the inverter output current as well as the tube current.

As a matter of fact, the secondary-side stray capacitance of the high-voltage transformer induces the ineffective reactive current through its secondary windings in addition to the decrease in the total efficiency of the resonant DC-DC converter with a high-frequency link.

III. NEWLY-DESIGNED HIGH-VOLTAGE TRANSFORMER

Fig.2 shows the structure of high-voltage transformer suitable for high-power delivering. The key point to the appropriate modeling lies in the method to estimate parasitic leakage-inductances, the internal resistances corresponding to iron and copper losses and lumped stray winding capacitances of the secondary winding of the high-voltage transformer.

The leakage-inductance Lr may be approximately treated as the lumped parameter. In the high-voltage transformer, the stray-capacitances exist between each layer of the secondary-windings which are with oiled paper. The distributed stray capacitances are also considered as a lumped stray-capacitance C_p. Besides, it is noted that power losses of the high-voltage transformer are to be represented. Some of them are proportional to the square of the applied voltage .and the others are determined by the current flowing through its windings. The former loss is equivalently denoted as iron loss and the latter loss is specified as stray-load loss.

As discussed above, an equivalent circuit of the high-voltage transformer is drawn in terms of a leakage inductance, the lumped stray capacitance and loss-equivalent iron and copper loss resistances which are represented by the lumped stray-load loss and the equivalent iron loss as no-load loss. Fig.3 shows the equivalent circuit of high-voltage transformer.

The lumped leakage inductance L_r of the high-voltage transformer is estimated as follows:

$$\chi_{L2} = 4\pi^2 f_{inv} N_2^2 \frac{u_1 + u_2}{2h}\left(\frac{\delta_1 + \delta_2}{3} + \delta_0\right) \times 10^{-7} \quad (1)$$

$$L_{r2} = X_{L2} / 2\pi f_{inv} \quad (2)$$

$$L_r = L_{r2} / n^2 \quad (3)$$

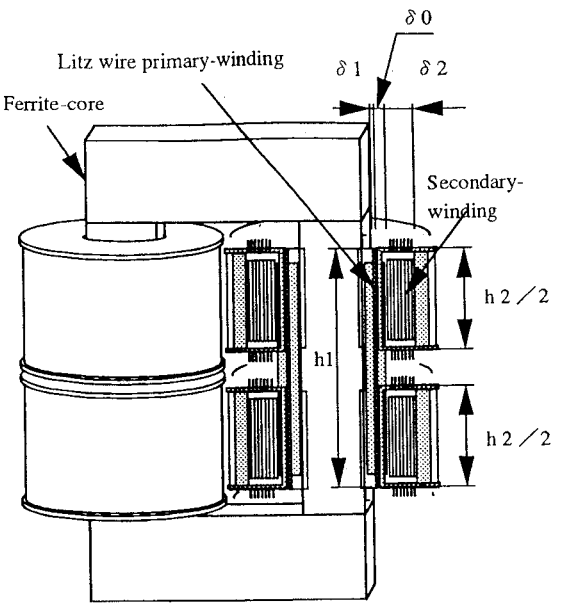


Fig2. High-voltage transformer for high-frequency link high-power

where χ_{L2}: the leakage reactance; L_{r2} : the secondary-side leakage inductance; L_r: the leakage inductance reduced into the primary side port; f_{inv} : the inverter operating frequency; N_2: the turn number of the secondary winding; n : the turn ratio of the high-voltage transformer; u_1 & u_2: the average one turn lengths of the primary and the secondary windings; $h, \delta_1, \delta_2 \& \delta_0$; geometric dimensions of the high-voltage transformer shown in Fig.3. The magnetizing inductance Lm is neglected. The lumped stray capacitance C_p of the high-voltage transformer is estimated by

$$C_p = C_{P2} n^2 = \frac{8\pi\varepsilon_e \varepsilon_0 r h_2 n^2}{3d(m-1)j^2 b} \quad (4)$$

where, C_{p2} : the stray capacitance of the secondary-side windings; C_p : the value C_p reduced the secondaryside capacitance into the primary-side port ; ε_0: electric permittivity of vacuum; ε_e : equivalent relative permittivity of the oiled paper ; γ : average radius of the secondary-side windings; h_2: the height of the primary and the secondary windings; d : the distance between two layers of the secondary windings; m: :the layer number of the secondary windings; j: the division number of the secondary windings for each leg; b : the number of the legs.

IV. CIRCUIT MODELING OF HIGH-VOLTAGE TRANSFORMER

Fig.4 illustrates three equivalent models of a parallel resonant tank circuit, series resonant tank circuit, and series-parallel resonant tank circuit. In this figure, V_{inv} is the sinusoidal component of the fundamental frequency of the inverter output voltage square wave and quasi square

PWM wave. C_p is a parallel resonant capacitance, C_s is an additional series resonant capacitance connected in series with a lumped leakage inductance of the high-voltage transformer, R_x is the variable load resistances in the primary side of the high-voltage transformer together with the high-voltage diode rectifier, the high-voltage cables and the X-ray tube. The filament heating current of X-ray tube is adjusted with a high-frequency converter.

X-ray tube is equivalently shown in variable resistances, which is varied by its filament current. The circuit parameters for the computer simulation presented here is indicated in Table 1.

As described above, the inputside equivalent capacitance C_L of the high-voltage cables behaves as the output smoothing filter. Therefore, R_x should be recognized filament current dependent resistances according to its transient stage. While charging C_L and rising the output DC voltage, R_x has smaller resistance value than a steady-state resistance.

Fig.4 shows the equivalent models of parallel, series, and series-parallel resonant tank power conversion circuit. Fig.4 (a) shows a parallel resonant circuit using a stray lumped capacitance *Cp* between the secondary-windings of the high-voltage transformer operated as a parallel resonant component with the leakage inductance *Lr*. In this case, the current resonance is activated when *Rx* is larger than a critical resistance required for current resonance. On the other hand, this critical resistance is determined by *Lr*, *Cp* and *Rx*.

Fig.4 (b) illustrates a series resonant circuit using an extremely-added capacitance *Cs* . At the series resonant circuit, the current resonance is activated when *Rx* is smaller than the other critical resistance determined by *Lr*, C_s and R_x. The lumped stray capacitance of the high-voltage transformer, however, can not be neglected so that this model can be prepared only in an ideal condition.

Fig.4 (c) presents a series-parallel resonant circuit using three reactive circuit elements L_r, C_s and *Cp*.

The series-parallel resonant circuit may behave as a complicated operation because of three reactive circuit elements.

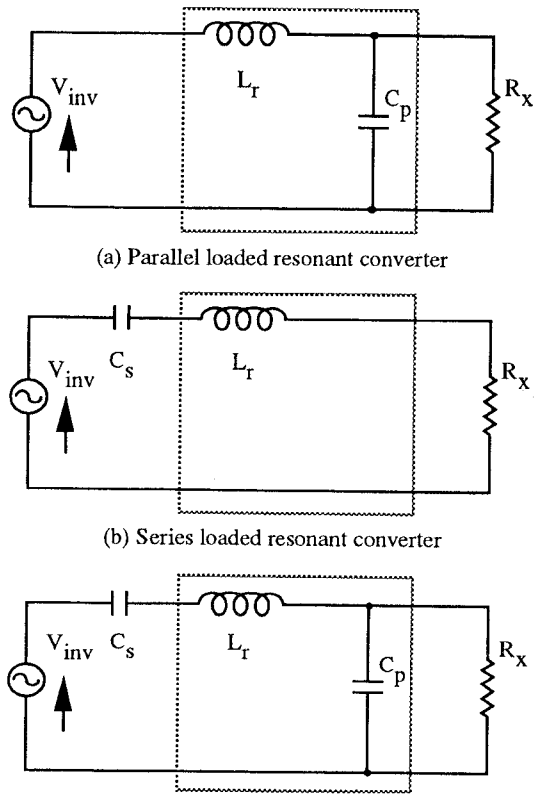


Fig. 4 Models of parallel, series, and series-parallel resonant tank power conversion circuit

TABLE 1
CIRCUIT PARAMETERS USED FOR SIMULATION

Symbols	Items / Circuit topologies	Parallel	Series	Series-Parallel
R_l	Lumped wiring resistance of main circuit (m Ω)	25	25	25
V_i	DC voltage source (V)	440	440	440
L_r	Leakage inductance of high-voltage transformer (μ H)	7.96	7.96	7.96
C_s	Series resonant capacitance (μ F)	-	7.96	7.96
C_p	Stray capacitance of high-voltage transformer (μ F)	7.96	-	7.96
C_L	Equivalent capacitance of high-voltage cable (μ F)	310	310	310
R_L	Load resistance model of X-ray tube (Ω) (Values reduced into the primary-side)	0.1 to 1000	0.1 to 1000	0.1 to 1000
R_i	Resistance corresponding to iron loss of high-voltage transformer (Ω)	280	280	280
R_r	Resistance corresponding to copper loss of high-voltage transformer (m Ω)	60	60	60
f_{inv}	Inverter frequency (kHz)	20	20	20
n	Turn ratio of high-voltage transformer	400	490	490

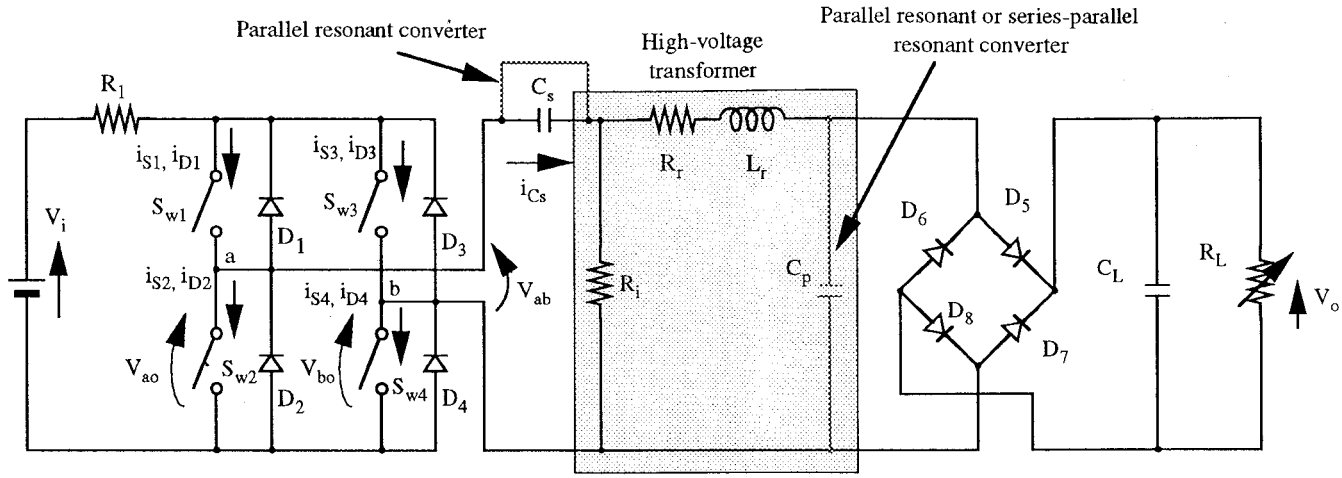
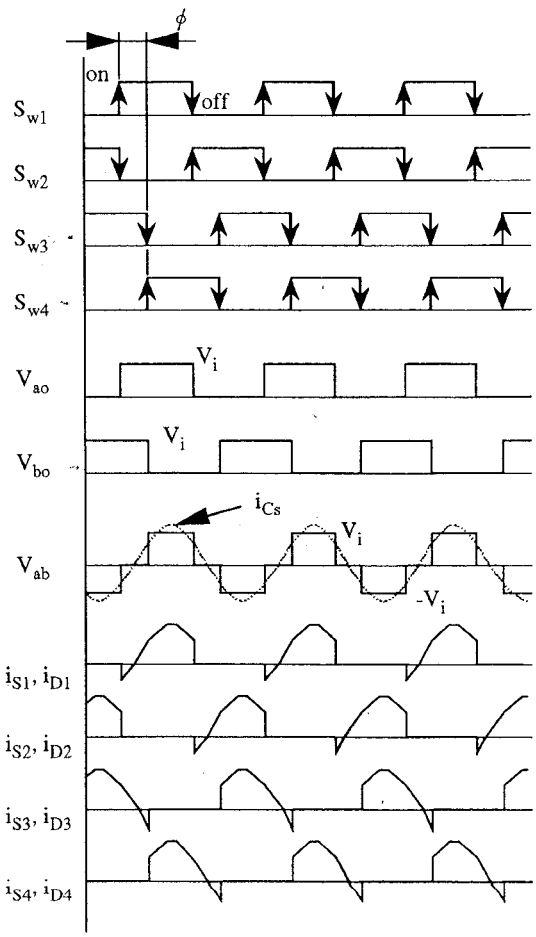


Fig.5 Circuit model of resonant tank inverter-fed DC-DC converter.



Vao,Vbo:Phase Voltages; Vab:Line-to-Line Voltage
ϕ :Phase-Shifted angle

Fig.6 Phase-shifted PWM signals and operating waveforms of the resonant inverter-fed type DC-DC converter

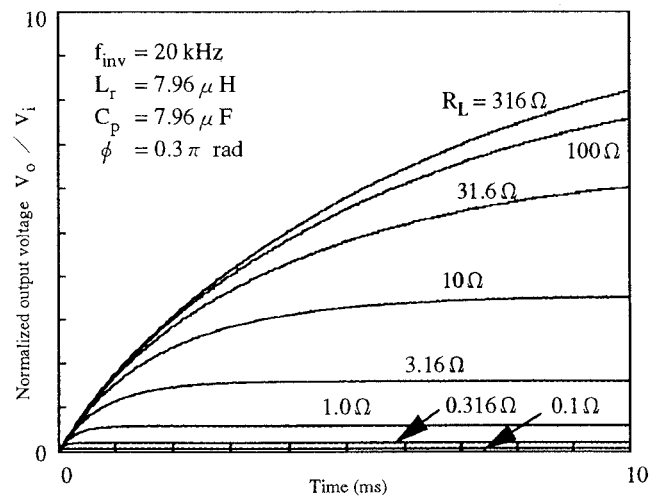


Fig.7 transient response of output voltage in parallel resonant converter

Fig.5 shows the whole approximated AC circuit model of three resonant inverter-fed converters type X-ray generator. Table 1 displays the circuit parameters used for the simulation analysis. There circuit models are treated under the following assumptions.

(1) The load resistance R_L *is* determined as the ratio of the tube voltage and the tube current
(2) The input capacitance of the high-voltage cables are utilized as the smoothing capacitor C_L
(3) R_L and C_L in the secondary-side of the high-voltage transformer are reduced into the primary side of the high-voltage transformer
(4) The high-voltage transformer includes the leakage inductance L_r, the stray capacitance Cp and the equivalent resistances Rr, Ri represented by the equivalent stray-load loss and iron loss.

Fig.6 illustrates the switching pulse sequence of the gate signals in this phase-shifted PWM resonant inverter.

These three resonant converters described here are controlled on the basis of PWM scheme instead of PFM(Pulse-Frequency-Modulation).

V. Simulation Results And Their Discussions

A. Parallel resonant converter

Fig.7 shows the step response waveform of output voltage, which is reduced into the primary-side of the high-voltage transformer. Their response curves are normalized. The output voltage of the parallel resonant converter behaves simply as a first-order lag system for any load resistances. It means that the parallel resonant converter can be controlled by only a proportional feedback control scheme with high loop gain. Therefore, the control circuit may be simple as well as the main circuit which needs no additional resonant component.

The power loss of the power conversion processing is apt to be high, however, as the ineffective current flows in the stray-capacitance C_p. In addition, sufficient output

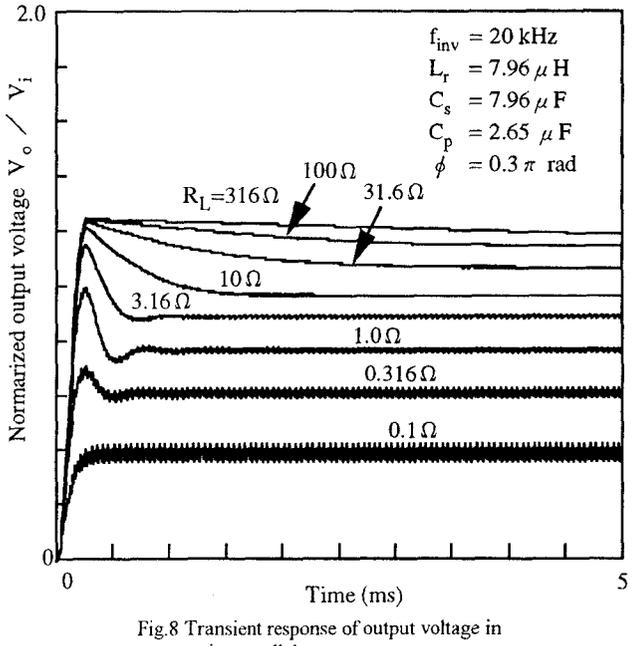


Fig.8 Transient response of output voltage in series-parallel resonant converter

voltage of this converter is not be able to obtain in the ranges of low load resistances.

B. *Series resonant converter*

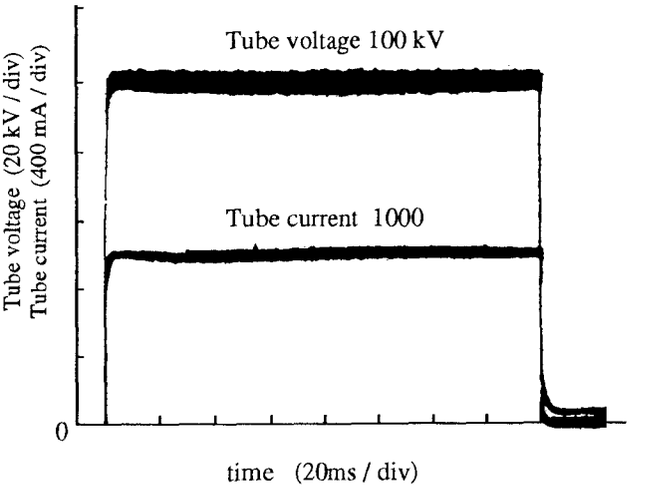
As the stray lumped capacitance between secondary-windings of the high-voltage transformer can not be negligible at all, the series resonant converter with a high-voltage transformer can not be practically realized for X-ray power generator.

C. Series-Parallel resonant converter

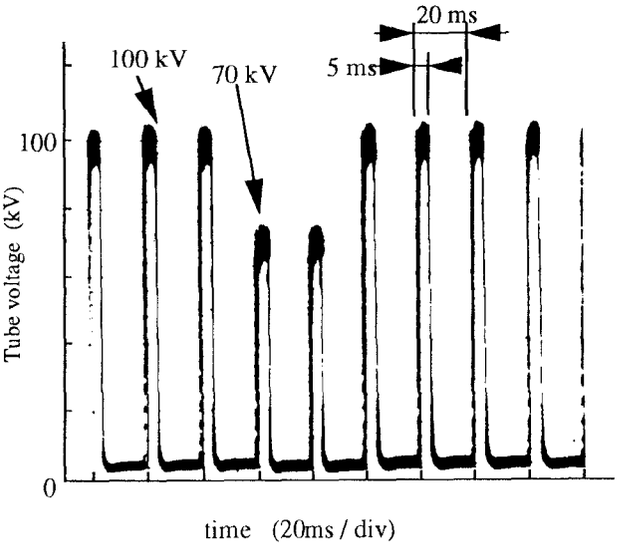
The series-parallel resonant converter has the most complicated characteristics in three resonant types of converters.

It can be considered that the mechanism of these phenomena is arisen by the effect of the resonant frequency of the inverter load circuit presented in Fig.4 according to the increased load resistance.

Fig.8 illustrates the step output voltage response in the series-parallel resonant converter. For the large wide range of load resistances, it can not be explained as the simple behavior in any linear systems. It seems difficult to apply the linear system control theory and the optimal control algorithm to such a wide load range. The control parameters such as the PID-gain parameters and the inverter input voltage ought to be suitably adjusted under each load condition.



(a) Tube voltage and tube current waveform.



(b) Output pulse tube voltage. (Tube current is 800 mA)

Fig.9 Examples of output waveform as experimental results

For the low resistance region, the series resonant converter is more advantageous than the parallel resonant converter. Consequently, it is obvious that the series resonant converter is more suitable for high power X-ray generator. According to these simulation results, the series-parallel resonant converter behaves just like the series resonant converter because the circuit parameters are basically determined as a series resonant converter.

VI. Experimental Results And Discussion

Fig.9 shows examples of output waveform as experimental results. Fig.9(a) demonstrates output voltage and current waveforms of the series-parallel resonant type X-ray generator as an example of experimental result. The load conditions are 100kV, 1000mA(100kW) for the X-ray tube load. The rising time of the output voltage is about 600 μ s. The ripple of the output voltage is about 3%.

Fig.9(b) shows high-voltage pulse output waveforms as other example. The pulse rate is 50 pulses per second. The tube current is 800mA and the maximum power rating is 800kW. These high-voltage pulses are used for medical diagnosis of the moving organs, for instance, the blood vessels and the heart. In the Fig.10(b), the reference high-voltage is changed from 100kV to 70kV, and from 70kV to 100kVagain. It is obvious that the output voltage responds quickly as soon as the reference value is changed. This quick response in the output voltgae is one of the significant characteristics of the series-parallel resonant converter.

VII Conclusions

Some particular characteristics and beneficial features of series resonant type, parallel resonant type and series-parallel resonant type DC-DC power converters with a high-voltage transformer link for the medical-use X-ray high-voltage generator have been presented from a practical viewpoint. It has been discussed how to treat the harmful parasitic circuit parameters of the high-voltage transformer by three types of resonant tank circuit topologies under the comparison of the load ranges in the X-ray power generator on the-basis of some simulated results.

The parallel resonant converter can be easily controlled because of its simple transient characteristics in the open loop scheme. If the stray capacitance in the secondary windings of the high-voltage transformer is adequately designed, the influences of its harmful leakage inductance can be compensated without any additional resonant component.

The series resonant converter can not be realized practically in medical-use X-ray power generator because the stray capacitance of the high-voltage transformer is not negligible for such a wide load range. The most significant feature of the series resonant converter is to be able to obtained the high output current for the low load resistance.

Furthermore, it was clearly proved that the series-parallel resonant converter is more suitable and acceptable for high power X-ray high-voltage generator for medical applications, though the overshoot of the output voltage in this inherent open loop system should be controlled by an adequate methodology using feedback control scheme.

VIII. Reference

[1] Y.Cheron, H.Foch and J.Salesses: "Study of a Resonant Converter Using Power Transistor in a 25-kW X-Ray Tube Power Supply", Proceedings of IEEE Power Electronics Specialists Conference, ESA Proceedings, 295, June, 1985

[2] H.Hino, T.Hatakeyama, M.Nakaoka: "Resonant DC-DC Converter Using Parasitic Impedances of High-Voltage Transformer", Proceedings of PCIM-USA Conference, Vol. 1, 15, October, 1987

[3] H. Takano, H. Uemura, M. Nakaoka: "Advanced Constant-Frequency PWM Resonant DC-DC Converter with Real Time Digital Control for X-Ray Power Generator", Proceedings of EPE Conference,Vol.1,544, October, 1991

[4] J.M.Sun, H.Takano, Y.L.Feng and M.Nakaoka;"Feasible Characteristic Evaluations Resonant PWM Inverter-Link DC-DC High-Power Converte rs using High-Voltage Transformer Parasitic Components", Proceedings of International Conference and Exhibition on Power Electronics, Drives and Motion-German(PCIM '96), pp.629-638,May,1996

[5] J.M.Sun, H.Takano, K.G.D.Lakunath, M.Nakaoka;"Feasible Charac teristic Evaluations of Resonant PWM Inverter-Linked DC-DC Po wer Converter using High-Voltage Transformer Parasitic Circuit C omponents", Proceedings of Power Electronics and Variable Speed Drives (PEVD96)-United Kingdom, pp.525-533,September,1996

[6] J.M.Sun, E.Hiraki, M.Nakaoka, H.Takano; "Digital Controlled Res onant PWM DC-DC Converter Bsaed On 32-Bit RISC Processor", Proceedings of 1996 JIASC-Japan,E-44-49, August,1996

[7] J.M.Sun, H.Takano and M.Nakaoka; "Transformer Parasitic High-Frequency Inverter-Fed DC-DC Converter For Medical-Use X Ray Power Generator and Its Digital Control", Proceedings of The IEEE International Conference on Industrial Technology (ICIT), PP.400-405, December, 1996

Performance Characteristics of the Combined Zero-Voltage Switching Inverter with the Auxiliary Input-Current Controller

Lishan Tu*, Fujio Kurokawa*, Hirofumi Matsuo* and Nanjo Aoike**

*Nagasaki University, Nagasaki, 852 JAPAN
**Toshiba Lighting & Technology Corporation, Kanagawa, 237 JAPAN

Abstract—Recently, the combined zero-voltage switching inverter with a single main power switch has been proposed as an electronic ballast for fluorescent lamps, in which the zero-voltage switching active filter and inverter are combined, and a main power switch in the active filter is used commonly as that in the inverter. This combined inverter has the superior advantages of simple circuit configuration, high power efficiency, high power factor, low distortion factor and so forth. However, the power factor and distortion factor of this combined inverter deteriorate when the ac input voltage or load vary.

This paper presents a new control circuit to improve the performance characteristics such as the power factor, distortion factor of the input current, the crest factor of the output voltage, the voltage stress of the main power switch and so forth even when the ac input voltage or load vary.

I. INTRODUCTION

Recently, the International Electrotechnical Commission(IEC), the Ministry of International Trade and Industry in Japan and so forth presented the guide-line with regard to the suppression of the harmonics in the electrical and electronic apparatuses, which is a serious low-frequency electromagnetic interference(EMI) problem. Especially, the guide-line is most severe in the lighting apparatus.

To find one solution of this harmonics problem, the combined zero-voltage switching inverter with a single main power switch has been proposed as an electronic ballast for fluorescent lamps[1],[2], in which the zero-voltage switching active filter and inverter are combined, and a main power switch in the active filter is used commonly as that in the inverter. This combined inverter has the superior advantages of simple circuit configuration, high power efficiency, high power factor, low distortion factor of the input current, low crest factor of the output voltage and so forth. However, it has a serious defect that the relatively large voltage stress is imposed on the main power switch[1]. Also, the power factor and distortion factor deteriorate when the ac input voltage or load vary.

The purpose of this paper is to present a new control strategy and to improve the performance characteristics of the combined zero-voltage switching inverter. After reviewing the operation principle of this combined inverter briefly, we proceed to examine and compare the performance characteristics of the combined inverter with the conventional[3] and new control circuits. As a result, it is clarified that the combined inverter with a new control circuit can achieve the high power factor, low distortion factor and low crest factor when the ac input voltage or load vary, that the maximum limits of distortion factor and the crest factor in IEC1000-3-2 Class C are satisfied, and that in this case, the voltage stress on the main power switch is sufficiently suppressed.

II. CIRCUIT CONFIGURATION

Fig.1 shows the circuit configuration of the combined zero-voltage switching inverter[1],[2], which is applied to electronic ballasts of fluorescent lamps. This circuit consists of the input filter of an inductor L_F and capacitors C_{F1} and C_{F2}, the bridge rectifier of diodes D_{11}, D_{12}, D_{13} and D_{14}, a MOSFET main switch T_r, a diode switch D_2, a reactor L_1, the parallel resonant circuit of an inductor L_2 and a capacitor C_3, a ballast choke L_3, a smoothing capacitor C_1, a capacitor C_2 to connect the active filter part with the main switch T_r, and a capacitor C_4 to preheat the fluorescent lamp. T_r is the common main power switch in both of the active filter and the inverter. So, the combined inverter has the feature that the circuit configuration is simple and that the power efficiency is high compared with the active filter method. In this figure, e_{ac} is the commercial ac line voltage, i_{ac} is the ac input current, V_{DS} is the drain-source voltage of the main switch T_r and e_o is the output voltage. Fig.2 shows the proposed control circuit, in which the circuit in the dotted line block is newly added to the conventional control circuit, and the distortion of the input current i_{ac} is suppressed by referring i_{acr}, which is proportional to the sinusoidal ac input voltage e_{ac}. In the

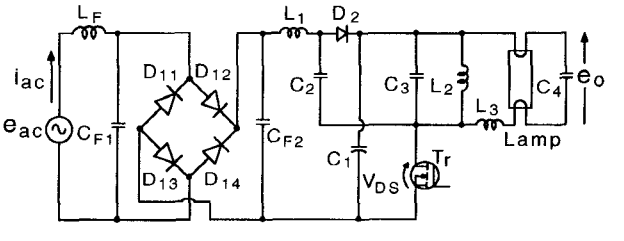


Fig.1 Circuit configuration of the combined zero-voltage switching inverter.

conventional control circuit in Fig.2, the delay circuit is used to induce the high voltage across the both terminals of the fluorescent lamp when the ac input power starts to be supplied. In the peak detector, the low frequency variation of the mean value E_{ac} of the sinusoidal ac input voltage e_{ac} is detected by that of the peak voltage V_{DSP} across the drain and source terminals of the MOSFET main switch T_r. In the dotted line block of Fig.2, the ac input voltage e_{ac} and the output signal G_V from the delay circuit and the peak detector are multiplied and the current reference i_{acr} is produced. The difference of i_{ac} and i_{acr} is sent to the voltage controlled oscillator VCO. So, the oscillation frequency f_s of the VCO is determined by the difference of i_{ac} and i_{acr} as follows;

$$f_S = f_S^* + G_f (i_{ac} - i_{acr}) \qquad (1)$$

where f_S^* is the oscillation frequency of the equilibrium point when i_{ac} is equal to i_{acr}. Also, f* is adjusted by the bias voltage E_B of the control circuit. G_f is the current gain which is determined by the product of the gains of the VCO and pre-amplifier. As shown in Fig.2, the output from the VCO drives the MOSFET switch T_r. Therefore, f_S in (1) is the switching frequency of T_r.

III. PERFORMANCE CHARACTERISTICS

Figs. 3(a) and 3(b) show the power factor and distortion factor of the input current, respectively, when the mean value E_{ac} of the ac input voltage e_{ac} is varied. E_{ac}^* is the rating voltage. The variation range of E_{ac} is $\pm 10\%$. Similarly, Figs. 4(a) and 4(b) show the power factor and distortion factor, respectively, when the load resistance R as a fluorescent lamp is varied in the steady state. R* is the

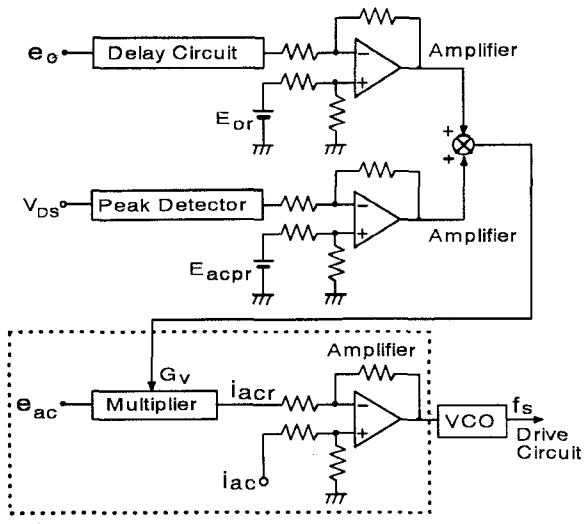
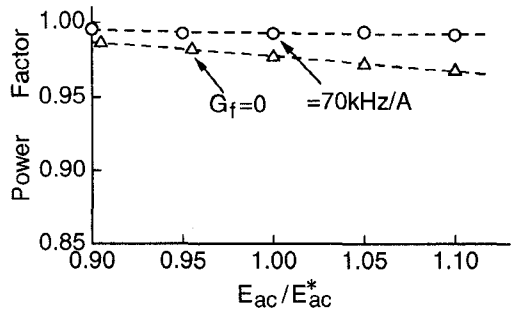
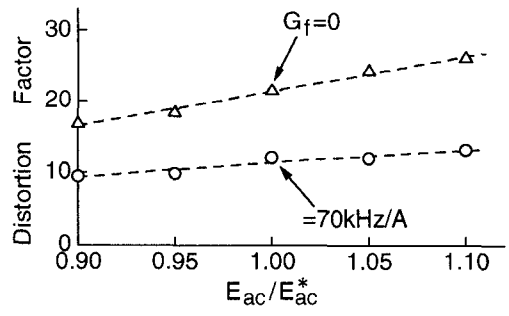


Fig.2 Proposed control circuit.

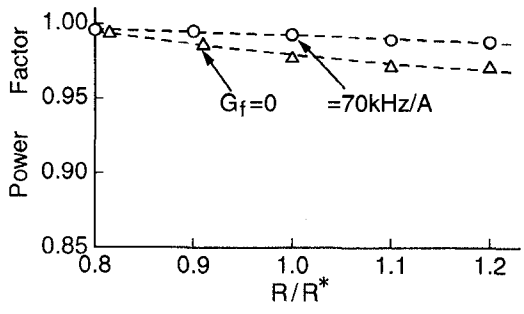


(a) Power factor.

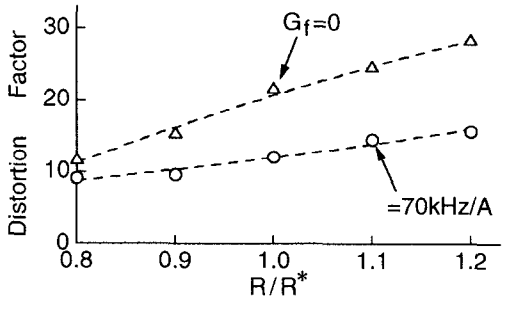


(b) Distortion factor.

Fig.3 Characteristics for the variation of the input voltage E_{ac}.



(a) Power factor.

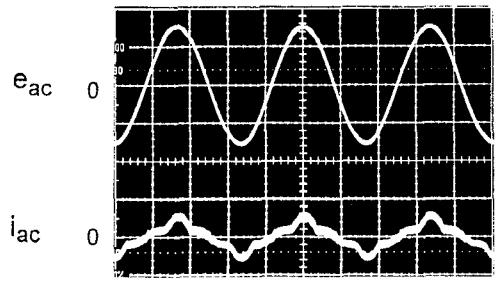


(b) Distortion factor.

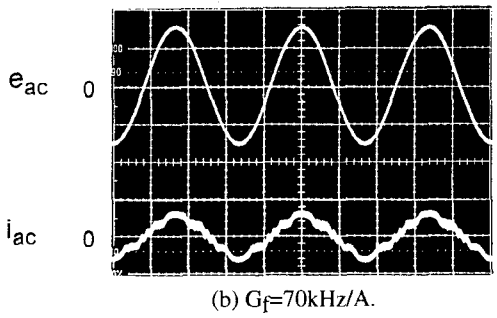
Fig.4 Characteristics for the variation of the load resistance R.

rating load resistance. The variation range of R is ±20%. Circuit conditions are : E_{ac}*=20V, E_O=6V, R*=15Ω, L_F=12.4mH, C_{F1}=C_{F2}=0.22μF, C_1=68μF, C_2=0.01μF, C_3=0.02μF, C_4=0.006μF, L_1=0.16mH, L_2=L_3=0.28mH and the characteristic impedance Z_n (=$\sqrt{L_2/C_3}$) of the resonant circuit is equal to 118Ω. In these case, V_{DSP}/E_{acp} is less than 3.7, where V_{DSP} is the peak value of the voltage V_{DS} across the drain and source terminals of the main switch T_r, and E_{acp} is the amplitude of the ac input voltage e_{ac}. Therefore, it is noted that the voltage stress of T_r is suppressed sufficiently. It is seen in Figs.3 and 4 that the combined zero-voltage switching inverter with the auxiliary input-current controller can achieve the power factor over 0.98 and distortion factor less than 15% when the current gain G_f is set to be 70kHz/A. In these figures, the case of G_f=0 corresponds to the characteristics of the combined inverter with the conventional control circuit.

Figs.5 and 6 show the observed waveforms of the ac input voltage e_{ac} and ac input current i_{ac} in cases of E_{ac}/E_{ac}*=1.10 and R/R*=1.20, respectively. Figs.7 and 8 show the input current harmonic distortion characteristics which are corresponding to the current waveforms shown in Figs.5 and 6, respectively. In these figures, the eleventh harmonic content ratio represents the maximum value of that in eleventh through thirty-ninth harmonics. The symbol of ● denotes the maximum limit of IEC1000-3-2 Class C, the symbols of ○ and △ denote the characteristics



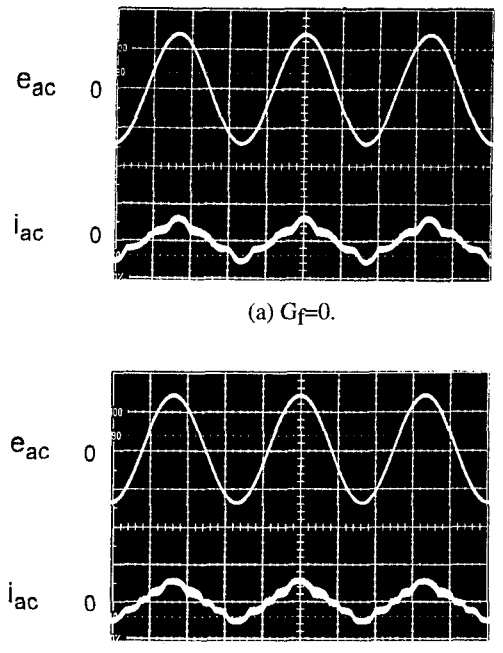
(a) G_f=0.



(b) G_f=70kHz/A.

Horizontal : 5msec./div.
Vertical : e_{ac} ; 20V/div. , i_{ac} ; 0.4A/div.

Fig.5 Waveforms of the ac input voltage e_{ac} and ac input current i_{ac} in case of E_{ac}/E_{ac}*=1.10.



(a) G_f=0.

(b) G_f=70kHz/A.

Horizontal : 5msec./div.
Vertical : e_{ac} ; 20V/div. , i_{ac} ; 0.4A/div.

Fig.6 Waveforms of the ac input voltage e_{ac} and ac input current i_{ac} in case of R/R*=1.20.

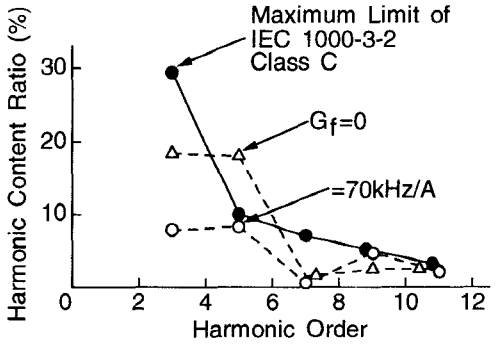


Fig.7 Harmonic content ratio of the ac input current i_{ac} in case of E_{ac}/E_{ac}*=1.10.

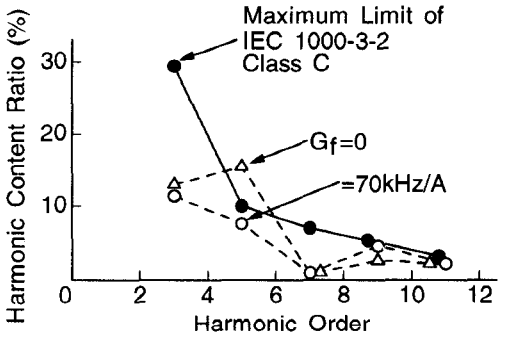
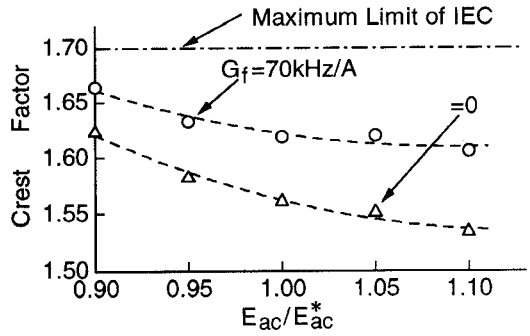
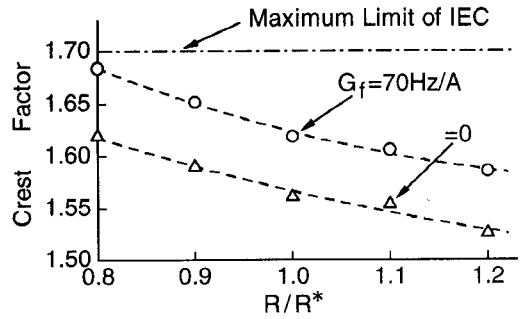


Fig.8 Harmonic content ratio of the ac input current i_{ac} in case of R/R*=1.20.



(a) For the variation of the input voltage E_{ac}.



(b) For the variation of the load resistance R.

Fig.9 Crest factor characteristics.

obtained by the new and conventional control circuits. It is seen in Fig.5 through Fig.8 that the maximum limit of IEC1000-3-2 Class C is satisfied by the proposed method.

Figs.9(a) and (b) show the crest factor characteristics of the output voltage for the variations of the input voltage E_{ac} and the load resistance R, respectively. The circuit parameters and variables of the inverter are the same as in Figs.3 and 4. The current gain G_f is set to be relatively large in order to suppress the distortion factor of the ac input current sufficiently. In this case, the crest factor of the combined inverter with the new control circuit is a little higher than that of the inverter with the conventional control circuit. However, these crest factors are less than 1.7 of the maximum limit of IEC 1000-3-2 Class C when the ac input voltage E_{ac} varies within $\pm 10\%$ when the load resistance R varies within $\pm 20\%$.

IV. CONCLUSION

A new control strategy of the combined voltage resonant inverter has been proposed and the performance characteristics have been examined. The conclusions are as follows:

1) The combined voltage-resonant inverter with a new simple control circuit can be achieved the power factor over 0.98 and distortion factor less than 15% in case of $\pm 10\%$ change of the input voltage or $\pm 20\%$ change of the load resistance as a fluorescent lamp.
2) High power factor, low input current distortion factor, low voltage stresses on the main switch and low crest factor of the output voltage can be realized when the current gain is selected at an adequate value.
3) The maximum limit of IEC1000-3-2 Class C is satisfied by the proposed control strategy when the ac input voltage or load resistance vary.

The performance characteristics and design oriented analysis of the practical prototype are being studied and will be reported in a separate paper.

The authors would like to express their appreciation to Mr. Kitajima of Nagasaki University for his assistance.

REFERENCES

[1] H. Matsuo, N. Aoike, F. Kurokawa and A. Hisako:"A new combined voltage-resonant inverter with high power factor and low distortion factor", IEEE PESC Record, pp.331-335(June 1994).

[2] H. Matsuo, F. Kurokawa, N. Aoike and Xu Hong :" Performance characteristics of the combined voltage-resonant inverter", IEEE PESC Record, pp.1159-1164(June 1995).

[3] K. Shimizu, T. Itoh and H. Fujii:"Electronic ballast for office lighting using single-transistor inverter", Toshiba Review, vol.45, no.10, pp.810-822(Oct. 1990).

SIMULATION AND ANALYSIS OF HYBRID SYSTEMS USING PROBABILISTIC TECHNIQUES

Fadia M.A.GHALI * **M.M.ABD EL AZIZ **** **Fathy A. SYAM ***

*** Electronics Research Institute**
El-Tahrir St.-Dokki- Egypt
Fax: 00202/ 3351631
E-mail: Fadia @ eri.sci.eg

**** Faculty of Engineering**
Cairo University
Egypt

ABSTRACT: **- In this paper, a PV / Wind hybrid autonomous system with a battery bank as a storage subsystem is optimally designed to supply pre-specified load. The implemented design criteria is the Loss of Power Supply Probability (LPSP). For selected locations, long term data of wind speed and irradiance recorded for every hour of the day are deduced to produce the probability density function of combined generation. For considered load distribution, the probability density function of the storage is obtained and consequently The battery size is calculated to give the relevant level of the system reliability using the LPSP technique. Different combinations of PV / Wind system are tested, for each the optimum size of storage facility is determined.**

I . INTRODUCTION

Interest in renewable energy sources is at its highest level since the oil embargo of 1973. In addition to the realization of the economic and geopolitical goals of existing and planned conventional non-renewable energy power plants, environmental concerns are playing an important role emphasizing the need to renewable energy sources. Economic aspects of renewable energy technologies are sufficiently promising at present to cope with the development of markets. One of the most promising markets for renewables exists in supplying energy to remote areas specially in developing countries.

For technical, economic and environmental reasons, it should be kept in mind to avoid the implementation of a variety of locally available resources to supply the demand by employing Integrated Renewable Energy System (IRES). As known, the renewables are intensive global energy scenarios[1].Thus moving towards reality, the question of designing IRES optimize an objective function such as capital cost or cost of energy takes on an increasing importance. The wide variety of renewable energy resources and their highly site- specific and variable nature, coupled with different types and qualities of energy needs, pose a challenging problem to the designers of IRES.

Today, wind and PV generators are utilized in many applications such as water pumping, lighting, electrification and telecommunication in remote areas. Such systems are usually equipped with diesel generators to meet the deficit in power generated. Diesel generators requires the control of their interactive operation and insured supply of fuel. Therefore the cost of the whole system along with its maintenance is comparatively expensive. To eliminate the need of a diesel generator, a battery bank can be used.

Now, the question that the designers have to answer is; which hybrid configuration is the optimum for a specific load ? Previous works attempted to find out the best configuration by changing the number of PV-modules only[2]. Several approaches have been proposed to design IRES such as linear programming, goal programming and probabilistic approach involving loss of power supply probability[3],[4].

The purpose of this paper is to implement the loss of power supply probability technique to find the optimum size of the battery storage sub-system coupled with a hybrid PV-Wind autonomous system.

II . SYSTEM DESCRIPTION AND MODELS

A . System Description

The system under study is shown in figure (1). a WECS is connected to the control unit through an appropriate electrical interface. In parallel a PV-array is also connected to the control unit. Interaction with the storage system is assumed to be bi-directional; excess energy generated by the WECS and PV-system is conditionally supplied to the batteries to be charged. On the other hand, deficit of energy will be drawn from the batteries in the discharging phase to supply the demand as needed.

Thus the performance of the hybrid system under study can be assessed by employing suitable models for the power output of WECS and PV-system and for the load.

B . Wind Energy Conversion System Model

To determine the output power of the WECS it is basically evident that the wind speed distribution for selected sites as well as the the chosen wind turbine type are the factors to be considered.

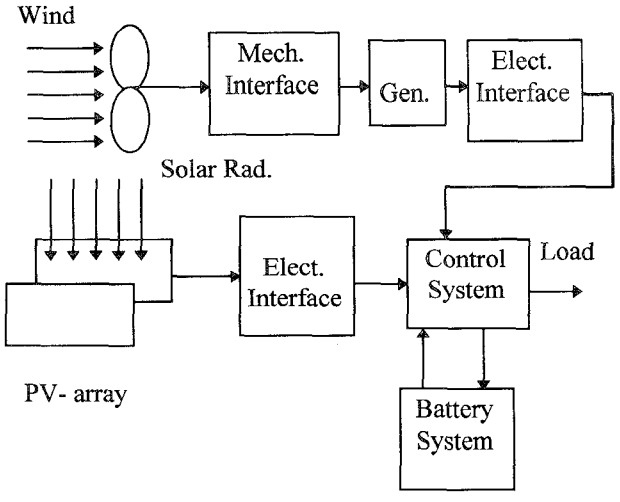


Fig.(1) : Schematic diagram of the system under study

Since the wind speed is a random variable, a long term meteorological data is desirable to describe the sites of wind energy potential. As a case study of Egypt, the measured wind speeds for sites on the north-west coast and on the Red-Sea coast are considered in this study [5].

The characteristics of the WECS can be described as a function of the wind speed as follows:

$$P_w(v) = \begin{cases} \dfrac{(v - v_c)}{(v_r - v_c)} P_r & \text{for } v_c \le v \le v_r \\ P_r & \text{for } v_r \le v \le v_f \\ 0 & \text{for otherwise} \end{cases} \quad (1)$$

Based on the available wind speed range, a wind turbine is selected. whose The technical parameters are given in appendix A. It is to be mentioned, that the chosen wind turbine has a speed working range wider than the available wind speeds. Therefore, the wind turbine will deliver power for all wind speeds.

C . Photovoltaic System Model

On an hourly basis, having the solar radiation data for the selected sites, the power output of the PV - module can be calculated [6],[7]. a PV - module is selected for this study. The technical parameters of this module are given in appendix B. The characteristic equations of the PV - module are :

$$V = -0.9I + 23.68 \ln\left(\frac{14.4\Phi - I}{0.009} + 1\right) \quad (2)$$

$$P = V I \quad (3)$$

A Maximum Power Point Traker (MPPT) is used to extract the maximum available power at every insolation level.

D . Load Model

As known, in the design phase the load to be considered could be a combination of existing load and forecasted load. The estimation of the second portion of load depends on the available data, the skill and techniques used by the designer. Therefore, to accommodate the variety of loads that are encountered in practice, the load is assumed to be uniformly distributed between a maximum value of L_{max} and a minimum value of L_{min} The corresponding probability density function is given as :

$$f_L(\ell) = \begin{cases} \dfrac{1}{L_{max} - L_{min}} & \text{for } L_{min} \le \ell \le L_{max} \\ 0 & \text{for otherwise} \end{cases} \quad (4)$$

III . LPSP CALCULATION

The power input C to storage system is controlled by the following equation :

$$C(t) = P(t) - L(t) \quad (5)$$

where, $P(t) = P_w(t) + P_{pv}(t)$ (6)

It is to be noticed that since the power generated by the hybrid system and the load supplied are time dependent, the amount of energy stored is also time dependent. However, C(t) can not be allowed to fall below a certain minimum value or to exceed a certain maximum value, both specified based on lifetime and safety considerations. The probability of encountering that minimum value in which the whole system would not be able to supply the load is the Loss of Power Supply Probability (LPSP).

Assuming that P(t) and L(t) are statistically independent, the probability density function $f_c(c)$ for the random variable C is found by convolving the pdf of P and L [8]. Thus, the pdf of power input to storage is given as :

$$f_c(c) = f_p(p) * f_L(-\ell) \quad (7)$$

A typical duration curve for the random variable C " power input to storage " is shown in figure(2). If a value of C can be found such that the difference between the

areas E_1 , E_2 is the allowable energy depletion from the storage system, Then the value of LPSPis given by :

$$LPSP = \frac{\int_{P_{min}-L_{max}}^{-c_1} f_c(c)\ dc}{} \qquad (8)$$

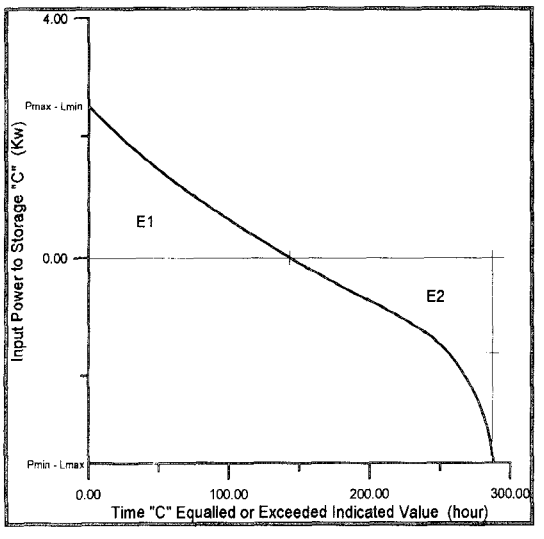


Fig.(2): Duration curve for the power input to storage

In design phase, LPSP is one of the design control parameters having certain value (say 0.01) depending on the nature of the load supplied.

IV . RESULTS

To show the significance of the LPSP technique in optimally design hybrid systems, keeping in mind to satisfy the technical constraints as well as the economic constraints, a case study is introduced. The assumptions of this case study are as follows:

1- The LPSP is to be kept at 1% level.

2- A forecasted load is uniformly distributed between a minimum value of 1 Kw and maximum of 4 Kw.

3- The metreological data of the north-west coast and Red-Sea coast of Egypt are used to choose the WECS and PV-module ratings of 2 kw , 1.5 kw respectively .

Apply the LPSP technique to design the hybrid system needed to supply the given load, two variants are considered; which are:

-- Variant I :

Starting from the base case of having one unit of each of the WECS and PV-module, the number of PV-modules is increased in steps. At each step , the capacity of the storage system required is calculated. The results are given in figure (3), from which it can be seen that increasing the number of PV-modules from 1 to 4 causes a battery capacity reduction of 16.6 Ah; 5% of the base case.

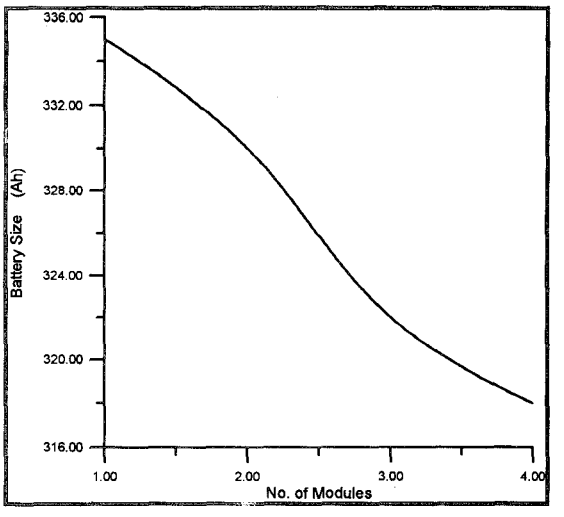


Fig.(3) : Required battery capacity for different No. of PV-modules

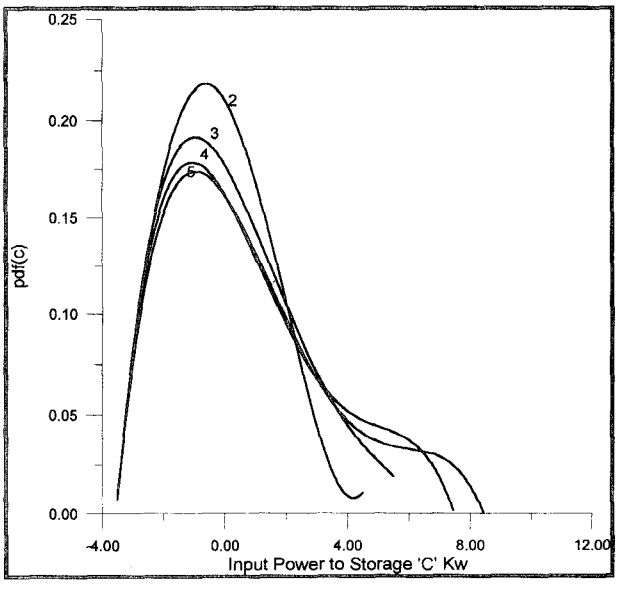


Fig.(4) : Probability density function of input power to storage for different No. of PV- modules

Figure (4) shows the pdf of input to storage for different No. of PV-modules. Numbers given to the curves indicate the number of PV-modules installed. For all cases, only one WECS is considered. Since the quantity (Pmin-Lmax) depends on the number of WECS used and maximum load, all the cases studied would have the same starting point. However, for increased number of PV- modules, the pdf-curves should be shifted from the right.

-- Variant II :

For this variant, starting again from the base case, the number of WECS is increased in steps, for each the pdf

and energy input to storage are calculated. In analogy with variant I, the numbers given to the curves indicate the number of wind turbines installed, e.g. number 2 refers to the dotted curve as well as describes the results of a combination of 1 PV- module and 2 wind turbines. As seen from figure (5), the pdf of input to storage is shifted to the right each time the number of WECS is increased. Also, the ratio between the charging area E_1 and discharging area E_2 is altered, showing an upwards shifting of the power curve. Figure (6) shows this behavior for load range 1: 4 Kw. The same trend is given in figure (7) for load range 3: 6 Kw.

Figure (8) shows the reduction of the battery capacity required with increased number of WECS for two different loading conditions. For case 1, a reduction of 75 % from the base case is gained by adding 4 units of WECS's. This reduction is almost equivalent to 200 Ah. For case 2, the reduction is 46 % of the base case.

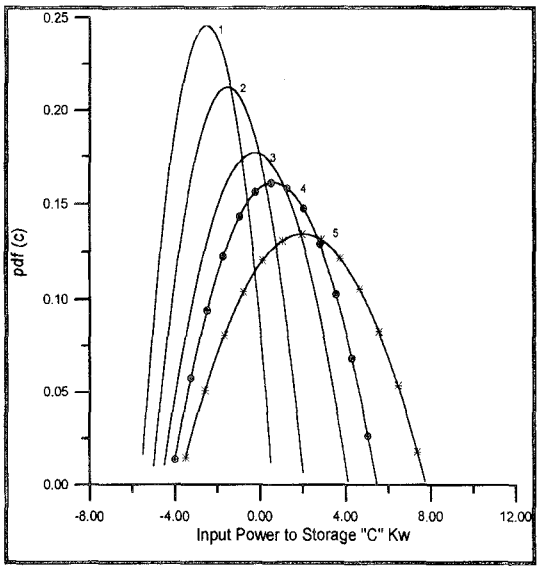


Fig.(5) : Probability density function of input power to storage for different No. of WECS

V . CONCLUSION

It is evident that, the LPSP technique is a powerfull tool to be implemented in the design phase of hybrid systems. It has the capability to encounter the probabilistic nature of the load demanded and the energy generated. It also enables the designer to test different variants. The first variant tested shows that , changing the number of PV-modules is not that much effective in reducing the storage capacity required. While the second variant declares the direct effect on the pdf of input to storage from higher tendency of discharging mode (the most left), to higher tendency of charging mode (the moat right). These two extreme cases are practically unaccepted . Thus changing the combination between WECS and PV-modules to ascertain a charging area higher than discharging area

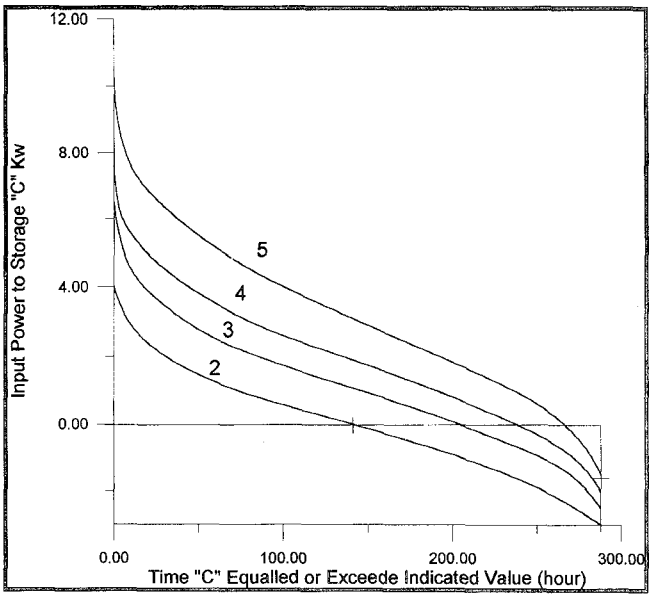


Fig.(6): Duration curves for the input power to storage for different No. of WECS Lmin = 1 Kw , Lmax = 4 Kw

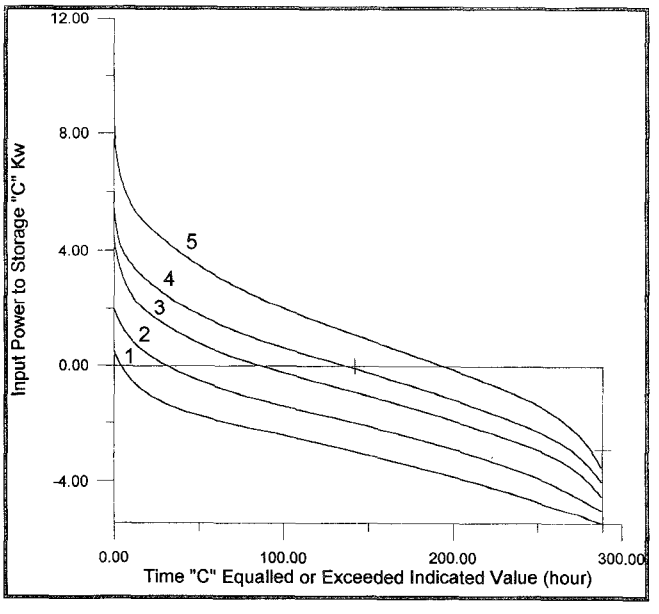


Fig.(7) : Duration curves for the input power to storage for different No. of WECS Lmin = 3 Kw , Lmax = 6 Kw

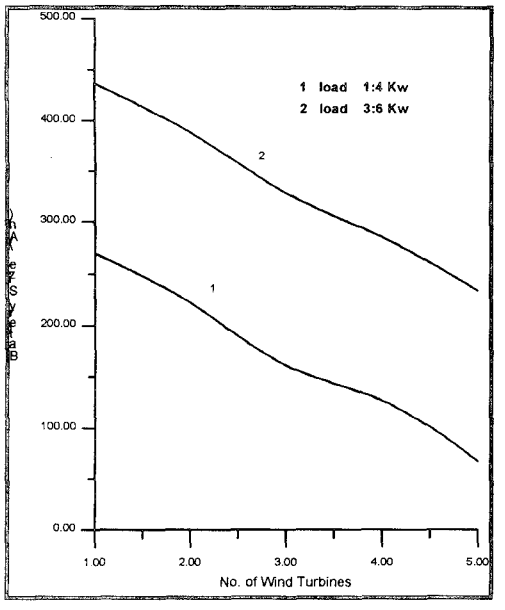


Fig.(8) : Required battery capacity for different No. of WECS

would be the lower limit, upon which the suboptimal design is to be figured. The upper limit to be realized is the economical features of the whole system , which finally specifies the optimal configuration of the hybrid system. In the economical evaluation, capital and running costs of all the system components are to be included.

REFERENCES

[1] R.Ramakumar, et. al., "Design Scenarios for Integrated Renewable Energy Systems", IEEE Trans. on Energy Conversion, Vol.10, No.4, December 1995, pp.736-746.

[2] B.S.Borowy, Z.M.Salameh, "Optimum Photovoltaic Array Size for a Hybrid Wind/ PV System" , IEEE Trans. on Energy Conversion, Vol.9, No.3, September 1994, pp482-488.

[3] I. Abouzahr, R.Ramakumar, "Loss of Power Supply Probability of Stand-Alone Photovoltaic Systems: A Closed Form Solution Approach" ,IEEE Trans. on Energy Conversion, Vol.6,No.1, March 1991, pp.1-10.

[4] I.Abouzahr,R.Ramakumar, "Loss of Power Supply Probability of Stand-Alone Wind Electric Conversion Systems: A Closed Form Solution Approach", IEEE Trans. on Energy Conversion,Vol.5, No.3, September 1990, pp.445-452.

[5] Wind Atlas For The Gulf of Suez, Prepared by Egyptian Renewable Energy Development Organization, EREDO, October 1994.

[6] A.Balouktsits, PH. Tsalides, "Stochastic Simulation Model of Hourly Total Solar Radiation", Solar Energy, Vol.37,No.2,1986,pp.119-126.

[7] M.A.MosalamShaltout, .T.Y.Tadros, "Typical Solar Radiation Year for Egypt", Renewable Energy, Vol.4, No.4,1994,pp.387-393.

[8] Operations Research , Hamdy A. Taha, Macmillan Publishing Co., Inc., 1982.

APPENDIX A

The manufacturer's parameters of the wind turbine used in the study :

* Manufacturer :North Wind Power Co.
* Type : Horizontal - Axis
* Rated power output 2 KW@ 9.8 m / s
* Cut- in wind speed : 3.6 m / s
* Rated wind speed : 9.8 m / s
* Cut- off wind speed : 22 m /s
* Rotor blade diameter : 4.15 m

APPENDIX B

The manufacturer's parameters of the PV generator used in the study :

* No. of parallel strings : 18
* No. of cells in each string : 324
* Resistance of each cell : 0.05 ohm
* Reverse saturation current : 0.5 mA
*Photocurrent for 100% insolation : 0.8 A

Modeling Analysis and Simulation of Motor Parameter Variation in Vector Controlled Electrical Drives

Goran Rafajlovski , Emil Ratz* ,D.Manov
Department of elektrical machines, Electrotechnical Fakulty, University "St.Kiril and Metodij"
Karpos II b.b POB 574, 91000 Skopje, MACEDONIA
tel: ++ 389 91 36 35 66, fax: ++ 389 91 36 42 62
E-mail: goran@cerera.etf.ukim.edu.mk
*Technical University Sofia Faculty of Sliven

Abstract - **The aim of this paper is to compare the influence of parameter uncertainties on the performance of two vector oriented control schemes of electrical drive with induction motor.**

In the first one the field oriented control method is used to control the speed of induction motor. In this system the spatial vector of the stator current is transformed into a i_{1q} component which creates the torque, and into a i_{1d} component which creates the flux. If d-axis component of the stator current is of constant value, the motor drives with a constant flux and the torque can be altered rapidly by means of the q-axis component of the stator current i_{1q}. Two components U_{1d}, U_{1q} of stator voltages in d-q coordinate system which must be applied to the stator d-q equivalent windings, are generated by two PI regulators controlling the two components: flux-generating and torque generating stator current.

In the second one the stator flux oriented control method is used to control the torque of induction motor. By using instantaneous voltage space vectors with selection of optimum inverter switching modes employing vector modulation technique, the direct control of torque and stator flux is achieved.

I. INTRODUCTION

In practice, frequently there are significant deviations between the parameter values of the model and the real parameter values of the engine in the working mode: Depending on the drive mode of the machine and due to the different heating and magnet utilization of the machine there is a change of the parameter values. An error can also appear during measurement, i.e. acquisition of parameters [1,2,7]. With some control concepts [2], this deviations between the parameter value can cause impermissible deviations of the regular values. Also, the variation of the different parameters in the machine as the stator resistance R_1, the rotor resistance R_2, the magnetizing reactance X_m, the leakage reactances $X_{1\sigma}, X_{2\sigma}$, have a different influence on the individual regular values of the stator spatial flux vector $\vec{\psi}_1$, the rotor spatial flux vector $\vec{\psi}_2$ the stator spatial current vector $\vec{i}_1$, the developed torque M and the speed n. For the purpose of decreasing or eliminating it, the error caused by the variation of the motor parameter values, should be observed and corrected if necessary. For that purpose, in this part an observation will be carried out of the influence of variation of the induction motor parameter values on the different spatial vectors in the machine, of the two previously analyzed vector regulation systems.

The first control strategy based on rotor flux vector considered in this paper is shown in fig.1 [7,9]. The second scheme based on stator flux oriented control method is presented on fig.2 [3,4,5,7,8].

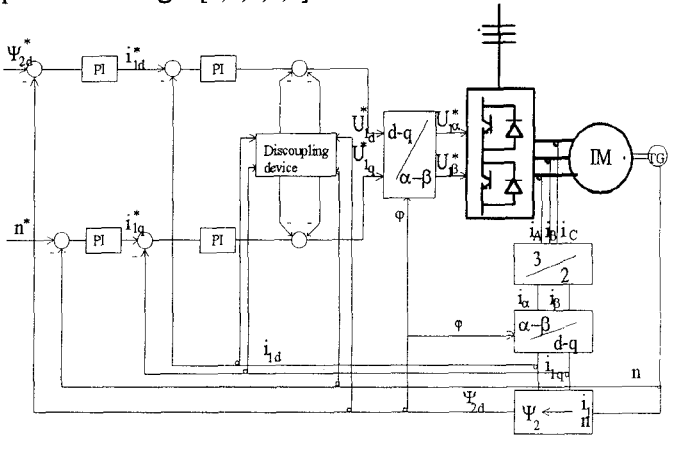


Fig.1 Field-oriented control of an induction motor

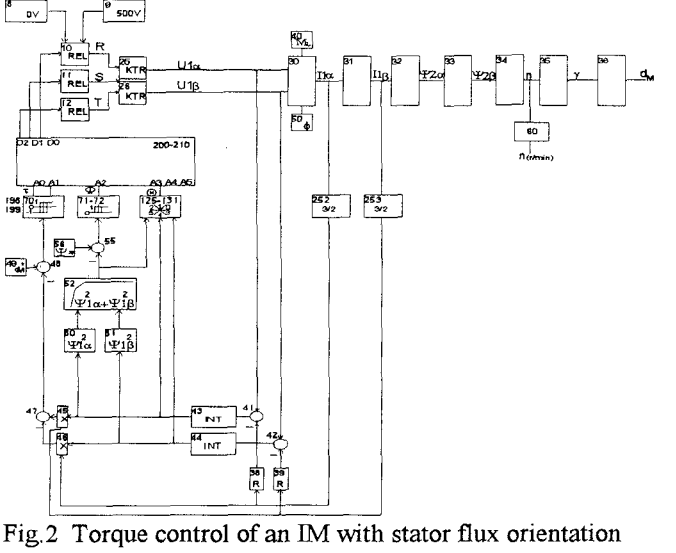


Fig.2 Torque control of an IM with stator flux orientation

II. INFLUENCE OF PARAMETERS VARIATION UPON VECTOR CONTROL

A. *Definition and assessment of error vector*

In this part a qualitative-quantitative assessment will be carried out of the error of certain controlling values of the induction motor as a consequence of the variation of the parameters of the induction motor model. From [8,9] can be obtained the following state equations of the induction motor in a matrix form:

$$\begin{bmatrix} \dot{\Psi}_{1x} \\ \dot{\Psi}_{1y} \\ \dot{\Psi}_{2x} \\ \dot{\Psi}_{2y} \end{bmatrix} = \begin{bmatrix} -\frac{R_1}{\sigma \cdot X_1} & n_k & \frac{R_1 \cdot X_m}{\sigma \cdot X_1 \cdot X_2} & 0 \\ -n_k & -\frac{R_1}{\sigma \cdot X_1} & -0 & \frac{R_1 \cdot X_m}{\sigma \cdot X_1 \cdot X_2} \\ \frac{R_2 \cdot X_m}{\sigma \cdot X_1 \cdot X_2} & 0 & -\frac{R_2}{\sigma \cdot X_2} & n_k - n \\ 0 & \frac{R_2 \cdot X_m}{\sigma \cdot X_1 \cdot X_2} & -(n_k - n) & -\frac{R_2}{\sigma \cdot X_2} \end{bmatrix} \cdot \begin{bmatrix} \Psi_{1x} \\ \Psi_{1y} \\ \Psi_{2x} \\ \Psi_{2y} \end{bmatrix} + \begin{bmatrix} 1 & 0 \\ 0 & 1 \\ 0 & 0 \\ 0 & 0 \end{bmatrix} \cdot \begin{bmatrix} u_{1x} \\ u_{1y} \end{bmatrix}$$

$$\dot{\underline{\Psi}}(t) = \underline{A} \cdot \underline{\Psi}(t) + \underline{B} \cdot \underline{U}(t) \qquad (1)$$

$$\begin{bmatrix} i_{1x} \\ i_{1y} \end{bmatrix} = \begin{bmatrix} \frac{1}{\sigma \cdot X_1} & 0 & -\frac{X_m}{\sigma \cdot X_1 \cdot X_2} & 0 \\ 0 & \frac{1}{\sigma \cdot X_1} & 0 & -\frac{X_m}{\sigma \cdot X_1 \cdot X_2} \end{bmatrix} \cdot \begin{bmatrix} \Psi_{1x} \\ \Psi_{1y} \\ \Psi_{2x} \\ \Psi_{2y} \end{bmatrix} \qquad (2)$$

$$\underline{I}_1(t) = \underline{C} \cdot \underline{\Psi}(t)$$

The equation of the torque balance can be represented as:

$$\dot{n} = \frac{1}{T_A}\left[\frac{X_m}{\sigma \cdot X_1 \cdot X_2} \cdot \left(\Psi_{2x} \cdot \Psi_{1y} - \Psi_{2y} \cdot \Psi_{1x}\right) - M_t\right] \qquad (3)$$

The matrixes $\underline{A}$ (system matrix), $\underline{B}$ (regulation matrix) and $\underline{C}$ (resulting matrix) contain the parameters of the control system, i.e. the induction motor. In order to differentiate between the model and the real system, the equations of the model shall be marked by the index "m" (example of the flux $\overset{m}{\Psi}$).

$$\dot{\underline{\Psi}}^m(t) = \underline{A}^m \cdot \underline{\Psi}^m(t) + \underline{B}^m \cdot \underline{U}(t) \qquad (4)$$

$$\underline{I}^m{}_1(t) = \underline{C}^m \cdot \underline{\Psi}^m(t) \qquad (5)$$

Figure 3 represents the principal structural block scheme of the induction motor in working mode and its model which in the following two chapters is used for assessment of the error in the control values.

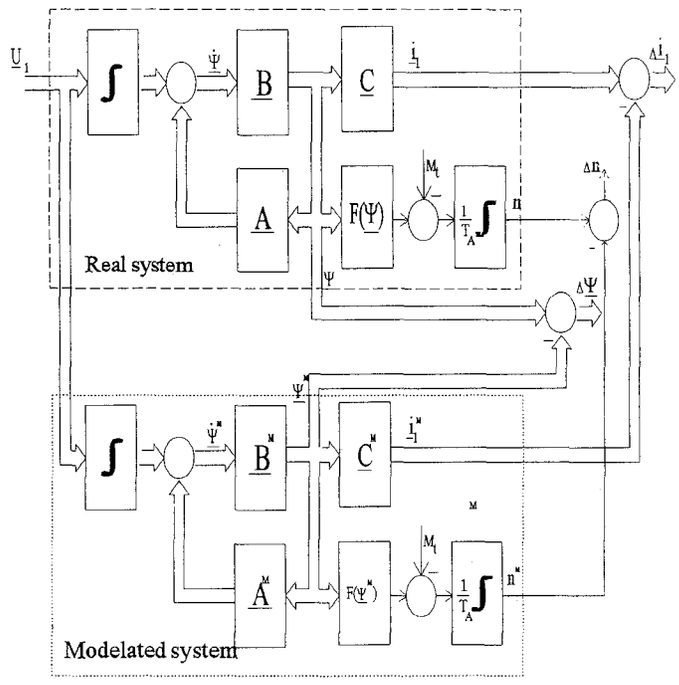


Fig.3 Block scheme for quantitative and qualitative error assessment

The deviation of the spatial vectors in the machine $\vec{i}_1$, $\vec{\Psi}_1$, $\vec{\Psi}_2$ from the spatial vectors of the model $\vec{i}_1^m$, $\vec{\Psi}_1^m$, $\vec{\Psi}_2^m$ conditioned by the variation of the parameter values in the induction machine can be represented mathematically by the error vector fig.3:

$$\Delta \vec{V} = \vec{V} - \vec{V}^m \qquad (6)$$

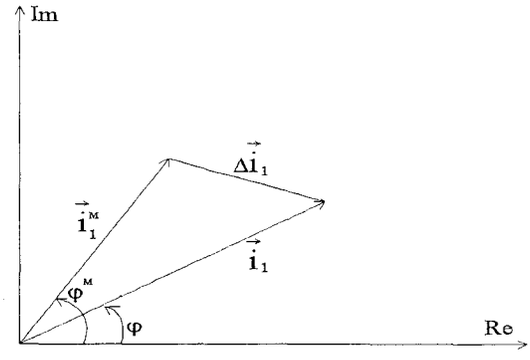


Fig.4 Definition of stator current error space vector

In (6) by $\vec{V}$ is represented a random spatial vector, while the index "m" denotes that it is a matter of parameters of spatial vector which belongs to the model.

For qualitative-quantitative assessment of the error the phase error $\Delta\varphi$ is used, as well as the amplitude error $\left|\Delta\vec{V}\right|$ defined by the equations (7) and (8) respectively.

$$\Delta\varphi = \varphi^{m} - \varphi \tag{7}$$

$$\left|\Delta\vec{V}\right| = \frac{\left|\vec{V}\right| - \left|\vec{V}^{m}\right|}{\left|\vec{V}\right|} \tag{8}$$

B. *Quantitative and qualitative error assessment*

In this part, investigated will be the influence of the variation of the parameters of the machine (R_1, R_2, X_1, X_2) on the estimation of the spatial vectors of the rotor flux $\vec{\psi}_2$, the stator flux $\vec{\psi}_1$, the stator current $\vec{i}_1$ as well as on the developed torque, i.e. the speed in dynamic and stationary work mode. Assessment of the influence of the variation of the parameter values of the induction motor on the control values shall be derived by the use of the amplitude and the phase error, in accordance with the functional block scheme represented by Fig.4. While assessing the phase and the amplitude error, analyzed in more detail shall be the following error vectors:

$\Delta\vec{i}_1^{R}(t)$, $\Delta\vec{\psi}_2^{R}(t)$, $\Delta\vec{\psi}_1^{R}(t)$ --- Spatial stator current error vectors, stator flux and rotor flux respectively, in relation with the active stator R_1 and rotor resistance R_2 (it is supposed that both the stator and rotor resistance are varied simultaneously and by equal values).

$\Delta\vec{i}_1^{X_\sigma}(t)$, $\Delta\vec{\psi}_2^{X_\sigma}(t)$, $\Delta\vec{\psi}_1^{X_\sigma}(t)$ --- Spatial stator current error vectors, stator flux and rotor flux respectively, in relation to the variation of the leakage reactance's $X_\sigma = 2X_{\sigma 1} = 2X_{\sigma 2}$.

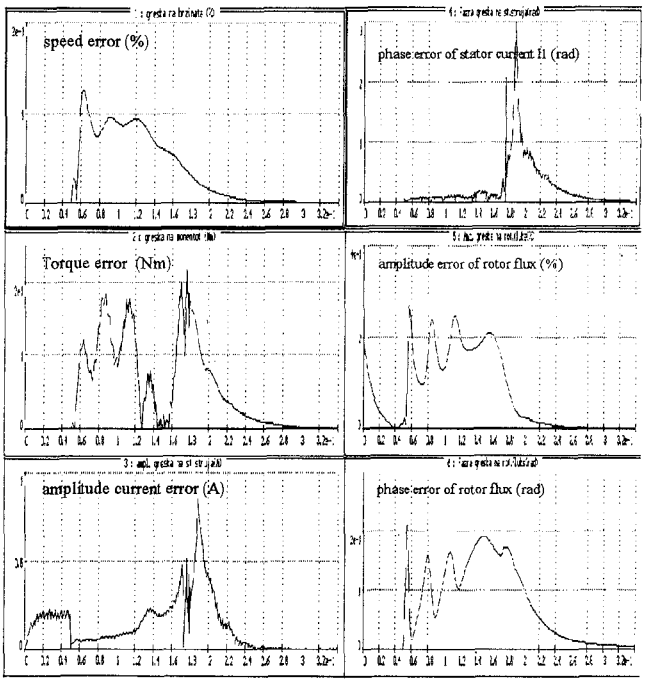
$\Delta\vec{i}_1^{X_m}(t)$, $\Delta\vec{\psi}_2^{X_m}(t)$, $\Delta\vec{\psi}_1^{X_m}(t)$ --- Spatial stator current error vectors, stator flux and rotor flux respectively, in relation to the variation of the magnetizing reactance X_m.

Further on, separately analyzed shall be the influence of the variation of the parameters on the vector control systems.

III ERROR ASSESSMENT IN FIELD ORIENTED CONTROL SYSTEM

On the basis of the functional block scheme represented by Figure 3, which has been adapted to the structural control scheme represented by Fig.1, observation shall be carried out and analysis of the amplitude and phase error of the rotor flux spatial vectors $\vec{\psi}_2$, the stator current $\vec{i}_1$, as well as on the developed torque, i.e. the speed in the dynamic and stationary working mode. The oscillograph (Figure 5) represent the influence of the variation of individual parameters on the speed, the torque, the stator current spatial vector and the rotor flux.

Figure 5.a) represents the errors of the speed, torque, stator current spatial vector $\Delta\vec{i}_1$ and the rotor flux $\Delta\vec{\psi}_2$, at variation of the values of the stator resistance R_1 and rotor resistance R_2 by 15% of the previously defined values. The speed error is $\Delta n = 12\%$ and is the largest at the initial part of the establishment of the nominal speed, while at reaching stationary speed it shows tendency of decreasing all the way down to zero. Similar is the oscillograph of the torque error with maximum error of $\Delta M = 8-10\%$. The amplitude error of the stator current spatial vector is almost insignificant, amounting to 1-2%, as a short time impulse which appears when the stationary speed is reached. This impulse appears at the moment of decreasing of the i_{1q}-component of zero value, and is due to the momentary increase of the angle error of the value of $\approx 3rad(172^{\circ})$. The amplitude and phase errors of the rotor flux spatial error $\vec{\psi}_2$ range from 20% (0.2rad) in the transient mode, to 0.1% in the stationary mode, respectively.



5.a) Variation of the parameter values R_1 and R_2 by 15%.

The oscilograms of Figure 5.b) represent the influence of the variation of the parameters $X_{1\sigma}, X_{2\sigma}$ by

15% of the previously acquisition values. In this case the speed error is biggest in the transient mode (≈30%), while in the stationary mode it shows certain decrease by up to 12%. The range of the torque error is similar: with a value of ≈ 50% in the transient mode, and value of 15% in the stationary mode, which is impermissibly large deviation in relation to the regular values in the regulation system. The amplitude error of the stator current spatial vector show similar characteristics as in the previous case, but in this case the error in the stationary mode does not drop to zero but remains at a constant value of 2% (amplitude error) and 0.99 rad. (56.75°)(phase error). That is the consequence of the stationary errors in the i_{1q}- and i_{1d}- components. The amplitude error of the rotor flux spatial vector $\vec{\psi}_2$ ranges from 50% in the transient mode to ≈18% in the stationary mode. Also significant is the constant phase error in the stationary mode of 0.5 rad (28.66°). This impermissible deviation of the rotor flux spatial vector $\vec{\psi}_2$ is due to the great sensitivity of the i_{1d}- component to the variation of the parameters $X_{1\sigma}, X_{2\sigma}$.

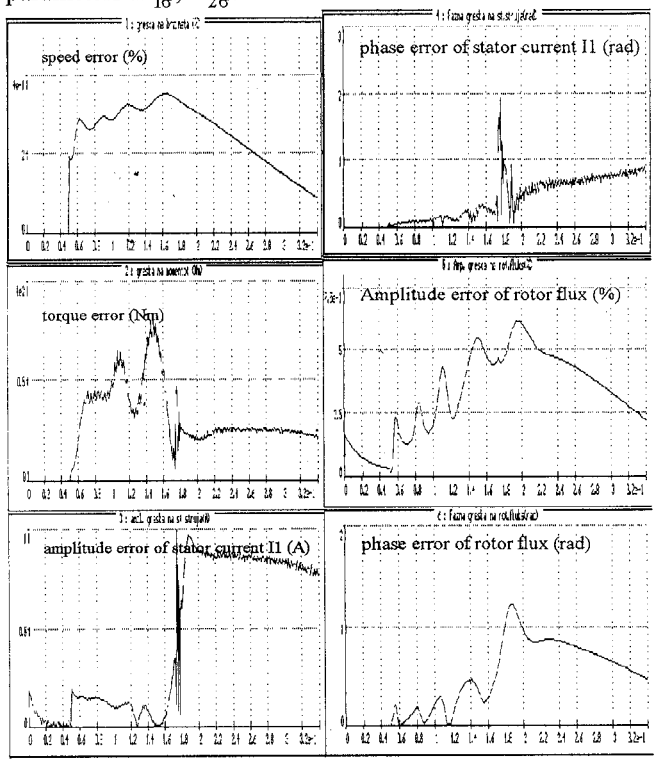


Fig.5.b) Variation of the parameters $X_{1\sigma}, X_{2\sigma}$ by 15%

Figure 5.c) represents the influence of the variation of X_m by 15% of the previously acqusitioned value. The range of the oscilograms is similar to the appropriate ones represented by Fig. 5.a). It is evident here that is the negligibly small stationary error of $\vec{i}_1$ and $\vec{\psi}_2$ of 0.5%.

As a conclusion stands the fact the largest, and at the same time impermissible deviation in the control values and vectors of this vector control system can be notice while varying the values of the leakage reactance $X_{1\sigma}$ and $X_{2\sigma}$.

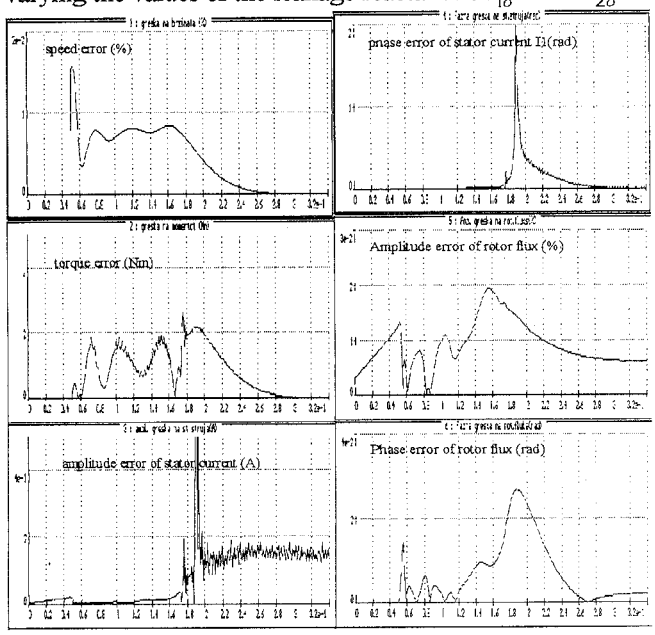


Fig.5.c) Variation of the parameters X_m by 15%

IV. ERROR ASSESSMENT IN DIRECT VECTOR CONTROL SYSTEM

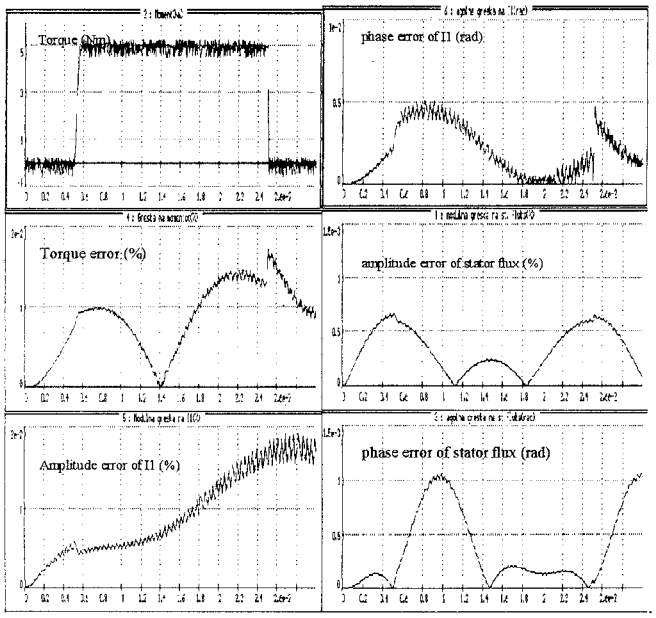
In this segment represented shall be the quantitative-qualitative assessment of the spatial vectors $\vec{i}_1, \vec{\psi}_1$ and the developed electromagnetic torque in the machine. For that purpose the detailed regulation structural block scheme is used represented by Figure 3, adapted to the principal block scheme for assessment of the spatial error vectors already represented by Figure 4.

Figure 6.a) represents the time diagrams of the developed torque in a time span of 30ms, the torque error as well as the amplitude and the phase errors of the spatial vectors $\vec{i}_1$ and at a variation of the parameter values R_1 and R_2 by 15%. The amplitude error of $\vec{i}_1$ is limited to 2%, while the angle error to only 0.28°. The amplitude error of $\vec{\psi}_1$ is even lesser than 0.6%, while the angle are is 0.05°

The maximum error in the developed torque is 1.5%. Evidently this regulation structure maintains the excellent dynamics and shows excellent stability to in the face of variation of the parameters R_1 and R_2. At the same time this is one more prove to the benefit of this control structure.

The oscillograms in Fig.6.b) represent the influence of the variation of the parameters $X_{1\sigma}$ and $X_{2\sigma}$ on the errors of the torque, the stator current spatial vector $\Delta\vec{i}_1$ and the stator flux $\Delta\vec{\psi}_1$. In this case too at a variation of $X_{1\sigma}$

and $X_{2\sigma}$ by 15% significant is the maximum error in the developed torque of 19%, the average stationary amplitude error of $\vec{i}_1$ of 10% and of $\vec{\psi}_1$ of 3%. The angle errors are small: the current is 0.02 rad, while the angle error of the stator flux id 0.01 rad.



a) Variation of the parameter values R_1 and R_2 by 15%.

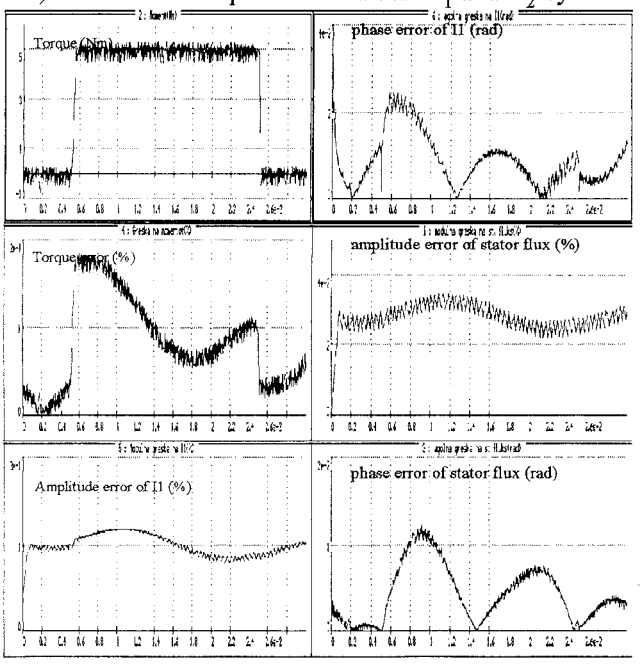


Fig.6.b) Variation of the parameters $X_{1\sigma}$ and $X_{2\sigma}$ by 15%

Figure 6.c) represents the influence of the variation of X_m by 15% of the previously acqusitioned value. The range of the oscilograms represented by Fig. 6.b) is similar to the appropriate ones represented by Fig. 6.a). Noticeable is the negligibly small stationary angle error of the spatial vectors $\vec{i}_1$ and $\vec{\psi}_1$ of 0.03rad and 0.01rad respectively. However, the amplitude errors are big and they are $\Delta\left|\vec{i}_1\right| = 10\%$, $\Delta\left|\vec{\psi}_1\right| = 3\%$. The impermissibly big error appears in the developed electromagnetic torque of 20%.

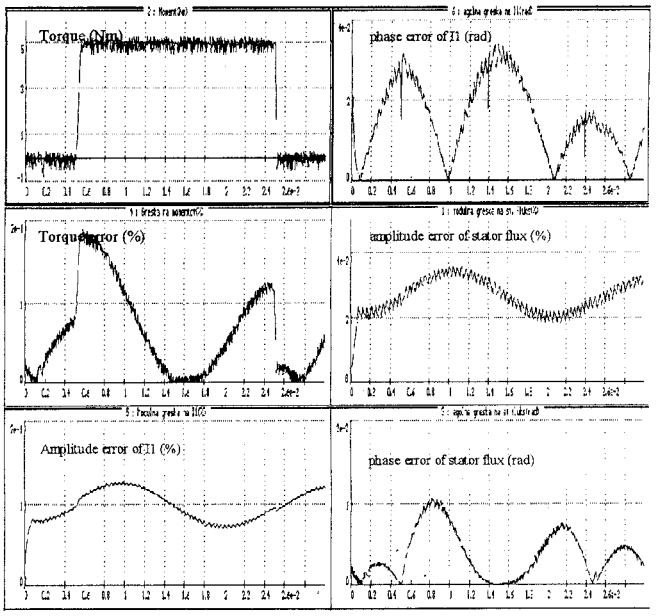


Fig.6.c) Variation of the parameter X_m by 15%

V. CONCLUDING REMARKS

On the basis of the analyzed results it can be concluded that most critical are the cases represented by Fig. 5.b), Fig. 6.b) and Fig.6.c). Also, it can be noticed that the system of direct control of the stator spatial flux vector $\vec{\psi}_1$ shows significant advantages compared to the system oriented on vectors $\vec{i}_1$ and $\vec{\psi}_2$, in relation to the:

- dynamics and
- stability of maintaining the regulation features at variation of the machine parameters.

VI. REFERENCES

[1]. Gerhard Pfaff: Regelung elektrischer antriebe I, R.Oldenbourg Verlag München, Wien 1987.

[2]Walter Zägelain: Drehzahlregelung des Asynchronmotors unter Vervendug eines Beobachters mit geringer Parameter-empindlichkeit, Disertation Erlangen 1984

[3] M.Depenbrock: Directe Selbstregelung (DSR) für hochd-ynamische Drehfeldantriebe mit Strom-richterschaltung, etz Archiv Bd.7 (1985)H.7.

[4] Takahaschi I.,Kanmachi T: Ultra wide speed control with a quick torque responce AC servo by a DSP, EPE Firenze 1991.

[5] M. Jänecke, R.Kremer, G.Steuerwald: Direct self control a novel method of controlling AM in traction application, EPE Aachen 1989, p.75-80.

[6].Ansim- Analogrechner Simulation Version 7.0, Institut für Elektrische Antriebe und Steurungen,Uni-Erlangen,1991

[7].G.Rafajlovski: Simulation verschiedener feldorientierter Regelkonzepte für die Asynchronmaschine, Lehrstuhl für El. Antriebe und Steuerungen der Universität Erlangen 1993, (Unveröffentlich)

[8]. Rafajlovski Goran, Emil Ratz, Manov Dionis, Slobodan Mircevski: Modeling and Simulation of Voltage Inverter Fed Induction Motor with Stator Flux Orientation, 1995 IEEE-IAS ANNUAL MEETING, Orlando Florida U.S.A.

[9]. Rafajlovski Goran, Manov Dionis: Digital simulation of field oriented control using ANSIM program, 1996 IEEE region 8, 8-th Mediterranean Electrotechnical Conference, MELECON '96 Bari ITALY

Effect of Slot-Combination on Electromagnetic Vibration of Squirrel-Cage Induction Motor under Loaded Condition

Isao Hirotsuka*, Kazuo Tsuboi**, Fuminori Ishibashi***
*, ** Department of Electrical Engineering, Chubu University,
1200, Matsumoto-cho, Kasugai-shi, Aichi 487, Japan
Fax: +81-568-51-1141, Phone: +81-568-51-1111
E-Mail: * hiro@solan.chubu.ac.jp, ** tsuboi@solan.chubu.ac.jp
*** Toshiba Co., Asahi-cho, Mie-gun, Mie, 512, Japan
Fax: +81-593-76-6186, Phone: +81-593-76-6113

Abstract — **A squirrel-cage induction motor produces electromagnetic vibration and noise caused by interaction between many harmonic fluxes in air gap. However, the vibration of the motor under loaded condition is not clarified enough. First, this paper theoretically describes effect of slot-combination on electromagnetic force wave of a squirrel-cage induction motor under loaded condition. Next, using the experimental data of the vibration, the characteristics of dominant electromagnetic vibration are studied for the various number of poles and the various number of rotor slots.**

I. Introduction

A three-phase squirrel-cage induction motor (abbr. IM) has been widely used because of lower cost, easier maintenance, and so on. In the air gap of IM, however, there are many harmonic fluxes. The harmonic fluxes produce the electromagnetic vibration causing electromagnetic noise. Recently, reduction of electromagnetic noise and vibration becomes very important from viewpoint of environmental improvement. Although a considerable number of studies have been done on the electromagnetic noise and vibration[1], the vibration of IM under loaded condition is not clarified enough. Since the vibration of IM under loaded condition is affected by loaded machine, the analysis of the vibration is rather difficult work. For reduction of the vibration, the authors have studied the characteristics and the cause of the vibration. From the results, a general equation of main electromagnetic force wave, which produced dominant electromagnetic vibration, was deduced. Using this equation, the cause and force wave mode of dominant electromagnetic vibration were clearly classified. Furthermore, the electromagnetic vibration for various loaded condition was analyzed in detail and classified.

In this paper, the effect of slot-combination on dominant electromagnetic vibration of IM under loaded condition is experimentally studied, and characteristics of the vibration are described. First, general equations are described to express physical concept of electromagnetic force waves, and it is theoretically analyzed that two kinds of radial force waves produce in a same frequency under loaded condition. Next, the characteristics of the force wave for the number of poles and of slots is described. Finally, based on experimental results, some characteristics of electromagnetic vibration are described for the slot-combination of IM.

II. Dominant Electromagnetic Force Wave Under Loaded Condition

The authors have already deduced the radial electromagnetic force wave under loaded condition[2]. In this paper, a general equation of the force waves from the previous paper[2] is shown to express physical concept of the force waves. First, let's consider that there are stator flux *bs* and rotor flux *br* in the air gap of IM. The stator flux *bs* can be expressed as follows.

$$bs \propto Fs \times Ps \times Pr \qquad (1)$$

Where *Fs* is stator magnetomotive force, and *Ps* and *Pr* are stator and rotor permeance, respectively.

The rotor flux *br* can be expressed as follows, as same as *bs*.

$$br \propto Fr \times Ps \times Pr \qquad (2)$$

Where, *Fr* is rotor magnetomotive force.

The sum of (1) and (2) is air gap flux *bg*. Since the radial force wave *fr* in the air gap is proportional

0-7803-3823-5/97/$10.00© 1997 IEEE

to square of bg[1], (3) is given.

$$fr \propto (bs+br)^2$$
$$\propto bs^2 + br^2 + 2bsbr$$
$$\propto frss + frrr + frsr \quad (3)$$

Where $frss = bs^2$, $frrr = br^2$, $frsr = 2bsbr$.

frss is a force wave generated by interaction between stator fluxes. Since main harmonic of *bs* is fundamental wave, the frequency producing *frss* is twice frequency of source voltage. This frequency is very low, so, the *frss* is not considered in this paper.

frrr is a force wave generated by interaction between rotor fluxes. At no-load, as slip s is nearly equal to zero, the fundamental current of rotor is nearly equal to zero[3]. Therefore, the main component of *br* is high order of harmonic rather than the fundamental component. In this case, since *frrr* consists of higher harmonic fluxes, *frrr* can't be a cause of dominant force at no-load. Under loaded condition, as the fundamental rotor current grows up, the fundamental component of *br* becomes main component. In this case, the frequency producing *frrr* is low as same as *frss*, so *frrr* can't be a cause of dominant force, too.

From what has been said in above, *frsr* can be regarded as the main cause of dominant electromagnetic vibration. Substituting *Fs*, *Fr*, *Ps* and *Pr*[1] into *frsr*, following equation is obtained .

$$frsr = \sum_{\nu e'} \sum_{ks} \sum_{kr} \sum_{ks'} \sum_{kr'} frsr\nu e' ks kr ks' kr'$$
$$\times \left[\cos\left[\left\{ \frac{kr-kr'}{p'} n\,(1-s) \right\} \omega t - \left\{ (\nu_e' + ks\,ns + kr\,n) - (p' + ks'ns + kr'n) \right\} \phi \right] + \cos\left[\left\{ \frac{kr+kr'}{p'} n\,(1-s) + 2 \right\} \omega t - \left\{ (\nu_e' + ks\,ns + kr\,n) + (p' + ks'ns + kr'n) \right\} \phi \right] \right] \quad (4)$$

Where ν_e' is the order of low stator magnetomotive force harmonic wave, *ks* and *ks'* are the orders of stator slot permeance and independent integers of each other, *kr* and *kr'* are the orders of rotor slot permeance and independent integers of each other, n_s and n are the number of stator and rotor slot, p' is the number of pole pairs, ω is angular frequency of source voltage, ϕ is angular position on stator expressed by electrical angle and t is time.

In (4), *ks*, *ks'*, *kr* and *kr'* are defined as follows; if neither *ks* nor *kr* are zero, then both *ks'* and *kr'* are zero, or if both *ks* and *kr* are zero, then neither *ks'* nor *kr'* are zero. Defined ν_s' by the order of stator harmonic flux *bs* and ν_r' by the order of rotor harmonic flux *br*, the term in first brackets multiplying ϕ is ν_s', and second is ν_r'.

Table 1 shows the frequencies and the modes of the force waves in (4). In this table, *ks* and *ks'* are substituted $\pm K$, and *kr* and *kr'* for $\pm L$, and each force wave is numbered for following explanation. At no-load, the force wave [I], which is generated by interaction between fundamental stator flux and harmonic rotor flux, are considered. Under loaded condition, in addition to the force wave [I], the force wave [II] is produced, which is generated by interaction between harmonic stator flux and fundamental rotor flux. Table 1 shows that two kinds of these force waves [I] and [II] produce in the same frequency under loaded condition.

Substituting each character expressing harmonics shown in Table 1 by numerically harmonic orders, Table 2 is obtained. In this table, the force waves with smaller mode are shown. In Table 2, one mode, for example "3(1)", means as producing two kinds of force waves [I] and [II] in the same frequency. When two force waves are produced in the same frequency, a vector sum of these force waves provides a resultant force wave in the frequency[4]. Changing load, the amplitudes of each force wave and the phase difference between two force waves varies. The amplitude of resultant force wave does not simply increase or simply decrease against the load. Affected by mechanical resonance and stator magnetomotive force waves, dominant electromagnetic vibration may be produced by force waves besides the force waves shown in Table 2.

Table 1 Dominant electromagnetic force wave.

No.	Vibrating frequency fM [Hz]	Mode M (Order of bs: ν_s') ± (Order of br: ν_r')
①	$\left\{\frac{Kn}{p'}(1-s)-2\right\}f$	[I] : $\lvert(\nu_e')+(p'+Ln_S-Kn)\rvert$
		[II] : $\lvert(\nu_e'+Ln_S-Kn)+(p')\rvert$
②	$\left\{\frac{Kn}{p'}(1-s)\right\}f$	[I] : $\lvert(\nu_e')-(p'\pm Ln_S\mp Kn)\rvert$
		[II] : $\lvert(\nu_e'\pm Ln_S\mp Kn)-(p')\rvert$
③	$\left\{\frac{Kn}{p'}(1-s)+2\right\}f$	[I] : $\lvert(\nu_e')+(p'-Ln_S+Kn)\rvert$
		[II] : $\lvert(\nu_e'-Ln_S+Kn)+(p')\rvert$

Table 2 Dominant electromagnetic force waves caused by lower slot-harmonics.

n	Example of n	for p'= 2 and 3	for p'=2		for p'=3	
		②	①	③	①	③
n_S-9	27					3(1)
n_S-8	28					2(1)
n_S-7	29			3(1)		1(1)
n_S-6	30			2(1)		
n_S-5	31			1(1)		1(1)
n_S-4	32					2(1) 2(2)
n_S-3	33	3(1)		1(1) 2(2)		3(1) 3(3)
n_S-2	34	2(1)		2(1) 2(3)		2(2)
n_S-1	35	1(1) 2(2) 3(3)		3(1) 2(2) 1(3)		3(3)
n_S	36					
n_S+1	37	1(1) 2(2) 3(3)	3(1) 2(2) 1(3)		3(3)	
n_S+2	38	2(1)	2(1) 2(3)		2(2)	
n_S+3	39	3(1)	1(1) 2(2)		3(1) 3(3)	
n_S+4	40				2(1) 2(2)	
n_S+5	41		1(1)		1(1)	
n_S+6	42		2(1)			
n_S+7	43		3(1)		1(1)	
n_S+8	44				2(1)	
n_S+9	45				3(1)	

NOTE: For example, "3(1)" means that there is much possibility producing dominant electromagnetic force waves [I] and [II] with $M=3$ and $L=K=1$.

III. Test Motors And Experimental Apparatuses

Table 3 shows the specification of the test motors. The motors are 4-pole and 6-pole stators with the number of 36 slots, and 19 kinds of rotors with the same dimension but different the number of slots. All stators and rotors are not skewed. In Table 3, natural frequencies measured at room temperature are shown for each test motor. These natural frequencies may be changed more or less, because the temperature rises under loaded condition.

Figure 1 shows the arrangement of experimental apparatuses. IM is set on the common base with the resilient rubber base. Applied voltage is sine wave and 60Hz. Loaded condition is defined as "load factor" Lp, which at no-load $Lp=0$ percent and at full-load $Lp=100$ percent. In case of $Lp=0$ percent, because IM is connected to the load set, load condition of IM is not precisely no-load. However, as the results of many preparatory experiments, the vibration at $Lp=0$ percent has been verified to agree

Table 3 Specification of the test machine.

The number of phases	3	
The number of poles	4	6
Rated output	1.5 kW	0.75 kW
Rated Voltage	200 V	
Rated Frequency	60 Hz	
The number of stator slots n_S	36	
The number of rotor slots n	27 ~ 45	
Skew	No-skew	
Natural frequencies	625, 1700, 3300, 4000 Hz	650, 1550, 1625, 3150, 3975 Hz

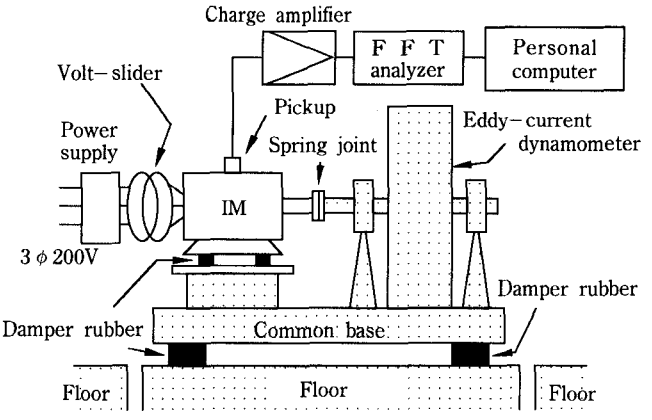


Fig. 1. Arrangement of experimental apparatuses.

with the data measured on IM alone. Acceleration pickup sets on the top on the frame of IM. Vibratory acceleration fa, frequency fv and over all value Fva up to 10kHz of vibration detected by the pickup are analyzed by the FFT analyzer and transferred to the personal computer. Since fv varies for Lp, the fv is represented by a multiple of source frequency f at $s = 0$.

IV. Experimental Results

Figure 2 shows the analyzed data of vibration at $p'=2$, $n=34$. As shown in this figure, increasing Lp, fv of each vibration is decreased. Because of the electromagnetic force wave and mechanical resonance, fa varies with Lp. In Fig. 2, at $Lp=0$ percent, main cause of $17.0f$ component is a force wave with mode $M=2$. At $Lp=100$ percent, fa of $17.0f$ component and $19.0f$ component are increased by force wave [II] in Table 1, which is generated by interaction between a harmonic stator flux and a fundamental rotor flux. As fa of dominant vibration is increased, Fva is increased.

Figure 3 and 4 show the characteristics of dominant vibration for n with the stator of $p'=2$ and $p'=3$. In each figure, (a) shows at $Lp=0$ percent,

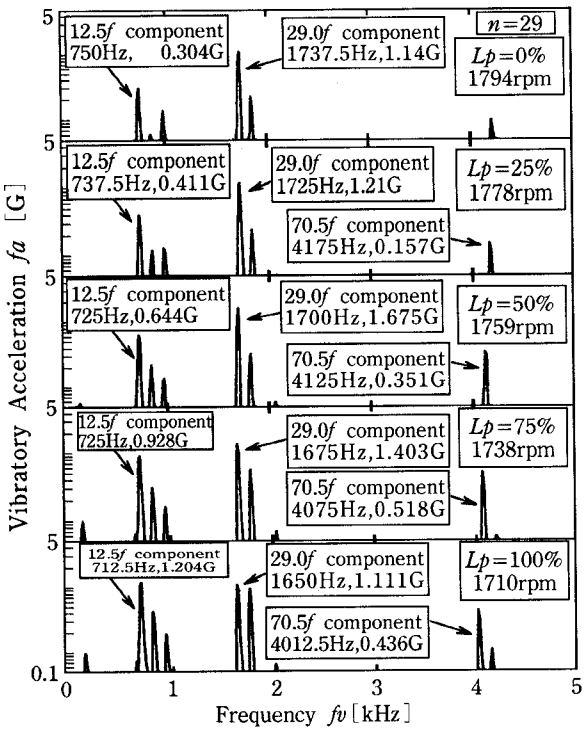


Fig. 2. Measured electromagnetic vibration.

(b) shows at Lp=50 percent and (c) shows at Lp=100 percent. In these figures, the horizontal axis is n, and the virtual axis is fv and f_M. The mark "○" means as producing dominant vibration produces, the size of "○" indicates magnitude of fa and leaned lines indicate f_M.

From Fig. 3, for p'=2, the following results are obtained:

(1) Combined rotor, of which slots n=28, 32, 40 or 44; that is, n is a multiple of $2p'$, IM does not tend to produce dominant vibration.

(2) Combined rotor, of which slots n=30, 34, 38 or 42; that is, n is a multiple of p' except $2p'$, IM tends to produce dominant vibration with K=1, but IM does not tend to produce dominant vibration with $K \geqq 2$.

It is clear that the above characteristics of dominant vibrations agrees well with Table 2, which shows the force waves with the smaller mode.

From Fig. 4, for p'=3, the following results are obtained:

(3) Dominant vibration is produced by the force wave with K=1 for any rotors. This characteristics is different from the case of p'=2. These dominant vibrations may be produced by not only the force waves in Table 2 but also other force waves causing, for example, lower harmonics of stator magnetomotive force, because f_M of these force waves correspond to the natural frequency 650Hz of the test motor.

Example data with influence of mechanical resonance is shown in Fig. 5. This figure shows two kinds of experimental data; that is, one is a data that the frequency f of source voltage is kept constant while changing Lp, and other is a data that the fv is kept constant at fv=4230Hz by changed f while changing Lp. From the result of "fv : constant", it is clear that the force wave causing the fv=4230Hz component is simply increasing with increasing Lp, if influence of mechanical resonance keep constant. From the other result of "f : constant", fa is increases with Lp because of affected by natural frequency at 4100Hz. Increasing Lp further, fa is decreased because fv leaves away from this natural frequency. When a force wave except one shown in Table 2 produces near the natural frequency of the motor, the force wave may become main cause of dominant vibration, due to mechanical resonance.

(4) Combined rotor, of which slots is a multiple of $2p'$, IM does not tend to produce especially dominant vibration with $K \geqq 2$.

In Fig. 3 and 4, some dominant vibrations appear at the frequency different from f_M. The details of the cause of these vibrations will be described an another paper.

Figure 6 shows overall value of vibratory acceleration up to 10kHz; Fva for various rotor. In most rotor, Fva is increased. This increase is due to the increase of many vibrations. However, for a examples, at p'=2, n=44, Fva is decreased. The decrease has been confirmed due to mechanical resonance[6] as same as mentioned above. In case of combined rotor, of which slots is a multiple of $2p'$, with stator of p'=2 or a multiple of p' with stator of p'=3, Fva tends to be relatively small. However, increasing ratio of Fva for Lp is various for n. Almost increasing ratio of Fva of p'=3 is smaller than the ratio on p'=2.

V. Conclusion

In this paper, some experimental results are shown due to provide the characteristics of electromagnetic vibration for various slot-combination.

In this paper, the follows are confirmed.

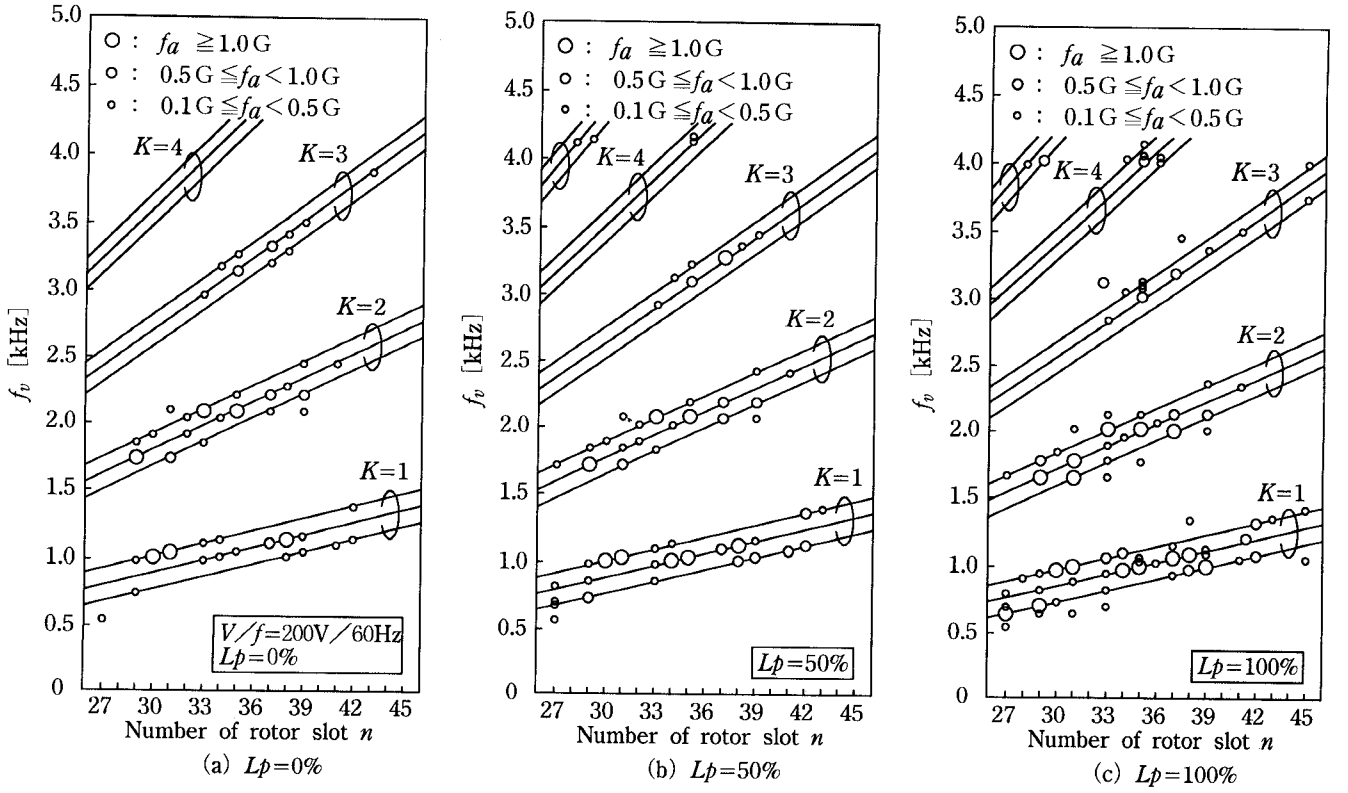


Fig. 3. Features of the electromagnetic vibration vs. rotor slot ($p'=2$) .

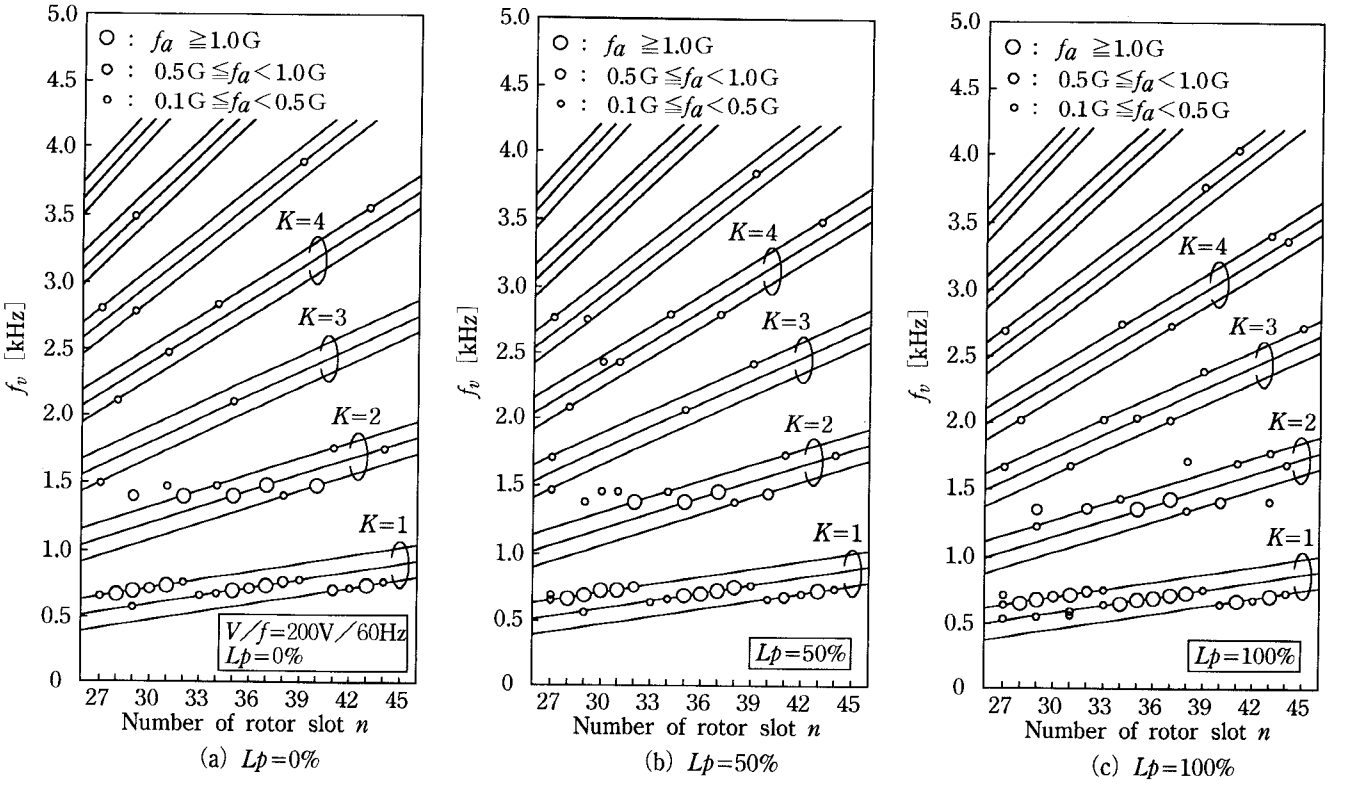


Fig. 4. Features of the electromagnetic vibration vs. rotor slot ($p'=3$) .

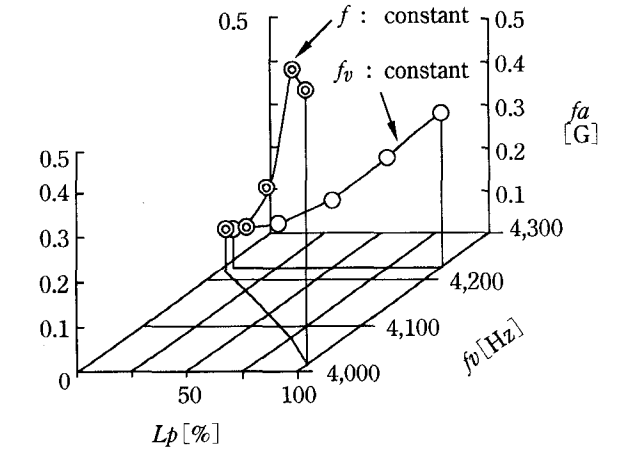


Fig. 5. Measured electromagnetic vibration vs. load factor Lp.(n=29, fv=70.5f component)

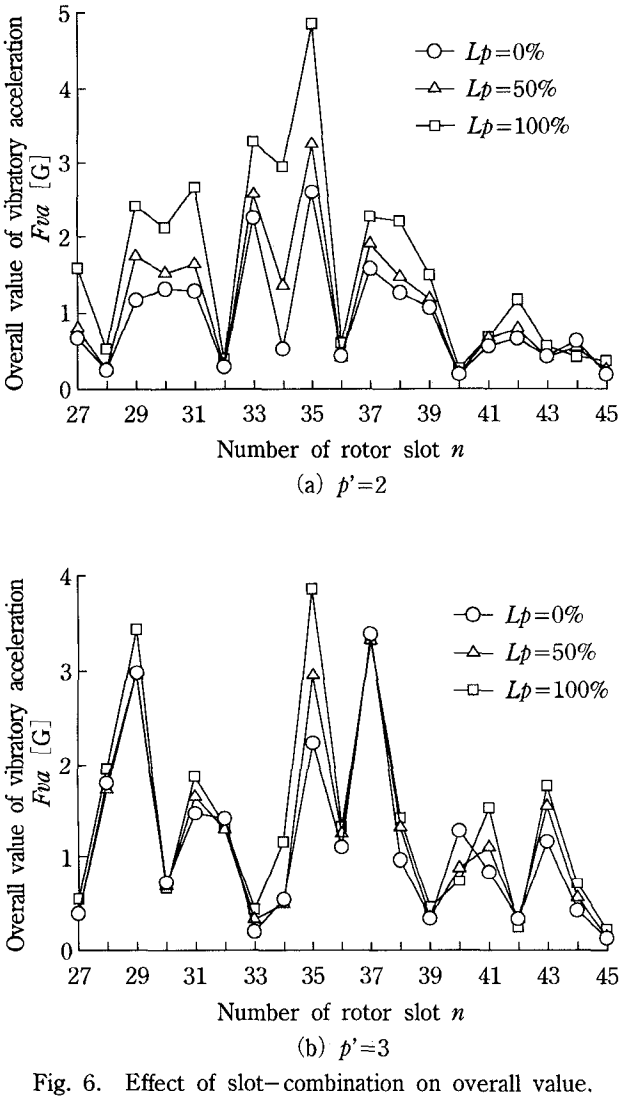


Fig. 6. Effect of slot-combination on overall value.

Combined rotor, of which the number of slots is a multiple of the number of poles, with stator of p'=2, IM does not tend to producing dominant vibration. Combined rotor, of which the number of slots is a multiple of the number of pole pairs except above rotors, IM does not tend to producing dominant vibration, because the force waves with smaller mode is not caused by more than 2nd slot harmonics. Combined rotor, of which the number of slots is a multiple of number of pole pairs, with stator of p'=3, IM does not tend to producing dominant vibration. However, on the test motor, dominant vibration is caused by 1st slot harmonics and affected by mechanical resonance.

As the results, with p'=2, it is cleared that *Fva* is relatively small in the case of that rotor slot is a multiple of number of poles. With p'=3, it is cleared that *Fva* is relatively small in the case of that rotor slot is a multiple of number of pole pairs. The reason is that the force waves of smaller mode do not produce, and it is qualitatively cleared based on the theory in previous paper. Hereafter, we will perform an analysis these data in detail.

ACKNOWLEDGMENT

The authors' special thanks are due to graduate research workers of the Electrical Engineering program of the Department of Technology of Chubu University for their assistance in experimental output and data.

REFERENCES

[1] For example; S.J.Yang, "Low-noise electrical motors", Clarendon Press, Oxford, 1981.

[2] K.Tsuboi, I.Hirotsuka, F.Ishibashi, "Causes and Characteristics of the Electromagnetic Vibration of A Squirrel Cage Induction Motor under Loaded Condition", The Trans. of I.E.E., Japan, Vol.117-D, No. 2, Feb., 1997.

[3] H.Sekino, C.Usuda, S.Kajitani, "Effect of Slot Combination and Skew on Magnetic Noise of Squirrel Cage Induction Motors", Tech. Rep. of Mitsubishi Elec., Vol. 31, No. 4, p44, 1957.

[4] I.Hirotsuka, K.Tsuboi, Y.Nakamura, F.Ishibashi, "A Study of the Electromagnetic Vibration of a Squirrel-Cage Induction Motor Caused by Time-Harmonic Voltages", The Trans. of I.E.E., Japan, Vol.113-D, No.3, Mar., 1993.

[5] I.Hirotsuka, K.Tsuboi, "Experimental Study on the Electromagnetic Vibration Caused by the slot Combination of a Squirrel-Cage Induction Motor", The Trans. of I.E.E., Japan, Vol. 109-D, No. 5, May, 1989.

[6] K.Muromachi, I.Hirotsuka, K.Tsuboi, F.Ishibashi. Record of 1995 Tokai-Section Joint Conference of the Six Institutes of Electrical and Related Engineers, No.224.

Analysis and Computer Simulation of Cycloconverter Operation Based on the Energy Equation.

I. Katz; M.A.Slonim.

Department of Electrical and Computer Engineering, Ben-Gurion University of the Negev,

P.O.Box 653, Beer-Sheva, 84105, Israel;

phone: 972-07-6461507; fax: 972-07-6472949;

e-mail: inna@newton.bgu.ac.il; Slonim@bguee.bgu.ac.il

Abstract - **A new method for the analysis and computer simulation of cycloconverters is proposed. Lagrange equations are used to obtain differential equations governing cycloconverter processes. These differential equations are derived and solved for each interval of the period of cycloconverter operation. The solutions obtained are sewed together and a difference equation governing the whole period of cycloconverter operation is derived. A computer program realizing these equations has been developed.**

The program allows us to obtain the instantaneous voltages and currents for different cycloconverter topologies, taking into consideration their parameters, number of phases and control of firing angles. In the paper appear examples of applications of the program.

I. INTRODUCTION

AC-AC power converters or cycloconverters are defined as devices converting the input AC voltage U_{in} of frequency f_{in} in the output AC voltage U_{out} of frequency f_{out} where $f_{in} \neq f_{out}$. In this article generic topology cycloconverter is discussed. The analysis treats the ideal multipoles Π that contain only ideal elements - ideal valves and ideal transformers (Fig.1).

For the cycloconverter the normal operation in steady-state and transient conditions is determined by periodical ignitions and extinctions of valves (transistors, SCRs, ect.). Particular sequence of ignitions and extinctions during half period of output e.m.f frequency composes repetition interval. Therefore it is possible to analyze the entire process by analyzing one repetition interval. In the following, such a basic situation will be analyzed. On every time segment, there is uninterrupted output current for all schemes.

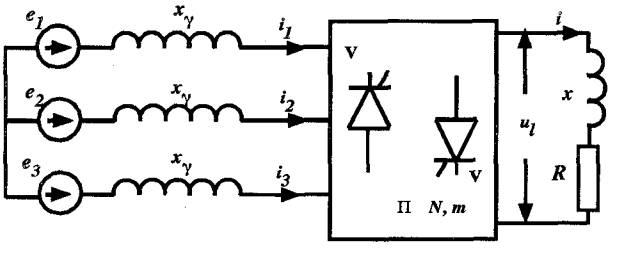


Fig.1. General structure of cycloconverter as multipole Π.

II. THE ANALYZING MODEL AND ITS OPERATING CONDITIONS.

The cycloconverter contains three phase or single phase input transformer, the ideal multipoles Π and single phase output (Fig.1).

The applied input voltage on the first side of the ideal transformer are labeled e_k $(k=1,2,3)$. Because, the phase voltages are symmetrical, then

$$e_k = E_m \cos(\Theta - (k-1)\,2\pi/3) \qquad (1)$$

where $k = 1, 2, 3$, for three phase input,

E_m is the amplitude of the phase voltage, $\Theta=\omega t=2\pi f_{in} t$.

In each phase there are phase current i_k and inductive reactance x_γ. The reactances x_γ is calculated at the supply voltage frequency f_{in}.

On the primary side of transformer, the following equation will be correct for the phase current i_k to all types of cycloconverters

$$i_1+i_2+i_3=0, \qquad (2)$$

The equations (1) and (2) are obvious for three phase system. In the case of a single phase system transformer has only one winding and correspondingly only one voltage e_1 and one current i_1.

The output of the cycloconverter is the AC circuit that includes an active resistance r and inductive reactance x, calculated at the supply frequency f_{in}. Through the resistor r and reactance x the single phase alternating current i flows. Each half wave of the current i is created by particular group of valves which conducts the current in one direction, correspondingly positive and/or negative one.

The multipole Π contains two anti parallel converters and will be called an *"m, N"* phase cycloconverter, if *"m"* is possible number of ignitions of the valves in the converter during one period of the input frequency and *"N"* is total number of valve's ignitions during half period of the output frequency.

In the steady state there are *"N"* time segments during half period of the output current i, where time segment (TS) is one between two consequent ignitions of valves. This sequence of *"N"* TS is called repetition interval (RI). During the RI all possible ignitions and/or extinctions of the valves of one particular converter occur.

It is convenient to choose the RI in such a manner that it starts at instant of appearing pulse across the grid of the first valve in the particular converter conducting current to one direction and stops at instant of appearing pulse across the grid of the first valve in the opposite converter.

On can prove that duration of the RI equal to

$\Delta=(N-q)*2\pi/m+\pi$, where $q=1,2,3$ depend on firing sequence.

Each TS contains commutation and intercommutation modes. It is assumed that during the intercommutation interval there is only one and during the commutation interval there are two independent current loops in the system. After every ignitions of valves commutation mode is begun. It is finished with the extinction of valve conducted before the ignition. After every extinction, an intercommutation mode is begun. It is finished with the ignition of a next valve. The processes analyzed are those where the commutation interval is less than the time between two consequent ignitions. The time segment also depends on the firing angles α_n of the valves $(1<n\leq N)$.

Based on the formulation of these problems, there may be found the general characteristics of converters, such as: the phase AC current and voltage on the first side of the transformer and/or load current and voltage. All specific characteristics such as currents and voltages of valves and the phase current and voltage on the second side of the transformer, may be found as linear combinations of the general characteristics.

In this article the energy Lagrange equations will be used to derive the sets of equations governing processes in the cycloconverters. The Lagrange equations allow to analyze the processes and obtain solution to the cycloconverter with arbitrary topology which is called above as multipole Π (Fig.1). The general equations will be obtained and solved.

III. ENERGY EQUATION OF THE CYCLOCONVERTER

For the ideal converter Π, the energy of the sources are equated to the energy of the elements and dissipative energy of load and the terms are arranged as follows:

$$\sum_{k=1}^{3} i_k\psi_k = \frac{1}{2\omega}(x\,i^2+x_\gamma \sum_{k=1}^{3} i_k^2)+r\,i^2/2 \qquad (3)$$

here $\psi_k = \int e_k\,dt$ is the magnetic flux of the phase k.

The right-hand part of the equation (3) is the sum of electrokinetic energy of the elements labeled T and dissipative energy labeled D, the left-hand part is the energy of sources T_e. Using Lagrange equation of the second kind

$$(d/dt)(\partial T_e/\partial q'_\nu) = (d/dt)(\partial T/\partial q'_\nu)+\partial D/\partial q'_\nu \qquad (4)$$

here ν is index number of independent loop, q_ν is a generalized coordinate for the loop ν, which is equal to the electrical charge in the loop; i.e. $q'_\nu = i_\nu$ where i_ν is the current in loop ν.

Using (3) and (4)

$$\sum_{k=1}^{3} (\partial i_k/\partial i_\nu)e_k = x_\gamma \Sigma\,[(d/d\Theta)\,i_k(\partial i_k/\partial i_\nu)]+x\,(d/d\Theta)\,i(\partial i/\partial i_\nu)+r\,i(\partial i/\partial i_\nu) \qquad (5)$$

where ψ_k is flux linkage of the phase number k; i_ν is the current in independent loop number ν.

Equation (5) is the Lagrange equation for the analysis of the electromagnetic process in cycloconverters. It is general analytical equation described of the cycloconverter. It does not depend on the cycloconverter scheme.

IV. THE INTERCOMMUTATION INTERVAL EQUATIONS.

Duration of the intercommutation interval of the TS number *"n+1"* of the RI number *"l+1"* is

$$\Theta(\gamma_n)=\tau+l^*\Delta+(2n-1)^*\pi/m+\alpha_n+\gamma_n\le\Theta\le$$
$$\le\tau+l^*\Delta+(2n+1)^*\pi/m+\alpha_{n+1}=\Theta(n+1)$$

Here α_n is the firing angle of the valve (the ignition of the valve that determines the beginning of the TS); α_{n+1} is the firing angle of the next valve (the ignition of this valve determines the end of the TS); τ is the phase shift between the phase voltage e_1 and the first time segment of the output e.m.f.; γ_n is the commutation angle for the TS *"n+1"*.

During intercommutation interval there is only one independent current loop in the cycloconverter. The current loop includes the load current i, which is uninterrupted. That is why it is convenient to choose the load current i as the current in independent loop number ν, i_ν. In this case equation (5) is in the form:

$$\sum_{k=1}^{3}(\partial i_{k,n+1}/\partial i)e_k = x_\gamma\Sigma\,(di/d\Theta)\,(i_{k,n+1}\,\partial i_{k,n+1}/\partial i)$$
$$+\,x\,(di/d\Theta)+r\,i \qquad (6)$$

The left-hand part of the equation (6) is the e.m.f. on the cycloconverter poles. For all cycloconverters, for TS number *"n+1"* of the RI number *"l+1"* this voltage may be written in the form

$$e_{out}=E_{cm}^*\cos(\Theta-\tau-l^*\Delta-n^*2\pi/m) \qquad (7)$$

where E_{cm} is the amplitude of the e.m.f. of the cycloconverter output.

After developing one can obtain

$$i_{k,n+1}=(2/3)(E_{cm}/E_m)^*\cos(\tau+l^*\Delta+n^*2\pi/m)^*i,$$
$$k=1,2,3 \qquad (8)$$

Substituting (7) and (8) in equation (6) there results:

$$x_\Sigma(di/d\Theta)+r\,i=E_{cm}^*\cos(\Theta-\tau-l^*\Delta--n^*2\pi/m) \qquad (9)$$

where $(2/3)(E_m/E_{cm})^2=a^2$ and

$$x_\Sigma=a^2x_\gamma+x$$

V. THE COMMUTATION INTERVAL EQUATIONS.

Duration the commutation interval

$$\Theta(n)=\tau+l^*\Delta+(2n-1)^*\pi/m+\alpha_n\le\Theta\le$$
$$\le\tau+l^*\Delta+(2n-1)^*\pi/m+\alpha_n+\gamma_n=\Theta(\gamma_n)$$

During the commutation interval there are two independent loops in the converter II. The first loop is the loop with the current i. This loop conducts during the intercommutation interval which is before the commutation which begins at time $\Theta(n)$. The second loop arises at time $\Theta(n)$ and includes the ignition circuits. The current in this loop is j, which is derivative of a second generalization coordinate. Using the superposition principle, each phase current i_k may be written:

$$i_k=c'i+c''j \qquad (10)$$

where c' and c'' are coefficients.

Founding the coefficients and using equation (8) on can obtain set equations

$$x_\gamma a^2\sin^2(\pi/m)(di/d\Theta)-2x_\gamma a^2\sin^2(\pi/m)(dj/d\Theta)=$$
$$=E_{cm}^*(1/2)\,[\cos(\Theta-\tau-l^*\Delta-(n-1)^*2\pi/m)-$$
$$\cos(\Theta-\tau-l^*\Delta-n^*2\pi/m)] \qquad (11)$$
$$x_\gamma a^2(di/d\Theta)-2x_\gamma a^2\sin^2(\pi/m)(dj/d\Theta)+x(di/d\Theta)+ri=$$
$$=E_{cm}^*\cos(\Theta-\tau-l^*\Delta-(n-1)^*2\pi/m);$$

After transposing the equation for commutation interval of every time segment *"n+1"* of the RI *"l+1"* is found

$$x_{\Sigma\gamma}(di/d\Theta)+r\,i=E_{cm}^*\cos(\Theta-\tau-l^*\Delta-$$
$$-(2n-1)^*\pi/m)^*\cos(\pi/m) \qquad (12)$$

where $x_{\Sigma\gamma}=x_\gamma a^2*\cos^2(\pi/m)+x$

The equations (9) and (12) are the general cycloconverter equation for every intercommutation interval of TS *"n+1"*. This equation is independent on the scheme of the cycloconverter and only depends on fire sequence.

VI. COMPUTER SIMULATION OF CYCLOCONVERTER OPERATION

Equations (9) and (12) are solved for each interval of the period of cycloconverter operation and a difference equation for TS is developed.

$$i(n+1)=[i(n)-I_{m\gamma}\cos(\alpha_n-\Psi_\gamma)] *e^{-[(r/x_{\Sigma\gamma})\gamma_n+(r/x_\Sigma)(\alpha_{n+1}-\alpha_n-\gamma_n+2\pi/m)]} +[I_{m\gamma}\cos(\alpha_n+\gamma_n-\Psi_\gamma)-I_m\cos(\alpha_n+\gamma_n-\pi/m-\Psi_\Sigma)]* e^{-(r/x_\Sigma)(\alpha_{n+1}-\alpha_n-\gamma_n+2\pi/m)}+I_m\cos(\alpha_{n+1}+\pi/m-\Psi_\Sigma) \quad (13)$$

where $\Psi_\Sigma=\arctan x_\Sigma/r$; $I_m=E_{cm}/\sqrt{x_\Sigma^2+r^2}$;

$\Psi_\gamma=\arctan x_{\Sigma\gamma}/r$ and

$I_{m\gamma}=E_{cm}*\cos(\pi/m)/\sqrt{x_{\Sigma\gamma}^2+r^2}$

Using (13) a difference equation governing the whole RI of cycloconverter operation is derived. Thus the initial conditions for each interval of the cycloconverter operation are found. Using these conditions the general expressions for the instantaneous current of the cycloconverter are obtained.

The program to calculate the current has been developed. The program allows us to obtain the instantaneous currents for different cycloconverter topologies, taking into consideration their parameters, number of phases and control of firing angles.

Example of computer simulation of the current and voltage of three phase cycloconverter is presented in Fig. 2. Control method is $\alpha_n=\alpha_1+(\alpha_1/N)*(n-1)$. The simulation allows us to obtain the voltage and current value at any instant of cycloconverter operation and the current waveform for a cycloconverter with any topology. As we see it, the proposed analytical method significantly simplifies the solution of the problem. It allows one to obtain an exact analytical solutions of systems which include a cycloconverter.

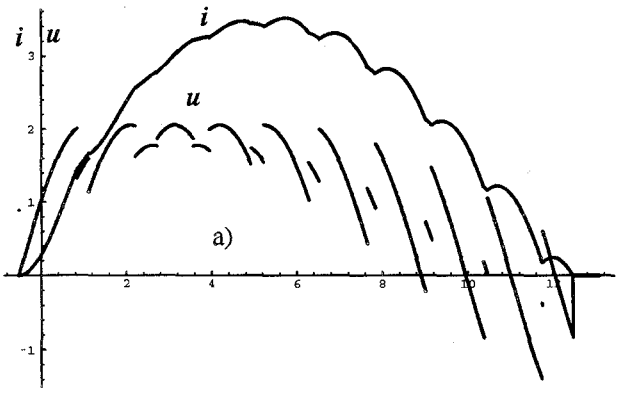


Fig.2 Cycloconverter current and voltage waveforms.

Steady-State Performance Analysis of Shaft Generator Systems

Shoji Nishikata, Akihiro Odaka, and Yohei Koishikawa
Tokyo Denki University
2-2 Kanda-Nishikicho, Chiyoda-ku, Tokyo, 101 JAPAN
Fax: +81-3-5280-3573, Tel: +81-3-5280-3313
E-mail: west@cck.dendai.ac.jp

Abstract **- Steady-state performance of a main-engine-driven shaft generator system, which is used in a ship to feed sufficient power to the electric apparatus, is discussed. A set of system equations, by which the total harmonic distortion of the output voltage, for example, can be estimated, is derived first, and the steady-state performance is analyzed in some detail. It is shown that if the reactance of ac reactor located in the output-side of the inverter is small, a wide operating range is obtained. The effects of leading angle of commutation of the inverter on the system performance are also clarified.**

I. INTRODUCTION

A shaft generator system feeds sufficient power to the electric apparatus in a ship by using a part of the power produced by the main engine [1]. This type of power generating system has been used since 60's mainly in large ships because it can reduce fuel and operation costs [2]. When the ship makes a voyage, the speed of the main engine can vary within a wide range. So, an inverter is needed to produce power with constant voltage and frequency. A typical configuration for a shaft generator system is shown in Fig. 1. As in the figure, the system consists of a shaft generator driven by the main engine, a thyristor rectifier, a current-source thyristor inverter, an AC reactor to reduce the harmonic components of the output voltage, and a synchronous condenser to provide reactive power for loads and for commutation of inverter thyristors. The output voltage and frequency are kept to be constant with controlling the field current and the speed, respectively, of the synchronous condenser. Also, the output voltage of the rectifier is regulated almost constant for a wide range of generator speed with the field current of the shaft generator and/or the firing angle of the thyristor rectifier.

The performance characteristics of the shaft generator system have been discussed little, and a detailed analysis of the system is presented in this paper. The system equations are given first, and the effects of system parameters on the steady-state performances are clarified.

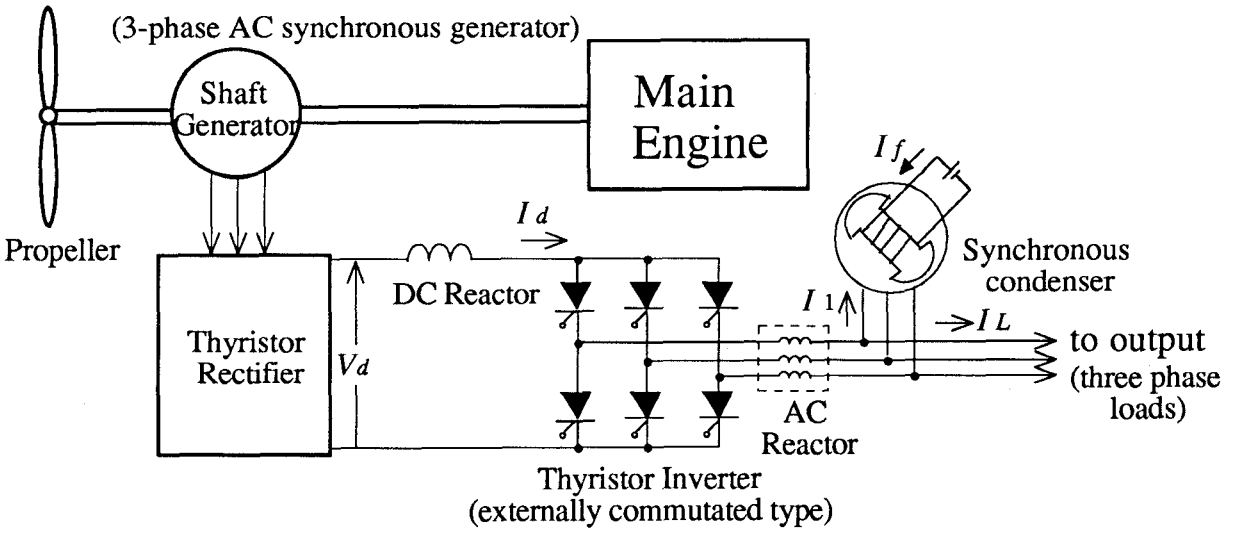


Fig. 1. Shaft Generator System.

II. SYSTEM EQUATIONS

Fig. 2 gives an equivalent circuit for the system shown in Fig. 1. The equivalent circuit for synchronous condenser is obtained by referring to [3]. In this figure, the resistances included in the system are neglected for the sake of convenience. We assume here the output terminal phase voltages e_U, e_V, and e_W without jumping and sinking due to commutation of thyristors to be sinusoidal. These voltage equations can be written:

$$\begin{aligned} e_U &= \sqrt{2}\, V_p \sin(\theta - \gamma + \pi/6) \\ e_V &= \sqrt{2}\, V_p \sin(\theta - \gamma - \pi/2) \\ e_W &= \sqrt{2}\, V_p \sin(\theta - \gamma + 5\pi/6) \end{aligned} \tag{1}$$

where, γ is leading angle of commutation, and the origin of θ is chosen to be the instant of the commutation from thyristor WP to UP.

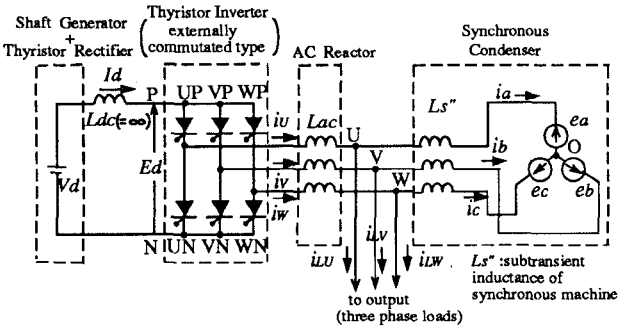


Fig. 2. Equivalent circuit of the system.

Output currents supplied to the load i_{LU}, i_{LV}, and i_{LW} are assumed to be sinusoidal because most loads are of inductive.

$$\begin{aligned} i_{LU} &= \sqrt{2}\, I_L \sin(\theta - \gamma + \pi/6 - \varphi) \\ i_{LV} &= \sqrt{2}\, I_L \sin(\theta - \gamma - \pi/2 - \varphi) \\ i_{LW} &= \sqrt{2}\, I_L \sin(\theta - \gamma + 5\pi/6 - \varphi) \end{aligned} \tag{2}$$

where, φ is lagging angle determined by the load.

In the conducting periods of inverter except the commutation periods in which two thyristors are conducting concurrently, since inverter output current can be regarded as constant, e_U, for example, can be obtained:

$$e_U = L_s'' \frac{d i_a}{d t} + e_a = L_s'' \frac{d(i_U - i_{LU})}{d t} + e_a = -L_s'' \frac{d i_{LU}}{d t} + e_a \tag{3}$$

Here, e_a is armature induced voltage of the synchronous condenser and can be assumed to be sinusoidal provided that the condenser has damper windings.

Therefore, we have equation for e_a as follows:

$$\begin{aligned} e_a &= e_U + L_s'' \frac{d i_{LU}}{d t} \\ &= \sqrt{2}\, V_p \sin(\theta - \gamma + \pi/6) + \sqrt{2}\, I_L X_s'' \cos(\theta - \gamma + \pi/6 - \varphi) \\ &\equiv \sqrt{2}\, V_i \sin(\theta - \gamma + \pi/6 + \varepsilon) \end{aligned} \tag{4}$$

$$V_i = \sqrt{(V_p + I_L X_s'' \sin\varphi)^2 + (I_L X_s'' \cos\varphi)^2} \tag{5}$$

$$\varepsilon = \tan^{-1} \frac{I_L X_s'' \cos\varphi}{V_p + I_L X_s'' \sin\varphi} \tag{6}$$

where, $X_s'' = \omega \cdot L_s''$, ω is angular velocity of θ.

Similarly, we have the equations for e_b and e_c :

$$e_b = e_V + L_s'' \frac{d i_{LV}}{d t} = \sqrt{2}\, V_i \sin(\theta - \gamma - \pi/2 + \varepsilon) \tag{7}$$

$$e_c = e_W + L_s'' \frac{d i_{LW}}{d t} = \sqrt{2}\, V_i \sin(\theta - \gamma + 5\pi/6 + \varepsilon) \tag{8}$$

From the preceding equations and the fact that the synchronous condenser does not produce any torque, we have a phasor diagram from which the relationship among the voltages and fundamental components of the currents can be clarified.

Fig. 3 shows such a phasor diagram, in which '1' denotes fundamental component. It should be noted that I_{a1} leads E_a by 90° because of no output power of synchronous condenser. Also, RMS value of $(\sqrt{6}/\pi) \cdot I_d$ for $\dot{I}_{U1}$ is derived from the trapezoidal waveform of inverter output currents [3].

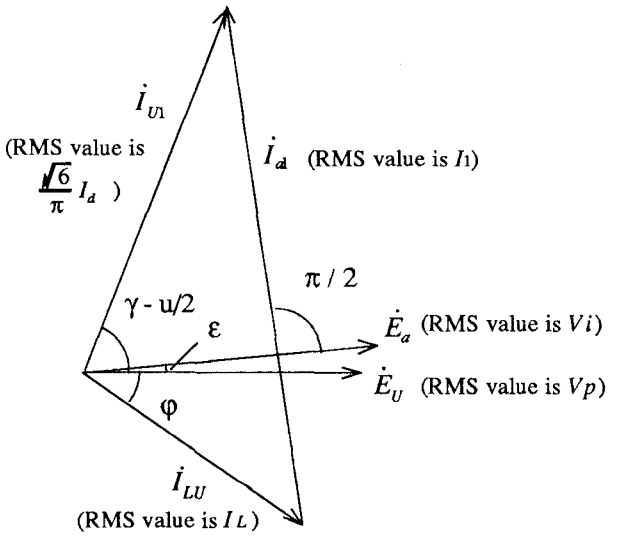


Fig. 3. Phasor diagram.

From Fig. 3, RMS value of the armature current in the synchronous condenser is

$$I_1 = \sqrt{\left(\frac{\sqrt{6}}{\pi} I_d\right)^2 + I_L^2 - 2\frac{\sqrt{6}}{\pi} I_d I_L \cos(\gamma + \varphi - u/2)} \quad (9)$$

where, u is angle of overlap of inverter output currents.

On the other hand, on referring to Fig. 2 voltage difference between points P and O e_{PO} and current equations in the period of overlap at the commutation from WP to UP, for example, are:

$$e_{PO} = L_{ac}\frac{di_U}{dt} + L_s''\frac{di_a}{dt} + e_a \quad (10)$$

$$e_{PO} = L_{ac}\frac{di_W}{dt} + L_s''\frac{di_c}{dt} + e_c \quad (11)$$

$$i_U = i_{LU} + i_a \quad (12)$$

$$i_W = i_{LW} + i_c \quad (13)$$

$$i_U + i_W = I_d = \text{constant.} \quad (14)$$

By adding (10) and (11), we have

$$\begin{aligned} e_{PO} &= \frac{1}{2}(e_a + e_c) + \frac{1}{2}L_s''\frac{d}{dt}(i_a + i_c) \\ &= \frac{1}{2}(e_a + e_c) - \frac{1}{2}L_s''\frac{d}{dt}(i_{LU} + i_{LW}) \\ &= \frac{1}{2}(e_U + e_W) \end{aligned} \quad (15)$$

By subtracting (10) from (11),

$$0 = L_{ac}\frac{d}{dt}(i_W - i_U) + L_s''\frac{d}{dt}(i_c - i_a) + (e_c - e_a) \quad (16)$$

Based on this equation, the inverter current in incoming phase i_U can be arranged through (12)-(14):

$$\begin{aligned} i_U &= \frac{1}{2(X_{ac} + X_s'')}\int_0^{\theta}(e_W - e_U)d\theta \\ &= \frac{1}{2(X_{ac} + X_s'')}\left[\sqrt{6}V_p \cos(\theta - \gamma)\right]_0^{\theta} \\ &= \frac{\sqrt{6}V_p}{2(X_{ac} + X_s'')}\left(\cos(\theta - \gamma) - \cos\gamma\right) \end{aligned} \quad (17)$$

where, $X_{ac} = \omega \cdot L_{ac}$.

Since i_U becomes I_d when the commutation is completed at $\theta = u$, we have the relationship between I_d and u as follows:

$$I_d = \frac{\sqrt{6}V_p}{2(X_{ac} + X_s'')}\left(\cos(u - \gamma) - \cos\gamma\right) \quad (18)$$

or,

$$u = \gamma - \cos^{-1}\left(\frac{2(X_{ac} + X_s'') \cdot I_d}{\sqrt{6}V_p} + \cos\gamma\right) \quad (18a)$$

The terminal voltages during the overlapping period are:

• Phase voltages

$$\begin{aligned} e_{UO} &= e_{PO} - X_{ac}\frac{d}{d\theta}i_U \\ &= e_U - \frac{X_s''}{(X_{ac} + X_s'')}\frac{\sqrt{6}V_p}{2}\sin(\theta - \gamma) = e_U + X_s''\frac{di_U}{d\theta} \end{aligned} \quad (19)$$

$$\begin{aligned} e_{WO} &= e_{PO} - X_{ac}\frac{d}{d\theta}i_W \\ &= e_W + \frac{X_s''}{(X_{ac} + X_s'')}\frac{\sqrt{6}V_p}{2}\sin(\theta - \gamma) = e_W + X_s''\frac{di_W}{d\theta} \end{aligned} \quad (20)$$

• Line-to-line voltage

$$\begin{aligned} e_{WU} &= e_{WO} - e_{UO} = 2X_{ac}\frac{d}{d\theta}i_U = -\frac{X_{ac}}{(X_{ac} + X_s'')}\sqrt{6}V_p \sin(\theta - \gamma) \\ &= \frac{X_{ac}}{(X_{ac} + X_s'')} \cdot (e_W - e_U) \end{aligned} \quad (21)$$

On the other hand, inverter dc side voltage E_d can be expressed by :

$$E_d = \frac{3\sqrt{6}}{\pi}V_p\frac{\left(\cos(\gamma - u) + \cos\gamma\right)}{2} \quad (22)$$

Based on the equations derived above, we can discuss the steady-state performance of the system as well as the quality of the terminal voltage.

III. Voltage Waveforms and Their Harmonic Content

Fig. 4 shows an example of measured output voltage of a shaft generator system. The system output was 280kW (rating). It can be seen that there are voltage jumping and sinking caused by commutation of inverter thyristors. The calculated waveforms for the measured waveform in Fig. 4

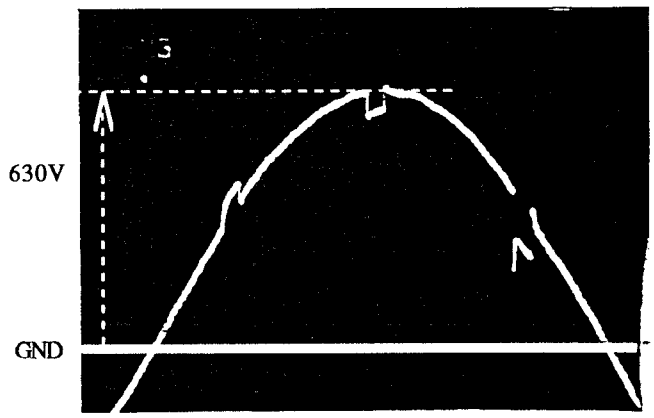


Fig. 4. Example of output voltage waveform.
(measured, 60Hz, line-to-line).

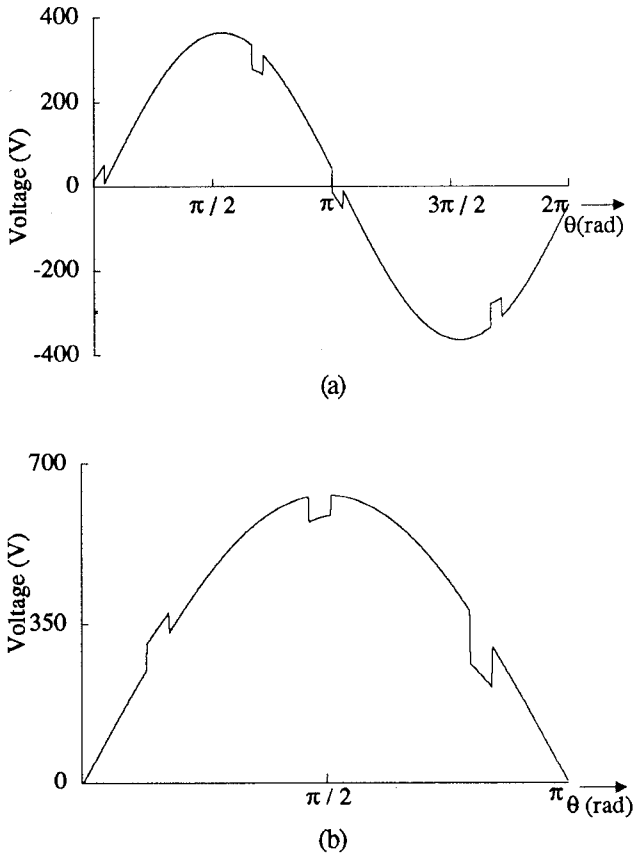


Fig. 5. Calculated waveform of output voltage.
((a): phase voltage, (b): line-to-line voltage)

are given in Fig. 5, in which phase voltage as well as line-to-line voltage are shown. The conditions needed to calculate these waveforms are : V_p = 257V (= 445V / $\sqrt{3}$), X_{ac} = 0.0279 Ω, X_s" = 0.0119 Ω, γ = 37°, I_d = 600 A.

It can be seen that the calculated waveform coincides well with the measured one, supporting the validity of the theory introduced here.

TABLE 1 THD AT AC LOADS OF 100%.

Shaft Generator Speed	I_d	γ	THD	
			Measured	Calculated
230rpm	608A	38°	5.9%	5.7%
150rpm	592A	55°	7.2%	6.9%
Output ratings: 280 / 196 kw 445V, 60 Hz				

The output voltage harmonic content is specified by means of a term called total harmonic distortion (THD). THD is defined as the ratio of the distortion component in the output voltage V_h and fundamental frequency component V_1, and can be expressed by Eq. (23):

$$\mathrm{THD} = {}^{V_h}\!/_{V_1} = \sqrt{{V_o}^2 - {V_1}^2}\,/_{V_1} = \left(\frac{1 + \frac{2}{\pi}\left(k^2 - \sqrt{3}k\right)\left(u - \sin u \cos\overline{2\gamma - u}\right)}{\left(1 - \frac{\sqrt{3}}{\pi}ku\right)^2 + \frac{3k^2}{2\pi^2}\left(1 - \cos 2u\right) + \left(1 - \frac{\sqrt{3}}{\pi}ku\right)\frac{\sqrt{3}}{\pi}k\left(\sin 2\gamma - \sin\overline{2\gamma - 2u}\right)} - 1 \right)^{\frac{1}{2}} \quad (23)$$

where, V_o : RMS value of output terminal voltage, $k = \dfrac{\sqrt{3}}{2}\dfrac{X_s^{"}}{X_{ac} + X_s^{"}}$.

Table 1 shows THD of the output voltage for two values of shaft generator speed at ac loads of 100%. The generator system investigated is the same as that for Fig. 4. In this case, it should be noted that when the speed of shaft generator is reduced to 150rpm the output rating is also reduced to 70% of the output rating for 230rpm, which is 280 kW. From this table the validity of Eq. (23) is found. It is also noticed that harmonic voltage limit THD for the shaft generator systems for ships is typically 15%, and THD for this system exists within this limit.

IV. STEADY-STATE CHARACTERISTICS

We can now analyze the steady-state characteristics of the shaft generator system through the equations derived in the

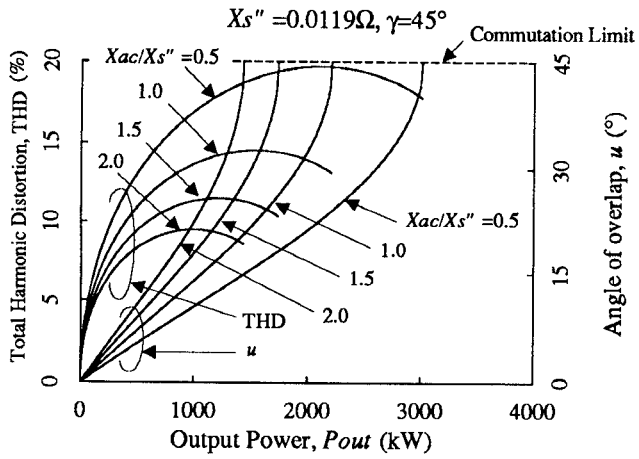


Fig. 6. Effects of X_{ac} on THD and u.

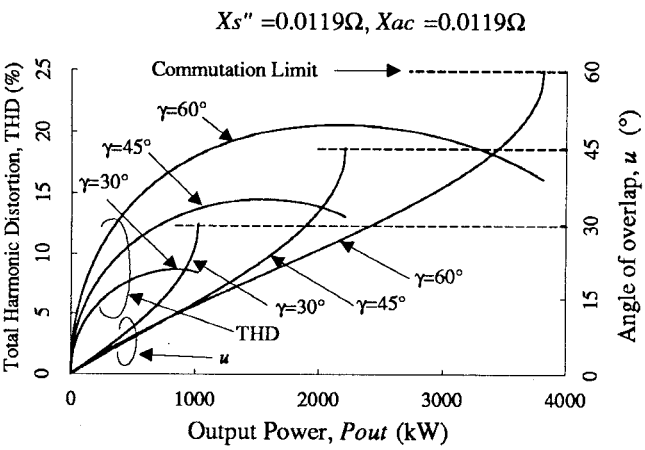


Fig. 7. Effects of γ on THD and u.

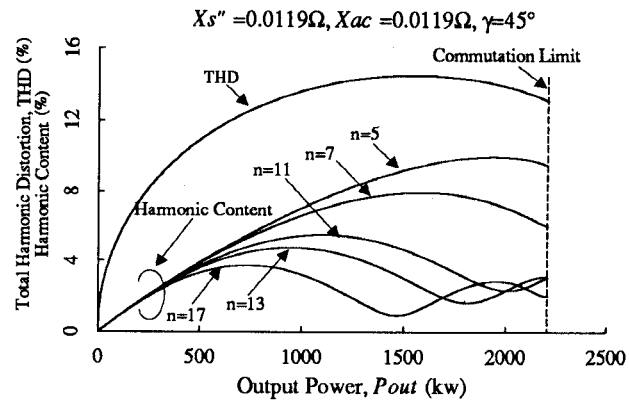


Fig. 8. Harmonic contents of output voltage vs. P_{out}.

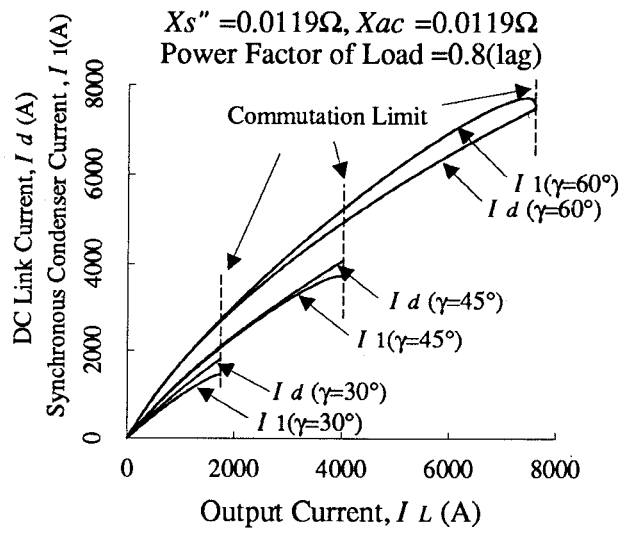


Fig. 9. I_d and I_1 vs. I_L.

foregoing sections. Here, the characteristics of total harmonic distortion THD and overlapping angle of inverter output currents are explored for various output power of the system. The relationships between output current and dc link and synchronous condenser currents are also investigated.

In Fig. 6, the characteristics of THD and angle of overlap u versus output power of the system P_{out}, which is equal to the input power to the inverter if losses can be neglected, are shown for various values of X_{ac}. In this case a constant output voltage of 445V(RMS) and a constant frequency of 60Hz are maintained throughout the calculation. It can be seen from the figure that the smaller X_{ac} is, the wider the operating range becomes, whereas THD increases when X_{ac} is small. From Eq. (18a) overlapping angle for a large value of X_{ac} becomes larger, resulting in reduction of maximum output as in the figure.

Fig. 7 gives the characteristics of THD and u versus P_{out} for various values of leading angle of commutation γ. It is clarified that if γ is large, u becomes small because large commutation voltage is obtained for a large value of γ, and operating range of the system can be widened with an increase of THD.

Fig. 8 shows the relationships between the harmonic contents of output voltage and output power P_{out} ($\gamma = 45$ °, $X_{ac} / X_s^{"} = 1$). The conditions are the same as those for Fig. 6 ($X_{ac} / X_s^{"} = 1$). It can be seen that the major harmonics are 5th, 7th, 11th, 13th ,…… components, and the magnitudes of these harmonics change with P_{out}.

In Fig. 9, the characteristics of dc link current I_d and the RMS value of the armature current of the synchronous condenser I_1 versus ac output current I_L are shown for various values of the leading angle of commutation γ. From the figure, it is shown that I_1 and I_d become large when γ increases since the reactive power needed in the

inverter increases for a large value of γ. Therefore, the VA capacity of synchronous condenser becomes larger than that of system output when γ is large. An approximate calculation shows that the ratio of synchronous condenser VA to system output is 1.33, for example, for γ =30°, and this ratio reduces if γ is decreased [4].

V. CONCLUSION

Steady-state performance of shaft-generator systems used in ships has been analyzed. A set of equations including one to express total harmonic distortion of the output voltage has first been derived. The validity of these equations has been shown by comparing the experimental results with theoretical ones. Based on the equations the steady-state performance of the system has been investigated, and it has been shown that if the reactance of ac reactor is small, operating range of the system is widened with an increase of output voltage distortion. It has also been clarified that synchronous condenser current and dc link current become large when leading angle of commutation of the inverter increases.

Although the equations and calculated results presented in this paper are useful in the design and control of the shaft generator systems, system losses, which were neglected in this analysis, must be incorporated to the analysis when we desire to obtain more accurate results. Moreover, dynamic performance of the system when loads are connected, for example, is also important. These are left for future study.

ACKNOWLEDGMENT

The authors wish to acknowledge the Research Institute for Technology of Tokyo Denki University for its financial support. They would also like to thank Mr. T. Namba, graduate student at Tokyo Denki University, for his cooperation in this work.

REFERENCES

[1] J. Nishiyama, H. Kotera, T. Kishimoto, M. Yamaji, and M. Tsuji, "Shaft driven AC generator for fixed pitch propeller," Journal of the M. E. S. J., Vol. 13, no. 6, pp. 442-449, June 1978

[2] H. Gundlach, "Static frequency converters for shaft generator systems," The Institute of Marine Engineers, London, UK, January 1972

[3] T. Kataoka and S. Nishikata, "Transient performance analysis of self-controlled synchronous motors," IEEE Trans. on Industry Applications, Vol. IA-17, pp. 152-159, March/April 1981

[4] I. Asada and S. Itano, "On the motoring mode operation of shaft generator systems," Trans. of Japan Society for Power Electronics, Vol. 17, pp. 157-162, 1991

Dynamic Model of Fluorescent Lamp Implemented in PSpice

K. J. Tseng
School of Electrical and Electronic Engineering, Nanyang Technological University
Blk S2, Nanyang Avenue, Singapore 639798
Fax: (65) 792-0415 E-mail: ekjtseng@ntu.edu.sg

Abstract - **This paper presents a discharge arc model which can represent approximately both static and dynamic characteristics of a typical fluorescent lamp controlled by a power electronic circuit. The proposed model was developed from the combination and modifications of the classical Cassie and Mayr equations. The equations have been expressed in a form suitable for incorporation into circuit simulators employing the nodal analysis method of equation solving. The model has been test implemented in the PSpice circuit simulator. Simulated and experimental results appear to be in good agreement.**

I. INTRODUCTION

In recent years, various electronic ballasts and control techniques have been proposed for fluorescent lamps to improve the lamp performances [1,2]. Besides the more obvious benefits such as efficiency and compactness which these electronic ballasts have over conventional passive ballasts, there are additional potentials such as dimming capability. The electronic ballast usually comprises of a power converter with a load resonant circuit. Therefore power electronics simulations would be useful to help in the design and optimization of ballast circuits. However there is an absence of reliable and accurate circuit simulation model of the fluorescent lamp. Circuit simulators such as SPICE and Saber simulators which are widely used in the industry and academic research centres do not incorporate realistic discharge lamp model. Therefore it is necessary to consider a practical model capable of representing both the static and dynamic behaviour of the fluorescent lamp and suitable for use in circuit simulators.

The fluorescent lamp phenomenon is basically a low pressure gas arc discharge. Owing to the very complex arc phenomena, the relationship between the lamp voltage and the lamp current is highly nonlinear. Initially the non-conducting gas has a very high resistance. This is followed by a negative resistance phase during gas breakdown, and followed finally by a small positive resistance phase once a stable arc is formed. Therefore modeling the lamp as a pure resistance does not provide sufficient accuracy. This approach is valid for very limited operating region, but has actually been reported for simulation of ballast circuits [3,4].

An improvement over the fixed resistance model has been reported recently, where the lamp resistance is a function of the average lamp power. Models of this type are useful in predicting the rms values of lamp voltage and current, but they cannot be used to predict lamp power factor and current crest factor because the instantaneous dynamic *v-i* characteristics of fluorescent lamps are nonlinear [5]. These models are also unable to provide realistic simulations of voltage and current stresses caused by the interaction of the lamp with the power electronic devices. In the model developed by Mader [6], the lamp voltage v is a cubic function of the lamp current I,

$$v(t) = A(\overline{p})i(t) + B(\overline{p})i^3(t) \quad (1)$$

where A and B are functions of average lamp power p. Both of these functions have three parameters each that must be experimentally determined.

$$A(\overline{p}) = a_1(\overline{p} + a_2)^{a_3} \quad (2)$$

$$B(\overline{p}) = b_1(\overline{p} + b_2)^{b_3} \quad (3)$$

Because of difficulty in obtaining the parameters, and convergence problems, Sun [5] proposed to modifiy Eq.1 to

$$v(t) = A(\overline{p})i(t) + [B(\overline{p})i(t)]^3 \quad (4)$$

where

$$A(\overline{p}) = a_1\overline{p}^{-1} + a_2 + a_3\overline{p} + a_4\overline{p}^2 \quad (5)$$

$$B(\overline{p}) = b_1\overline{p}^{-1} + b_2 + b_3\overline{p} + b_4\overline{p}^2 \quad (6)$$

However this model is still too intricate for its parameters to be estimated easily. A somewhat simpler model has been proposed by Moo [7] which is still dependent on the operating lamp power. All these models are basically empirical in nature, the form of their equations proposed on the basis of typical *v-i* characteristics of fluorescent lamp. They are not valid when the lamp arc is igniting from the cold or extinguishing.

A new approach is presented in this paper, in which the model of the discharge arc is formulated from the classical Cassie and Mayr equations used extensively in the past to study the arc phenomena in high-voltage circuit breakers. This proposed model describes the fluorescent lamp as a two-terminal device whose variables are the arc current and voltage. The lamp conductance is a function of the instantaneous lamp voltage and current, and the rate of change of lamp conductance. This differential equation is largely related to arc physics and is thus applicable to all dc and ac operating conditions. The model is amenable to computer-aided circuit analysis as most modern circuit simulators employ the nodal-analysis method of solution. This model was first proposed by the authors for the simulation of electric arc in general [8,9].

Section II describes the development of the lamp model. The implementation of the model in PSpice is

described in Section III. Parameter estimation for the model is discussed in Section IV. Experimental verification of the model is given in Section V.

II. Proposed Mathematical Model

Careful studies, both theoretical and experimental, have shown that the dynamic arc plasma phenomena are extremely complex in detail so that complete mathematical models of the arc comparable in simplicity and accuracy with engineering models of the connected power electronic circuit are not possible [10,11]. However, it has been recognized for many years that the relatively simple Cassie and Mayr differential equation models based on simplifications of principal power loss mechanisms and energy storage in the arc column, are useful for at least a qualitative understanding of the phenomena determining arc striking or extinction of the energy balance type [12]. An attempt is thus made here to modify and combine the Cassie and Mayr models to a form suitable for transient circuit simulation. It may then be used for simulation of any arc loads including fluorescent lamps.

Fig 1 shows typical arc characteristics in a quasi steady state condition. There are numerous factors affecting the characteristics, among which are the type of gas, the gas pressure, the electrodes separation distance, the electrode material and the geometry and position of the electrodes. The shape of the *v-i* curve may be explained by considering the mode of heat loss from the arc [11]. Consider a very simple arc model with a constant current density and a constant heat loss per unit area of the cylindrical surface of the arc. The circumference of the arc column, and therefore the heat loss=*vi* is then proportional to the arc radius. For a constant current density, arc radius is proportional to the square root of arc current. This gives a shape not unlike the typical characteristics in the low current range, but not for the high current range.

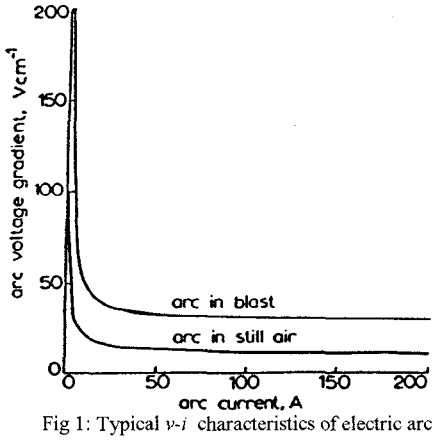


Fig 1: Typical *v-i* characteristics of electric arc

In the high current range, we can let the current density constant, but assume that the loss is proportional to the cross-sectional area of the arc, such as might occur with gas flowing through the arc and removing heat from the entire volume of the arc. In this case, v remains constant, and the model presents an acceptable reproduction of the curve in the high current region.

The simple heat loss processes considered so far can satisfactorily account for the static charcteristics. To understand the dynamic characteristics, the heat loss processes have to be considered in greater details. The temperature of the arc column at high pressure is sufficiently high for thermal ionization to be become an important factor in the maintenance of ionization, as evidenced from the well-known Saha's equation. The thermal ionization that maintains the arc is established by virtue of the high gas temperature, which in turn is established and maintained by the energy given up by the ions and electrons in collision with the gas particles. If the arc current changes abruptly, the arc exhibits a hysteresis effect, i.e. a time lag in the change in voltage compared to a change in current. This is because the arc plasma conductivity is a function of the gas temperature. Hence, when the current undergoes a positive rate of change, the conductance does not change instantaneously since the temperature change has a time lag due to the heat capacity of the gas. The result is a lower conductivity and a higher voltage drop than the steady state voltage for a given current.

Cassie postulated an arc model that has a constant current density, so that its cross-sectional area varied directly with the current [13]. It also has a constant resistivity and stored energy per unit volume. The air (or other materials) flow penetrated the whole cross-section of the arc, carrying away heat, and thus made the dissipation per unit volume constant as well. With the arc resistance R as the dependent variable, the Cassie equation is given by

$$\frac{1}{R}\frac{dR}{dt} = \frac{1}{\theta}\left(1 - \frac{v^2}{E_0^2}\right) \tag{7}$$

where E_0 is the constant steady-state arc voltage and θ is the arc time constant = ratio of energy stored per unit volume to energy loss rate per unit volume. This model has a drawback in that the modelled arc could not be interrupted. It in fact describes the behaviour of the arc when the current is large.

In Mayr's model, the heat loss is assumed to occur from the periphery of the arc only, and the conductance of the arc varied with the energy stored in it [14]. The Mayr equation is

$$\frac{1}{R}\frac{dR}{dt} = \frac{1}{\theta}\left(1 - \frac{vi}{P_0}\right) \tag{8}$$

where P_0 is the constant power loss. In the steady-state condition, when currents and voltages are changing very slowly, $vi = P_0$. Thus the steady-state characteristics are hyperbolic, which is a moderately good representation of the curves in the low current range (Fig 1). This equation does allow the arc to interrupt, since, with R high, vi/P_0 can still be less than unity, so that dR/dt is positive and the resistance continues to increase until the arc is extinguished.

In our experience with transient circuit simulations using iterative Newton-Raphson algorithm, convergence problems are frequently encountered whenever the value of resistance of any circuit element converges to a very small value during any of the iterations. Therefore we proposed to use the arc conductance G as the dependent variable instead of R. It can be shown that the original Cassie equation can be transformed to

$$G_C = \frac{vi}{E_0^2} - \theta \frac{dG_C}{dt} \tag{9}$$

and the original Mayr equation be transformed to

$$G_M = \frac{i^2}{P_0} - \theta \frac{dG_M}{dt} \tag{10}$$

As the Mayr equation is more valid for zero and low current regions while the Cassie equation is more representative of higher current regions, it is proposed here that an arc may be simulated by the combination of equations (9) and (10). One way of combining equations (9) and (10) into a single model is to define a transition current I_0 such that the arc conductance is given by

$$G = \frac{vi}{E_0^2} - \theta \frac{dG}{dt} \quad \text{if } i > I_0$$

$$G = \frac{i^2}{P_0} - \theta \frac{dG}{dt} \quad \text{if } i < I_0 \tag{11}$$

However this leads to a lack of defined derivative at the transition point between the two equations, which can give rise to a host of convergence problems in circuit transient simulation. To allow smooth transition between equations (9) and (10), it is possible to define a transition factor $\sigma(i)$ which is a function of arc current such that the arc conductance is given by

$$G = (1 - \sigma(i))G_C + \sigma(i)G_M \tag{12}$$

where G_C and G_M are the conductances given by equations (9) and (10) respectively. The transition factor $\sigma(i)$ varies between zero and unity, and should be a monotonic decreasing function when arc current i increases. A satisfactory form of $\sigma(i)$ used in our model is given by

$$\sigma = \exp\left[-\left|\frac{i}{I_0}\right|\right] \tag{13}$$

where I_o is the transition current. When current i is small, the value of σ is closed to unity, and G is dominated by Mayr conductance G_M. When i is large, σ is negligible and therefore G is now dominated by Cassie conductance G_C.

In addition, there has to be a finite though very small amount of conductance between any two electrodes when the arc is absent. The value of this constant, G_{min}, would depend on the distance between the electrodes, the geometry of the electrodes, the type of gas, and the temperature. The complete model is thus given by

$$G = G_{\min} + [1 - \exp(-\left|\frac{i}{I_0}\right|)]G_C + [\exp(-\left|\frac{i}{I_0}\right|)]G_M \tag{14}$$

$$i = |G|v \tag{15}$$

with G_C and G_M as given by Eqs.9 and 10.

Eqs.9, 10, 14 and 15 are amenable to implementation in industrial-standard circuit simulators such as SPICE and Saber. The parameters of the model are E_o, I_o, P_o, θ_C, θ_M and G_{min}.

III. MODEL IMPLEMENTATION IN PSPICE

Modern versions of some circuit simulators offer novel ways to implement new mathematical device models without having to modify the source code. They usually take the form of user defined controlled sources (UDCS) whose through variables (currents) and across variables (voltages) can be described by complicated mathematical equations. Examples are the SLICE simulator from Harris Semiconductor and the PSpice with the Analog Behavioral Modeling option. In SLICE each controlled source is used to reference a user written Fortran subroutine. In PSpice the equations are written into the netlist directly.

A new device model can thus be constructed as a sub-circuit of these special controlled sources, a kind of macro model with the detailed equations of a micro model. The advantages of such form of implementation are:

- It is relatively easy and straightforward to implement.
- It is easy to port the model from one user to another without having to compile and link the software.
- The model can be modified readily.

Compared with the embedded implementation, the disadvantages are:

- It is not able to convey to the simulator information which can aid convergence, e.g. preventing excessive voltage swing per iteration when the lamp arc extinguishes. As a result, the model can be prone to convergence problems if model equations are not properly formulated.
- The run-time memory requirement can be substantially higher, especially when the model appears many times in the circuit. However this is not usually the case when designing electronic ballasts.
- The execution speed may be slower.

The proposed fluorescent lamp model has been implemented using the Analog Behavioral Modeling option of PSpice. Under this option, two of the standard SPICE controlled sources, **E** and **G**, have been enhanced. The **E** device has voltage output and the **G** device has a current output. The standard SPICE implementation of these sources allows polynomial controlling functions

which have very limited applications. The enhanced sources allow transfer function for non-linear devices to be specified by mathematical expressions, look-up tables, Laplace transforms, or frequency response tables. Fig 2 shows the block diagram of the implementation.

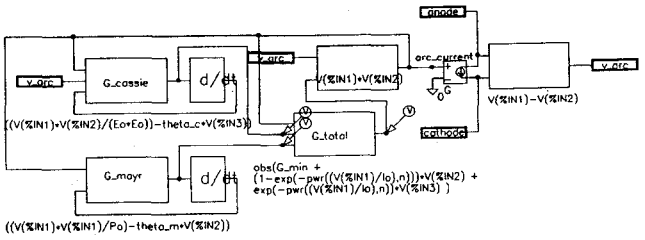


Fig. 2: Block diagram of model implementation in PSpice

IV. Parameter Estimation

It is important that the relative influence of the model parameters on the simulated charactersitics is well understood as this would help in the estimation of model parameters. This section discusses the contributions of each parameter to the simulated characteristics, using analytical analysis as well as from observations of trial simulations. From the discussed results, a procedure for the estimation of model parameters is proposed.

Figures 3, 4 and 5 each shows a family of simulated static characterstics obtained from PSpice simulations using the implemented lamp model. The simulated circuit consists of a voltage source in series with a resistance and an arc. Using the DC transfer function of the simulator, the voltage source is progressively stepped down to zero in true DC operating conditions to obtain the static characteristics. The above procedure is carried out repeatedly, each time the value of one chosen parameter, say E_0, is changed to a different value. In this way a family of static characteristics is obtained which clearly illustrates the influences of that parameter as it changes.

At high steady-state currents, it can be seen from Eqs.9 and 14 that the arc conductance is approximately

$$G \approx \frac{vi}{E_0^2} \tag{15}$$

Therefore $$v^2 \approx E_0^2 \tag{16}$$

Hence E_0 strongly governs the level of arc voltage at high currents. This is evidenced in Fig 3 which shows the simulated static characteristics for different values of E_o. At low steady-state currents, Eq.14 can be simplified to

$$G \approx \frac{i^2}{P_0} \tag{17}$$

Therefore $$v \approx \frac{P_0}{i} \tag{18}$$

Hence the static characteristic has a hyperbolic shape at low currents and is dependent on the value of parameter P_0, as can be seen in Fig 4. For the same arc current, the arc voltage is higher for larger values of P_0. For smaller values of P_0, the characteristics display a more pronounced positive differential resistance in the transition region.

From Fig 5, it can be observed that the parameter I_0 has important bearing on the current value at which the curve becomes dominated by the Cassie term. The value of arc voltage at high currents is virtually unaffected by P_0 and I_0.

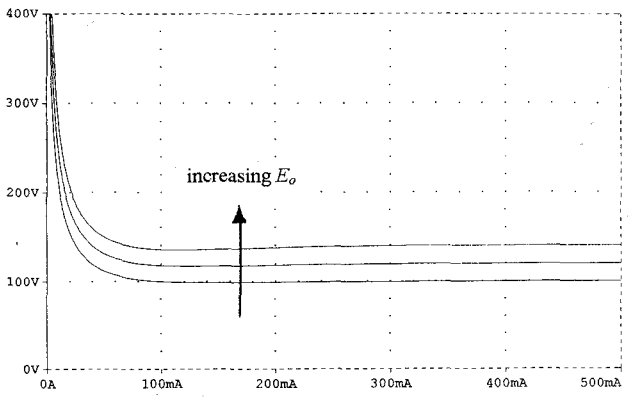


Fig 3: Effect of parameter E_o on static simulation

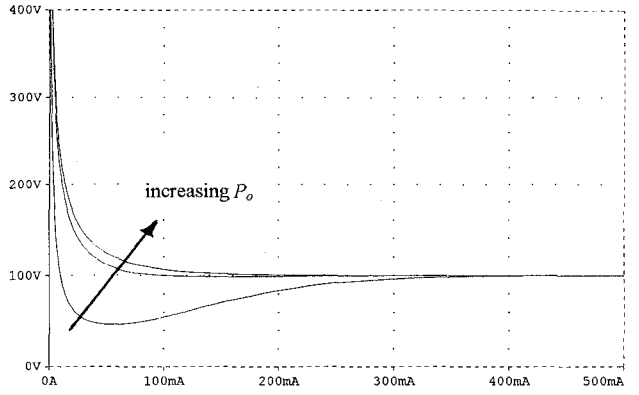


Fig 4: Effect of parameter P_o on static simulation

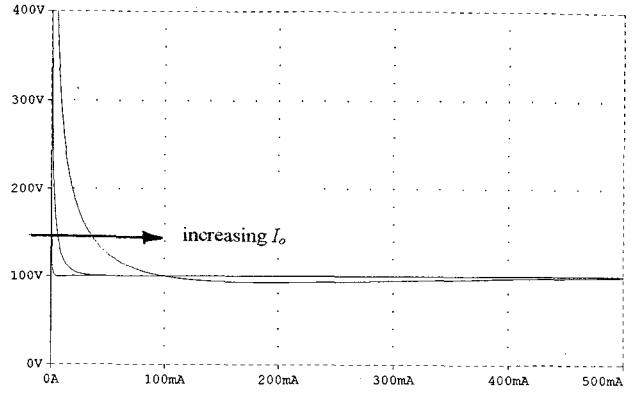


Fig 5: Effect of parameter I_o on static simulation

The parameters θ_C and θ_M, now termed as the arc conductance damping factors are defined as the respective ratio of instantaneous energy stored per unit volume to the instantaneous energy loss per unit volume. Their effect on the transient arc behaviour is analoguous to that of the damping factor used to characterize mechanical system behaviour. The dynamic characteristics of the model are determined by θ_C and θ_M besides E_0, P_0 and I_0. At low frequencies, the arc is momentarily extinguished whenever the current approaches zero. The lamp voltage then rises sharply until the 'hot' striking voltage is reached. This depends on the frequency and lamp temperature which in turn depends on the operating power. Once the arc is re-ignited, the voltage drops to the steady-state level Eo. At high frequencies, the dynamic v-i characteristics exhibit the typical cubic relationship as shown in Fig. 6. The effect of parameter θ_M on the simulated characteristics is also clearly evidenced.

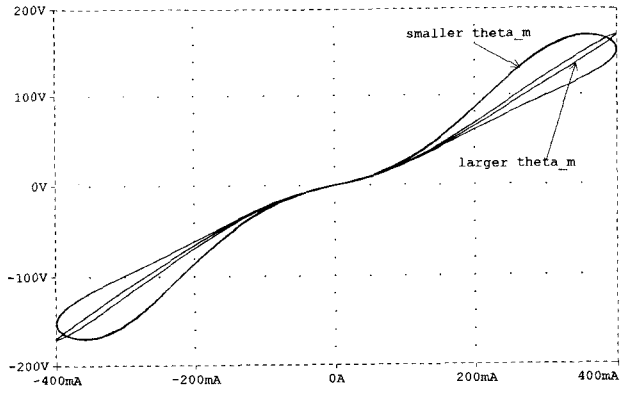


Fig 6: Effect of parameter θ_M on dynamic simulation

A simple multi-step parameter estimation procedure is proposed here for the fluorescent lamp model:

(1) Initial estimates for E_o and I_o are obtained from the lamp operating rms voltage and current respectively. Parameter P_o is estimated as E_oI_o.

(2) Experimental static characteristics are then obtained for the particular lamp and compared with the simulated static characteristics using the initial estimates for P_o, I_o and E_o. These parameters should then be adjusted iteratively until a satisfactory match between experimental and simulated results are obtained.

(3) Choose $\theta_C = \theta_M = 0.0001$. Experimental and simulated dynamic characteristics are then obtained and compared at two widely different frequencies, e.g. 50 Hz and 20 kHz. The parameters θ_C and θ_M should be adjusted until good correlations are obtained.

V. Experimental Verification

The fluorescent lamp model has been verified using experimental data obtained from a commercial 36 W straight tube 4-feet fluorescent lamp. The first test involved the excitation of the lamp using a DC power supply. The experimental and simulated static v-i characteristics are shown in Fig 7.

In the second test, the dynamic characteristics are measured at 50 Hz. To rule out any effects due to the non-linearities of an inductive ballast, the lamp was run and simulated on a purely resistive ballast. The experimental lamp voltage and current are shown in Fig 8(a) while the simulated traces are shown in Fig 8(b). The shape and form of the simulation results largely match the experimental data, despite the fact that the 50 Hz AC power supply obtained from the laboratory mains was not exactly sinusoidal due to harmonic pollution. The simulation results were based on the assumption of a perfectly sinusoidal excitation voltage.

The third test was done at a high frequency of 26 kHz using an electronic ballast. Experimental and simulated dynamic v-i characteristics are given in Fig 9, which again shows good correlation. All the simulation results in Figs 7, 8 and 9 are obtained using the same set of optimized parameters: $E_o = 120$, $I_o = 0.01$, $P_o = 30$, $\theta_C = 0.0003$ and $\theta_M = 0.0001$.

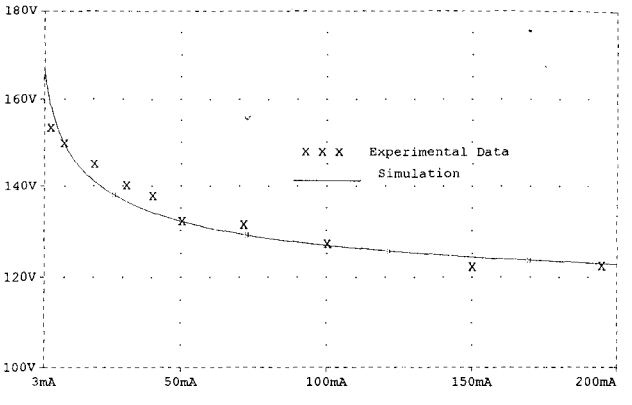
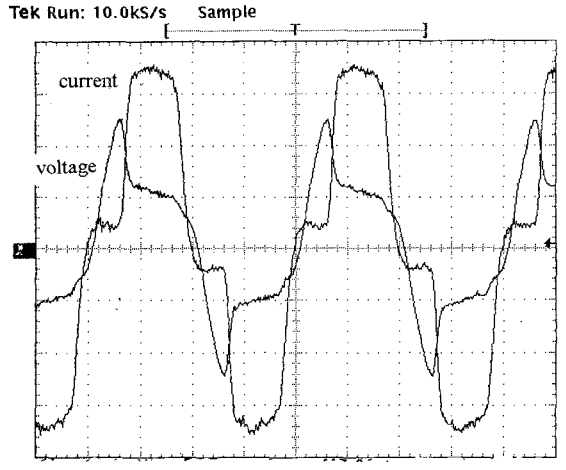


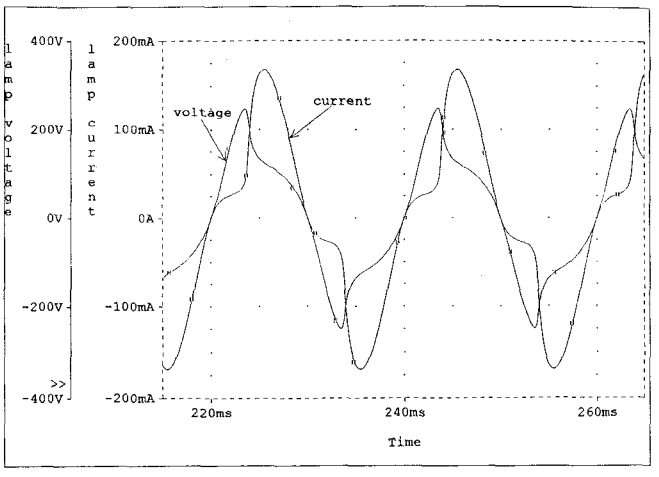
Fig 7: Comparision of simulated and experimental static characteristics

VI. Conclusion

A mathematical model of the electric arc has been implemented in the PSpice simulation program and was used to model the fluorescent lamp tube, a typical arc-type electric load. Both the static and dynamic characteristics of the lamp were studied by means of simulations. A set of model parameters was estimated for a 36 W fluorescent lamp. Closed correspondence between simulation and experimental results were obtained at DC, 50 Hz and 26 kHz operations.



(a) experimental: 50mA/div 100V/div



(b) simulation

Fig 8: Simulation and experimental results at 50 Hz

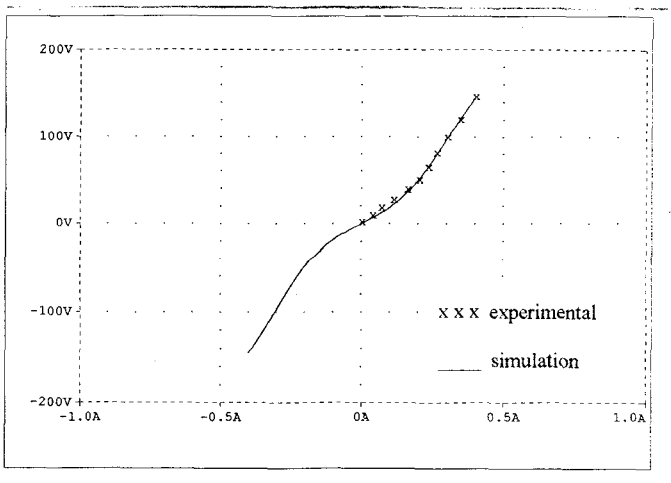


Fig 9: Simulation and experimental results at 26 kHz

REFERENCES

[1] Marian K.Kazimierczuk and Wojciech Szaraniec, "Electronic Ballast for fluorescent lamps". IEEE Transactions On Power Electronics, 1993, Vol.8, No.4., pp.386-395.

[2] D.Tadesse, et al (1993), "A comparison of Power Circuit Topologies and Control Techniques for a High Frequency Ballast", IEEE Transactions On Power Electronics, pp.2341-2347.

[3] Yu T.H., Huang H.M. and Wu T.F., "Self-excited half-bridge series resonant parallel loaded fluorescent lamp electronic ballasts," IEEE APEC Conference Record 1995, pp.657-664.

[4] Sun Y., "Using PSpice to determine lamp current variations due to electronic ballast component tolerance," IEEE IAS Conference Record 1994, pp.1974-1978.

[5] Sun N. and Hesterman B., "PSpice high frequency dynamic fluorescent lamp model," IEEE 11th Annual Power Electronics Conference and Exposition, APEC'96, San Jose, USA, pp.641-647.

[6] Mader U. and Horn P., "A dynamic model for the electrical characteristics of fluorescent lamps," IEEE IAS Conference Record 1992, Vol.2, pp.1928-1934.

[7] Moo C.S., Chuang Y.C., Huang Y.H. and Chen H.N., "Modeling of fluorescent lamps for dimmable electronic ballasts," IEEE ???, pp.2231-2236.

[8] Tseng K.J. and Wang Y., "Dynamic electric arc model for electronic circuit simulation", IEE Electronics Letters, 1996, Vol. 32, No.8, pp.705-707.

[9] Tseng K.J. and Wang Y., "An experimentally verified hybrid Cassie-Mayr electric arc model for power electronics simulations," IEEE Trans. on Power Electronics, May 1997.

[10] Cobine J. D., "Gaseous Conductors - theory and engineering applications," McGraw-Hill, 1941.

[11] Meek J.M. and Craggs J.D., "Electrical breakdown of gases," Oxford University Press, 1953.

[12] Browne T.E., "Practical modelling of the circuit breaker arc as a short line interrupt," IEEE Trans. Power Apparatus & Systems, Vol.PAS-97, No.3, Jun 1978, pp.838-847.

[13] Cassie A.M., "Arc rupture and circuit serverity: a new theory," CIGRE Report No.102, Paris, France, 1939.

[14] Mayr O., "Beitrage zur theorie des statischen und des dynamischen lichbogens," Archiv fur Elektrotechnik, Berlin, Germany, Vol.37, 1943, pp.588-608.

[15] *PSpice Circuit Analysis Reference Manual*, Microsim Corporation, Ver 6.2, Apr 1995

Stability Analysis and Performance Evaluation of AC Side Current Control System of Voltage Type Converters

A. Draou

Institute of Electrotechnics, University of Sciences and Technology of Oran U.S.T.O, BP 1505
El MNaouar, Oran, ALGERIA
Tel: + 213-6-452377 Fax: + 213-6-451581

Abstrast– A new control method for voltage type PWM ac to dc converters with reduced number of sensors is proposed. To reduce the waveform distortion and DC offset current of the supply current, state feedback control of the LC filter in the AC side is used. Analysis of the current control system, and stability analysis to determine optimum values of feedback gains are reported. The performance of the PWM rectifier with the proposed control strategy is confirmed by experiments, where the transient dynamic response was greatly improved.

I. INTRODUCTION

In recent years, a new generation of voltage type PWM ac to dc converters that offer unity power factor and sinusoidal line current have been proposed to replace conventional converters [1-3]. Such voltage type PWM ac to dc converters have been introduced into uninterruptible power supplies, battery chargers, traction applications and large industrial motor drives. Many papers on these PWM ac to dc converters have been published to date with various control strategies.
One of these control strategies is the phase and amplitude control, or indirect control method.
This control technique is simple and reliable because of its simple structure and constant switching frequency but, as mentionned in[1], one of its inherent limitations is slow response due to the presence of dc offset current. This cannot be corrected by the conventional control.
As was done in [4] better performance can be obtained by state feedback control, which acts simultaneously on all state variables as shown on Fig. 1. Clearly, this kind of control is not practical, since all state variables must be sensed and a suitable reference must be provided for each of them. In this paper we study the stability of the proposed control system and prove that some of these state variables might not be necessary to sense.

II.MAIN CIRCUIT AND CONTROL STRATEGY

A. Main Circuit Configuration

Fig.1 shows the main circuit and control block diagram of the proposed PWM AC-to-DC voltage type converter system.
In this configuration the bridge converter employs six fully controlled IGBT's switches that are turned on and off to synthesize three phase sinusoidal voltages at the converter terminals as well as bidirectional power conversion.
The bridge circuit is connected to the three phase supply through an LC filter composed of L_s, C'_s, and L_i as shown.
A load and a dc capacitor C_d are connected to the dc side of the converter. The inductor L_i performs the voltage boost operation in combination with the capacitor C_d, and at the same time acts as a filter for the ac line current.
Under regenerating conditions, it is assumed that a dc power source E_b with a series resistance R_e is connected in parallel with the load as shown by the dotted box in the figure.The filter inductor L_s and capacitor C'_s further reduce the current harmonic and improve the waveform of the ac line current.

In the ac side current control system, phase and amplitude control strategy is used to force the line

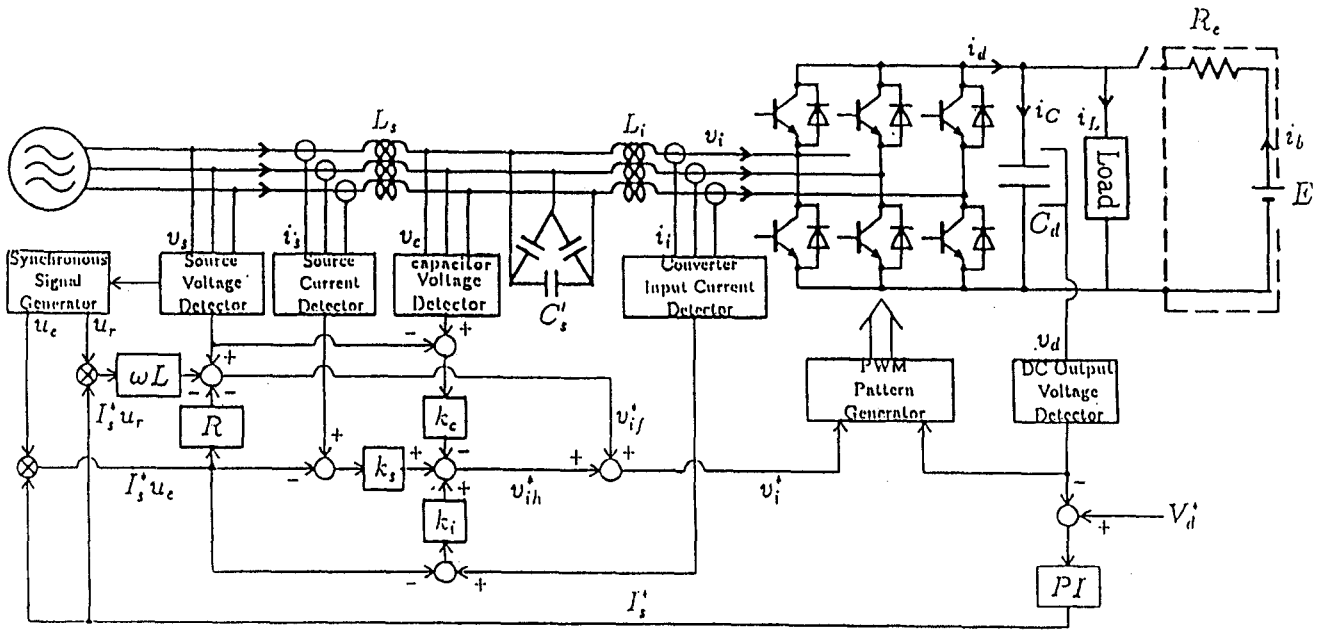


Fig. 1 Main and Control Circuit of the Proposed Converter System

current of the converter to follow a sinusoidal reference waveform.

B. Basic State Feedback Control Scheme

In order to achieve unity power factor operation of the converter, it is necessary to control the fundamental component of the converter input phase voltage and its relative phase angle δ with respect to the source voltage such that the power factor angle ϕ is equal to zero for rectifying operation and is equal to π for regenerating operation.

The expression for the reference signal of the converter ac side phase voltage v_i which allows the system to operate at unity power factor can be shown [3] to be given by

$$v_{if}^* = v_s - 2(Ru_c + \omega L u_r)I_s^* \qquad (1)$$

where v_{if}^* is the reference of the fundamental component of the converter ac side phase voltage in the steady state, u_c, and u_r are the unity amplitude sinusoidal phase reference signals which are in phase with the supply voltage and in time quadrature with the supply voltage, respectively. I_s^* is the amplitude of the source reference current i_s^*.

R = $(R_s + R_i)/2$ and L = $(L_s + L_i)/2$ in which R_s, R_i are the resistances of the inductors $L_s$and L_i, respectively.

It has been demonstrated mathematically that the supply current under transient conditions will contain a dc current component [5].

To compensate this DC offset current and improve the transient performance of the system, an additional component of the reference of the converter ac side phase voltage, the state feedback component v_{ih}^*, is introduced. The state feedback component v_{ih}^* is produced by detecting the state variables of the LC filter, that is, the inductor currents i_s and i_i and the capacitor voltage v_c. In this case only the deviations of the state variables from their steady state values are required to compensate the the dc offset current and the resulting oscillations on the dc output current and voltage waveforms. Therefore, the state feedback component v_{ih}^*, is given by

$$v_{ih}^* = k_s(i_s - i_s^*) + k_i(i_i - i_s^*) - k_c(v_c - v_s) \qquad (2)$$

where k_i, k_s, k_c are the feedback coefficients.

The total reference input voltage v_i^* of the ac input current control is obtained by summing the two

components given in equations (1) and (2) as

$$v_i^* = v_{if}^* + v_{ih}^* \tag{3}$$

which is applied to the PWM pattern generator shown in Fig.1 for the switching process of the power devices.

III. ANALYSIS OF THE CURRENT CONTROL SYSTEM

A. Derivation of Characteristic Equation

In this configuration the error component is due to the DC offset current and oscillations on the DC output current and voltage as explained above. Moreover, the supply voltage v_s is a pure sine wave and therefore the error component does not exist. Thus the system equation can be written as follows

$$\frac{d}{dt}\begin{bmatrix} i_{sf}+i_{sh} \\ v_{cf}+v_{ch} \\ i_{if}+i_{ih} \end{bmatrix} = \begin{bmatrix} -\frac{R_s}{L_s} & -\frac{1}{L_s} & 0 \\ \frac{1}{C_s} & 0 & -\frac{1}{C_s} \\ 0 & \frac{1}{L_i} & -\frac{R_i}{L_i} \end{bmatrix} \cdot \begin{bmatrix} i_{sf}+i_{sh} \\ v_{cf}+v_{ch} \\ i_{if}+i_{ih} \end{bmatrix} + \begin{bmatrix} 0 & \frac{1}{L_s} \\ 0 & 0 \\ -\frac{1}{L_i} & 0 \end{bmatrix} \begin{bmatrix} v_{if}+v_{ih} \\ v_s \end{bmatrix} \tag{4}$$

From the system equation (4) the state equations of the fundamental and harmonic components can be obtained from which a third order equation of S can be obtained

$$|sI - A| = s^3 + (\frac{R_s}{L_s} + \frac{R_i}{L_i})s^2 + (\frac{R_s R_i}{L_s L_i} + \frac{1}{L_s C_s} + \frac{1}{L_i C_s})s + \frac{R_s + R_i}{L_s L_i C_s} = 0 \tag{5}$$

It can be shown that by using routh stability criteria, the system can be unstable and thus needing to be stabized.

Thus a state feedback component is included to allow the system to work properly as represented by Fig.2.

A detailed investigation of the feedback gains k_s, k_i k_c of the ac control system for an experimental converter system has been carried out based on root locus method using the block diagram shown in Fig. 2. After an extensive derivation and mathematical manipulations the characteristic equation has yielded a third order polynomial of S [6].

$$|sI - A + bf| = s^3 + (\frac{R_s}{L_s} + \frac{R_i + k_i}{L_i})s^2 + (\frac{R_s(R_i + k_i)}{L_s L_i} + \frac{1}{L_s C_s} + \frac{1 + K_c}{L_i C_s})s + \frac{R_s(1 + k_c)}{L_s L_i C_s} + \frac{k_i + k_s + R_i}{L_s L_i C_s} = 0 \tag{6}$$

where **f** is the feedback component vector.

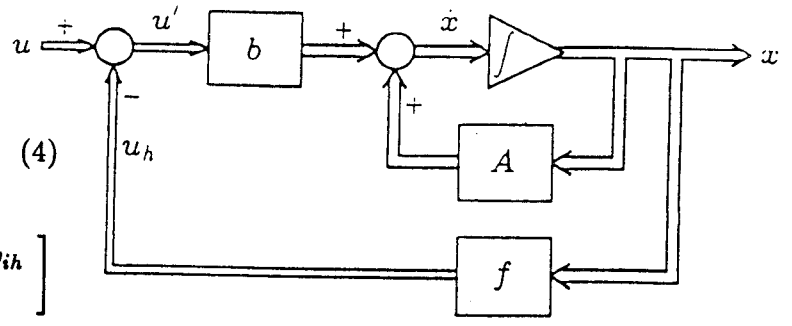


Fig. 2 Block Diagram of the AC Side Current Control System

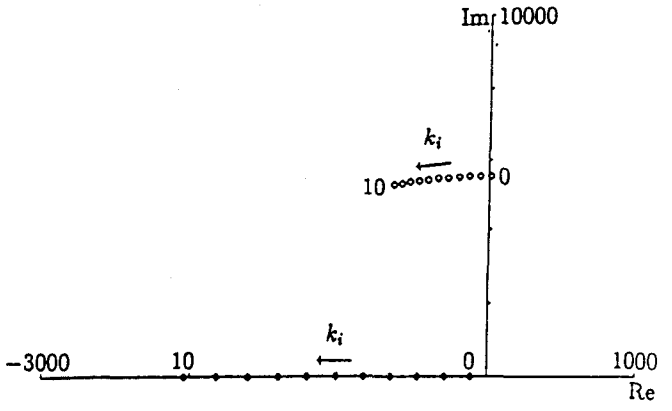
From the above the stability of the ac side current control system can be investigated for the variations of the various parameters. By varying one feedback gain, k_i, and keeping the others constant and the remaining circuit are set to the values used in the test system, the root locus in the S-plane is obtained. Then the range of the design parameter for which good transient performance and stable operation of the system is obtained can be found. Similarly, the other feedback gains can be selected under similar conditions.

B. Simulation Results

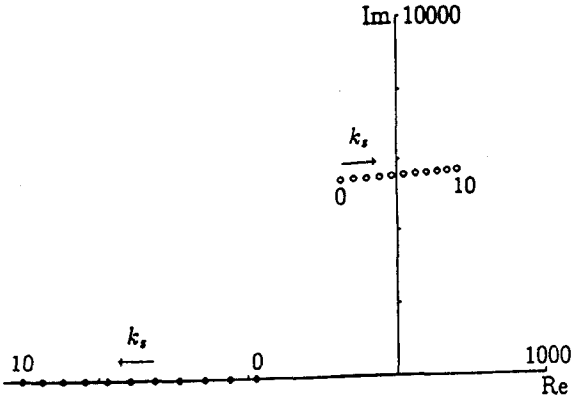
As an example of the investigations, root loci for the variation of the feedback coefficients k_i and k_s

is shown in Fig.3

Fig. 3 (a) shows the root locus for the variations of feedback k_i in the S-plane. It shows the variation of k_i from 0 to 10 and at k_i=0, the system is seen to be unstable. As k_i is increased the system becomes stable. However for higher values of k_i the transient response is not good, so considering this through simulation the value of k_i=5.0 was selected.



(a) Variation of k_i



(b) Variation of k_s

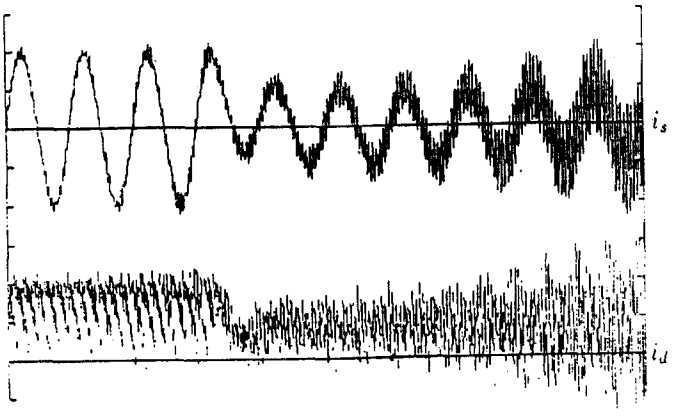
Fig. 3 Root Locus Variation of Feedback Constants k_i and k_s

Similarly, the feedback coefficients k_s and k_c can be selected where it can be shown that even for values of k_c=0 and k_s=0, the system is stable. Just for completeness Fig.3(b) is included to show the root locus of the variation of feedback coefficient k_s.

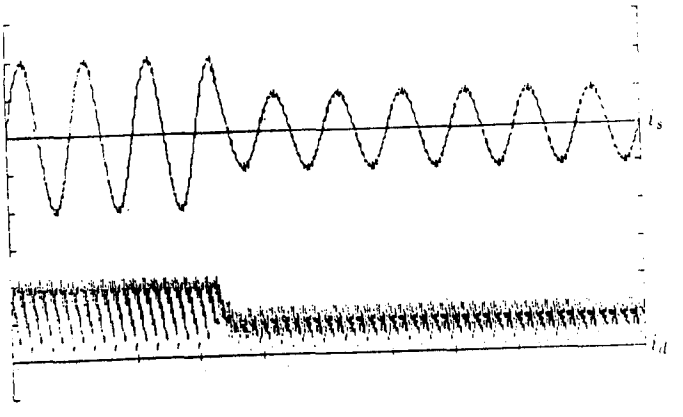
The selected values for the experimental system are: k_i = 5.0, k_s = 0.0, k_c = 0.0. Hence a reduction in the number of sensors is obtained since the supply current and the capacitor voltage might not be detected.

Fig.4 is included to show the simulation results for two values of k_i .

Fig.4(a) shows the case when k_i=0, it shows that the steady state waveform is distorted and at sudden change of the reference current, the distortion increases and the system becomes uncontrollable. However, when some feedback is included (k_i=1) as shown in Fig.4(b) the steady state waveform gets better and the transient response of both ac and dc currents are instantaneous with no offset or distortion. At k_i=5, the response is much better.



(a) Case when k_i=0



(b) Case when k_i=1.0

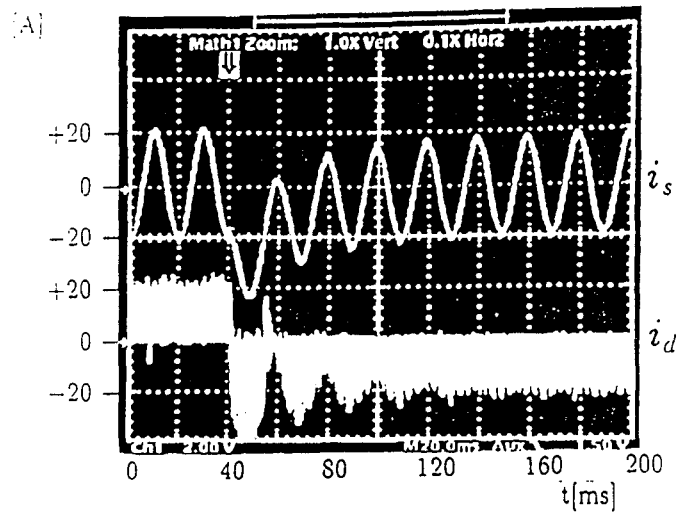
Fig.4 Simulation Results from the Stability Study

IV. EXPERIMENTAL INVESTIGATIONS

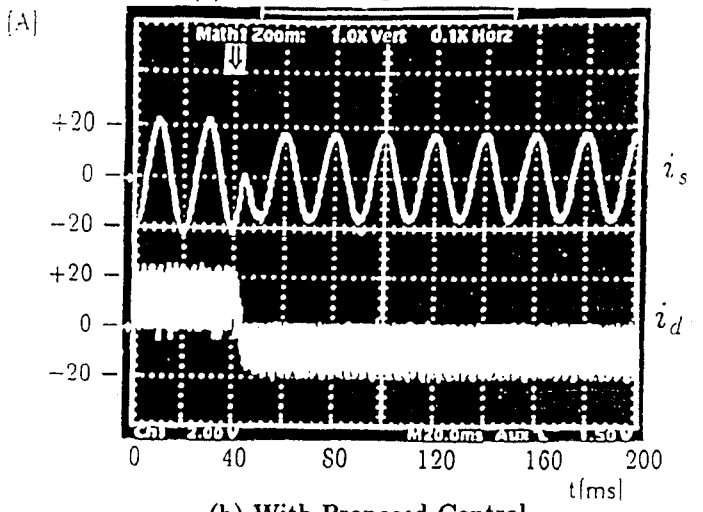
The specifications of the experimental prototype constructed to verify the effectiveness of the control method are given in Table 1.

TABLE 1
SPECIFICATION OF THE TEST SYSTEM

Supply Voltage	80 V r.m.s
LC Filter	L_s=2.5mH
	L_i=3.1mH
	C_s=24μF
Carrier Frequency	f_c=1.2kHz
Feedback Constants	k_s=0, k_c=0
	k_i=5.0



(a) Without Proposed Control



(b) With Proposed Control

Fig. 5 Experimental Transient Responses of AC and DC Currents at Sudden Reversal of Power

As a basic example for the usefulness of the proposed method, we examined the speed of response of the current control of the system for sudden power reversal.

Fig.5 shows the experimental results of the supply and dc output current at sudden power reversal. The amplitude of ac reference current was reversed from 20A to −20A at the instant shown by the arrow.

Fig. 5(a) shows the transient response of the system when the proposed control is not used. It shows that the sudden power reversal causes oscillations on the DC output current and DC offset current on the supply current. On the contrary, as we can see from Fig.5(b) the supply and dc output currents respond almost instantly to the reversal of power with no offset or oscillations. This control method shows that this system can dump its stored energy to the utility or get the energy from the utility.

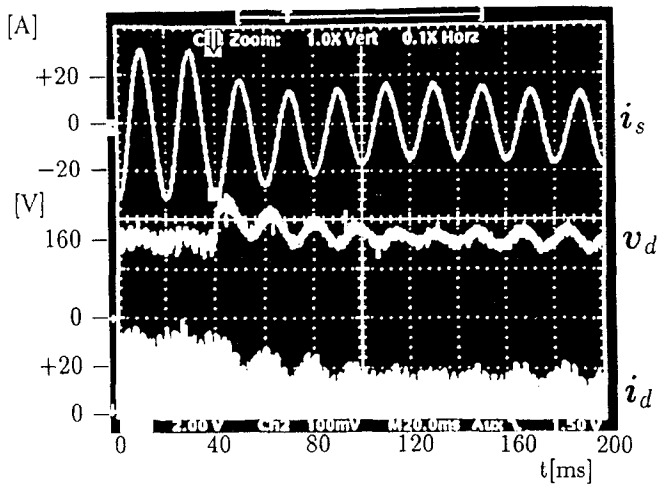
In the second stage, the amplitude of the reference I, I_s^* was generated by the external DC side voltage control loop. The transient behavior of the system is investigated for the case of a step increase in load resistance.

Fig 6 shows the dynamic response of the system when the load is changed from 10 to 20 Ω at the time shown by the arrow.

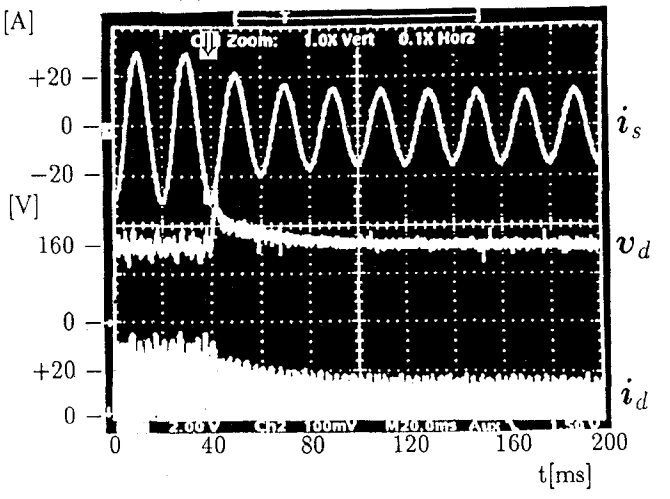
Fig. 6(a) shows that the step load change causes oscillations of the DC output current and voltage. The system tends to become unstagble as the oscillations gradually increases with time. However, when the proposed state feedback control is used, the oscillations are eliminated and the system is stabilized as shown in Fig.6(b).

V. CONCLUSIONS

A new technique to current control of voltage type PWM ac to dc converters with reduced number of sensors has been proposed. It has been shown that, this control method can effectively improve the dynamic performance of the system. The design of the power and control circuits required for the experimental implementation were briefely described. The experimental results show that the supply current waveform of the controlled converter, both in the rectifying and regenerating operations is kept good.



(a) Without Proposed Control



(b) With Proposed Control

Fig. 6 Experimental Transient Responses of Source current and DC Output Current and voltage at Sudden Change of Load Resistance for $C_d = 100\mu F$

REFERENCES

[1] E. Wernekinck, A. Kawamura, and R. Hoft, "A high frequency AC/DC converter with unity power factor and minimum harmonic distortion," IEEE Trans. Power electron. vol.6, no.3, pp. 364-371, Jul. 1991

[2] R. Wu, S.B.Dewan, and R.G.Slemon, "Analysis of a PWM AC to DC voltage source converter under the predicted current control with a fixed switching frequency," IEEE Trans. Ind. Applicat., vol. 27, no. 4, pp. 756-764, July/Aug.1991.

[3] T. Sukegawa, K. Kamiyama, J. Takahashi, T. Ikimi, and M. Matsutake,"A multiple PWM GTO line side converter for unity power factor and reduced harmonics," IEEE Trans. Ind. Applicat., vol. 28, no. 6, pp. 1302-1308, 1992.

[4] A.Draou, Y.Sato, and T.Kataoka, "A new state feedback based transient control of PWM AC to DC voltage type converters", IEEE Trans. Power electron. vol.10, no.6, pp. 716-724, Nov. 1995

[5] A.Draou " A New Improved Current Control method for Voltage Type PWM Rectifiers" Conf. Rec. IEEJ/ IPEC, pp 1536-1541, Yokohama, April 1995.

[6] A.Draou " Stability analysis of AC side current control system of voltage type converters", First Seminary of Electrical Eng. No. 33 pp.198-204, Biskra, Dec. 1995

The Use of a Single Microprocessor Board to Control Two Independent Invertors

I.A.El-Kassas*, L.N.Hulley and W.Shepherd****
***College of Technology Al-Ahsa,P.O.Box:804, 31982, Al-Hofuf, Saudi Arabia**
****Dept. Elec. & Elect. Eng., University of Bradford, Richmond Rd, BD7 1DP, U.K**

Abstract: The use of a microprocessor as controllers in ac drives and systems is now of intense interest. Nevertheless, a study on the microprocessor performance used in such a system revealed that only a fraction of the total processor capability is being used to generate the required PWM pattern. The performance of the microprocessor was carefully monitored to establish how many invertors could be pulse width modulated from a single board. Finally, the possibility of incorporating more control task is also investigated.

1.Introduction:

Microprocessor control of power electronic equipment is attractive because it offers the possibility of improved reliability and increase flexibility, particularly in the design of variable speed drives.

A wide range of microprocessor chips is now available. Their speed and capability continue to grow with a significant impact on the industry. However, the issue of evaluation and selection is a significant problem. The actual throughput of a particular generation of chips, is a function of the exact instruction sequence, displacements, data lengths, clock frequency, and other factors. The increase in the number of devices on a single piece accompanied by a more powerful instruction set, has led to an increase of throughput provided by a single chip, by two to three orders of magnitude over the past years

One of the main parameters of relevance in determining a processor performance is the execution time required to implement a given control algorithm on a given microcomputer. This is closely related to the clock frequency of the processor in addition to other parameters such as the storage and the accuracy requirements. Nevertheless, the CPU is only one component of a micro-controller, which also contains highly complex on-board peripherals. That is, it is essential to evaluate the interaction of the whole system in order to achieve the required optimal benefit.

The performance of the MC68020 was carefully monitored to establish how much of the total capability of the processor is being used. The possibility of controlling two PWM inverters by a single microprocessor board and incorporating more control tasks are also investigated.

2: PWM Strategy:

The production of adjustable magnitude sinusoidal voltages is closely approximated by using PWM technique. Different approaches may be used to formulate the PWM switching strategy. The regular sampling PWM is inherently a linear sampling process and allow sampling of the modulating waveform to be taken at regularly speed intervals

A practical implementation of a double edge asymmetric regular sampled PWM uses a triangular wave (sampling) to sample the sinusoidal waveform (Fig.1). The width of the resulting pulse or gap may be then defined as:

$$t_p = \{1/2p\ F_m\}[1=(-1)^{(n+1)}\ (M/2)*\{Sin[(n-1.5)\ (\pi/p) + Sin[(n-0.5)\ (\pi/p)]\}] \quad \text{Equ.1}$$

where M is the modulation index, P is the number of pulses, F_m the modulating frequency, n is the pulse or

gap number. This equation is suitable for direct simulation on a microprocessor system.

A microprocessor software control program responsible for generating the required PWM pattern is designed using assembly language [1].

3.Processor Performance:

Evaluation of a processor performance imposes a number of difficulties when based on parameters comparison alone (instruction speed, store access time, bus speeds, direct memory access speeds). A number of techniques are used to evaluate the processor performance, such as instruction execution times, instruction mixes, synthetic programs, benchmarks. However, the advanced architecture of the MC68020 makes exact instructions timing calculations difficult due to the effects of: An on chip instruction cache, Instruction prefetch, Operand misalignment and Instruction execution overlap.

Furthermore, the CPU is not the only component of a micro-controller. Additional on board peripherals may also add an extra burden on the processor and affect the execution time of some of the instructions. Together, all these factors cooperate to make the execution estimation of the MC68020 using the instruction execution time list provided by the manufacturer unpredictable.

A way to overcome this problem, which uses a Real Time Clock (RTC, MM58274) was adopted in this work.

4. Real Time clock:

The MVME133 bug system contains a RTC which measures time by counting pulses of a crystal oscillator. It can be as accurate as a quartz watch and can measure up to a fraction of a second. The clock is used to time the software. A time read system call is included at the beginning of the control program. The first time reading is then stored in a predetermined memory location. To improve the accuracy of the reading, the program was allowed to repeat within a loop for 2000 times. The reading at the end is read. The actual execution timing is then calculated by dividing the number of times the loop is repeated.

The computed time represents the actual time required to input the data, calculate the pulse widths, the phase shift and the corresponding phase addresses, transfer the pulses to the generation table, initialise the Programmable Timer Module (PTM, MC6840) and enable the interrupt.

It was found that only 1.2 ms was required to perform the above mentioned demands for: F_M=100Hz F_C=1KHz P=9. The processor is then released to check for new input data and to serve interrupt.

Figure 2 shows the outputs of the PTM for this case and its corresponding interrupts. From this figure it is clear that for each phase 18 interrupt request (I.R) are needed, that is, 54 I.R for a three-phase operation. Measurement showed that the interrupt latency is 22 μs and the total time required for one cycle is 2.455ms. And for a modulating waveform of 100Hz only 24.55% of the capacity is being used. This indicates that a good chance to control two inverters and to develop support facilities such as circuit protection is feasible. This is discussed next.

5 Time-Sharing of a CPU

In a typical microprocessor application, only one instruction is executed at a time. Nevertheless, the CPU must still manage several associated activities during a short period of time. The switching from one task to another is achieved by means of interrupts, which allows one task to be suspended temporarily so that another may run. In a MC68020 an interrupt can occur at one of eight levels of priority (0-7). So by assigning a different level of interrupt to each task an independent operating system for the system can be developed.

The operation starts by loading into the system the required programs and running the first task say A. The general outline for such a program is:

(1)- Read set of inputs., (2)- Compute with the inputs to produce a set of outputs., (3)- Load the PTM and serve I.R, (4)- Scan for new inputs, service I.R, call another task or terminate.

When the program reaches its fourth stage, the processor main task is to service the interrupt and scan for new inputs. Again for a modulating waveform of 100Hz only 12.54% of the processor capability is used, after terminating the required computation (calculate the pulse widths, the phase shift....). The second process (B) can then be called to be executed. The flowchart of this scheme is shown in Fig.3. Each task is assigned its own data area, or stack frame. Just before interrupt disabling, the three-pointers addresses are saved in a specific location defined at the beginning of the program . When the interrupt routine is called, after saving all the data and address registers, the pointers addresses are reloaded to the registers so as output generation could start. Just before returning from exception (RTE), all the pointers addresses are re-saved, so as to keep track of the exact location in the generation table. Figure 4 shows the PTM outputs of these two different tasks [2].

6 Experimental Tests

In order to test experimentally the time-sharing of a CPU, two different three-phase inverters were built and used. The power devices used were the power MOSFET and the IGBT. The outputs of the two Input/Output cards, which contain the PTMs, were connected to the driving circuit of each of the appropriate inverter. Each inverter was allocated a different level of priority according to the user need. In this case the power MOSFET had the higher priority state.

Figure 5 shows the outputs of both inverters at no load. The voltage harmonic spectra, shown in Fig. 6, was also measured and its content is identical for both the higher and the lower priority cases for the same conditions. The interrupt latency, which may occur when two inverter request services at the same time, has little effect on the waveform content.

The test was also repeated for the inverters when loaded with resistive loads. The inverters outputs are shown in Fig.7. The harmonic spectra for the above conditions are shown in Fig.8. Still, the harmonic voltage spectra of the time-shared case shown in Fig.9, display no discrepancy for the same condition when a single inverter is controlled by the microprocessor system.

7. Conclusion

A study on the microprocessor performance revealed that a fraction of the total processor capability is being used. An investigation into how many invertors could be pulse-width-modulated by a single processor revealed that two invertors could be controlled by the same processor. Furthermore, other control facilities could be included in the system. No extra hardware is required except for the Input/Output card which contains the PTM responsible of real-time pulse generation.

The flexibility of the system was tested with two different invertors. The output frequencies of each of the three-phase system could be varied up to 100 Hz and the modulation indexes up to 1 independently. The voltage harmonics spectra showed that the interrupt latency, has little effect on the harmonic contents of the waveforms.

References:

1. El-kąssas, I.A., Hulley, L.N., Shepherd, W., "**Microprocessor Based PWM Invereter with Third Harmonic Injection**", PEDS, 1995 Singapore.

2 .El-Kassas, I.A., "**Metal Oxide Devices in Microprocessor Controlled Inverters**" Ph.D. Thesis, University of Bradford, U.K., 1992

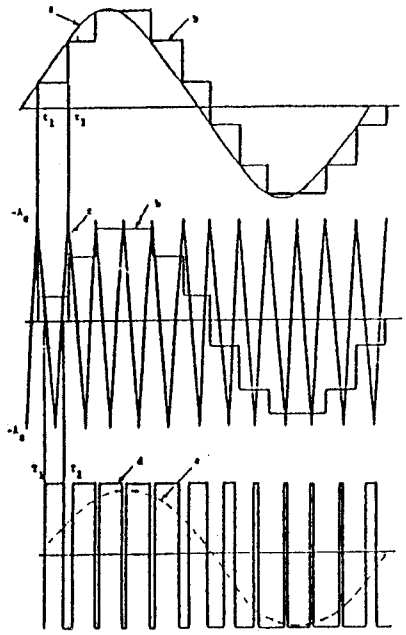


Fig.1 Regular Sampled PWM
(a) Modulating Signal
(b) Sample & hold modulating signal
(c) Carrier signal
(d) PWM waveforrm
(e) Fundamental of the PWM waveform

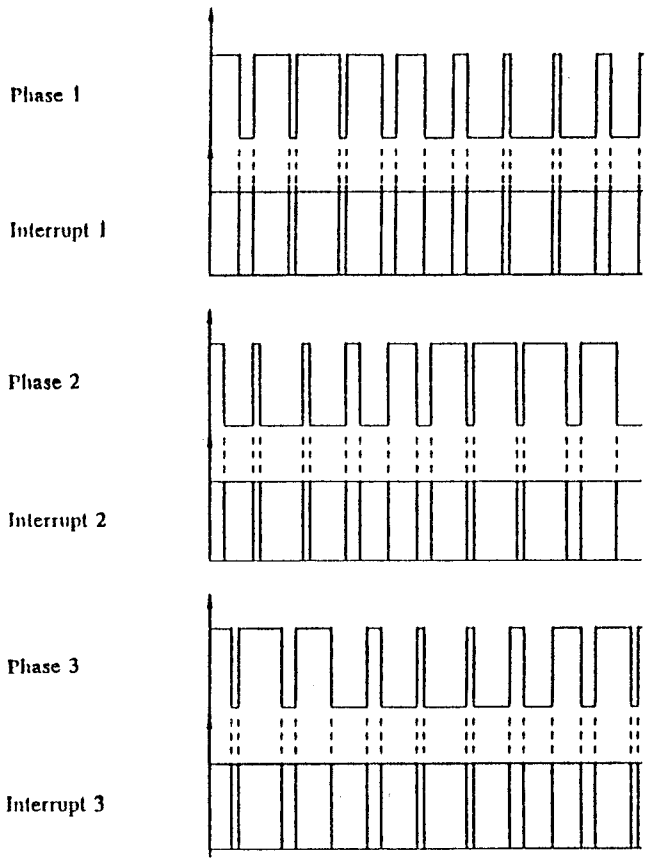
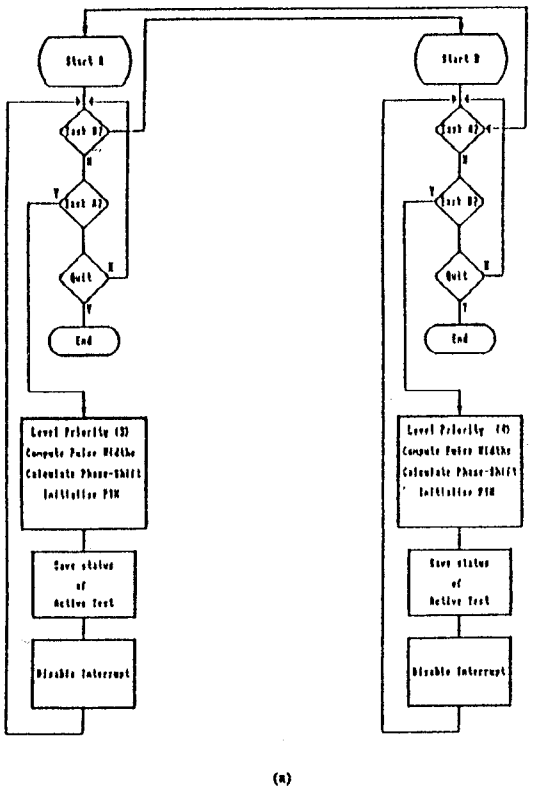
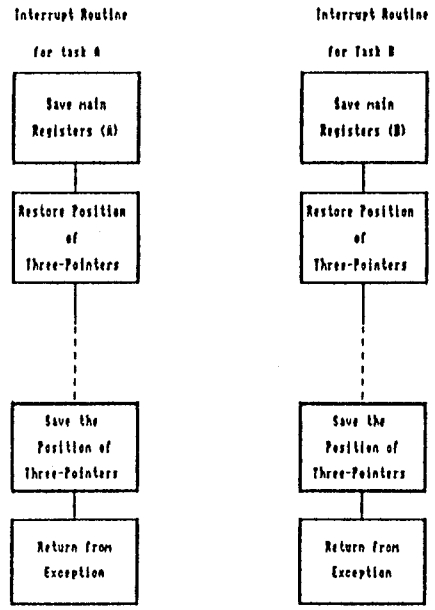


Fig.2 Output of the three-phase inverter and its corresponding interrupts



(a)



(b)

Fig.3 Flowchart of the time-sharing scheme (a&b)

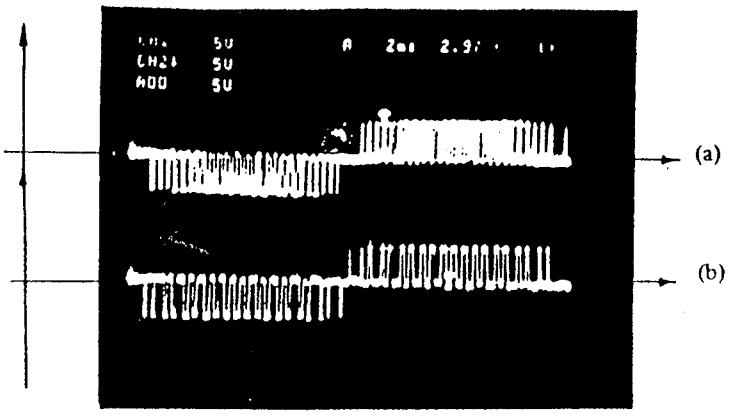


Fig.4 PTMs output for two different tasks
(a) F_c=2.85KHz, F_m=50Hz, M=0.8
(b) F_c=1.05KHz, F_m=50Hz, M=0.6

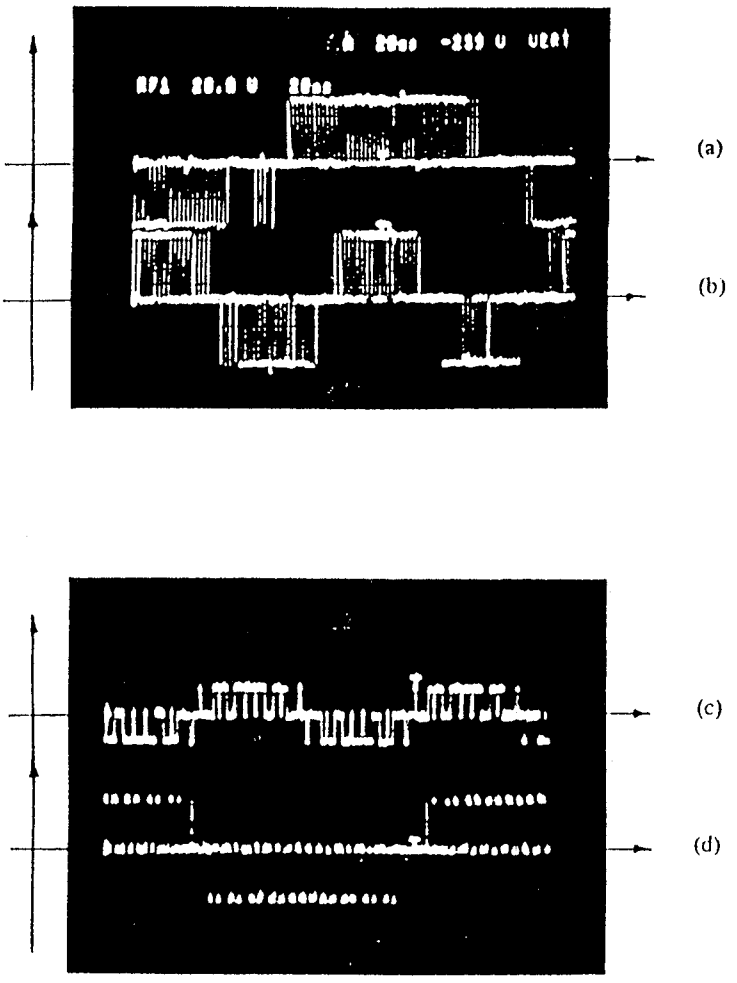
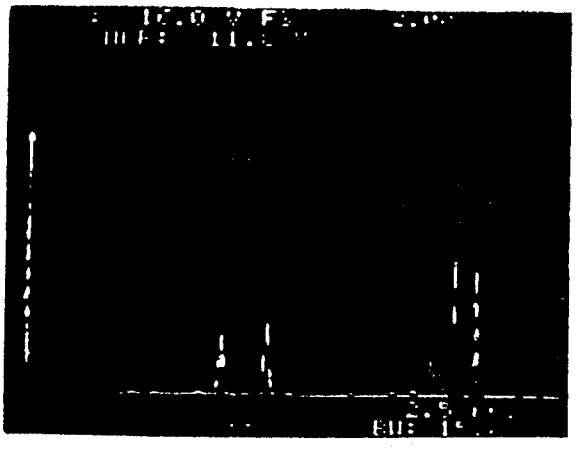
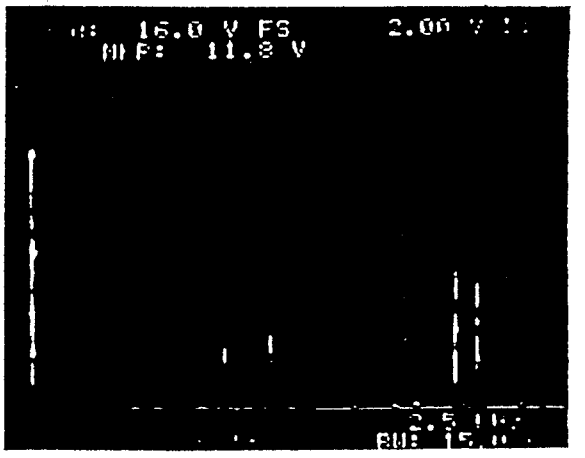


Fig.5 No load inverters outputs at different conditions
(a) F_c=.975KHz, F_m=5Hz, M=0.3
(b) F_c=1.05KHz, F_m=50Hz, M=0.8
(c) F_c=.9KHz, F_m=100Hz, M=0.9
(d) F_c=1.05KHz, F_m=50Hz, M=0.8



High Priority

(a) F_c=1.05KHz, F_m=50Hz, M=0.8



Low Priority

(b) F_c=1.05KHz, F_m=50Hz, M=0.8

Fig.6 Harmonic spectra for the higher & lower priority cases

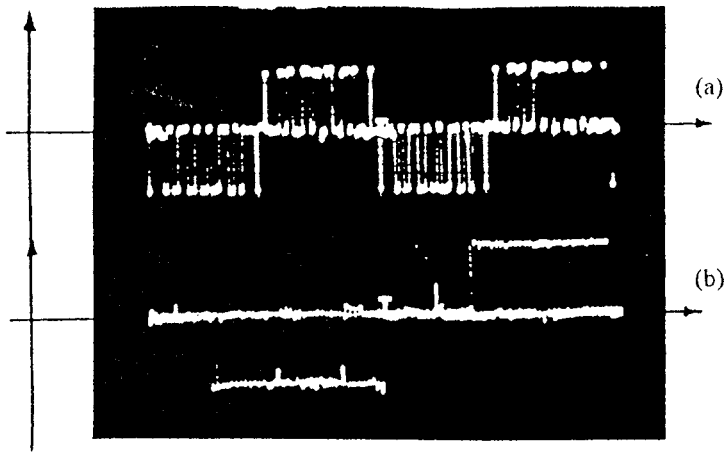


Fig.7 Resistance load test for two time-shared tasks
(a) F_c=.9KHz, F_m=100Hz, M=0.9
(b) F_c=.975KHz, F_m=5Hz, M=0.3

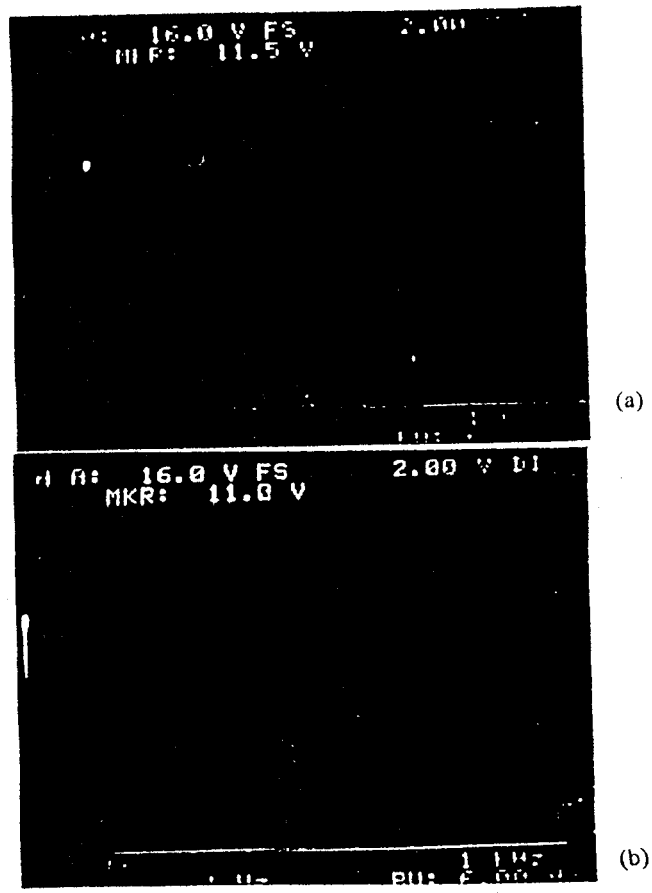


Fig.8 Harmonic spectra for the time-shared load test
(a) F_c=.9KHz, F_m=100Hz, M=0.9
(b) F_c=.975KHz, F_m=5Hz, M=0.3

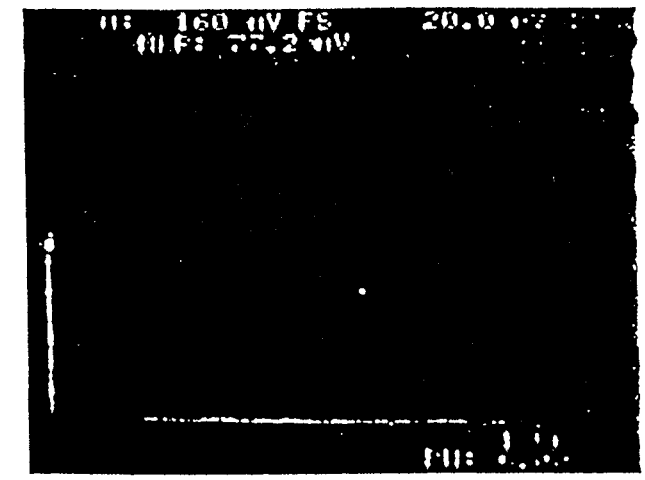


Fig.9 Harmonic spectra for
(a) time-shared controlled inverter
(b) Single inverter

RAPID PROTOTYPING TOOL FOR A FUZZY LOGIC BASED SOFT-STARTER

M.Rajendra Prasad and V.V.Sastry, Senior Member IEEE, FNAE
Department of Electrical Engineering
Indian Institute of Technology, Madras 600 036, INDIA.
Fax: +91 44 2350509, Phone: 2351365 Extn: 4007
E.Mail : sastry@acer.iitm.ernet.in

Abstract - **On account of the problems associated with the conventional starting techniques (D.O.L, Star-Delta, etc.) an efficient method of soft-starting is required with energy saving features and adaptive parameter setting capability. An optimal soft-starting is one that starts the motor with minimum voltage and reduced starting current limit (CURLIM). Starting current limit is different for motors of different ratings and for the same motor under different initial load conditions. Fuzzy logic has been adapted with a triangular membership function with a finite overlap between two membership grades to achieve the adaptive parameter setting capability. It features automatic setting of current limit and the optimality is achieved by performing the task with appropriate settings for a maximum firing angle (α_{max}), decrement of α ($\Delta\alpha$) and the delay time between the two successive decrements (Δt) calculated based on 'fuzzy logic'. The hardware interface is developed around a '8051 microcontroller based rapid prototyping tool' which interfaces the Personal Computer (PC) with the external world through its serial communication link. This tool improved the ease with which a prototype algorithm could be developed. All the algorithms are tested on different motors in the laboratory under different load conditions and found to be reliable and optimal. In all, a novel fuzzy logic based soft-start scheme for A.C. chopper fed induction motor drive is proposed and implemented using a rapid prototyping tool.**

I. INTRODUCTION

Electrical drives are playing a key role in all modern industrial applications because of their compactness in size, reliability, and ease in controllability. Owing to their importance, they require a highly reliable soft-start (vide Fig.1.). The algorithm involved in earlier developed soft-start schemes involved a gradual increase of voltage across the motor till the rated voltage appeared across the motor at the end of soft-start. It was observed that the efficiency and power factor were poor in that kind of soft-start under no load and light load conditions. If the system goes to the full conduction, the controllability over the system was some times lost and it was also leading to oscillations[2]. Moreover the starting current is different for motors of different ratings and for the same motor with different load conditions. So it requires man-machine interaction to set an appropriate current limit along with maximum firing angle (α_{max}), decrement of α ($\Delta\alpha$) and the delay time between the two successive decrements (Δt) based on the dynamics of the machine. Fuzzy logic based soft-start[4] eliminated all the above problems and the optimality is obtained by applying only an appropriate voltage with the

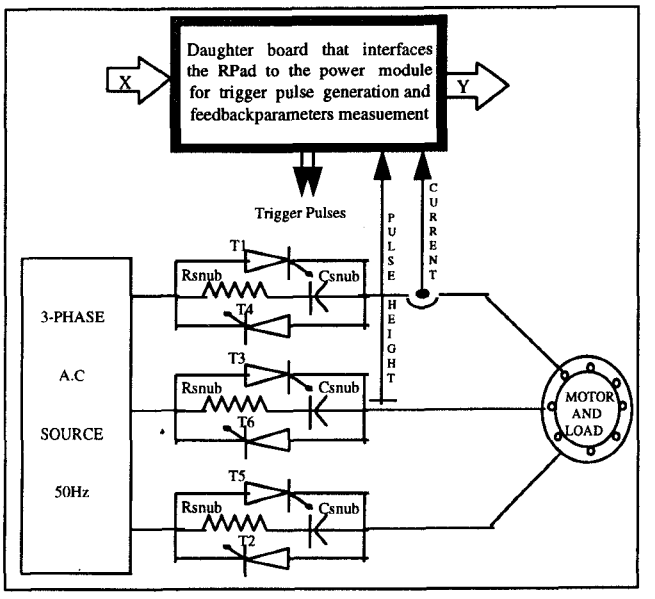


Fig.1. Voltage controller fed 3-phase Induction Motor Drive

parameters(α_{max}, $\Delta\alpha$ and Δt) set on line and detecting the end of soft-start based on the voltage across the non conducting thyristor (which will henceforth be called as pulse height)[5]. Pulse height is an indirect index of back e.m.f. and hence a drop of about 25% of its value at α_{max} is identified as end of soft-start. In the proposed scheme self-commissioning capability is established and the parameters are set on line based on 'fuzzy logic' with a triangular membership function implemented in a discrete function

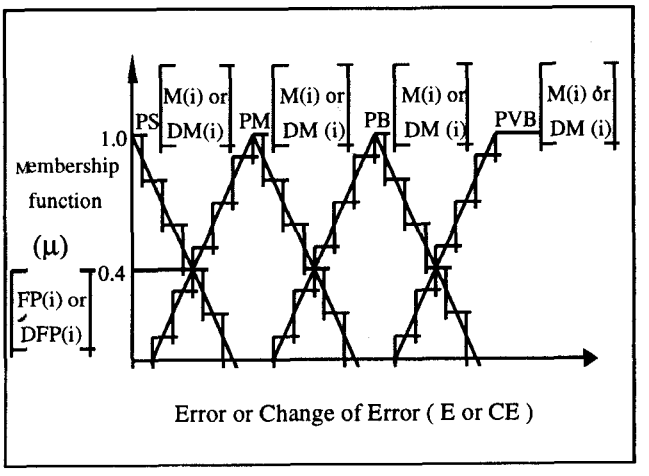


Fig.2. Membership function used in the 'Fuzzy Logic' based soft-start

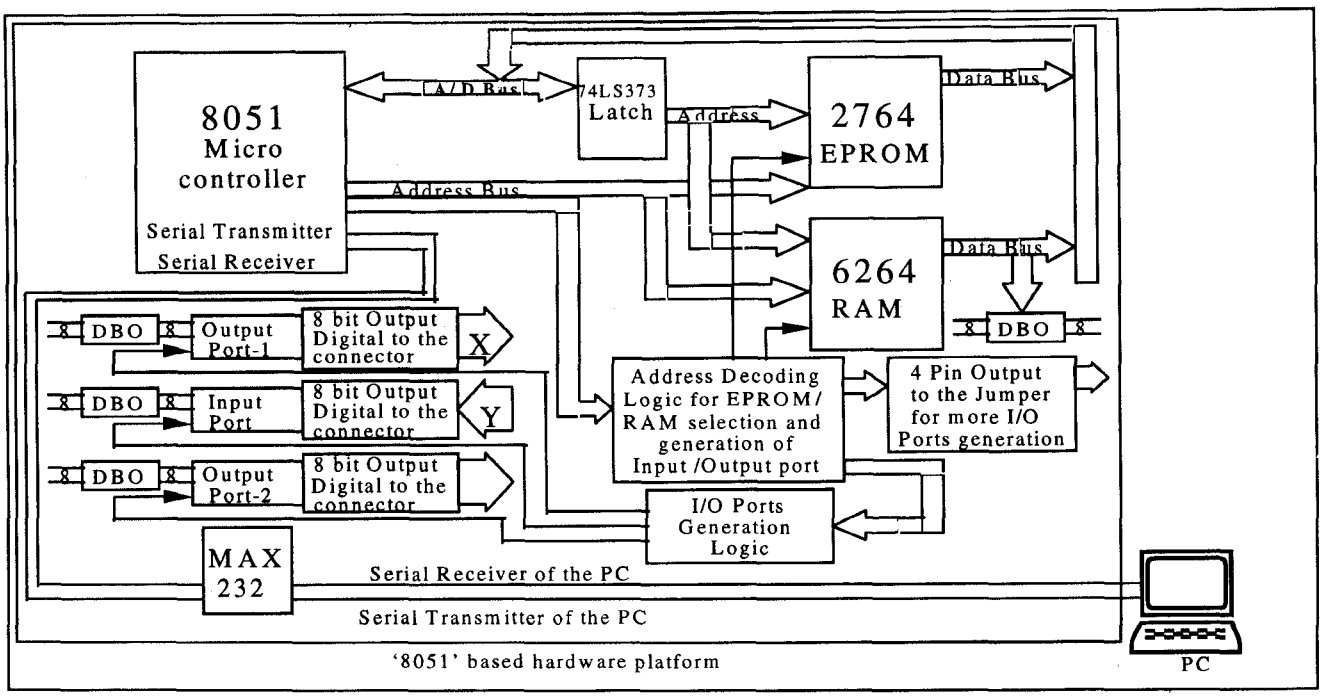


Fig.3. Block diagram representation of the 'Rapid Prototyping Tool' built around '8051' microcontroller

format with a finite overlap as shown in Fig.2. The earlier reported works[4],[5] deal with the implementation of the same logic with a rectangular membership function. This was implemented around '8085' microprocessor in the form of a simple look up table. Effective implementation of a complex membership in real-time for an improvement in performance using the earlier conventional development methods (involved erasing and fusing the 'EPROM' on a dedicated board) is tedious and time taking. To circumvent this difficulty a 'Rapid Prototype Algorithm Development Tool' (RPAD)is developed by which the control code is down loaded into the external RAM through RS232 serial link of the PC and executed with a microcontroller.

II. Hardware Development

Microcontroller is an appropriate tool for any real-time control application. The hardware development for the specific application and the corresponding software development are the two tasks involved in it. So there is a need for the development of basic hardware for any real-time control application. An 8 bit Microcontroller is used in the external world for a two way communication with the P.C. through it's duplex serial port. Fig.3 gives the over all block diagram of the tool. A daughter board is designed to interface the RPAD to the A.C voltage controller module. It consists of driver circuitries to connect the trigger pulses from the output port to the gate and cathode terminals of the thyristors. It also consists of the necessary circuitries for stepping down and filtering the control parameters Viz. current and voltage across the non-conducting thyristor to make them readable through the microcontroller using an ADC to implement the given control strategy in real time environment.

III. Methodology and Software Development

The methodology followed for the real-time implementation of fuzzy logic for the improvement of optimality is shown in Fig.4. The sequential procedure lies in finding out the error and change in error of the feed back variables (current and pulse height) and fuzzyfying them with a triangular membership function with a finite overlap. This fuzzified output is processed through the minimum-maximum compensation routine. Finally the de-fuzzification (DEFUZ) is performed with the center of gravity approach[7] using the variables decided based on a set of rules defined for different control parameters (α_{max}, $\Delta\alpha$ and CURLIM). The flow chart of the whole fuzzy logic based soft-start control algorithm is given in Fig.5. This

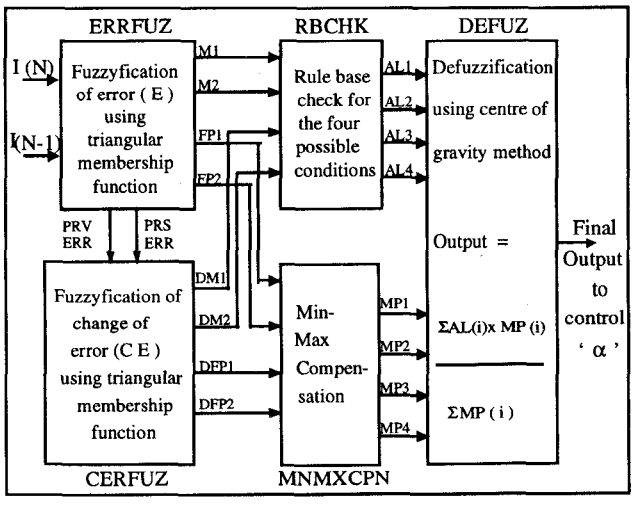


Fig.4. Methodology of 'Fuzzy Logic' implementation in real-time

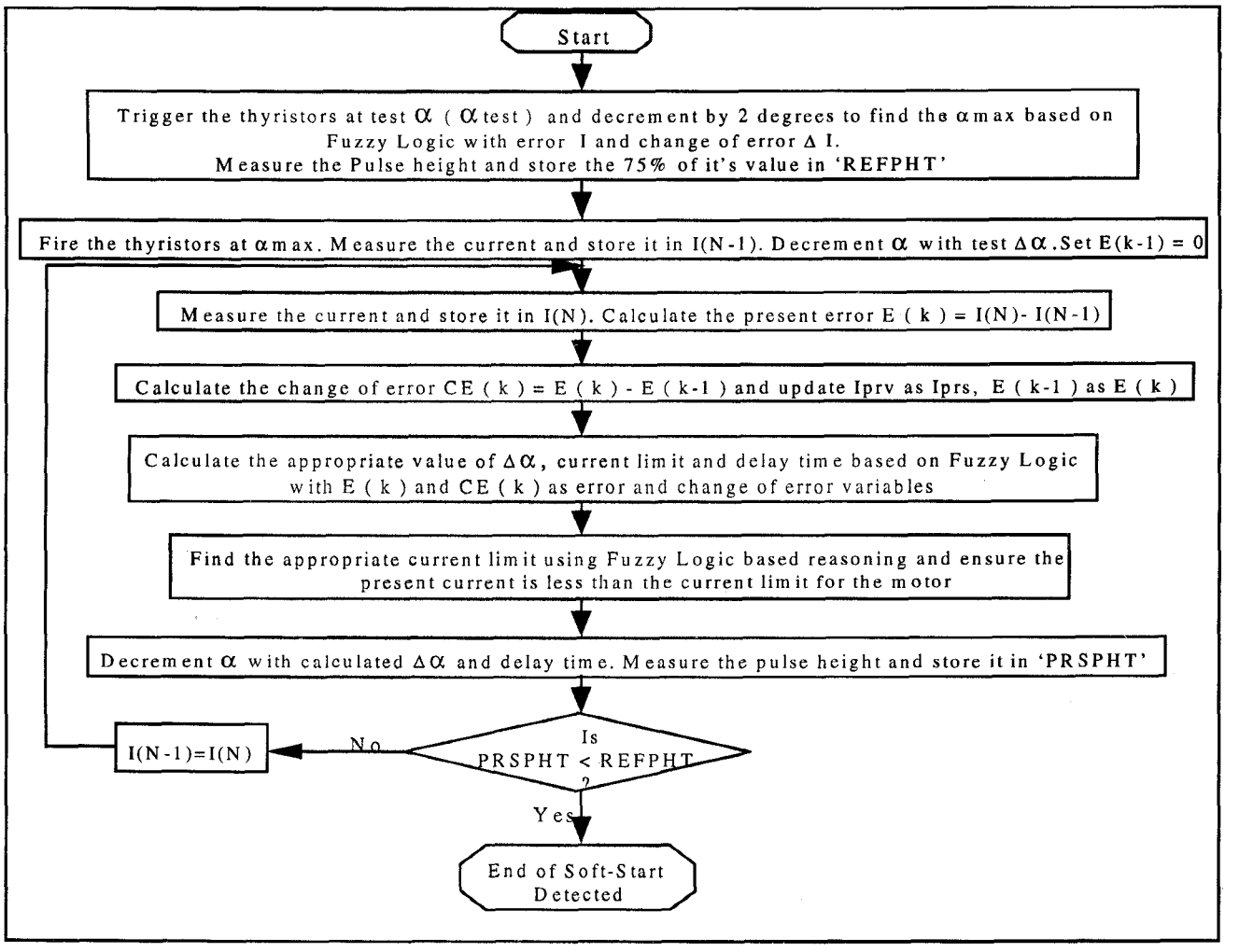


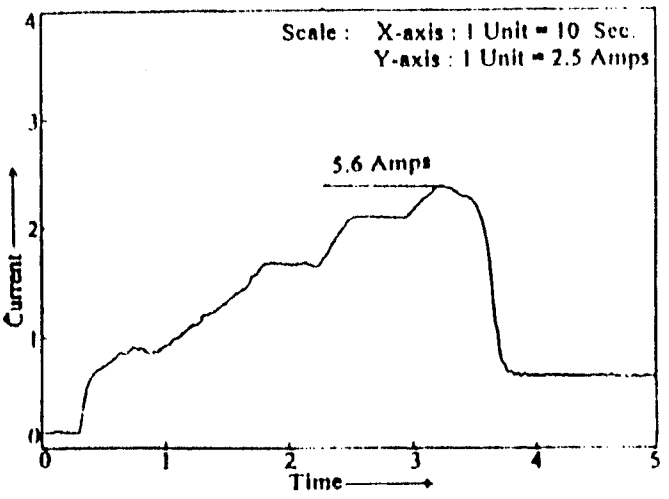
Fig.5. Flow chart of the whole process involved in 'Fuzzy soft-start scheme'

process starts by triggering the thyristors at α_{max}, decided based on 'fuzzy logic'. It is carried out till the end of soft-start is identified i.e., when the pulse height drops to 75% of its initial value[6]. Improvement in optimality compared to the earlier developed "Fuzzy Logic based soft-start with a rectangular membership function" [4] is achieved by performing the process with appropriate parameters calculated using a fuzzy algorithm. The experimental results for different soft-start algorithms recorded using a waveform analyzing recorder (of Yokogowa make) for a 2.2kW, 3-phase, 415V squirrel cage induction motor are given in Fig.6. The quantitative analysis of these results are represented in Table.1. It can be observed from Table.1 and Fig.6 that there is a reduction in the starting current limit and the terminal voltage at the end of soft-start in the present scheme when compared with the earlier reported schemes and thus achieving an improvement in the optimality of soft-start.

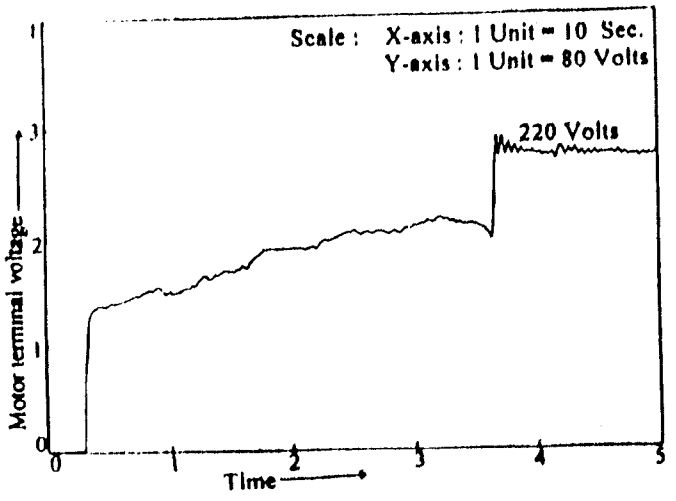
TABLE I

QUANTITATIVE ANALYSIS OF OPTIMALITY IN DIFFERENT TYPES OF SOFT-STARTING SCHEMES AT NO LOAD
(MOTOR RATINGS: 2.2 kW, 3-Phase, 415V, 4.5 Amps, 1470 RPM)

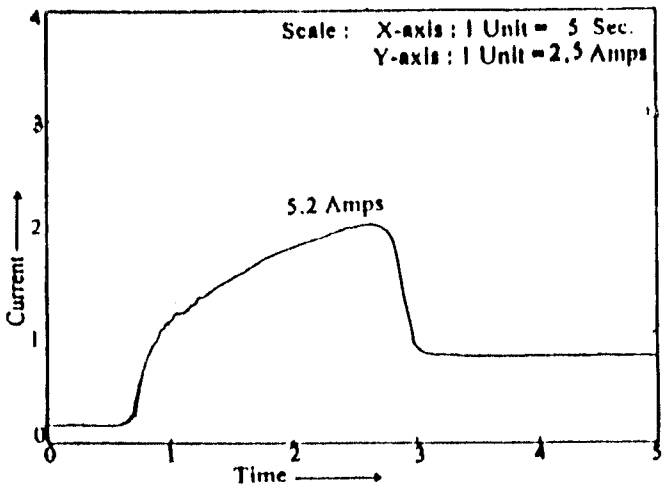
Type of soft-start scheme / Parameter	Novel soft-start with preset parameters	Fuzzy soft-start with rectangular membership function	Fuzzy soft-start with triangular membership function
Starting Current limit (in Amps)	7.9	5.6	5.2
Motor terminal voltage at the end of soft-start (in Volts)	295	220	202



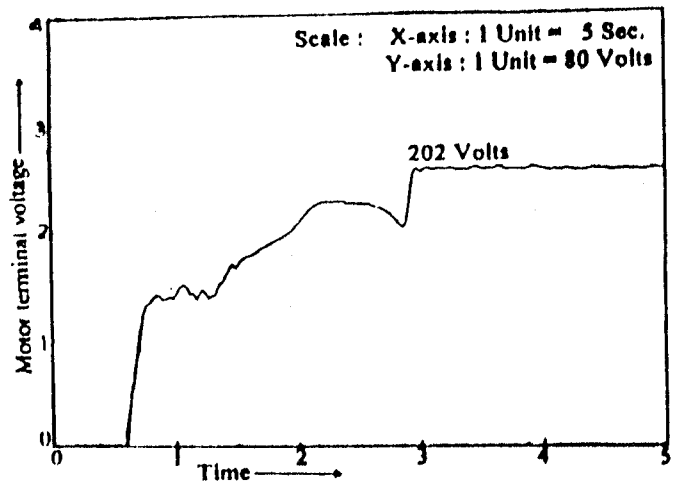
Current profile for 'fuzzy logic based soft-start' with rectangular membership function at no load



Profile of the motor terminal voltage for 'fuzzy logic based soft-start' with rectangular membership function at no load



Current profile for 'fuzzy logic based soft-start' with triangular membership function at no load



Profile of the motor terminal voltage for 'fuzzy logic based soft-start' with triangular membership function at no load

Fig.6. Experimental results for different soft-start schemes at no load

IV . CONCLUSIONS

This paper presents a fuzzy logic based soft-start scheme. The superiority of this scheme is the improvement in the optimality by a further reduction in the value of voltage applied to the motor terminals at the end of soft-start (vide Table.1). The improved optimality using a triangular membership function however increased the software complexity and overheads causing the external RAM capacity to be increased from 8Kbytes to 16Kbytes.The whole scheme is developed around a rapid prototyping tool and validated experimentally.

REFERENCES

(1) Timothy M . Rowan and Thomas A .Lipo, "A Quantitative Analysis of Induction Motor Performance Improvement by SCR Voltage Control", *IEEE Transactions on Industrial Applications*, July/August 1993, Vol.IA-19, No.4, pp. 545-553.

(2) G.Bhuvaneswari, *"An Intelligent solid-state Inauction Motor*, Ph.D Thesis, I.I.T., Madras, January 1992.

(3) R.S.Janardhana Iyengar *Novel techniques for energy efficient voltage controlled Induction Motor drives*, Ph.D Thesis, I.I.T., Madras, May 1995.

(4) R.S.Janardhana Iyengar and V.V.Sastry, "Fuzzy Logic based Soft-Start for Induction Motor Drives", *Proceedings of IEEE-IAS Annual Meeting*, Orlando(U.S), October 1995.

(5) G.Kaplan, Industrial Electronics, *IEEE Spectrum*, January 1996, pp. 96-100,

(6) V.V.Sastry, P.S.Ganesh and V.Madhavi, "High performance Induction Motor controller using Thyristor Voltage Feedback", *Proceedings of IEEE international conference on Power Electronics Drives and Energy Systems (PEDES-96) for Industrial Growth*, New Delhi, January 1996.

(7) Bart Kosko, *Neural networks and Fuzzy systems*, Prentice Hall, 1994.

Accurate Measurement of Instantaneous Voltage for Power Electronics Circuits

Tung-Hai Chin Motomu Nakano Takashi Hirayama

Sophia University, Dept. of Electrical and Electronics Engrg.
Kioi-cho 7-1, Chiyoda-ku, Tokyo 102, Japan
Tel: 03-3238-3335, Fax: 03-3238-3321
E-mail: chin@tokai.ee.sophia.ac.jp

Abstract **~ For power electronics circuits such as the inverter circuits, the measurement of the instantaneous average value of the output voltage is rather troublesome and has never been undertaken in a rigorous sense. However, it becomes important, when the inner states of the load connected to the inverter has to be calculated using the quantities of the load terminal voltages and currents, such as in the case of vector control of the induction motor without speed sensor. This paper tries to give an accurate measuring method for it. The voltage cluster from the inverter is integrated every half period of the switching. Then the output of the integrator will be reset to zero after its volt-second value has been detected digitally. Two groups of the circuit take the alternative operation. High accuracy and linearity of the measurement can be achieved. As the concerning subject, the measurement of the instantaneous current has also been discussed.**

1. Introduction

For power electronics circuits such as the inverter circuits, the measurement of the instantaneous average value of the output voltage during each period is rather troublesome and has never been undertaken in a rigorous sense. The reason may be that the exact value of the output voltage of the power electronics circuit is not essentially important, because it is the output current or the frequency which should be controlled accurately even for voltage source inverter in most cases. However, the measurement of voltage becomes important, when the inner states of the load connected to the inverter has to be calculated using the quantities of the load terminal voltages and currents, such as in the case of vector control of the induction motor without speed sensor, or in the case where on-line parameter identification is going to be undertaken. In the former case, the accurate measurement of the instantaneous average voltage is very important to exactly estimate the rotor speed and get stable operation, especially in the lower revolving speed range.

From another stand point, it is not desirable that there exists no accurate measuring method for the instantaneous voltage output from power electronics circuits, even though the technology of power electronics has already matured. This paper tries to give an accurate measuring method for it. And as the concerning subject, the measurement of the instantaneous current has also been discussed.

2. Issues of Instantaneous Voltage Measurement

Several methods of instantaneous voltage measurement for power electronics circuits have been reported. The most accurate method in them is to measure the width of the voltage cluster by some digital method and then to multiply its value by the input dc voltage which should also be detected using some adequate equipment [1]. This method is not so simple but expensive, and moreover, the error due to the voltage drop of the switching devices and the free-wheeling diodes, which becomes more prominent in lower output voltage range, can not been compensated. Fig. 1 shows the zero level voltage of the line voltage of an IGBT PWM inverter with rated voltage of 200 V. One can recognize that the zero level voltage varies from about 3 volts to minus 3 volts according the direction of the inverter output currents, even though the output PWM voltage is kept in the same polarity. This deviation of zero level voltage is induced by the forward drop of IGBTs and free-wheeling diodes of the inverter. The top flat peak value of the PWM wave-form, which is over scaled and not displayed in Fig. 1, will also be distorted in the same manner. This deviation of voltage will cause voltage measuring error of several tens percent in low revolving range, say 2 or 3 Hz.

0-7803-3823-5/97/$10.00© 1997 IEEE

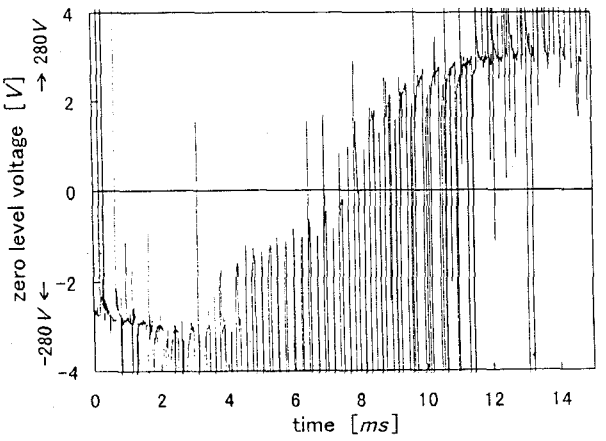


Fig. 1 The variation of the zero level voltage of the inverter line voltage. The top of the PWM wave is out of scale and not displayed. Inspecting the figure in detail, three steps of voltage changes during half cycle can be recognized.

Occasionally, the output voltage has been estimated indirectly from the source voltage value which has been used to decide the PWM pattern. In this case, not only the error due to the variation of the zero level voltage, but also the error due to the dead time will be induced.

There is also method where some low pass filter is used and then the voltage is digitally detected at the output of the filter. The premise of this method is not to measure the voltage instantaneously, but to measure it as a whole. In other words, the steady state voltage of the fundamental component is to be measured, and its instantaneous variation will be masked. Another problem of this method can be described as follows. The filter is inserted for voltage measurement, however it also acts as a circuit block in the whole control system. For example, in a sensor-less vector control system, an additional low pass filter will be inserted in the estimating loop for rotor speed, and it will affect the response or stability of the whole control system. Consequently, the effect of the low pass filter upon the control characteristics should be investigated.

3. HERE PROPOSED METHOD

Here proposed method for instantaneous voltage measurement is just to avoid the defects of the above-mentioned methods. At first, the voltage cluster within every half period of the inverter switching is integrated. After then, the integration is stopped, and the output of the integrator is hold during a defined interval for observation and digital detection of its volt-second value. At last, the integrator is reset to zero and waiting for the next operation. Consequently, two groups of the circuit are necessary for alternating operation of the measurement.

Fig. 2 shows the measuring circuit and Fig. 3 the timing chart and the wave-forms of the circuit. In Fig. 2, two groups of the integrator are used and they operate alternately every half switching period according to the sequence shown in Fig. 3. Here, the case of constant switching period is considered, and the timing pulse is given from the inverter circuit. As the switches shown in Fig. 2, MOS type analogue switch can be used, which acts as a variable resistance in the on-state. Comparing with the other resistance values of the circuit elements, the on resistance of the analogue switch is generally low, from 60 to 120 ohm for example, and will not cause significant effect on the circuit operation.

In Fig. 3, fictitious PWM pulse train of input voltage is given in (a) for description. The vertical dashed lines show the boundaries of the integration which correspond to the half period of the inverter switching. Figure (b) is the output of the upper group integrator, where the PWM voltage is integrated in the first half period (from t_1 to t_3) and the integrator holds its value for another one half of the half period for volt-second value measurement (from t_3 to t_4), after then the capacitor is discharged to zero for preparation of the next operation (at t_4). Figure (c) shows the output of the lower group integrator whose sequence shifts by half of the inverter switching period from that of the upper group integrator. Upper and lower groups of the integrator operate alternatively according the sequences shown in Fig. 3, and their outputs are sent out through the analogue switches. Figure (d) is the output wave-form of the measuring system. Only the value in the holding interval (t_3 - t_4, for example) is output for volt-second value measurement and observation.

The merits of here proposed method are as follows.

a) The integrated value is the volt-second value of the voltage cluster during every half switching period. Dividing it by the half period, the instantaneous average voltage defined for every half switching period can be gotten.

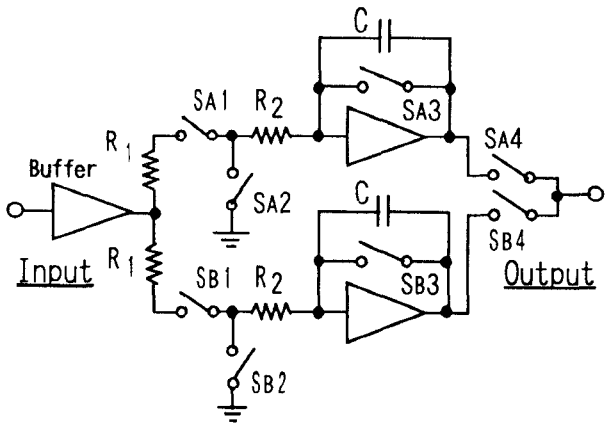


Fig. 2 The circuit diagram of the measuring circuit

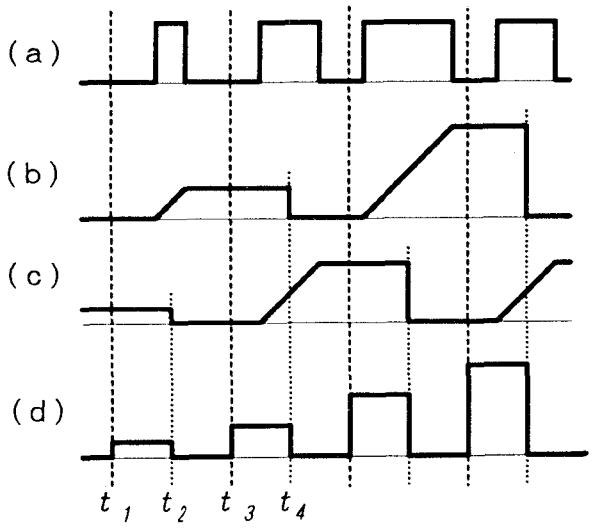


Fig. 3 Wave-forms of the circuit. The sequence of the switching is as follows.

t_1 : SA1, SB2, SB4= ON SB1, SA2, SA3, SA4=OFF

t_2 : SB3 = ON

t_3 : SB1, SA2, SA4 = ON SA1, SA2, SA3, SA4= OFF

t_4 : SA3 = ON

b) The integrator is reset to zero every half cycle, then the drift of the integrator will not cause trouble.

c) The full dynamic range of the integrator can be used for every measuring procedure, then the resolution of the measurement can be made high and precision measurement is possible.

d) The total circuit is simple and of low cost.

Fig. 4 shows the experimental wave-forms. Upper wave-form is the line voltage of an inverter, where the pulse train is just going from minus value to positive. DC source voltage is 280 V and switching half period is 240 μs. Lower wave-form is the output wave-form of the integrator, where the height of the pulse corresponds to the area of the PWM voltage at half switching period before it. The linearity and the accuracy of the measuring circuit is fundamentally depending on the design of the analogue integrating circuit. Resolution of the measurement over 8 digits after A/D transformation can easily be achieved.

Fig. 5 is another sample of the experimental wave-form. The height of the pulses indicates the average value of the voltage cluster from an vector control inverter on the market. One can recognize the voltage fluctuation on the particular part of the sinusoidal wave, which will not be detectable using other measuring method.

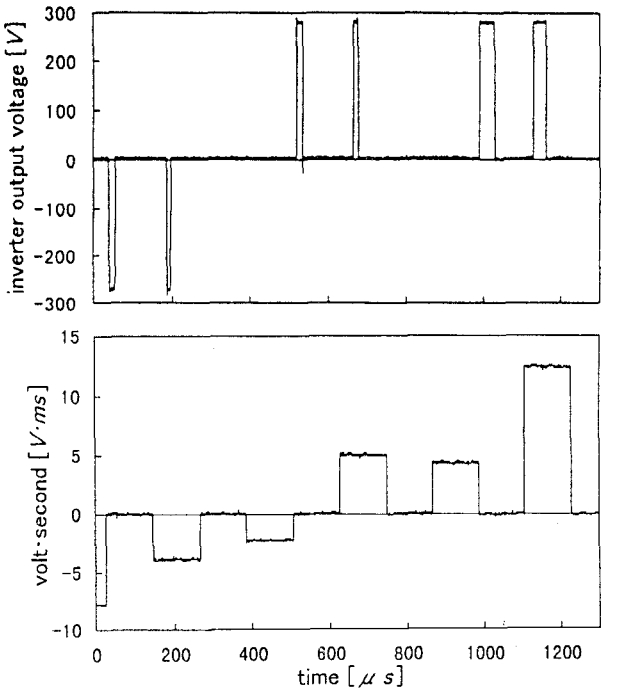


Fig. 4 Wave-form example of measurement upper: inverter line voltage, lower: volt-second value of the voltage cluster at one sample before it.

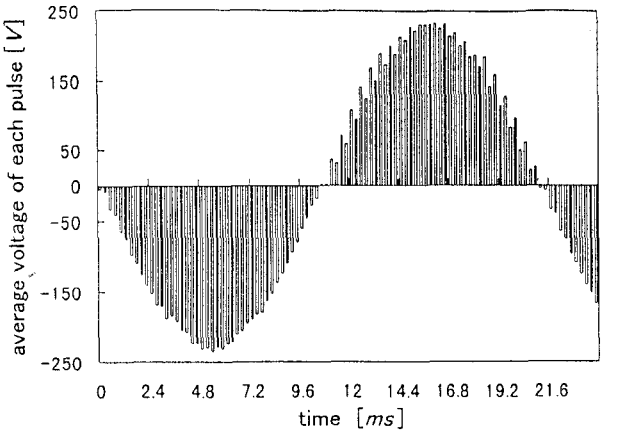


Fig. 5 Instantaneous average value of the output voltage (switching half period: 240 μs, output frequency: 50 Hz)

4. ABOUT THE MEASUREMENT OF THE INSTANTANEOUS CURRENT

The measurement of instantaneous current is also an important subject for power electronics. It has been reported that the current value sampled at the center of the switching period is nearly equal to the value of the fundamental component of the current at that instant [2]. The current wave-form of the inverter which fed PWM voltage to an induction motor has been simulated as shown in Fig. 6. The circles on the wave is the sampled current at the peak and bottom of the triangular carrier wave for PWM pattern generation. The indicated values of the circles are nearly equal to the value of the fundamental component at same instant, and the deviation between them is under one or two percent. So, the sample values at the switching boundaries and the center of the switching period can be used as the instantaneous value of the fundamental current wave at that instant, reminding their possible error.

The saw teeth wave shown in Fig. 6 is the integrated value of the current, but it has been reset to zero at the boundary of every switching period. The integrated values at the reset boundary are exactly the defined average value of the current. This value is also nearly equal to the value of the fundamental wave at the center point of the switching period, and the deviation is also under 1 to 2 percent. However, when the integration has been taken during half switching period, the deviation between the integrated value and the center value of the fundamental wave during the half period has been over 6 to 7 percent sometimes. This means that the harmonic currents in the fore half period is not symmetrical to that of the latter half period. One can recognize this asymmetry from the inclined slop of the saw teeth wave, which waves badly in some switching period. So, the integrated value of the current is really the average value as its definition, but the integration interval must be a full switching period. The reason is that, from the standpoint of the phase current, the voltage pattern is not symmetrical concerning the center of the switching period.

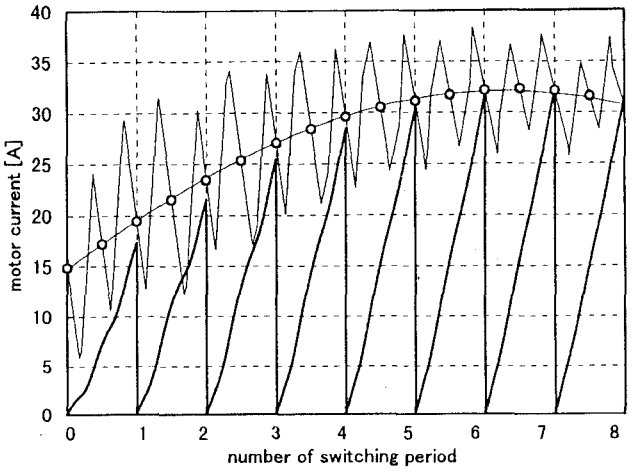


Fig.6 Simulation of motor current
motor rating: 4 poles, 25kW, 200 V, 50 Hz
(The condition of operation is50 Hz, 100 V. For emphasizing the harmonic components, the voltage is reduced.)

5. CONCLUSION

Method for precision measurement of the instantaneous average voltage during each period for the power electronics circuits is proposed. Because the intermediate voltage value among the switching interval has no meaning as a whole, the integration method is undertaken. By resetting the integrator every half period of the switching, the usually accompanying problem of the integrator can be solved and as well as the problem of measuring precision. A measuring system of instantaneous average value for power electronics equipment with resolution of 8 digits and good linearity can be realized. Good result is expected in its application. For example, when this method is applied to sensor-less vector control of induction motor, the stability of the control circuit is expected to be improved, especially in the low revolving speed range.

As the relative matter, the measurement of the current has also been discussed. To get the average value of the current, here proposed method can also be applied. However, the averaging interval should be one full switching period. Half period integration will cause large error.

REFERENCES

[1] G. Yang, T.H. Chin, "Instantaneous output voltage detector for voltage source inverter," JIEE National Conference, vol. 5, no. 489, p. 41, 1990

[2] Morita, Hayashi, Sato, "Method of vector control of induction motor with reduced torque pulsation," JIEE Seminar for semiconductor power conversion, SPC-87-55, p. 11, 1987

Analysis of the Tuned-Average Current-Mode Control of the Constant Frequency DC/DC Converters

Predrag Ninković, Marko Janković
EE Institute Nikola Tesla, Department of Automatic Control
Koste Glavinića 8A, Belgrade 11000, YUGOSLAVIA
Fax: +381-11-2351-823, Phone +381-11-2351-412
E-mail: ninkov05695p@buef31.etf.bg.ac.yu

Abstract **- This paper presents an original method for inductor current control of constant-frequency DC/DC converters operating in continuous current mode. It includes information about voltage in current loop. Its main features are stable operation over full range of duty cycle variations without subharmonic oscillations, fast dynamic response and inherent short-circuit protection. Therefore, no artificial means of stabilizing should be provided as with peak current-mode control. Excellent dynamic response is achieved compared to other existing control methods. Implementation is simple and advantageous. Since the converter is of a discrete nature, its sampled-data model is analyzed and small-signal analysis is performed. Experimental model of buck converter is tested, and the results of it's transient response are obtained. Boost and buck-boost converters are analyzed and the results are briefly reviewed.**

I. Introduction

Current-mode control seems to be the most suitable way to control DC/DC converters. Its origin is well-known peak current-mode[1,2,3]. Many of its modifications appeared in last few years[4,5,6,7]. Most of them suffer from the same disadvantage as their origin does - subharmonic oscillations exist, so artificial means of stabilizing should be provided [4,6,7]. Another approach is quasi-charge control[5] that does not suffer from subharmonics. Its disadvantage is nonlinear average inductor current to reference value ratio.

This paper presents another approach of current-mode control of inductor current in PWM DC/DC converters. Stable operation is achieved over full range of duty-cycle variations. There are no subharmonic oscillations and therefore, a need for stabilizing does not exist. Very good dynamic response and inherent short-circuit protection are maintained. Improvement is made in linear average inductor current to reference value ratio.

II. Theoretical Analysis

In this section some important aspects are analyzed, which include basics, stability analysis and transfer function. As an example, buck converter topology is analyzed. Since the control method is of a discrete nature, discrete-time analysis is more convenient for this purpose than the continuous one. Large-signal and small-signal models are derived and stability conditions are determined.

A. Basics

The basic idea is very simple. For simplicity, components are assumed to be ideal, the input voltage is constant and the output voltage ripple is negligible. The main goal is to control the average inductor current value on one switching period. If $V_{L,FALL}$ is inductor voltage during falling edge of its current, then, according to Fig.1 and Fig.2, in steady state, average inductor current $I_{L,AVG}$ is related to peak inductor current $I_{L,peak}$ as follows:

$$I_{L,peak} = I_{L,AVG} + \frac{1}{2} \cdot \int_{kT+t_{on}}^{kT+T} \frac{|V_{L,FALL}|}{L} \cdot dt, \qquad (1)$$

where kT is the beginning of the k-th cycle. The final form of (1) is:

$$I_{L,peak} = I_{L,AVG} + \frac{|V_{L,FALL}|}{2 \cdot L} - \frac{1}{2 \cdot L} \cdot \int_{kT}^{kT+t_{on}} |V_{L,FALL}| \cdot dt. \qquad (2)$$

One can notice that there is one resetable integrator, i.e. its value at the beginning of each cycle must be set to zero.

Eq.(2) can be implemented in practical converter as a constraint function [8] by substituting $I_{L,AVG}$ with the reference value. In this manner, the right-handed side of (2) becomes the main computational part of current loop and it is compared with the instant inductor current value. The moment these two values became equal, the switch turns off (the current reaches its peak value). At the beginning of next cycle, the integrator will be set to zero, and the switch will be turned on again.

In the case of buck converter, $|V_{L,FALL}|$ is equal to output voltage value in ideal model, and in real model it has some additional components:

$$|V_{L,FALL}| = V_{out} + R_L \cdot i_L + V_{diode}, \qquad (3)$$

where V_{out} is output voltage, R_L is inductor parasitic resistance and V_d is forward biased freewheeling diode voltage drop.

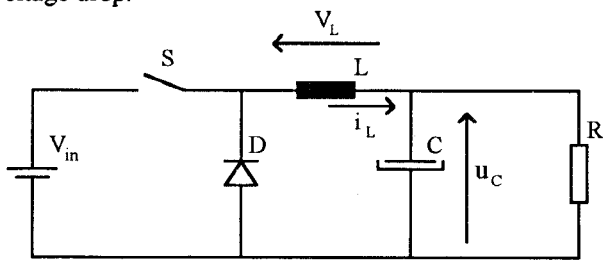


Fig.1 Buck converter schematic

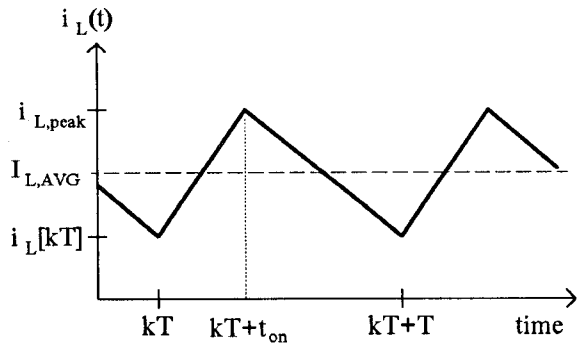


Fig.2. Steady-state inductor current vaweform in buck converter

B. Large-Signal Model

The discrete-time large-signal sampled-data model of buck converter has the form:

$$\begin{bmatrix} i_L[k+1] \\ u_C[k+1] \end{bmatrix} = \begin{bmatrix} 1 & -\frac{T}{L} \\ \frac{T}{C} & 1-\frac{T}{RC} \end{bmatrix} \cdot \begin{bmatrix} i_L[k] \\ u_C[k] \end{bmatrix} + \begin{bmatrix} \frac{d_k \cdot T}{L} & 0 \\ 0 & 0 \end{bmatrix} \cdot \begin{bmatrix} v_{in}[k] \\ I_{ref}[k] \end{bmatrix}, \quad (4)$$

where $i_L[k+1]$ and $i_L[k]$ are inductor current values sampled at the beginning of the k+1-st cycle and k-th cycle, respectively. The same reason is valid for the output filter capacitor voltage u_C, input voltage v_{in} and reference I_{ref}. T is the switching period, and d_k is the duty-cycle in the k-th cycle of operation. This model is derived from the continuous-time state-space model of buck converter by discretization.

In the case of ideal buck converter, substituting u_C as $|V_{L,FALL}|$ in (2), constraint function gets the form:

$$I_{L,peak} = I_{ref} + \frac{u_C}{2 \cdot L} - \frac{1}{2 \cdot L} \cdot \int_{kT}^{kT+t_{on}} u_C \cdot dt. \quad (5)$$

Constraint equation in a discrete-time takes the form:

$$0 = \frac{2 \cdot L}{T} \cdot (I_{ref}[k] - i_L[k]) + (1-d_k) \cdot u_C[k] - 2 \cdot d_k \cdot v_{in}[k]. \quad (6)$$

Obviously, this model is nonlinear, due to (6). Linearization around steady-state operating point will give the sampled-data small-signal model which can be easily analyzed.

C. Small-signal Model

By means of linearization[8], small-signal model is derived from (4) and (6):

$$\begin{bmatrix} \tilde{i}_L[k+1] \\ \tilde{u}_C[k+1] \end{bmatrix} = \begin{bmatrix} \frac{D}{2+D} & -\frac{T}{L} \cdot \frac{2D+1}{2+D} \\ \frac{T}{C} & 1-\frac{T}{RC} \end{bmatrix} \cdot \begin{bmatrix} \tilde{i}_L[k] \\ \tilde{u}_C[k] \end{bmatrix}$$

$$+ \begin{bmatrix} \frac{T}{L} \cdot \frac{D^2}{2+D} & \frac{2}{2+D} \\ 0 & 0 \end{bmatrix} \cdot \begin{bmatrix} \tilde{v}_{in}[k] \\ \tilde{I}_{ref}[k] \end{bmatrix} =$$

$$= [A] \cdot \begin{bmatrix} \tilde{i}_L[k] \\ \tilde{u}_C[k] \end{bmatrix} + [B] \cdot \begin{bmatrix} \tilde{v}_{in}[k] \\ \tilde{I}_{ref}[k] \end{bmatrix}, \quad (7)$$

where "~" denotes the small-signal perturbation, D is the steady-state duty-cycle, and *[A]* is known as the discrete-time system matrix.

Further developing of this linearized system brings out its characteristic polynomial. The goal is to obtain natural ratios (natural frequencies) from the relation:

$$\det(zI - A) = 0, \quad (8)$$

where I is the identity matrix.

If the modules of natural ratios lie inside the unit circle, than the system is said to be asymptotically stable. If one of them is less than one and positive, it causes exponentially damped component of transient response. Substituting *[A]* from (7) in (8), characteristic polynomial is obtained:

$$\det(zI - A) = \frac{D}{2+D} \cdot (1 - \frac{T}{RC}) + \frac{T^2}{LC} \cdot \frac{2D+1}{2+D}. \quad (9)$$

It is obvious that

$$\frac{T^2}{LC} \cdot \frac{2D+1}{2+D} < \frac{T^2}{LC} = M, \quad (10)$$

so, since M is negligible in a properly designed output filter, the characteristic polynomial has new form:

$$\det(zI - A) = \frac{D}{2+D} \cdot (1 - \frac{T}{RC}). \quad (11)$$

There are two natural ratios:

$$z_1 = \frac{D}{2+D}, \quad z_2 = 1 - \frac{T}{RC}. \quad (12)$$

Both of them are real. The first one is always less than one and positive. The other is less then one if

$$\frac{T}{RC} < 2, \quad (13)$$

which is true in the most cases.

The first natural ratio z_1 has origin in current loop response. The second one is obviously a natural ratio of parallel RC circuit with constant current injected into it. z_1 is always less than 1/3 and, assuming that C is sufficiently large and R is not too small, it is clearly distinguished from z_2. The closer z_1 is to zero, the current loop has faster response. This gives rise to an idea that as far as these two ratios are clearly distinguished from each other, the inner current loop can be viewed as pure gain if there is an outer voltage loop.

This analysis has shown that the system is stable for all values of duty-cycle, which means that there is no need for

additional means of stabilization. Also, if the switching period T is small enough, which is the common practice, then both natural ratios are positive, too. This fact means that transient response is purely exponential, without oscillatory terms.

D. Transfer Function

Two variables of interest are inductor current i_L and output voltage u_C. Considering them output variables, the vector of output variables can be formed:

$$y[k]=\begin{bmatrix}1 & 0\\ 0 & 1\end{bmatrix}\cdot\begin{bmatrix}i_L[k]\\ u_C[k]\end{bmatrix}=[C]\cdot\begin{bmatrix}i_L[k]\\ u_C[k]\end{bmatrix}. \tag{14}$$

With some algebraic operations, it can easily be obtained that (14) is equal to:

$$y[k]=[C]\cdot[zI-A]^{-1}\cdot[B]\cdot u[k]=[G]\cdot u[k]\,, \tag{15}$$

or:

$$\begin{bmatrix}\tilde{i}_L[k]\\ \tilde{u}_C[k]\end{bmatrix}=[G]\cdot\begin{bmatrix}\tilde{v}_{in}[k]\\ \tilde{I}_{ref}[k]\end{bmatrix}, \tag{16}$$

where matrix G is:

$$[G]=\begin{bmatrix}G_{11} & G_{12}\\ G_{21} & G_{22}\end{bmatrix}, \tag{17}$$

with its coefficients:

$$G_{12}=\frac{TD^2}{L(2+D)}\cdot\frac{1}{z-\frac{D}{2+D}}\,, \tag{18}$$

$$G_{12}=\frac{2}{2+D}\cdot\frac{1}{z-\frac{D}{2+D}}\,, \tag{19}$$

$$G_{21}=\frac{D^2T^2}{LC(2+D)}\cdot\frac{1}{(z-1+\frac{T}{RC})(z-\frac{D}{2+D})}\,, \tag{20}$$

$$G_{22}=\frac{2T}{C(2+D)}\cdot\frac{1}{(z-1+\frac{T}{RC})(z-\frac{D}{2+D})}\,. \tag{21}$$

Amplitude and phase characteristic of current loop gain G_{12} are shown in Fig.3 and Fig.4, respectively, for the following values of parameters: $C=560\mu F$, $L=115\mu H$, $R=0.5\Omega$, $T=25\mu s$ ($f_{sw}=40kHz$), with D as a running parameter.

As one can see, the current loop gain has very broad frequency passband with flat amplitude characteristic. In this way there is no resonant peak due to output LC filter, since the inductance can be viewed as constant current source. Also, as the steady-state duty-cycle is getting smaller, the frequency passband gets broader, because the pole is moving toward higher frequencies.

III. Short-circuit Protection

If short-circuit occurs on the converter output, the inherent short-circuit protection will limit the inductor current. According to (5), when the output filter capacitor voltage is zero, then the constraint function is:

$$I_{L,peak}=I_{ref}\,, \tag{22}$$

which means that as soon the instantaneous inductor current value reaches the reference value, the switch turns off. It is obvious that this control method in short-circuit acts like a peak-current mode with duty-cycle close to zero. Stability is achieved since the duty-cycle is well below 0.5 .

IV. Experimental Results

Experimental model of buck converter with following parameters: $C=560\mu F$, $L=115\mu H$, $R=1\Omega$, $T=25\mu s$ ($f_{sw}=40kHz$) was prepared for the testing purposes. Parasitic parameters were:

- capacitor series resistance $R_C=0.05\Omega$
- inductor series resistance $R_L=0.1\Omega$

Because of the presence of parasitic elements in the circuit which were not taken into account while deriving the constraint equation, some steady-state error will be introduced. Main cause of this error are inductor parasitic resistance and freewheeling diode voltage drop. They are included in $V_{L,FALL}$ so the measured value of output voltage should be increased by value of forward biased PN junction and additional term which is proportional to inductor current. This compensation had great success in experimental buck converter.

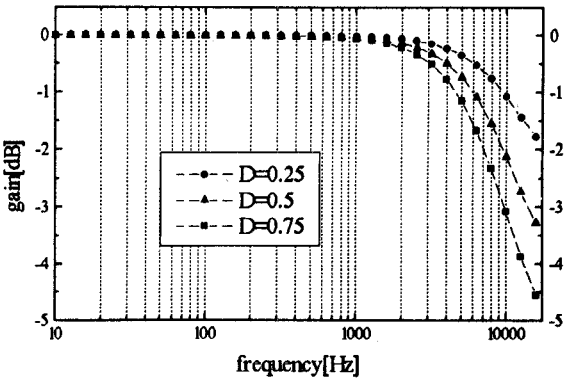


Fig.3. Amplitude characteristic of buck converter

In Fig.5 the transient response from zero-state to steady-state with the reference value of 5A is shown. Fig.6 shows converter's response to step-change of reference value from 5A to 15A. Reference value is the output of the microcontroller system with fast D/A converter.

One can easily see that inductor current envelope is exponential during transients, which is in accordance with the theoretical conclusion derived in section II.c. This

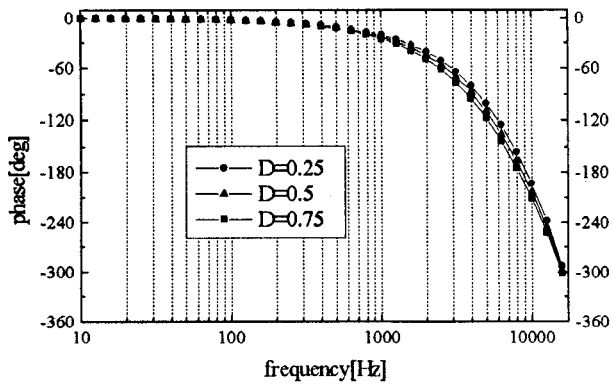


Fig.4. Phase characteristic of buck converter

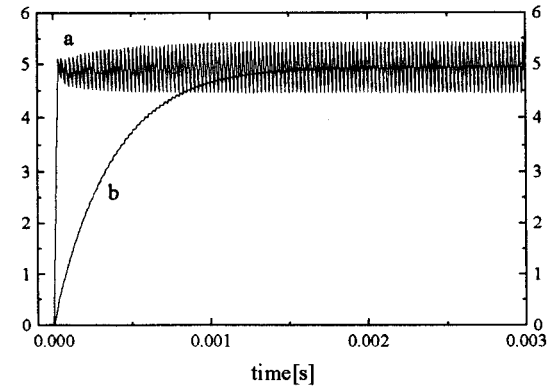


Fig.5. Buck converter transient response in a start-up sequence: a- inductor current(A), b- output voltage(V)

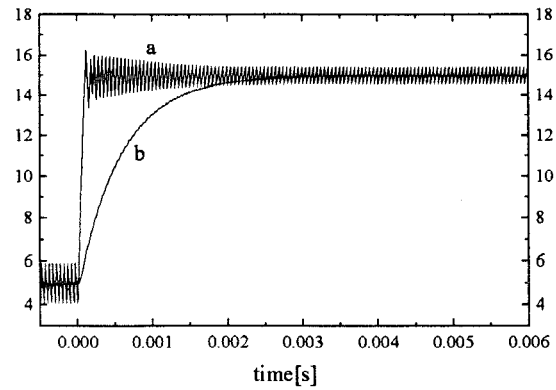


Fig.6. Buck convrter transient response in reference step-change sequence from 5A to 15A: a- inductor current(A), b- output voltage(V)

envelope is narrowing toward the horizontal straight line which is equal to steady-state average inductor current value. Output voltage rises exponentially which means that conclusion in section II.c is right. Fast current response is due to small inductor value. Large value of capacitance is needed for providing the output voltage ripple sufficiently small.

V. Other Converters

Brief review of theoretical analysis and simulation results for boost and buck-boost converters is performed. It includes large-signal model, constraint equation, stability conditions and some simulation results.

A. Boost Converter

Large-signal model for boost converter is:

$$\begin{bmatrix} i_L[k+1] \\ u_C[k+1] \end{bmatrix} = \begin{bmatrix} 1 & -\frac{T}{L}\cdot(1-d_k) \\ \frac{T}{C}\cdot(1-d_k) & 1-\frac{T}{RC} \end{bmatrix} \cdot \begin{bmatrix} i_L[k] \\ u_C[k] \end{bmatrix} + \begin{bmatrix} \frac{T}{L} & 0 \\ 0 & 0 \end{bmatrix} \cdot \begin{bmatrix} v_{in}[k] \\ I_{ref}[k] \end{bmatrix} \quad , \quad (23)$$

and the constraint equation is:

$$I_{L,peak} = I_{ref} + \frac{T}{2L}\cdot(V_{out}-V_{in}) - \frac{1}{2L}\cdot\int_{kT}^{kT+t_{on}}(V_{out}-V_{in})dt \quad , \quad (24)$$

since $|V_{L,FALL}|=V_{out}-V_{in}$.

After this model is linearized, assuming that M is negligible, two natural ratios are obtained:

$$z_1 = 1+\frac{2}{D-2}, \qquad z_2 = 1-\frac{T}{RC}\cdot\frac{3-D}{2-D}. \quad (25)$$

The first one describes the inductor current dynamics and since it is real and less than one for all values of D, the inductor current response is always stable. The other ratio is related to output voltage response, and it shows that parallel connection of output capacitor and load resistance is charged with constant current (if average inductor current is constant, then the average diode current is constant).

Simulation of ideal boost converter has been performed. Fig.7 shows inductor current response from zero state to 45A reference value and then step-change to 80A. The output capacitor was initially charged with voltage equal to input voltage. The circuit parameters were: $L = 115\mu H$, $C=1000\mu F$, $R=1\Omega$.

Limiting output current in short-circuit condition with single-switch boost converter is impossible by its nature, so this control method can not provide it. However, the switch will not be activated according to (24) and it can not be destroyed by overcurrent.

Fig.7 also shows time delay in output voltage response when reference is changed. This is because the control circuit will not activate the switch until it estimates that average inductor current in that cycle will be equal to reference. This phenomenon is quite negative if rapid output voltage drop is not allowed, but this is an extreme case when the reference value is changed instantly to a new value. If it is changed continuously and slow, output

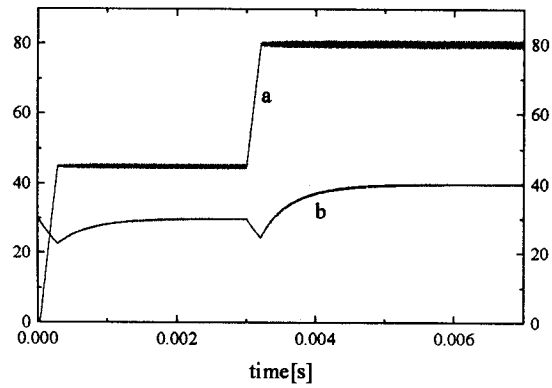


Fig.7. Boost converter response: a- inductor current(A), b- output voltage(V)

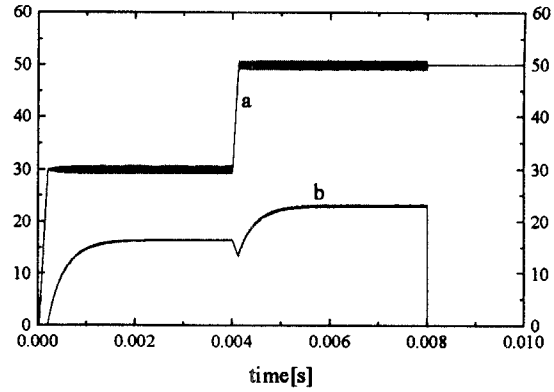


Fig.8. Buck-boost converter response: a-inductor current(A), b-output voltage(V)

voltage drop can be avoided.

B. Buck-boost Converter

Large-signal model for boost converter is:

$$\begin{bmatrix} i_L[k+1] \\ u_C[k+1] \end{bmatrix} = \begin{bmatrix} 1 & -\frac{T}{L}\cdot(1-d_k) \\ \frac{T}{C}\cdot(1-d_k) & 1-\frac{T}{RC} \end{bmatrix} \cdot \begin{bmatrix} i_L[k] \\ u_C[k] \end{bmatrix}$$

$$+ \begin{bmatrix} \frac{T}{L}\cdot d_k & 0 \\ 0 & 0 \end{bmatrix} \cdot \begin{bmatrix} v_{in}[k] \\ I_{ref}[k] \end{bmatrix} \quad , \quad (26)$$

and the constraint equation is:

$$I_{L,peak} = I_{ref} + \frac{T}{2L}\cdot V_{out} - \frac{1}{2L}\cdot \int_{kT}^{kT+t_{on}} V_{out}\,dt \ , \quad (27)$$

since $|V_{L,FALL}|=V_{out}$

After this model is linearized, assuming that M is negligible, two natural ratios are obtained:

$$z_1 = \frac{D}{2-D}, \qquad z_2 = 1-\frac{T}{RC}\cdot\frac{2}{2-D} \ . \quad (28)$$

The first ratio is real, positive and less then one for all values of steady-state duty-cycle, so the current response is always asymptotically stable with exponential envelope. The other ratio has the form and function similar to those in buck and boost converters.

Simulation results are performed with the same circuit parameters as with boost converter. The simulation sequence is: start-up to reference value of 30A, then step-change to 50A, and at the end the output short-circuit was simulated. The inherent short-circuit protection is active since the switch can limit the input current, and therefore, it can limit energy supplied to the load. According to (27),just like with buck converter, the current control loop acts like peak-current control loop, since output voltage is zero. The duty-cycle is well bellow one half, too, so the stability is achieved in short-circuit condition. Fig. 8 shows inductor current and output voltage response. Time delay is noticeable during sudden reference change, because the control loop will not turn the switch off until it estimates that the inductor current has risen enough to average inductor current become equal to reference value in current cycle. As for the output voltage drop, the same recomedation is valid as in the case of boost converter.

VI. Conclusion

This brand new control method shows very good performances. Stable operation with very fast dynamic response is achieved for all values of duty-cycle if converter is properly designed. No subharmonic oscillations exist, so there is no need for any means of stabilization, unlike other current-control methods (peak-current mode, average-current mode). The average inductor current is linearly proportional to reference value. Therefore, this reference value can be directly involved into current loop, without internal function generator. Also, bi-directional current flow is available if convenient converter is imployed (e.g. two-quadrant chopper), without changing the control loop. In this way, the same converter with the same control circuit can be used as a battery charger or discharger. Another important characteristic is that the same control circuit can be used for all tree mentioned types of topology, with (2) as constraint equation. The difference between topologies will be made in measuring $|V_{L,FALL}|$. Control circuit consists of one resetable integrator and a few components that will do the summing operations and comparison. This is actually very easy to implement. Of course, one must know the inductor value as accurate as it is possible because the error in this value can introduce steady-state error. But, since the value of L appears as a simple gain, this gain can be tuned to fit the real value.

The future works with this method will be aimed to extending it onto power-factor-correction circuits, since they sink continuous current except around zero-crossings. Also, all insulated DC/DC converters that have output

inductor are of interest. Finally, single-phase and tree-phase PWM inverters with current control can be controlled with this method since they are buck-derived converters.

REFERENCES

[1] R.D.Middlebrook, "Topics in Multiple-Loop Regulators and Current-Mode Programming," *IEEE Trans. Power Electronics*, Vol. PE-2, no. 2, Apr. 1987, pp. 109-124.

[2] R.D.Middlebrook, "Modeling Current-Programmed Buck and Boost Regulators," *IEEE Trans. Power Electronics*, Vol. 4, no. 1, Jan. 1989, pp. 36-52.

[3] Y.Liu and P.C.Sen, "A General Unified Large Signal Model for Current Programmed DC-to-DC Converters," *IEEE Trans. Power Electronics*, Vol. 9, no. 4, July 1994, pp. 414-424.

[4] W.Tang, F.C.Lee and R.B.Ridley, "Small-Signal Modeling of Average Current-Mode Control," *IEEE Trans. Power Electronics*, Vol. 8, no. 2, Apr. 1993, pp. 112-119.

[5] F.A.Huliehel, W.Tang, F.C.Lee and B.H.Cho, "Modeling, Analysis, and Design of the Quasi-Charge Control," *IEEE Trans. Power Electronics*, Vol. 10, no. 5, Sept. 1995, pp. 597-604.

[6] M.Jankovic, P.Ninkovic, Z.Janda, "A Novel Approach to Current-Mode Control of the Constant Frequency Power Converters," in *Proceedings of the 1996 IEEE International Symposium on Industrial Electronics*, Vol. 1, pp.488-492.

[7] P.Ninkovic, Z.Janda and M.Jankovic, "Stability Analysis of the Quasi-Charge and Novel Average Current-Mode Control," *in Proceedings of the 1996 Power Electronics and Motion Control Conference*,Vol. 1, pp.263-267.

[8] J.G.Kassakian, M.F.Schlecht and G.C.Verghese, *Principles of Power Electronics*, Addison-Wesley Publishing Company, 1991.

Analysis of Single Phase Diode Rectifiers with Power Factor Correction Circuits

Akiteru Ueda, Toshiko Shinohara, Masaru Matsubara, Akihiro Torii
Aichi Institute of Technology
1247, Yachigusa, Yakusa-cho, Toyota, 470-03, JAPAN
Fax: +81-565-48-0010, Phone: +81-565-48-8121, Ext.2016
E-mail: aueda@ee.aitech.ac.jp

Abstract — **Single phase diode rectifiers with single switch boost chopper and their variation of soft switching circuits are analyzed. It is found that the voltage fluctuation at an ac filter capacitor is not so small that it can be neglected. Then an analytical calculation method is developed with the consideration of the voltage fluctuation at the ac filter capacitor. The developed method is very useful for circuit design of high power factor converters.**

I . INTRODUCTION

Capacitor input type rectifiers are widely used for the dc power supply of many home appliances and other electrical equipment for the advantage of simple circuit configuration. They have the problems, however, that the ac input current contains a lot of higher harmonic components and that the input power factor is low.

To solve these problems much research has been done. An active power factor correction technique for a diode rectifier with a single switch boost chopper has been proposed [1] - [3]. The major advantage of the circuit is simple control, because higher harmonics of an ac input current is considerably eliminated with discontinuous mode operation of a reactor current. And to take advantage of this, the circuit is usually open loop controlled.

In the above stated circuit (called "the basic circuit" hereafter) the switching device is turned-on in zero current switching, but it is turned-off abruptly from the maximum current in hard switching. Then it suffers switching stress. So, the variation circuit with a loss-less snubber added to the basic circuit is proposed (called "the soft switching circuit" hereafter) [4]. In this circuit the switching device is turned-off in soft switching by the function of the snubber capacitor even when the control is the same as that of the basic circuit.

To obtain the design method of the circuit, an analytical calculation formula is necessary. The analytical calculation so far is done by neglecting the ac filter components. But the analytically calculated output voltage (called "the rough approximation" hereafter) by neglecting a LC filter has considerable calculation error. This paper presents a method for calculating output voltage analytically (called "the analytical value" hereafter) by considering LC filter both in the case of the basic circuit and the soft switching circuit.

In this calculation method, at first the approximate equation of the filter capacitor voltage is derived. Then the output voltage is calculated using the approximate equation and it is in good agreement with the simulation result.

II . CIRCUIT CONFIGURATION AND OPERATION

The basic circuit and its variation of a soft switching circuit are shown in Fig.1.

A. The basic circuit

Fig.1(a) shows the well known basic circuit. At first a switching device Tr1 is turned-on at a constant interval, then the switch Tr1 is turned-off after the predetermined constant period. The operation of the circuit is divided into the following three modes.

Mode I :

When the switch Tr1 is turned-on, the current flows through the power supply es, the commutation reactor Lr, and the switch Tr1. The current in the reactor Lr increases and energy is stored in the reactor. The current in the load resistor R flows from the smoothing capacitor Cr.

Mode II :

When the switch Tr1 is turned-off, the energy stored in the reactor Lr is discharged to the load side and the reactor current iLr decreases.

Mode III :

When the reactor current iLr is zero, the mode is moved to Mode III . The current in the load resistor R flows from the smoothing capacitor Cd. This mode finishes when the switch Tr1 is turned-on again.

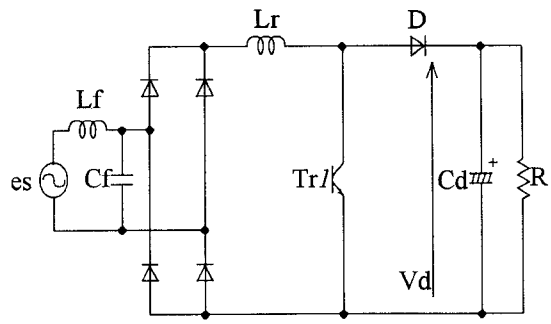
B. The soft switching circuit

The soft switching circuit is shown in Fig.1(b). In this circuit the operation mode corresponding to Mode I and Mode II of the basic circuit is divided to two modes each and thus the one switching cycle is divided into the following five modes.

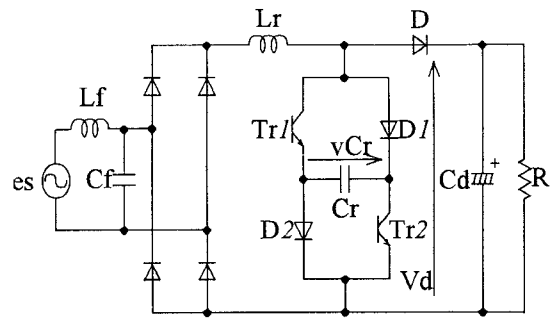
Mode I :

At the beginning of this mode the snubber capacitor Cr was charged to the output voltage Ed. The current flows through the power supply es, the commutation reactor Lr, the switch Tr1, the snubber capacitor Cr, and the switch Tr2 when the switch Tr1 and Tr2 is turned-on simultaneously. Energy is stored in the reactor Lr by this current. The increasing rate of the current is large compared with that of Mode I of the basic circuit because the rate is determined

0-7803-3823-5/97/$10.00© 1997 IEEE



(a) basic circuit



(b) soft switching circuit

Fig.1 Circuit configurations

by the sum of the supply voltage es and the voltage of capacitor Cr. And then the voltage of the capacitor decreases in this mode.

Mode II :

The mode is moved to Mode II when the voltage of the capacitor Cr is zero. In this mode, the current flows through the two paths; one is the switch Tr1 and the diode D2, the other is the diode D1 and the switch Tr2. Energy is also stored to the commutation reactor Lr by the current in this mode. The increasing rate of the current, however, is smaller than that of Mode I because it is excited only by the supply voltage es. It is the same rate as that of Mode I in the case of the basic circuit.

Mode III :

When the switches Tr1 and Tr2 are turned-off, the current flow through the diode D1, the snubber capacitor Cr and the diode D2, and then the capacitor Cr is charged.

Mode IV :

Mode III is moved to Mode IV when the snubber capacitor Cr is charged to the output voltage Ed. Energy stored in the reactor Lr is discharged to the load side, and the current in the reactor decreases.

Mode V :

The mode is moved to Mode V when the reactor current iLr is zero. The current in the load resistor R flows from the smoothing capacitor Cd. This mode finishes when the switches Tr1 and Tr2 are turned-on again.

III . The APPROXIMATE EQUATION OF THE FILTER CAPACITOR VOLTAGE

The output voltage characteristics obtained by the simulation are compared with the theoretically calculated output voltage obtained by neglecting the ac filter as is shown later. It is clear that the theoretically calculated value differs considerably from the simulation results. It is found by close survey that the difference is caused by the voltage fluctuation at the ac filter capacitor. It is not so small that we can neglect it. Then the voltage fluctuation in the ac filter capacitor is studied by using the simulation results. The equation of the filter capacitor voltage is necessary for calculating the output voltage analytically.

A. The basic circuit

The operating waveforms for explanation in the case of the basic circuit are shown in Fig.2. The origin of t-axis in Fig.2 is the turn-on timing of the switching device. The filter capacitor voltage can be expressed by the sum of the source voltage and the ripple voltage. The ripple voltage is approximated to be a cosine function with a phase lag referring to the switching-on timing. And the peak to peak value of its amplitude is calculated by dividing the integral value of the current discharged from the filter capacitor by the filter capacitance Cf. The phase lag corresponds to the time interval from the turn-on of the switching device and the time when the reactor current is equal to the input current.

At first, the amplitude of the ripple voltage of the filter capacitor is calculated from the integral of iCf during the period of iLr ≧ iLf. The integral of iCf is expressed by Eq.(1).

$$q_{Cf}=\int_{T1a}^{T1} i_{Cf}dt=\frac{I_m'(T_{1b}+T_{2a})}{2} \qquad (1)$$

where

$$i_{Cf}=i_{Lr}-i_{Lf} \quad , \quad I_m'=I_m-i_{Lf} \quad , \quad I_m=\frac{es}{Lr}T_1$$

$$T_{1b}=T_1-T_{1a} \quad , \quad T_{1a}=\frac{i_{Lf}\cdot Lr}{es}$$

$$T_{2a}=\frac{Lr(I_m-i_{Lf})}{Ed-es}$$

The amplitude (vCfa) is obtained by dividing the half of Eq.(1) by the filter capacitance Cf and expressed as Eq.(2).

$$v_{Cfa}=\frac{1}{2}\frac{q_{Cf}}{Cf} \qquad (2)$$

The phase lag (θ 1) of the ripple voltage is derived from the time interval (t1'= T1a) between the turn-on

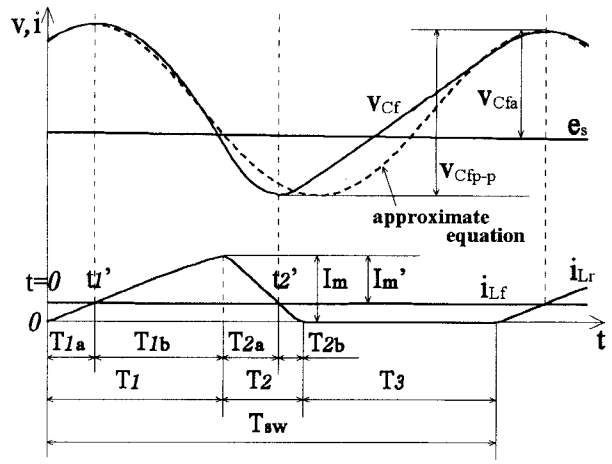


Fig.2 Waveforms of capacitor voltage and reactor current in basic circuit

timing and the time when iLr is equal to iLf and it is expressed by Eq.(3).

$$\theta_1 = 2\pi f_{sw} \cdot T_{1a} \tag{3}$$

Then the voltage at the ac filter capacitor can be approximated by Eq.(4).

$$v_{Cf} = v_{Cfa}\cos(\omega_s t - \theta_1) + es \tag{4}$$

where $\omega s = 2\pi$ fsw and fsw is the switching frequency.

B. The soft switching circuit

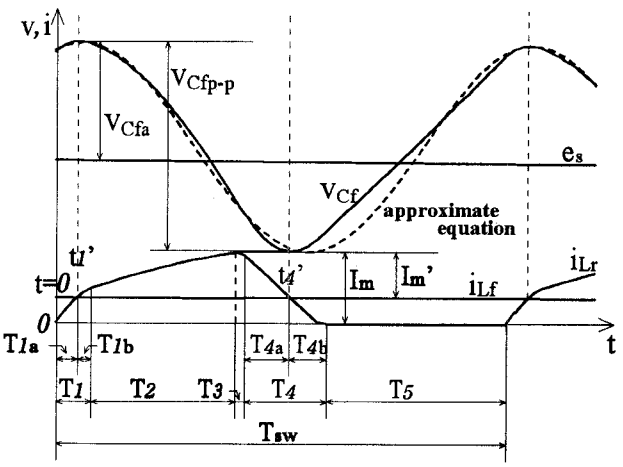
Each part of the operating waveforms for explanation in the case of the loss-less snubber circuit are shown in Fig.3. In this case, the operation which is corresponded to Mode I of the basic circuit is divided into two modes, these are Mode I , and Mode II . Therefore, there are two cases according to whether the timing point when the input current iLf equals the reactor current iLr (named "equal current timing") is in Mode I or Mode II . Fig.3(a) shows the former case and Fig.3(b) shows the latter case. Equations of filter capacitor voltage differs in each case.

1) When equal current timing is in Mode I

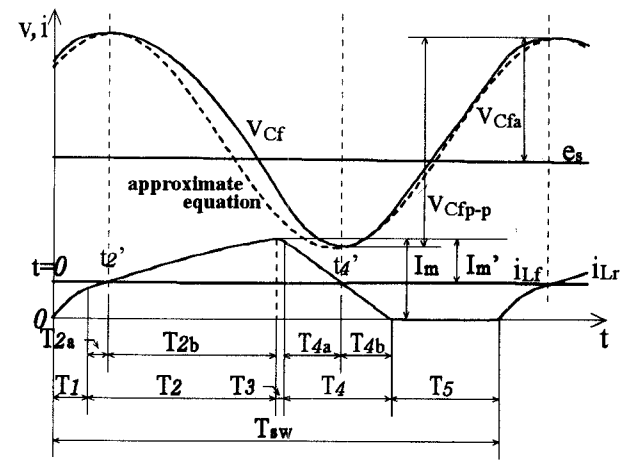
The amplitude of the filter capacitor ripple voltage can be derived from the integral of iCf during the period of iLr ≧ iLf similar to the basic circuit and it corresponds to the peak to peak value. Eqs.(5) - (8) show the integral of the current iCf in each mode respectively. The current Im1', Im2',Im3' are given by subtracting input current iLf from the maximum reactor current value (Im1, Im2, Im3) of each mode respectively.

Mode I :

$$q_{11} = \int_{T1a}^{T1} i_{Cf}dt = \frac{I_m' \cdot T_{1b}}{2} \tag{5}$$



(a) When equal current timing is in Mode I



(b) When equal current timing is in Mode II

Fig.3 Waveforms of capacitor voltage and reactor current in soft switching circuit

where

$$I_{m1}' = I_{m1} - i_{Lf} \quad , \quad I_{m1} = \frac{1}{\sqrt{\frac{Lr}{Cr}}}\sqrt{Ed^2 + 2es \cdot Ed}$$

$$T_{1b} = T_1 - T_{1a}$$

$$T_1 = \sqrt{Lr \cdot Cr}\cos^{-1}\left(\frac{es}{es+Ed}\right) \quad , \quad T_{1a} = \frac{\sin^{-1}\left(\frac{i_{Lf}\sqrt{\frac{Lr}{Cr}}}{es+Ed}\right)}{\omega_r}$$

$$\omega_r = \frac{1}{\sqrt{Lr \cdot Cr}}$$

Mode II :

$$q_{21} = \int_{T1}^{T1+T2} i_{Cf}dt = I_{m1}'T_2 + \frac{(I_{m2} - I_{m1})T_2}{2} \tag{6}$$

where

$$I_{m2}=\frac{es}{Lr}T_2+I_{m1} \quad , \quad T_2=D\cdot T_{sw}-T_1$$

Mode Ⅲ :

$$q_{3\,I}=\int_{T1+T2}^{T1+T2+T3} i_{cf}dt=I_{m2}'\cdot T_3+\frac{(I_{m3}-I_{m2})T_3}{2} \tag{7}$$

where

$$I_{m2}'=I_{m2}-i_{Lf}$$

$$I_{m3}=I_{m2}\cos\omega_r T_3+\sqrt{\frac{Cr}{Lr}}\,es\cdot\sin\omega_r T_3$$

$$T_3=\sqrt{Lr\cdot Cr}\,\{\sin^{-1}(\frac{Ed-es}{\sqrt{es^2+\frac{Lr}{Cr}I_{m2}^2}})-\theta_3\}$$

$$\theta_3=\sin^{-1}(-\frac{es}{\sqrt{es^2+\frac{Lr}{Cr}I_{m2}^2}})$$

Mode Ⅳ :

$$q_{4\,I}=\int_{T1+T2+T3}^{T1+T2+T3+T4a} i_{cf}dt=\frac{I_{m3}'\cdot T_{4a}}{2} \tag{8}$$

where

$$I_{m3}'=I_{m3}-i_{Lf}$$

$$T_{4a}=\frac{Lr(I_{m3}-i_{Lf})}{Ed-es}$$

Therefore the whole integral qCf Ⅰ is calculated by Eq.(9).

$$q_{cf\,I}=q_{1\,I}+q_{2\,I}+q_{3\,I}+q_{4\,I} \tag{9}$$

The amplitude of the ripple voltage is approximated by dividing Eq.(9) by two and the filter capacitance Cf and is expressed by Eq.(10).

$$v_{cfa\,I}=\frac{1}{2}\frac{q_{cf\,I}}{Cf} \tag{10}$$

The phase lag (θ 1) of the ripple voltage is derived from the time interval (t1' = T1a) between the turn-on timing and the time when iLr is equal to iLf. It is expressed by Eq.(11).

$$\theta_{1\,I}=2\pi f_{sw}\cdot t_1' \tag{11}$$

Then the voltage at the ac filter capacitor can be approximated by Eq.(12).

$$v_{cf\,I}=v_{cfa\,I}\cos(\omega_s t-\theta_{1\,I})+es \tag{12}$$

2) When equal current timing is in Mode Ⅱ

In this case, the amplitude of the filter capacitor ripple voltage can be derived from the integral of iCf during the period of iLr ≧ iLf similar to the basic circuit and it corresponds to the peak to peak value. Eqs.(13) - (15) show the integral of the current iCf in each mode respectively.

Mode Ⅱ :

$$q_{2\,II}=\int_{T1+T2a}^{T1+T2} i_{cf}dt=\frac{I_{m2}\cdot T_{2b}}{2} \tag{13}$$

where

$$T_{2b}=T_2-T_{2a} \quad , \quad T_{2a}=\frac{Lr(i_{Lf}-I_{m1})}{es}$$

Mode Ⅲ :

$$q_{3\,II}=\int_{T1+T2}^{T1+T2+T3} i_{cf}dt=I_{m2}'\cdot T_3+\frac{(I_{m3}-I_{m2})T_3}{2} \tag{14}$$

Mode Ⅳ :

$$q_{4\,II}=\int_{T1+T2+T3}^{T1+T2+T3+T4a} i_{cf}dt=\frac{I_{m3}'\cdot T_{4a}}{2} \tag{15}$$

Therefore the whole integral qCf Ⅱ is calculated by Eq.(16).

$$q_{cf\,II}=q_{2\,II}+q_{3\,II}+q_{4\,II} \tag{16}$$

The amplitude of the ripple voltage is approximated by dividing Eq.(16) by two and the filter capacitance Cf and is expressed by Eq.(17).

$$v_{cfa\,II}=\frac{1}{2}\frac{q_{cf\,II}}{Cf} \tag{17}$$

The phase lag (θ 2) of the ripple voltage is derived from the time interval (t2') between the turn-on timing and the time when iLr is equal to iLf. It is expressed by Eq.(18).

$$\theta_{1\,II}=2\pi f_{sw}\cdot t_2' \tag{18}$$

where

$$t_2'=\frac{Lr(i_{Lf}-I_{m1})}{es}+T_1$$

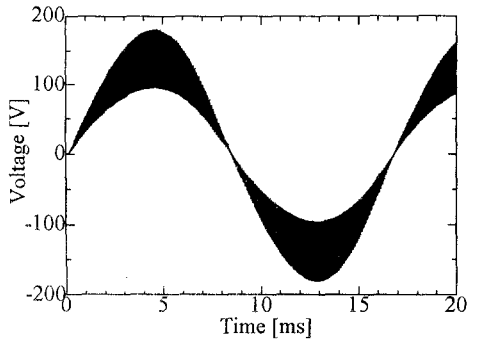
Then the voltage at the ac filter capacitor can be approximated by Eq.(19).

$$v_{cf\,II}=v_{cfa\,II}\cos(\omega_s t-\theta_{1\,II})+es \tag{19}$$

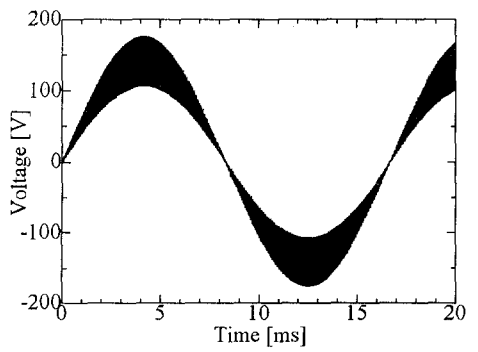
Ⅳ. ANALYTICAL METHOD FOR CALCULATING OUTPUT VOLTAGE

A method for calculating output voltage analytically by considering the LC filter is as follows.

First, the ac source voltage, the circuit parameters



(a) Waveform by simulation



(b) Waveform by analytical calculation

Fig.4 Voltage waveforms at filter capacitor of basic circuit (D=0.4, R=200)

including the load resistance R and the duty factor D are given. Next, the average current value of the reactor current is calculated in the mode which the energy of the commutation reactor Lr is discharged to the load side (Mode II in the basic circuit or Mode III and IV in the soft switching circuit). It is calculated by using the equation of the reactor current obtained by neglecting the LC filter. The rough approximation value of the output voltage is then calculated from the average current value (iq) and the load resistance R.

The approximate equation of the filter capacitor voltage is derived through the method stated in Section 3. The output voltage depends on the maximum value of the reactor current and it is subjected to the reactor voltage during the turn-on period of the switching device. Therefore, the average value VCf(on) is calculated by averaging the filter capacitor voltage during the turn-on period. Then, by substituting the average value VCf(on) for the input voltage es in the equation neglecting the LC filter, the reactor current can be calculated. The output voltage Ed is calculated analytically by the way similar to the rough value.

V . DIGITAL SIMULATION

The circuit is operated in the fixed duty factor at the discontinuous reactor current mode region. The circuit

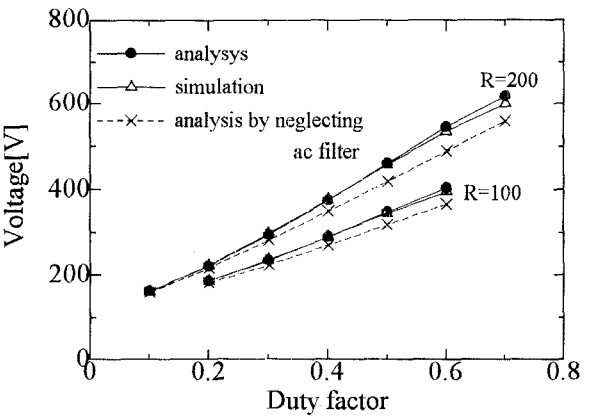


Fig.5 Output voltage of basic circuit

parameters in the simulation are as follows: ac source voltage = 100V, ac frequency = 60Hz, ac filter reactor Lf = 3mH, ac filter capacitor Cf = 3 μ F, commutation reactor Lr = 100 μ H, smoothing capacitor Cd = 100 μ F, and loss-less snubber capacitor Cr = 0.1 μ F. The load resistance R is 100 Ω or 200 Ω respectively. The switching frequency fsw is 20 kHz. The power switching devices are assumed to be ideal.

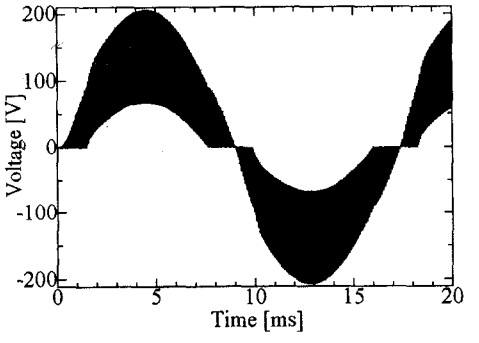
A. The basic circuit

The waveforms of the ac filter capacitor voltage calculated by using the approximate equation and by the simulation are compared with each other. The ac filter capacitor voltage obtained by the simulation is shown in Fig.4(a) and that calculated by the approximate equation is shown in Fig.4(b). From Fig.4 the ripple amplitude of the ac filter capacitor voltage calculated by the approximate equation is slightly small compared with the simulation, but we can say both waveforms agree well.

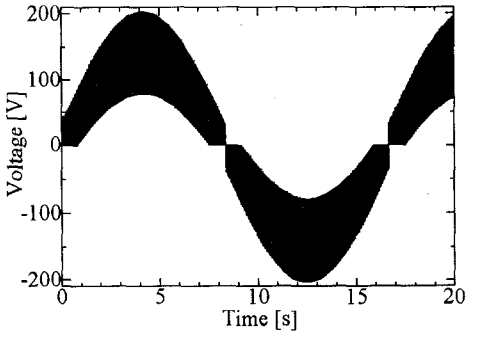
The output voltage characteristics calculated by the approximate equation and by the simulation are shown in Fig.5. The output voltages obtained by the rough approximation by neglecting the ac filter are shown in Fig.5 as references. The output voltage value calculated by the approximate equation is much closer to the output voltage value by the simulation. And therefore the effectiveness of the ac filter capacitor voltage derived by the approximate equation is confirmed.

B. The soft switching circuit

The waveforms of the ac filter capacitor voltage calculated by the approximate equation and by the simulation are compared. The ac filter capacitor voltage obtained by the simulation is shown in Fig .6(a) and that calculated by the approximate equation is shown in Fig.6(b). From Fig.6, the difference of the ripple voltage is slightly



(a) Waveform by simulation



(b) Waveform by analytical calculation

Fig.6 Voltage waveforms at filter capacitor of soft switching circuit (D=0.4, R=200)

bigger than in the case of the basic circuit.

The output voltage characteristics calculated by using the approximate equation and by the simulation are shown in Fig.7. The output voltages obtained by the rough approximation by neglecting the ac filter are also shown in Fig.7. From the characteristics in Fig.7, in the smaller range of the duty factor, output voltage calculated by the approximate equation is in good agreement with the output voltage calculated by the simulation. In the bigger range of the duty factor, however, the output voltage calculated by the approximate equation differed considerably from the output voltage calculated by the simulation. This difference may be caused by the approximation error of the equation of the filter capacitor voltage and its improvement will be expected for the future study.

The effectiveness of the ac filter capacitor voltage derived by the approximate equation is partly shown because the output voltage calculated by using the approximate equation of the ac filter capacitor voltage is in good agreement with that by simulation in the smaller range of the duty factor.

VI . CONCLUSION

In the single phase high power factor converter, conventional analysis of the output voltage characteristic has been done by neglecting the LC filter and the result has a

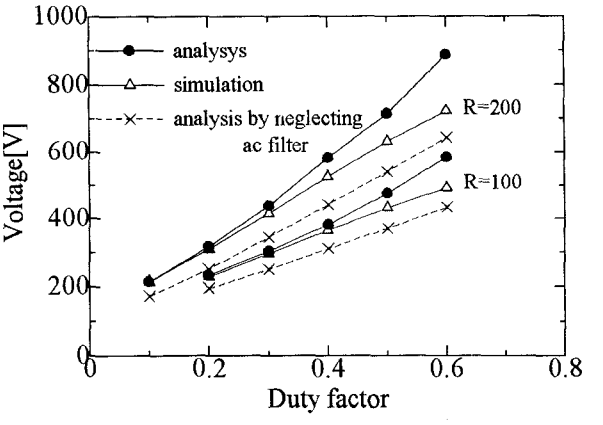


Fig.7 Output voltage of soft switching circuit

considerably large calculation error. Therefore, we studied a method for deriving the approximate equation of the ac filter capacitor voltage waveform from the simulation results. The ripple voltage of the filter capacitor is approximated to be a cosine function with a phase lag referring to the turn-on timing. And we derived the equation of the ac filter capacitor voltage and analytical method for calculating the output voltage.

Before calculation of the output voltage, the voltage waveforms of the ac filter capacitor both in the basic circuit and the soft switching circuit using the derived approximate equation are compared with the simulation results and they indicate good agreement. The output voltage analytically calculated by considering the ac filter capacitor agreed well with the simulation results.

Therefore the developed method is very useful for the circuit design of the high power factor converters.

REFERENCES

[1] A.R.Prasad, P.D.Ziogas and S.Manias, "An Active Power Factor Correction Technique for Three-Phase Diode Rectifiers", IEEE Trans. on Power Electronics, Vol.6, No.1, pp.83-92 (1991)

[2] T.C.Chen and C.T.Pan, "Modelling and design of a single phase AC to DC converter", IEEE Proceedings - B, Vol.139, No.5, pp.465-470 (1992)

[3] J.W.Kolar, H.Ertl and F.C.Zach, "A Comprehensive Design Approach for a Three-Phase High-Frequency Single-switch Discontinuous-Mode Boost Power Factor Correcter Based on Analytically Derived Normalized Converter Component Ratings", IEEE Trans. on Industry Appl. Vol.31, No.3, pp569-582 (1995)

[4] N.Kimura, K.Nishiyama and K.Taniguchi, "High Power Factor Active Converter with New Soft-Switching Circuit using Loss-less Snubber", Proceedings of IPEC-Yokohama'95, pp.843-847

Improvement of Current Waveform for 200V Input Single-Phase Rectifiers Using Modified Voltage-Doubler Circuit

Kenichiro Fujiwara and Hiroshi Nomura
Kochi National College of Technology
200-1 Monobe, Nangoku, Kochi 783 JAPAN
Fax :+81-888-64-5541, Phone:+81-888-64-5544
E-mail:fujiwara@ee.kochi-ct.ac.jp

Abstract – **To improve the current waveform of rectifiers, we propose a new operating principle for the voltage-doubler rectifiers with 200V utility voltage. For the limited input range, 0.3[kW] ~ 1.6[kW], the conventional diode voltage-doubler rectifier can be designed such that the input current satisfies the harmonic guidelines. A high power factor of 97% and efficiency of 98% are experimentally obtained. The proposed method seems to be very attractive for an air conditioner dc source using inexpensive and reliable components.**

I .INTRODUCTION

In the application of the single-phase diode rectifiers with large capacitor on the dc side, the rectifiers draw highly distorted current from the electric utility. Now and even more in the future, the harmonic guidelines will limit the amount of current distortion into the electric utility, and the diode rectifiers without any waveform improvement may not be allowed to use.

Many works have been done concerning this matter. Most of them employ the PWM boost-type converters[1]-[3] and a few works without PWM strategy[5]-[7].

A new circuit to improve the current waveform of the single-phase rectifiers with 200V utility voltage is proposed. The circuit configuration is basically the same as the voltage-doubler diode rectifiers. But two capacitors, which are for voltage doubling function in conventional voltage-doubler, are chosen much smaller in value and behave as a LC filter to improve the line current waveform.

Prior to the experiment, the circuit is analyzed by PSpice simulation to determine the best circuit parameters, from which a 12[mH] ac line inductance and 16[μ F] filter capacitances are obtained. The experimental results show that the input current satisfies the harmonic guidelines and agrees well with the simulation results.

II . CIRCUIT CONFIGURATION AND OPERATING MODES

The proposed rectifier circuit is shown in Fig.1, which appears to be the voltage-doubler rectifier, but capacitance of C1 and C2 have been chosen to be reasonably small, so that voltage boosting function is minimized. The circuit parameters shown in Fig.1 are determined by the PSpice simulation. The operating modes and corresponding waveforms are shown in Fig.2. Prior to the positive half interval of the ac source, v_{C1}, the voltage of C1, is zero and v_{C2} equals to v_d in the steady state operation as shown in Fig.2(d).

Mode 1 At the instance when the source voltage goes to positive, diode D1 conducts and the line current flows through C1 and C2. This mode has the main role of improving the line current waveform, whereas, in the conventional recifiers, the current starts to flow when the peak of ac input voltage comes near, which results in narrow pulses.

Mode 2 When the voltage v_{C2} discharges and becomes zero, diode D2 conducts and no current flows through C2. This mode ends when the stored energy in L is delivered to the load.

Mode 3 In this mode, the ac line current becomes zero and remains zero until the next negative half cycle of the ac voltage begins.

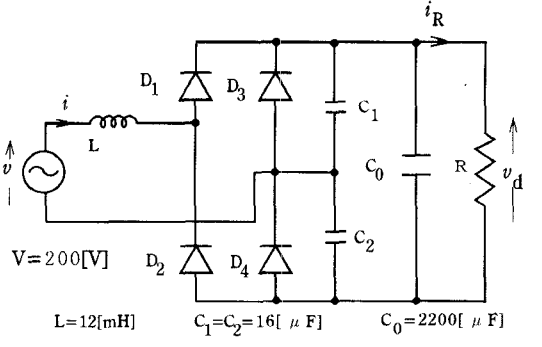


Fig.1. Proposed Rectifier Circuit.

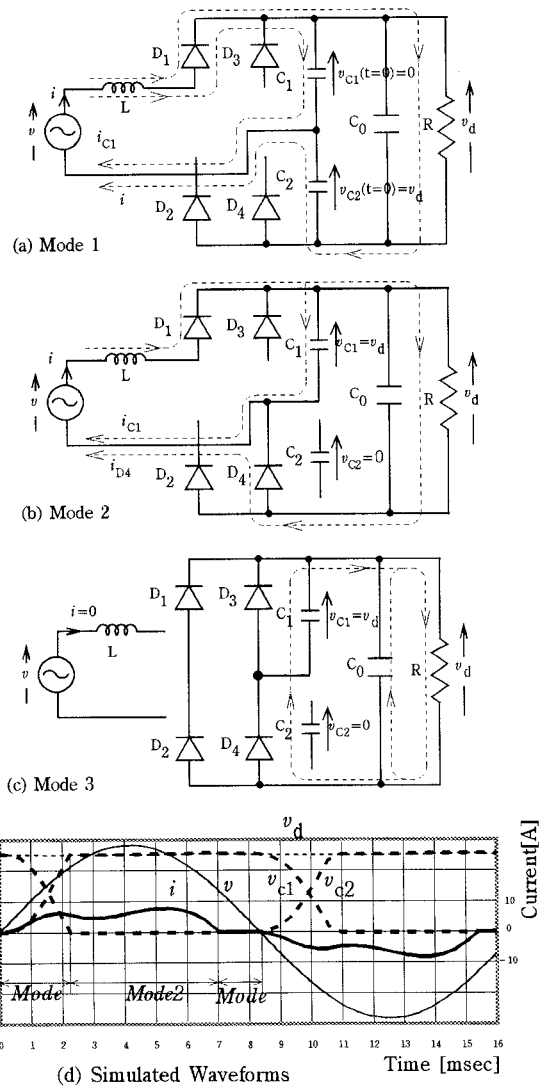


Fig.2 Operating Modes and Waveforms of Fig.1.

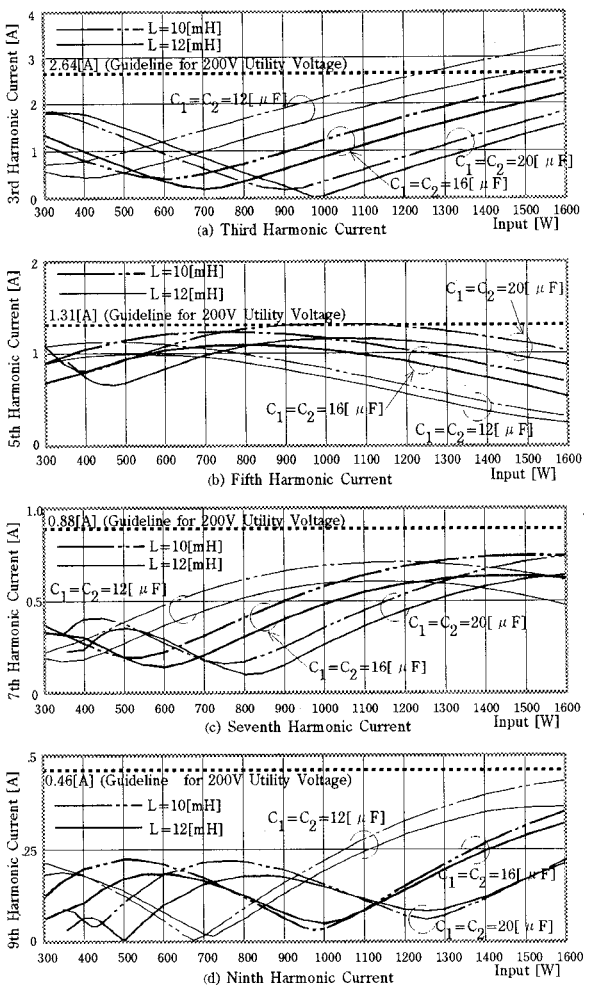


Fig.3 Harmonic Currents Obtained by Simulation.

III. Simulation And Experimental Results

A. *Harmonic Currents Obtained by PSpice Simulation*

Although the proposed circuit looks simple, it is rather complex to analyze. The simplest way of confirming operation of the circuit is computer simulation and PSpice is used to analyze the circuit. Figure 3 shows detailed simulation results of harmonic currents. A larger filter inductance is effective to reduce all the harmonics. However, with the recent rquirements of reducing size and weight, reactive components would be chosen to be as small as possible. Figure 3.(a) shows that a inductance of 10[mH] and capacitance of 16[μ F] are required to satisfy the guideline of the third harmonic current. Considering the

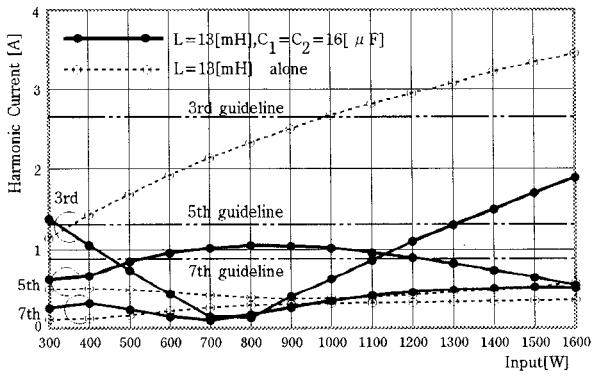


Fig.4 Experimental Results of Harmonic Currents
(L=13[mH],C=16[μ F])

margin of safty for the third harmonic current, inductance of 12[mH] is preferable. The fifth harmonic current with 20[μ F] capacitance gets near the guideline at 1[kW] input. This implies that a larger capacitance is not necessarily effective to reduce the fifth harmonic current. Therefore, capacitance of 16 [μ F] was chosen and used in experiments.

B. Experimental results

The characteristics of the proposed rectifier have been verified by experiments and the results are shown in Fig.4 and Fig.5. In the experiments, 13[mH] filter inductor is employed instead of 12[mH] used in simulation. To show the role of C1 and C2, the harmonic currents of the rectifier without C1 and C2 (referred to as conventional rectifier in the following discussions) are also shown in Fig.4. The proposed circuit satisfies the harmonic guidelines, whereas, the conventional one does not meet the guideline of the third harmonic current.

The input–output characteristics are shown in Fig.5. Comparing the output voltage and power factor of the proposed rectifier with that of the conventional rectifier, the role of C1 and C2 are well understood. The maximum power factor of the proposed rectifier shows 98%, while the one of conventional rectifier is 77%. Because of the voltage boosting function of C1 and C2, the output voltage of the proposed rectifier gives 273[V] at 0.6[kW] input, which is 40[V] higher than that of the conventional one.

Figure 6 shows the typical waveforms of the input current at 0.6, 1.0 and 1.6[kW] input. The first resonant current waveform in each half interval of the ac voltage is determined by L and C, whenever v_{C1} or v_{C2} discharges to zero, as shown in Fig.2(d). The second resonant waveform of the input current depends on the output voltage. At low input, the output voltage is charged up to near the peak value of the ac voltage. Therefor, the conduction interval of the current is narrowed and the current through L can not be built up to reasonable value. The waveforms of Fig.5 clearly explain the basic operation of the proposed circuit.

IV .CONCLUSION

To improve the current waveform and power factor of rectifiers with a line voltage of 200[V], we propose a new operating principle for the voltage–doubler rectifiers. For the limitted input range, 0.3[kW] ~ 1.6[kW], the conventional diode voltage–doubler rectifier can be designed such that the input current

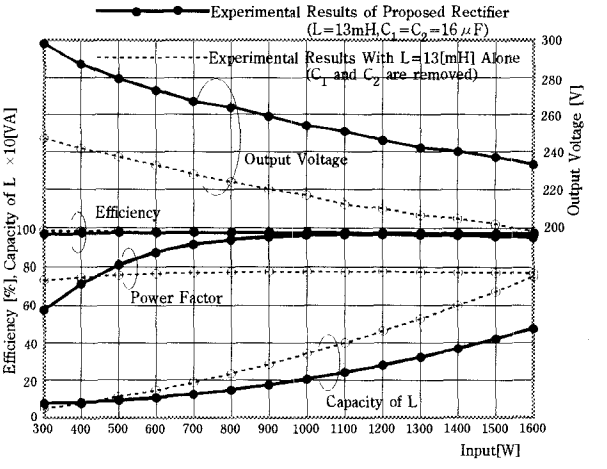
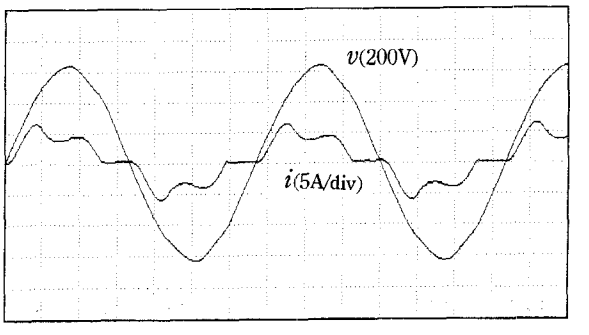
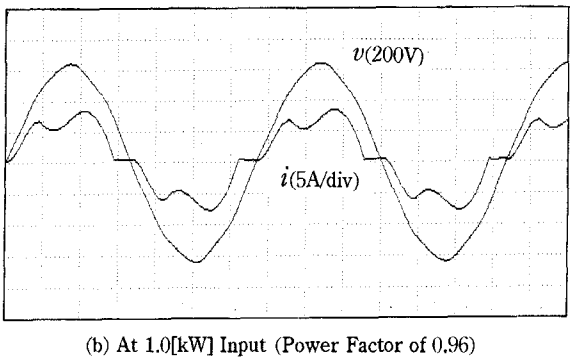


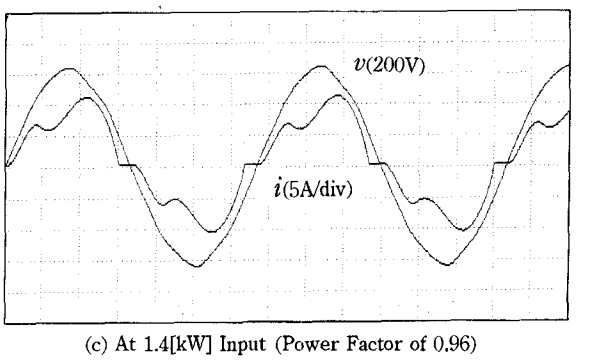
Fig.5 Input–Output Characteristics



(a) At 600[W] Input (Power Factor of 0.88)



(b) At 1.0[kW] Input (Power Factor of 0.96)



(c) At 1.4[kW] Input (Power Factor of 0.96)

Fig.6. Input Current Waveforms.
(Input Voltage:200[V], Current:5[A/div])

satisfies the harmonic guidelines. The circuit is analyzed to determine the best circuit parameters, from which a 12[mH] ac line inductance and 16[μ F] filter capacitance are obtained. The simulation results are comfirmed by experiment and agrees well with the simulation results. The experimental verification shows that the input current satisfies the harmonic guidelines. A high power factor of 97% and efficiency of 98% are obtained. The proposed rectifier seems to be very attractive for an air conditioner dc source using inexpensive and reliable components.

REFERENCES

[1] J.C. Salmon,"Circuit Topologies for Single-Phase Voltage-Doubler Boost Rectifier" IEEE Transactions on Power Electronics, Vol.8, No4, 1993

[2] K.Taniguchi, K. Nishiyama and N. Kimura,"Soft-Switching Converter with High Power Factor Using Loss Less Snubber" The Transaction of The Institute of Electrical Engineers of Japan, Vol. 115-D, No.1, 1995

[3] I. Suga, M. Kimata and R. Uchida, "A Simple Switching Method The Transaction of The Institute of Electrical Engineers of Japan, Vol.116-D, pp.420-426, 1996

[4] I. Takahashi and R. Y. Igarashi" A Switching Power Supply of 99% Power Factor by The Dither Rectifier", IEEE INTELE Proceedings, pp.714-719,1990

[5] K. fujiwara and H. Nomura, "A Power Factor Correction for Single-phase Diode Rectifiers without Employing PWM Strategy", Proceedings of 1995 International Power Electoronics Conference in Yokohama, pp.1501-1506

[6] I. Takahashi and K. Hori, "Single Phase Rectifier Having Small Input Harmonic Currents" ,The Transactions of The Institute of Electrical Engineers of Japan, Vol.115-D, pp.1215-1220,1995

[7] I.Takahashi, K. Hori,"Improvement of Input Current Waveforms of a Single Phase Diode Rectifier by Passsive Devices" The Transactions of The Institute of Electrical Engineers of Japan, Vol.117-D, No.1, pp.13-18,1997

Power Factor and PWM Controller TDA 16888

by
M. Herfurth / L. Lorenz

Siemens AG
Semiconductor Group
Balanstr. 73
81541 Munich

Short form description

TDA 16888 is designed for Off-line switched mode power supplies (SMPS) with optional universal input and Power Factor Correction e.g. for PCs, Monitors, CTVs and industrial applications. Combi-IC TDA 16888 includes the pulse width modulated (PWM) control for a SMPS and the control for the preconverter to improve the power factor and to reduce the harmonics of the AC input current. Both sections are internally synchronized on the same operating frequency.
The preferred topology of the PFC-preconverter is boost, but also flyback is possible. The PWM section can be designed as a forward or as a flyback converter. Maximum duty cycle of the PFC is about 95%, in order to achieve minimal line current gaps. Maximum duty cycle of the PWM is limited to 50% to prevent transformer saturation.
In normal operation the PFC section operates with dual loop control. A first control loop controls the shape of the line current by average current control enabling either continuous or discontinuous operation mode. The second loop controls the DC bus voltage. There is a third control loop available that enables the PFC section as an auxiliary power supply even during disabling the PWM section. During standby operation mode (disabled PWM) the PFC section is operating with half of its nominal operating frequency in order to save operating power.
The PWM section operates with improved current mode control, with effective slope compensation, spike suppression and especially with amplified signal levels at the pulse width comparator. The PWM section can be disabled by a short (controlled by transistor Q4) across the softstart capacitor.
There are monitoring and protection functions such as broken connection detection in order to monitor the bus voltage, undervoltage and dual step overvoltage monitoring of the bus voltage, peak current limitation for PFC and PWM section and undervoltage lockout of the IC supply voltage. The Combi-IC TDA 16888 is designed in respect to FMEA (failure mode effect analysis).
The limitation of the PWM duty cycle, the leading edge PFC- and the trailing edge PWM-operation are done in a digital way by flipflops. Handling the signals this way meets the requirements for an external synchronisation. On the other hand an oscillator is necessary that operates at twice of the operating frequency. For a lower current consumption and higher EMI resistance the capacitor of the oscillator is integrated. The operating frequency is set by only one resistor. Operating frequency can be increased by a sink current in parallel to this resistor. There is an additional synchronisation input that can be used for low changes in frequency or for supporting a phase locked operation.

0-7803-3823-5/97/$10.00© 1997 IEEE

PFC Preconverter

Rectification of an AC voltage and smoothing with an electrolytic capacitor effects a peak current during the peak input voltage and a break in current flow during the rest of the half period of the line frequency. The RMS value of such a pulsed input current is about twice of a sinusoidal current and the harmonics of that pulsed current effect EMI to other devices.
The power factor is the relation between real input power to apparent input power. With a typical mains voltage rectification in electronic devices the power factor is about 0,5. There are standards to improve power factor that become effective in the near future. But system cost must not increase by introduction of power factor correction. It depends on the output power and features like the option to supply a device from different line voltages.
The most efficient way to correct the power factor with an active circuitry is to use a boost converter. Most part of the energy flowing from input via rectifier to the bus capacitor bypasses the switching transistor of the boost converter. Connecting the boost preconverter to the line, an inrush current occurs due to charging the bus capacitor. As the capacity of the bus capacitor is between three to ten times lower than with conventional rectification, the inrush current is much smaller even without additional measures like NTCs.
There is a peak current limitation (Pin 6) to prevent an overload to the boost transistor during inrush currents and during maximum load which occurs for example after turn on to charge the bus capacitor. The turn off threshold is designed at +1V to meet FMEA requirements. A broken wire to Pin 6 activates the current limitation. Another comparator (C2) at Pin 19 is detecting a broken wire to the bus voltage sense. At least 20% of nominal bus voltage is necessary to make the Combi-IC active. This feature has to be taken into account when testing the IC at low input voltages.
The typical startup of the Combi-IC is supported by the undervoltage lockout (UVLO) feature of the IC. Via a highohmic resistor (R2) a capacitor (C11) is charged up to a threshold of 14V at Pin 9. During this operation the current consumption of the IC is less than 100µA. Reaching this threshold the IC becomes active sending drive pulses to the boost transistor Q1. During this operation the PWM section is not yet active in order to save supply current. The same reason is for driving the boost transistor with only half of the nominal operating frequency. Capacitor C11 has to be designed so big that the circuitry is able to supply the IC before the voltage at Pin 9 reaches the turn off threshold of 11V.
The power supply of the Combi-IC can be realized by a separate winding on the boost converter choke. Our proposal is to use a bridge rectifier on the auxiliary winding AUX 1. So a current can flow at low input voltages in flyback mode and at high input voltages in forward mode. The minimum supply voltage at capacitor C18 will occur at a input voltage level half of the bus voltage.
There is another operating condition when the supply voltage at C18 becomes low: at disabled PWM section and high input voltages. This condition may be the worst for the auxiliary power supply. In a first application test we got enough power to supply the Combi-IC during all operating conditions and to offer an isolated auxiliary voltage of 5V/20mA in addition. How to increase the output power of the auxiliary power supply will be part of future applications.

In order to finish the description of the auxiliary power supply there is a separate control loop and a separate output of the boost converter via Diode D6. This additional circuitry is necessary to get a fast response at load changes. There are operating conditions resulting in an overshoot at the bus voltage that would stop the boost transistor for more than 100ms. With the second output of the boost converter via D6 a not working transistor can be detected within 100µs and the transistor can be turned on in a way, that the auxiliary output gets power but not the main output to the bus capacitor. During the standby operation the bus voltage remains at nominal level The separate control loop can be activated by itself, when the second output of the boost converter via D6 is designed for a output voltage slightly below the nominal bus voltage (e.g. 5%). The load (R2) which is necessary at the second output can be used for the startup of the Combi-IC.
The PFC section is working initially at half of the nominal operating frequency until a level of 20% below the nominal bus voltage is reached. Then the PWM section is able to run with a soft-start (Pin 13) with nominal operating frequency on both sections or it is disabled by transistor Q4, then the system is running in the standby mode with half of nominal operating frequency.
Usually there is an overshoot during the charging of the bus capacitor. The reason is the long response time of the bus voltage control loop. There is a first overvoltage threshold at 10% above nominal bus voltage. The operation of the boost transistor is turned down via OTA2 and the Multiplier to avoid increasing bus voltage. A second threshold at 20% above nominal bus voltage will stop PFC and PWM section immediately until the bus voltage reaches a level of 10% above nominal bus voltage. This feature protects the power supply during hazardous mains overvoltages in combination with varistor R30.
The typical operating mode of the PFC section is a DC output signal with a low superimposed AC rippel of the voltage error amplifier at Pin 18. This signal is multiplied by the current at Pin 1, derived from the rectified AC input voltage. That forces a shape like the input voltage at the multiplier output that can be varied in amplitude by the voltage error amplifier OP1. A second error amplifier OP2 controls the input current like the set value of the multiplier output. In order to enlarge the effect of the voltage error amplifier there is an exponential function at the input (M2) of the multiplier included. Furthermore there is an OTA3 that cares for the stability of the bus voltage during light load and no load conditions.
The ramp voltage of the PFC pulse width modulation starts from a higher voltage level (6V) decreasing to the lower peak (1V). The reason for this shape which is invers to the common ramp voltages is that the feedback can be connected to the sense input (Pin 4). Doing this the sensed signal is smoothed and the operation level of the input must not operate below zero.

PWM Converter

The PWM Converter starts with a soft start at a bus voltage higher than 80% of its nominal value. Operating frequency is the nominal and the same like that of the PFC Preconverter. The transistor of the boost converter turns on with leading edge and that

of the PWM turns on with trailing edge, delayed in minimum 50% of the operation period.
The way of control is an improved current mode. There is a capacitor at Pin 15, which on a basic ramp voltage is generated for slope compensation. This voltage is superimposed by the times 5 amplified voltage drop across the shunt resistor (R15) fed over an internal 10K resistor in order to suppress spikes. The result is a ramp voltage with a maximum level up to 6,5V. So the active input range of the PWM input (Pin 14) is from 0,4V to 7V. The higher level on the PWM comparator cares for better resistance against EMI and better stability of operation. The current sense input (Pin 11) feeds a fast comparator (threshold = 1V) for current limitation in addition.

PFC and PWM Gate Drive

There is a new design for the Gate drive on both sections. This totem pole configuration avoids cross conduction currents and has a voltage modulated turn on slope. The turn on slope increases moderately between 0V and 3V, increases slowly between 3V and 5V and increases moderately above 5V up to the limitation on a level of 12V. The reason for this is a possible fast turn off as soon as the current limitation is activated, a continuously reduceable duty cycle down to zero and a soft current commutation from boost or output diode to the transistor. The voltage modulation guarantees the effect independent of load capacitance. The turn off is fast with a current capability of about 1,5A peak.
Operating the Combi-IC below the undervoltage threshold, the drive outputs are active low.

Oscillator and Synchronisation

The oscillator operates with a integrated low tolerance capacitor and a current mirror set by only one external resistor at Pin 16. The integration of this capacitor operating with a ramp voltage of 5V increases the resistance against EMI and saves supply current due to the low capacitance which can be used. The internal oscillator operates with twice of the external operating frequency for exact limitation of the PWM duty cycle below 50% by flipflops. In the same way the leading edge turn on of the PFC and the trailing edge turn on of the PWM is generated. Therefor the operating frequency can be changed during operation only by bypassing a current to the set resistor R24.
Changing the frequency by the set current at Pin 16 does not influence the amplitude of the internal ramp voltage of the PFC pulse width modulation but will influence the external ramp voltage of the PWM at the external capacitor C13.
There is a synchronisation input Pin 12. A high level signal (3,5V-7,5V) discharges the internal oscillator capacitor. Corresponding a low level signal (below 0,4V) enables the charging with the set current (R24). The internal oscillator can completely be super-imposed by an external synchronisation signal. But the influence to the internal ramp voltages have to be taken into account. For a synchronisation over a wide frequency range the variation of the set current at Pin 16 is to prefer. For a synchronisation which will increase the set frequency up to factor 1,5 the synchronisation input may be the better choice.

OPERATING BEHAVIOUR OF POWER COMBI - IC
TDA 16888

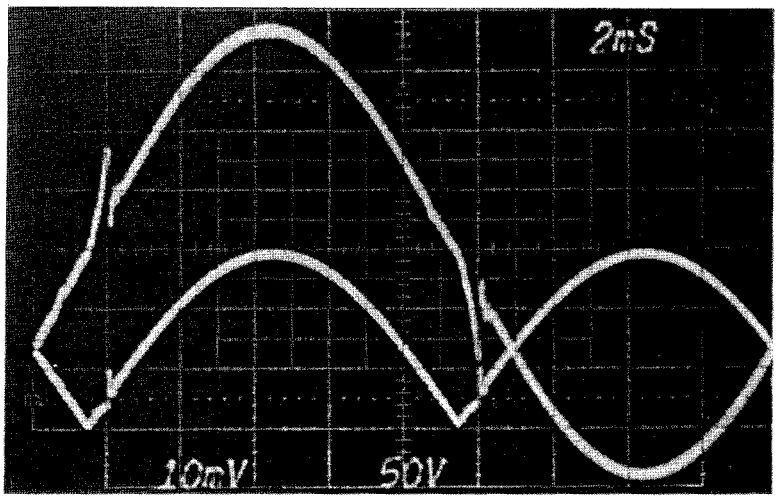


FIG 1:
AC INPUT CURRENT
(0,5A/DIV; UPPER TRACE)
RECTIFIED AC INPUT VOLTAGE
(50V/DIV; LOWER TRACE)
THE SPIKE DURING ZERO
CROSSING RESULTS
FROM THE FAST AUXILIARY
CONTROL LOOP

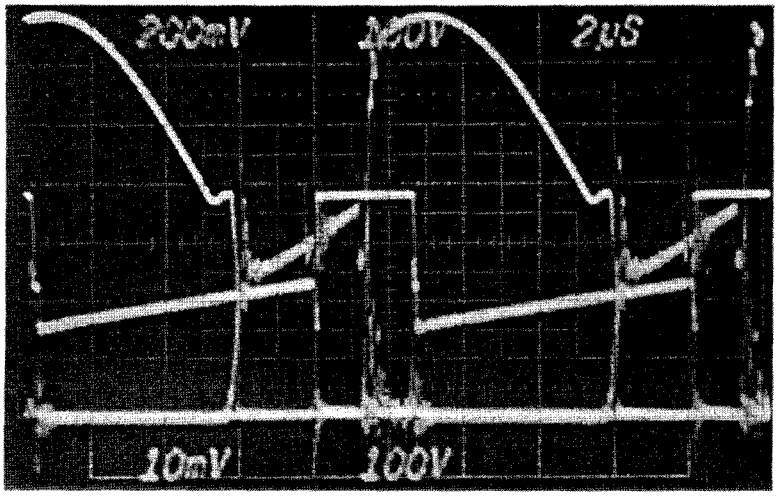


FIG 2:
DRAIN SOURCE VOLTAGE PWM
(100V/DIV; ON-TIME 3,5µs,L)
SOURCE CURRENT PWM
(0,2A/DIV; ON-TIME 3,5µs,H)
DRAIN-SOURCE VOLTAGE PFC
(100V/DIV; ON-TIME 7,5µs,L)
DRAIN CURRENT PFC
(0,5A/DIV; ON-TIME 7,5µs)
LEADING EDGE PFC AND
TRAILING EDGE PWM

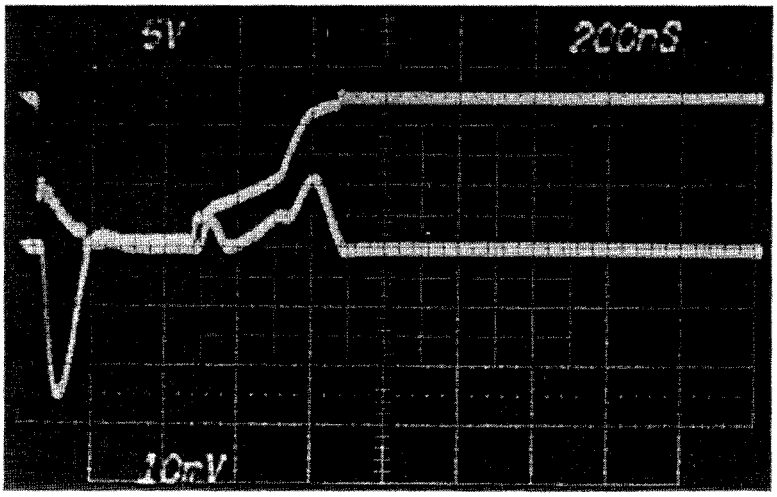
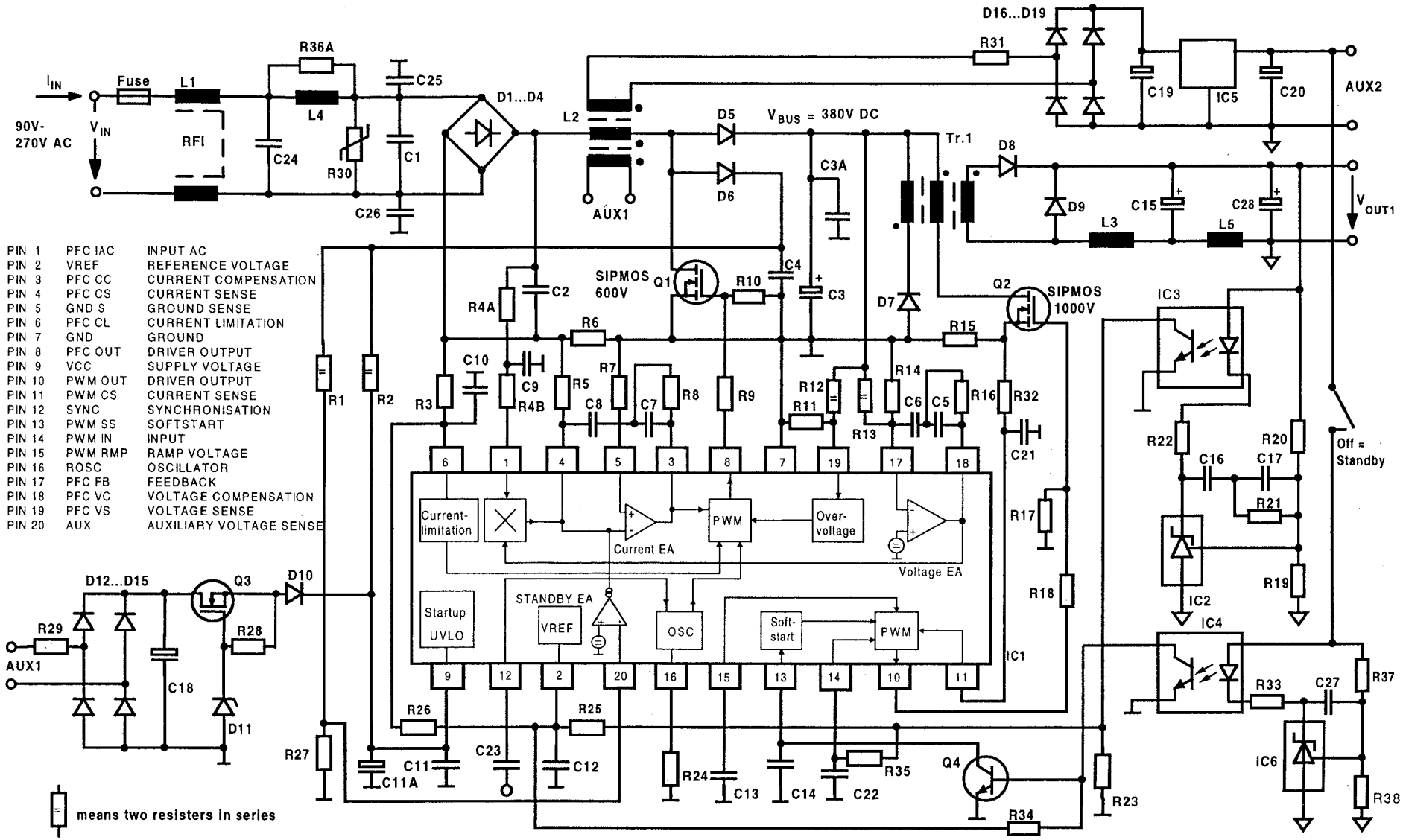


FIG 3:
GATE DRIVE VOLTAGE
(5V/DIV; UPPER TRACE)
DRIVE CURRENT TO BUZ91
(0,5A/DIV; LOWER TRACE)
TURN OFF SLOPE WITH 1,3A
PEAK CURRENT
TURN ON SLOPE WITH
MODULATED GATE VOLTAGE



12V/150W SMPS WITH POWER FACTOR CORRECTION AND UNIVERSAL INPUT

HL LH TM 4

CBI70423.DRW 04/97

Improved Circuit of AC Choppers for Single-Phase Systems

Nabil Abd El-Latif Ahmed, Kenji Amei and Masaaki Sakui
Faculty of Engineering
Toyama University
3190 Gofuku, Toyama 930, Japan
Tel. 0764-45-6713
Fax. 0764-45-6713

Abstract —**In this paper, an improved circuit of AC choppers for single-phase systems are proposed and investigated. This new circuit employs a DC chopper modulated switch with a diode bridge rectifier and two switches to provide freewheeling path for the load current when the modulated switch is off. The attractive feature of this improved circuit is that, it uses only a single modulated switch. The improved circuit has many advantages compared with the conventional ac choppers such as simple design requirements, easy implementation, higher power capacity, fast dynamic response, high reliability, high power factor, low cost, low switching loss and consequently high efficiency. By digital simulation several characteristics are investigated.**

I. INTRODUCTION

AC voltage regulators are widely used to obtain variable ac voltage from fixed ac source. The phase angle control of regulators are extensively employed in many applications such as industrial heating, lighting control, soft starting of induction motors and speed controllers for fans and pumps. Triacs or thyristors pairs (anti-parallel) connected are usually employed as the power control elements of such controllers. Such techniques offer some advantages as simplicity and ability of controlling large amount of power economically. However, delayed firing angle causes discontinuity and plentiful harmonics in load current, the size of the passive circuit becomes bulky and also a lagging power factor occurs at the ac side even though the load is completely resistive specially when the firing angle increases.

These problems can be improved by modifying the power circuit with freewheeling path or by using the PWM AC chopper [1-11]. This chopper offers several advantages such as sinusoidal input current with unity power factor, fast dynamic and significant reduction in the filter size. Several PWM AC choppers have been articulated in a number of technical papers [5-7, 9]. In the PWM the switching patterns are critical and an alternate path has to be provided for current when both switches are turned off. This alternate path is implemented using additional bilateral switches or by using standard switches with RC bypass snubbers [2, 7, 9]. In these techniques, the switching losses are very high and as more power capacity is increased, more the power loss of RC bypass snubbers is increased. Thus, such techniques are difficult, expensive, bulky and inefficient for high-power applications.

The present paper describes an improved circuit of AC choppers for single-phase systems, the proposed circuit is a modified version of the circuit proposed in [2]. In this circuit the number of controlled switches has been reduced to three with the aid of a diode bridge rectifier. The reduction in the number of switches is essential for the control simplicity, cost, high switching frequency with small switching loss, good efficiency and reliability. Also, standard power switches can be used instead of bilateral switches.

0-7803-3823-5/97/$10.00© 1997 IEEE

Ⅱ. PRINCIPLE OF OPERATION

Fig. 1 shows a schematic diagram of the proposed ac chopper circuit which consists of a main switch S connected in series with a diode bridge rectifier and a one standard switch modules with two switches and two freewheeling diodes S2, S3 connected across the load to provide the freewheeling path for the load current. The switching patterns are decided by the polarity of the source voltage and load current. The main switch S is always modulated with a constant duty cycle. When the load voltage and current are of similar polarity, normal switching takes place. In which one of the parallel switches S2 or S3 is completely turned on and the other is completely turned off according to the polarity of the supply voltage. In other words , when the supply voltage is positive S2 is turned on and S3 is turned off and vice-versa. This is not the case when the load voltage and current are of different polarity, where the on-switch from the parallel switches S2 and S3 is gated by the complementary signal of the modulated switch S instead of continuous conduction and normal switching is resumed at the instant where the load current reverses its direction as shown in Fig. 2. By such switching patterns, the current path always exists whatever the load current direction. Since only single switch is modulated and only single switch is always turned on during the most half period of the voltage source, the switching losses is significantly reduced and consequently high efficiency is approached.

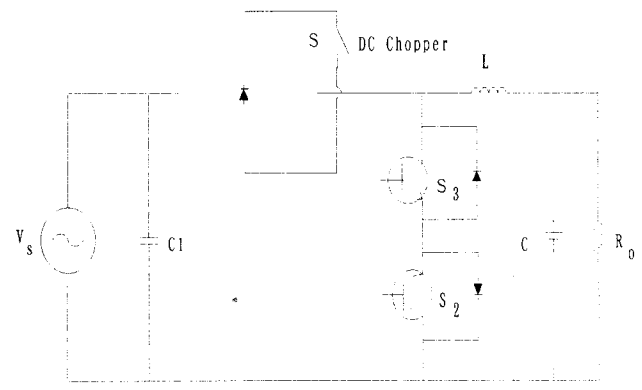


Fig. 1. Improved circuit of single-phase ac chopper.

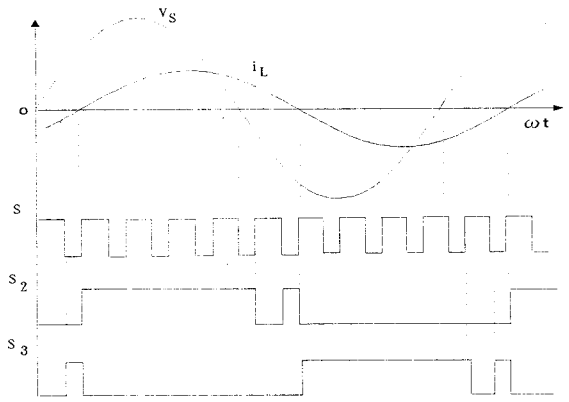


Fig. 2 . Switching patterns of the driving signal.

The operation modes are divided into two modes active and freewheeling modes. The active mode is defined when the modulated switch S is turned on, during the active mode the current is forced to flow from the voltage source into the load circuit through the modulated switch S during its on-state periods and the power flows to the load. The freewheeling mode is defined when the modulated switch S is turned off and the load current paths can be formed by the direction of the load current, i.e. in the freewheeling mode, the load current freewheels and naturally decays through the freewheeling switches S2 or S3 according to the direction of the load current. Fig. 3 shows the system's equivalent circuit during the two modes. High chopping frequency can be used, thereby, reducing the losses in the load by reducing the output-current harmonics.

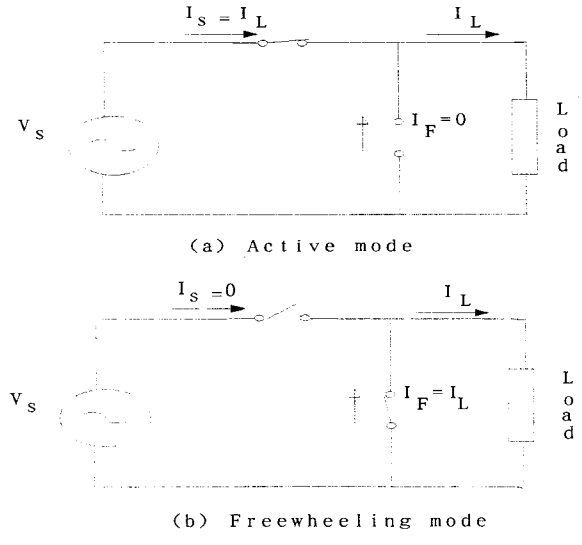


Fig. 3. System's equivalent circuit during the operating modes.

Voltage regulation is obtained by changing the duty cycle (D) of the switch S. By digital simulation, the proposed circuit is investigated and several characteristics such as total distortion factor of output voltage and current and input power factor are evaluated. Some results are also compared with those of PSPICE simulated

Ⅲ. ANALYSIS

The input source voltage is defined as follows:

$$v_s(t) = V_{sm}\cos(\omega t) \quad (1)$$

Where ω and V_{sm} are the angular frequency and the magnitude of the input voltage respectively. The fourier series of the square wave control signal with a switching frequency ω_s and a constant duty ratio D is given by:

$$S(\omega_s t) = D + \sum_{k=1}^{\infty} \frac{2V_{sm}\sin kD\pi}{k\pi}\cos(k\omega_s t) \quad (2)$$

Then the intermediate modulated voltage is given by:

$$v_r(t) = S(\omega_s t)v_s(t)$$

$$= DV_{sm}\cos(\omega t) + \sum_{k=1}^{\infty} \frac{V_{sm}\sin kD\pi}{k\pi}\cos(k\omega_s \pm \omega)t \quad (3)$$

The output filter reduces the harmonics of the load current and the output voltage. The total harmonic distortion factor (THD) in the output voltage and the load current are defined as follows.

$$THD_V = \frac{1}{V_{of}}\sqrt{\sum_{k=1}^{\infty} V_{ok}^2} \quad (4)$$

$$THD_i = \frac{1}{I_{of}}\sqrt{\sum_{k=1}^{\infty} I_{ok}^2} \quad (5)$$

Where V_{of}, I_{of}, V_{ok} and I_{ok} are the magnitude of the fundamental and harmonic elements in the output voltage and current respectively. The equivalent circuits of the harmonic and fundamental elements of the output voltage and input current are shown in Fig. 4 (a) to (c). From which the, the input current and the input power factor can be represented by the following :

$$I_S = I_{L1} + I_{c1} \quad (6)$$

$$PF = \cos \angle I_S \quad (7)$$

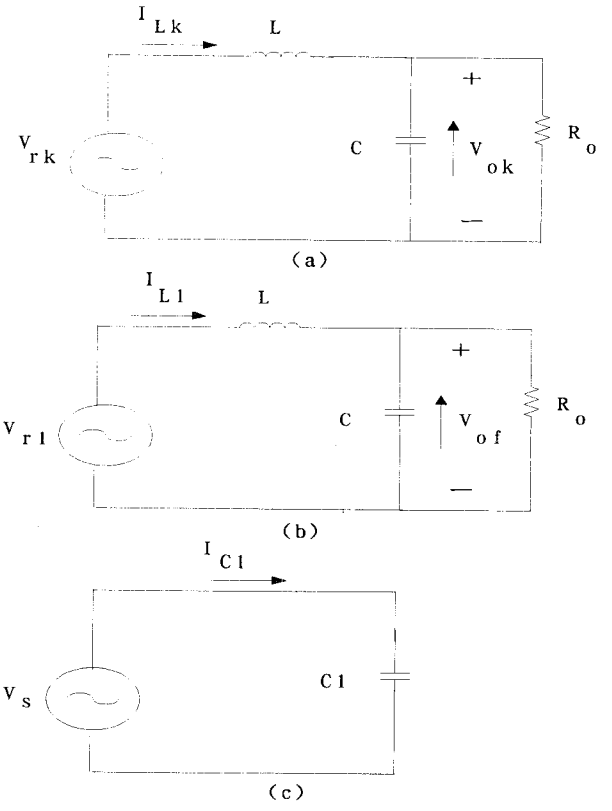


Fig. 4. Equivalent circuits for harmonic elements and fundamental current.

Ⅳ. RESULTS AND DISCUSSIONS

Figs. 5 and 6 show the percentage total harmonic distortion factor of the output voltage THD_V as a function of the filter capacitor C and inductor L. While the total harmonic distortion factor of the output current THD_i is demonstrated in Figs. 7 and 8. It is interesting to note that with a proper choice of the parameters C and L, the total harmonic distortion factor of the output voltage and current can be considerably improved. This is not just a claim but it is clearly evident from the Figs. 5-8. Fig. 6 demonstrates that the total harmonic distortion factor of the output voltage has a small effect by the value of the inductor L and it is highly effected by the capacitor C as shown in Fig. 5. Also, Fig. 7 shows that the total harmonic distortion factor of the output current is not dependent on the output filter capacitor C, it is dependent only on the inductor L as represented in Fig. 8.

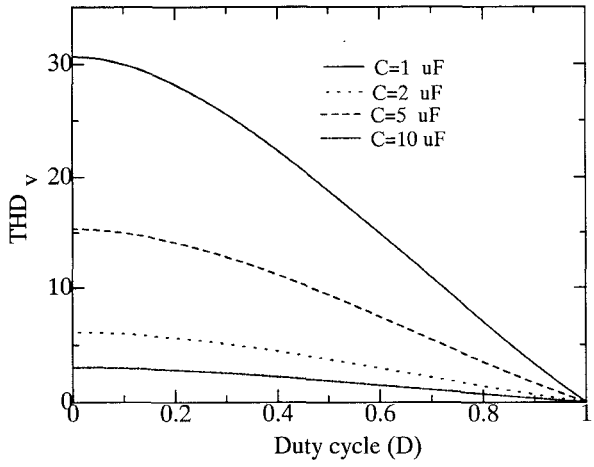


Fig. 5. Total harmonic distortion factor of output voltage. L=0.5 mH, Ro=10 Ohm.

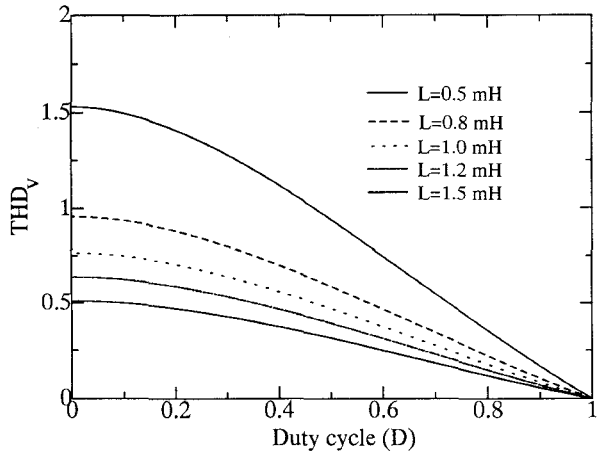


Fig. 6. Total harmonic distortion factor of output voltage, C=20 uF, Ro=10 Ohm.

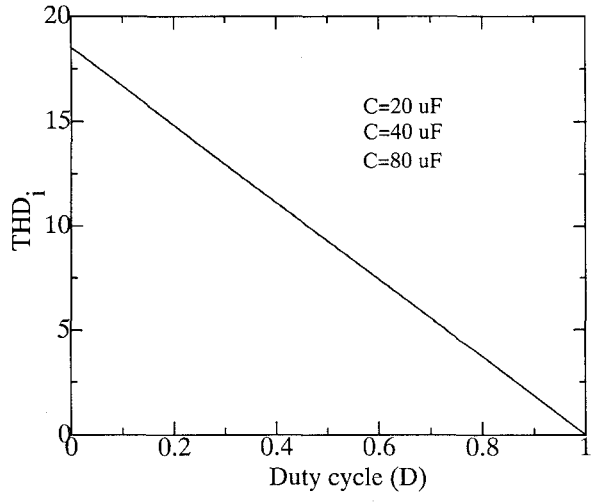


Fig. 7. Total harmonic distortion of the output current, L=1.0 mH, Ro=10 Ohm

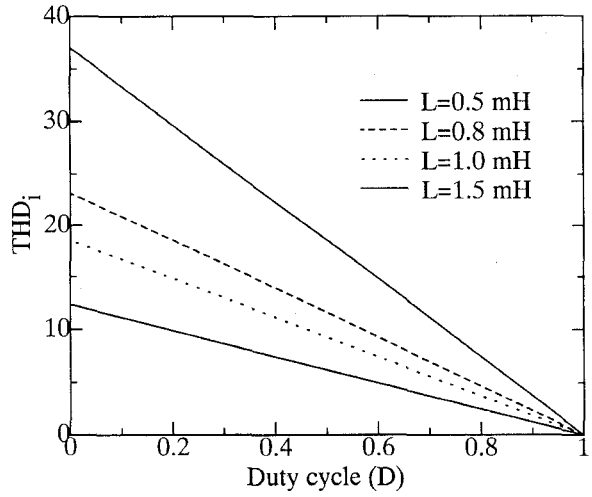


Fig. 8. Total harmonic distortion factor of output current, C=20 uF, Ro-10 Ohm.

Figs. 5-8 can be used for the selection of the system parameters C and L to maintain the total harmonic distortion factor of the output voltage and current within the value required in the system .

The input power factor according to (6) and (7) and for a different values of the power system parameters is demonstrated in Figs. 9-12. From these figures, it is depicted that almost unity input power factor is remarkably maintained over most of the control range with a proper choice of the power system parameters.

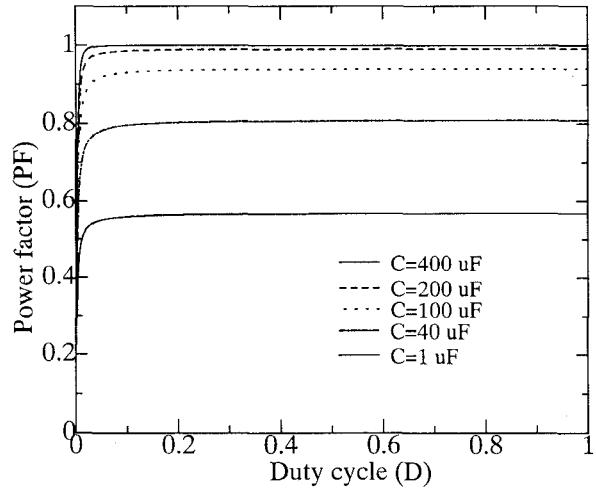


Fig. 9. Input power facator.
C1=1 uF, L=0.5 mH, Ro=10 Ohm.

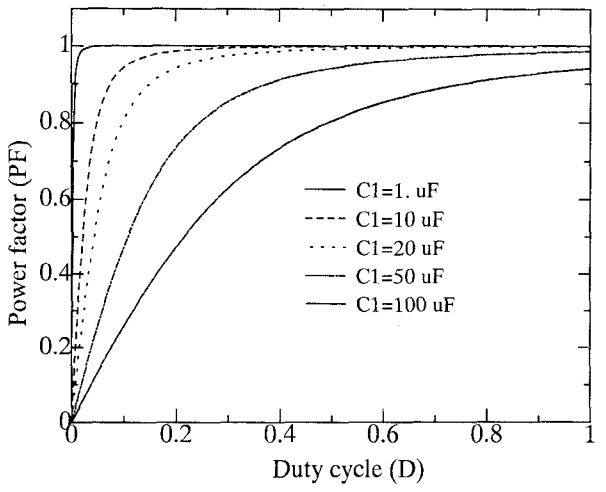


Fig. 10. Input power facator.
C=1 uF, L=0.5 mH, Ro=10 Ohm.

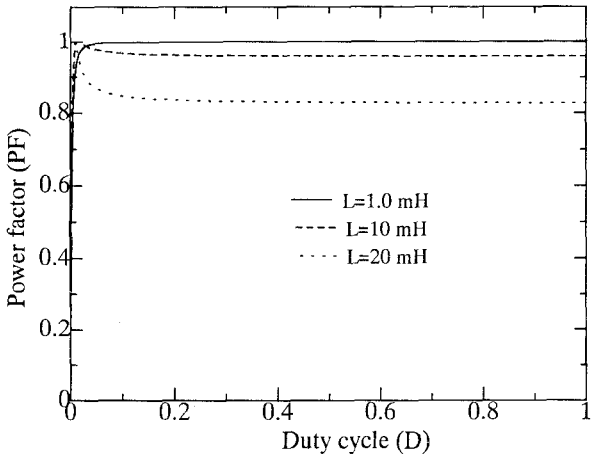


Fig. 11. Input power facator.
C=20 uF, C1=1uF, Ro=10 Ohm.

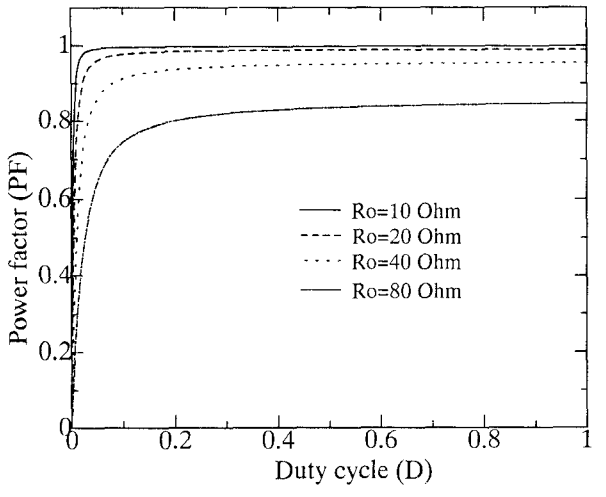


Fig. 12. Input power facator.
C=20 uF, C1=1 uF, L=0.5 mH.

Finally, a comparison between the calculated percentage total harmonic distortion factor of the output voltage and current using (4) and (5) with that obtained by PSPICE software program for different values of the filter capacitor and inductor are shown in Figs. 13 and 14. The evident good agreements between the calculated and PSPICE simulated results enhances the accuracy of the analysis.

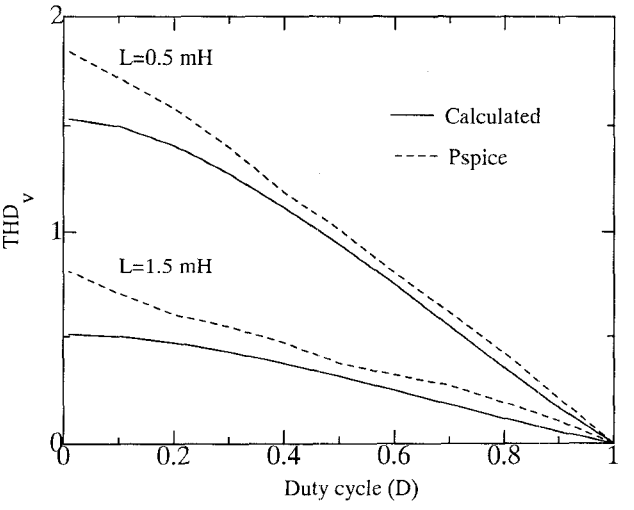


Fig. 13. Comparision between calculated and PSPICE simulated total harmonic distortion factor of output voltage.

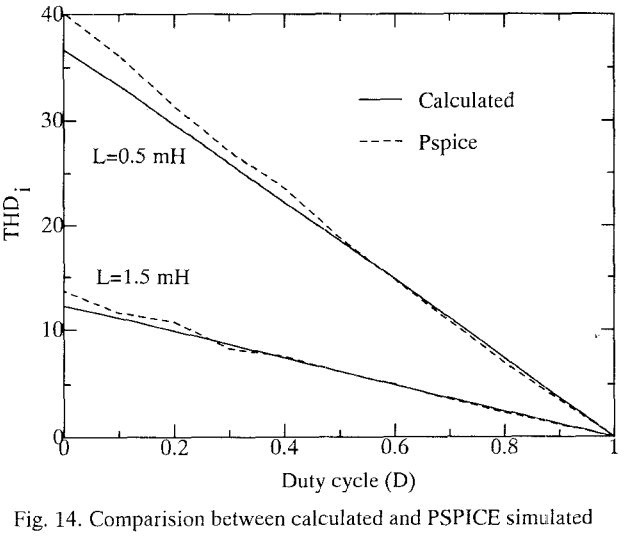


Fig. 14. Comparision between calculated and PSPICE simulated total harmonic distortion factor of output current.

V. CONCLUSION

The paper presents an improved circuit of AC choppers for single-phase systems with a reduced number of switches

and simple control circuit. Since only one switch is modulated and one switch is always turned on during the most half period of the supply voltage, the switching loss is significantly reduced and consequently high efficiency can be approached. Using the polarity of the input voltage and the load current, the switching patterns are decided to make the current path possible whatever the load current and the operation modes are divided into active and freewheeling modes. Advantages of the proposed circuit for AC choppers include increased input power factor, fast dynamic, high efficiency, high reliability, high power capacity and it is more economic owing to simple design requirements, less number of switches and low cost. Digital simulation have shown that the proposed circuit give a good performance.

REFERENCES

[1] B. Cotta, M. Mazzuchelli and G. Sciuto, "AC Chopper Regulation Using Power Transistors", in the Proceedings of Conference POWERCON 8, 1981, Vol. G1-4, PP. 1-8.

[2] B. H. Kwon, B. D. Min and J.-H. Kim, " Novel topologies of AC choppers", in the Proceedings of IEE on Electric Power Applications., Vol. 143, No. 4, July 1996, PP. 323-330.

[3] B. W. Willams, "Asymmetrically modulated AC chopper", IEEE Trans. on Industrial Electronics Vol. IE-29, No. 3, August 1982, PP. 181-185.

[4] D. A. Deib and H. W. Hill, "Optimal Harmonic Reduction in AC/AC Chopper Converters", in the Proceedings of the IEEE Conference PESC'91, pp.1055-1060.

[5] D. H. Jang, J. S. Wong and G. H. Choe "AN Improved PWM Technique for AC Chopper", in the Trans. of IEEE on Power Electronics, Vol. 4, No. 4, October 1989, PP. 496-505.

[6] G. H. Choe, A. K. Wallace, and M. Park, "Asymmetrical PWM method of AC chopper with improved input power factor", in the Proceedings of IEEE Conference PESC'91, PP. 838-845.

[7] L. Salazar, C. Vasquez and E. Weichmann, "On the characterastics of a PWM AC Controller using Four Switches", in the Proceedings of IEEE Conference PESC'91, PP. 307-313.

[8] M. M. Mazzuchelli , L. Puglisi, G. Sciuto and P. Tenti, "Improving The Performance of AC/AC Static Converters With High Frequency AC Chopper", in the Proceedings of Conference POWERCON 9, 1982, Vol. I-3, PP. 1-9.

[9] P. D. Ziogas, D. Vincenti and G. Joos, "A Practical PWM AC Controller Topology", in the Proceedings of IEEE Conference IECON'91, PP. 554-559.

[10] S. A. Hamed, "Steady-state modeling, analysis, and performance of transistor-controlled AC power conditioning systems", IEEE Trans. on Power Electronics Vol. 5, No. 3, July 1990, PP. 305-3013.

[11] S. Ashoka, K. Bhat, J. Vithayathilams, "A simple multiple pulse width modulated AC chopper", IEEE Trans. on Industrial Electronics Vol. IE-29, No. 3, August 1982, PP. 185-189.

[12] S. Iida, and S. Miyairi, "Effects of PWM applied in single-phase AC chopper control", Trans. of JIEE, Vol. 103-B(1), Jan. 1983, PP. 7-14.

A New Topology for Single Phase UPS Systems

Gui-Jia Su and Tetuhiko Ohno
Sanken Electric Co., Ltd.
677 Ohnohara, Shimoakasaka, Kawagoe, Saitama 350-11, Japan
Phone: 0492-66-8031, Fax: 0492-66-8084

Abstract —**This paper presents a new converter topology, based on a single switch ac/dc or dc/dc boost converter combined with a half bridge inverter, suitable for on-line single phase UPS systems. The converter uses only four active switches, including the one for maintaining the charge of storage battery, to realize very desirable features. These include sinusoidal input currents, a common neutral connection – eliminating the requirement of an isolation transform, low voltage storage battery as well as its charge/discharge regulations. Further, higher ac-dc conversion efficiency can be obtained due to reduced voltage stresses on the switch in the boost converter during normal operation, compared with conventional half bridge converters. Detailed simulation results and experimental results are included in this paper.**

I. INTRODUCTION

Uninterruptible power supply (UPS) systems are being widely used for a wide variety of critical loads including computers, telecommunication systems and medical equipment to overcome the disruption in utility power supply that may occur in the form of outage, voltage sag or voltage surge. Although UPSs have been applied in the past for large computers, increased dependency of businesses and industries on small or personal computers (PCs) has created a tremendous increase in the use of small capacity UPSs operating off a single phase supply. Given the decreased cost of computer capability and increased installation volume of PCs, these single phase UPSs are extremely sensitive to cost.

On-line systems are preferred where highly reliable uninterruptible power supply is required. Among various topologies for the on-line UPS systems of 3 kVA and lower ratings reported in literature [1][2], UPS systems based on a half bridge converter combined with a half bridge inverter, as shown in Fig. 1, seem to have attracted attentions in recent research and development for low power range applications in computers and telecommunication systems. Compared with systems based on full bridge converters with a high frequency or commercial ac line frequency isolation transform[3], this topology offers several advantages including a simple power conversion circuit with possibly fewest switching device count, no need of an isolation transformer. Adding other desirable features such as sinusoidal ac line currents with unity power factor, and load regulation with non-linear loads, it can thus provide the potential for realizing compact, low cost and high performance systems. However, since a storage battery is connected directly to the dc bus, many battery cells connected in series are required to obtain a high voltage for matching with the dc link voltage, which is usually raised to a level higher than the doubled peak line voltage for shaping the input current waveform. This requirement of high voltage storage battery leads to increased cost and reduced reliability, since storage battery is the most expensive part in low power range UPS systems.

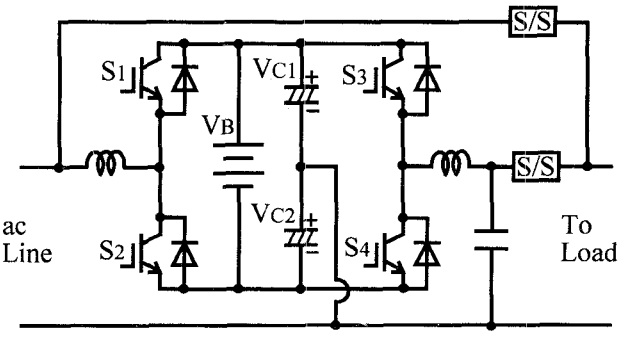


Fig. 1 Single phase UPS system based on half bridge converters.

Several schemes have been reported to overcome the high battery voltage issues. One is to add one more leg to the dc bus, which forms a bi-directional chopper circuit for connecting a low voltage battery to the dc bus [4]. The bi-directional chopper steps down the dc link voltage for the charge of battery, or steps up the battery voltage to support the dc link during ac line outages. A low voltage battery can thus be adopted at the expense of a bi-directional chopper. Moreover, all six switches are exposed to a boosted high dc link voltage – around 350 V for 100 V ac input, causing increased voltage stress and switching loss.

Another approach is to utilize an auxiliary inverter of full bridge type to connect a low voltage battery to the line input side [5]. Upon detecting ac line failure, the battery is brought on line through the auxiliary inverter operating synchronized with the UPS output voltage. This arrangement requires at least four additional switches and a dedicated battery charger.

This paper presents a new approach to realizing single phase on-line UPS systems. Taking advantage of the fact that net power flow in most UPS applications is completely unidirectional, i.e. from ac

line to load, a single switch ac/dc (during normal operation) or dc/dc boost converter (during battery powered operation) is introduced to replace the half bridge converter in Fig. 1. Combining with a half bridge inverter at dc/ac conversion stage maintains the benefits inherent in the half bridge scheme, i.e. a common neutral line, thus eliminating the requirement for an isolation transform. The proposed circuit uses only four active switches and allows full control of the ac line currents and load voltages, and battery charge/discharge regulations. Moreover the switch in the boost converter has greatly reduced voltage stresses during normal operation, contributing to decrease switching loss and improve reliability. The system operates with a near unity input power factor, and delivers a high quality sinusoidal voltage waveform to loads.

II. Proposed Single Phase UPS System

A. Configuration of Proposed Single Phase UPS

The basic schematic of the proposed converter for realizing single phase UPS systems is shown in Fig. 2, which is mainly consisted of a single switch ac/dc or dc/dc boost converter, a half bridge PWM inverter and a step-down chopper for battery charge. Switch S_1 and inductor L_1 plus diodes $D_1 \sim D_6$ form an ac/dc boost converter to obtain sinusoidal ac line currents when operating off an ac line, or a dc/dc boost converter to support the dc link voltage from the storage battery during line outages. The step-down chopper consisting of switch S_2, diodes D_7 and D_8, and inductor L_2 performs the charge control for the storage battery. Switches S_3 and S_4, capacitors C_1 and C_2 construct a half bridge inverter for supplying loads.

Two transfer switches, S_a and S_b, are used to transfer the input for the boost converter from the ac line to the storage battery, or vice versa. Either static switches or electromagnetic contacts may be used. Generally, the use of electromagnetic contacts presents a longer transfer time at the moment of power loss, but this can be tolerated by choosing large dc bus capacitors. In addition two by-pass switches (S/S) for reverting to ac line in the event of UPS failure or overload are also employed. Static switches are used for realizing no transfer time. Moreover an EMI noise filter is inserted into the ac input line for blocking switching-operation produced high frequency currents from entering to utility, and an L-C low-pass filter is used at the output side for eliminating unwanted harmonic components from the output voltage.

B. Description of Converter Operation Modes

The operation of the ac/dc or dc/dc boost converter can be divided into four normal operation modes for operating off ac line, two battery powered operation modes for ac line outages. In addition, three modes for the charge regulation of the battery occur simultaneously with the normal operation modes.

1) Normal operation modes: In the normal operation modes, switch S_a is kept on and S_b off. The current in the inductor L_1 is regulated by PWM control of the ac/dc boost converter so as to obtain a sinusoidal ac line current while maintaining a constant voltage across the dc link capacitors. For positive ac line voltage v_s if Switch S_1 is turned on, a current is produced in the path of $v_s \rightarrow L_1 \rightarrow D_2 \rightarrow S_1 \rightarrow D_3 \rightarrow v_s$, storing energy in the inductor L_1 (denoted as normal operation mode 1). Notice that the EMI filter is ignored for simplifying the discussion. Then turning off S_1 changes the current path so as to transfer power from the ac line to dc bus

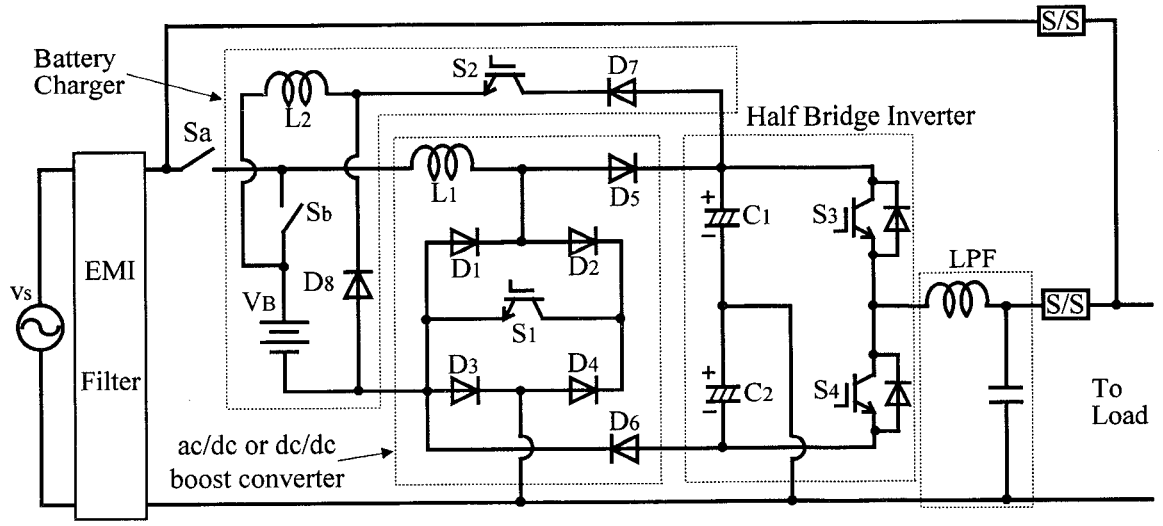


Fig. 2 Schematic of proposed single phase UPS system.

and to release part of the stored energy. A current is also provided for charging the upper dc capacitor C_1 through the path of $v_s \rightarrow L_1 \rightarrow D_5 \rightarrow C_1 \rightarrow v_s$ (normal mode 2). Similarly, for negative v_s two other operation modes, S_1 on as normal operation mode 3 and S_1 off as normal mode 4, can be established. The lower dc capacitor C_2 is charged during mode 4 with a current flowing in the path of $v_s \rightarrow C_2 \rightarrow D_6 \rightarrow D_1 \rightarrow L_1 \rightarrow v_s$.

2) Battery powered operation modes: Upon identifying failure of ac line, switch S_a is turned off and S_b on, transferring the input from the ac line to the storage battery for the boost converter, which now functions as a dc/dc step-up chopper to continue supplying to loads. To support the dc link voltage switch S_1 is first turned on for a certain interval, generating a current through the path of $V_B \rightarrow L_1 \rightarrow D_2 \rightarrow S_1 \rightarrow V_B$ and storing energy in the inductor L_1 (battery powered mode 1). After S_1 is turned off, part of the stored energy in the battery and L_1 is then transferred to loads through dc bus, and a current for charging the dc capacitors is also produced in the path of $V_B \rightarrow L_1 \rightarrow D_5 \rightarrow C_1 \rightarrow C_2 \rightarrow D_6 \rightarrow V_B$ (battery powered mode 2).

3) Battery charge regulation modes: The charge regulation of battery is achieved by the control of switch S_2 during the normal operation modes. There are two possible current paths for charging the battery by turning on S_2, depending on which normal operation modes is involved. Turning on S_2 during each one of the first three normal operation modes results in a current flowing in the path of $C_1 \rightarrow D_7 \rightarrow S_2 \rightarrow L_2 \rightarrow V_B \rightarrow D_3 \rightarrow C_1$, charging the battery while storing energy in L_2 (charge regulation mode 1). On the other hand, if S_2 is turned on in the normal mode 4, a charging current is provided in the path of $C_1 \rightarrow D_7 \rightarrow S_2 \rightarrow L_2 \rightarrow V_B \rightarrow D_1 \rightarrow L_1 \rightarrow v_s \rightarrow C_1$(battery charge regulation modes 2). Then turning off S_2 releases the energy stored in L_2 to the battery (charge regulation mode 3).

The proposed topology provides several advantages worthy of mentioning over conventional schemes. It is apparent that the proposed boost converter possesses no possibility of shoot-through accident as that may happen in half bridge converters. From the above discussion, it is also revealed that during the normal operation modes, the voltage stresses on the switch S_1 are reduced to half of dc link voltage, compared again with the case of conventional half bridge converters where all switches are exposed to full dc bus voltage. It can thus be expected to reduce the switching loss and thus to improve the ac/dc conversion efficiency and reliability.

C. Control Strategy

Control strategies for realizing sinusoidal current for a boost converter of full-wave rectifier have been well studied [6], but most of the reported methods can not be readily applied to the proposed converter due to the differences in circuit configuration. A rather simple control strategy is adapted for the proposed boost converter, with current shaping compensation, from the one designed for half bridge converters. Fig. 3 shows the control block diagram for both normal and battery powered operations. During normal operation, the input current reference is derived from the requirements of dc bus regulation and balancing the two capacitor voltages. A PI controller is used to accomplish the dc bus voltage regulation. The output of the PI controller is clamped to zero as the lower boundary since power can only flow from ac line to the dc bus with the boost converter. The difference of voltage between the upper and lower capacitors is detected and put through a low pass filter with a fairly large time constant, denoted by τ, to obtain a capacitor voltage unbalance compensation signal. This signal is then used to bias the input current reference so that the voltages can be balanced over half cycle basis. The voltage unbalance may be caused by loads that draw unequal power over each half cycles such as in the transient states for non-linear loads.

Another PI controller is used to regulate the input current. The PI controller output is compared with a triangle wave to produce a pulse width modulation (PWM) signal for the control of switch S_1. The PWM signal is delivered to S_1 for positive v_s and the logically reversed one is directed to S_1 for negative v_s. This is accomplished by the logic circuit gated by the zero-crossing signal of v_s. For reducing audible noises a switching frequency higher than 16 kHz is preferred.

Compared with the case of half bridge converter a much higher P gain for the current controller is required to obtain near sinusoidal current waveform, especially for shaping the current waveform around zero-crossing moment of ac line voltage.

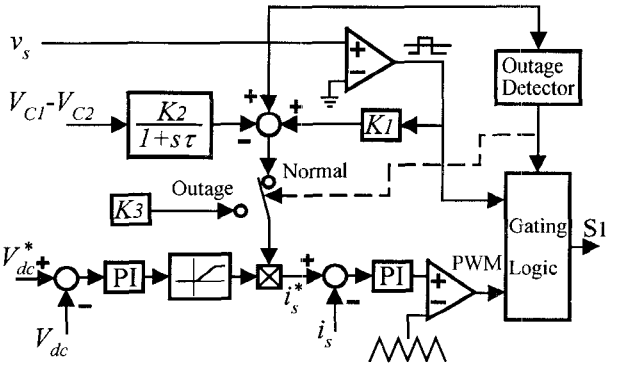


Fig. 3 Boost converter control block diagram.

This can be easily explained by examining the operation of the converters around zero-crossing region. In half bridge converters, with the help of a high dc capacitor voltage, even for small voltage of v_s around zero-crossing region a desired current can be produced in a short conduction period of the corresponding switch for boost operation. Taking positive v_s for example (ref. to Fig. 1), when S_2 is turned on, the lower capacitor voltage V_{C2} is included in the direction of increasing the input current. But this is not the case for the boost converter where the dc capacitors are not involved in generating a desired current when the switch in the boost converter is conducting. Therefore to generate a desired current around the zero-crossing with a small line voltage, the switch must be kept on for a longer period. This requires a high P gain to produce a suitable level control signal from the current error.

However the gain can not be raised too high otherwise the system can become unstable due to the interference with the dc bus voltage controller. Also a high gain is not desirable from preventing the influence of noises in the control circuit. A wave shaping compensation signal is therefor injected into the current reference to overcome the high gain issue. The signal is a rectangular wave derived from the zero-crossing of v_s, and is added to v_s after passing a gain element K_1 for generating the input current reference as shown in the control block diagram.

Upon detection of a power failure, the controller is switched to battery powered operation. The input current reference for battery current is generated only from the requirement of dc bus voltage regulation by multiplying the output of the dc bus voltage PI controller with a gain element K_3, as shown in the control block diagram.

In order to obtain good output voltage regulation, an average voltage regulator combined with an instantaneous waveform controller is used for generating PWM control signal for the half bridge inverter. In addition a disturbance (i.e. load current) compensator is added to the waveform controller to achieve good dynamic response, especially in the presence of non-linear loads.

III. Simulation and Experimental Results

The proposed circuit was extensively simulated on a SPICE based computer simulator. Fig. 4 shows typical operation waveforms in the normal modes; (a) for positive v_s while (b) for negative v_s, where V_{S1}, V_{S2}, V_G ,V_{dc} and I_B represent the voltages across switches S_1, S_2 and their gate control voltages, dc bus voltage, and battery charging current, respectively. The charging current was set at 1 A, which was chosen only for verifying the operation

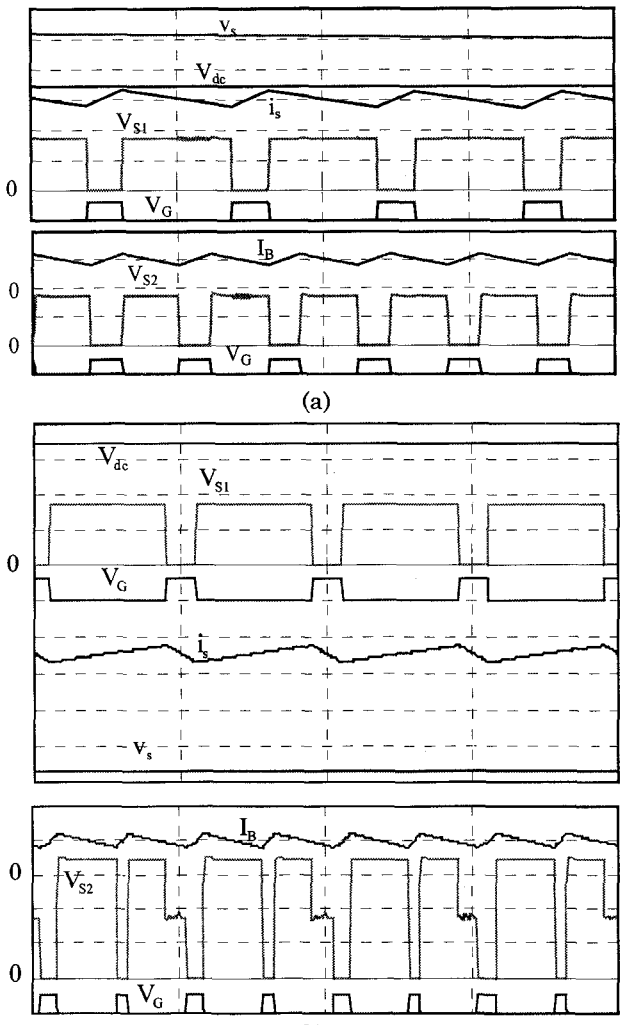
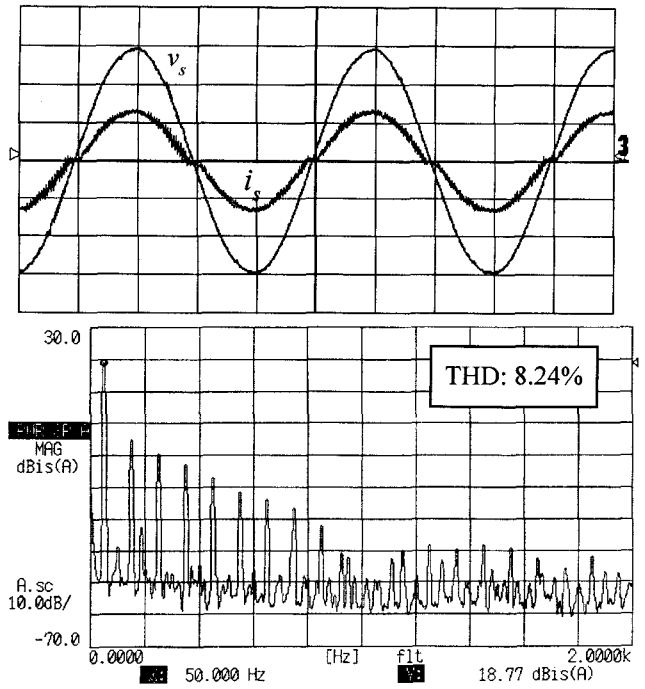


Fig. 4 Simulation Results. (a) for positive v_s, (b) for negative v_s. Time: 50us/div, V_{dc}, V_{S1}, V_{S2}:100V/div, v_s:25V/div i_s:2.5A/div, I_B:1A/div

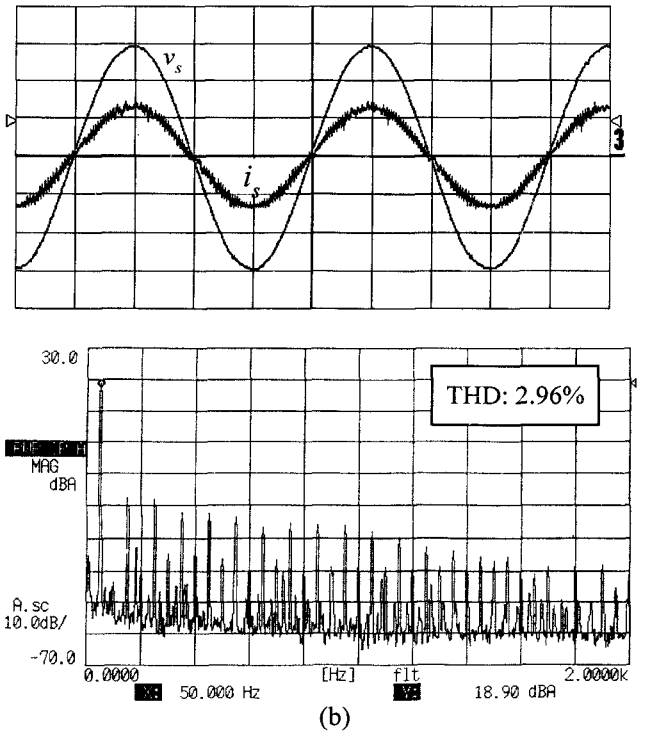
mode analysis given in the previous section. It can be seen that voltage stress for switch S_1 in the boost converter is reduced to half of the dc bus voltage, conforming the above discussion. And the voltage stress for switch S_2 in the battery charger is also half of the dc bus voltage for positive v_s, but either half or full dc bus voltage for negative v_s depending on whether switch S_1 is conducting or not.

A prototype was built for 1 kVA UPS systems. IGBTs were used at a switching frequency of 18 kHZ, and a battery bank with a rated voltage of 48 V was employed to demonstrate operation performances at ac line outages.

Fig. 5 shows input current waveforms and their harmonic spectra before and after using the wave-shaping compensation at a rated load power. While a zero-current zone around zero-crossing can be observed in the current waveform without the compensation as shown in figure (a), it disappears and a sinusoidal current is obtained after compensation, confirming the efficacy of the wave-shaping com-



(a)



(b)

Fig. 5 Input current waveform and its spectrum.
(a) without wave shaping compensation.
(b) with wave shaping compensation.
Upper: input voltage (50V/div) and current (10A/div)
Time scale: 5ms/div
Lower: input current spectrum (10dB/div)

pensation technique. The lower order harmonic components are significantly reduced with a total harmonic distortion (thd) decreased from 8.24 % to 2.96 %. Fig. 6 gives a detailed comparison of thd

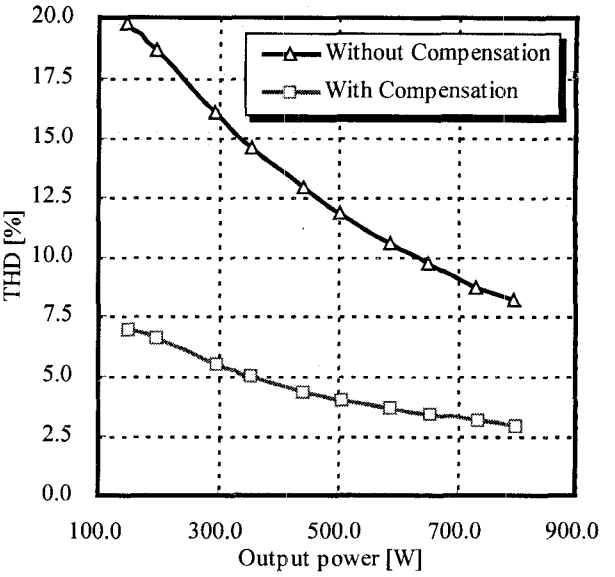


Fig. 6 THD v.s. output power.

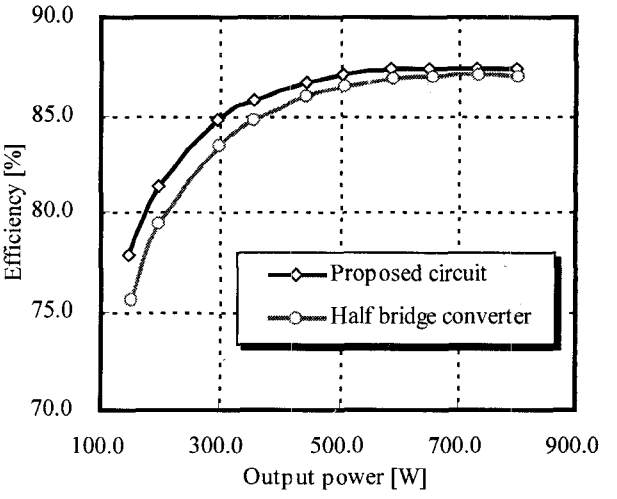


Fig. 7 Efficiency v.s. output power.

versus output power. The thds are greatly reduced to below 7.5 % over the entire load range by use of the wave-shaping compensation technique.

Fig. 7 depicts a comparison of efficiency at resistive loads between the proposed circuit and conventional schemes using a half bridge converter at ac-dc power conversion stage. Although one may expect for the half bridge converter to have higher efficiency due to the reduced device count and thus conduction loss. But this is betrayed because of increased switching loss caused by a higher voltage stress on the switching devices in the half bridge converter, as explained in section II. This is shown clearly from the figure. The efficiency at a rated load is 87.0% for half bridge converter and 87.4% for the boost converter. Also it can be seen that the efficiency gains more improvement as load power decreases. This can be explained by considering the weight of switching loss against conduction loss

which becomes higher as load power decreases.

Fig. 8 illustrates operations at a power outage, where the ac line was intentionally disconnected for about 1 second and then reconnected. Good dynamic regulation of the output voltage is demonstrated. The time for transferring the input from ac line to storage battery is about 60 ms due to the use of electromagnetic contact switches for S_a and S_b. During this transfer period the energy in the dc capacitors is released to continue supplying loads, as indicated by the slight decrease in the dc bus voltage. And it took about 160 ms to transfer back to ac line after the ac line voltage was recovered. These transfer time can be shortened, if necessary, by employing static switches and reducing the time constant of the outage detection circuit.

IV. CONCLUSIONS

To summarize, the advantages of the proposed single phase UPS systems over conventional schemes using a half bridge converter at ac-dc power conversion stage can be restated as follows;

- Fewer active switches,
- Reduced voltage stress on the switch in the boost converter,
- Improved efficiency and reliability.

The proposed single phase UPS systems also satisfy other desirable features including sinusoidal ac line currents with near unity power factor, a common neutral connection, high quality sinusoidal load voltage even with non-linear load, and low voltage storage battery. The successful operation of the proposed scheme is demonstrated by both simulation and experimental results.

REFERENCES

[1] M. Nakamura, Y. Fujitani and S. Kawauchi, "Several Recent Circuits in the Small Power UPS System", *National Convention Record, IEE IAS Japan (JIASC)*, vol.2, No. S-1-2-2, 1995.

[2] K. Kuroki, "The Main Circuit Configuration of UPS", *JIASC*, vol.2, No.S.1-3, 1995.

[3] R. Krishnan, "Design and Development of a High Frequency On-Line Uninterruptible Power Supply", *IEEE IECON*, vol. 1, pp. 578-583, 1995.

[4] K. Hirachi, et al, "Cost-Effective Practical Developments of High-Performance and Multi-Functional UPS with New System Configurations and Their Specific Control Implementations", *IEEE PESC*, pp. 480-485, 1995.

[5] K. Hirachi, et al, "Practical Developments of High-Performance UPS with New System Configurations and Their Specific Control Implementations", *IPEC-Yokohama*, pp. 1278-1283, 1995.

[6] D. Maksimović, "Design of the Clamped-Current High-Power-Factor Boost rectifier", *IEEE Tran. IAS*, vol. 31, No. 5, pp. 1826-1831, Sept./Oct. 1995.

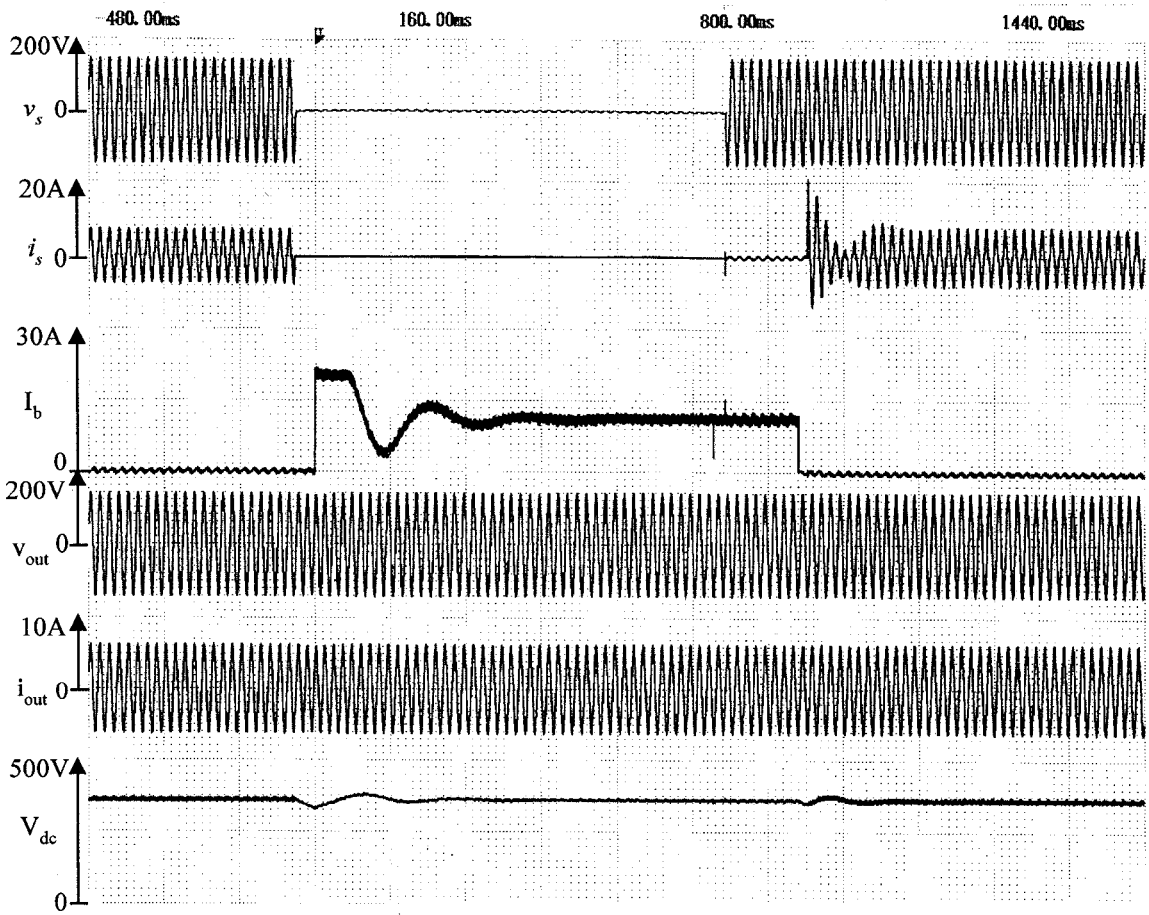


Fig. 8 Operation at a power outage. Time scale: 160ms/div, (a) ac line voltage, (b) ac line current, (c) Battery current, (d) Output voltage, (e) Load current, (f) dc bus voltage.

A Design Concept of DC Filters for Magnet Power Supplies

Hyosung KIM °

Dept. of Control & Measurement Eng.
Cheonan National Technical College
275-1 Budae Cheonan Chungnam
330-240, Korea
TEL: 82-417-550-0286
FAX: 82-417-63-3689 or 62-8080
Email: hyoskim@dragon.cntc.ac.kr

Jaeho CHOI *

School of Electrical & Electronics Eng.
Chungbuk National University
San 48 Gaesin Cheongju Chungbuk
360-763, Korea
TEL: 82-431-61-2425
FAX: 82-431-276-6520
Email: choi@choijae.chungbuk.ac.kr

Abstract - **Passive filters are essentially used for attenuating current/voltage harmonics generated from pulse-modulation type converters which are prevail in high-power magnet power supplies (MPS). But the passive filter limits the operation range of the output dc current, causes harmful filter resonance, and makes the system equation more complicate. This paper presents, a systematic and simple filter design method which considers not only filtering but also controlling the magnet current. The design algorithm is extended to the applications on superconducting magnetic energy storage (SMES) systems.**

I. INTRODUCTION

Magnet power supplies (MPS) which are used in high energy physics and its applications such as magnetic levitated vehicles (Maglev), computerized axial tomographies (CAT), magneto hydro dynamics (MHD) generations and superconducting magnetic energy storages (SMES) require high power and precise output current control.

In the view of efficiency and cost, pulse modulation type switching converters such as chopper, thyristor converter and pulse width modulation (PWM) converter, are prevail in this field.[1,2,3,4,7] Although passive filters are necessary to attenuate the current/voltage harmonics generated from the input/output terminals of these converters, they raise many problems such as the limitation of the operation range of converters, resonances with converter switching, and the complexity of system equations.[5,6,7,8]

This paper proposes a simple and systematic DC filter design method in the view of filtering and controlling the magnet current. Design data are provided as a per-unit representation to be applied for the various electrical conditions easily. The design algorithm is extended to the applications on SMES systems.

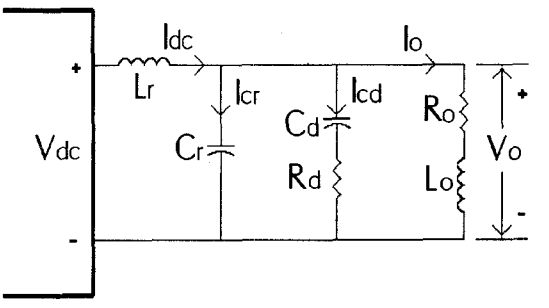


Fig.1. Circuit diagram of the proposed DC output filter with magnet load.

II. CONFIGURATION OF DC FILTER

Fig.1 shows the configuration of the proposed DC output filter which is composed of a conventional L-C filter and an additional R-C damper. The R-C damper circuit allows only the high-frequency ripple current which may resonate between the filter capacitor C_r and the high inductive magnet inductance L_o. The magnet load is composed of the resistance R_o and inductance L_o.

As an operation limitation of the output current for converters, Ripple Factor (RF_{io}) is defined as (1).

$$RF_{io} = \frac{\left(\sum_{k=1,2,3,\ldots}^{31} I_{ok}^2\right)^{1/2}}{I_{oavg}} \times 100\ (\%) \qquad (1)$$

where,
I_{ok}: Magnitude of k-th order harmonics of load current
I_{oavg}: Average value of load current.

III. FILTER DESIGN ALGORITHM

A. Modelling For DC Circuit

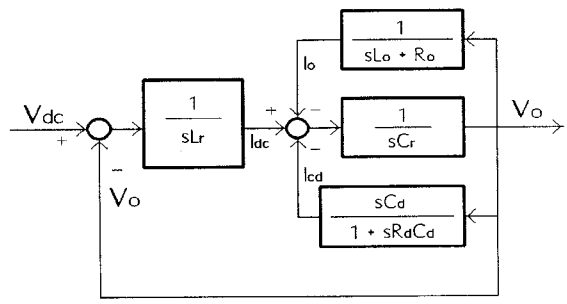


Fig.2. Block diagram of DC output filter with magnet load.

There are two considerations in designing the DC filter; one is the harmonic attenuation and the other is the dynamic response of the magnet current. Although the DC filter attenuates the voltage harmonics of the converter output terminal, it makes the system equation complicate and deteriorates the dynamic response of the magnet current.

Fig.2 shows the block diagram between the converter output voltage V_{dc} and the filter output voltage V_o related with the DC filter and a magnet load. Equation (2) shows the transfer function of the block diagram.

$$\frac{V_o}{V_{dc}} = \frac{N(s)}{D(s)} = \frac{b_2(s-z_1)(s-z_2)}{a_4s^4+a_3s^3+a_2s^2+a_1s+a_0} \tag{2}$$

where,

$$z_1 = -\frac{1}{R_dC_d}$$
$$z_2 = -\frac{R_o}{L_o}$$
$$a_4 = L_oL_rC_rR_dC_d$$
$$a_3 = L_oL_rC_r + L_oL_rC_d + R_oL_rC_rR_dC_d$$
$$a_2 = R_oL_rC_r + R_oL_rC_d + L_rR_dC_d + L_oR_dC_d$$
$$a_1 = L_r + L_o + R_oR_dC_d$$
$$a_0 = b_0 = R_o$$
$$b_2 = L_oR_dC_d$$
$$b_1 = R_oR_dC_d + L_o.$$

B. Filter Design Algorithm

If the conditions of (3) and (4) are satisfied with the DC filter, the transfer function of the load output voltage will be a 2nd order differential equation as (5).

$$R_d = R_o \tag{3}$$

$$C_d = \frac{L_o}{R_o^2} \tag{4}$$

$$\frac{V_o}{V_{dc}} = \frac{1}{L_rC_r(s^2+2\zeta\omega_cs+\omega_c^2)} \tag{5}$$

where,

$$\omega_c = \frac{1}{\sqrt{L_rC_r}} \tag{6}$$

$$\zeta = \frac{1}{2R_o}\sqrt{\frac{L_r}{C_r}}. \tag{7}$$

The harmonic attenuation is depend on the setting of the cutoff frequency ω_c, and the dynamic response is depend on the setting of the damping factor ζ. Since the parameters of the resistive capacitance leg R_d and C_d are already fixed by the parameters of the magnet load R_o and L_o, only pure filter parameters L_r and C_r are determined according to the setting of the ω_c and ζ.

Besides, the resistive capacitance C_d has a practical limitation. Let's define a capacitance ratio m between C_d and C_r as (8).

$$m = \frac{C_d}{C_r} \tag{8}$$

The power rating of the resistive capacitance C_d becomes m-times larger than that of the pure filter capacitance C_r because each average dc voltage applied to the two capacitors is same in steady state. Thus, if the ratio m increases without limitation, the power rating of the resistive capacitance C_d becomes too large to be practical.

Combining (4), (6) and (7), the capacitance ratio m can be calculated as (9).

$$m = \frac{C_d}{C_r} = \frac{2\omega_c\zeta L_o}{R_o} = 2\omega_c\zeta\tau_o \tag{9}$$

where, $\tau_o = \frac{L_o}{R_o}$ [sec].

If $m \le 10$, the cut-off frequency is limited as (10).

$$\omega_c \le \frac{5}{\zeta\tau_o} \tag{10}$$

For example, if the magnet time constant $\tau_o = 20$ [ms] and the damping ratio $\zeta = 0.6$, the cut-off frequency ω_c is limited under 416.7 [rad/s] (f_c<66.8[Hz]).

C. Application For Superconducting Magnet

1) LC-RC type filter: In the application of superconducting magnets which have no internal resistance, the transfer function of the DC circuit can be expressed as (11).

$$\frac{V_o}{V_{dc}} = \frac{L_o R_d C_d\left(s+\frac{1}{R_d C_d}\right)}{a_3 s^3 + a_2 s^2 + a_1 s + a_0} \tag{11}$$

where,

$a_3 = L_o L_r C_r R_d C_d$

$a_2 = L_o L_r C_r + L_o L_r C_d$

$a_1 = L_o R_d C_d + L_r R_d C_d$

$a_0 = L_o + L_r$.

Same with the section B, if the conditions of (12) and (13) are satisfied with the DC filter, the transfer function of the load output voltage will be a 2nd order differential equation as (14).

$$L_r \ll L_o \tag{12}$$

$$C_d = \frac{L_o}{R_d^2} \tag{13}$$

$$\frac{V_o}{V_{dc}} = \frac{1}{L_r C_r\left(s^2 + 2\zeta\omega_c s + \omega_c^2\right)} \tag{14}$$

where,

$$\omega_c = \frac{1}{\sqrt{L_r C_r}} \tag{15}$$

$$\zeta = \frac{1}{2R_d}\sqrt{\frac{L_r}{C_r}} \quad . \tag{16}$$

To investigate design limitations of the filter, let's define an inductance ratio M between L_o and L_r as (17).

$$M = \frac{L_o}{L_r} \tag{17}$$

Thus, combining (13) and (17) to (16), the damping factor of the DC circuit composed of the filter and superconducting magnet can be rewritten as (18).

$$\zeta = \frac{1}{2}\sqrt{\frac{m}{M}} \tag{18}$$

If the M is very large, compared with the m, the damping factor ζ is decreased too small to properly damp the load ripple current.

2) L-C-R type filter: If the pure filter capacitor is disconnected in Fig.1, the filter configuration becomes L-C-R type. Including the magnet inductance, the transfer function between the input and output voltage of the filter becomes as (19).

$$\frac{V_o}{V_{dc}} = \frac{\frac{R_d}{L_r}\left(s+\frac{1}{R_d C_d}\right)}{s^2 + s\left(\frac{R_d}{L_o}+\frac{R_d}{L_r}\right)+\left(\frac{1}{L_o C_d}+\frac{1}{L_r C_d}\right)} \tag{19}$$

If $L_o \gg L_r$, the transfer function can be represented as (20).

$$\frac{V_o}{V_{dc}} = \frac{R_d / L_r (s+z)}{s^2 + 2\zeta\omega_c s + \omega_c^2} \tag{20}$$

where,

$$z = \frac{1}{R_d C_d} \tag{21}$$

$$\omega_c = \frac{1}{\sqrt{L_r C_d}} \tag{22}$$

$$\zeta = \frac{R_d}{2}\sqrt{\frac{C_d}{L_r}} \quad . \tag{23}$$

The cutoff frequency ω_c must be lower enough than the lowest harmonic frequency of V_{dc}, to attenuate the voltage harmonics. Besides, since the zero z in (20) increases the gain of the transfer function as +20[dB/dec] for the higher frequency band than z, z must be larger than ω_c for normal filtering. This means that the damping factor is limited to $\zeta \leq 0.5$ and that the damping resistance is limited as (24).

$$R_d \leq \sqrt{\frac{L_r}{C_d}} \tag{24}$$

IV. Simulation

A. DC Filter Design

TABLE I
SPECIFICATIONS OF THE PROPOSED MAGNET POWER SUPPLY SYSTEM.

Items		Specification
AC input voltage		3φ, 220[V]±10%, 60[Hz]
DC output voltage range		50 ~ 250[V]
DC output current range		40 ~ 200[A]
Output current ripple		≤ 10[ppm] peak to peak
Magnet load	Inductance	21.49[mH]
	Resistance	1.0746[Ω]

Table I shows the specification of the proposed magnet power supply system. A Current Source (CS) PWM converter which adopts hysteresis comparison switching method is used for the magnet power supply

system. The output power of the converter is 60 [kVA]. The magnet load which has time constant of 20[ms] is operated in ambient temperature. The DC filter data designed for the proposed system is shown in Table II.

TABLE II
FILTER DESIGN DATA FOR THE SIMULATION SYSTEM.

Filter inductor[mH]	5.37
Filter capacitor[μF]	1163
Damping capacitor[μF]	18610
Damping resistor[Ω]	1.0746

B. Per-unit System

Using per-unit system, the system performance can be represented as a more simple form, and the filter design data can be easily applied to other rated systems. The per-unit system of the DC side is defined as follows;

$$V_{dbase} = V_{avg} = 3\frac{\sqrt{2}}{\pi} V_{rated} \quad (25)$$

$$I_{dbase} = \frac{P_{out}}{V_{dbase}} = \frac{\pi}{\sqrt{6}} I_{rated} \quad (26)$$

$$Z_{dbase} = \frac{V_{dbase}}{I_{dbase}} \quad (27)$$

Table III shows the per unit representation of the filter design data. The per-unit representation can be applied to any CS PWM converter system which has the same average switching frequency and same modulation index.

TABLE III
PER UNIT REPRESENTATION OF THE DC FILTER.

ω_c[rad/s]	400
ζ	1.0
x_{Lr}[p.u]	1.378
y_{Cr}[p.u]	0.645
r_d[p.u]	0.731
y_{Cd}[p.u]	10.313

C. Simulation Results

Fig.3 shows simulation results. Fig.3(a) shows the waveform of the converter output voltage. The ripple factor of the DC output voltage RF_{vdc} is about 48[%]. Fig.3(b) shows the waveform of the magnet current. The ripple factor of the magnet current RF_{io} is about 9.5[ppm]. Fig.4(c) shows the harmonic ripple current

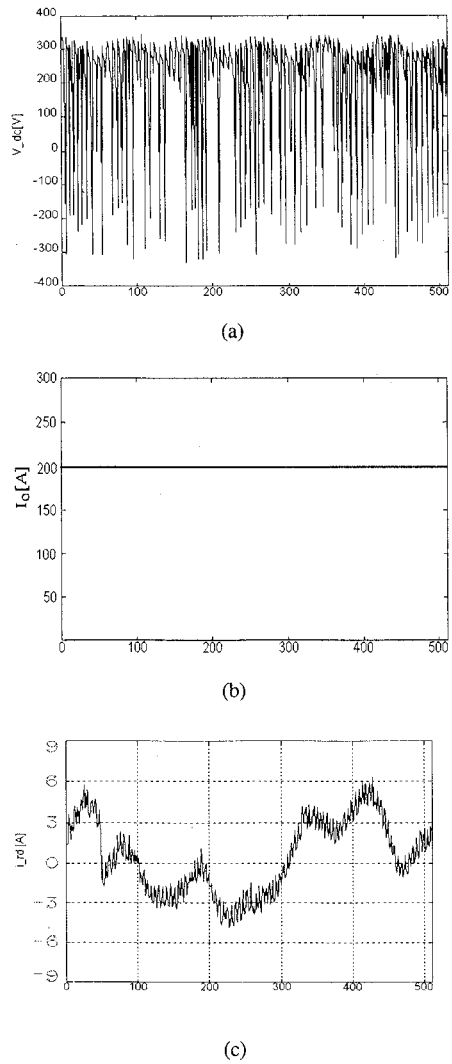


Fig.3. Simulation results; (a) waveform of the converter output DC voltage V_{dc}, (b) waveform of the load DC current I_o, (c) waveform of the ripple current flows into the damping resistor I_{Rd}.

which flows into the filter damping resistor of the DC filter. The peak value of the ripple current is under 3[%] of the average DC load current.

IV. EXPERIMENTAL RESULTS

A. Specification Of Pilot System

The power rating of the pilot system is 1[kVA] which is 60 times smaller than that of the simulation model. Eventhough, the same filter design data represented with the perunit system are applied to the pilot system to verify the theory. Table IV shows the specification of the pilot system. Table V shows the filter design data for the pilot system according to the per-unit system.

TABLE IV
SPECIFICATION OF THE PILOT SYSTEM.

AC input condition	No. of phases	3
	Frequency[Hz]	60
	Rated voltage[V]	220
	Rated power[kVA]	1.0
DC output condition	Output voltage[V]	50~250
	Output current[A]	1.0~3.3
Magnet Load	Inductance[mH]	1289.5
	Resistance[Ω]	64.48
	Time constant[ms]	20

TABLE V
FILTER DESIGN DATA FOR THE PILOT SYSTEM.

ω_c[rad/s]	400
ζ	1.0
L_r[mH]	322
C_r[μF]	20
R_d[Ω]	64.48
C_d[μF]	310

B. Experimental Results

Fig.4 shows the experimental results. The experimental wave forms closely coincide with the simulated wave forms which have 60 times larger power rating. This means that the filter design data represented with the per unit system can be applied to any power rated system. The peak value of the ripple current which flows into the filter damping resistor is under 4[%] of the average magnet load current. This also closely coincides with the simulated result.

Fig.4(c) shows the transient response of the AC/DC currents when the reference value of the load current was changed from about 30[%] to about 90[%]. The load current is perfectly damped and completely settled within 100[ms].

VI. CONCLUSION

A DC filter design of magnet power supply systems which require high power and high precision current control was studied. Analyzing the transfer functions of the DC filters with magnets provided simple and systematic filter design algorithm which satisfies both requirements of the filtering and controling performances. The filter design data were represented by a per-unit system so that they can be easily applied to any power rated system. The design algorithm is expanded to the applications of SMES systems.

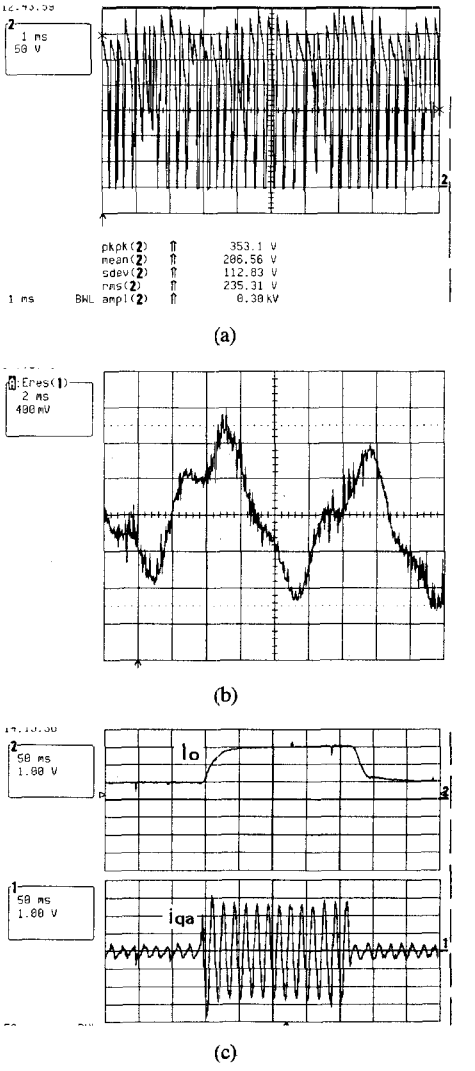


Fig.4. Experimental results; (a) waveform of the converter output DC voltage V_{dc}(50V/div, 1ms/div), (b) waveform of the ripple current flows into the damping resistor I_{Rd}(0.05A/div, 2ms/div), (c) waveforms of the load current I_o(1A/div, 50ms/div) and the converter input current i_{qa}(1A/div, 50ms/div) in a transient state.

ACKNOWLEDGMENT

This paper was supported (in part) by NON DIRECTED RESEARCH FUND, Korea Research Foundation, 1996.

REFERENCES

[1] H. Jin, "Low ripple ac/dc one quadrant switch mode magnet power supply," *Ph.D. Thesis, University of Toronto, 1991.*

[2] D. Ciscato, L. Malesani, L. Storari, L. Rossetto, P. Tenti, G.

L. Basile, and F. Voelker, "Optimum Control of PWM Rectifiers for Magnet Supply," *EPE Firenze*'91, vol. 2, pp. 89-93, 1991.

[3] D. Ciscato, L. Malesani, L. Rossetto, P. Tenti, G. L. Basile, M. Pasti, and F. Voelker, "PWM Rectifier with Low DC Voltage Ripple for Magnet Supply," *IEEE Trans. on IA*, vol. 28, no. 2, pp. 414-420, Mar./Apr. 1992.

[4] D. Xu, J. Baba, E. Masada, H. Ohsaki, "GTO PWM Current Converter Array For Superconducting Magnetic Energy Storage," *Japan Industry Applications Society Conference(JIASC)'96 E.38-E.43, 1996.*

[5] N. R. Zargari, G. Joos, "A Current-Controlled Current Source Type Unity Power Factor PWM Rectifier," *IEEE/IAS'93*, pp. 793-799, 1993.

[6] N. R. Zargari, G. Joos, and P. D. Ziogas, "Input Filter Design for PWM Current-Source Rectifiers," *Proceedings of APEC'93*, pp. 824-830, 1993.

[7] H. Chikaraishi, S. Yamada, S. Tanahashi, S. Kitagawa, T. Satow, J. Yamamoto, O. Motojima, T. Satoh and H. Niwa, "DC Power Systems for Superconducting Magnets of LHD," *IPEC'95-Yokohama*, pp. 904-909, 1995.

[8] H. S. Kim, " Modelling and Design of Magnet Power Supply System using CS PWM Converter," *Ph.D. dissertation, Chung-buk National University*, Korea, Feb. 1995.

Electric Load Controlled by Computer Simulator having Power Regeneration Ability

Itaru Ando, *member, IEEE*, Isao Takahashi, *fellow, IEEE*
Nagaoka University of Technology
1603-1 Kamitomioka Nagaoka 940-21, JAPAN
FAX:+81-258-47-9500, phone:+81-258-47-9515
E-mail : andoh@vos.nagaokaut.ac.jp

Yuichi Tanaka, Mitsuo Ikehara
Tsuken Electric Co., Ltd.
301 21st Century Research Center
2-1-40 Takamori Izumi-ku Sendai 981-32, JAPAN
FAX:+81-22-374-3238, Phone:+81-22-374-3301

Abstract — **This paper describes on the newly developed electric load having a real time computer simulator and power regeneration ability. This electric load can be utilized the various load-test equipment for the inverter and the converter. The developed single phase load has following ability.**

(1) It has the isolated power regeneration ability, and realizes small size and light weight because of high efficiency.

(2) By compensating the input current waveform of the test equipment using active filter ability of the electric load, the unity power factor and the sinusoidal input current of the total system can be achieved.

(3) It can simulate various type of loads such as R-L, R-C or rectifier circuits, and changing their circuit device values by real time simulator of the personal computer.

As a experimental result, it is possible to obtain excellent simulation of loads including rapid load fluctuations and rush currents.

I . INTRODUCTION

According to development of the material techniques, a resistance, a reactor and a capacitor become small size and high performances. But, the large capacity resistances are not so low price. The factories have the power source capacity over than the usual power because of the large capacity testing of the equipment.

By the way, developing high speed switching devices, it become possible to realize various electronic impedance devices whose characteristics are electronically variable by controlling current and voltage with high speed. [1][2][3][4][5]

However, a conventional electric load equipment does not use of the power effectively because the input power is usually consumed in resistances inside the equipment.

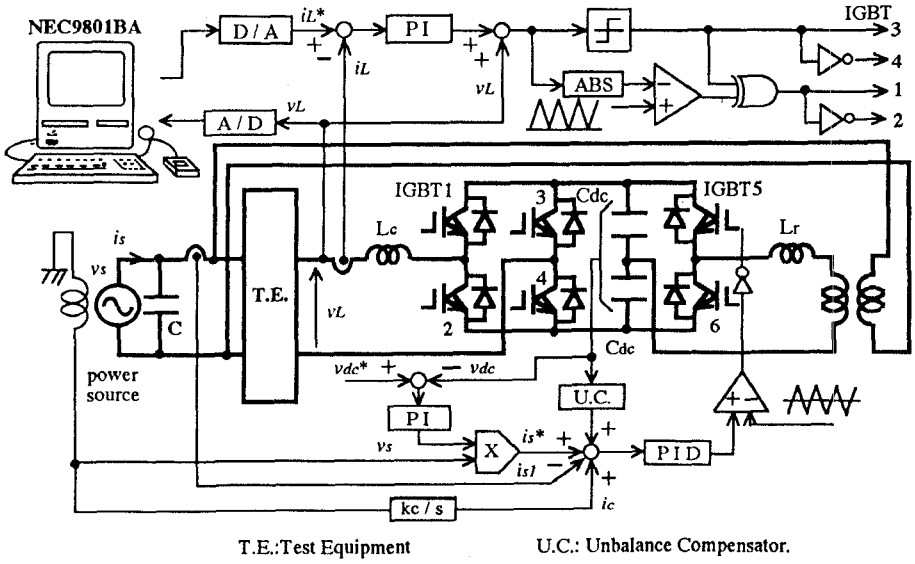
This paper describes on the newly developed electric load having computer simulators and power regeneration ability. The developed electric load can be employed the various load-test of the inverter and the converter and has following ability.

(1) It realizes small size, light weight and high efficiency.
(2) By using active filter ability, the unity power source power factor can be obtained.
(3) It can simulate to various type loads such as R-L, R-C or rectifiers by real time computer simulator.

II . MAIN AND CONTROL CIRCUITS

The main circuit and its control block diagram of the developed regeneration type electric load is shown in Fig.1.

In this circuit, the left converter has load simulator ability and the right inverter has active power regeneration and source current compensation ability, respectively. The



T.E.:Test Equipment U.C.: Unbalance Compensator.
L=0.6mH,C=50mF,Cdc=4700mF

Fig.1. Main circuit and its control block diagram.

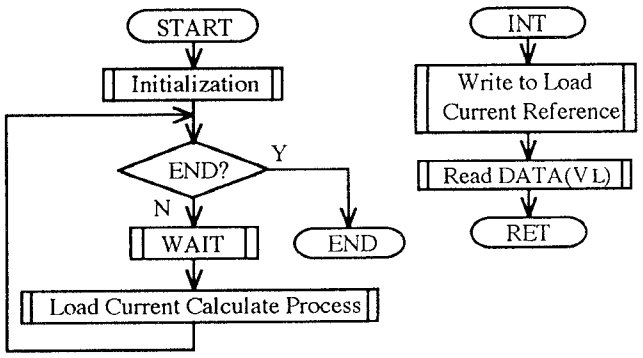
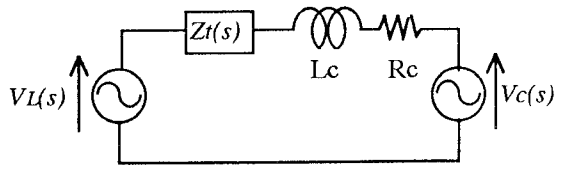


Fig.2. Control flowchart of the load simulator.



Zt(s) : internal impedance of the test equipment
VL(s) : output voltage of the test equipment.
Vc(s) : output voltage of the load system.

Fig.3. Equivalent circuit of the load system.

left converter [IGBT1,2,3,4] has to be constructed by full bridge construction to simulate the various loads included direct current power.

The current of the load is controlled by the high speed follow-up method. The PI compensator controls the only input reactor voltage of the load converter side because the output voltage v_L of the test equipment is added to the output of the PI compensator. The simulated load current reference i_L* is determined using the personal computer in real time by sensing the output voltage v_L of the test equipment.

The right regenerative inverter regenerates the active power to the power source and acts as an active filter to achieve unity power factor and the sinusoidal current of the power source side. The regenerative inverter is also controlled by the current follow-up method to get the above ability. The dc link voltage v_{dc} of this electric load is kept constant by controlling the amplitude of the current reference i_s* on the power source side. As the countermeasure of low input power factor at light load simulating by the filter capacitor C, the compensating current i_c of the capacitor current has to be added to the current reference i_s*.

Fig.2 shows the control flowchart of the load simulator by the personal computer (NEC9801BA, CPU:80486DX2, 40/20MHz). The load simulator can be selected from various menus of loads such as R-L, R-C and the capacitor input rectifier load circuits, etc. The computer can sample the output voltage of the test equipment in every 200μs. The each simulated device values are only input by the keyboard. The simulated load current reference i_L* is output in real time to the D/A converter (12bit, 3ms) by

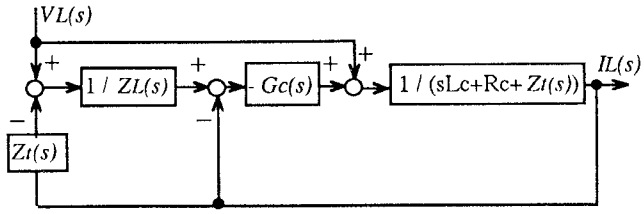
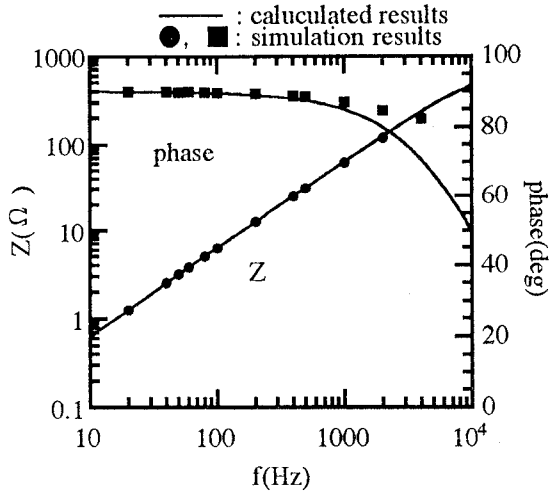
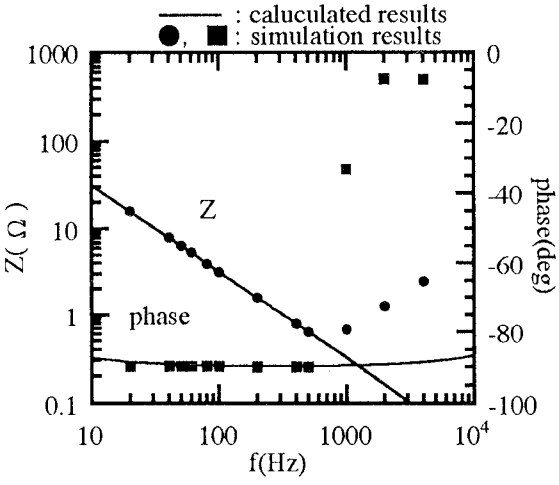


Fig.4. Control block diagram of the load system.



(a) Simulation results of L (10mH).



(b) Simulation results of C (500μF).

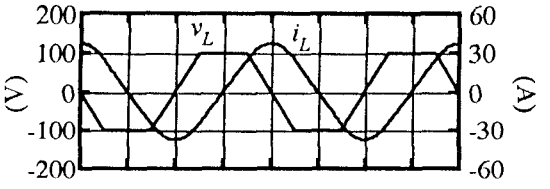
Fig.5. Frequency characteristics on the load system.

solving the load circuit differential equation using the Runge-Kutta-Gill method.

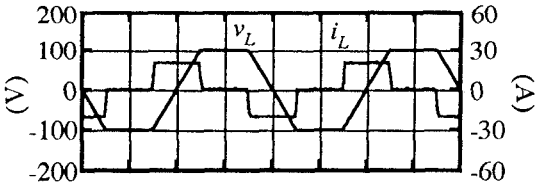
Ⅲ . ANALYSIS OF ELECTRIC LOAD RESPONSE

(a) Response of the electric load system.

Fig.3 and Fig.4 show a equivalent circuit of the Electric load system and its control block diagram, respectively. The trial impedance *Z(s)* is given by the equation (1).



(a) case of L (10mH).



(a) case of C (500μF).

Fig.6. Simulation rezults in the case of the trapezoidal voltage v_L.

$$Z(s)=\frac{V_L(s)}{I_L(s)}=\frac{Z_L(s)(sL_c+R_c-G_c(s))}{Z_L(s)-G_c(s)} \quad (1)$$

Where, $G_c(s)$ and $Z_L(s)$ are the transfer function of the PI compensator and the simulated load impedance, respectively. It can realize to the desired load on high gain $G_c(s)$ because of the equation (1) is expanded $Z(s) = Z_L(s)$.

Fig.5 shows the frequency characteristics of $Z(s)$ when L (10mH) and C (500mF) are simulated on this load converter. The simulation results differ over 1kHz from the theory of this main circuit and the control gain as shown in Fig.4. Because, the current exceeds the permissible range of current control in this converter and carrier frequency of 16kHz. It shows that this is adequately effective as a load simulator under 1kHz.

Fig.6 shows the simulation results when the test equipment output trapezoidal voltage waveform v_L. It can be realized to good simulation in the case of the voltage waveform v_L included the harmonic components.

(b) Regeneration system

Fig.7 and Fig.8 show the equivalent circuit of the regeneration system and its block diagram, respectively. Where, $Z_a(s)$ and $G_c(s)$ are summarization of the test equipment and the load system and the transfer function of the PID compensator, respectively.

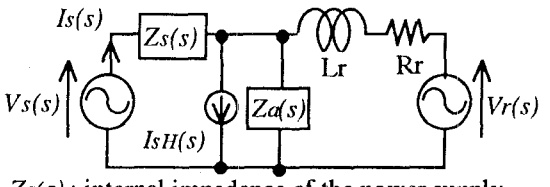
When the dc link capacitor is large enough, the time constant of the dc link voltage variation is enough longer than that of the source current. Therefore, it is notes that the dc link voltage control can be achieved if the source current is controlled in stability.

The current $I_s(s)$ is given by equation (2) from Fig.8.

$$I_s(s)=\frac{Z_a(s)G_c(s)I_s^*(s)+Z_a(s)V_s(s)+Z_r(s)V_s(s)}{Z_a(s)G_c(s)+Z_r(s)Z_a(s)} \quad (2)$$

where, $Z_s(s)$ is assumed 0 and $Z_r(s)$=sL_r+R_r.

It is clear that the source current $I_s(s)$ can be equal its sinusoidal reference $I_s(s)^*$ on high control gain $G_c(s)$ by



$Zs(s)$: internal impedance of the power supply.
$Vr(s)$: output voltage of the regeneration system.
$IsH(s)$: harmonics current source.

Fig.7. Equivalent circuit of the regeneration system.

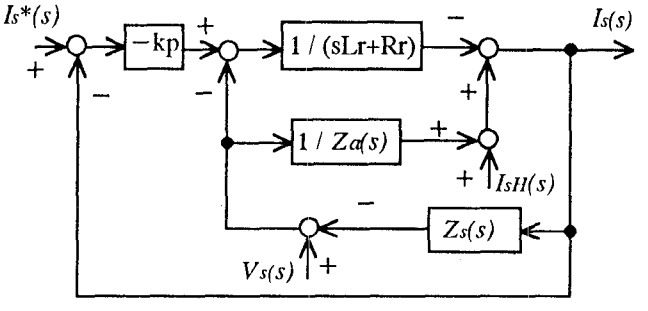


Fig.8. Control block diagram of the regeneration system.

equation (2).

The control transfer function $G_{ref}(s)(=I_s(s)/I_s(s)^*)$, the disturbance transfer function $G_i(s)(=I_s(s)/V_s(s))$ and the harmonic current disturbance transfer function $G_{sH}(s)(=I_s(s)/I_{sH}(s))$ are given by following equations, respectively.

$$G_{ref}(s)=\frac{Z_a(s)G_c(s)}{Z_r(s)(Z_a(s)+Z_s(s))+Z_s(s)Z_a(s)+G_c(s)Z_a(s)} \quad (3)$$

$$G_i(s)=\frac{(Z_a(s)+Z_r(s))\,Z_r(s)}{Z_r(s)\,Z_a(s)\,(Z_r(s)+G_c(s))+(Z_a(s)+Z_r(s))\,Z_r(s)\,Z_s(s)} \quad (4)$$

$$G_{sH}(s)=\frac{Z_r(s)\,Z_a(s)}{Z_a(s)\,(Z_r(s)+G_c(s)+Z_s(s))-Z_r(s)\,Z_s(s)} \quad (5)$$

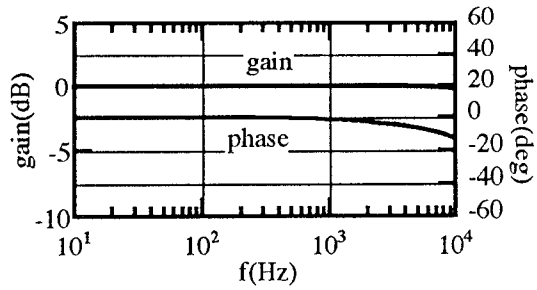
They show that the source current $I_s(s)$ can be followed up to its sinusoidal reference $I_s(s)^*$ on the high gain $G_c(s)$. Because $G_{ref}(s)$=1, $G_i(s)$=0 and $G_{sH}(s)$=0 are given in this case.

Fig.9 shows frequency characteristics of $G_{ref}(s)$, $G_i(s)$ and $G_{sH}(s)$ with $Z_a(s)$=R=50Ω, respectively. It is clear that the effect of the disturbance $V_s(s)$ and $I_{sH}(s)$ can be almost compensated by the system PID compensator under 1kHz. [6][7][8]

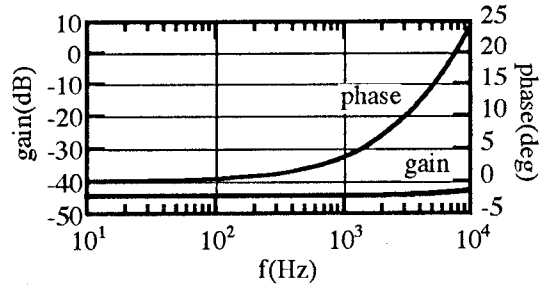
Ⅳ. Experimental Results

The experiment is performed by using following two kinds of 1kVA (100V/50Hz) UPS as the tested equipment having a carrier frequency of 16kHz.

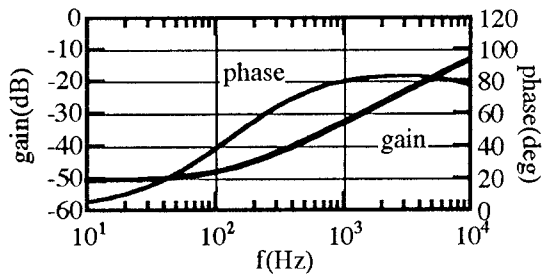
UPS1 : A asynchronous type 1 phase UPS with the capacitor input diode rectifier.



(a) Frequency characteristics of the $G_{ref}(s)$.

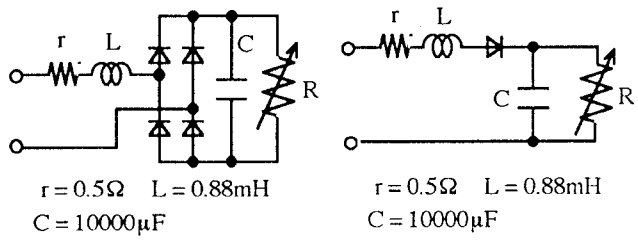


(b) Frequency characteristics of the $G_f(s)$.



(c) Frequency characteristics of the $G_{sH}(s)$.

Fig.9. Frequency characteristics of $G_{ref}(s)$, $G_f(s)$ and $G_{sH}(s)$.



(a) Full-wave rectifier circuit. (b) Half-wave rectifier circuit.

Fig.10. Simulated rectifier load circuits.

UPS2 : A synchronous type 1 phase UPS with the sinusoidal PWM converter.

Fig.10 shows the two types of simulated rectifier loads.

Fig.11 shows the steady state characteristics of the electric load simulator of the resistance R simulating in case of UPS1. The power factor on the power source side is achieved 99% in over 0.5kW load. The dc link voltage V_{dc} is kept constant and its regulation is also obtained within 1%.

Regenerative power W_r and total efficiency η with R simulating with UPS2 are shown in Fig.12. The regenerative power W_r is linearly increased and the total efficiency η from load converter to regenerative inverter included

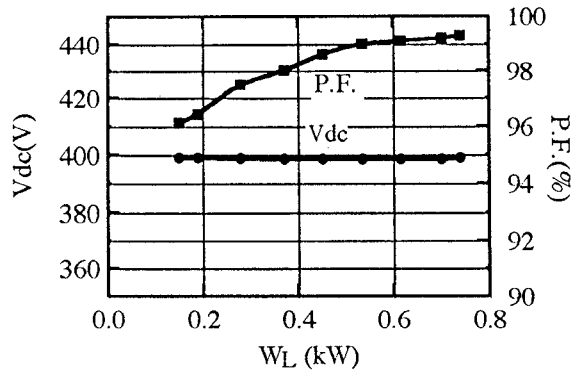


Fig.11. Steady state characteristics of the electric load simulator of the resistance R.

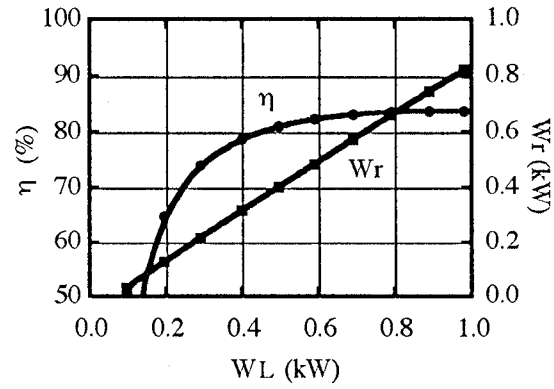


Fig.12. Regenerative power Wr and total efficiency η characteristics.

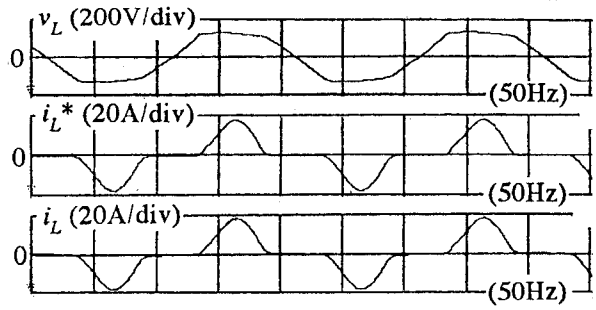


Fig.13. Waveforms of load current reference i_L* and load current i_L.

isolation transformer has achieved over 80% over 0.5kW load. Because the efficiency of the isolation transformer is about 95%, the result is not so bad.

Fig.13 and 14 show the waveforms of various parts on the capacitor input rectifier load (load power factor of 80%) and a R-L series load with UPS1. The good simulation results for these loads are also obtained. The input power factor P.F. on the power source side becomes over 99%. And total harmonic distortion THD of the power source current i_s is obtained 3.3%.

Fig.15 shows the load power factor variation characteristics using UPS1 in which the R-L and R-C loads is simulated with the current i_L fixed at 9Arms . The input power factor P.F. on the power source side is exceeded

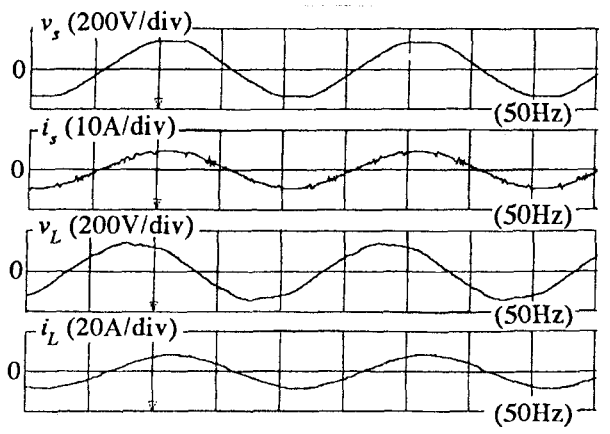
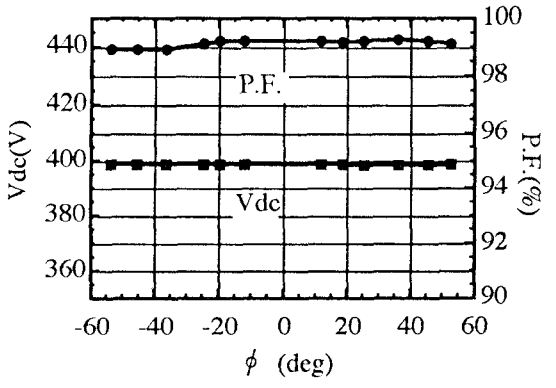
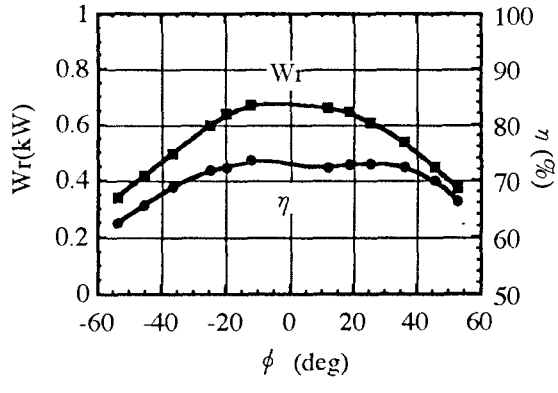


Fig.14. Waveforms of various parts with R-L load.



(a) Power factor P.F. of the power source side and the dc link voltage Vdc of the electric load simulator.



(b) Regenerative power Wr and the total electric load efficiency η.

Fig.15. Load power factor variation characteristics.

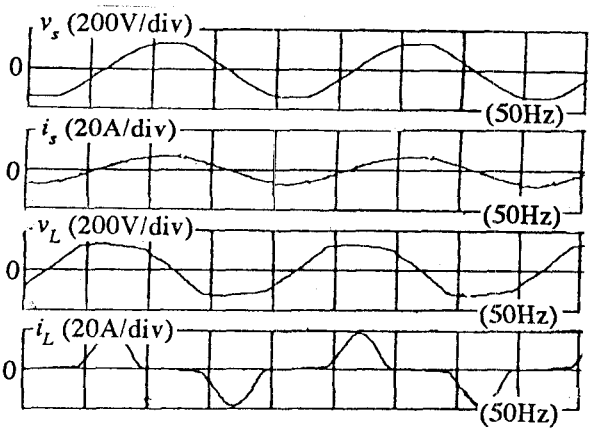


Fig.16. Waveforms of various parts with rectifier load

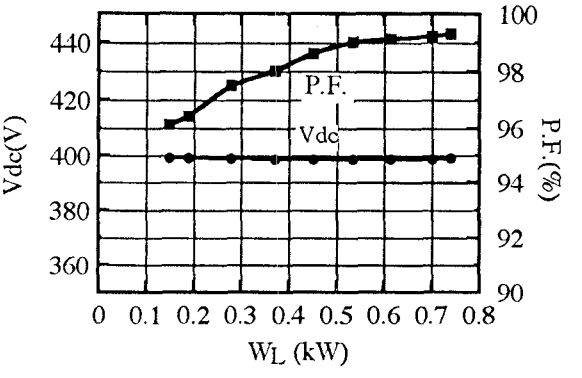


Fig.17. Steady state characteristics of the electric load simulator with rectifier load.

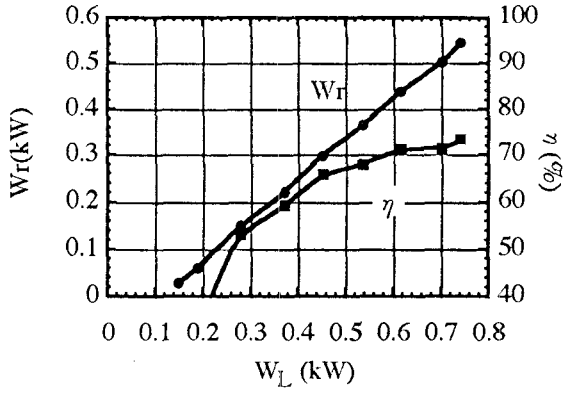


Fig.18. Regenerative power Wr and the total efficiency η of the electric load simulator with rectifier load.

99%, total efficiency η from load converter to regenerative inverter included isolation transformer reaches about 70%.

Fig.16 and Fig.17 show the waveforms of UPS1 of the various parts and the steady state basic characteristics during the full-wave type capacitor input rectifier load variation (load power factor of over 60%).

The regenerative power W_r and efficiency characteristics η are shown in Fig.18. The input power factor P.F. is over 99% and the total efficiency η from load converter to regenerative inverter included isolation transformer has achieved over 70% over 0.6kW load.

Sometimes, the voltage of the every dc link capacitor becomes unbalance by the direct current simulating or the control offset and the its drift. Fig.19 shows the simple unbalance compensator of the every dc link capacitor voltage. The unbalance voltage is detected by photo couplers. And the unbalance compensation is achieved by adding the appropriate offset voltage to the source current reference i_s^*.

Fig.20 shows the waveforms on the half-wave rectifier

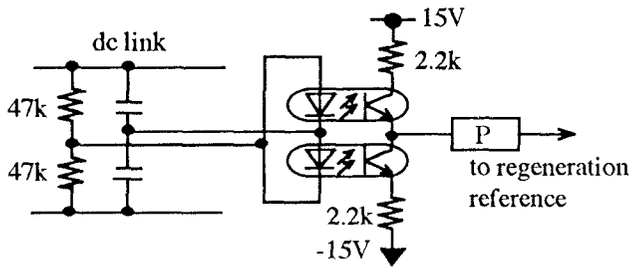


Fig.19. Unbalance compensator of the dc link capacitor voltage.

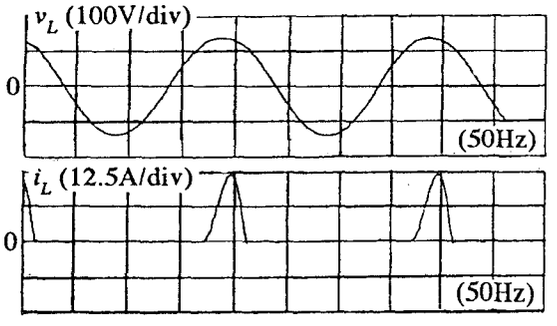


Fig.20. Waveforms of the load voltage and current on the half-wave rectifier simulating.

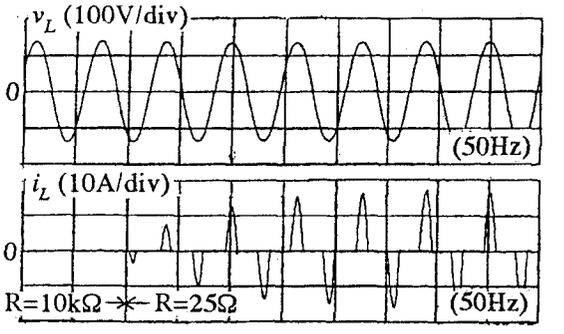


Fig.21. Transisent waveforms with changing load resistance.

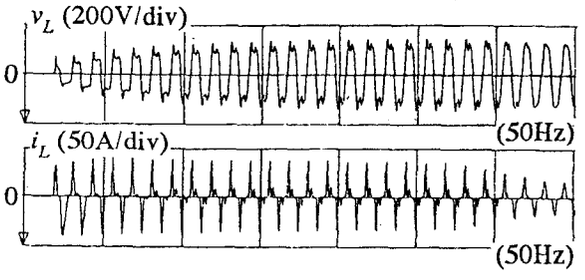


Fig.22. Transient waveforms on rectifier load simulating with adding the UPS output voltage

load simulating with UPS2. Its simulated result is excellent and the every dc link capacitor voltage difference is controlled under 2V by the unbalance compensator.

Fig.21 and Fig.22 show the transient state of the tested UPS2 and UPS1 output waveforms having the developed load equipment simulated the rectifier load, respectively. It is clear that electric load can simulate the desired load even on load sudden change. Although the UPS1 output voltage drops at the rush current of the rectifier load, it may be noted that the good characteristic of the electric load simulator is obtained even at transient states.

V . Conclusion

This paper describes on attempting the trial production of the electric load controlled by computer simulator having power regeneration ability, and developing the real time simulator program of the various loads.

As the results, it is not only possible to obtain excellent simulation of various loads including rapid load fluctuations and rush currents but also possible to confirm effectiveness in the case of test equipments including harmonics.

Acknowledgment

The authors would like to express their appreciation to Power Electronics Laboratory members of Nagaoka University of Technology.

References

[1] I.Takahashi, "Variable Impedance, Voltage and Current Source using Switching Devices" *Proceedings of the Joint Conference of Hokuriku Chapters of Institutes of Elec. Engrs.*, Japan , A-54, 1987

[2] S.Singer, "Realization of Loss-Free Resistive Elements" *IEEE Trans. CAS*, 37, No1, 1990

[3] M.Takeuchi, H.Nakano and I.Takahashi,"Variable Electric Impedance Equipment using Switching Devices" *Proceedings of the Joint Conference of Hokuriku Chapters of Institutes of Elec. Engrs.*, Japan , A-58, 1987

[4] H.Funato and A.Kawamura, "Active-passive Power Circuit" *IEEJ Trans. on IAS*, Japan, vol.113-D, 1993

[5] H.Funato and A.Kawamura, "Variable Active-Passive Reactance for Power Circuit without DC voltage Source" *IEEJ Trans. on IAS*, Japan, vol.114-D, 1994

[6] I.Ando, I.Takahashi, Y.Tanaka and M.Ikehara, "Development of Electric Load Controlled by Computer Simulator having Power Regeneration Ability" *IEEJ Techcical committee of Semiconductor-Power Converter*, Japan, SPC-95-119, 1995

[7] I.Ando, I.Takahashi, Y.Tanaka and M.Ikehara, "Development of a Variable Electric load System with Power Regenerative Ability using Load Simulator by a Personal Computer" *IEEJ National Convention Record*, Japan, No.802, 1996

[8] I.Ando, I.Takahashi, Y.Tanaka and M.Ikehara, "Development of a Computer Controlled Electric Load having Power Regeneration Ability" *IEEJ National Convention Record-IAS*, Japan, No.80, 1996

New NPC Multi-Level Four-Quadrant DC-DC Converter Controlled by the Integrated-Voltage-Control Method.

Hideyuki Okui
(Osaka Polytechnic College)
1778_Inaba-cho, Kishiwada, Osaka, 596-01_JAPAN
[Phone] 0724-89-2121, [Fax] 0724-79-1751
[E-mail] okui@osaka-pc.ac.jp

Hisaichi Irie
(Osaka Electro-Communication University)
18-8_Hatsu-cho, Neyagawa, Osaka, 572_JAPAN
[Phone/Fax] 0720-25-4675
[E-mail] irie@isc.osakac.ac.jp

Abstract : **A switching mode DC-DC Converter controlled by the Integrated-Voltage-Control Method works stablely and has no steady state error and a quick response time. We propose a new NPC (Neutral-Point-Clamped) Multi-Level Four-Quadrant DC-DC Converter controlled by the Integrated-Voltage-Control Method. It consists of eight hysteresis comparators driven by an error voltage integrator. The working region is divided into eight regions and one of eight power transistors driven by one of eight comparators to on/off in each prearranged region. The Neutral-point voltage can also be kept at a constant value by a new restrain control scheme.**

I · Introduction

In recent years, the NPC (Neutral-Point-Clamped) Multi-Level Inverter has been developed and applied to a high voltage inverter which drives the motor for a steel rolling-mill machine or for an electric train etc. The NPC Inverter has some advantages : a higher output voltage can be obtained for the same device ratings; less harmonics are contained in the output for the same switching frequency than ordinary inverters. However, the conventional NPC Inverter has the following two large problems. The control characteristics are discontinuous among operating voltage levels especially with GTOs which need minimum on-time and minimum off-time. The Neutral-point voltage obtained by a voltage divider with two capacitors tends to fluctuate, especially for very low frequency single or DC to DC conversion.

In this paper, we propose a new NPC Multi-Level Four-Quadrant DC-DC Converter controlled by the Integrated-Voltage-Control method. It is developed from the Four-Quadrant DC-DC Converter which we have already proposed [2]. It can operate as an inverter with a sinusoidal signal.

The driving circuit of the new NPC Converter has prearranged eight hysteresis comparators driven in parallel by an error voltage integrator. The operation of the new NPC Converter is divided into four quadrants and eight regions. In each region, one of eight hysteresis comparators is active and drives regularly one of eight power transistors to on/off. As one error voltage integrator is used, the discontinuous distortion of control characteristics among regions are prevented. The Neutral-point voltage is kept at a constant value

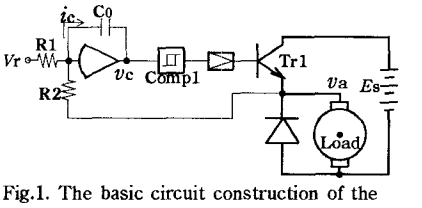


Fig.1. The basic circuit construction of the Integrated-Voltage-Control method.

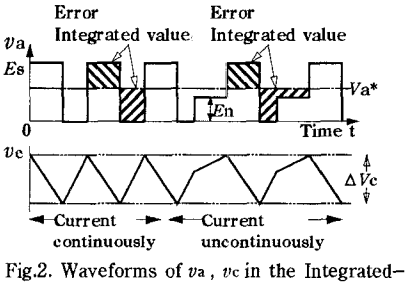


Fig.2. Waveforms of v_a, v_c in the Integrated-Voltage-Control method.
(ΔV_c = Hysteresis width of Compl)

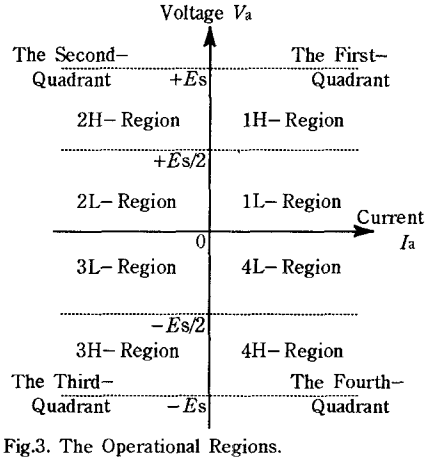


Fig.3. The Operational Regions.

by a new control scheme proposed in this paper. The minimum on-time and minimum off-time are ensured in this new NPC Converter without control error.

It is also described in this paper that operations and characteristics of this new NPC Converter are confirmed experimentally.

II · The Integrated-Voltage-Control Method

The basic circuit of the Integrated-Voltage-Control method is shown in Fig.1 and the waveforms are shown in Fig.2. A hysteresis comparator Comp1 has a hysteresis width ΔV_c which is the voltage difference between the lower and the upper thresholds. The voltage v_c represents the integrated value of the error voltage between the instantaneous output voltage v_a and the setting output voltage V_a^*. IF Tr1 is in an on-state and v_a is higher than V_a^*, v_c decreases and reaches the lower threshold of Comp1, then Comp1 drives Tr1 to an off-state. When Tr1 is an off-state and v_a is less than V_a^*, v_c increases and reaches the upper threshold, then Comp1 drives Tr1 to an on-state. Thus the voltage v_c shuttles between two thresholds of Comp1 and Tr1 repeats switching to turn-on and turn-off.

As shown in Fig.2, the positive error integrated value for the area drawn by the error voltage $v_a - V_a^*$ is always equal to the negative error integrated value in each cycle. Consequently, the average output voltage V_a is always controlled equal to V_a^* independent of any current continuous/uncontinuous condition, the fluctuation of the power supply voltage, the voltage drop and the delay time of the power transistor etc.

III · The Circuit Constitution and The Operation Principle of The New NPC Converter

The circuit constitution of the new NPC Multi-Level Four-Quadrant DC-DC Converter controlled by the Integrated-Voltage-Control method is shown in Fig.4. There are eight power transistors Tr1 ~ Tr8 and twelve diodes D1 ~ D8, DC1 ~ DC4 in the main circuit, they are arranged into a general NPC type bridge-circuit. DC power supply E_s is divided into two $E_s/2$s by two capacitors C1 and C2 which have the same capacity. The control circuit of this new NPC Converter is divided into a block for the output voltage control circuit and a block for the Neutral-point voltage fluctuation restraint circuit.

The block for the output voltage control circuit is composed of a feedback loop for the instantaneous output voltage v_a, one integrator and eight hysteresis comparators Comp1 ~ Comp8. The Comp1 ~ Comp8 drive eight transistors Tr1 ~ Tr8 regularly. The order of threshold voltage levels of the Comp1 ~ Comp8 are arranged by voltage Er1 ~ Er8. Voltage Er1' ~ Er8' are prearranged voltage for Er1 ~ Er8.

Two FlipFlop circuits in the driving circuits for Tr2-Tr3 or Tr6-Tr7 prevent all transistors from making a short circuit even in a starting transient state.

The block for the Neutral-point voltage fluctuation restraint control circuit is composed of a comparator CompN which compares the Neutral-point voltage v_N with voltage $E_s/2$, and decides set or reset of a D-FlipFlop. The output signal Q and $-Q$ of the D-F.F. are added to Er1' ~ Er8' and Er1 ~ Er8 are rearranged as set or reset of the D-F.F. The voltage v_N is controlled by changing the arrangement of Er1 ~ Er8 in the new NPC Converter.

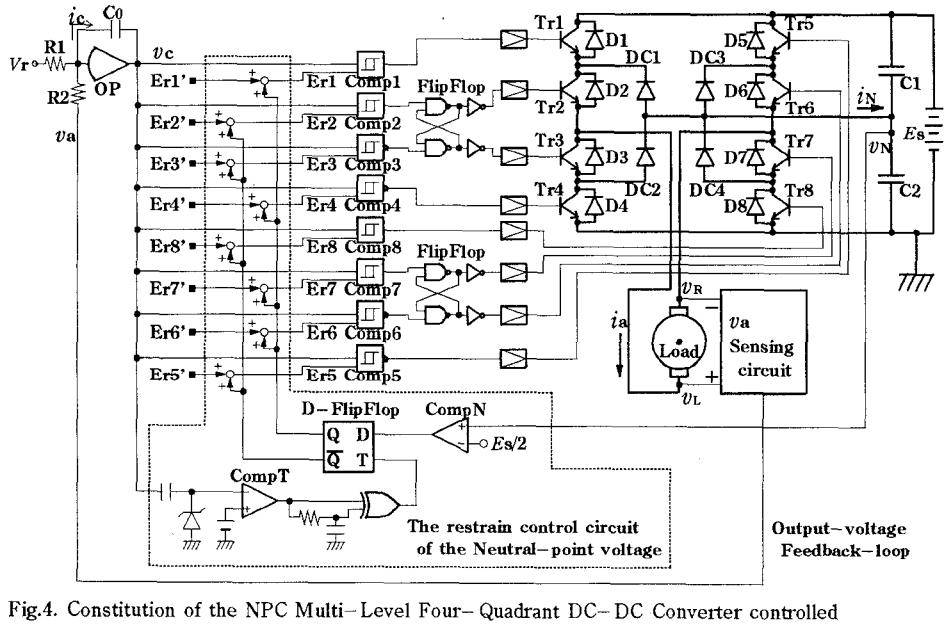


Fig.4. Constitution of the NPC Multi-Level Four-Quadrant DC-DC Converter controlled by the Integrated-Voltage-Control method.

Table1. Switching pattern table of the eight Regions.

Region		Load Current v_L	i_a	v_R	Output Voltage v_a	Power–Transistor 1 2 3 4	5 6 7 8	N–point Voltage v_N
1H	(b)	++	→	0	++	●●	●○	↗
		++	→	+	+	●●	●■	
	(a)	++	→	0	++	○●	●●	↘
		+	→	0	+	■●	●●	
1L		++	→	+	+	●●	○●	↗
		++	→	++	0	●●	△■	
	(b)	++	→	+	+	○●	●●	↗
		+	→	+	0	■●	●●	
	(a)	+	→	0	+	●●	●○	↘
		+	→	+	0	●●	●■	
		+	→	0	+	○●	●●	↘
		0	→	0	0	■△△	●●	
2H	(a)	++	←	+	+	△△	●●	↘
		++	←	0	++	△△	■△△	
	(b)	+	←	0	+	●●	△△	↗
		++	←	0	++	△△■	△△	
2L		++	←	++	0	△△	○●	↘
		++	←	+	+	△△	■●	
	(a)	+	←	+	0	●○	●●	↘
		++	←	+	+	△■	●●	
	(b)	+	←	+	0	●●	○●	↘
		+	←	0	+	●●	■△△	
		0	←	0	0	●○	△△	↗
		+	←	0	+	●■	△△	
3H	(b)	0	←	++	−−	●○	●●	↗
		+	←	++	−	●■	●●	
	(a)	0	←	++	−−	●●	○●	↘
		0	←	+	−	●●	■●	
3L		+	←	++	−	●○	●●	↗
		++	←	++	0	△■	●●	
	(b)	+	←	++	−	●●	○●	↗
		+	←	+	0	●●	■●	
	(a)	0	←	+	−	●○	●●	↘
		+	←	+	0	●■	●●	
		0	←	+	−	●●	○●	↘
		0	←	0	0	●●	■△△	
4H	(a)	+	→	++	−	○●	△△	↘
		0	→	++	−−	■△△	△△	
	(b)	0	→	+	−	△△	○●	↗
		0	→	++	−−	△△	△■	
4L		++	→	++	0	○●	△△	↘
		+	→	++	−	■●	△△	
	(a)	+	→	+	0	●○	●●	↗
		+	→	++	−	●■	△△	
	(b)	+	→	+	0	○●	●●	↘
		0	→	+	−	■△△	●●	
		0	→	0	0	△△	●○	↗
		0	→	+	−	△△	●■	

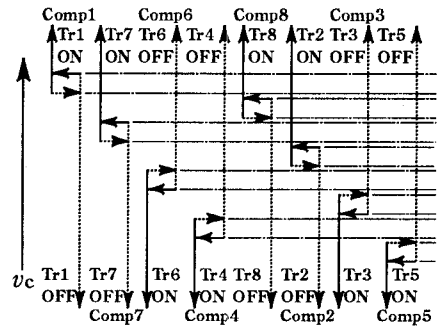
【 Note 】

v_L : Left–side Voltage of the Load.
v_R : Right–side Voltage of the Load.
(a)_mark : Switching_Pattern taken by the Table2(a).
(b)_mark : Switching_Pattern taken by the Table2(b).
++ : $+E_s$, + : $+E_s/2$
−− : $-E_s$, − : $-E_s/2$
↘ : v_N decreasing.
↗ : v_N increasing.
△ : Conducting through the anti–paralleled Diode.
● : ON–state.
| : OFF–state.
■ : Switching Now.
■ : ↑

Table2. Switching pattern arrangement table.

(a) In the case of Decreasing of the Neutral–point Voltage.

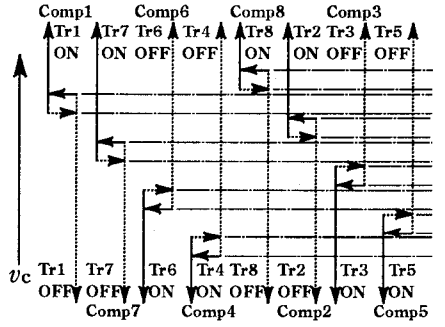
Region	Load Current v_L	i_a	v_R	Output Voltage v_a	Power–Transistor 1 7 8 2	6 4 3 5	N–point Voltage v_N
1H	++	→	0	++	○●●●		↘
	+	→	0	+	■●●●		
1L	+	→	0	+	○●●●		↘
	+	→	+	0	■●●●		
4L	+	→	+	0	○●●●		↘
	+	→	++	−	■●●●	△ △	
4H	+	→	++	−	○●●●	△ △	↘
	0	→	++	−−	■●●●	△△△△	
2H	++	←	0	++	△△△△	■●●●	↘
	++	←	+	+	△ △	○●●●	
2L	++	←	+	+	△ △	●■●●	↘
	+	←	+	0	●●●●		
3L	+	←	+	0	●●●●		↘
	0	←	+	−	●●●●		
3H	0	←	+	−	●●●●		↘
	0	←	++	−−	●●●●		



Changing by comparing voltage v_N and voltage $E_s/2$

(b) In the case of Increasing of the Neutral–point Voltage.

Region	Load Current v_L	i_a	v_R	Output Voltage v_a	Power–Transistor 1 7 8 2	6 4 3 5	N–point Voltage v_N
1H	++	→	0	++	○●●●		↗
	++	→	+	+	■●●●		
1L	++	→	+	+	○●●●		↗
	+	→	+	0	■●●●		
4L	+	→	+	0	○●●●		↗
	0	→	+	−	■●●●	△ △	
4H	0	→	+	−	○●●●	△ △	↗
	0	→	++	−−	■●●●	△△△△	
2H	++	←	0	++	△△△△	■●●●	↗
	+	←	0	+	△ △	○●●●	
2L	+	←	0	+	△ △	●■●●	↗
	+	←	+	0	●●●●		
3L	+	←	+	0	●●●●		↗
	+	←	++	−	●●●●		
3H	+	←	++	−	●●●●		↗
	0	←	++	−−	●●●●		



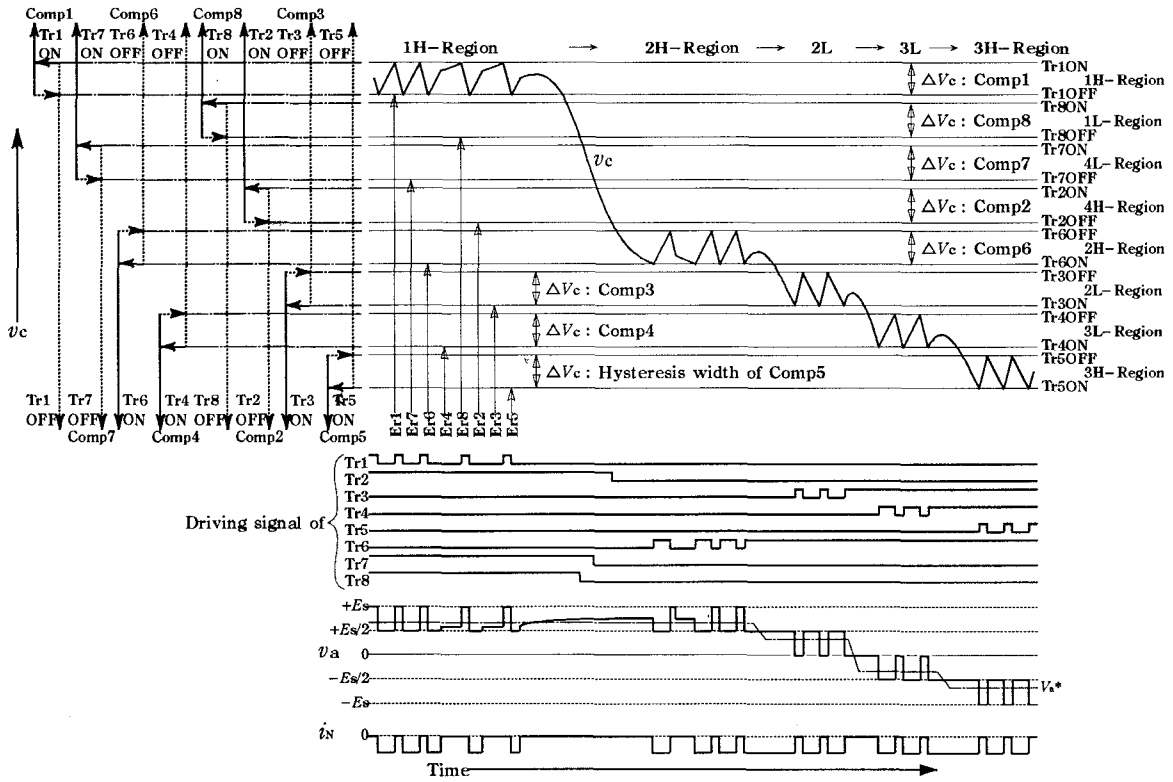


Fig.5(a). Waveforms of v_C , v_a , i_N and driving signals of eight transistors. (Decreasing the Neutral−point voltage v_N .)

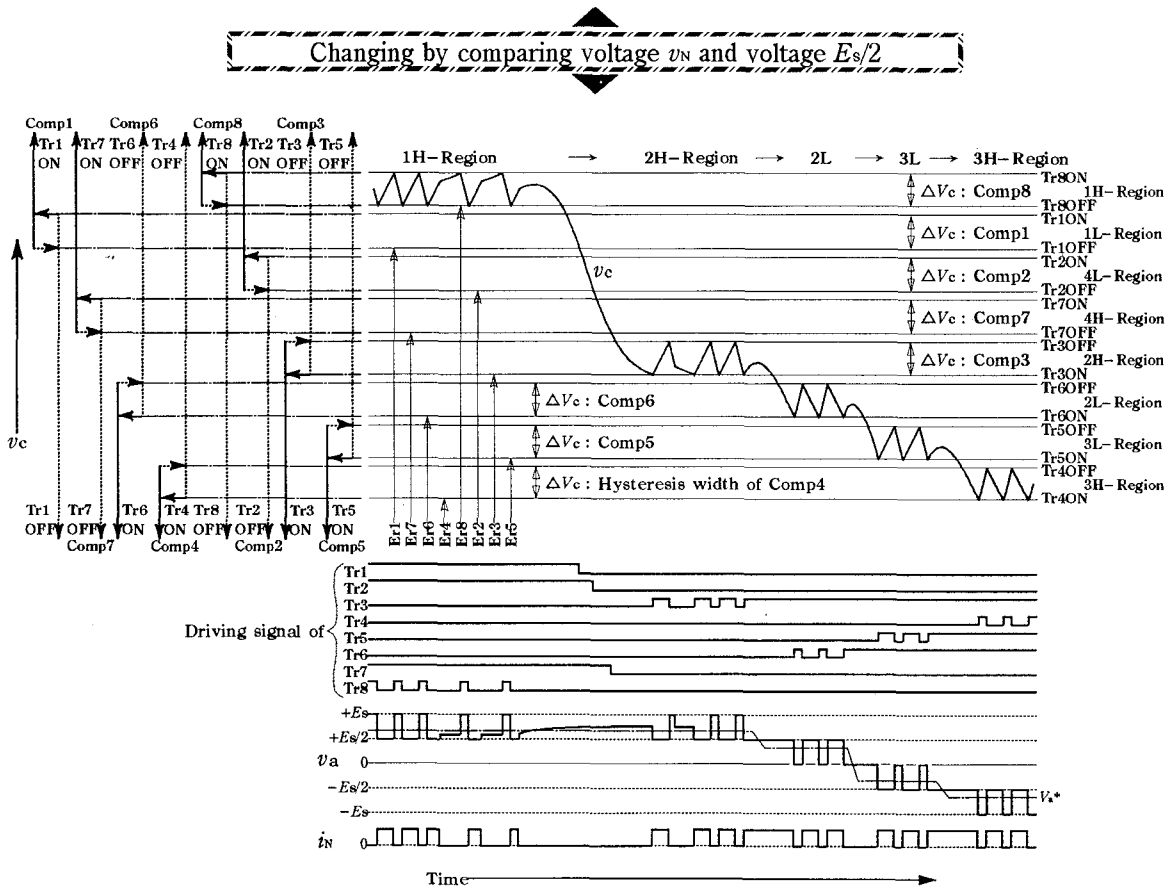


Fig.5(b). Waveforms of v_C , v_a , i_N and driving signals of eight transistors. (Increasing the Neutral−point voltage v_N .)

The classification of the eight operational regions in this new NPC Converter is shown in Fig.3. The current is assigned to a horizontal axis and the voltage is assigned to a vertical axis. A plane shown in Fig.3 is divided into a total of four quadrants which are from the First-Quadrant to the Fourth-Quadrant by the current and voltage axes. Beside this, the plane is divided into a total of eight operational regions by dividing each quadrant into two stages which are a high voltage and a low voltage stage.

In this paper, these eight operational regions are labeled as follows : the upper region in the First-Quadrant is the "1H-Region" and the lower region is the "1L-Region", in the Second-Quadrant, the "2H-Region" and the "2L-Region", and so on as shown in Fig.3.

All switching patterns of Tr1 ~ Tr8 in each operational region is shown in Table1. Each of the 1H ~ 4H-Regions has two switching patterns and each of the 1L ~ 4L-Regions has four ones. Basically, only one power transistor is switching and the other seven power transistors stay in an on- or off-state in one operational region as shown in Table1.

When the instantaneous output voltage v_a is $+E_s$ or 0 or $-E_s$, the current into the Neutral-point i_N doesn't flow. When v_a is $+E_s/2$ or $-E_s/2$, current i_N flows out from or flows into the Neutral-point, consequently the Neutral-point voltage v_N decreases or increases.

Table2(a) shows v_N decreasing switching patterns in order of the output voltage and the load current direction. Table2(b) shows v_N increasing switching patterns in same order. In the new NPC Converter, thresholds of Comp1 ~ Comp8 or Er1 ~ Er8 are arranged in order of Table2(a) or 2(b) as follows.

(a) arrangement for v_N decreasing.
Er1 > Er8 > Er7 > Er2 > Er6 > Er3 > Er4 > Er5

(b) arrangement for v_N increasing.
Er8 > Er1 > Er2 > Er7 > Er3 > Er6 > Er5 > Er4

Comparing the voltage arrangement (a) and (b), it can be found that there are two groups Group1 and Group2 as follows.

(Er1 Er7 Er6 Er4)-------- Group1
(Er8 Er2 Er3 Er5)-------- Group2

In the new NPC Converter, Group1 and Group2 are shifted by output signals Q and -Q of the D-F.F. inversely, to change the voltage arrangement (a) and (b) according to CompN as shown in Table4.

Decreasing or increasing of the voltage v_N are depended on the arrangement Er1 ~ Er8. The voltage v_N can be controlled by choosing Table2(a) or 2(b) as $v_N > E_s/2$ or $v_N < E_s/2$ at every switching moment. Consequently, the fluctuation of voltage v_N is restrained with no effect upon the block for the output voltage control.

IV • Changing Operation Across Regions

In the new NPC Four-Quadrant DC-DC Converter controlled by the Integrated-Voltage-Control method, an active comparator is chosen automatically among eight comparators according to the operating region only by a voltage feedback. The operating region is depended on the setting voltage V_a^* and the direction of the current which is determined by the difference between V_a^* and counter emf E_n in the load. When the operating point transfers across 1H → 2H → 2L → 3L → 3H-Region, several waveforms are shown in Fig.5(a) for Table2(a) and Fig.5(b) for Table2(b).

In the 1H-Region, the voltage v_c shuttles within the hysteresis width of Comp1, Tr1 is switching and the average output voltage V_a is controlled to be equal to the setting voltage V_a^*. Other transistors Tr2, Tr7 and Tr8 are in the on-state, and Tr3 ~ Tr6 are in the off-state. If the load counter emf E_n increases and the load current i_a becomes discontinuous, then E_n appears on the instantaneous output voltage v_a, the off-time extends, as V_a remains equal to V_a^*.

If voltage E_n becomes larger than V_a^*, the operating point transfer from 1H- to 2H-Region. As voltage v_a is equal to E_n and v_a is larger than V_a^*, voltage v_c decreases even though Tr1 is in the off-state and v_c goes through the lower threshold of Comp1. Voltage v_c also goes through the lower threshold of Comp8, Comp7 and Comp2, then Tr8, Tr7 and Tr2 turn-off, finely v_c reaches the lower threshold voltage of Comp6. When v_c reaches the lower threshold of Comp6, Tr6 turns-on, v_a is clamped $E_s/2$, v_a is less than V_a^*, and v_c changes the inclination to increase. Now, v_c shuttles within the hysteresis width of Comp6, Tr6 is switching and the average output voltage V_a is still controlled equal to V_a^* in the 2H-Region.

If the setting voltage V_a^* moves $E_n > V_a^* \rightarrow E_s/2 \rightarrow 0 \rightarrow -E_s/2 \rightarrow > -E_n$, then the operating point transfers automatically as shown in Fig.5. The only difference between waveforms of Fig.5(a) and Fig.5(b) is the directions of the Neutral-point i_N.

As always only one transistor is switching and always there is zero current interval when the operating point transfers across the vertical axis, the new NPC Converter requires no blanking-time which all of the ordinary NPC Inverters require.

V • The Experimental Results

Oscillograms of the experimental circuit with an R-L load (32 Ω and 87mH) are shown in Fig.6 for sinusoidal setting voltage V_a^* (77.5Hz). The DC source voltage E_s is 50V and the Neutral-point voltage is formed by a voltage divider with two capacitors which have the same capacitance 220 μ F.

A total of five-level voltage switching appears on

the instantaneous output voltage v_a following V_a^* and the average value V_a is always controlled to it. As the phase of the load current i_a is lag behind the voltage, there are eight operating regions in one-cycle as shown in Fig.3. The operating point transfers smoothly across regions.

The Neutral-point current i_N flows during $v_a = \pm E_s/2$ and has the same magnitude as the current i_a. The plus or minus polarity of i_N express the current flows out from or flows into the Neutral-point respectively. The polarity of i_N is determined at every switching moments according as the voltage v_N is lower than E_n or not. Consequently, the fluctuation of v_N is restrained within 7%.

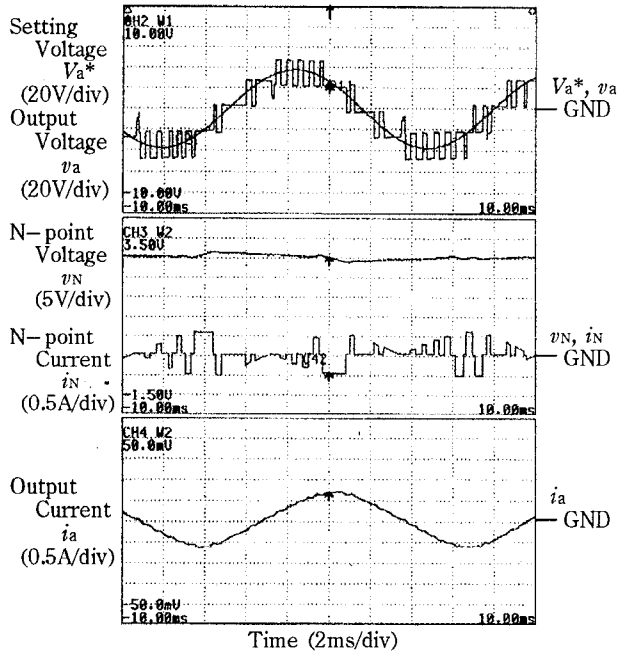


Fig.6. Oscillograph of the experimental circuit.
(E_s = 50V, Frequency f = 77.5Hz)
(R = 32 Ω , L = 87mH, Power_Factor = 0.6)

VI · Conclusion

A new NPC Multi-Level Four-Quadrant DC-DC Converter controlled by the Integrated-Voltage-Control method with eight hysteresis comparators has been presented. A new restraint control technique for the Neutral-point voltage fluctuation has also been presented.

The advantages of the Integrated-Voltage-Control method are as follows.

(1) The control circuit is simple.
(2) The average output voltage is always controlled equal to the setting voltage.
(3) The minimum on-time and the minimum off-time of switching devices are ensured.
(4) The response is very fast.
(5) As one transistor is switching at one time, there is no short-circuit mode at switching without blanking-time.
(6) The addition of the current restriction circuit is easily provided.

Adding to the above, the advantages of the new NPC Multi-Level Four-Quadrant DC-DC Converter controlled by the Integrated-Voltage-Control method which is proposed in this paper are as follows.

(7) The main circuit is a general NPC type bridge circuit.
(8) The operating point transfers automatically across eight operational regions only with a voltage feedback. Current feedback is unnecessary.
(9) The control circuit for the Neutral-point voltage is simple, can be operate even for DC signal and has no influence on voltage control.

The new NPC Multi-Level Four-Quadrant DC-DC Converter is suitable for a high voltage and large scale DC power supply, a single-phase AC power supply and the servo-amplifier etc.

References

[1] A.Nabae, I.Takahashi & H.Akagi : "A New Neutral-Point-Clamped PWM Inverter", IEEE Trans. IAS, Vol.IA-17, No.5 (1981)

[2] H.Irie, H.Okui & T.Hirasa : Integrated Voltage Control Method for the Four-Quadrant Chopper Driving", Trans. of IEEJ, Vol.109D, No.4, PP.259-266 (1989)

[3] H.Okui & H.Irie : "Four-Quadrant Multi-Level DC-DC Converter Using Integrated-Voltage-Control Method Restrained Voltage Fluctuation of Neutral Point", 1996 National Convention Record IEEJ-IAS, 84 (1996)

[4] Y.Ota, H.Irie & H.Okui : "Experimental Results of Four-Quadrant Multi-Level DC-DC Converter Using Integrated-Voltage-Control Method", Record of the Kansai-Section Joint Convention of IEEJ G3-23 (1996)

Induction Motor Control for Electric Vehicle Application Using Low Resolution Position Sensor and Sensorless Vector Control Technique

Giuseppe Guidi
Dipartimento di Ingegneria Elettrica
Università Degli Studi Dell'Aquila
Phone: + 39-746-482387
Fax: + 39-746-274755
E-mail: lalloguidi@email.telpress.it

Hisao Kubota
Department of Electrical Engineering
Meiji University
Phone: +81-44-934-7296
Fax: +81-44-934-7909
E-mail: kubota@isc.meiji.ac.jp

Yoichi Hori
Department of Electrical Engineering
The University of Tokyo
Phone: +81-3-3812-2111 ext.7680
Fax: +81-3-5800-3865
E-mail: hori@kaya.t.u-tokyo.ac.jp

Abstract **– In this paper an induction motor drive for electric vehicle applications is proposed. The system joins a robust very low resolution position sensor with both an instantaneous speed observer algorithm and a sensorless technique, achieving satisfactory speed identification and control. Simulation results show that the proposed system offers promising performances in the whole set of significant operating conditions.**

I. INTRODUCTION

Induction motors (IM) are very popular in many industrial applications where ruggedness, low cost and good efficiency are required; if field oriented control (FOC) is achieved, they can also be used in several applications requiring high dynamic performances such as servodrives, robots and electric vehicles. Usually, high performance drives include optical encoders for rotor speed measurement; unfortunately this kind of sensor is not suitable for harsh environments such as electric vehicles (EV) because it is very sensitive to mechanical vibrations, temperature variations and dust. In order to overcome this problem, several sensorless techniques have been presented in literature [1, 2]. Typically, those algorithms are very sensitive to parameter variations which occur during operations (e.g. stator and rotor resistance variations with temperature or inductance variations due to non-linearity of the magnetic core), requiring complex adaptation techniques and highly decreasing reliability.
The aim of this paper is to show how a very low resolution speed sensor, which is quite insensitive to vibrations, can be successfully used for speed identification, overcoming most of the problems listed above. This kind of sensor is already mounted on the shaft of most of the existing vehicles and it is only used for displaying its actual speed.
Due to the very limited number of encoder pulses, an instantaneous speed observer [3] is used for rebuilding the exact rotor speed even between two consecutive pulses from the sensor; furthermore, since no information about motor shaft direction is available, a simple sensorless technique is used to draw it out. The observed speed is passed to a linearizing non-linear controller [4] which provides to speed and flux reference tracking. The resulting IM controller can be considered similar to Direct FOC, but having a different theoretical base.
This paper firstly deals with the description and the analysis of the whole control system, then shows some simulation results obtained using parameters measured from an existing EV, showing the behavior of the vehicle under significant operating conditions (e.g. EV start-up in the presence of a steep slope). The influence of typical motor parameter variations are also investigated, highlighting promising performances in view of the practical implementation.

II. THE PROPOSED CONTROL SYSTEM

The basic idea of the proposed EV drive is the use of the tachometer included in most of vehicles for speed detection, obtaining a system which is less sensitive to measurement noise, parameters and load variations in comparison with the pure sensorless. Information from this sensor, which is a very low resolution pulse generator (typically 20 ppr), is used by an instantaneous speed observer algorithm in order to achieve IM drive control and vehicle speed tracking in a wide range of operation i.e. in presence of accelerations, decelerations, sudden changes in slope and so on. Notice that since the sensor is mounted on a shaft coupled with the motor through a

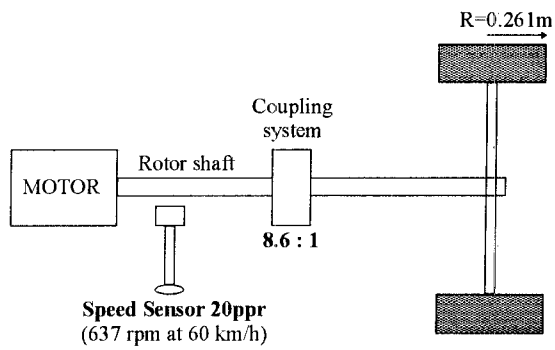


Fig. 1. Simplified schematic of the vehicle

transmission gear having a ratio of 8.25:1 (Fig. 1), the actual resolution available for the control system is 2.42 ppr, which is very low in respect of the one provided by a typical industrial incremental encoder (1024 ppr or more). Another drawback of this kind of sensor is the lack of information related to rotor direction. In the proposed system this problem is overcome employing a further estimation algorithm which only requires stator current and DC bus voltage measurements.

Non-linear control system theory is then used for designing a controller which allows flux and torque decoupling and tracking. The resulting control system is shown in Fig. 2.

III. Instantaneous Speed Observer

Due to the poor information from the position sensor, there is the need of an algorithm which can calculate the actual speed between two consecutive pulses (Fig. 3).

The mechanical behavior of the vehicle can be described by the following equation:

$$J \cdot \frac{d\omega}{dt} = T_{em} + T_L \ , \tag{1}$$

where ω is the angular speed, J is the inertia coefficient, T_{em} and T_L are respectively the generated and load torque, which also includes all the friction effects.

If both T_{em} and T_L are known, it is possible to estimate the rotor speed at the sampling instant [m, k], starting from its value estimated in the previous sampling instant [m, k-1]:

$$\hat{\omega}[m,k] = \hat{\omega}[m,k-1] + \frac{T_2}{2} \cdot \left(\frac{T_{em}[m,k] + T_L[m] + T_{em}[m,k-1] + T_L[m]}{J} \right) . \tag{2}$$

Starting from this quantity, it is easy to estimate the rotor position:

$$\hat{\theta}[m,k] = \hat{\theta}[m,k-1] + \frac{T_2}{2} \cdot \left(\hat{\omega}[m,k] + \hat{\omega}[m,k-1] \right) . \tag{3}$$

When a pulse is detected from the sensor, assuming that the rotor direction is known, the actual angular position is also exactly known, and it is possible to evaluate the

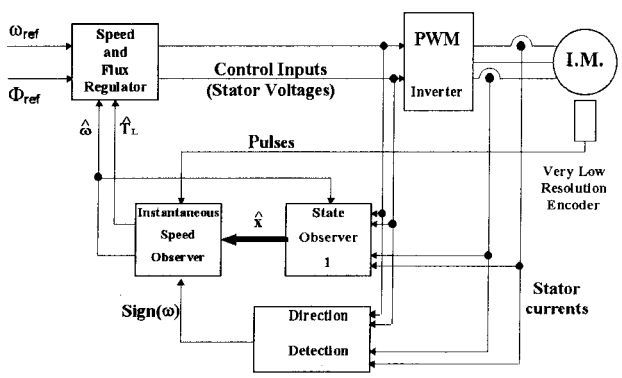


Fig. 2. The Proposed Control System

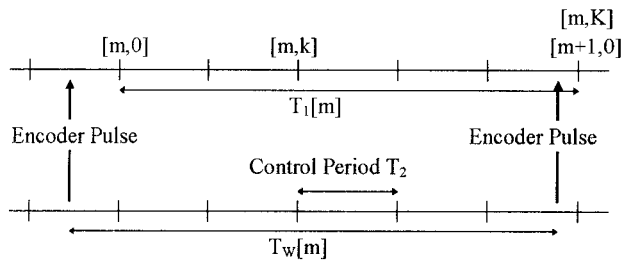


Fig. 3. Timing diagram.

average speed between the last two pulses:

$$\overline{\omega}[m] = \frac{\theta_0}{T_w[m]} , \tag{4}$$

where θ_0 is the sensor resolution in radians.

Assuming that the speed is almost constant over the sampling interval (EV inertia is considerable), the actual angular position is given by:

$$\theta[m+1,0] = \theta[m,0] + \overline{\omega}[m] \cdot T_1 . \tag{5}$$

T_1 is shown in Fig. 3.

The position estimation error at [m+1] is:

$$\Delta\theta[m+1] = \hat{\theta}[m,K] - \theta[m+1,0] . \tag{6}$$

The key is to find an updating rule which starting from this error, determines the convergence of the estimated speed and position toward their actual value. In [3] and [5], assuming that the error is due to both an erroneous initial value of the speed and an uncertainty on the load torque, the following laws have been proposed:

$$\Delta\hat{\omega}[m+1] = \frac{\gamma_1 \cdot \Delta\theta[m+1]}{T_1}$$

$$\Delta\hat{T}_L[m+1] = \frac{2 \cdot J \cdot \gamma_2 \cdot \Delta\theta[m+1]}{T_1^2} , \tag{7}$$

providing also a load torque estimation. Coefficients γ allow to assign the desired estimation error dynamics.

This algorithm has been successfully investigated with DC motors, where em torque can be easily evaluated starting from a current measurement. This is not the case of IM, where the generated torque is expressed as a function of inaccessible quantities (rotor fluxes or currents):

$$T_{em} = \frac{p \cdot L_m}{L_r} \cdot \left(i_\beta \cdot \Phi_\alpha - i_\alpha \cdot \Phi_\beta \right) , \tag{8}$$

where p is the number of pole pairs, L_m and L_r are the equivalent magnetizing and rotor inductances, $i_{\alpha,\beta}$ and $\Phi_{\alpha,\beta}$ are respectively the components of the stator current and of the rotor flux, expressed in the well known stationary reference frame.

Since the em torque is needed in (2), a state observer is built starting from the following IM model:

$$\frac{d}{dt}\begin{pmatrix}\underline{i}_s\\ \underline{\Phi}_r\end{pmatrix}=\begin{pmatrix}A_{11} & A_{12}\\ A_{21} & A_{22}\end{pmatrix}\cdot\begin{pmatrix}\underline{i}_s\\ \underline{\Phi}_r\end{pmatrix}+\begin{pmatrix}B_1\\ 0\end{pmatrix}\cdot\underline{v}_s \tag{9}$$

where

$\underline{i}_s=\begin{pmatrix}i_\alpha & i_\beta\end{pmatrix}^T$ stator current

$\underline{\Phi}_r=\begin{pmatrix}\Phi_\alpha & \Phi_\beta\end{pmatrix}^T$ rotor flux

$\underline{v}_s=\begin{pmatrix}v_\alpha & v_\beta\end{pmatrix}^T$ stator voltage

$$A_{11}=-\left(\frac{R_s}{\sigma\cdot L_s}+\frac{1-\sigma}{\sigma\cdot\tau_r}\right)\cdot\boldsymbol{I}=a_{r11}\cdot\boldsymbol{I}$$

$$A_{12}=\frac{L_m}{\sigma\cdot L_s\cdot L_r}\cdot\left(\frac{1}{\tau_r}\cdot\boldsymbol{I}-p\cdot\omega\cdot\Im\right)=a_{r12}\cdot\boldsymbol{I}+a_{i12}\cdot\Im$$

$$A_{21}=\frac{L_m}{\tau_r}\cdot\boldsymbol{I}=a_{r21}\cdot\boldsymbol{I}$$

$$A_{22}=-\frac{1}{\tau_r}\cdot\boldsymbol{I}+p\cdot\omega\cdot\Im=a_{r22}\cdot\boldsymbol{I}+a_{i22}\cdot\Im$$

$$B_1=\frac{1}{\sigma\cdot L_s}\cdot\boldsymbol{I}$$

$$\boldsymbol{I}=\begin{pmatrix}1 & 0\\ 0 & 1\end{pmatrix}\qquad\Im=\begin{pmatrix}0 & -1\\ 1 & 0\end{pmatrix}$$

R_r, R_s	stator and rotor resistance
L_r, L_s, L_m	stator, rotor and mutual inductance
$\sigma=1-L_m^2/(L_rL_s)$	leakage factor
$\tau_r=L_r/R_r$	rotor time constant

When the rotor speed is constant, (9) describes a linear system and the Luenberger observer can be applied, having the form:

$$\frac{d}{dt}\begin{pmatrix}\hat{\underline{i}}_s\\ \hat{\underline{\Phi}}_r\end{pmatrix}=\begin{pmatrix}A_{11} & A_{12}(\omega)\\ A_{21} & A_{22}(\omega)\end{pmatrix}\cdot\begin{pmatrix}\hat{\underline{i}}_s\\ \hat{\underline{\Phi}}_r\end{pmatrix}+\begin{pmatrix}B_1\\ 0\end{pmatrix}\cdot\underline{v}_s+K\cdot\left(\hat{\underline{i}}_s-\underline{i}_s\right) \tag{10}$$

where ^ denotes observed quantities. The vector K allows to assign the desired dynamics to the observation error.
This kind of observer still works properly in the case of slow speed variation, as in EV systems.
Since the actual speed is not known, the observed one given by (2) is used, assuming that $A(\omega)\cong A(\hat{\omega})$ and generating the feedback shown in Fig. 2. There is not yet a strict demonstration of the closed loop stability for that system, but low sensibility of matrix A with respect to the rotor speed, make this kind of adaptation not so critical.

IV. Direction Detection

Since the employed encoder does not give any information about direction, a Model Reference Adaptive System approach (MRAS) is used with the objective of rotor speed and stator resistance estimation, ensuring overall closed loop stability. Only the sign of the estimated speed is then used by the control algorithm.

According to [2], another state observer is to be calculated, having the same structure of (10). Matrix $A=A(\omega)$ must be evaluated with the sensorless estimated value for the rotor speed $\hat{\omega}_{sl}$.
From (9) and (10), the estimation error on the state variables is described by the following equation:

$$\frac{de}{dt}=(A_{sl}+K_{sl}C)\cdot e-\Delta A_{sl}\cdot\hat{x}_{sl} \tag{11}$$

where

$$e=x-\hat{x}_{sl}=\begin{pmatrix}\underline{i}_s\\ \underline{\Phi}_r\end{pmatrix}-\begin{pmatrix}\hat{\underline{i}}_s\\ \hat{\underline{\Phi}}_r\end{pmatrix}_{sl}$$

$$\Delta A_{sl}=A_{sl}-A=\begin{pmatrix}0 & -\Delta\omega\cdot\Im/m\\ 0 & \Delta\omega\cdot\Im\end{pmatrix}$$

$m=(\sigma\cdot L_s\cdot L_r)/L_m$; $\Delta\omega=\hat{\omega}_{sl}-\omega$.

Subscript sl in the previous equations, denotes sensorless quantities and it is add in order to avoid any confusion with the analogous quantities which appear in the state observer used by the instantaneous speed observer algorithm.
It is convenient to define the following Lyapunov function candidate:

$$V=e^T\cdot e+(\hat{\omega}_{sl}-\omega)^2/\lambda \tag{12}$$

where λ is a positive constant.
The time derivative of V is:

$$\frac{dV}{dt}=e^T\left(\left(A+K_{sl}C\right)^T+\left(A+K_{sl}C\right)\right)e+$$
$$-2\Delta\omega\cdot\left(e_{i\alpha}\cdot\hat{\Phi}_\beta-e_{i\beta}\cdot\hat{\Phi}_\alpha\right)/m+ \tag{13}$$
$$+2\Delta\omega\cdot\frac{d\hat{\omega}}{dt}/\lambda$$

where $e_{i\alpha}=i_\alpha-\hat{i}_{\alpha_{sl}}$, $e_{i\beta}=i_\beta-\hat{i}_{\beta_{sl}}$.
By equalizing the third term to the second term in (13) and providing that K_{sl} is chosen so that the first term in the same equation is negative-semidefined, the proposed algorithm is stable. It results in the following adaptive law:

$$\frac{d\hat{\omega}_{sl}}{dt}=\frac{\lambda}{m}\cdot\left(e_{i\alpha}\cdot\hat{\Phi}_\beta-e_{i\beta}\cdot\hat{\Phi}_\alpha\right) \tag{14}$$

In practice, (14) is replaced by a PI law, in order to improve the response of the speed estimation:

$$\hat{\omega}_{sl}=K_P\cdot\left(e_{i\alpha}\cdot\hat{\Phi}_{\beta_{sl}}-e_{i\beta}\cdot\hat{\Phi}_{\alpha_{sl}}\right)+K_I\cdot\int\left(e_{i\alpha}\cdot\hat{\Phi}_{\beta_{sl}}-e_{i\beta}\cdot\hat{\Phi}_{\alpha_{sl}}\right)dt \tag{15}$$

where

$e_{i\alpha,\beta}=i_{\alpha,\beta_{sl}}-\hat{i}_{\alpha,\beta_{sl}}$	sensorless current estimation error
K_P, K_I	arbitrary positive gains

It is worth to remark that there is no need to know exactly the rotor speed. In fact, due to the presence of the instantaneous speed observer, only the sign of ω is required. This means that the gains in (15) can be chosen very small, highly increasing noise immunity in comparison with the typical sensorless systems.

V. Flux and Speed Control

A non-linear controller has been used in order to track the speed reference and to keep the rotor flux at the desired value.
The non-linear description of the IM is:

$$\begin{cases} \dfrac{di_\alpha}{dt} = -a\cdot i_\alpha + b\cdot\Phi_\alpha + b\cdot p\cdot\omega\cdot\Phi_\beta + \dfrac{1}{\sigma L_s}\cdot v_\alpha \\ \dfrac{di_\beta}{dt} = -a\cdot i_\beta + b\cdot\Phi_\beta - b\cdot p\cdot\omega\cdot\Phi_\alpha + \dfrac{1}{\sigma L_s}\cdot v_\beta \\ \dfrac{d\Phi_\alpha}{dt} = \dfrac{L_m}{\tau_r}\cdot\Phi_\alpha - \dfrac{1}{\tau_r}\cdot\Phi_\beta - p\cdot\omega\cdot\Phi_\beta \\ \dfrac{d\Phi_\beta}{dt} = \dfrac{L_m}{\tau_r}\cdot\Phi_\beta - \dfrac{1}{\tau_r}\cdot\Phi_\alpha + p\cdot\omega\cdot\Phi_\alpha \\ \dfrac{d\omega}{dt} = -\dfrac{B}{J}\cdot\omega + \dfrac{1}{J}\cdot(T_{em} + T_L) \end{cases} \tag{16}$$

where

$$a = \frac{R_s + \left(\frac{L_m}{L_r}\right)^2\cdot R_r}{\sigma\cdot L_s} \quad \text{and} \quad b = \frac{L_m}{\tau_r\cdot\sigma\cdot L_s\cdot L_r},$$

which is put in the canonical form

$$\dot{x} = f(x) + g(x)\cdot u,$$

where

$x = \begin{pmatrix} i_\alpha & i_\beta & \Phi_\alpha & \Phi_\beta & \omega \end{pmatrix}^T$ system state

$u = \begin{pmatrix} v_\alpha & v_\beta \end{pmatrix}^T$ control input (stator voltage)

$f: \Re^5 \to \Re^5$ and $g: \Re^5 \to \Re^{5\times 2}$ are easily obtainable from (16). Notice that (9) and (16) are exactly the same, except for the mechanical equation which does not appear in the former.
According to non-linear control theory, it is possible to find a feedback from the system state which achieves torque-flux linearization and allows speed reference tracking and rotor flux regulation. Due to the space limitation, the controller calculation is not presented here. This can be found in [4]. The control input, in terms of stator voltage is given by:

$$\begin{pmatrix} v_\alpha \\ v_\beta \end{pmatrix} = \begin{pmatrix} L_f^2 h_1(x) + c_{0\omega}\cdot\left(h_1(x) - \omega_{ref}\right) + c_{1\omega}\cdot L_f h_1(x) \\ L_f^2 h_2(x) + c_{0\Phi}\cdot\left(h_2(x) - \Phi_{ref}\right) + c_{1\Phi}\cdot L_f h_2(x) \end{pmatrix} \tag{17}$$

where

$$\beta(x) = \frac{\sigma\cdot L_s\cdot\tau_r\cdot J}{2\cdot L_m\cdot c\cdot\left(x_3^2 + x_4^2\right)}\cdot\begin{pmatrix} \frac{c}{J}\cdot x_3 & -\frac{2\cdot L_m}{\tau_r}\cdot x_4 \\ \frac{c}{J}\cdot x_4 & \frac{2\cdot L_m}{\tau_r}\cdot x_3 \end{pmatrix}$$

$$c = \frac{3}{2}\cdot p^2\cdot\frac{L_m}{L_s}$$

$$h_1(x) = x_5 \qquad \text{rotor speed}$$

$$h_2(x) = \left(x_3^2 + x_4^2\right) \qquad \text{rotor flux module} \tag{18}$$

and

$$L_f h_2(x) = 2\cdot x_3\cdot f_3 + 2\cdot x_4\cdot f_4$$

$$L_f^2 h_2(x) = 2\cdot\left(\frac{L_m}{\tau_r}\cdot x_3\cdot f_1 + \frac{L_m}{\tau_r}\cdot x_4\cdot f_2 + \left(\frac{L_m}{\tau_r}\cdot x_1 - \frac{2}{\tau_r}\cdot x_3\right)\cdot f_3 + \left(\frac{L_m}{\tau_r}\cdot x_2 - \frac{2}{\tau_r}\cdot x_4\right)\cdot f_4\right)$$

$$L_f h_1(x) = f_5$$

$$L_f^2 h_1(x) = -\frac{c}{J}\cdot x_4\cdot f_1 + \frac{c}{J}\cdot x_3\cdot f_2 + \frac{c}{J}\cdot x_2\cdot f_3 - \frac{c}{J}\cdot x_1\cdot f_4 + -\frac{B}{J}\cdot f_5$$

are the Lie derivatives of the output functions (18) along the vector field f.
It is important to notice that the controller is always well defined, except when the rotor flux module is zero. That is not a real limitation, because it only occurs in the very beginning of motor operations.
Feeding the IM according with (17), the behavior of the whole system can be described by the following transfer function:

$$\begin{pmatrix} \Omega(s) \\ \Phi(s) \end{pmatrix} = \begin{pmatrix} \frac{1}{s^2 + c_{1\omega}\cdot s + c_{0\omega}} & 0 \\ 0 & \frac{1}{s^2 + c_{1\Phi}\cdot s + c_{0\Phi}} \end{pmatrix}\cdot\begin{pmatrix} \Omega_{ref}(s) \\ \Phi_{ref}(s) \end{pmatrix} \tag{19}$$

which clearly stresses the decoupled structure. Furthermore, properly choosing the c constants in (17), it is extremely easy to assign system dynamics.
Since the whole state cannot be measured, in evaluating the control input (17), the observed quantities given by (10) are used, achieving only asymptotic decoupling and linearization, instead of the exact one

VI. Simulation Results

Several simulations have been carried out, using the MATLAB software tools, in order to investigate the behavior of this control system. A vehicle start has been simulated, involving steep road modeled with a load torque as shown in Fig. 5 (100 Nm constant torque, plus a friction term which is proportional to the vehicle speed). The reference rotor speed has been fixed to 30 rad/s, which

corresponds to a vehicle speed of about 1 m/s, while the flux reference has been kept constant to 0.15 Wb.

Fig. 4 shows the motor speed in comparison with its estimation, evaluated by the Instantaneous Speed Observer. Notice that the proposed algorithm converges toward the true values for both speed and load torque very quickly. In the very low speed region (less than 5 rad/s), there is practically no more information from the used sensor, resulting in an erroneous value for both the estimated load and speed. It is not critical from the EV point of view, considering that this condition only occurs when the vehicle stops and, of course, speed can be easily fixed to zero by using the mechanical brakes, once its value is small enough. The resulting error on the estimated speed does not affect flux estimation, which is fundamental for not to lose the control action.

Fig. 6 shows the actual rotor flux module. The desired flux level is reached quickly and is kept well enough even during sudden speed changes.

The behavior of the system in presence of significant variations on motor parameters has also been investigated.

Regarding to the inertia coefficient, since the proposed system is intended to be used in EV applications, only small variations are significant. Simulations show how an erroneous value for $J = J_n \pm 20\%$ only slightly affects the performances of the instantaneous speed observer, thus no adaptation is required.

A wrong value for the rotor resistance, due for example to the motor heating, can affect the rotor flux level, while the speed is still well controlled, since there are the sensor pulses which allow exact speed measurement.

Heating effect also determines a stator resistance variation. That represents a problem only in the very low speed range. Due to the presence of the transmission gear (Fig.1), there is no reason to operate in such conditions and the R_s value can be critical only during vehicle startup. Following the same method presented in section IV, it is also possible to build an adaptation mechanism for both stator resistance and rotor speed. The resulting adaptation law is given by:

$$\hat{R}_s = -K_{Is} \cdot \int \left(e_{i\beta} \cdot \hat{i}_{\beta_{sl}} + e_{i\alpha} \cdot \hat{i}_{\alpha sl} \right) dt \qquad (20)$$

Since resistance variations are typically very slow, the adaptation gain K_{Is} in (20) can be chosen small enough, in order to increase noise immunity.

TABLE I
MOTOR PARAMETERS

p	2	
R_s	0.877	Ω
R_r	1.47	Ω
L_s	0.1651	H
L_r	0.1651	H
L_m	0.1608	H
J	20	kgm^2

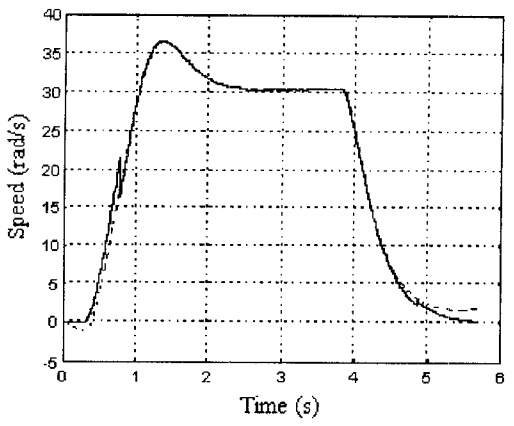


Fig. 4 Actual (dashed) and observed rotor speed

VII. CONCLUSIONS AND FURTHER DEVELOPMENTS

In this paper an induction motor drive mainly intended for electric traction purposes is proposed. The control system uses a very low resolution tachometer encoder (available in most of modern vehicles as a speed sensor) an instantaneous speed observer algorithm and a sensorless technique; estimated quantities are then used by a non-linear controller, achieving speed and flux tracking. Simulation results obtained using parameters measured on an existing EV highlight good performances in a complete set of significant operating conditions. At present, work is in progress in order to experimentally verify the proposed control system.

REFERENCES

[1] C. Schauder, "Adaptive speed identification for vector control of induction motor without rotational transducers", in *Conf. Rec. 1989 IEEE IAS Annu. Mtg.*, pp. 493-499.

[2] H. Kubota, K. Matsuse, T. Nakano, "DSP-Based Speed Adaptive Flux Observer of Induction Motor", *IEEE Trans. on Industry Applications*, Vol. 29, no. 2, March/April 1993.

[3] Y. Okamura, Y. Chun, Y. Hori, " Inertia Moment Identification in the Average Speed-Type Instantaneous Speed Observer", *Electrical Engineering in Japan*, Vol. 115, no. 7, 1995.

[4] C. Cecati, G. Guidi, F. Marinelli, "An Adaptive Non-linear Control Algorithm for Induction Motor Drives". in *Conf. Rec. IECON* Taiwan, Taipei, August 1996.

[5] Konno and Hori, "Instantaneous Speed Observer with higher order disturbance estimation", Trans. IEE Japan, Vol. 122-D, p. 539, 1992.

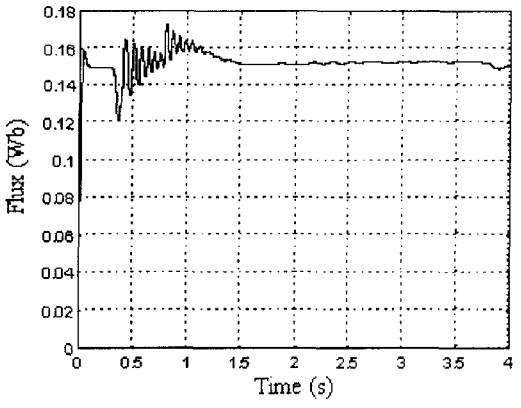


Fig. 6. Rotor flux module

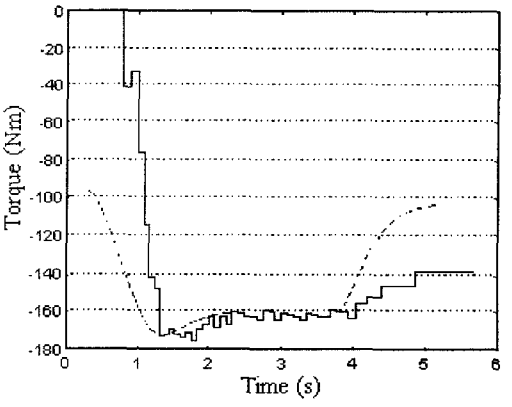


Fig. 5. Actual (dashed) and estimated load torque

Residual Capacity Estimation of Sealed Lead-Acid Batteries for Electric Vehicles

Takahiro Yanagihara* Atsuo Kawamura**

Dept. of Elec. and Comp. Eng.
Yokohama National University
79–5 Tokiwadai, Hodogaya-ku
Yokohama 240 JAPAN
E-mail: * yanagi@kawalab.dnj.ynu.ac.jp
E-mail: ** kawamura@kawalab.dnj.ynu.ac.jp

Abstract— **The various estimation methods for the residual capacity of the the sealed lead-acid battery have been proposed. However, any method can not accurately predict the residual capacity.**

It is known that the internal resistance and the electromotive force are related to the residual capacity [3][4]. The equation of estimating the residual capacity of the sealed lead-acid battery is proposed. The experiments were performed for verification of the proposal estimation.

I. Introduction

The electric vehicles(EV) are not yet widely accepted for replacement with the internal combustion engine car. One reason is the short driving rang of the EV with the present battery technology. This problem makes drivers afraid of exhausting all of the battery energy before the arrival in the destination.

This anxiety is solved by the exact estimation of the residual capacity. As a result, the excess discharge and the excess charge are avoided, and a life of the battery becomes longer.

This paper proposes one estimation method of the residual capacity of the sealed lead–acid battery based on the internal resistance and electromotive force.

II. Theory of generation of electricity

The lead–acid battery consists of PbO_2, Pb and H_2SO_4.

The electromotive reaction is expressioned as (1), (2).

$$PbO_2 + 4H^+ + SO_4^{2-} + 2e^- \rightarrow PbSO_4 + 2H_2O \quad (1)$$

$$Pb + SO_4^{2-} \rightarrow PbSO_4 + 2e^- \quad (2)$$

These reaction cause the discharge. And the electromotive force is expressed as (3)[1].

$$E = 2.04 + 0.0591 \log a_{H_2SO_4}/a_{H_2O} \quad (3)$$

Equation (1) and (2) show that the discharge reaction reduces H_2SO_4 and increases H_2O. Thus the density of the electrolyte decreases, as the residual capacity decreases. Equation (3) indicates the electromotive force (E) decreases, as the residual capacity decreases.

III. Assumptions for Residual Capacity Estimation Experimental Set-up for discharge and charge

The proposed residual capacity estimation was verified by the experiments. Thus, in this section the assumptions and conditions for the experimental set-up are described.

A. Tested Battery

We used the 24 Ah sealed lead–acid battery.

B. Equipments of Experiments

B.1 Equipments and Assumptions for Discharge

Fig.1 shows the equipment for discharge. The battery is discharged by the chopper (switching frequency about 20 kHz), using a resistance for load. The battery is discharged at a constant current (about 4A) till the terminal voltage becomes 10.5 [V]. The capacity is determined by the product of the current and the duration of discharge. And the residual capacity is determined by subtraction of the discharged capacity from the whole capacity, which is assumed the total discharged energy when the terminal voltage decreases to 10.5 [V].

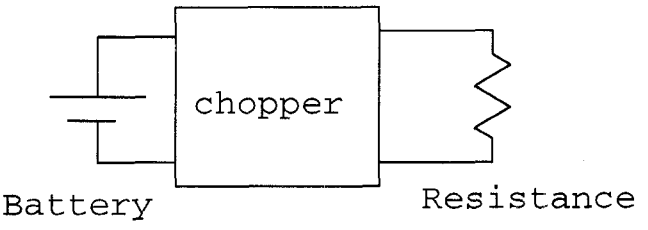


Fig. 1. Equipment for Experiment of Discharge

B.2 Equipments and Assumptions for Charge

Fig.2 shows the equipment for charge. The battery is charged by the chopper. The battery is charged at a constant current (about 2.4A) till the amount of the charge, which is determined by the product of the current and the duration of discharge, becomes 26 Ah.

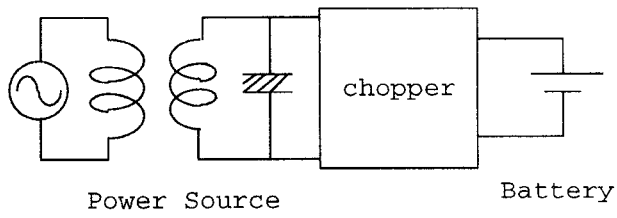


Fig. 2. Equipment for Experiment of Charge

IV. Conventional estimation

The following estimation methods of the sealed lead–acid battery are known in [3], [4], [5] and [6].

- Estimation based on the electromotive force [3]
- Estimation based on current integration [6]
- Estimation based on the internal resistance [4] [6]

A. Estimation based on the electromotive force

Equation (3) shows that the relationship between residual capacity of a lead-acid battery and electromotive force [1][3]. The electromotive force drops as the residual capacity reduces as shown in Fig.3, in which three kind of discharge experiments are illustrated.

But the electromotive force suddenly drops, when the residual capacity is almost zero. The reason for this sudden voltage drop is that the shortage of sulfuric acid (H_2SO_4)and the surface of electrodes are covered with the resultings($PbSO_4$).

But, before the sudden voltage drop the residual capacity is estimated as (4).

$$C = 100(V_e - 11.7)/(12.8 - 11.7) \qquad (4)$$

where V_e is the electromotive force and C is the residual capacity [3].

In case of discharging, the terminal voltage drop is equal to the internal resistance times the current.Thus, the electromotive force can be estimated from this relationship. However, in case of the pulse discharging, the estimation of the electromotive force is very difficult, because the non-uniform distribution of the electrolyte around the electrodes causes the electromotive force to vary in a short time.

B. Estimation based on current integration

If the total integration of the charged current is correctly known, the residual capacity is estimated by integrating the discharge current.[2] The current waveform of the discharged experiment is shown in Fig. 4. It is observed that the current waveform is warped by switching. It is difficult to integrate the discharged current. And even if the amount of the charge is known, the state of the previous discharge has an effect on the residual capacity. This method has difficulty in this point.

C. Estimation based on the internal resistance

As the amount of discharge increases, the active material in the battery decreases. As a result, the internal resistance increases.

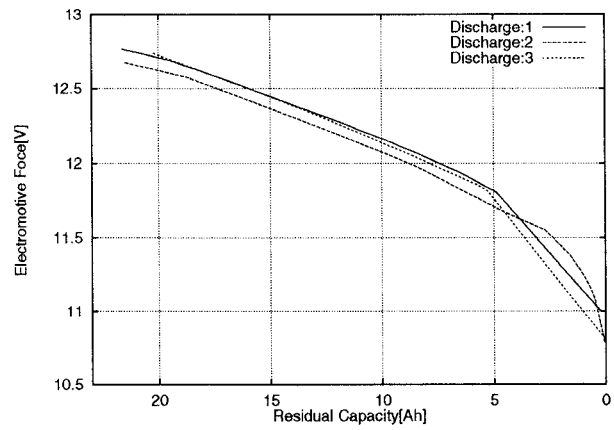


Fig. 3. Relation between electromotive force and integration of discharge current

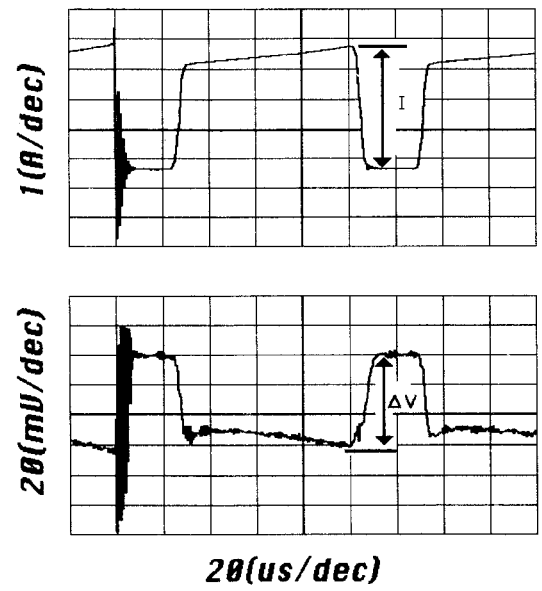


Fig. 4. waveform of the current with switching

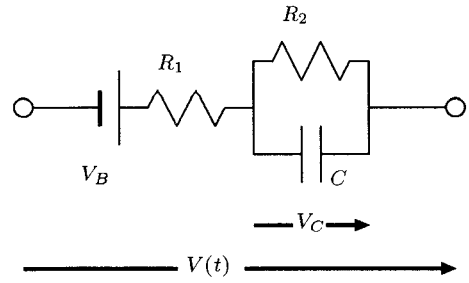


Fig. 5. Equivalent Circuit of Battery

Fig.5 shows an equivalent circuit of a battery which has been proposed in [4] and [5]. In Fig.5 R_1 is the electrolyte resistance including the electrode resistance. R_2 is the charge transfer resistance at the interface between the electrode and electrolyte solution, and C is the electric double layer static capacity formed at the interface between the electrode and electrolyte solution.

Using the equivalent circuit shown in Fig.5, the terminal voltage is given as (5).

$$V(t) = V_B - I(R_1 + R_2) + R_2 I \cdot e^{-\frac{t}{CR_1}} - V_C \cdot e^{-\frac{t}{CR_2}} \quad (5)$$

, where $V(t)$ and I are shown in Fig.4. From (5), the steady state is given as (6).

$$V(t) = V_B - I(R_1 + R_2) \quad (6)$$

Thus, the internal resistance is obtained as (7).

$$R_1 + R_2 = \Delta V / I \quad (7)$$

In Fig.4, the wave form is in the steady state. Thus, we assume the follow conditions in order to measure the internal resistance.

1. The state of the discharge current is not the pulse, but we suppose that the maximum value of the discharge current is the pulse current (I).
2. The terminal voltage is not the stable, but we suppose the voltage at the point where the discharge current is maximum, is the value of the stable voltage.

The internal resistance obtained from (7) is shown in Fig.6, from which we see that as the residual capacity

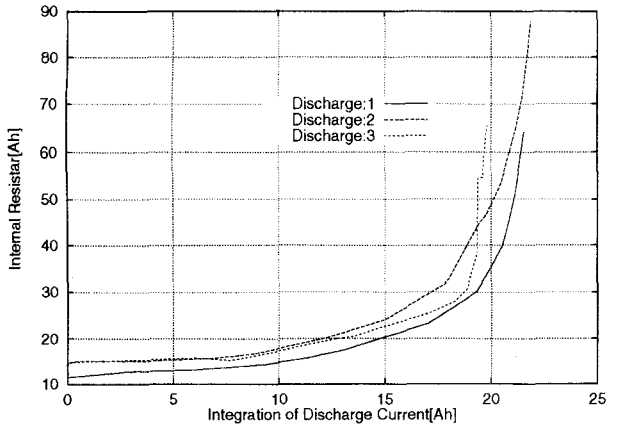


Fig. 6. Relationship between the internal resistance and the residual capacity

decreases, the internal resistance increases. And the internal resistance is in reversely proportional to the residual capacity. As mentioned before, the residual capacity is able to estimated by the internal resistance to a certain degree.

But the following is the problem.

- The terminal voltage depends on the temperature. Thus, the adjustment is required when the temperature changes.
- When the residual capacity is about full, the gradient of the internal resistance is not large.

Thus, the estimation only using the internal resistance is difficult.

Besides, the acid battery contains the inductance. When the frequency of the pulse discharge changes, the internal resistance seems to change. Fig.7 shows the internal resistance with another frequency of the pulse discharge.

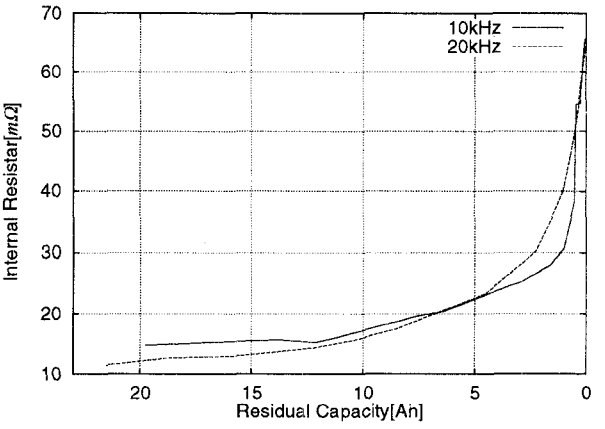


Fig. 7. The internal resistance with other frequency

And the curves of the internal resistance are a little different each other. Thus, we may say that the suitable frequency exists for the pulse discharge.

V. Proposed estimation method for the lead-acid battery

The Fig.3 shows that the electromotive force decreases at some rate before the residual capacity is about 3 Ah. The Fig.6 indicates that the gradient of internal resistance increases, as the amount of discharge current increases.

We propose the next equation to estimate the residual capacity using the electromotive force and the internal resistance.

$$C_{resi} = \alpha V_e + \beta r_{in} + \gamma \frac{\partial r_{in}}{\partial Ah} + f(T, V_e, r_{in}) + Const \quad (8)$$

C_{resi}:residual capacity, V_e:the electromotive force, r_{in}:internal resistance, T:temperature, Ah:ampere-hour

The following is explanation for each term.

- The first term is the electromotive force, and it has relation to the residual capacity until the residual capacity becomes a little.
- The second term is the internal resistance.
- The third term is the gradient of the internal capacity, and it has relation to the residual capacity after the residual capacity becomes a little.
- The fourth is the correctional term for the temperature.
- The fifth term is the constant.

A. Decision of the parameters

Assuming that the fourth term is negligible, we can say that the number of the parameters including the constant term is four.

Thus, the parameters are obtained from the measured data by the least square error (LSE) method.

First, from (8) the residual capacity at nth point can be expressed as (9)

$$C_n = \alpha V_n + \beta R_n + \gamma R'_n + Const \tag{9}$$

Where C_n is the nth residual capacity, R_n is equal to $R_1 + R_2$ in (7) and R'_n is equal to $\frac{\partial(R_1+R_2)}{\partial Ah}$.

If n points of measured data are used, (9) is expressed as (10). If n is equal to four, the inverse exists. If n is larger than four, the pseudo inverse matrix is used.

$$\begin{bmatrix} C_1 \\ C_2 \\ \vdots \\ C_n \end{bmatrix} = \begin{bmatrix} V_1 & R_1 & R'_1 & 1 \\ V_2 & R_2 & R'_2 & 1 \\ \vdots & \vdots & \vdots & \vdots \\ V_n & R_n & R'_n & 1 \end{bmatrix} \begin{bmatrix} \alpha \\ \beta \\ \gamma \\ Const \end{bmatrix} \tag{10}$$

B. Calculation of the gradient of the internal resistance

Fig.6 shows that the point of measure is a little, because we do not measure the internal resistance automatically. Thus it is difficult to find the precise gradient of the internal resistance.

However, the value of the internal resistance can be expressed as a hyperbola of the residual capacity in (11).

$$r_{in} = \frac{a}{Ah - b} + c \tag{11}$$

where a, b, and c is constant. The three parameters are decided by the regression method. From (11) the gradient of the internal resistance is obtained.

VI. Experiment Result

The results are shown in Fig.8 and Fig.9. The Fig.9 shows the estimation error between the estimated and the actual residual capacity.

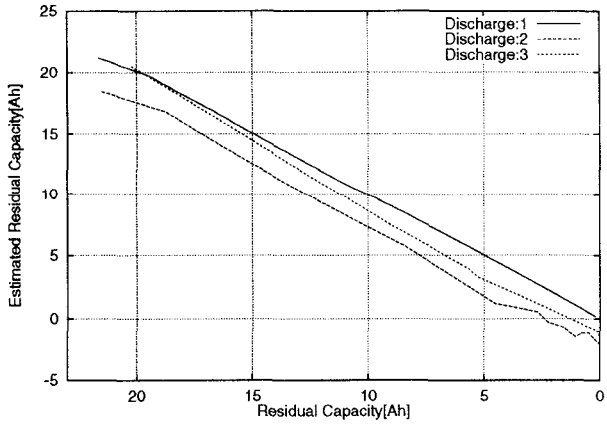


Fig. 8. Estimation of the residual capacity from propose method

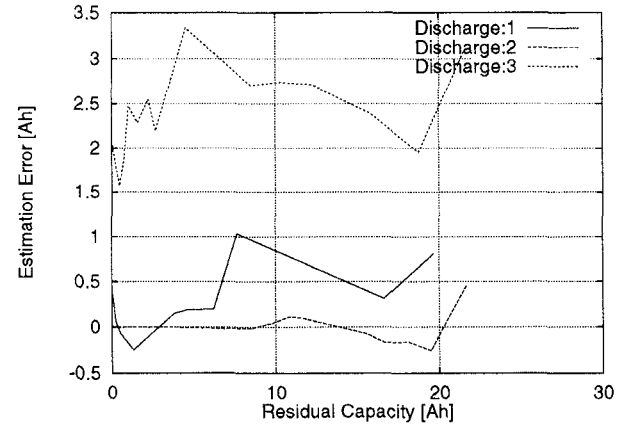


Fig. 9. Estimation error between the proposed method and the residual capacity

The Fig.9 shows that the residual capacity is estimated to some extent. But the error is large as the residual capacity becomes small. The internal resistance increases suddenly and the electromotive force decreases suddenly around this region. And the ΔV and I were measured by an oscilloscope not automatically but manually. Thus the number of the measurement point of the internal resistance at one discharge is fifteen.

The gradient of the internal resistance is obtained by the regression method of the internal resistance. The four parameters in (8) may not be optimal, because of the shortage of the points measurement.

VII. Conclusion

We proposed the residual capacity estimation of the lead-acid battery using the internal resistance and the electromotive force. We confirmed that the residual capacity could be estimated by the proposed equation and the error was below ±15%. The proposed estimation method seems to have more accuracy if the number of data used for experiments becomes longer.

In future, we think that the automatic measurement to improves the overall accuracy. And the residual capacity estimation of the combination battery is also important.

References

[1] Japan Battery Company:" Newest Practical Secondary Battery" ,Nikkan Kougyou Shinbunsha(1995)

[2] Kitagawa Shibuya Tkehara Kasaki Ookugo:" Development of Mater of Residual Capacity of Sealed Lead-Acid Batteries for Electric Vehicle" ,,pp. 176–186(1995)

[3] ShimomuraF"Deterioration Estimation and Residual Capacity Estimation for Sealed Lead-Acid Batteries", Technical Meeting Report(in japanese) , pp. 75–76 (1996).

[4] Yamamoto Ogata Takano Konya:"Deterioration Estimation Method for 200Ah Sealed Lead-Acid Batteries ",NTT R&D, **43**, 10, pp. 91–96 (1994).

[5] Ogata, Takano, Kouno, YoshidaF ."Deterioration Estimation Method Using Pulse Discharge and Charge Characteristics of Lead- Acid Batteries", Trans IEICE B–I, **j76–B–I**, 10, pp. 719–726 (1993).

[6] Kitagawa, Shibuya, Takehara, kasaki, ookubo, "Development of Residual Capacity Mater for EV ",Electric Vehicle Forum'95, pp.176–186.

Total Efficiency of a Hybrid Electric Vehicle

Sadao Imai *@, Nobuaki Takeda, Yusuke Horii
Mitsubishi Motors Corporation
4-21-1,Shimomaruko,Ohta-ku,Tokyo 146, Japan
Fax: +81-03-3757-7369, Phone: +81-03-3757-7342
E-mail: sadao_imai@fuso.mitsubishi-motors.co.jp

Abstract —**Generally, the efficiency of a motor for electric vehicles is extremely high compared with an internal combustion engine. And the electric vehicle doesn't produce emission during running. Including fuel production and generation, however, the efficiency falls and emissions are produced. Therefore it is necessary to consider total efficiency and emissions. Mitsubishi Motors Corporation has developed hybrid electric light-duty truck Canter HEV that equipped LPG powered engine-generator and electric motors. Canter HEV has achieved low fuel consumption and low emissions. This paper describes comparison of total fuel consumption and emissions of diesel and electric and hybrid electric vehicle.**

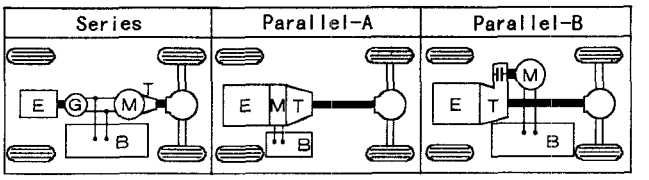
I. Introduction

Petroleum resources being exhausted, global warming by carbon dioxide and air pollution in urban areas by nitrogen oxides are getting serious these days. These problems are closely related with the automobile industry. Of the total energy consumption in Japan, 24% is consumed in the transportation sector and its some 90% is by automobiles. Accordingly, the sector accounts for 19% of the total carbon dioxide emission. As for nitrogen oxides, as much as 53% of the total emission is attributable to automobiles in some districts. In this situation, the automobile industry has been making active efforts to develop low-pollution vehicles improved in fuel consumption and emission. Main efforts are directed to CNG (Compressed Natural Gas) vehicles, methanol vehicles, electric vehicles, hybrid electric vehicles, etc. CNG vehicles can somewhat reduce CO_2 and NOx, but fuel tanks are heavy, one-charge travel distance is short and the fuel supply infrastructure is not so easy to establish. Methanol vehicles generate much CO_2 in the process of fuel production and, similar to CNG vehicles, are not easy to construct the fuel supply infrastructure. Electric vehicles, including hybrid ones, have begun to be developed actively. But electric vehicles are inferior in one-charge travel distance and carrying capacity although emissions can be eliminated at all. It is not practical to develop electric trucks. Meanwhile, hybrid electric vehicles can secure sufficient travel distance and carrying capacity. Our company has developed the Canter HEV, a series type hybrid electric vehicle featuring sufficient travel distance and low pollution.

Generally, motors used in electric vehicles are very efficient as compared with internal combustion engines. However, production of electric power, the energy source of motors, is less efficient than the fuel production for internal combustion engines. Therefore, in comparison with an diesel vehicle, this report evaluates our developed hybrid electric truck in terms of the total energy efficiency, fuel consumption and emissions, taking into account the production efficiencies of energy sources (electric power, LPG and diesel oil) and the amounts of emissions during production. Efficiency, fuel consumption and emissions during travel were measured with a chassis dynamo.

II. Hybrid Electric Vehicle System

Hybrid electric vehicles may fall into two types: series type and parallel type. A series type vehicle is driven by a motor while electric power is generated by "engine + generator". Meanwhile, a parallel type vehicle can be driven either by an engine or a motor. Figure 1 shows hybrid electric vehicle system.



E;Engine, M;Motor G;Generator, B;Battery, T;Transmission

Fig.1. Hybrid Electric Vehicle System

III. Overview of Canter HEV

A. System Configuration

Canter HEV is a series type hybrid vehicle which is

driven exclusively by motors. Figure 2 shows the system configuration of Canter HEV. There are two AC induction motors (40 kW x 2). Figure 3 shows the motor characteristics. One is operated when the load is low while both are operated when the load is heavy, realizing high efficiency drive. The battery unit consists of 28 valve regulated lead acid batteries, supplying electric power at 336V. The battery can be charged by a charger and by the mounted generation engine unit. The generation engine is a taxi-use 1.8 L- LPG engine which generates 20 kW at 2000 rpm, realizing high efficiency power generation. The generation efficiency is 27%. Combined with the effect of the catalytic converter, emissions are remarkably reduced. In addition, when the vehicle is braked, the motor can function as a generator to charge the battery by converting the braking energy to electric power. This greatly contributes to improving the vehicle efficiency.

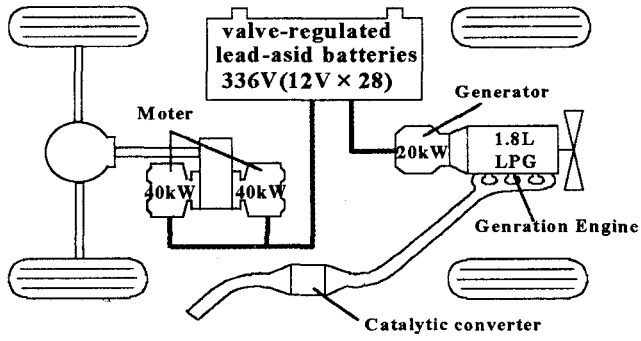


Fig.2. System Configuration

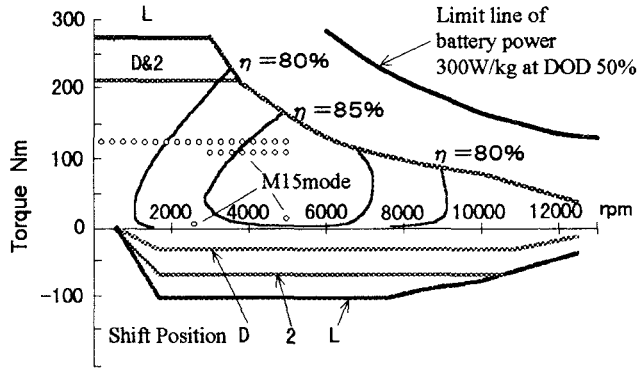


Fig.3. Motor Characteristics

B. Drive Modes

Canter HEV is driven by the motor while the SOC (State of Charge) of the battery is high. In this battery drive mode, it runs as a clean vehicle free of emissions. In this paper, this part is considered to be the EV. If the SOC becomes lower than 50%, the vehicle enters the hybrid drive mode with the engine and generator forced to start power generation. When the battery is charged to a SOC of 55%, the vehicle enters the battery drive mode, again. Although charging efficiency is low when the battery is almost fully charged, Canter HEV maintains the SOC between 50 and 55% in the hybrid drive mode. Therefore, much of the braking energy can be collected as electric power. These parts are considered to be the HEV. Figure 4 shows the driving modes.

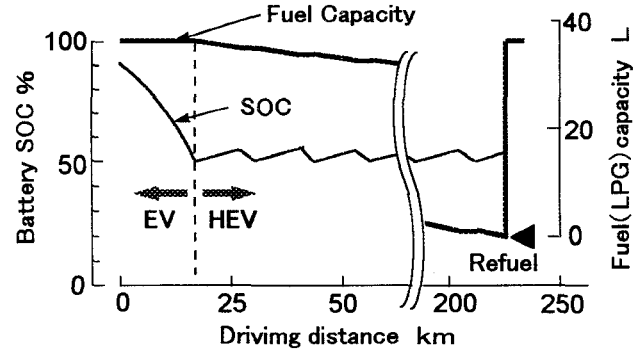


Fig.4. Driving Mode

IV. Theoretical Drive Energy

In preparation of calculating the vehicle efficiency and total efficiency, we calculated the theoretical drive energies of Canter HEV and a comparable equivalent class diesel vehicle in various drive modes. Table I shows characteristics of the vehicles under test.

TABLE I

CHARACTERISTICS OF THE VEHICLES UNDER TEST

		Canter HEV	Diesel(A/T)
empty weight kg		2800	2170
gross weight kg		3855	3225
roll.resist.co.		0.0052	0.0088
air resist.co. kgf/{m²·(km/h)²}		0.0035	←
frontal area m²		2.7	←
tire radius m		0.338	0.324
transmission gear ratio	1st	3.000	3.068
	2nd	—	1.570
	3rd	—	1.000
	4th	—	0.724
final gear ratio		5.285	4.875

Mainly due to the weight of the battery, Canter HEV is heavier by 630kg than the diesel vehicle. However, thanks to the low rolling resistance tires employed, Canter HEV requires less energy to cope with the rolling resistance than the diesel vehicle. Regarding the energy to cope with the air resistance, there is no difference between the two vehicles. Therefore, the theoretical drive energy required by the Canter HEV traveling at constant velocity is smaller than required by the diesel vehicle. In the M15 mode, however, Canter HEV requires more energy than the diesel

vehicle because of the increased total vehicle weight raises the acceleration resistance.

V Test Calculation Result

A. Energy Production Efficiency

We examined the efficiency of the energy production. Figure 5 shows the energy production efficiency.

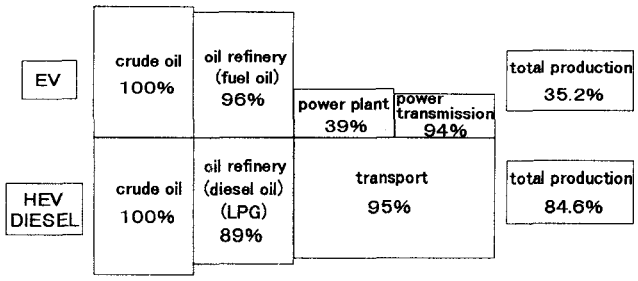


Fig.5. Energy Production Efficiency

B. Vehicle Efficiency

Figure 6 shows the way of thinking the vehicle efficiency. In the case of EV, AC is converted into DC with the charger, and the battery is charged. The motor is driven by the power saved in the battery. When the vehicle is braked, the battery is charged by converting the braking energy to electric power. The vehicle efficiency is the value that divided theoretical drive energy by the AC side electric energy of the charger. In case of HEV, same as EV, the motor is driven by the battery power in the battery drive. In the hybrid drive, the motor is driven by the power generated with the generation unit. A part of generated output charges the battery under the low load condition. In addition to generated output, power is taken from the battery under the high load condition. The vehicle efficiency is the value that divided theoretical drive energy by the LPG's calorific power.

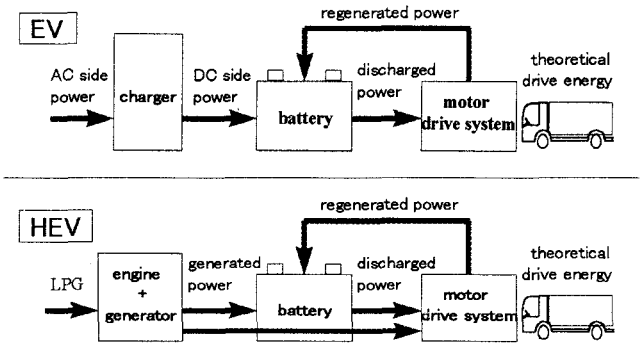


Fig.6. Vehicle Efficiency

In Japan, since this vehicle is included in the GVW class of more than 2.5 tons, emission gas measurement is carried out in operation of the engine alone. Therefore, although the drive mode on actual vehicle is not specified by the emission gas measurement regulation, M15 mode was used in our evaluation. This is the drive mode in a city for trucks. Figure 7 shows M15 mode pattern.

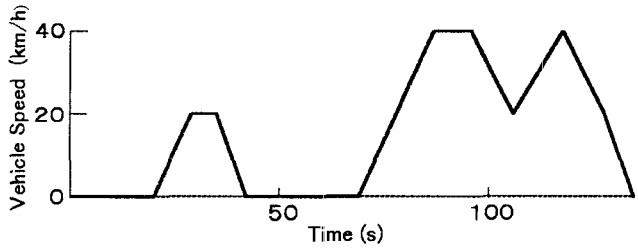


Fig.7. M15 mode pattern

Fuel consumption in each mode by EV is calculated from the travel distance covered by Canter HEV during battery drive with a SOC between 100% and 50%. That by HEV is calculated from the travel distance and measured fuel consumption when the charge and discharge were balanced (SOC: 55%→50%→55%). Because the energy source of each vehicle varies, the fuel consumption is compared with calorific value base.

C. Total Efficiency

The total energy efficiency, fuel consumption, CO_2 emission and NOx emission of each vehicle are calculated by taking into account the efficiency and gas emissions during fuel production. Figures 8 through 11 show these calculation results. Note that the gas emissions by EV include those which are calculated by assuming thermal power generation only.

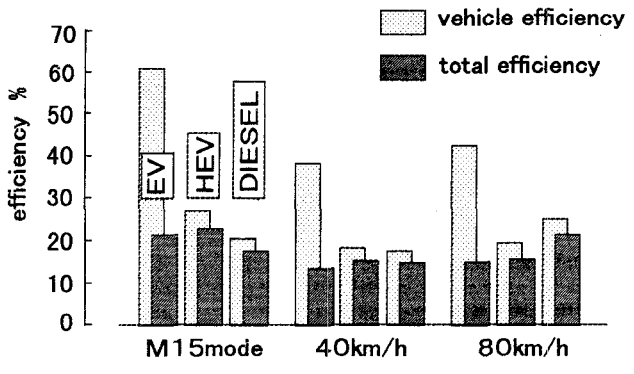


Fig.8. Efficiency

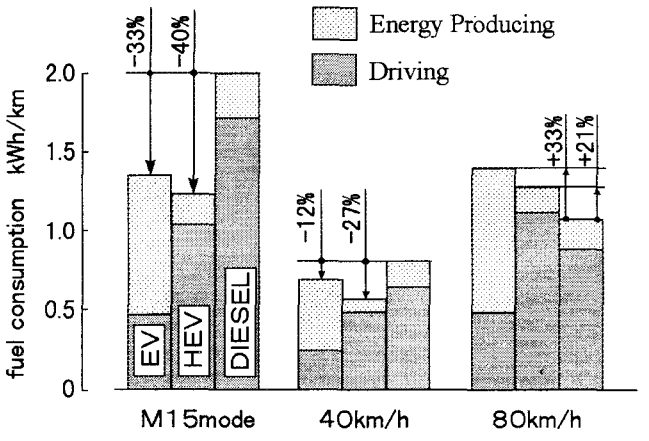


Fig.9. Fuel Consumption

Efficiency and fuel consumption; The EV and HEV are superior to the diesel vehicle in the M15 mode involving acceleration and deceleration because regenerated energy can be collected. In travel at constant velocity, improvement is large at 40 km/h while deteriorated at 80 km/h. This may be because the thermal efficiency of the diesel engine is high at 80 km/h.

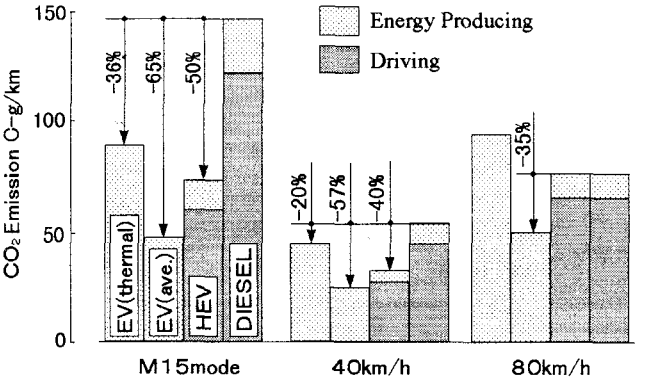


Fig.10. CO_2 Emission

CO_2 emission; The EV and HEV are superior in the M15 mode and constant-speed travel at 40 km/h but in constant-speed travel at 80 km/h, the EV (thermal power generation only) is inferior. Apart from the diesel vehicle, the EV (average power generation) is best, followed by the HEV and then the EV (thermal power generation only) in any drive mode.

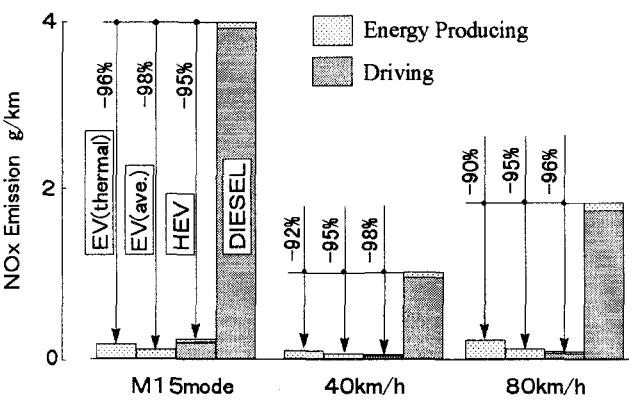


Fig.11. NOx Emission

NOx emission; The EV and HEV are much superior to the diesel vehicle in any drive mode. HEV got large improvement effect by running the LPG engine at constant speed with constant load.

VI. Summary

According to the results of this report, it is verified that EV and HEV show relatively high superiority as energy-saving low-pollution vehicles. In particular, the improvement effect is big during relatively low and middle speed drive involving frequent acceleration and deceleration. In this reason, EV and HEV are most suitable for delivery truck in urban areas. By performance up of power generation unit, battery, regeneration brake, motor and these most suitable control, we are aimed at further raising the efficiency and reducing gas emissions. For environmental improvement, we expect these vehicles to be introduced widely before long.

References

[1] Nobuaki Takeda, Naotake Kumagai, "Development of a HEV for Light-Duty Trucks" EVS-13 (1996-10)

[2] Nobuyuki Iwai, "Study on Efficiency of Hybrid Vehicles"

[3] The Environmental Agency, "A Proposal for a large quantity of Spread of low pollution vehicles"

[4] "Nisseki Technical Review" 1993 vol.35/No3-203

[5] Takeshi Saito "Technical Review and Future Trend of Low-Emission, Alternative Fueled Vehicles in Japan"

Maximum Adhesive Force Control in Super High Speed Train

Yoshiki Ishikawa*

Dept. of Elec. and Comp. Eng.
Yokohama National University
79–5 Tokiwadai, Hodogaya-ku
Yokohama 240 JAPAN
E-mail: * yoshiki@kawalab.dnj.ynu.ac.jp

Atsuo Kawamura**

Dept. of Elec. and Comp. Eng.
Yokohama National University
79–5 Tokiwadai, Hodogaya-ku
Yokohama 240 JAPAN
E-mail: ** kawamura@kawalab.dnj.ynu.ac.jp

Abstract— **When the wheels of the train slip on the rails, the torque is decreased to avoid the continuously slipping condition. It is well known that the coefficient between the wheels and the rails has a peak at a certain slipping velocity. Thus, in this paper, we proposed to estimate the friction force and the derivative by an observer, and the optical slipping velocity is estimated. As a result, the torque is controlled such that the train is driven by the maximum adhesive force.**

I. Introduction

It is well known that the friction coefficient between the wheels and the rails increases a little when the slipping speed between the wheels and the rails increases. However as the slipping speed goes to high, the coefficient now goes down. And also the wet rails on account of raining, misting or frosting lower a friction coefficient compared with the dry rail. The friction coefficient becomes over 0.3 at the dry condition, and it drops to 0.03 at the wet condition. Thus once the wheels start to slip in the acceleration period, for example due to rain, and the torque of the motor is maintained to be constant, the only wheel speed goes to very high, while the train speed is kept at the low speed. This might be called "gross-sliding". To avoid the phenomena the torque control of the motor is required for the maximum adhesion control of the wheel.

II. Simulation Model for One Axis Train

Fig.1. is an illustration of the one axis train model in our simulation and we set up motion equations (1)(2)(3) which are the differential equations for the wheel,the whole train and the relation of the friction between the rail and wheel, respectively.

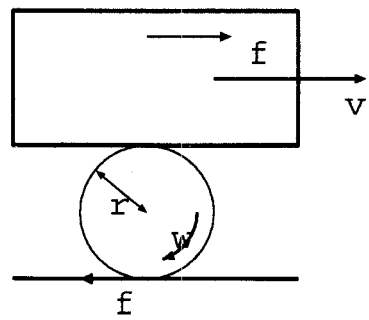


Fig. 1. One Axis Train Model

$$J\frac{dw}{dt} = Te - f \cdot r - b \cdot w \tag{1}$$

$$W\frac{dv}{dt} = f - c \cdot v^2 \tag{2}$$

$$f = \mu \cdot W \cdot g \tag{3}$$

where w is the motor speed, v is the train speed, and f is the adhesive force. Other parameters are shown at Table I

The slip velocity is defined as the absolute value of the difference between the train body velocity and the wheel velocity, as follows.

$$slip = w \cdot r - v \tag{4}$$

A friction coefficient is assumed to be as follows,

$$\mu = c \cdot exp(-a \cdot slip) - d \cdot exp(-b \cdot slip) \tag{5}$$

The parameter a, b, c and d are designed depending on the rail surface conditions.

J	Te	r	b	W	c	g
wheel moment	input torque	wheel radius	viscocity resistance	train weight	aerodynamic coefficient	gravity
37.6		0.5	0.32	20000	0.63	9.8
$[kg \cdot m]$	$[N \cdot m]$	[m]	$[kg \cdot m/sec]$	[kg]	$[m^3/sec^2]$	$[m/sec^2]$

TABLE I
Parameters

a	a	b	c	d
Wet Condition	0.54	1.2	0.29	0.29
Dry Condition	0.54	1.2	1.0	1.0

TABLE II
PARAMETERS FOR FRICTION COEFFICIENT IN (5)

Usually $a < b$. And the parameter is shown TABLE II.

Fig.2 is an illustration of the friction coefficient, and from (3), the driving force f (or adhesive force) is obtained.

III. MAXIMUM ADHESIVE CONTROL

A. The Slip Detector of the Adhesive Force Control

The slip detector judges that the wheel is slipping, if the difference angular velocity or the difference acceleration velocity between the wheel and the train body goes over beyond a certain value.

B. Change of Friction Coefficient

We changed the friction coefficients under the assumption that the train went into the tunnel under a dry condition of the rail. But when it came out from the tunnel, it dropped into slipping because it rained outside the tunnel. We also assumed that the friction had a peak around slip=1.0(km/h) (See Fig.2)

C. Possible Conventional Adhesive Force Control

Once the train wheel slips, the motor torque is lowered to the eight-tenth to avoid the wheels damage (the sticking or the flat). For the duration of 200 [ms] the motor torque is maintained, and again the slip velocity is cheked. The flow chart of the possible conventional method is shown Fig.3.

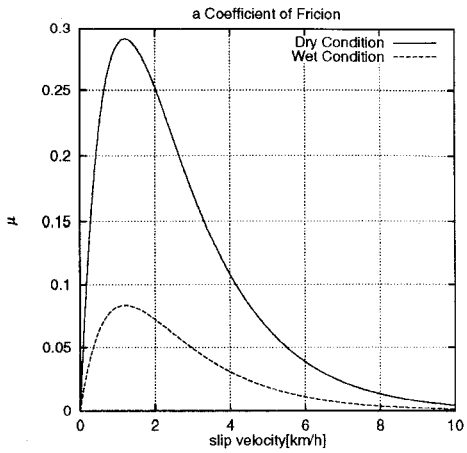


Fig. 2. Coefficient of Friction

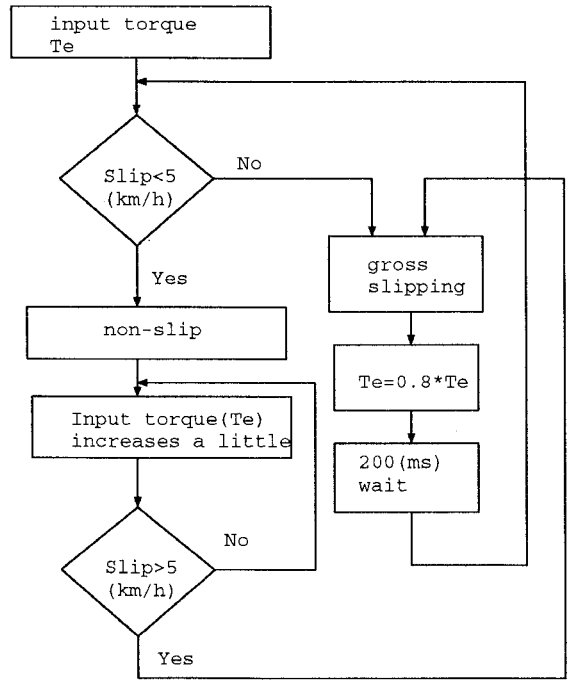


Fig. 3. Flow Chart of Possible Conventional Maximum Adhesive Force Control

D. Proposed Adhesive Force Control

Fig.4 is the block diagram of the proposed adhesive force control. We knew the torque reference (Te) and measure the speed (or the motor speed). Thus the full order observer is designed to estimate the adhesive force ($\hat{f}$) and the derivative of the adhesive force($\hat{f}\prime$). It is assumed that the adhesive force is in the order of one, thus the ramp friction type force will be obtained. The equation is shown in (6)

$$\frac{d}{dt}\begin{bmatrix}\hat{w}\\ \hat{f}\\ \hat{f}\prime\end{bmatrix} = \begin{bmatrix}\frac{1}{j} & \frac{r}{j} & 0\\ 0 & 0 & 1\\ 0 & 0 & 0\end{bmatrix}\begin{bmatrix}\hat{w}\\ \hat{f}\\ \hat{f}\prime\end{bmatrix} + \begin{bmatrix}\frac{1}{j}\\ 0\\ 0\end{bmatrix} Te + \boldsymbol{K}(w-\hat{w}) \qquad (6)$$

The gain K is selected so that the poles of (6) have triple poles at the negative real axis. The slip velocity generator generates the suitable slip refernce so that the maximum adhesive force may be obtain. The algorithm in this block is as follows.

1. if $\frac{df_k}{dslip_k} = 0$, then the slip reference($slip_{ref}$) in the previous sampling priod is maintained.
2. if $\frac{df_k}{dslip_k} \neq 0$, then ${slip_{ref}}^{k+1} = {slip_{ref}}^{k} + \alpha\frac{df_k}{dslip_k}$
3. return to 1,

where α is a constant, and $\frac{df}{dslip}$ is obtained by

$$\frac{df}{dslip} = \frac{df}{dt}\cdot\frac{dt}{dslip} \qquad (7)$$

, and the wheel velocity reference is given as

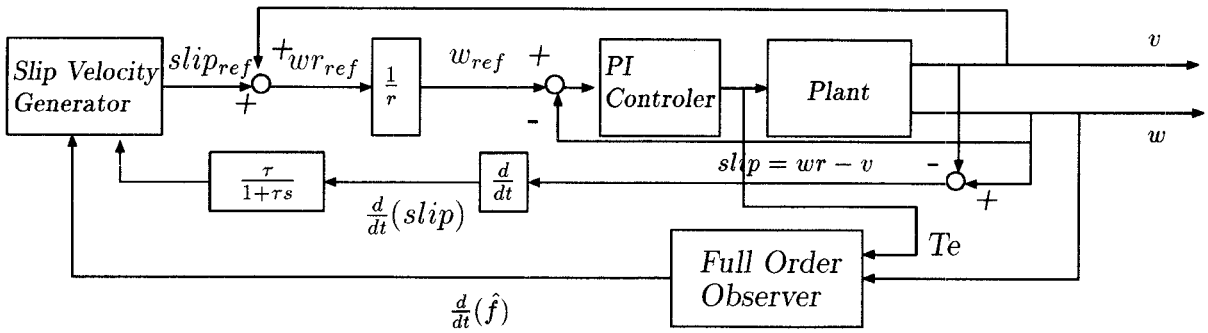


Fig. 4. Block Diagram

$$w_{ref} = \frac{slip_{ref}}{r} + \frac{v}{r} \tag{8}$$

IV. Simulation Results

First the train began to run at $t = 0[s]$ and after $t = 30[s]$ the friction coefficient was changed as shown in Fig.2. In Fig.5, we can find that in the proposal method the slip velocity is around 1[km/h], but in the possible conventional method it is around 1.5[km/h]. Fig.6 and Fig.7 are the illustration of the adhesive force vs slip velocity in the possible conventional method and the proposal method. It is obvious that the adhesive force stays around the maximum point in the proposal algorithm. Second, we changed the friction coefficient at t=30[s] at the same way. But after t=40[s] we changed the friction coefficient as shown in Fig.8. From Fig.9 and Fig.10, it is clear that the adhesive force stays near the peak value in the proposed method.

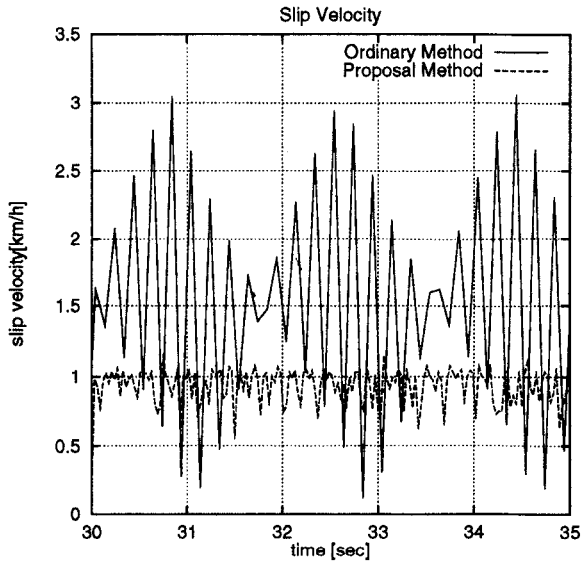


Fig. 5. Comparison of Slip Velocity

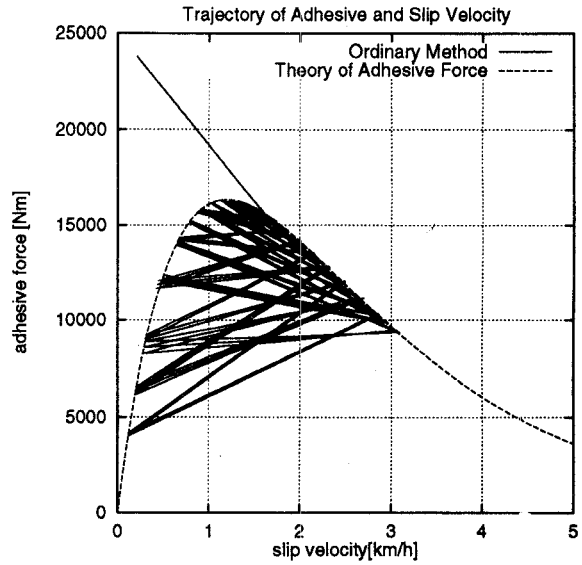


Fig. 6. Trajectory of Adhesive and Slip Velocity(Ordinary Method)

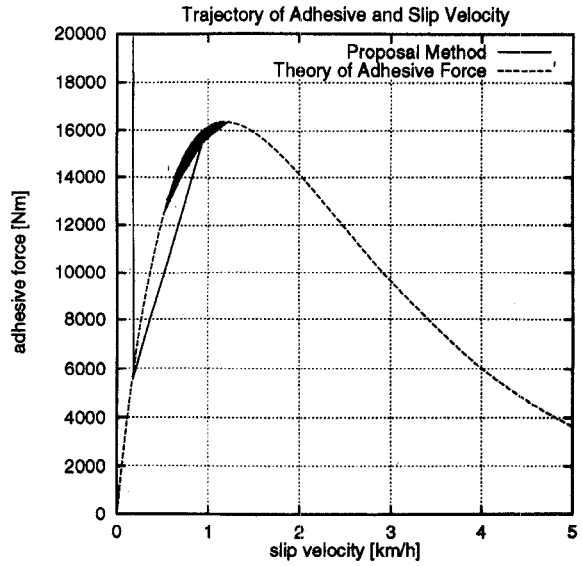


Fig. 7. Trajectory of Adhesive and Slip Velocity(Proposal Method)

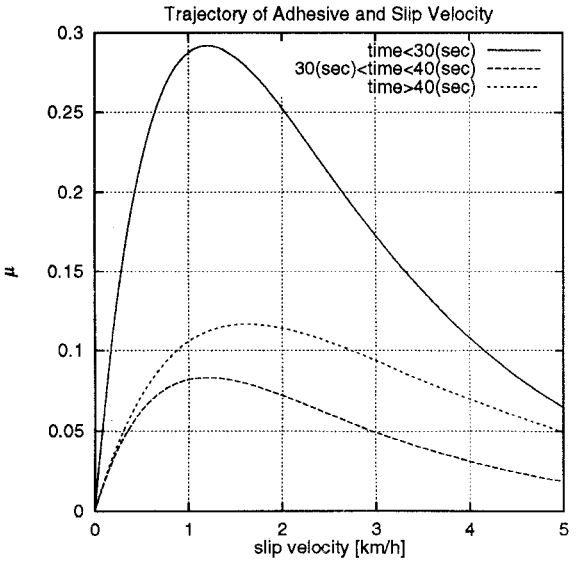


Fig. 8. a coefficient friction

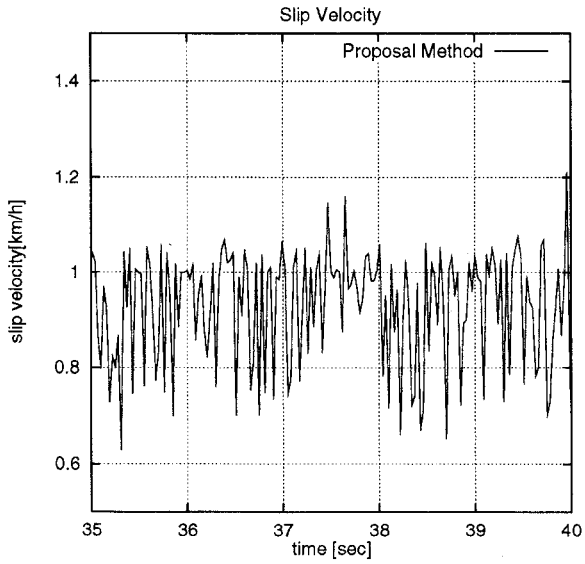


Fig. 9. Comparison of Slip Velocity

V. Conclusion

The adhesive force control for super high speed trains has been investigated and the maximum adhesive control force was achieved even though the friction coefficient changed abruptly. We put the slip velocity generator in front of the PI controller, and applied the steepest gradient method for searching the maximum adhesive force. The simulation results indicate that the adhesive force is maintained around the peak point.
The direct torque control in Fig.4 will be studied in future.

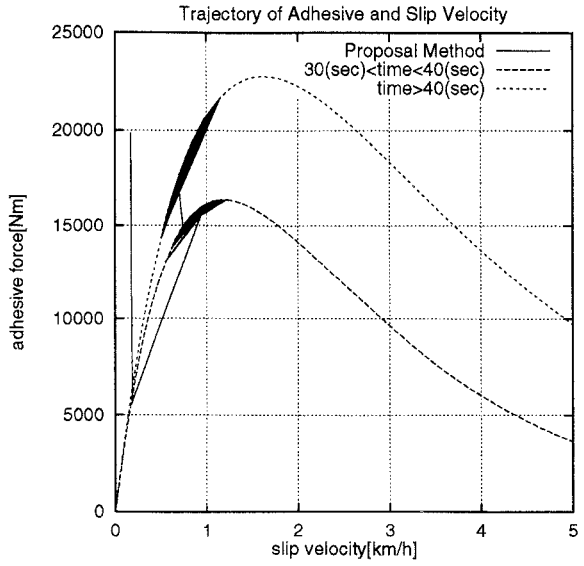


Fig. 10. Trajectory of Adhesive and Slip Velocity(Proposal Method)

References

[1] S. Ohe, T. Watanabe, K. Kawaguchi(Railway Technical Research Institute), Shunji Tamaoki(Hokkaido Railway Company),"Multi-modal anti-skid brake control", No 150, pp635-638,JIASC 1996 (in Japanese) Institute), Shunji Tamaoki(Hokkaido Railway Company),"Multi-modal anti-skid brake control", No 150, pp635-638,JIASC 1996 (in Japanese)

[2] S. Ohe, T. Watanabe(Railway Technical Research Institute), Masanao Sekimoto, Shigeru Nakamura(East Japan Railway Company), "Results of Running Test of Wheel Slip/readhesion Control, using Micro Slip Detection, in Inverter Controlled Electric Motor Vehicle", No 1182, Vol 5, pp325-326, National Convention I.E.E Japan, 1995 (in Japanese)

[3] T. Watanabe, S. Ohe, M. Ogasa(Railway Technical Research Institute), M. Sekimoto, K. Hoshi, S. Nakamura(East Japan Railway Company),"Practical Method Readhesion Control in time of wheel slip/slide for Inverter Controlled Electric Motor Vehicles", National Convention I.E.E Japan, 1995 (in Japanese)

[4] K. Nagase, H. Nakamura, and H. Kobayashi,"Influence of Weather Condition upon Adhesive between Rails and Running Wheels on Main Lines (Results Investigated on JR Nikko Line by Slipping Adhesion Test Truck)", No.89-0490, B, pp 271-276, Transactions of the Japan Society of Mechanical Engineers, May 1990 (in Japanese)

[5] T Hhyama, S Uchida,"Behavior of Traction Force between Wheel and Rail from Microslip to Gross Slipping(Some Experiments under Water Lubrication with Static and Dynamic Contact Loads)", No.93-1721, Vol.60, C, pp206-212, The Japan Society of Mechanical Engineers, June, 1994 (in Japanese)

[6] N Kumagaya(Railway Technical Research Institute), "Break System in Rolling Stocks", Vol.41, pp293-298, , 1996 (in Japanese)

[7] T Tsujimura, H Yasuda (Railway Technical Research Institute), "Friction Materials for Rolling Stock Brakes", Vol.41, pp299-304, , 1996 (in Japanese)

Compensation of Voltage Drop Using Static Var Compensator at Sectioning Post in AC Electric Railway System

Keiji KAWAHARA, Shin-ichi HASE, Yoshifumi MOCHINAGA, Yasuji HISAMIZU
Railway Technical Research Institute
2-8-38, Hikari-cho, Kokubunji city, Tokyo 185, JAPAN
Fax: +81-425-73-7388, Phone: +81-425-73-7334
E-mail: kkawa@rtri.or.jp

Takashi INOUE
West Japan Railway Company
2-4-24, Shibata, Kita-ku, Osaka city, Osaka 530, JAPAN
Fax: +81-6-376-6079 Phone: +81-6-375-8963

Abstract—**In this paper, the authors describe the application of SVC(Static Var Compensator) to AC electric railway system, outlines SVC installed at Shin-syo sectioning post on San-yo Shinkansen and report on the result of verifiable site investigations.**

Single-phase SVC can reduce the voltage drop in the feeding circuit and improve the power factor at substation by compensating the reactive power.

In the case of compensating the voltage drop, it is more effective to locate SVC at sectioning post than at substation.

The site investigation has revealed that SVC can reliably suppress the voltage drop.

I. Introduction

In Japan, AC electric railway system with single phase and commercial frequency is adopted on main lines such as Shinkansen. The allowance range of feeding voltage is 22.5 ~ 30kV for Shinkansen and 16 ~ 22kV for narrow-gauge lines.

In recent years, the service load tends to increase with an increased operation of trains, an increased speed and multiplied power. As the load capacity of train becomes larger, reactive power of load causes a larger voltage drop. It is feared that the feeding voltage would drop below lower bound of above-mentioned range.

The voltage drop used to be compensated by canceling the reactance of the feeding transformer using series capacitors or by controlling tap-changing system of step-up transformer using thyristors, which is called AC line voltage regulator , ACVR for short.

With advance of power electronics technology, nowadays the voltage drop in a feeding line and the voltage fluctuation in 3-phase side can be reduced, and the power factor at substation can be improved by compensating the reactive power using a single-phase static var compensator , SVC for short.

In the case of compensating the voltage drop over AC feeding system, SVC should be located at sectioning post, that is at the end of feeding circuit. The capacity of SVC can be reduced to half by locating it at sectioning post instead of at substation.

There are some control methods for SVC. One is continuous control using combination of fixed capacitors with a thyristor-controlled reactor, TCR[1] for short. The other is stepwise control using a thyristor-switched capacitor, TSC[2][3] for short. Each method with its own characteristics is used properly considering the actual situation of line sections.

This paper describes the principle of the voltage compensation using SVC, outlines SVC with TSC installed in West Japan Railway Company's Shin-syo sectioning post and summarizes the results of a site investigation.

II. Principle of Voltage Compensation Using SVC at Sectioning Post

A. Principle of voltage compensation using SVC

The voltage drop occurs at the load point due to a load current through the impedance ($Z=R+jX$) of feeding circuit as shown in Fig.1.

Vector diagrams of compensation using SVC are given in Fig.2. The voltage drop ratio $\varepsilon(\%)$ is expressed as follows.

$$\varepsilon = \frac{V_0 - V_R}{V_0} \times 100 \tag{1}$$

where V_0 represents the voltage at the load point without load current and, V_R, with load current. When the phase angle between V_0 and V_R is very small, (1) is rewritten as follows.

$$\begin{aligned} \varepsilon &= \frac{I_L \times Z}{V_0} \times \cos(\theta - \gamma) \times 100 \\ &= \frac{I_L \times Z}{V_0} \times (\cos\gamma\cos\theta + \sin\gamma\sin\theta) \times 100 \\ &= \frac{1}{V_0^2} \times (P_L R + Q_L X) \times 100 \end{aligned} \tag{2}$$

where
$$\begin{cases} Z = \sqrt{R^2 + X^2} \\ \gamma = \tan^{-1}\dfrac{X}{R} \\ P_L = V_0 I_L \cos\theta \\ Q_L = V_0 I_L \sin\theta \end{cases}$$

where Z represents absolute value of line impedance; R, resistance component; X, reactance component; and, P_L, active power.

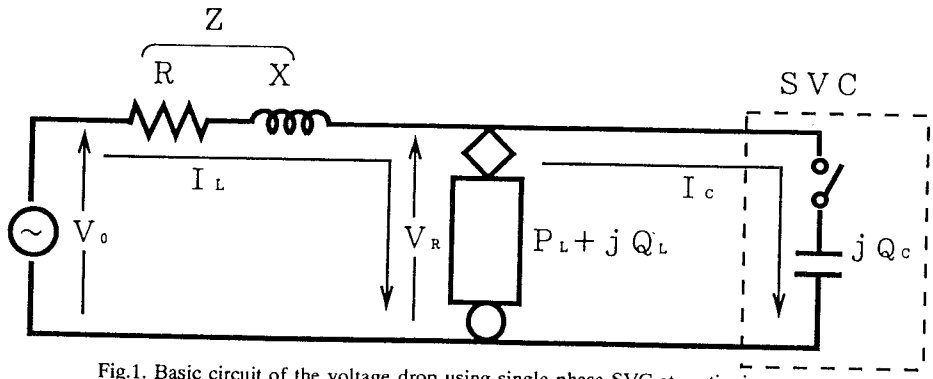
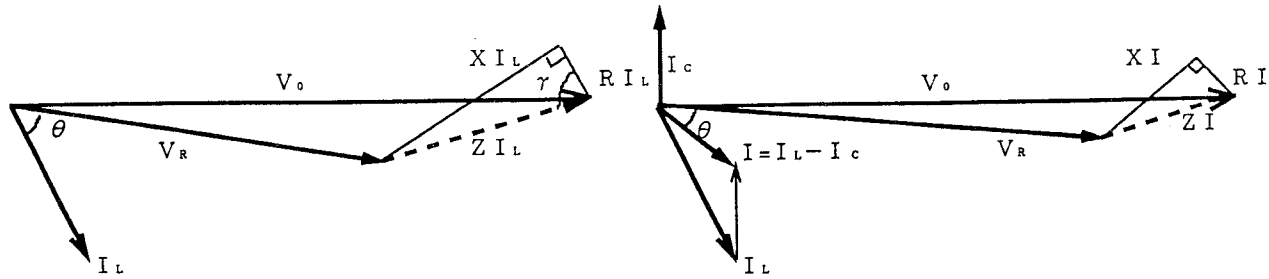


Fig.1. Basic circuit of the voltage drop using single-phase SVC at sectioning post



(a) Vector diagram before compensation using SVC

(b) Vector diagram after compensation using SVC

Fig 2. Principle of voltage compensation using SVC

TABLE I

COMPARISON BETWEEN TSC AND TCR

	TSC	TCR
Method of control	Stepwise	Continuous
Withstand voltage of thyristor	Double SVC voltage	SVC voltage
Power losses under nocompensation	None	Large
Generation of harmonics	None	Much
Volume of equipment	Capacitor	Capacitor + Reactor

TABLE II

CONDITIONS OF CALCULATION

Impedance of power source	j 0.36 Ω
Impedance of feeding transformer	0.09+j1.55 Ω
Impedance of feeding circuit	0.19 Ω/km∠76°
Feeding distance	25 km

R and X are determined by the feeding circuit, P_L is determined uniquely by the load. Thus we can control the reactive power Q_L to suppress the voltage drop. When SVC at sectioning post generates reactive power Q_C, (2) is rewritten as follows.

$$\varepsilon = \frac{1}{V_0^2} \times \{P_L R + (Q_L - Q_C) X\} \times 100 \quad (3)$$

When SVC generates reactive power Q_C expressed by (4), the voltage drop at the load point becomes zero theoretically.

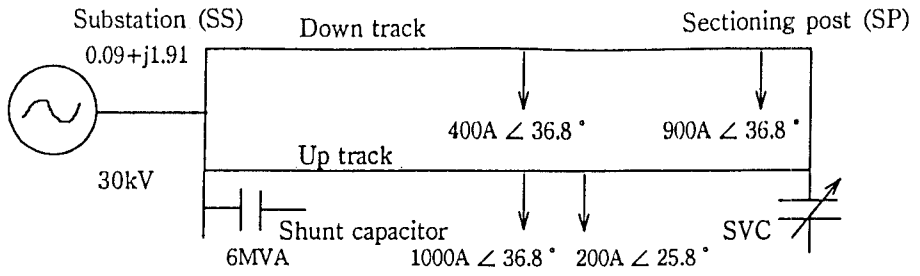
$$Q_C = Q_L + \frac{R}{X} P_L \quad (4)$$

B. Comparison between TSC and TCR

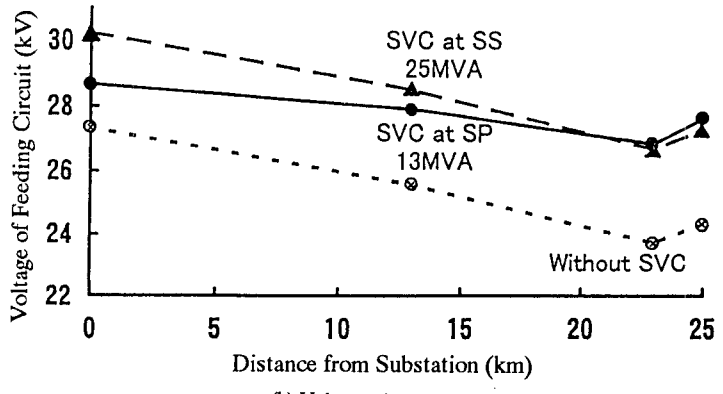
Table I shows comparison between TSC and TCR. Each method with its own characteristics is adopted properly considering the actual situation of line sections.

III. LOCATION AND CAPACITY OF SVC

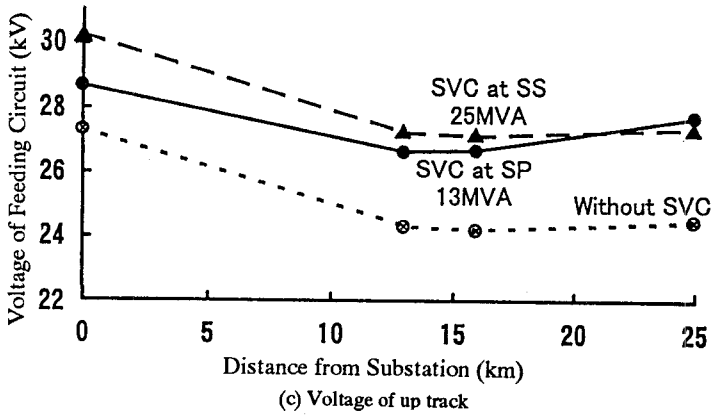
Fig.3 illustrates calculation results of the voltage at load point. Calculation model is San-yo Shinkansen. Table II shows parameters used in calculation.



(a) Feeding system and loads



(b) Voltage of down track



(c) Voltage of up track

Fig.3. Distribution of voltage

SVC at sectioning post can compensate the voltage over the feeding circuit equally. To keep the feeding voltage over 27kV, the rated capacity of SVC at substation needs to be at least 25MVA. On the other hand, SVC at sectioning post needs only 13MVA. Therefore it is confirmed that the capacity of SVC can be reduced to half by locating it at sectioning post unlike the case at substation.

IV. Outline of SVC at Sectioning Post

A. Configuration of SVC

Fig.4 shows an overview of SVC with TSC method installed at Shin-syo sectioning post on San-yo Shinkansen.

The electrification of San-yo Shinkansen between Shin-Osaka and Hakata is under AT (auto-transformer) feeding system.

As shown in Fig.5, the SVC is connected between the contact wire and the rail. The SVC compensates the voltage drop by applying two banks of capacitors in order. The capacity of compensation is 15MVA in the direction of Hakata and 20 MVA in the direction of Shin-Osaka. Because train load in the direction of Shin-Osaka is heavier than in the direction of Hakata.

Table III shows the specification of SVC.

The high impedance transformer performs the function of suppressing the transient phenomena and fixing its reactance such that resonance of the third higher harmonic current from train load does not spread into the feeding circuit. It also has the function to reduce the voltage in secondary side, considering the withstand voltage of thyristors.

The cooling system for thyristors adopts the demineralized water method. The power source for the cooling system uses 3-phase power transformed from single-phase power of the feeding circuit by the converter.

A connection diagram of the SVC is shown in Fig.6. The SVC detects the fluctuation of the feeding voltage using the voltage sensor and operates thyristor switches by the gate circuit.

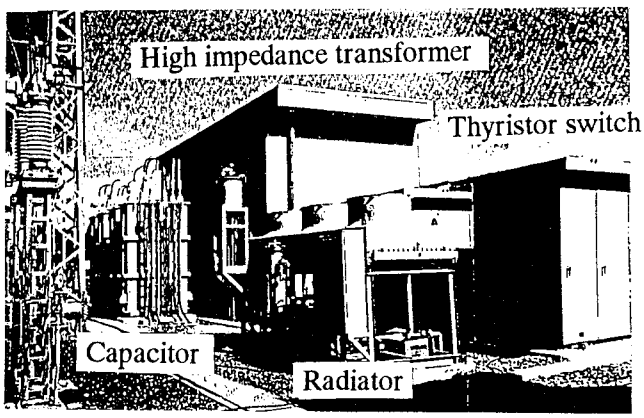


Fig.4. Overview of SVC

TABLE III

SPECIFICATION OF SVC

Transformer for thyristor

Number of phases	Single phase
Frequency	60 Hz
Rated primary voltage	30 kV
Rated secondary voltage	5.5 kV/5.5kV
Rated capacity	20/10/10 MVA
Impedance voltage	15%

Capacitor bank and thyristor

Number of phases	Single phase
Frequency	60 Hz
Circuit voltage	5000 V
Circuit current	2000 A
Capacity	11.5 MVA
L/C	15%
Withstand voltage of a thyristor	4000 V
Connection of thyristor	9S1P×2G

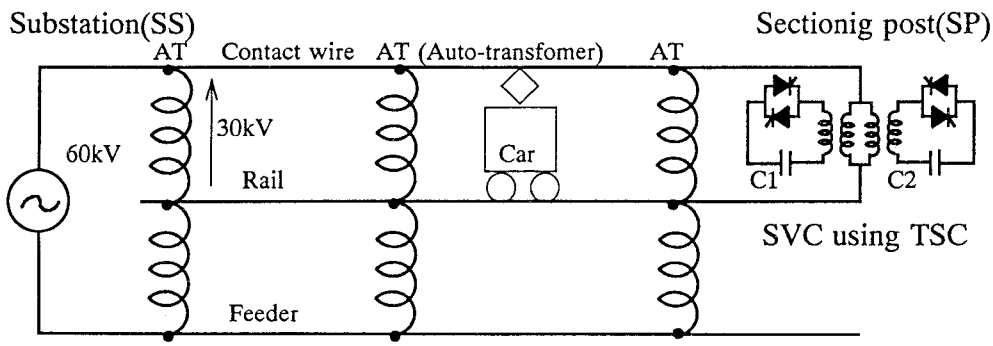


Fig.5. AT feeding system using SVC at sectioning post

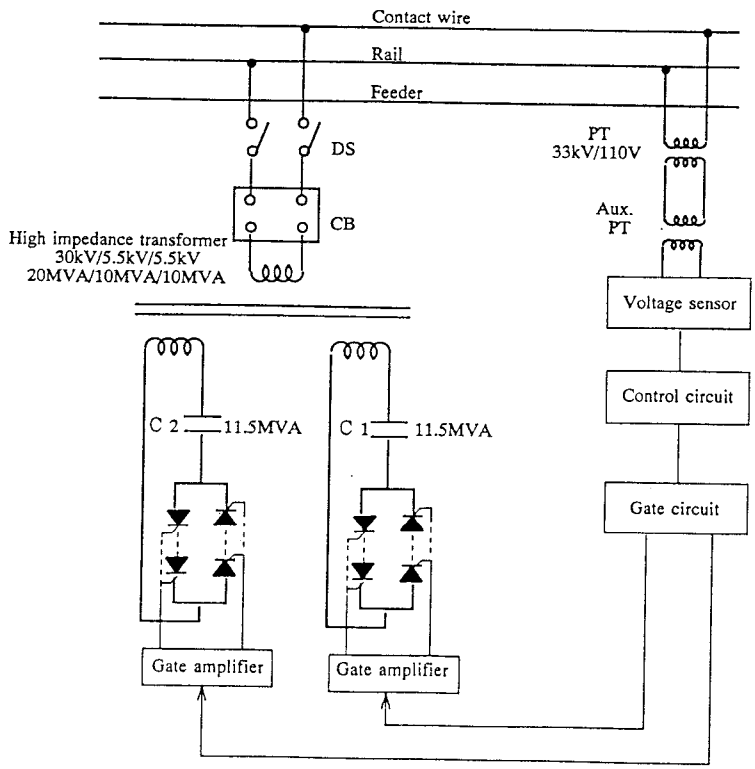


Fig.6. SVC using TSC

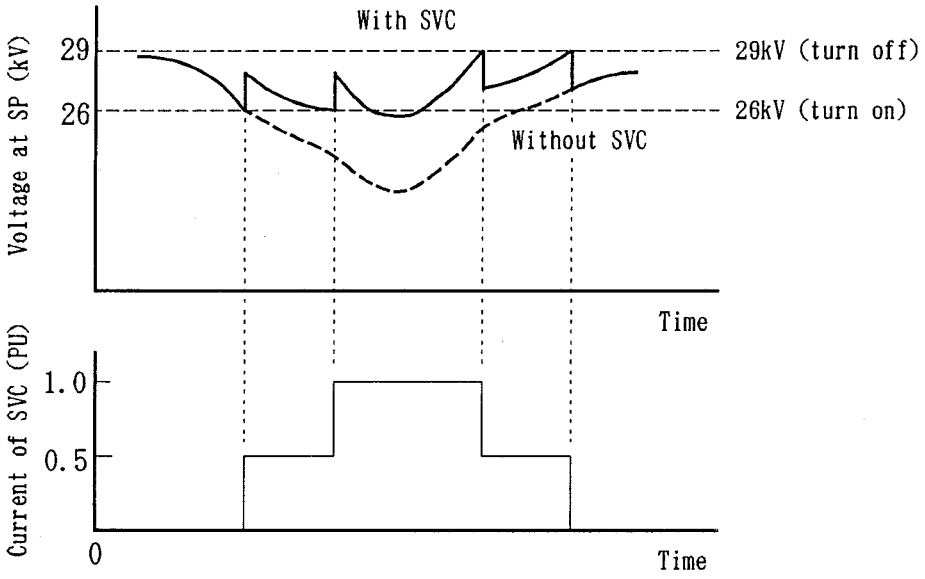


Fig.7. Outline of voltage compensation using SVC

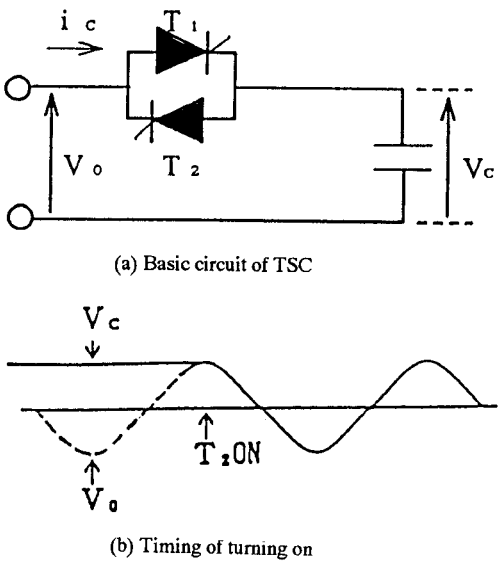


Fig.8. Charging maximum voltage method using SVC

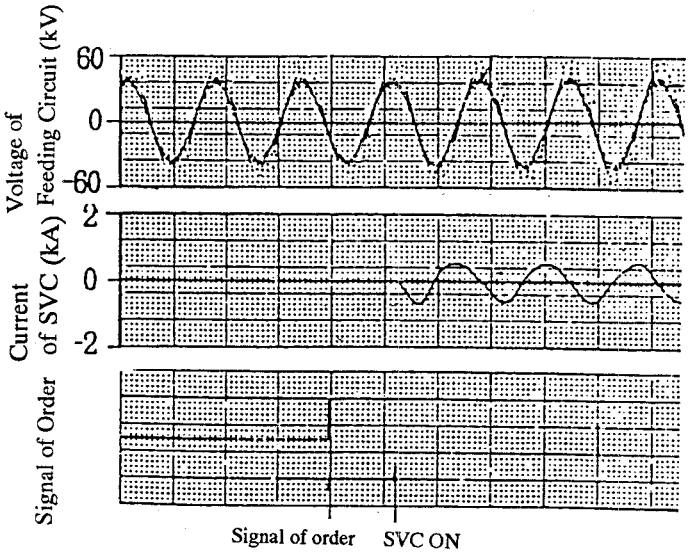


Fig.9. Feeding voltage and current of SVC turning on

When the feeding voltage drops below the set point(26kV in Fig.7), capacitor(C1) is turned on. When the feeding voltage drops under the setting point again, capacitor(C2) is turned on, too. Then, when the feeding voltage restores to the set point to turn off(29kV in Fig7), the capacitor is turned off.

As shown in Fig.8, the capacitor of SVC is always charged to be equal to the maximum value of feeding voltage by applying thyristor(T1) as a diode, to prevent the transient phenomena when the SVC is turned on.

B. Cooperation with feeding circuit and protecting system

1) Cooperation with feeding circuit: Because SVC the detects the fluctuation of the feeding voltage using the voltage sensor, there is a possibility that the SVC is turned on by a transition voltage drop when a fault should occur in the feeding circuit or a train load approaches feeding area with the SVC from adjoining feeding area. As shown in Fig.9, after detecting the voltage drop, the SVC is turned on about 100ms later. If a fault should occur on the feeding circuit with SVC turned on, the SVC, located at sectioning post that is at the end of feeding circuit, is turned off at once after an accident happens.

2) Cooperation with protecting system: When the capacity of SVC is large, a fault locator using AT neutral current accurately measures the location of the fault by AT neutral current in consideration of SVC current.

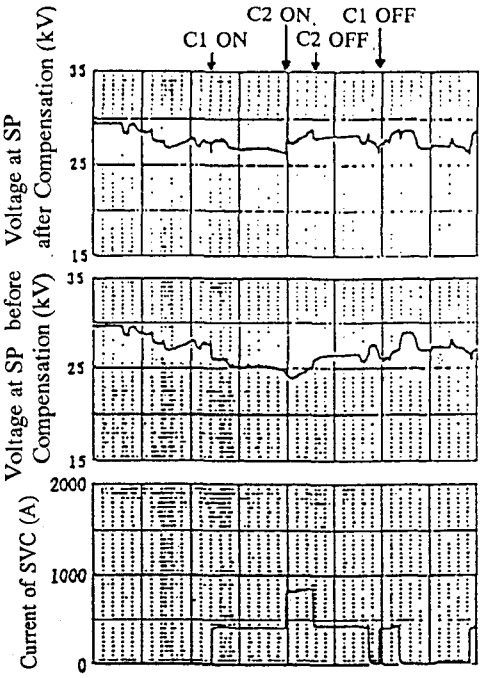


Fig.10. Oscillogram of voltage at SP before and after compensation using SVC

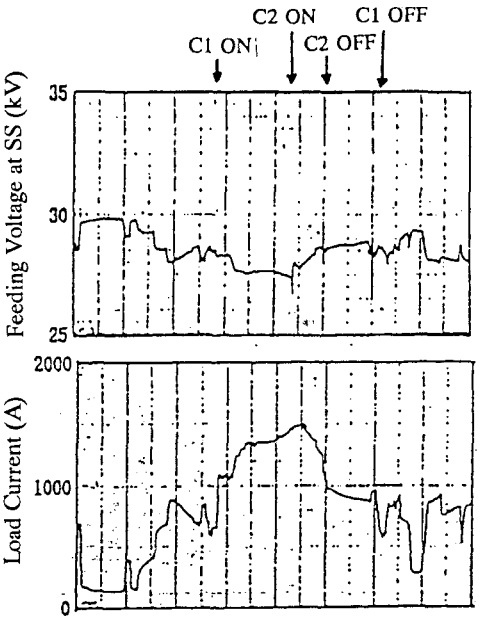


Fig.11. Oscillogram of voltage and load current at SS

V. Result of Measurements at Actual Loads

A. Effect of compensation using SVC at sectioning post

Fig.10 shows an oscillogram of the feeding voltage at Sin-syo sectioning post before and after the compensation, and Fig.11 shows an oscillogram of the feeding voltage and load current at the substation. When the voltage in the feeding line got below the set point 26kV and over 29kV, the SVC was turned on and off respectively. It is seen that the SVC as a bank can rise about 1.5kV by compensating the reactive power.

B. Load zone measuring at substation

Fig.12 shows the load zone in resistance－reactance(R－X) plane of trains with SVC measuring at substation. It is confirmed from this figure that the power-factor angle of trains is about 30～45 degrees without SVC, but the power factor is improved with SVC.

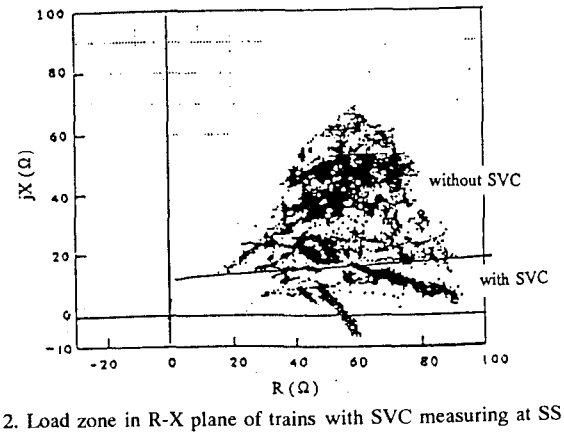


Fig.12. Load zone in R-X plane of trains with SVC measuring at SS

VI. Conclusions

In compensating the voltage drop in AC feeding system using SVC, it is more effective to locate SVC at sectioning post than at substation.

The verifiable site tests of the SVC with TSC at Shin-syo sectioning post on San-yo Shinkansen have revealed that the SVC can reliably suppress the voltage drop in the feeding circuit. It is noted that the compensation of the voltage drop using SVC at sectioning post contributes to improvement of load power-factor and reduction of absolute value of load current.

VII. Acknowledgment

The author would like to express his gratitude for the guidance and encouragement received from colleagues who carried out much of the experimental and constructional work.

References

[1] Y.Mochinaga and M.Kayama, "Practical Use of SVC in AC Electric Railway ", Transactions of IEE Japan, Vol.113-D, No.10, pp.1228, 1993

[2] Y.Mochinaga,:et.al, "Countermeasure for Voltage Drop using SVC at SP in San-yo Shinkansen", IEE Japan, Papers of technical meeting on transportation and electric railway, TER-93-35, pp.31-40, 1993

[3] Y.Mochinaga,:et.al, "Countermeasure for Voltage Drop using SVC at SP in Kagoshima narrow-gauge line", National convention of IEE Japan, 1073, pp.8-209, 1993

Optimal Formation of Trainsets

Satoru Ito
Rolling Stock Development Center
Hitachi, Ltd. Mito Works
Ichige 1070, Hitachinaka-shi
Ibaraki-ken, 312 JAPAN
Tel.: +81-29-276-6663, Fax: +81-29-276-6662
e-mail: Ito@cm.mito.hitachi.co.jp

Klemens Heumann, Prof. Dr.-Ing.
Institut für Meß- und Automatisierungstechnik
Technische Universität Berlin
Sekr. E2, Einsteinufer 19
D-10587 Berlin, Germany
Tel.: +49-30-314-25855, Fax: +49-30-314-25717

Abstract - **In this paper, the authors identify the optimal formation of a high-speed train, considering mainly weight, axle load and adhesion utility, which are important indices for trainset formation. Trainset models are constructed based on data collected worldwide for major high-speed trains and high-performance locomotives, and formations are clarified that can reduce the indices. The method and the results will be useful when basic specifications of high-speed trains are being set.**

I. Introduction

Worldwide, many kinds of trainset formations are in use. Some are hauled by a locomotive, some have power units at each end, and some are EMUs (electric multiple units) with distributed traction motors. Though the question has been often asked which train formation is appropriate, it has not been fully answered yet. In this paper, the authors consider the question again, mainly for high-speed trains and from the viewpoint of an electric traction system.

An evaluation method of trainset models, which are based on train data collected in Europe and Japan, and the characteristics obtained through the evaluation are described. Then the formations and numbers of traction units are clarified that can reduce weight, axle load and adhesion utility. Finally, the optimal formation is compared with formation of actual high-speed trains.

II. Definitions of Indices for Trainset Model Evaluation

In the following, indices, codes and words used in this study are defined.

A. Train Performance

The train performance index T_{ea} is calculated as follows:

$$T_{ea} = \int_0^{v_{max}} F_{dd}(v)dv \quad [\text{MNkm/h}] \tag{1}$$

where

- v train speed [km/h],
- v_{max} train maximum speed [km/h],
- F_{dd} tractive effort [kN].

The rated power is not used to represent the performance of trains in this paper. Because of the difference in definitions of rated powers in Europe and Japan, and the difference in tractive effort profiles of each train [1]-[5], it can not be used for a fair comparison.

B. Adhesion Utility

The adhesion utility index (*Traktionswert* [6]) T_w is used to compare adhesion utility of trains:

$$T_w = \frac{\int_0^{v_{max}} F_{dd}(v)dv}{W_r g \int_0^{v_{max}} u(v)dv} \tag{2}$$

where

- W_r adhesion weight of the train (= sum of driving axle loads) [t],
- g gravity acceleration,
- $u(v)$ adhesion coefficient [7], $u(v) = 0.161 + \frac{7.5}{v+44}$.

C. Structures of Electric Tractive Equipment and Traction Unit

In order to represent structures of transformers, power converters and motors in a traction unit easily, the electric tractive system structure code *Cet* is defined as follows:

$$C_{et}=[N_{tr} \quad N_{pcs} \quad N_{tm}] \tag{3}$$

where

- N_{tr} number of transformers in a traction unit (normally =1),
- N_{pcs} number of power converters connected to one transformer,
- N_{tm} number of traction motors connected to one power converter.

Similarly, the traction unit structure code *Ctu* is defined which can describe the structure and the assignment of apparatuses in a traction unit:

$$C_{tu} = \begin{bmatrix} n_{tr1} & n_{pcs1} & n_{tm1} \\ n_{tr2} & n_{pcs2} & n_{tm2} \\ & \cdots & \end{bmatrix} \tag{4}$$

where

- n_{tri} number of transformers on car No. i,

n_{pcsi} number of power converters on car No. i,
n_{tmi} number of traction motors on car No. i.

D. *Train Rolling Resistance*

Sauthoff's formula is used here to calculate the train rolling resistance:

$$R_L = [1 + 0.0025 \cdot v + 0.70 \frac{n_w + 2.7}{W} (\frac{v + 15}{10})^2] g \frac{W}{1000} \quad (5)$$

where
R_L train rolling resistance (kN),
n_w number of cars,
W train mass (t).

E. *Number of Traction Unit*

The number of traction units in a train is referred as N_{tu}. A traction unit is defined as the smallest group of cars which can run from the viewpoint of the electric tractive system. An example traction unit is shown in Fig. 1 when $C_{et} = [1\ 2\ 4]$ and $C_{tu} = \begin{bmatrix} 1 & 1 & 4 \\ 0 & 1 & 4 \end{bmatrix}$.

III. Evaluation Method of Trainset Model

A. *Basic Specifications of Trainset Model*

Basic specifications of trainset models are shown in Table I. They are decided so that they well represent typical high-speed trains in this paper. When a train under some specific conditions is of interest, the table can be changed accordingly.

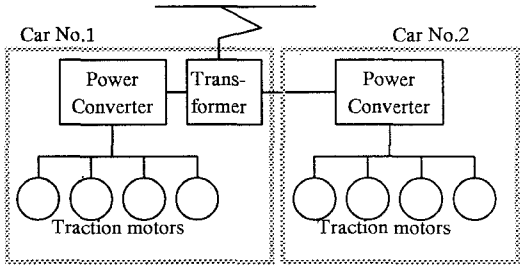


Fig.1. Example traction unit ($C_{et} = [1\ 2\ 4]$ and $C_{tu} = \begin{bmatrix} 1 & 1 & 4 \\ 0 & 1 & 4 \end{bmatrix}$)

TABLE I
BASIC SPECIFICATIONS OF TRAINSET MODEL

Supply voltage	AC commercial frequency
Power converter	GTO power converter
Max. speed	100 - 350 km/h
Car length	25m
Train length	400m (16 cars)
Car weight	45t/car (except electric traction system)

B. *Relations of Weight and Performance*

Based on collected data of trains, data of weight vs. performance of transformers, power converters and traction motors are plotted. Then, the relations between weight and performance are obtained.

Fig.2 shows data for transformers. Each point corresponds to a transformer. The performance-weight characteristics are derived as a combination of linear equations, for easier handling using spread sheet software.

The following performance-weight characteristics of transformers, power converters, and traction motors are obtained from the collected train data:

$$W_{tr} = \min(2.42e^{-5} \cdot P_{tr} + 2.38,\ 1.07e^{-4} \cdot P_{tr} + 1.99,\ 4.01e^{-4} \cdot P_{tr} - 6.06) \quad (6)$$

$$W_{pcs} = \min(3.58e^{-5} \cdot P_{pcs} + 2.08,\ 3.24e^{-4} \cdot P_{pcs} - 2.10) \quad (7)$$

$$W_{tm} = \min(1.07e^{-4} \cdot P_{tm} + 0.164,\ 2.44e^{-4} \cdot P_{tm} - 0.25,\ 3.82e^{-4} \cdot P_{tm} - 1.52) \quad (8)$$

where
W_{tr}, W_{pcs}, W_{tm} weight of a transformer, power converter, and traction motor,
P_{tr}, P_{pcs}, P_{tm} performance per transformer, power converter, and traction motor,
min(X, Y, Z, ...) a function which gives the minimum of the values.

C. *Train Performance*

Taking the maximum speed as a parameter, a tractive effort profile is decided so that it balances at the maximum speed. Then the train performance index can be derived using equation (1).

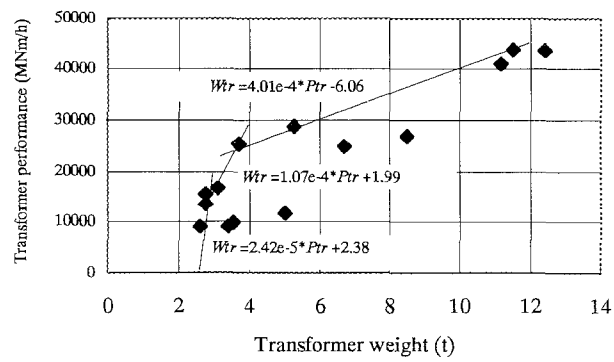


Fig.2. Performance vs. weight of transformers

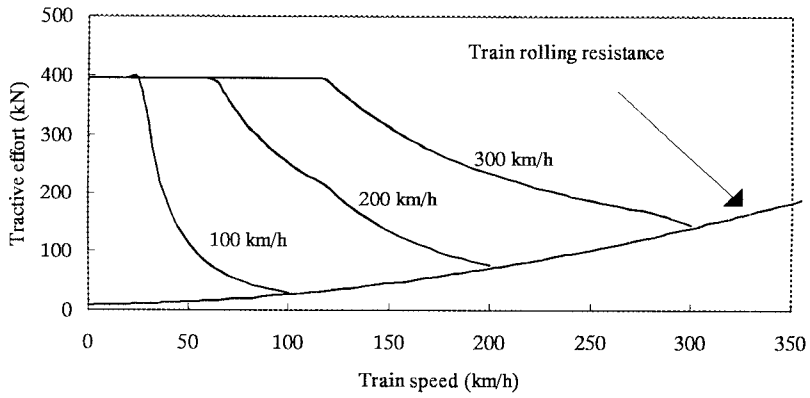


Fig.3. Example tractive effort profiles

Example tractive effort profiles with maximum speeds of 100, 200, and 300 km/h are shown in Fig. 3. Their train performance indices are 18,500, 51,300, and 85,500, respectively.

D. Structure of Trainset

Having derived a train performance index, the structure of the electric tractive system in a train is taken as the parameters: the number of traction units in a train N_{tu}, the electric tractive system structure C_{et}, and the traction unit structure C_{tu}. The total number in a train of transformers, power converters, and traction motors can be obtained by multiplying N_{tu} and C_{et},. Performance of each apparatus can be calculated by dividing train performance index by the respective total numbers. Then the performance-weight characteristics of equations (6) - (8) are used to derive weights of each apparatus.

E. Weight, Axle Load and Adhesion Utility

The weight of the electric tractive system is derived as the sum of weights of each apparatus.

The traction unit structure C_{tu} is to calculate weight of each car and then axle load. Finally, adhesion utility index can be derived using equation (2).

IV. Results of Trainset Model Evaluation

A. Characteristics Obtained through Trainset Model Evaluation

Figs. 4 - 6 show the characteristics diagrams of electric tractive system weight, axle load and adhesion utility at the train performance of 100,000 MNm/h (= that at the maximum speed of 350 km/h).

The curves of weight characteristics in Fig. 4 look like the letter "v" and the minimum is located at N_{tu}=4 when C_{et}=[1 2 4].

As shown in Fig. 5, the larger the number of traction units N_{tu} is, the lower the axle load becomes. However, the reduction is almost saturated when N_{tu} is larger than about 6. Generally, a heavy axle load results when a transformer and a power converter are installed on a car at the same time, and it is better to avoid this. Sometimes it costs about a 100 % increase of the weight to reduce the axle load by only 1 t in this region.

The adhesion utility index T_w at larger N_{tu} in Fig. 6 tends to be lower, which means slips and slides are expected less frequently. However, values of some existing trains are more than 1.0 with appropriate adhesion controls. There is no benefit gained in reducing the adhesion utility index T_w too much.

Fig. 7 shows the numbers of transformers, power converters, and motors vs. the train performance when they give the minimum weight, while Fig. 8 shows their performances. Here, the number of transformers equals the number of traction units N_{tu} . For weight reduction, at most four traction units in a trains are suitable.

Similarly, Figs. 9 and 10 show the numbers and performance when the minimum axle load is given. The number of traction units which gives the minimum axle load tends to be larger than the number when the minimum weight is given.

According to Figs. 8 and 10, the weights of the transformer, power converter and traction motor when they give the minimum weight or axle load do not depend on the train performance very much. This suggests the possibility that combinations of a few kinds of pre-designed traction equipment, for example power converters, should suffice rather than individual designs for each train. This would result in higher reliability and easier maintenance because of compatibility of the parts.

B. Guidelines Derived from the Evaluation

(1) A moderately distributed traction system with at most four traction units results in weight reduction.

(2) In order to reduce the axle load, a transformer should be installed in a car in which a power converter is not installed.

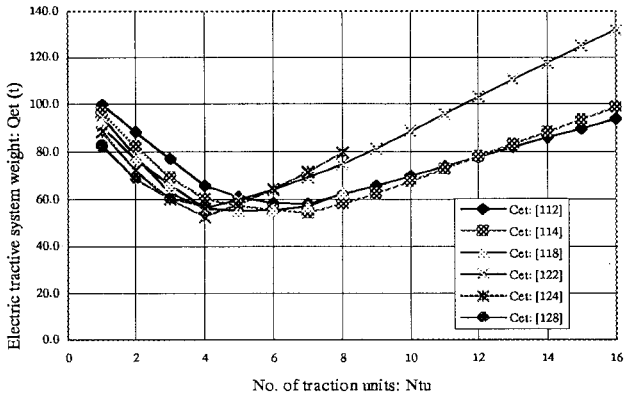


Fig. 4. Electric Tractive System Weight

(Tea=100,000 MNm/h)

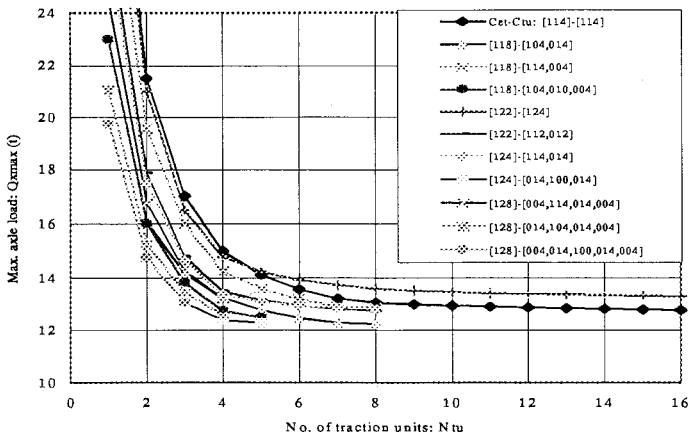


Fig. 5. Axle Load

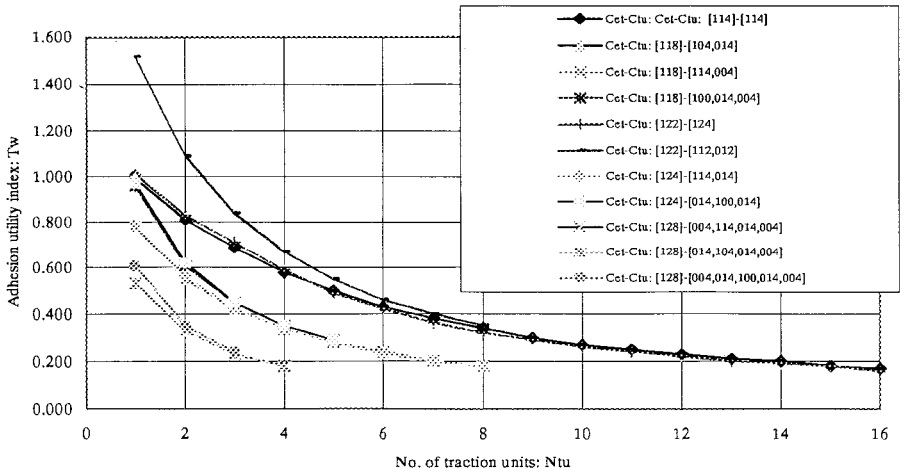


Fig. 6. Adhesion Utility Index

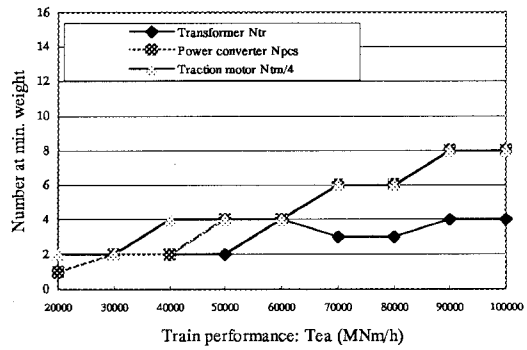


Fig. 7. Number of Each Apparatus at Min. Weight

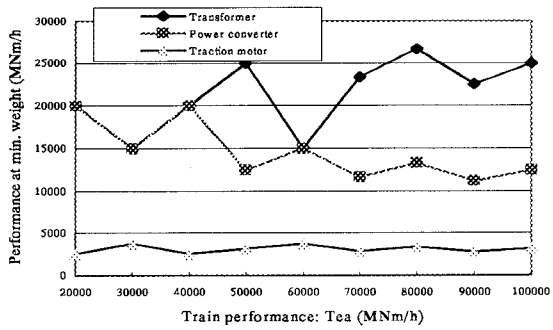


Fig. 8. Performance of Each Apparatus at Min. Weight.

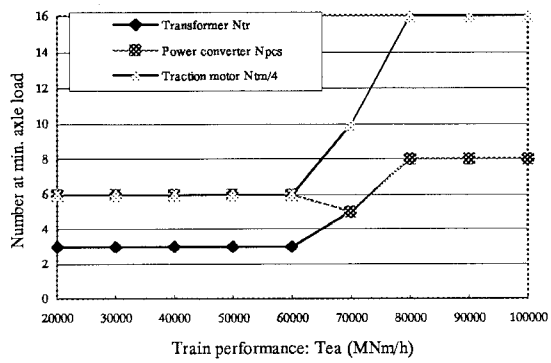


Fig. 9. Number of Each Apparatus at Min. Axle Load

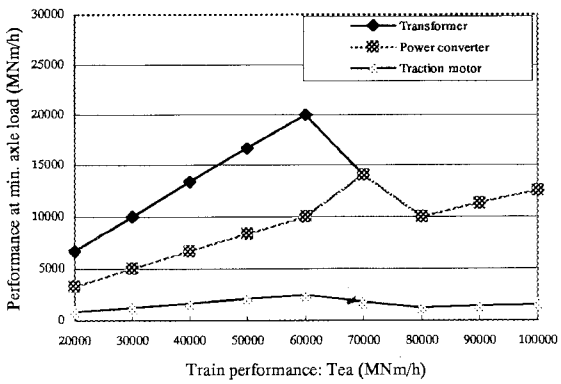


Fig. 10. Performance of Each Apparatus at Min. Axle Load

(3) The larger the numbers of traction units and driven axles become, the lower the adhesion utility index becomes, which results in lower possibility of slip and slide.

The number of traction units N_{tu} plays a more important role than the number of motor cars. Therefore, it should be carefully decided. For example, the larger the number of traction units is, the lower the axle load and the adhesion utility index become. However, it should be noted that this is an issue of trading-off with the increase of total weight.

V. Conclusion

In this paper, the method to identify the optimal formation of high speed trains and results of the trainset model evaluation were described. The numbers of traction units, power converters, and traction motors may be slightly modified in a practical application, so that they fit indices like cost, reliability, flexibility of formations, etc. which are also important but were not considered in this study.

As the results showed, a moderately distributed traction system is the optimal formation for high-speed trains at present and in the near future. Centralized as well as too-distributed traction systems will become less popular as formations of high-speed trains. In fact, the formations of high-speed trains developed in the last few years are getting closer to the moderately distributed traction system described in this paper. The French TGV-A, German ICE-3 [8], and Japanese Shinkansen E1 [9] are good examples of this. As shown in Table II, their formations agreed with the optimal formation when they were converted to a 400 m long train.

Acknowledgments

The authors are grateful to the personnel of the railway companies and the manufacturers in Europe and Japan for helping them to collect the train data and providing kind and informative advice.

The authors are also grateful to their colleagues at TU Berlin and Hitachi, whose kind support helped them to finish this work successfully.

References

[1] B. Hartmann "Die Triebkopfe des InterCityExpress," *Elektrische Bahnen* Vol. 89 No. 5, pp.131-146, May 1991

[2] S. Ishikawa "Shinkansen-Triebzüge Serie 300 "Nozomi"," *Elektrische Bahnen* Vol. 92 No. 8, pp.223-228, August 1994

[3] G. Petit "TGV A La maîrise du 300 km/h," *Revue Généale des Chemins de Fer* Vol.110 No. 10, pp.29-35, October 1991

[4] F. Jonard "Die Geschiwindigkeitssteuerung und der im TGV-ATLANTIQUE verwendete selbstgeführte Synchronmotor," *Elektrische Bahnen* Vol. 87 No. 12, pp.351-355, December 1989

[5] H. Hata, "ICE2, ICE2.2 and VT610 (1)," *Rolling Stock & Technology* Vol.1 No.2, pp.49-51, September 1995 *(in Japanese)*

[6] K. Bauermeister, A. Jaekel and M. Nießen, "Traktionswert von Triebfahrzeugen," *Elektrische Bahnen* Vol. 92 (1994) No. 12, pp.337-340, December 1994.

[7] E.W. Curtius and A. Kniffler, "Neue Erkenntnisse über die Haftung zwischen Treibrad und Schiene," *Elektrische Bahnen* Vol. 21 No. 9, pp.201-210 September 1950

[8] A. Weschta, "Die Elektrische Ausrüstung der Schnellverkehrstriebzüge ICE 2.2 und ICT der Deutschen Bahn AG," *ZEV+DET Glas. Ann.* 119 (1995) Nr. 9/10 (September/Oktober), pp.425-435

[9] "Shinkansen Double Deck EMU Train Series E1 for East Japan Railway Company," *Rolling Stock in Japan* No.61, August 1994

Table II
Comparison of Existing High-Speed Trains and the Optimal Formation as Clarified in this Paper

Name of train	Max. operational speed	Approx. train length	Number of traction units	Number of power converters	Number of motor cars	Notes
TGV-A (SNCF)	300 km/h	400 m (200 m)	4 (2)	8 (4)	4 (2)	Data when two 200 m trains are coupled.
ICE-3 (DB)	330 km/h	400 m (200 m)	4 (2)	8 (4)	8 (4)	Data when two 200 m trains are coupled.
Shinkansen E1 (JR-East)	240 km/h	400 m (300 m)	4 (3)	8 (6)	8 (6)	Data converted from those of an actual 300 m train to a 400 m one.
Optimal formation (Example at the train performance index of 85,500 MNm/h)	300 km/h	400 m	4	8	8	Optimal formation when the weight is the minimum.

(): Data of actual trains.

3300V 400A, 600A and 1200A High Power IGBT Modules with High Reliability for Traction Applications

Akira Tanaka, Mutsuhiro Mori, Hirokazu Inoue, Yoshihiko Koike
Tadao Kushima, Hideo Shimizu, Kiyoshi Nakamura*, Ryuichi Saito

Hitachi Research Lab., Hitachi, Ltd.,
7-1-1, Omika-cho, Hitachi-shi,
Ibaraki-ken, 319-12 Japan
Tel:+81-294-52-5111
Fax:+81-294-52-7612

*Transportation Systems Div., Hitachi, Ltd.,
6, Kanda-surugadai 4-chome, Chiyoda-ku,
Tokyo, 101 Japan
Tel:+81-3-5295-5169
Fax:+81-3-3258-5481

Abstract - **Newly developed 3300V IGBT modules with current ratings of 400A, 600A and 1200A for traction applications are described. Single or parallel use of these modules can provide coverage of the whole motor range of GTO inverter systems for traction applications. The IGBT modules consist of newly developed IGBT chips with improved terminations for high blocking voltage and soft and fast recovery diode chips with high reverse recovery di/dt capability. The new IGBTs have a lower switching loss as compared with a conventional IGBT. A baseplate with low thermal expansion extends their fatigue lifetime to more than 5 times that of a conventional module. Low thermal impedance is achieved by a simple module structure with optical arrangement of IGBT and diode chips for both thermal and electric characteristics. Solder and wire-bonding reliabilities of the modules are kept high throughout the fatigue lifetime despite their large size.**

I. Introduction

Today, lower cost, smaller size and higher performance are demanded for high capacity inverter systems for traction applications. Therefore high blocking voltage IGBT modules are being used, in place of GTOs. 2000V IGBT modules have been used to construct a three-level traction inverter directly connected to a DC 1500V catenary line (1)-(3). 3300V IGBT modules have been developed for use in a two-level traction inverter with a DC 1500V catenary line (4). The two-level inverter circuit has fewer parts, compared with the three-level inverter circuit. No clamping diode modules are required and the number of IGBT modules is cut in half. The adoption of 3300V IGBT modules can lead to a compact and low cost inverter system. The inverter power unit size of the two-level inverter is decreased by approximately 30% as compared with that of the three-level inverter (5).

Fig.1 shows an applicability range of 3300V IGBT modules for traction inverters. A motor current range of 2000A GTO is equivalent to the single use of 3300V 1200A IGBT module or 2 parallel use of 3300V 600A IGBT modules. 4000A GTO is equivalent to 2 parallel use of 3300V 1200A IGBT modules or 4 parallel use of 3300V 600A IGBT modules. Hence, single or parallel use of each of the 3300V 400A, 600A and 1200A modules is able to cover the entire motor current range for traction uses. Table 1 shows the high power IGBT module line-up for traction applications. These five kinds of IGBT modules satisfy the configuration of inverter circuits for traction applications. 2000V and 3300V clamping diode modules have also been developed for three-level inverter circuits.

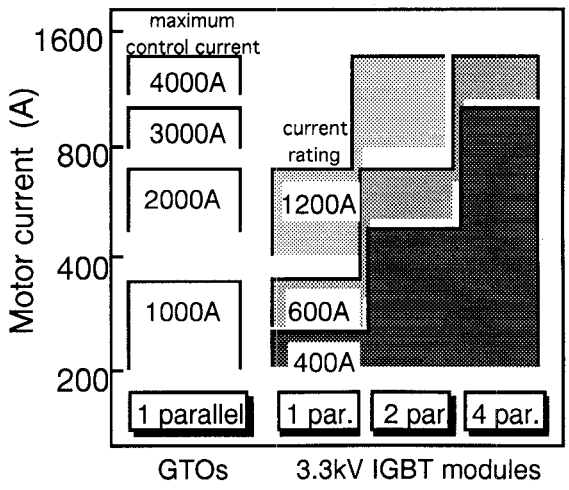


Fig.1 Applicability range of 3300V IGBT modules for traction inverters

Table 1 High power IGBT module line-up

	400A	600A	1200A
2000V (1-in-1)	MBN400C20	MBN600C20	——
3300V (1-in-1)	MBN400C33	MBN600C33	MBN1200C33

II. Module design

Fig.2 shows the newly developed 3300V 400A, 600A and 1200A IGBT modules. These modules provide features of the original package concept from the 2000V 500A IGBT module (2). Therefore, they have :

1) a low thermal expansion plate for high reliability; and

2) a U-SFD (Ultra-Soft & Fast Recovery Diode) for low electrical noise characteristics.

Moreover the newly developed modules add the following features to the package concept:

3) high speed switching and low loss IGBT chips; and

4) an improved copper bonded AlN ceramic plate for high thermal reliability.

The modules in the two-level inverter receive a high fluctuation voltage compared with that of the three-level inverter, because the circuit length of the former is shorter than that of the latter. Effective inductance of the inverter circuit is decreased and current slew rate, di/dt, as switching is increased. Low noise and high breakdown voltage IGBT and diode chips have been developed and applied to these modules (7). The IGBT and diode chips are mounted on the copper bonded AlN ceramic plate which provides improved fracture endurance in the thermal cycling test.

As module capacity increases, module size also increases. Larger module size means higher stresses of module components. It is important that the modules keep good mechanical and electric reliabilities with larger size. The 3300V 400A module is the same size as the 2000V 500A IGBT module, but the 3300V 600A IGBT module is 1.2 times as large as the former. The 3300V 1200A IGBT module is the double size of 3300V 600A module. The IGBT and diode chips are mounted in a number proportional to the output capacity of the module. Fig.3 shows a cross-sectional sketch of the 3300V IGBT module series. The power chips on the copper bonded AlN ceramic plates are connected in parallel in each module. The baseplate is made of low thermal expansion material. Wire bonding technology (8) is used to realize high reliability for traction motor drives.

Emitter and collector terminals are closely set in the design and they have a short length inside the modules in order to reduce the internal inductance of the terminals. Diode chips are arranged near an emitter internal terminal in order to decrease fluctuation of the electric potential of the control terminals during high current switching. The gate terminal position is kept away from the emitter and collector terminals in order to decrease the effect of electric noise.

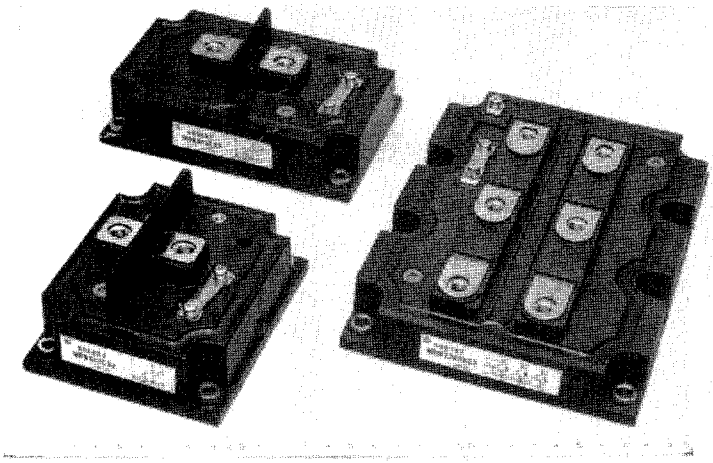


Fig.2 3300V 400A, 600A, 1200A IGBT modules

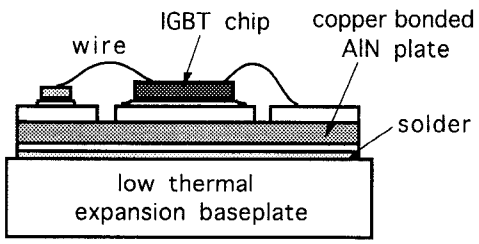


Fig. 3 A cross-sectional sketch of power chip mounted on the baseplate

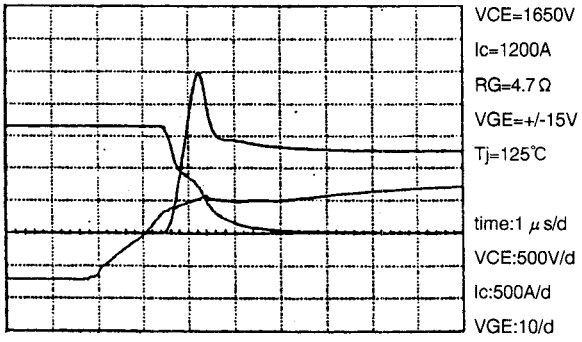
III. Electrical characteristics

Table 2 shows ratings and main electrical specifications of 3300V 400A, 600A and 1200A IGBT modules. New carrier distribution control technology is applied to improve the trade - off relation for the IGBT and diode. The high blocking voltage of the IGBT has a uniform and stable of the electric field due to the original FLR (Field Limiting Ring) and field plate structure. The newly developed IGBT has a wider RBSOA (Reverse-Bias Safe Operating Area) than a conventional GTO does.

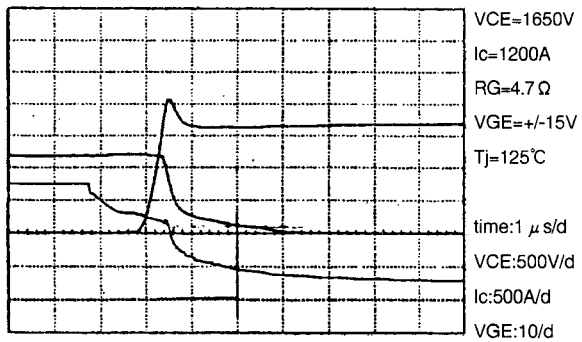
Fig.4 shows typical switching wave forms of the 3300V 1200A IGBT module at 125℃. A high frequency turn-off wave is realized. The di/dt endurance for the two-level inverter with low inductance is also realized by relaxation of current concentration in the chip. Fig.5 shows the trade-off between switching loss and Vce(sat) at 125℃. The new developed 3300V 1200A IGBT module which uses local lifetime control has a lower switching loss than a conventional IGBT. Because of the soft and fast recovery characteristics of the diode, electrical noise at recovery is effectively eliminated.

Table 2 Ratings and main electrical specifications of 3300V 400A, 600A, 1200A IGBT modules (Tc=25℃) (*:Tc=125℃)

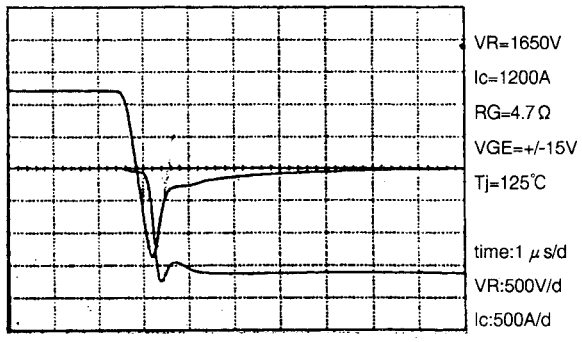
Items		Symbols	Units	Value			Test Conditions
Collector Emitter Voltage		VCES	V	3300			
Continuous Collector Current		IC	A	400	600	1200	
Isolation Voltage		-	V(RMS)	6000	6000	6000	AC 1 minute
Collector Emitter Saturation Voltage		VCE(sat)	V	typ.4.8*	typ.4.8*	typ.4.8*	Ic=rating, VGE=15V
Peak Forward Voltage Drop		VF	V	typ.3*	typ.3*	typ.3*	IF=rating, VGE=0V
Switching Time	Turn-on Time	ton	μS	typ.1.5	typ.1.5	typ.1.5	Vcc=1500V
	Turn-off Time	toff	μS	typ.1.5	typ.1.5	typ.1.5	Ic=rating
Reverse Recovery Time		trr	μS	typ.0.6	typ.0.6	typ.0.6	VGE=±15V
Thermal Impedance	IGBT	Rth(j-c)	℃/kW	Max.25	Max.17	Max.8.3	Junction to case
	Diode	Rth(j-c)	℃/kW	Max.50	Max.33	Max.16.6	
Outer Dimensions of Module		-	mm	96x113	93x140	140x190	



(1) Turn-on wave form



(2) Turn-off wave form



(3) Reverse recovery wave form

Fig.4 Switching wave forms of 3300V 1200A IGBT module

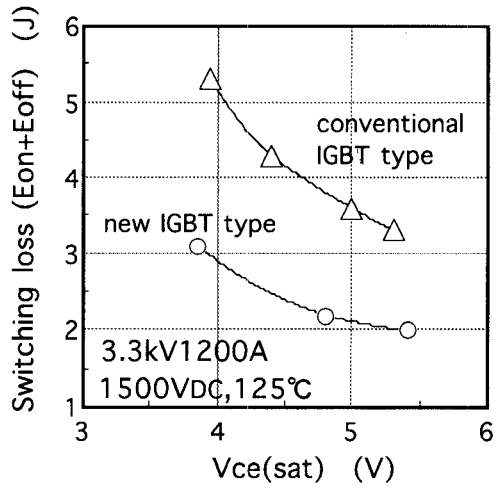


Fig.5 Switching loss of 3300V 1200A IGBT modules

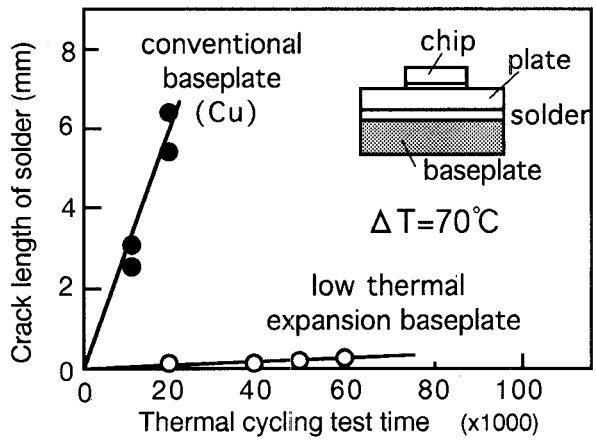


Fig.6 Reliability of solder between insulated plate and baseplate

Ⅳ. Thermal capabilities

As a large capacity module has many power chips, thermal management is important. It is necessary to arrange power chips so they do not interfere with each other's heat dissipation. The power chips are scattered in the new modules for effective heat dissipation. Their thermal impedance is lower than that of the conventional type.

In order to extend the fatigue lifetime of IGBT modules, a low thermal expansion baseplate is applied to the newly developed modules which better matches the thermal expansion coefficient between module components. The thermal expansion mismatch between power chips, the AlN ceramic plate and the low thermal expansion plate is about one-tenth that using conventional copper base material. Fig.6 shows the crack propagation in solder between the copper bonded insulated ceramic plate and baseplate under thermal test. Crack length of solder in the low thermal expansion baseplate module is much shorter than that of the conventional copper baseplate module.

The copper bonded AlN plate also receives large stresses under thermal loads. Boundary stress is generated at the interface between copper and AlN ceramic in a copper bonded AlN plate under thermal loads. This stress concentrates on the end of the copper layer which is contacted with the AlN plate. As the AlN plate size increases, the stress concentration increases. When the electric terminal contact area is brought close to the edge of the copper layer, the stress concentration is increased much more. In order to decrease the stress concentration, the arrangement of the electric terminal contact area in the conventional copper bonded AlN plate is designed to be kept away from the edge of the copper layer. The newly developed copper bonded AlN plate has a stress relaxation structure which can be arranged for high density packaging of module components. It was checked in thermal cycling tests (-40℃ to +125℃). The conventional copper bonded AlN plates in modules have several cracks in a ceramic layer after about 100 cycles under the test conditions, but no cracks are observed in the newly developed copper bonded AlN plates in modules after 1000 cycles.

When the improved copper bonded ceramic plate is applied, module thermal reliabilities are kept high in spite of a large module size (e.g. 3300V 1200A IGBT module, 140x190mm).

Ⅴ. Conclusion

3300V high power IGBT modules with current ratings 400A, 600A and 1200A for traction applications were developed with the following features.

(1) Single or parallel use of modules provided coverage of the entire motor current range of GTO inverter systems for traction applications.

(2) The new IGBTs and diodes had lower switching loss than a conventional IGBT.

(3) The thermal reliabilities of the modules were kept high by using a low thermal expansion baseplate and stress relaxation copper bonded AlN plates, in spite of their large size.

Acknowledgments

The authors would like to thank Dr. T. Kariya, Mr. K. Akabane, Dr. N. Monma and Dr. Y. Kobayashi for their helpful suggestions and encouragement. They also wish to acknowledge Dr. M. Kitano, Dr. Y. Kurihara and Messrs. K. Suzuki, M. Koizumi, S. Kuribayashi, H. Kobayashi, K. Koga, Y. Wakisawa, T. Saiki, T. Saito, M. Ito and H. Kokubun for the design and fabrication of the modules.

References

(1) M. Mori et al., "A High Power IGBT Module for Traction Motor Drive" Proceeding of ISPSD'92 p.287 (1992)

(2) A. Tanaka et al., "2000V 500A High Power IGBT Module " Proceeding of ISPSD'95 p.80 (1995)

(3) A. Nakata et al., "A three-level Traction Inverter with IGBTs for EMU " Conf. Rec. IEEE IAS Annual Meeting, Oct. (1994)

(4) H. Brunner et al., "3300V IGBT Module for Traction Application" Proceeding of EPE'95 p.56 (1995)

(5) K. Nakata et al., "Two-level Inverter with 3.3kV IGBT" Cybernetics Symposium for Traction, p.208 (1996)

(6) E. Toyoda et al., "High Blocking Voltage IGBT and Applications" Cybernetics Symposium for Traction, p.197 (1996)

(7) H. Kobayashi et al., "3.5kV IGBT" Annual Meeting of the Institute of Electrical Engineers of Japan, 4-66 (1996)

(8) J. Onuki et al., "Reliability of Thick Al Wire Bonds in IGBT Modules for Traction Motor Drives" Proceeding of ISPSD'95 p.428 (1995)

Efficient Ozonizer using PDM and PWM Controlled Resonant Inverter and its Performance Evaluations

Y.Konishi
Section Design Department, Kobe Factory
Fuji Electric Co.Ltd, Kobe, 651-22, Japan.

S.P.Wang, M.Ishibashi, Y.L.Feng and M.Nakaoka
The Graduate School of Engineering and Science,
Yamaguchi University, Yamaguchi, 755, Japan.

Abstract — **This paper presents a high-frequency voltage source-fed load-resonant IGBT inverter with a series-compensated resonant inductor for ozonizer, which incorporates the power control strategy on the basis of Pulse Density Modulation (PDM). The inverter system configuration is illustrated through the circuit modeling of the silent discharge-based ozone generating tube as well as high-voltage transformer. The state-of-the art ozonizer using a voltage-fed type high-frequency load resonant inverter is demonstrated, and its operating principle is described for driving ozone generating tube. It is noted that the pulse density modulated series resonant high-frequency inverter using IGBTs makes an ozone generating system simple, thus leading to improve the ozone generation efficiency. Finally, it is proved that the series load-resonant inverter type ozonizer developed in this paper provides stable silent discharge characteristics over a wide output power range from 10% to 100%.**

Ⅰ. INTRODUCTION

In recent years, ozone has been widely used for the chemical processing pipe line treatment of water and exhausted smoke, deodorization, color removal and disinfection and the forth. Because ozone gas has an extremely strong oxidizing power, this is widely used as well as fluorine. But it is also known that a variety of applications of ozone is hindered primarily because of its low efficient ozone gas generation. It is indispensable to improve the total appliance efficiency of the ozonizer. In order to improve the ozone gas generating characteristics, a new pattern-based pulse density modulation (PDM) power control scheme in the voltage source type IGBT resonant inverter using a series-compensated inductor provides good performances for the ozonizer appliance .

This paper presents a novel efficient ozonizer using the voltage-source type IGBT resonant inverter with a series-compensated resonant inductor for ozonizer, which operates on the basis of the digitally-regulated power control-based pulse density modulation (PDM) scheme. The voltage-source type load resonant inverter with a series compensated resonant inductor is designed so as to operate at a constant output frequency. The average output power of this inverter can be linearly regulated with PDM control strategy. The ozonizer prototype developed in this paper provides excellent ozone generating characteristics over a wide output power range from 10% to 100%.

The analysis of the load resonant IGBT inverter for ozonizer appliance including high-frequency transformer modeling and ozone generating tube modeling is carried out under a condition of PDM control scheme. The conceptual operation principle of this inverter is described herein including the principle of power control based on pulse density modulation (PDM) scheme. It is noted that the application-specific high-frequency load resonant inverter using the new generation IGBTs can efficiently operate under a principle of effective PDM control strategy.

Ⅱ. SILENT DISCHARGE OZONIZER

In general, it is understood that the ozone gas can be produced on the basis of silent discharge phenomena, radiative irradiation, electrolytic, optochemical reaction and so forth. Among them, the silent discharge is most widely used in some various industrial fields. The principle of ozone gas generation with silent discharge is illustrated in Fig.1.

A high-frequency AC exciting voltage generated by the high-frequency load resonant inverter is applied to ozone generation tube which has two electrodes. This is composed of discharge gap and the dielectric material of glass inserted into two electrodes, which are shown in Fig.1 (a). The equivalent circuit modeling of the silent

0-7803-3823-5/97/$10.00© 1997 IEEE

discharge type ozonizer is indicated as Fig.1 (b). A section of the discharge gap includes a capacitance Ca in series with the capacitance Cg of the glass when the silent discharge does not occurred, and discharge voltage source Vz called discharging sustaining voltage is connected in parallel with Ca as soon as the silent discharge occurs. On the other hand, the part of glass dielectric substrate is shown as a capacitor Cg in series with Ca.

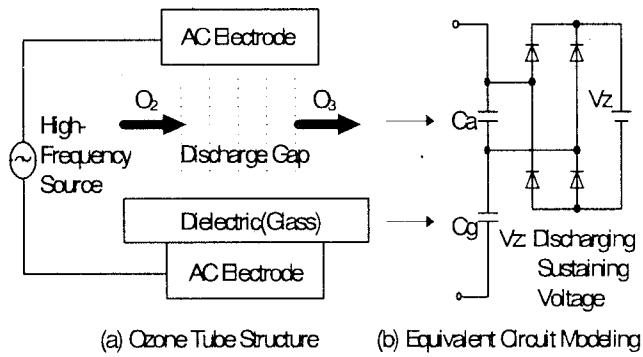


Fig.1: Principle of Silent Discharges Type Ozonizer.

Ⅲ. HIGH-FREQUENCY INVERTER SYSTEM

Fig.2 shows a total power conversion system configuration for an ozonizer using the voltage source-fed load resonant inverter. The DC power supply of this inverter consists of three-phase bridge rectifier with a DC smoothing capacitor. Three-phase diode rectifier is effectively replaced by the active three-phase power factor correction converter using IGBTs which operates at a sinewave current shaping scheme. The power conversion processor consists of a single-phase voltage source-fed full-bridge inverter using IGBT modules. The high-frequency output of this resonant inverter is connected to a series-compensated resonant circuit and a high-frequency transformer with turn-ratio.

In order to achieve the appropriate discharge on air gap portion between two electrodes of ozonizer, it is necessary to apply a high frequency and high voltage AC to two electrodes. The ozonizer is depicted with a capacitive load for matching with the inverter in spite of discharging in air gap or not, so the inverter circuit with a matching transformer is practically utilized. The load resonant circuit with a high frequency transformer is composed of series compensated inductance Ls and the capacitance Ca of the gap in series with the capacitance Cg of the glass dielectric substrate as the ozone generating tube. Strictly speaking, the capacitive load parameter is changed with an discharge and in case of discharge period, the discharge sustaining voltage Vz is connected in parallel with Ca. The switching frequency of the inverter is designed for 7 kHz. The optimum value of the series-compensated inductor Ls is estimated so as to realize a tuned resonant condition by the computer-aided simulation technique.

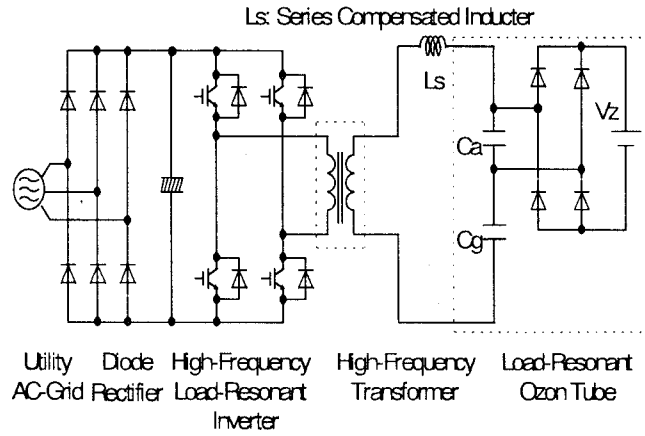


Fig.2: Configuration of the new type ozonizer system

Ⅳ. POWER REGULATION SYSTEM

In order to control a producing quantity of ozone gas, it is dispensable to regulate an discharge power in the ozonizer. Fig.3 illustrates the relationship between the output power of inverter and ozone production.

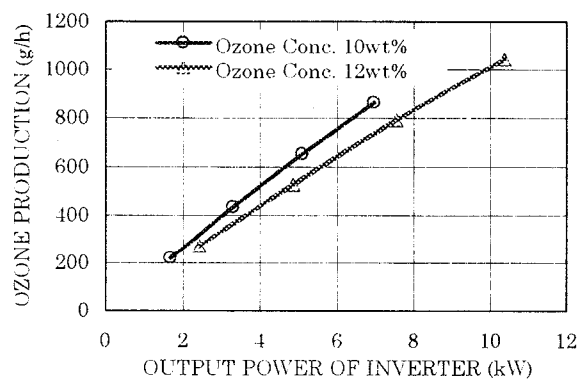


Fig.3: The relationship between the output power of inverter and ozone production

A peak voltage across two electrodes must keep for sustaining a stable discharge, even though an output power is lowered. The power regulation principle of PDM control strategy is basically illustrated in Fig.4. The effective power delivered from the ozone generating tube can be continuously controlled by means of high-frequency ac pulse density modulation. This modulation procedure is based upon a time ratio control of high-frequency ac voltage pulse group which is generated by the voltage-fed load resonant inverter using IGBTs, which is operating at a constant frequency of 7kHz.

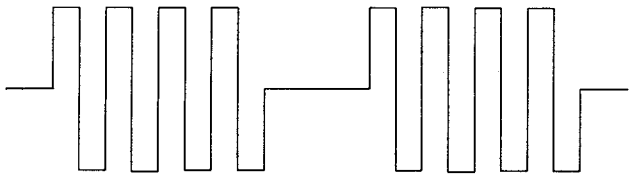


Fig.4: Principle of PDM control

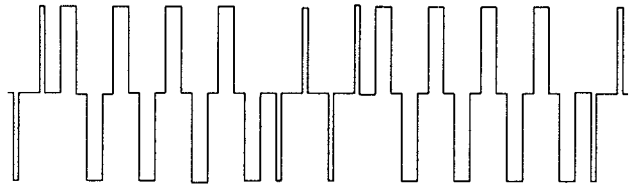


Fig.5: Principle of PDM&PWM control

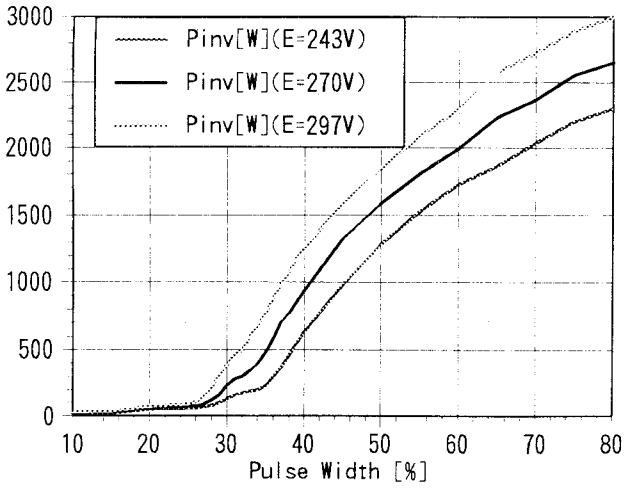


Fig.6: Relationship between the output power and pulse width

In this ozonizer, PDM and PWM hybrid-based power control method is effectively proposed for ozone generating tube load. The principle of PDM and PWM hybrid-based power control is shown in Fig.5. In case of no power injection mode in PDM control scheme, the additional PWM control is effective to increase the rising time of the injected current when the power of ozone generating tube is delivered from the inverter.

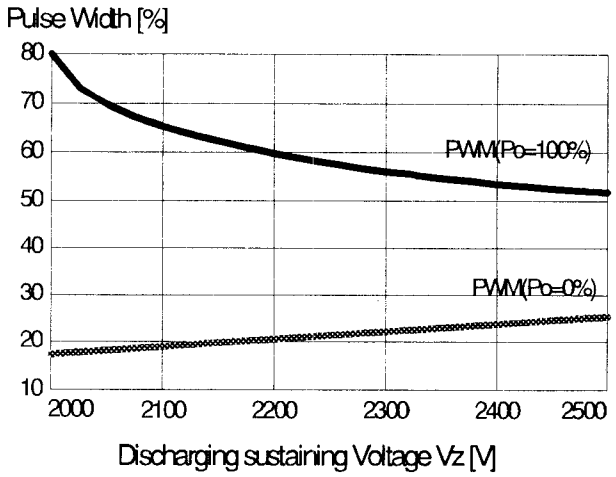


Fig.7: The relationship between pulse width and discharging sustaining voltage Vz

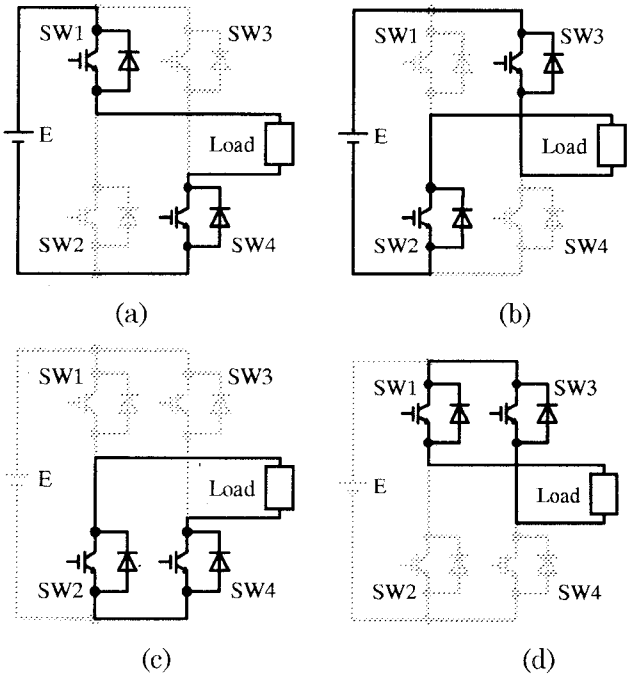


Fig.8: Operating Modes of inverter

In order to control the output power of the inverter, it is necessary to regulate the pulse width in accordance with the input side voltage fluctuations of the inverter

and the variations of discharging sustaining voltage Vz. The relationship between output power of the inverter and pulse width with the input side voltage source E fluctuating with in $\pm$10% is shown in Fig.6. In addition, the relationship between pulse width and the discharging sustaining voltage Vz is estimated graphically in Fig.7.

Fig.8 illustrates the operating modes of voltage-fed series load resonant inverter using IGBTs for ozonizer when the output power is regulated by pulse density modulation.

V. PERFORMANCE EVALUATIONS

Fig.9 shows a set-up of experimental ozone generation system. This system is made up of three major parts, that is the DSP computer control system, the inverter power supply system, and the ozone generating equipment.

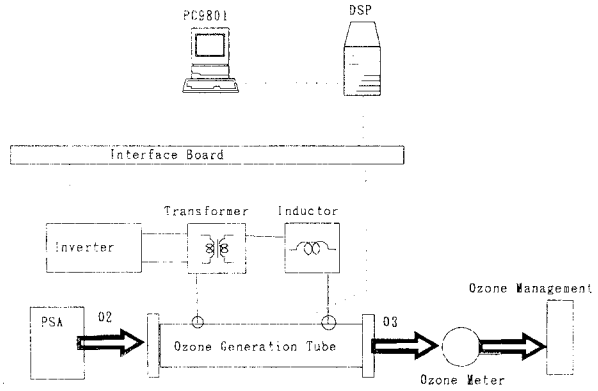


Fig.9 The experimental ozone generation system configuration

The inverter operating waveforms which are controlled by a new PDM&PWM hybrid regulation scheme are shown in Fig.10 in case of Pulse Density Modulation rate 15%. This measured waveforms are illustrated in Fig.11. The experimental voltage and current waveforms of the ozone generating tube are illustrated in Fig.12. The operation includes positive charging and discharging modes in ozone generating tube as well as negative charging and discharging modes.

The silent discharge of ozone generating tube does not caused almost when the voltage across discharge gap is below a certain voltage value to start a discharge phenomena occurred in this gap. The voltage across the discharge gap in discharge mode maintains the voltage Vz when this gap exceeds the voltage to start discharge, it is noted that the discharge sustaining voltage Vz has a non-linear characteristics. So, the applied voltage across the ozone generating tube has to be a specified peak value (9kV-10kV) when the power is delivered from the inverter. If the applied high-frequency AC voltage across two electrodes is much lower, the discharge phenomena doesn't occur at all and reveals a partial discharge phenomena. To raise over a voltage across two electrodes, the insulation is distracted on an edge of an ozone generating tube and an arc discharge generates around two electrodes.

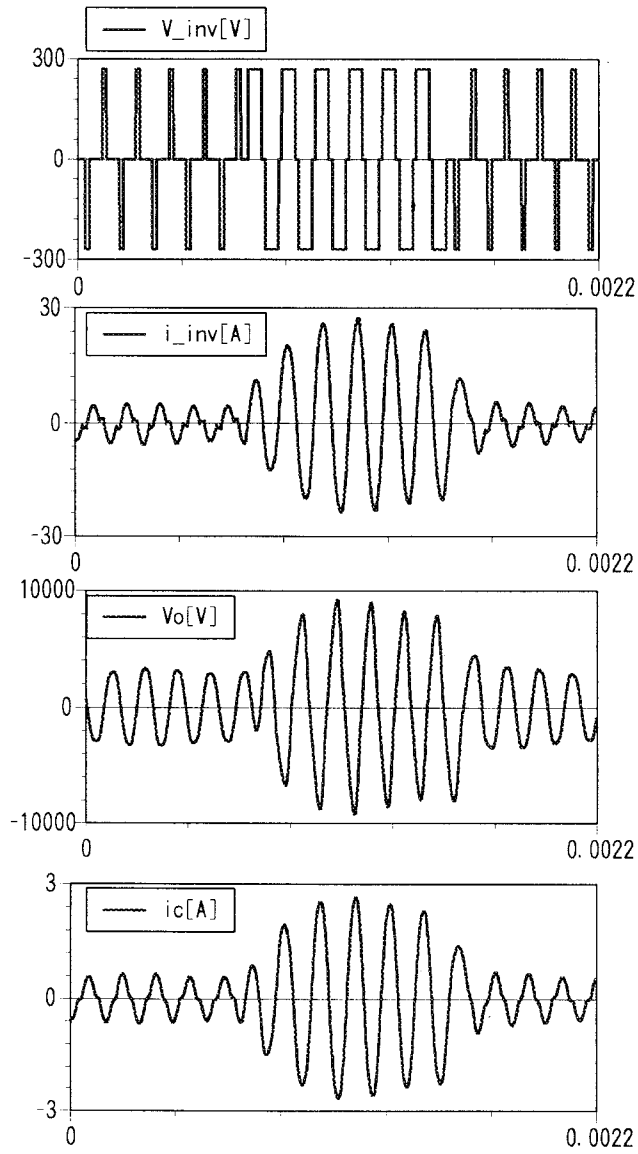


Fig.9: Voltage and current waveforms

Fig.13 shows lissajous figure of the ozone generating tube when the output power is regulated by

PDM&PWM hybrid controll scheme. There are discharging period, non-discharging period and incomplete discharging period. The internal area of lissajous figure as *v-q* characteristics of ozone generating tube corresponds to an output power.

Fig.14 indicates a relationship between the pulse density modulation rate and the output power of the inverter. The PDM control scheme under a constant output frequency of the inverter is more effective in order to perform a stable discharge when the output power delivered to the ozone generating tube is lowered. The output power on the basis of this PDM scheme is regulated linearly over wide ranges within duty ratio 10 % to 100 %.

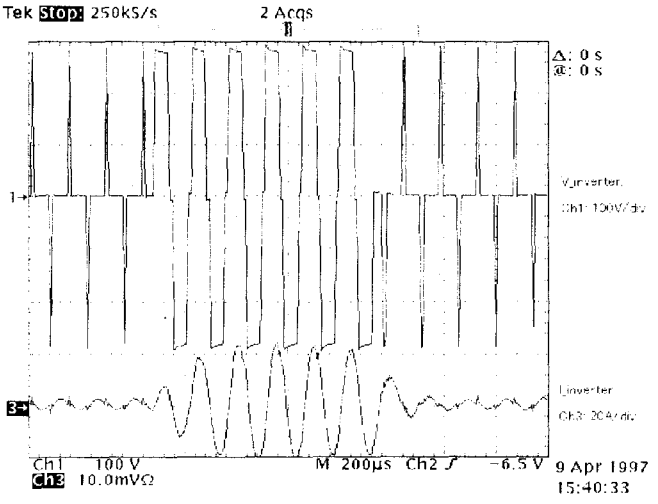


Fig.10: Experimental output voltage and current waveforms of the inverter

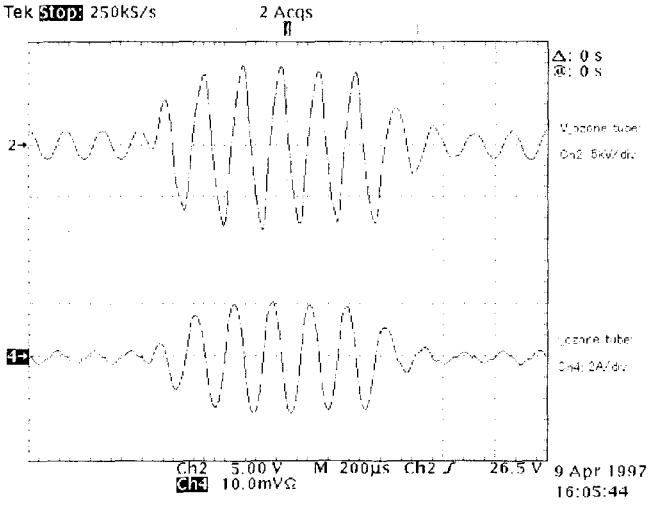


Fig.11: Experimental voltage and current waveforms of ozone tube

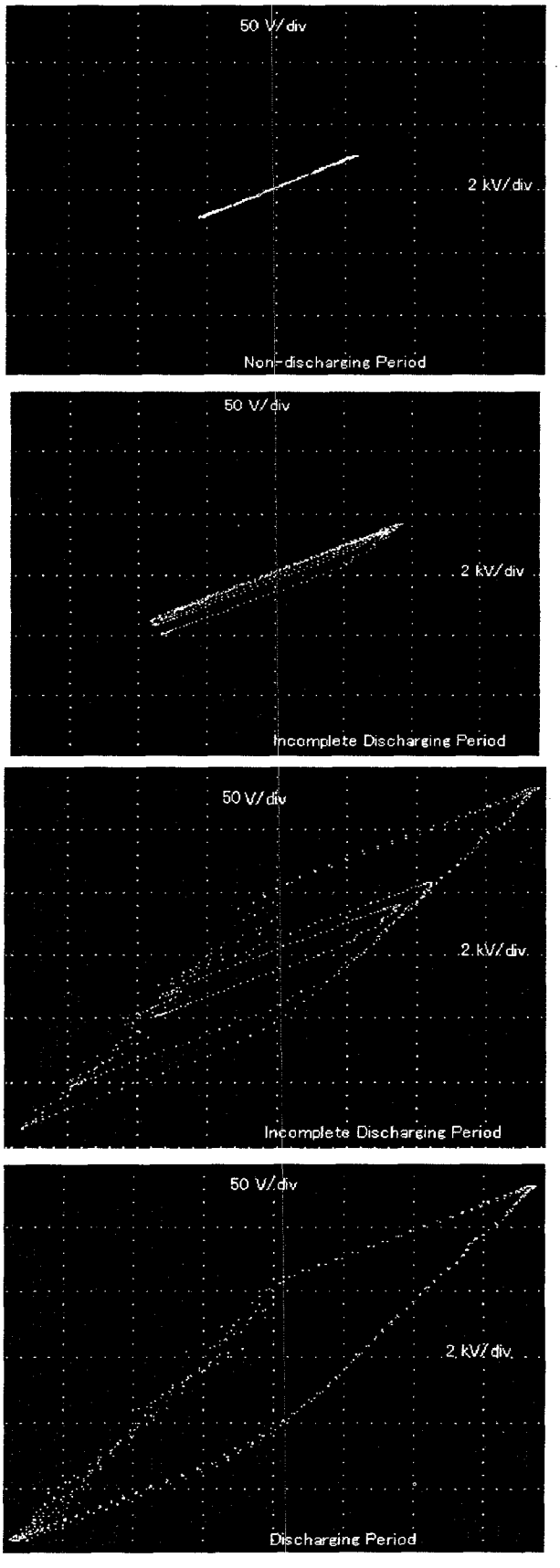


Fig.12: Lissajous figure

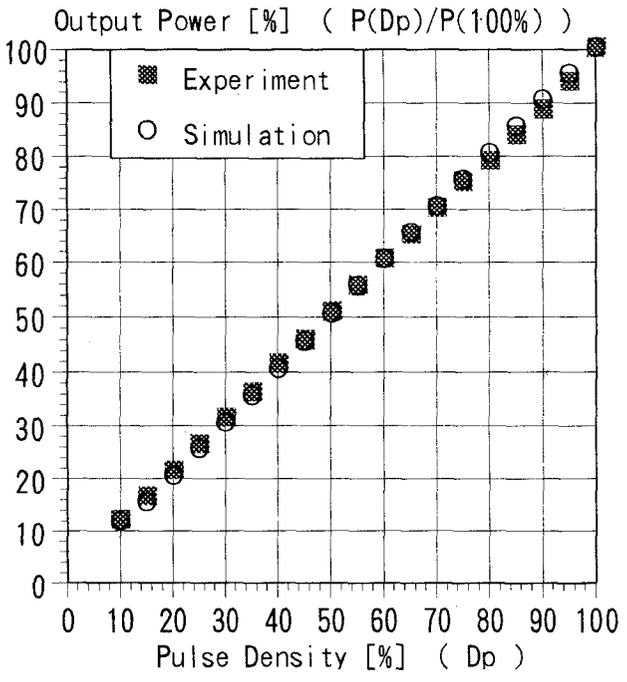


Fig.13: Steady-state characteristics in case of PDM control scheme

VI. CONCLUSIONS

A novel type pulse density modulated load-resonant inverter using the IGBT modules which is designed for the ozonizer appliance has been developed. The operating principle of the inverter working under PDM and PWM hybrid control strategy has been described and evaluated for ozonizer, along with the ozonizer power regulation performances as well as the ozonizer characteristics. The effectiveness of the ozonizer using PDM&PWM control based voltage source type load resonant inverter has been demonstrated from a practical point of view.

In this future, the pulse density modulated high-frequency resonant inverter for ozonizer which can operate under a principle of soft-switching transition scheme should be developed and evaluated. The ozonizer using a current-fed type load resonant inverter should be evaluated as compared with the ozonizer using voltage-fed type load resonant inverter with PDM control strategy.

REFERENCES

[1]. H.Fujita, H.Akagi "Pulse-Density-Modulation Power Control of a 4kHz Voltage-Source Inverter for Induction Melting Applications", IEEE Transactions on Industry Applications, Vol.32, No.2, pp.279-286, 1996.

[2]. S.P.Wang, M.Nakaoka & H.Omori, "A constant frequency variable power regulated ZVS-PWM load-resonant inverter for induction heated cooking", Proceedings of JIASC'96 Japan, pp.E-68~E.73, 1996.

INNOVATIVE DEVELOPMENT OF ELECTROMAGNETIC INDUCTION-BASED FLUID-HEATING SYSTEM USING RESONANT PWM INVERTER

A.Kajiyama(Student Member), B.Guo(Student Member) and M.Nakaoka(Member)
Department of Electrical and Electronics Engineering, Yamaguchi University, Ube, Yamaguchi, 755,Japan
FAX +81-836-35-9449, E-mail kajiyama@pe-news1.eee.yamaguchi-u.ac.jp

Y.Uchihori (Member)
Advanced Research & Development Division, Seta Kosan Chemical Industry Co.Ltd., Osaka,567,Japan

Abstract- *This paper presents a novel prototype of a new conceptual electromagnetic induction-based fluid heating appliance using series capacitor-compensated load resonant high-frequency IGBT inverter using IGBT modules, which operates at a phase-shifted PWM and a power factor correction schemes. Its operating characteristics in a steady-state are illustrated and evaluated on the basis of its computer-aided circuit simulation and experimental results. The promising cost effective applications of this electromagnetic induction-heated fluid-heating appliances is proposed including induction-heated boiler, induction-heated dryer and induction-heated hot air producer, which is more suitable for industrial,chemical and consumer utilizations from a practical point of view.*

I. Introduction

In recent years, the electromagnetic induction-based heating energy processing systems which are controlled by voltage-fed or current-fed high-frequency resonant inverter circuits and systems using the latest IGBTs have attracted special interest from the advantageous viewpoints of high-frequency, high-reliability, safety, cleannes, compactness in volumetric size, light weight, controllability in quick temperature rising response as well as stable temperature tracking and precise temperature control characteristics.

This paper presents a technological innovation of the electromagnetic induction-based fluid heating appliance using a soft-switched PWM voltage source type high-frequency resonant inverter which is composed of a phase-shifted PWM series loaded-resonant inverter using the new generation IGBT modules, the latest auto-tuning PID gain controller, and specially-designed-package laminated steel plate type induction heater incorporated into the vessel or tank in the pipeline plants. Its inherent steady-state operating characteristics are illustrated as an efficient heat exchanger and evaluated as induction-heated boiler, induction-heated hot water producer and evaporator from a practical point of view. Finally, the advanced high-frequency resonant inverter topology with a constant frequency soft-switched PWM scheme is also introduced newly, which can operate under ZVS and ZCS hybrid modes in spite of PWM regulation process.

II. Electromagnetic Induction Fluid-Heating Appliance

Fig.1 shows a schematic system configuration of the electromagnetic induction-based fluid (liquids or gases)-heating appliance using a voltage-fed type series resonant PWM inverter with an active power filtering scheme. This unique fluid-heating appliance used in the industrial chemical and consumer pipeline systems is composed of a three-phase diode rectifier without the smoothing DC capacitor filter link, a high-pass and high-block LC filter, a voltage-fed full-bridge type series load resonant inverter using IGBT modules, which operates at a constant frequency phase-shifted PWM power regulation scheme, a specially-designed heater made of electromagnetic induction type fluid-through thin metallic layer assembly with many flow-though spots and wave-like fluid channel slits. For fluid direct heating, the state-of-the art power electronic product can be considered for

0-7803-3823-5/97/$10.00© 1997 IEEE

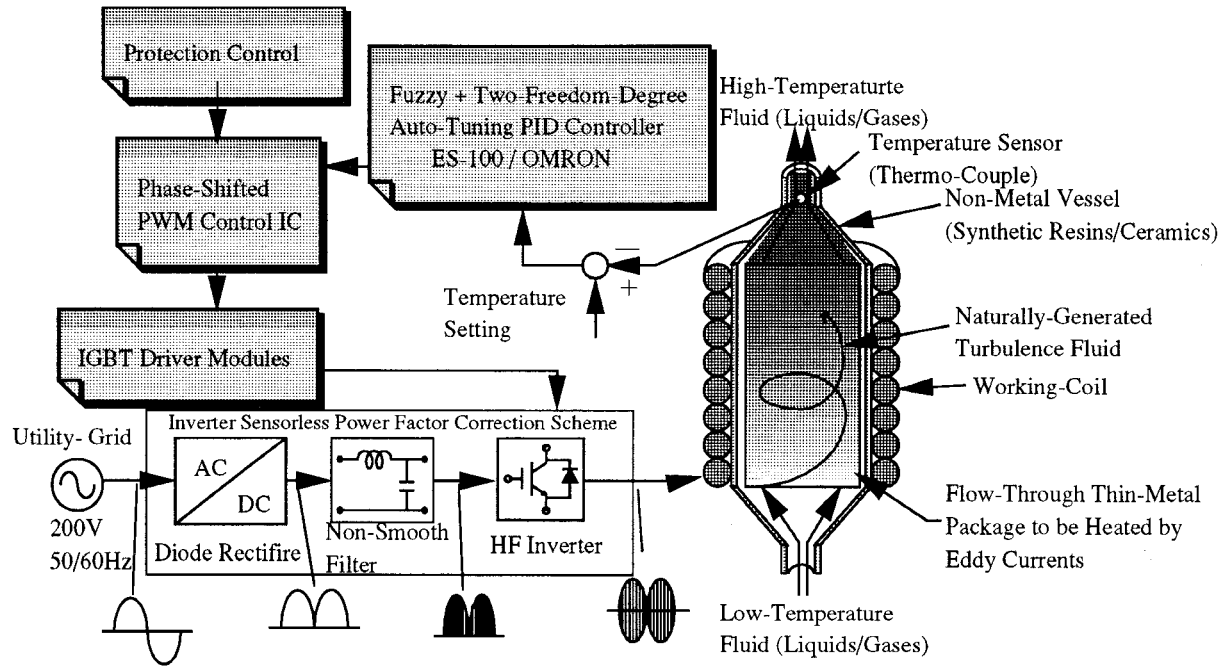


Fig.1 New schematic induction-heated electrical energy conversion & utilization system

operation under the conditions of a unity power factor correction and active harmonic current compensation.

III. High-Frequency Series Resonant Inverter

Fig.2 shows the voltage-fed full-bridge type series loaded-resonant PWM inverter using IGBT modules with their optical fiber connected intelligent driver circuit modules. The operating voltage and current waveforms of the series- loaded resonant PWM in-

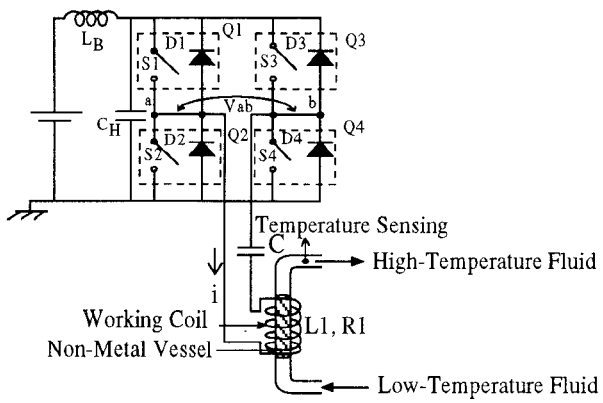


Fig.2 A voltage-fed full-bridge type series loaded-resonant inverter

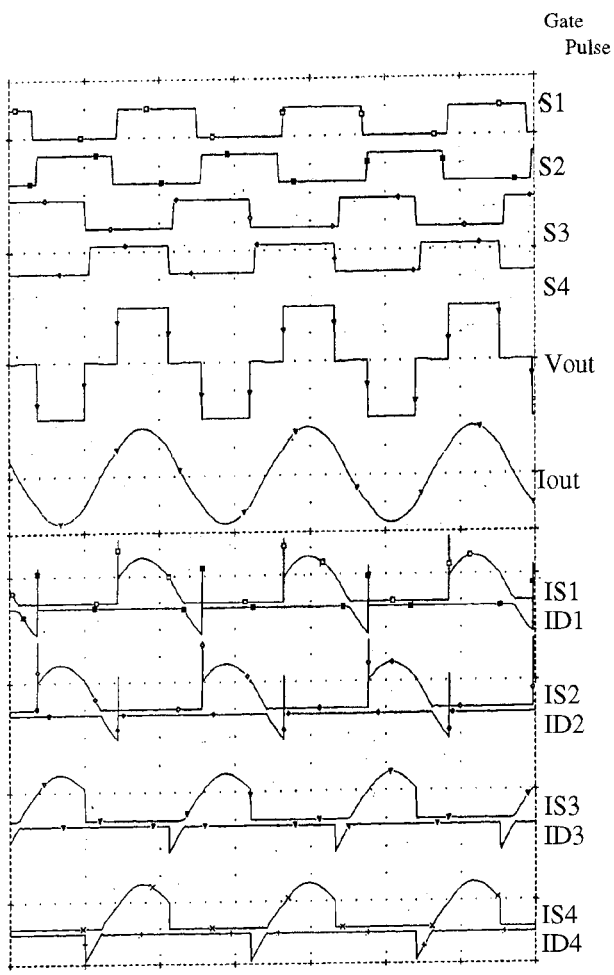


Fig.3 Voltage and current waveforms

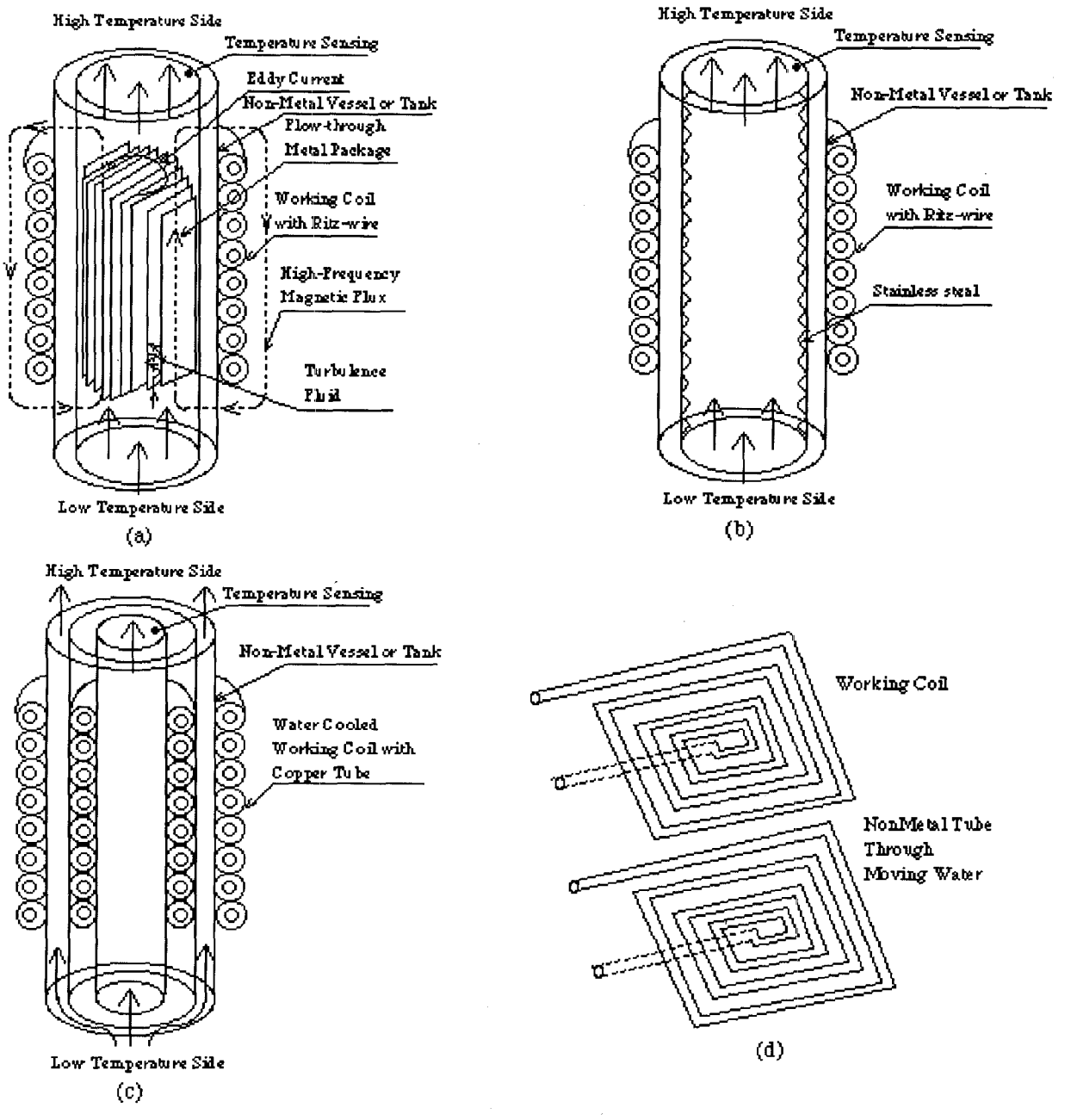


Fig.4 Heating package in the vessel and tank used in the pipeline system

verter operating at a phase-shifted PWM mode are illustrated in Fig.3. The output voltage of this full-bridge resonant PWM inverter can be continuously regulated by the phase-shifted PWM scheme at a constant frequency. As can be observed in Fig.3, the turn-on switching currents through S1/S2 in the left bridge leg are both positive in PWM regulation mode. As a result, S1/S2 operate at hard-switching turn-on. However, S1/S2 can realize a soft-switching turn-off operation under a condition of zero current and zero voltage commutation in spite of phase-shifted PWM control process and wide load parameter variations.

On the other hand, S3/S4 in the right bridge leg can turn-on under a condition of the zero current and zero voltage soft switching in spite of phase-shifted PWM processing and load parameter variations. In case of fo>fr (fo : Inverter frequency, fr : Series resonant frequency), the switches S3/S4 must always turn off at hard switching condition.

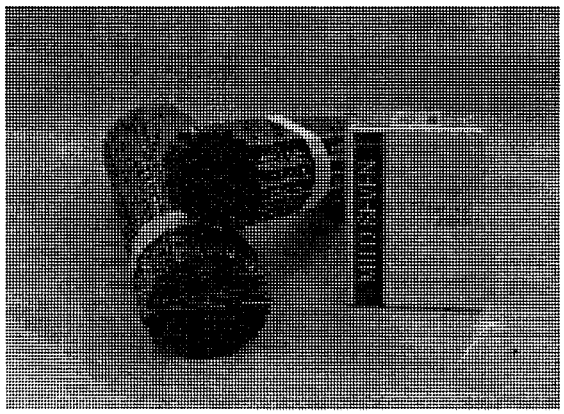


Fig.5 Induction-heated metallic package

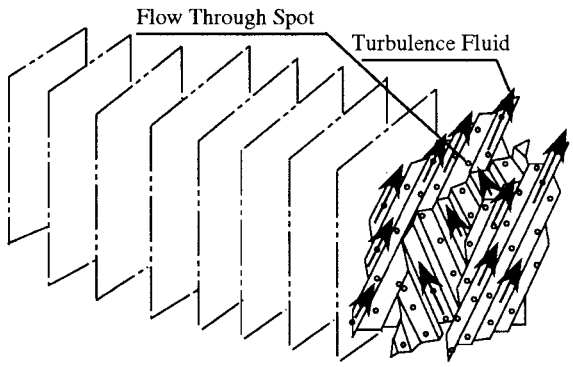


Fig.6 Internal structure fluid-through specially designed metal layer packing to generate turbulence fluid

IV.Induction-Heated Flow-Through Metallic Package Assembly

Fig.4(a) indicates a specially-designed fluid-through eddy current-heated metallic package developed by the authors. Fig.4(b) and (c) indicates the other type of induction-heated assembly incorporated into the vessel or tank, which are newly proposed in place of the induction-heated assembly shown in Fig.4(d). A mechanically-processed wave-like thin stainless-steel layer package with many spots and fluid-flow channels in the cylindrical induction-heated assembly is demonstrated in Fig.5. Detail internal structure of this metallic layer (stainless steel plate) package to be heated directly by the eddy current-based losses is displayed Fig.6.

The overview of induction-heated metal package is indicated in Fig.7.

In addition, the fluid turbulence can be naturally generated by using specially-designed dual package induction-heating assembly. When the fluid (liquids or gases) flows through the inherent package in-

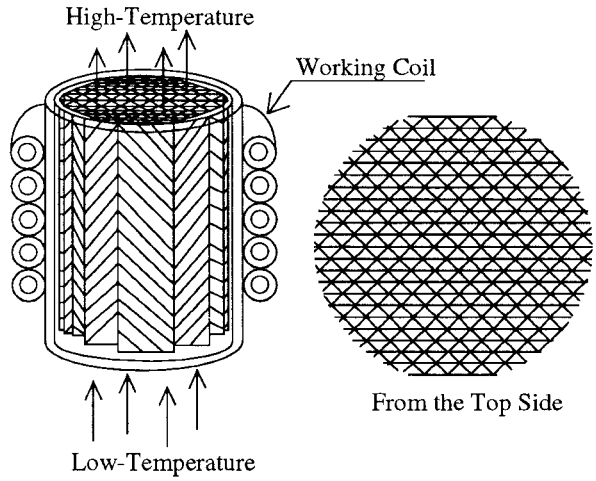


Fig.7 Overview of induction-heated matal package

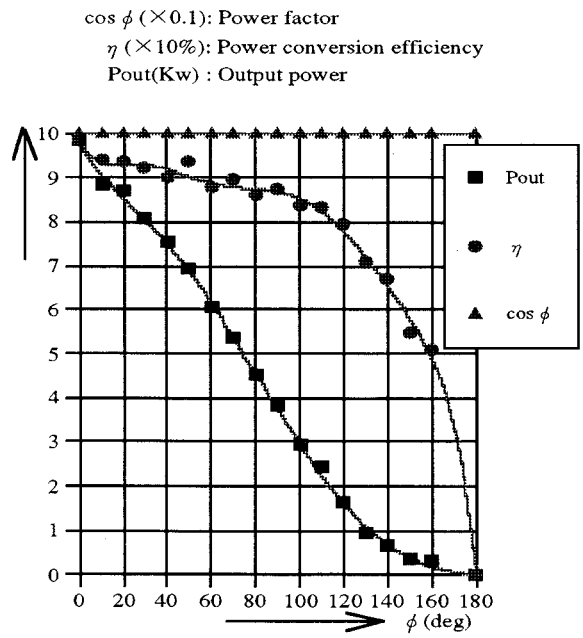


Fig.8 Steady-state characteristics of inverter-fed induction-heated boiler

serted into the ceramic vessel or tank with a work coil, which is distributively located to actual the pipeline system.

This turbulence fluid is to be heated instantaneously and uniformly by using the induced eddy current based-heat energy in order to be generated in both surfaces of thin stainless-steel package. Induction-heated energy can efficiently transferred and exchanged into the moving fluid heat energy.

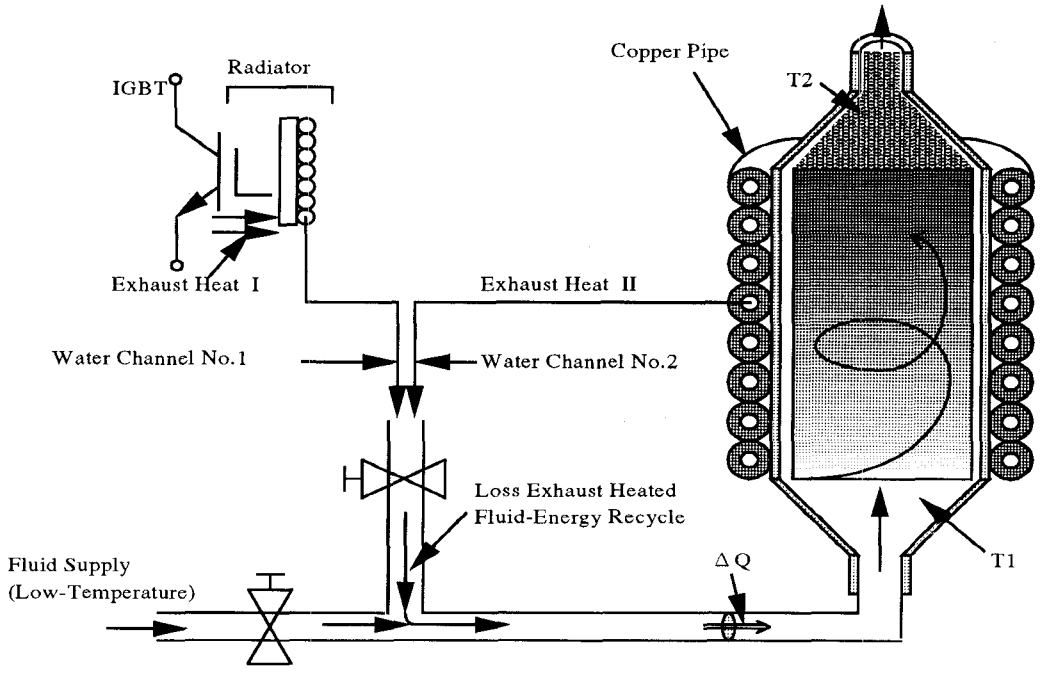


Fig.9 Improved energy conversion utilization system of induction-heated fluid heating appliance

V. New Applications of Experimental Set-Up and Peformance Evaluations

Fig.8 illustrates the steady-state total operating characteristics in case of this electromagnetic induction-heated boiler. Observing operating characteristics in Fig.8, the output power can be continuously regulated according to the phase-shifted angle ϕ from 0° to 180° . Power conversion efficiency η is estimated by,

$$\eta = \frac{P_{OUT}}{P_{IN}} \times 100\ [\%] \tag{1}$$

$$P_{OUT} = c\,\Delta T \frac{\Delta Q}{860} \times 1000\ [W] \tag{2}$$

where, Pin : input power

Pout : output power estimated by equation(2)

T1 : temperature in inlet of the vessel

T2 : temperature in outlet of the vessel

$\Delta T = T2 - T1$, $c \cong 1.0$ (Specific Heat)

VI. Conclusions

In this paper, a novel prototype of electromagnetic induction-based fluid-heating appliance has been successfully proposed on the basis of a series loaded resonant PWM high-frequency inverter using IGBT modules and their related driver circuit modules, and its self-tuning PID temperature control scheme, which can efficiently operate at soft-switched PWM scheme.

It was emphasized that epoch-making and new conceptual fluid-heating principle of this new appliance is based upon joules heat due to the electromagnetic-induced eddy current which is generated in a flow-through thin metallic package incorporated into the nonmetallic vessel or tank in the pipeline system.

In this innovative appliance, the voltage-fed series-loaded resonant PWM inverter using IGBT modules has grid AC bus.

It has been practically proved that this new heating appliance could be more cost-effective for electromagnetic induction-heated boiler, heat exchanger, steamer, dryer, hot air producer, hot water producer and evaporator as well as induction heated hot water supplier because of compactness in volumetric physical size, cleanness, high-efficiency conversion, quick temperature response, stable and precise temperature control realization.

In the future, this promising electromagnetic induction-type fluid heating appliance using the current-fed parallel resonant inverter should be investi-

gated and evaluated as compared with the induction fluid-heating appliance employing voltage-fed inverter appliance treated in this paper.

References

[1] M.Nakaoka, S.Nagai ; New Phase-Shifted Soft-Switching PWM High-Frequency Series Resonant Inverter Topologies and Their Practical Evaluations; 1994, Proceedings of International IEEE-CAS (Circuits and Systems) Symposium on Power Electronics Circuits(ISPEC), pp.25-28, June.

[2] Y.Uchihori, Y.Kawamura, H.Yasutsune, M.Nakaoka ; Novel Electromagnetic Induction Flow-Through Package in Pipeline Type Fluid Heating Appliance using Series Resonant PWM Inverter with Self-Tuning PID Controller-based Feedback Loop; 1995, Proceedings of International Power Electronics Conference (IPEC)-Yokohama, pp.660-665, April.

[3]Y.UchihoriÅ@Y.KawamuraÅ@M.Nakaoka H.Yasutune S.MoritaÅG"The State-of-the-Art Electromagnetic Induction Flow-Through Pipeline Package Type Fluid Heating Appliance using Series Resonant PWM Inverter with Self-Tuning PID Controller-Based Feedback Implementation" International IEEE/IAS Conference pp.14-21 May 1995(in Taipei) IPEC-Yokohama pp.660-665 April 1995(in Japan)

Switching Modes And Short-circuit Considerations In Very High Frequency, Very High Power Resonant Inverters For Induction Heating Applications

E.J.Dede, J. Jordan, V. Esteve, J.M. Espi*, A. Ferreres*

G.H.ELIN International S.A. P.O.BOX 8056(46080) Valencia, SPAIN Fax: 34-6 -135.04.78
*University of Valencia, Dep. of Electronics Dr. Moliner, 50 Burjassot (Valencia) Fax: 34-6-364.23.45

***Abstract*-The aim of the paper is to present, from the practical point of view, the optimum switching strategy in very high frequency very high power current-fed inverters for induction heating applications in general and for tube welding applications in particular as well as the presentation of some practical considerations for short-circuit behaviour of the heating coil.**

I. INTRODUCTION

Practical industrial current-fed inverters for induction heating are basically constructed with two different lay-outs. In the first case, as shown in Fig.1, the capacitor bank is very close to the inverter so that the effect of the parasitic wiring inductance can be neglected (topology n° 1). In the second case, Fig.2, the capacitor bank is connected to the inverter with a flexible cable so that, in this case, the effects of the parasitic wiring inductance Lp has to be considered (topology n° 2).

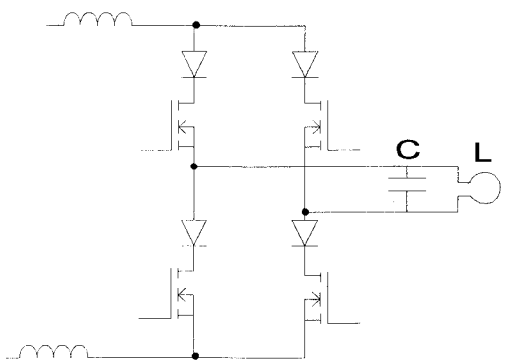


Fig.1. Current-fed inverter with capacitor bank very close to it.

Fig.3 shows a practical implementation of topology n° 2 while Fig.4 shows a practical implementation of an inverter featuring the n° 1 topology characteristics.

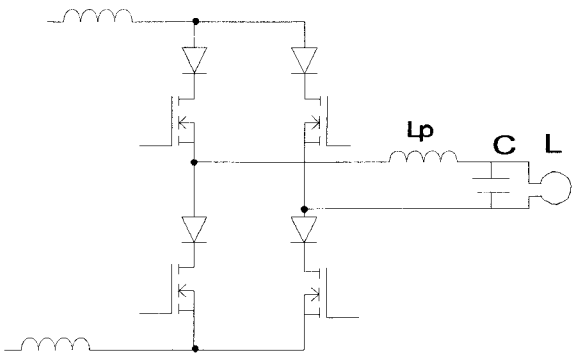


Fig.2. Current-fed inverter with capacitor bank not close to it.

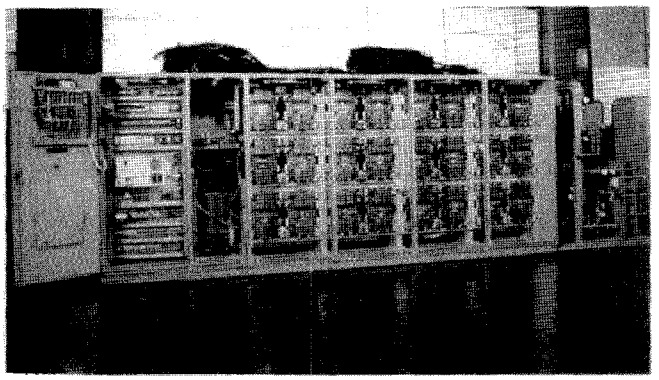


Fig. 3. 600kW, 400 kHz MOS Generator for Tube Welding

Both topologies have advantages and disadvantages. Topology shown in figure 1 is more attractive for very high frequencies but from the user point-of-view is not an optimum one in several applications like hardening where topology shown in Fig.2 is more attractive as the heating station is connected to the inverter with a flexible cable. Discussion on the advantages and disadvantages of both topologies, from the electrical point-of-view as well as from the user point-of-view can be found in [1].

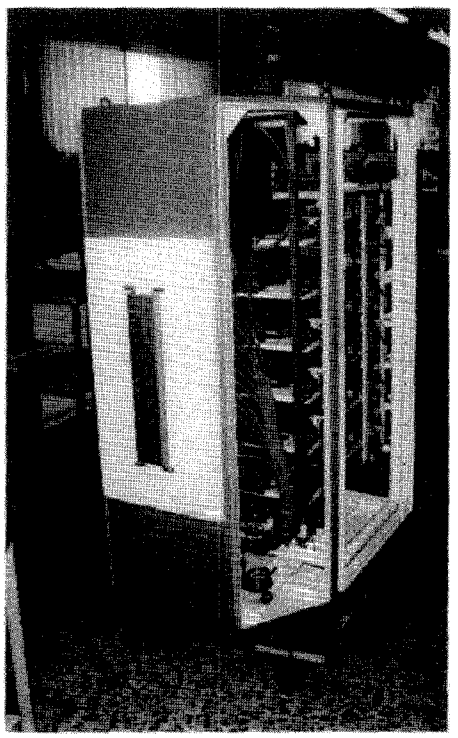


Fig. 4. 300 kW, 700 kHz inverter for tube welding with capacitor bank directly connected to the inverter.

0-7803-3823-5/97/$10.00© 1997 IEEE

In practical working conditions, there are in both topologies two possible modes of operation of the inverter: the inductive mode and the capacitive mode. In this paper the two modes of operation are analysed as well as its extension to short-circuit conditions in the case of short-circuit of the heating inductor.

II. SWITCHING MODES AND SHORT CIRCUIT BEHAVIOUR FOR TOPOLOGY N° 1

The equivalent circuit for topology n° 1 can be seen in Fig.3.

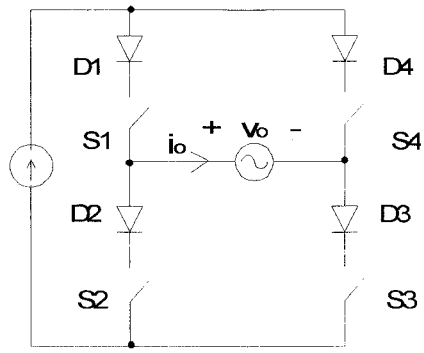


Fig.3 Topology n° 1

The commutation constrains are as follows:

A. General

The turn-on switching must lead the turn-off switching (overlapping)

B. Turn-off switching

Suppose S4 has been turned-on and S1 is going to be turned-off. In this case the two possible situations can be seen in Fig.4.

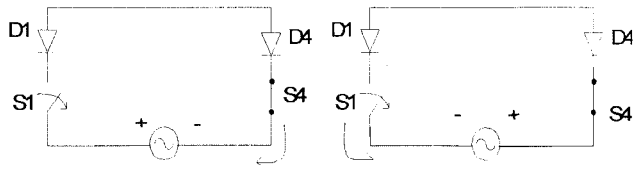


Fig.4a Fig .4b

1) In this case D1 blocks the output voltage V0, so that the turn-off switching of S1 is ZCS, Fig.4a.
2) Before the turn-off of S1, D4 blocks the output voltage: When S1 turns-off, D4 turns on: in this case there are turn-off losses for the transistor but the commutation process is not problematic due to the fact that there is no reverse recovery current in D1, Fig.4b.

C. Turn-on switching

Suppose that S4 is conducting and S1 is going to be turned-on. In this case the two situations are as shown in Fig.5.

1) In this case D1 blocks the output voltage Vo so that the commutation occurs under ZVS conditions, Fig.5a.
2) In this case the turn-on of S1 implies the turn-off of series diode D4. There are turn-on losses for S1 and reverse recovery problems with the series diode D4, Fig.5b.

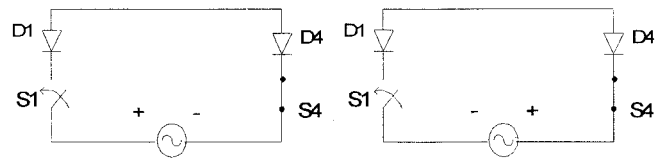


Fig.5a Fig .5b

D. Conclusions

1) The only problematic commutation occurs when the turn-on of the transistors implies the turn-off of a series diode
2) For voltage leading (inductive phase or $f<f_0$) ,cases B.2. and C.1., there are no turn-on switching losses and there is no problematic commutation.
3) For current leading (capacitive phase or $f>f_0$) cases B.1. and C.2. there are no turn-off losses and the turn-on of a transistor implies the turn-off of a series diode so that in this case the commutation process is problematic.
4) The optimum drive for the actual case where the effect of the parasitic wiring inductance has been neglected (topology 1) is with an inductive phase.
5) It can be also concluded that in the case of a short-circuit, where the resonant frequency abruptly increases, and in this case problematic commutation appears. For this reason it is imperative to have very fast series diodes and in some cases also the antiparallel diodes of the switches should be very fast.
6) In order to protect effectively the transistors in the case of a short-circuit the case C.2. should be avoided. That means that the protection strategy has to implement a circuit that inhibits the turn-on of a transistor when this transistor has positive voltage.

III. SWITCHING MODES AND SHORT CIRCUIT BEHAVIOUR FOR TOPOLOGY N° 2 CONSIDERING IDEAL DIODES

The equivalent circuit for topology n° 2 can be seen in Fig.6.

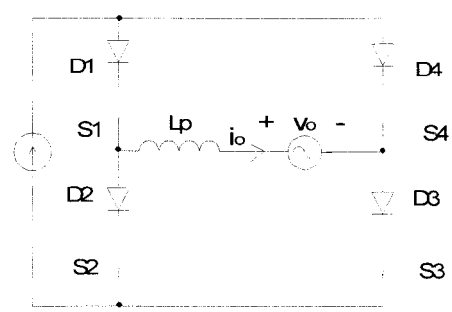


Fig. 6: Equivalent circuit for topology n°2.

The commutation constrains are as follows:

A. General

As in the previous case turn-on must lead turn-off

B. Turn-off switching

As for topology 1, suppose that S4 has been turned-on and S1 is going to be turned-off. In this case two possible situations can be seen in , Fig.7.

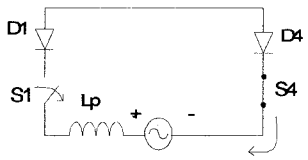


Fig.7a

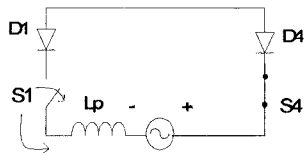


Fig .7b

1) In this case as D1 blocks the output voltage V0, turn-off of S1 happens exactly as in case B.1. for the topology n° 1, so that for this type of commutation the presence of Lp has no effect on the commutation Fig.7a.
2) As in case B.2. for the topology n° 1 the turn-off S1 implies the turn-on of D4 and also there are turn-off losses in S1 but a very high overvoltage appears on S1 due to the high di/dt on Lp when S1 turns-off. This commutation appears as very problematic and has to be avoided, Fig. 7 b.

C. *Turn-on switching*

Suppose that S4 is conducting and S1 is going to be turned-on. Again two situations appaers as shown in Fig. 8.

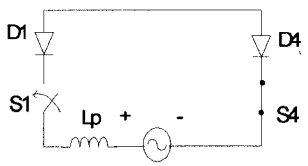


Fig.8a:

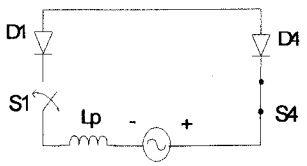


Fig.8b

1) It can be easily seen that in this case, Fig.8a, the turn-on of S1 happens exactly as in case C.1. for the toplogy n° 1 so that the presence of the wiring inductance Lp has no effect on this commutation
2) In this case Fig.8b the turn-on of S1 implies the turn-off of series diode D4 but with limited di/dt by the inductance Lp. In this case turn-on of S1 occurs with reduced turn-on losses and with softer turn-off commutation of D4. Lp acts in this case as lossless turn-on snubber.

D. Conclusions

1) The only problematic commutation occurs in case B.2. A high overvoltage is generated with very high turn-off losses.
2) For inductive phase, cases B.2. and C.1., there are no turn-on losses but a high overvoltage appears at turn-off.
3) For capacitive phase, cases B.1. and C.2. there are reduced turn-on losses due to the fact that the parasitic wiring inductance acts like a lossles turn-on snubber.
4) As a consequence of the former, the optimum drive is with capacitive phase instead of inductive as for topology n° 1.
5) In the case of a short-circuit of the heating coil problematic commutation type B.2 may appear generating dangerous overvoltages.

IV. SWITCHING MODES AND SHORT CIRCUIT BEHAVIOUR FOR TOPOLOGY N° 2 CONSIDERING REAL SERIES DIODES

In this case the transistor drive has to be as in the former case that is with a capacitive phase. In this case due to the reverse recovery of the series diodes, the antiparallel diodes conduct at the turn-off of the transistors In this case an overvoltage is generated due to the reverse recovery current of the antiparallel diodes. To limit this overvoltage, FREDFED Mosfet's should be used. Optimum drive for this case are discussed in [2] and [3].

REFERENCES

[1] E.J. Dede et al."Practical Considerations for Current-Fed Resonant Inverters for Induction Heating Applications" PCIM'96-Nurenberg (Germany).
[2] E.J. Dede et al."On the Design of High Power Current-Fed Inverters for Tube Welding Applications" PCIM'93- Nurenberg (Germany).
[3] .J. Dede et al. "On the Design and Control Strategy of High Power, High Frequency Converters for Tube Welding Applications" PCC'93 Yokohama (Japan).

New Type of Ballast for HID Lamps Using Distributed Constant Line

Masato H. OHSATO, Hideki OHGUCHI,
Toshihisa SHIMIZU, Gunji KIMURA

Dept. of Electrical Eng, Tokyo Metropolitan Univ.
1−1, Minami−osawa, Hachi−oji, Tokyo 192−03, Japan
Phone: +81−426−77−2747 Fax: +81−426−77−2737
e−mail: ohsato@eei.metro−u.ac.jp

Hiroyuki TAKAGI

Kandenko Corporation
4−8−33, Shibaura, Minato−ku
Tokyo 108, Japan

Abstract − **This paper presents a new type of solid state ballast, which operates in the MHz−range frequency. A circuit composed of a voltage−fed half−bridge inverter, a distributed constant line, and a parallel LC resonant circuit has been developed for this purpose. An HID (High Intensity Discharge) lamp is connected to the output terminal of the inverter through the distributed constant line. Here, since the length of the line is adjusted to 1/4 of the propagation wavelength λ, the output voltage of the voltage−fed inverter can be converted to a current source at the load side. From the experimental results, the following issues are considered. The ballast can supply not only high voltage to the HID lamp for igniting for discharge but also constant current to it during discharge condition. The proposed ballast has the capability of dimming control.**

I. Introduction

The recent developments of the HID (High Intensity Discharge) lamp have attracted increasing amounts of affection due to its highly efficient operation and excellent color characteristics. This lamp may be used in various applications, for example, automobile head lamps, back−lights for projectors and so on [1].

The HID lamp exhibits negative resistance characteristics in the operating regions as well as an ability to change its resistance with time. Therefore, a current−limiting device called a ballast is necessary to ensure stable operation.

A conventional type of ballast which operates at low frequency (50 or 60 [Hz]) is not the most practical solution due to its large size, heavy weight and low efficiency.

In order to reduce the size of the ballasts for HID lamps, high frequency (10k−20k[Hz]) ballasts have been developed. However, the arc in the HID lamp tends to be unstable at specific frequency operation ranges. This phenomenon is called "acoustic resonance".

One method for avoiding this phenomenon is to operate at a frequency above this range. However, the switching loss on the ballast becomes greater as the operating frequency increases [2]. In order to reduce the switching loss, a resonant−type inverter is used to provide an electric ballast for a fluorescent lamp [3].

The authors have researched on various types of electric ballasts for use in HID lamps [4]−[7]. In this paper, a novel type of solid state ballast is presented which operates in the MHz−range frequency.

II. Circuit Configuration

The circuit configuration of the proposed ballast is shown in Fig. 1. This circuit is composed of a voltage−fed half−bridge inverter (1 [MHz]), a

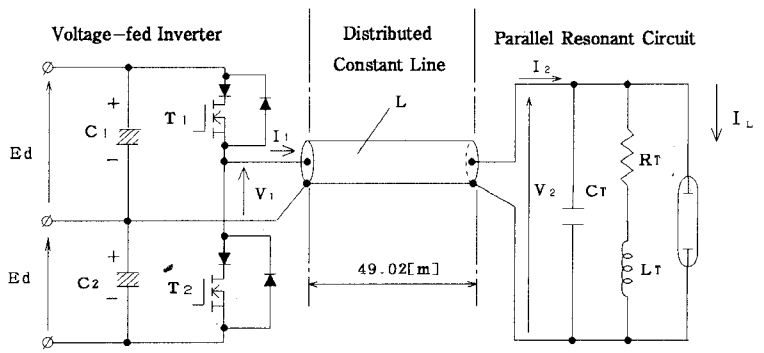


Fig. 1. Circuit configuration.

Key words: Voltage−fed Inverter, HID Lamp, Metal Halide Lamp, MHz Operation, Distributed Constant Line, Ballast.

TABLE I
PARAMETERS OF PROPOSED CIRCUIT.

Device	Part No.	Specification
Power MOSFET T_1, T_2	2SK1020 (Fuji Electric)	V_{DS} : 500 [V] I_D : 30 [A]
Capacitor C_1, C_2		1000 [μF]
C_T		0.01 [μF]
Inductor L_T		2.54 [μH]
R_T		0.46 [Ω]
HID Lamp	HQI-TS (OSRAM)	70 [W]
Distributed Constant Line L	10D-2V (Furukawa Electric)	Z_W : 50 [Ω] C: 102 [nF/km] D: 9.7 [mm] (49.02 [m])
Fast Recovery Diode	ESAC82 (Fuji Electric)	I_0 : 8.0 [A] V_{FM} : 0.55 [V] T_{rr} : 50 [ns]

distributed constant line, a parallel LC resonant circuit, and an HID lamp.

The length of the distributed constant line is selected to be 1/4 of its propagation wavelength λ. This paper examines a 70 [W] metal-halide lamp as one of an HID lamp. The operation frequency is taken as 1 [MHz] in order to avoid the acoustic resonance.

The parameters of the proposed circuit are shown in Table I.

III. CIRCUIT ANALYSIS [8]

The stable operation of the circuit(Fig. 1) is analyzed. The Voltages and currents at the sending and receiving ends of the distributed constant line (length: X shown in Fig. 2) are defined as V_1, I_1, V_2, and I_2, respectively. In order to simplify the equation, loss on the distributed constant line is assumed to be negligible.

The above mentioned voltage and current can be expressed by the following equations:

$$\begin{pmatrix} V_1 \\ I_1 \end{pmatrix} = \begin{pmatrix} \cos \beta X & j Z_w \sin \beta X \\ j \frac{1}{Z_w} \sin \beta X & \cos \beta X \end{pmatrix} \begin{pmatrix} V_2 \\ I_2 \end{pmatrix} \quad (1)$$

where

Z_w : characteristic impedance of the transmission line

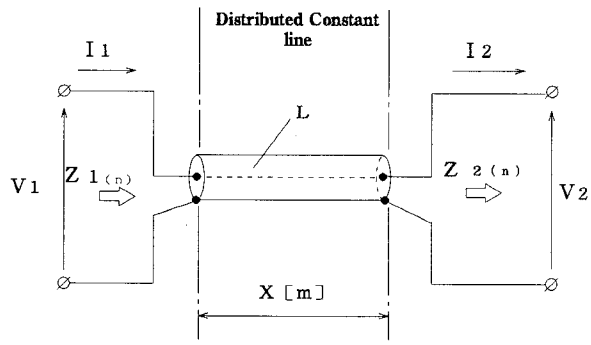


Fig. 2. Distributed constant line.

β : phase constant of the transmission line
($\beta = 2\pi f/v = 2\pi/\lambda$,
v : propagation velocity
λ : propagation wavelength of the transmission line).

When the length of the distributed constant line is set to $\lambda/4$, the coefficient βX becomes :

$$\beta X = \frac{2\pi}{\lambda} \frac{\lambda}{4} = \frac{\pi}{2} \quad . \quad (2)$$

By substituting (2) into (1), the following equation is obtained:

$$\begin{pmatrix} V_1 \\ I_1 \end{pmatrix} = \begin{pmatrix} 0 & j Z_w \\ j \frac{1}{Z_w} & 0 \end{pmatrix} \begin{pmatrix} V_2 \\ I_2 \end{pmatrix} \quad (3)$$

Equation (3) clearly shows that the voltage at the sending end is converted to current at the receiving end and current at the sending end is converted to voltage at the receiving end when the length of the distributed constant line is set to $\lambda/4$.

Now the impedance Z_2 at the receiving end is expressed as :

$$V_2 = Z_2 I_2 \quad . \quad (4)$$

The impedance Z_1 at the sending end is given by (1) and (4):

$$Z_1 = \frac{V_1}{I_1} = \frac{Z_2 \left(\cos \beta X + j \frac{Z_w}{Z_2} \sin \beta X \right)}{\cos \beta X + j \frac{Z_2}{Z_w} \sin \beta X} \quad (5)$$

Therefore, the n-th harmonic impedance $Z_{1(n)}$ at the sending end is given by the following equation:

$$Z_{1(n)} = \frac{Z_2 \left(\cos n\beta X + j \frac{Z_w}{Z_2} \sin n\beta X \right)}{\cos n\beta X + j \frac{Z_2}{Z_w} \sin n\beta X} \quad (6)$$

Equation (6) shows that the harmonic impedance at sending end varies according to the propagation distance or propagation frequency, when the distributed constant line is utilized as an electric power distribution.

Figs. 3(a) and 3(b) show the calculated results of the absolute values of n−th harmonic frequency impedance $|Z_{1(n)}|$ for the transmission line length X, where the fundamental frequency is 1 [MHz].

Fig. 3(a) shows the result before discharging of the HID lamp, and Fig. 3(b) shows the result during discharging of it. Note that the sending end impedance $|Z_{1(n)}|$ varies with the length of the transmission line.

In case that the length of the distributed constant line is selected to $\lambda/4$, the harmonic components in the output current of the inverter is reduced. As a result, the current supplied from the inverter forms a sinusoidal waveform with the fundamental frequency.

IV. Experimental Results

A. Experimental Waveforms

Experimental waveforms are shown in Fig. 4 − 7, respectively. Fig. 4 and Fig. 5 show the waveforms (before discharging of the HID lamp) of the sending and receiving ends on the distributed constant line.

These results demonstrate that the output voltage of the voltage−fed inverter is converted to the current source at the receiving end. Furthermore, the voltage of the ballast is high enough to ignite the discharge of the HID lamp.

Figs. 6 and 7 show the waveforms (discharging condition of the HID lamp) at the load sides. Fig. 6 shows the waveforms of the receiving end on the distributed constant line in detail, and Fig. 7 shows the waveforms at the HID lamp side.

Note that the voltage and current waveforms in Fig. 7 are sinusoidal, that is , the high−order harmonic components are eliminated in the lamp current.

The metal−halide lamp can be regarded as having a variable resistance R. The impedance of the lamp

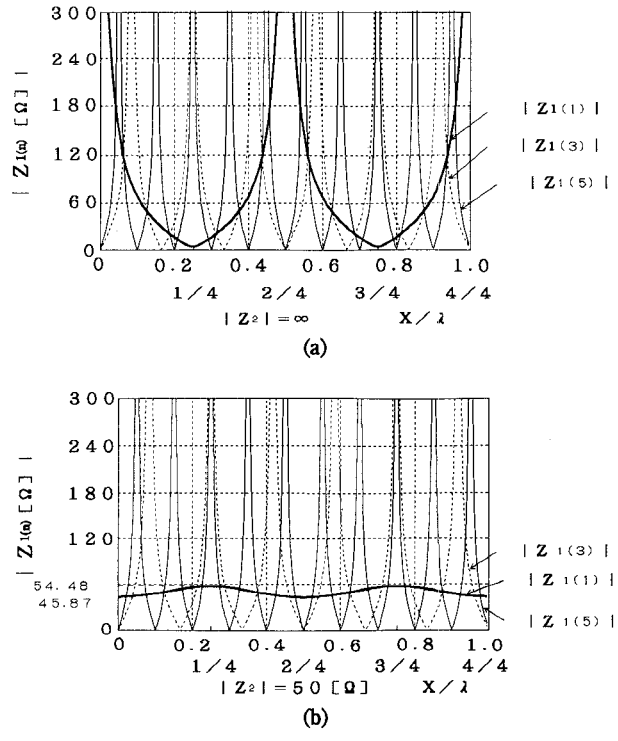


Fig. 3. Calculation results of sending impedance $|Z_1|$ and length of transmission line X/λ : (a) condition before discharge ; (b) condition on discharge of HID lamp.

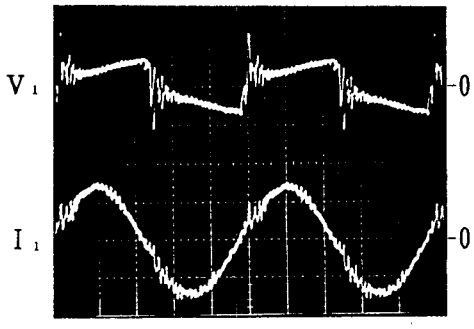


Fig. 4. Waveforms of sending end on distributed constant line: V_1 = 50 V/div, I_1 = 10 A/div, time = 0.2 μ s/div (before discharge).

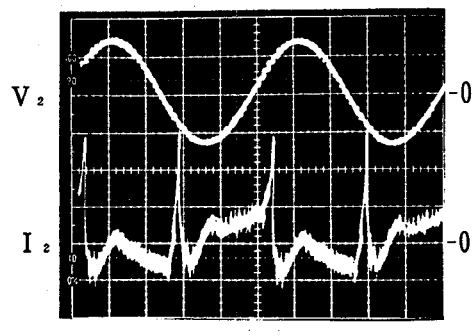


Fig. 5. Waveforms of receiving end on distributed constant line: V_2 = 500 V/div, I_2 = 1.0 A/div, time= 0.2 μ s/div (before discharge).

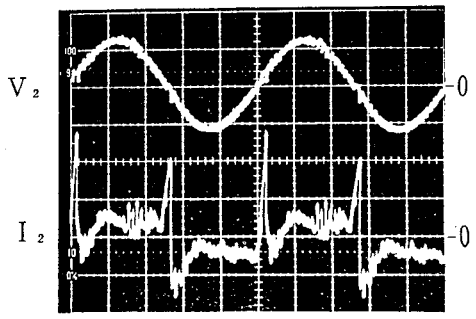


Fig. 6. Waveforms of receiving end on distributed constant line: V 2 =100 V/div, I 2 = 1.0 A/div, time= 0.2 μ s/div (on discharge).

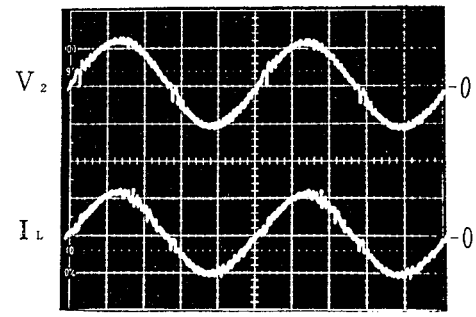


Fig. 7. Waveforms at HID lamp side: V 2 =100 V/div, I L = 0.5 A/div, time=0.2 μ s/div (on discharge)

varies according to the electrical condition of the HID lamp. The proposed ballast is suitable for HID lamps based on its ability to supply high voltage before discharge and low voltage during discharge.

B. Dimming Control

By varying the input voltage 2E d of the inverter, the lamp current and the related lamp power are controlled. Therefore, the dimming control is possible. The dimming characteristics is shown in Fig. 8. Note that the luminous flux varies in proportion to the input voltage in Fig. 8.

V. Conclusions

The basic features of the ballast could be summarized as follows:

1) A novel type of ballast has been developed for HID lamps. The analysis and the characteristics of the ballast are described.
2) The ballast can supply enough high voltage to ignite discharge of a HID lamp.
3) The output voltage of the voltage-fed inverter can be converted to a current source at the load side by using the distributed constant line with 1/4 of the propagation wavelength λ .

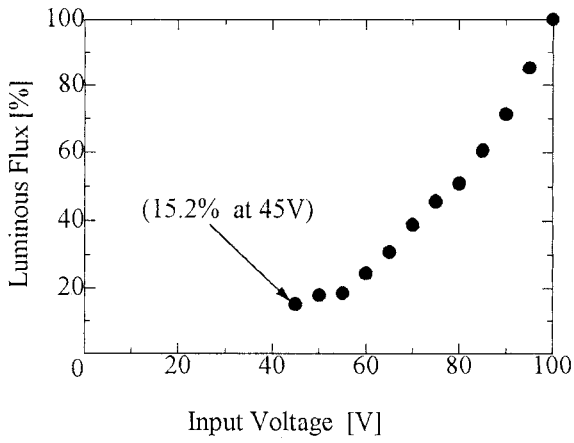


Fig. 8. Dimming characteristics of HID lamp.

4) The proposed ballast has the capability of dimming control.

Acknowledgement

The authors would like to thank Miss M. Matsushiro and Mr. M. HAYASHI, students of Tokyo Metropolitan University, for their experimental assistance.

References

[1] "Special Issue for Metal Halide Lamps and its Applications," *J. Illum. Engng. Inst. Jpn.*, Vol. 77, No. 12, pp. 4-35, 1993 (in Japanese).

[2] M. Nakamichi and M. Ihara, "Trends of Electronic Tech-nologies for HID Lamps Luminaries," *J. I llum. Engng. Inst. Jpn.*, Vol. 77, No. 5, pp. 233-237, 1993 (in Japanese).

[3] M. C. Cosby, Jr. and R. M. Nelms, "A Resonant Inverter for Electronic Ballast Applications," *IEEE Trans. Ind. Electron.*, Vol.41, No.4, pp. 418-425, Aug. , 1994.

[4] M. H. Ohsato, S. Inarida, G. Kimura, M. Shioya, and T. Kawaguchi, "New Type of Ballast for HID Lamps Using Series Resonant Circuit," *Proc. of IECON'92*, Vol. 1, pp. 191-195, 1992.

[5] T. Yamada, M. H. Ohsato, T. Shimizu, G. Kimura, and T. Kanaoka, "New Type of Ballast for HID Lamps with a Single-Ended Resonant-Type Inverter Circuit Using Leakage inductance," *Proc. of IPEC-Yokohama'95*, Vol.3, pp. 1266-1271, 1995.

[6] Q. Mao, M. H. Ohsato, T. Shimizu, G. Kimura, Y. Takuchi, and H. Takagi,"MHz Operation of Voltage-fed Inverter for HID Lamps Using Distributed Constant Line," *Proc. of IAS'96*, Vol. 4, pp.2120-2125, 1996.

[7] M.H. Ohsato, H. Ohguchi, T. Shimizu, G. Kimura, and H. Takagi, "High Frequency Operation of HID Lamps Using Distributed Constant Line," *Papers of Technical Meeting on Semiconductor Power Conversion of IEEJ*, SPC-96-118, 1996 (in Japanese).

[8] T. Shimizu and M. Shioya, "Characteristics of Electric Power Transmission on High-Frequency Inverter Having Distributed Constant Line at Load Side," *IEEE Trans. Ind. Electron.*, Vol.38, No.2, pp. 115-120, Apr. 1991.

All Digital Controlled Three-Phase UPS without Inverter-Transformer

Akihiko Kanouda, Yoshimi Sakurai, Kenji Kubo, *Keizou Shimada,
*Hideaki Kunisada, and *Hideyasu Umetsu
Hitachi Research Laboratory, *Hitachi Works, Hitachi Ltd.
1-1, Omika-cho 7-chome, Hitachi-shi 319-12, JAPAN
Fax: +81-294-52-7599, Phone: +81-294-52-7564
E-mail: akanouda@hrl.hitachi.co.jp

***Abstract* —A fully digital-controlled three-phase UPS (Uninterruptible Power System) is developed which does not have an inverter- transformer. To remove the transformer, a different type of main circuit from the conventional UPS is adopted. One phase of the input AC is regarded as the common voltage of the main circuit. A DC voltage stabilizer solves problems caused when this transformer-less circuit is applied to the UPS. A digital controller with two RISC (Reduced Instruction Set Computer) processing micro-computers to operate the circuit is also proposed. Experiments show the THD (Total Harmonic Distortion) of the input current is less than 5%, and that of the output voltage is less than 3.6% under non-linear load.**

I. INTRODUCTION

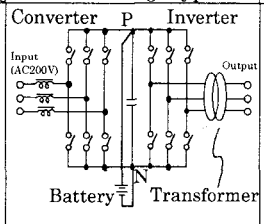
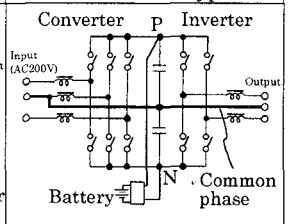
Nowadays, it is important for a UPS (Uninterruptible Power System) to have a reduced size and weight so that its loaded computer systems becoming smaller than the conventional. However, in the case of the three- phase UPS, an inverter-transformer is needed to isolate the voltage caused by PWM switching between the DC line and output lines. So for this UPS it is difficult to cut the size and weight [1]. Therefore we adopted a V- connection type circuit [2] for the main circuit of the UPS, to eliminate the transformer. But voltages of DC capacitors of the V- connection type UPS fluctuate when the inverter phase is not equal to the converter phase because of the difference in input and output current flows through the DC capacitors. In this paper, we give a method for stabilizing voltages of the DC capacitors as one of the functions of the converter. The V- connection type converter controls three- phase input currents with two line voltage vectors, so it is different from the conventional full bridge type converter which controls them with three- phase voltage vectors. This is why it is more difficult for the V- connection type converter to restrain distortion of input currents than the conventional.

In this paper, we analyze the relation between the ACR (Automatic Current Regulator) response and the distortion and compare these results with experimental results. The V- connection type inverter has to make sinusoidal three- phase output voltages with two line voltage vectors. It is important for the inverter to reduce harmonic distortion of the output voltage particularly in the case of an non- linear load. Then we present an output voltage waveform control scheme with two compensating methods to restrain harmonic distortion. Comparison between the results of simulation and experimentation is made. We made the waveform controller using two RISC (Reduced Instruction Set Computer) processing microcomputers without a DSP (Digital Signal Processor).

II. CONSTITUTION OF DEVELOPED UPS

Table 1 shows main circuit types for three- phase UPS.

Table 1 Main Circuit Types for Three-Phase UPS

	Full bridge type	V-connection type
Circuit		
V_{PN}[V]	290−410	600−700
Number of SW devices	Converter: 6 Inverter: 6 Total: 12	Converter: 6 Inverter: 4 Total: 10
Inverter-transformer	Necessary	Not Necessary

The full bridge type main circuit is generally used for the conventional UPS. DC voltage between P and N is from 290V to 410V under 200V AC input condition. However, an inverter- transformer is

necessary to isolate the voltage caused by the PWM switching between the DC line and output lines for this type UPS. The other type is the V- connection [2,3]. One of its features is that one phase, called the *common phase* of the power source, is connected to connect point of the two DC capacitors, and loaded directly. The number of switching devices which constitute a converter is six, the same as in the conventional full bridge type. But an inverter can constitute four arms of the switching devices. This type of main circuit does not need the inverter-transformer because voltage between the DC line and output lines is stable because of the common phase. Therefore we select the V- connection type for the UPS.

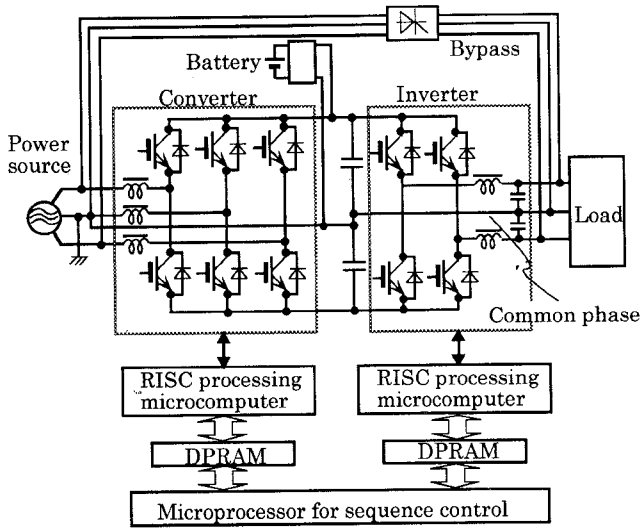


Fig.1 Constitution of Fully Digital- Controlled UPS without Inverter-Transformer

Fig. 1 shows a constitution of the developed transformer- less UPS. This main circuit use IGBT (Insulated Gate Bipolar Transistor) devises and diodes for converter and inverter. Two RISC processing microcomputers control the main circuit. Operating commands, sent by the microprocessor to control sequence, inform the RISC microprocessors via the DPRAM (Dual port Random Access Memory).

III. CHARACTERISTICS OF THE V- CONNECTION TYPE MAIN CIRCUIT

Fig. 2 shows the stability problem of the V-connection type UPS. Generally, constitution of the V- connection type converter is the same as for the V-connection type inverter shown in Fig. 1. When frequency and phase of the inverter are not completely synchronized with those of the power source, I_{in} which flows as the common phase from the power source is not equal to I_{out} which flows as the common phase for the load. Voltages of DC capacitors, V_{c1} and V_{c2}, fluctuate because different currents of I_{in} and I_{out} flow through the DC capacitors. Voltage fluctuation shortens the lifetime of the DC capacitors. Harmonic distortion of input current and output voltage are also increased by the fluctuation.

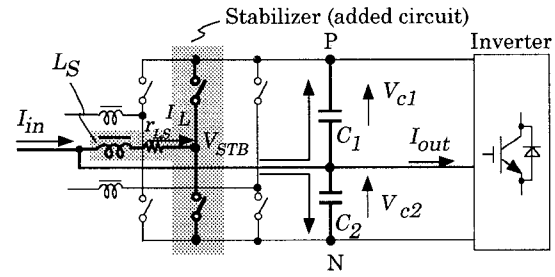


Fig. 2 Principle of a Voltage Stabilizer for the DC Capacitors

In order to suppress the voltage fluctuation, we add a circuit consisting of a reactor L_S and two switching devices. This circuit is called a voltage stabilizer for the DC capacitors and is shown in Fig. 2.

IV. VOLTAGE STABILIZER FOR THE DC CAPACITORS

Fig. 3 shows a circuit model of the stabilizer.

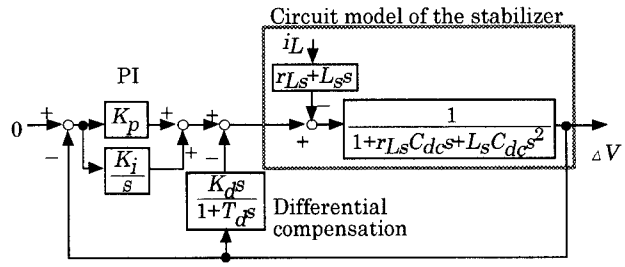


Fig. 3 Circuit Model of the Stabilizer

DC capacitors C_1 and C_2 can be regarded as parallel connected in the case of the voltage fluctuation, and the following equation is used.

$$C_{dc} = C_1 + C_2 \quad (1)$$

Therefore C_{dc}, L_S and r_{LS} (wiring resistance of L_S) make a series resonant circuit. To control this circuit, PI control with feed- back voltage fluctuation ΔV is used. However the control object has a secondary delay function, so gain of the control object increases

and its phase is delayed 180 degrees near the resonant frequency. As a result, the controller become unstable. In order to improve the damp characteristics at the resonant frequency, differential compensation (shown in Fig. 3) is added.

Fig. 4 shows a digital control block diagram of the stabilizer for the DC capacitors.

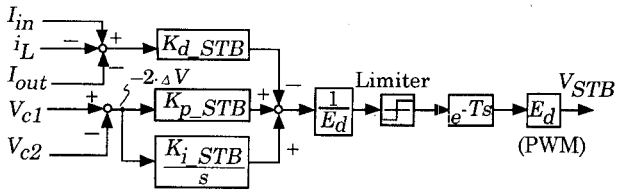


Fig.4 A Digital Control Block Diagram of the Stabilizer

Using V_{c1} and V_{c2} , we can calculate ΔV as follows:

$$\Delta V = -\frac{1}{2}(V_{c1} - V_{c2}). \quad (2)$$

DC voltage E_d is defined as follows:

$$E_d = \frac{V_{PN}}{2}. \quad (3)$$

Differential compensation is realized by using the current i_{dc} which flows into the DC capacitors.

$$i_{dc} = I_{in} - i_L - i_{out} \quad (4)$$

$$\frac{d\Delta V}{dt} = \frac{1}{C_{dc}} i_{dc} \quad (5)$$

$$K_{p_STB} = \frac{K_p}{2} \quad (6)$$

$$K_{i_STB} = \frac{K_i}{2} \quad (7)$$

$$K_{d_STB} = \frac{K_d}{C_{dc}} \quad (8)$$

Performance of the stabilizer is confirmed with a simulation which can includes circuit elements and control block. In this simulation, the current difference between I_{in} and I_{out} is the standard value of the input current, and it is expressed as a current source.

Fig. 5 shows the characteristics of V_{c2} and response with the differential compensation gain K_{d_STB}. Voltage variation which is expressed as a rated value based on E_d decreases with increasing K_{d_STB}, but when considering the response too, K_{d_STB} is selected as 0.008.

Fig. 6 shows the characteristics of proportional gain of the stabilizer: K_{p_STB}. The stabilizer cannot be operated when K_{p_STB} is greater than 10 because of instability. K_{p_STB} is therefore set to 7.0. In this case, the variation of V_{c2} (and V_{c1}) is less than 1 %, and the response is about 22 ms. Integrated gain K_{i_STB} which is 0 in this simulation is set to a very small value in the real controller.

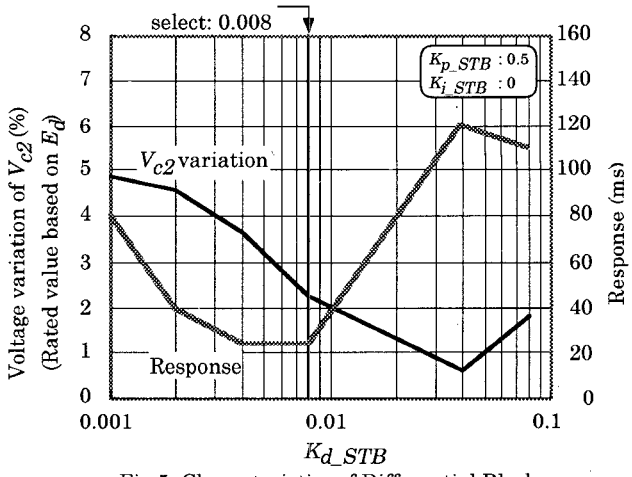


Fig.5 Characteristics of Differential Block

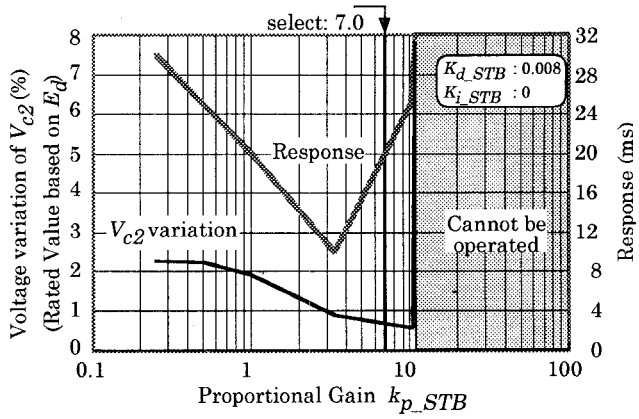


Fig.6 Characteristics of the Stabilizer

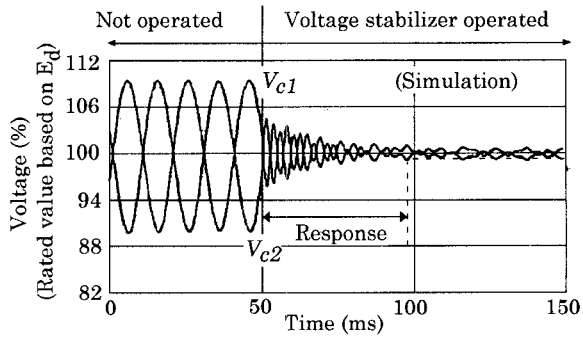


Fig.7 Voltage Waveforms of DC Capacitors

Fig. 7 shows the simulated voltage waveforms of DC capacitors. The waveform of V_{c1} is almost equal to V_{c2}. $Vc1$ and $Vc2$ fluctuate about 20 % alternately when the stabilizer is not operated. The DC

capacitor voltage is less than 2 % with a defined response when the stabilizer is operated.

Other experimental results, not shown in these figures, have less than 2 % variation of DC capacitor voltage under a different current which is double the standard value of the input current.

V. CHARACTERISTICS OF THE INPUT CURRENT CONTROLLER

Fig. 8 shows the converter circuit and voltage vectors of the V- connection type converter.

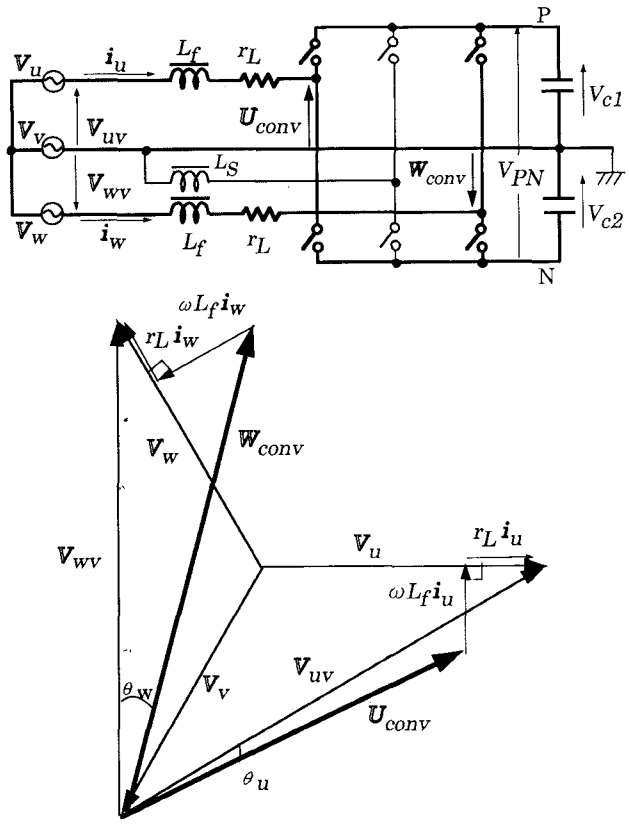


Fig.8 Voltage Vectors of the V-Connection Type Converter

The phases of the input currents i_u and i_w which are sinusoidally operated are kept equal to the phases of the voltages V_u and V_w, respectively. From this condition, output voltage vectors of the converter $\mathbb{U}_{conv}$ and $\mathbb{W}_{conv}$ have to become as shown in Fig. 8. They are expressed as follows:

$$\mathbb{U}_{conv} = \mathbb{V}_{uv} - \omega L_f \mathbb{i}_u - r_L \mathbb{i}_u, \qquad (9)$$

$$\mathbb{W}_{conv} = \mathbb{V}_{wv} - \omega L_f \mathbb{i}_w - r_L \mathbb{i}_w. \qquad (10)$$

The absolute values of the converter voltages are the same as in the case of the full bridge type converter, but $\mathbb{W}_{conv}$ is larger than $\mathbb{U}_{conv}$ for the V-connection type converter, as can be seen in this figure.

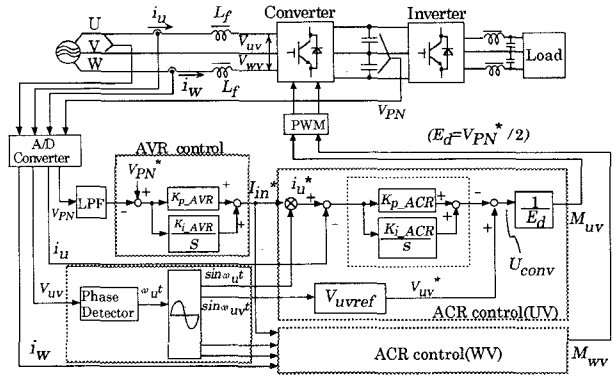


Fig. 9 A Block Diagram of PWM Input Current and DC Voltage Controller

Fig. 9 shows a block diagram of the input current and DC voltage controller. The sensed DC voltage V_{PN} is compared with the voltage reference V_{PN}^*. The AVR (Automatic Voltage Regulator) block calculates the input current reference I_{in}^*. Current reference I_{in}^* is multiplied by sine waves $\sin \omega_u t$ and $\sin \omega_w t$, and I_u^* and I_w^* are outputted. The two ACR blocks compare the sensed current signals Iu and Iw with I_u^* and I_w^*, respectively. PWM control signals to operate the converter voltages V_{uv} and Vwv are obtained for every ACR output [4].

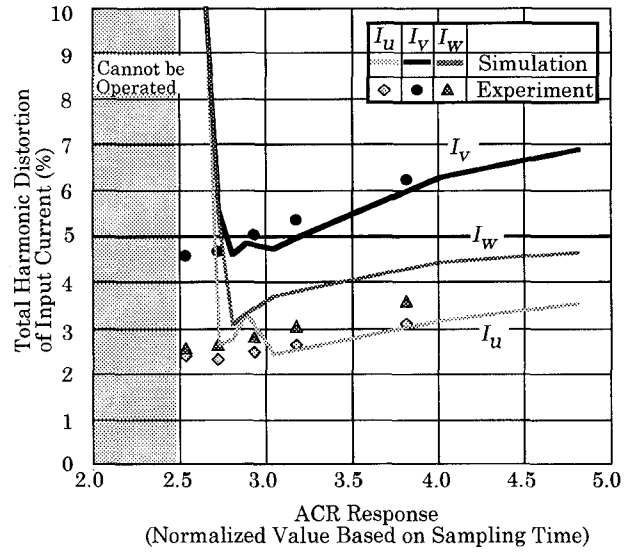


Fig. 10 THD of Input Current

Fig. 10 compares simulation and experiment results for the digital controlled converter using the control block shown in Fig. 9. ACR response is expressed as the normalized value based on the sampling time. Therefore ACR response becomes higher when the sampling time is smaller.

The higher the ACR response, the more the THD of the input currents decrease. But input currents are not able to controlled when ACR response is higher than about 2.5. Experimental values agree well with the simulation results. Input current *Iv* is more distorted than the other phases because the controller cannot control *Iv* directly. According to these results, the THD of the input current is lowered by less than 5 % when the ACR response is set at 2.7.

VI. INVERTER CONTROL BLOCK

Fig. 11 shows the inverter control block diagram. V- connection type inverter controls output line voltage V_{uvo} and V_{wvo}.

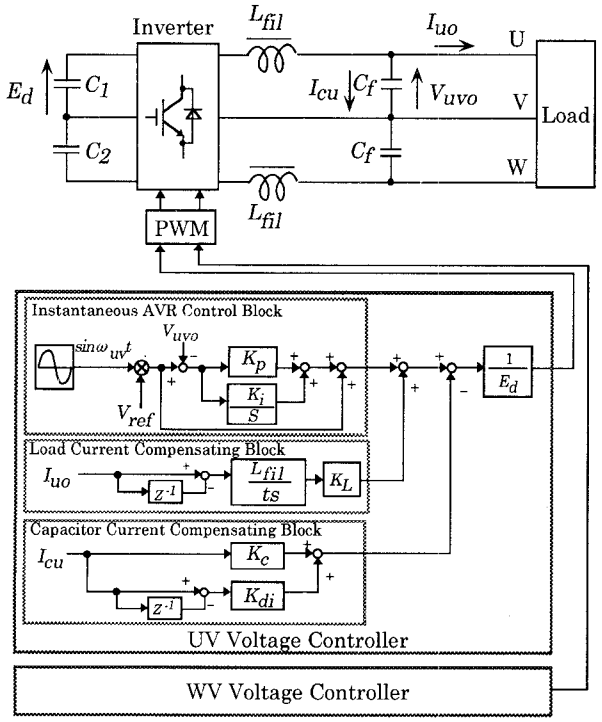


Fig. 11 Inverter Control Block Diagram

There is a UV voltage controller and a WV voltage controller which have the same composition. The UV voltage controller is divided into three blocks. The instantaneous AVR block compares the voltage reference and the sensed voltage signal V_{uvo}. In addition to the AVR control block, two types of compensating blocks are prepared in the controller to restrain the harmonic distortion of the output voltage, particularly in the case of non- linear load [5].

The capacitor current compensating block computes the voltage drop of the filter capacitor C_f using the sensed capacitor current I_{cu}. The load current compensating block computes the voltage drop of L_{fil}. These compensating blocks operate efficiently in the case of sudden changes of the load current.

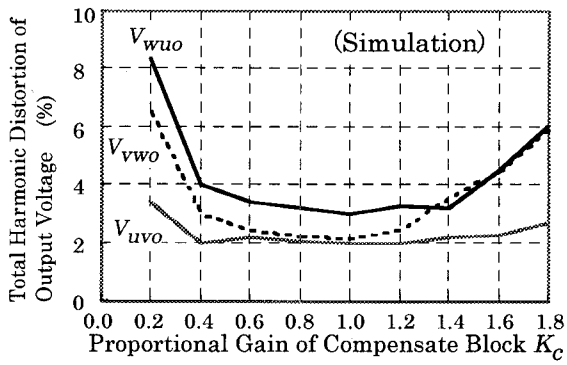


Fig.12 THD Dependence on Capacitor Current Compensating Block (100% Rec. Load)

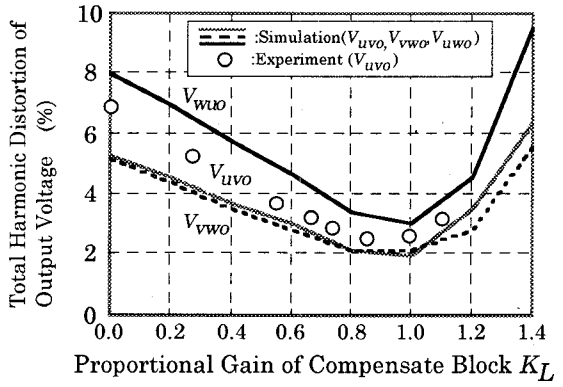


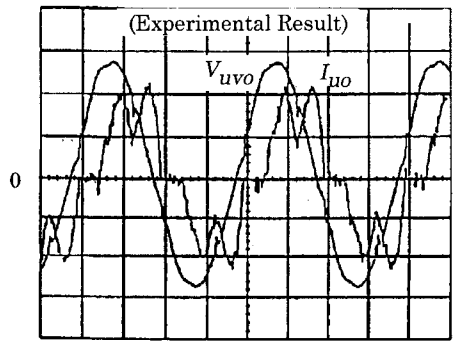
Fig.13 THD Dependence on Load Current Compensating Block (100% Rec. Load)

Fig. 12 shows simulation results to verify the effect of the capacitor current compensating block under a 100 % rectifier load condition. V_{uvo} has a flat characteristic compared with the two other line voltages concerned with the proportional gain K_c . Output voltage V_{wuo} is most distorted because it is not controlled. The minimum point of THD is when Kc is set at 1.0.

Fig. 13 shows simulation and experimental results under a 100 % rectifier load condition. The experimental results differ from the simulation results, but the trend is the same. The minimum point of THD is when K_L is set at 1.0. This result agrees well with the theoretical characteristics of the compensating block.

Fig. 14 shows the waveforms of output voltage and current under a 100 % rectifier load condition. The THD of the voltage waveform is 2.37 % for V_{uvo}.

V_{wuo} is the most distorted of the three phases, and the value is 3.58 %.



(V_{uvo}: 100V/div. I_{uo}: 125A/div. Time: 5ms/div)

Fig. 14 Output Voltage and Current (100% Rec. Load)

VII. CONCLUSION

In this paper, we developed a V- connection type three- phase transformer- less UPS system. It includes a voltage stabilizer for the DC capacitors to solve the stability problem when the V- connection type main circuit is applied to the UPS. We also offered an all digital- controller for the UPS circuit. Control gain to stabilize voltages of the DC capacitors was obtained. Experimental values agreed well with the simulation results concerned with the converter. The THD of the input current of the converter was lowered by less than 5 % in experiments. According to the experimental results of the inverter, THD of the output voltages was less than 3.6 % under a 100 % rectifier load condition.

REFERENCES

[1] Fact -finding and survey committee for the new type power supply system, "Trend of the Uninterruptible Power Supply System ", IEE Japan Technical Report, No. 596, July 1997

[2] A. Kanouda, et al. , "A Digital Controlled Three-Phase Uninterruptible Power System without Inverter-Transformer", National Convention Record IEE Japan, No. 918, pp. 4-217-218, April 1997

[3] M. Mishima and I. Takahashi, "Development of a Simple Flywheel UPS having Active Filter Ability", National Convention Record IEE Japan, JIASC '91, No. 112, pp. 490-495, August 1991

[4] K. Sakai, et al., "Control Schemes for Three-Phase PWM Converters", National Convention Record IEE Japan, No. 729, Vol. 4, pp. 29- 30, March 1996

[5] M. J. Ryan and R. D. Lorentz, "A High Performance Sine Wave Inverter Controller with Capacitor Current Feedback and "Back-EMF" Decoupling", University of Wisconsin- Madison, Research Report 95- 22, August 1995

Steady-State Characteristics of an Overload-Protected Frequency-Compensated Current-Feedback Magnetic Multivibrator

Akihiko KATSUKI, Masaki OUCHIYAMA, and Tomoko TAKESHITA
Department of Computer Science and Electronics
Faculty of Computer Science and Systems Engineering
Kyushu Institute of Technology
680-4 Kawazu, Iizuka-shi, Fukuoka 820, JAPAN
Fax: +81-948-29-7651, Phone: +81-948-29-7677
E-mail: katsuki@cse.kyutech.ac.jp

Abstract — Current-feedback magnetic multivibrator (Wilson-Moore circuit) is highly efficient and the number of components is extremely small. However, this circuit has no ability of overload protection and the frequency of oscillation depends much on the load current. So, we proposed an improved current-feedback magnetic multivibrator with overload protection and frequency compensation. In this paper, steady-state characteristics of this circuit are investigated in detail.

1. Introduction

Push-pull-transistor magnetic multivibrators are widely used as power supply for electronic equipment rated at several kilowatts or less. These circuits of self-excitation are reliable and the number of components is extremely small. Royer circuit[1], Jensen circuit[2], and Wilson-Moore circuit[3] are especially well-known.

Since switching transistors of Royer circuit and Jensen circuit are voltage-feedback driven, these circuits can protect themselves from overloading. However, with light loading, the transistors are overdriven and the efficiency decreases. In Jensen circuit, collector-current spike can be removed by the use of linear output transformer. However, the frequency of oscillation depends on the load current as well as the power supply voltage, because p-n junction voltages are utilized to determine the frequency.

In contrast to these circuits, Wilson-Moore circuit employs a technique of the current feedback. Consequently, the efficiency is kept high over a wide range of the load current and this circuit is suitable for high-frequency operations. However, this circuit has no ability to protect itself from overloading. In addition, the frequency of oscillation varies much according to the load current by the same reason as Jensen circuit's.

So, we proposed a new current-feedback magnetic multivibrator with frequency compensation and overload protection[4]. In this paper, steady-state characteristics of this circuit are presented by experimental results with respect to both ac load and dc load. Operations with capacitive ac load are also considered.

2. Circuit

Fig.1 shows basic circuit of the overload-protected frequency-compensated current-feedback magnetic multivibrator. The power supply voltage is represented by E_S. The diode D_7 and the resistor R_S construct the start circuit. SR is the current-feedback transformer with a saturable core and T_3 the output linear transformer. N_B, N_C, N_1, N_2, and N_3 represent turns numbers of windings.

The circuit for cessation of oscillation[5] is constructed by the linear transformer T_1 (directed by T_{1a}, T_{1b}, T_{1c}, and T_{1d} in Fig.1), the diodes D_1~D_6, and the resistor R_F. And the circuit for compensation of oscillation frequency[6] is constructed by the linear transformer T_2 (directed by T_{2a}, T_{2b}, and T_{2c} in Fig.1) and the resistor R_C. N_D, N_F, N_P, N_Q, N_R, N_S, and N_T represent turns numbers of windings.

For dc loading, a diode-full-wave-rectifier bridge by the diodes D_8~D_{11} and a capacitor C-input smoothing circuit are inserted between the secondary winding N_2 of T_3 and the load resistor R_L. The dc load current is represented by I_L.

3. Circuit Operations

In the following discussions, we consider the positive half-cycle in which the transistor T_{r1} operates and T_{r2} is cutoff. In this case, D_1, D_2, and D_3 are reverse-biased by the voltage e_B ($\fallingdotseq v_{BE} + v_{D7}$) induced in the base winding N_B of the saturable core SR and these are cutoff, where v_{BE} and v_{D7}

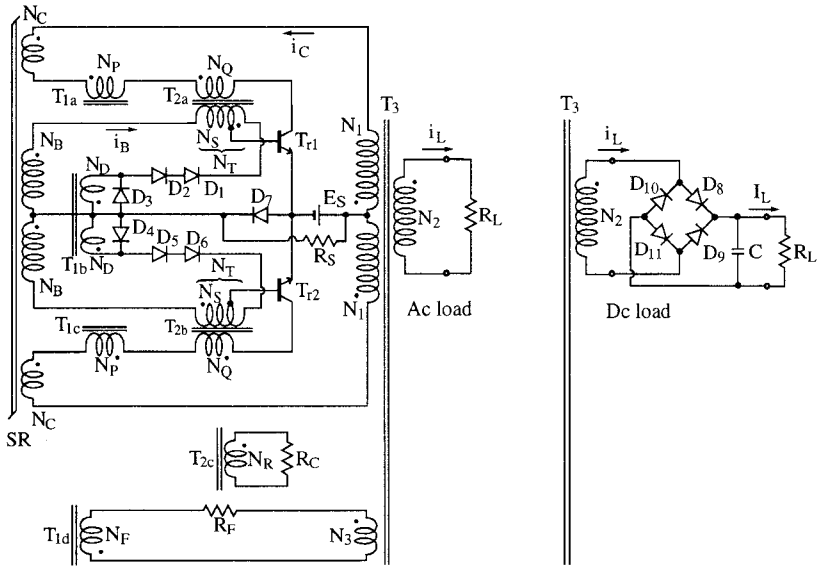


Fig.1. Overload-protected frequency-compensated current-feedback magnetic multivibrator.

are the base-emitter voltage of T_{r1} and the forward-voltage drop of D_7 respectively.

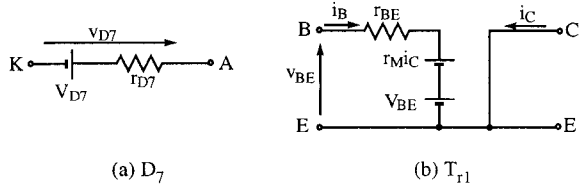
The undermentioned assumptions are made for simplicity of the analysis. (1) SR has the ideal rectangular magnetizing curve. (2)The equivalent circuit of D_7 for the conducting state is expressed by Fig.2(a). (3)The equivalent circuit of T_{r1} for the on state is shown by Fig.2(b). (4)The resistance of R_S is infinite.

A. Light loading

Circuit operations are explained by Fig.3 when the load current i_L satisfies the following relation

$$i_L < \frac{N_F N_3 E_S}{N_P N_2 R_F}. \tag{1}$$

D_4 conducts and the current i_{D4} flows. D_5 and D_6 are nonconducting though these diodes are slightly forward-biased by the voltage $v_{D5} + v_{D6}$ ($\fallingdotseq v_{BE} + v_{D7} - v_{D4}$). v_{D4}, v_{D5}, and v_{D6} are the forward-voltage drops in D_4, D_5, and D_6 respectively. Because the base current i_B is proportional to the collector current i_C, T_{r1} is current-feedback driven.



(a) D_7 (b) T_{r1}

Fig.2. Equivalent circuits of D_7 and T_{r1} for the on state.

B. Heavy loading

When the following relation

$$i_L > \frac{N_F N_3 E_S}{N_P N_2 R_F}. \tag{2}$$

is satisfied, circuit operations are expressed by Fig.4. D_5 and D_6 conduct, and the current i_{D5} flows. D_4 is nonconducting because this diode is almost zero-biased by the voltage v_{D4} ($\fallingdotseq v_{BE} + v_{D7} - v_{D5} - v_{D6}$).

If the following relation

$$\frac{N_C}{N_B} = \frac{N_P}{N_D}. \tag{3}$$

is satisfied, i_B is proportional to E_S. In this case, T_{r1} is voltage-feedback driven.

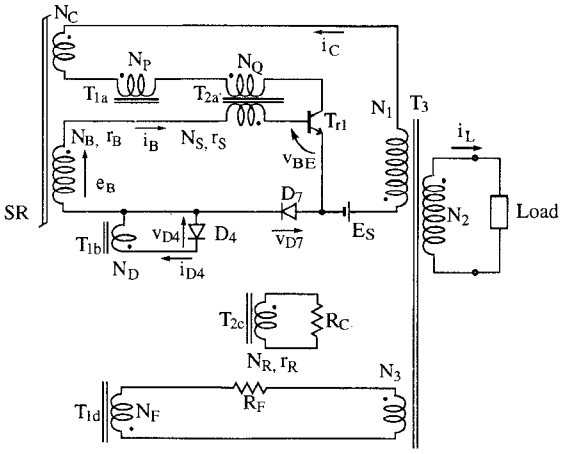


Fig.3. Circuit operations with light loading.

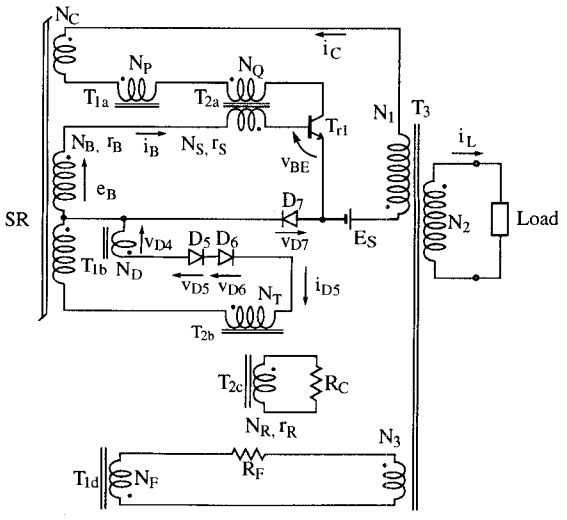


Fig.4. Circuit operations with heavy loading.

4. Conditions for Frequency Compensation

Here, we explain the conditions for that the oscillation frequency f becomes indepedent of i_L and E_S.

A. Dependence of f on i_L

With light loading, f is independent of i_L when the following relation on R_C

$$R_C + r_R = \frac{r_M + \frac{N_C}{N_B}(r_B + r_S + r_{BE} + r_{D7})}{\left(\frac{N_S}{N_R}\right)^2\left(\frac{N_Q}{N_S} - \frac{N_C}{N_B}\right)} \qquad (4)$$

is satisfied, where r_B, r_R, and r_S are resistances of the windings N_B, N_R, and N_S respectively.

Next, the case of heavy loading is considered. It is impossible to exchange R_C in operation. In this case, it is necessary for N_T to be determined according to the following relation.

$$\frac{N_T}{N_S} = 1 + \frac{r_B + r_S + r_{BE} + r_{D7}}{r_M + \frac{N_C}{N_B}(r_B + r_S + r_{BE} + r_{D7})}\left(\frac{N_Q}{N_S} - \frac{N_C}{N_B}\right). \qquad \text{..... (5)}$$

The winding N_T of T_{2b} plays an important role in the frequency compensation.

B. Dependence of f on E_S

When the circuit is light-loaded, f does not depend on E_S originally. If (4) and (5) are satisfied, it is derived with heavy loading that f becomes indepedent of E_S. Therefore, determination of R_C and N_T by (4) and (5) makes f independent of i_L and E_S throughout light loading and heavy loading.

5. Conditions for Cessation of Oscillation

When i_L increases and the relation $i_C = h_{FE} i_B$ is satisfied, T_{r1} operates in the active region and the oscillation stops. h_{FE} is the common-emitter static forward current transfer ratio. The maximum load current i_{Lm} is given by the following equation

$$i_{Lm} = \frac{h_{FE}\frac{N_F N_3 E_S}{N_D N_2 R_F}}{1 - \left(\frac{N_C}{N_B} - \frac{N_P}{N_D}\right)h_{FE}}. \qquad (6)$$

i_{Lm} means the load current at cessation of oscillation.

6. Experimental Results

In this paper, experimental results are shown with respect to both ac load and dc load. Fig.5 shows the relations between the maximum load currents i_{Lm}, I_{Lm} and R_F (the characteristics of overload protection). Next, the characteristics of frequency compensation are given in Fig.6 (the relations between f and i_L, I_L) and Fig.7 (the relations between f and E_S). It is seen from these figures that the data on ac load are almost in accord with those on dc load.

For reference, graphs on the current-feedback magnetic multivibrator (see Fig.A1) are presented. This circuit is obtained by adding the base-bias circuit (in other words, the starting circuit) to original Wilson-Moore circuit. Usually, the circuit shown in Fig.A1 is called the current-feedback magnetic multivibrator. The relations between f and i_L, I_L are presented in Fig.A2 and the relations between f and E_S in Fig.A3.

With respect to the fequency-compensated current-feedback magnetic multivibrator (see Fig.A4) and the overload-protected current-feedback magnetic multivibrator (see Fig.A7), circuit diagrams and their characteristics are shown in APPENDIX.

Fig.8 presents the characteristics of oscillation frequency with capacitive ac load. A series-combination circuit of capacitor C_L and resistor R_L (see Fig.8) was used as load in

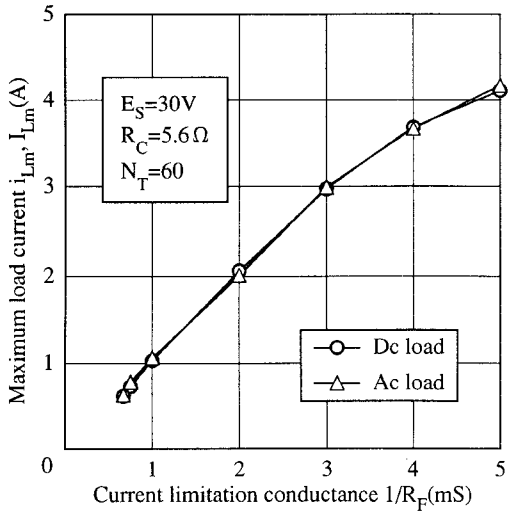


Fig.5. Characteristics of overload protection.

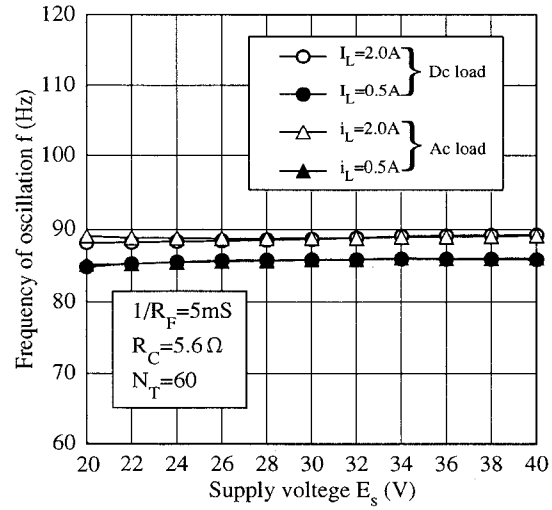


Fig.7. f vs. characteristics of E_S.

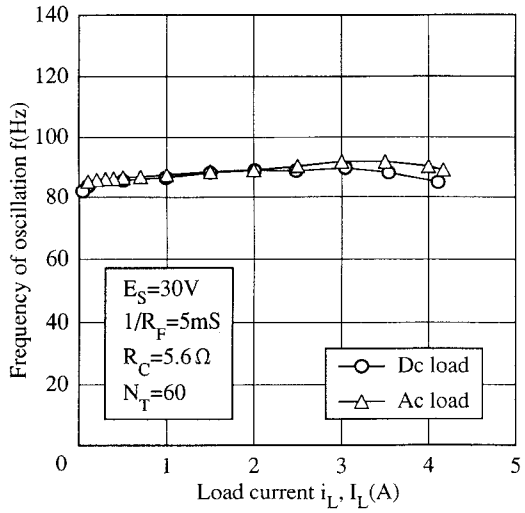


Fig.6. f vs. characteristics of i_L and I_L.

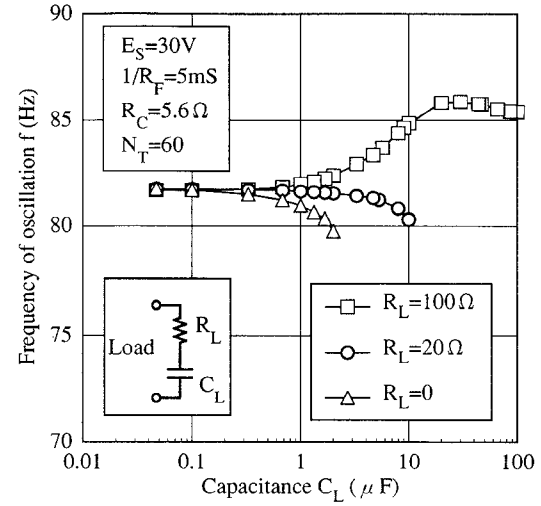


Fig.8. Characteristics of f with capacitive ac load.

measurements. It is seen from Fig.8 that this circuit can operate normally with pure-capacitive load.

The semiconductors used in experiments and the values of parameters are as follows:

T_{r1}, T_{r2}: Silicon transistors 2SD641, D_1~D_7: Silicon diodes U05E, D_8~D_{11}: Silicon diodes 12FC12, C: Aluminum electrolytic capacitor 4400μF, V_{BE} = 0.75V, V_{D7} = 0.78V, r_{BE} = 0.10Ω, r_M = 0.038Ω, r_{D7} = 0.08Ω, r_S = 0.067Ω, r_B = 0.13Ω, r_R = 0.26Ω, $N_1 = N_2 = N_3$, $N_B = N_D = N_F$ = 100, $N_C = N_P = N_Q$ = 10, N_S = 50, N_R = 150.

7. Conclusion

Steady-state characteristics of the proposed overload-protected frequency-compensated current-feedback magnetic multivibrator were investigated and experimental results were presented on both ac load and dc load. It was confirmed that both functions of frequency compensation and overload protection act well. Operations with inductive ac load will be reported in another article.

References

[1] G.H.Royer, "A switching transistor d-c to a-c converter having an output frequency proportional to the d-c input voltage," Trans. Commun. Elect., AIEE, vol.74, pp.322-326, July 1955.

[2] J.L.Jensen, "An improved square-wave oscillator circuit," Trans. Circuit Theory, IRE, vol.4, pp.276-279, September 1957.

[3] T.G.Wilson and E.T.Moore, "Inverter for use with very low input voltages," Trans. Commun. Elect., IEEE, vol.83, pp.424-428, July 1964.

[4] A.Katsuki, M.Ouchiyama, and M.Matsushima, "Overload-protected frequency-compensated current-feedback magnetic multivibrator," will be presented at the IEEE PESC'97, St. Louis, Missouri, USA, June 22-27, 1997.

[5] A.Katsuki, M.Matsushima, and M.Ouchiyama, "Analysis of an overload-protected current-feedback magnetic multivibrator," in IEEE

PESC'96 Record, June 1996, pp.975-980.

[6] A.Katsuki and M.Matsushima, "Current feedback magnetic-multivibrator with compensated frequency of oscillation," in IEEE PESC'94 Record, June 1994, pp.1205-1211.

APPENDIX

A. Current-feedback magnetic multivibrator

Fig.A1 shows a circuit diagram of the current-feedback magnetic multivibrator. This circuit is obtained by removing T_1, T_2, the winding N_3 of T_3, D_1~D_6, R_F, and R_C from the circuit shown in Fig.1. Fig.A2 and Fig.A3 are oscillation-frequency characteristics of this circuit.

B. Fequency-compensated current-feedback magnetic multivibrator

Next, the current-feedback magnetic multivibrator with frequency compensation[6] is presented in Fig.A4. This circuit is obtained by removing T_1, the windings N_T's of T_2, D_1~D_6, and R_F from the circuit of Fig.1. It is seen from Fig.A5 and Fig.A6 that deviation in oscillation frequency is effectively decreased.

C. Overload-protected current-feedback magnetic multivibrator

The current-feedback magnetic multivibrator with overload protection[5] is shown in Fig.A7. This circuit is obtained by removing T_2 and R_C from the circuit of Fig.1. Fig.A8 presents the characteristics of overload protection. Fig.A9 and Fig.A10 are characteristics of oscillation frequency. From Fig.A10, we can see that the frequency of oscillation is slightly dependent of E_S.

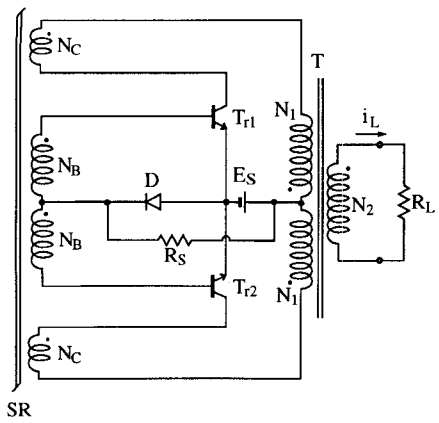


Fig.A1. Current-feedback magnetic multivibrator.

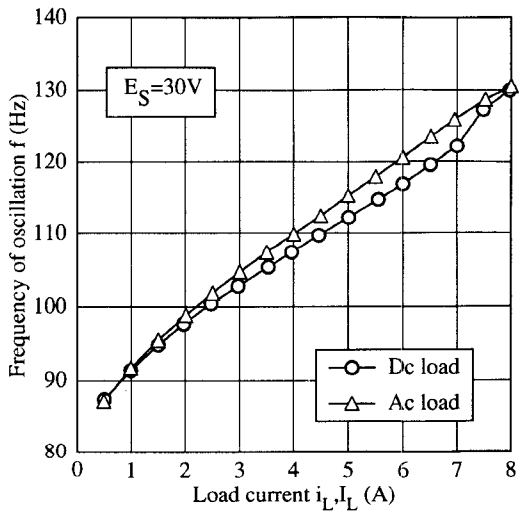


Fig.A2. f vs. characteristics of i_L and I_L in the circuit of Fig.A1.

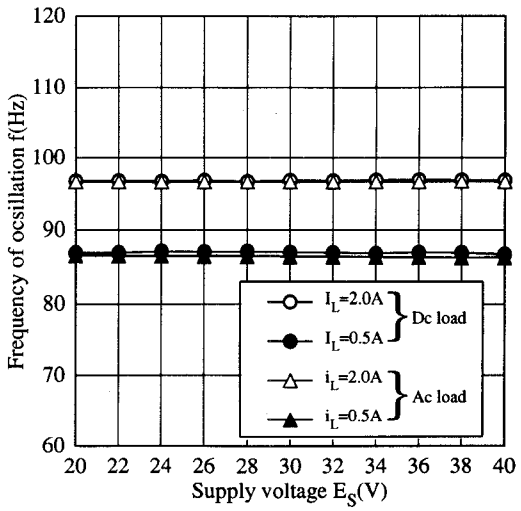


Fig.A3. f vs. characteristics of E_S in the circuit of Fig.A1.

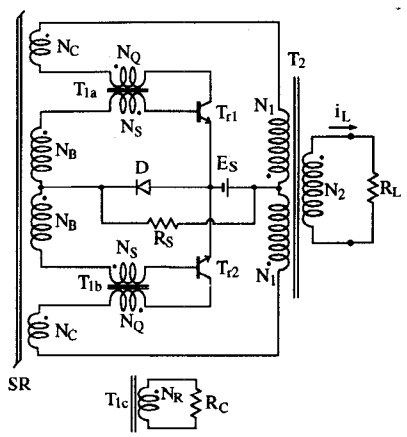


Fig.A4. Fequency-compensated current-feedback magnetic multivibrator.

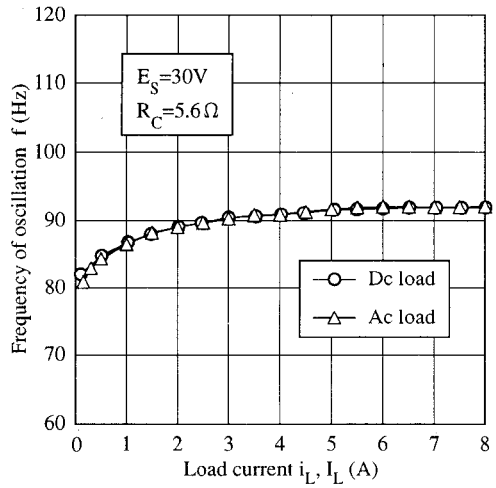


Fig.A5. f vs. characteristics of i_L and I_L in the circuit of Fig.A4.

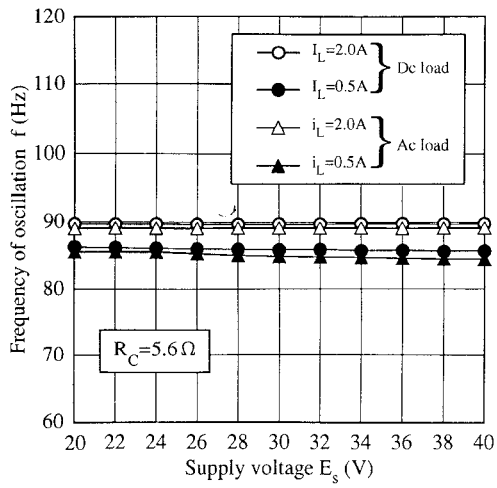


Fig.A6. f vs. characteristics of E_S in the circuit of Fig.A4.

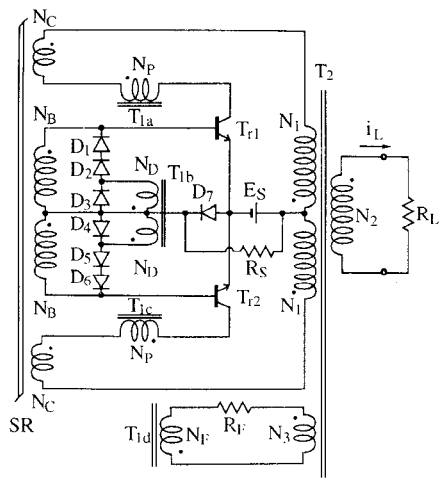


Fig.A7. Overload-protected current-feedback magnetic multivibrator.

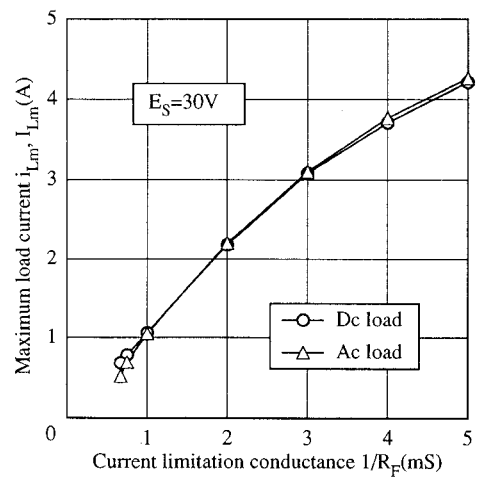


Fig.A8. Characteristics of overload protection in the circuit of Fig.A7.

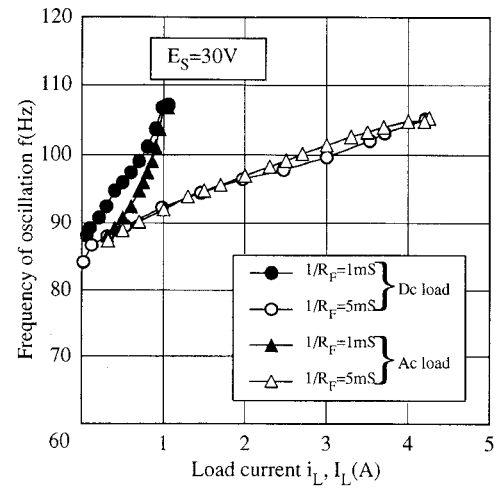


Fig.A9. f vs. characteristics of i_L and I_L in the circuit of Fig.A7.

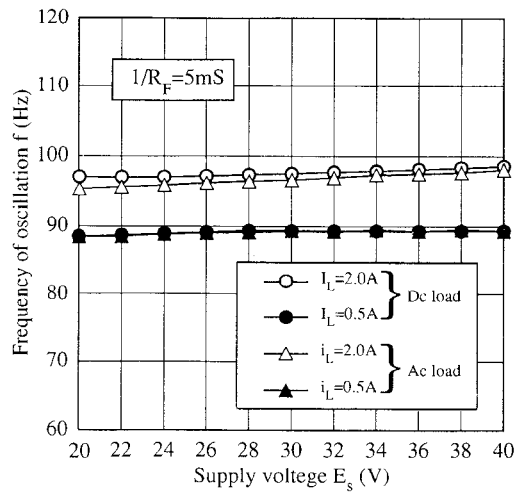


Fig.A10. f vs. characteristics of E_S in the circuit of Fig.A7.

Rare-Metal Free Thin Film Solar Cell

Hironori Katagiri, Masato Nishimura, Takeshi Onozawa, Shinichi Maruyama
Masato Fujita, Toshiyuki Sega and Taku Watanabe
Nagaoka National College of Technology
888, Nishikatakai, Nagaoka 940, Japan
Fax & Phone: +81-258-34-9240
E-mail: hiro@nagaoka-ct.ac.jp

Abstract — **Cu_2ZnSnS_4 (CZTS) thin films have been successfully formed on a soda lime glass substrate by vapor phase sulfurization of precursors of E-B evaporation. This semiconductor dose not contain any rare-metal such as indium. In this study, we estimated the optical band gap energy as 1.45 eV and the optical absorption coefficient was in the order of 10^4 cm^{-1}. From these optical properties, this CZTS film is very suitable for thin film solar cell. Fabricated solar cells, Al/ZnO/CdS/CZTS/Mo/Soda Lime Glass, showed an open circuit voltage up to 522 mV.**

I. Introduction

Cu_2ZnSnS_4(CZTS) is one of the promising materials for low cost thin film solar cell, because of a suitable band gap energy of 1.4～1.5 eV, and the large absorption coefficient over 10^4 cm^{-1}. All constituents of this film are abundant on the crust of the earth, and are not toxic [1, 2, 3]. In the study by K. Ito and T. Nakazawa, fabricated solar cell using CZTS thin films prepared by sputtering technique showed the open circuit voltage of 250 mV [2]. In our previous work, the stoichiometric CZTS thin films were prepared by sulfurization of E-B evaporated precursors, and physical properties of them were examined. Fabricated thin film solar cells, Al/ZnO/CdS/CZTS/Mo/Soda Lime Glass, showed an open circuit voltage of 400 mV [4, 5]. In this study, in order to optimize the physical properties of the CZTS film for solar cell, we examined both the thickness of Cu layer of the precursors and the sulfurization condition. By this optimization, an open circuit voltage has drastically increased from 400 mV [4, 5] to 522 mV, which may be one of the top data in this field.

II. Fabrication of CZTS Films

Cu/Sn/Zn stacked layers were deposited by E-B evaporation sequentially on soda lime glass substrates which were heated up to 100 °C. At the first, a Zn layer in the thickness of 1600 Å was deposited on the substrate. Then, a Sn layer in the thickness of 2300 Å was deposited on the Zn layer. Finally, we obtained the precursor by depositing a Cu layer of 1200～1800 Å in thickness on the Sn layer. Each of film thicknesses was estimated by atomic weight and density for preparation of the near-stoichiometric CZTS films. The purities of source materials were 99.999%.

In order to obtain the CZTS films, we sulfurized precursors by heating up to 500 °C in the atmosphere of N_2+ H_2S(5%) in an electric furnace. Precursors were set in a Pyrex glass tube mounted in the furnace. Using rotary pump and N_2 gas, undesirable air was purged from this tube. Then the reactive gas flowed at room temperature. In the sulfurization, the flow rate of reactive gas was set as 10 sccm. Fig.1 shows the temperature history of precursor in the sulfurization. In this study, we set each ramp-up rate as constant value and varied only the Hold Time. The hold times were 0 min., 150 min. and 300 min. for the sulfurization conditions of Type 1, Type 2 and Type 3, respectively.

III. Physical Properties of CZTS Films

A. Crystallinity and Optical Properties

In order to optimize the sulfurization condition, we fabricated the CZTS films by different sulfurization conditions by using the same precursors. The thickness of the Cu layer in all precursors was fixed to 1800 Å. Thus, a crystallinity and an optical property of the CZTS films were examined.

By using an X-ray diffractometer of Cu-K α radiation, the crystal structure of the CZTS films was characterized. For all of the films, the peaks due to (002), (112), (200), (220) and (312) planes of CZTS were confirmed, which are due to the characteristic stannite structure [6]. From the results of these peaks, the lattice constants of the films were estimated. From the peaks of (220), (002) plane, we estimated the lattice constant a and c. Table 1 shows the estimated lattice constants.

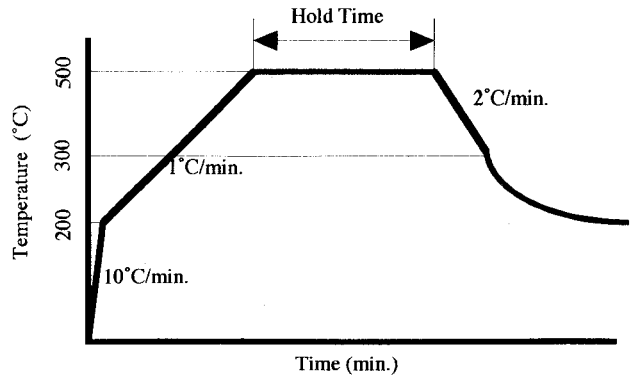


Fig.1. Temperature history of precursor in the sulfurization.

TABLE I
ESTIMATED LATTICE CONSTANTS
OF THE CZTS FILMS.

Sulfurization condition	Lattice constant a	c
Type 1	5.424 [Å]	10.802 [Å]
Type 2	5.424 [Å]	10.810 [Å]
Type 3	5.427 [Å]	10.818 [Å]

These estimated values are in good agreement with the previous data for a single crystal of CZTS, namely 5.427 Å and 10.848 Å by W. Schäfer and R. Nitsche [7]. These lattice constants of the sample Type 3 are closer to those of the previous data than those of the other samples.

The transmittance and reflectance of CZTS films were measured by using a photo spectrometer. Owing to the specimen chamber with an integral sphere, we could measure a reflectance spectra precisely. We used a Ge-photo diode with a liquid nitrogen coolant as the photo detector. Fig.2 shows the squared absorption coefficient of the film as a function of the photon energy. All the samples in this study have a large absorption coefficient in the order of 10^4 cm^{-1} near a fundamental absorption edge. For the sample Type 1, the absorption of the tail part is larger than those of the others. For the sample Type 3, the absorption increases more steeply at 1.5 eV than those of the sample Type 2. We determined the band gap energy of this film as 1.45 eV by extrapolating these plots. From these optical properties, this CZTS is very suitable for solar cells.

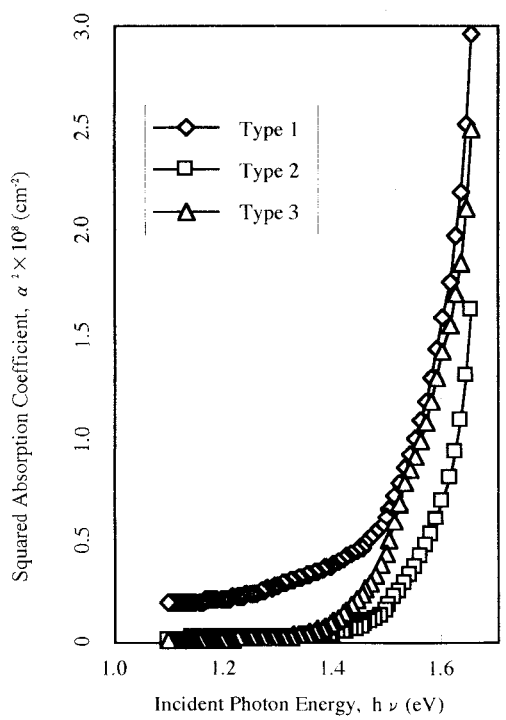


Fig.2. Relation between the squared α and photon energy of the CZTS films.

Both of the crystallinity and the optical properties in this study show clearly that the sulfurization condition of Type 3 is more appropriate than those of the others.

B. Chemical Composition

By using an electron probe microanalysis (EPMA) with $CuFeS_2$, pure Zn, pure Sn as the standard samples, the chemical composition of the film was determined. The EPMA system used in this study was JEOL JXA-8800, and a wave dispersive spectrometry (WDS) measurement was performed. The accelerated voltage and the probe current were set as 10 kV and 5.0×10^{-8} A respectively. The chemical composition of the CZTS films was estimated by using those X-rays with intensities of Cu-L α , Zn-L α , Sn-L α and S-K α .

Fig. 3 shows the dependence of the chemical composition of the CZTS films on the thickness of the Cu layer of the precursors. All of the films were fabricated by the sulfurization condition of Type 3. With the increase in the thickness of the Cu layer, the ratio of Cu/(Zn+Sn) increases monotonically from 0.751 to 0.992 and the ratio of S/Metal decreases slightly from 1.11 to 1.08. The decrease in the ratio of S/Metal is due to the increase of the ratio of Cu/(Zn+Sn). This tendency can be commonly observed in $CuInSe_2$.

C. SEM Observation

A photograph of a scanning electron microscopy (SEM) revealed both the surface morphology and the film thickness. The SEM system used in this study was Hitachi S-4100, which is field emission (FE)-SEM. In order to examine the surface morphology, we tilted the sample setting by 45°. From the SEM observation, the grain sizes of the films are extremely large (about 3 μm) compared with the film thickness of 2.0 μm.

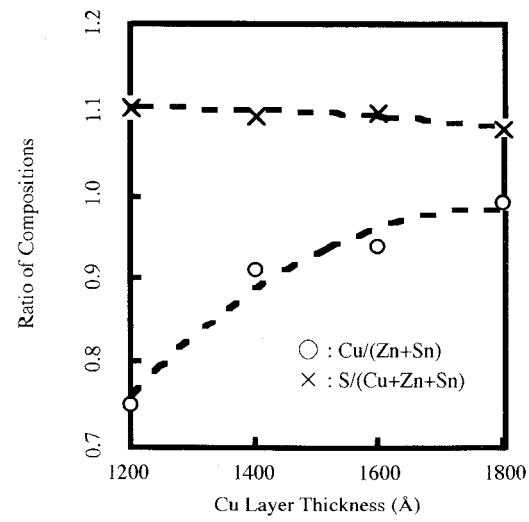


Fig.3. Dependence of the ratio of composition on the Cu layer thickness.

D. Electrical Properties

In this study, the conductivity type of all the films was shown to be p-type by a hot probe method. By the 4-probe method, the resistivity of the films were estimated as 4.9×10^5, 7.0×10^5, 3.2×10^5 and 3.2×10^5 Ωcm for the thickness of the Cu layer of 1200, 1400, 1600 and 1800 Å, respectively.

IV. Properties of Photovoltaic Cell

In order to fabricate a photovoltaic cell, we deposited Al/ZnO/CdS/CZTS stacked layers on Mo-coated soda lime glass substrates. The thickness of CdS buffer layer is less than 20 nm on the thin CZTS film absorber by a chemical bath deposition (CBD) process with Cd sulfate, thiourea, ammonia solution and deionized water in a CBD solution at a temperature of 60 °C. Then, the thickness of ZnO window layer is 0.6 μm by a RF sputtering technique. In order to decrease the resistivity of this layer, we used a ZAO($ZnO+Al_2O_3$:1 wt%) target and introduced H_2 gas of 2 sccm to a normal sputtering gas, Ar gas, of 20 sccm. Finally, in order to decrease the resistive losses, we deposited an Al top grid on the ZnO window layer by a vacuum evaporation method.

Fig. 4 shows an I-V characteristics of a CZTS solar cell. This cell showed a short-circuit current of 3.13 mA/cm², an open-circuit voltage of 522 mV, and a fill factor of 0.299 under AM 1.5 illumination. The conversion efficiency was 0.489%. Fig. 5 shows a photospectral response of this solar cell. The photospectral response is in a wide wavelength range from 400 to 850 nm. The short- and long-wavelength cut-offs correspond to the bandgaps of ZnO and CZTS, respectively. In the region of long-wavelength, the photospectral response increases. The wavelength at the maximum collection efficiency is about 730 nm.

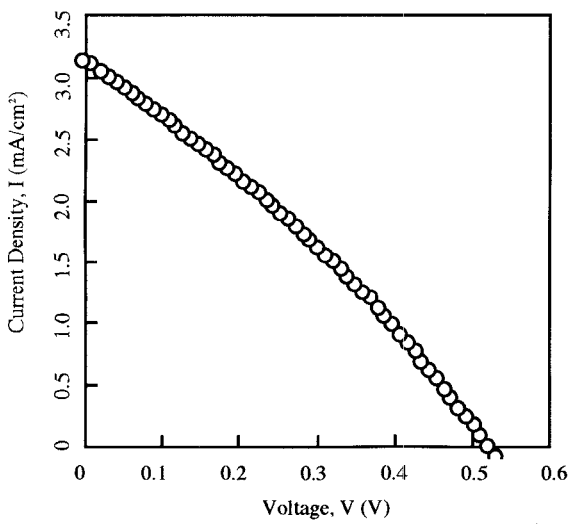


Fig.4. Illuminated I-V characteristics of CZTS thin-film solar cell.

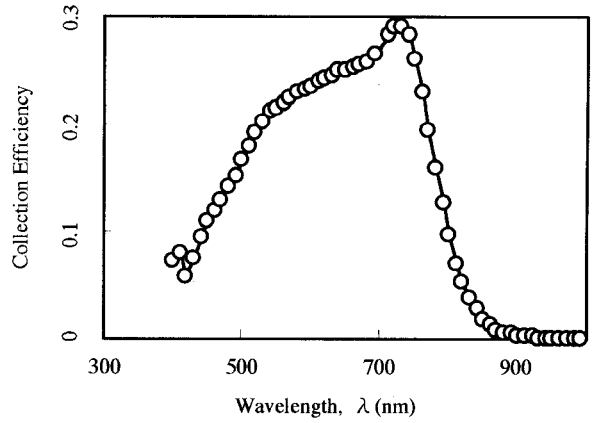


Fig.5. Spectral response of CZTS thin-film solar cell.

From these results, we can see some points to improve the cell performance. The first point is an optimization of a thickness of an absorption layer. Our cell shows an open circuit voltage of 522 mV, however, the conversion efficiency was very low; 0.489%, which was attributed to the degraded fill factor. A fill factor strongly depends on a series resistance of a solar cell. The fill factor of this cell must be degraded owing to the high resistance of the absorption layer. In this study, we fabricated a CZTS layer of about 2.0 μm in thickness as the absorption layer. But the resistivity of this film was in the order of 10^5 Ωcm. Therefore, this absorption layer is too thick to reduce the series resistance of the solar cell. The second point is on the property of window layer, especially it's transmittance. From the photospectral response, the collection efficiency is very small, less than 30%, over the whole region of the wavelength. Hence, the transmittance of the window layer is not so high enough for the incident photons to reach a n-CdS/p-CZTS heterojunction. In order to increase the transmittance and the conductivity of the window layer, optimization of the preparing condition of a ZnO film is needed.

V. Conclusions

The CZTS film could be prepared successfully with suitable physical properties for solar cell. This semiconductor does not contain any rare-metal such as indium. This film has a band gap energy of 1.45 eV which is very close to the optimum value for a solar cell absorber. Fabricated solar cell using the CZTS film shows an open circuit voltage of 522 mV. However, the conversion efficiency was very low; 0.489%, which was attributed to the degraded fill factor. In order to improve the fill factor and the conversion efficiency, further study to optimize the preparing condition of CZTS and ZnO films is now in progress. In this study, we could show the possibility of a very low cost solar cell.

ACKNOWLEDGMENT

The courtesy of Shinanogawa Technopolis Development Organization for using EPMA system in the measurement of chemical composition of CZTS films is greatly appreciated.

The authors would like to express their sincere thanks to the helpful and stimulating discussions by Prof. K. Ito of Shinsyu University and Prof. M. Konagai of Tokyo Institute of Technology.

The authors express their sincere thanks to the financial support in part by the Uchida Energy Science Promotion Foundation, the Niigata Engineering Science Promotion Foundation and the New Energy Enterprise Cooperative Union (NECO) for this study.

REFERENCES

[1] K. Ito and T. Nakazawa, "Electrical and Optical Properties of Stannite -Type Quaternary Semiconductor Thin Films," Japanese Journal of Applied Physics, vol. 27, pp. 2094-2097, 1988.

[2] K. Ito and T. Nakazawa, "Stannite-Type Photovoltaic Thin Films," in Proc. 4th Int. Conf. Photovoltaic Science & Engineering, Sydney, 1989, pp. 341-346.

[3] N. Nakayama and K. Ito, "Sprayed films of stannite Cu_2ZnSnS_4," Applied Surface Science, vol. 92, pp. 171-175, 1996.

[4] H. Katagiri et.al., "Preparation and Evaluation of Cu_2ZnSnS_4 Thin Films by Sulfurization of E-B Evaporated Precursors," Technical Digest of the International PVSEC-9, Miyazaki, 1996, pp. 745-746.

[5] H. Katagiri et.al., "Preparation and Evaluation of Cu_2ZnSnS_4 Thin Films by Sulfurization of E-B Evaporated Precursors," to be published in Solar Energy Materials and Solar Cells.

[6] JCPDS (Joint Committee on Powder Diffraction Standards) card 26-575 .

[7] W. Schäfer and R. Nitsche, "TETRAHEDRAL QUATERNARY CHALCOGENIDES OF THE TYPE Cu_2-II-IV-$S_4(Se_4)$," Mater. Res. Bull. vol. 9, pp. 645-654, 1974.

A Method To Measure EMI Due To Electric Field Coupling On PCB

Bryan M.H. Pong Angus C.M. Lee
Department of Electrical & Electronic Engineering, Hong Kong University
Pokfulam Road, HONG KONG
Fax : +852-25598738, Phone : +852-28597099
E-mail : mhp@hkueee.hku.hk

Abstract — **A new method to measure electric field coupling between PCB copper traces is presented. This method enables measurement of noise from waveforms obtainable from breadboard prototypes, which is available in an early stage in the design process. The measurement result can then be analyzed and provide information for further PCB design. This method is verified by experiments and applied to an off-line flyback converter.**

I. INTRODUCTION

Electromagnetic Interference (EMI) generated by switching power supplies have received a lot of attention in the industry. More and more countries have established regulations against products which generate EMI. The switching nature of switch mode power supply makes it an inevitable source of EMI. Engineers and researchers are striving to reduce EMI by various methods. From experience it is well known that circuit layout design on a printed circuit board (PCB) plays a very important part in the reduction of EMI. A good circuit layout can very often solve EMI problems without any changes in circuit topology or components in the circuit. However, there is very little information available on the EMI performance of a switching power supply circuit until the circuit is fully laid out on a PCB and tested. Even when the circuit is breadboarded only the functional performance of the power supply can be tested, very little EMI performance information are available because the circuit layout of the breadboard prototype will be very different from the final layout. This makes overall EMI measurement in the breadboard stage meaningless. However, it will be extremely useful for the engineer who lay the circuit on a PCB have as much information as possible on circuit parts with high emission so that these parts can be dealt with carefully. Computer modeling of the whole circuit including details of all components and PCB layouts is an overwhelming task even for state of the art technology. Even though one can manage the modeling and simulations, the results will definitely be too complex to understand and hard to be translated to useful information. Very often one has to resort to actual measurements.

Every EMI problem comprises three elements, namely a source, a receiver and a mechanism which couples interference from the source to the receiver as in Fig.1.

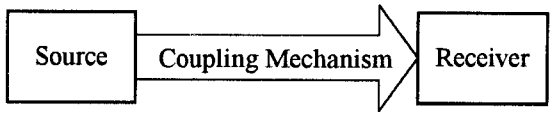


Fig.1. Basic Elements in EMI Problems

Coupling mechanism can be categorized into *conducted coupling* and *non-conducted coupling*. Conducted coupling refers to interference along a conductor which links up the source and the receiver. Non-conducted coupling comprises of electric field coupling, magnetic field coupling and a combination of both. In switching power supplies, electric field coupling has considerable contribution to overall EMI especially those circuits which involve high voltage transients. This paper describes a simple and low cost method to measure *electric field coupling* at circuit nodes. This method can be applied to breadboard prototypes and potential sources of electric field interferences can be identified. Measurement results will provide electric coupling information at various circuit nodes. PCB designer can make use of these information in the layout design.

II. ELECTRIC FIELD COUPLING ON PCB

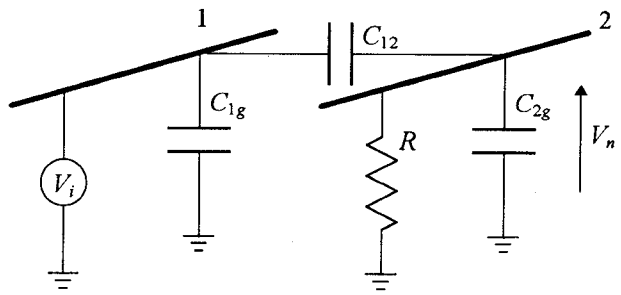


Fig.2. Electric Field Coupling Model

A simple representation of electric field coupling [1] between PCB traces is shown in Fig.2. Noise source V_i is connected to conductor 1 and the interference noise couples to conductor 2 through capacitor C_{12}.

The noise voltage picked up by conductor 2 is represented by

$$V_n = \frac{j\omega\left[\frac{C_{12}}{\left(C_{12}+C_{2g}\right)}\right]}{j\omega+\frac{1}{R\left(C_{12}+C_{2g}\right)}}V_i \qquad (1)$$

In most practical cases,

$$R \ll \frac{1}{j\omega\left(C_{12}+C_{2g}\right)} \tag{2}$$

and (1) can be simplified to

$$V_n = j\omega R C_{12} V_1 \tag{3}$$

III . APPARATUS

The principle of the measurement method is to pick up the noise source from nodes of the circuit under test, and connect it to a fixed structure which simulates electric field coupling on PCB. The coupled noise voltage on the receiver end is analyzed by a measurement instrument.

The apparatus comprises of two copper traces which are printed on a PCB. One of the traces is to be connected to the circuit under test. Another trace is to be connected to measurement instrument which is typically a spectrum analyzer. A schematic diagram of the apparatus is shown in Fig.3.

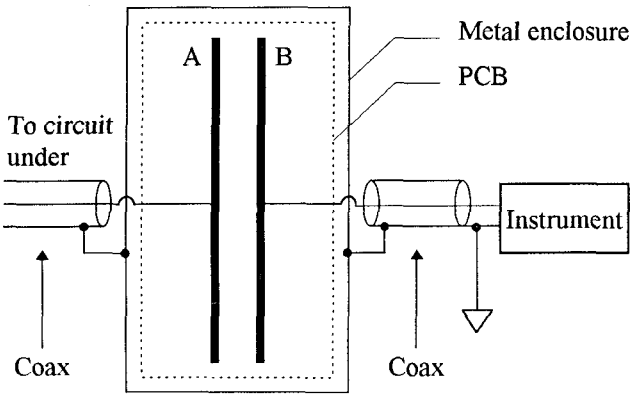


Fig.3. Schematic Diagram of Apparatus Setup

On the PCB there are copper traces A and B which are laid parallel to one another. Traces A and B are separated by a fixed distance. Trace A is connected to the circuit under test via a coaxial cable. Trace B is connected to a measurement instrument via another coaxial cable. The shield of the coaxial is grounded together with the instrument ground and the metal enclosure. There is no electrical connection between traces A and B.

A coaxial cable from the apparatus is connected to two nodes of interest in a switching circuit by which the noise signal is brought up to the apparatus. These two nodes may be, say, the drain and the source of a MOSFET in a switching power supply circuit, or any other nodes which is likely to be noise generator. Note that the shield of the coaxial cable is connected to Ground at earth potential. So precaution must be made so that when connecting earth to the circuit under test. The signals picked up are differential mode noise between the two nodes. This can be modeled by the equivalent circuit in Fig.2.

V_i is the noise source which generates an electric field. The spectrum of the electric field is strongly dependent on the voltage wave shape. C_{1g} is the capacitance of the interconnection between the circuit under test and the apparatus. In this case C_{1g} is the capacitance the interconnection coaxial cable, plus the capacitance between trace A and the metal enclosure.

$$C_{1g} = C_{(\text{coax in})} + C_{(A\&M)} \tag{4}$$

C_{12} is the capacitance between copper trace A and copper trace B

$$C_{12} = C_{(A\&B)} \tag{5}$$

C_{2g} is the capacitance between copper trace B and the metal enclosure, plus the capacitance of the interconnection cable which connects to the measurement instrument.

$$C_{2g} = C_{(B\&M)} + C_{(\text{coax out})} \tag{6}$$

The spectrum analyzer to be used has an input impedance R of 50 ohm, which can satisfy the condition described in (2), and hence the noise voltage in (3) is valid in this case. From (3), the noise voltage V_n is independent of C_{1g} and C_{2g}. In other words, the coaxial cable length is not a critical parameter provided that its length is much smaller than the wavelength of the harmonics to be measured.

The coupling noise will be the capacitive coupling of the noise voltage if a copper trace is laid on a PCB with a length and a distance the same as traces A and B. Other length and distances can be obtained by correction factors.

IV . EXPERIMENTAL VERIFICATION USING A SIGNAL GENERATOR

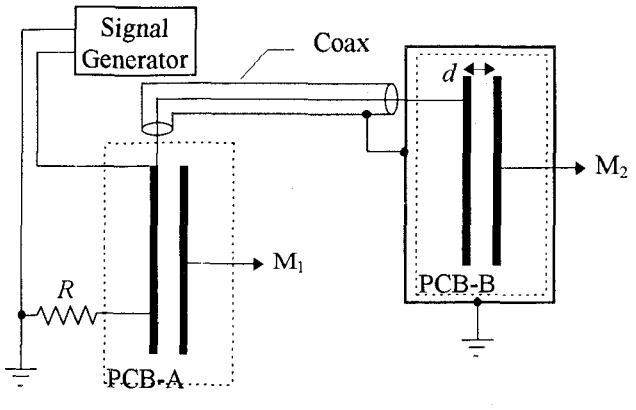
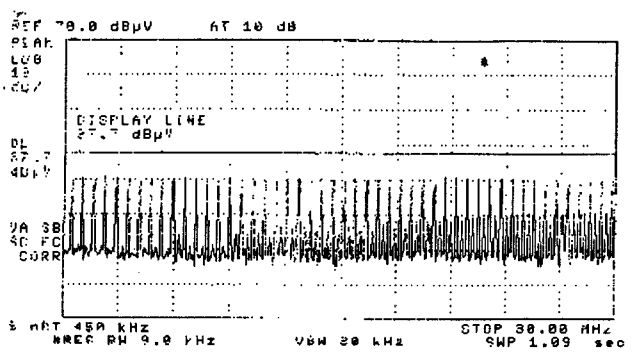


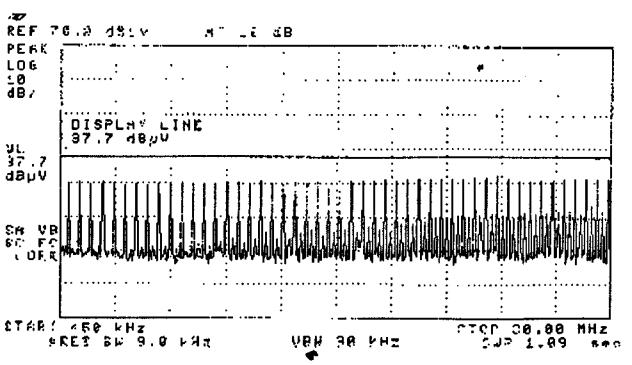
Fig.4. Experimental Verification Using a Signal Generator

An experiment is set up to verify the principle of electric field coupling. Two identical PCB are fabricated and they are connected with a resistor as shown in Fig.4. PCB-A is connected to a signal generator through a resistor to simulate the tracks inside the PCB of the convertors, while PCB-B is part of the apparatus described in Fig.3 which is housed in a metal enclosure with coaxial cables as input and output connections. The signal input to PCB-A simulates a switching waveform coupling to an adjacent copper trace inside the converter. The same signal is then transferred to the apparatus described in the previous section. Measurement are taken at M_1 and M_2 respectively and compared with each other.

The comparison of the spectrums obtained with square wave at 300 kHz input are shown in Fig.5a and Fig.5b. It can be seen that the two spectrum closely resemble each other and this shows that the electric field coupling between internal traces can be represented through the connection of a pair of external parallel traces. Hence the measurement method in the previous section is validated.



(a) Spectrum Measured at M_1



(b) Spectrum measured at M_2

Fig.5. Spetrum measured with a square wave input from signal generator. trace length l = 4 mm, trace separation d = 3 mm, trace width w = 1 mm, frequency = 300 kHz, amplitude = 2 $V_{p\text{-}p}$

A more precise measurement is achieved by generating a sine wave and apply to the same circuit as shown in Fig.4. As the sine wave contains a single frequency only, an unique peak is detected in the spectrum analyzer. The peak values at M_1 and M_2 are recorded for different input frequency.

Table I indicates the coupling voltages at M_1 and M_2 match closely with less than 1 dBμV inside the measuring frequency range. This further confirms the validity of the measuring technique.

TABLE I
PEAK VOLTAGE RECORDED WITH SINE WAVE INPUT

Frequency (MHz)	Voltage at M_1 (dBμV)	Voltage at M_2 (dBμV)
1	32.1	32.8
5	45.5	45.8
10	51.7	52.5

trace length l = 54 mm, trace separation d = 2 mm, trace width w = 1 mm, signal = sine wave amplitude = 1 $V_{p\text{-}p}$

In practice, the traces may have different track length l track width w and track separation d. It affects the capacitance C_{12} mainly because the characteristics follow (2) in most practical case. Walker [1] gives the equation for the variation in these parameters to the effect of C_{12}

$$C_{12} = \frac{27.8\varepsilon_{r(eff)}}{\ln\left[\frac{\pi(d-w)}{w+t}+1\right]} \times l \tag{7}$$

where l is the trace length in meter, d is the trace separation in meter, w is the trace width in meter and t is the trace thickness in meter.

For a new set of capacitance C'_{12} and coupling voltage V'_n

$$\frac{C'_{12}}{C_{12}} = \frac{\ln\left[\frac{\pi(d-w)}{w+t}+1\right]}{\ln\left[\frac{\pi(d'-w')}{w'+t'}+1\right]} \times \frac{l'}{l} = \frac{V'_n}{V_n} \tag{8}$$

The correction factor F can be expressed in dB as

$$\mathrm{F} = 20\log\left[\frac{l'}{l}\frac{\ln\left[\frac{\pi(d-w)}{w+t}+1\right]}{\ln\left[\frac{\pi(d'-w')}{w'+t'}+1\right]}\right] \tag{9}$$

and

$$20\log V'_n - 20\log V_n = \mathrm{F} \tag{10}$$

or

$$V'_n - V_n = \mathrm{F} \text{ in dB} \tag{11}$$

The experimental setup in Fig.4 is also used to verify the validity of the scaled coupling effect of (11). A sine wave is generated from the signal generator, instead of a square wave. It is conducted with the tracks with different

separation d. The reference voltage V_n' is measured with a pair of arbitrary traces. Then other the coupling voltage of other traces are recorded as V_n in Table II.

According to (11), the correction factor F is equal to the difference between the V_n' and V_n. Close matching of measured and calculated results in Table II shows that the correction factor F can perform the trace transformation in a high degree of accuracy, given that the trace separation d is small comparing with trace length l.

TABLE II
EXPERIMENTAL VERIFICATION OF CORRECTION FACTOR F

			Measured	Calculated
Trace separation d (mm)	Voltage at M_2 V_n' (dBμV)	Reference voltage V_n (dBμV)	$V_n' - V_n$ (dBμV)	Calculated F (dBμV)
5	37.5	29.7	7.8	7.1
10	31.3	29.7	1.6	1.6
20	27.1	29.7	- 1.4	- 1.3

trace thickness t = 0.1 mm, frequency = 1 MHz, amplitude : 1 V_{p-p}
V_n :
trace length l = 54 mm, trace width w = 2 mm, trace separation d = 1 mm
V_n' :
trace length l' = 100 mm Trace width w' = 3 mm

V . EXPERIMENT WITH AN LISN AND A FLYBACK CONVERTER

This experiment demonstrates the application of this measuring technique on a flyback converter. A typical flyback converter comprises a bridge rectifier, a flyback transformer, a MOSFET and a series of filter capacitors as shown in Fig.6. The significant node pairs are labeled from A to F. A coaxial cable is connected two nodes, for example A+ and A-, so that the noise voltage across A+ and A- is brought up to one side of the parallel traces. The other side of the parallel traces is connected to a spectrum analyzer for measurement. Fig.7 describes the experimental setup. The shielding of the coaxial cables connects to each other at the metal enclosure such that external noise is inhabited in this environment. It is noted that the converter circuit and the measuring circuit should be isolated. The differential mode noise waveform from nodes A to F observed at the spectrum analyzer is recorded in Figs.8(a) to Fig.8(f). The spectrum across nodes A+ and A- shows a very low noise level as it is the input side of the converter, in which no switching noise is presented. Also the capacitor across A+ and A- filters out the surge in the input. Same situation is found at nodes B+ and B- as well since it does not produce high frequency noise through the bridge rectifier. Nodes C+ and C- are electrically equivalent to nodes B+ and B- so that a low noise level is expected. The most significant noise comes from the switching of the MOSFET. Fig.8(d) shows the noise spectrum of node D+ and D- which is measured across the drain and source of the switch MOSFET; a very high noise level is found. The switch noise is coupled through the transformer to the secondary side of the converter. The noise voltage is recorded across nodes E+ and E- as shown in Fig.8(e). It shows a

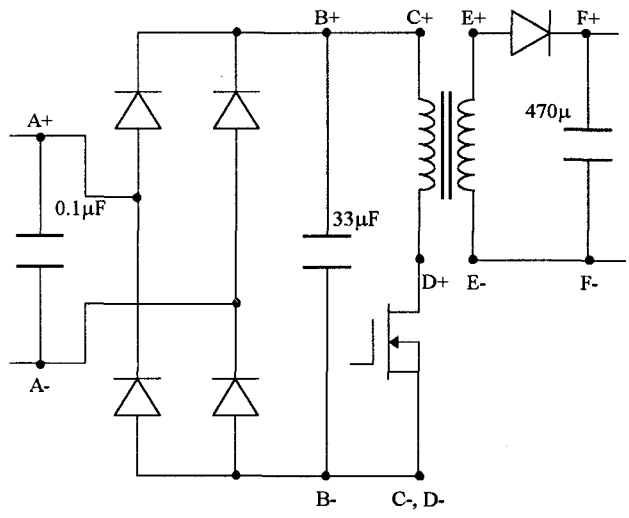


Fig.6. Schematic diagram of a typical Flyback Converter

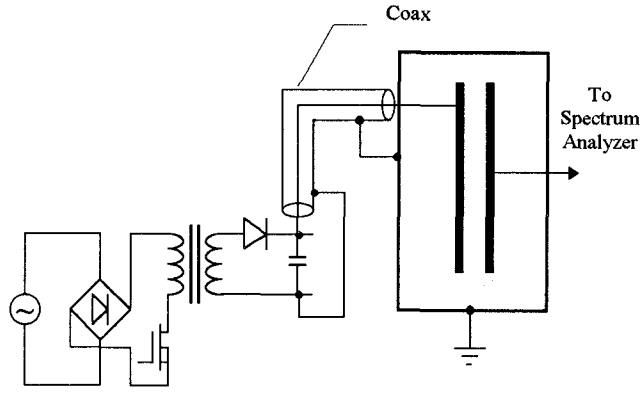


Fig.7. Experimental Setup Using a Flyback Converter

medium noise level throughout the whole measuring frequency. The noise is suppressed by the capacitor across nodes F+ and F- to produce a low noise spectrum.

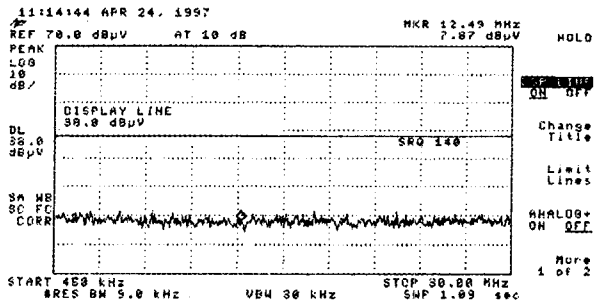
The experiment verifies the critical noise source in the flyback converter circuit. Both nodes D and E are strong sources of noise. Although the noise level at node E is not as high as that at node D in general, a wide frequency range of noise is observed. PCB designer should pay attention to these important nodes.

The converter is then tested for overall conducted noise using the standard noise measurement method through a line impedance stabilization network (LISN) and the observed spectrum is shown in Fig.9. Comparing the spectrum obtained through the LISN, the spectrum obtained at nodes D+ and D- represents a very similar profile. This result shows that the conducted noise is highly affected by the electric field coupling from the traces connected to these switching points.

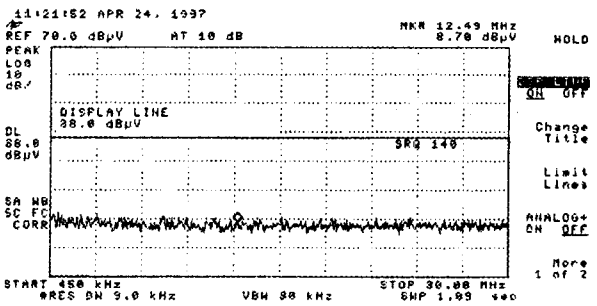
The previous section verifies the relationship between the electric field coupling and traces dimension. The result can be applied together with the spectrums obtained to

provide information on optimum trace separation in the PCB layout, such that electric field coupling is suppressed in the circuit.

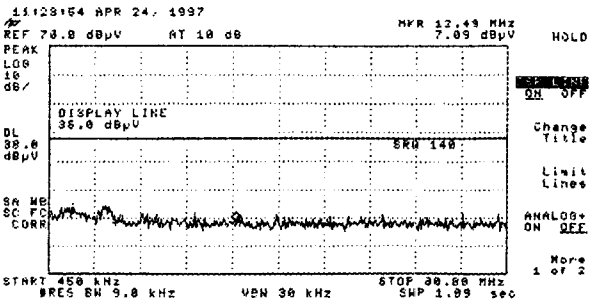
The peak voltage between the PCB traces may approach 500 V in the switching of power electronic devices. The high surge can cause flash-over between the traces and damage the spectrum analyzer or other devices. Therefore one should take a note on the separation between the two PCB traces.



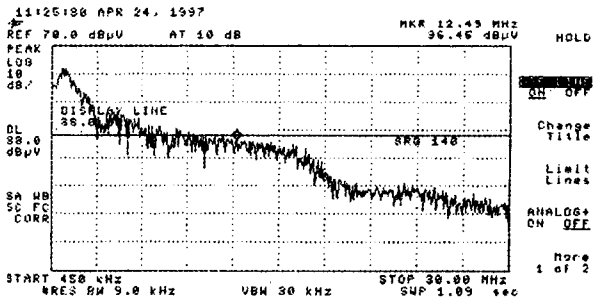
(a) Spectrum measured at point A



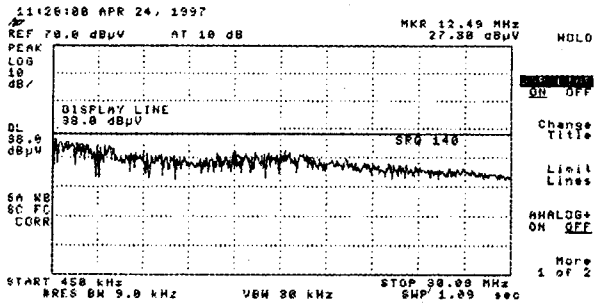
(b) Spectrum measured at point B



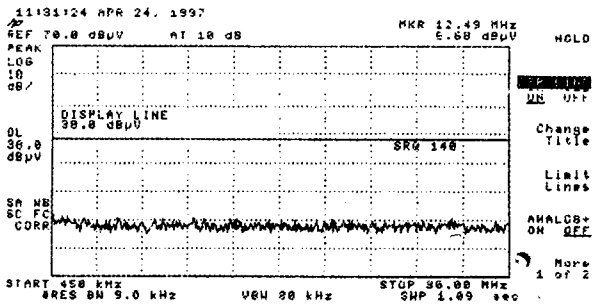
(c) Spectrum measured at point C



(d) Spectrum measured at point D



(e) Spectrum measured at point E



(f) Spectrum measured at point F

Fig.8. EMC Measurement of a Flyback Converter

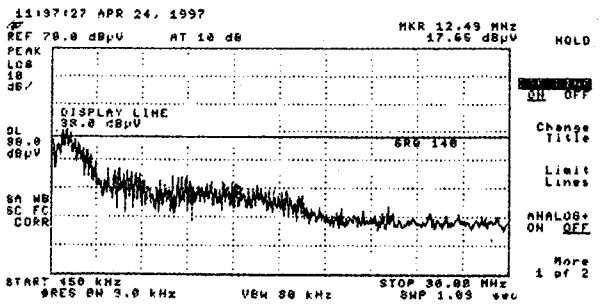


Fig.9. Spectrum Measured at Line Input Through a LISN

VI . CONCLUSION

This paper describes a new method to estimate EMI due to electric field coupling between PCB traces in which its effect is significant in the switching nature of the model power electronic system. A simple set of apparatus is required and the test can be achieved easily. Experimental results prove the accuracy of this method.

Moreover, it provides a means for engineers to estimate the electric field coupling between copper traces from spectrums which are obtainable from prototypes. This provides useful information to PCB designer on the required dimensions and separation of trace layout and avoids EMI problems in an early stage in the design process, such that the PCB design can still be changed in a convenience way.

REFERENCES

[1] C. S. Walker, *Capacitance, Inductance and Crosstalk Analysis.* Artech House, 1990.

[2] H. W. Ott, *Noise Reduction Techniques in Electronic Systems.* 2nd Edition, Wiley, New York, 1988.

[3] M. Mardiguian, *Controlling Radiated Emissions by Design.* Van Nostrand Reinhold.

[4] L. Tihanyi, *Electromagnetic Compatibility in Power Electronics.* IEEE Press, 1995.

[5] L. B. Gravelle and P. F. Wilson, "EMI/EMI in Printed Circuit Boards - A Literature Review," *IEEE Transactions on Electromagnetic Compatibility*, vol. 34, no. 2, May 1992.

[6] J. C. Fluke, Sr., *Controlling Conducted Emission by Design.* Van Nostrand Reinhold.

[7] C. R. Paul, *Introduction to Electromagnetic Compatibility.* 1st Edition, Wiley, New York, 1992.

[8] T. N. Bahr and E. J. MacMahon, *Electrostatic Discharge Control.* Hayden, New York, 1983.

[9] A. N. Faught, "An Introduction to Shield Joint Evaluation using EMU Gasket Transfer Impedance Data," in *Proceedings of the IEEE Symposium*, pp. 38-44, 1982.

[10] J. Goedbloed, *Electromagnetic Compatibility.* Prentice Hall, New York, 1990.

[11] R. J. Mohr, "Evaluation Technique for EMI Seams," in *Proceedings of the IEEE Symposiumon Electromagnetic Compatibility*, pp. 81-84, 1987.

[12] B. Keiser, *Principles of Electromagnetic Compatibility*, 3rd Edition, Aertech House, Norwood, MA, 1987.

[13] E. D. Knowles and L. W. Olson, "Cable Shielding Effectiveness Testing," *IEEE Transaction on Electromagnetic Compatibility*, EMC-16, February, 1974.

[14] C. R. Paul and K. B. Hardin, "Diagnosis and Reduction of Conducted Emissions," *in Proceeding of the IEEE Symposium on Electromagnetic Compatibility*, pp. 19-23, 1988.

[15] C. R. Paul and W. W. Everett III, "Printed Circuit Board Crosstalk," *in Proceedings of the IEEE Symposium on Electromagnetic Compatibility*, pp. 452-459, 1985.

[16] J. L. N. Violette, D. R. J. White and M. F. Violette, *Electromagnetic Compatibility Handbook*, Van Nostrand Reinhold, New York, 1987.

NOVEL DIGITAL CONTROL TOPOLOGY OF A HIGH POWER RESONANT DC-DC CONVERTER FOR X-RAY HIGH-VOLTAGE APPLICATIONS

H. Takano* , T. Hatakeyama*, L. Gamage#, J.M. Sun#, and M.Nakaoka#
*Hitachi Medical Corporation, Chiba, 277 Japan
#Yamaguchi University, Yamaguchi, 755 Japan

Abstract - This paper describes 32-bit RISC processor-based digital feedback control scheme for a series-parallel resonant high power DC-DC converter using its high-voltage transformer parasitic LC circuit components which is applied for medical use X-ray high-voltage generator . In the converter system, I-PD feedback control algorithm with a nonlinear compensator for steady-state voltage regulation characteristics and an input voltage fluctuation compensator are presented in this paper. A practical estimation procedure to obtain the adequate I-PD gains specified by logarithmic interpolation from some regulation points is established under conditions of extremely wide load ranges as the medical use X-ray high-voltage generator. High speed processing hardware for the digital feedback control scheme with 20kHz sampling frequency are also discussed as well as programing guidelines. Finally, the performances of this application-specific converter and the effectiveness of the proposed gain parameter estimation procedure of I-PD compensator are demonstrated on the basis of experimental results.

Keywords - RISC processor, Digital control scheme, I-PD controller, Medical use X-ray generator, Transformer parasitic reactive circuit components, Series-parallel resonant DC-DC converter, High-frequency isolated link

1. INTRODUCTION

Series-parallel resonant inverter-fed DC-DC power converters using MOS gate controlled power transistors have been introduced for medical use X-ray high-voltage generator operating under extremely-wide load ranges, which can reduce the impedance of the high-voltage transformer and can obtain high output power up to 100kW[1][2][4]-class. DSP (Digital signal processor) -based digital control scheme has been introduced to these DC-DC power converters in order to obtain the desirable output high-voltage waveforms with rapid rise-time and stable flat voltage responses[3]. The operating frequency of this resonant inverter in the converter is designed for identical being to the digital sampling frequency10kHz.

Higher operating frequency of the resonant inverter is required to reduce the physical size and weight of the high-voltage transformer and to get optimal output high-voltage waveforms. In recent years, 20kHz to 50kHz operating frequency can be applied to these high-power converters by using third generation IGBTs. However, it seems difficult to apply higher digital sampling-based control more than 20kHz for this converter application.

In this paper, the I-PD feedback control algorithm with a nonlinear steady-state voltage regulation characteristic compensator and an input voltage fluctuation compensator, and a practical estimation procedure to obtain the adequate I-PD gains estimated by logarithmic interpolation from some regulation points on the basis of using the high-performance 32-bit RISC (Reduced Instruction Set Computing) microcontroller are presented so as to get desirable output high-voltage waveforms in dynamic and steady-states .

2. CHARACTERISTICS OF DC-DC CONVERTER AND X-RAY TUBE LOAD

2.1 DC-DC converter for medical use X-ray high-voltage generator

Fig. 1 illustrates a newly-developed power conversion processing system composed of the resonant inverter-fed type X-ray power generator with a high-frequency high-voltage transformer parasitic resonant link. The solid-state X-ray high-voltage power generator using high-frequency IGBTs inverter mentioned above consists of a single-phase or three-phase thyristor bridge rectifier, a fixed frequency phase-shifted PWM control-based high-frequency resonant inverter with a specially-designed high-voltage transformer link, a high-voltage diode rectifier connected into the high-voltage cables, and an X-ray tube as a load of this resonant DC-DC converter using the parasitic LC circuit parameters of the high-voltage high-frequency transformer.

In this whole system, the thyristorized bridge type rectifier and the phase-shifted PWM resonant inverter-fed converter are controlled by a 32-bit RISC processor-based I-PD control circuit scheme.

The remarkable features of this X-ray power generator are to make the most of the parasitic lumped leakage-inductance and the secondary-side lumped parallel capacitance of the high-voltage high-frequency transformer as the LC resonant circuit components in addition to the input-side equivalent capacitance of the high-voltage DC cables used as the output smoothing DC filter. The series resonant capacitor only is to be externally connected to the primary-side of the high-voltage high-frequency transformer.

2.2 v-i characteristics of X-ray tube load

The medical use X-ray tube is a kind of two electrodes-vacuum tube. The v-i characteristics of the X-ray tube may be roughly modeled by a pure resistance which is specified in accordance with the filament heating current in its cathode. This current is regulated by the another type resonant inverter with a high-frequency transformer isolated link. However, strictly speak-

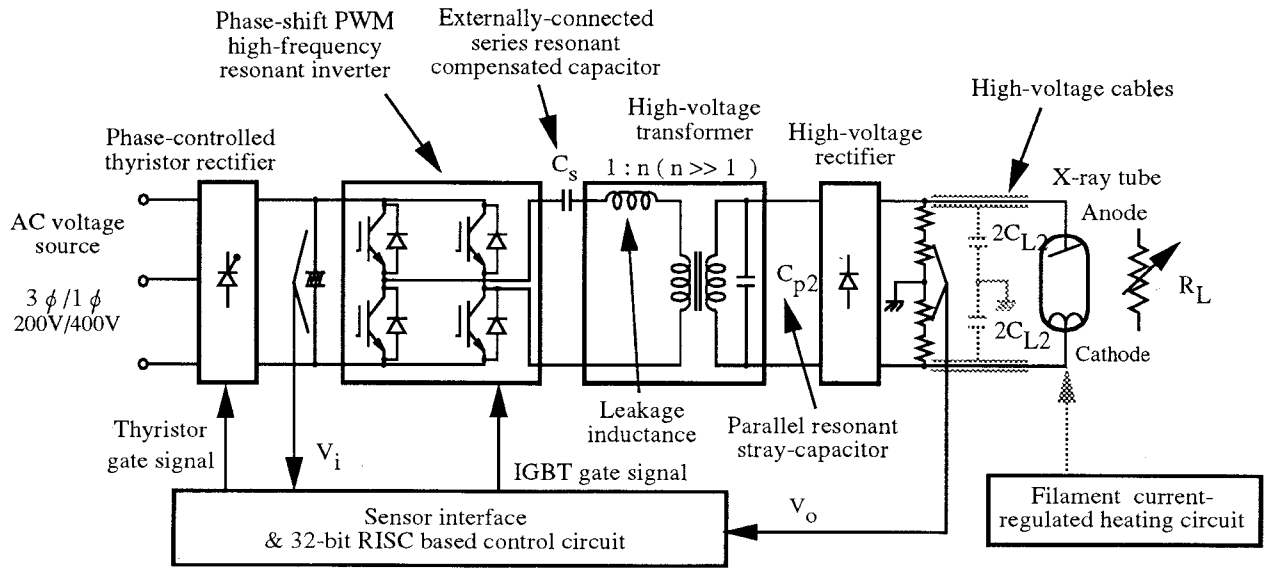


Fig. 1. Schematic main circuit configuration of transformer resonant DC-DC converter type X-ray high-voltage generator.

ing, the X-ray tube has nonlinear characteristics owing to space charge limit current and thermal limit current.

Fig. 2 shows the v-i characteristics of the X-ray tube (UH-6GE-55T, Hitachi), in case of the load resistance R_L = 1 Ω reduced into the primary side of the high-voltage transformer . As well known, the v-i characteristics of the X-ray tube depend upon the structure of its cathode and the distance between the anode and the cathode. Its v-i characteristics for the same load resistance have similar configurations as shown in Fig. 2. As an another unique characteristic of this two electrodes-vacuum tube, high-voltage discharge begins at certain voltage determined by filament current. The authors call it respective discharge start voltage, which has the same value.

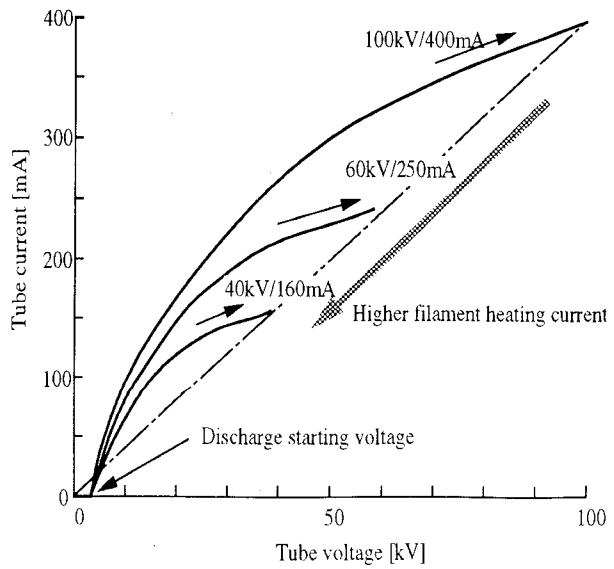


Fig. 2. v-i characteristics of X-ray tube. Load resistance (primary side) R_L = 1.0 Ω; X-ray tube: UH-6GE-55T (Hitachi); Large focal spot.

For the purpose of the optimal output high-voltage waveforms, the feedback control parameters of the I-PD gains should be preciously adjusted for each combination of the output voltage and the output current even if the same load resistance, so that influences of the discharge start voltage can not be negligible under extremely low power condition.

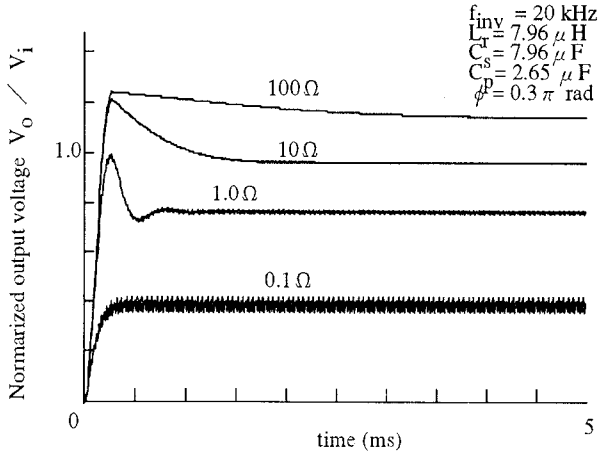


Fig. 3. Transient response of output voltage in the transformer resonant DC-DC converter in case of open-loop system.

Fig. 3 shows the open-loop step output voltage response characteristics in the series-parallel resonant DC-DC power converter. The step output voltage response under the extremely wide range of the load resistance cannot be explained as the simple behavior in any linear systems except heavy load conditions. It seems to be difficult that the linear system control theory such as the AC analysis, the pole assignment system design and the optimal control algorithm applies for wide load ranges of the high-voltage X-ray generating system.

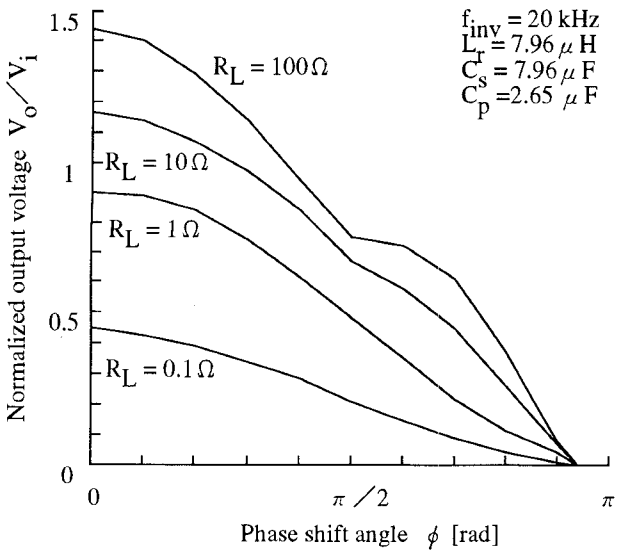


Fig. 4. Steady-state characteristics of the phase shift PWM control.

Fig. 4 illustrates the steady-state characteristics of the converter with phase shifted PWM control scheme. In the steady-state simulation, the relations between its phase-shifted PWM angle and the output voltage can not be approximated by any operating curves like the simple cosine function characteristics because of its load resistance dependent-characteristics. On the other hand, some nonlinear steady-state characteristics compensators with weighting gain parameters for each load condition may be available to obtain feasible controllability in addition to conventional feedback control scheme.

3. FEEDBACK CONTROL SCHEME

3.1 I-PD control scheme using interpolation from some adjusting points

The output voltage over shoot is undesirable for the medical-use X-ray generator because the output voltage waveform sensitively affects quality of the X-ray images. The higher output voltage than the allowable voltage causes abnormal discharge in the high-voltage components, for example, the high-voltage transformer, high-voltage cables and the X-ray tube. Since the X-ray dose and the X-ray energy ought be continuously changed according to the output load setting conditions, the same output voltage waveforms are demanded for every combination of the reference output voltage and the output current. Though, in fact, the I-PD gains can not be manually adjusted for every combination on account of terribly many combinations.

If the X-ray tube load can be regarded as an ideal resistance, simple resistance representation can be applied to the X-ray tube load model instead of 2 dimensional combinations for each output voltage and current. However, it is difficult that the X-ray tube load shown in Fig. 2 is regarded as an ideal resistance which is continuously adjusted by its heater current control. Therefore, as a feasible approach, the authors propose to decide the adequate I-PD gains for each load condition by interpolation from some manually-adjusted combination points in a load resistance vs. X-ray tube voltage map.

Fig.5 indicates this load resistance map as a domain of the reference output voltageV_{ref} (tube voltage) and the output current (tube current).These load resistance are determined by the ratio of the output voltage and the current, and reduced to the primary side of the high-voltage transformer for its turn ratio n (n = 490). Although the reference output voltage is set 1kV-step practically, it is summarized with 5kV-step in Fig. 5. Hatching points on this map indicate the adjusted points of the I-PD gains in the converter control implementation.

First, the I-PD gains are regulated for the tuning points in advance by trial and error, and then, adequate I-PD gains are calculated using interpolation in the log-log scale from 2 or 4 adjusted points encircling the set conditions. The interpolation in the log-log scale is more suitable than linear interpolation for such wide load domain.

Interpolation function in the log-log scale $f_{ip}(x_1, x_2, y_1, y_2, x)$ is given by $f_{ip}(x_1, x_2, y_1, y_2, x)$

$$= 10^{\left\{\frac{\log(y_2) - \log(y_1)}{\log(x_2) - \log(x_1)} \left(\log(x) - \log(x_1)\right) + \log(y_1)\right\}} \quad (1)$$

where, y_1 and y_2 : y-axis values of adjusted point 1 and point 2; x_1 and x_2: x-axis values of adjusted point 1 and point 2 ; x: x-axis value.

For example, in case that the reference output voltage is 80kV and the output current is 200mA, adequate I-PD gains are given as follows.

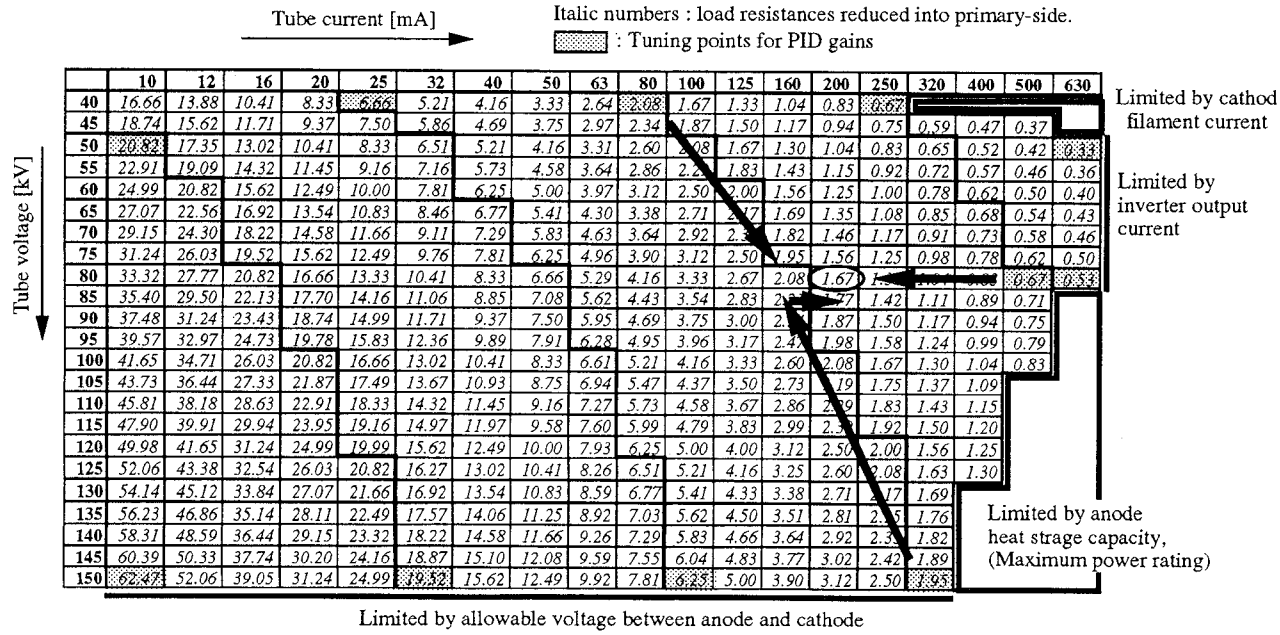
(1) Three adjusted points, (40kV, 80mA, 2.08Ω), (150kV, 320mA, 1.95Ω) , approximately the same load resistance, and (80kV, 500mA, 0.67Ω), the same output voltage, encircling the set condition (80kV, 200mA, 1.67Ω) are selected in the load resistance map.

(2) An intermediate gain at (80kV,160mA, 2.08Ω) is estimated from the first point (40kV, 80mA, 2.08Ω) and the second adjusted point (150kV, 320mA, 1.95Ω) by equation (1).

(3) The adequate gain of the set condition (80kV, 200mA, 1.67Ω) is given from the intermediate gain at (80kV,160mA, 2.08Ω) and the third adjusted point (80kV,500mA,0.67Ω) by equation (1)

3.2 Input voltage compensator and steady-sate nonlinear compensator

It is considered necessary to control and stabilize the periodical input voltage fluctuation and abrupt voltage disturbance, and to compensate the steady-state nonlinear voltage regulation characteristics into the quasi linear system in order to increase high-performance controllability. Therefore, the newly-developed tube volt-



	10	12	16	20	25	32	40	50	63	80	100	125	160	200	250	320	400	500	630
40	16.66	13.88	10.41	8.33	6.66	5.21	4.16	3.33	2.64	2.08	1.67	1.33	1.04	0.83	0.67				
45	18.74	15.62	11.71	9.37	7.50	5.86	4.69	3.75	2.97	2.34	1.87	1.50	1.17	0.94	0.75	0.59	0.47	0.37	
50	20.82	17.35	13.02	10.41	8.33	6.51	5.21	4.16	3.31	2.60	2.08	1.67	1.30	1.04	0.83	0.65	0.52	0.42	0.33
55	22.91	19.09	14.32	11.45	9.16	7.16	5.73	4.58	3.64	2.86	2.2	1.83	1.43	1.15	0.92	0.72	0.57	0.46	0.36
60	24.99	20.82	15.62	12.49	10.00	7.81	6.25	5.00	3.97	3.12	2.50	2.00	1.56	1.25	1.00	0.78	0.62	0.50	0.40
65	27.07	22.56	16.92	13.54	10.83	8.46	6.77	5.41	4.30	3.38	2.71	2.17	1.69	1.35	1.08	0.85	0.68	0.54	0.43
70	29.15	24.30	18.22	14.58	11.66	9.11	7.29	5.83	4.63	3.64	2.92	2.3	1.82	1.46	1.17	0.91	0.73	0.58	0.46
75	31.24	26.03	19.52	15.62	12.49	9.76	7.81	6.25	4.96	3.90	3.12	2.50	1.95	1.56	1.25	0.98	0.78	0.62	0.50
80	33.32	27.77	20.82	16.66	13.33	10.41	8.33	6.66	5.29	4.16	3.33	2.67	2.08	1.67				0.67	0.53
85	35.40	29.50	22.13	17.70	14.16	11.06	8.85	7.08	5.62	4.43	3.54	2.83	2		1.42	1.11	0.89	0.71	
90	37.48	31.24	23.43	18.74	14.99	11.71	9.37	7.50	5.95	4.69	3.75	3.00	2	1.87	1.50	1.17	0.94	0.75	
95	39.57	32.97	24.73	19.78	15.83	12.36	9.89	7.91	6.28	4.95	3.96	3.17	2.4	1.98	1.58	1.24	0.99	0.79	
100	41.65	34.71	26.03	20.82	16.66	13.02	10.41	8.33	6.61	5.21	4.16	3.33	2.60	2.08	1.67	1.30	1.04	0.83	
105	43.73	36.44	27.33	21.87	17.49	13.67	10.93	8.75	6.94	5.47	4.37	3.50	2.73	2.19	1.75	1.37	1.09		
110	45.81	38.18	28.63	22.91	18.33	14.32	11.45	9.16	7.27	5.73	4.58	3.67	2.86	2.29	1.83	1.43	1.15		
115	47.90	39.91	29.94	23.95	19.16	14.97	11.97	9.58	7.60	5.99	4.79	3.83	2.99	2.3	1.92	1.50	1.20		
120	49.98	41.65	31.24	24.99	19.99	15.62	12.49	10.00	7.93	6.25	5.00	4.00	3.12	2.50	2.00	1.56	1.25		
125	52.06	43.38	32.54	26.03	20.82	16.27	13.02	10.41	8.26	6.51	5.21	4.16	3.25	2.60	2.08	1.63	1.30		
130	54.14	45.12	33.84	27.07	21.66	16.92	13.54	10.83	8.59	6.77	5.41	4.33	3.38	2.71	2.17	1.69			
135	56.23	46.86	35.14	28.11	22.49	17.57	14.06	11.25	8.92	7.03	5.62	4.50	3.51	2.81	2.25	1.76			
140	58.31	48.59	36.44	29.15	23.32	18.22	14.58	11.66	9.26	7.29	5.83	4.66	3.64	2.92	2.33	1.82			
145	60.39	50.33	37.74	30.20	24.16	18.87	15.10	12.08	9.59	7.55	6.04	4.83	3.77	3.02	2.42	1.89			
150	62.47	52.06	39.05	31.24	24.99	19.52	15.62	12.49	9.92	7.81	6.25	5.00	3.90	3.12	2.50	1.95			

Fig. 5. Load resistance map (primary-side value).

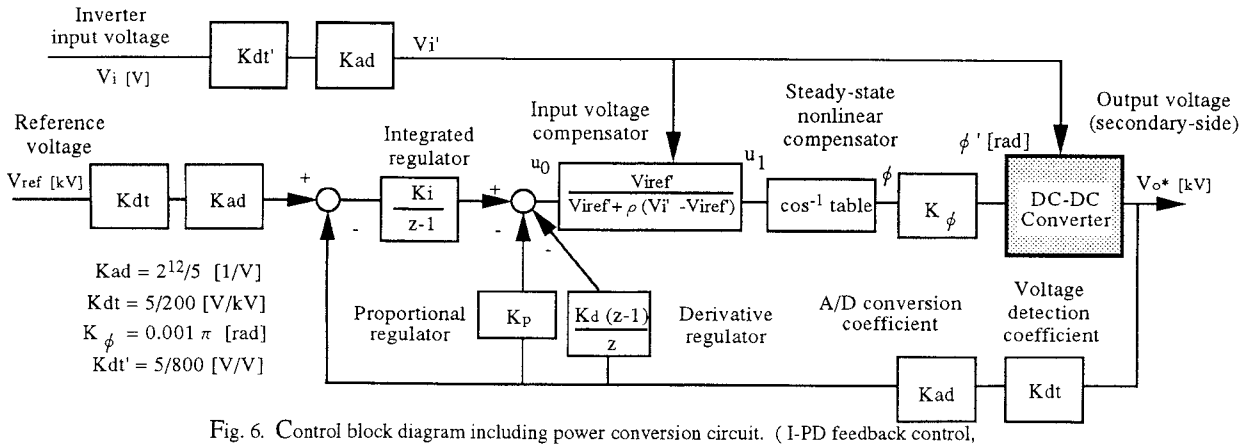


Fig. 6. Control block diagram including power conversion circuit. (I-PD feedback control, input voltage compensation and linearization for steady-state characteristics)

age feedback controller consists of the basic I-PD regulators and two compensators which are the input voltage and the steady-state nonlinear compensators. Fig. 6 shows the I-PD feedback control block diagram including the power conversion circuit, the input voltage fluctuation compensator and the steady-state nonlinear compensator using cosine function curve.The input voltage feed forward compensator which adaptively and dynamically modifies the feedback loop gain as

$$u_1 = \frac{V_{iref}'}{V_{iref}' + \rho (V_i' - V_{iref}')} u_0 \qquad (2)$$

where, u_0, u_1, V_{iref}' and V_i' are new intermediate variables shown in Fig. 6. r is definite as inverter input voltage compensation coefficient.

The nonlinear loop compensator which modifies the relationship of the steady-state voltage regulation characteristics (see Fig. 4) based upon the phase-shifted control scheme, the dead-time t_d determined by the time interval between the left side and the right side switching power devices of the inverter (see Fig. 1), and the inverter frequency f_{inv} is operated under the control law as

$$\phi = \cos^{-1}(u_1) - 2\pi t_d f_{inv} \qquad (3)$$

where, f_{inv} : inverter operating frequency; and u_1 are new intermediate variable shown in Fig. 6.

3.3 Digital control hardware implementation

Table 1 shows specifications of a representative embedded use microcontroller and a DSP (Digital signal processor). Although some high performance processors with floating point unit can be recently available, these processor make the control circuit board cost up and large size. Therefore, the processors without floating point unit in the output voltage feedback and feedforward digital control scheme are introduced as the converter control scheme.

As well known, DSP TMS320C25 (Texas Instruments) had been widely applied for embedded use because of its progressive high-speed processing ability. On the other hand, DSP has disadvantage because it dose not have peripheral interfaces such as PWM timers,

A/D converters or parallel input/output ports. Moreover, in the 16-bit integer processing, calculation overflow occurs frequently in the multiplication and the numerical integration in the I-PD process. Therefore, the overflow of the calculation results ought be checked and limited frequently in the feedback control program. High speed sampling can not be realized unexpectedly because of these incidental processes.

SH-1 (Hitachi:SH7034) is single-chip 32-bit RISC microcontroller and has more processing abilities than 16-bit DSP. This microcontroller has 64-kbyte on-chip ROM, 4-kbyte on-chip RAM, 8-channel 10-bit A/D converter with 6.7μs conversion time, 2-channel serial ports, 16 priority interrupt controller and integrated timer units including 3-channel PWM units. SH-1 is basically 32-bit 5-stage pipeline microprocessor; nevertheless, the multiplier is 16-bit configuration. This microcontroller has advantages in order to avoid the overflow in the feedback processing using 32-bit,dynamic range of integer variables.

The authors had applied TMS320C25 to 10kHz sampling digital feedback control for the inverter-fed X-ray generator[3] and recently SH-1 to 20kHz sampling one.

Table 1. Specifications of embedded-use microcontroller and DSP.

Type	SH-1 (SH7034) 32-bit RISC	TMS320C25 16-bit DSP
Maker	HITACHI	TI
Clock Frequency	20MHz	40MHz
Minimum instruction time	50 ns	100 ns
Pipeline	5-stage	3-stage
Dhrystone MIPS	16 MIPS	10 MIPS
General Purpose Registors	32-bit×16	16-bit×8
ROM	64-kbyte	-
RAM	4-kbyte	1-kbyte
Multiplyer	16×16-bit (50~150 ns)	16×16-bit (100 ns)
A/D	10-bit×8ch, 6.7μs	-
Timer for PWM	16-bit×3ch.	-
SCI	2-ch.	1-ch.
Package	QFP-112	PLCC-68

4-EXPERIMENTAL RESULTS

4.1 Programing guidelines for high-speed control processing

Fig. 7 shows digital control processing time chart for phase-shifted PWM the DC-DC converter with a high-frequency high voltage transformer link. If it is possible, local variables should be used instead of global variables in the feedback control program. Because the memory access for a global variable requires 4-byte indirect address code in addition to its 2-byte instruction code access. In general, division instruction takes several processing steps for such processors , therefore, these division instructions had better be replaced with shift instructions for high speed processing.

A/D conversions take 6.7μs to get the output voltage V_o' (intermediate digital value) and the inverter input voltage V_i' (intermediate digital value), so internal abnormal check to protect against over current of the inverter or X-ray tube, and I-PD control processing must be run parallel with the A/D conversions.

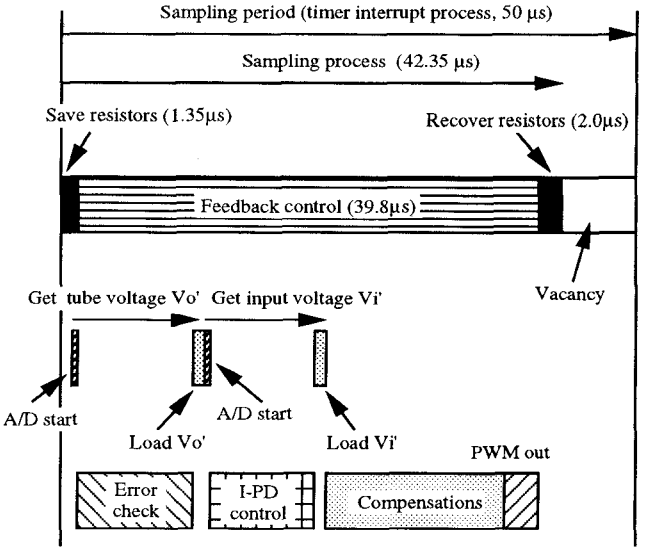


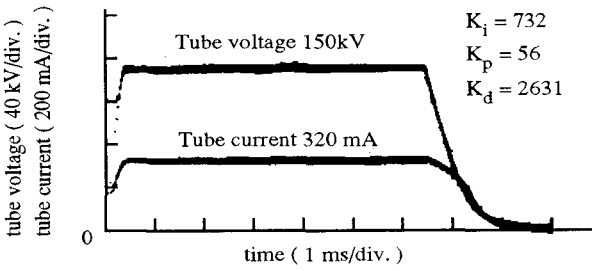
Fig. 7. Digital control processing time chart for the DC-DC converter.

4.2 Experimental response waveforms in feedback control scheme

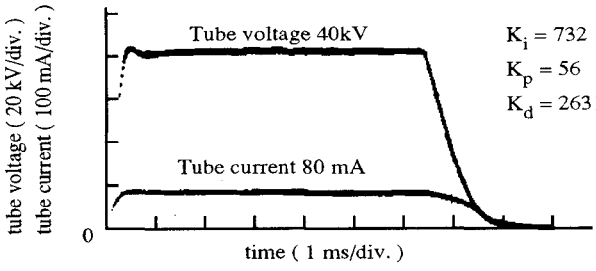
Fig. 8 shows experimental output waveforms of this converter system. Fig. 8 (a) shows the output high-voltage and the current waveforms in case of 150kV, 320mA, R_L=1.95 (approximate 2Ω) as an adjusted point for the I-PD gains. The same I-PD gains(the integrated gain Ki=732, the proportional gain Kp=56 and the derivative gain Kd=2631) are applied to the second waveforms shown in Fig. 8(b) at the load condition 40kV, 80mA and R_L=2.08Ω (approximate 2Ω). The slight overshoot voltage in the rise time can be seen in the high-voltage waveform in Fig. 8(b). The overshoot voltage causes variations of the X-ray dose in the short time exposure and affects photographic density of X-ray image even if the slight overshoot.

Fig. 8(c) shows the output waveforms with I-PD gains which are adjusted manually by trial and error. Obviously the better high-voltage waveform is obtained than Fig. 8(b). As illustrated here, these adjustments of the I-PD gains are required for the optimum output high-voltage waveforms even though the load resistances are identical.

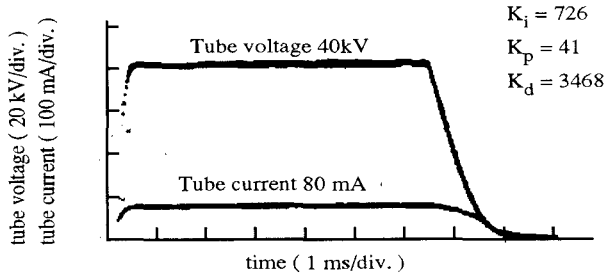
Fig. 8(d) shows the output high-voltage and the current waveforms with I-PD gain parameters, which are estimated by the logarithmic interpolation from the three adjusted points; 40kV, 80mA(2.08Ω); 150kV,320mA(1.95Ω) and 80kV,500mA(0.67Ω) according to equation (1). The I-PD gains of the first and the second conditions are indicated in Fig. 8(a) and Fig. 8(c). The I-PD gains of the last condition are Ki=797, Kp=260 and Kd=3404. It is obvious that a favorable high-voltage waveform is obtained by the proposed



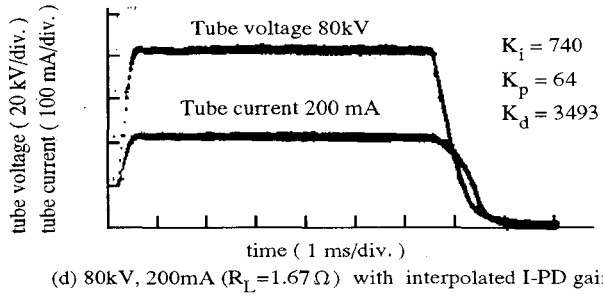
(a) 150kV, 320mA (R_L=1.95 Ω) with adjusted I-PD gains .



(b) 40kV, 80mA (R_L=2.08 Ω) with the same I-PD gains of (a).



(c) 40kV, 80mA (R_L=2.08 Ω) with adjusted I-PD gains.



(d) 80kV, 200mA (R_L=1.67 Ω) with interpolated I-PD gains.

Fig.8 Experimental output high-voltage waveforms

logarithmic interpolation for I-PD gains. In this case, the rise time is about 400μs and the voltage ripple is less than 2% for the all output waveforms shown in Fig. 8

5-CONCLUSIONS

The embedded 32-bit RISC microcontroller-based digital feedback control scheme has been described in order to apply to the series-parallel resonant type high power high-frequency inverter-fed DC-DC converter with a high-voltage transformer link for X-ray power generator, which operators under condition of extremely wide load ranges and nonlinear load resistance characteristics. The practical estimation procedure to obtain the desirable I-PD gains by logarithmic interpolation from some tuning points around the set load condition has proposed according to the load resistance vs, tube voltage map. High speed processing hardware and programing guidelines of the digital feedback control were also presented. The steady-state and dynamic state performances of the converter for X-ray power generator and the feasible effectiveness of the proposed estimation procedure to obtain the adequate I-PD gains in the control implementation have been confirmed by experimental results.

In the future, the knowledge-based nonlinear feedback algorithms such as fuzzy logic control, neural-network and learning software control should be investigated so as to be incorporated into this type of resonant DC-DC power converter for X-ray power generator the DC-DC converter a high-voltage transformer link in order to supply desirable output high-voltage DC waveforms in steady-state and dynamic state.

REFERENCES

[1] Hino, H., Hatakeyama, T. and Nakaoka, M.: Resonant PWM inverter linked d.c.-d.c. power converter utilizing parasitic circuit constants of high-voltage transformer and cables, International Journal of Electronics, 66, No.6, 1989, pp. 969-983

[2] Hino, H., Hatakeyama, T. and Nakaoka, M.: Digitally controlled resonant converter for X-ray generator utilizing parasitic circuit constants of high voltage-transformer and cables, Proceedings of EPE '89, 1, 1989, pp.361-365

[3] Takano, H., Uemura, H., Nakaoka, M.: "Advanced Constant-Frequency PWM Resonant DC-DC Converter with Real Time Digital Control for X-Ray Power Generator", Proc. of EPE, 1991, 1, 544-549

[4] Takano, H., Takahashi, J., Hatakeyama, T. and Nakaoka, M. :"Feasible Characteristic Evaluations of Resonant Tank PWM Inverter-Linked DC-DC High-Power Converters for Medical-Use High-Voltage Application", Proc. of IEEE-APEC, 1995, 2, 913-919

[5] Single Chip RISC Microcomputer SH7032, SH7034 Hardware Manual, Hitachi Ltd., 1993

[6] SIEMENS Microcomputer components C167 16-bit CMOS Microcontroller Data Sheet, Siemens AG, 1993

[7] TMS320C25 Digital Signal Processor User's Manual, Texas Instruments, 1987

Address of the authors

H. Takano and T. Hatakeyama, R & D Center, Hitachi Medical Co., 2-1 Shintoyofuta, Kashiwa, Chiba, 277, Japan

L. Gamage, J.M. Sun ,E.Hiraki and M.Nakaoka, Dept, of Electrical and Electronics Engineering, Yamaguchi University., 2557, Tokiwadai, Ube, Yamaguchi, 755, Japan

The Power Conversion Conference-Nagaoka is supported by the following foundations, companies and so on.

The Ministry of Education

Nagaoka-City

Tokyo Electric Power Co., INC.

Kansai Electric Power Co., INC.

Chubu Electric Power Co., INC.

Hitachi, Ltd.

Toshiba Corporation

Mitsubishi Electric Corporation

Tohoku Electric Power Co., LTD.

Electric Power Development Co., Ltd.

Fuji Electric Co., Ltd.

Meidensha Corporation

Sanken Electric Corporation

Nissan Motor Co., LTD.

Eye Lighting Systems Corporation

DAIKIN INDUSTRIES, LTD.

Nissin Electric Corporation

Toyo Electric Mfg. Co., LTD.

TDK Corporation

Sharp Corporation

Shindengen Electric Mfg. Co.

NEMIC LAMBDA K.K.

Neturen Co., LTD.

Yaskawa Electroc Corporation

Research Foundation for the lectrotechnology of Chubu

Shinko Electric CO., LTD.

Nippon Telegraph and Telephone Corporation

Shikoku Research Institute Inc.

Seiko Seiki CO., LTD.

Motor Company, Matsushita Electric Industrial Co., Ltd.

JAPAN STORAGE BATTERY CO., LTD.

Oriental Motor Co., Ltd.

Origin Electric Co., Ltd.

Nippon Steel Corporation

Mitsubishi Heavy Industries Ltd.

NIKON CORPORATION

TOYOTA MOTOR CORPORATION

Sanyo Denki Co., Ltd.

FANUC LTD.

Yuasa Corporation

DENSO CORPORATION

TAKAOKA ELECTRIC MFG. CO., LTD.

Kawasaki Steel Corporation

Railway Technical Research Institute

NSK Ltd.